Intraseasonal Variability in the Atmosphere-Ocean Climate System

William K. M. Lau
Duane E. Waliser

Second Edition

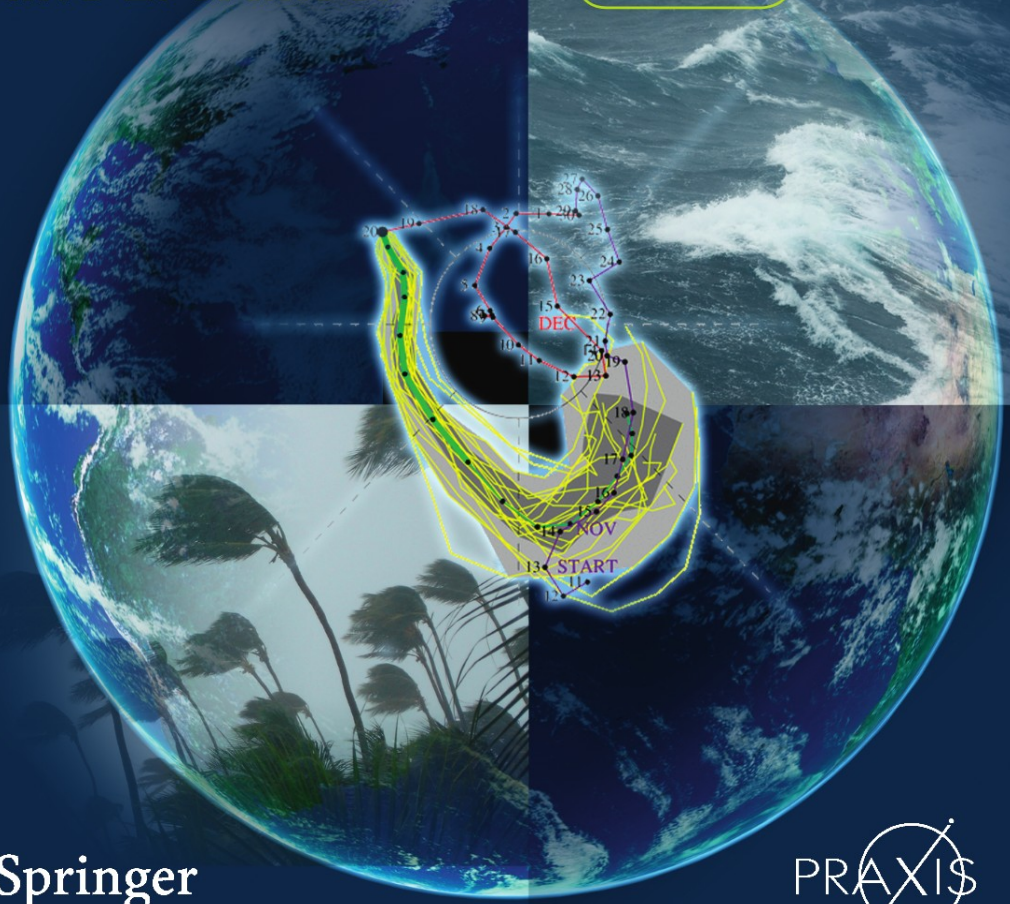

Springer
PRAXIS

Intraseasonal Variability in the Atmosphere–Ocean Climate System

(Second Edition)

William K. M. Lau and Duane E. Waliser

Intraseasonal Variability in the Atmosphere–Ocean Climate System

(Second Edition)

Springer

Published in association with
Praxis Publishing
Chichester, UK

PRAXIS

Dr. William K. M. Lau
Chief, Laboratory for Atmospheres
NASA/Goddard Space Flight Center
Greenbelt
Maryland
U.S.A.

Dr. Duane E. Waliser
Chief Scientist
Earth Science and Technology Directorate
Jet Propulsion Laboratory
California Institute of Technology
Pasadena
California
U.S.A.

About the cover
Madden–Julian Oscillation index phase plot [see Wheeler and Hendon (2004) and Chapter 5 for more information and the reference] for an example forecast from the U.S. National Oceanographic and Atmospheric Administration's (NOAA's) National Weather Service (NWS) Global Ensemble Forecast System (GEFS). The RMM1 (x-axis) and RMM2 (y-axis) values for the most recent 40 days prior to the forecast are given along with the forecast values for the subsequent 15 days. The green line is the mean of the 21-member ensemble forecast (forecast days 1–7: thick line, forecast days 8–15: thin line) along with all 21 individual ensemble forecast members (yellow lines). The light gray shading represents the area in which 90% of forecast members reside and the dark gray shading represents the area in which 50% of forecast members reside.

Courtesy Jon Gottschalck—Climate Prediction Center/NWS/NOAA
(see also Gottschalck et al. 2010 reference in Chapter 12)

SPRINGER–PRAXIS BOOKS IN ENVIRONMENTAL SCIENCES

ISBN 978-3-642-13913-0 e-ISBN 978-3-642-13914-7
DOI 10.1007/978-3-642-13914-7

Springer Heidelberg Dordrecht London New York

Library of Congress Control Number: 2011922055

First Edition published 2005

Cover design: Jim Wilkie
Project management: OPS Ltd., Gt Yarmouth, Norfolk, U.K.

Printed on acid-free paper

Springer is part of Springer Science + Business Media (www.springer.com)

Contents

Preface to the Second Edition

In the Preface to the First Edition of this book, we wrote about the goal to provide a one-stop reference text on intraseasonal variability (10–90 days) to bridge the gap between weather forecasts (a few days to a week), and climate predictions (seasonal, yearly, and longer timescales). We seek to further this goal in the Second Edition. The years since the publication of the First Edition have seen significant advances in our understanding of the physical processes, multiscale interactions, and predictability associated with intraseasonal variability in the tropical ocean–atmosphere system. These advances have been achieved by the scientific community at large through (a) increased capabilities in high-resolution global modeling and data assimilation, (b) in-depth theoretical studies, and (c) improved diagnostics mostly from new global satellite observations and improved reanalysis products.

At present, a realistic simulation of the Madden and Julian Oscillation (MJO) is considered a prerequisite for climate models to produce reliable predictions of interannual variability and longer term projections of regional impacts and extreme events from climate change. Common metrics for MJO prediction and diagnostics have been developed and adopted by the scientific community so that model validations and empirical forecasts of the MJO can be compared and evaluated. Operational forecast centers such as the U.S. National Oceanic and Atmospheric Administration Climate Prediction Center, the U.K. Meteorological Office, and the European Center for Medium-range Weather Forecasts, among many others, are producing routine forecasts of the MJO. Predictions of onsets and breaks in major monsoon regions around the world are now focused on the propagation and evolution of regional intraseasonal oscillations (ISOs). International and national organizations such as the World Climate Research Programme and the World Weather Research Programme have joined to sponsor working groups and task forces to organize international projects and workshops to facilitate and coordinate research on the MJO and ISOs. The science community has now coined the term "seamless prediction" to address the continuum of temporal and spatial scales linking weather and climate. Indeed, the MJO and associated regional ISOs represent critical linkages between global weather forecasts and regional climate

predictions. Another critical factor spurring the recent rapid advance in our understanding of the MJO and ISO phenomena was the advent of a series of NASA Earth-observing satellites launched between the early 2000s and the present. As a result, the scientific community has access to unprecedented information regarding propagation, horizontal and vertical structures of rainfall, clouds, moisture, and temperature. Such information is essential to define the characteristics of the MJO and associated regional ISOs and their far-field impacts. Other derived quantities such as latent heating profiles and cloud microphysics derived from satellite data and field campaigns are setting the stage for the next level of understanding and improved model fidelity associated with the MJO and ISOs. Studies documenting the influence of the MJO on ozone, aerosols, and carbon dioxide fluctuations in the atmosphere and in ocean productivity are emerging, further demonstrating the far-reaching importance of the MJO and ISOs not only in the physical domain but also in the biogeochemical component of the climate system. Given these momentous recent developments, the Second Edition of the book seems opportune.

The organization of the Second Edition is as follows. The first 12 chapters are either original chapters (Chapters 1, 8, 9), or original chapters with updates (Chapters 2, 3, 4, 5, 6, 7, 10, 11, 12). Chapters 13-18 are new shorter chapters that cover new topics or significant recent advances. In some cases, the latter can also serve as updates or complements to the original chapters. Specifically, the new chapters are: Chapter 13 on ''Africa and West Asia'' by M. Barlow; Chapter 14 on ''Tropical and extratropical interactions'' by P. Roundy; Chapter 15 on ''Oceans and air–sea interaction'' by J.-P. Duvel; Chapter 16 on ''Vertical structure from recent observations'' by C. Zhang; Chapter 17 on ''Multiscale theories'' by A. Majda and S. Stechmann; and Chapter 18 on ''Chemical and biological impacts'' by B. Tian and D. Waliser.

The Second Edition of this book would not have been possible without the support and dedicated efforts of the contribution authors, both old and new. Special thanks are due to Xiouhua Fu, George Kiladis, Tim Li, Jiaylin Lin, Adrian Matthews, Mitch Moncrieff, Benjamin Pohl, David Strauss, Chung-Hsiung Sui, Mike Wallace, Sun Wong, and Klaus Weickmann who have provided constructive comments in reviewing the new chapters. The co-Chief Editors also thank the Earth Science Division of the National Aeronautics and Space Administration, the Office of Global Programs of the National Oceanic and Atmospheric Administration, the Large-scale Dynamics Programs of the Atmospheric Science Division of the National Science Foundation, and the Atmospheric Radiation Measurement and Climate Research Program of the Department of Energy for providing support for years of research of observations and modeling of the MJO and related phenomena. We would also like to express our thanks to the World Climate Research Programme and the World Weather Research Programme for their programmatic sponsorship of a number of panels, working groups, and task forces that have greatly facilitated research on intraseasonal variability and its transition to operational utility.

William K. M. Lau and Duane E. Waliser
June, 2011.

Preface to the First Edition

On the subject of extended range weather forecasts, one of the pioneers of numerical weather forecasts, John von Neumann (1955) wrote:

> "The approach is to try first short-range forecasts, then long-range forecasts of those properties of the circulation that can perpetuate themselves over arbitrarily long periods of time ... and only *finally* to attempt forecast for medium–long time periods which are too long to treat by simple hydrodynamic theory and too short to treat by the general principle of equilibrium theory."

In modern phraseology, von Neuman's short-range forecasts would mean weather forecasts extending out to about 5 days, long-range forecasts would be equivalent to climate predictions extending out to a season or longer, and medium to long-range forecast would refer to intraseasonal predictions having lead times of the order of 2 to 8 weeks. Numerical weather forecasting has seen tremendous improvement since its inception in the 1950s. Today, human activities are often so dependent on skillful short-term weather forecasts, that many have come to the unrealistic hope, and even expectation, that weather forecasts should be accurate all the time. However, any basic textbook on weather forecasting will point out that there exists a natural limit on *deterministic* weather forecasts of about 2 weeks, which is strongly dependent on initial conditions and atmospheric flow regimes.

Recently, the public has been made aware of high-impact climate phenomena such as El Niño and La Niña, which can affect weather patterns all over the world. Thanks in large part to the international climate research program, Tropical Ocean Global Atmosphere (TOGA), scientists now have the observational resources, the knowledge, and the models to make useful (deterministic) predictions of El Niño and La Niña with lead times up to 9–12 months. These predictions in turn have been helpful in making *probabilistic* seasonal-to-interannual forecasts of weather patterns (not deterministic forecasts of individual weather events) more skillful over certain

spacetime domains (e.g., wintertime temperature over North America and summer rainfall over the Asian monsoon region and South America). Because the lead time for climate prediction is typically a season or longer—a time long enough for the atmosphere to lose memory of its initial state—the skill of prediction is no longer dependent on the initial conditions of the atmosphere. In contrast to weather forecasts, seasonal-to-interannual climate predictions owe their skill to a dependence on slowly changing boundary conditions at the Earth's surface, such as sea surface temperature, snow cover, and soil moisture, and the considerable impact these boundary conditions have on determining the statistics of observed weather patterns. In the forecasting community, it is often said that weather forecasting is an initial value problem and climate prediction is more akin to a boundary value problem. What about the timescales in between (e.g., lead times between about 2 weeks and 2 months)? Are there atmosphere–ocean phenomena with these timescales that are predictable, and how do these phenomena and their predictability respond to the changing boundary conditions at the Earth's surface? These are among some of the issues to be addressed in this book.

Given the progress in weather forecasting and seasonal-to-interannual climate prediction, it is apparent that we are ready to more formally and thoroughly address forecasting of, in von Neuman's words, the "medium–long time periods". Improving extended range (i.e., intraseasonal) forecasts requires fundamental knowledge built on sound research, realistic models of the atmosphere, ocean, and land components of the climate system, and the training of a new generation of scientists and forecasters. Today, we have many textbooks and research reference books on weather and climate variability, and prediction, but there has been none focused specifically on intraseasonal variability (ISV). There has been a large body of scientific studies showing that ISV is far from a simple interpolation between weather and climate scales/processes, and is not just a red-noise extension of weather variability. Indeed, there are specific and unique modes of ISV that are ubiquitous and can be found in the atmosphere, the ocean, and the solid Earth, as well as in the tropics and the extratropics.

To improve prediction in the intermediary timescale (2 weeks to less than a season) of the atmosphere–ocean, it is vital to improve our understanding of the phenomena that are inherently intraseasonal and the manner in which they interact with both shorter (weather) and longer (climate) timescales. Thus one of the overarching goals of this book is to summarize our current understanding of IV and its interactions with other weather and climate processes. However, in developing the framework for this book, we found that including all aspects of ISV would require too much material for one book. Thus, in order to limit the scope of this book, we have chosen to focus primarily on ISV in the tropical ocean and atmosphere, including its interactions with the extratropics whenever appropriate. Using this guideline, topics directly related to midlatitude atmospheric blocking or extratropic annular modes, for example, will not be treated in their own right in this book, but rather discussed in the context of their interaction with tropical ISV (TISV).

Central to TISV is the Madden–Julian Oscillation (MJO) phenomenon, known also as the 40 to 50-day or 30 to 60-day oscillation. However, TISV in general refers to a broad spectrum of phenomena: some quasi-periodic, some non-periodic, some with global reach, and others with regional manifestations. To avoid possible confusion in

this book with the various terminologies used in the literature, we refer throughout this book to all variability longer than synoptic timescales ($\sim$2 weeks) and shorter than a season (90 days) as ISV. The MJO is specifically referred to as the atmosphere–ocean entity that exhibits a coherent eastward propagation along the equator with quasi-periodicity of 30 to 60 days. In the general case, when a quasi-periodic oscillation can be identified, the term intraseasonal oscillation (ISO) will be used. When specially referring to ISV or ISO in the tropics, the acronyms TISV or TISO will be used as appropriate. In this nomenclature, MJO is a special case of a TISO.

This book is intended to be a one-stop reference book for researchers interested in ISV as well as a textbook for senior undergraduate and graduate students in Earth science disciplines. The book contains 12 chapters, each with a comprehensive bibliography. Chapter 1 provides a historical account of the detection of the MJO by R. Madden and P. Julian, who discovered the phenomena. The regional characteristics of TISV on South Asia, East Asia, the Americas, and Australia/Indonesia are covered in Chapters 2–5, respectively. Air–sea interactions and oceanic ISV are discussed in Chapters 6 and 7. Chapter 8 discusses atmospheric and solid Earth angular momentum and Earth rotation associated with ISV. Chapter 9 is on El Niño Southern Oscillation (ENSO) connections to ISV. Chapters 10, 11, and 12 are devoted to the theory, numerical modeling, and predictability of ISV, respectively. The chapters are written with self-contained material and frequent cross-referencing to other chapters, so that they need not be read in sequence. Readers are encouraged to jump to their chapters of interest if they so desire. However, we strongly recommend everyone to read the Preface and Chapter 1 first to obtain the proper perspective of the subject matter and objectives of the book.

This book could not have been possible without the support and the dedicated efforts of the contributing authors, who provided excellent write-ups for the chapters in a timely manner. Everyone we contacted regarding this book was very enthusiastic and supportive. In addition, we thank Drs. H. Annamalai, Charles Jones, Huug van den Dool, T. C. (Mike) Chen, Klaus Weickmann, Chidong Zhang, Ragu Murtugudde, William Stern, George Kiladis, and Steve Marcus, and one anonymous reviewer for providing very constructive comments in reviewing various chapters of this book. The co-chief editors will also like to thank the Earth Science Enterprise of the National Aeronautics and Space Administration, the Office of Global Programs of the National Oceanographic and Atmospheric Administration, and the Climate Dynamics and Large-Scale Dynamic Meteorology Programs of the Atmospheric Sciences Division of the National Science Foundation for providing support over the years for research on ISV.

REFERENCE

von Neumann, J. (1955) Some remarks on the problem of forecasting climate fluctuations. *Dynamics of Climate: The Proceedings of a Conference on the Application of Numerical Integration Techniques to the Problem of the General Circulation*. Pergamon Press, p. 137.

William K. M. Lau and Duane E. Waliser
Goddard Space Flight Center, Greenbelt, Maryland
October, 2004

Figures

Abbreviations

AAM	Atmospheric Angular Momentum
ACC	Antarctic Circumpolar Current
ADCP	Acoustic Doppler Current Profiler
AGCM	Atmospheric General Circulation Model
AI	Aerosol Index
AMIP	Atmospheric Model Intercomparison Project
AMY	Asian Monsoon Year
ARGO	Array for Real-time Geostrophic Oceanography
AS	Arabian Sea
AVHRR	Advanced Very High Resolution Radiometer
BAC	Bivariate Anomaly Correlation
BFA	Break Followed by Active
BISO	Boreal IntraSeasonal Oscillation
BLEP	Boundary Layer Ekman Pumping
BNFA	Break Not Followed by Active
BoB	Bay of Bengal
BOBMEX	Bay Of Bengal Monsoon EXperiment
BSISO	Boreal Summer ISO
BSISV	Boreal Summer IntraSeasonal Variability
CAM	Community Atmospheric Model
CAPE	Convective Available Potential Energy
CCA	Canonical Correlation Analysis
CCM	Community Climate Model
CCW	Convectively Coupled Wave
CFS	Coupled Forecast System
CG	Chatterjee and Goswami
CGCM	Coupled GCM
CID	Convective Interaction with Dynamics

CIN	Convective INhibition
CINDY2011	Cooperative INDian Ocean experiment on intraseasonal variability in Year 2011
CISK	Convective Instability of the Second Kind
CISO	Climatological IntraSeasonal Oscillation
CLIVAR	CLImate VARiability and Predictability
CM	Center of Mass
CMAP	CPC Merged Analysis of Precipitation
CMIP	Coupled Model Intercomparison Project
CMT	Convective Momentum Transport
COARE	TOGA–Coupled Ocean Atmosphere Response Experiment
COLA	Center for Ocean Land Atmosphere
CRM	Cloud Resolving Model
DERF	Dynamical Extended Range Forecast
DOD	Department of Ocean Development
DWL	Diurnal Warm Layer
DYNAMO	DYNAMics of the Madden–Julian Oscillation
EA/WNP	East Asian and Western North Pacific
ECMWF	European Centre for Medium-range Weather Forecast
EEOF	Extended Empirical Orthogonal Function
EIO	Equatorial Indian Ocean
EMT	Eddy Momentum Transfer
ENSO	El Niño Southern Oscillation
EOF	Empirical Orthogonal Function
EPM	Eastward Propagating Mode
EPP	Empirical Phase Propagation
ER	Equatorial Rossby
ERA-40	ECMWF 40-year ReAnalysis
EUC	Eastward equatorial UnderCurrent
EWP	Empirical Wave Propagation
EWT	Equivalent Water Thickness
FCI	Frictional Convergence Instability
FGGE	First GARP Global Experiment
GCM	General Circulation Model; Global Circulation Model
GFDL	Geophysical Fluid Dynamics Laboratory
GHCN	Global Historical Climatology Network
GLA	NASA Goddard Laboratory for Atmospheres
GLAS	Goddard Laboratory for Atmospheric Sciences
GMS	Geostationary Meteorological Satellite; Gross Moist Stability
GP	Genesis Potential
GPCP	Global Precipitation Climatology Project
GSOD	Global Summary of the Day
GTS	Global Telecommunication System

IAV	InterAnnual Variability
IB	Inverted Barometer
IFA	Intensive Flux Array
IMR	India Monsoon Rainfall
INCOIS	Indian National Centre for Ocean Information Services
IO	Indian Ocean
IOD	Indian Ocean Dipole
ISI	IntraSeasonal to Interannual
ISO	IntraSeasonal Oscillation
ISV	IntraSeasonal Variability
ISVHE	IntraSeasonal Variability Hindcast Experiment
ITAC	Indian Ocean (east of 115°E), Timor and Arafura Seas, and Gulf of Carpentaria
ITCZ	Intertropical Convergence Zone
ITF	Indonesian ThroughFlow
JASMINE	Joint Air–Sea Monsoon INteraction Experiment
KE	Kinetic Energy
LF	Low Frequency
LIM	Linear Inverse Model
LLJ	Low Level westerly Jet
LP	LowPass
LPS	Low Pressure System
MBF	Meiyu/Baiu Front
MCA	Moist Convective Adjustment
MCS	Mesoscale Convective System
MEM	Maximum Entropy Method
MISMO	Madden–Julian Oscillation (MJO)–Convection Onset
MISO	monsoon ISO
MJO	Madden–Julian Oscillation
MJOTF	MJO Task Force
MJOWG	MJO Working Group
MLD	Mixed Layer Depth
MONEX	MONsoon EXperiment
MRF	Medium Range Forecast
MRG-TD	Mixed Rossby Gravity wave–Tropical Disturbance
MSI	MultiScale Interaction
MT	Monsoon Trough
NAME	North American Monsoon Experiment
NCAR	National Center for Atmospheric Research
NCEP	National Center for Environmental Prediction
NDVI	Normalized Difference Vegetation Index
NEC	North Equatorial Current
NECC	North Equatorial CounterCurrent
NICAM	Nonhydrostatic ICosahedral Atmospheric Model

NMC	National Meteorological Center
NOAA	National Oceanic and Atmospheric Administration
NWP	Numerical Weather Prediction
OGCM	Ocean General Circulation Model
OLR	Outgoing Longwave Radiation
OLRA	Outgoing Longwave Radiation Anomaly
PC	Principal Component
PNA	Pacific North American
POAMA	Predictive Ocean–Atmosphere Model for Australia
POP	Principal Oscillating Pattern
PSA	Pacific–South American
PV	Potential Vorticity
QBM	Quasi Biweekly Mode
QSM	Quasi Stationary Mode
RAMA	Research moored Array for African–Asian–Australian Monsoon Analysis and prediction
RHC	Relative Humidity Criterion
RMM	Real time Multivariate MJO
RMS	Root Mean Square
SA	South Asian
SACZ	South Atlantic Convergence Zone
SALLJEX	South American Low Level Jet EXperiment
SCC	SuperCloud Cluster
SCTR	Seychelles–Chagos Thermocline Ridge
SD	Seychelles Dome
SeaWiFS	Sea-viewing Wide-Field-of-view Sensor
SEC	South Equatorial Current
SLR	Satellite Laser Ranging
SOI	Southern Oscillation Index
SPCAM	Super-Parameterized Community Atmospheric Model
SPCZ	South Pacific Convergence Zone
SSA	Singular Spectrum Analysis
SSH	Sea Surface Height
SST	Sea Surface Temperature
SSTA	Sea Surface Temperature Anomaly
SSWJ	SubSurface Westward Jet
STCC	SubTropical CounterCurrent
SVD	Singular Value Decomposition
TAO	Tropical Atmosphere and Ocean
TC	Tropical Cyclone
TCO	Total Column Ozone
TCZ	Tropical Convergence Zone
TIGGE	THORPEX Interactive Grand Global Ensemble
TISO	Tropical IntraSeasonal Oscillation
TISV	Tropical IntraSeasonal Variability

TIW	Tropical Instability Wave
TMI	TRMM Microwave Imager
TOGA	Tropical Ocean Global Atmosphere
TRMM	Tropical Rain Measuring Mission; Tropical Rainfall Measuring Mission
TTT	Tropical Temperate Trough
UEMT/UWMT	eddy-induced Upscale Easterly/Westerly Momentum Transfer
UM	Met Office Unified Model
VAMOS	Variability of American Monsoon Systems
VLBI	Very Long Baseline Interferometry
VP200	Velocity Potential at 200 hPa
WCRP	World Climate Research Program
WGNE	Working Group on Numerical Experimentation
WHOI	Woods Hole Oceanographic Institution
WIG	Westward-propagating Inertial–Gravity wave
WISHE	Wind Induced Surface Heat Exchange
WWE	Westerly Wind Event
WWRP	World Weather Research Program
WWW	World Weather Watch
YOTC	Year of Tropical Convection
ZC	Zebiak and Cane (1987)

1

Historical perspective

Roland A. Madden and Paul R. Julian

1.1 INTRODUCTION

The 1960s was a remarkable decade for research in tropical meteorology. Tropical climatology was already reasonably understood, but little was known of its variability or that of daily tropical weather. Regularly sampled data and access to computers to process data became more readily available. The excitement of looking at these data, which no one else had studied before, must have been something like that of polar explorers in the early part of the century who made their way to places no one had ever been before. The decade opened with descriptions of the remarkable Quasibiennial Oscillation (QBO) showing that neither the formerly identified ''Krakatoa Easterlies'' nor the ''Berson Westerlies'' were steady features of the equatorial stratosphere (Ebdon, 1963). By the mid-1960s a theory tailored specifically to waves in the equatorial region was published, and soon after some of them were observed. These were, arguably, the first identifications of large-scale waves in the atmosphere predicted by theory. By the end of the decade the tropical atmosphere was a topic of research given similar attention to that of the midlatitudes.

The surprising discovery of the QBO (Ebdon, 1960; Reed *et al*., 1961) kindled new interest in the meteorology of the tropics leading eventually to the discovery, at the beginning of the next decade, of an equally surprising tropical oscillation with an intraseasonal timescale. That feature is often referred to as the Madden–Julian Oscillation (MJO)[1] after papers appearing in the *Journal of the Atmospheric*

[1] Madden and Julian called the phenomenon the ''40–50 Day Oscillation'' (1971, 1972). Weickmann *et al*. (1985) referred to the ''intraseasonal (30–60 day) fluctuations''. Other authors defined it similarly by its approximate period. Some referred in their text to a form of MJO: for example, ''Madden and Julian's 40–50 day oscillation'' (Gruber, 1974a), or ''Madden and Julian's 40–50 day wave'' (Webster, 1987). The Madden Julian Oscillation began to be used more regularly after it appeared in the title of two papers published in 1988 (Swinbank *et al*., 1988 and Lau *et al*., 1988).

W. K. M. Lau and D. E. Waliser (Editors), *Intraseasonal Variability in the Atmosphere–Ocean Climate System* (Second Edition).

Sciences (Madden and Julian, 1971, 1972). The discovery of the MJO resulted from the serendipitous convergence of this new interest in the tropics, new tropical data, new computers, and the increasing application of spectrum analysis. Basic features of the MJO are described here but, first, the research environment that led to its discovery is outlined.

Graystone (1959) showed the zonal wind, u, or wind blowing from west to east, in a time–height section of the lower stratosphere from October 1956 through to August 1958. With only 23 months of data, Graystone could not have recognized the very regular change in the u-wind from westerlies to easterlies and back with an approximate 26-month period, even though, in retrospect, it is clearly evident. He did "note the interesting lack of an annual variation in the data." It took a longer time series to bring out the QBO (Reed *et al*., 1961). The QBO, a phenomenon so unexpected yet so unmistakable and so amazing, proved that the tropics was not, excepting an occasional tropical storm, a dull and uninteresting place meteorologically.

The QBO begged for an explanation and tropical meteorologists, most notably at the Universities of Tokyo and Washington, began searching for one. Yanai and Maruyama (1966) reported on wave-like disturbances in the meridional wind, v, or south to north component, in the tropical lower stratosphere with a timescale of 5 days, a horizontal lengthscale of 10,000 km, and a westward phase speed of about $23\,\mathrm{m\,s^{-1}}$. Motivation for their work was a search for large-scale waves in the equatorial stratosphere. It was thought that such waves might play a role in the momentum convergence needed to explain the QBO. It is now understood that the waves Yanai and Maruyama discovered do play a minor role, but more importantly their discovery marked one of the first unambiguous identifications of theoretically predicted, large-scale atmospheric waves. A theory of equatorial waves had been laid out in that same year by Matsuno (1966). It is interesting to note that Matsuno submitted his manuscript in November 1965, in which he thanks Yanai for reading it; yet Yanai and Maruyama did not immediately recognize the connection between their observational paper submitted in July 1966 and Matsuno's theory—it did not take long though. In the following year Maruyama published a second paper on the waves and identified them as mixed Rossby gravity waves, predicted by the theory (Maruyama, 1967).

At almost the same time, Wallace and Kousky (1968) were studying the u-wind in the tropical stratosphere. Their motivation was similarily related to the QBO. They stated: "This study of synoptic-scale disturbances in the tropical stratosphere was originally motivated by certain unsolved problems relating to the momentum budget of the quasi-biennial oscillation." They found waves with 15-day periods, lengthscales of 20,000 km to 40,000 km (zonal wavenumbers 2 and 1), and 6 km to 10 km vertical scales. They identified them as Kelvin waves predicted by Matsuno's theory.

In the above and subsequent papers, Yanai *et al*. (1968), Wallace and Chang (1969), and colleagues showed the power of spectrum analysis in extracting the most out of widely scattered tropical observations and how to interpret results in the context of theoretical predictions. Their work provided a vantage point for the

analysis of tropical data beginning at the National Center for Atmospheric Research (NCAR) in Boulder, Colorado. The Center was collecting longer time series than had been available to the research community earlier, and it had the fastest computers devoted to meteorological studies: a Control Data Corporation (CDC) 6600, and in 1971 a CDC 7600. The computers were advanced for the time, but clock speeds and memories were only 10 mHz and 64 kb, and 36 mHz and 65.5 kb, respectively. Today a typical laptop computer (e.g., Dell 8600) has a clock speed of 1,400 mHz and 262,144 kb of random access memory.

Another fortuitous development at the time was that of the fast Fourier transform, or FFT (Cooley and Tukey, 1965), which made it feasible to perform spectrum analysis of long time series on these machines. Before the development of the FFT, a Fourier transform of an N-member time series required $N \times N$ complex multiplies. The FFT reduced that requirement to $N \times \log(N)$ which for a 10-year record of daily values reduced multiplications by a factor of 100.

In the fall of 1970, we embarked on a study "designed to provide analysis over a broader frequency range and to study the non-stationary aspects of the aforementioned wave modes" (Madden and Julian, 1971). The aforementioned wave modes were those discovered by Yanai and Maruyama and Wallace and Kousky. What we found was a variation with a timescale longer than these waves and shorter than any component one could attribute to seasonal variations, and one not predicted by any theory.

1.2 THE INTRASEASONAL, TROPOSPHERIC OSCILLATION

For our initial analysis, rawinsonde data from Kanton Island (3°S, 172°W) for the period June 1957 to March 1967 were available with only about 2.5% of observations below 500 hPa missing, and approximately 5% missing above that level. Data were one sample per day, usually taken at 00:00 GMT, and they included surface pressure, winds, temperatures, and humidity often extending to pressure levels higher than the tropopause which is at about 100 hPa near the equator. Though difficult to appreciate now, analyses of 10 years of daily observations pushed computer memory to its limit.

The rawinsonde data were contained on magnetic tapes: one station per tape. Magnetic tapes required an operator to physically mount them on a tape drive. Cross-spectra among data from two stations would require two tape mounts. Since the computers served all NCAR scientists and visitors, the need to mount tapes often meant long delays. To avoid these delays, initial analyses involved reading the data from the tapes and putting out values on punched cards. Data on cards were read in with the program and there was no need for further tape mounts. Of course this meant that decks of as many as 2,000 cards containing Fortran routines and data had to be fed through the card reader, and, in any case, "turnaround" was still slow relative to today. This was not all bad since it allowed plenty of time to digest the results of one run before the return of a second.

Resulting cross-spectra between the *u*-wind in the lower troposphere below about 500 hPa and that in the upper troposphere above 500 hPa showed negative values with large magnitudes in the co-spectra occurring at approximately 50-day periods. A cross-spectrum of two time series gives information on the covariability between them as a function of frequency or period. This covariability is contained in the co-spectrum and the quadrature spectrum. The co-spectrum is that part of the co-variability at some frequency that is either exactly in phase or exactly out of phase. It turned out that, near 50-day periods, upper tropospheric *u*-winds were out of phase with lower tropospheric *u*-winds, or, put another way, the phase shift between the two was 180°. If the phase shift had been different, then some, all in the case of an exactly 90° phase shift, of the covariability would have been found in the quadrature spectrum.

Figure 1.1 presents an example of those negative co-spectra along with a positive one between the 850 hPa *u* and the surface pressure. Corresponding coherence squares, a correlation as a function of frequency which includes both the co-spectrum and the quadrature spectrum parts of the covariability, are plotted at the bottom of the figure. All results have relative extrema in the 40 to 50-day period range. Madden and Julian (1971) were able to see these low-frequency maxima where others had not by virtue of the relatively long record from Kanton that we could analyze. Phase angles (not shown) indicated that the 850 hPa *u* was out of phase with *u* at tropospheric levels above 600 hPa to 500 hPa. Surface pressure was very nearly in phase with the 850 hPa *u*. Coherence squares of 0.25 demark the 0.1% prior confidence level for a null hypothesis of zero coherence. A null hypothesis is a hypothesis about the data that can be tested statistically and accepted or rejected. In this case the null, zero coherence, is that the upper and lower tropospheric *u*-winds are not related.

A short digression is in order to explore statistical confidence levels. A 5% prior confidence level is one that 5% of estimates are likely to exceed due to sampling variability even if the null hypothesis were true. The kind of study we were doing might be termed "exploratory data analysis" because we had no "a priori" reason, that is no reason before we looked at the data to expect anything unusual at 50-day periods. When doing exploratory data analysis with no prior reason to expect any difference from a null, prior confidence levels are not particularly discriminatory. A "significant peak" at an arbitrary frequency may well be one of the 5% of such peaks expected. A stronger test is in order. The bandwidth of the analysis whose results are shown in Figure 1.1 is 0.0081 cycles/day. As a result there are just over 60 (0.5/0.0081) non-overlapping, independent estimates. Even if the null hypothesis of zero coherence were true, the 5% prior significance level would have, on average, three values (60×0.05) in a single sample spectrum exceeding it. The 0.1% prior significance level would have, on average, 0.06 values exceeding it in a single sample spectrum, or six values in 100 such sample spectra. In this case the 0.1% "prior confidence level" can be thought of as the 6% "posterior confidence level". A posterior confidence level is considerably more stringent than a prior one. Most of the coherence-squared values and spectral peaks reported in Madden and Julian (1971) exceeded zero-coherence and

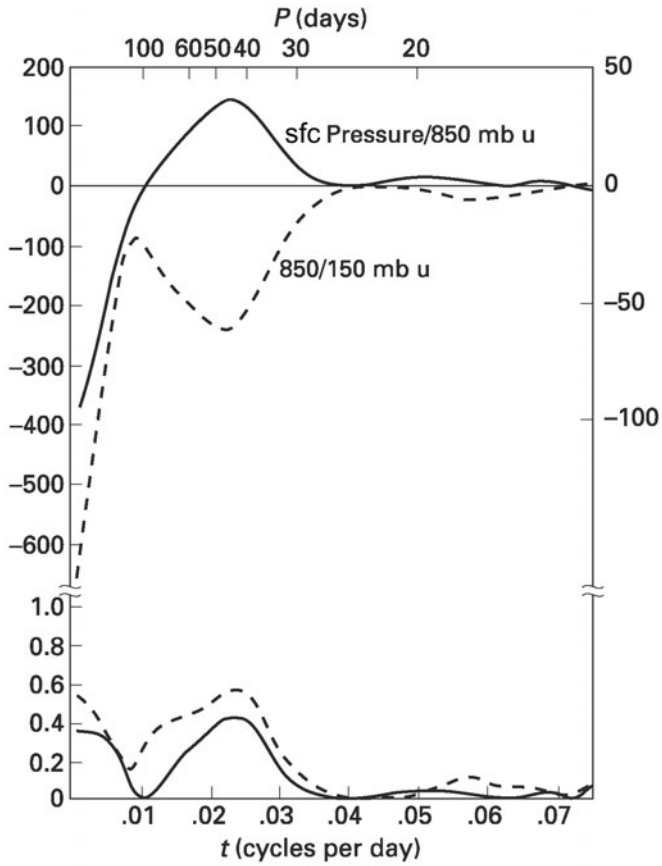

Figure 1.1. (Top) The co-spectrum of the 850 hPa and 150 hPa *u*-wind (dashed line and left ordinate values), together with the co-spectrum of the station (sfc) pressure and the 850 hPa *u*-wind (solid line and right ordinate values) for Kanton Island. (Bottom) The coherence-squared statistic for the 850 hPa and 150 hPa *u*-wind (dashed line) and for the station pressure and 850 hPa *u*-wind (solid line). The 0.1% prior (6% a posteriori) confidence level on the null hypothesis of no coherence is 0.25 (from Madden and Julian, 1971).

smooth background spectral null hypotheses by the stringent 6% posterior confidence levels.

Madden and Julian (1971) concluded that at Kanton the oscillation was a relatively broadband phenomenon with maxima in coherence and power typically in the 41 to 53-day period range. The *u*-wind and pressure oscillations were in phase with each other at a given level, but out of phase between the lower and upper troposphere. There was a nodal surface in the 600 hPa to 500 hPa levels. The *v*-wind did not appear to be involved. This last conclusion proved wrong and resulted from not distinguishing results by season (see Section 1.7).

1.3 THE ELEMENTARY 4-D STRUCTURE

Cross-spectra between locations and the technique of compositing indicated that the pressure disturbance probably began in the Indian Ocean and propagated eastward moving at more than $30\,m\,s^{-1}$ from Singapore (1°N, 104°E) to the Balboa Canal Zone (9°N, 80°W). Pressure oscillations were largest within 10° of the equator and from at least Singapore to Curaçao (12°N, 69°W) in the Carribean. Data from six widely spaced rawinsonde stations indicated that the oscillation extended all the way around the world in the upper equatorial troposphere. In the lower troposphere the oscillations in the *u*-wind appeared to be limited to the Indian and western Pacific Oceans.

Tropospheric temperature variations supported the out-of-phase nature of the vertical structure of the *u*-wind. Low pressures at the surface of the central Pacific are accompanied by high tropospheric temperatures. This nearly out-of-phase relationship through the troposphere changes to a nearly in-phase relationship at 100 hPa. Low 100 hPa temperatures, possibly indicating a higher tropopause, are associated with low surface pressures. The temperature amplitude was of the order of 0.5°C in the troposphere and about twice that at 100 hPa. At least at Singapore and Chuuk (7°N, 152°E), high water vapor mixing ratios also accompanied low surface pressures.

Convergence of the lower-level *u*-wind, divergence of the upper-level *u*-wind, higher tropospheric temperatures and mixing ratios, and possibly higher tropopause were circumstantial evidence that deep convection accompanied low surface pressures. Figure 1.2 summarizes the evidence about the oscillation. Relative dates in the figure are indicated symbolically by letters in the left of each panel, and they relate to the surface pressure oscillation at Kanton. Date "A" is the time when pressure is low and "E" when it is high at Kanton. Other "dates" are intermediate ones. For a 48-day period there would be 6 days between each panel with time increasing from top to bottom. The pressure oscillation is indicated at the bottom of each panel with negative anomalies shaded. The streamlines reflect *u*-wind anomalies. Assumed associated convection is indicated by the cumulus and cumulonimbus clouds. Tropopause height (relatively high above surface low pressure and convective regions) is depicted by the wavy line at the top of each panel.

The behavior of the oscillation as indicated in Figure 1.2 is as follows: a negative pressure anomaly is present over East Africa and the Indian Ocean, and large-scale convection begins over the Indian Ocean (F); the pressure anomaly propagates eastward past the Date Line as does the eastern edge of the zonal circulation cell (G); by the time of lowest pressure at Kanton the zonal circulation cells have a zonal wavenumber 1 character and the convection has moved across Indonesia (A); pressures begin to rise over the Indian Ocean and convection weakens over and east of the Date Line (B–C); finally there is highest pressure over Kanton, subsiding motion there, and possibly weak rising motions over the Atlantic Ocean (E).

Figure 1.2 provides a simplified 3-D picture of the oscillation. The fourth,

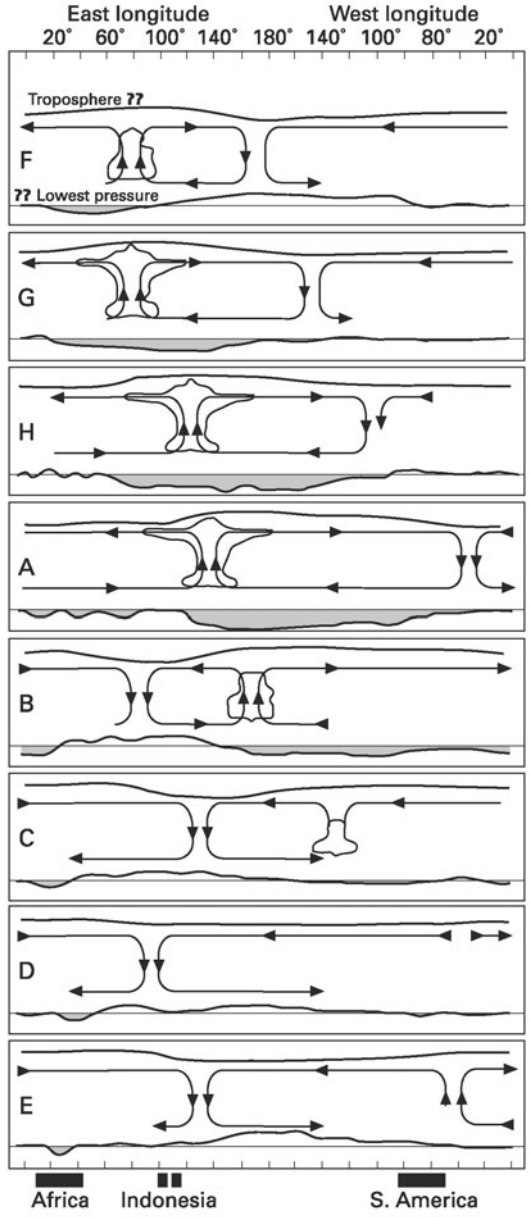

Figure 1.2. A schematic of the approximate structure of the oscillation in the equatorial plane. The situations summarized in each panel are about 4 to 8 days apart with time increasing downward. Cartoon clouds indicate large regions of increased convection. Streamlines show the east–west circulation with convergence into and divergence out of the convective areas in the lower and upper troposphere, respectively. The wavy line at the top represents the tropopause and that at the bottom changing sea level pressure (from Madden and Julian, 1972).

south–north dimension is, to first approximation, characterized by a simple weakening of the signal as one looks farther from the equator.

1.4 OTHER EARLY STUDIES OF THE OSCILLATION

To our knowledge, the oscillation was not reported before 1971. Aspects were discussed in the later 1970s. Evidence of eastward-propagating clouds speculated by Madden and Julian (1972) was presented by Gruber (1974b) who found eastward, zonal wavenumber 1 variance near 50 days in a spacetime spectrum of cloud brightness data near the equator. Zangvil (1975) similarly reported eastward, zonal wavenumber 1 and wavenumber 2 variance near 40 days in equatorial cloud data. In addition to this eastward movement, a northward propagation of cloud zones over India with 30 to 40-day timescales was suggested by spatial correlations computed by Murakami (1976). A related paper published in the same year contained Dakshinamurti and Keshavamurty's (1976) spectral analyses of winds over India. They showed relative maxima in variance near 30-day periods that were associated with south-to-north movements of the monsoon trough. Later, Yasunari (1979) argued that the eastward-propagating equatorial clouds and the northward movement of cloud systems in the monsoon trough were related.

Parker (1973) found the oscillation in the 100 hPa u-winds and temperatures over the equator. Parker considered the oscillation to be sufficiently like a Kelvin wave to be considered as such. Like the Madden and Julian references, Parker concluded that the oscillation affected u and not v-winds and, at least at Gan Island, u and pressure were about in phase. These are basic characteristics of the Kelvin wave. Equatorial Kelvin waves move eastward and the disturbance associated with the oscillations in variables moved eastward. The disturbance was symmetric about the equator, fell off in amplitude away from the equator, and 100 hPa temperature variations tended to lead to u-wind variations by 0.25 of a cycle—all properties of the Kelvin wave. At about the same time, Holton (1973) and Lindzen (1974) presented modeling and theoretical evidence that the oscillation could be the manifestation of an atmospheric Kelvin wave. Later it was suggested that the oscillation resulted from an eastward-moving, forced Kelvin–Rossby wave pair as contained in Matsuno (1966) and others' work and studied by Gill (1980) (see also Yamagata and Hayashi, 1984; Madden, 1986).

We cannot pretend to provide an adequate summary of the considerable related theoretical work that has followed. That is found in Chapter 10. However, this section provides the opportunity to give a brief overview of its development. Theoretical work began with the aforementioned studies of Kelvin waves but, because of the large vertical scale of the oscillation, this theory typically predicted phase speeds that were much faster than observed. Adding linear damping to the equations resulted in modes with more realistic eastward speeds (Chang, 1977). Convection was always recognized as an essential part of the oscillation, but early Kelvin wave theories did not explain what caused the convection. In addition, the recognition that convective heating near the equator forced a Kelvin–Rossby wave

pair made unclear why eastward propagation associated with the Kelvin wave was selected over the westward propagation of the Rossby waves.

Wave CISK (conditional instability of the second kind), in which the low-level moisture convergence of an existing wave produces convection and warming that acts, in turn, to reinforce the wave, could explain the convection. A problem was that most CISK formulations favor small-scale convection—not the very large scale that is observed. In addition eastward propagation is not a necessary consequence. Lau and Peng (1987) introduced "mobile wave CISK" which included "positive-only heating" unlike the wavy heating of traditional approaches. Their model favored more realistic large-scale convection and the eastward-propagating Kelvin wave part of the response. To get relatively slow propagation, the heating profile they used had what is likely an unrealistic maximum at low tropospheric levels.

A different mechanism that could explain the formation of convection and the eastward movement was "wind-induced surface heat exchange" (WISHE) (Emanuel, 1987; Neelin *et al*., 1987). Here, surface winds of the large-scale wave affect fluxes of latent heat from the ocean to preferably support new convection to the east of old convection. Unfortunately, WISHE favors smaller scale convection just as traditional CISK does.

None of these theories explains all of the complex features of the MJO. Undoubtedly many of the physical processes that they describe are important, as are boundary layer friction (Wang, 1988; Hendon and Salby, 1994) and radiative effects (Hu and Randall, 1994). Chapter 10 adds details of the theories and describes a model that incorporates many of their influences. Here, we continue to describe the oscillation from an observational point of view.

1.5 THE OSCILLATION IN 1979

We separate out 1979 as a key time in the history of research into intraseasonal variations in the tropics because the meteorological research community invested considerable effort in the First Global Atmospheric Research Program (GARP) Global Experiment (FGGE) during that year. There were several MJOs in 1979. Two particularly strong oscillations passed over the region of the Monsoon Experiment (MONEX) between May and August, and interest in them was renewed.

Lorenc (1984) computed the empirical orthogonal functions (EOFs) of daily values of the 200 hPa velocity potential during FGGE and found that the two leading EOFs (explaining most of the variance after the annual cycle had been removed) represented a zonal wavenumber 1, eastward-propagating pattern, that circled the equator in 30 to 50 days, much like the upper-tropospheric divergent circulations indicated in Figure 1.2. Lorenc noted negative velocity potential (upper-level divergence) near India during the 1979 monsoon onset in mid-June and monsoon revival, or an active period, in late July. In contrast, positive velocity potential (upper-level convergence) ruled during a break in mid-July and during withdrawal in mid August.

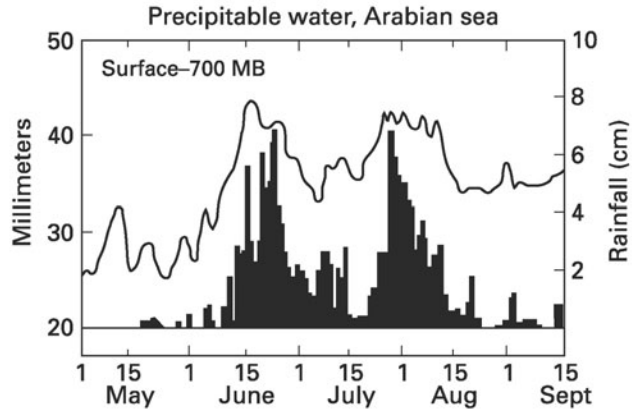

Figure 1.3. Time series of precipitable water from the surface to 700 hPa over the Arabian Sea (thin line) from TIROS-N, and precipitation along the west coast of India during MONEX (adapted from Cadet, 1986).

The importance of wax (active periods) and wane (break periods) in the monsoon is illustrated in Figure 1.3. There are very large variations in Indian rainfall with roughly 40 days between maxima. These variations are associated with northward movement of the monsoon trough and accompanying clouds. The cloud systems also moved eastward along the equator. This particular northward and eastward-moving event is clearly documented in Lau and Chan (1986b). We note that sometimes the term MJO is limited to systems whose dominant propagation is eastward, and those with considerable latitudinal movement are considered as members of a broader class of intraseasonal oscillations (ISOs; see Chapter 10).

The MONEX period also revealed related variations in latent heat flux over the Bay of Bengal with amplitudes of 40 $W\,m^{-2}$ about an average of about 200 $W\,m^{-2}$ (Krishnamurti *et al.*, 1988). There were strong winds over the Bay of Bengal and accompanying positive anomalies in latent heat flux in mid-June and in late July coincident with the heavy rains over India (Figure 1.3). At those same times strong easterlies were found over the entire tropical Pacific (Madden, 1988). The resulting varying surface friction and exchange of angular momentum between the atmosphere–ocean–Earth system played an important role in angular momentum changes discussed in Section 1.8.

1.6 COMPLEXITY OF CLOUD MOVEMENT AND STRUCTURE

Although Figure 1.2 captures the essential nature of the oscillation in convection, it is a simplified picture. Wang and Rui (1990) stratified movement of cloud complexes related to the oscillation into three categories: (1) strictly eastward near the equator from Africa to the central Pacific; (2) similarily eastward over the Indian Ocean and

then northward or southward over the western Pacific; and (3) eastward as above but connected to cloud systems that moved northward into southern Asia or into the north Pacific. Three out of four of the strictly eastward-moving cloud complexes occurred from September to May. Complexes that moved eastward and then southward into the south Pacific also tended to occur during the northern winter half of the year, while those that moved into the north Pacific did so from April to December. This points to a tendency for meridional movement to be into the summer hemisphere as was observed during MONEX. Other seasonal variations are described in Section 1.7.

High temporal and spatial resolution satellite-measured cloud data reveal added complexity in the makeup of individual cloud complexes. Figure 1.4 is a schematic that summarizes some of this complexity. The intraseasonal variability (ISV) depicted by Nakazawa (1988) corresponds to the large-scale cloud complexes indicated in Figure 1.2. Their east–west scale is of the order of 5,000 km to 10,000 km and they move eastward halfway around the Earth in about 20 days. Finer spatial resolution reveals that these large-scale complexes are made up of eastward-propagating supercloud clusters (SCCs) having 2,000 km to 4,000 km horizontal scales. The SCCs, in turn, are composed of westward-moving cloud clusters (CCs) which continually develop to the east and decay to the west. The lifetimes of the CCs are only 1 to 2 days.

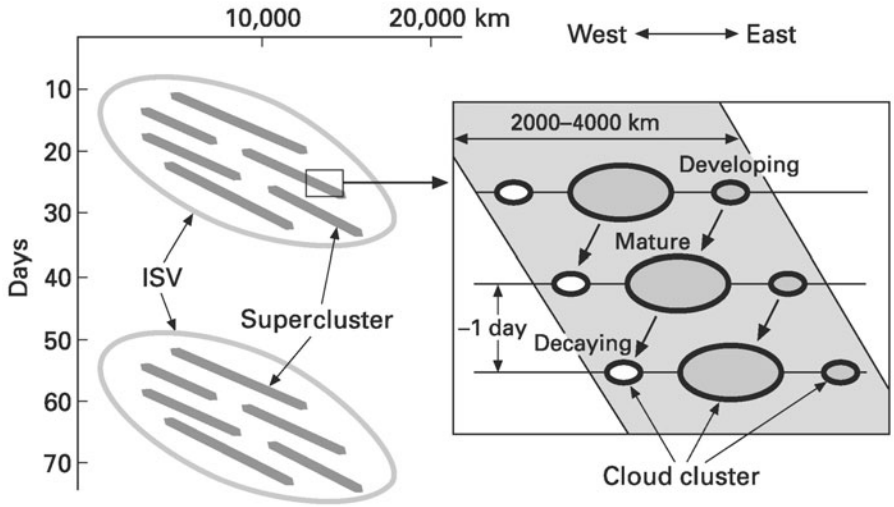

Figure 1.4. Schematic describing the details of large-scale eastward-propagating cloud complexes (slanting ellipses marked ISV on the left-hand side). Slanting emboldened lines represent supercloud clusters (SCCs) within the larger ISV. The right-hand side illustrates the fine structure of the SCC with smaller westward-moving cloud clusters (CCs) that develop, grow to maturity, and decay in a few days (from Nakazawa, 1988).

1.7 SEASONAL VARIATIONS IN THE OSCILLATION

Some interesting seasonal variations are revealed when one isolates spectral and cross-spectral quantities as a function of the time of year (Madden, 1986). The out-of-phase relationship between the lower and upper troposphere evident in the Indian and western Pacific equatorial regions is strongest at stations in the summer hemisphere. This is consistent with a close connection with the divergent motions of the Intertropical Convergence Zone (ITCZ). In this regard, the oscillation often modulates large monsoons of the summer hemisphere. Examples for the northern summer are those during MONEX discussed above. Chapters 2, 3, 4, and 5 of this book cover variations in the monsoons in detail.

Another seasonal result reveals a role of the v-wind and illustrates the danger in interpreting spectral results of non-stationary time series. Estimates of seasonally varying coherence and phase between u and v-winds in a frequency band centered on 1/47 day at 150 hPa over Chuuk reveal that the coherence is large twice a year. In northern winter (summer) u and v are out-of-phase (in-phase) manifesting surges in the climatological southeasterlies (northeasterlies) in that season. This reflects a connection to changing upper-level outflow from the ITCZ. The coherence between time series of u and v-winds that are not stratified by season is small because the negative relation during northern winter cancels the positive one during northern summer.

Variance in the 1/47-day frequency band generally exceeds that in adjacent bands by the largest amount during December, January, and February so, by that measure, the oscillation is strongest in those months. There is no obvious change in the period of the oscillation with season. It averages from 45 to 48 days but individual oscillations range from a few weeks to more than 60 days. There is subjectivity in deciding if an MJO is present, but two methods of identification—one using winds (Madden, 1986) and one using May to October clouds (Knutsen *et al.*, 1986)—suggest that they are active between 50% and 75% of the time. Considering a 45-day period, we might expect that there would be between four and six oscillations in a typical year. They are slightly more likely to occur during the northern winter half of the year since on average there are fewer occurrences during June, July, and August than during other seasons (Madden, 1986; Wang and Rui, 1990).

1.8 THE OSCILLATION IN THE ZONAL AVERAGE

Figure 1.2 shows that the surface pressure anomaly is not a simple sinusoid but reflects changes in the zonal average as well. Another striking example of a zonally averaged component in the oscillation is in relative atmospheric angular momentum (RAAM). RAAM is a mass-weighted integration of the u-winds over the entire globe. Figure 1.5 shows RAAM during MONEX. There are two marked relative maxima about 45 days apart: one at the end of June and a second in mid August. Because the angular momentum of the atmosphere–ocean–Earth system

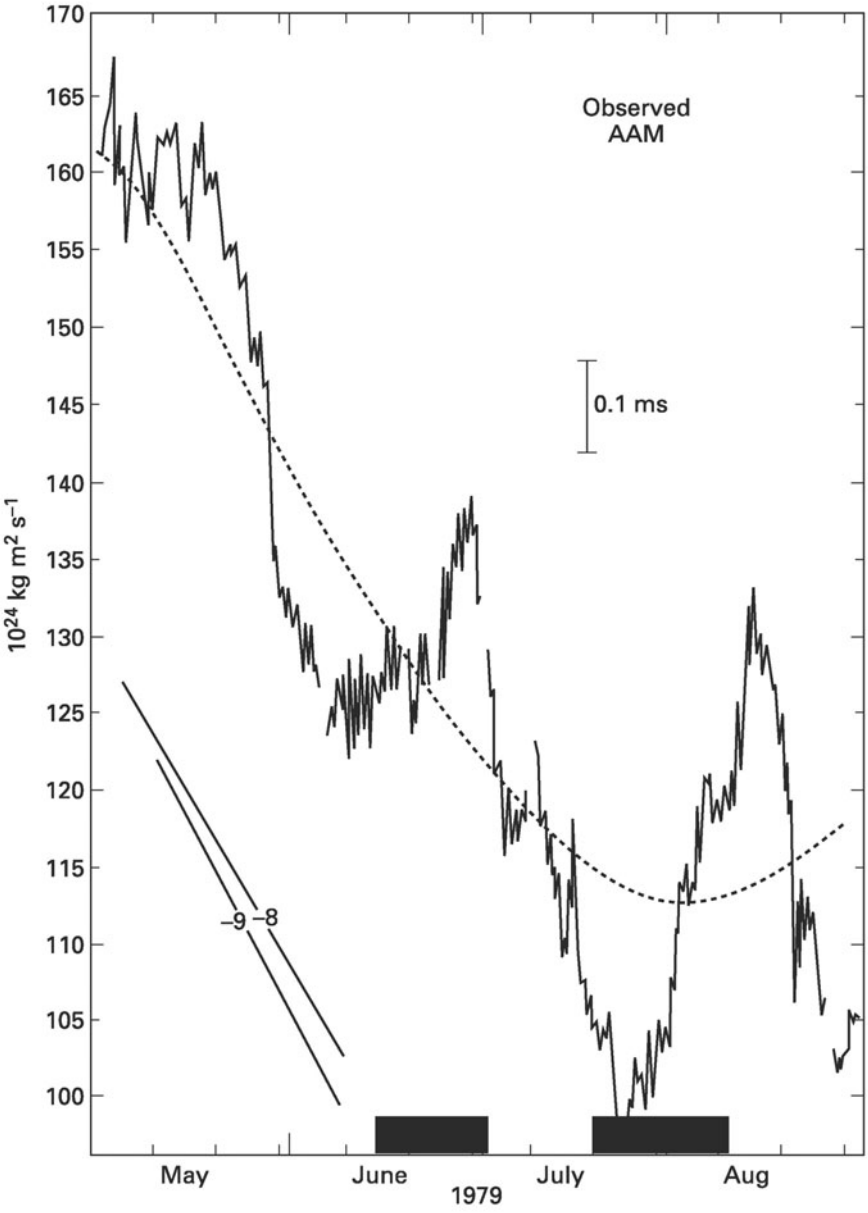

Figure 1.5. Observed relative atmospheric angular momentum (RAAM) during MONEX (thin irregular line). The dotted curved line represents approximate seasonal variation. Slanting lines on the lower left are expected seasonal variations based on two estimates of northern springtime climatalogical torques in units of $10^{18}\,\mathrm{kg\,m^2\,s^{-2}}$ (Newton, 1971; Wahr and Oort, 1984). The amplitude of a corresponding 0.1 ms change in length of day (LOD) is indicated. Thick lines at the bottom mark times of heavy monsoon rains from Figure 1.3 (from Madden, 1988).

remains nearly constant, a change in RAAM can be reflected in changes in the momentum of the ocean or solid Earth. Feissel and Gambis (1980) reported on a 50-day oscillation in the angular momentum of the solid Earth as reflected in measurements of the length of day (LOD) during the MONEX period of about 0.35 ms (10^{-3} s) peak-to-trough amplitude. The LOD change corresponding to a change in RAAM is indicated in Figure 1.5 and reveals that peak-to-trough amplitudes of about 0.2 ms (June) to more than 0.3 ms (August) would result if all changes in RAAM went to increasing the angular momentum of the solid Earth. LOD is longest (solid Earth momentum smallest) when RAAM is greatest. This is but one example of the consistency between RAAM and LOD that occurs on all timescales less than a few years. It is a credit to our observing systems that these two disparate time series—irregularly measured winds averaged over the Earth and estimates of tiny changes in the LOD—are so well related.

The evolving surface wind and pressure distributions during an oscillation result in changing frictional and mountain torques that vary the exchange of momentum between the atmosphere–ocean–Earth system. As the cloud complex moves east the torques combine to increase RAAM. First, frictional torques increase, reflecting stronger trades over the tropical Pacific. Then mountain torques reach relative maxima, sometimes with relatively high pressure to the east of the Rocky Mountains, while relatively low–pressure systems approach from the west. This results in an anomaly surface pressure gradient directed from west to east across the mountains and a positive anomaly in the mountain torque. Anomaly pressure gradients across the Himalayas (Weickmann and Sardeshmukh, 1994) and the Andes (Salstein and Rosen, 1994) are sometimes also important. RAAM tends to reach a relative maximum shortly after the propagating clouds reach the central Pacific (Madden and Speth, 1995). Chapter 8 in this book considers the intraseasonal exchange of momentum between the atmosphere–ocean–Earth system more thoroughly.

1.9 OTHER EFFECTS OF THE OSCILLATION

A tropical phenomenon as large as the MJO is certain to affect midlatitude weather. Weickmann *et al.* (1985) described the reach of the oscillation into midlatitudes, and Lau and Phillips (1986) linked it to wavetrains propagating across the Pacific to North America. Propagation to midlatitudes is now a research area of intense interest. Wavetrain propagation is dependent on background flow, and its ever changing character results in widely differing midlatitude responses to very similar MJOs. With the growing bank of observations and improved modeling it is likely that MJOs will contribute to added skill in midlatitude weather forecasts in the 5-day to 3-week range (e.g., Ferranti *et al.*, 1990; Jones *et al.*, 2004).

We have seen evidence of the oscillation in many aspects of the tropical atmosphere. In addition, the development of tropical cyclones is favored in

regions of the upper-level, negative velocity potential of the MJO as well (Nakazawa, 1986; Liebmann *et al.*, 1994; Maloney and Hartman, 2000; Mo, 2000; Hall *et al.*, 2001). At this point, though promising, it is not clear how this relation might aid in tropical storm prediction.

Section 1.5 contains evidence that the oscillation affects the Indian Monsoon. It also influences the Australian Summer Monsoon. Holland (1986) found an average of 40 days between its active bursts. More recently, Wheeler and Hendon (2004) found a tripling of the probability of extreme (highest quintile) monsoon rainfall between the wet and dry phases of the oscillation. The oscillation has also often been implicated in the special case of the annual onset of the monsoon (Hendon and Liebmann, 1990a; Hung and Yanai, 2004; Wheeler and Hendon, 2004). It should be noted that none of these results translates into spectral evidence for a favored 40-day period in monsoon rainfall (Hendon and Liebmann, 1990b; Drosdowsky, 1996). While the effect of the oscillation is unmistakable, the discussion in Chapter 5 will show that it is only one part of a myriad of intraseasonal monsoon phenomena.

The underlying ocean plays a part in the oscillation as well. Related ocean current variations are apparent. McPhaden (1982) found that low-level winds at Gan Island (1°S, 73°E) and 100 m deep currents, were coherent on 30 to 60-day timecales. Similarly, Mysak and Mertz (1984) concluded that variations in wind stress or in wind stress curl drove 40 to 60-day oscillations that they found in the Somali Current. They found that during 1979 both u and v-wind stresses in the region have spectral peaks in the 40 to 50-day range.

Another response to the surface wind oscillation is the excitation of ocean Kelvin waves along the equator. They move eastward and then north and south along the west coast of the Americas. There is a clear 40 to 60-day variation in sea level height from at least the Peruvian coast northward to northern California (Enfield, 1987). Luther (1980) had already reported 35 to 80-day spectral peaks in sea level height from Kanton to the Galapagos (1°S, 91°W). These variations result from Kelvin waves that are excited in the far western Pacific by surface winds of MJOs.

The oscillation affects the underlying ocean, and it can be assumed that the ocean affects the oscillation. For example, there are changes in the oscillation that appear to be driven by the El Niño/La Niña cycle (e.g., Lau and Chan, 1986a). On the other hand, evidence is growing that MJOs can play an important role in the timing of the ocean cycle itself. Lau and Chan (1986a) were the first to propose a link between MJOs and the onset of El Niño. It may also be important in the demise of El Niño (Takayabu *et al.*, 1999). The physical mechanism may be that both the anomalous surface westerlies and easterlies of the MJO can excite downwelling and upwelling ocean Kelvin waves, respectively, that then influence sea surface temperatures (McPhaden, 1999). The El Niño/La Niña cycle is important for global climate, and the possiblity that MJOs influence its timing has kindled additional interest in them since the late 1980s. More on this important topic follows in Chapters 6 and 7.

1.10 SUMMARY

The discovery of the QBO was important for subsequent discoveries of mixed Rossby gravity waves and Kelvin waves, and they, in turn, were the motivation for work that led to the discovery of the MJO. A basic description of the MJO is presented here. The oscillation affects tropical clouds and precipitation, planetary-scale divergence patterns, the Asian and Australian Monsoons, zonally averaged pressures, atmospheric angular momentum and the LOD, midlatitude weather, and the ocean beneath it. These introduced features are brought up to date in subsequent chapters based on the burgeoning research that has taken place in the last 25 years.

1.11 REFERENCES

Cadet, D. L. (1986) Fluctuations of precipitable water over the Indian Ocean during the 1979 summer monsoon. *Tellus*, **38A**, 170–177.

Chang, C.-P. (1977) Viscous internal gravity waves and low-frequency oscillations in the tropics. *J. Atmos. Sci.*, **34**, 901–910.

Cooley, J. W. and J. W. Tukey (1965) An algorithm for the machine calculation of Fourier series. *Math. Comput.*, **19**, 297–301.

Dakshinamurti, J. and R. N. Keshavamurty (1976) On oscillations of period around one month in the Indian summer monsoon. *Indian J. Meteor. Hydrol. Geophys.*, **27**, 201–203.

Drosdowsky, W. (1996) Variability of the Australian summer monsoon at Darwin: 1957–1992. *J. Climate*, **9**, 85–96.

Ebdon, R. A. (1960) Notes on wind flow at 50 mb in tropical and sub-tropical regions in January 1957 and January 1958. *Quart. J. Roy. Meteor. Soc.*, **86**, 540–542.

Ebdon, R. A. (1963) The tropical stratospheric wind fluctuation. *Weather*, **18**, 2–7.

Emanuel, K. A. (1987) Air–sea interaction model of intraseasonal oscillations in the tropics. *J. Atmos. Sci.*, **44**, 2324–2340.

Enfield, D. B. (1987) The intraseasonal oscillation in eastern Pacific sea levels: How is it forced? *J. Phys. Oceanogr.*, **17**, 1860–1876.

Feissel, M. and D. Gambis (1980) La mise en evidence de variations rapides de la durée de jour. *C. R. Hebd. Séances Acad. Sci., Sér. B*, **291**, 271–273 [in French].

Ferranti, L., T. N. Palmer, F. Molteni, and E. Klinker (1990) Tropical–extratropical interaction associated with the 30–60 day oscillation and its impact on medium and extended range prediction. *J. Atmos. Sci.*, **47**, 2177–2199.

Gill, A. E. (1980) Some simple solutions for heat-induced tropical circulation. *Quart. J. Roy. Meteor. Soc.*, **106**, 447–463.

Graystone, P. (1959) Meteorological Office discussion: Tropical meteorology. *Met. Mag.*, **88**, 113–119.

Gruber, A. (1974a) Wavenumber–frequency spectra of the 200 mb wind field in the tropics. *J. Atmos. Sci.*, **32**, 1615–1625.

Gruber, A. (1974b) Wavenumber–frequency spectra of satellite-measured brightness in the tropics. *J. Atmos. Sci.*, **31**, 1675–1680.

Hall, J. D., A. J. Matthews, and D. J. Karoly (2001) The modulation of tropical cyclone activity in the Australian region by the Madden–Julian Oscillation. *Mon. Wea. Rev.*, **129**, 2970–2982.

Hendon, H. H. and B. Liebmann (1990a) A composite study of onset of the Australian summer monsoon. *J. Atmos. Sci.*, **47**, 2227–2240.

Hendon, H. H. and B. Liebmann (1990b) The intraseasonal (30–50 day) oscillation of the Australian summer monsoon. *J. Atmos. Sci.*, **47**, 2909–2923.

Hendon, H. H. and M. L. Salby (1994) The life cycle of the Madden–Julian Oscillation. *J. Atmos. Sci.*, **51**, 2225–2231.

Holland, G. J. (1986) Interannual variability of the Australian summer monsoon at Darwin: 1952–82. *Mon. Wea. Rev.*, **114**, 594–604.

Holton, J. R. (1973) On the frequency distribution of atmospheric Kelvin waves. *J. Atmos. Sci.*, **30**, 499–501.

Hu, Q. and D. A. Randall (1994) Low-frequency oscillations in radiative–convective systems. *J. Atmos. Sci.*, **51**, 1089–1099.

Hung, C.-W. and M. Yanai (2004) Factors contributing to the onset of the Australian summer monsoon. *Quart. J. Roy. Meteor. Soc.*, **130**, 739–758.

Jones, C., D. E. Waliser, K. M. Lau, and W. Stern (2004) The Madden–Julian Oscillation and its impact on Northern Hemisphere weather predictability. *Mon. Wea. Rev.*, **132**, 1462–1471.

Knutsen, T. R., K. M. Weickmann, and J. E. Kutzbach (1986) Global-scale intraseasonal oscillations of outgoing longwave radiation and 250 mb zonal wind during northern hemisphere summer. *Mon. Wea. Rev.*, **114**, 605–623.

Krishnamurti, T. N., D. K. Oosterhof, and A. V. Mehta (1988) Air–sea interaction on the time scale of 30 to 50 days. *J. Atmos. Sci.*, **45**, 1304–1322.

Lau, K.-M. and P. H. Chan (1986a) The 40–50 day oscillation and the El Niño/Southern Oscillation: A new perspective. *Bull. Amer. Meteor. Soc.*, **67**, 533–534.

Lau, K.-M. and P. H. Chan (1986b) Aspects of the 40–50 day oscillation during northern summer as inferred from outgoing longwave radiation. *Mon. Wea. Rev.*, **114**, 1354–1367.

Lau, K.-M. and L. Peng (1987) Origin of low-frequency (intraseasonal) oscillations in the tropical atmosphere, Part 1: Basic theory. *J. Atmos. Sci.*, **44**, 950–972.

Lau, K.-M. and T. J. Phillips (1986) Coherent fluctuations of extratropical geopotential height and tropical convection in intraseasonal time scales. *J. Atmos. Sci.*, **43**, 1164–1181.

Lau, N.-C., I. M. Held, and J. D. Neelin (1988) The Madden Julian Oscillation in an idealized general circulation model. *J. Atmos. Sci.*, **45**, 3810–3832.

Liebmann, B., H. H. Hendon, and J. D. Glick (1994) The relationship between tropical cyclones of the western Pacific and Indian Oceans and the Madden–Julian Oscillation. *J. Meteor. Soc. Jap.*, **72**, 401–412.

Lindzen, R. S. (1974) Wave-CISK and tropical spectra. *J. Atmos. Sci.*, **31**, 1447–1449.

Lorenc, A. C. (1984) The evolution of planetary-scale 200-mb divergent flow during the FGGE year. *Quart. J. Roy. Meteor. Soc.*, **110**, 427–441.

Luther, D. S. (1980) Observations of long period waves in the tropical oceans and atmosphere. PhD. thesis, Massachusetts Institute of Technology–Woods Hole Oceanographic Institution, 210 pp.

Madden, R. A. (1986) Seasonal variations of the 40–50 day oscillation in the Tropics. *J. Atmos. Sci.*, **43**, 3138–3158.

Madden, R. A. (1988) Large intraseasonal variations in wind stress over the tropical Pacific. *J. Geophys. Res.*, **93**, 5333–5340.

Madden, R. A. and P. R. Julian (1971) Description of a 40–50 day oscillation in the zonal wind in the tropical Pacific. *J. Atmos. Sci.*, **28**, 702–708.

Madden, R. A. and P. R. Julian (1972) Description of global-scale circulation cells in the tropics with a 40–50 day period. *J. Atmos. Sci.*, **29**, 1109–1123.

Madden, R. A. and P. Speth (1995) Estimates of atmospheric angular momentum, friction, and mountain torque during 1987–1988. *J. Atmos. Sci.*, **52**, 3681–3694.

Maloney, E. D. and D. L. Hartmann (2000) Modulation of eastern North Pacific hurricanes by the Madden–Julian Oscillation. *J. Climate*, **13**, 1451–1460.

Maruyama, T. (1967) Large-scale disturbances in the equatorial lower stratosphere. *J. Meteor. Soc. Jap.*, **45**, 391–408.

Matsuno, T. (1966) Quasi-geostrophic motions in the equatorial area. *J. Meteor. Soc. Jap.*, **44**, 25–43.

McPhaden, M. J. (1982) Variability in the central equatorial Indian Ocean: Ocean dynamics. *J. Mar. Res.*, **40**, 157–176.

McPhaden, M. J. (1999) Genesis and evolution of the 1997–1998 El Niño. *Science*, **283**, 950–954.

Mo, K. C. (2000) The association between intraseasonal oscillations and tropical storms in the Atlantic basin. *Mon. Wea. Rev.*, **128**, 4097–4107.

Murakami, T. (1976) Cloudiness fluctuations during the summer monsoon. *J. Meteor. Soc. Jap.*, **54**, 175–181.

Mysak, L. A. and G. J. Mertz (1984) A 40-day to 60-day oscillation in the source region of the Somali Current during 1976. *J. Geophys. Res.*, **89**, 711–715.

Nakazawa, T. (1986) Intraseasonal variations of OLR in the tropics during the FGGE year. *J. Meteor. Soc. Jap.*, **64**, 17–34.

Nakazawa, T. (1988) Tropical super clusters within intraseasonal variations over the western Pacific. *J. Meteor. Soc. Jap.*, **66**, 823–828.

Neelin, J. D., I. M. Held, and K. H. Cook (1987) Evaporation–wind feedback and low-frequency variability in the tropical atmosphere. *J. Atmos. Sci.*, **44**, 2341–2348.

Newton, C. W. (1971) Global angular momentum balance: Earth torques and atmospheric fluxes. *J. Atmos. Sci.*, **28**, 1329–1341.

Parker, D. E. (1973) Equatorial Kelvin waves at 100 millibars. *Quart. J. Roy. Meteor. Soc.*, **99**, 116–129.

Reed, R. J., W. J. Campbell, L. A. Rasmussen, and D. G. Rogers (1961) Evidence of a downward-propagating, annual wind reversal in the equatorial stratosphere. *J. Geophys. Res.*, **66**, 813–818.

Salstein, D. A. and R. D. Rosen (1994) Topographical forcing of the atmosphere and a rapid change in the length of day. *Science*, **264**, 407–409.

Swinbank, R., T. N. Palmer, and M. K. Davey (1988) Numerical simulations of the Madden and Julian Oscillation. *J. Atmos. Sci.*, **45**, 774–778.

Takayabu, Y. N., T. Iguchi, M. Kachi, A. Shibata, and H. Kanzawa (1999) Abrupt termination of the 1997–98 El Niño in response to a Madden–Julian Oscillation. *Nature*, **402**, 279–282.

Wahr, J. M. and A. H. Oort (1984) Friction and mountain torques and atmospheric fluxes. *J. Atmos. Sci.*, **41**, 190–204.

Wallace, J. M., and C.-P. Chang (1969) Spectrum analysis of large-scale wave disturbances in the tropical lower troposphere. *J. Atmos. Sci.*, **26**, 1010–1025.

Wallace, J. M. and V. E. Kousky (1968) Observational evidence of Kelvin waves in the tropical stratosphere. *J. Atmos. Sci.*, **25**, 900–907.

Wang, B. (1988) Dynamics of tropical low-frequency waves: An analysis of the moist Kelvin wave. *J. Atmos. Sci.*, **45**, 2051–2065.

Wang, B. and H. Rui (1990) Synoptic climatology of transient tropical intraseasonal convection anomalies. *Meteor. Atmos. Phys.*, **44**, 43–61.

Webster, P. J. (1987) The variable and interactive monsoons. In: J. S. Fein and P. L. Stephens (Eds.), *Monsoons*, John Wiley & Sons, New York, 632 pp.

Weickmann, K. M. and P. D. Sardeshmukh (1994) The atmospheric angular momentum cycle associated with the Madden–Julian Oscillation. *J. Atmos. Sci.*, **51**, 3194–3208.

Weickmann, K. M., G. R. Lussky, and J. E. Kutzbach (1985) Intraseasonal (30–60 day) fluctuations of outgoing longwave radiation and 250 mb stream function during northern winter. *Mon. Wea. Rev.*, **113**, 941–961.

Wheeler, M. C. and H. H. Hendon (2004) An all-season real-time multivariate MJO index: Development of an index for monitoring and prediction. *Mon. Wea. Rev.*, **132**, 1917–1932.

Yamagata, T. and Y. Hayashi (1984) A simple diagnostic model for the 30–50 day oscillation in the tropics. *J. Meteor. Soc. Jap.*, **62**, 709–717.

Yanai, M. and T. Maruyama (1966) Stratospheric wave disturbances propagating over the equatorial Pacific. *J. Meteor. Soc. Jap.*, **44**, 291–294.

Yanai, M., T. Maruyama, T. Nitta, and Y. Hayashi (1968) Power spectra of large-scale disturbances over the tropical Pacific. *J. Meteor. Soc. Jap.*, **46**, 308–323.

Yasunari, T. (1979) Cloudiness fluctuations associated with the Northern Hemisphere summer monsoon. *J. Meteor. Soc. Jap.*, **57**, 227–242.

Zangvil, A. (1975) Temporal and spatial behavior of large-scale disturbances in tropical cloudiness deduced from satellite brightness data. *Mon. Wea. Rev.*, **103**, 904–920.

2

South Asian monsoon

B. N. Goswami

2.1 INTRODUCTION

2.1.1 South Asian summer monsoon and active/break cycles

As the word "monsoon" (derived from an Arabic word meaning "seasons") indicates, the South Asian (SA) summer monsoon is part of an annually reversing wind system (Figure 2.1c, d) (Ramage, 1971; Rao, 1976). The winds at low levels during the summer monsoon season are characterized by the strongest westerlies anywhere in the tropics at 850 hPa over the Arabian Sea, known as the low-level westerly jet (LLJ) (Figure 2.1d), and a large-scale cyclonic vorticity extending from the north Bay of Bengal (BoB) to western India known as the monsoon trough (Figure 2.1d) (Rao, 1976). The easterly jet (Figure 2.1f) centered around 5°N and the Tibetan anticyclone centered around 30°N are important features of upper-level winds over the monsoon region during northern summer. Millions of inhabitants of the region, however, attach much greater importance to the associated seasonal changes of rainfall. Wet summers and dry winters (Figure 2.1a, b) associated with the seasonal changes of low-level winds are crucial for agricultural production and the economy of the region. The monsoon, or the seasonal changes of winds and rainfall, in the region could be interpreted as a result of northward seasonal migration of the east–west oriented precipitation belt (Tropical Convergence Zone, TCZ) from the southern hemisphere in winter to the northern hemisphere in summer (Gadgil, 2003). The largest northward excursion of the rain belt takes place over the Indian monsoon region where it moves from a mean position of about 5°S in winter (Figure 2.1a) to about 20°N in northern summer (Figure 2.1b) (Waliser and Gautier, 1993). In the upper atmosphere (200 hPa), the equatorial easterlies are weak and confined between 5°N and 10°S while the subtropical westerlies intrude all the way to 10°N during northern winter (Figure 2.1e). The subtropical westerlies recede to north of 30°N during northern summer and a strong easterly jet

W. K. M. Lau and D. E. Waliser (Editors), *Intraseasonal Variability in the Atmosphere–Ocean Climate System* (Second Edition).

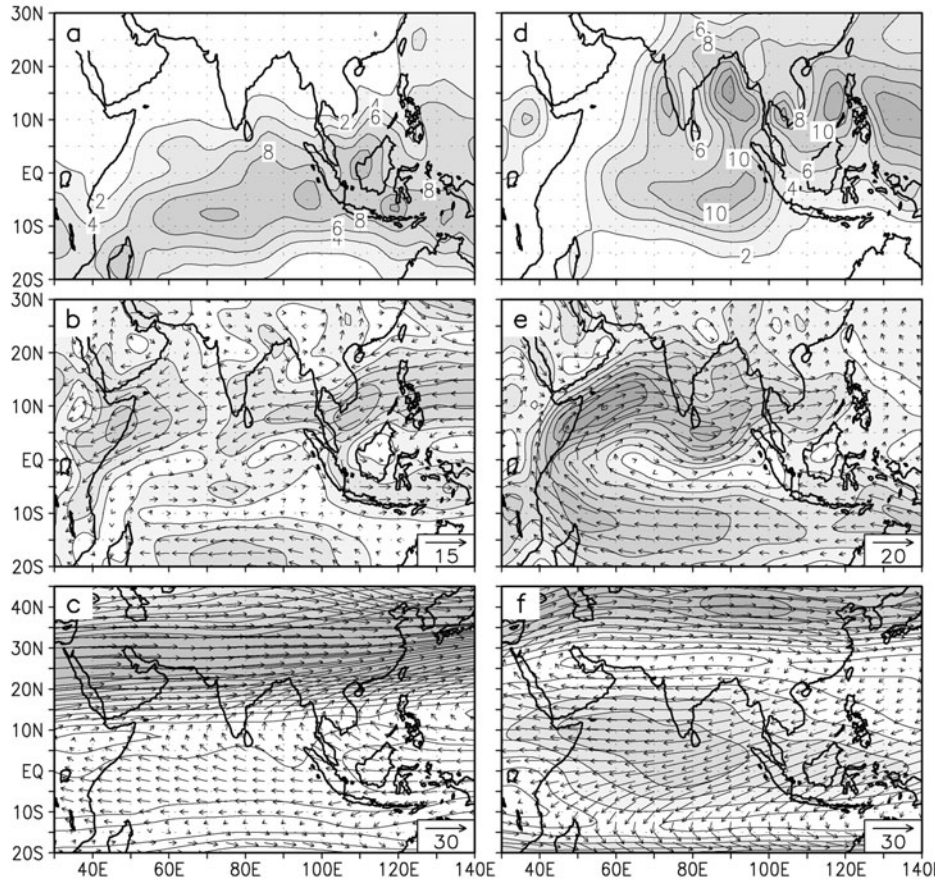

Figure 2.1. Climatological mean precipitation (mm/day) based on CMAP during (a) boreal winter (DJF) and (b) summer (JJAS). (c) and (d) Same as (a) and (b) but for winds ($m\,s^{-1}$) at 850 hPa based on NCEP reanalysis. The contour interval for isotachs is $2\,m\,s^{-1}$ with the minimum contour being 2. (e) and (f) Similar to (c) and (d) but for winds at 200 hPa. The contour interval for isotachs is $5\,m\,s^{-1}$ with the minimum contour being 5. For better depiction of the subtropical westerly jetstream in winter and the Tibetan anticyclone in summer, a larger meridional domain is used for 200 hPa winds (e) and (f).

characterizes the equatorial upper atmosphere in the region (Figure 2.1f). Year-to-year variation of long-term seasonal mean precipitation over the Indian region is strongly correlated with food production in the region (Parthasarathy *et al.*, 1988; Webster *et al.*, 1998; Abrol and Gadgil, 1999). Extremes in year-to-year variations of long-term mean precipitation manifest themselves in the form of large-scale floods and droughts (Parthasarathy and Mooley, 1978; Shukla, 1987; Mooley and Shukla, 1987) and cause devastating human and economic loss.

The seasonal mean rainfall of approximately $8\,mm\,day^{-1}$ does not pour as a continuous deluge but is punctuated by considerable variations within the season.

In addition to the day-to-day fluctuations of weather (e.g., lows and depressions) with timescales of 5–7 days (also known as synoptic disturbances), a characteristic feature of monsoon rainfall is the prolonged spells of dry and wet conditions often lasting for 2–3 weeks. Examples of such spells can be seen in the time series of rainfall averaged over central India between June 1 and September 30, 1972, 1994, and 2002 (Figure 2.2). As seen during 1972, the evolution of rainfall over the season generally goes through extended periods of above-normal conditions (wet spells) followed by extended periods of below-normal conditions (dry spells). Extended above-normal rain spells can be seen to represent epochs when the monsoon was vigorous or active while the dry spells represent periods when the monsoon took a break from its activity (Ramamurthy, 1969; Raghavan, 1973) and hence are known as active and break conditions, respectively. Frequent or prolonged breaks within the monsoon season, as in the case of 1972 and 2002 (Figure 2.2), lead to drought conditions and adversely affect agricultural production (Gadgil, 1995; Webster *et al*., 1998). Similarly, the above-normal seasonal rainfall in 1994 was a result of the occurrence of more active spells and an absence of extended break spells within the season. Thus, frequency of occurrence of active and break spells influences seasonal mean rainfall and hence agricultural production. For example, long breaks in critical growth periods of agricultural crops also lead to substantially reduced yields (Gadgil and Rao, 2000). As a consequence of their influence in agricultural production and water resources, considerable attention has been paid toward understanding the nature of monsoon breaks and the possible mechanism responsible for them. In fact, the earliest reference to monsoon breaks was made more than a century ago by Blanford (1886), where he refers to the periods between two active spells as intervals of droughts. Using upper-air data over the Indian continent and its neighborhood, large-scale circulation changes associated with active and break conditions have been identified (Ramamurthy, 1969; Raghavan, 1973; Krishnamurti and Bhalme, 1976; Sikka, 1980; Alexander *et al*., 1978). The active (break) condition is generally associated with an increase (decrease) of cyclonic vorticity and decrease (increase) of surface pressure over the central Indian monsoon trough region and strengthening (weakening) of the LLJ. Movement of the low-level trough (monsoon trough) to the foothills of the Himalayas during break conditions have been recorded (Ramamurthy, 1969; Raghavan, 1973; Krishnamurti and Bhalme, 1976; Sikka, 1980; Alexander *et al*., 1978). Weakening of the Tibetan anticyclone in the upper atmosphere and extension of a large-amplitude trough in midlatitude westerlies up to northern Indian latitudes are also associated with monsoon breaks (Ramaswamy, 1962).

The dry and wet spells of active and break conditions represent subseasonal or intraseasonal variation (ISV) of the monsoon with timescales longer than synoptic variability (1–10 days) but shorter than a season. Studies have also shown (Dakshinamurthy and Keshavamurthy, 1976; Alexander *et al*., 1978) certain preferred periodicities are associated with the monsoon ISV indicating that certain oscillations (intraseasonal oscillations, or ISOs) are involved in generating ISV. Early studies on monsoon ISV that manifest in active and break cycles were based on station rainfall data and soundings from a few upper-air stations. The availability

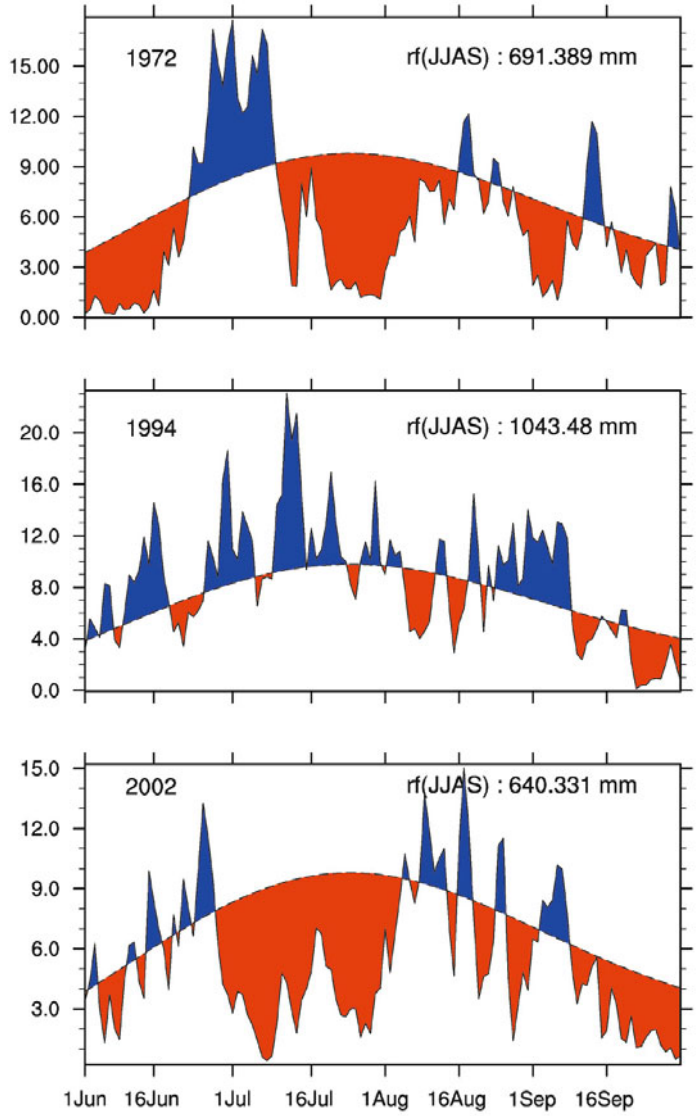

Figure 2.2. Daily rainfall (mm day^{-1}) averaged over 72.5°E–85.5°E and 10.5°N–25.5°N based on high-resolution daily gridded rainfall data (IMD) over the Indian subcontinent during the summer monsoon season for 3 years: 1972, 1994, and 2002. Departures from the mean annual cycle (shown as the envelope) are shaded. Seasonal mean rainfall for each year is also shown in the top-right corners.

of daily satellite cloudiness data and operational analysis in the mid 1970s with global coverage brought new insight regarding the large-scale spatial structure and relationship between the convection and circulation of monsoon ISV. Progress in modeling during the past three decades has also provided new insight regarding the

origin of monsoon ISV. Recently made available gridded daily rainfall data over continental India for more than 50 years (Rajeevan *et al.*, 2006) also helps in bringing out the spatial patterns of anomalies of rainfall associated with different phases of ISV. This dataset has also allowed better delineation of the active and break spells of the Indian monsoon (Rajeevan *et al.* 2010). During this period, we have also learned how monsoon ISOs interact with different scales of motion. At one end of the spectrum, they interact with the annual cycle influencing the seasonal mean, its interannual variability (IAV), and limiting the predictability of the seasonal mean, while at the other end they modulate synoptic activity and cause spatial and temporal clustering of lows and depressions. In this chapter, we attempt to provide a synthesis of the observed spatial and temporal scale of monsoon ISOs, their regional propagation characteristics, relationships with large-scale regional and global circulation, together with a review of theories for their scale selection. The mechanism through which monsoon ISOs influence the seasonal mean and its IAV will also be highlighted. The variety of observations utilized and analysis methodology employed to highlight these different aspects of summer monsoon ISOs are described in the appendix to this chapter (p. 64).

2.1.2 Amplitude and temporal and spatial scales

Distinct from the synoptic disturbances (lows and depressions), the ISOs of monsoons essentially have timescales between 10 and 90 days. In order to get an idea of the amplitude of intraseasonal variability (ISV), it is compared with that of the interannual variability of the seasonal mean and the annual cycle in Figure 2.3. The standard deviation of 10 to 90-day filtered rainfall from GPCP (Figure 2.3a) shows that the amplitude of the ISV is much larger than that of interannual variability of the seasonal mean (Figure 2.3b) and comparable with the amplitude of the seasonal cycle (Figure 2.3c). Thus, the ISV of Asian monsoon rainfall represents a very large–amplitude low-frequency signal. This aspect of monsoon ISV provides some hope for extended range prediction of the active/break spells associated with them (see Section 2.6).

Insight regarding the spatial structure of ISOs and coupling between different variables may be obtained by constructing an index of monsoon ISOs. We construct such an index based on 10 to 90-day bandpass-filtered GPCP precipitation averaged over the box between 70°E–90°E and 15°N–25°N during June 1 and September 30 of each year. The time series normalized by its own standard deviation (2.35 mm day^{-1}) (hereafter referred to as the ISO index) $> +1$ (< -1) represents active (break) conditions as seen from Figure 2.4, where a sample of the ISO index for 10 summer seasons (122 days in each season) is shown.

A lag regression analysis of 10 to 90-day filtered winds from U.S. National Center for Environmental Prediction/National Center for Atmospheric Research (NCEP/NCAR) reanalysis (Kalnay *et al.*, 1996; Kistler *et al.*, 2001) at a number of vertical levels and 10 to 90-day filtered GPCP precipitation with respect to the ISO index brings out the vertical structure and relationship between convection and circulation of the ISV. Simultaneous regressions of GPCP rainfall and 850 hPa

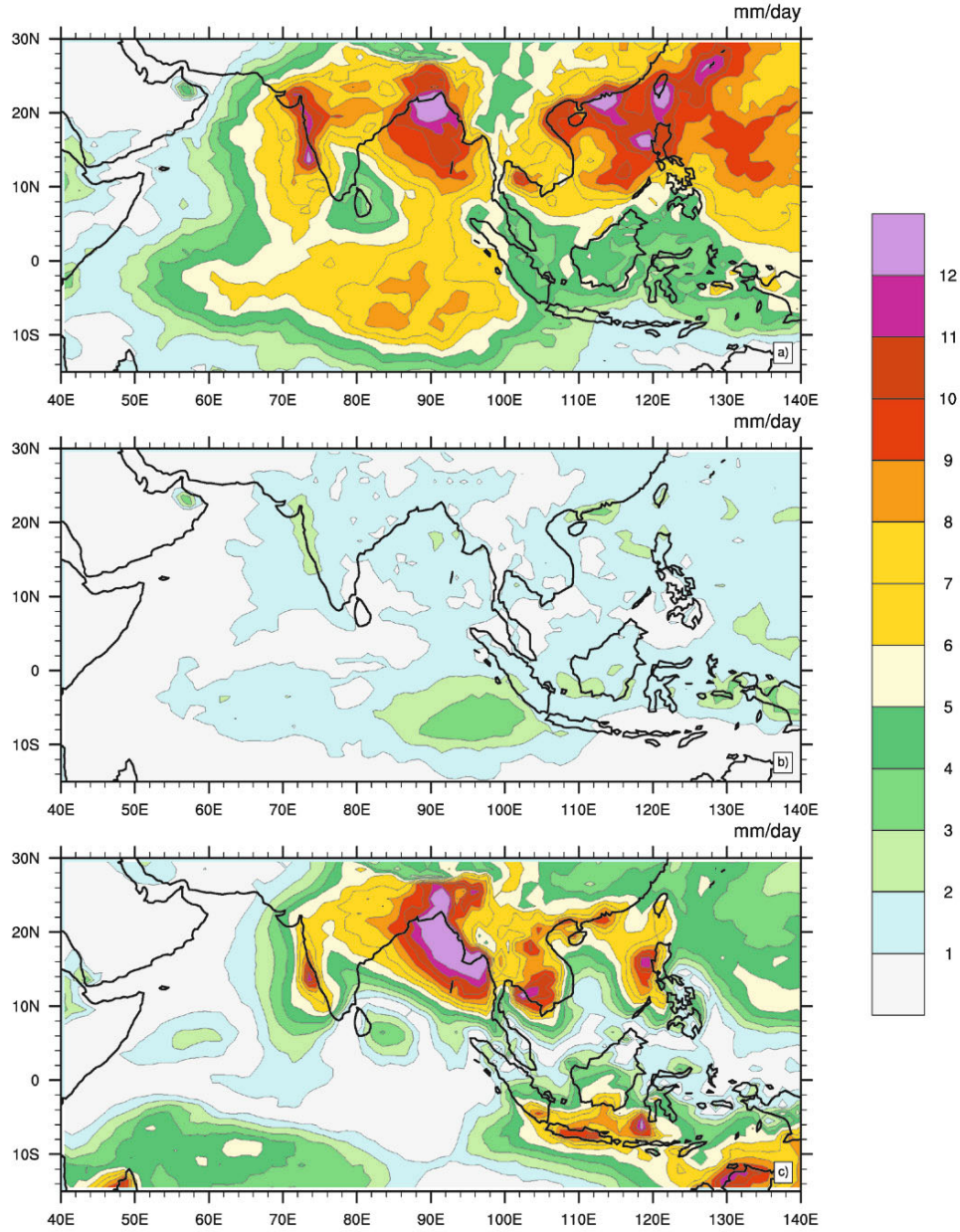

Figure 2.3. (a) Standard deviation of 10 to 90-day filtered GPCP precipitation anomalies (mm/day) based on 1997–2007 JJAS seasons. (b) Standard deviation of IAV of JJAS seasonal mean for the period 1997–2007. (c) Amplitude of the annual cycle. Climatological mean absolute value of the difference between JJAS mean and DJF mean for the 1997–2007 period from GPCP.

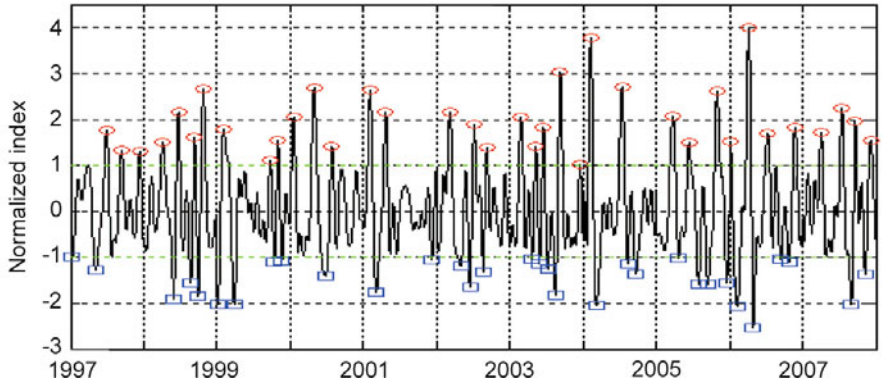

Figure 2.4. Time series of normalized monsoon ISO index between June 1 and September 30 (122 days) for a sample of 11 (1997–2007) summer seasons. The ISO index is defined as 10 to 90-day filtered GPCP rainfall anomaly averaged between 70°E–90°E and 15°N–25°N. The time series is normalized by its own standard deviation. Open circles and squares indicate peaks of active and break conditions, respectively.

winds and those with a lag of 14 days are shown in Figure 2.5a, b. The spatial pattern of precipitation during active and break cycles over the Indian continent corresponds well with active (break) patterns described in other studies (Singh *et al*., 1992; Krishnamurthy and Shukla, 2000; Rajeevan *et al*. 2010). The composite from GPCP within the Indian continent is very similar to that obtained from station data. It also illustrates that monsoon ISV with active/break phases is not confined to the Indian continent but has a much larger spatial scale and is associated with enhanced (decreased) rainfall extending from the western Pacific to the north BoB and central Indian continent. This observation also highlights that ISV during northern summer over the SA monsoon region and ISVs over the East Asian and western North Pacific (EA/WNP) monsoon region are interlinked (see also Chapter 3). One important characteristic of SA monsoon ISV is the north–south dipole in precipitation with active (break) conditions being associated with enhanced (decreased) precipitation over the monsoon trough region and decreased (enhanced) precipitation over the eastern equatorial Indian Ocean (IO) (Goswami and Ajaya Mohan, 2001). Another aspect of the spatial structure of the dominant ISV is a dipole-like structure of opposite sign over the western equatorial Pacific and western North Pacific (Annamalai and Slingo, 2001).

The anomalous meridional circulation associated with active (0 lag) and break (14-day lag) phases are shown in Figure 2.5c, d based on regressions of meridional and vertical velocities with respect to the ISO index averaged between 70°E and 90°E. The low-level wind anomalies associated with ISOs (Figure 2.5a, b) are consistent with a linear response to corresponding precipitation anomalies, indicating that monsoon ISV and active/break conditions are opposite phases of large-scale convectively coupled oscillation. Anomalous Hadley circulation of opposite sign associated with active and break phases shows that regional monsoon Hadley

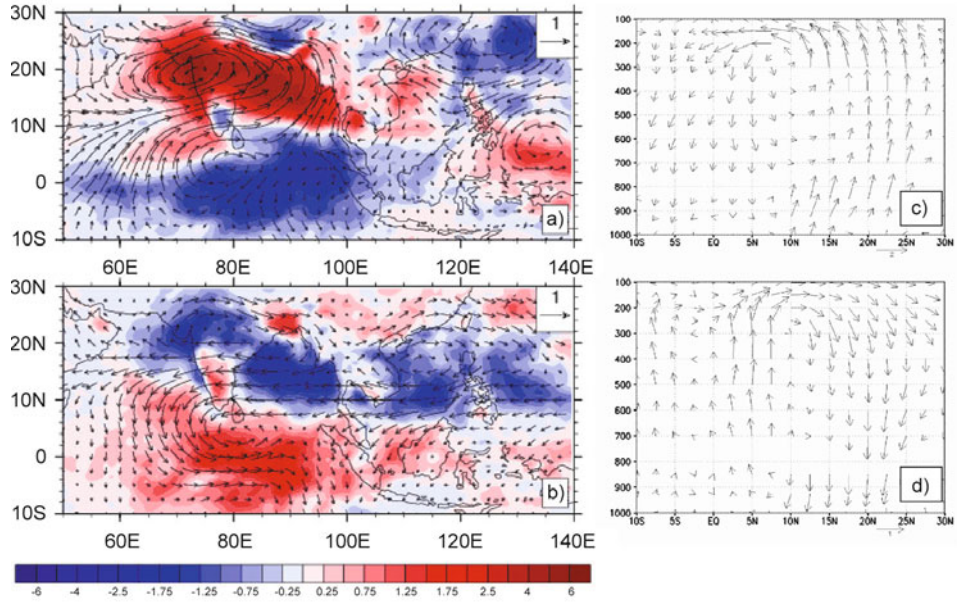

Figure 2.5. Horizontal and vertical structure of dominant ISV. Regressed 10 to 90-day filtered GPCP (shaded, mm day^{-1}) and zonal and meridional wind anomalies at 850 hPa (vectors, m s^{-1}) with respect to the ISO index (Figure 2.4) at (a) 0 lag (active condition) and (b) 14-day lag (break condition). (c) and (d) The anomalous regional Hadley circulation associated with active and break conditions, respectively. Regressed meridional and vertical wind anomalies at a number of vertical levels averaged over 75°E–85°E. Vertical wind anomalies (h Pa s^{-1}) have been scaled up by a factor of 100.

circulation is significantly strengthened (weakened) during the active (break) phase. The anomalous Hadley circulation also indicates a baroclinic vertical structure for monsoon ISV.

Within the broad range of 10 to 90-day periods, two period ranges, with periodicities between 10 and 20 days and 30 and 60 days, respectively, are particularly prominent. Several early studies (Murakami, 1976; Krishnamurti and Bhalme, 1976) showed the existence of a 10 to 20-day oscillation in a number of monsoon parameters. Later studies (Krishnamurti and Ardunay, 1980; Chen and Chen, 1993) show that the 10 to 20-day oscillation is a westward-propagating mode closely related to monsoon active/break conditions. In addition to the 10 to 20-day oscillation, a prominent oscillation with a 30 to 60-day period is seen in monsoon circulation (Dakshinamurthy and Keshavamurthy, 1976), cloudiness, and precipitation (Yasunari, 1979, 1980, 1981; Sikka and Gadgil, 1980). Most of these early studies estimated the spectral peaks based on limited data and, hence, it was not possible to establish the statistical significance of the peaks. The existence of significant power in the two frequency ranges is illustrated in Figure 2.6 where the power spectra of four representative time series are shown. One (Figure 2.6a) is of

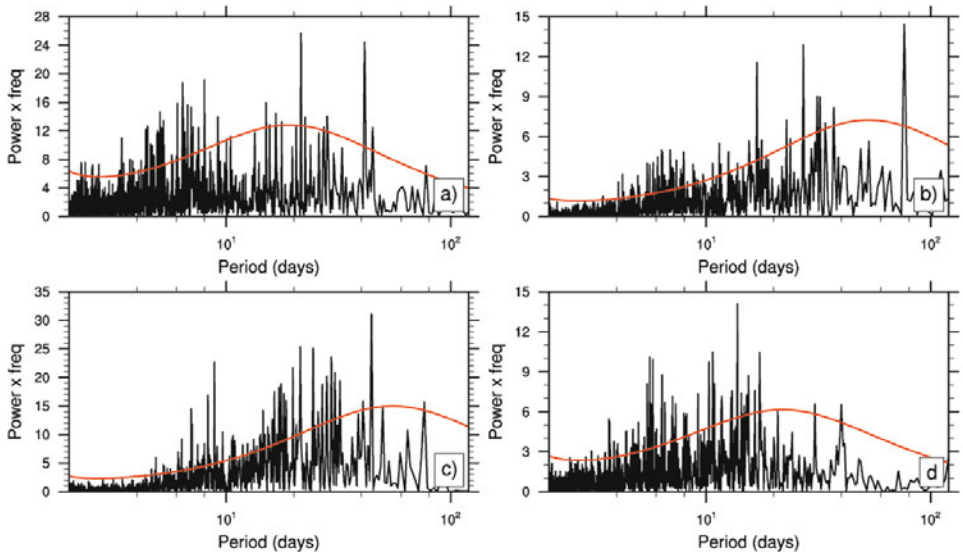

Figure 2.6. Spectrum of (a) rainfall anomalies for 20 (1979–1998) summer seasons (June 1–September 30) from IMD high-resolution gridded rainfall data averaged over 75.5°E–85.5°E and 15.5°N—25.5°N, and (b) zonal wind anomalies at 850 hPa for 20 (1979–1998) summer seasons from NCEP reanalysis averaged over 55°E–65°E and 5°N–15°N (Arabian Sea). (c) Same as (b) but averaged over 85°E–90°E and 10°N–15°N (Bay of Bengal). (d) Same as (b) but for meridional wind anomalies averaged over 80°E–85°E and equator–5°N. Spectra are calculated using the periodogram method and the dotted lines represent a 95% confidence level with respect to a red noise null hypothesis.

daily precipitation anomalies from the raingauge data (Rajeevan *et al*., 2006) averaged over 75.5°E–85.5°E and 15.5°N–25.5°N (central India) for 20 (1979–1998) summer seasons (June 1–September 30) while two others (Figure 2.6b, c) are of daily zonal wind anomalies at 850 hPa from NCEP reanalysis averaged over 55°E–65°E and 5°N–15°N (Arabian Sea, or AS) and over 85°E–90°E and 10°N–15°N (BoB) also for 20 summer seasons, respectively. The last one (Figure 2.6d) is of meridional wind anomalies averaged over 80°E–85°E and equator–5°N. A strong quasi-biweekly period is seen in the precipitation time series (Figure 2.6a) distinct from synoptic variability (period <10 days) and the lower frequency 30 to 60-day mode. Significant power at the 10 to 20-day range is also noted in the two zonal wind time series. It is also noted that the zonal winds at low levels over the BoB (Figure 2.6c) have higher power at this frequency range than those over the AS (Figure 2.6b). The meridional wind over the central equatorial IO (Figure 2.6d) shows prominent power at 10 to 20-day timescales well separated from synoptic disturbances and the low-frequency 40-day mode. There is also significant power at the 30 to 60-day ranges in all the four time series.

To put the role of these two oscillations in the context of variability of full daily anomalies, zonal wind anomalies at 850 hPa between June 1 and September 30 for 20

years were bandpass-filtered to retain periods between 10–20 days and 30–60 days using a Lanczos filter. The ratio between variances of the 10 to 20-day modes and of the 30 to 60-day modes and that of total daily anomalies are shown in Figure 2.7. It may be noted that variance of zonal winds at low level contributed by each of these modes is considerable, ranging between 15% and 25% of total daily variance. However, the importance of the two ISO modes go far beyond these percentages of total daily variance explained, as ISOs strongly modulate the synoptic activity (see Section 2.4) responsible for a large fraction of total daily variability. The global structure of the 30 to 60-day oscillation has been explored in a number of studies (Krishnamurti *et al*., 1985; Knutson *et al*., 1986; Lau and Chen, 1986; Murakami *et al*., 1986; Knutson and Weickmann, 1987; Nakazawa, 1986). In contrast, the spatial structure and propagation characteristics of the 10 to 20-day mode has been addressed only by a few studies (Krishnamurti and Ardunay, 1980; Chen and Chen, 1993; Goswami and Ajaya Mohan, 2001; Chatterjee and Goswami, 2004). It may be noted that the 10 to 20-day and 30 to 60-day ISV is not unique to the SA monsoon. The EA/WNP monsoon also exhibits 12 to 24-day and 30 to 60-day variability during boreal summer (see Chapter 3).

The primary features of the horizontal and vertical structures of the two modes are summarized here. The QBW mode (12–24 days) tends to occur regionally and is found to be associated with monsoons. Kikuchi and Wang (2009) identify three

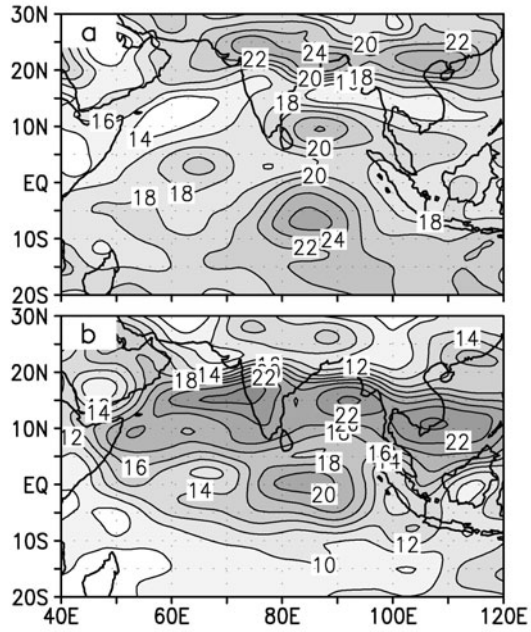

Figure 2.7. Percentage of total daily variance of 850 hPa zonal winds explained by (a) 10 to 20-day mode and (b) 30 to 60-day mode during the summer monsoon season (June 1–September 30) for 20 years (1979–1998).

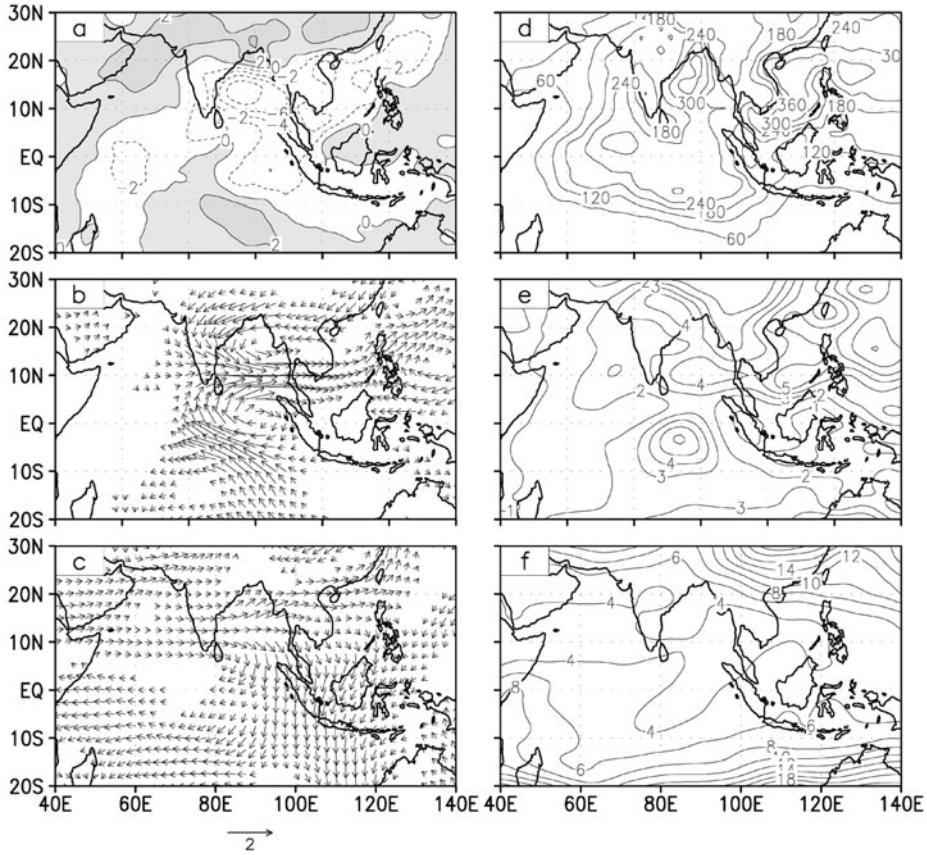

Figure 2.8. Spatial structure and amplitude of the 10 to 20-day mode. Regressed 10 to 20-day filtered anomalies of (a) OLR (in $W\,m^{-2}$), (b) 850 hPa winds, and (c) 200 hPa winds (in $m\,s^{-1}$) with respect to a reference time series of 10 to 20-day filtered zonal winds averaged over 85°E–90°E and 5°N–10°N with 0 lag. Only regressed wind anomalies significant at 95% confidence level are plotted, with a mean variance of 10 to 20-day filtered (d) OLR (in $W^2\,m^{-4}$), (e) 850 hPa, and (f) 200 hPa zonal winds (in $m^2\,s^{-2}$) based on 20 (1979–1998) summers (June 1–September 30).

boreal summer QBW modes in the Asia–Pacific, Central America, and subtropical South Pacific regions. They also find five austral summer QBW modes in the Australia–southwest Pacific, South Africa–Indian Ocean, South America–Atlantic, subtropical North Pacific, and North Atlantic–North Africa regions. The horizontal and vertical structure of the 10 to 20-day mode is illustrated in Figure 2.8. A reference time series is constructed by averaging 10 to 20-day filtered zonal winds at 850 hPa over a box between 85°E–90°E and 5°N–10°N during the summer season (June 1—September 30) for 20 years (1979–1998). The reference box is selected to be in a region of high variance of 10 to 20-day filtered zonal winds at 850 hPa. Lag

regressions with the reference time series of 10 to 20-day filtered zonal and meridional winds at 850 hPa and 200 hPa, together with that of outgoing longwave radiation (OLR) at all gridpoints, are constructed. Simultaneous regressed OLR and wind vector anomalies at 850 hPa and 200 hPa are shown in Figure 2.8a, b, c, respectively. The low-level wind structure of the mode is characterized by two vortices: one centered around 18°N while the other has its center close to the equator around 3°S. It may be recalled that the gravest meridional mode ($n = 1$) equatorial Rossby wave is also characterized by two vortices similar to those in Figure 2.8b, but centered around the equator (Matsuno, 1966; Gill, 1982). It has recently been shown (Chatterjee and Goswami, 2004) that the low-level spatial structure of the mode may be interpreted as the gravest meridional mode ($n = 1$) equatorial Rossby wave with a wavelength of about 6,000 km but shifted to the north by about 5° by the background summer mean flow. The phase of the vortices in the vertical remain the same from the surface up to 200 hPa and change sign around 150 hPa, indicating its vertical structure to have a significant barotropic component (see also Chen and Chen, 1993) together with a baroclinic component. The figure also contains average variance associated with 10 to 20-day filtered OLR zonal winds at 850 hPa and 200 hPa (Figure 2.8d, e, f). Significant fluctuations of OLR (standard deviation of 15–20 $W\,m^{-2}$) and zonal winds at both lower and upper levels (2 $m\,s^{-1}$) are associated with this oscillation. Coherent evolution of the OLR and the circulation anomalies throughout the oscillation indicate that convective coupling is involved with the genesis and propagation of the mode. This is further illustrated in Figure 2.9 where regressed OLR and divergence at 925 hPa averaged over 5°N–15°N are shown as a function of

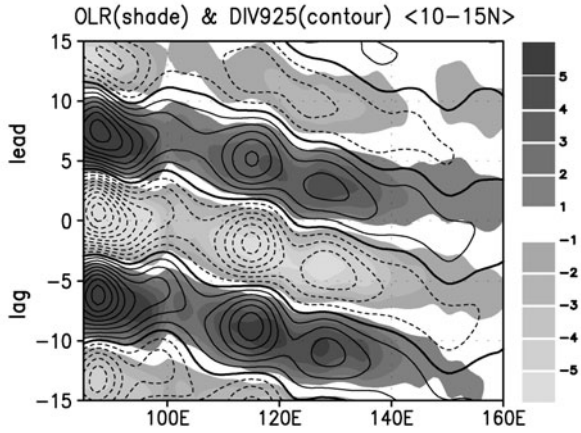

Figure 2.9. Coupling between convection and low-level winds for the 10 to 20-day mode. Lag–longitude plot of regressed 10 to 20-day filtered anomalies of OLR (in $W\,m^{-2}$; shaded) and divergence of 925 hPa winds (contour) with respect to the same reference time series described in Figure 2.8 averaged over 10°N–15°N. Solid (dashed) lines indicate positive (negative) divergence, with a contour interval of $0.1 \times 10^{-6}\ s^{-1}$, and with thick lines showing the zero contour.

longitudes and lags. The close association between boundary layer convergence (divergence) and negative (positive) OLR anomalies is apparent. Also the convergence center being slightly west of the OLR center seems to be responsible for the westward propagation of the mode.

The horizontal structure of the 30 to 60-day mode is studied in a similar manner by constructing a reference time series of 30 to 60-day filtered zonal winds at 850 hPa averaged over 80°E–90°E and 10°N–15°N and calculating lag regressions of 30 to 60-day filtered zonal and meridional winds and OLR everywhere. The simultaneous OLR and vector wind anomalies at 850 hPa and 200 hPa associated with the mode are shown in Figure 2.10a, b, c, respectively. The mean variance associated with the

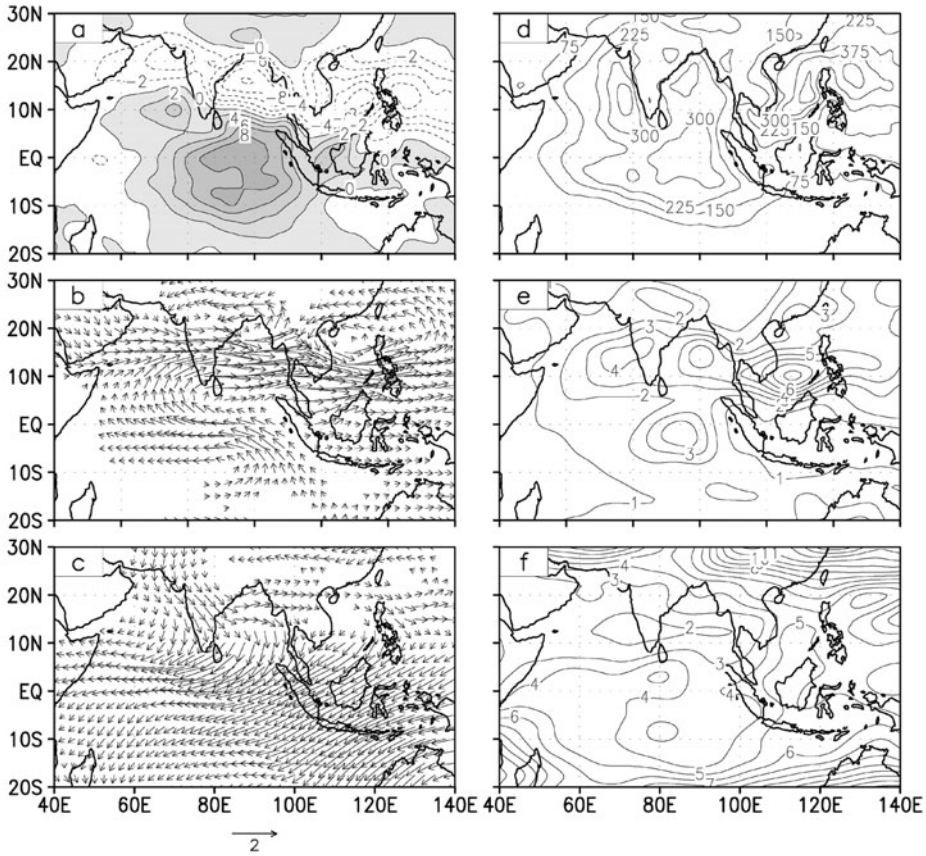

Figure 2.10. Spatial structure and amplitude of the 30 to 60-day mode. Regressed 30 to 60-day filtered anomalies of (a) OLR (in $W\,m^{-2}$), (b) 850 hPa winds, and (c) 200 hPa winds (in $m\,s^{-1}$) with respect to a reference time series of 30 to 60-day filtered zonal winds averaged over 85°E–90°E and 5°N–10°N with 0 lag. Only regressed wind anomalies significant at 95% confidence level are plotted, with a mean variance of 30 to 60-day filtered (d) OLR (in $W^2\,m^{-4}$), (e) 850 hPa, and (f) 200 hPa zonal winds (in $m^2\,s^{-2}$), based on 20 (1979–1998) summers (June 1–September 30).

30 to 60-day filtered OLR and zonal winds at 850 hPa and 200 hPa are shown in Figure 2.10d, e, f, respectively. The spatial structure of OLR and low-level winds associated with the mode are similar to those found in various studies (e.g., Annamalai and Slingo, 2001; Goswami and Ajayamohan, 2001; Webster *et al.*, 1998). The horizontal scale of the 30 to 60-day mode (half-wavelength of about 10,000 km) is much larger than that of the 10 to 20-day mode (Figure 2.8) which is rather regional in character. The other interesting point to note is that the low-level wind anomaly associated with the 30 to 60-day mode (Figure 2.10b) has a structure similar to that of the seasonal mean (Figure 2.10d), strengthening (weakening) the seasonal mean in its active (break) phases. It may also be noted that the horizontal structure of the 30 to 60-day mode around the Indian longitudes is characterized by two vortices of opposite sign flanked on either side of a vortex centered close to the equator, similar to the spatial structure of $n = 2$ equatorial Rossby mode. The difference between the two (e.g., asymmetry in the strength of the northern and the southern vortices and a shift of the vortices to the north) is likely to be due to the modification of the Rossby wave by the summer mean background flow. Comparison of Figure 2.5 and Figure 2.10 indicates that the large-scale structure of active/break conditions seems to come largely from the 30 to 60-day modes. The 200 hPa anomalies associated with the 30 to 60-day mode are opposite to those at low levels but with a tilt to the west. Phase transition takes place (not shown) at around 500 hPa. Therefore, a first baroclinic mode vertical structure emerges for the mode.

In order to gain insight into the spatiotemporal scales associated with boreal summer ISV, spacetime spectra of GPCP rainfall and 850 hPa zonal winds in the east–west direction between 10°S and 25°N are calculated using the procedure followed by Wheeler and Kiladis (1999). The dominant power in both precipitation and low-level winds (Figure 2.11a, b) indicate that the dominant mode with period between 30 and 60 days is eastward propagating with a zonal scale between wavenumbers 1 and 3 and is strongly convectively coupled. To examine the northward propagation characteristics, the spacetime spectra of GPCP rainfall and 850 hPa zonal winds in the north–south direction were also carried out by taking the data between 20°S and 35°N and averaging the spectra between 60°E and 110°E. The dominant mode with period between 30 and 60 days has a strong northward propagation with northward-propagating power between wavenumbers 1 and 3 being nearly four times larger than southward-propagating power of the same wavenumber and frequency band. The strong convectively coupled nature of monsoon ISOs is also demonstrated by Chattopadhyay *et al.* (2008) who show that different nonlinear phases of rainfall ISO can be uniquely identified by a set of dynamical parameters, without explicitly involving rainfall itself.

Coherent evolution of OLR and relative vorticity anomalies at 850 hPa shown in Figure 2.12 over a cycle of the oscillation indicate strong convective coupling for the 30 to 60-day mode also. The evolution of OLR anomalies over a cycle of the 30 to 60-day mode is similar to that found in other studies (e.g., Annamalai and Slingo, 2001) using other methods. One interesting point that emerges from this figure is that

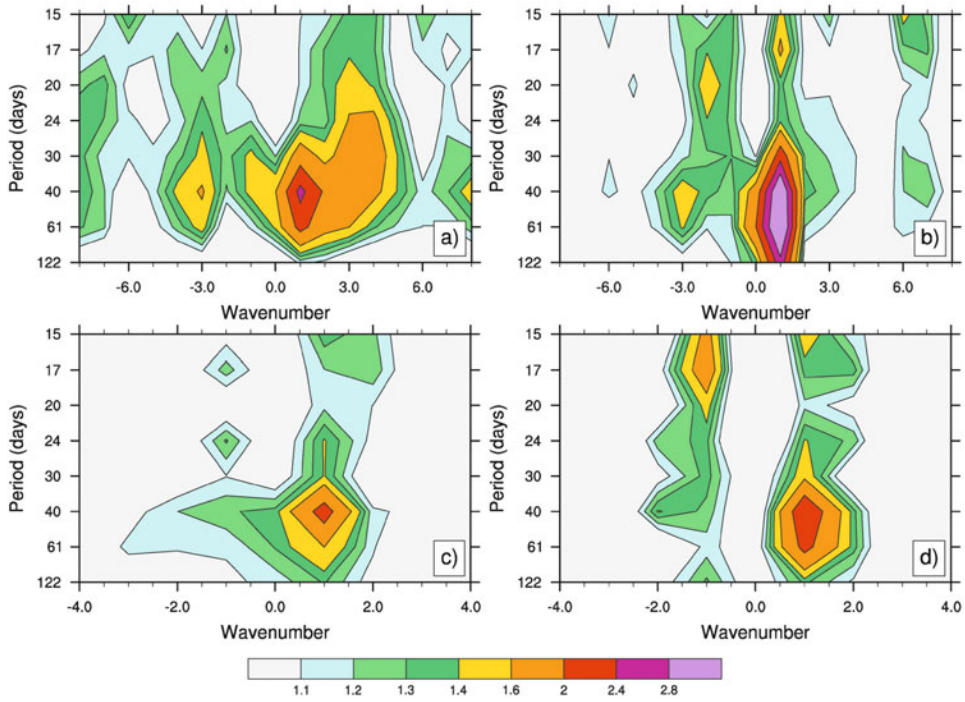

Figure 2.11. Th top panel shows symmetric east–west wavenumber–frequency spectra normalized by its red background calculated for 11 JJAS seasons for the 1997–2007 period calculated using (a) precipitation (GPCP) and (b) U850 anomalies. The bottom panel shows north–south wavenumber–frequency spectra normalized by its red background calculated for 11 JJAS seasons for the 1997–2007 period (60°E–100°E,12.5°S–29.5°N) calculated using (c) precipitation (GPCP) and (d) U850 anomalies.

the 30 to 60-day variability over the SA monsoon region and that over the EA/WNP region (see Chapter 3) during boreal summer is governed by the same 30 to 60-day mode of variability. The main difference being that the phase of northward propagation of the mode in the EA/WNP is shifted with respect to that over the SA monsoon region by about 10 days. The convection first starts in the equatorial IO (day −20) and moves northward to about 10°N (day −10) when convection starts in the south China Sea region. When the convection reaches 25°N in the SA region by day 0, it progresses to about 15°N in the EA/WNP region. Another important point to note is that bands of cyclonic (anticyclonic) relative vorticity at 850 hPa move coherently northward with bands of negative (positive) OLR anomalies with relative vorticity maxima being about 3°N of convection maxima. We shall show later (see Section 2.2.1.1) that this phase relationship between convection and low-level relative vorticity is important for understanding the mechanism of northward propagation of the mode.

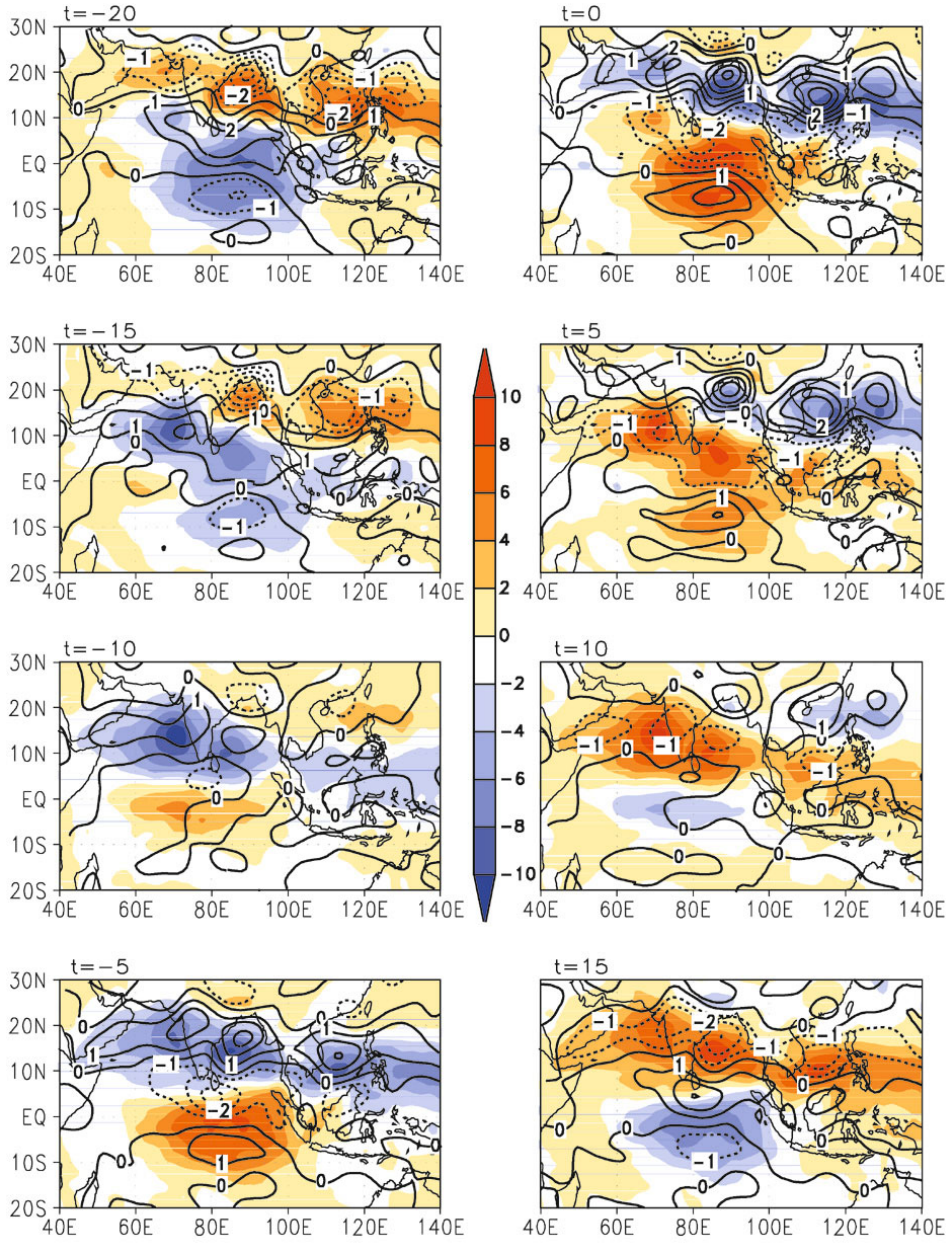

Figure 2.12. Evolution of convection and relative vorticity at 850 hPa over a cycle of the 30 to 60-day mode. Regressed 30 to 60-day filtered anomalies of OLR (in $\mathrm{W\,m^{-2}}$; shaded) and relative vorticity of 850 hPa winds (contour) with respect to the same reference time series described in Figure 2.10 from a lag of 20 days ($t = -20$) to a lead of 15 days ($t = 15$). Solid (dashed) lines indicate positive (negative) relative vorticity, with a contour interval of $1 \times 10^{-6}\ \mathrm{s^{-1}}$, and with thick lines showing the zero contour.

2.1.3 Regional propagation characteristics

The seminal work of Yasunari (1979) and Sikka and Gadgil (1980) led to the discovery that the zonally oriented cloud band of the Tropical Convergence Zone (TCZ) repeatedly propagates northward starting from south of the equator to the foothills of the Himalayas during the summer monsoon season and that the propagation of this cloud band is intimately associated with the active and break cycles of monsoon ISV (Krishnamurti and Subrahmanyam, 1982; Murakami *et al.*, 1984; Webster *et al.*, 1998). In terms of the two modes, northward propagation is primarily associated with the 30 to 60-day mode. Regressed anomalies of relative vorticity based on 30 to 60-day filtered data for 20 summer seasons averaged over 80°E–90°E (Figure 2.13a) illustrate that, on the average, the mode propagates northward north of the equator up to about 25°N and southward south of the equator to about 10°S (not shown). The phase speed of northward propagation is about 1° latitude per day. Similar regressed anomalies averaged between 10°N and 20°N as a function of longitude and lag (Figure 2.13b) indicate a rapid eastward phase propagation at a rate of about $10\,m\,s^{-1}$ for the mode at this latitude belt between 40°E and 80°E and almost stationary in character between 80°E and 140°E. Although the northward propagation characteristics of the mode over Indian longitudes is rather robust, there is considerable event-to-event and year-to-year variability (not shown). In some years (e.g., 1979) there were several

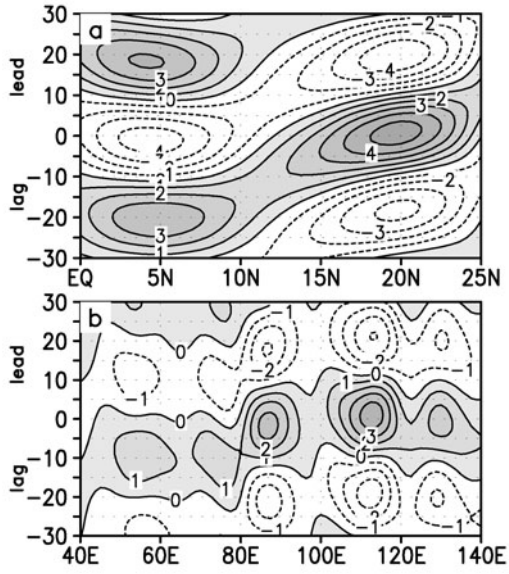

Figure 2.13. (a) Lag–latitude section of regressed anomalies of 30 to 60-day filtered 850 hPa relative vorticity ($10^{-6}\,s^{-1}$) with respect to the same reference time series described in Figure 2.10 and averaged over 80°E–90°E. (b) Lag–longitude section of regressed anomalies of 30 to 60-day filtered 850 hPa relative vorticity ($10^{-6}\,s^{-1}$) with respect to the same reference time series described in Figure 2.10 and averaged over 10°N–20°N.

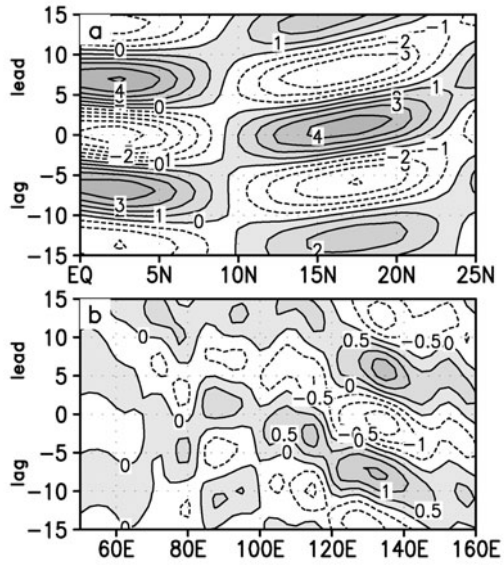

Figure 2.14. (a) Same as Figure 2.12(a), but for the 10 to 20-day mode. (b) Same as Figure 2.13(b), but for the 10 to 20-day mode of regressed anomalies averaged over 5°N–15°N. The reference time series used is the same as that described in Figure 2.8.

regular northward-propagating periods extending up to 25°N while in some other years (e.g., 1981), the northward-propagating periods seem to be terminated at about 15°N. In yet other years (e.g., 1986) there were very few clear northward-propagating periods. While the averaged northward propagation (Figure 2.13a) is a measure of regularity and predictability, it coexists with a certain amount of irregularity that limits the predictability of the mode.

A plot similar to Figure 2.12a for the 10 to 20-day mode (Figure 2.14a) shows that this mode is not associated with any significant northward propagation (Krishnamurti and Ardunay, 1980; Yasunari, 1981; Chen and Chen, 1993). However, the mode is clearly associated with westward propagation from the western Pacific to about 70°E (Figure 2.14b). Both Figure 2.9 and Figure 2.14b indicate that the phase speed of westward propagation is about 4.5 m s^{-1} (Krishnamurti and Ardunay, 1980; Chen and Chen, 1993; Chatterjee and Goswami, 2004). Another point to note from Figure 2.9 and Figure 2.14b is that the 10 to 20-day mode over the SA monsoon region is closely linked with that over the EA/WNP monsoon region during northern summer and that westward propagation from the EA/WNP monsoon region influences the 10 to 20-day variability over the SA monsoon region (Fukutomi and Yasunari, 1999; Annamalai and Slingo, 2001).

2.1.4 Relationship between poleward-propagating ISOs and monsoon onset

SA summer monsoon ISOs are strongly tied up with the annual evolution of the mean monsoon. A notable event in the seasonal evolution of the Indian summer

monsoon is the onset, representing a sudden transition from dry to wet conditions of the annual cycle. Although no objective criterion exists for fixing the date of onset of the SA monsoon, the primary indicator from early days of Indian meteorology has been a sharp and sustained increase in rainfall at a group of stations in Kerala in the southern tip of the Indian continent (Ananthakrishnan *et al.*, 1967). Dramatic changes in some of the regional circulation features are known to occur around the time of the onset (Pearce and Mohanty, 1984; Krishnamurti, 1985; Ananthakrishnan and Soman, 1988a, b; Soman and Krishna Kumar, 1993; Joseph *et al.*, 1994). A dramatic feature of the onset is the sudden increase in precipitation over the monsoon region (70°E–110°E, 10°N–30°N) followed by a sudden increase of the kinetic energy (KE) over the low-level jet (LLJ) region (55°E–65°E, 5°N–15°N) by a factor of 5 to 10. This is illustrated in Figure 2.15 where the northward propagation of precipitation anomalies (from CMAP) averaged over 70°E–90°E together with the KE of winds at 850 hPa averaged over 55°E–65°E and 5°N–15°N for 3 years are shown. Almost invariably, onset of the monsoon is triggered by a poleward-propagating monsoon ISOs. It may also be noted that a northward-propagating ISO pulse in April or early May does not lead to onset. A northward-propagating pulse of convection and precipitation in early May, as in 1979 (also in 1995 and 2002) is often called a bogus onset (Flatau *et al.*, 2001, 2003) and sometimes could be confused as the real onset. The bogus onset is usually associated with a bifurcation of the Madden–Julian Oscillation (MJO) over the BoB. While the dynamic and thermodynamic conditions over the Indian region are not yet ready for the onset, they lead several days later to onset of the East Asian or south China Sea monsoon (Lau *et al.*, 2002) (see also Chapter 3). Real onset is substantially delayed during years with a bogus onset. Delayed onset (as in 1979) or early onset (as in 1984), therefore, depend on the phase of the first pulse of the northward-propagating monsoon ISOs. The interannual variability of the phase of the first monsoon ISO and, hence, that of the onset seems to be related to, among others, sea surface temperatures (SSTs) over the south tropical IO and western equatorial Pacific (Joseph *et al.*, 1994; Flatau *et al.*, 2003).

While the high level of mean KE of the LLJ is maintained by the large-scale non-adiabatic tropospheric heat source that is set up by Tibetan Plateau heating and deep convection over India and the BoB (Li and Yanai, 1996), the fluctuations of total KE of the LLJ within the season are closely related with the intraseasonal fluctuations of precipitation (non-adiabatic heating) over India and BoB. The northward-propagating pulse of precipitation ISOs over India and the BoB in September, however, does not accelerate the LLJ over the AS. This may be understood if we keep in mind that the wind response depends on the spatial structure of the non-adiabatic heat source. The center of non-adiabatic heating moves eastward with the season and is centered around 10°N and 100°E in September due to a decrease of sensible heating over the Tibetan Plateau (Yanai and Tomita, 1998). As a result, the cross-equatorial flow shifts to the central and eastern IO during September and is not reflected in the KE of western IO winds.

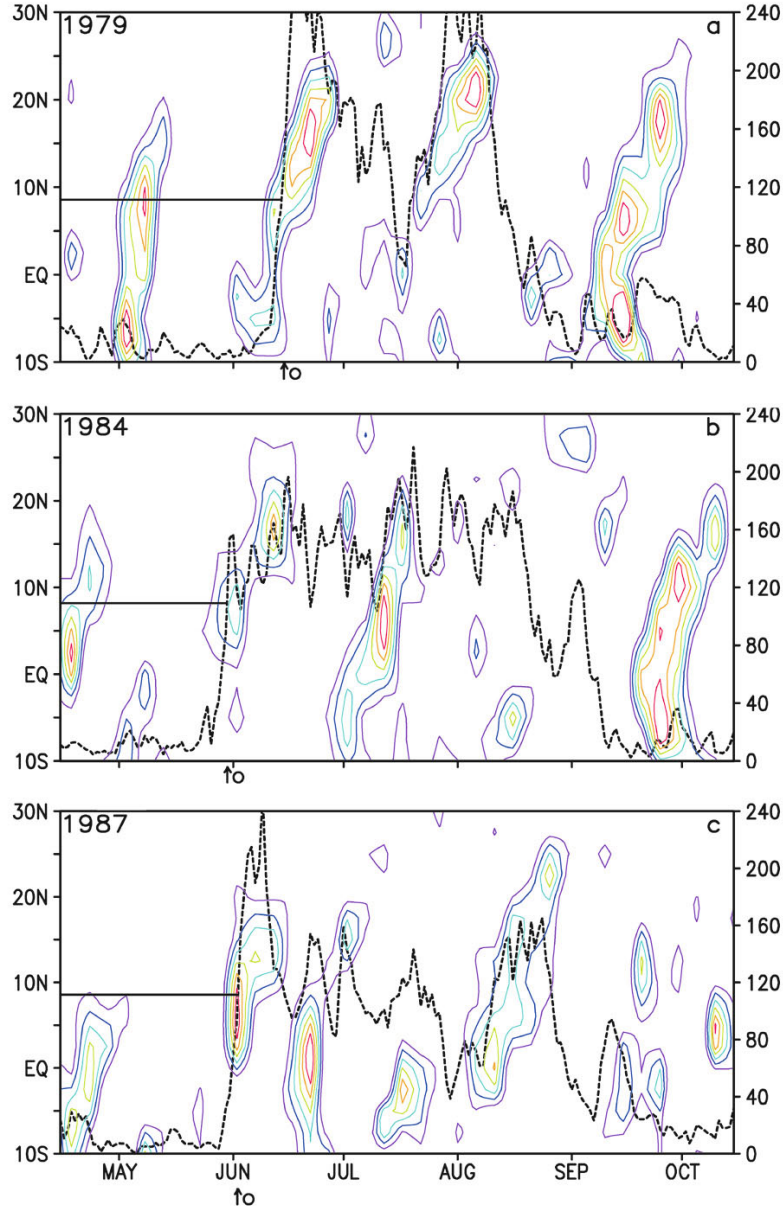

Figure 2.15. Time–latitude section of CMAP anomalies (unfiltered) averaged over 70°E–90°E. Only positive anomalies greater than 2 mm day^{-1} with a contour interval of 2 mm day^{-1} are plotted. Northward-propagating wet spells can be seen. The dashed line shows the evolution of total KE of winds at 85O hPa averaged over the LLJ (55°E–65°E, 5°N–l5°N). The scale for the KE (m s^{-1})^2 is on the right. The latitude of Kerala (southern tip of India) is shown by the horizontal line. The monsoon onset over Kerala is shown by the arrow and roughly corresponds to KE exceeding 100(m s^{-1})^2 and precipitation exceeding 4 mm day^{-1}.

2.1.5 Relationship with the MJO

An oscillation with a period between 30 and 60 days confined around the equator, generally known as the MJO, was discovered in the early 1970s and has since been studied extensively (see Chapters 1 and 7–12 for details). The MJO is strongest during the boreal winter and spring seasons when it appears as an eastward-propagating large-scale system in convection, zonal winds, and upper-level velocity potential (Hendon and Salby, 1994). During boreal summer, while the MJO is typically weaker and more complex in character (Madden, 1986; Madden and Julian, 1994), the northward-propagating monsoon ISO is vigorous. The similarity in temporal character of the two ISOs raises a natural question: Are the two in any way related? This question led some authors (Yasunari, 1979; Lau and Chen, 1986; Madden and Julian, 1994) to suggest that the northward-propagating convection over the Indian monsoon region is related to eastward-propagating clouds along the equator. Tracing all the 122 intraseasonal systems in pentad mean intraseasonal OLR (equivalent to 10 to 90-day filtered) data between 1975 and 1985, Wang and Rui (1990) conclude that almost half of the northward-propagating events during boreal summer were not associated with eastward-propagating equatorial convection (MJOs). Building on the study of Wang and Rui (1990), a comprehensive study based on 24 years of convection data was carried out by Jones *et al.* (2004) using more objective tracking of convection anomalies. They arrived at conclusions similar to those of Wang and Rui (1990) for the summer ISOs. With the higher sample size compared with that of Wang and Rui (1990), they could also study some IAVs of summer ISOs. Using an index of ISV based on the first two empirical orthogonal functions (EOFs) of 25 to 80-day filtered OLR anomalies between 1975 and 1999 (excluding 1978), Lawrence and Webster (2001) conclude that about 78% of northward-moving convection is associated with eastward-moving convection at the equator, although they also found some independent northward-moving events. The discrepancy between their study and that of Wang and Rui (1990) on the fraction of independent northward-propagating events appear to be partly due to the fact that only a small fraction (about 20%) of the total ISO variance is represented by the ISO index of Lawrence and Webster (2001), and partly due to a different criterion being used in the latter study to define independent northward-moving events. While a fraction of boreal summer events are associated with an eastward-propagating MJO, a significant fraction (up to 50%) of them are independent northward-moving events. The northward-propagating character, larger meridional scale, and weaker eastward penetration make summer ISOs distinct from the winter MJO (Jones *et al.*, 2004). As a result, MJO theories may not be sufficient to explain the genesis or northward movement of the full spectrum of summer monsoon ISOs.

Pai *et al.* (2009) examine the association of different phases of the MJO as defined by Wheeler and Hendon (2004) MJO indices (RMM1 and RMM2) with active and break phases of the monsoon over India. While no strong signal has emerged, they find that the initiation as well as the duration of the break phases seem to occur with MJO phases 7, 8, 1, and 2. They also find that possibility for

onset of active events was relatively higher during phases 3 to 6. A new linkage between an eastward-propagating MJO and a northward-propagating summer ISO has come to light recently (Joseph *et al*. 2009), though there is considerable interannual variation of MJO power (with a period between 30 and 60 days and an eastward wavenumber between 1 and 3) during boreal summer. While MJO power is strong during winter and weak during summer, in the summer of Indian monsoon drought years it is found to be as strong as during winter. On the other hand, during the summer of Indian monsoon flood years, eastward-propagating power is even weaker than westward-propagating power (fig. 6 of Joseph *et al*. 2009). During drought years, the MJO triggers an air–sea interaction, leads to a ''long break'', and plays a crucial role in creating the drought.

2.2 MECHANISM FOR TEMPORAL-SCALE SELECTION AND PROPAGATION

As noted in Figure 2.7, both ISOs are significant, each explaining 15% to 25% of daily variability. Although they are not single-frequency sinusoidal oscillations, peak power around the broadband spectrum indicates preferential excitation and amplification around these frequencies. A question naturally arises: What is responsible for the preferential excitation and amplification around these frequencies? Such a mechanism must also explain the very large horizontal scale and northward movement of the 30 to 60-day mode and smaller horizontal scale and westward propagation of the 10 to 20-day mode. We also noted that evolution of circulation is strongly coupled with that of convection and precipitation for both modes. The interaction between organized convection and flow (circulation) must, therefore, be at the heart of explaining not only the basic preferred periodicities but also their propagation characteristics.

2.2.1 30 to 60-day mode

The seasonal mean summer monsoon is characterized by two maxima in rainfall: one over the monsoon trough region between 15°N and 25°N and another in the IO between the equator and 10°S. Both locations are associated with low-level cyclonic vorticity and represent two preferred locations of the TCZ. The oceanic preferred location is associated with an SST maximum (Hastenrath and Lamb, 1979) in the region, and the oceanic TCZ is maintained by the meridional gradient of SST and zonally symmetric dynamics discussed in several studies (Schneider and Lindzen, 1977; Held and Hou, 1980; Goswami *et al*., 1984). The off-equatorial location is along the monsoon trough (MT), a low-level quasi-stationary cyclonic vorticity arising from the interaction of cross-equatorial flow and the Himalayan topography. Cross-equatorial flow is set up by a large-scale pressure gradient due to the large-scale non-adiabatic heating gradient. Tomas and Webster (1997) study the role of inertial instability in maintaining such off-equatorial precipitation when the zero potential vorticity line is located off the equator due to the large-scale north–south

surface pressure gradient. Since the horizontal scale of the 30 to 60-day mode is large and similar to that of the seasonal mean (Figure 2.10), the mode appears as fluctuations of the TCZ between the two preferred locations (Sikka and Gadgil, 1980; Krishnamurti and Subrahmanyam, 1982; Goswami, 1994). The dynamics of the zonally symmetric TCZ, therefore, provide a paradigm for understanding the genesis and northward propagation of the 30 to 60-day mode (Webster, 1983; Goswami and Shukla, 1984; Nanjundiah *et al*., 1992; Srinivasan *et al*., 1993). Webster (1983) simulated northward-propagating ISOs in a zonally symmetric model with land north of 14°N and an advective mixed layer ocean south of it (hereafter referred to as the W-model). The simulated ISOs, however, had a period of about 15 days and, unlike observed ISOs, started from the land–ocean boundary. Using a zonally symmetric version of the GLAS (Goddard Laboratory for Atmospheric Sciences) global circulation model (GCM), Goswami and Shukla (1984) simulate the ISO of the TCZ during northern summer as having a period and northward propagation similar to those observed. The simulated unfiltered precipitation band (fig. 4 in Goswami and Shukla, 1984) starts from about 5°S and has a longer residence time over the northern location of the TCZ, similar to the characteristics of the observed cloud band (Sikka and Gadgil, 1980). They further show that the simulated ISO with a period similar to that observed arises due to an interaction between organized convection and large-scale Hadley circulation. According to their convection–thermal relaxation feedback mechanism, convective activity results in an increase of static stability which depresses the convection itself. Meanwhile, dynamic processes and radiative relaxation decrease moist static stability and bring the atmosphere to a new convectively unstable state.

Gadgil and Srinivasan (1990) and Srinivasan *et al*. (1993) derive additional insight regarding factors responsible for determining the period of the oscillations by experimenting with the W-model. They show that poor simulation of the period of the ISO by the original W-model was due to the model not taking the thermal inertia of land and low moisture holding capacity into consideration. With the W-model modified to include the increased thermal inertia of the land and increased moisture holding capacity (from 10 cm to 30 cm), Srinivasan *et al*. (1993) are able to simulate the observed periodicity of ISOs. The zonally symmetric mixed layer in the W-model had a large cold bias in simulating the meridional structure of SST over the IO region. The prescription of observed SST avoided this bias and allowed simulation of northward propagation of the oscillations from near the equator.

The very large zonal scale compared with the meridional scale of the dominant summer monsoon ISO invited zonally symmetric dynamics to be invoked as an explanation of the genesis and temporal-scale selection. However, these theories do not shed light on the observed zonal phase propagation of a large fraction of the summer ISOs. Therefore, wave dynamics needs to be involved for a fuller explanation of the genesis and phase propagation of ISOs. Krishnan *et al*. (2000) indicate that westward-propagating Rossby waves are important in causing the transition from an active to a break phase of summer ISOs. As the theory for

genesis and eastward-propagating MJO is much better developed (see Chapter 10) in terms of an equatorial convectively coupled Kelvin–Rossby couplet, some attempts have been made (Lau and Peng, 1990; Wang and Xie, 1997) to seek an explanation for scale selection and northward propagation of summer monsoon ISOs within the same framework. Lau and Peng (1990) show that the interaction of eastward-propagating equatorial ISOs with mean monsoon flow can lead to an unstable quasi-geostrophic baroclinic Rossby wave with a wavelength of 3,000 km to 4,000 km over the Indian monsoon region between 15°N and 20°N. As these waves grow, low-level air is drawn northward resulting in rapid northward propagation of the area of deep convection. Based on the results of a modeling study, Wang and Xie (1997) describe summer ISOs as a convection front formed by continuous emanation of equatorial Rossby waves from convection in the equatorial western Pacific. An initial convection cell over the equatorial IO moves eastward as a Kelvin wave and forms Rossby wave cells on either side with a typical scale of 2,000 km to 4,000 km. Feedback from convection and westward propagation of emanated Rossby waves makes the convection front tilt northwestward from the equator to 20°N, resulting in an apparent northward movement. The westward-propagating Rossby waves eventually decay over the AS due to a dry airmass from Africa sinking while a southern cell initiates equatorial perturbation and starts the next cycle. The lifecycle takes about 4 weeks.

Thus, convectively coupled wave dynamics involving a Kelvin and Rossby wave pair can give rise to an ISO with a timescale of 30–40 days. This mechanism is probably responsible for summer monsoon ISOs that are associated with eastward propagation at the equator. A significant fraction of summer ISOs have northward-moving events not associated with eastward-moving equatorial disturbances. Zonally symmetric dynamics is required to explain these summer ISOs as wave dynamics cannot explain the genesis of this fraction of summer ISOs. Thus, both wave dynamics and zonally symmetric physics are required to explain the full range of the summer monsoon 30 to 60-day mode.

2.2.1.1 Mechanism for poleward propagation of the 30 to 60-day mode

As described in Section 1.3, a major characteristic of the 30 to 60-day mode is its poleward propagation. Hence, a considerable amount of literature has been devoted to understanding the poleward propagation of this mode. However, temporal-scale selection and northward propagation are intimately related. Therefore, here we describe how different mechanisms for temporal-scale selection, discussed above, address the question of observed northward propagation of the mode. Webster (1983) propose that the northward gradient of sensible heat flux is responsible for the poleward propagation of the cloud band. Goswami and Shukla (1984) also indicate that ground hydrology feedback may be responsible for northward propagation. Later, Gadgil and Srinivasan (1990) and Nanjundiah *et al.* (1992) show that the northward gradient of moist static stability (the poleward side being more unstable than the equatorward side) is responsible for the poleward propagation of the cloud band. The existence of a meridional gradient of near surface background humidity in this region contributes to the meridional gradient of moist

static stability. While these studies followed a zonally symmetric paradigm and identified some processes that are important for northward propagation, a few other studies (Lau and Peng, 1990; Wang and Xie, 1997) attempted to explain the basic genesis and northward propagation resulting from unstable Rossby waves interacting with the background monsoon mean flow. However, the physical mechanism that led to the northward component of Rossby wave propagation was not clearly identified in these studies. Keshavamurthy *et al.* (1986) also indicate that northward propagation may arise from a zonally symmetric component of an eastward-propagating equatorial oscillation interacting with the mean flow over the Asian monsoon region.

To gain some insight regarding the mechanism responsible for the poleward propagation of the cloud band, a diagnostic analysis is presented here. Lag regression of 30 to 60-day filtered OLR, relative vorticity at 850 hPa, and divergence at 925 hPa with respect to the same reference time series used in Figure 2.10 were carried out. A lag–latitude plot of regression of OLR and 850 hPa relative vorticity averaged over 80°E–90°E are shown in Figure 2.16a, while that for 850 hPa relative vorticity and divergence at 925 hPa are shown in Figure 2.16b. It is seen from Figure 2.16a that, at any given time, cyclonic (anticyclonic) vorticity at 850 hPa is to the north of the negative (positive) OLR anomalies representing cloudy (clear) belts. This is consistent with observations made from Figure 2.12. The cyclonic (anticyclonic) vorticity at 850 hPa is associated with convergence (divergence) of moisture in the boundary layer as seen by the in-phase relationship between the two in Figure 2.16b. Atmospheric circulation driven by diabatic

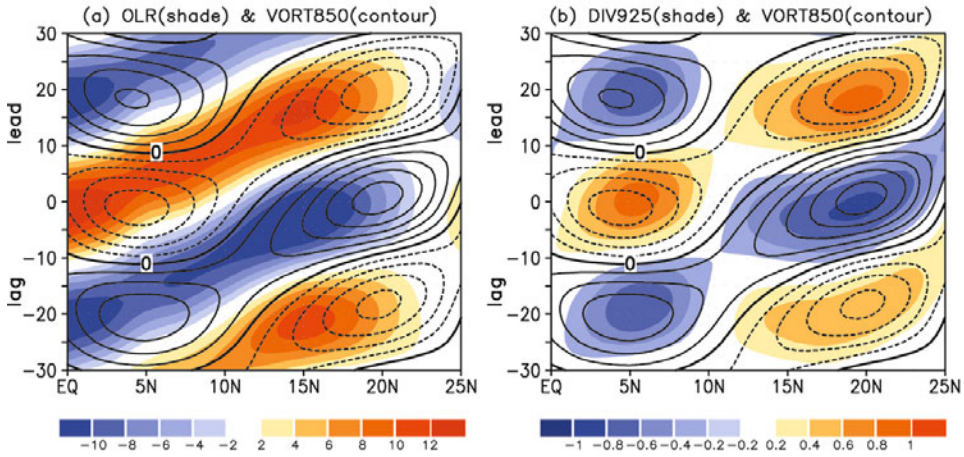

Figure 2.16. (a) Regressed 30 to 60-day filtered anomalies of OLR (shaded; $W\,m^{-2}$) and 850 hPa relative vorticity (contour, positive solid and negative dashed, contour interval $1 \times 10^{-6}\,s^{-1}$) with respect to the reference time series described in Figure 2.10 averaged over 80°E–90°E. (b) Regressed 30 to 60-day filtered anomalies of 850 hPa relative vorticity (contour, positive solid and negative dashed, contour interval $1 \times 10^{-6}\,s^{-1}$) and divergence at 925 hPa (shaded; $10^{-6}\,s^{-1}$) with respect to the same reference time series.

heating (Gill, 1980) associated with the zonally oriented cloud band in the presence of background mean flow with easterly vertical shear produces a cyclonic vorticity with a maximum about 3°N of the center of the cloud band. Cyclonic vorticity drives frictional convergence in the planetary boundary layer and leads to higher moisture convergence north of the cloud band. The meridional gradient of mean boundary layer moisture also helps in making moisture convergence larger to the north of the cloud band. This leads the convection center to move northward. Kemball-Cook and Wang (2001) and Lawrence and Webster (2001) also indicate that the planetary boundary layer convergence maximum, being north of the convection maximum, is responsible for the northward propagation of the summer monsoon 30 to 60-day oscillation. Hsu and Weng (2001) also suggest that a similar frictional convergence driven by low-level vorticity is responsible for the northwestward movement of the EA/WNP monsoon 30 to 60-day oscillations.

The crucial question for northward propagation of the 30 to 60-day mode is to understand what is responsible for producing the low-level vorticity maximum north of the convection maximum. Also, northward propagation takes place from about 5°S, but frictional convergence is ineffective near the equator. Therefore, an alternative mechanism is required to explain northward propagation near the equator. Although several earlier studies (Goswami and Shukla, 1984; Gadgil and Srinivasan, 1990; Nanjundiah *et al.*, 1992), using zonally symmetric dynamics, identified some processes as important for northward propagation of the mode, a clear physical picture had not emerged. Using a simple zonally symmetric model to interpret results from a GCM simulation and observations, Jiang *et al.* (2004) provide a clearer picture of the physical processes responsible for poleward propagation. They proposed that a combination of a vertical windshear mechanism and moisture–convection feedback mechanism is responsible for poleward propagation of the convection band. They showed that easterly mean vertical shear in the region gives rise to the generation of barotropic vorticity to the north of the convection center, which in turn generates barotropic divergence in the free atmosphere north of the convection center. This leads to boundary layer convergence north of the convection maximum. The mean flow and mean boundary layer humidity during the summer monsoon season also allow perturbation moisture convergence to be maximum north of the convection center. Both these processes contribute to poleward propagation of the mode. Near the equator, the moisture–convection feedback mechanism is the dominant mechanism producing poleward propagation. Although this mechanism is essentially based on zonally symmetric dynamics, a similar mechanism may be at work in producing the northward component of the Rossby wave motion in the presence of the background summer mean flow (see Chapter 10).

Bellon and Srinivasan (2006) argue that the f-plane model used by Jiang *et al.* (2004) could not explain scale selection correctly and contended that a linear theory may be sufficient to explain all aspects of northward propagation of BISO. However, Drbohlav and Wang (2005) show that, even in a β-plane model, the northward propagation of BISOs is governed by the mean easterly vertical shear and meridional gradient of low-level mean humidity. The role of these two parameters is further

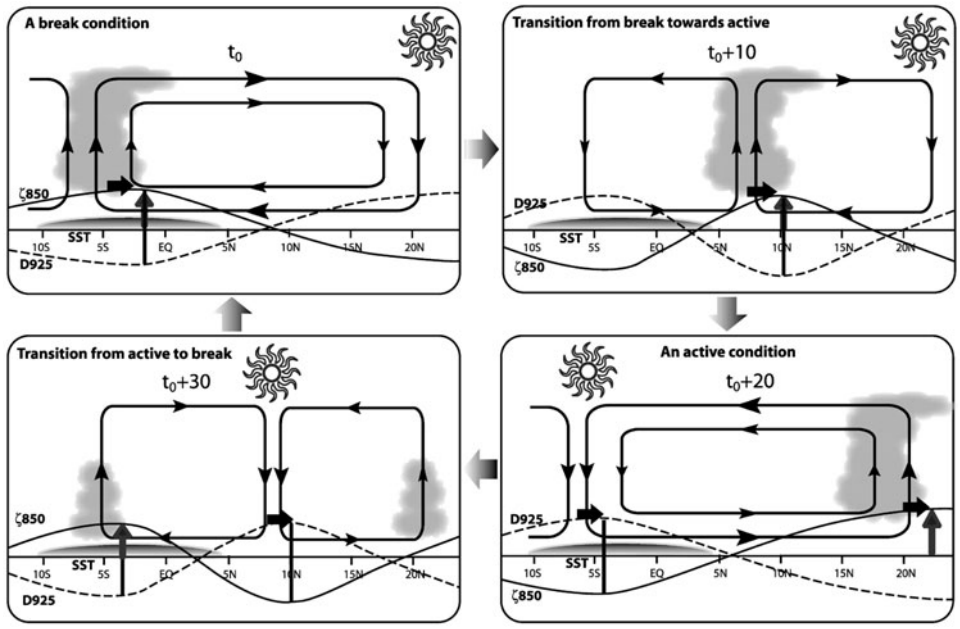

Figure 2.17. A schematic representation of the evolution and northward propagation of the meridional circulation associated with the 30 to 60-day mode in the meridional plane. The thin arrows indicate the anomalous Hadley circulation. The thick vertical arrow indicates the location of the center of boundary layer moisture convergence, while the thick horizontal arrow indicates the direction of poleward motion of the cloud band. The thin solid (dotted) line indicates the phase of relative vorticity at 850 hPa (divergence at 925 hPa) with the positive (negative) phase above (below) the base line. The location of clear sky conditions is shown by the Sun-like symbol.

highlighted by the observation that northward propagation of simulated BISOs in AGCMs and coupled GCMs is strongly linked to the ability of the models to simulate the easterly vertical shear and meridional gradient of low-level humidity (Ajaya Mohan and Goswami, 2007; Ajaya Mohan *et al*. 2010).

Based on understanding the genesis of the large-scale (zonally symmetric) component of the 30 to 60-day mode from modeling studies (e.g., Goswami and Shukla, 1984), and understanding the poleward propagation from diagnostic studies (Figure 2.16) and theoretical analysis (e.g., Jiang *et al*., 2004), the evolution of the mode in the meridional plane over the SA monsoon region is schematically shown in Figure 2.17. The low-level convergence of moisture associated with the SST gradient in a conditionally unstable atmosphere produces organized convection and intensifies the TCZ over the SST maximum over the equatorial IO with subsidence and clear conditions over the MT region (Figure 2.17a). The anomalous Hadley circulation has ascending motion over the oceanic position and descending motion over the MT region. This situation corresponds to a break condition. It is also associated with anomalous cyclonic vorticity over the oceanic location and

anticyclonic vorticity over the MT. Cyclonic vorticity at low levels and the associated boundary layer moisture convergence is maximum north of the zone of maximum convection and makes it move northward (also see Figure 2.16). After about 10 days ($t_0 + 20$, Figure 2.17b) the convection zone reaches about 10°N, with both the MT and oceanic region being under subsidence and clear sky. After another 10 days ($t_0 + 20$, Figure 2.17c), the convection zone reaches the MT zone around 25°N with a divergence maximum slightly north of the anticyclonic vorticity maximum over the oceanic zone (SST maximum). The anomalous Hadley circulation has descending motion over the oceanic position and ascending motion over the MT region. This situation corresponds to an active monsoon condition. During the next 10 days ($t_0 + 30$), the convection over the MT moves farther northward to the foothills of the Himalayas and the clear conditions over the equatorial zone also move northward from 5°S. The decrease in subsidence over the oceanic zone is associated with weak winds, and the continued clear conditions raise the surface temperature as the net heat flux at the surface becomes positive (see also Section 2.3). This acts against subsidence and eventually brings about convection. The convection builds up to become maximum over the oceanic zone in about 10 more days, repeating the cycle.

2.2.2 10 to 20-day mode

In contrast to the considerable attention received by the genesis and scale selection of the summer monsoon 30 to 60-day mode, the 10 to 20-day mode has received very little attention. Having observed that both cloudiness and moist static stability have a quasi-biweekly oscillation, Krishnamurti and Bhalme (1976) propose a mechanism in terms of the cloud–radiation–convection feedback. According to them, the net radiative effect warms up the surface over the MT region under normal summer monsoon conditions and builds up dry and moist static stability of the lower atmosphere. This leads to moist convection, increase in cloud cover, and reduction of solar radiation at the surface. The resultant surface cooling and warming of the middle layer of the atmosphere due to latent heat release associated with the convection stabilizes the temperature profile and cuts down convection. With the dissipation of clouds and increase in solar radiation at the surface, moist instability again builds up and the process can repeat itself. While this is a plausible scenario, Krishnamurti and Bhalme did not demonstrate that the mechanism would preferentially select the quasi-biweekly period. In fact, modeling studies (Goswami and Shukla, 1984; Gadgil and Srinivasan, 1990) indicate that a very similar mechanism leads to the 30 to 60-day oscillation. Chen and Chen (1993) make a comprehensive study of the structure and propagation characteristics of the quasi-biweekly mode (QBM) but did not address the question of scale selection. Using a shallow-water model with a fixed vertical structure and a relaxation timescale for the moisture variable, Goswami and Mathew (1994) propose that the QBM is an unstable mode of the tropical atmosphere driven by the evaporation–wind feedback in the

presence of background westerlies. However, the exact nature of the unstable mode is unclear as the meridional structure is not shown. Also, the zonal wavelength of their most unstable mode is between 9,000 km and 12,000 km, much larger than observed. Chatterjee and Goswami (2004) (hereafter referred to as CG) provide a mechanism for scale selection of the QBM. As shown in Figure 2.8b, c they noted that the horizontal structure of the QBM at low levels resembles that of a first meridional mode ($n = 1$) equatorial Rossby wave with a wavelength of about 6,000 km, but shifted to the north by about 5°. What makes the Rossby wave unstable and affects the selection of observed horizontal scale? A pure $n = 1$ equatorial Rossby wave has two vortices centered around the equator. What is responsible for the northward shift in the structure of the QBM in the meridional direction (Figure 2.8b)? According to CG, the QBM is an equatorial Rossby wave that is driven unstable by convective feedback in the presence of a frictional boundary layer and modified by the summer mean flow.

Using a two-layer atmosphere and a steady Ekman boundary layer with simple parameterization for convective heating, CG showed that convective feedback forced by boundary layer convergence drives an $n = 1$ Rossby wave unstable with maximum growth corresponding to a period of 16 days and a wavelength of 5,800 km. The westward phase speed of the unstable Rossby mode corresponding to this period and wavelength is close to the observed westward phase speed of about 4.5 m s^{-1}. The positive feedback arises from the fact that the baroclinic component of low-level vorticity for the $n = 1$ Rossby wave drives in-phase boundary layer Ekman convergence. As vorticity is in phase with the baroclinic component of potential temperature, latent heat release from boundary layer moisture convergence increases the potential temperature perturbation leading to positive feedback. They noted that turbulent entrainment in the planetary boundary layer is important in achieving the in-phase relationship between convergence in the boundary layer and potential temperature perturbation at the top of the boundary layer. They also demonstrated that inclusion of realistic summertime mean flow in their model results in a shift of the unstable Rossby wave to the north by about 5° without seriously affecting the preferred periodicity and wavelength. The shift of the spatial structure to the north by about 5° can be interpreted as the "dynamic equator" effect. As a free symmetric Rossby wave has the tendency to be centered around background zero absolute vorticity (sum of relative vorticity and Earth's vorticity), the zero background absolute vorticity line may be called the "dynamic equator". The vorticity of background mean flow can make the dynamic equator shift from the geographical equator. It may be noted that low-level summer mean flow makes the zero absolute vorticity line move to about 5°N in the IO/Indonesian region (Tomas and Webster, 1997). The observed shift of the structure of the QBM appears to be due to the shift of the dynamic equator by background mean flow. Thus, this model explains both the scale selection and propagation characteristics of the QBM. It is also shown that the same model may explain the genesis and scale selection of the northern winter QBM observed in the western Pacific.

2.3 AIR–SEA INTERACTIONS

As noted in Section 2.1.2, monsoon ISOs are associated with significant fluctuations of cloudiness and surface winds and, hence, one may expect considerable fluctuations in net heat flux at the surface. What is the amplitude of the net heat flux (Q_{net}) associated with monsoon ISOs? What is the amplitude of intraseasonal SST fluctuations? Do intraseasonal SST fluctuations have a large spatial scale similar to that of atmospheric parameters and Q_{net}? What is the role of SST fluctuations in determining the periodicities and northward movement of monsoon ISOs? We shall attempt to get some answers to these questions in this section.

The first evidence that ISOs involve significant fluctuations of SST and latent heat flux at the interface over the BoB and western Pacific came from Krishnamurti *et al.* (1988) who examined data during 1979 from FGGE (First GARP Global Experiment). While tropical atmosphere and ocean (TAO) moorings in the Pacific have given good data on SST fluctuations associated with the MJO, very little high-resolution direct measurement of SST is available in the IO region. Recent measurements on a few moored buoys by the Department of Ocean Development (DOD) of India (Sengupta and Ravichandran, 2001) have shown large intraseasonal fluctuations of SST and net heat flux over the BoB. Measurements during special field experiments such as BOBMEX (Bhat *et al.*, 2001) and JASMINE (Webster *et al.*, 2002) also show large intraseasonal fluctuations of net heat flux. However, the large-scale structure of ISV of SST was not available, as the IR-based satellite which derived weekly SST (Reynolds and Smith, 1994) was shown to be inadequate to represent observed intraseasonal SST variability (Sengupta and Ravichandran, 2001). With the availability of reliable high-resolution SST measurements using microwave sensors—such as the TMI (TRMM Microwave Imager) on board the TRMM (Tropical Rain Measuring Mission) satellite—it became possible to describe the spatial distribution of ISV of SST over the IO region. Using TMI SST, wind speed, and NOAA OLR data, Sengupta *et al.* (2001) show that an intraseasonal SST oscillation with an amplitude of 0.6°C to 0.8°C has a large horizontal scale similar to that of atmospheric ISOs (Figure 2.5) and possesses northward movement in the region coherent with OLR, surface wind speed, and Q_{net} during the 1998, 1999, and 2000 summer monsoon seasons. Such coherent evolution of 10 to 90-day filtered anomalies of Q_{net}, surface wind speed, precipitation, and SST for the summer season of 2002 is shown in Figure 2.18. The components of net heat flux are estimated using the same formulation used in Sengupta *et al.* (2001). It is noteworthy that the amplitude of interseasonal Q_{net} fluctuations is quite large (70–90 $W\,m^{-2}$). The phase lag between SST and precipitation bands (Figure 2.18, lower panels) is another important aspect of observed summer monsoon ISOs. The warm (cold) SST band follows the dry (rainy) band with a time lag of 7–10 days. Vecchi and Harrison (2002) indicate that this phase relation could be exploited to predict monsoon breaks. The speed of northward movement of SST is the same as that for atmospheric fields but lags behind Q_{net} by about 7 days. The quadrature relationship between SST and Q_{net} indicates that intraseasonal SST fluctuations are essentially being driven by atmospheric ISV through Q_{net}. The quadrature relationship between

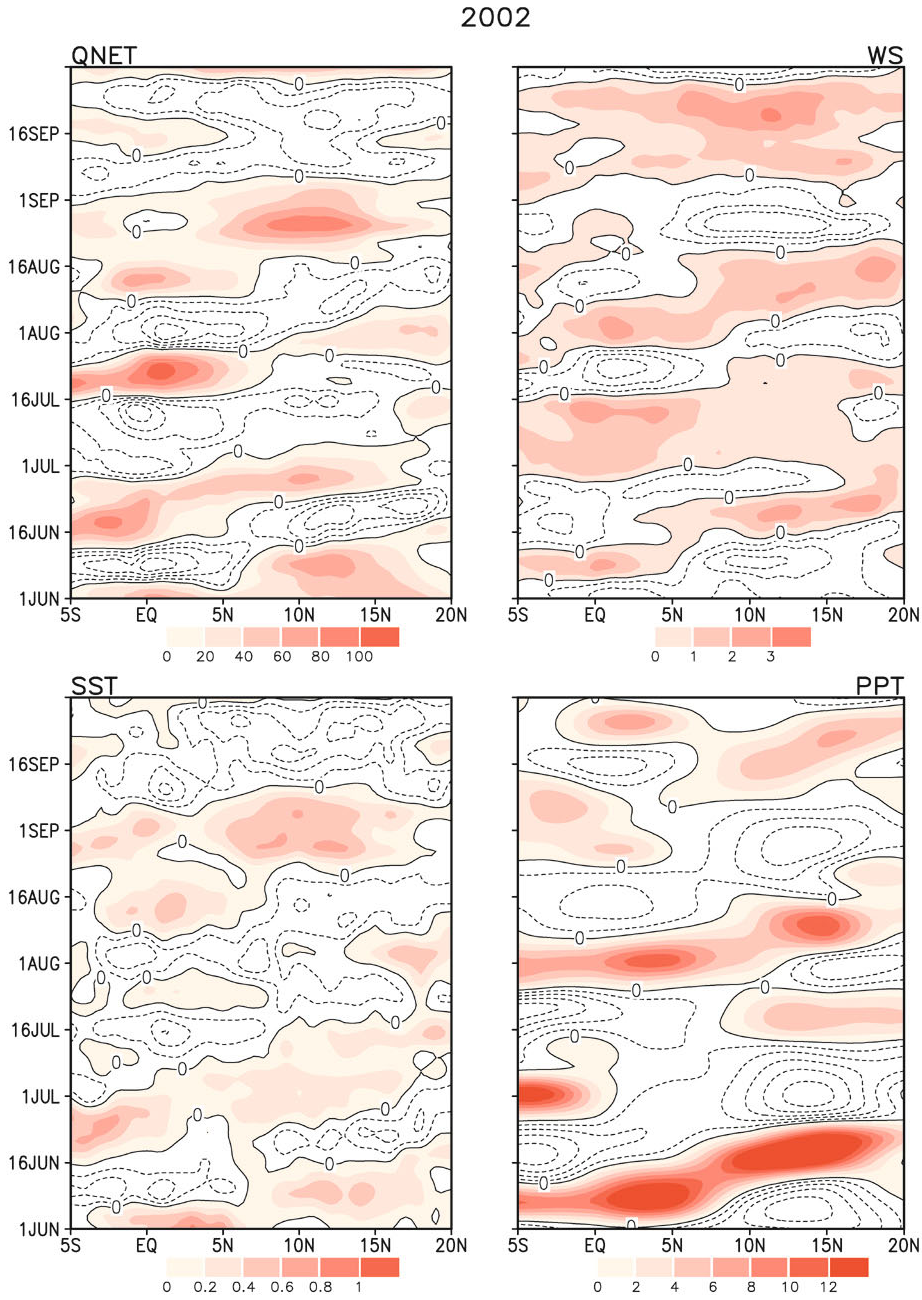

Figure 2.18. Time–latitude section of 10 to 90-day filtered net heat flux (Q_{net}; $W\,m^{-2}$), surface wind speed (WS; $m\,s^{-1}$), SST (°C), and CMAP precipitation (PPT; $mm\,day^{-1}$) for the 2002 summer season averaged over 85°E–90°E. Positive (negative) anomalies are shown with shading (contours). Contour intervals are the same for both positive and negative anomalies.

SST and Q_{net} is not found to hold good over the equatorial IO and the western IO coastal region (Sengupta *et al.*, 2001), where ocean dynamics also seems to play a role in determining SST. Waliser *et al.* (2003b) study an ocean model with a mixed layer using the daily wind stresses and heat fluxes associated with atmospheric ISOs. While the net heat flux associated with ISOs is a major forcing, they found that mixed layer depth (MLD) variations tended to contribute positively to SST variations. Further, contributions from advection and/or entrainment within the Somali Current region and equatorial IO are significant.

From the above discussion, it is clear that atmospheric ISOs do force ISO in SST over the IO. However, the role of intraseasonal fluctuations of SST in determining either the scale selection or northward movement of Asian monsoon ISOs is unclear. Is air–sea coupling crucial for the existence of observed ISOs? Air–sea coupling is certainly important for observed summer ISOs as the quadrature phase relationship between atmospheric convection (or precipitation) and SST cannot be simulated by an AGCM forced by observed daily SST (Wu *et al.*, 2002; Fu *et al.*, 2003). Although intraseasonal variations of SST in this region may act almost like a slave to atmospheric ISV, the coupling between ocean and atmosphere is essential to simulate the correct phase relationship between convection and SST. This was demonstrated by Fu *et al.* (2003) when they coupled an AGCM to a relatively simple ocean model without flux corrections and were able to simulate the observed period, northward movement, and phase relationship between precipitation and SST reasonably well. When the AGCM is forced by daily SST from the coupled run, the AGCM-simulated precipitation band is in phase with SST. Several recent studies (Rajendran *et al.*, 2004; Zheng *et al.*, 2004; Rajendran and Kitoh, 2006; Pegion and Kirtman, 2007) compared simulation of a coupled GCM (CGCM, an AGCM coupled to an OGCM) with simulations of the AGCM forced by CGCM SSTs, and found that the coupling not only improves simulation of the spatial structure of the summer ISOs, but also is essential in simulating the observed quadrature relationship between precipitation and SST. Fu *et al.* (2007) using a hybrid coupled ocean–atmosphere model show that atmospheric ISO forces coherent SST fluctuations in the ocean which in turn provides external forcing for atmospheric ISO, making it more coherent. They further show that such coupling can lead to enhancement of the limit on potential predictability of the ISO by 7 days. Is the air–sea interaction crucial for the existence of summer ISOs? As discussed in Sections 2.1 and 2.2, the theories of atmospheric ISOs indicate that the basic temporal-scale selection and northward propagation of atmospheric summer ISOs arise from internal feedback within the atmosphere. Several AGCMs forced by prescribed SST exhibit ISV levels at or above those found in observations with spatial patterns that resemble the observed pattern (Kemball-Cook and Wang, 2001; Waliser *et al.*, 2003b; Jiang *et al.*, 2004; Klingaman *et al.* 2008; Liu *et al.* 2009) and include some form of northward propagation. This also supports the hypothesis that the basic oscillation and northward propagation may be of internal atmospheric origin. Air–sea interactions can modify these internally triggered oscillations in amplitude, frequency domain, and northward propagation characteristics. Kemball-Cook and Wang (2001) find that air–sea coupling enhances northward propagation of summer

ISOs significantly. Waliser *et al.* (2004) find that air–sea coupling also improves the spacetime characteristics of summer ISOs over the IO. Fu *et al.* (2002) also find that ocean–atmosphere coupling improves simulation of the amplitude and northward propagation characteristics of ISOs. However, some of these results could be influenced by mean state bias of individual components of the coupled model. Therefore, quantitative estimation of modification of summer ISOs by air–sea coupling is still not well established. One particular aspect of the air–sea interaction that is still not clear from all these studies is how the ISV of SST feeds back to the convective activity of the atmosphere and modifies ISO characteristics. Modeling of air–sea interactions associated with northern summer monsoon ISOs is still in its early days. More studies are required to unravel the quantitative role played by the SST in determining the amplitude and phase propagation of monsoon ISOs.

2.4 CLUSTERING OF SYNOPTIC EVENTS BY ISOS

The modulation of synoptic activity by the large-scale circulation anomalies associated with the MJO has been demonstrated by Liebmann *et al.* (1994) and Maloney and Hartmann (2000). The horizontal structure of low-level winds associated with the summer monsoon 30 to 60-day mode (Figure 2.10b) also has large scales and is similar to that of the seasonal mean (Figure 2.1e). Therefore, the meridional shear of low-level zonal winds and cyclonic vorticity at 850 hPa are significantly enhanced (weakened) during an active (break) phase of ISOs. Hence, conditions for cyclogenesis are much more favorable during an active phase than a break phase. Similar to the MJO, do monsoon ISOs modulate synoptic activity in the region during northern summer? Using genesis and track data for low-pressure systems (LPSs) for 40 years (1954–1993), Goswami *et al.* (2003) show that the genesis of an LPS is nearly 3.5 times more favorable during an active condition (147 events corresponding to normalized index $> +1$) than with a break condition (47 events corresponding to normalized index < -1) of monsoon ISOs. They also show that LPSs are spatially strongly clustered to be along the MT region under active conditions (Figure 2.19). Day-to-day fluctuations of precipitation are essentially governed by synoptic activity. As synoptic activity is clustered in time and space by ISOs, a prediction of ISO phases about 3 weeks in advance may allow one to also predict the probability of high (low) rainfall activity with such a lead time. Using daily rainfall data and LPS data during 1901–1970, Krishnamurthy and Shukla (2007) find that seven times more depressions occur during active phases than during break phases. A more detailed analysis of the association between different phases of monsoon ISOs and LPSs has recently been carried out by Krishnamurthy and Ajaya Mohan (2010) using data over a longer period (1901–2003).

Due to the much larger horizontal scale of monsoon ISOs and the MJO compared with that of synoptic disturbances, all these studies (Liebmann *et al.*, 1994; Maloney and Hartmann, 2000; Goswami *et al.*, 2003) argue that the collective effect of randomly occurring synoptic disturbances could not influence the structure of ISOs significantly. However, a recent study by Straub and Kiladis (2003) indicates

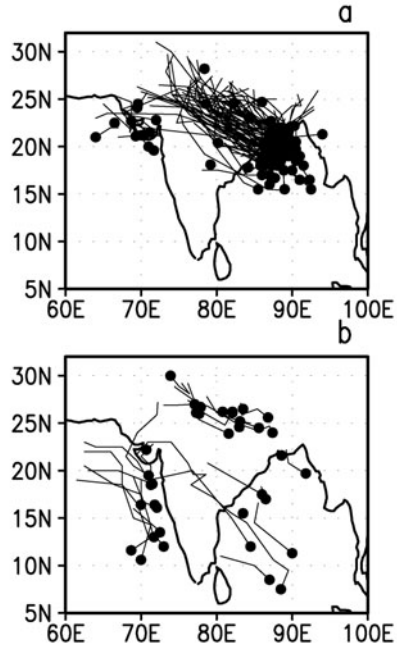

Figure 2.19. Tracks of LPSs for the period 1954–1983 during extreme phases of monsoon ISOs. (a) Active ISO phase (MISI $> +1$) and (b) break ISO phase (MISI > -1). The MISI (monsoon ISO index) used here is the 10 to 90-day filtered relative vorticity during the summer monsoon season (June 1–September 30) averaged over 80°E–95°E and 12°N–22°N. Dark dots represent the genesis point and the lines show their tracks. Large number of LPSs during the active phase are strongly clustered along the MT. The few LPSs that form during breaks clearly avoid the MT region and form either near the foothills of the Himalayas or off the western coast and move westward (after Goswami *et al.*, 2003; © American Geophysical Union).

that westward-propagating mixed Rossby–gravity wave–tropical disturbance (MRG-TD) type synoptic disturbances may have some influence on the structure of summer ISOs.

2.5 MONSOON ISOS AND PREDICTABILITY OF THE SEASONAL MEAN

The prediction of summer monsoon rainfall at least one season in advance is of great importance for the agro-based economy of the region. For over a century, attempts have been made to predict seasonal mean monsoon rainfall using statistical methods involving local and global antecedent parameters that correlate with monsoon rainfall (e.g., Blanford, 1884; Walker, 1923, 1924; Gowarikar *et al.*, 1989; Sahai *et al.*, 2003; Rajeevan *et al.*, 2004). Linear or nonlinear regression models as well as

neural network models (Goswami and Srividya, 1996) indicate a degree of skill when the monsoon is close to normal (about 70% of years over the past 130-year period) but fails to predict the extremes with a level of skill that is useful. Almost all statistical models failed to predict the droughts of 2002, 2004, and 2009. Delsole and Shukla (2002) argue that regression models with many predictors (e.g., the 16-parameter model of the Indian Meteorological Department; Gowarikar *et al.*, 1989) may possess a degree of artificial skill and often regression models with two or three parameters produce better forecasts on average than regression models with multiple predictors. Thus, the usefulness of statistical models is limited. A series of sensitivity studies (Charney and Shukla, 1981; Shukla, 1981, 1987; Lau, 1985) have shown that the tropical climate is, in general, much less sensitive to initial conditions and, hence, more predictable than the extratropical climate. These studies laid the foundation for deterministic climate prediction in the tropics, and dynamical prediction of the seasonal mean monsoon using state-of-the-art climate models appears to be a logical alternative to statistical prediction. Although climate models have improved significantly over the years in simulating mean climate, they still do not have a higher level of skill than statistical models in predicting the seasonal mean monsoon (Kang *et al.*, 2002b; Wang *et al.*, 2004). Almost all present day climate models have serious difficulty in simulating the seasonal mean monsoon climate and its interannual variations (Sperber and Palmer, 1996; Gadgil and Sajani, 1998; Kang *et al.*, 2002a, b; Wang *et al.*, 2004). Even though the climates of certain tropical regions show very little sensitivity to initial conditions (e.g., Shukla, 1987), the Indian summer monsoon appears to be an exception within the tropics and appears to be quite sensitive to initial conditions (Sperber and Palmer, 1996; Sperber *et al.*, 2001; Krishnamurthy and Shukla, 2001), making it probably the most difficult climate system to simulate and predict.

What makes the Indian monsoon such a difficult system to simulate and predict? The sensitivity of the monsoon climate to initial conditions indicates the existence of significant internal low-frequency (LF) variability in the monsoon region (Goswami, 1998). The predictability of the monsoon is going to be determined by the extent to which internal LF variability governs the IAV of the monsoon. What is responsible for such internal LF variability in the monsoon region? We recall (see Section 2.2) that monsoon ISOs arise due to the internal dynamical feedback between organized convection and large-scale circulation with the possibility of SST coupling playing a role. Could monsoon ISOs lead to any significant LF internal variability? If they do, that part of monsoon IAV would be unpredictable. Ajaya Mohan and Goswami (2003) make estimates of the internal IAV of circulation based on daily data from NCEP–NCAR reanalysis for more than 40 years and convection data for more than 20 years, and show that almost all internal IAV in the tropics arises from ISOs. Hoyos and Webster (2007) also find that a proportion of the interannual modulation of monsoon rainfall is the direct result of the cumulative effect of rainfall variability on intraseasonal (25–80 day) timescales.

How do ISOs influence the seasonal mean and its IAV? We noted in Section 2.1.2 that the spatial structure of the 30 to 60-day mode (Figure 2.10) is similar to that of the seasonal mean (Figure 2.1), strengthening (weakening) the seasonal mean

in its active (break) phases. As shown in Figure 2.20, the ISV and IAV of the Asian monsoon are, in fact, governed by a common spatial mode of variability (Fennessy and Shukla, 1994; Ferranti *et al*., 1997; Goswami *et al*., 1998; Goswami and Ajaya Mohan, 2001; Goswami and Xavier, 2005). As the horizontal structures of ISOs and the seasonal mean are similar, there is a higher probability of active (break) conditions within a season resulting in a stronger (weaker) than normal monsoon. If monsoon ISOs were a single-frequency sinusoidal oscillation, this could not happen. However, due to the existence of a band of frequencies, ISOs are rather quasi-periodic and hence there is ahigher probability of active (break) phases within a season taking place. Goswami and Ajaya Mohan (2001) and Goswami *et al*. (2006) show that a strong (weak) Indian monsoon is associated with the higher probability of occurrence of active (break) conditions. Sperber *et al*. (2000) also show that the ISV and IAV of the Asian monsoon are governed by a common mode of spatial variability and that strong (weak) monsoons are associated with a higher probability of occurrence of active (break) conditions. In a series of interesting studies, Krishnamurthy and Shukla (2007, 2008) examine how ISOs influence the seasonal mean and—using multi-channel singular spectrum analysis—were able to separate the seasonally persisting component of ISV that influences the seasonal mean. Further work is required to elucidate the origin of the seasonally persisting component of ISV. Is it a result of nonlinear interaction between the oscillatory components of ISV as well as of higher frequency oscillation? Or, is it driven by some slowly varying external forcing? The fact that ISV influences the seasonal mean and its predictability is a conclusion reached by Waliser *et al*. (2003b), who compare simulation of the seasonal mean and ISV using a number of AGCMs and find that higher ISV is associated with higher intra-ensemble variance (internal variability) and poorer predictability of the seasonal mean.

The predictability of the seasonal mean monsoon is governed by the relative contribution of slowly varying external components of forcing (such as that associated with the ENSO) and internal variability to the observed IAV of the monsoon. High (low) predictability is associated with a higher (lower) contribution of external forcing to the IAV than that from internal variability. How much of the total IAV of the Asian monsoon is actually governed by LF internal variability? Estimates made using AGCMs (Goswami, 1998; Goswami and Xavier, 2005) and using long observations (Ajaya Mohan and Goswami, 2003) indicate that about 50% of the total IAV of the Asian monsoon is governed by the internal component coming primarily from ISOs. Thus, ISOs make the Asian monsoon a difficult system to predict by making the unpredictable noise comparable with the externally forced predictable signal. For many years, a consensus on the fraction of total IAV of the Indian monsoon governed by ISOs was lacking. However, a consensus towards what is concluded here is slowly evolving. Therefore, the seasonal mean summer monsoon will remain a difficult system to predict. Clever methods will have to be devised to simulate and identify the weak signal from a background of noise of comparable amplitude. The prospect of predicting the seasonal mean monsoon would have improved if the statistics of summer ISOs were strongly modulated (or constrained) by slowly varying forcing (such as that associated with the ENSO). Modeling studies

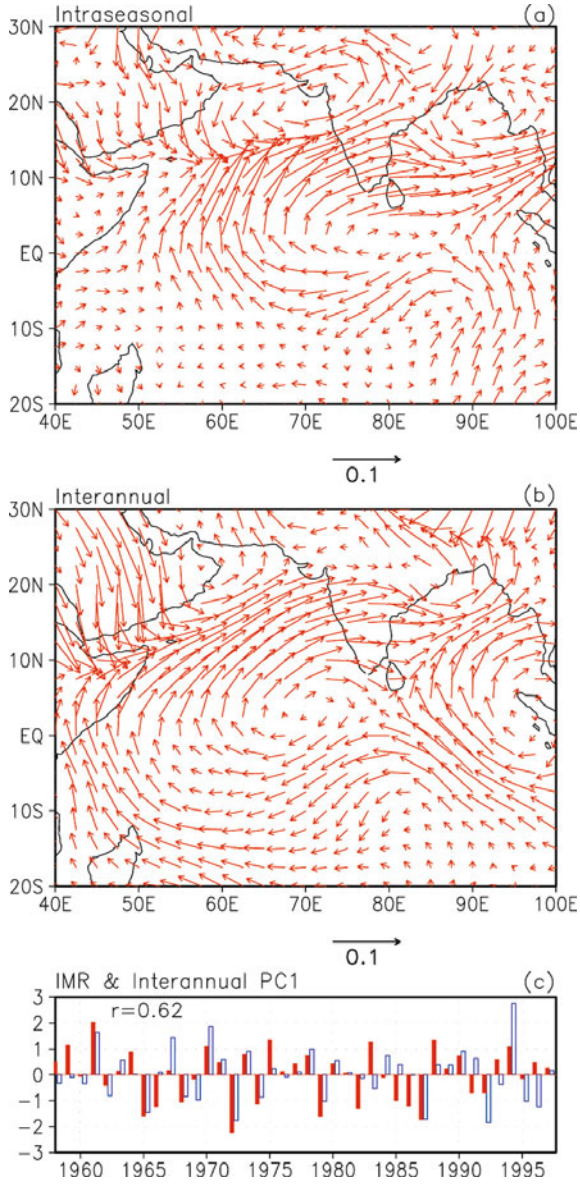

Figure 2.20. First EOF of intraseasonal and interannual 850 hPa winds. (a) Intraseasonal EOFs are calculated using ISO-filtered winds for the summer months (June 1–September 30) for a period of 20 years (1978–1997). (b) Interannual EOFs are calculated using seasonal mean (JJAS) winds for a 40-year period (1958–1997). The units of vector loading are arbitrary. (c) Relation between all India monsoon rainfall (IMR; unfilled bars) and interannual PC1 (filled bar). Both time series are normalized by their own standard deviation. Correlation between the two time series is shown ((a) and (b) are from Goswami and Ajaya Mohan, 2001; (c) is copyright © of the American Meteorological Society).

so far, however, indicate that summer monsoon ISOs over the Asian monsoon region are not sufficiently influenced by the slowly varying SST changes associated with the ENSO.

2.6 AEROSOLS AND MONSOON ISOS

An emerging area of interest is the interaction between aerosols and monsoon ISOs (MISOs). The Asian monsoon region is known to have high concentrations of natural as well as anthropogenic aerosols that significantly influence the regional climate through direct radiative forcing (Jayaraman, 2001; Pandithurai *et al*., 2008; Ramanathan and Carmichael, 2008). Some studies (Ramanathan *et al*., 2005) indicate that aerosols may lead to weakening of the seasonal mean Indian monsoon through cooling the land and weakening the north–south surface temperature gradient. Some other studies (e.g., Lau *et al*. 2006), on the other hand, indicate that—due to the absorbing nature of some aerosols—the Indian monsoon may strengthen through the elevated heat pump mechanism. While considerable attention has been paid to address how aerosols may influence the seasonal mean monsoon (Meehl *et al*., 2008; Collier and Zhang, 2009), not many studies have addressed the issue of how aerosols might influence monsoon ISOs and vice versa. There is, however, the basis to think that aerosols and MISOs may interact with each other. MISOs can give rise to significant oscillation of aerosol concentrations as a result of the washout effect during active phases and to accumulation and buildup during break phases. In addition to surface cooling over land during a break phase, warming of the atmosphere in the 1 km to 3 km layer due to absorbing aerosols could affect the stability of the atmosphere and influence the transition to active phase and, hence, the periodicity of MISOs.

In a recent study, Manoj *et al*. (2011) show that the aperiodicity of MISOs—associated with the fact that some long breaks go over to an active spell while many other long breaks do not transit to an active spell—may be related to an interaction between absorbing aerosols and ISO circulation. It is shown that breaks that are followed by active conditions (BFA cases) are characterized by a much higher concentration of absorbing aerosols (AI index) compared with breaks that are not followed by active (BNFA cases) conditions (Figure 2.21a–c). The circulation associated with BFA allows desert dust to be transported (see Manoj *et al*., 2011) and helps the accumulation of locally generated absorbing aerosols (such as black carbon) while that associated with BNFA cases not only does not allow transport from west to northwest but also allows the locally generated aerosols to be transported out of central India (Figure 2.21d–f). The difference in the circulation in the two types of breaks is that in the BNFA cases there is increased organized convection over eastern India, Myanmar, the south China Sea and Southern China (Figure 2.21f). Manoj *et al*. (2011) show that heating of the 1 km to 3 km layer by absorbing aerosols in BFA cases compared with the pristine region over the equatorial Indian Ocean culminates in a significant north–south temperature gradient resulting in strong low-level moisture transport to central India that is able to overcome the

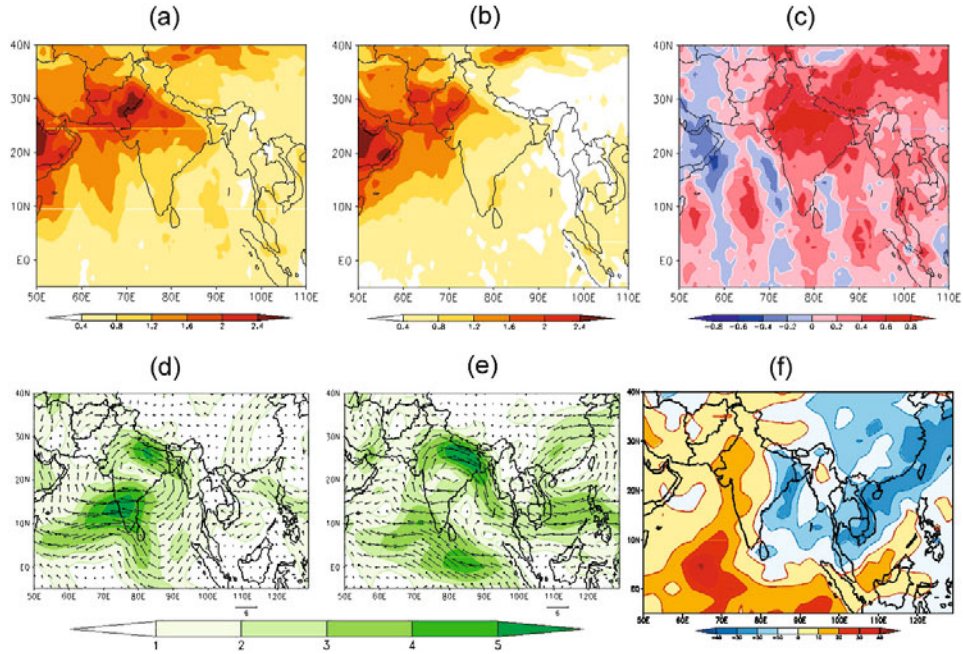

Figure 2.21. (a) Composite AI index for BFA cases. (b) Composite AI index for BNFA cases. (c) Difference between BFA and BNFA composite AI index. (d) Same as (a) but for 850 hPa winds. (e) Same as (b) but for 850 hPa winds. (f) Difference of OLR ($W\,m^{-2}$) composites between BFA and BNFA cases (BFA – BNFA).

stability effect and facilitate a quick transition to an active phase. In BNFA cases, stability cannot be overcome easily due to lack of such a temperature gradient and low-level moisture transport. This demonstration that aerosols are intrinsically linked with transitions of MISOs indicates that thermodynamically active aerosols must be included in any comprehensive theory and prediction of MISOs.

2.7 PREDICTABILITY AND PREDICTION OF MONSOON ISOS

While monsoon ISOs make the seasonal mean monsoon difficult to predict, they themselves may possess predictability beyond the current skill of medium-range prediction by virtue of their quasi-periodic nature. Prediction of long dry spells 2 to 3 weeks in advance is important to farmers when planning sowing, harvesting, and water management. What is the limit on the prediction of dry and wet spells or break and active phases of monsoon ISOs? These and other issues related to predictability and extended range prediction of summer monsoon ISOs are discussed at length in Chapter 12 and, hence, will not be repeated here. Two important findings are summarized here. The first finding is that the potential predictability of monsoon

breaks is much higher than that for monsoon active conditions (Goswami and Xavier, 2003; Waliser *et al*., 2003a). Second, simple empirical models developed during the last couple of years (Goswami and Xavier, 2003; Webster and Hoyos, 2004) demonstrate a potential for predicting summer monsoon ISOs up to 3 weeks in advance. A limitation of some of these empirical models was that they were not suitable for real time predictions due to endpoint problems arising from the use of some form of time filters. The development of analogue models for real time forecasting of summer monsoon ISOs with a level of skill that is useful up to 3 weeks in advance (Xavier and Goswami, 2007; Chattopadhyay *et al*., 2008) during the past couple of years may be considered a major advance in this direction. These developments in the real time prediction of summer ISOs as well as of the MJO are reviewed in Goswami *et al*. (2011).

2.8 SUMMARY AND DISCUSSION

A synthesis of the large-scale spatial and temporal structure and regional propagation characteristics of Asian summer monsoon ISV is presented in this chapter, based on advances made in global observations. Such observations have revealed that the active and break phases of the SA monsoon or the wet and dry spells over the Indian continent are manifestations of the superposition of 10 to 20-day and 30 to 60-day oscillations. Both the 10 to 20-day oscillation and the 30 to 60-day oscillation contribute roughly equally to total ISV in the SA monsoon region. While 30 to 60-day oscillation has a very large zonal scale encompassing both the SA and the EA/WNP monsoon regions, the 10 to 20-day oscillation has a smaller zonal scale and is regional in character. The 30 to 60-day mode is characterized by northward propagation while the 10 to 20-day mode is characterized by westward propagation. The ISV on a 30 to 60-day timescale over the EA/WNP region (see Chapter 3) and that over the SA region are closely related through the evolution (northward propagation) of the large spatial structure associated with the 30 to 60-day mode. Also the 10 to 20-day variability over the SA region is associated with the 10 to 20-day oscillation propagating from the western Pacific and amplification over the BoB. Thus, ISVs over the SA and EA/WNP monsoon regions are intimately related.

Advances made in understanding the scale selection for the 30 to 60-day mode and its northward propagation and that for the 10 to 20-day mode and its westward propagation are reviewed based on an analysis of observations and a hierarchy of modeling studies. Two mechanisms seem to contribute to the temporal-scale selection of the 30 to 60-day mode. One is a ''convection–thermal relaxation feedback mechanism'', according to which convective activity results in an increase of static stability which depresses convection itself. As convection dies, dynamical processes and radiative relaxation decrease moist static stability and bring the atmosphere to a new convectively unstable state. This mechanism does not involve wave dynamics and may be responsible for northward-propagating 30 to 60-day oscillations not associated with the eastward propagation of convection in

the equatorial region. The other mechanism involves the eastward propagation of convection over the equatorial IO in the form of a Kelvin wave and west to northwest propagation of Rossby waves emanated over the western Pacific. The timescale is determined in this case by the propagation time of the moist Kelvin wave from the eastern IO to the western Pacific and the moist Rossby waves from the western Pacific to the AS where they decay and a new equatorial perturbation is generated.

An important advance has also been made in understanding the poleward propagation of the 30 to 60-day mode. Several modeling studies have indicated that the ground hydrology and meridional gradient of moist static stability were important for the northward propagation of the mode. However, a clear physical picture has not emerged. Some diagnostic studies then showed that low-level relative vorticity drives boundary layer moisture convergence that is maximum about 3°N of the convection maximum. What is responsible for low-level vorticity to be maximum about 3°N of the convection maximum has been elucidated in some recent modeling and theoretical studies. The easterly vertical shear of summer mean flow couples the barotropic and baroclinic components of response to convective heating and generates a barotropic vorticity maximum north of the convection maximum. The barotropic vorticity maximum forces boundary layer moisture convergence to be maximum to the north of the heating maximum. Thus, a better understanding is emerging for mean northward propagation. However, we recall that northward propagation is rather intermittent within a summer season and varies from year to year. For the predictability of ISO phases, we need to understand the cause of the variability of northward propagation of the 30 to 60-day mode. This is still an important outstanding problem and more theoretical and modeling work is required in this direction.

Another major advance has been made in understanding the genesis and scale selection of the 10 to 20-day mode. Until recently, no clear physical mechanism for selection of the 10 to 20-day mode period, wavelength, and westward phase propagation was known. A unified model now explains the spatial structure (wavelength), period, and westward phase speed of both summer and winter 10 to 20-day oscillations or the QBM. It is demonstrated that the QBM is an $n = 1$ equatorial Rossby wave, with a wavelength about 6,000 km and a period of 14–16 days, which is shifted to the north (south) of the equator by about 5° by summer (winter) background mean flow (Chatterjee and Goswami, 2004). For some time, the driving mechanism for the observation of equatorial Rossby waves with a 10 to 20-day timescale was a puzzle, as some theoretical studies indicated that convective feedback could not make the $n = 1$ equatorial Rossby mode unstable. A recent study (Chatterjee and Goswami, 2004) shows that inclusion of a proper boundary layer (inclusion of turbulent entrainment) allowed the $n = 1$ equatorial Rossby mode to become unstable with a maximum growth rate corresponding to the observed period and wavelength.

The interaction between the ocean and the atmosphere on intraseasonal timescales during the northern summer and its role in the scale selection and northward propagation of monsoon ISOs are also reviewed. This is an area where

our knowledge has just begun to grow. Two things became clear during the last couple of years. A reasonable estimate of ISV of net heat flux at the surface (made possible by the availability of reliable SST from TMI, surface winds from QuikSCAT, and NOAA OLR on daily timescales) showed that ISV of heat flux is a major driving force for the ISV of SST over most of the tropical IO, although advection and entrainment play roles in the equatorial IO and the Somali Current region. It is also noted that there exists a quadrature phase relationship between the northward propagation of SST and precipitation on the 30 to 60-day timescale and that air–sea coupling is crucial for this observed phase relationship between SST and precipitation. Thus, atmospheric ISOs seem to lead to ISOs in SST (largely through heat fluxes) and the air–sea coupling is certainly required for the observed phase relationship between SST and precipitation. However, it is still unclear how ISOs in SST feed back to ISOs in convection and modify them. It appears that the basic genesis, temporal-scale selection, and northward phase propagation may arise from atmospheric internal dynamics and that air–sea coupling modifies the spatio-temporal character in some way. However, the quantitative contribution of air–sea coupling to spacetime spectra and northward propagation is not well settled at this time. Much more theoretical and modeling work is required to resolve these issues.

Developing coupled ocean–atmosphere GCMs for the Asian monsoon region is a challenging task, although some initial work is being made. This is because almost all AGCMs have large systematic errors in simulating mean SA monsoon and most OGCMs have more than a 1°C error in simulating mean SST over the IO. These systematic errors of component models lead to a drift of the coupled model climate that may influence the quantitative estimates sought above. However, the following observation provides a silver lining. We note that the signal in SST fluctuations on the intraseasonal timescale (1°C) is larger than that on the interannual timescale (0.5°C) during northern summer over the IO. Also, the amplitude of the dominant forcing—namely, net surface heat flux—on the intraseasonal timescale (60–80 $W m^{-2}$) is much larger than that on the interannual timescale.

The interactions between summer monsoon ISOs and various scales of motion have also been summarized. What started in the mid 1970s (Dakshinamurthy and Keshavamurthy, 1976; Alexander *et al.*, 1978) and the early 1980s (Yasunari, 1979; Sikka and Gadgil, 1980) as innocuous quasi-periodic oscillations that contribute to the active and break spells within the monsoon season, has now developed into the ISOs of the SA monsoon emerging as a major building block of the SA monsoon itself. On the one hand, they produce spacetime clustering of the synoptic disturbances (lows and depressions) and control the day-to-day fluctuations of precipitation while, on the other hand, they influence the seasonal mean and contribute significantly to the IAV of seasonal mean precipitation. It is estimated that modulation of the seasonal mean monsoon by slowly varying external forcing is rather weak and up to 50% of the total IAV may be contributed by internal variability arising from monsoon ISOs. This leads to poor predictability of the seasonal mean SA monsoon, as ISOs are primarily of internal atmospheric origin and the component of IAV of the seasonal mean contributed by ISOs may be unpredictable. The potential predictability of the monsoon would have been enhanced if the statistics of ISOs were also

modulated by slowly varying external forcing. Currently available studies indicate that ISO statistics over the Asian monsoon region is only weakly modulated by slowly varying SST forcing. However, we now know that air–sea coupling is involved in the ISV of the SA monsoon. Coupled evolution of SST and circulation and precipitation on the intraseasonal timescale may introduce certain constraints on the internal variability generated by ISOs. However, this question is just being raised and no study has addressed it so far. In the coming years, CGCMs should investigate whether predictability of the seasonal mean monsoon is enhanced by air–sea coupling of summer monsoon ISOs. Monsoon predictability could also be influenced by interdecadal variability of external forcing and interdecadal variability of ISO statistics. The role of ISOs in the interdecadal variability of predictability of the SA monsoon needs to be studied using long observations and coupled models.

Exploiting the quasi-periodic nature of ISOs, it has been shown (Goswami and Xavier, 2003; Webster and Hoyos, 2004; Xavier and Goswami, 2007; Chattopadhyay *et al*., 2008) that the phases of ISOs could be predictable up to 3 weeks in advance. This knowledge is likely to be put to practical use in extended range forecasting of the dry and wet spells of the monsoon and flood forecasting. Improvement in the extended range forecasting of ISO phases, however, may come only from better understanding and simulation of within-season and year-to-year variability of northward-propagating events. Fundamental work is required to advance the understanding of this aspect of ISOs.

For better long-range prediction of the seasonal mean and for better extended range prediction of ISOs themselves, it is apparent that CGCMs must simulate the climatology of ISOs correctly. However, ISOs do influence the annual cycle, and ISO activity is related to the internal variability of the seasonal mean. Waliser *et al*. (2003b) find that AGCMs with higher (lower) internal variability are associated with a stronger (weaker) annual cycle. Thus, ISO activity may be indirectly tied to the hydrological cycle of a model. The hydrological cycle of a model, in turn, depends on various parameterizations of the model, such as the cumulus scheme, land surface processes, etc. Model-to-model variability in simulating the statistics of ISOs may be related to differences in these parameterization schemes. Correct simulation of the climatology of observed ISOs, therefore, remains a challenging task and continued focused efforts must be made to improve summer ISO simulations in GCMs.

2.9 ACKNOWLEDGMENTS

This work was partially supported by the Department of Ocean Development, Government of India and the Indian National Centre for Ocean Information Services (INCOIS), Hyderabad. I thank D. Sengupta for his comments on the draft of this manuscript. I am grateful to Duane, Bill, and an anonymous reviewer for detailed and constructive comments that significantly improved the presentation of the chapter. Some of the results presented in the chapter grew out of work done in collaboration with my colleague D. Sengupta and students R. S. Ajaya Mohan,

Retish Senan, and Prince Xavier. I am thankful to Prince Xavier, Neena Mani Joseph, and E. Suhas for help in preparing the manuscript.

2.10 APPENDIX

Several datasets have been utilized in preparing the figures presented in this chapter. Primary among them are the daily circulation data from NCEP–NCAR reanalysis (Kalnay *et al*., 1996; Kistler *et al*., 2001), daily interpolated outgoing longwave radiation (OLR) data (Liebmann and Smith, 1996), and daily precipitation estimates from GPCP (Huffman *et al*. 2001). We have also used high-resolution daily rainfall data over India compiled by the India Meteorological Department (Rajeevan *et al*., 2006) based on 1,803 stations distributed over the country. For the large-scale pattern of precipitation climatology, we have used CMAP data (Xie and Arkin, 2006). NCEP–NCAR reanalysis, interpolated OLR, and CMAP precipitation are available at $2.5^\circ \times 2.5^\circ$ horizontal resolution. The daily precipitation from GPCP (Huffman *et al*., 2001) and IMD are available at $1^\circ \times 1^\circ$ horizontal resolution. Daily anomalies are constructed as deviations from daily observations from an annual cycle defined as the sum of the annual mean and the first three harmonics. To extract bandpass-filtered data we have generally used a Lanczos filter (Duchon, 1979). The surface winds and SST were obtained from the microwave imager on board the TRMM satellite (Wentz *et al*., 2000) and were not affected by clouds, aerosols, and atmospheric water vapor. A 3-day running mean provided data at $0.25^\circ \times 0.25^\circ$ horizontal resolution.

2.11 REFERENCES

Abrol, Y. P. and S. Gadgil (Eds.) (1999) *Rice in a Variable Climate*. APC Publications, New Delhi, 243 pp.

Ajaya Mohan, R. S. and B. N. Goswami (2003) Potential predictability of the Asian summer monsoon on monthly and seasonal time scales. *Meteorol. Atmos. Phys*., doi: 10.1007/s00703-002-0576-4.

Ajaya Mohan, R. S. and B. N. Goswami (2007) Dependence of simulation of boreal summer tropical intraseasonal oscillations on the simulation of seasonal mean. *J. Atmos. Sci*., **64**, 460–478.

Ajaya Mohan, R. S., H. Annamalai, Jing-Jia Luo, J. Hafner, and T. Yamagata (2010) Poleward propagation of boreal summer intraseasonal oscillations in a coupled model: Role of internal processes, *Climate Dynamics*, doi: 10.1007/s00382-010-0839-6.

Alexander, G., R. Keshavamurty, U. De, R. Chellapa, S. Das, and P. Pillai (1978) Fluctuations of monsoon activity. *J. Meteorol. Hydrol. Geophys*., **29**, 76–87.

Ananthakrishnan, R. and M. Soman (1988a) The onset of the south-west monsoon over Kerala: 1901–1980. *J. Climatol*., **8**, 283–296.

Ananthakrishnan, R. and M. Soman (1988b) Onset dates of the south-west monsoon over Kerala for the period 1870–1900. *Int. J. Climatol*., **9**, 321–322.

Ananthakrishnan, R., U. R. Acharya, and A. R. R. Krishnan (1967) *On the Criteria for Declaring the Onset of the Southwest Monsoon over Kerala* (forecasting manual, FMU Rep. No. IV-18.1). India Meteorological Department, Pune, India, 52 pp.

Annamalai, H. and J. M. Slingo (2001) Active/break cycles: Diagnosis of the intraseasonal variability of the Asian summer monsoon. *Climate Dynamics*, **18**, 85–102.

Bellon, J. and J. Srinivasan (2006) Comments on "Structures and mechanisms of the northward propagating boreal summer intraseasonal oscillation." *J. Climate*, **19**, 4738– 4743.

Bhat, G., S. Gadgil, S. Kumar, P. V. Hareesh Kalsi, S. R. Madhusoodanan, P. Murty, V. S. N. Prasada Rao, C. V. K. Babu, and V. Ramesh Rao (2001) BOBMEX: The Bay of Bengal monsoon experiment. *Bull. Amer. Meteorol. Society*, **82**, 2217–2243.

Blanford, H. F. (1884) On the connection of the Himalaya snowfall with dry winds and seasons of drought in India. *Proc. Royal Society London*, **37**, 3–22.

Blanford, H. F. (1886) Rainfall of India. *Mem. India Meteorol. Department*, **2**, 217–448.

Charney, J. G. and J. Shukla (1981) Predictability of monsoons. In: J. Lighthill and R. P. Pearce (Eds.), *Monsoon Dynamics*. Cambridge University Press, Cambridge, U.K., pp. 99–108.

Chatterjee, P. and B. N. Goswami (2004) Structure, genesis and scale selection of the tropical quasi-biweekly mode. *Quart. J. Roy. Meteorol. Soc.*, **130**, 1171–1194.

Chattopadhyay, R., A. K. Sahai, and B. N. Goswami (2008) Objective identification of nonlinear convectively coupled phases of monsoon intraseasonal oscillation: Implications for prediction. *J. Atmos. Sci.*, **65**, 1549–1569.

Chen, T.-C. and J.-M. Chen (1993) The 10–20-day mode of the 1979 indian monsoon: Its relation with the time variation of monsoon rainfall. *Mon. Wea. Rev.*, **121**, 2465–2482.

Collier, J. C. and G. J. Zhang (2009) Aerosol direct forcing of the summer Indian monsoon as simulated by the NCAR cam3. *Climate Dynamics*, **32**, 313–332.

Dakshinamurthy, J. and R. N. Keshavamurthy (1976) On oscillations of period around one month in the Indian summer monsoon. *Ind. J. Meteorol. Geophys.*, **27**, 201–203.

Delsole, T. and J. Shukla (2002) Linear prediction of Indian monsoon rainfall. *J. Climate*, **15**(24), 3645–3658.

Drbohlav, H. K. L. and Bin Wang (2005) Mechanism of the northward-propagating intraseasonal oscillation: Insights from a zonally symmetric model. *J. Climate*, **18**, 952–972

Duchon, C. (1979) Lanczos filtering in one and two dimensions. *J. Appl. Meteorol.*, **18**, 1016–1022.

Fennessy, M. and J. Shukla (1994) Simulation and predictability of monsoons. Paper presented at *Proceedings of the International Conference on Monsoon Variability and Prediction, WMO/TD619, Trieste*, pp. 567–575.

Ferranti, L., J. M. Slingo, T. N. Palmer, and B. J. Hoskins (1997) Relations between interannual and intraseasonal monsoon variability as diagnosed from AMIP integrations. *Quart. J. Roy. Meteorol. Soc.*, **123**, 1323–1357.

Flatau, M., P. Flatau, and D. Rudnick (2001) The dynamics of double monsoon onsets. *J. Climate*, **14**, 4130–4146.

Flatau, M., P. Flatau, J. Schmidt, and G. Kiladis (2003) Delayed onset of the 2002 Indian monsoon. *Geophys. Res. Lett.*, **30**(14), 1768, doi: 10.1029/2003GL017,434.

Fu, X., B. Wang, and T. Li (2002) Impacts of air–sea coupling on the simulation of mean Asian summer monsoon in the ECHAM4 model. *Mon. Wea. Rev.*, **130**, 2889–2904.

Fu, X., B. Wang, T. Li, and J. McCreary (2003) Coupling between northward propagating, intraseasonal oscillations and sea-surface temperature in the Indian ocean. *J. Atmos. Sci.*, **60**(15), 1755–1753.

Fu Xiouhua, Bin Wang, D. E. Waliser, and Li Tao (2007) Impact of atmosphere–ocean coupling on the predictability of monsoon intraseasonal oscillations. *J. Atmos. Sci.*, **64**, 157–174.

Fukutomi, Y. and T. Yasunari (1999) 10–25 day intraseasonal variations of convection and circulation over east Asia and western north Pacific during early summer. *J. Meteorol. Soc. Japan*, **77**(3), 753–769.

Gadgil, S. (1995) Climate change and agriculture: An Indian perspective. *Curr. Sci.*, **69**, 649–659.

Gadgil, S. (2003) The Indian monsoon and its variability. *Annu. Rev. Earth Planet. Sci.*, **31**, 429–467.

Gadgil, S. and P. R. S. Rao (2000) Famine strategies for a variable climate: A challenge. *Curr. Sci.*, **78**, 1203–1215.

Gadgil, S. and S. Sajani (1998) Monsoon precipitation in the AMIP runs. *Climate Dynamics*, **14**, 659–689.

Gadgil, S. and J. Srinivasan (1990) Low frequency variation of tropical convergence zone. *Meteorol. Atmos. Phys.*, **44**, 119–132.

Gill, A. E. (1980) Some simple solutions for heat-induced tropical circulation. *Quart. J. Roy. Meteorol. Soc.*, **106**, 447–462.

Gill, A. E. (1982) *Atmosphere–Ocean Dynamics* (Vol. 30 of International Geophysics Series). Academic Press, San Diego, CA, 666 pp.

Goswami, B. N. (1994) Dynamical predictability of seasonal monsoon rainfall: Problems and prospects. *Proc. Ind. Nat. Acad. Sci.*, **60A**, 101–120.

Goswami, B. N. (1998) Interannual variations of Indian summer monsoon in a GCM: External conditions versus internal feedbacks. *J. Climate*, **11**, 501–522.

Goswami, B. N. and R. S. Ajaya Mohan (2001) Intraseasonal oscillations and interannual variability of the Indian summer monsoon. *J. Climate*, **14**, 1180–1198.

Goswami, B. N. and J. Shukla (1984) Quasi-periodic oscillations in a symmetric general circulation model. *J. Atmos. Sci.*, **41**, 20–37.

Goswami, B. N. and P. Xavier (2003) Potential predictability and extended range prediction of Indian summer monsoon breaks. *Geophys. Res. Lett.*, **30**(18), 1966, doi: 10.1029/2003GL017,810.

Goswami, B. N. and P. K. Xavier (2005) Dynamics of ''internal'' interannual variability of the Indian summer monsoon in a GCM. *J. Geophys. Res.*, **110**, D24104, doi: 10.1029/2005JD006042.

Goswami, B. N., J. Shukla, E. Schneider, and Y. Sud (1984) Study of the dynamics of the intertropical convergence zone with a symmetric version of the GLAS climate model. *J. Atmos. Sci.*, **41**, 5–19.

Goswami, B. N., D. Sengupta, and G. Sureshkumar (1998) Intraseasonal oscillations and interannual variability of surface winds over the Indian monsoon region. *Proc. Ind. Acad. Sci. (Earth and Planetary Sciences)*, **107**, 45–64.

Goswami, B. N., R. S. Ajaya Mohan, P. K. Xavier, and D. Sengupta (2003) Clustering of low pressure systems during the Indian summer monsoon by intraseasonal oscillations. *Geophys. Res. Lett.*, **30**, 8, doi: 10.1029/2002GL016,734.

Goswami, B. N., G. Wu, and T. Yasunari (2006) The annual cycle, intraseasonal oscillations, and roadblock to seasonal predictability of the Asian summer monsoon. *J. Climate*, **19**, 5078–5098.

Goswami, B. N., M. C. Wheeler, J. C. Gottschalck, and D. E. Waliser (2011) Intraseasonal variability and forecasting: A review of recent research. In: C. P. Chang *et al.* (Eds.), *The Global Monsoon System: Research and Forecast*, Second Edition, World Scientific, Singapore, Ch. 23, pp. 389–409

Goswami, P. and V. Mathew (1994) A mechanism of scale selection in tropical circulation at observed intraseasonal frequencies. *J. Atmos. Sci.*, **51**, 3155–3166.

Goswami, P. and Srividya (1996) A novel neural network design for long-range prediction of rainfall pattern. *Curr. Sci.*, **70**, 447–457.

Gowarikar, V., V. Thapliyal, R. P. Sarker, G. S. Mandel, and D. R. Sikka (1989) Parametric and power regression models: New approach to long range forecasting of monsoon rain in India. *Mausam*, **40**, 125–130.

Hastenrath, S. and P. Lamb (1979) *Climatic Atlas of the Indian Ocean, Part I: Surface Climate Atmosphere Circulation*. University of Wisconcin Press, Madison.

Held, I. and A. Hou (1980) Nonlinear axially symmetric circulations in a nearly inviscid atmosphere. *J. Atmos. Sci.*, **37**, 515–533.

Hendon, H. and M. Salby (1994) The life cycle of Madden–Julian Oscillation. *J. Atmos. Sci.*, **51**, 2207–2219.

Hoyos, C. D. and P. J. Webster (2007) The role of intraseasonal variability in the nature of Asian monsoon precipitation. *J. Climate*, **20**, 4402–4424.

Hsu, H.-H. and C.-H. Weng (2001) Northwestward propagation of the intraseasonal oscillation in the western north Pacific during the boreal summer: Structure and mechanism. *J. Climate*, **14**, 3834–3850.

Huffman, G. J., R. F. Adler, M. Morrissey, D. T. Bolvin, S. Curtis, R. Joyce, B. McGavock, and J. Susskind (2001) Global precipitation at one-degree daily resolution from multi-satellite observations. *J. Hydrometeorol.*, **2**, 36–50.

Jayaraman, A. (2001) Aerosol radiation cloud interactions over the tropical Indian Ocean prior to the onset of the summer monsoon. *Curr. Sci.*, **81**(11), 1437–1445.

Jiang, X., T. Li, and B. Wang (2004) Structures and mechanisms of the northward propagation boreal summer intraseasonal oscillation. *J. Climate*, **17**, 1022–1039.

Jones, C., L. M. V. Carvalho, R. W. Higgins, D. E. Waliser, and J. K. E. Schemm (2004) Climatology of tropical intraseasonal convective anomalies: 1979–2002. *J. Climate*, **17**, 523–539.

Joseph, P., J. Eischeid, and R. Pyle (1994) Interannual variability of the onset of the Indian summer monsoon and its association with atmospheric features, El Nino and sea surface temperature anomalies. *J. Climate*, **7**, 81–105.

Joseph, S., A. K. Sahai, and B. N. Goswami (2009) Eastward propagating MJO during boreal summer and Indian monsoon droughts. *Climate Dynamics*, **32**, doi: 10.1007/s00382-008-0412-8, pp. 1139–1153.

Kalnay, E., M. Kanamitsu, R. Kistler, W. Collins, D. Deaven, L. Gandin, M. Iredell, S. Saha, G. White, J. Woollen *et al.* (1996) The NCEP/NCAR 40-year reanalysis project. *Bull. Amer. Meteorol. Society*, **77**, 437–471.

Kang, I.-S., K. Jin, K.-M. Lau, J. Shukla, V. Krishnamurthy, S. D. Schubert, D. E. Waliser, W. Stern, V. Satyan, A. Kitoh *et al.* (2002a) Intercomparison of GCM simulated anomalies associated with the 1997–98 El Nino. *J. Climate*, **15**, 2791–2805.

Kang, I.-S., K. Jin, B. Wang, K.-M. Lau, J. Shukla, V. Krishnamurthy, S. D. Schubert, D. E. Waliser, W. Stern, V. Satyan, *et al.* (2002b) Intercomparison of the climatological variations of Asian summer monsoon precipitation simulated by 10 GCMs. *Climate Dyn.*, **19**, 383–395.

Kemball-Cook, S. R. and B. Wang (2001) Equatorial waves and air–sea interaction in the boreal summer intraseasonal oscillation. *J. Climate*, **14**, 2923–2942.

Keshavamurthy, R. N., S. V. Kasture, and V. Krishnakumar (1986) 30–50 day oscillation of the monsoon: A new theory. *Beitr. Phys. Atmo.*, **59**, 443–454.

Kistler, R., W. Collins, S. Saha, G. White, J. Woollen, E. Kalnay, M. Chelliah, W. Ebisuzaki, M. Kanamitsu, V. Kousky *et al*. (2001) The NCEP–NCAR 50-year reanalysis: Monthly means CD-ROM and documentation. *Bull. Amer. Meteorol. Society*, **82**, 247–267.

Kikuchi, K. and Bin Wang (2009) Global perspectives of the quasi biweekly oscillation. *J. Climate*, **22**, 1340–1359.

Klingaman, N. C., P. M. Inness, H. Weller, and J. M. Slingo (2008) The importance of high-frequency sea surface temperature variability to the intraseasonal oscillation of Indian monsoon rainfall. *J. Climate*, **21**, 6119–6140.

Knutson, T. and K. Weickmann (1987) 30–60 day atmospheric oscillations: Composite life cycles of convection and circulation anomalies. *Mon. Wea. Rev.*, **115**, 1407–1436.

Knutson, T. R., K. M. Weickmann, and J. E. Kutzbach (1986) Global scale intraseasonal oscillations of outgoing longwave radiation and 250 mb zonal wind during northern hemispheric summer. *Mon. Wea. Rev.*, **114**, 605–623.

Krishnamurthy, V. and R. S. Ajaya Mohan (2010) Composite structure of monsoon low pressure systems and its relation to Indian rainfall. *J. Climate*, **23**, doi: 10.1175/2010JCLI2953.1.

Krishnamurthy, V. and J. Shukla (2000) Intraseasonal and interannual variability of rainfall over India. *J. Climate*, **13**, 4366–4377.

Krishnamurthy, V. and J. Shukla (2001) Observed and model simulated interannual variability of the Indian monsoon. *Mausam*, **52**, 133–150.

Krishnamurthy, V. and J. Shukla (2007) Intraseasonal and seasonally persisting patterns of Indian monsoon rainfall. *J. Climate*, **20**, 3–20.

Krishnamurthy, V. and J. Shukla (2008) Seasonal persistence and propagation of intraseasonal patterns over the Indian monsoon region. *Climate Dynamics*, **30**, 353–369, doi: 10.1007/s00382-007-0300-7.

Krishnamurti, T. N. (1985) Summer monsoon experiment: A review. *Mon. Wea. Rev.*, **113**, 1590–1626.

Krishnamurti, T. N., P. Jayakumar, J. Sheng, N. Surgi, and A. Kumar (1985) Divergent circulations on the 30–50 day time scale. *J. Atmos. Sci.*, **42**, 364–375.

Krishnamurti, T. N., D. Oosterhof, and A. Mehta (1988) Air–sea interactions on the time scale of 30–50 days. *J. Atmos. Sci.*, **45**, 1304–1322.

Krishnamurti, T. N. and P. Ardunay (1980) The 10 to 20 day westward propagating mode and breaks in the monsoons. *Tellus*, **32**, 15–26.

Krishnamurti, T. N. and H. N. Bhalme (1976) Oscillations of monsoon system, Part I: Observational aspects. *J. Atmos. Sci.*, **45**, 1937–1954.

Krishnamurti, T. N. and D. Subrahmanyam (1982) The 30–50 day mode at 850 mb during MONEX. *J. Atmos. Sci.*, **6**(39), 2088–2095.

Krishnan, R., C. Zhang, and M. Sugi (2000) Dynamics of breaks in the Indian summer monsoon. *J. Atmos. Sci.*, **57**, 1354–1372.

Lau, K. M. and P. H. Chen (1986) Aspects of 30–50 day oscillation during summer as inferred from outgoing longwave radiation. *Mon. Wea. Rev.*, **114**, 1354–1369.

Lau, K. M. and L. Peng (1990) Origin of low-frequency (intraseasonal) oscillations in the tropical atmosphere, Part III: Monsoon dynamics. *J. Atmos. Sci.*, **47**(12), 1443–1462.

Lau, K. M., X. Li, and H. T. Wu (2002) Change in the large scale circulation, cloud structure and regional water cycle associated with evolution of the south China Sea monsoon during May–June, 1998. *J. Meteorol. Soc. Japan*, **80**, 1129–1147.

Lau, K. M., M. K. Kim, and K.-M. Kim (2006) Asian summer monsoon anomalies induced by aerosol direct forcing: The role of the Tibetan Plateau. *Climate Dynamics*, **26**, 855–864.

Lau, N. C. (1985) Modelling the seasonal dependence of atmospheric response to observed El Niño in 1962–1976. *Mon. Wea. Rev.*, **113**, 1970–1996.

Lawrence, D. M. and P. J. Webster (2001) Interannual variations of the intraseasonal oscillation in the south Asian summer monsoon region. *J. Climate*, **14**, 2910–2922.

Li, C. and M. Yanai (1996) The onset and interannual variability of the Asian summer monsoon in relation to land–sea thermal contrast. *J. Climate*, **9**, 358–375.

Liebmann, B. and C. A. Smith (1996) Description of a complete (interpolated) out-going longwave radiation dataset. *Bull. Amer. Meteorol. Society*, **77**, 1275–1277.

Liebmann, B., H. H. Hendon, and J. D. Glick (1994) The relationship between tropical cyclones of the western Pacific and Indian oceans and the Madden–Julian Oscillation. *J. Meteorol. Soc. Japan*, **72**, 401–412.

Liu Ping, Y. Kajikawa, Bin Wang, Akio Kitoh, T. Yasunary, Tim Li, H. Annamalai, X. Fu, K. Kikuchi, R. Mizura, K. Rajendran, D. E. Wand, and D. Kim, (2009) Tropical intraseasonal variability in the MRI-20km60L AGCM. *J. Climate*, **22**, 2006–2022.

Madden, R. A. (1986) Seasonal variations of the 40–50 day oscillation in the tropics. *J. Atmos. Sci.*, **43**, 3138–3158.

Madden, R. A. and P. R. Julian (1994) Detection of a 40–50 day oscillation in the zonal wind in the tropical Pacific. *Mon. Wea. Rev.*, **122**, 813–837.

Maloney, E. D. and D. L. Hartmann (2000) Modulation of hurricane activity in the gulf of Mexico by the Madden–Julian Oscillation. *Science*, **287**, 2002–2004.

Manoj, M. G., P. C. S. Devara, P. D. Safai, and B. N. Goswami (2011) Absorbing aerosols facilitate transition of Indian monsoon breaks to active spells. *Climate Dynamics*, doi: 10.1007/s00382-010-0971-3.

Matsuno, T. (1966) Quasi-geostrophic motions in the equatorial area. *J. Meteorol. Soc. Japan*, **44**, 25–43.

Meehl, G. A., J. M. Arblaster, and W. D. Collins (2008) Effects of black carbon aerosols on the Indian monsoon. *J. Climate*, **21**, 2869–2882.

Mooley, D. A. and J. Shukla (1987) *Tracks of Low Pressure Systems which Formed over India, Adjoining Countries, the Bay of Bengal and Arabian Sea in Summer Monsoon Season during the Period 1888–1983*. Center for Ocean Land Atmosphere Studies, Calverton, MD [available from J. Shukla of COLA].

Murakami, M. (1976) Analysis of summer monsoon fluctuations over India. *J. Meteorol. Soc. Japan*, **54**, 15–31.

Murakami, T., T. Nakazawa, and J. He (1984) On the 40–50 day oscillation during 1979 northern hemisphere summer, Part I: Phase propagation. *J. Meteorol. Soc. Japan*, **62**, 440–468.

Murakami, T., L. X. Chen, and A. Xie (1986) Relationship among seasonal cycles, low frequency oscillations and transient disturbances as revealed from outgoing long wave radiation. *Mon. Wea. Rev.*, **114**, 1456–1465.

Nakazawa, T. (1986) Mean features of 30–60 day variations inferred from 8 year OLR data. *J. Meteorol. Soc. Japan*, **64**, 777–786.

Nanjundiah, R. S., J. Srinivasan, and S. Gadgil (1992) Intraseasonal variation of the Indian summer monsoon, Part II: Theoretical aspects. *J. Meteorol. Soc. Japan*, **70**, 529–550.

Pai, D. S., J. Bhate, O. P. Sreejith, and H. R. Hatwar (2009) Impact of MJO on the intraseasonal variation of summer monsoon rainfall over India. *Climate Dynamics*, doi: 10.1007/s00382-009-0634-4.

Pandithurai, G., S. Dipu, K. K. Dani, S. Tiwari, D. S. Bisht, P. C. S. Devara, and R. T. Pinker (2008), Aerosol radiative forcing during dust events over New Delhi, India. *J. Geophys. Res.*, **113**, D1309, doi: 10.1029/2008JD009804.

Parthasarathy, B. and D. Mooley (1978) Some features of a long homogeneous series of Indian summer monsoon rainfall. *Mon. Wea. Rev.*, **106**, 771–781.

Parthasarathy, B., A. Munot, and D. Kothawale (1988) Regression model for estimation of Indian food grain production from Indian summer rainfall. *Agric. For. Meteorol.*, **42**, 167–182.

Pegion, K. and B. Kirtman (2007) The impact of air–sea interactions on the simulation of tropical intraseasonal variability. *J. Climate*, **21**, 6616–6635.

Pearce, R. P. and U. C. Mohanty (1984) Onsets of the Asian summer monsoon, 1979–1982. *J. Atmos. Sci.*, **41**, 1620–1639.

Raghavan, K. (1973) Break-monsoon over India. *Mon. Wea. Rev.*, **101**(1), 33–43.

Rajeevan, M., D. S. Pai, S. K. Dikshit, and R. R. Kelkar (2004) IMD's new operational models for long-range forecast of southwest monsoon rainfall over India and their verification for 2003. *Curr. Sci.*, **86**(3), 422–431.

Rajeevan, M., J. Bhate, J. D. Kale, and B. Lal (2006) High resolution daily gridded rainfall data for the Indian region: Analysis of break and active monsoon spells. *Curr. Sci.*, **91**, 296–306.

Rajeevan, M., S. Gadgil, and J. Bhate (2010) Active and break spells of the Indian summer monsoon. *J. Earth Sys. Sci.*, **119**, 229–248.

Rajendran, K., and A. Kitoh, (2006) Modulation of tropical intraseasonal oscillations by ocean–atmosphere coupling. *J. Climate*, **19**, 366–391.

Rajendran, K., A. Kitoh, and O. Arakawa (2004) Monsoon low frequency intraseasonal oscillation and ocean–atmosphere coupling over the Indian ocean. *Geophys. Res. Lett.*, **31**, doi: 10.1029/2003GL019,031.

Ramage, C. S. (1971) *Monsoon Meteorology* (Vol. 15 of International Geophysics Series). Academic Press, San Diego, CA, 296 pp.

Ramamurthy, K. (1969) *Monsoon of India: Some Aspects of "Break" in the Indian South West Monsoon during July and August* (forecasting manual, Part IV.18.3). India Meteorological Department, New Delhi.

Ramanathan, V. and G. Carmichael (2008) Global and regional climate changes due to black carbon. *Nature Geoscience*, **1**, 221–227.

Ramanathan, V., P. J. Crutzen, J. Lelieveld, A. P. Mitra, D. Althausen, J. Anderson, M. O. Andreae, W. Cantrell, G. R. Cass, C. E. Chung *et al.* (2001) Indian Ocean Experiment: An integrated analysis of the climate forcing and effects of the great Indo-Asian haze. *J. Geophys. Res.*, **106**, 28371–28398, doi: 10.1029/2001JD900133.

Ramanathan, V., Chung, C., Kim, D., Bettge, T., Buja, L., Kiehl, J. T., Washington, W. M., Fu, Q., Sikka, D. R., and Wild, M. (2005) Atmospheric brown clouds: Impacts on South Asian monsoon climate. *Proceedings of the National Academy of Sciences U.S.A.*, **102**(15), 5326–5333.

Ramaswamy, C. (1962) Breaks in the Indian summer monsoon as a phenomenon of interaction between the easterly and the sub-tropical westerly jet streams. *Tellus*, **XIV**, 337–349.

Rao, Y. P. (1976) *Southwest Monsoon* (meteorological monograph). India Meteorological Department, New Delhi, 366 pp.

Reynolds, R. W. and T. M. Smith (1994) Improved global sea surface temperature analyses using optimum interpolation. *J. Climate*, **7**, 929–948.

Sahai, A. K., A. M. Grimm, V. Satyan, and G. B. Pant (2003) Long-lead prediction of Indian summer monsoon rainfall from global SST evolution. *Climate Dynamics*, **20**, 855–863.

Schneider, E. and R. Lindzen (1977) Axially symmetric steady state models of the basic state of instability and climate studies, Part I: Linearized calculations. *J. Atmos. Sci.*, **34**, 263–279.

Sengupta, D. and M. Ravichandran (2001) Oscillations of Bay of Bengal sea surface temperature during the 1998 summer monsoon. *Geophys. Res. Lett.*, **28**(10), 2033–2036.

Sengupta, D., B. N. Goswami, and R. Senan (2001) Coherent intraseasonal oscillations of ocean and atmosphere during the Asian summer monsoon. *Geophys. Res. Lett.*, **28**(21), 4127–4130.

Shukla, J. (1981) Dynamical predictability of monthly means. *J. Atmos. Sci.*, **38**, 2547–2572.

Shukla, J. (1987) Interannual variability of monsoon. In: J. S. Fein and P. L. Stephens (Eds.), *Monsoons*. John Wiley & Sons, New York, pp. 399–464.

Shukla, J. (1998) Predictability in the midst of chaos: A scientific basis for climate forecasting. *Science*, **282**, 728–731.

Sikka, D. R. (1980) Some aspects of large-scale fluctuations of summer monsoon rainfall over India in relation to fluctuations in planetary and regional scale circulation parameters. *Proc. Ind. Acad. Sci. (Earth and Planetary Sciences)*, **89**, 179–195.

Sikka, D. R. and S. Gadgil (1980) On the maximum cloud zone and the ITCZ over Indian longitude during southwest monsoon. *Mon. Wea. Rev.*, **108**, 1840–1853.

Singh, S. V., R. H. Kriplani, and D. R. Sikka (1992) Interannual variability of the Madden–Julian Oscillations in Indian summer monsoon rainfall. *J. Climate*, **5**, 973–979.

Soman, M. and K. Krishna Kumar (1993) Space-time evolution of meteorological features associated with the onset of Indian summer monsoon. *Mon. Wea. Rev.*, **121**, 1177–1194.

Sperber, K. R. and T. N. Palmer (1996) Interannual tropical rainfall variability in general circulation model simulations associated with atmospheric model intercomparison project. *J. Climate*, **9**, 2727–2750.

Sperber K. R., J. M. Slingo, and H. Annamalai (2000) Predictability and the relationship between subseasonal and interannual variability during the Asian summer monsoons. *Quart. J. Roy. Meteorol. Soc.*, **126**, 2545–2574.

Sperber, K. R., C. Brankovic, T. Palmer, M. Deque, C. S. Frederiksen, K. Puri, R. Graham, A. Kitoh, C. Kobayashi, W. Tennant, *et al.* (2001) Dynamical seasonal predictability of the Asian summer monsoon. *Mon. Wea. Rev.*, **129**, 2226–2248.

Srinivasan, J., S. Gadgil, and P. Webster (1993) Meridional propagation of large-scale monsoon convective zones. *Meteorol. Atmos. Phys.*, **52**, 15–35.

Straub, K. and G. Kiladis (2003) Interactions between the boreal summer intraseasonal oscillations and higher-frequency tropical wave activity. *Mon. Wea. Rev.*, **131**, 945–960.

Tomas, R. and P. Webster (1997) The role of inertial instability in determining the location and strength of near-equatorial convection. *Quart. J. Roy. Meteorol. Soc.*, **123**(541), 1445–1482.

Vecchi, G. and D. E. Harrison (2002) Monsoon breaks and subseasonal sea surface temperature variability in the Bay of Bengal. *J. Climate*, **15**, 1485–1493.

Waliser, D. E. and C. Gautier (1993) A satellite-derived climatology of the ITCZ. *J. Climate*, **6**, 2162–2174.

Waliser, D. E., K. Lau, W. Stern, and C. Jones (2003a) Potential predictability of the Madden–Julian Oscillation. *Bull. Amer. Meteorol. Society*, **84**, 33–50.

Waliser, D. E., K. Jin, I.-S. Kang, W. F. Stern, S. D. Schubert, M. L. C. Wu, K.-M. Lau, M.-I. Lee, V. Krishnamurthy, A. Kitoh, *et al.* (2003b) AGCM simulations of intraseasonal variability associated with the Asian summer monsoon. *Climate Dynamics*, doi: 10.1007/s00382-003-0337-1.

Waliser, D. E., R. Murtugudde, and L. Lucas (2004) Indo-Pacific ocean response to atmospheric intraseasonal variability, Part II: Boreal summer and the intraseasonal oscillation. *J. Geophys. Res., Oceans*, **109**, C03030, doi: 10.1029/2003JC002002.

Walker, G. T. (1923) Correlation in seasonal variations of weather, VIII: A preliminary study of world weather. *Mem. Indian Meteorol. Dept.*, **24**, 75–131.

Walker, G. T. (1924) Correlation in seasonal variations of weather, IV: A further study of world weather. *Mem. Indian Meteorol. Dept.*, **24**, 275–332.

Wang, B. and H. Rui (1990) Synoptic climatology of transient tropical intraseasonal convection anomalies: 1975–1985. *Meteorol. Atmos. Phys.*, **44**, 43–61.

Wang, B. and X. Xie (1997) A model for the boreal summer intraseasonal oscillation. *J. Atmos. Sci.*, **54**(1), 71–86.

Wang, B., I.-S. Kang, and J.-Y. Lee (2004) Ensemble simulations of Asian–Australian monsoon variability by 11 AGCMs. *J. Climate*, **17**, 699–710.

Webster, P. J. (1983) Mechanism of monsoon low-frequency variability: Surface hydrological effects. *J. Atmos. Sci.*, **40**, 2110–2124.

Webster, P. J. and C. Hoyos (2004) Prediction of monsoon rainfall and river discharge on 15–30 day time scales. *Bull. Amer. Meteorol. Society*, **85**, 1745–1767.

Webster, P. J., V. O. Magana, T. N. Palmer, J. Shukla, R. T. Tomas, M. Yanai, and T. Yasunari (1998) Monsoons: Processes, predictability and the prospects of prediction. *J. Geophys. Res.*, **103**(C7), 14451–14510.

Webster, P. J., E. F. Bradley, C. W. Fairall, J. S. Godfrey, P. Hacker, R. A. Houze Jr., R. Lukas, Y. Serra, J. M. Hummon, T. D. M. Lawrence *et al.* (2002) The JASMINE pilot study. *Bull. Amer. Meteorol. Society*, **83**(11), 1603–1630.

Wentz, F., C. Gentemann, D. Smith, and D. Chelton (2000) Satellite measurements of sea surface temperature through clouds. *Science*, **288**, 847–850.

Wheeler, M. C. and H. H. Hendon (2004) An all-season real-time multivariate MJO Index: Development of an index for monitoring and prediction. *Mon. Wea. Rev.*, **132**, 1917–1932.

Wheeler, M. C. and G. N. Kiladis (1999) Convectively coupled equatorial waves: Analysis of clouds and temperature in the wavenumber–frequency domain. *J. Atmos. Sci.*, **56**, 374–399.

Wu, M., S. Schubert, I.-S. Kang, and D. Waliser (2002) Forced and free intraseasonal variability over the south Asian monsoon region simulated by 10 AGCMs. *J. Climate*, **15**(20), 2862–2880.

Xavier, P. K. and B. N. Goswami, (2007) An analog method for real time forecasting of summer monsoon subseasonal variability. *Mon. Wea. Rev.*, **135**, 4149–4160.

Xie, P. and P. A. Arkin (1996) Analyses of global monthly precipitation using gauge observations, satellite estimates and numerical predictions. *J. Climate*, **9**, 840–858.

Yanai, M. and T. Tomita (1998) Seasonal and interannual variability of atmospheric heat sources and moisture sinks as determined from NCEP–NCAR reanalysis. *J. Climate*, **11**, 463–482.

Yasunari, T. (1979) Cloudiness fluctuation associated with the northern hemisphere summer monsoon. *J. Meteorol. Soc. Japan*, **57**, 227–242.

Yasunari, T. (1980) A quasi-stationary appearance of 30–40 day period in the cloudiness fluctuation during summer monsoon over India. *J. Meteorol. Soc. Japan*, **58**, 225–229.

Yasunari, T. (1981) Structure of an Indian summer monsoon system with around 40-day period. *J. Meteorol. Soc. Japan*, **59**, 336–354.

Zheng, Y., D. E. Waliser, W. Stern, and C. Jones (2004) The role of coupled sea surface temperatures in the simulation of the tropical intraseasonal oscillation. *J. Climate*, **17**(21), 4109–4134.

3

Intraseasonal variability of the atmosphere–ocean–climate system: East Asian monsoon

Huang-Hsiung Hsu

3.1 INTRODUCTION

The intraseasonal oscillation (ISO) is one of the major systems affecting the summer monsoon system in East Asia and the Western North Pacific (EA/WNP). This has become known to the scientific community since the late 1970s and early 1980s. Studies (e.g., Krishnamurti and Bhalme, 1976; Murakami, 1976; Yasunari, 1979; Krishnamurti and Subrahmanyan, 1982) report the prominent northward ISO propagation at both 10 to 20-day and 30 to 60-day periods in the Asian summer monsoon region. The passage of these intraseasonal fluctuations tended to be in phase with the onsets[1] (i.e., beginning of wet phases) and breaks (i.e., beginning of dry phases) of the Indian summer monsoon. It was noted that northward movement also tended to occur simultaneously in EA/WNP (e.g., Yasunari, 1979). Other intraseasonal features in EA/WNP were also documented. For example, Murakami (1980) found 20 to 30-day perturbations propagating westward along 10°N–20°N and northward over the South China Sea.

Studies on the EA/WNP summer ISV flourished after the First GARP Global Experiment (FGGE). The summer monsoon experiment provided a dataset that for the first time documented the entire Asian summer monsoon in detail. The completeness of this dataset spawned a great number of studies on the summer ISO not only in South Asia but also in EA/WNP. These studies (e.g., Lorenc, 1984; Murakami, 1984; Murakami *et al.*, 1984a, b; Nakazawa, 1986; Ninomiya and Muraki, 1986; Chen, 1987; Chen and Murakami, 1988; Hirasawa and Yasunari, 1990 provide us with a basic understanding of summer EA/WNP ISV and lay the foundation for further exploration on this subject. Interestingly and incidentally, intraseasonal variability in the summer FGGE year (i.e., summer of 1979)

[1] The summer monsoon is characterized by rainy and dry periods that often occur intermittently. "Onset" ("active") and "break" are often used to refer to the beginning of the rainy and dry periods.

W. K. M. Lau and D. E. Waliser (Editors), *Intraseasonal Variability in the Atmosphere–Ocean Climate System* (Second Edition).

happened to be one of the most pronounced in recent history. Although the FGGE experience might not yield a general understanding of EA/WNP ISV, it certainly paved the way for many important findings and stimulated ideas over the past two to three decades. One of the intriguing characteristics of EA/WNP ISV is its close relationship with the monsoon system. As will be discussed below, ISO has been reported to fluctuate concurrently with monsoon onset and withdrawal in this region. This concurrence is most evident in the boreal summer. It has been obvious for many years that ISV in this region cannot be examined and studied independently of the monsoon system. The complex land–sea contrast and topography create a complicated monsoon system in EA/WNP that evolves through several stages in the summer. Seasonal evolution of the monsoon, in which ISO embeds itself, inevitably affects ISO spatial distribution and temporal evolution. This in-phase relationship with the annual cycle leads to a seasonally and regionally prominent ISV.

The East Asian summer monsoon is a system involving both tropical and extratropical fluctuations, a unique characteristic that cannot be found in other monsoon areas. Tropical–extratropical interaction is an inherent property of EA/WNP ISV. In addition to these unique features, the WNP is one of the major breeding regions for tropical cyclones and typhoons. These intraseasonal fluctuations, associated with strong variation in convective activity and large-scale circulation, are found to modulate typhoon activity in the Western North Pacific. EA/WNP ISV is under the influence of the tropical intraseasonal oscillation (TISO), which propagates eastward from the Indian Ocean to the Western Pacific (e.g., Lorenc, 1984; Lau and Chan, 1986; Chen *et al.*, 1988). However, it is also likely that some of this variability is inherently regional and independent of the TISO (Wang and Rui, 1990).

This chapter summarizes the major characteristics of summertime ISV in the EA/WNP monsoon system. The content includes the general characteristics of the monsoon system; seasonality, periodicity, regionality in ISV; the close relationship with the summer monsoon system; the spatial structure and temporal evolution of the ISO; its modulating effect on and upscale feedback from typhoon activity.

3.2 GENERAL CHARACTERISTICS OF EA/WNP MONSOON FLOW

Before the ISV discussion, it is essential to understand the general characteristics of the background monsoon flow in which intraseasonal fluctuations exhibit prominent seasonality and regionality. The Asian monsoon—which covers South Asia, Southeast Asia, tropical and extratropical East Asia, and the Western North Pacific—is the largest monsoon system on Earth. Although this system is basically a tropical system in South and Southeast Asia, it extends well into extratropical East Asia. In other words, the monsoon system exhibits both tropical and extratropical circulation characteristics. Because of the complex land–sea contrast and the high-rising topography, the Asian monsoon exhibits prominent regionality, especially in the summer. This regional characteristic can be divided into several subsystems

according to their distinctive characteristics (e.g., Murakami and Matsumoto, 1994; Wang and LinHo, 2002). The EA/WNP monsoon is the easternmost subsystem that affects the weather and climate in East Asia and the Western North Pacific.

The summer season definition used here is unconventional. The four-season concept is based on the astronomical calendar. However, a natural season—often defined based on distinct weather/climate characteristics—does not always fall into these four categories. It is common practice in climate research to define the seasons based on natural season characteristics. Since the summer monsoon can begin as early as May and begins withdrawing southward in September, the long-term circulation and convection means averaged from May to September (MJJAS) are defined here to represent the summer mean state.

Figure 3.1a presents summer precipitation[2] and 850 hPa circulation.[3] Note that the major precipitation in this region during the summer is generally collocated with deep convection. Large precipitation and deep convection are therefore used interchangeably here. In contrast to precipitation in South Asia and the Indian Ocean, which tends to cluster in relatively limited areas (e.g., the Bay of Bengal), the precipitation in EA/WNP exhibits banded structures that are zonally elongated. Two such banded structures exist in the tropics and extratropics. The tropical band extends eastward from the South China Sea to the dateline and the weaker extratropical band extends eastward from Japan to the Central North Pacific. Between these two precipitation bands, a region of suppressed precipitation exists.

The major precipitation in the South China Sea and the extratropical precipitation band tend to lie near a region of strong low-level southwesterly winds. For example, a southwesterly wind band extends from the Arabian Sea eastward all the way to the South China Sea and the western Philippine Sea. This southwesterly wind band is associated with the continental thermal low (i.e., the cyclonic circulation in the Asian continent) and the monsoon trough in the Western North Pacific (i.e., this troughlike circulation and the major precipitation region extends southeastward from the Indochina Peninsula to the tropical Western North Pacific). Another southwesterly wind band extends from southeast China to Japan. These two southwesterly wind bands collocate with regions that endure major precipitation. The tropical precipitation band in the tropical Western North Pacific occurs in a confluent zone where westerly and easterly winds merge. The subtropical anticyclone occupies a vast area in the Western North Pacific where convection is inactive. The existence of this anticyclone is the main reason for separation of the two precipitation bands. The southern precipitation band is associated with monsoon trough variation in the Western North Pacific, while the northern band is associated with the Meiyu (in China), Baiu (in Japan), and Changma (in Korea), which are the major precipitation and circulation systems embedded in the East

[2] The pentad data of the CPC Merged Analysis of Precipitation (CMAP) from 1979 to 1992 were used here. The precipitation data on a $2.5^\circ \times 2.5^\circ$ grid are a combination of gauge precipitation, various satellite observations, and numerical model outputs (Xie and Arkin, 1997).

[3] The European Centre for Medium-Range Weather Forecast (ECMWF) reanalysis from 1979 to 1993 (Gibson *et al.*, 1997) is used to illustrate the circulation.

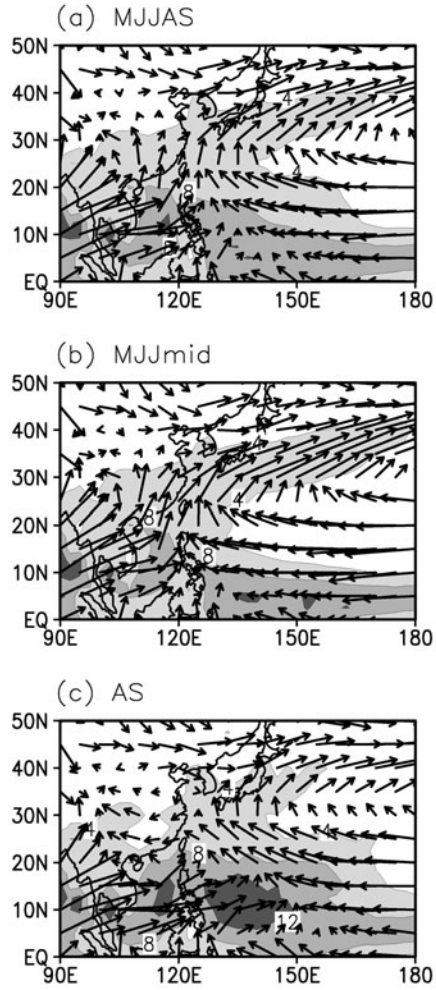

Figure 3.1. Climatological mean precipitation and 850 hPa winds during (a) May to September, (b) May to mid July, and (c) August to September. Areas where precipitation is greater than 4 mm/day are shaded. The contour interval is 4 mm/day.

Asian summer monsoon. The continental thermal low, the East Asian monsoon trough, and the subtropical Pacific anticyclone are the three major components of the EA/WNP monsoon during the northern summer. Intraseasonal variability in the different regions of East Asia and the Western North Pacific is closely related through these circulation systems.

The EA/WNP summer monsoon, which is characterized by abrupt changes, can be divided into several stages (e.g., Matsumoto, 1992; Murakami and Matsumoto, 1994; Ueda *et al*., 1995; Wang and Xu, 1997; Wu and Wang, 2001; Wang and LinHo, 2002). An excellent historical review on the division in natural seasons can

be found in Matsumoto (1992). One of the most notable phenomena is the abrupt change in convection and circulation in late July (e.g., Ueda and Yasunari, 1996; Wu, 2002; Wu *et al*., 2009). As will be discussed in the following section, this abrupt change has a significant influence on ISV seasonality and regionality.

Figures 3.1b, c illustrate contrasting circulation and convection characteristics during the first and second half of the summer. During the first half period (i.e., May to mid July), the monsoon trough extends eastward only to the Philippines and the subtropical anticyclonic ridge extends westward over Taiwan and southeast China. The tropical westerly and easterly winds between the equator and 20°N merge near the Philippines where a confluent zone is located. Strong southerly and southwesterly winds are located at the western and northern flanks of the subtropical anticyclone. The southwesterly winds extending from the Indochina Peninsula and the South China Sea reach as far north as Japan. Two notable precipitation bands are located to the south and north of the anticyclone where winds are strong.

During the second half period (i.e., August to September, Figure 3.1c), the monsoon trough penetrates as far east as 150°E while the subtropical anticyclonic ridge shifts northward to Japan. East China and Japan are under the influence of a southeasterly wind from the Pacific, in contrast to the southwesterly from the South China Sea during the first half period. Large-scale precipitation distribution is very different from its counterpart in the first half period. The convection in the Philippine Sea is fully developed and shifts northward to around 15°N. At the same time, the extratropical precipitation band appearing in the first half of summer weakens. The precipitation characteristics shown in Figure 3.1 are consistent with results based on infrared equivalent blackbody temperature (e.g., Kawamura and Murakami, 1995) and high-cloud amount (e.g., Kang *et al*., 1999).

3.3 PERIODICITY, SEASONALITY, AND REGIONALITY

Two frequency bands equivalent to the 30 to 60-day and 10 to 30-day periods dominate the EA/WNP ISV. These two periodicities are also characterized by strong seasonal and regional dependence. In a study on East Asian summer rainfall variability, Lau *et al*. (1988) find the coexistence of 40-day and 20-day oscillation. The 40-day oscillation occurred in the period from April to September, while the 20-day oscillation was active only from July to September. They suggest that the 40-day oscillation was associated with the TISO, while the 20-day oscillation was a local phenomenon. Tanaka (1992) find that the 20 to 25-day mode existed north of 13°N while the 30 to 60-day mode was active south of 13°N. Chen *et al*. (2000) identify the presence of two well-separated spectral peaks with periods around 30–60 days and 12–24 days in the South China Sea and the Meiyu/Baiu front region (i.e., East China and Japan). Similar observations have been identified in many studies (e.g., Chen and Chen, 1995; Wang and Xu, 1997; Fukutomi and Yasunari, 1999; Kang *et al*., 1999).

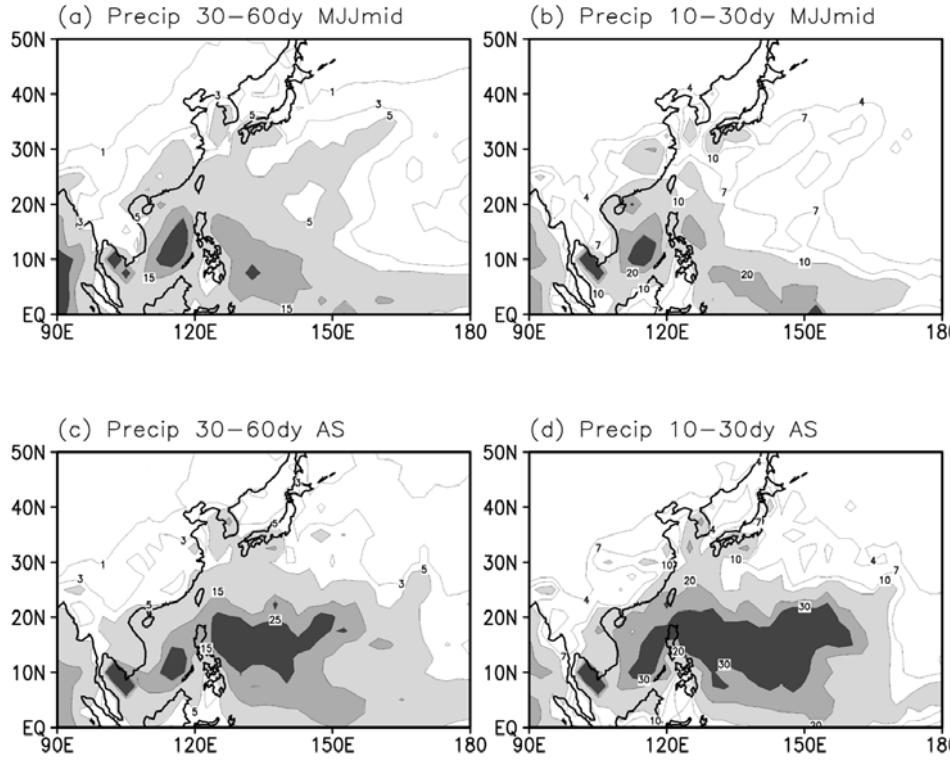

Figure 3.2. Precipitation variance for 30 to 60-day (left) and 10 to 30-day (right) perturbations during (a, b) May to mid July, and (c, d) August to September. The contour interval is 10 mm^2/day^2 for precipitation greater than 5 (10) mm^2/day^2 for 30 to 60 (10 to 30)-day perturbations. Contour lines are also drawn for smaller levels of precipitation as indicated in the figures.

Based on the previous results, it is logical to examine ISV in two periodicities: 30–60 days and 10–30 days. A Butterworth recursive filter was used to isolate the signals in these two periodicity bands (Kaylor, 1977; Hamming, 1989). Figure 3.2 presents the 30 to 60-day and 10 to 30-day precipitation variance distributions during the first (early) and second (late) half of summer. As shown in Figure 3.2, large variability in both frequency bands is largely restricted to south of 30°N during the entire summer. The major 30 to 60-day variance center in early summer is located in the South China Sea and a secondary center is observed in the western Philippine Sea south of 15°N (Figure 3.2a). Weaker variance is seen in Japan, Korea, and a band extending from Taiwan to 160°E along 25°N. These maximum variance regions are collocated with the two precipitation bands shown in Figure 3.1b. This indicates that precipitation fluctuates more widely in regions where mean precipitation is large.

In late summer (Figure 3.2c), the largest variability observed in the Philippine Sea extends eastward to 170°E. Comparison between Figure 3.2a and 3.2c indicates

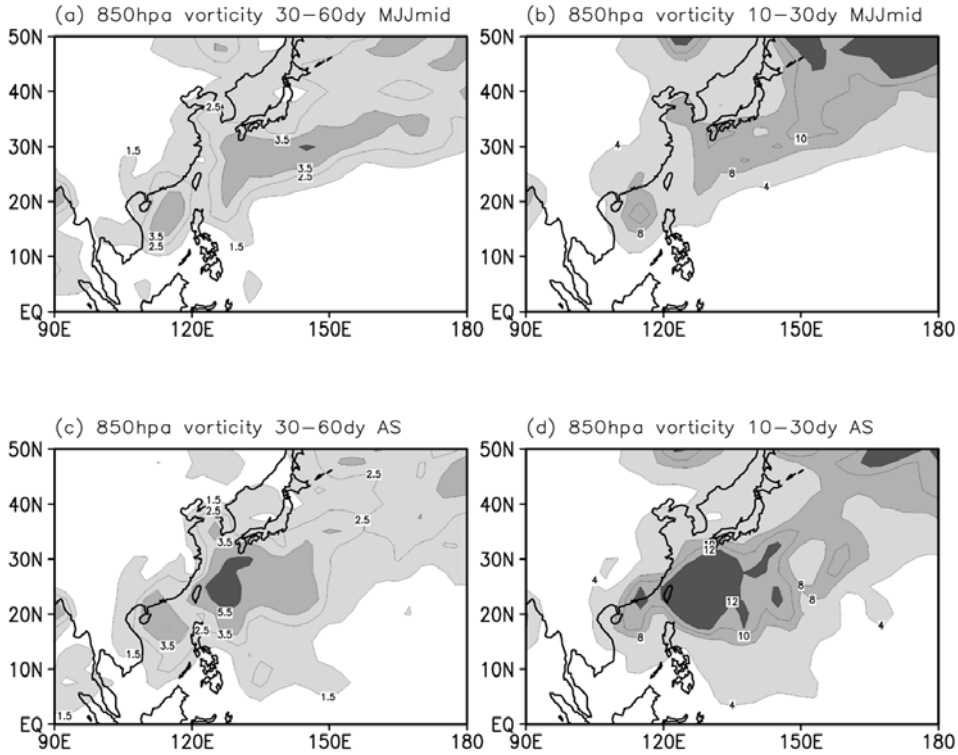

Figure 3.3. The same as Figure 3.2 except for 850 hPa vorticity. The contour intervals are $1 \times 10^{-10}\,s^{-2}$ and $4 \times 10^{-10}\,s^{-2}$ for the 30 to 60-day and 10 to 30-day disturbances, respectively.

that the major activity in 30 to 60-day perturbations shifts eastward from the Bay of Bengal and the South China Sea to the Western North Pacific during the seasonal march from early to late summer. The most notable change in the Western North Pacific is the northward shift of the maximum variance region from 5°N to 10°N–15°N. This change occurs concurrently with the northward shift of the tropical precipitation band and the subtropical anticyclone seen in Figure 3.1b and 3.1c. The 10 to 30-day variance is about 1.5 times as large as the 30 to 60-day variance (Figure 3.2b and 3.2d). Seasonal and regional dependences similar to those seen in the 30 to 60-day variability are also observed in the 10 to 30-day variability. The contrast in the Philippine Sea between the early and late summer is more prominent than that in the 30 to 60-day band.

The 850 hPa vorticity variance, which exhibits more pronounced extratropical variability, is shown in Figure 3.3 to illustrate ISV in low-level atmospheric circulation. During the northern summer, 850 hPa vorticity variance in the tropics and subtropics is closely associated with precipitation variability in both frequency bands. The major 850 hPa vorticity variance centers tend to be located to the

north of precipitation variance centers. The significant variance in the extratropics reflects the dominance of extratropical circulation fluctuations, which are less closely coupled with deep convection.

In early summer, a northeast to southwest–oriented banded structure is observed in both the 30 to 60-day and 10 to 30-day variance in the Western North Pacific southeast of Japan (Figure 3.3a, b). This structure is associated with the elongated secondary maximum precipitation variance located to its south (Figure 3.2a, b). This feature reflects the strong intraseasonal activity of the Meiyu (Baiu) quasi-stationary fronts, which is a prominent phenomenon during the period from mid June to mid July in East China and Japan. Note that during this period the subtropical 850 hPa southwesterly wind prevails in the region extending from East China to the Pacific southeast of Japan (Figure 3.1b). This windy region is located near the large 850 hPa vorticity and precipitation variance regions for both 30 to 60-day and 10 to 30-day bands. Another variance maximum is located in the northern South China Sea, where the monsoon trough and the precipitation variance maximum reside (Figures 3.1b, 3.2a, c). Despite the tendency for collocation between the large 850 hPa vorticity and precipitation variance, the maximum 850 hPa vorticity variance is located mostly to the north of 20°N, while the maximum precipitation variance is located mostly to the south of 15°N. This contrast reflects the weaker coupling between deep convection and low-level circulation in early summer.

In late summer, the 30 to 60-day and 10 to 30-day vorticity variance exhibits similar spatial distributions (Figures 3.3c, d). The subtropical banded structure no longer exists because of the Meiyu (Baiu) withdrawal. Instead, a bullseye-shaped 850 hPa vorticity variance is found in the Western North Pacific between 15°N and 35°N. This variability is associated with major precipitation variance located to the south in a latitudinal band between 10°N and 25°N (Figures 3.2c, d). In contrast to the well separation between the precipitation and 850 hPa vorticity variance maxima in early summer, the coupling between convection and low-level circulation is apparently much more significant in late summer. The phase relationship between precipitation and vorticity variance is likely associated with the westward and northwestward-propagating intraseasonal perturbations prevailing in this area (see the discussion in Section 3.4). During this period, the monsoon trough and the westerly wind extend southeastward into the Philippine Sea while the subtropical Pacific anticyclone shifts to the north with the ridge sitting around Japan. The prevailing wind in East Asia and the subtropical Western North Pacific is a southeasterly wind instead of a southwesterly wind as in the early summer. The largest 850 hPa vorticity variance is embedded in the strong southeasterly wind region. These changes in ISV occur concurrently with circulation changes between early and late summer. It again reflects the in-phase relationship between ISV and monsoon seasonal evolution.

The variance distributions shown above confirm the regionality and seasonality of the EA/WNP ISV, as has been reported in many previous studies (e.g., Lau *et al.*, 1988; Nakazawa, 1992; Tanaka, 1992; Kawamura and Murakami, 1995; Kawamura *et al.*, 1996; Wang and Wu, 1997; Wang and Xu, 1997; Fukutomi and Yasunari,

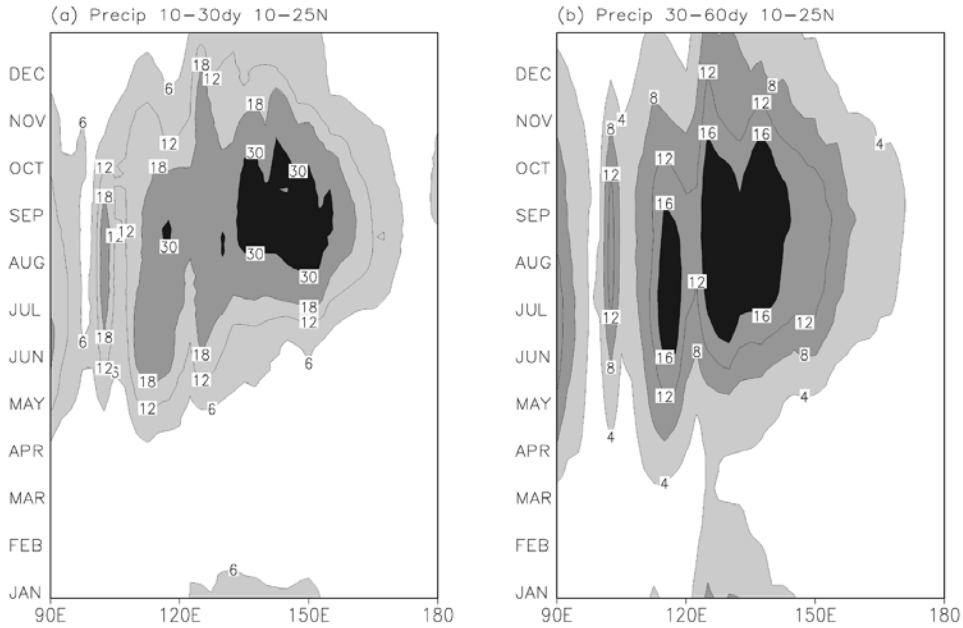

Figure 3.4. Hovmöller diagrams of running variance (see text for explanation) for the (a) 10 to 30-day and (b) 30 to 60-day precipitation perturbations averaged over 10°N–25°N. The contour intervals are 6 mm^2/day^2 and 4 mm^2/day^2 for the 10 to 30-day and 30 to 60-day perturbations, respectively.

1999; Kang *et al.*, 1999). To summarize the seasonal dependence of ISV, variances were computed for each calendar date (from January 1 to December 31) based on data from a certain period (or window) that centered on the corresponding calendar date. Since this is an approach similar to the way running means are calculated, the computed variance is called running variance.[4]

The longitudinal–time running variance diagrams for precipitation averaged over 10°N–25°N in the 10 to 30-day and 30 to 60-day bands are presented in Figure 3.4a, b, respectively. For the 10 to 30-day band, the earliest activity takes place in the South China Sea (e.g., 110°E–120°E) in mid May, followed by activity in the far western Philippine Sea (e.g., 120°E–130°E) and the West Indochina Peninsula (e.g., 100°E) in late May, and finally the Western North Pacific (e.g., 130°E–150°E) in mid August. The most significant contrast is between the South China Sea and the Western North Pacific. The 10 to 30-day activity in the South China Sea lasts from May to September, while its counterpart in the Western North Pacific does not occur

[4] Different window lengths might result in different results. Tests based on various window lengths yielded similar results except that the longer lengths yielded a smoother temporal evolution. In other words, a running variance is not particularly sensitive to the window length as long as the length is long enough compared with corresponding intraseasonal timescales. Running variances based on 60 and 120-day window lengths are shown here for the 10 to 30-day and 30 to 60-day bands, respectively. The variance was calculated from all years and, therefore, contains the interannual variation of ISV.

until late July and early August and lasts through November. The sudden convection flareup in the Western North Pacific is consistent with the abrupt change in WNP circulation, as documented by many studies (e.g., Matsumoto, 1992; Murakami and Matsumoto, 1994; Ueda *et al*., 1995; LinHo and Wang, 2002). This result is consistent with the findings of Hartmann *et al*. (1992). They find that the spectral peak around 20–25 days was most significant in the tropical Western North Pacific and exhibited the largest amplitudes during the September–December season.

The seasonal evolution of 30 to 60-day precipitation variability takes places in an order similar to its 10 to 30-day counterpart. However, the maximum variance in the South China Sea and the Western North Pacific tends to appear earlier than the 10 to 30-day perturbations. Maximum variability in the Western North Pacific occurs in June almost concurrently with activity in the South China Sea. This feature is the major contrast to 10 to 30-day variability, which does not become active in the Western North Pacific until late summer.

3.4 INTRASEASONAL OSCILLATION PROPAGATION TENDENCY

The TISO is well known for its eastward propagation along the equator (as shown in previous chapters). Similarly, the EA/WNP ISO has been known to propagate in certain directions. One of the most prominent features is the northward/northwestward propagation in the Western Pacific during the boreal summer, which has been documented in many studies (e.g., Lau and Chan, 1986; Nitta, 1987; Chen *et al*., 1988; Wang and Rui, 1990). These studies found that the eastward-propagating TISO could trigger northward-propagating intraseasonal perturbations in the equatorial Western Pacific. This time lag relationship can also be seen clearly in Figure 4.10. However, Wang and Rui (1990) note that many northward-propagating intraseasonal perturbations observed in the Western North Pacific were spawned in the equatorial Western Pacific and were independent of the TISO. The other prominent feature is the westward propagation from the Western North Pacific to East Asia and sometimes to the Indochina Peninsula and India (e.g., Murakami, 1980; Wang and Rui, 1990; Chen and Chen, 1995).

This propagation tendency has been explored most intensively in the studies discussed above. Wang and Rui (1990) document the ISO propagation paths for all seasons using a semi-subjective approach. The more objective approach taken by Jones *et al*. (2004) yielded similar results in describing the TISO eastward propagation. Another way to present the overall ISO propagation tendency is to use a propagation tendency vector derived from lagged correlation maps. This technique, used in many studies (e.g., Lau and Chan, 1986; Nitta, 1987; Hsu and Weng, 2001; LinHo and Wang, 2002; Hsu *et al*., 2004a), provides information about the propagation tendency at every location in the most efficient way.

Previous studies report that the 10 to 30-day and 30 to 60-day perturbations exhibit different propagation characteristics in different seasons (e.g., Wang and Xu, 1997; Fukutomi and Yasunari, 1999; LinHo and Wang, 2002). It is therefore sensible to examine the propagation tendency of both the 10 to 30-day and 30 to 60-day

perturbations during early and late summer. The propagation tendency vectors[5] for the 850 hPa vorticity anomalies shown in Figure 3.5 were derived from the 5-day and 2-day lagged correlation maps for the 30 to 60-day and 10 to 30-day bands, respectively. In early summer (Figure 3.5a), the major propagating features for the 30 to 60-day band are the northwestward propagation in the South China Sea, the East China Sea, and the western Philippine Sea, and the northward propagation in South China. Other propagation features include westward propagation in the eastern Philippine Sea and southward propagation from 50°N to 20°N between 140°E and 160°E. In lagged correlation terms, the westward and northwestward propagation are the most prominent features.

In late summer (Figure 3.5c), northwestward propagation extends to Southeast China and becomes the most dominant feature in EA/WNP. To the east of this northwestward propagation region, a westward propagation region exists. It will be shown in Section 3.7 that the northwestward-propagating features in the Philippine Sea often originate from the westward-propagating features occurring between 150°E and the dateline. Propagation in other directions, seen in early summer, is then no longer evident. Southward propagation (e.g., to the east of Japan) in early summer is replaced by a northward propagation region that extends all the way to north Japan.

For the 10 to 30-day band during early summer (Figure 3.5b), westward propagation is the predominant feature in the whole domain between 5°N and 15°N. Southwestward propagation is found in the region from Japan to the northern Philippine Sea, indicating an extratropical origin for the 10 to 30-day ISO. In late summer (Figure 3.5d), the westward propagation in the Philippine Sea seen in early summer is replaced by northwestward propagation, while the southward propagation to the east of Japan is replaced by northward propagation. The clockwise-rotating propagation tendency vectors in the Western North Pacific might be related to the frequent recurrence of recurving tropical cyclones in late summer (Schnadt *et al.*, 1998). The contrast between early and late summer seen in the 30 to 60-day band is also evident in the 10 to 30-day band.

One of the major contrasts between early and late summer is the northern limit for northward tropical origin ISO penetration. Northward propagation is restricted mostly to tropical and subtropical regions in early summer but penetrates farther north to the extratropics in late summer. Conversely, southward propagation of extratropical origin ISO was only active in early summer. This contrast indicates

[5] It should be noted that these tendency vectors represent only the local tendency and do not provide information about the full path along which an ISO propagates. Conversely, one can easily infer ISO propagation in regions where most vectors point in the same direction. This approach usually yields results similar to those obtained based on the approaches taken by Wang and Rui (1997) and Jones *et al.* (2004). To construct such a map, one must compute the lagged correlation coefficients between every gridpoint (i.e., base point) and all gridpoints in the chosen domain with the time series at the base point leading other points by 5 (2) days. One can then draw an arrow from a base point to the point where the lagged correlation coefficient is the largest. This arrow indicates the most probable path for an anomaly at the base point to propagate in the next 5 (2) days. A larger lagged correlation coefficient indicates a stronger propagation tendency. The results shown here were calculated based on the bandpass-filtered data already smoothed using a T24 spectral smoothing technique (Sardeshmukh and Hoskins, 1984). Spatial smoothing yielded a more coherent propagation tendency spatial distribution.

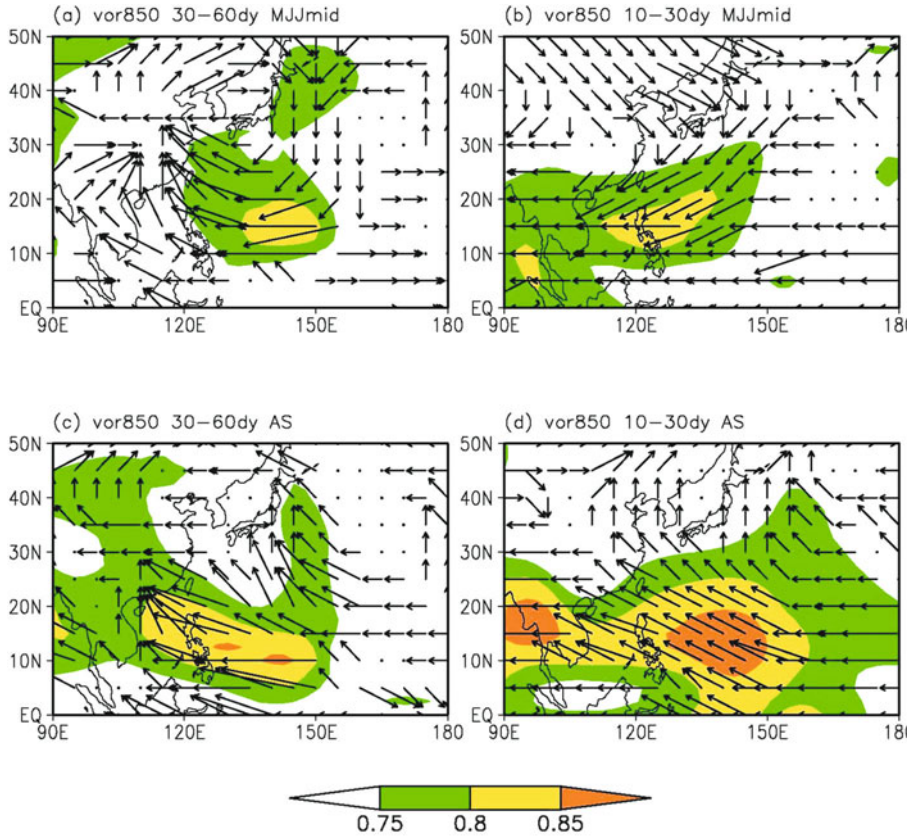

Figure 3.5. Propagation tendency vectors derived from the 5-day and 2-day lagged correlation maps for the 30 to 60-day (left) and 10 to 30-day (right) 850 hPa vorticity perturbations for (a, b) May to mid-July and (c, d) August to September. Shading represents lagged correlation coefficients greater than 0.75 and the contour interval is 0.05. The vector denotes the direction and distance that an anomaly at the base point most likely travels in the next 5 or 2 days. The unit arrow denotes the length of a three-gridpoint distance (i.e., 7.5°).

the different nature of ISV in early and late summer. Extratropical influence is still evident in early summer, while tropical influence dominates in late summer. All these contrasts seem to occur concurrently with the northward penetration of the East Asian summer monsoon (Tao and Chen, 1987; LinHo and Wang, 2002). It once again illustrates that the nature of the ISO is modulated by the seasonal evolution of the East Asian summer monsoon.

3.5 RELATIONSHIP WITH MONSOON ONSETS AND BREAKS

Prominent active and break periods, which are closely associated with the ISO, characterize the EA/WNP summer monsoon (e.g., Lau and Chan, 1986; Lau *et*

al., 1988; Ding, 1992; Nakazawa, 1992; Tanaka, 1992; Wang and Xu, 1997; Kang *et al*., 1989, 1999; Chen *et al*., 2000; Wu and Wang, 2001). For example, two ISO spells propagated northward in East Asia during the 1998 summer, coinciding with the Yangtze River floods in June and July (Mu and Li, 2000; Xu and Zhu, 2002; Wang *et al*., 2003; Ding *et al*., 2004; Hsu *et al*., 2004b). Similar events occur from year to year.

This northward propagation was found to be often associated with the TISO. Lau and Chan (1986) identify the leading intraseasonal OLR pattern that propagated northward in the Indian Ocean to the Indian monsoon region, northwestward from the Philippine Sea to the northern South China Sea and Taiwan, and eastward along the equator from the Indian Ocean to the maritime continent. The OLR anomaly near Borneo also propagated northward to the northern South China Sea. A similar evolution can be seen clearly in Figure 4.10. This result indicates the close relationship between the TISO and the fluctuation in the EA/WNP summer monsoon. Many studies confirm this relationship. For example, it was suggested (e.g., Chen and Murakami, 1988; Chen *et al*., 1988; Chen and Chen, 1993b) that the Meiyu/Baiu convergence zone fluctuated on an intraseasonal timescale in response to eastward TISO propagation.

The onset of the monsoon in the South China Sea signals the beginning of the East Asian summer monsoon (Tao and Chen, 1987; Lau and Yang, 1997; Wang and LinHo, 2002). It is likely that such a pattern occurring in mid May could trigger the onset of the East Asian summer monsoon as suggested by Lau and Chan (1986). This TISO effect on East Asian summer monsoon onset has been observed for many years. Chen and Chen (1995) study the onset and lifecycle of the South China Sea monsoon during the 1979 summer. They find that onset (break) was triggered by the simultaneous arrival of a westward-propagating 12 to 24-day monsoon low (high) and a northward-propagating 30 to 60-day monsoon trough (ridge) in the northern section of the South China Sea. They point out that northward-propagating 30 to 60-day monsoon perturbation was coupled with the eastward-propagating 30 to 60-day ISO in the tropics. Hung and Hsu (2008) find that most of the sharp onsets of the first transition of the Asian summer monsoon (Yanai *et al*., 1992, Hsu *et al*., 1999), which usually coincides with monsoon onset in the South China Sea in May, are associated with the TISO propagating into the region from the Indian Ocean.

Since the ISO is a large-scale feature, different parts of the monsoon flow often oscillate concurrently with one another under the influence of the ISO. One example is the interaction between summer convection in East Asia and the South China Sea on the intraseasonal timescale. Chen *et al*. (2000) identify a coherent intraseasonal north–south oscillation existing between the Meiyu/Baiu front (MBF, representing East Asia convection) and the Intertropical Convergence Zone (ITCZ, representing South China Sea convection). In between the MBF and the ITCZ is a subtropical anticyclone. Convection activities at the MBF and ITCZ tended to fluctuate out of phase. Figure 3.6a shows the differences between the anomalous 850 hPa streamlines and convection activity composites for the 30 to 60-day ISO during strong (active) and weak (break) monsoon periods in the South China Sea. As seen in Figure 3.6a, when MBF convection was suppressed and ITCZ convection was active, a cyclonic circulation anomaly appeared between 5°N and 30°N, signaling an enhanced

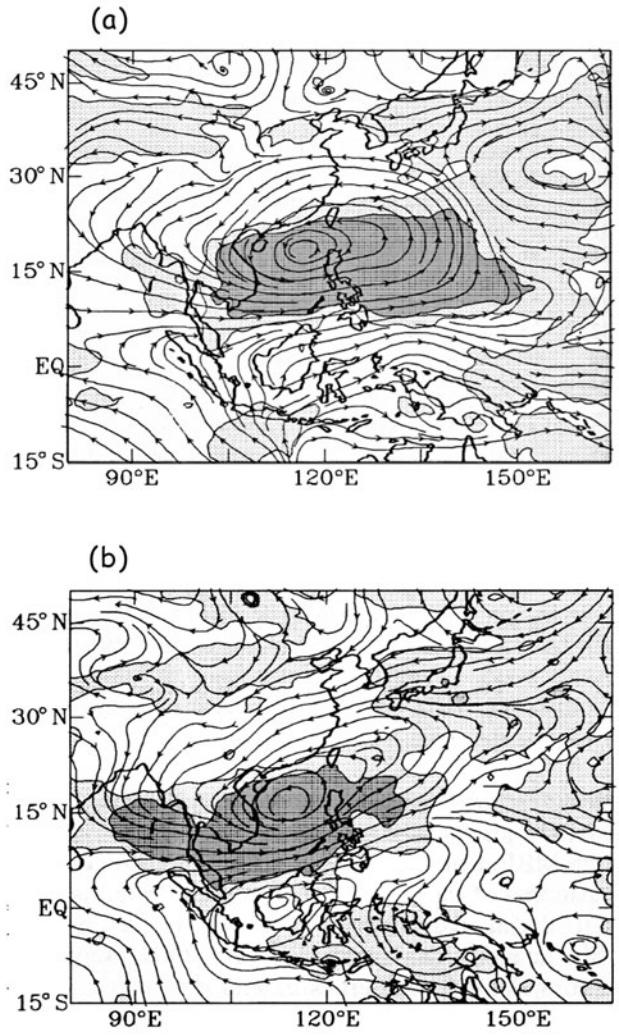

Figure 3.6. Differences between the composite streamline and equivalent blackbody temperature anomaly ($\Delta T_{BB} = 270K - T_{BB} \geq 0$ or $= 0$ if $270K - T_{BB} < 0$) during active and break phases of the westerly anomaly in the South China Sea for the (a) 30 to 60-day and (b) 12 to 24-day mode. The values of $0 \leq \Delta T_{BB} \leq 5K$ and $5K \leq \Delta T_{BB}$ are lightly and heavily stippled, respectively. Positive ΔT_{BB} denote stronger convection (adapted from Chen *et al.*, 2000).

monsoon trough in the region. The reverse situation, which can be inferred from Figure 3.6a by reversing signs, was characterized by enhanced MBF convection, weakened ITCZ convection, and an anticyclonic circulation anomaly in between. This anomalous circulation corresponded to the southwestward penetration of the subtropical anticyclonic ridge or a weaker monsoon trough. Figure 3.6b shows a

similar composite except for the 10 to 24-day ISO. The circulation and convection characteristics are essentially the same as in the 30 to 60-day counterpart, shown in Figure 3.6a, except that the circulation centered at the South China Sea tended to tilt in the northeast–southwest direction and exhibited a larger zonal scale and smaller meridional scale. Apparently, the oscillation in MBF and ITCZ convection was associated with intraseasonal oscillation in the anticyclone on both 30 to 60-day and 12 to 24-day timescales. It was found that the opposite phase variation between MBF and ITCZ convection was caused by the anomalous circulation associated with the northward-propagating 30 to 60-day monsoon trough/ridge from the equator to 20°N and the westward-propagating 12 to 24-day monsoon low/high along the 15°N–20°N latitude. The similar northward-propagating 30 to 60-day oscillation and westward-propagating 10 to 30-day oscillation, clearly evident in Figure 3.2, were found to be the two major intraseasonal features affecting the EA/WNP monsoon. More examples will be discussed below.

Despite the large interannual variability of the EA/WNP summer monsoon, the climatological intraseasonal variation tends to be in phase with the climatological seasonal evolution of the EA/WNP monsoon (i.e., long-term data averages at the same date of the year). Many studies report this interesting characteristic (e.g., Lau *et al*., 1988; Kang *et al*., 1989, 1999; Nakazawa, 1992; Tanaka, 1992; Wang and Xu, 1997; Wu and Wang, 2001). Figure 3.7 (adapted from Lau *et al*., 1988) presents a time–latitude diagram of climatological 10-day mean precipitation averaged over East China (100°E–115°E). The rainy season begins in South China (25°N–30°N) around mid May, signaling the onset of the East Asian summer monsoon. The northward propagation of the maximum precipitation region in June coincides with the onset of the Meiyu in Central China and the Baiu in Japan. The rain band continues moving to about 40°N in early July when the Meiyu suddenly

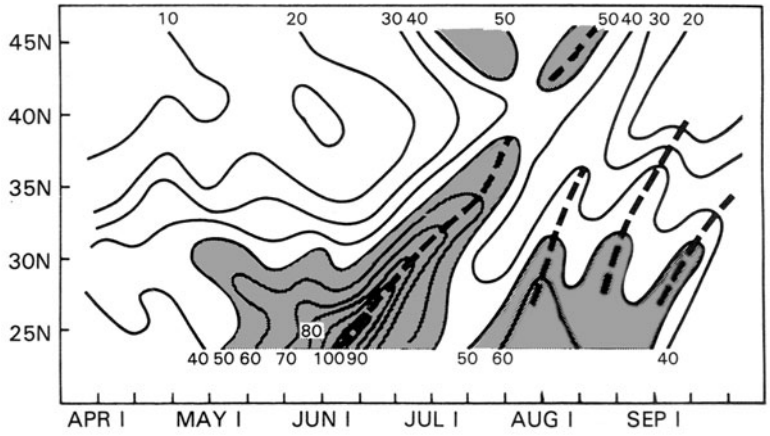

Figure 3.7. Time–longitude section of 10-day mean rainfall over East China (110°E–115°E). Units in millimeters. Regions of heavy rain (>50 mm) are shaded. The heavy dashed lines indicate northward propagation of rain bands (adapted from Lau *et al*., 1988).

ceases, indicating the Meiyu (Baiu) withdrawal in central East China and Japan. Northward propagation weakens slightly in late July and revives again in North China in early August, coinciding with the beginning of the rainy season in the region. The precipitation south of 30°N recovers around early August about 40–50 days after first onset in June. During the period from mid July to early September, an oscillation with a period around 20 days is the major feature observed south of 35°N, while the rainy season ends and the dry period begins in the northern region.

Many studies examine this climatological in-phase relationship. In an examination of fluctuations in high-cloud amount in East Asia, Southeast Asia, and the Western North Pacific, Tanaka (1992) find that the climatological onsets and retreats of convection were associated with the northward-propagating 30 to 60-day ISO from the equator to 13°N, the westward-propagating 20 to 25-day ISO north of 13°N, and seasonal evolution. After close examination, Tanaka (1992) divide the seasonal evolution of the EA/WNP monsoon into seven stages. Each stage corresponds to distinctive characteristics of monsoon flow and convection. Wang and Xu (1997) name this climatological intraseasonal feature embedded in the seasonal evolution of the EA/WNP monsoon as the "climatological intraseasonal oscillation" (CISO). To isolate the CISO, Wang and Xu (1997) first compute the long-term averages of pentad mean data (e.g., OLR) at the same pentad for every year to construct the climatological annual cycle. The first four harmonics are then removed from the time series to filter out fluctuations with periods longer than 90 days. This procedure isolates ISO signals with periods of 10–90 days. Kang *et al.* (1999) examine data on high-cloud amount, representing deep convection, and find that the CISO explained more variance than smoothed seasonal variation (i.e., the sum of the first four harmonics) did in regions of weak seasonal variation (e.g., the Western Pacific between 20°N and 30°N, near Japan, and the southern part of the South China Sea).

Figure 3.8 shows some CISO features in time–latitude and time–longitude plots adapted from Wang and Xu (1997). For the OLR CISO averaged over 122.5°E–132.5°E, there were four spells of northward propagation from 10°S to 20°N during the May–October period (Figure 3.8, left). Northward propagation was most active from May to July and became less organized in mid July. During August and September, northward propagation occurred mostly in the subtropics. These propagation events tended to occur every 30 to 40 days. For the OLR CISO averaged over 12.5°N–22.5°N, four spells of westward propagation associated with northward propagation were observed (Figure 3.8, right). In contrast to northward propagation, westward propagation was more prominent in late summer than in early summer. The OLR CISO in August and September propagated westward all the way to the Bay of Bengal, while propagation in early summer occurred mostly to the east of 120°E. The contrasting propagation characteristics between early and late summer is associated with the abrupt change occurring in late July.

The seven stages and four cycles classified by Tanaka (1992) and Wang and Xu (1997), respectively, are similar although the data type and length are different. The corresponding monsoon characteristics in the four cycles (marked by "w" and "d" in Figure 3.8) defined by Wang and Xu (1997) are described as follows. The peak wet

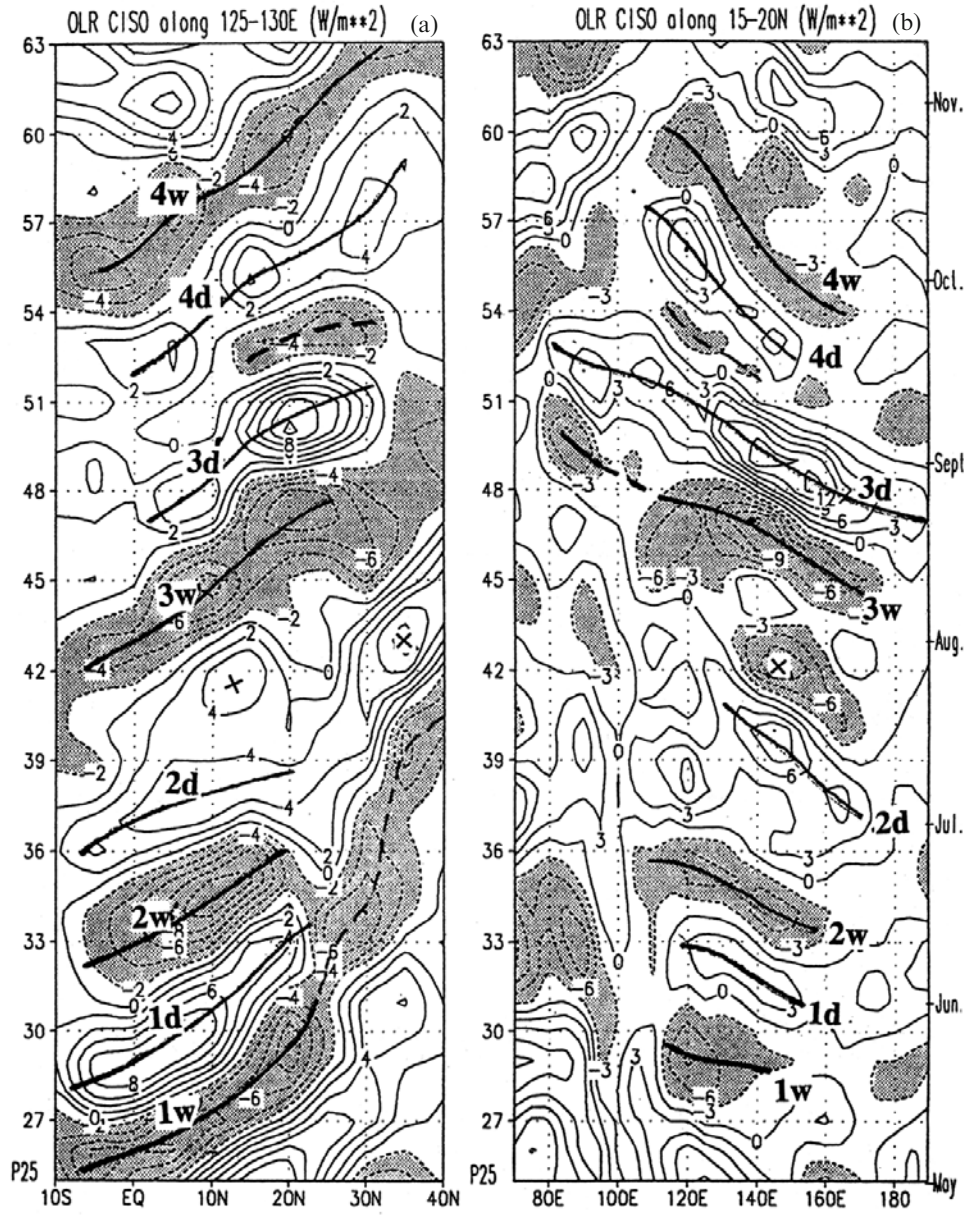

Figure 3.8. Hovmöller diagrams of the outgoing longwave radiation (OLR) CISO averaged over (a) 122.5°N–132.5°N and (b) 12.5°N–22.5°N. Four major propagation episodes are indicated by heavy lines and labels. The labeled numbers indicate the sequence of events and the "d" and "w" denote the dry and wet phases, respectively. The numbers at left-hand side of each panel denote the pentad number (e.g., P25 denotes the 25th pentad—May 1–5—of the year. Note that 1 year is divided into 72 pentads (adapted from Wang and Xu, 1997).

phase of the first CISO cycle occurring between May 16 and May 20 reflects the onset of the South China Sea–Philippine summer monsoon. The following dry phase between May 26 and June 4 corresponds to the pre-monsoon dry period of the Indian summer monsoon, the WNP summer monsoon, and the Meiyu/Baiu region. The peak wet and dry phases of cycle II—occurring between June 15 and June 19 and between July 10 and July 14, respectively—coincide with simultaneous monsoon onsets and breaks in the above three regions. The extremely wet phase of cycle III between August 14 and August 18 marks the peak of the WNP monsoon, while the dry phase of cycle III is characterized by the prominent westward propagation shown in Figure 3.7, which coincides with the second break in the WNP monsoon and the Indian summer monsoon. The wet phase of cycle IV in mid October is associated with the last active monsoon in the Western North Pacific and terminates the Indian summer monsoon.

While the ISO and monsoon seasonal evolution tend to synchronize, the two do not always evolve in phase. The tempo between the two can vary from year to year. This means that one needs to understand how much ISV is explained by the CISO. The CISO variance distribution for precipitation is shown in Figure 3.9a. It exhibits maximum variance in the South China Sea, the Western North Pacific around 20°N, and near Japan. It is interesting to note that CISO variance tends to be larger over the ocean than the land. Kang *et al.* (1999) showed a similar spatial distribution using high-cloud amount. Both results are derived from data representing convection, which is generally larger over the ocean in this area and, therefore, emphasizes variation over the ocean. For comparison, intraseasonal variation (20 to 100-day ISO) was extracted from the CMAP data for every summer. The ratio between ISO variance and total variance is shown in Figure 3.9b. Total variance was computed relative to the long-term mean without any filtering. It therefore includes interannual, seasonal, and intraseasonal variability. The ISO explains more than 50% of total variance in the South China Sea and the Western North Pacific around 20°N, indicating again the importance of the ISO in the EA/WNP monsoon region. While the ISO contributes a large amount of variance, it would be interesting to know how much of that portion is explained by the CISO. Figure 3.9c, which presents the percentage of ISO variance explained by the CISO, reveals that the CISO explains less than 20% of ISO variance in most areas, which is equivalent to less than 10% of total variance. The largest percentage is seen near Japan where the CISO is most active. This result indicates that the interannual variability of the ISO is much larger than CISO variability. Interestingly, only a few studies on the interannual variability of ISOs have been published so far. One of the recent studies is Teng and Wang (2003). They show that westward and northwestward-propagating ISOs in the Western North Pacific are enhanced in July–October during the developing El Niño. This enhancement is due to increased easterly vertical shear over the tropical Western Pacific, which favors northwestward emanation of Rossby waves from the equatorial Western Central Pacific (Wang and Xie, 1996; Xie and Wang, 1996). Lin and Li (2008) further find that intraseasonal northward propagation is strengthened (weakened) over the Western Pacific (east of 140°E) during the El Niño (La Niña) developing summer, while it is suppressed (enhanced) over the South

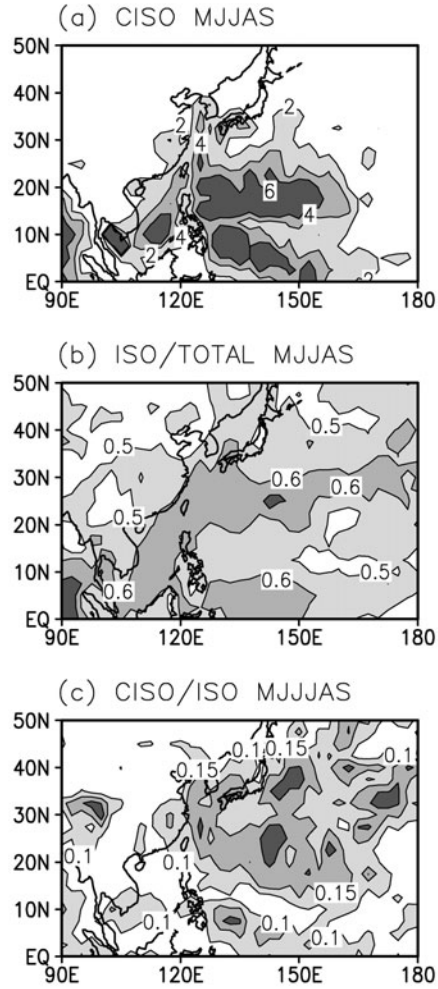

Figure 3.9. (a) Precipitation CISO variance during the May–September period, (b) ratio of precipitation ISO variance to total variance, and (c) ratio of precipitation CISO variance to ISO variance. The contour intervals are $2\,mm^2/day^2$ for (a), and 0.1 and 0.05 for (b) and (c), respectively.

China Sea and the Western Pacific during the El Niño (La Niña) decaying summer. They attribute this contrast to asymmetry of the background mean flow change associated with the developing and decaying phases of ENSO.

The cause and effect between the CISO and the background smoothed annual cycle is an interesting and yet unsolved problem. To understand this, we have to consider the multiscale nature of the ISO and the interaction between phenomena with different time and spatial scales. The processes involved in these multiscale interactions are poorly understood. The following is a scenario based on intuitive

thinking. It has been shown that the TISO tends to flare up under favorable background conditions (e.g., high sea surface temperature, abundant moisture content, etc.). During the seasonal evolution of the EA/WNP summer monsoon, large-scale circulation and moisture distribution evolve slowly and create a breeding ground for the ISO in different regions at different stages of this seasonal evolution. The ISO is therefore more likely to spawn in these regions at the right time of the season. The in-phase relationship between the ISO and seasonal evolution of the EA/WNP monsoon would then occur naturally. The right conditions needed to breed the ISO and how the ISO feeds back into background monsoon flow are other interesting topics for future study.

3.6 THE 10 TO 30-DAY AND 30 TO 60-DAY BOREAL SUMMER ISO

3.6.1 The 30 to 60-day northward/northwestward-propagating pattern

Northwestward propagation in the Philippine Sea is clearly documented in the propagation tendency vectors shown in Figure 3.5. This propagation, which occurs concurrently with northward propagation in South Asia, as seen in Figure 4.10, often appears as one component of a large-scale seesaw pattern dominating summertime intraseasonal variability in the Asian summer monsoon region (Lau and Chan, 1986; Chen and Murakami, 1988; Zhu and Wang, 1993). The evolution of the 850 hPa vorticity and OLR anomalies associated with northwestward-propagating 30 to 60-day disturbances documented by Hsu and Weng (2001) is presented in Figure 3.10. Before the appearance of a positive vorticity anomaly in the Philippine Sea on day –5 (Figure 3.10c), two negative OLR anomalies (one from the west along the equator, the other from the east in the subtropics) located to the east of positive vorticity anomalies merge in the Philippine Sea (Figure 3.10b). This merging results in the large OLR anomaly in the Philippine Sea and enhancement of the 850 hPa vorticity anomaly, which has been propagating westward in the subtropics and is a part of the wavelike structure extending northeastward from the South China Sea to the Central North Pacific (Figure 3.10c). The coupled convection–circulation system then propagates northwestward toward Taiwan and Southeast China and dissipates when it approaches the land area (Figure 3.10d–e).

Kawamura *et al.* (1996) document the northward propagation in the 110°E–160°E longitudinal band and present results similar to those shown in Figure 3.10. Kawamura *et al.* (1996) summarize the circulation and convection characteristics during the period when the 30 to 60-day deep convection is active in the South China Sea and the Philippine Sea, equivalent to Figure 3.10c. At this stage, both the southwesterly wind from the Indian Ocean and the southeasterly wind from the Pacific were enhanced. This indicates enhancement of the east–west vertical circulations across the Indian Ocean and the Western Pacific, corresponding to enhanced convection in the South China Sea and the Philippine Sea. The north–south vertical circulations between 110°E and 160°E, with rising motion between 10°N and 20°N and sinking motion to the north and south, are also enhanced.

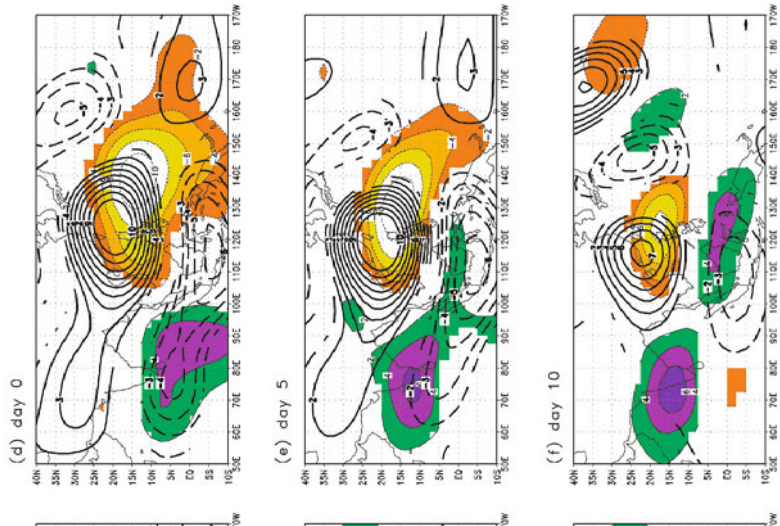

Figure 3.10. Evolution of the 30 to 60-day OLR and low-level circulation patterns in the Western North Pacific (adapted from Hsu and Weng, 2001). Lagged regression coefficients between the OLR anomaly averaged in 120°E–160°E, 0–20°N and the OLR (shaded) and 850 hPa vorticity (contoured) at (a) day −15, (b) day −10, (c) day −5, (d) day 0, (e) day 5, (f) day 10. The ontour intervals are 2 W/m^2 and 1×10^{-7} s^{-1} for OLR and vorticity, respectively. Dark shading and solid lines indicate positive values, while light shading and dashed (and dotted) lines indicate negative values. The regression coefficients have been multiplied by one standard deviation of the OLR index, and only those that are significant at the 0.05 level are plotted.

Many mechanisms have been proposed to explain the eastward-propagating TISO. In comparison, the mechanisms responsible for the northward/northwestward propagation are poorly understood. Nitta (1987) document a similar feature in the Western North Pacific and suggest that propagation was probably due to advection by the southeasterly prevailing in the Philippine Sea during the summer. However, Hsu and Weng (2001) find that the pattern propagated at a speed much faster than the background wind speed. Wang and Xie (1997) simulate northwestward propagation in a shallow-water model. They suggest that the propagating disturbance was an equatorial Rossby wave breaking away from the Kelvin–Rossby wave packet, which propagates from the Indian Ocean into the Pacific and dissipates near the equatorial Central Pacific. However, an equatorial Rossby wave would not propagate northwestward unless there is a strong potential vorticity (PV) gradient in the northeast–southwest direction. Since such a PV gradient was not observed, other mechanisms have to be considered to explain the northwestward propagation of the ISO.

Hsu and Weng (2001) suggest that the frictional convergence associated with the Rossby wave–like circulation might result in northwestward propagation of the system. During the evolution, surface friction results in frictional convergence near the center of the Rossby wave–like cyclonic circulation, which is located to the northwest of the deep convection (e.g., day 0 in Figure 3.10c). The anomalous southwesterly in the southwestern quarter of the 850 hPa vorticity anomaly extracts surface latent heat flux from the Indian Ocean and the South China Sea and transports moisture into the center of the anomalous circulation. The anomalous moisture convergence northwest of the deep convection not only fuels the anomalous convection and circulation but also helps create less stable conditions in the lower troposphere, a precondition for further northwestward propagation. This interpretation is consistent with Kawamura *et al.* (1996) who conclude that moisture convergence occurring north of the deep convection is responsible for northward propagation.

Jiang *et al.* (2004) propose that the combination of the vertical shear mechanism and moisture–convection feedback mechanism leads to northward propagation of the ISO in the boreal Asian monsoon region. The first mechanism generates barotropic vorticity due to the coupling between the free atmosphere baroclinic and barotropic modes in the presence of the vertical shear of the mean flow. The induced barotropic vorticity in the free atmosphere further causes a moisture convergence in the planetary boundary layer, leading to northward shift of convective heating. Tsou *et al.* (2005) conclude from a vorticity budget calculation that the combined effect of surface-diabatic heating and vorticity advection causes intraseasonal circulation and convection to develop and propagate simultaneously northwestward in the Western North Pacific.

The atmosphere–ocean interaction has been proposed as an important mechanism for the eastward-propagating TISO (e.g., Flatau *et al.* 1997). Hsu and Weng (2001) explore the relationship between atmospheric circulation, sea surface temperature, and surface heat fluxes. They find that, although positive SST anomalies were found in the region located to the northwest of the anomalous

convection, analysis of surface heat flux anomalies indicated less heat fluxes from the ocean surface to the atmosphere in this positive SST anomaly region. Instead, evaporation in the ocean located to the southwest of the cyclonic circulation, where anomalous southwesterly winds prevailed (e.g., day −5 to day 10 in Figure 3.10), was the major source of moisture, which was transported to the center of the cyclonic circulation by the southwesterly wind anomalies. This result suggests that the ocean northwest of anomalous convection does not play an active role in destabilizing the lower troposphere by heating the lower atmosphere. Hsu and Weng (2001) conclude that the atmosphere–ocean interaction might help maintain the northwestward-propagating ISO, but the ocean played a passive role by supplying moisture in response to atmospheric forcing. On the other hand, a recent study by Zhou and Li (2010) finds that rectified surface latent heating due to synoptic-scale variability contributes to the propagation. While many processes have been identified for their contribution to propagation of the WNP ISO, their relative importance has yet to be evaluated. One thing we do know is that the mechanism responsible for ISO propagation in the WNP is likely quite different from that for eastward propagation of the MJO.

The evolution shown in Figure 3.10 exhibits certain characteristics that are not observed in the circulation and convection associated with the TISO (e.g., Figure 4.10). One of the most notable features is the Rossby wave–like perturbation extending from the South China Sea to the extratropical WNP. This suggests that the 30 to 60-day ISO in EA/WNP is not entirely a response to the TISO, as suggested in previous studies. Instead, it is also affected by perturbations originated in EA/WNP. The presence of the wavelike structure indicates that the tropical–extratropical interaction could be an important process affecting the 30 to 60-day ISO in EA/WNP. Nitta (1987) note a similar wavelike pattern, which exhibits strong variability on both intraseasonal and interannual timescales. The wavelike pattern exhibits a phase reversal between the 850 hPa and 200 hPa circulations in the South China Sea and the Philippine Sea, where the tropical heating perturbations were located, and essentially a barotropic vertical structure in the extratropics (Kawamura *et al.*, 1996). Because of its similarity to theoretical results (e.g., Hoskins and Karoly, 1981), this wave pattern was interpreted as Rossby wave dispersion forced by northward-propagating convection in the Philippine Sea (e.g., Kawamura *et al.*, 1996; Hsu and Weng, 2001). While the Rossby wave–like packet develops continuously downstream into the extratropical North Pacific, an individual cyclonic (anticyclonic) anomaly along with the active (suppressed) convection to its southeast propagates westward like a Rossby wave. When these individual circulation and convection anomalies reach the South China Sea, they trigger another wavelike packet with reversed polarity, which again emanates into the extratropical North Pacific. Another round of ISOs with opposite signs is then ready to repeat their predecessors' paths.

Kawamura and Murakami (1995) study the interaction between mean summer monsoon flow and 45-day perturbations similar to those shown in Figure 3.10. They find that 45-day waves in the Western North Pacific amplified barotropically by weakening the sheared mean zonal and meridional flow, while corresponding extratropical 45-day perturbations were maintained by the moist baroclinic instability

poleward of the Pacific anticyclone. Their study indicates that the wave pattern described above contributes to the development of the extratropical ISO. Through this tropical–extratropical interaction, the 30 to 60-day ISO becomes one of the most prominent features that strongly interact with EA/WNP summer monsoons.

3.6.2 The 10 to 30-day westward-propagating pattern

As shown in Figures 3.2b and 3.2d, westward propagation between 5°N and 20°N is one of the most prominent characteristics associated with the 10 to 30-day ISO (e.g., Nakazawa, 1986; Tanaka, 1992; Chen and Chen, 1993a, 1995; Wang and Xu, 1997; Chen and Weng, 1999; Fukutomi and Yasunari, 1999). These perturbations, which are most evident in early summer (Figure 3.2b), often propagate from the tropical Western North Pacific, through the South China Sea and the Indochina Peninsula, and on to the Bay of Bengal (Chen *et al*., 2000). The 12 to 30-day westward-propagating ISO documented by Chen *et al*. (2000) exhibits a spatial structure similar to the one shown in Figure 3.6b. This type of propagation exhibits characteristics resembling those of an equatorial Rossby wave and is often accompanied by convection fluctuations at both its northern and southern sides, which tend to be out of phase with each other. When viewed in variables representing convection, two westward propagation paths—one near 15°N and the other near the equator—were observed (e.g., fig. A2 in Chen *et al*., 2000). Since the vorticity anomaly is located between the northern and southern convection anomalies, the westward propagation of the vorticity anomaly predominantly between 5°N and 15°N (Figures 3.2b and 3.2d) is consistent with the propagation paths of convection anomalies.

As shown in Figure 3.2, the 10 to 30-day ISO exhibits a maximum variance in the South China Sea. Fukutomi and Yasunari (1999, 2002) use the 10 to 25-day filtered OLR averaged over 10°N–20°N, 110°E–120°E as an index for composites and examine the spatial and temporal evolution of the corresponding 10 to 25-day intraseasonal perturbations during the June–August season. The result turns out to be another type of westward-propagating 10 to 30-day ISO, which prevails in higher latitudes around 30°N. In contrast to the westward-propagating ISO in the lower latitudes, which is essentially tropical in nature, this westward-propagating ISO exhibited both tropical and extratropical characteristics.

Fukutomi and Yasunari (1999, 2002) divide a complete cycle of the corresponding 10 to 30-day ISO evolution into eight categories. Figure 3.11a shows the OLR, 850 hPa streamfunction, and wind anomalies at category 3, which corresponds to the phase when convection in the South China Sea is most active, as indicated by the dark shading in the figure. The negative OLR anomaly (representing anomalous convection) in the South China Sea is accompanied by a cyclonic circulation located to the northwest. Downstream is a wavelike pattern extending eastward along the 20°N–40°N latitudinal band. The corresponding 200 hPa circulation is shown in Figure 3.11b. The 200 hPa circulation anomalies tend to have the same signs as their 850 hPa counterparts, indicating an equivalent barotropic vertical structure in the extratropics. However, the 850 hPa and

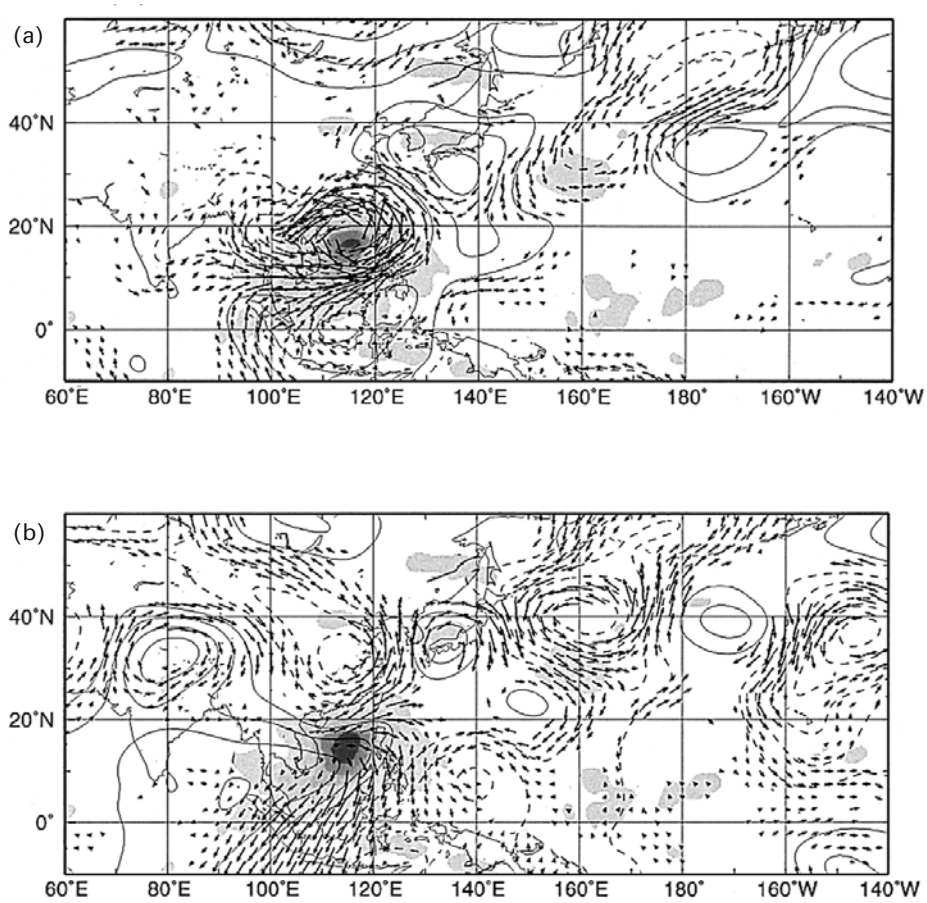

Figure 3.11. The spatial distribution of composite OLR and (a) 850 hPa and (b) 200 hPa winds and streamfunction anomalies in the 10 to 25-day band when convection is strongest in the South China Sea. The contour interval is 3.0×10^5 m^2 s^{-1}. OLR anomalies less (greater) than -5 (5) W m^{-2} are darkly (lightly) shaded. Only locally significant wind vectors are shown (adapted from Fukutomi and Yasunari, 1999).

200 hPa circulation anomalies near East China and the South China Sea tend to be out of phase, indicating a first baroclinic mode vertical structure. During the period from category 3 to category 6, the wave pattern moves westward, while the anomalous low-level anticyclonic circulation, originally located in the 20°N–40°N and 120°E–140°E region, moves southwestward to the South China Sea where the OLR anomaly becomes positive (not shown). This anticyclonic anomaly continues moving westward near 20°N to the Bay of Bengal at category 8 (not shown).

It is interesting to note that the anomaly circulation associated with the wave pattern switches from an equivalent barotropic vertical structure to a first baroclinic mode vertical structure when it reaches the South China Sea. Fukutomi

and Yasunari (1999) suggest that southwestward movement of the anomalous anticyclonic (cyclonic) circulation into the South China Sea initiated a convection-inactive (active) state in the South China Sea, which in turn triggered the downstream Rossby wave–like pattern. The existence of this wavelike pattern modulated the Pacific anticyclone, the monsoon trough, and the convection. They suggest that the mutual interaction between the tropics and the extratropics on the 10 to 25-day timescale played an important role in the variability of monsoon convection and circulation in EA/WNP.

Fukutomi and Yasunari (2002) find that the wavelike pattern and the tropical–extratropical interaction were most pronounced during the June–July period and less pronounced in August. This result is consistent with southwestward propagation in the region between Japan and the northern Philippine Sea, which is observed in early summer but not in late summer (Figure 3.2b and 3.2d). The wavelike pattern occurred in the background southwesterly wind, which served as a waveguide for downstream development of a Rossby wave. They also suggest that southwestward propagation of the circulation anomaly into the South China Sea was similar to the retrograding Rossby wave along a westerly duct.

Ko and Hsu (2006) identify a 7 to 30-day wavelike pattern, which exhibits a wavelength of about 4,000 km and propagates north-northwestward at a speed of $5\,m\,s^{-1}$ from the tropical Philippine Sea to the East China Sea. This wave pattern is most active between mid July and September and is usually accompanied by tropical cyclones (TCs) in its cyclonic circulation. Both TCs and the wave pattern tend to recurve northeastward after reaching the East China Sea. The relation of this TC/submonthly wave pattern with the ISO will be discussed further in Section 3.7.

3.7 RELATIONSHIP WITH TROPICAL CYCLONE ACTIVITY

The EA/WNP monsoon trough extends southeastward into the tropical Western North Pacific where the sea surface temperature is higher than 26°C in the boreal summer and the moisture in the lower troposphere is abundant. In addition, the region occupied by the monsoon trough is a region of cyclonic relative vorticity in the lower troposphere and anticyclonic relative vorticity in the upper troposphere. The vertical shear of horizontal winds is also smaller than the surrounding regions. These characteristics are among the favorable environmental factors for tropical cyclone formation (Gray, 1968, 1998; Elsberry, 2004). Many studies confirm that most typhoons occur in an active monsoon trough environment (e.g., McBride, 1995; Harr and Elsberry, 1995; Elsberry, 2004). Other studies find that the eastern end of the monsoon trough, where the tropical westerly and easterly meet to result in a confluent zone in the lower troposphere, is also a region favorable for tropical cyclone formation (e.g., Harr and Elsberry, 1995; Briegel and Frank, 1997). Tropical disturbances with a period of 8–9 days—originated in this confluent zone—were found to propagate northwestward in the Western North Pacific (Lau and Lau, 1990; Chang *et al.*, 1996; Kuo *et al.*, 2001). These results all indicate that the monsoon trough in the Western North Pacific is a breeding ground for tropical

cyclones. Its fluctuation in both structure and amplitude can significantly affect tropical cyclone formation and track. Elsberry (2004) gives an informative review on this subject.

Since ISV in EA/WNP is closely associated with monsoon trough fluctuation (e.g., contraction and expansion of the trough in the east–west direction and/or meridional shifts of the trough), it is likely that the ISO modulates typhoon activity in the Western North Pacific. Gray (1978) notes that tropical cyclogenesis tended to cluster in an active period of 1–2 weeks and was separated by a 2 to 3-week inactive period. A similar clustering phenomenon was also observed in the Western North Pacific. In a study of the intraseasonal variations of the tropical OLR during the FGGE year, Nakazawa (1986) finds that the generation and growth of tropical cyclones tended to occur during the convection-active phase of the ISO on both the 15 to 25-day and 30 to 60-day timescales in both northern and southern hemisphere summers. Heta (1990) studies the relationship between tropical wind and typhoon formation during the 1980 summer (July to October) in the tropical Western Pacific. In that particular year, the confluent region in the Western North Pacific moved westward and eastward on a timescale of 10–30 days, and most of the tropical cyclones and storms appeared when the westerly wind region expanded eastward (i.e., a strengthened monsoon trough).

An unusually strong and regular 32 to 76-day fluctuation of the monsoon trough occurred in the 2004 typhoon season and had a clear clustering effect on TCs, which were active (suppressed) during the cyclonic (anticyclonic) phase of the ISO (Nakazawa, 2006; Hsu *et al.*, 2008a). This unusual coupling between TC and ISO resulted in the record-breaking number (10) of typhoon landfalls on Japan. The 2004 ISO in the Western North Pacific had a strong clustering effect on both TC genesis and tracks. These findings were consistent with the above discussion on the effect of the confluent zone on tropical cyclogenesis. When the confluent zone shifts zonally on the intraseasonal timescale, the region of tropical cyclogenesis might shift in the similar manner.

Hartmann *et al.* (1992) finds that the 20 to 25-day OLR anomalies in the Western North Pacific were most active during the September–December period. The 20 to 25-day interval appeared to be the most preferred recurrence frequency for tropical cyclones in the Western North Pacific, although other recurrence frequencies also existed. It was concluded that the 20 to 25-day oscillation played a modest role, although not a dominant one, in setting the pace of typhoon development in this region and season. Schnadt *et al.* (1998) also identified the relationship but found that the 15 to 25-day spectral peak did not exist in some years.

While the findings discussed above might be affected by the EA/WNP ISO that was not necessarily associated with the TISO, other studies document the modulating effect of the TISO on typhoon activity in the Western North Pacific. For example, Liebmann *et al.* (1994) finds that tropical cyclones in the Northern Indian Ocean and Western Pacific tended to spawn in the wet phase of the 35 to 95-day TISO, which propagated eastward along the equator. The development of tropical cyclones was associated with the low-level vorticity and divergence anomalies located to the northwest of anomalous TISO convection. Intraseasonal

perturbation strongly modulated large-scale tropical convection fluctuations to create an environment favoring the development of tropical cyclones. However, they note that increased tropical cyclone activity also occurred in active monsoon troughs, which were not associated with the TISO.

The findings discussed above are consistent with the observations that the 3 to 10-day tropical disturbance activity increased during the westerly phase of the TISO (Nakazawa, 1986; Yamazaki and Murakami, 1989; Sui and Lau, 1992; Maloney and Hartmann, 2001; Maloney and Dickinson, 2003; Straub and Kiladis, 2003). Figures 3.12a–c (adapted from Maloney and Dickinson, 2003) present the 2.5 to 12-day 850 hPa vorticity variance during the entire June–August period, TISO westerly events, and TISO easterly events, respectively. Among the three periods, the

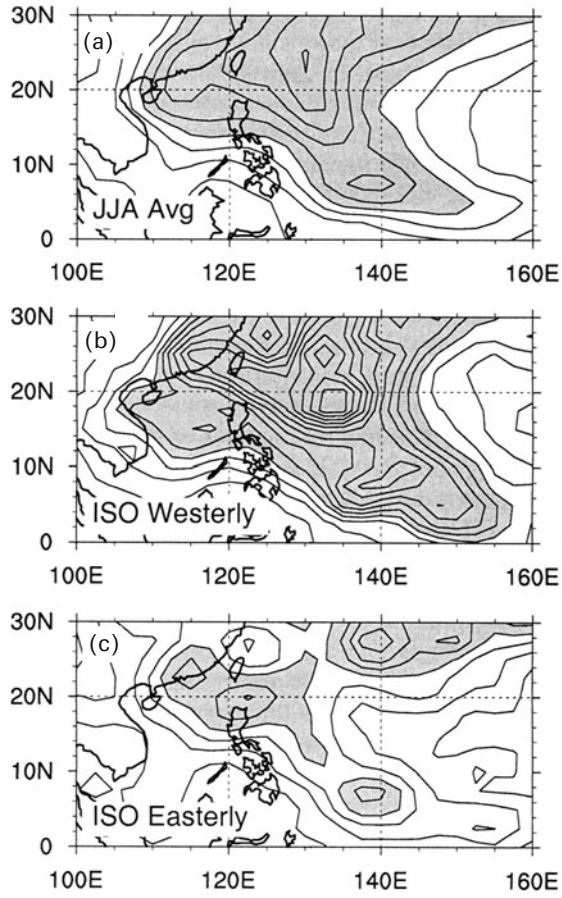

Figure 3.12. The 850 hPa perturbation vorticity variance in the 2.5 to 12-day band averaged during (a) June–August, (b) ISO westerly events, and (c) ISO easterly events. The contour interval is $2 \times 10^{-11}\,s^{-2}$. Values greater than $10 \times 10^{-11}\,s^{-2}$ are shaded (adapted from Maloney and Dickinson, 2003).

variance was largest during westerly events and smallest during easterly events. The maximum variance during westerly events was located in a northwest–southeast elongated region from South China to the southeastern Philippine Sea. The monsoon trough in the Philippine Sea deepened during westerly phases and was almost missing during easterly phases (not shown). The energetic analysis done by Maloney and Dickinson (2003) indicates enhanced barotropic energy conversion and enhanced conversion from perturbation available potential energy to perturbation kinetic energy during westerly phases. This result suggested favorable conditions for the growth of tropical disturbances during TISO westerly events. The deepened monsoon trough during westerly phases apparently acts as a breeding ground for tropical synoptic disturbances, which might develop into tropical cyclones.

The ISO modulates not only TCs but also submonthly perturbations. The TC/submonthly wave pattern identified by Ko and Hsu (2006) is better organized when the ISO in the tropical Western North Pacific is in its wet/cyclonic phase (i.e., anomalously strong westerly and convection in the South China Sea and the Philippine Sea), reflecting an enhanced monsoon trough (Figure 3.13). The corresponding stronger-than-normal low-level moisture convergence and cyclonic vorticity provide a favorable background for the development of the TC/submonthly wave pattern (Ko and Hsu, 2009). On the contrary, the pattern is poorly organized during the dry/anticyclonic phase of the ISO, because of moisture divergence and negative vorticity anomalies in the lower troposphere. After reaching the East China Sea, the pattern often triggers downstream development of Rossby wave–like perturbation toward the extratropical northeastern Pacific and North America through the jetstream waveguide in the extratropical North Pacific (Ko and Hsu, 2010). This downstream development is likely to affect the weather in western North America.

An event of ISO–submonthly wave–TC coupling occurred in early August 2009 when the monsoon trough was enhanced due to the arrival of a submonthly wave from the tropical Philippine Sea and three typhoons appeared simultaneously in the monsoon trough (Hong *et al.*, 2010). One of the three typhoons made landfall on Taiwan, precipitated almost 3,000 mm of rainfall in 3 days, and caused record-breaking damage to the island country.

3.8 UPSCALE EFFECT OF TC AND SYNOPTIC SYSTEMS

While the lower frequency (e.g., 30 to 60-day) ISO has a modulating effect on both the 10 to 30-day perturbation and TC activity, recent studies reveal the possible upscale effect of TCs on the ISO. Hsu *et al.* (2008b) purposely remove TCs from the 850 hPa wind field and compare vorticity variance with and without TCs. The comparison indicated that removing TCs reduced intraseasonal variance by 40% to 50%. While the ISO modulates TC activity and leads to the spatiotemporal clustering of TCs, the clustering of strong TC vortices significantly increases positive vorticity during the cyclonic phase of the ISO, while weak TC activity during the

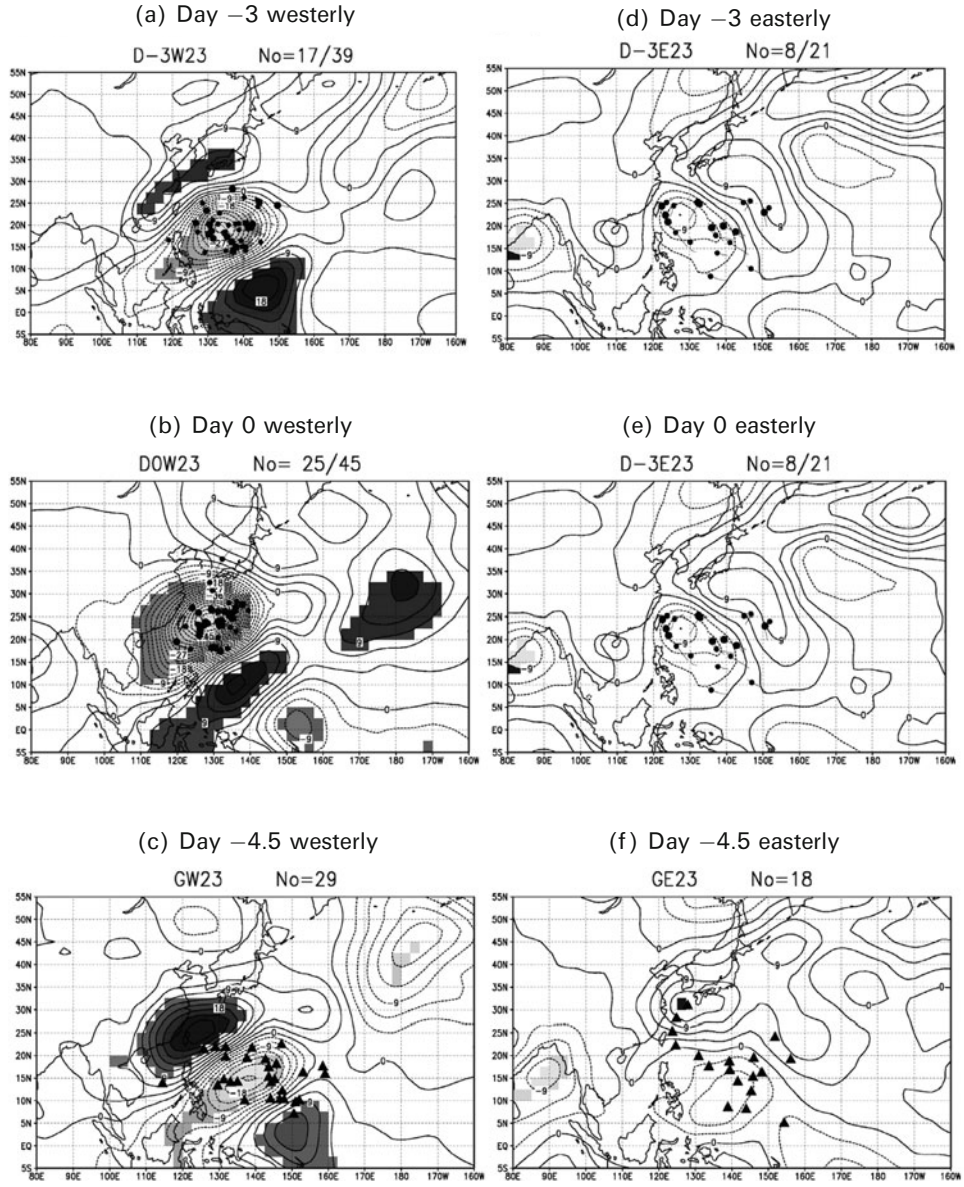

Figure 3.13. The TC submonthly wave pattern in the (a–c) westerly and (d–f) easterly phase of the WNP ISO. The 850 hPa composite filtered streamfunction (TC cases) on (a, d) day −3; (b, e) day 0; and (c, f) day −4.5 for 23 July–September summers (1979–2001). The interval is $3(\times 10^5)\,m^2\,s^{-1}$. Also shown for (a, d) and (b, e) are the typhoon positions—with past 1-day tracks, and big dots representing a wind speed ≥ 64 kt—associated with the composite cases. (c, f) The typhoon genesis positions between day −1.5 and day −7.5. The shaded areas represent a streamfunction that exceeds the 95% confidence limit (adapted from Ko and Hsu, 2009).

anticyclonic phase of the ISO has little effect on the overall amplitude of the ISO. Intraseasonal variance is therefore enlarged with the occurrence of TCs.

Zhou and Li (2010) identify a similar upscale effect. While synoptic-scale variability is modulated by the ISO in the Western North Pacific during the boreal summer as demonstrated in previous studies, it enhances the intraseasonal surface latent heat flux ahead of deep convection by 20% to 30% and contributes to the northwestward propagation of the ISO. These two studies suggest the importance of the two-way interaction between TC/synoptic-scale variability and the ISO. In other words, the ISO is an inseparable part of multiscale weather/climate variability in the Western North Pacific during the boreal summer. A seamless approach treating the TC/synoptic perturbation, submonthly wave, and ISO as an integrated system is needed to fully understand the mechanism of the ISO and to improve model capability in simulation and prediction.

3.9 FINAL REMARKS

This review summarized the interesting characteristics of the EA/WNP ISV during the boreal summer. We can identify more phenomena than we can explain. Many outstanding issues remain to be solved. Some of these issues are discussed as follows.

3.9.1 Close association with the EA/WNP monsoon

The close relationship between monsoon onsets/breaks and the ISO is remarkable. The good timing match between the ISO and abrupt changes in monsoon circulation does not necessarily yield the cause and effect. The passage of an ISO certainly affects convective activity and precipitation in various regions. However, whether it leads to abrupt changes in circulation remains to be seen.

The ISO behaves differently during different periods of the EA/WNP summer monsoon. We need to understand how background monsoon flow affects ISO characteristics. The ISO propagation tendency exhibits strong geographical dependence in the northern summer: northward in the South China Sea, northwestward in the Philippine Sea, and westward in the subtropical Western North Pacific. Although there are already some explanations proposed for these characteristics (e.g., mechanisms for propagation), little has been said about the reason for geographical dependence. Background flow property, land–sea contrast, ocean–atmosphere interaction, scale interaction, etc., are among the possible mechanisms.

3.9.2 The CISO vs. interannual variability

The CISO helps us understand the in-phase relationship between the ISO and the annual cycle. This in-phase relationship is often referred to as phase lock. However, the term ''phase lock'' does not necessarily give us a better understanding of the interaction between the ISO and the annual cycle. Is there an interaction between the ISO and smoothed background monsoon evolution? Or, could it be simply that

slowly evolved monsoon flow sets up an environment favorable for ISO development? Moreover, the CISO explains less than 20% of total ISV and is prominent only in certain regions. The interannual variability of the ISO is much larger than the CISO variability. Little is known about the cause for this large interannual variability. It is probably affected by interannual fluctuation of the background flow, which in turn is induced by ocean–atmosphere interaction such as the El Niño/South Oscillation (e.g., Teng and Wang, 2003; Lin and Li, 2008), the atmosphere–land interaction in the Eurasian continent (e.g., the Tibetan Plateau heating effect, snow cover), the internal dynamics in the atmosphere, etc.

3.9.3 Multiperiodicities and multiscale interaction

Another interesting phenomenon is the existence of two spectral peaks around 30–60 days and 10–30 days in the summer. Are these two the intrinsic modes in monsoon background flow? What are the reasons for their prominent seasonality and regionality? ISO variability is also closely related to the TC and synoptic activity in the Western North Pacific through a two-way interaction. All these facts indicate that the ISO is likely one component of a multiscale system, which involves interannual, annual, intraseasonal, and TC/synoptic-scale variability in EA/WNP. The multiscale interaction between features of these timescales appears to be one of the most important issues that must be addressed in future EA/WNP ISO studies.

3.9.4 Others

One area that has been hardly touched on for the EA/WNP ISO is the cloud-radiative effect. Several studies (e.g., Slingo and Madden, 1991; Hu and Randall, 1994, 1995; Mehta and Smith, 1997) report on the possible effects of the cloud-radiative process on the TISO. Wang *et al.* (2004) recently identified the dramatic weakening of cloud-radiative cooling in East Asia after East Asian summer monsoon onset in June. The cloud-radiative process could also have a strong effect on the ISO. The complexity of this problem and the lack of reliable data have hindered this research for a long time. Fortunately, the rapidly increasing availability of satellite cloud-related data (e.g., CloudSat, TRMM, etc.) in recent decades has been very helpful in diagnosing the vertical and horizontal distribution and the variability of cloud types (Lin *et al.*, 2004; Zhang and Hagos, 2009; Jiang *et al.*, 2010). Such diagnostics shed light on our understanding of the diabatic heating distribution of the MJO and ISO as a whole. A combination of modeling and empirical evidence is likely to shed light on this issue and to add another dimension toward a better understanding of the EA/WNP ISV.

3.10 REFERENCES

Briegel, L. M. and W. M. Frank (1997) Large-scale influences on tropical cyclogenesis in the western North Pacific. *Mon. Wea. Rev.*, **125**, 1397–1413.

Chang, C.-P., J. M. Chen, P. A. Harr, and L. E. Carr (1996) Northwestward-propagating wave patterns over the tropical western North Pacific during summer. *Mon. Wea. Rev.*, **124**, 2245–2266.

Chen, T.-C. (1987) 30–50 day oscillation of 200-mb temperature and 850-mb height during the 1979 northern summer. *Mon. Wea. Rev.*, **115**, 1589–1605.

Chen, T.-C. and J.-M. Chen (1993a) The 10–20-day mode of the 1979 Indian monsoon: Its relation with the time variation of monsoon rainfall. *Mon. Wea. Rev.*, **121**, 2465–2482.

Chen, T.-C. and J.-M. Chen (1993b) The intraseasonal oscillation of the lower-tropospheric circulation over the western Pacific during the 1979 northern summer. *J. Meteorol. Soc. Japan*, **71**, 205–220.

Chen, T.-C. and J.-M. Chen (1995) An observational study of the South China Sea monsoon during the 1979 summer: Onset and life cycle. *Mon. Wea. Rev.*, **123**, 2295–2318.

Chen, T.-C. and M. Murakami (1988) The 30–50 day variation of convective activity over the western Pacific Ocean with emphasis on the northwestern region. *Mon. Wea. Rev.*, **116**, 892–906.

Chen, T.-C. and S.-P. Weng (1999) Interannual and intraseasonal variations in monsoon depressions and their westward-propagating predecessors. *Mon. Wea. Rev.*, **127**, 1005–1020.

Chen, T.-C. M.-C. Yen, and M. Murakami (1988) The water vapor transport associated with the 30–50 day oscillation over the Asian monsoon regions during 1979 summer. *Mon. Wea. Rev.*, **116**, 1983–2002.

Chen, T.-C., M.-C. Yen, and S.-P. Weng (2000) Interaction between the summer monsoon in East Asia and South China Sea: Intraseasonal monsoon modes. *J. Atmos. Sci.*, **57**, 1373–1392.

Ding, Y. (1992) Summer monsoon rainfall in China. *J. Meteorol. Soc. Japan*, **70**, 373–396.

Ding, Y., C. Li, and Y. Liu (2004) Overview of the South China Sea Monsoon Experiment (SCSMEX). *Adv. Atmos. Sci.*, **21**, 343–360, doi: 10.1007/BF02915563.

Elsberry, R. L. (2004) Monsoon-related tropical cyclones in East Asia. In: C.-P. Chang (Ed.), *East Asian Monsoon* (World Scientific Series on Meteorology of East Asia Vol. 2). World Scientific, Singapore, pp. 463–498.

Flatau, M., P. Flatau, P. Phoebus, and P. Niller (1997) The feedback between equatorial convection and local radiative and evaporation processes: The implications for intraseasonal oscillation. *J. Atmos. Sci.*, **54**, 2373–2386.

Fukutomi, Y. and T. Yasunari (1999) 10–25 day intraseasonal variations of convection and circulation over East Asia and Western North Pacific during early summer. *J. Meteorol. Soc. Japan*, **77**, 753–769.

Fukutomi, Y. and T. Yasunari (2002) Tropical–extratropical interaction associated with the 10–25-day oscillation over the Western Pacific during the northern summer. *J. Meteorol. Soc. Japan*, **80**, 311–331.

Gibson, J. K., P. Kallberg, S. Uppala, A. Hernandez, A. Nomura, and E. Serrano (1997) *ECMWF Re-analysis Project Report Series, 1: ERA Description*. European Centre for Medium-Range Weather Forecasts, Reading, U.K., 72 pp.

Gray, W. M. (1968) Global view of the origin of tropical disturbances and storms. *Mon. Wea. Rev.*, **96**, 669–700.

Gray, W. M. (1978) Hurricanes: Their formation, structure and likely role in the tropical circulation. In: D. B. Show (Ed.), *Meteorology over the Tropical Oceans* Royal Meteorological Society, pp. 155–218.

Gray, W. M. (1998) The formation of tropical cyclones. *Meteorol. Atmos. Phys.*, **67**, 37–69.

Hamming, R. W. (1989) *Digital Filters*. Prentice-Hall, Englewood Clliffs, NJ, 284 pp.

Harr, P. A. and R. L. Elsberry (1995) Large-scale circulation variability over the tropical western North Pacific, Part I: Spatial patterns and tropical cyclone characteristics. *Mon. Wea. Rev.*, **123**, 1225–1246.

Hartmann, D. L., M. L. Michelsen, and S. A. Klein (1992) Seasonal variations of tropical intraseasonal oscillations: A 20–25-day oscillation in the Western Pacific. *J. Atmos. Sci.*, **49**, 1277–1289.

Heta, Y. (1990) An analysis of tropical wind fields in relation to typhoon formation over the western Pacific. *J. Meteorol. Soc. Japan*, **68**, 65–76.

Hirasawa, N. and T. Yasunari (1990) Variation in the atmospheric circulation over Asia and the Western Pacific associated with the 40-day oscillation of the Indian summer monsoon. *J. Meteorol. Soc. Japan*, **68**, 129–143.

Hong, C. C., M. Y. Lee, H. H. Hsu, and J. L. Kuo (2010) Role of submonthly disturbance and 40–50 day ISO on the extreme rainfall event associated with Typhoon Morakot (2009) in Southern Taiwan. *Geophys. Res. Lett.*, **37**, L08805, doi: 10.1029/2010GL042761.

Hoskins, B. J. and D. J. Karoly (1981) The steady linear response of a spherical atmosphere to thermal and orographic forcing. *J. Atmos. Sci.*, **38**, 1179–1196.

Hsu, H.-H. and M.-Y. Lee (2005) Topographic effects on the eastward propagation and initiation of the Madden–Julian Oscillation. *J. Climate*, **18**, 795–809.

Hsu, H.-H. and C.-H. Weng (2001) Northwestward propagation of the intraseasonal oscillation in the Western North Pacific during the boreal summer: Structure and mechanism. *J. Climate*, **14**, 3834–3850.

Hsu, H.-H., C.-T. Terng, and C.-T.Chen (1999) Evolution of large-scale circulation and heating during the first transition of Asian summer monsoon. *J. Climate*, **12**, 793–810.

Hsu, H.-H., C.-H. Weng, and C. H. Wu (2004a) Contrasting characteristics between the northward and eastward propagation of the intraseasonal oscillation during the boreal summer. *J. Climate*, **17**, 727–743.

Hsu, H.-H., Y.-C. Yu, W.-S. Kau, W.-R. Hsu, W.-Y. Sun, and C.-H. Tsou (2004b) Simulation of the 1998 East Asian summer monsoon using Purdue regional model. *J. Meteorol. Soc. Japan*, **82**, 1715–1733.

Hsu, H.-H., Y.-L. Chen, A.-K. Lo, C.-H. Hung, W.-S. Kau, and C.-C. Wu (2008a) Intraseasonal oscillation–tropical cyclone coupling in the Western North Pacific during the 2004 typhoon season. In: K. N. Liou and M. D. Chou (Eds.), *Recent Progress in Atmospheric Sciences: Applications to the Asia–Pacific Region*. World Scientific, Singapore, pp. 49–65.

Hsu, H.-H., C.-H. Hung, A.-K. Lo, C.-C. Wu, and C.-W. Hung (2008b) Influence of tropical cyclones on the estimation of climate variability in the tropical Western North Pacific. *J. Climate*, **21**, 2960–2975.

Hu, Q. and D. A. Randall (1994) Low-frequency oscillations in radiative–convective systems. *J. Atmos. Sci.*, **51**, 1089–1099.

Hu, Q. and D. A. Randall (1995) Low-frequency oscillations in radiative–convective systems, Part II: An idealized model. *J. Atmos. Sci.*, **52**, 478–490.

Hung, C.-W. and H.-H. Hsu (2008) The first transition of the Asian summer monsoon, intraseasonal oscillation, and Taiwan Meiyu. *J. Climate*, **21**, 1552–1568.

Jiang, X., T. Li, and B. Wang (2004) Structures and mechanisms of the northward propagating boreal summer intraseasonal oscillation. *J. Climate*, **17**, 1022–1039.

Jiang, X., D. E. Waliser, J.-L Li, and C. Woods (2010) Vertical structures of cloud water associated with the boreal summer intraseasonal oscillation based on CloudSat observations and ERA-Interim reanalysis. *Climate Dynamics*, doi: 10.1007/s00382-010-0853-8.

Jones, C., L. M. V. Carvalho, R. W. Higgins, D. E. Waliser, and J.-K. E. Schemm (2004) Climatology of tropical intraseasonal connective anomalies: 1979–2002. *J. Climate*, **17**, 523–539.

Kang, I. S., S.-I. An, C.-H. Joung, S.-C. Yoon, and S.-M. Lee (1989) 30–60 day oscillation appearing in climatological variation of outgoing longwave radiation around East Asia during summer. *J. Korean Meteorol. Soc.*, **25**, 149–160.

Kang, I. S., C.-H. Ho, and Y.-K. Lim (1999) Principal modes of climatological seasonal and intraseasonal variations of the Asian summer monsoon. *Mon. Wea. Rev.*, **127**, 322–340.

Kawamura, B. and T. Murakami (1995) Interaction between the mean summer monsoon flow and 45-day transient perturbations. *J. Meteorol. Soc. Japan*, **73**, 1087–1114.

Kawamura, B., T. Murakami, and B. Wang (1996) Tropical and mid-latitude 45-day perturbations over the Western Pacific during the northern summer. *J. Meteorol. Soc. Japan*, **74**, 867–890.

Kaylor, R. E. (1977) *Filtering and Decimation of Digital Time Series* (Tech. Note BN 850). Institute of Physical Science Technology, University of Maryland, College Park, 42 pp.

Ko, K.-C. and H.-H. Hsu (2006) Sub-monthly circulation features associated with tropical cyclone tracks over the East Asian monsoon area during July–August season. *J. Meteorol. Soc. Japan*, **84**, 871–889.

Ko, K.-C. and H.-H. Hsu (2009) ISO modulation on the submonthly wave pattern and recurving tropical cyclones in the tropical Western North Pacific. *J. Climate*, **22**, 582–599.

Ko, K.-C. and H.-H. Hsu (2010) Downstream development of the summertime TC/sub-monthly wave pattern in the extratropical North Pacific. *J. Climat*, **23**, 2223–2229.

Krishnamurti, T. N. and H. N. Bhalme (1976) Oscillations of a monsoon system, Part I: Observational aspects. *J. Atmos. Sci.*, **33**, 1937–1954.

Krishnamurti, T. N. and D. Subrahmanyam (1982) The 30–50 day mode at 850 mb during MONEX. *J. Atmos. Sci.*, **39**, 2088–2095.

Kuo, H.-C., J.-H. Chen, R. T. Williams, and C.-P. Chang (2001) Rossby waves in zonally opposing mean flow: Behavior in northwest Pacific summer monsoon. *J. Atmos. Sci.*, **58**, 1035–1050.

Lau, K.-H. and N.-C. Lau (1990) Observed structure and propagation characteristics of tropical summertime synoptic scale disturbances. *Mon. Wea. Rev.*, **118**, 1888–1913.

Lau, K.-M. and P.-H. Chan (1986) Aspects of the 40–50 day oscillation during the northern summer as inferred from outgoing longwave radiation. *Mon. Wea. Rev.*, **114**, 1354–1367.

Lau, K.-M. and S. Yang (1997) Climatology and interannual variability of the southeast Asian summer monsoon. *Adv. Atmos. Sci.*, **14**, 141–162.

Lau, K.-M., G.-J. Yang, and S.-H. Shen (1988) Seasonal and intraseasonal climatology of summer monsoon rainfall over East Asia. *Mon. Wea. Rev.*, **116**, 18–37.

Liebmann, B., H. H. Hendon, and J. D. Glick (1994) The relationship between tropical cyclones of the western Pacific and Indian Ocean and the Madden–Julian oscillation. *J. Meteorol. Soc. Japan*, **72**, 401–412.

Lin, A. and T. Li (2008) Energy spectrum characteristics of boreal summer intraseasonal oscillations: Climatology and variations during the ENSO developing and decaying phases. *J. Climate*, **21**, 6304–6320.

Lin, J., B. Mapes, M. Zhang, and M. Newman (2004) Stratiform precipitation, vertical heating profiles, and the Madden–Julian Oscillation. *J. Atmos. Sci.*, **61**, 296–309.

LinHo and B. Wang (2002) The time-space structure of the Asian–Pacific summer monsoon: A fast annual cycle view. *J. Climate*, **15**, 2001–2018.

Lorenc, A. C. (1984) The evolution of planetary scale 200-mb divergences during the FGGE year. *Quart. J. Roy. Meteorol. Soc.*, **110**, 427–441.

Maloney, E. D. and M. J. Dickinson (2003) The intraseasonal oscillation and the energetics of summertime tropical Western North Pacific synoptic-scale disturbances. *J. Atmos. Sci.*, **60**, 2153–2168.

Maloney, E. D. and D. L. Hartmann (2001) The Madden–Julian oscillation, barotropic dynamics, and North Pacific cyclone formation, Part I: Observations. *J. Atmos. Sci.*, **58**, 2545–2558.

Matsumoto, J. (1992) The seasonal changes in Asian and Australian monsoon regions. *J. Meteorol. Soc. Japan*, **70**, 257–273.

McBride, J. L. (1995) Tropical cyclone formation. Chapter 3 in *Global Perspectives on Tropical Cyclones* (Tech. Doc. WMO/TD No. 693). World Meteorological Organization, Geneva, Switzerland, pp. 63–105.

Mehta, A. V. and E. A. Smith (1997) Variability of radiative cooling during the Asian summer monsoon and its influence on intraseasonal waves. *J. Atmos. Sci.*, **54**, 941–966.

Mu, M. and C. Li (2000) On the outbreak of South China Sea summer monsoon in 1998 and activities of atmospheric intraseasonal oscillation. *J. Climate Environ. Res.*, **5**, 375–387 [in Chinese].

Murakami, M. (1976) Analysis of summer monsoon fluctuations over India. *J. Meteorol. Soc. Japan*, **54**, 15–32.

Murakami, M. (1984) Analysis of the deep convective activity over the Western Pacific and Southeast Asia, Part II: Seasonal and intraseasonal variations during northern summer. *J. Meteorol. Soc. Japan*, **62**, 88–108.

Murakami, T. (1980) Empirical orthogonal function analysis of satellite-observed outgoing longwave radiation during summer. *Mon. Wea. Rev.*, **108**, 205–222.

Murakami, T. and J. Matsumoto (1994) Summer monsoon over the Asian continent and Western North Pacific. *J. Meteorol. Soc. Japan*, **72**, 719–745.

Murakami, T., T. Nakazawa, and J. He (1984a) On the 40–50 day oscillations during the 1979 Northern Hemisphere summer, Part I: Phase propagation. *J. Meteorol. Soc. Japan*, **62**, 440–468.

Murakami, T., T. Nakazawa, and J. He (1984b) On the 40–50 day oscillations during the 1979 Northern Hemisphere summer, Part II: Heat and moisture. *J. Meteorol. Soc. Japan*, **62**, 469–484.

Nakazawa, T. (1986) Intraseasonal variations of OLR in the tropics during the FGGE year. *J. Meteorol. Soc. Japan*, **64**, 17–34.

Nakazawa, T. (1992) Seasonal phase lock of intraseasonal oscillation during the Asian summer monsoon. *J. Meteorol. Soc. Japan*, **70**, 597–611.

Nakazawa, T. (2006) Madden–Julian Oscillation activity and typhoon landfall on Japan in 2004. *Scientific Online Letters on the Atmosphere*, **2**, 136–139, doi: 10.2151/sola.2006-035.

Ninomiya, K. and H. Muraki (1986) Large-scale circulation over East Asia during Baiu period of 1979. *J. Meteorol. Soc. Japan*, **64**, 409–429.

Nitta, T. (1987) Convective activities in the tropical Western Pacific and their impact on the Northern Hemisphere summer circulation. *J. Meteorol. Soc. Japan*, **65**, 373–390.

Sardeshmukh, P. D. and B. J. Hoskins (1984) Spatial smoothing on the sphere. *Mon. Wea. Rev.*, **112**, 2524–2529.

Schnadt, C., A. Fink, D. G. Vincent, J. M. Schrage, and P. Speth (1998) Tropical cyclones, 6–25 day oscillations, and tropical–extratropical interaction over the Northwestern Pacific. *Meteorol. Atmos. Phys.*, **68**, 151–169.

Slingo, J. M. and R. A. Madden (1991) Characteristics of the tropical intraseasonal oscillation in the NCAR community climate model. *Quart. J. Roy. Meteorol. Soc.*, **117**, 1129–1169.

Straub, K. H. and G. N. Kiladis (2003) Interactions between the boreal summer intraseasonal oscillation and high frequency tropical wave activity. *Mon. Wea. Rev.*, **131**, 781–796.

Sui, K.-H. and K.-M. Lau (1992) Multiscale phenomenon in the tropical atmosphere over the western Pacific. *Mon. Wea. Rev.*, **120**, 407–430.

Tanaka, M. (1992) Intraseasonal oscillation and onset and retreat dates of the summer monsoon over east, southeast Asia and the western Pacific region using GMS high cloud amount data. *J. Meteorol. Soc. Japan*, **70**, 613–629.

Tao, S. and L. Chen (1987) A review of recent research on the East Asian summer monsoon in China. In: C.-P. Chang and T. N. Krishnamurti (Eds.), *Monsoon Meteorology*. Oxford University Press, Oxford, U.K., pp. 60–92.

Teng, H. and B. Wang (2003) Interannual variations of the boreal summer intraseasonal oscillation in the Asian–Pacific region. *J. Climate*, **16**, 3572–3584.

Tsou, C.-H., P.-C. Hsu, W.-S. Kau, and H.-H. Hsu (2005) Northward and northwestward propagation of 30–60 day oscillation in the tropical and extratropical Western North Pacific. *J. Meteorol. Soc. Japan*, **83**, 711–726.

Ueda, H. (2002) Processes for the northeastward advance of the summer monsoon over the western North Pacific. *J. Meteorol. Soc. Japan*, **80**, 67–83, doi: 10.2151/jmsj.80.67.

Ueda, H. and T. Yasunari (1996) Maturing process of the summer monsoon over the western North Pacific: A coupled ocean/atmosphere system. *J. Meteorol. Soc. Japan*, **74**, 493–508.

Ueda, H., T. Yasunari, and R. Kawamura (1995) Abrupt seasonal changes of large-scale convective activity over the Western Pacific in the northern summer. *J. Meteorol. Soc. Japan*, **73**, 795–809.

Wang, B. and LinHo (2002) Rainy season of the Asian–Pacific summer monsoon. *J. Climate*, **15**, 386–398.

Wang, B. and H. Rui (1990) Synoptic climatology of transient tropical intraseasonal convection anomalies: 1975–1985. *Meteorol. Atmos. Phys.*, **44**, 43–61.

Wang, B. and X. Xie (1996) Low-frequency equatorial waves in vertically sheared zonal flow, Part I: Stable waves. *J. Atmos. Sci.*, **53**, 449–467.

Wang, B. and X. Xie (1997) A model for the boreal summer intraseasonal oscillation. *J. Atmos. Sci.*, **54**, 72–86.

Wang, B. and X. Xu (1997) Northern hemisphere summer monsoon singularities and climatological intraseasonal oscillation. *J. Climate*, **10**, 1071–1085.

Wang, B. and R. Wu (1997) Peculiar temporal structure of the South China Sea summer monsoon. *Adv. Atmos. Sci.*, **14**, 177–194.

Wang, W.-C., W.-S. Kau, H.-H. Hsu, and C.-H. Tu (2004) Characteristics of cloud radiative forcing over East Asia. *J. Climate*, **17**, 845–853.

Wang, Y., O. L. Sen, and B. Wang (2003) A highly resolved regional climate model (IPRC-RegCM) and its simulation of the 1998 severe precipitation event over China, Part I: Model description and verification of simulation. *J. Climate*, **16**, 1721–1738.

Wu, C.-H., W.-S. Kau, and M.-D. Chou (2009) Summer monsoon onset in the subtropical western North Pacific. *Geophys. Res. Lett.*, **36**, L18810, doi: 10.1029/2009GL040168.

Wu, R. (2002) Processes for the northeastward advance of the summer monsoon over the western North Pacific. *J. Meteorol. Soc. Japan*, **80**, 67–83, doi: 10.2151/jmsj.80.67.

Wu, R. and B. Wang (2001) Multi-stage onset of the summer monsoon over the western North Pacific. *Climate Dynamics*, **17**, 277–289.

Xie, P. and P. A. Arkin (1997) Global precipitation: A 17-year monthly analysis based on gauge observations, satellite estimates and numerical model outputs. *Bull. Amer. Meteorol. Society*, **78**, 2539–2558.

Xie, X. and B. Wang (1996) Low-frequency equatorial waves in vertically sheared flow, Part II: Unstable waves. *J. Atmos. Sci.*, **53**, 3589–3605.

Xu, G. and Q. Zhu (2002) Feature analysis of summer monsoon LFO over SCS in 1998. *J. Tropical Meteorol.*, **18**, 309–316.

Yamazaki, N. and M. Murakami (1989) Intraseasonal amplitude modulation of the short-term tropical disturbances over the western Pacific. *J. Meteorol. Soc. Japan*, **67**, 791–807.

Yanai, M., C. Li, and Z. Song (1992) Seasonal heating of the Tibetan Plateau and its effects on the evolution of the Asian summer monsoon. *J. Meteorol. Soc. Japan*, **70**, 319–351.

Yasunari, T. (1979) Cloudiness fluctuations associated with the northern hemisphere summer monsoon. *J. Meteorol. Soc. Japan*, **57**, 227–242.

Zhang, C. and S. M. Hagos (2009) Bi-modal structure and variability of large-scale diabatic heating in the tropics. *J. Atmos. Sci.*, **66**, 3621–3640.

Zhou, C. and T. Li (2010) Upscale feedback of tropical synoptic variability to intraseasonal oscillations through the nonlinear rectification of the surface latent heat flux. *J. Climate*, **23**, 5738–5754.

Zhu, B. and B. Wang (1993) The 30–60 day convection seesaw between the tropical Indian and Western Pacific Oceans. *J. Atmos. Sci.*, **50**, 184–199.

4

Pan America

Kingtse C. Mo, Charles Jones, and Julia Nogués Paegle

4.1 INTRODUCTION

Rain has a strong socioeconomic impact for the 850 million inhabitants of the American continents. Both continents depend on rainfall to sustain agriculture, hydroelectric power, and to maintain their waterways. Rainfall over Pan America has large interannual and intreaseasonal variability. In the interannual band, ENSO has a strong impact on total seasonal rainfall (Ropelewski and Halpert, 1987, 1989) over the region, while the occurrence of extreme rainfall episodes is more likely modulated by intraseasonal oscillations. The persistence of atmospheric patterns during episodes of strong intraseasonal events raises expectations of converting this information into predictability enhancement beyond the current limitation of about 1 week for weather forecasts. This would be of great value to optimize crop management, particularly in South America, where regional economies are largely based on agriculture and livestock.

The impact of intraseasonal oscillations on Pan America within a global perspective was first discussed by Weickmann (1983) and Weickmann *et al.* (1985), who identified large-scale patterns of variability in tropical outgoing longwave radiation and in expansions and contractions of subtropical and extratropical jets for selected boreal winters. They found that tropical–extratropical linkages in the intraseasonal band are remarkably similar to those found in the interannual band. The responses of circulation anomalies to the Madden Julian Oscillation (MJO) are similar to the responses associated with tropical sea surface temperature anomalies (SSTAs) in the Pacific Ocean on interannual timescales (Horel and Wallace, 1981). Kousky (1985a) also finds similarities between the interannual (ENSO) and intraseasonal signatures in relationships between northeast Brazil rains and circulation patterns over the Atlantic and the North American subtropical jet. This jet extends from the Caribbean towards the east–northeast across the Atlantic into North Africa and is also a component of the global patterns of intraseasonal variability

W. K. M. Lau and D. E. Waliser (Editors), *Intraseasonal Variability in the Atmosphere–Ocean Climate System* (Second Edition).

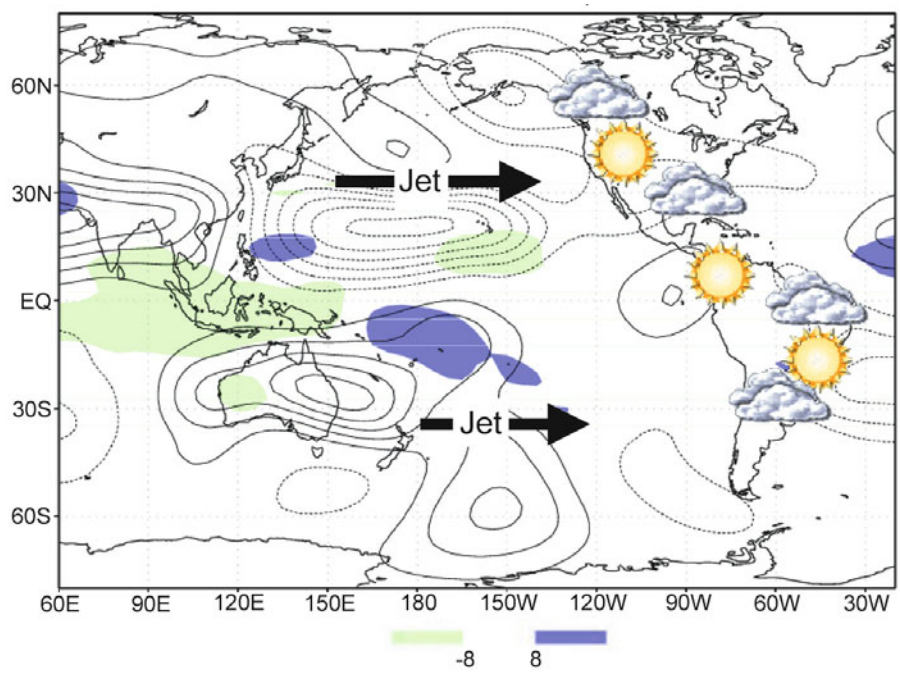

Figure 4.1. Schematic drawing of the impact of the TIS.

(Weickmann, 1983; Weickmann *et al*., 1985). Other intense weather events, such as hurricanes, appear to preferentially form and develop within intraseasonal regimes with convection patterns that resemble those during an ENSO cold phase.

Carvalho *et al*. (2004) find that the MJO modulates the persistence (enhanced convection lasting more than 4 days) of the South Atlantic Convergence Zone (SACZ), which is defined as an elongated band that originates in the Amazon Basin and extends into the subtropical Atlantic Ocean. There is a 25% to 30% increase of rainfall over eastern tropical Brazil for the MJO phase with enhanced convection over the Central Pacific (Figure 4.1). The persistence of the oceanic part of the SACZ is more frequent during warm ENSO events and can provoke states of emergency in southeastern Brazil due to an increase in the number of floods and mudslides. The implications of these studies are that there may be internal patterns of atmospheric variability associated with diabatic heating on the intraseasonal timescale that play a role similar to that of SSTAs on the interannual scale. Jones *et al*. (2004a) find no statistical significant differences in the frequency of the MJO during warm and cold ENSO phases. That does not rule out the possibility that the warm phase of ENSO sets up conditions over the equatorial Pacific that are conducive to excitation of intraseasonal oscillations or vice versa (see Chapter 9 for more on the ENSO connection).

The expansion and contraction of subtropical and extratropical jets mentioned above are components of wavetrains with alternating positive and negative upper air

height anomalies that extend from the tropical Pacific into midlatitudes. These are referred to as the Pacific–North American (Wallace and Gutzler, 1981) and the Pacific–South American modes (e.g., Mo and Nogués-Paegle, 2001). These wavetrains affect the weather over North and South America by modulating Pacific storm tracks—a modulation that is strongest during boreal winter (Figure 4.1). During this season they regulate precipitation on the west coast of North America. The tropical continent of South America is also regulated by the rich spectrum of frequencies contained within the intraseasonal band.

In the intraseasonal band, the wavetrains previously mentioned can be excited by two different modes. One mode is the well-known Madden Julian Oscillation (MJO). This is an eastward-propagating mode with convective amplitude that dampens as convection moves over the cold water of the eastern Pacific Ocean (Chapter 1). This mode has characteristics typical of Kelvin and tropical Rossby modes (Nogués-Paegle *et al.*, 1989). In addition to the MJO, there are submonthly modes with smaller spatial scales and periods of 20–28 days. They were originally observed in the Indian Ocean and the Pacific (Krishnamurti and Bhalme, 1976; Fukutomi and Yasunari, 1999). Although these modes do not contribute much to variance in the tropics, they are known to modulate the Indian and the Asian monsoons. Over the Pan American region, they influence rainfall over both South and North America. For example, strong flooding in California is often associated with the submonthly mode. Figure 4.2a shows 5-day running mean precipitation averaged over nine stations during the 1996/1997 winter (Mo, 1999). Five coastal stations (Brookings, Los Angeles, Pendleton, San Diego, and San Francisco) and four inland stations (Blue Canyon, Fresno, Stockton, and Thermal) were used. There were four wet episodes roughly 20 days apart with breaks in between. These alternating wet and dry events occur often in California during winter. Over South America, submonthly oscillations are also found over the SACZ. Liebmann *et al.* (1999) examine power spectra of 90-day highpass-filtered outgoing longwave radiation anomalies (OLRAs) at several gridpoints. They find peaks near 27, 16, 10, and 8 days for a point in the SACZ (solid thick line, Figure 4.2b). In contrast, there is no 27-day peak for the point in the Amazon Basin (dashed thin line, Figure 4.2b). This is consistent with other studies that find strong diurnal and seasonal cycles of Amazon convection, while it is over eastern tropical and subtropical South America that intraseasonal variability is most pronounced (e.g, Kiladis and Weickmann 1992a, b). The following sections focus on the influence of ISOs over the Americas based on EOF analysis of OLRAs and related atmospheric circulation anomalies.

4.2 VARIATIONS IN THE IS BAND

To indicate the seasonal variations of convection associated with intraseasonal oscillations, Figure 4.3 plots standard deviations of OLRAs in the lowpass (LP, greater than 10 days) 10 to 90-day and 10 to 30-day bands. The largest standard deviations of LP-filtered OLRAs follow the annual evolution of convection and are

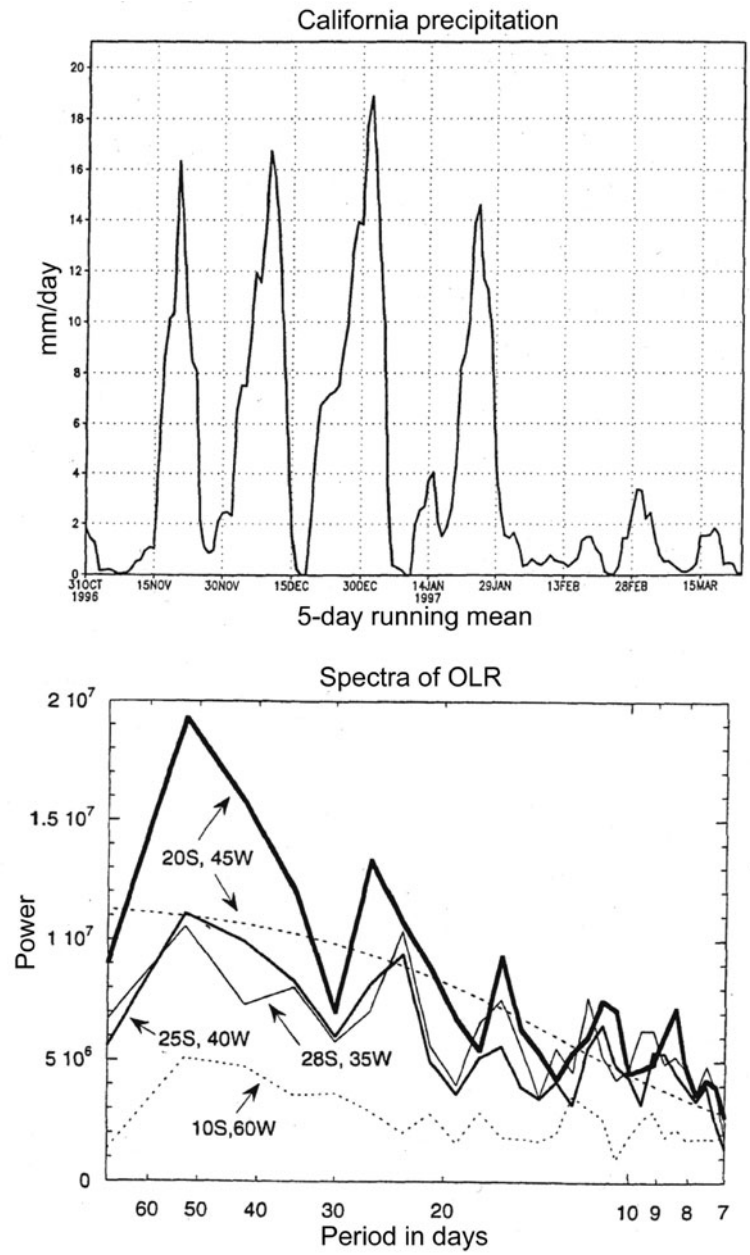

Figure 4.2. (a) 5-day running mean of California precipitation averaged over 9 stations (Brookings, Los Angeles, Pendleton, San Diego, San Francisco, Blue Cayan, Fresno, Stockton, and Thermal) during the 1996/1997 winter (from Mo, 1999). The unit is millimeters per day. (b) Average power spectra of OLR for points at locations marked in the figure. Also shown is the red-noise spectrum for the uppermost curve, computed from the lag 1 autocorrelation (from Liebmann *et al.*, 1999).

concentrated mostly in the summer hemisphere (Fig. 4.3). For DJFM, large standard deviations are located over the Indian Ocean and the Western and Central Pacific predominantly south of the equator (Figure 4.3a). As the season progresses, the largest values show a northward displacement of 20° to 30° of latitude over the same longitude from winter (DJFM) to summer (JJAS) (Figure 4.3b). The largest standard deviations in the 10 to 90-day band (Figures 4.3b, e) are located in the Indian Ocean and the Western and Central Pacific, where the contribution to lowpass-filtered OLRA variance can range from 50% to as large as 75%. Such contributions are smaller at equatorial latitudes east of the dateline, where convection is largely due to interannual variations related to ENSO. In the western hemisphere, the largest values are located along the west coast of North America and in the Eastern Pacific just above the equator, due to variations of the ITCZ. For JJAS, large values are also located over Mexico and the southern United States. Large contributions from the 10 to 90-day band are evident in the SACZ and subtropical plains over South America, where the contributions to LP-filtered OLRA variance can range from 50% to as large as 75%. Figure 4.3c, f shows the contribution on submonthly timescales. They exhibit a similar global imprint to that of the 10 to 90-day band contributing less than 50% to LP variance.

For DJFM, convection related to the TISO modulates the Australian monsoon over the Western Pacific and Australia (Chapter 5). Large values of OLR also extend into the SPCZ and the SACZ. For JJAS, TISO modulation of the Indian monsoon is evident from standard deviations higher than 30 $W\,m^{-2}$ that extend from the Indian Ocean to the Indian continent (see Chapters 2 and 3). The band that extends from the South China Sea to Japan indicates TISO modulation of the Asian monsoon and the East Asian Meiyu. Over North America, large values over Mexico and the southwestern United States during JJAS represent intraseasonal modulation of the North American monsoon. Over South America, large standard deviations during boreal winter are also found over the SACZ and the subtropical plains, where both the 30 to 60-day band, related to the MJO. and the submonthly oscillation modulate the South American monsoon.

4.3 IS VARIABILITY IN DECEMBER–MARCH

IS variability is described next by empirical orthogonal function (EOF) analysis of OLR anomalies. This methodology has been extensively used to isolate the dominant patterns of large-scale variability. The technique is not as useful when looking at local phenomena (e.g., Carvalho *et al.*, 2004).

4.3.1 EOF modes

Empirical orthogonal function (EOF) analysis was performed on OLRAs from 40°S to 50°N for DJFM. OLRAs were filtered to retain variability on a 10 to 90-day band and the resolution was reduced to 5° prior to EOF analysis. Both spectral analysis and singular spectrum analysis (Vautard and Ghil, 1989) identify the leading modes

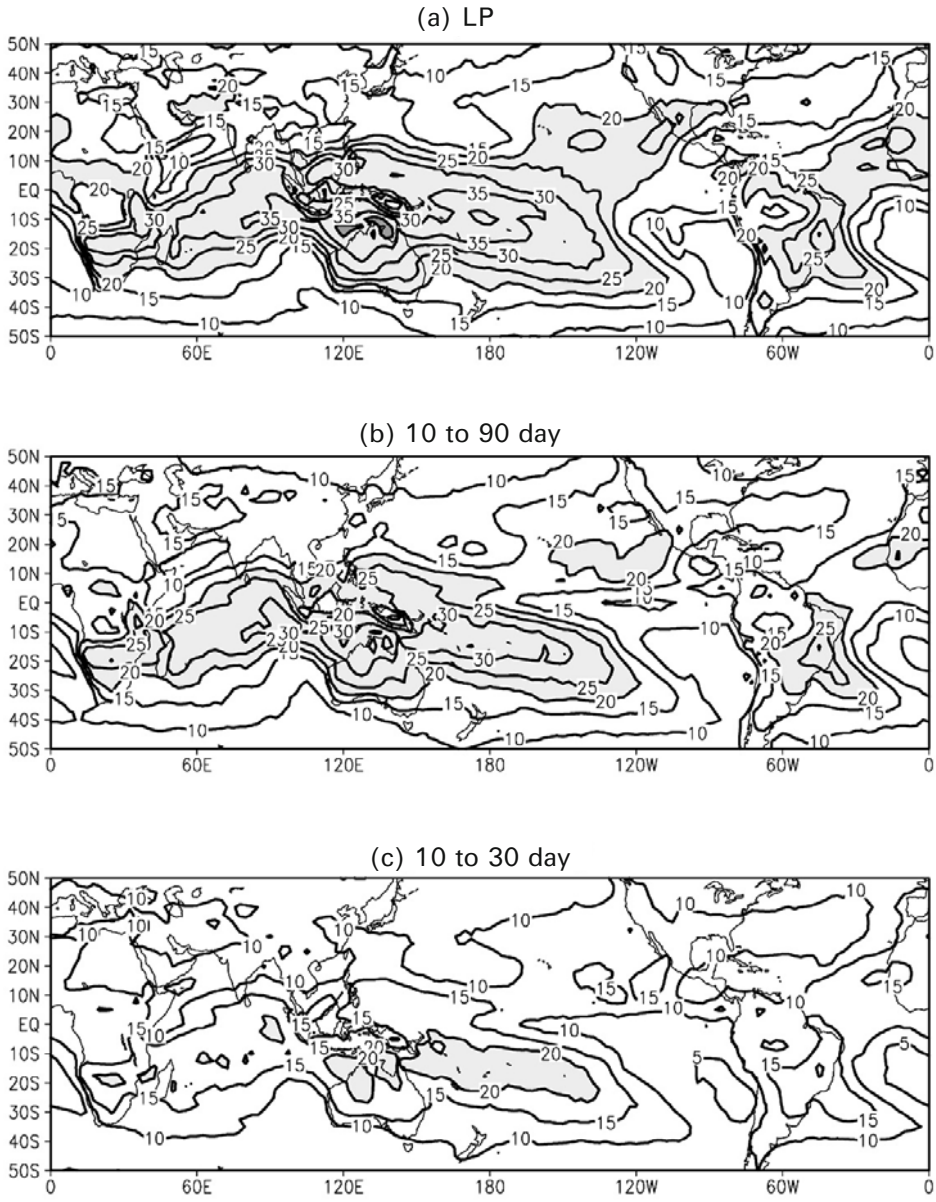

Figure 4.3. (a) Standard deviation for the lowpass-filtered (>10 days) of outgoing longwave radiation anomalies obtained from daily averages of NOAA satellites (Liebmann and Smith, 1996) for the period January 1, 1979 to December 31, 2001 for DJFM (boreal winter). Anomalies are computed as departures from the seasonal cycle defined as the grand mean plus the annual and semi-annual cycles. The contour interval is $5\,W\,m^{-2}$. Values greater than $20\,W\,m^{-2}$ are shaded. (b) Same as (a), but for 10 to 90-day filtered OLRAs. (c) Same as (a), but for 10 to 30-day filtered OLRAs.

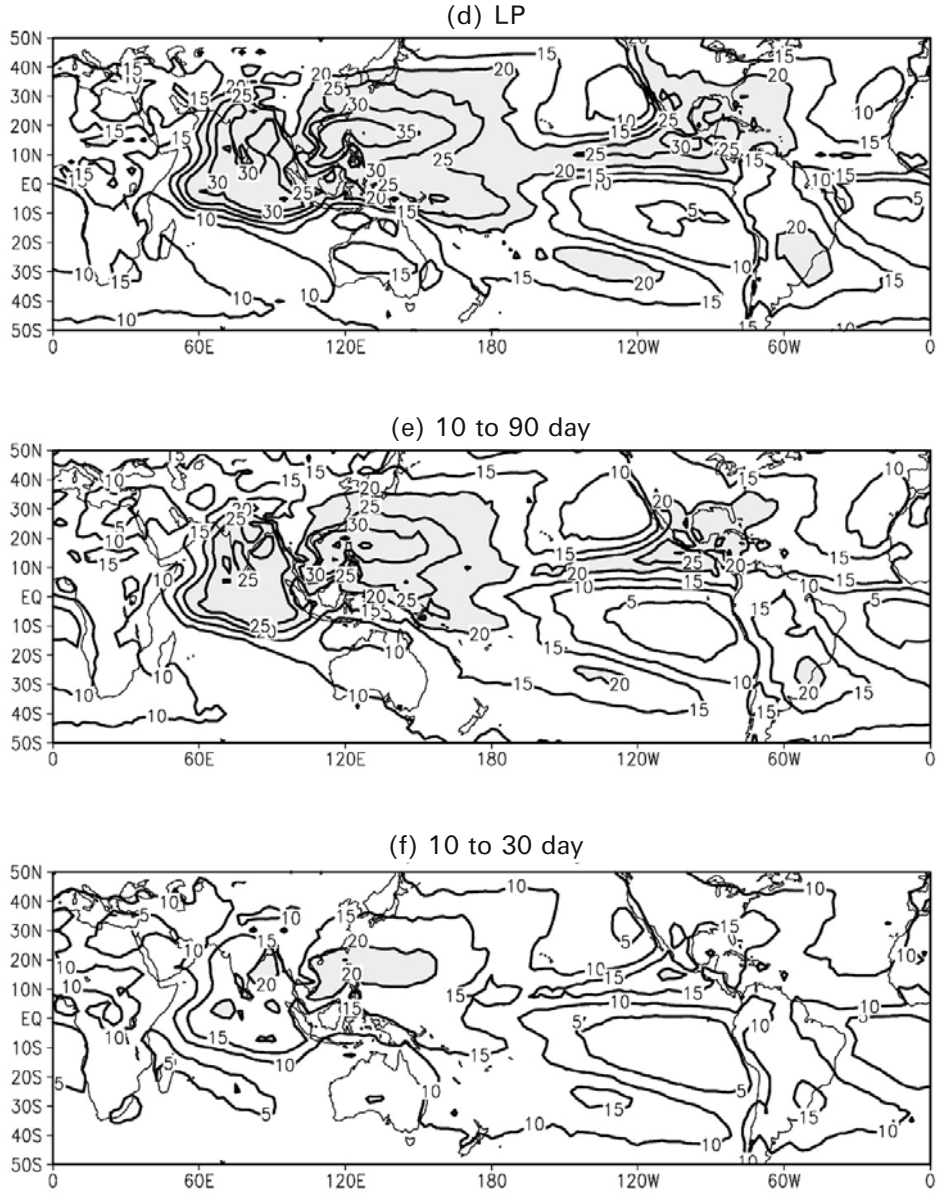

Figure 4.3. (*cont.*) (d)–(f) Same as (a)–(c), but for JJAS (boreal summer). Anomalies are filtered using the minimum bias window developed by Papoulis (1973).

(EOF 1 and EOF 2) with a period of 40–48 days. They are in quadrature in time as well as space and explain nearly the same percentage of variance (about 4.7%). Together, they represent the MJO (Figure 4.4a, b). In the Indian–Pacific sector, they are similar to the patterns isolated by the pioneering work of Lau and Chan (1985) and the EEOF (Chapter 1). EOF 1 (Figure 4.4a) shows suppressed convection over the Western Pacific accompanied by enhanced convection in the Central Pacific and the Indian Ocean. Over the Pan American region, enhanced convection extends from northeastern Brazil through the tropical Atlantic to the west coast of Guinea. EOF 2 (Figure 4.4b) shows a longitudinal dipole with two centers located at 90°E and 165°E, respectively. Positive loadings are also located in the SPCZ and the SACZ. Rainfall patterns do not map into OLRAs over the African desert north of 10°N and, therefore, OLRAs should not be interpreted as precipitation anomalies in this region (Waliser *et al.*, 1993).

While the first two EOFs project strongly onto a wavenumber 1 structure in longitude with centers over the Indian Ocean and Pacific sector (Figure 4.4a, b), the next two EOFs exhibit a more complex structure with at least two positive and two negative centers (Figure 4.4c–, d). EOFs 3 and 4 are also orthogonal to each other and explain nearly 2.9% of total variance. EOF 5 explains only 1.6% of total variance. They are well separated from EOF 2 and EOF 5 by the North criterion (North *et al.*, 1982). The second pair of EOFs represent oscillations with timescales of 22–28 days. They are similar to the leading EOFs in the 10 to 30-day band (Mo, 1999). Even though they do not explain a large percentage of total variance, the submonthly modes are stronger than the MJO for certain years. During these periods, they have a large influence on rainfall over Pan America. As discussed in the introduction, strong submonthly oscillations are often responsible for winter floods in California (Mo, 1999). Carvalho *et al.* (2002) and Liebmann *et al.* (2004) relate the occurrence of extreme wet events over tropical southeastern South America with contributions from the TISO.

Both EOFs 3 and 4 (Figure 4.4c, d) show high loadings extending from centers at the equator near the dateline to the west coast of North and Central America, indicating their large influence on rainfall over the Pan America region. EOFs 3 and 4 both show a dipole with positive loadings over California and negative loadings to the south. Over South America, EOF 3 exhibits a three-cell structure, with positive values over northeastern Brazil, flanked by a negative arch-shaped pattern that extends from northern South America into the South American subtropics.

4.3.2 The Madden Julian Oscillation

The evolution of OLRAs and atmospheric circulation anomalies associated with the MJO were examined with a compositing approach obtained as follow: 10 to 90-day filtered OLRAs were projected onto EOF modes 1 and 2 to obtain a time series of principal components (PCs). For each PC, the standard deviation was computed. A positive (negative) day was selected when the PC for that day was above 1.2 (below −1.2) standard deviations. This date is also defined as the onset day.

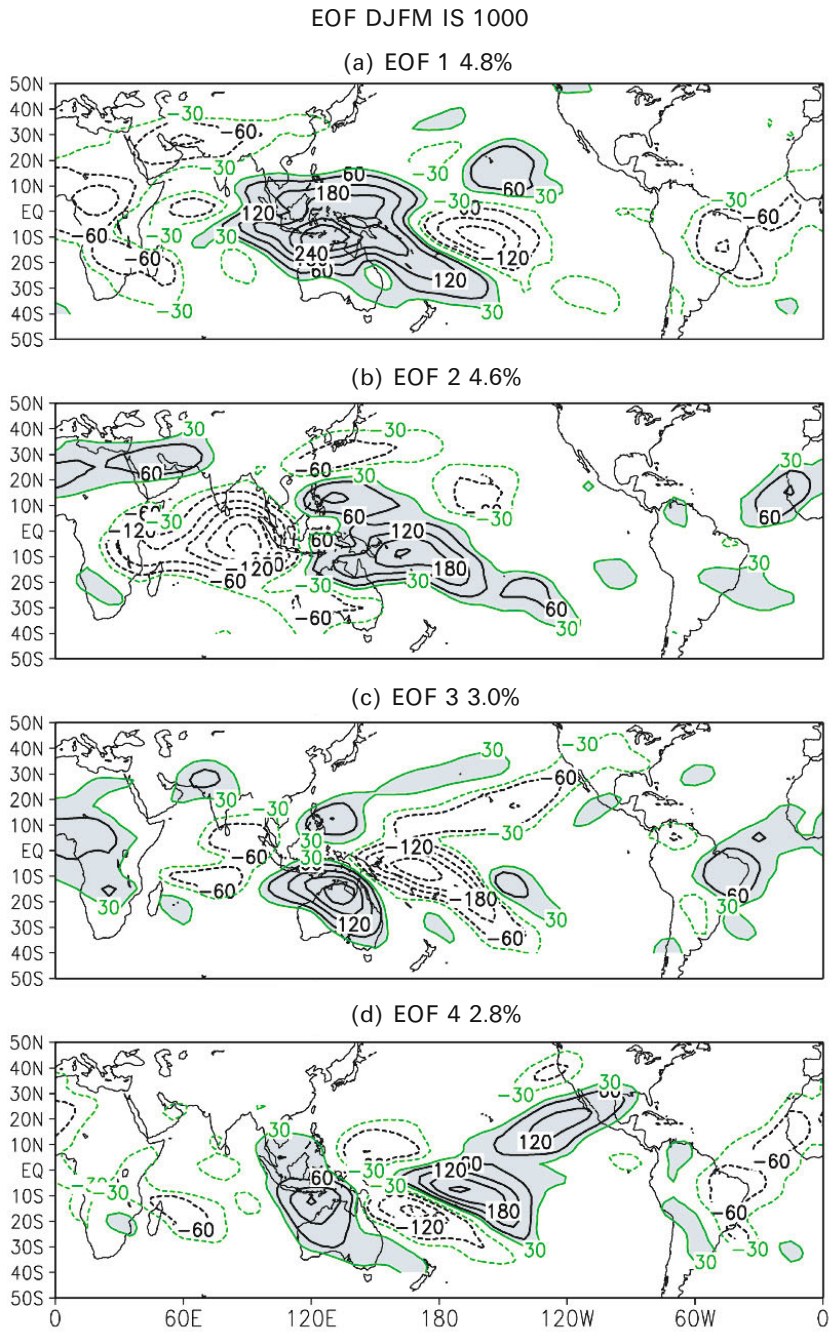

Figure 4.4. (a) EOF 1, (b) EOF 2, (c) EOF 3, and (d) EOF 4 for the domain from 40°S to 50°N. The contour interval is 60 non-dimensional units. Zero contours are omitted. Contours −30 and 30 non-dimensional units are added for (a) to (d). Positive values are shaded.

Composites of the 10 to 90-day filtered 200 hPa eddy streamfunction (with zonal means removed) and OLRAs were formed from 20 days before to 20 days after the onset day. There were more than 300 days in each composite. To assure that OLRA composites represented rainfall, the OLRA composites were compared with composites of pentad rainfall anomalies from the CMAP (Xie and Arkin, 1997; Xie *et al.*, 2003). From the above daily PC time series, the 5-day means were computed. The same composite procedures were used to obtain pentad rainfall anomalies. Overall, OLRAs and rainfall composites were similar except in areas over West Africa north of 10°N, where OLRAs did not represent rainfall (Waliser *et al.*, 1993). The statistical significance of each map was tested using Student *t* tests. The degrees of freedom were determined by assuming 6 days as the decorrelation time. Composites for positive and negative events were similar with a sign reversal; therefore, composite differences between positive and negative events were presented to amplify the signal. OLRA composite evolution is shown in Figure 4.5 based on PC 1. Areas with anomalies in the corresponding rainfall composite and daily OLRA composites with statistical significance at the 5% level are shaded.

Figure 4.5 shows an eastward-propagating pulse and a stationary component that is most evident over South America between the equator and 20°S. A negative center (enhanced convection) propagates from the western Pacific to the central Pacific in 15 days (Figures 4.5a–d, 4.6a). South America acts as a bridge linking convection from the Central Pacific to the tropical Atlantic. As negative OLRAs shift towards the Central Pacific east of the dateline, a link is established between the center over eastern Brazil at 20°S and the western African coast of Guinea (Figure 4.5d). The compensatory branch of suppressed convection is found over the tropical Atlantic (Figure 4.5f, g). This is indicative of meridional displacements of the Atlantic ITCZ. As negative OLRAs proceed eastward farther into the Central Pacific east of the dateline, negative anomalies extend southeastward from West Africa to South Africa and connect to anomalies in the Indian Ocean (Figure 4.5f). With the enhancement of convection in the Indian Ocean, positive OLRAs are found in the Western Pacific and another cycle starts (Figure 4.5g, h). At the same time, the Atlantic convective branch between South America and Africa weakens. The OLRA composite at day −10 resembles EOF 2 (Figure 4.4b), showing that PC 1 has evolved into PC 2 in 10 days, in about one quarter of the total period.

Circulation anomalies and rainfall over the Pan American region depend on the location of tropical convection. The strongest large-scale upper-level response to the MJO in the Pan American region is at day 5 based on the PC 1 composite (Figure 4.6c), when enhanced convection is located east of the dateline centered at 140°E–150°E and over the Indian Ocean (Figure 4.5f). The response represented by the 200 hPa streamfunction difference shows that anomalies are symmetric in the tropics and exhibit a four-cell pattern with high-pressure centers (i.e., anticyclonic flow) flanking strengthening convective activity in the Pacific. There is also a wavetrain extending from the convective region in the tropics to both North and South America (Weickmann *et al.*, 1985). Over North America, there are negative anomalies near the west coast of the United States, positive anomalies over

Canada, and negative anomalies over the east coast of North America. This closely represents a Pacific North American (PNA) pattern. Liebmann and Hartmann (1984) examine tropical–extratropical connections and find a similar wavetrain pattern to that of day 5 (Figure 4.6c). The location of anomalies in the North Pacific at days 0 to 5 is also the region where blocking and persistent anomaly events are most likely to form (Higgins and Mo, 1997). It is likely that tropical forcing related to the MJO sets up favorable conditions for persistent weather anomalies.

Consistent with the above discussion, the response of North American west coast rainfall also depends on the location of tropical convection anomalies. At day 5, the rainfall response exhibits a dipole pattern with centers located over California and the Pacific Northwest (Figure 4.6f), which resembles the response during warm ENSO events except for the negative anomaly center shifting from the southern plains into the Ohio Valley during ENSO. The rainfall response is partly due to a westward shift of the stormtrack to California, which contributes to dry conditions in the Pacific Northwest and wet conditions over California (Mo and Higgins, 1998a, b).

The evolution of the MJO cycle and downstream responses are shown in terms of Hovmöller diagrams (Figure 4.6). When tropical OLRAs move eastward (Figure 4.6a), the dipole response in the 200 hPa streamfunction propagates eastward in concert (Figure 4.6b) (Weickmann, 1983; Knutson and Weickmann, 1987). In midlatitudes, the wavetrain (Figure 4.6f) propagates from the convective region downstream to North America. The rainfall response is consistent with circulation anomalies. It shows a dipole pattern depicting a seesaw between the Pacific Northwest and California. In South America, responding OLRAs propagate from the subtropics to the equator (Figure 4.6d). The largest influence is over northeast Brazil when suppressed convection is located in the Eastern Pacific (Figures 4.5e, 4.6a). The OLRA pattern also shows a dipole with centers over northeast Brazil and the SACZ (Figure 4.6e).

As previously mentioned, extreme precipitation oftentimes is associated with significant social and economic impacts. Observational studies have shown clear linkages between the MJO and extreme precipitation in the Pan American region. Mo and Higgins (1998a), for instance, find that heavy precipitation in California is accompanied by dry conditions over Washington, British Columbia, and along the southeastern coast of Alaska and reduced precipitation over the subtropical Eastern Pacific. Higgins *et al.* (2000) conclude that extreme events occur at all phases of ENSO, but the largest fraction of these events occurs during neutral winters prior to the onset of an El Niño, which tend to be characterized by enhanced tropical intraseasonal activity. Jones (2000) also finds that the frequency of extreme events in California is more common when tropical convective activity associated with the MJO is high, as opposed to quiescent phases of the oscillation. Significant relationships between the MJO and flooding events in Oregon and Washington have also been shown (Bond and Vecchi, 2003).

Likewise, an important modulation of the MJO on extreme precipitation events in South America has been identified. Carvalho *et al.* (2004) determine that the MJO

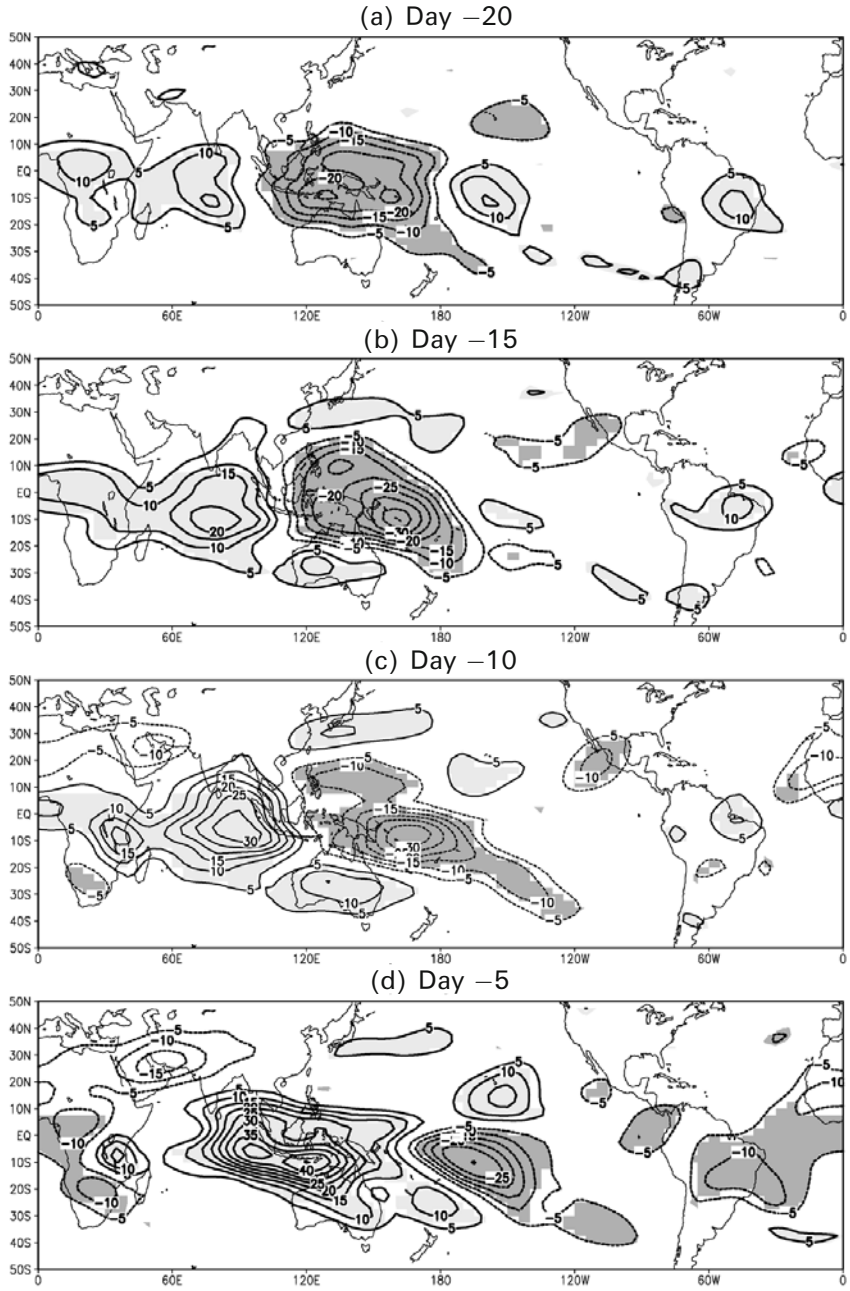

Figure 4.5. OLRA (IS1090) composite difference between positive and negative events for (a) day −20, (b) day −15, (c) day −10, (d) day −5. The contour interval is $5\,W\,m^{-2}$. Zero contours are omitted. Areas where positive (negative) anomalies are statistically significant at the 5% level are shaded light (dark).

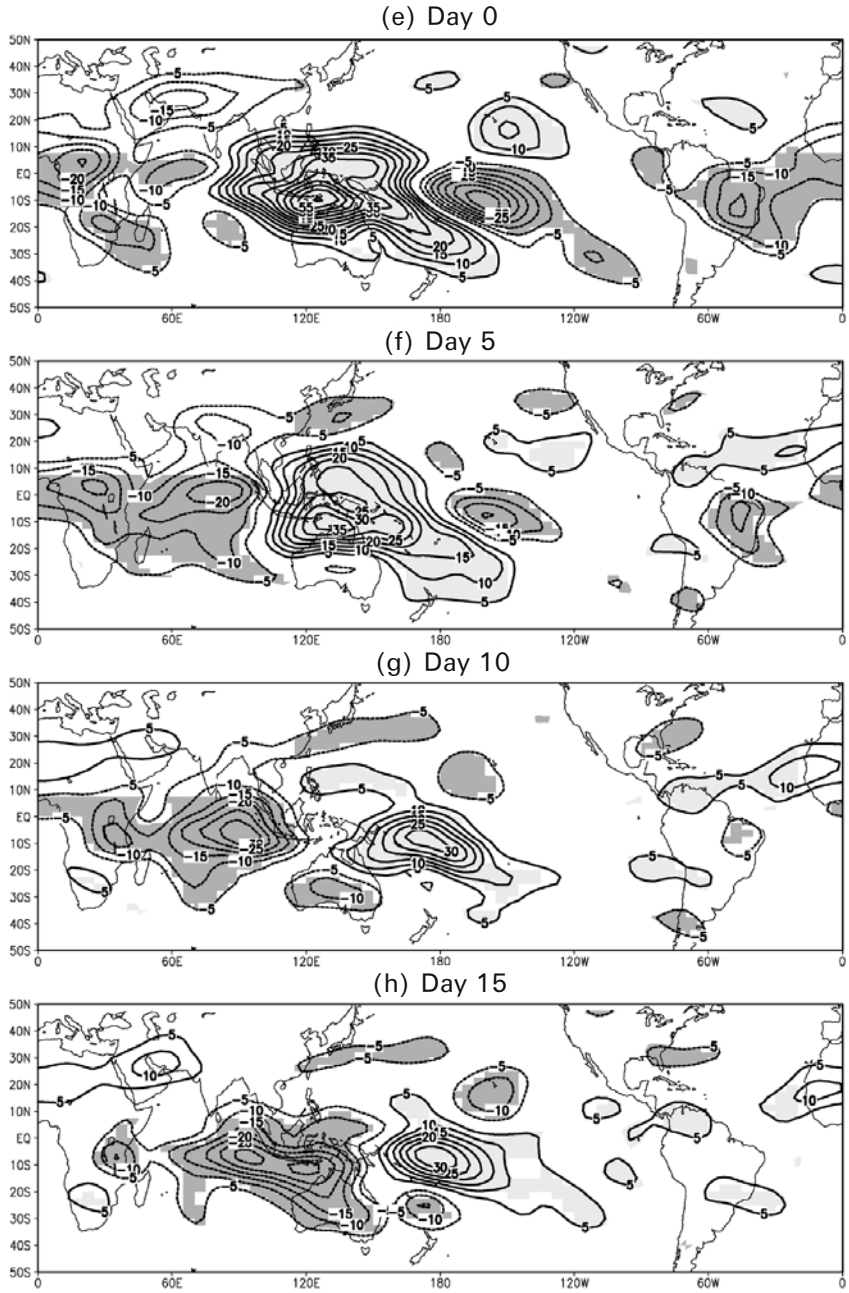

Figure 4.5. (*cont.*) (e) day 0, (f) day 5, (g) day 10, and (h) day 15 based on PC 1 for DJFM.

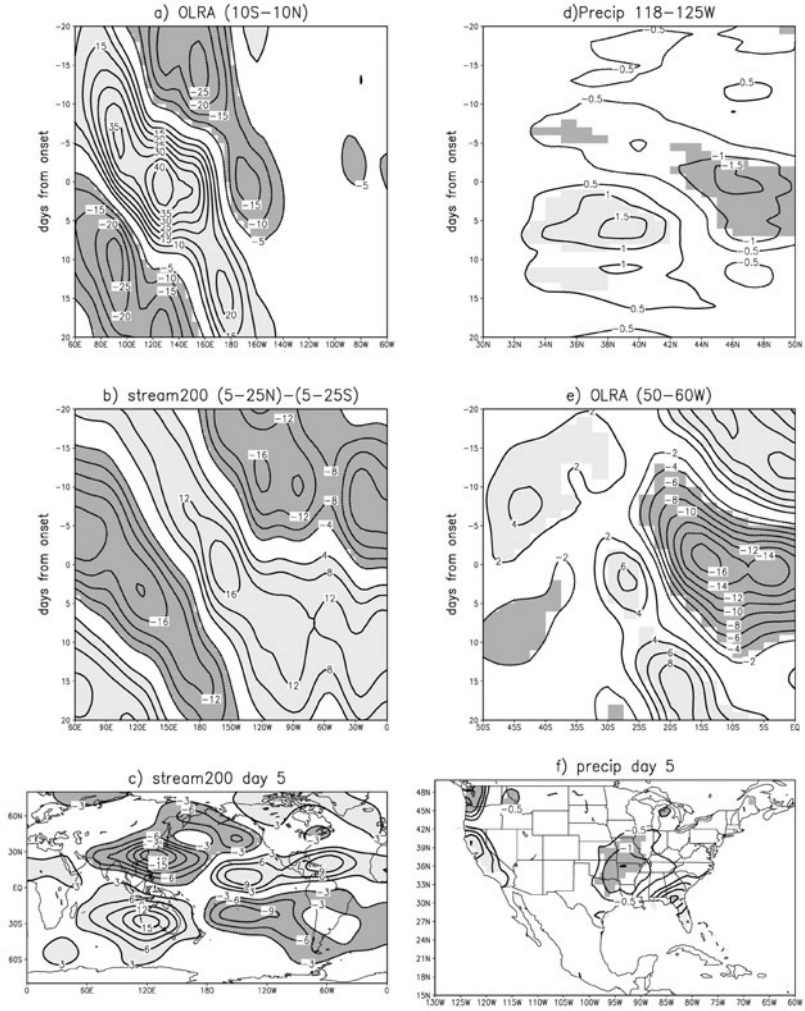

Figure 4.6. (a) Time and longitude plot of OLRA composite difference averaged from 10°S to 10°N between positive and negative events from 20 days before to 20 days after onset of PC 1. The contour interval is $5\,W\,m^{-2}$. Areas where positive (negative) values are statistically significant at the 5% level are shaded light (dark). (b) Same as (a), but for composite of 200 hPa streamfunction difference between mean from 5°N–25°N and 5°S–20°S. (c) Composite of 200 hPa streamfunction between positive and negative events for day 5 based on PC 1 for DJFM. The contour interval is $3 \times 10^6\,m^2\,s^{-1}$. Zero contours are omitted. Areas where positive (negative) anomalies are statistically significant at the 5% level are shaded light (dark). (d) Same as (a), but the time–latitude plot of precipitation difference averaged from 118°W–125°W is over land. The contour interval is $0.5\,mm\,day^{-1}$. (e) Same as (d), but for OLRA averaged from 50°W to 60°W. (f) Same as (c), but for precipitation difference. The contour interval is $0.5\,mm\,day^{-1}$. The 200 hPa streamfunction was obtained from NCEP/NCAR reanalysis (Kalnay *et al.*, 1996). Daily observed precipitation over the U.S.A. and Mexico was derived from unified gridded daily data (Higgins *et al.*, 2000).

modulates intense SACZ episodes with persistence longer than 3 days. They additionally find that the MJO phase characterized by suppression of convective activity over Indonesia and enhancement over the Central Pacific increases the 95th daily precipitation percentile over north/northeastern Brazil, whereas the opposite features are observed during enhancement of convection over Indonesia and suppression over the Central Pacific. Liebmann *et al*. (2004) investigate the variability of extreme precipitation events and associations with the SACZ and the South American low-level jet. They obtain statistically significant variations associated with precipitation both downstream of the jet and in the SACZ. They further speculate that a slowly varying dipole feature is a consequence of the preferred phasing of synoptic waves due to variations of the MJO.

The importance of the MJO in modulating extreme precipitation is further investigated by Jones *et al*. (2004b). On a global scale, extreme events during active MJO periods are about 40% higher than in quiescent phases of the oscillation in locations of statistically significant signals. Furthermore, predictability experiments indicate the mean number of correct forecasts of extreme precipitation during active MJO periods to be nearly twice the correct number of extremes during quiescent phases of the oscillation.

4.3.3 The submonthly oscillation

In addition to the influence of the MJO, the submonthly oscillation (depicted by EOFs 3 and 4) also influences rainfall over the Pan American region. The evolution of OLRAs and streamfunction anomalies was determined by projecting OLRAs into EOFs 3 and 4 to obtain the time series of PCs. These composites were computed following the methodology described in the previous section for the MJO. Selected time sequences of OLRA, 200 hPa streamfunction, and precipitation anomaly composites are depicted in Figures 4.7 and 4.8 to illustrate their temporal behavior. The typical eastward propagation of the MJO is not apparent on submonthly timescales. Instead, westward propagation of OLRAs is dominant along 10°N–20°N (Figure 4.7a, d; shading) from the Central Pacific into the Indian Ocean. It may be better represented by the Hovmöller diagrams of OLRAs based on both PC 3 and PC 4 (Figure 4.8b, a). In addition to propagation, there are standing components with centers located at 150°E and 120°W for PC 4 (Figure 4.8a) and 120°E and 150°W for PC 3 (Figure 4.8b). The timescale is about 20–22 days. When convection associated with the submonthly mode moves westward, circulation anomaly composites (Figure 4.7a–d; contours) show a northward displacement into the midlatitudes of anomalies, extending from the subtropics to Mexico and North America (Figure 4.7). Northwestward travel of circulation anomalies was first reported by Branstator (1987) when he analyzed circulation patterns in 1979. The composites also indicate a modulation on timescales of 20–28 days of the so-called ‘‘pineapple express’’, characterized by moisture plumes that feed wet conditions over western North America and are oftentimes associated with extreme precipitation (e.g., Higgins *et al*., 2000; Jones, 2000).

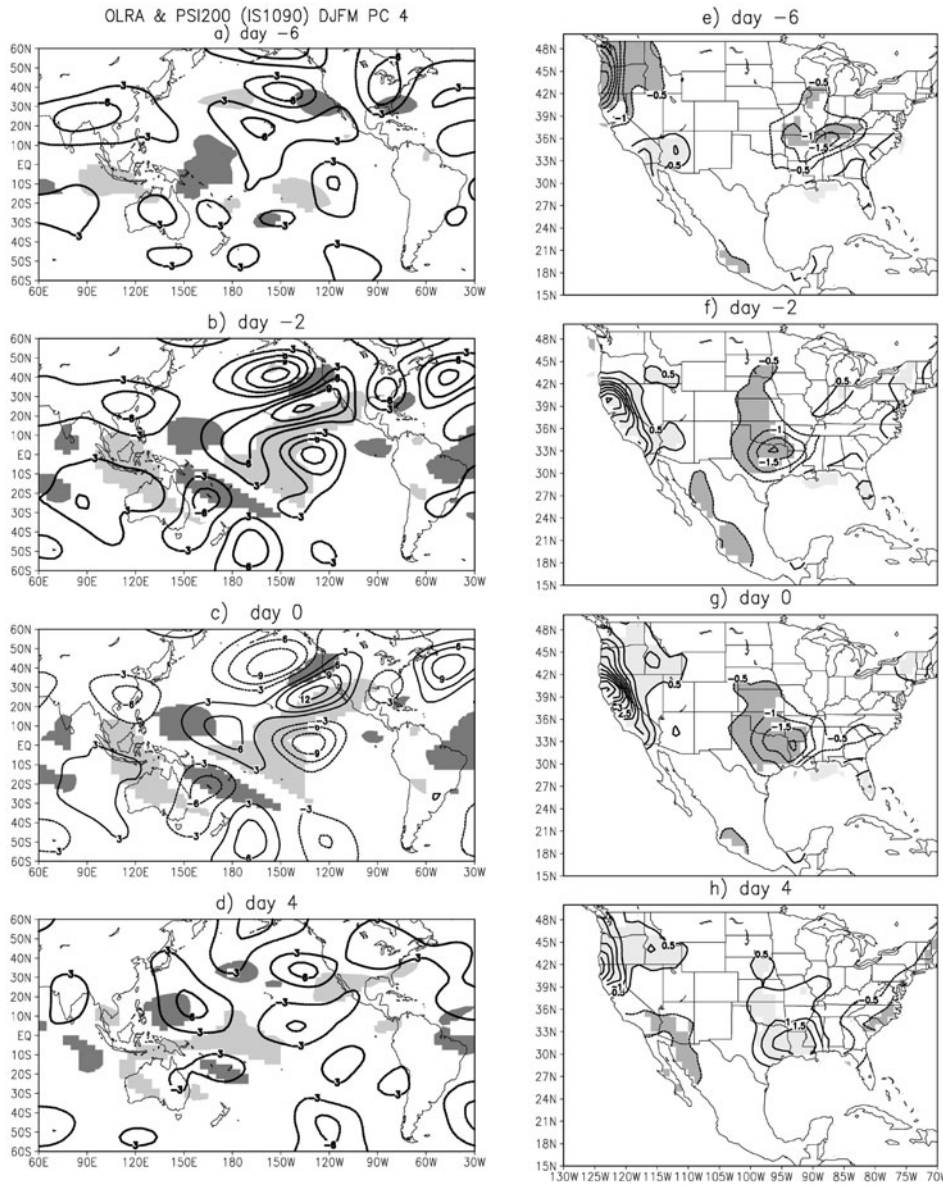

Figure 4.7. OLRA (shaded) and 200 hPa streamfunction (contoured) composite difference between positive and negative events for (a) day −6, (b) day −2, (c) day 0, and (d) day 4 based on PC 4 for DJFM. Areas where OLRAs are greater (less) than 6 (−6) W m^{-2} and are statistically significant at the 5% level are shaded light (dark). The contour interval for the 200 hPa streamfunction composite is 3×10^6 m^2 s^{-1}. Zero contours are omitted. (e)–(h) Same as (a) and (d), but for precipitation. The contour interval is 0.5 mm day^{-1}. Areas where positive (negative) anomalies are statistically significant at the 5% level are shaded light (dark).

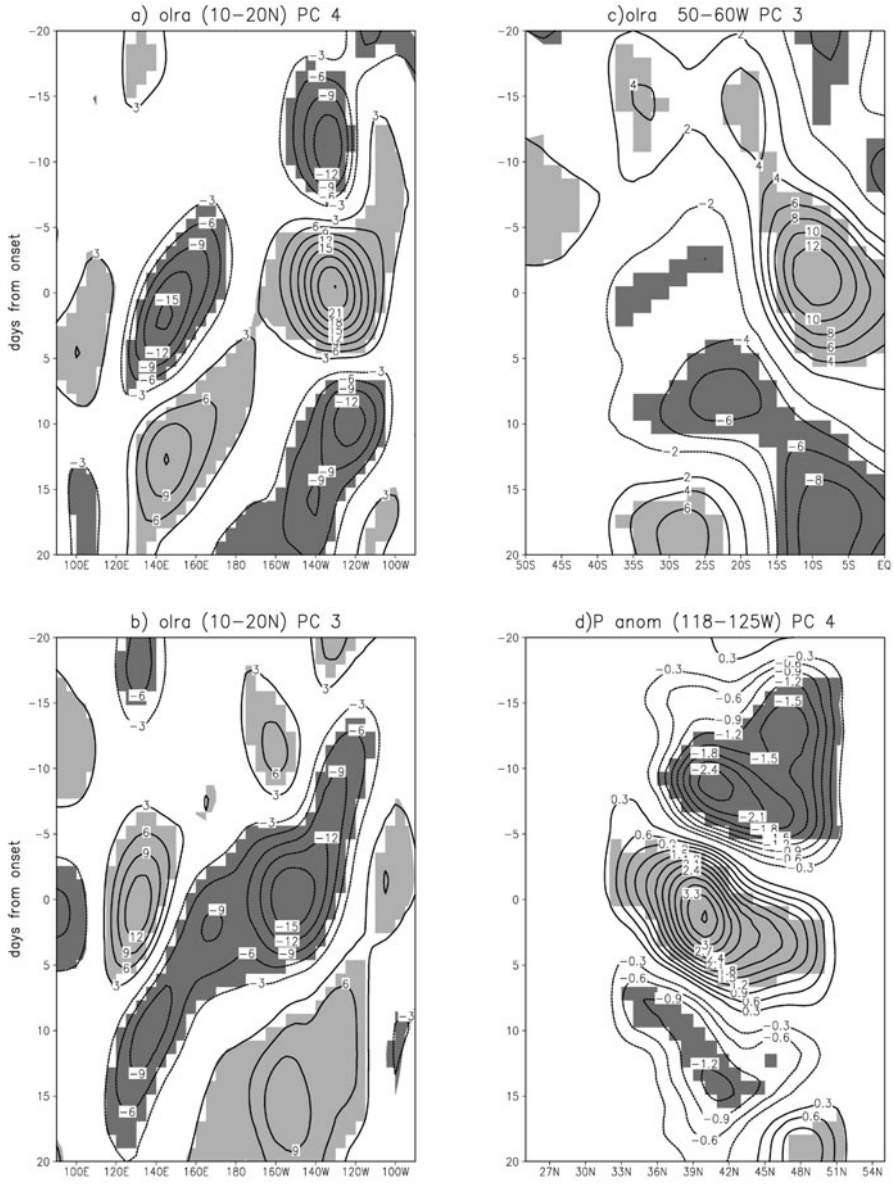

Figure 4.8. (a) Time and longitude plot of OLRA composite difference averaged from 10°N to 20°N between positive and negative events from 20 days before to 20 days after onset of PC 4 for DJFM. The contour interval is $3\,W\,m^{-2}$. Areas where positive (negative) values are statistically significant at the 5% level are shaded light (dark). (b) Same as (a), but based on PC 3. (c) Same as (a), but for time–latitude plot of OLRA composite difference averaged from 50°W to 60°W based on PC 3. The contour interval is $2\,W\,m^{-2}$. (d) Same as (c), but for precipitation difference averaged from 118°W to 125°W over land based on PC 4. The contour interval is $3\,mm\,day^{-1}$.

The evolution of precipitation over the west coast of North America shows a three-cell pattern with negative anomalies over the Pacific Northwest, positive anomalies over Southern California, and negative anomalies over the Pacific Northwest at day −6. The rainfall pattern shifts northward along the west coast in response to circulation changes. For example, positive anomalies originating from Southern California move to northern California at day –2 and reach the Pacific Northwest at day 4. The time–latitude plot of rainfall anomalies averaged over the west coast demonstrates the northward movement of rainfall (Figure 4.8d). Over the United States, composites (Figure 4.7e–h) also show a phase reversal of rainfall anomalies between southern California and the Southern Plains.

In contrast, OLRAs over tropical South America originate in the subtropics and propagate into the deep tropics (Figure 4.8c). This is related to submonthly modulation of the wavetrain response to the MJO. This timescale has been identified by several studies (e.g., Nogués-Paegle and Mo, 1997; Liebmann *et al*., 1999; Nogués-Paegle *et al*., 2000; Mo and Nogués-Paegle, 2001) and linked to Rossby trains over the Pacific Ocean, in which low-level cold air moves northward channeled by the Andes and triggers enhanced convection along the SACZ. Liebmann *et al*. (1999) point out that convection over the southwestern Amazon Basin on submonthly timescales appears to propagate from the south, while convection over the southeastern Amazon is accompanied by disturbances moving from the Atlantic. This is consistent with the early results of Kousky (1985b) that relate rainfall anomalies over tropical Brazil to cold fronts moving from the south with an enhanced Atlantic subtropical high and enhanced easterlies over the continent that persist for periods commensurate with those of the ISO.

The synoptic picture described above is complemented by previous studies related to other tropical convective bands. Kodama (1992, 1993) discuss common characteristics of the SPCZ, SACZ, and the Baiu frontal zone over South Asia. These convergence zones originate from equatorial convection extending poleward and eastward. Moisture has a dominant monsoonal origin in the tropical portion of these bands and is advected poleward by subtropical highs. In the case of South America, the poleward moisture flux is modified by the steep orographic relief of the Andes, which deflects the prevailing trade winds southward, transporting large amounts of water vapor into subtropical South America. These characteristics of the time mean South American climate have been shown to also typify submonthly oscillation (Nogués-Paegle and Mo, 1997). The SACZ and the fertile plains of South America located towards the south of the SACZ constitute a dipole of convection, such that low-level moist-laden flow from the tropics fuels convection over the plains prior to cold air moving northward and triggering enhancements of the SACZ. The central South American low-level jet constitutes an integral part of the South American convective dipole and is strongly modulated by TISOs (Nogués-Paegle and Mo, 1997).

Recently, Carvalho *et al*. (2010) used indices for the South American monsoon and SACZ to investigate variations of moisture transport on intraseasonal timescales. Wet events over the South American monsoon were observed to amplify wave activity in the northern hemisphere and enhance northwesterly cross-equatorial

moisture transport over tropical continental South America. Enhanced SACZ episodes were observed with moisture transport from the extratropics of the southern hemisphere. Simultaneous wet events over the continent and SACZ were associated with cross-equatorial moisture transport along with moisture transport from the subtropical southwestern Atlantic.

4.4 IS VARIABILITY IN JUNE–SEPTEMBER

4.4.1 EOF modes

EOF analysis was performed on OLRAs for June through September (JJAS). The procedures are similar to those used to obtain EOFs for DJFM. The first two EOFs are nearly in quadrature with each other and singular spectrum analysis indicates that the leading temporal mode has a period of 40–48 days. Together, they represent the MJO (Figure 4.9a–c). EOF 3 also has a spectrum peak with a period of 40–48 days, which suggests additional modulation of the MJO. The complexity in OLRA patterns introduced by convection associated with the Asian monsoon requires three EOFs during boreal summer to adequately represent the MJO during this season, unlike the case during boreal winter when most of the convection is found over oceanic areas. EOF 1 (Figure 4.9a) shows positive loadings north of the equator extending from the Western Pacific to the Central Pacific with negative loadings in the Indian Ocean. Over the Pan American region, the largest negative loadings are found over Central America. The largest loading in the vicinity of Central America indicates modulations of the North American monsoon by the much stronger intraseasonal anomalies of the eastern hemisphere. Weak negative loadings extend across South America into the Atlantic. EOF 2 (Figure 4.9b) has a four-cell structure in the eastern hemisphere with two dipoles, opposite in phase, straddling the equator. EOF 3 (Figure 4.9c) is similar to EOF 1 over the Americas, but it exhibits sign reversals from that of EOF 1 over the eastern hemisphere. EOF 1 over the Indian–Pacific sector resembles the second EOF for 20 to 60-day filtered OLRAs (Lau and Chan, 1986). Such agreement is lacking in subsequent EOFs, possibly due to differences in the analysis domain and width of the time filter.

EOF 4 (Figure 4.9d) explains about 2.6% of total variance. This mode is found in the 10 to 30-day band and the dominant temporal mode has a period of 20–24 days. This mode together with the MJO establishes linkages between convection over the South China Sea associated with the Asian monsoon and summer precipitation over the Pan American region in the intraseasonal band. The dominant feature is a four-cell pattern with two dipoles, opposite in sign, located over the Western and Central Pacific. There are positive loadings over the South China Sea (5°N–15°N, 100°E–130°E) and negative loadings to the east with a wave of alternating positive and negative anomalies towards the northeast. A three-cell OLR anomaly pattern along the west coast of North America is noted. In South America there are positive loadings over the SACZ.

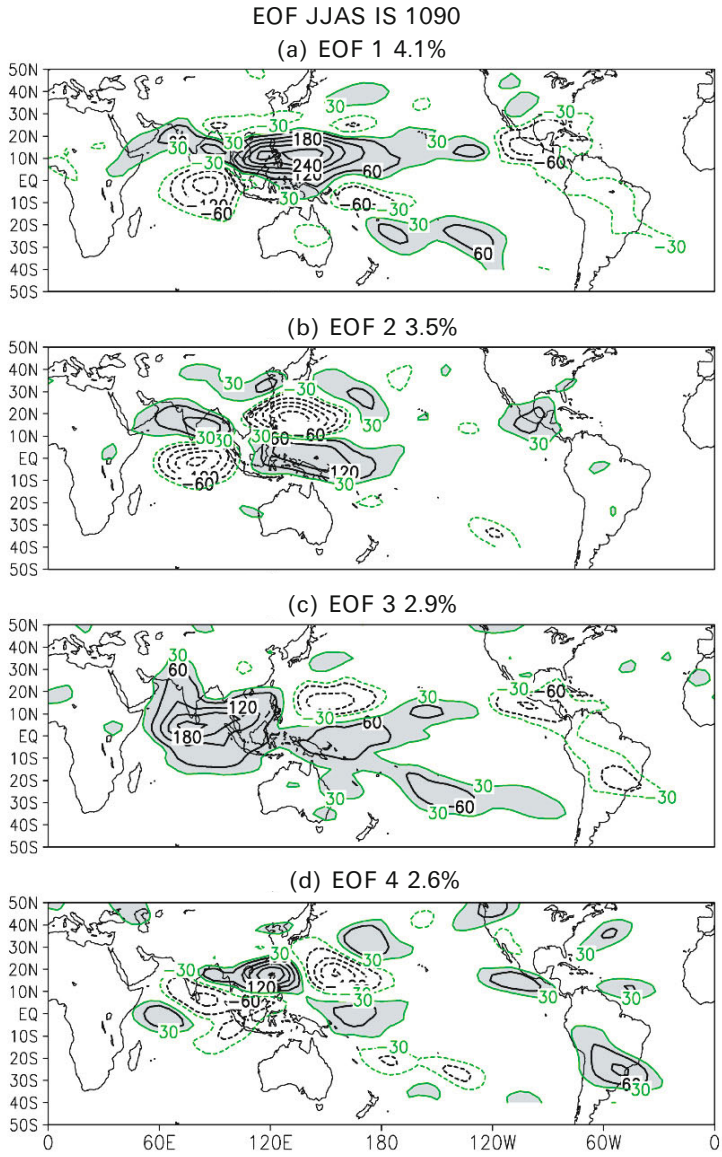

Figure 4.9. Same as Figure 4.4, but for JJAS.

Composites of 10 to 90-day filtered OLRAs, 200 hPa streamfunctions, and precipitation anomalies were formed for JJAS using the same compositing procedures as for DJFM. The composites for positive and negative events are similar but with sign reversal, so the composite differences between positive and negative events are given. Areas where features are statistically significant at the 5% level are shaded.

4.4.2 Madden–Julian Oscillation

The OLRA composites (Figure 4.10) show the evolution of EOF 1. In addition to eastward propagation there is also a northward shift of OLRAs in the Indian Ocean. The positive OLRAs centered in the Indian Ocean at day −20 (Figure 4.10a) shift from 5°S to 10°N at day −5 (Figure 4.10d) and extend into the Western Pacific. From day −5 on, a negative center is established in the equatorial Indian Ocean which expands northward and eastward such that by day 15 (Figure 4.10h), mostly negative OLRAs are found over the eastern hemisphere. The connection with the Americas is evident only after negative OLRAs are established at equatorial latitudes (day −5 through day 15). They take the form of a band of convection that extends from Mexico into South America (day 0, see also Figure 4.10a), which evolves into an opposite phase by day 15 (Figure 4.10h). The evolution over the eastern hemisphere is consistent with well-known features associated with the Asian monsoon (Gadgil, 1983; Krishnarmurti *et al.*, 1985; Lau and Chan, 1986; see Chapters 2 and 3 for a review). The composite at day 0 is an amplified version of the composite at day −20 with a phase reversal, indicating a period near 40–48 days. The composite at day −10 is similar to EOF 3 (Figure 4.9c) west of the dateline in agreement with the notion that all three leading EOFs represent different phases of the MJO.

Figure 4.11b shows rainfall anomaly patterns for days 0–2 based on PC 1, when the strongest anomalies are found over North America, consistent with the OLRA composites shown in Figure 4.10e. MJO modulation of the North American monsoon is characterized by an anomaly that extends from the core of the monsoon over southern Mexico (Higgins and Shi, 2001) across the Gulf of Mexico. There are also anomalies over the southeastern United States, which (except for areas near the Gulf of Mexico) are not significant at the 5% level. Rainfall anomalies with opposite sign are found centered over the Great Plains and New Mexico. The circulation response to the MJO is shown in Figure 4.11a in terms of the 200 hPa streamfunction difference based on PC 1. It is characterized by global wavenumber 1 with maximum values located in subtropical latitudes. The pattern indicates high (low) pressure in the western (eastern) hemisphere at this time, with an enhancement of equatorial easterlies and subtropical westerlies over the Americas and the Eastern Pacific. These results are consistent with those of Nogués-Paegle and Mo (1987) for the 1979 FGGE year. That study linked planetary divergent and rotational circulation and concluded that the seasonal northward displacement of OLRAs from South into Central America was triggered by the passage of intraseasonal oscillations over the Americas during 1979. The results presented here suggest the validity of this conclusion for a longer time period.

The evolution of OLRAs and circulation anomalies associated with the MJO is directly related with precipitation variability in the Pan American region. Barlow and Salstein (2006) analyze rainfall data in Mexico and Central America during boreal summer. Their analysis shows significant increases in precipitation during the MJO phase that favors enhanced convection in the region including the occurrence of extreme events. Lorenz and Hartmann (2006) also show that positive zonal

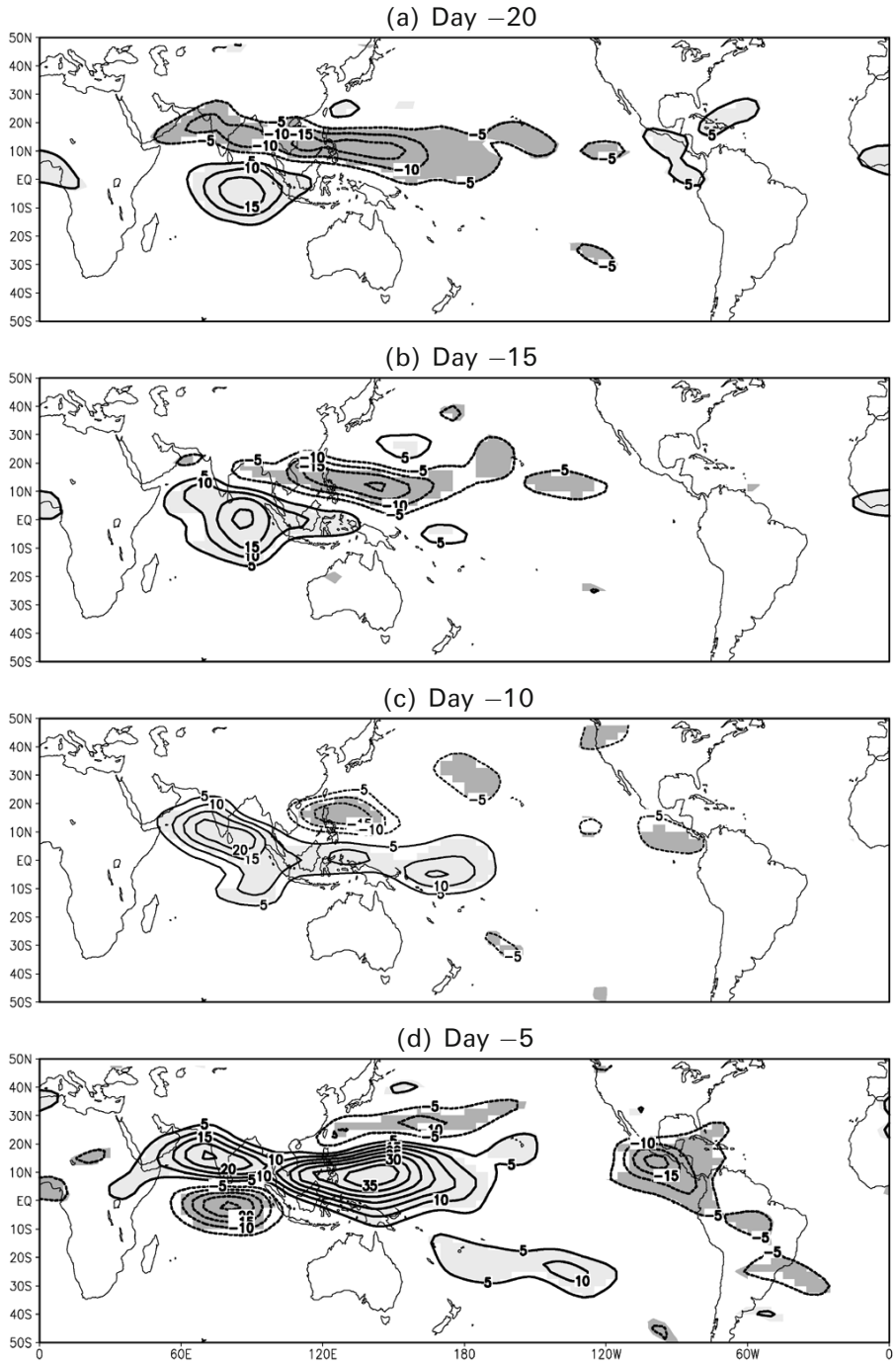

Figure 4.10. Same as Figure 4.5, but for JJAS based on PC 1.

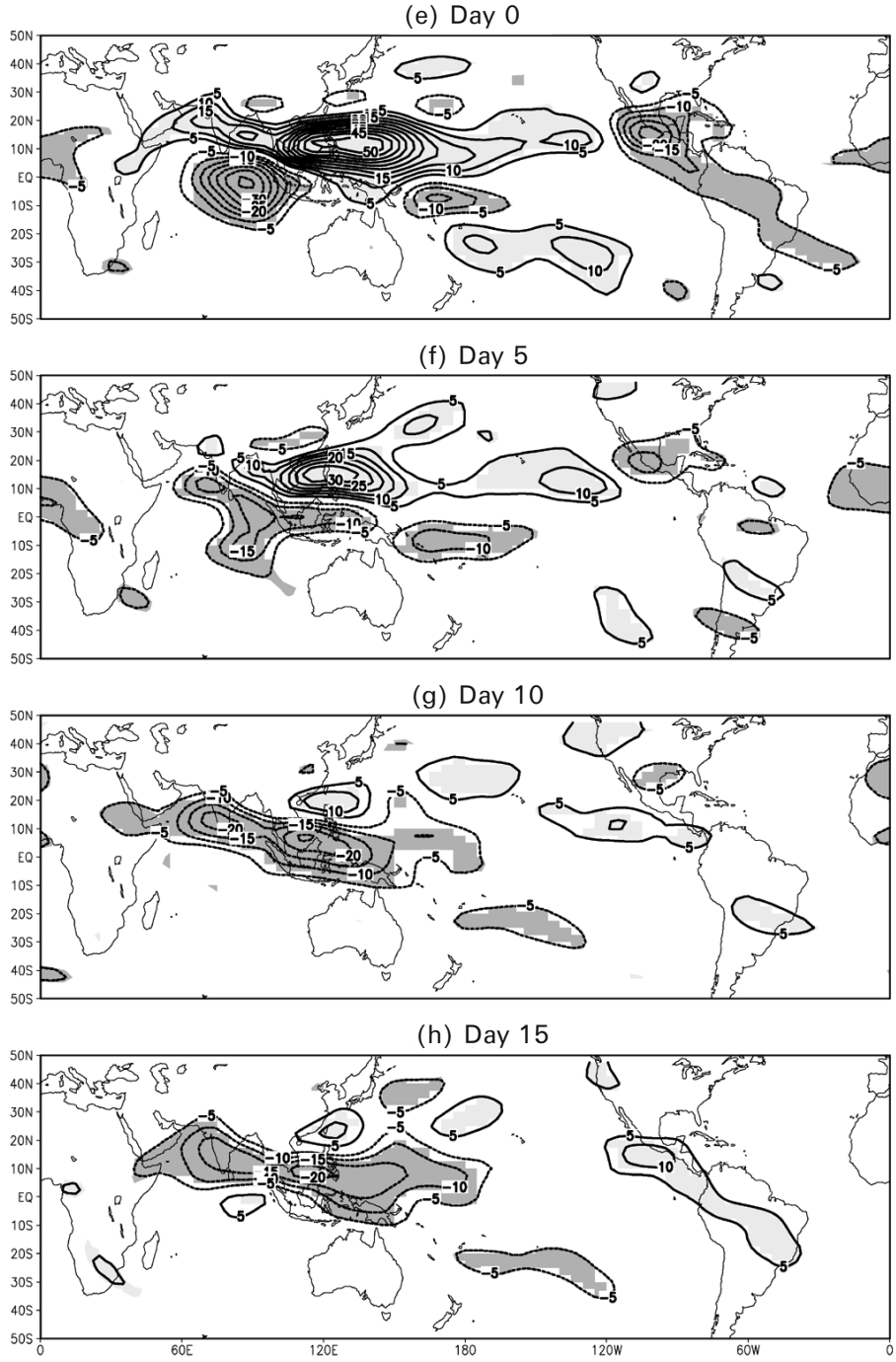
(e) Day 0
(f) Day 5
(g) Day 10
(h) Day 15
50N
40N
30N
20N
10N
EQ
10S
20S
30S
40S
50S
0
60E
120E
180
120W
60W
0

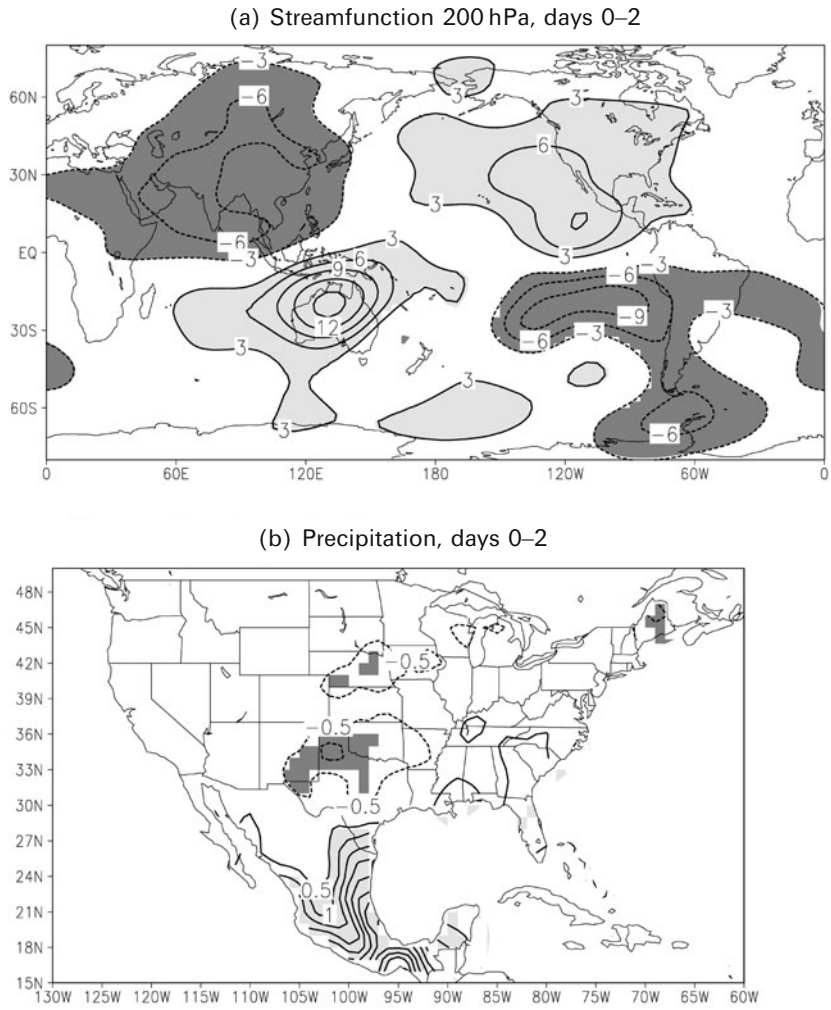

Figure 4.11. The 200 hPa streamfunction composite difference between positive and negative events averaged from days 0–2 for JJAS based on PC 1. The contour interval is 3×10^6 m^2 s^{-1}. Zero contours are omitted. Areas where positive (negative) anomalies are statistically significant at the 5% level are shaded light (dark). (b) Same as (a), but for precipitation. The contour interval is 0.3 mm day^{-1}.

wind anomalies in the eastern tropical Pacific are related to MJO results in above-normal precipitation in northwest Mexico and Arizona. They postulate that this association between the MJO and the North American monsoon is limited to regions influenced by moisture surges from the Gulf of California. In these regions, the MJO modulates the strength of low-level easterly waves off the coast of Mexico which then triggers the development of a gulf surge.

The strongest TIO influence on South America can be represented by two dominant wavetrain patterns known as the Pacific–South American (PSA) modes (Mo and Nogués-Paegle, 2001), given here as the leading two EOFs of the 200 hPa streamfunction eddy anomalies over the southern hemisphere (Mo and Higgins, 1998c). The wavetrains extend from the tropics into the midlatitudes and bend northward into South America. The two wavetrains are in quadrature with each other. The PSA 2 pattern shows a region of positive anomalies centered about 120°W and 60°S, a region of frequent blocking in the southern hemisphere (e.g., Kiladis and Mo, 1998), predominantly in austral winter. Composites of 10 to 90-day filtered OLRAs and 200 hPa eddy streamfunctions based on PCs associated with PSA patterns were obtained using the same technique as composites based on OLRA PCs.

There is good correspondence between the evolution of the PSA modes and tropical convection related to the TISO (Mo and Higgins, 1998c), with major contributions from the MJO. The connection with the TISO is demonstrated by the composites of 10 to 90-day filtered OLRAs based on PSA PCs (Figure 4.12c, d). For JJAS, PSA 1 is excited when EOF 1 is strong (Figure 4.9a) with enhanced convection centered over the Western Pacific and suppressed convection over the Indian Ocean. This pattern is associated with suppressed convection over northeastern Brazil. For DJFM, PSA 2 is linked to enhanced convection (light shading) in the Western Pacific and suppressed convection in the Central Pacific. In South America, PSA 2 is associated with suppressed rainfall over the SACZ and enhanced convection over the subtropical plains. This dipole pattern is the prominent convection pattern during the South American winter (Nogués-Paegle and Mo, 1997).

4.4.3 Submonthly oscillation

Submonthly modes with periods around 10–28 days play an important role in modulating the Indian monsoon (Krishnamurthi and Andanuy, 1980) and the Asian monsoon (Krishnamurthi and Bhalme, 1976; Krishnamurthi *et al.*, 1985; Chen and Chen, 1993; Wu *et al.*, 1999). These are reviewed in Chapters 2 and 3. A submonthly mode with fluctuations in the 10 to 25-day range has also been reported by Fukutomi and Yasunari (1999). When enhanced convection is located over the South China Sea, a wavetrain extends from the convective region to the North Pacific. They suggest that interactions between the tropics and the subtropics play important roles in development of the Baiu front. Linkages between the Asian monsoon and OLRAs over the Americas are described with composites based on PC 4 (Figure 4.13), at days 0–2.

The OLRA composite (Figure 4.13a) indicates suppressed convection over the South China Sea flanked by enhanced convection in the Indian Ocean to the southwest and over the Pacific to the northeast. From the convective area, a wavetrain extends to the United States with positive anomalies over the Pacific Northwest, negative anomalies over the central United States, and positive anomalies over the east coast (Figure 4.13b). This is consistent with rainfall anomalies and OLRAs. Over the west coast of North America, there is suppressed

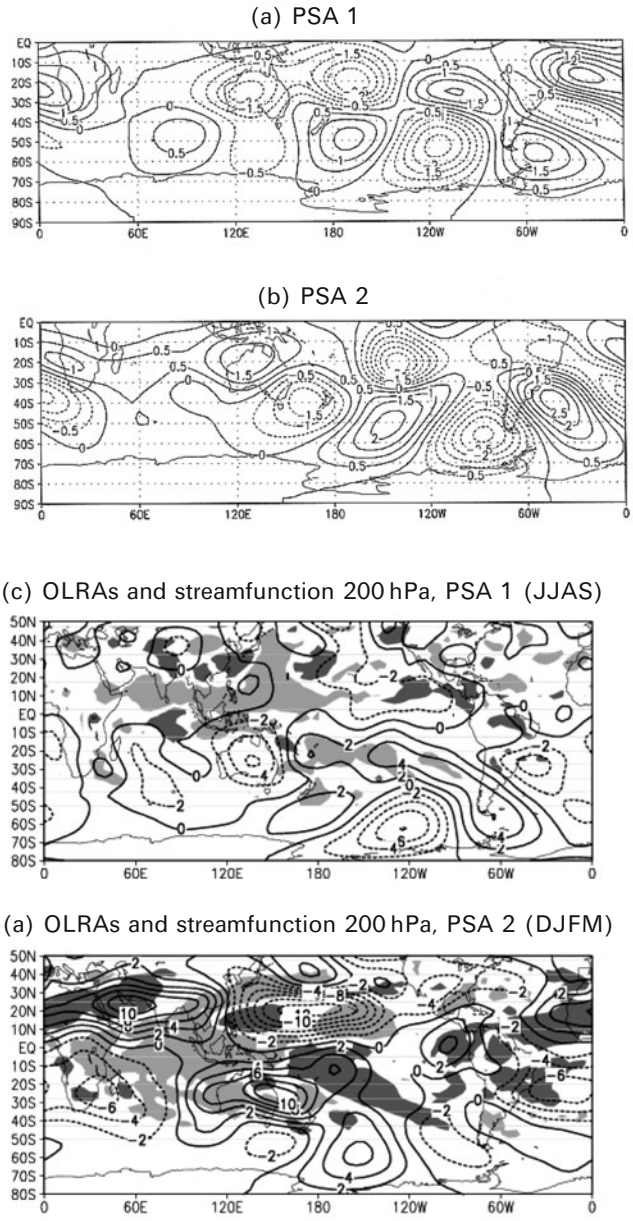

Figure 4.12. (a) PSA 1 and (b) PSA 2 from the first two EOFs for the 200 hPa streamfunction with zonal means removed. EOFs are normalized to 1 and time 100. The contour interval is 0.5 non-dimensional units (from Mo and Higgins, 1998c). (c) Composites of 10 to 90-day filtered OLRAs (shading) and 200 hPa streamfunction eddy difference (contour) between positive and negative PSA 1 events for JJAS. Areas where OLRAs are greater (less) than $3\,\mathrm{W\,m^{-2}}$ are shaded dark (light). The contour interval for the 200 hPa streamfunction composite is $2 \times 10^6\ \mathrm{m^2\,s^{-1}}$. (d) Same as (c), but for PSA 2 events for DJFM.

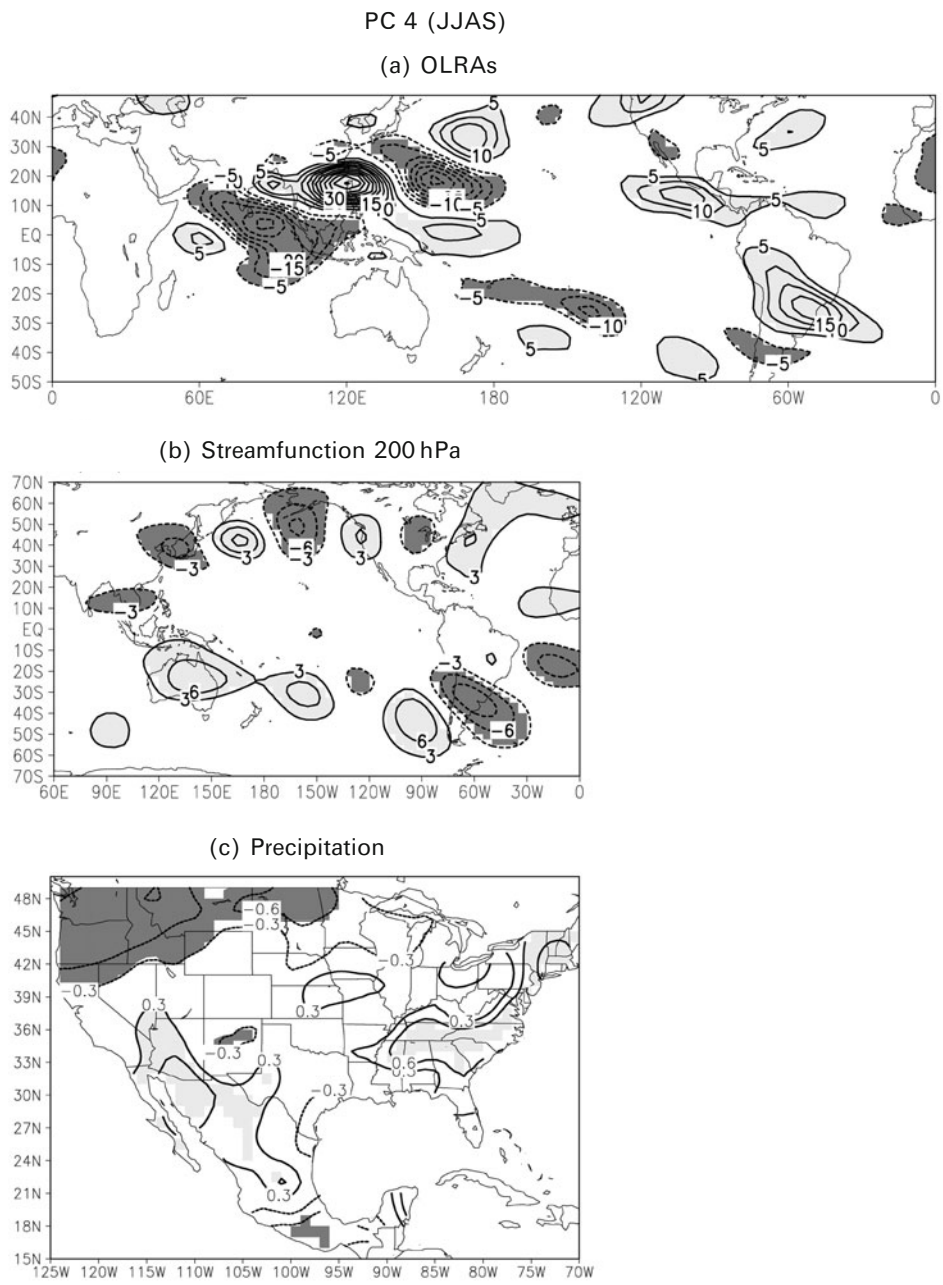

Figure 4.13. OLRA composite difference between positive and negative events averaged from days 0–2 for JJAS based on PC 4. The contour interval is 5 W m^{-2}. Zero contours are omitted. Areas where positive (negative) anomalies are statistically significant at the 5% level are shaded light (dark). (b) Same as (a), but for 200 hPa streamfunction. The contour interval is 3×10^6 m^2 s^{-1}. (c) Same as (a), but for precipitation. The contour interval is 0.3 mm day^{-1}.

convection over southern Mexico (Figure 4.13c), enhanced convection over northern Mexico and Arizona, and negative anomalies over the Pacific Northwest. The linkages between rainfall over the South China Sea and North America also exist in the interannual band (Lau and Weng, 2000), but the wavetrain there has a longer wave length than the wavetrain in the intraseasonal band (Figure 4.11b). During JJAS, the influence of the MJO on rainfall over the Southwest is not large. The dominant mode that influences rainfall active and break periods over the Southwest is a mode of 20–28 days (Mo, 2000a), which is near the range of PC 4. In the southern hemisphere, there is also a wavetrain extending from the Indian Ocean downstream to South America. Corresponding OLRAs show positive anomalies over central South America and negative anomalies to the south.

4.5 INTRASEASONAL MODULATION ON HURRICANES

Previous sections have emphasized IS variability on large and synoptic scales. Nevertheless, there are also impacts on severe weather events such as hurricanes. The following discussion documents this for North America since these violent storms are not observed over South America. In the Atlantic, hurricanes tend to occur during August–October when sea surface temperature anomalies (SSTAs) are warm (Gray, 1984; Landsea, 1993). Hurricanes are most likely to develop in the area extending from the west coast of Africa to the tropical Atlantic (5–20°N), which was identified by Goldberg and Shapiro (1996) as the main development region for Atlantic hurricanes. In the Eastern Pacific, the tropical storm/hurricane season starts in June over the region close to the west coast of Mexico (10–20°N) (Maloney and Hartmann, 2000a). The major factor that controls the development of hurricanes is vertical wind shear, with low values favoring hurricane formation (Goldberg and Shapiro, 1996).

In the interannual band, the occurrence of hurricanes or tropical storms in the Atlantic are modulated by ENSO (Gray, 1984), SSTAs in the Atlantic (Shapiro and Goldberg, 1998), and decadal SSTA trends in the Pacific. Enhanced convection related to warm SSTAs in the Central Pacific caused by a warm ENSO or by decadal warm trends in the 1990s generates high wind shear in the main development region of the Atlantic sector and below-normal hurricane occurrence. The situation reverses for cold SSTAs.

While the MJO does not influence the total number of tropical storms and hurricanes in the Atlantic or Eastern Pacific, it does influence the periods when storms are most likely to occur. The positive phase of EOF 1 (Figue 4.10a), with suppressed convection in the central tropical Pacific and enhanced convection over the Indian Ocean, favors more tropical storms in the Atlantic (Mo, 2000b) similar to the influence of cold ENSO events. The atmospheric response to this convection pattern is suppressed vertical wind shear in the Atlantic. Maloney and Hartmann (2000a, b) examine the impact of the MJO on tropical storms in the eastern North Pacific and the Gulf of Mexico. They find that the occurrence of hurricanes and tropical storms is regulated by MJO-related convection over the Eastern Pacific.

MJO modulation of tropical storm occurrence is not limited to the Eastern

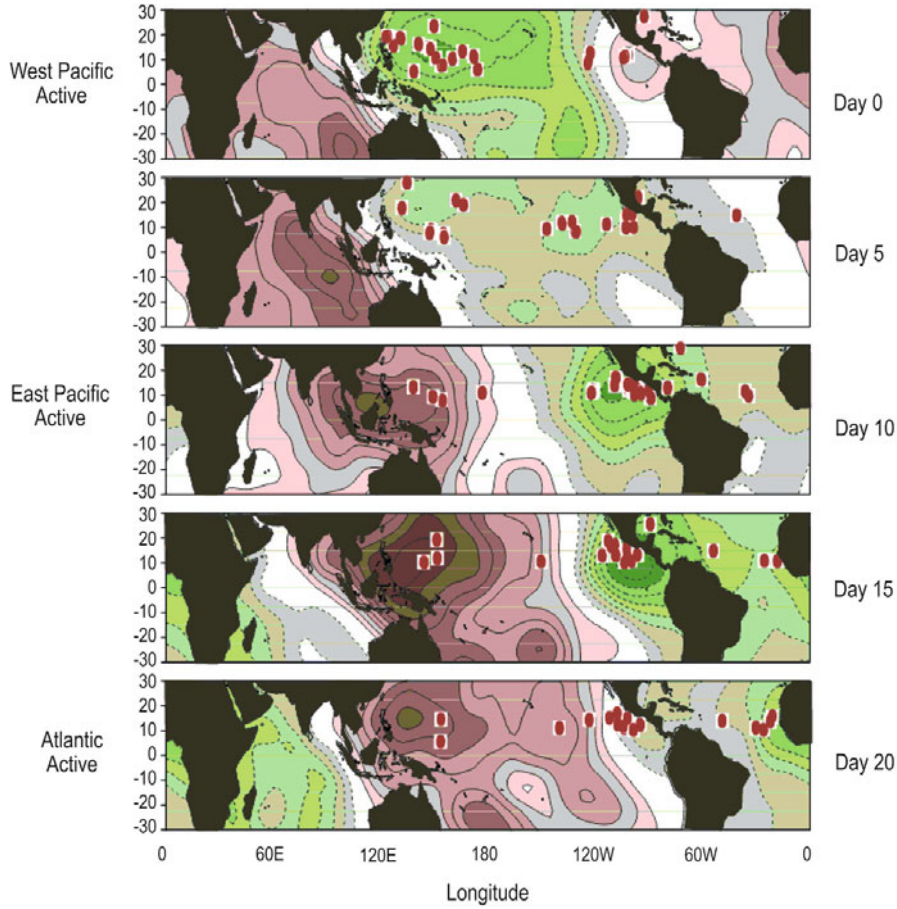

Figure 4.14. Composite evolution of 200 hPa velocity potential anomalies together with points of origin of tropical cyclones that developed into hurricanes/typhoons (open circles) for the 35-day period from day −15 to day +15. Composites are based on 21 events. Hurricane track data for JAS 1979–1997 were used. The contour interval is 0.5×10^6 m^2 s^{-1}. Negative contours are dashed and zero contours are omitted (from Higgins and Shi, 2001). *Note*: "O" indicates points of origin of tropical cyclones that become hurricanes or typhoons.

Pacific and the Atlantic. Higgins and Shi (2001) examine the points of origin of tropical cyclones that developed into hurricanes/tropical storms in the Western Pacific, the Eastern Pacific, and the Atlantic (Figure 4.14). They composite the numbers of tropical storms originated at any given location according to the phases of the MJO, as indicated by the 200 hPa velocity potential from July through September. Strong tropical storms (open circles) are more likely to develop in regions where the MJO favors enhanced convection. As the MJO moves eastward, the favored region of storm development also moves eastward from the Western Pacific to the Eastern Pacific and into the Atlantic Basin.

Recently, Aiyyer and Molinari (2008) showed that the MJO modulated the frequency and location of tropical cyclogenesis over the Eastern Pacific and the Gulf of Mexico during August–September 1998. When convective activity during the MJO lifecycle was suppressed, convection and low-level cyclonic vorticity were forced by the ITCZ. In contrast, during the convective phase of the MJO, low-level cyclonic vorticity and convergence expanded into the northeastern Pacific and Gulf of Mexico. This process was associated with enhanced eddy kinetic energy and barotropic energy conversions. In addition, idealized numerical experiments indicated that, during the convective phase of the MJO, stronger southerlies steer easterly waves into the Gulf of Mexico.

The influence of the MJO in modulating the genesis, intensification, and landfall patterns of tropical cyclones and hurricanes in the North Atlantic and Eastern Pacific have been demonstrated in more comprehensive climatological studies (Barret and Leslie, 2009; Camargo *et al.*, 2009; Klotzbach, 2010). In this regard, since the MJO is potentially predictable up to about 20–30 days into the future (see Chapter 12 on MJO predictability), some exciting new perspectives exist to improve forecasts of high-impact weather such as tropical cyclones and hurricanes. Vitart (2009) uses 46-day hindcasts from the European Centre for Medium-Range Weather Forecast (ECMWF) system to show that the MJO has a significant impact on the statistics of tropical storms generated by a dynamical model. Furthermore, this study indicates that the risk of landfall over Australia and North America varies significantly with phases of the MJO.

4.6 SUMMARY

Convection associated with the TISO is an important source of circulation and precipitation variability in the vicinity of the region of maximum variability on intraseasonal timescales (see Chapters 2, 3, and 5). It also has an effect on the Pan American region. This chapter shows linkages to the Pan American region that are established by wavetrains to both North and South America (Mo and Nogués-Paegle, 2001). The geomorphology of these two continents is quite different. The North American landmass lies mostly in the midlatitudes, while South America is a tropical continent. Though both continents have extensive meridionally oriented mountain ranges, the Rockies gently slope towards the east, while the Andes abruptly decrease from a high-level plateau with average heights of 4,000 m down to sea level in a few hundred kilometers. In spite of these differences there are remarkable similarities in the circulation and rainfall response over Pan America and its vicinity. Pacific North American and Pacific South American patterns act as guides to modulate weather anomalies over these continents in sync with variations in tropical convection. Over both the North and South Pacific, there is a center of marked response to the TISO in regions of frequent atmospheric blocking. OLRAs over the two continents exhibit dipole structures and the impact of the TISO is stronger in the winter hemisphere. Over South America, this is apparent

in modulation of the SACZ and establishment of a rainfall dipole between the SACZ and the subtropical plains. Over North America, a rainfall dipole with centers at the Pacific Northwest and California is regulated by the TISO. The similarity of the response on intraseasonal and interannual timescales is also of interest. This is evident not only in modulations of the dipole patterns of convection, but also in the generation and development of hurricanes.

Identification of the sources of variability in the two continents is of great social and economic significance. Both continents possess fertile subtropical plains (the Great Plains of North America and the Pampas of South America) where agriculture and hydroelectric energy generation depend highly on the weather. There are also some important waterways in these plains: the Mississippi and La Plata river basins and their tributaries are used to transport goods downstream. The Amazon Basin is a treasure trove of natural resources, with pristine botanical and zoological marvels. This has given impetus to efforts to better understand and measure the processes responsible for major weather anomalies that result in extended periods of floods and droughts. The expectation is that this will result in improved predictions and, as a consequence, a positive impact on regional economies. Nogués-Paegle *et al.* (1998) find that errors that develop early in the forecast during suppressed convection in the SACZ are smaller than when convection is enhanced. Since SACZ events last from 5 to 10 days, they are influenced by both the MJO and the submonthly mode. Jones and Schemm (2000) extend their results to examine 50-day forecasts for 5 years. They confirm that forecast skill depends on TISO regimes. The model has relatively high reliability during a strong SACZ dominated by the MJO. However, reliability is low if the SACZ is dominated by the submonthly mode.

There are several national and international initiatives aimed at improving long-term predictability. In the operational environment, for instance, the U.S. Climate Prediction Center routinely monitors MJO development and uses statistical and dynamical model forecasts for hazard assessment (Gottschalck *et al.*, 2010). In addition, international efforts have been organized under the aegis of the CLIVAR/VAMOS (Variability of the American Monsoon Systems) panel to address a number of issues related to improved prediction of summer rainfall. In the U.S.A., the USCLIVAR/PANAM (Pan American) panel has parallel objectives with a focus on North America. Two important field experiments, NAME (North American Monsoon Experiment) and SALLJEX (South American Low Level Jet Experiment), have compiled unique datasets that help understand, among other goals, moisture fluxes that fuel massive convective systems over the continents. These experiments have also contributed to answering questions relevant to the global water cycle, to quantify the variability of the water cycle and to assess the degree to which it is predictable. SALLJEX was a 3-month experiment (November 15, 2002–February 15, 2003) and included a marked ISO that appears to have had a positive impact on 2-week prediction by global models over South America. Unique datasets collected during these experiments offer a scientific challenge to translate observational improvements into consistent predictability gains by numerical model improvements. Such gains will be realized when models are capable of correctly simulating diurnal cycles, the formation and development of tropical convection

through better parameterizations, and the intraseasonal variability observed in nature.

4.7 REFERENCES

Aiyyer, A. and J. Molinari (2008) MJO and tropical cyclogenesis in the Gulf of Mexico and Eastern Pacific: Case study and idealized numerical modeling. *J. Atmos. Sci.*, **65**, 2691–2704.

Barlow, M. and D. Salstein (2006) Summertime influence of the Madden-Julian Oscillation on daily rainfall over Mexico and Central America. *Geophys. Res. Lett.*, **33**, L21708, doi: 10.1029/2006GL027738.

Barret, B. S. and L. M. Leslie (2009) Links between tropical cyclone activity and Madden–Julian Oscillation phase in the North Atlantic and Northeast Pacific Basins. *Mon. Wea. Rev.*, **137**, 727–744.

Bond, N. A. and G. A. Vecchi (2003) The influence of the Madden-Julian oscillation on precipitation in Oregon and Washington. *Weather and Forecasting*, **18**, 600–613.

Branstator, G. (1987) A striking example of the atmosphere leading traveling pattern. *J. Atmos. Sci.*, **44**, 2310–2323.

Camargo, S. J., M. C. Wheeler, and A. H. Sobel (2009) Diagnosis of MJO modulation of tropical cyclogenesis using an empirical index. *J. Atmos. Sci.*, **66**, 3061–3074.

Carvalho, L. M. V., C. Jones, and B. Liebmann (2002) Extreme precipitation events in southeastern South America and large-scale convective patterns in the South Atlantic Convergence Zone. *J. Climate*, **15**, 2377–2394.

Carvalho, L. M. V., C. Jones, and B. Liebmann (2004) The South Atlantic Convergence Zone: Intensity, form, persistence and relationships with intraseasonal to interannual activity and extreme rainfall. *J. Climate*, **17**, 88–108.

Carvalho, L. M. V., A. E. Silva, C. Jones, B. Liebmann, and H. Rocha (2010) Moisture transport and intraseasonal variability in the South America monsoon system. *Climate Dynamics*, doi: 10.1007/s00382-00010-00806-00382.

Chen, T. C. and J. M. Chen (1993) The 10–20 day mode of the 1979 Indian monsoon: Its relation with the time variation of monsoon rainfall. *Mon. Wea. Rev.*, **121**, 2465–2482.

Fukutomi, Y. and T. Yasunari (1999) 10–25 day intraseasonal variations of convection and circulation over east Asia and western north Pacific during early summer. *J. Meteorol. Soc. Japan*, **77**, 753–769.

Gadgil, S. (1983) Recent advances in monsoon research with particular reference to the Indian monsoon. *Australian Meteorol. Mag.*, **36**, 193–204.

Goldberg, S. B. and L. J. Shapiro (1996) Physical mechanisms for the association of El Niño and West African rainfall with Atlantic major hurricane activity. *J. Climate*, **9**, 1169–1187.

Gottschalck, J., M. Wheeler, K. Weickmann, F. Vitart, N. Savage, H. Lin, H. Hendon, D. Waliser, K. Sperber, M. Nakagawa *et al.* (2010) A framework for assessing operational Madden–Julian Oscillation forecasts: A Clivar MJO Working Group project. *Bull. Amer. Meteorol. Society*, **91**, 1247–1258.

Gray, W. M. (1984) Atlantic seasonal hurricane frequency, Part I: El Niño and 30 mb quasi biennial oscillation influences. *Mon. Wea. Rev.*, **112**, 1649–1668.

Higgins, R. W. and K. C. Mo (1997) Persistent North Pacific circulation anomalies and the tropical intraseasonal oscillation. *J. Climate*, **10**, 223–244.

Higgins, R. W. and W. Shi (2001) Intercomparison of the principal modes of intraseasonal and interannual variability of the North American monsoon system. *J. Climate*, **14**, 403–417.

Higgins, R. W., J. K. E. Schemm, W. Shi, and A. Leetmaa (2000) Extreme precipitation events in the western United States related to tropical forcing. *J. Climate*, **13**, 793–820.

Horel, J. D. and M. J. Wallace (1981) Planetary scale atmospheric phenomena associated with the Southern Oscillation. *Mon. Wea. Rev.*, **109**, 813–929.

Jones, C. (2000) Occurrence of extreme precipitation events in California and relationships with the Madden–Julian oscillation. *J. Climate*, **13**, 3576–3587.

Jones, C. and J. K. E. Schemm (2000) The influence of intraseasonal variations on medium to extended range weather forecasts over South America. *Mon. Wea. Rev.*, **128**, 486–494.

Jones, C., L. M. V. Carvalho, R. W. Higgins, D. E. Waliser, and J. K. E. Schemm (2004a) Climatology of tropical intraseasonal convective anomalies: 1979–2002. *J. Climate*, **17**, 523–539.

Jones, C., D. E. Waliser, K. M. Lau, and W. Stern (2004b) Global occurrences of extreme precipitation and the Madden–Julian oscillation: Observations and predictability. *J. Climate*, **17**, 4575–4589.

Kalnay E., M. Kanamitsu, R. Kistler, W. Collins, D. Deaven, L. Candin, M. Iredell, S. Saha, G. White, J. Woollen *et al.* (1996) The NMC/NCAR CDAS/Reanalysis Project. *Bull. Amer. Meteorol. Society*, **77**, 437–471.

Kiladis, G. N. and K. C. Mo (1998) Interannual and intraseasonal variability in the Southern Hemisphere. In: D. Karoly and D. G. Vincent (Eds.), *Meteorology of the Southern Hemisphere*. American Meteorological Society, Boston, Chapter 8, pp. 307–335.

Kiladis, G. N. and K. M. Weickmann (1992a) Circulation anomalies associated with tropical convection during northern winter. *Mon. Wea. Rev.*, **120**, 1900–1923.

Kiladis, G. N. and K. M. Weickmann (1992b) Extratropical forcing of tropical Pacific convection during northern winter. *Mon. Wea. Rev.*, **120**, 1924–1938.

Klotzbach, P. (2010) On the MJO–Atlantic hurricane relationship. *J. Climate*, **23**, 282–293.

Knutson, T. R. and K. M. Weickmann (1987) 30–60 day atmospheric oscillations: Composite life cycles of convection and circulation anomalies. *Mon. Wea. Rev.*, **115**, 1407–1436.

Kodama, Y.-M. (1992) Large scale common features of subtropical precipitation zones (the Baiu frontal zone, the SPCZ and the SACZ), Part I: Characteristics of subtropical frontal zones. *J. Meteorol. Soc. Japan*, **70**, 813–835.

Kodama, Y.-M. (1993) Large scale common features of subtropical precipitation zones (the Baiu frontal zone, the SPCZ and the SACZ), Part II: Conditions of the circulations for generating the STCZs. *J. Meteorol. Soc. Japan*, **71**, 581–610.

Kousky, V. (1985a) Atmospheric circulation changes associated with rainfall anomalies over tropical Brazil. *Mon. Wea. Rev.*, **113**, 1951–1957.

Kousky, V. (1985b) Frontal influences on Northeast Brazil. *Mon. Wea. Rev.*, **107**, 1140–1153.

Krishnamurti, T. N. and P. Andanuy (1980) The 10–20 day westward propagating mode and breaks in the monsoon. *Tellus*, **32**, 15–26.

Krishnamurti, T. N. and H. Bhalme (1976) Oscillations of a monsoon system, Part 1: Observational aspects. *J. Atmos. Sci.*, **33**, 1937–1954.

Krishnamurti, T. N, P. K. Jayaakaumar, J. Sheng, N. Surgi, and A. Kumar (1985) Divergent circulation on the 30–50 day time scale. *J. Atmos. Sci.*, **42**, 364–375.

Landsea, C. W. (1993) A climatology of intense (major) Atlantic hurricanes. *Mon. Wea. Rev.*, **121**, 1703–1713.

Lau, K. M. and P. H. Chan (1985) Aspects of the 40–50 day oscillations during the northern winter as inferred from outgoing longwave radiation. *Mon. Wea. Rev.*, **113**, 1889–1909.

Lau, K. M. and P. H. Chan (1986) Aspects of the 40–50 day oscillation during the northern summer as inferred from outgoing longwave radiation. *Mon. Wea. Rev.*, **114**, 1345–1367.

Lau, K. M. and H. Weng (2000) Recurrent teleconnection patterns linking summer time precipitation variability over East Asia and North America. *J. Meteorol. Soc. Japan*, **80**, 1309–1324.

Liebmann, B. and D. L. Hartmann (1984) An observational study of tropical–midlatitude interaction on intraseasonal time scales during winter. *J. Atmos. Sci.*, **41**, 3333–3350.

Liebmann, B. and C. A. Smith (1996) Description of a complete (interpolated) outgoing longwave radiation dataset. *Bull. Amer. Meteorol. Society*, **77**, 1275–1277.

Liebmann, B., G. N. Kiladis, J. A. Marengo, T. Ambrizzi, and J. D. Glick (1999) Submonthly convective variability over South America and the South Atlantic convergence zone. *J. Climate*, **12**, 1877–1891.

Liebmann, B., G. N. Kiladis, C. S. Vera, A. C. Saulo, and L. M. V. Carvalho (2004) Subseasonal variations of rainfall in South America in the vicinity of the low-level jet east of the Andes and comparison to those in the South Atlantic convergence zone. *J. Climate*, **17**, 3829–3842.

Lorenz, D. J. and D. L. Hartmann (2006) The effect of the MJO on the North American monsoon. *J. Climate*, **19**, 333–343.

Maloney, E. D. and D. L. Hartmann (2000a) Modulation of eastern North Pacific hurricanes by the Madden Julian oscillations. *J. Climate*, **13**, 1451–1460.

Maloney, E. D. and D. L. Hartmann (2000b) Modulation of hurricane activity in the Gulf of Mexico by the Madden Julian Oscillation. *Science*, **287**, 2002–2004.

Mo, K. C. (1999) Alternating wet and dry episodes over California and intraseasonal oscillations. *Mon. Wea. Rev.*, **127**, 2759–2776.

Mo, K. C. (2000a) Intraseasonal modulation of summer precipitation over North America. *Mon. Wea. Rev.*, **128**, 1490–1505.

Mo, K. C. (2000b) The association between intraseasonal oscillations and tropical storms in the Atlantic basin. *Mon. Wea. Rev.*, **128**, 4097–4107.

Mo, K. C. and R. W. Higgins (1998a) Tropical convection and precipitation regimes in the western United States. *J. Climate*, **11**, 2404–2423.

Mo, K. C. and R. W. Higgins (1998b) Tropical influences on California precipitation. *J. Climate*, **11**, 412–430.

Mo, K. C. and R. W. Higgins (1998c) The Pacific South American modes and tropical convection during the Southern Hemisphere winter. *Mon. Wea. Rev.*, **126**, 1581–1596.

Mo, K. C. and J. Nogués-Paegle (2001) The Pacific South American modes and their downstream effects. *Int. J. Climatol.*, **21**, 1211–1229.

North, G. R., T. L. Bell, R. F. Cahalan, and F. J. Moeng (1982) Sampling errors in the estimation of empirical orthogonal functions. *Mon. Wea. Rev.*, **110**, 699–702.

Nogués-Paegle, J. and K. C. Mo (1987) Spring-to-summer transitions of global circulations during May–July 1979. *Mon. Wea. Rev.*, **115**, 2088–2102.

Nogués-Paegle, J. and K. C. Mo (1997) Alternating wet and dry conditions over South America during summer. *Mon. Wea. Rev.*, **125**, 279–291.

Nogués-Paegle, J., B.-C. Lee, and V. Kousky (1989) Observed modal characteristics of the intraseasonal oscillation. *J. Climate*, **2**, 496–507.

Nogués-Paegle, J., K. C. Mo, and J. Paegle (1998) Predictability of the NCEP–NCAR reanalysis model during austral summer. *Mon. Wea. Rev.*, **126**, 3135–3152.

Nogués-Paegle, J., A. Byerle, and K. C. Mo (2000) Intraseasonal modulation of South American summer precipitation. *Mon. Wea. Rev.*, **128**, 837–850.

Papoulis, A. (1973) Minimum bias windows for high resolution spectral estimates. *IEEE Trans. Infor. Theory*, **19**, 9–12.

Roplewski, C. F. and H. S. Halpert (1987) Global and regional precipitation patterns associated with the El Niño/Southern Oscillation. *Mon. Wea. Rev.*, **115**, 1606–1626.

Roplewski, C. F. and H. S. Halpert (1989) Precipitation patterns associated with the high index phase of the Southern Oscillation. *J. Climate*, **2**, 268–284.

Shapiro, L. J. and S. B. Goldberg (1998) Atlantic sea surface temperatures and tropical cyclone formation. *J. Climate*, **11**, 578–590.

Vautard, R. and M. Ghil (1989) Singular spectrum analysis in non linear dynamics with applications to paleoclimatic time series. *Physica D*, **35**, 392–424.

Vitart, F. (2009) Impact of the Madden Julian Oscillation on tropical storms and risk of landfall in the ECMWF forecast system. *Geophys. Res. Lett.*, **36**, L15802, doi: 10.1029/2009GL039089.

Wallace, J. M. and D. S. Gutzler (1981) Teleconnections in the geopotential height field during the Northern Hemisphere winter. *Mon. Wea. Rev.*, **109**, 784–812.

Waliser, D. E., N. E. Graham, and C. Gautier (1993) Comparison of the high reflective cloud and outgoing longwave radiation data sets for use in estimating tropical deep convection. *J. Climate*, **6**, 331–353.

Weickmann, K. M. (1983) Intraseasonal circulation and outgoing longwave radiation modes during Northern Hemisphere winter. *Mon. Wea. Rev.*, **111**, 1838–1858.

Weickmann, K. M., G. R. Lussky, and J. Kutzbach (1985) Intraseasonal circulation and outgoing longwave radiation modes during Northern Hemisphere winter. *Mon. Wea. Rev.*, **111**, 1838–1858.

Wu, M. L., S. Schubert, and N. E. Huang (1999) The development of the South Asian summer monsoon and intraseasonal oscillation. *J. Climate*, **12**, 2054–2075.

Xie, P. and P. A. Arkin (1997) Global precipitation: A 17-year monthly analysis based on gauge observations, satellite estimates, and numerical model outputs. *Bull. Amer. Meteorol. Society*, **78**, 2539–2558.

Xie, P. P., J. E. Janowiak. P. A. Arkin, R. Alder, A. Gruber, R. Ferraro, G. J. Huffmann, and S. Curtis (2003) GPCP pentad precipitation analyses: An experimental data set based on gauge observations and satellite estimates. *J. Climate*, **16**, 2197–2214.

5

Australasian monsoon

M. C. Wheeler and J. L. McBride

5.1 INTRODUCTION

This chapter describes the intraseasonal climate and weather variability of the "Australasian monsoon" region comprising northern Australia, Indonesia, New Guinea, the surrounding seas, and the near equatorial southwest Pacific. This region has a marked seasonal cycle in winds and precipitation characteristic of a monsoon (e.g., Troup, 1961; McBride, 1987, 1998; Suppiah, 1992; Figure 5.1). At lower tropospheric levels, the mean winds shift from being easterly in austral winter, with correspondingly small rain totals, to westerly in summer, with much enhanced cumulonimbus convection and rainfall. This monsoonal character of the region has long been recognized; for both northern Australia and Indonesia, reference to this nature dates back at least as far as the early 19th century.[1]

Given these defining monsoon characteristics, there is understandably a large climatic influence on the biogeography (e.g., Bowman *et al*., 2009) and lifestyles and practices of the people of the area. In particular, the monsoon seasonal cycle has a governing influence on agriculture and, in times past, has had a large influence on navigation and trade. Such influences have undoubtedly played an important role for the highly populated islands of Indonesia (e.g., Java and Bali), making research on year-to-year variability of the monsoon obviously important. Consequently, there has been a long history of studies of interannual variability, with multiple examples

[1] For northern Australia, the climatologists of the early 20th century used the word monsoon to describe the climate of the region (e.g., Hunt *et al*., 1913). During the same period the term monsoon (or in Dutch, "moesson") was used by government meteorologists of the Netherlands Indies (modern day Indonesia) to describe the climate of southern hemisphere parts of Indonesia. For example, Braak (1919) described the region of the Malay Archipelago as "the most typical monsoon region of the world". The term was sufficiently entrenched that it appears in even earlier writings about the region such as in the journals of explorers Matthew Flinders (1814) and Alfred Russel Wallace (1891). Indeed, the Indonesian language provides no distinction between the words for "season" and "monsoon", for which they use the word "musim".

W. K. M. Lau and D. E. Waliser (Editors), *Intraseasonal Variability in the Atmosphere–Ocean Climate System* (Second Edition).

from both the colonial period (e.g., Berlage, 1927; de Boer, 1947) and the modern research era (e.g., Nicholls, 1981; Hastenrath, 1987; Naylor *et al.*, 2001; Lo *et al.*, 2007; Hendon *et al.*, 2011). Yet, as is the case for the other monsoon areas of the world, intraseasonal variability (ISV) is also prominent.

The accepted beginning of published research on ISV in the region is the seminal paper by Troup (1961). Troup, concentrating on the Australian component of the monsoon system, used the term "bursts" to describe spells of excessively wet or low-level westerly conditions occurring for periods shorter than the overall summer season. "Onset" was then naturally defined as being the beginning of the first westerly burst in each wet season. Such bursts, by definition, are the manifestation of subseasonal variability of the monsoon system, for which a very large variance component falls within the range we classify here as ISV. Since Troup's paper, many authors have referred to active (burst) and break events in the context of the Australian monsoon (e.g., Murakami and Sumi, 1982; McBride, 1983; Holland, 1986; Gunn *et al.*, 1989; Drosdowsky, 1996; McBride and Frank, 1999; Pope *et al.*, 2009), and the current operational definitions of onset and active vs. break periods follow the framework Troup developed.

Yet there have been other influences on the development of the region's research. Due partly to the utility of Darwin in northern Australia as a base for meteorological field experiments, the Australasian monsoon has received focused attention and review in the last few decades (e.g., McBride, 1987, 1998; Manton and McBride, 1992; Suppiah, 1992; Keenan *et al.*, 2000; Wheeler and McBride, 2005; May *et al.*, 2008). In parallel with this work, internationally there has been a recognition of the influence of variability on intraseasonal timescales in tropical weather and climate, and in particular on the role of the Madden Julian oscillation (MJO) as a large-scale control (e.g., Madden and Julian, 1971, 1994; Lau and Chan, 1985; Weickmann *et al.*, 1985; Knutson and Weickmann, 1987; Wang and Rui, 1990; Hendon and Salby, 1994). Consequently, a number of research papers have suggested an important role for the MJO in the Australasian monsoon (Hendon *et al.*, 1989; Hendon and Liebmann, 1990a, b; Wheeler and Hendon, 2004; Matthews and Li, 2005; Hidayat and Kizu, 2009). Yet other papers have seemingly implied very little or no MJO impact (e.g., Davidson *et al.*, 1983; Drosdowsky, 1996).

More recently there has been an increased recognition of other "modes" of ISV within the monsoon and equatorial regions, besides just the MJO. In particular, increasing attention is being paid to convectively coupled equatorial waves (Takayabu, 1994; Wheeler and Kiladis, 1999) as they have now been well observed to produce prominent perturbations in near equatorial monsoons (e.g., Wheeler *et al.*, 2000; Wheeler and Weickmann, 2001; Straub and Kiladis, 2002; Roundy and Frank, 2004; Kiladis *et al.*, 2009).

Within this context then, this chapter provides a review and synthesis of the topic of ISV within this monsoon region, drawing heavily on our previous review chapter (Wheeler and McBride, 2005) and concentrating on the extended southern hemisphere summer season (namely, approximately October–April). Included in the content of this chapter is a general description of the climatological seasonal cycle of the region, as it is this that forms the necessary background state about which ISV

appears (Section 5.2). ISV is usually defined as covering all timescales of variability beyond the synoptic limit (~10 days) to less than a season (~90 days), and we adopt this definition here. The earliest work concerning variability within this broad range in the Australasian monsoon region is discussed in Section 5.3. The frequency-only power and coherence spectra of standard monsoon variables are examined in Section 5.4. While the MJO is the only prominent spectral peak, the fact that much variance does exist in the intraseasonal band, much of which is highly coherent, is important to appreciate.

Irrespective of its source, the local manifestation of ISV of the monsoon is the bursts and breaks, the general meteorology of which is discussed in Section 5.5. Section 5.6 is then specifically devoted to the character and influence of the MJO. The discussion of the previous sections is then contrasted and compared with the evolution of two individual monsoon years, 1983/1984 and 1987/1988 (Section 5.7). Importantly, the fact that all years show at least some degree of burst or break activity (and hence have ISV), but not necessarily show strong MJO variability, is highlighted.

Section 5.8 then addresses the contrasting views that have been expressed on the importance of the role of the MJO, especially with regard to the timing of monsoon onset. We then discuss other sources and modes of ISV in the region (Section 5.9), the modulation of tropical cyclones in the region by ISV (Section 5.10), and intraseasonal extratropical–tropical interaction (Section 5.11). Finally, we provide some discussion of ISV prediction in Section 5.12, followed by conclusions in Section 5.13. In accordance with the areas that have received the most attention in recent years, the most significant additions to this review compared with Wheeler and McBride (2005) are: (a) a new section devoted to ISV prediction in the Australasian monsoon region; (b) increased discussion of the impact of the MJO through the islands of Indonesia and New Guinea; and (c) greater emphasis on the intraseasonal modulation of tropical cyclones.

5.2 SEASONAL CYCLE OF BACKGROUND FLOW

The focus in this chapter is on the tropical region south of the equator and within the longitude bounds of about 100°E–170°E. Included in the region are southern Sumatra, Java, Bali, Sulawesi, Flores, Timor, New Guinea, New Britain, and the Solomon islands, along with northern Australia. As has been presented in several papers (e.g., Troup, 1961; Meehl, 1987; Drosdowsky, 1996), the mean seasonal cycle of the region is characterized by a reversal in lower-tropospheric winds and a marked change in rainfall. An appreciation of such seasonal changes can be made with reference to the climatological monthly mean fields of Figure 5.1. Shown are 850 hPa level winds as representative of winds of the lower troposphere, and the satellite-observed outgoing longwave radiation (OLR) field as representative of the cold cloud tops of rain-producing deep-convective systems. Twenty-four years of data have been used.

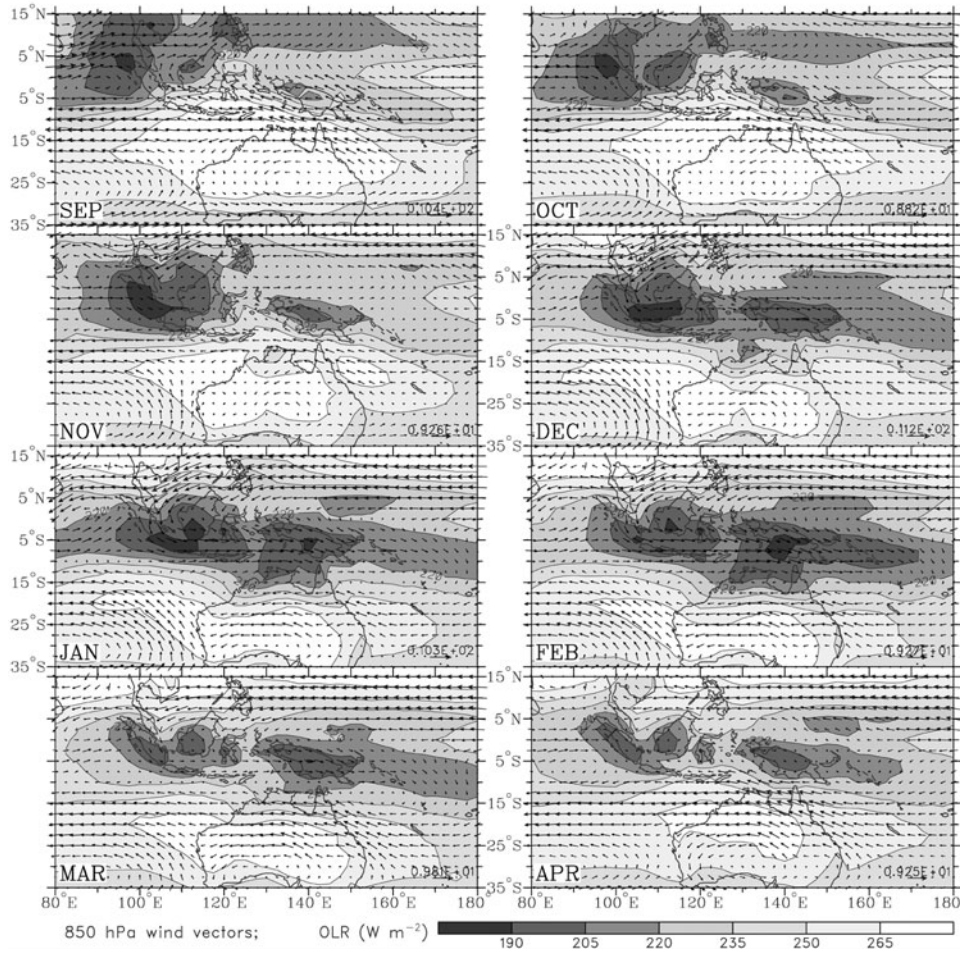

Figure 5.1. The seasonally evolving structure of the Australasian monsoon as revealed by the monthly climatology of NOAA satellite-observed outgoing longwave radiation (OLR) and NCEP/NCAR reanalysis 850 hPa level winds. All wind vectors are scaled the same, and the maximum vector for each panel is as displayed in the bottom right corner. Low values of OLR are indicative of cold cloud tops as produced by precipitationg cumulonimbus convection (based on data from 1979–2002).

In September, the prevailing mean 850 hPa winds across the region are southeasterly trade winds emanating from the subtropical ridge lying along about 25°S. The strength of these trade winds is between about $5\,m\,s^{-1}$ to $9\,m\,s^{-1}$. At this time of year, the strongest convective activity (as represented by OLR less than $220\,W\,m^{-2}$) is restricted to being mostly north of the equator, especially in the

northwest of the plotted domain. This convective activity is associated with the northern hemisphere summer (wet) monsoon still being active; and the line of convection (low OLR) along the northern boundary of the domain denotes the location of the Inter Tropical Convergence Zone (ITCZ). As the seasonal cycle progresses into the months of October and November, there is an overall decrease in the low-level easterlies together with a shift of the strongest convective activity southward and eastward. This is first marked by a buildup of convection over the large islands of Sumatra, Borneo, and New Guinea during October to November, coinciding with (wet) monsoon onset on those islands by some definitions (e.g., Tanaka, 1994). By December, convective activity has transformed into a continuous line across the region centered near 5°S and represents the ITCZ having shifted south of the equator.

As the ITCZ becomes established south of the equator in December, westerly winds appear between the equator and 10°S, while the trade winds retreat southwards over the Australian continent. At this time a small portion of strong convective activity ($\mathrm{OLR} < 220\,\mathrm{W\,m^{-2}}$) has reached the Australian continent at Darwin (12.5°S, 130.9°E), consistent also with the late December mean monsoon onset date there (Holland, 1986; Hendon and Liebmann, 1990a; Drosdowsky, 1996; Pope *et al.*, 2009). By January to February, the peak of southern hemisphere summer season tropical convective activity is reached. This peak occurs earlier in the west (e.g., Java) than the east (e.g., New Guinea). The defined region of interest is now mostly occupied by westerlies, with magnitudes up to $9\,\mathrm{m\,s^{-1}}$. At this stage the trade wind easterlies have also strengthened across the southern part of the plotted domain. Consequently, along about 10°S to 15°S there is a well-defined monsoon shear line marked by the line of strong cyclonic ($-\partial u/\partial y$) shear separating lower-latitude westerlies from higher-latitude easterlies (McBride and Keenan, 1982; McBride, 1995).

For much of the domain of interest, the overall character of the sequence from October through to February is thus a replacement of dry easterlies by convective westerlies. This seasonal character, as is the case for other monsoon regions, is thought mostly to occur due to the existence of land–sea thermal contrast, resulting in this case from the location of the off-equatorial Australian continent (e.g., Webster *et al.* 1998). As modeled by Yano and McBride (1998), however, there is also a forcing due to the seasonal excursion of the warmest sea surface temperatures south of the equator during the southern summer months. At the location of Darwin, the changes in rainfall are from a peak in the climatological mean of around $12\,\mathrm{mm\,day^{-1}}$ in February to less than $1\,\mathrm{mm\,day^{-1}}$ from June to September (Drosdowsky, 1996). Further seasonal changes that are known to occur are an increase in upper-level easterlies around Darwin during the summer months and a southward movement of the southern hemisphere subtropical jet (Troup, 1961). As will be discussed next, however, the appearance of any particular year can be quite different from this slowly evolving mean seasonal cycle.

5.3 BROADBAND INTRASEASONAL BEHAVIOR: BURSTS AND BREAKS

As stated in the introduction (Section 5.1), the accepted beginning of published research on ISV in the region is Troup (1961). In examining time series of daily mean winds and rainfall in the Darwin area, Troup demonstrated that each wet season consisted of a number of spells of heavy rains, or "bursts", each lasting on the order of a few days to a week or more. Similarly, the seasonal changes in winds in each year were the result of more frequently occurring and longer lasting wind spells, and not necessarily from the establishment of a steady regime. Heavy rain bursts tended to coincide with low-level westerly wind bursts and, in the 4 years Troup examined, there were between one and six bursts per summer season (namely, from December through March)—the in-between dry spells being called "breaks". The yearly "monsoon onset" he defined corresponded to the first such wet or westerly burst and, when viewed relative to these individual monsoon onset dates, the transition to active monsoon conditions took only a matter of days.

A very similar appreciation of the intraseasonal behavior of the region can be obtained from the multiple panels of Figure 5.2. The upper curve in each panel shows the satellite OLR field averaged over the indicated area encompassing a large section of the monsoon region. The lower curve shows rainfall averaged over a much smaller area in northern Australia. The only time smoothing that has been applied is a 3-day running mean.[2] Superimposed on the OLR curve is the climatological seasonal cycle (dashed curve) computed from the long-term mean and three harmonics, with shading to denote anomalies. Given that downward excursions of the OLR curve represent convectively active conditions, a reasonably close correspondence between large-scale convective conditions and smaller scale rainfall is apparent. Also apparent are the characteristic monsoon bursts, many appearing in both OLR and rainfall. For example, during the 1984/1985 monsoon season there are two notable bursts in OLR, both showing similarly timed peaks in rainfall. In 1987/1988, there are three notable bursts, also with matching peaks in rainfall. Much of the variance of these bursts can be identified as being that of ISV (i.e., having a timescale in the range of 10 to 90 days).

Given our identification of the bursts in Figure 5.2 as ISV, one important aspect of the region's ISV is revealed: its amplitude appears just as large or larger than that of the seasonal cycle. One way that this can be appreciated is through consideration of the absolute minimum OLR value reached in each year. By the seasonal cycle alone, this value is only $200\,\mathrm{W\,m^{-2}}$ but, due to the presence of ISV, it actually reaches minimum values below $180\,\mathrm{W\,m^{-2}}$ and usually below $160\,\mathrm{W\,m^{-2}}$; this can occur at any time between December and the end of March. Conversely, in at least half of the years, mid-summer monsoon breaks are strong enough to fully negate the effects of the seasonal cycle (in OLR), causing conditions equivalent to the dry season. The break of late February/early March 1988 is a good example.

[2] A 3-day running mean effectively serves as a lowpass filter with a half-power point near a period of 6 days and passing 90% power at a period of 9 days.

Within the framework of "burst" definition by Troup (1961), there also came a natural definition of the "onset" of the monsoon as being the first such burst of each wet season. Following this methodology, a number of authors have developed objective definitions of onset for the Australian portion of the monsoon system, as also presented in Figure 5.2. Hendon and Liebmann (1990a) based their definition on the simultaneous satisfaction of two criteria: that the lowpass-filtered (1–2–3–2–1) daily time series of 850 hPa wind at Darwin become positive (westerly) and that the average rainfall rate for Australian stations equatorward of 15°S exceed 7.5 mm per day. Thus, their definition was based on the concept of the first occurrence of "wet westerlies". Hung and Yanai (2004) have a similar definition based on 850 hPa zonal wind over the region 2°S–15°S, 115°E–150°E, and simultaneous satisfaction of a criterion that OLR over the same box be less than a threshold value. Drosdowsky's (1996) definition, on the other hand, is based purely on zonal winds at Darwin, requiring the mean lower tropospheric (surface to 500 hPa) wind to be westerly, with an additional requirement being that the upper-tropospheric (300–100 hPa) wind be easterly. Obviously, each definition is subtly different but, for the sake of the current discussion, we have simply taken all their dates of onset and indicated them on Figure 5.2 with arrows. The main point portrayed is that for each of the years shown—as we have also confirmed is generally the case for all years—all the defined onset dates coincide with a large-scale OLR-measured intraseasonal burst. Further, as intraseasonal bursts have no apparent phase locking to the seasonal cycle, their timing plays a role in interranual variation in defined monsoon onsets. For example, in the 6 years shown, the onset dates vary anywhere from early December to mid January.

As seen in Figure 5.2, a consequence of strong ISV within the monsoon is that the changes occurring at the time of each year's monsoon onset are much more rapid than those implied by the mean seasonal cycle alone. A natural extension of defining monsoon onset is thus to view circulation changes with respect to that onset date, and not just with respect to the seasonal cycle. Each of the studies of Hendon and Liebmann (1990a), Drosdowsky (1996), and Hung and Yanai (2004) employed such a view. An example, as adapted from Drosdowsky (1996), is seen in the time–height cross-section of zonal winds at Darwin in Figure 5.3. The first panel shows the 35-year mean composite of the seasonal cycle, while the second shows a 30-day time slice of the wind data when composited with respect to the onset dates. The second panel is thus an average view of the first intraseasonal burst of the wet season. In the seasonal cycle plot, wet-season low-level westerlies do not exceed a value of $2\,\mathrm{m\,s^{-1}}$ at heights greater than 800 hPa. In the plot depicting onset burst, however, westerlies of a magnitude of $2\,\mathrm{m\,s^{-1}}$ reach as high as 400 hPa. Thus, not only is the transition to westerlies much more rapid when viewed with respect to the first intraseasonal burst, but their vertical extent into the troposphere is greater and considerably unlike that seen even at the peak of the seasonal cycle. It is this deep westerly view of the active monsoon that seems the most applicable at any instant during any individual monsoon burst (and not just the first one of the season). Indeed, the collective experience gained from forecasters in Darwin (Drosdowsky having been one) and that gained from a number of field experiments (e.g., Gunn *et*

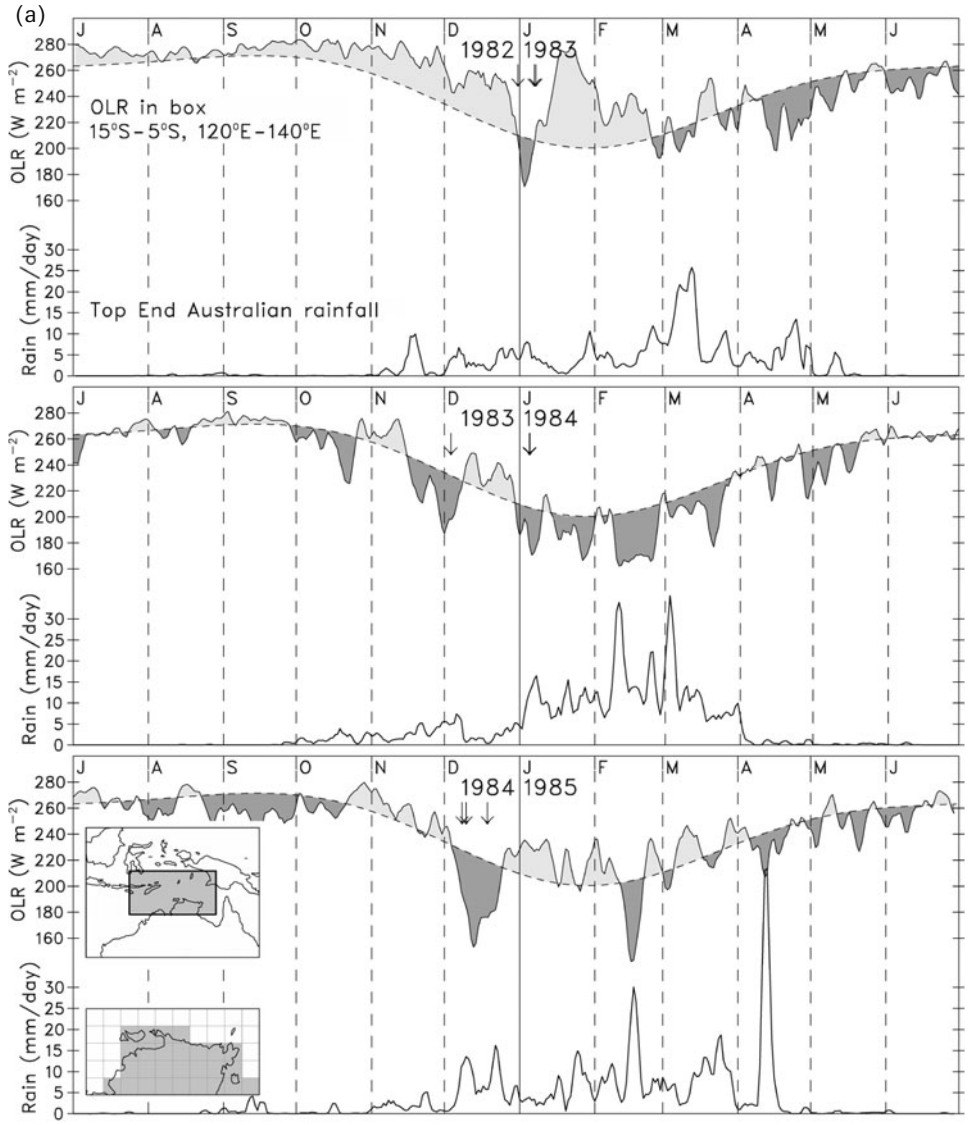

Figure 5.2. Intrinsic intraseasonal structure of the monsoon as revealed by a 3-day running mean time series of NOAA satellite-observed OLR, averaged for the box 15°S to 5°S and 120°E to 140°E, and Australian Top End rainfall, averaged for all available Australian Northern Territory stations north of 15°S for (a) 1982/1983, 1983/1984, and 1984/1985 and (b) 1985/1986, 1986/1987, and 1987/1988. Dashed line (for OLR) shows the climatological

al., 1989), substantiates the view of an active monsoon as being characterized by deep westerlies near Darwin.

From the combination of observations discussed above then, we are left with a somewhat different perspective on the region's monsoon system than that obtained

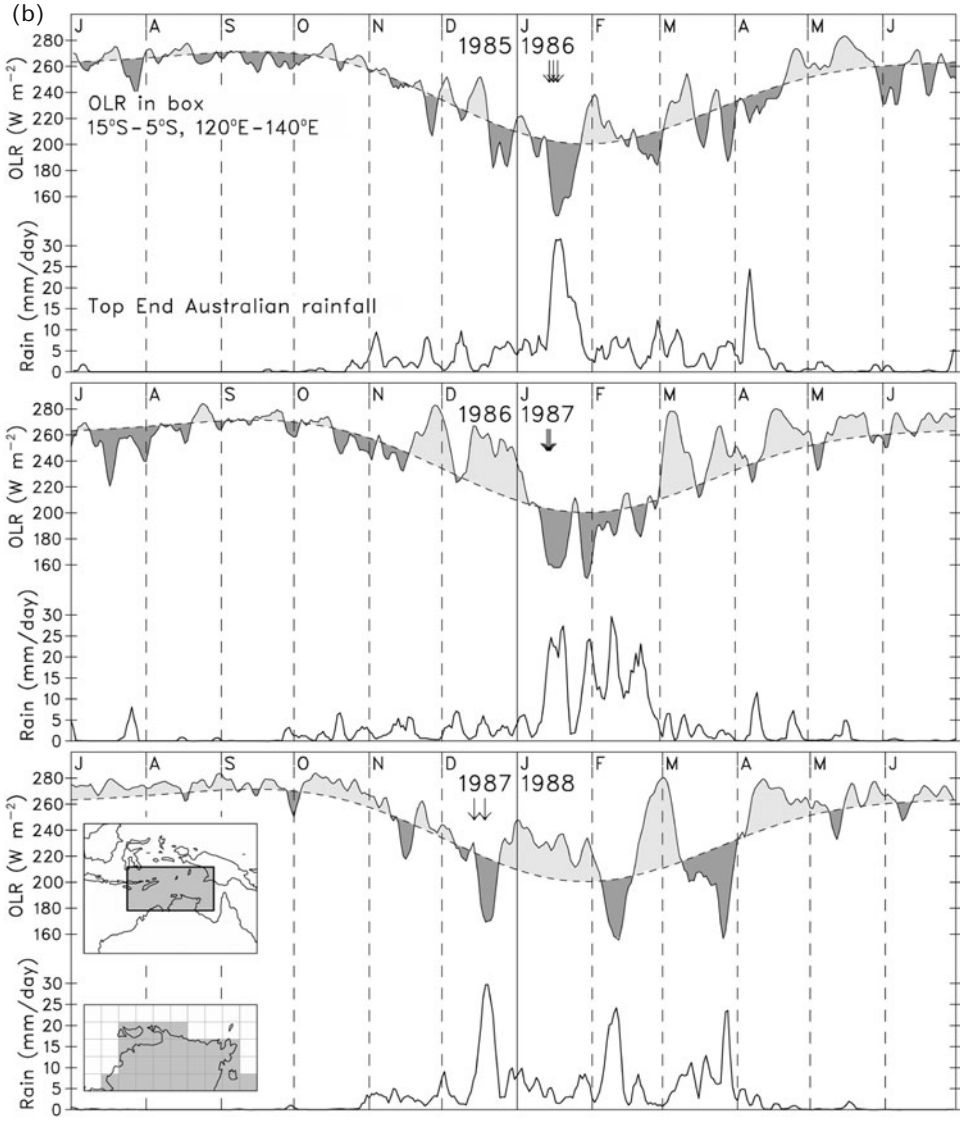

seasonal cycle created by taking the mean and the first three harmonics of 1979 to 2001 climatology. Dark/light shading (for OLR) are indicative of times of anomalously active/inactive convection. Also shown (arrows above the OLR curve) are monsoon onset dates as defined by Hendon and Liebmann (1990a), Drosdowsky (1996), and Hung and Yanai (2004). Key maps for the areas used for OLR and rainfall are shown at the bottom left.

from the previous section. Instead of being wholly a consequence of the seasonal cycle, the Australasian monsoon system has been shown to have a broad range of ISV as an intrinsic component. Many aspects of the monsoon that we take for granted (e.g., the bursts of deep westerlies) would appear not to occur without the

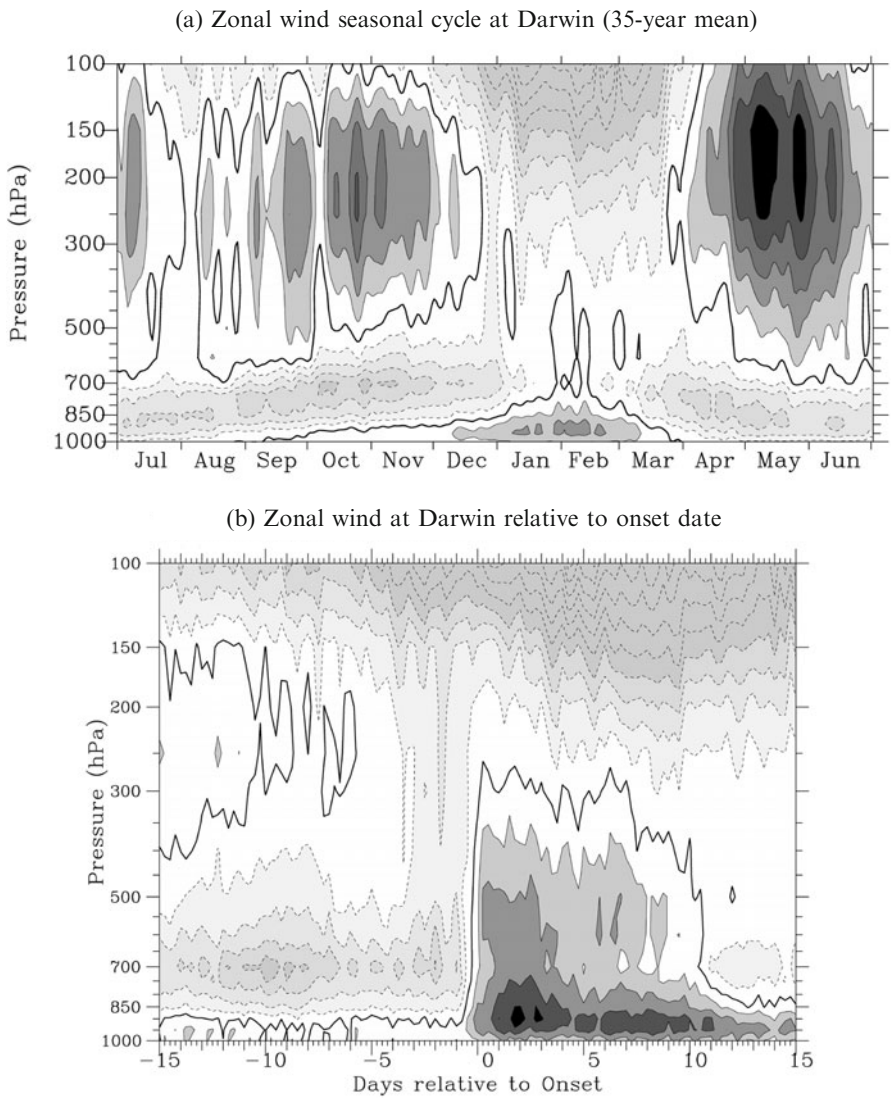

Figure 5.3. Time–height sections of station zonal wind at Darwin when composited for (a) the 35-year mean seasonal cycle (July 1957 to June 1992) and (b) relative to the 35 annual onset dates of Drosdowsky (1996). The contour interval is $2\,\mathrm{m\,s^{-1}}$, the zero contour is a heavy solid line, and negative (easterly) contours are dashed (adapted from Drosdowsky, 1996).

presence of ISV. This view that ISV is an intrinsic component of the monsoon was the basis of the theoretical model of Yano and McBride (1998) and is also a recurring theme in the work of Peter Webster and collaborators on the northern summer (India and Indochina) monsoon system (e.g., Webster *et al.*, 1998; Lawrence and Webster, 2002; Hoyos and Webster, 2007).

5.4 BROADBAND INTRASEASONAL BEHAVIOR: SPECTRAL ANALYSIS

For increased understanding of ISV, it is of interest to know the range of timescales that are covered and if there is a particular timescale that dominates. This knowledge can be obtained through spectral analysis techniques. Among the most enlightening use of such techniques has been that of Lau and Chan (1988), Hendon and Liebmann (1990a), and Drosdowsky (1996). Lau and Chan showed that the Australasian monsoon region is close to being at the global maximum of intraseasonal OLR variance during austral summer, confirming the impression given above of the occurrence of considerable ISV in this region. By comparison, the region is neither at the global maximum for variance in interannual nor 1 to 5-day bands. They further showed in spectra that the region's ISV is particularly enhanced in the 30 to 60-day band, as indicated by a rather broad spectral peak in the OLR. Hendon and Liebmann (1990a) showed a similar spectral peak in Darwin 850 hPa zonal wind, although they did not find any significant peaks in the spectrum of north Australian rainfall.

Confirmation of some of these results is provided in Figure 5.4 through the use of power spectra computed for OLR and rainfall data averaged over the same regions as used in Figure 5.2. These spectra have been computed in the same manner as Hendon and Liebmann (1990a). Starting from anomaly data (smoothed seasonal cycle removed) spectra were calculated for 212-day segments of length starting on October 1 each year. As such, the spectra represent subseasonal variability acting during the months of October through April in all available years. Twenty-seven years/segments are used for the OLR data (Figure 5.4a) and 49 for the rainfall (Figure 5.4b). Each segment was padded with zeroes to 256 days, giving a bandwidth of 1/256 cpd. The resulting spectral power from each year was then averaged, providing multiple degrees of freedom (d.o.f.) for each spectral estimate (up to 54 d.o.f. for the OLR spectrum and 98 d.o.f. for the rainfall spectrum). The displayed "AR1 noise" reference spectra are computed by performing the same procedure on a very long (20,000-year) time series generated from a first-order autoregressive model with the same lag 1 autocorrelation as the segmented data. The 99% confidence curves are based on this noise spectrum and the chi-squared distribution. The spectrum of OLR closely follows the AR1 noise curve at higher intraseasonal frequencies (0.04 to 0.12 cpd), has a broad spectral peak in the 30 to 80-day range (which exceeds the computed 99% significance around 45 days), and then has a sharp reduction in power for longer periods. The spectrum of rainfall, on the other hand, shows no statistically significant spectral peaks.

Why a broad 30 to 80-day spectral peak exists for the multiyear OLR dataset but not for the rainfall is difficult to understand. It appears to be not just a question of scale: the spectrum of a smaller area average of OLR still shows a statistically significant spectral peak around 40 days (not shown). It is perhaps related to the greater degree of noise inherent in the rainfall field (e.g., see Figure 5.2). Despite their different-shaped spectra, OLR and rainfall still show a close correspondence when viewing their individual time series, as evidenced in Figure 5.2, and this

(a) Spectrum of OLR in 15°S–5°S, 120°E–140°E

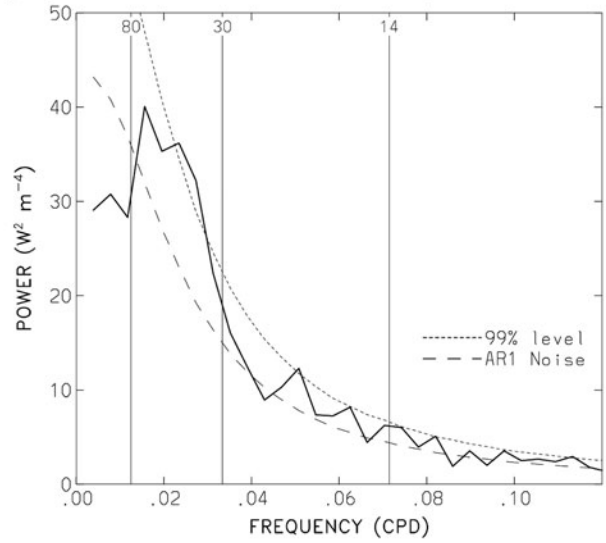

(b) Spectrum of Top End rainfall, 1950–1999

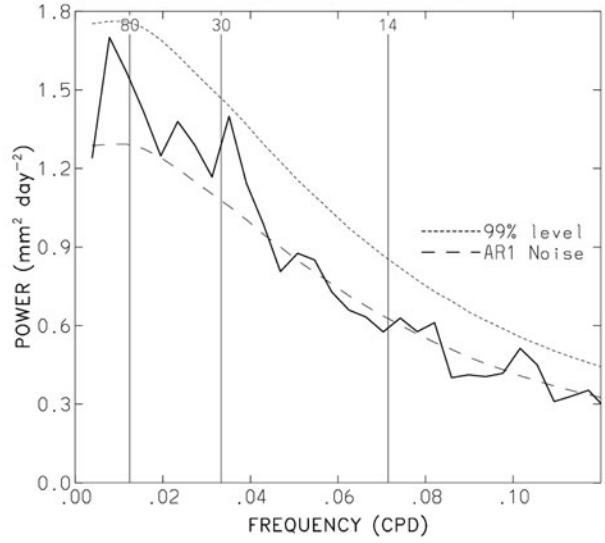

Figure 5.4. (a) Power spectrum of daily OLR anomalies averaged for the box 15°S to 5°S and 120°E to 140°E, using October to April data for all available seasons from 1974 to 2003. The bandwidth is 1/256 cpd, and the reference frequencies corresponding to periods of 80, 30, and 14 days are marked with a vertical line. "AR1 Noise" refers to the similarly computed spectrum of a time series generated from a first-order autoregressive model, and "99% level" is the signficance level. (b) As in (a), except using area-weighted station rainfall data from all available stations in the Top End region (approximately 15°S to 10°S and 128°E to 138°E, as in Figure 5.2) of northern Australia for the years 1950 to 1999.

correspondence is even stronger when the same areas are taken for both OLR and rainfall (not shown).

Quantification of the relationship between two time series, as a function of frequency, can be obtained by the application of cross-spectra. Through use of this technique Hendon and Liebmann (1990b) were able to show that, although rainfall shows no obvious preference for a particular frequency, very coherent rainfall fluctuations accompany the pronounced 30 to 80-day fluctuations that exist in other monsoon variables. Two examples of cross-spectra are presented in Figure 5.5. They have been computed using total fields (i.e., the seasonal cycle was retained) and using all days of the available multiyear time series. Figure 5.5a shows the cross-spectrum between large-scale OLR and large-scale 850 hPa zonal wind. Most striking is the high coherence between the two fields for frequencies around the annual cycle and its harmonics. The phase relationship at these annual harmonics is such that positive zonal wind anomalies tend to occur in conjunction with negative OLR anomalies (i.e., westerly winds with enhanced convection). Relatively high coherence also exists in the 30 to 80-day range, especially when compared with the coherence for frequencies just outside this range. The phase within the 30 to 80-day range is such that enhanced convection (negative OLR) slightly leads (by about an eighth of a cycle) the westerly zonal winds—the same relationship that generally occurs across the whole ISV range. The results for Australian "Top End" rainfall and zonal wind (Figure 5.5b) are essentially the same; coherence steadily increases with increasing period from 5 days to 1 year, but with notable bumps around the annual harmonics and within the 30 to 80-day range. In the whole ISV range, rainfall slightly leads the westerly wind.

On the whole, multiyear frequency spectra of fields like OLR and rainfall in the region are notable for their general lack of statistically significant spectral peaks—the only robust peak being the broad 30 to 80-day peak in OLR. Nonetheless, the spectra of Figure 5.4 still indicate the existence of a great deal of ISV in these fields, occurring over a rather broad range of frequencies. Much of this variance, however, appears to be a consequence of the continuum of scales from "weather" to "climate", being well characterized by the lag 1 autoregressive model of red noise. The spectra also show the subjectivity that must be involved in any definition of ISV itself, as there is no spectral gap between intraseasonal and higher frequency scales. Increased wind–rain coherence seen at ISV scales, however, is at least one distinguishing aspect of ISV and the broad 30 to 80-day spectral peak appears particularly coherent. This spectral peak is with little doubt associated with the global-scale MJO (Madden and Julian, 1971, 1994), arguably the most important defined "mode" of ISV for the region. We return to its discussion in Section 5.6.

5.5 METEOROLOGY OF THE BURSTS AND BREAKS

The first views of the structural details of Australasian monsoon bursts and breaks, irrespective of their source, were published in the 1980s. Using infrared imagery from the geostationary meteorological satellite (GMS) during the summer of 1978/1979,

(a) Cross-spectrum of box-averaged OLR and wind

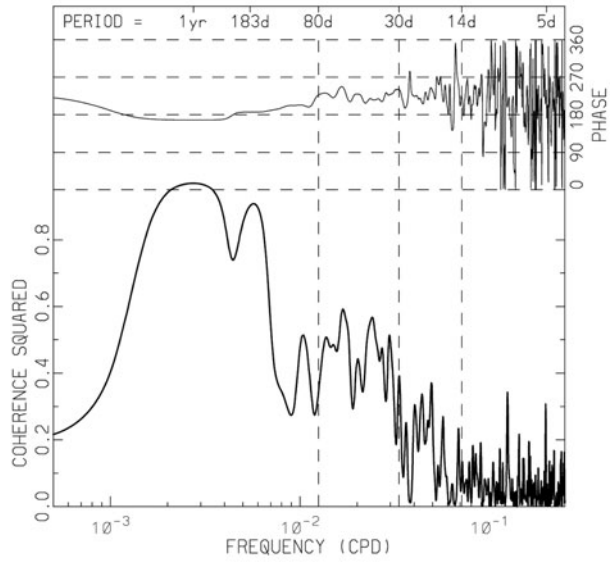

(b) Cross-spectrum of Top End rainfall and wind

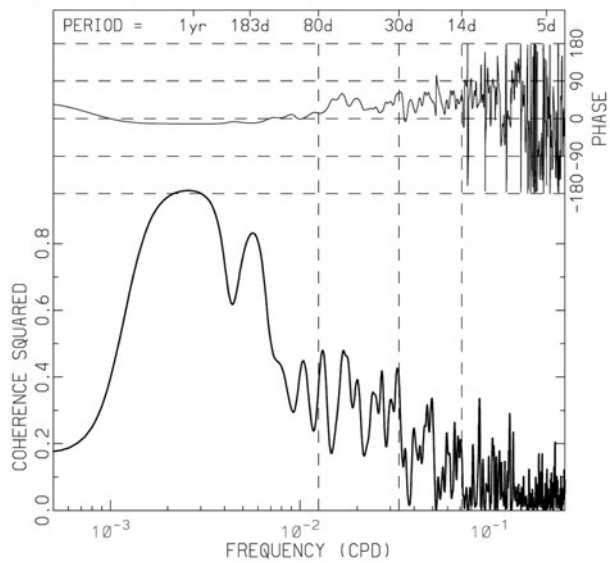

Figure 5.5. (a) Coherence-squared and phase between multiyear time series (using all days of the year) of OLR and 850 hPa zonal wind, both averaged for the box 15°S to 5°S and 120°E to 140°E (same box as in Figure 5.2). Multiple passes of a 1–2–1 filter were applied to the co-spectra and quadrature spectra before computing the phase and coherence resulting in an effective bandwidth of 2.5×10^{-3} cpd. A 90° phase relationship means that OLR is leading the wind by a quarter cycle. (b) As in (a), except between Top End averaged rainfall (see box in Figure 5.2) and 850 hPa zonal wind averaged over the box 15°S to 10°S and 130°E to 135°E.

McBride (1983) found the bursts in that year to be associated with large-scale envelopes of enhanced convective activity, each spanning approximately 35° longitude and 15° latitude, moving either eastward or westward.[3] Davidson (1984) and Keenan and Brody (1988) built on this earlier work by constructing composites of active (burst) and break periods which they identified using time–longitude representations of satellite imagery. Davidson's study emphasizes the differences in structure of tropical wind flow, demonstrating enhanced southern hemisphere Hadley circulation during active periods, and movement of the ITCZ closer to the equator during breaks. Keenan and Brody conclude that a major factor governing tropical convection is the location of upper-level (200 hPa) subtropical troughs and ridges associated with the circumpolar westerly flow at upper levels. In particular, the regions of tropical convection in their composite were associated with the eastern side of an upper trough. How these results have stood the test of time is difficult to gauge as neither has been exactly repeated with more recent data. Importantly, all the authors emphasize that the large-scale envelopes of tropical convective and suppressed regions undergo slow eastward and westward movements, with speeds of between $4\,\mathrm{m\,s^{-1}}$ and $10\,\mathrm{m\,s^{-1}}$ (3° and 8° per day). This primarily zonal movement of the convective envelopes was notably unlike the poleward movement seen in the northern hemisphere monsoon near India (e.g., Yasunari, 1979; Sikka and Gadgil, 1980).

Since the time of the aforementioned studies, at least some of the *eastward movement* of the large-scale envelopes of convection has become identified as being a result of the MJO, as will be described in the following section. The predominance of the MJO in current mainstream thought, however, due largely to the initial work of Hendon and Liebmann (1990a, b), is such that *westward-moving* envelopes have received less attention. Yet, as can be seen in the time–longitude strips for the 1978/1979 season in McBride's paper (also shown in Davidson and Hendon, 1989) and the strips for 1983/1984 shown in Keenan and Brody (1988), westward movements do exist. Most likely some of the westward systems are associated with equatorially trapped Rossby waves, as will be discussed in Section 5.9.

Further details on broadband active and break periods have come from McBride and Frank (1999). They studied the thermodynamic structure of active vs. break periods using data from a radiosonde array surrounding the Gulf of Carpentaria in tropical Australia during the Australian Monsoon Experiment (AMEX). They found major changes in the lapse rate of virtual temperature and that the differences between large-scale active and break regions far exceeded any higher frequency differences between convective and non-convective soundings within the active envelope. Thus, it was interpreted that mid-tropospheric temperatures are primarily adjusted by dynamical processes acting over large scales, rather than by in situ processes acting on the scale of individual convective cells. This is

[3] McBride (1983), as was common with other authors at the time, used the term "synoptic-scale" to refer to the envelopes of convective activity, of order 35° longitude across, that he observed. In this chapter, as is common with more recent treatments (e.g., Hendon and Liebmann, 1990b), we reserve use of the term "synoptic" to refer to a timescale that is shorter than that of intraseasonal variability (ISV).

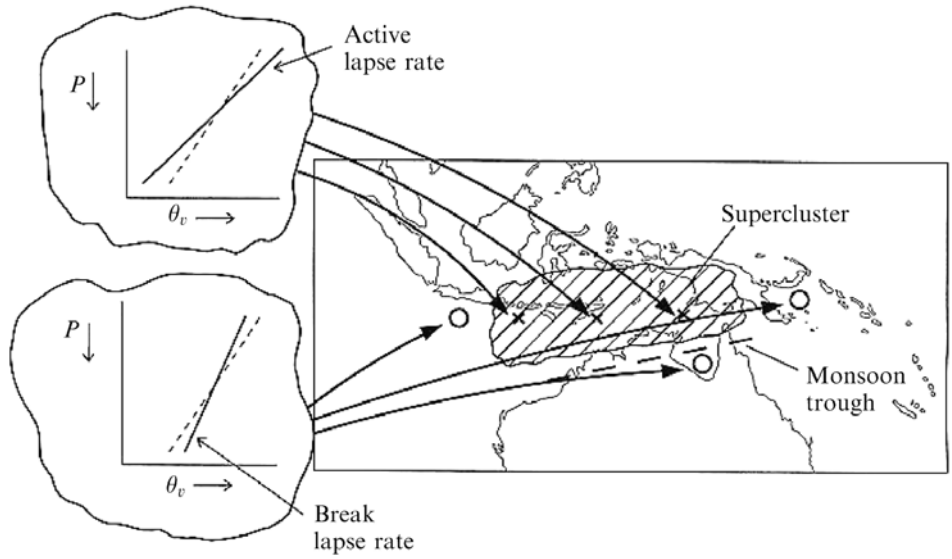

Figure 5.6. A schematic overview of the Australasian monsoon region showing the envelope of active convection or "supercluster" (although we now prefer not to use this overly bandied term), with the break regions being outside the envelope. The nature of variations in the lapse rate of virtual potential temperature are indicated to the left of the map, with X marks on the map showing active regions and O marks showing break regions (reproduced from McBride and Frank, 1999).

illustrated schematically in Figure 5.6. As shown, based on their observations, monsoon active regions are characterized by a warm upper troposphere and a cold lower troposphere, with the reverse in suppressed or break regions (i.e., active monsoon conditions are actually associated with increased mid-tropospheric static stability).

Hendon and Liebmann (1990b) studied the intraseasonal structure of the Australian monsoon specifically in the 30 to 60-day band. They defined active events as having a peak in both wind and rain in their bandpass-filtered data. Once events were defined, the composite structure from 20 days prior to 20 days after the westerly maximum was obtained by averaging unfiltered gridpoint analysis data. Their composite structure in both wind and rainfall was very similar to the eastward-moving fields typically associated with the MJO, as will be described in the following section. Further, their thermodynamic structure was similar to that described by McBride and Frank (1999), with a warm anomaly of the order of 0.9 K in the upper troposphere and a cold anomaly of similar size in the lower troposphere.

Following the methodology of Troup (1961), Drosdowsky (1996) produced a bar chart showing periods of deep westerly flow and of area-averaged rain events for the Darwin area over all monsoon seasons from 1957/1958 through to 1991/1992. Despite a "less than obvious" relationship between the two, both he and Hendon

and Liebmann (1990a) did calculate a statistically significant coherence between wind and rain over a wide range of intraseasonal timescales, especially for timescales greater than about 20 days (see also Figure 5.5). As will be discussed in the following section, the zonal wind vs. rain phase relationship is now well established as a feature of the MJO, yet these coherence calculations show that this is in fact a common property of much of the intraseasonal band.

Since the mid 1980s, Darwin has been the base for a series of both international and Australian meteorological field experiments. It has also been the site of numerous radar deployments. This has led to a number of research papers on the fundamental properties of tropical convection (e.g., Frank and McBride, 1989; Webster and Houze, 1991; Keenan and Carbone, 1992; Mapes and Houze, 1992; Rutledge *et al*., 1992; Williams *et al*., 1992; May and Rajopadhyaya, 1999; McBride and Frank, 1999; Keenan *et al*., 2000; Hamilton *et al*., 2004; May and Ballinger, 2007; May *et al*., 2008). Usually, in these papers the characteristics of convection are interpreted in terms of its occurrence during active vs. break monsoon conditions. However, for one of the major field experiments (AMEX in 1986/1987) the "break" period was only of the order of several days (Gunn *et al*., 1989), thus it not clear to what extent some of these studies are relevant on the intraseasonal (namely, greater than ~10-day) timescale.

One consistent and useful theme to emerge from the various convection studies utilizing data from the Darwin site is that convection has different properties depending on whether the background flow is a deep westerly monsoonal flow as distinct from a deep easterly (break) trade flow. The convective cells present during pre-monsoon and break periods have high vertical development, intense updrafts, high electrical activity, strong diurnal modulation with an afternoon maximum, and a lack of large stratiform decks (e.g., Keenan and Carbone, 1992; Williams *et al*., 1992; May and Ballinger, 2007). In comparison, the convection present during monsoon westerly bursts is often associated with squall-like structures within large mesoscale stratiform decks, warm rain coalescence processes, weak updrafts, and weaker diurnal variation (Mapes and Houze, 1992; Keenan and Rutledge, 1993; Hamilton *et al*., 2004). Thus, while active monsoon conditions result in more rain, the individual convective cells involved are generally less intense. To some extent these differences at Darwin can be attributed to a continental (for the break) as opposed to a maritime (for the monsoon burst) source of the airstream in which the convection is embedded. However, such differences are also consistent with the general large-scale static stability changes found by McBride and Frank (1999); thus, it is likely that some of the observed active vs. break differences in convective type may also apply to oceanic conditions away from the continent. However, as has been recently demonstrated for the diurnal cycle and its modulation by the large-scale flow (Ichikawa and Yasunari, 2008; Rauniyar and Walsh, 2011), the result summarized above for Darwin (of a stronger diurnal cycle during the suppressed phase) certainly does not apply everywhere. Instead, these recent studies have highlighted the complex interaction of large-scale flows with the high topography of the region and the complicated consequences of the diurnal cycle (see also Wu and Hsu, 2009).

5.6 CHARACTERISTICS AND INFLUENCE OF THE MJO

As discussed, the MJO has been identified as the strongest mode of ISV in the Australasian monsoon region. Consistent with the first studies on the MJO (Madden and Julian, 1971, 1972), the MJO is responsible for the statistically significant spectral peak with a central period near 45 days which we identified in Figure 5.4a. It was from the similar appearance of near 45-day peaks in spectra of wind and pressure data that Madden and Julian gave it the name "40–50 day oscillation". However, the MJO has since been determined to contribute variance across a broader range of timescales: namely, 30–80 days (Weickmann, 1983; Lau and Chan, 1985; Salby and Hendon, 1994; Wheeler and Hendon, 2004). This and its other defining characteristics of being of planetary scale, eastward propagating, and mostly confined to the tropics, has led to it now being more universally called the "Madden Julian Oscillation".

For the correct interpretation of some of the previous work on the MJO, it needs to be stressed that not all the variance existing in the 30 to 80-day band should be ascribed to it. Instead, it is only the component that is associated with large-scale eastward propagation that should be included, as this is one of the essential characteristics of the MJO. Calculations show that the large-scale eastward-propagating component of tropical variability (e.g., eastward planetary wavenumbers 1 through 6) accounts for only about half the variance in the 30 to 80-day band in fields of OLR and zonal wind (on a 2.5° grid) across the equatorial Indian and Western Pacific Oceans (Hendon *et al.*, 1999). Outside the near equatorial band, the portion of atmospheric 30 to 80-day variance that is attributable to the MJO is likely to be even less. In the Australasian monsoon region, even without the restriction to large-scale eastward propagation, the coherence calculations of Figure 5.5a suggest that only half the 30 to 80-day variance may be attributed to a coherent mode (coherence squared of 0.5). When considering the influence and characteristics of the MJO in any region then, such an attribution must be kept firmly in mind.

In this context, the results of the earliest studies that pertain to the influence of the MJO on the Australasian monsoon region must be viewed with some caution. The first two studies to propose that the active–break cycle in the Australasian monsoon is associated with the MJO were those of Holland (1986) and McBride (1987). As was common practice at the time, McBride (1987) used a rather narrow bandpass filter (half-power response at 37 and 54.7 days) on the local wind at Darwin and interpreted the resulting time series as being the signal of the MJO. In light of developments since, this interpretation is not entirely correct. However, McBride's work did serve to demonstrate the out-of-phase character between upper-level (100 hPa) and lower-level (850 hPa) zonal winds for this frequency band as well as the general correspondence between peaks and troughs of the filtered winds and the active and break periods of the monsoon.

Another early piece of work that is often quoted in the context of the MJO's influence on the Australian monsoon is that of Holland (1986). Holland defined active bursts of the monsoon by filtering the 850 hPa zonal wind at Darwin, and found that the mean period between active bursts is 40 days, with a standard

deviation of 10 days. Holland interpreted this recurrence interval as evidence of an influence by the MJO. However, as discussed by Drosdowsky (1996), Holland's cubic spline filter was effectively a lowpass filter with a cutoff at approximately 30 days. Consequently, Holland's result of a 40-day mean recurrence interval could have equally as well been made with an input of red noise and, hence, did not necessarily imply an MJO influence.

Beyond these earliest pieces of work, Hendon and Liebmann (1990b) provided a much more detailed picture. Using the techniques of cross-spectra and compositing relative to a 30 to 60-day filtered time series at Darwin, they were able to show the dominance of large-scale eastward propagation in this frequency range. Again, however, some caution needs to be given with regard to the attribution of structures they presented to the MJO. As Hendon and Liebmann used a 30 to 60-day filtered time series of wind and rain near Darwin as the predictor about which to composite (i.e., a local index), their composites likely contain a contribution from more aspects of variability than just the MJO. One likely symptom of this is that the anomaly of enhanced convection within their composite is seen to be traceable from the southern Indian Ocean at a latitude around 10°S (their fig. 10), rather than the usual equatorial Indian Ocean as seen in composites made with more global indices of the MJO (e.g., Knutson and Weickmann, 1987; Wang and Rui, 1990; Wheeler and Hendon, 2004; see also Figure 5.8). Nevertheless, other aspects of Hendon and Liebmann's results provide a picture of the influence of the MJO that has remained accurate to this day. With a composite comprising 91 events from 30 wet seasons (1957–1987), they found the amplitude of the "oscillation" at Darwin to be about $5\,\mathrm{m\,s^{-1}}$ in zonal wind, $0.75\,\mathrm{m\,s^{-1}}$ in meridional wind, 5 mm rainfall per day, and 10% in relative humidity. The deep baroclinic structure in zonal wind had its node at about 300 hPa, much like that of the westerly burst of Figure 5.3b. The amplitude of the associated OLR anomaly near Darwin was found to be about $30\,\mathrm{W\,m^{-2}}$, placing the broadband intraseasonal variations of Figure 5.2 in perspective.

Compared with the aforementioned work, more recent studies on the influence of the MJO have tended to use MJO indices that are based on data from a much larger region, consistent with its planetary scale. One common approach for identifying the MJO is to employ filtering in both frequency and wavenumber. This allows for selection of variability with the largest zonal spatial scales (low zonal wavenumber), as well as of variability that is propagating to the east (e.g., Wheeler and Kiladis, 1999; Hendon *et al.*, 1999). Another common approach is to employ empirical orthogonal function (EOF) analysis of tropical fields such as OLR and zonal wind (e.g., Hendon *et al.*, 1999; Hall *et al.*, 2001; Waliser *et al.*, 2003; Wheeler and Hendon, 2004). Provided the seasonal cycle and interannual variability are prior removed, structures akin to our current view of the MJO are well described by the leading EOF pair and projection of global data onto those EOFs extracts the large-scale, predominantly eastward-propagating, signal of the MJO. While such approaches appear superior to using a locally defined index for the MJO, they are not without their own caveats, and there will always be the concern that an index may contain contributions from non-MJO variability and/or be missing some of that variability. Nevertheless, here we present results using the EOF approach of Wheeler

and Hendon (2004) for identifying the MJO. This will serve to provide a useful comparison with both earlier work and for presenting some new calculations.

Wheeler and Hendon's (2004) MJO-defining EOFs are displayed in Figure 5.7a. They are the leading EOF pair of the combined analysis of near equatorially averaged fields of OLR, 850 hPa zonal wind, and 200 hPa zonal wind, using daily data for all seasons. As can be seen, the EOFs show the predominantly zonal wavenumbers 1 and 2 structure of the MJO and, when taken as a pair, can describe its eastward propagation. Indeed, as shown in Figure 5.7b, projection of daily observed data onto the EOFs yields principal component (PC) time series that vary mostly on the 30 to 80-day timescale of the MJO. These PCs are approximately in quadrature with PC1 leading PC2, implying predominantly eastward propagation. Taken together, the two PC time series are used as the MJO index and, as this index was developed for real time use, they have been called the real-time multivariate MJO series 1 (RMM1), and 2 (RMM2). By the analysis of Wheeler and Hendon (2004), RMM1 and RMM2 are able to represent the essential characteristics of what most scientists consider as the "MJO". In particular, the state of the MJO can be measured in the phase space defined by RMM1 and RMM2 (Figure 5.7c): eight different phases are used when the MJO is considered relatively strong, and a "weak MJO" phase when the (RMM1,RMM2) vector has an amplitude of less than 1.0. When individual sequences of days of strong MJO activity are viewed in the phase space, their paths trace large anticlockwise circles. On average, each phase lasts for about 6 days, but there can be considerable variability in this number from one MJO event to the next.

Given the description of the MJO by the (RMM1, RMM2) phase space, composites may be formed by averaging the observed anomaly fields occurring for the days that fall within each of the defined phases. Here, in Figure 5.8, we present such a composite for the December–January–February season using data from the 1974 to 2010 period. About 250 days of data were averaged for each of the presented eight MJO phases, while 1,164 days were rejected for being at a time of weak MJO amplitude (representing 36% of the time). The composite of phase 1 shows suppressed convection (positive OLR anomalies) over the Australasian monsoon region, with OLR anomalies reaching values greater than 22.5 $W\,m^{-2}$. Anomalous tropical easterlies (at the 850 hPa level) accompany this suppressed convection, especially in the west of the domain. As time progresses through each of the phases, the patterns shift to the east. In phase 2 the easterly wind anomalies are at their greatest around 130°E, with a magnitude of about 5 $m\,s^{-1}$. By phase 3, a large negative OLR anomaly has appeared over the eastern equatorial Indian Ocean. At the same time, there is evidence of tropical–extratropical interaction, with a negative OLR anomaly associated with cyclonically turning winds over extratropical Western Australia.

As time progresses beyond phase 3 in the composite (Figure 5.8), the main tropical convective signal shifts farther eastward and at the same time expands southward over the north of Australia. In phase 5, the negative OLR anomaly has reached its most southward extent, being centered at 12°S, with a value of less than $-30\,W\,m^{-2}$. Maximum westerly anomalies are placed coincident and somewhat to

(a) EOF spatial structures for real time multivariate MJO (RMM) index

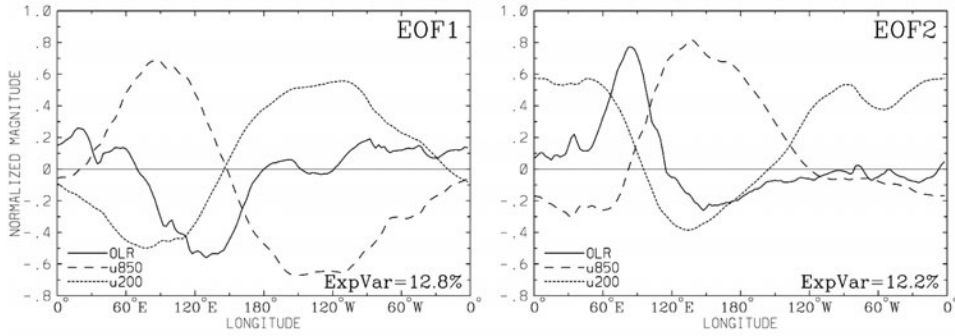

(b) PC time series (RMM1 and RMM2) for 1987/1988

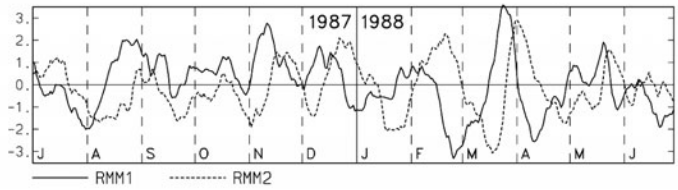

(c) (RMM1, RMM2) phase space for January 22, 1988 to April 27, 1988

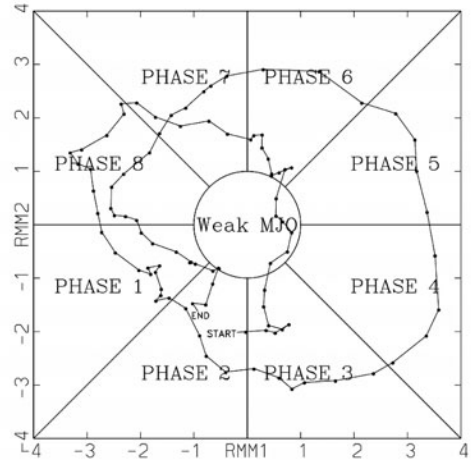

Figure 5.7. (a) Structure of EOFs designed to isolate the signal of the MJO using 15°S–15°N averaged fields. See text for further details. (b) Example series of RMM1 (PC1) and RMM2 (PC2). (c) (RMM1, RMM2) phase space for January 22, 1988 to April 27, 1988 (adapted from Wheeler and Hendon, 2004).

the west of the enhanced convection, with maximum values of about $5\,\mathrm{m\,s^{-1}}$. In the vicinity of Darwin (12.5°S, 130.9°E) there is a signal in the meridional wind as well, with northerly anomalies (phase 4) leading the westerlies (phases 5–7). The largest amplitude signals in the OLR tend to be over the sea. In contrast, the islands of New

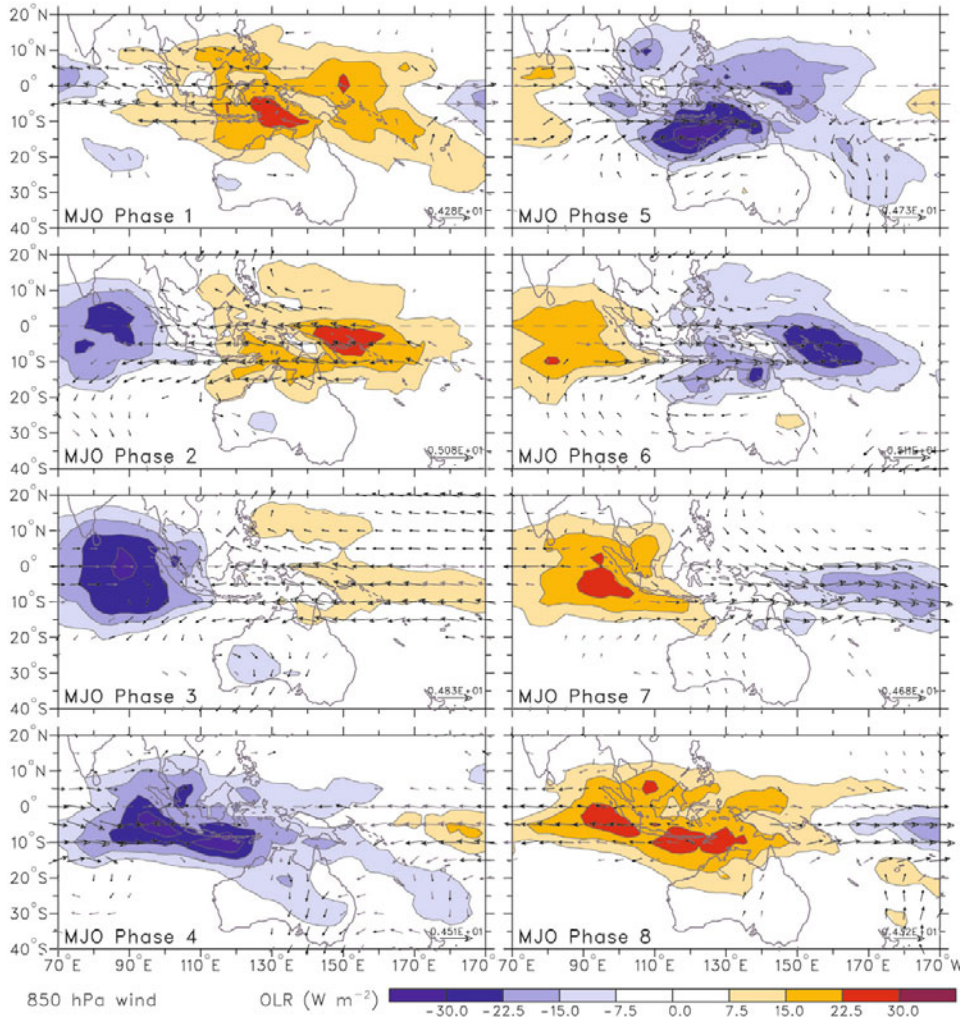

Figure 5.8. MJO composites of OLR and 850 hPa wind anomalies for the December–January–February season for RMM phases 1–8, using data for 1974–2010. The OLR contour interval is 7.5 W m^{-2} with the zero contour omitted (see also the color scale provided). Black vectors indicate wind anomalies that are statistically significant at the 10% level, based on their local standard deviation and the Student *t* test, and gray vectors at the 20% level. The magnitude of the largest vector is shown at the bottom right of each panel.

Guinea and Borneo have a reduced amplitude OLR anomaly in many of the phases. Also of note is the lesser degree to which convection moves poleward when compared with what occurs over the Indian monsoon region in the opposite season (Wheeler and Hendon, 2004). On the whole, many of these features of this composite are equivalent to those of the study of Hendon and Liebmann (1990b).

Importantly, magnitudes are favorably high when compared with the broadband ISV bursts and breaks of Figures 5.2 and 5.3b, thus suggesting the relative importance of the MJO for producing some of that variability.

The influence of the MJO on rainfall in the region has recently been studied in some detail by Hidayat and Kizu (2009), Wheeler *et al*. (2009), and Rauniyar and Walsh (2011). Over northern Australia and the surrounding seas the rainfall signal associated with the MJO closely matches the large-scale OLR signal that is illustrated in Figure 5.8, with positive rainfall anomalies occurring during the same MJO phases as negative OLR anomalies. Wheeler *et al*. (2009) show that in the land area around Darwin the rainfall anomaly maximizes at about $5\,\mathrm{mm\,day^{-1}}$ in phase 5. Hidayat and Kizu (2009) and Rauniyar and Walsh (2011) compute a similar rainfall anomaly over the Timor Sea, Arafura Sea, and Gulf of Carpentaria in about the same MJO phase. However, over the large islands of Sumatra, Borneo, Java, Sulawesi, and New Guinea, composite rainfall anomalies have been computed to be much smaller (Hidayat and Kizu, 2009) and may in fact be reversed (Rauniyar and Walsh, 2011) (i.e., with weakly negative rainfall anomalies occurring over the islands in the "convectively-active" phases of the MJO). Rauniyar and Walsh (2011) provide evidence which suggests it is the interaction of the MJO with the strong diurnal cycle over the islands that is the cause of this curious result. This absence (or perhaps even reversal) of the rainfall signal over the aforementioned islands is only weakly apparent in the OLR composite of Figure 5.8. This may be partly explained by the relatively coarse resolution of the OLR data (2.5° grid), but also suggests that OLR is not always a faithful indicator of local rainfall.

One research question that has been little addressed in the aforementioned research papers is the extent to which the MJO can account for the broadband ISV bursts and breaks discussed in the last three sections. We explore this question in Figure 5.9. Shown is the same OLR time series as Figure 5.2, except solid bars have been added to indicate times when the MJO is diagnosed to be in either phases 4, 5, or 6 (i.e., times when the composite MJO has negative OLR anomalies in the region of interest). If the MJO/burst relationship is strong, the solid bars should coincide with the negative excursions of the OLR time series below the seasonal cycle. Sometimes the relationship appears strong (e.g., during 1987/1988) and at other times weak (e.g., 1982/1983 and 1983/1984). Quantification of the relationship is given by the multiple correlation coefficient squared, R^2, between the 3-day running mean OLR anomaly and the RMM1 and RMM2 values, calculated for the November through April months only. The value of $R^2 = 0.58$ in 1987/1988 indicates that 58% of the variations of 3-day running mean OLR can be linearly accounted for by variations in this EOF-based global measure of the MJO.[4] In 1982/1983 and 1983/1984, the amount is less than 10%. Thus, it is indicated that there is a great deal of interannual variability in the MJO/

[4] In some sense the calculated R^2 are an overestimate of the variability accounted for by the MJO, and in another it is an underestimate. It is an overestimate in the sense that some of the fluctuations of the RMM indices, especially at higher frequencies, are presumably not associated with the MJO but may provide some additional correlation with box-averaged OLR. Underestimation comes from the fact that just two spatial structures (EOF 1 and EOF 2) presumably cannot capture all the real world MJO variability.

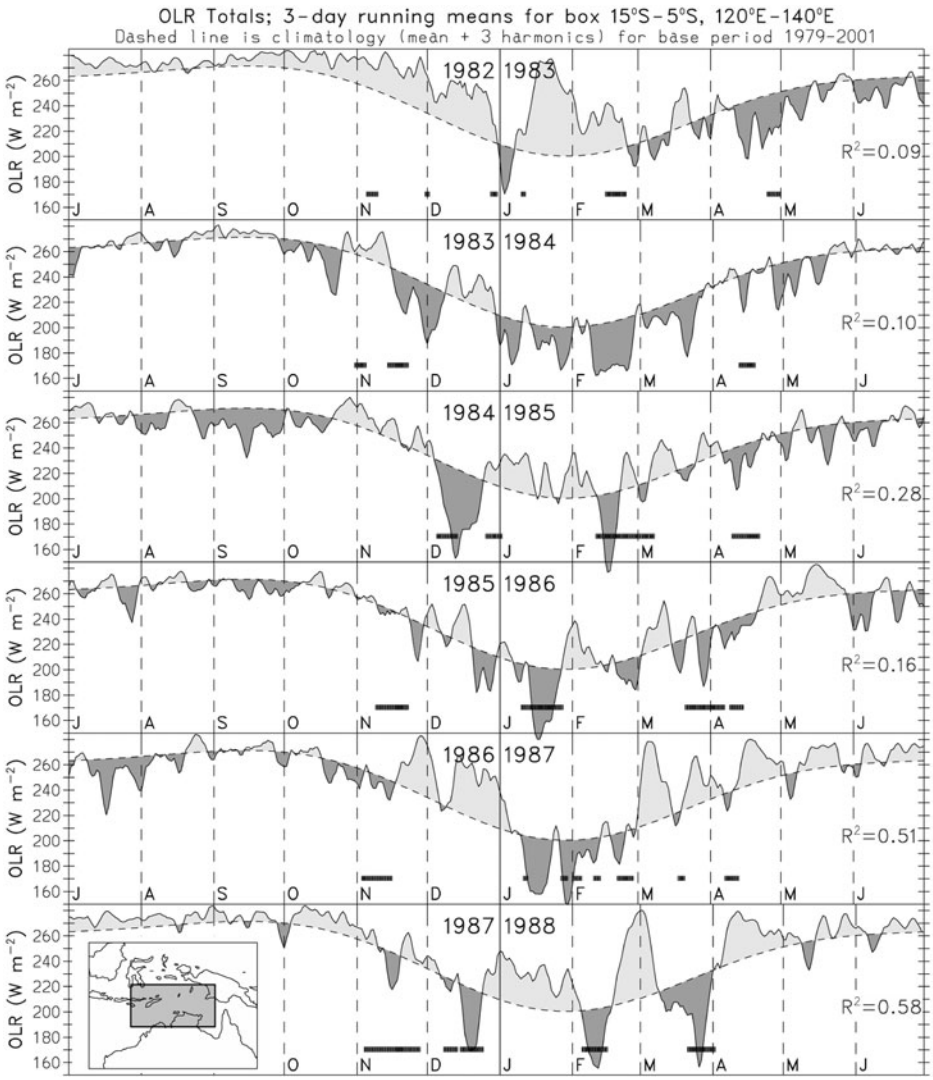

Figure 5.9. As in Figure 5.2, except showing just the OLR series and a solid bar when the phase of the MJO, as defined by the (RMM1, RMM2) phase space, was within either phase 4, phase 5, or phase 6, for the months of November through April only. Also given is the square of the multiple correlation coefficient between the OLR anomaly time series and the RMM1 and RMM2 values calculated for the November through April months.

ISV burst relationship. Some of this variability is likely related to interannual variability in the strength of the MJO itself (e.g., Hendon *et al.*, 1999). In some years the MJO is essentially absent (e.g., 1982/1983 and 1983/1984), and in those years it is difficult to imagine that the relationship can be anything but weak.

5.7 1983/1984 AND 1987/1988 CASE STUDIES

Many of the subtleties of the MJO, and its relation to ISV bursts and breaks and the monsoon seasonal cycle, can be well illustrated by case studies. Here we provide a fuller view of two cases, the summers of 1983/1984 and 1987/1988. They were chosen because the monsoon ISV of 1983/84 shows little relation to the MJO and that of 1987/1988 shows quite a strong relationship (Figure 5.9).

As has been mentioned, much of the ISV of the region tends to be characterized by either eastward or westward movement of large-scale envelopes of convection (e.g., McBride, 1983), while the MJO is characterized as showing large-scale eastward movement. Time–longitude plots show such movements and thus provide a useful comparison. Here in Figures 5.10 and 5.11 we show time–longitude plots of OLR and 850 hPa vector wind averaged over the latitudes from 15°S to the equator. Most striking about the two figures is the presence of three large-scale eastward-moving envelopes of convection in 1987/1988, oscillating with a period around 50 days, and the absence of such a clear oscillation in 1983/1984. The three dramatic intraseasonal events of the 1987/1988 summer are with no doubt produced by the MJO, and the 1987/1988 summer has often been used in previous studies to provide a clear example of the MJO (e.g., Hendon and Liebmann, 1994; Matthews, 2000). Further, many of the features of the composite MJO, as presented in Figure 5.8, are present for the individual events in Figure 5.11. For example, for each of the three dominant events, the regions of strongest convection (lowest OLR) tend to be coincident with, or somewhat leading, the regions of strongest westerly winds, and these coupled convection–wind patterns mostly move across the domain to the east. However, there are some exceptions to this rule. For example, in the first 2 weeks of January, there is a coupled convection–wind signal in the eastern part of the plotted domain (between 130°E and 160°W) that is moving to the west. As previously computed (Figure 5.9), the squared multiple correlation coefficient (R^2) tells us that there is still a sizable portion (~42%) of subseasonal 3-day running mean variance in the 120°E to 140°E box that cannot be accounted for by the MJO in the 1987/1988 season. This westward-moving feature would comprise one component of that unaccounted variance.

Compared with the 1987/1988 season, the 1983/1984 season (Figure 5.10) provides an interesting contrast. Rather than the nearly 50-day periodic bursts and breaks, the 1983/1984 season shows no clear periodicity. Instead, there appears to be a greater amount of high-frequency variability, with around a 1 to 2-week timescale, imbedded within a low-frequency envelope of convection lasting for much of the monsoon season. An early wet westerly burst of the monsoon occurs at the longitudes of Australia and Indonesia (near 130°E) at the end of November, followed by a break in mid December. Monsoon westerlies then return at the end of December and, except for a brief time in February, don't change back to easterly until late March. Yet there is still a lot of intraseasonal variability occurring during this time. For example, the OLR returns to values greater than 220 W m^{-2} on four occasions (at 125°E) during the 3 months of sustained westerlies. Interestingly, much of this latter variability can be visually associated with westward propagation

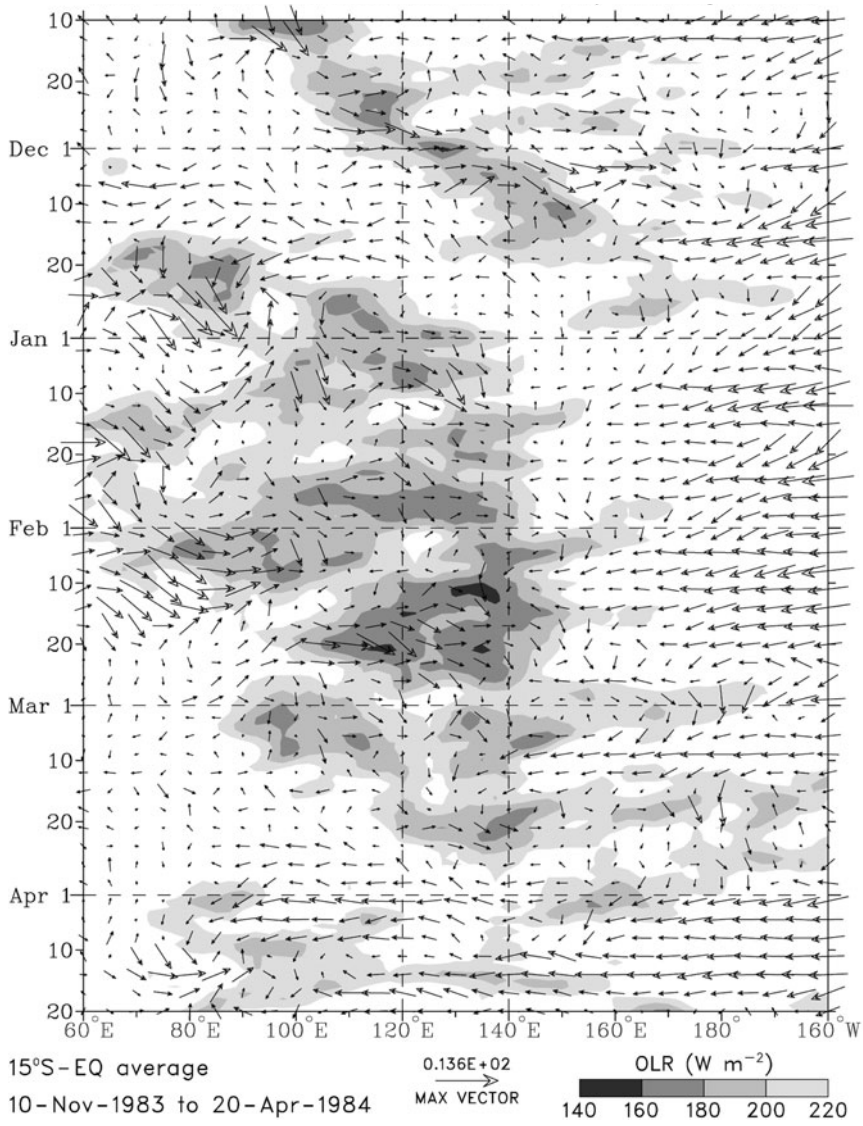

Figure 5.10. Time–longitude plot of 3-day running mean total 850 hPa wind and OLR averaged from 15°S to the equator for the monsoon season of 1983/1984.

originating in the Pacific. Some of this westward-propagating variability can be identified as equatorially trapped Rossby waves, as we will discuss in Section 5.9. Except during the early monsoon burst in November/December, however, large-scale eastward propagation is mostly absent.

A further view of the two periods can be had by looking at time series of rainfall, as shown in Figure 5.12 for the locations of Bali (approximately 115–116°E, 8–9°S)

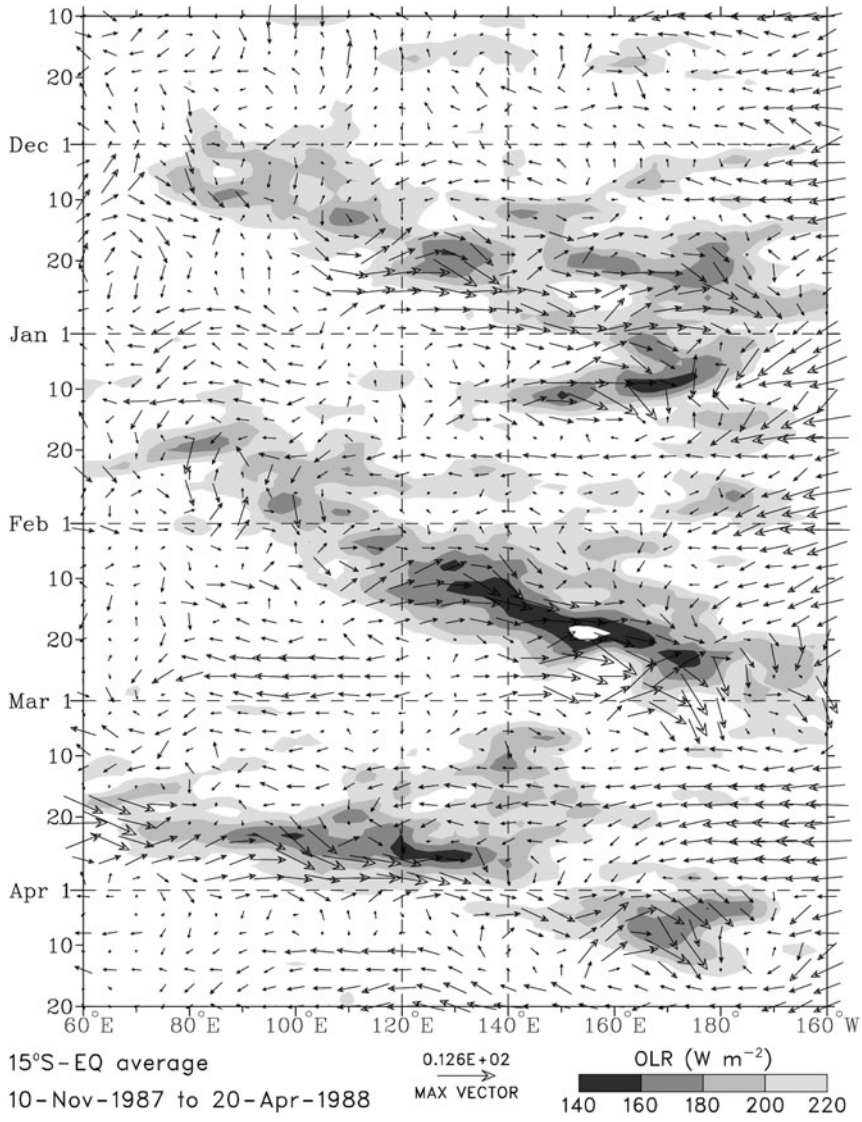

Figure 5.11. As in Figure 5.10, except for 1987/1988.

and the northern Australian Top End region (as defined in Figure 5.2). The Bali series is an average of 10 stations on the island,[5] while the Australian series comprises information from about 100 stations which were averaged in an area-weighted fashion. As has already been mentioned, station rainfall data tend to be

[5] The Bali stations used were Abiansemal, Bangli, Bebandem, Bukti, Candikuning, Gerokgak, Gianyar, Rambutsiwi, Ngurah Rai, and Kubu.

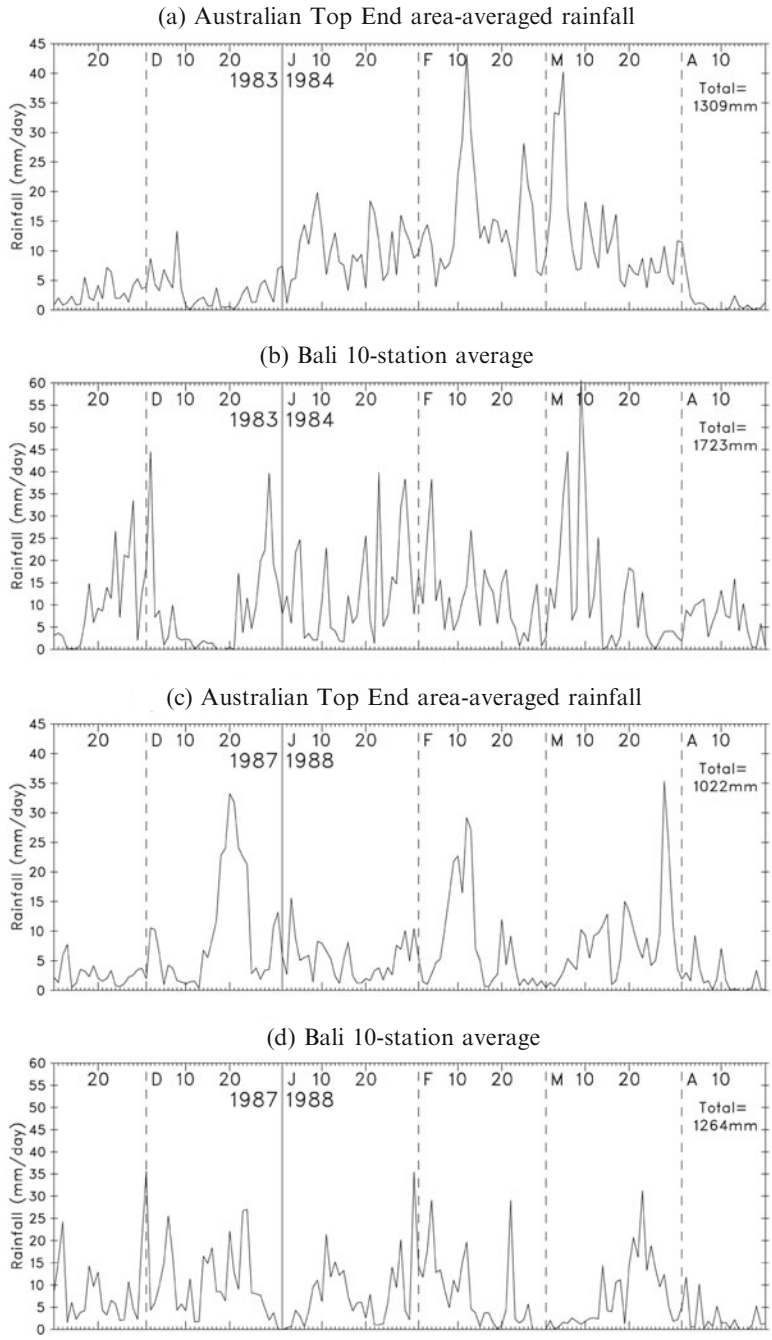

Figure 5.12. Daily precipitation averaged for the Top End region (northern Australia, as in Figure 5.2) and for the island of Bali (approximately 115–116°E, 8–9°S) for the 1983/1984 and 1987/1988 wet seasons. The total rainfall amount in each season is given.

more noisy than satellite-observed OLR data, yet many of the same features observed in OLR can be seen. For example, at both locations the 1983/1984 season has an early burst of rainfall in late November/early December, then a more continuous period of rainfall from late December through to late March. In the 1987/1988 season, on the other hand, the Australian series is seen to be comprised of three major bursts spaced about 50 days apart, characteristic of the MJO. Those three bursts are also somewhat apparent in the 1987/1988 Bali series as well, albeit occurring a little earlier, and obscured by a much greater component of noise. Thus, knowing that 1987/1988 was a time of strong MJO activity (e.g., Slingo *et al.*, 1999; Wheeler and Hendon, 2004) and that activity had a strong correlation with large-scale variations in the monsoon (e.g., Figure 5.9), this example shows how it can still be very difficult to observe an MJO impact in small-area station rainfall data, such as the Bali data, especially for stations from the region's islands (see also Hidayat and Kizu, 2009 and Rauniyar and Walsh, 2011).

One further point that can be made with regard to Figure 5.12, is the fact that in both locations total season rainfall is greater in 1983/1984 than 1987/1988. This is consistent with the relationship found by Hendon *et al.* (1999): enhanced MJO activity tends to occur in conjunction with positive season mean OLR anomalies over northern Australia. Thus, there is the suggestion that it is the monsoon break (i.e., highly suppressed) periods produced by the MJO that distinguish those monsoon years with strong MJO activity from others.

5.8 MJO INFLUENCE ON MONSOON ONSET

As mentioned in the introduction (Section 5.1), some of the research literature pertaining to the region's monsoon onset gives the impression of a widely varying role for the MJO. On the one hand, Hendon and Liebmann (1990a) suggest that monsoon onset in each year is "strongly influenced by the 40–50 day oscillation" and that in 27 out of 30 years onset fell within 4 days of the passage of the "oscillation". Composites of atmospheric fields constructed relative to their onset dates showed that onset coincided with the arrival of an eastward-propagating convective anomaly originating in the Indian Ocean. On the other hand, the study by Davidson *et al.* (1983) examined the evolution of the large-scale flow at monsoon onset in 6 years and, although they suggested an important role for a number of different triggers, no relationship was suggested with the propagation of MJO-like perturbations from the Indian Ocean. Part of the reason for the omission of the MJO in the Davidson *et al.* study was that, although the Madden and Julian (1971, 1972) papers long preceded their work, the MJO was still relatively unknown among researchers at the time. Yet, later studies on monsoon onset have also seemingly downplayed the influence of the MJO. Drosdowsky (1996), for example, in relation to the similarly defined "active periods" stated, "in contrast to a number of recent studies that have highlighted the so-called 40–50-day oscillation in the Australian summer monsoon, no dominant timescales are found in the length of the active periods or in the recurrence time between active phases." Of course, the latter statement doesn't specifically refer to

monsoon onset, but given that monsoon onset is universally defined as the beginning of the first active period in each wet season, it can be difficult to reconcile this statement given the earlier work of Hendon and Liebmann (1990a).

A partial re-evaluation of the onset/MJO relationship is made by Wheeler and Hendon (2004), using the information presented here in Figure 5.13. This figure shows the relationship between the RMM phase space definition of the MJO and the monsoon onset definition of Drosdowsky (1996), updated with data up to 2008. A definite relationship with Drosdowsky's locally defined onset dates appears. Considering only the dates that lie outside the central unit circle (i.e., those occurring when the MJO is not weak), 85% (17 of 20) of the dates occur in phases 4–7 (when MJO low-level westerlies are in the vicinity of northern Australia in Figure 5.8) and only 15% (3 of 20) of the onset dates occur in the other phases (when northern Australia is under the influence of MJO easterlies). The same overall result is achieved with the newer definition of monsoon onset provided by Pope *et al*. (2009) (not shown).

Importantly, however, the spread of onsets from phases 4 to 7 covers a time window of half the period of the MJO (i.e., about 20 to 30 days), a significantly greater spread than the ±4 days found by Hendon and Liebmann (1990a). Thus, it appears that, while the planetary-scale MJO is limiting monsoon onset to be within its active half-cycle as lasting for a few weeks, the actual day of onset (as defined at the point location of Darwin by Drosdowsky and others) is often being set by other

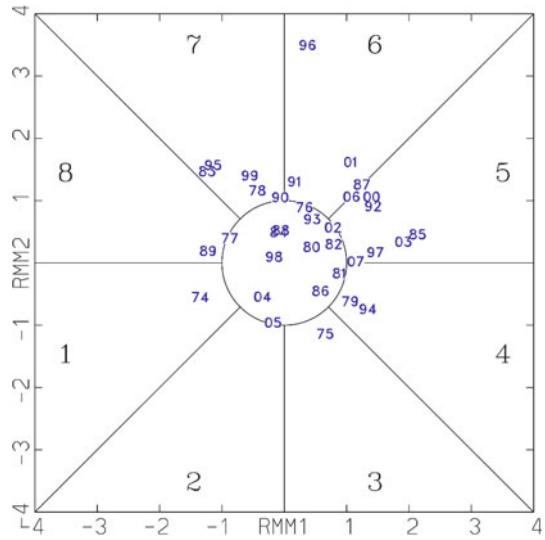

Figure 5.13. (RMM1, RMM2) phase space points (as marked by the blue numbers) for the days on which the monsoon was defined to onset, based on the daily deep-layer mean zonal wind, at Darwin, Australia. The blue numbers refer to the monsoon year, being that of the nearest December. The monsoon dates are defined and taken (with updates) from Drosdowsky (1996) and cover all wet seasons from 1974/1975 to 2007/2008.

presumably shorter timescale phenomena. This view is in essence the same as that of Hung and Yanai (2004) and the much earlier study of Hendon *et al.* (1989), both of whom find the large-scale low-frequency influence of the MJO to be only one of a number of factors that determine monsoon onset.

How then did Hendon and Liebmann (1990a) get a much closer correspondence between the MJO and Australian monsoon onset? The reason is their less stringent definitions of monsoon onset and the MJO. For monsoon onset they used a 1–2–3–2–1 lowpass filter of Darwin winds and northern Australian rainfall, and for their "40 to 50-day oscillation" they used a 30 to 60-day filtered series of the same winds and rainfall. Obviously, dates defined from such similar series are likely to have a closer correspondence than those coming from unfiltered winds (as in the case of Drosdowsky's onset dates) and a series using information from planetary-scale fields of winds and OLR (as in the case of the RMM MJO index). Thus, while the MJO was a notable oversight as a potential onset mechanism in Davidson *et al.*'s (1983) work, its dominance, we feel, was overstated by Hendon and Liebmann (1990a).

5.9 OTHER MODES AND SOURCES OF ISV

With good reason, the majority of research work on ISV of the Australasian monsoon has concentrated on the MJO. This is a reflection of the fact that the MJO is responsible for the most robust intraseasonal peak in frequency spectra of the standard atmospheric variables (e.g., Figure 5.4a). When looking at time–longitude plots of atmospheric fields for the region (e.g., Figures 5.10 and 5.11), much of the large-scale coherent eastward propagation can be identified as MJO events. Yet, cases of large-scale coherent westward propagation have also been observed (Sections 5.5, 5.7; McBride, 1983; Davidson *et al.*, 1983; Keenan and Brody, 1988; Hendon *et al.*, 1989). Although it can be quite varied, the phase speed of the westward convective envelopes that have been observed is often about the same as that of the eastward MJO, being on the order of $5\,\mathrm{m\,s^{-1}}$ ($\sim 4^\circ$ per day). Usually these westward envelopes are maximized off the equator and can be accompanied by large variations in rotational wind as well. Such characteristics are suggestive of an influence on the monsoon by equatorial Rossby (ER) waves (e.g., Kiladis *et al.*, 2009), the "mode" that is perhaps the next most important for this monsoon region.

Since the mid 1990s, evidence for the lowest order ($n = 1$) ER waves has become relatively common in studies of the tropical Pacific (e.g., Kiladis and Wheeler, 1995; Numaguti, 1995; Pires *et al.*, 1997; Kiladis, 1998; Wheeler and Kiladis, 1999). The evidence presented is of westward-propagating disturbances with structures much like the theoretical shallow water ER waves of Matsuno (1966). Some evidence has also been presented linking variations of the Australasian monsoon with these waves (McBride, 1983; Hendon *et al.*, 1989; Wheeler and McBride, 2005). While ER waves do not readily appear in the frequency spectra of individual time series of monsoon variables (e.g., OLR as in Figure 5.4a), wavenumber–frequency spectra, using data from multiple longitudes, has had success at showing their existence above the red-noise background (e.g., Wheeler and Kiladis, 1999). The suggested broad frequency

band of the waves is 1/7 cpd to 1/40 cpd, which corresponds well with what we define as intraseasonal. Filtering for their specific zonal wavenumbers and frequencies has revealed that they have maximum variance in OLR in the far Western Pacific and account for a useful portion of the variance across the whole Australasian monsoon region (Wheeler and Kiladis, 1999; Roundy and Frank, 2004; Masunaga, 2007). Concentrating on this signal, Wheeler *et al.* (2000) show a typical structure of the "convectively coupled" ER waves at 150°E (near their longitude of maximum variance) as reproduced here as Figure 5.14. It was constructed by computing lagged linear regressions of predictand variables against a reference time series of wavenumber–frequency filtered OLR. The waves' structure of symmetric circulation cells on either side of the equator is clearly depicted, as is a clear indication of an influence on winds and convection within the Australasian monsoon region.

A case of $n = 1$ ER waves in the region is presented in Figure 5.15, as taken from a small portion of the 1983/1984 season that was previously shown and discussed in relevance to Figure 5.10. In particular, we focus on late February to early April 1984, during which a number of westward-propagating features were previously identified. Given the $n = 1$ ER wave's symmetry about the equator, averages over the latitude band of 15°S–15°N are shown. In the total OLR data of Figure 5.15a, there is a clear indication of flareups of convection occurring in the 120°E–140°E domain with a period between 10 and 20 days. Applying the wavenumber–frequency filtering of Wheeler and Kiladis (1999), as shown by the contours, indicates a close correspondence between those flareups and the ER wave's canonical wavenumber–frequency spectral peak (from which the filtering was defined). Yet further consistency with the ER wave is given in Figure 5.15b, showing a clear signal of the waves in the intraseasonally filtered (10–90 days) antisymmetric meridional wind $[(V_{\text{north}} - V_{\text{south}})/2]$. Obviously, much of the broadband intraseasonal variance can be accounted for by ER waves during this particular period and similar cases can be found in many other years as well.

There are also a number of other types of convectively coupled equatorial waves (Wheeler and Kiladis, 1999). Of the others, it is only the convectively coupled Kelvin wave that is expected to have a direct influence in the intraseasonal frequency band, the others having frequencies higher than the defined intraseasonal limit. Using the same regression procedure as that applied for the ER wave above, Figure 5.16 shows the typical structure of a convectively coupled Kelvin wave, as computed near its point of maximum variance (0°, 90°E) by Wheeler *et al.* (2000). It is eastward moving, faster than the MJO, with its convective signal more confined near the equator, and primarily has a zonal wind component signal only. Being more confined near the equator, the Kelvin wave is expected to have a greater influence in the Indonesian part of the monsoon system. A typical phase speed of this convectively coupled wave is around 15 m s^{-1}, and its structure is a close match to observed disturbances described in the earlier works of Williams (1981), Nakazawa (1986, 1988), Hayashi and Nakazawa (1989), Takayabu and Murakami (1991), and Dunkerton and Crum (1995), and the more recent work of Murata *et al.* (2006). The terminology for the wave has not always been consistent, however, with some of these earlier studies using the term "supercluster" when referring to them in the

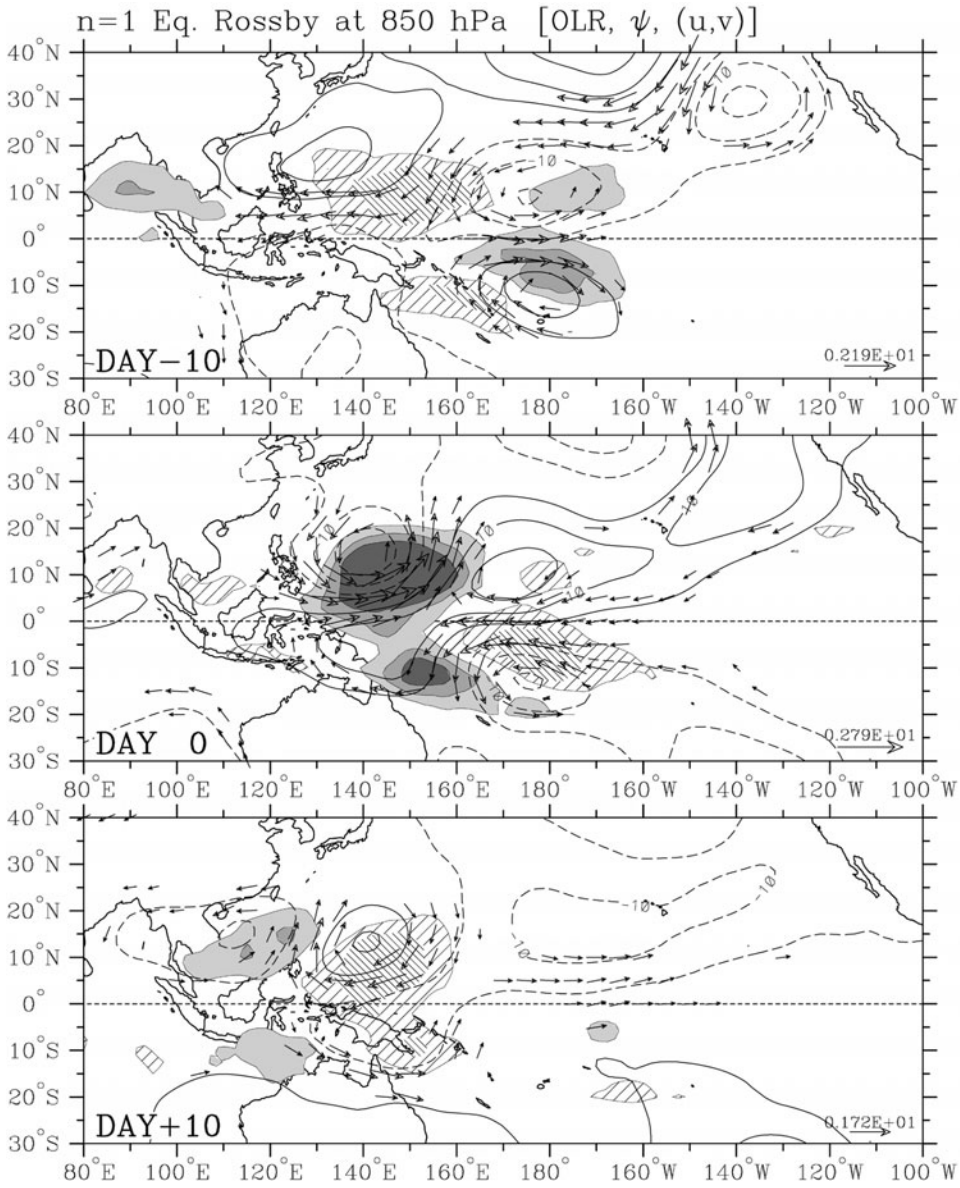

Figure 5.14. Typical horizontal structure of a convectively coupled $n = 1$ equatorial Rossby (ER) wave over a sequence spanning 21 days, as computed using lagged regression based on a 2 standard deviation anomaly in the ER wave filtered OLR series at 10°S, 150°E. Shading/cross-hatching shows negative/positive OLR anomalies at the levels of −15, −10, −5, 5, and 10 W m^{-2}. Contours are streamfunctions at the 850 hPa level, having an interval of 5×10^5 m^2 s^{-1}, with negative contours dashed and the zero contour omitted. Vectors are 850 hPa wind anomalies, plotted only where the local correlation of either wind component is statistically significant at the 99% level (reproduced from Wheeler *et al.*, 2000).

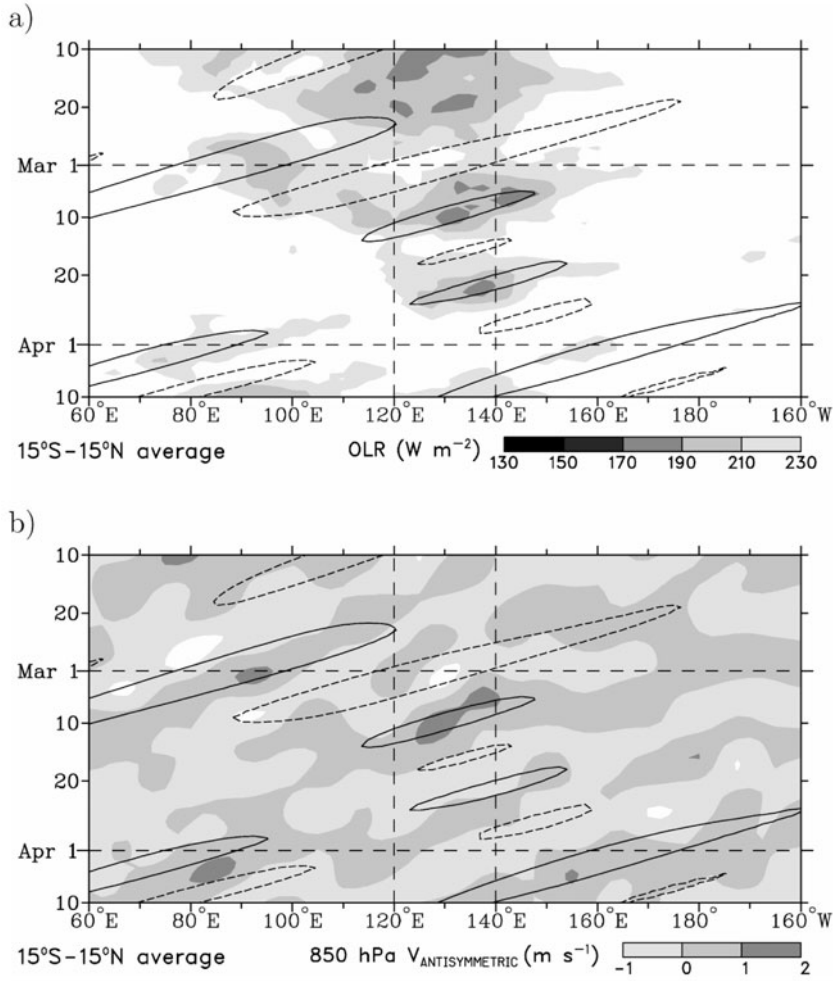

Figure 5.15. (a) Time–longitude plot of 3-day running mean total OLR (shading) and $n = 1$ ER wave filtered OLR (contours) averaged from 15°S to 15°N for a 2-month period in 1984. The contour interval for filtered anomalies is 10 W m^{-2}, with the positive contour dashed and the zero contour omitted. (b) As in (a), except showing shading for the antisymmetric component of the 10 to 90-day bandpass-filtered 850 hPa meridional wind $[(V_{\text{north}} - V_{\text{south}})/2]$.

context of rapid eastward components embedded within the MJO. They need not always be associated with the MJO, however, as has been shown by Dunkerton and Crum (1995) and Wheeler and Kiladis (1999).

An example case period for convectively coupled Kelvin waves is shown in Figure 5.17. The first panel is a time series of area-averaged OLR over the period from late 1997 to mid 1998. Crosses are drawn for days when Kelvin wave filtered OLR (as in Wheeler and Kiladis, 1999) reaches a value less than −15 W m^{-2}. Despite

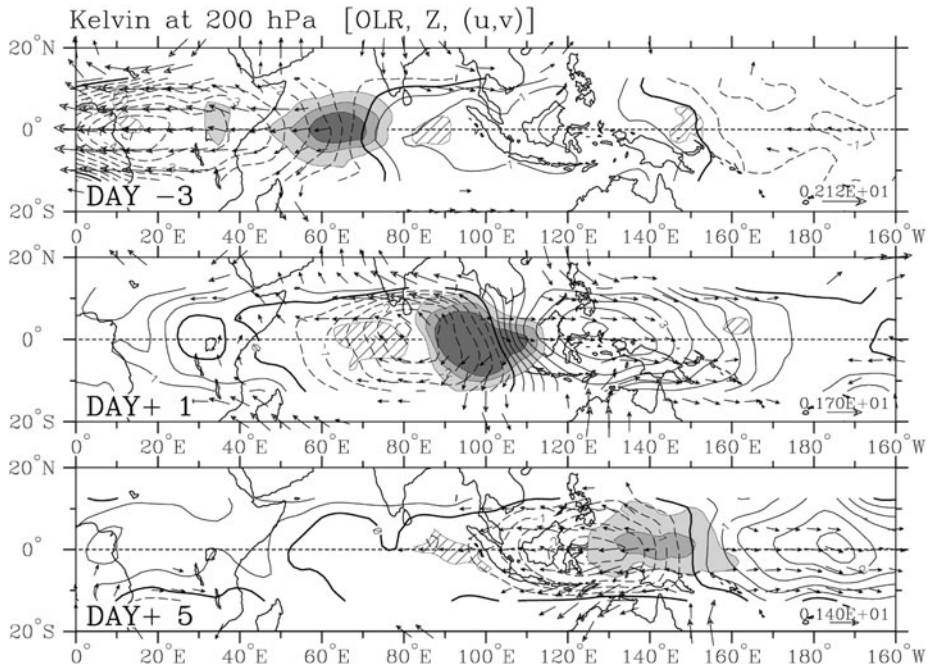

Figure 5.16. As in Figure 5.14, except for the convectively coupled Kelvin wave. The contours of 200 hPa geopotential height (contour interval of 0.5 m) and 200 hPa wind vector anomalies are shown using the Kelvin wave filtered OLR series at 0°S, 90°E (reproduced from Wheeler *et al.*, 2000).

the fact that OLR is generally higher than the climatology, owing to the occurrence of the strong 1997/1998 El Niño, Kelvin wave episodes correspond quite well with total area-averaged convective variations during this whole period. Concentrating on the three episodes during January and February, the latter two panels (Figure 5.17b, c) give a clear indication of the fast eastward propagation of the waves, not only in convection (Figure 5.17b) but in the intraseasonally filtered zonal wind field as well (Figure 5.17c). As calculated by Wheeler *et al.* (2000), February through July is typically the time that such Kelvin waves are most active near Indonesia.

Besides the contribution of variance from the abovementioned "modes" of ISV, there may also be a significant source of intraseasonal variance originating from tropical cyclones (TCs). Though these systems are primarily considered "synoptic" in both time and space (~5 days, ~1,000 km), their large-amplitude perturbations can significantly project onto lower frequencies and the largest scales as well. The same can be said for any other large-amplitude non-periodic "weather"-like disturbance. Thus, for example, Gunn *et al.* (1989) and Webster and Houze (1991) noted the simultaneous existence of a number of cyclones and monsoon depressions during the AMEX–EMEX experiments, and while present they dominated the structure of large-scale flow. Moreover, in examining the large-scale flow averaged over the 1978/1979 season, McBride (1987) noted that the location of the mean

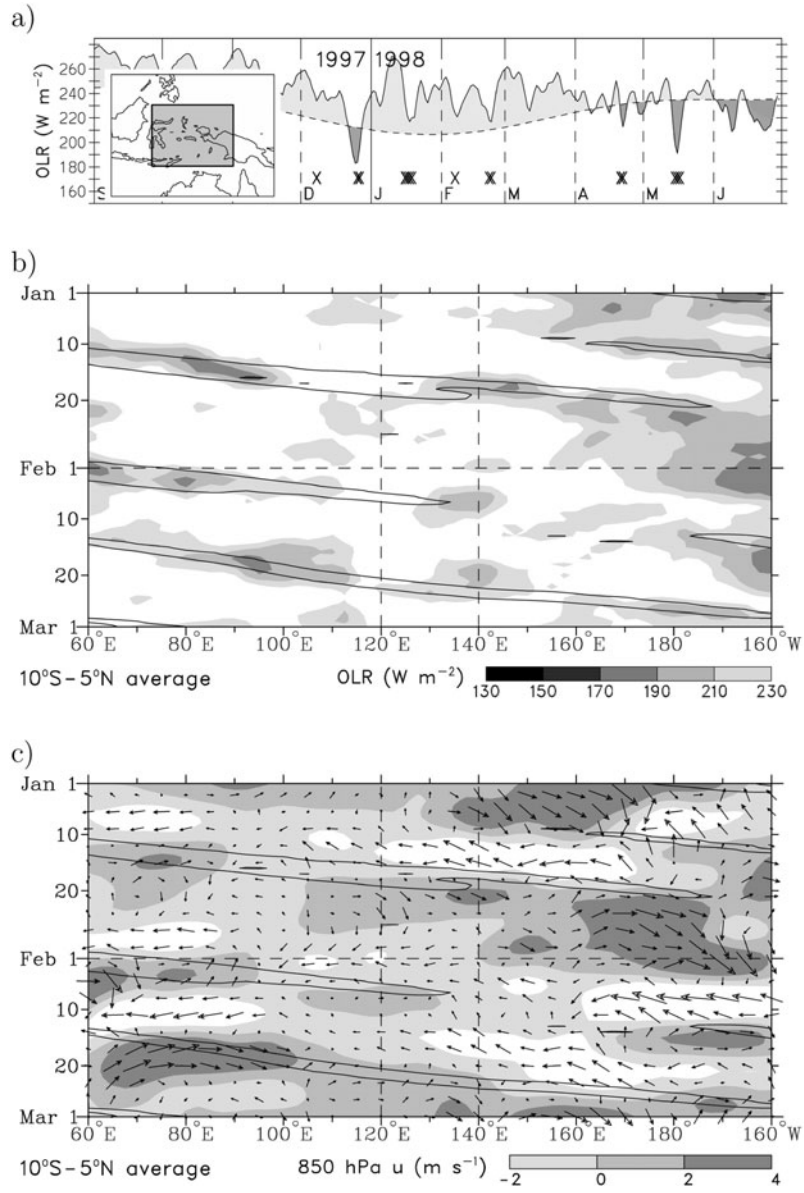

Figure 5.17. (a) As in Figure 5.2, except for OLR averaged over the box from 10°S to 5°N and 120°E to 140°E. The monsoon period covers just 1997/1998. Also shown are crosses marking the days on which the Kelvin wave filtered component of area-averaged OLR reaches a value of less than $-15\,\mathrm{W\,m^{-2}}$. (b) As in Figure 5.15a, except for a 2-month period in 1998, an average from 10°S to 5°N, and showing contours (negative only; the contour interval is $15\,\mathrm{W\,m^{-2}}$) of the Kelvin wave filtered OLR. (c) As in (b), except showing shading for the 10 to 90-day bandpass-filtered 850 hPa zonal wind and vectors for the 10 to 90-day filtered 850 hPa total wind.

upper-level velocity potential maximum (or center of large-scale divergent outflow) was within 6° longitude of the genesis location of five TCs. Thus, McBride hypothesized that a major contribution to the 3-month mean velocity potential map came from these cyclones, amounting to a projection of these synoptic-scale events on to the large-scale low-frequency structure. It is possible, however, that such observations are the result of ISV modulating TCs, rather than the reverse (as discussed in Section 5.10).

Another potential source of ISV within the Australasian–Indonesian monsoon region is the cross-equatorial influence of cold surges in the South China Sea. Occurring during the northern hemisphere winter, these surges are characterized by periods (of the order of several days) of strong northerly winds, anomalously low temperatures, and an increase in surface pressure from the East Asian continent to the South China Sea (e.g., Lau and Chang, 1987). Compo *et al.* (1999) found submonthly (6 to 30-day) timescale surges were directly related to convective activity south of Indonesia. Sumathipala and Murakami (1988), on the other hand, found no contribution of lower frequency, 30 to 60-day, northerly surges of East Asian origin to convection in the Australasian monsoon. Instead, they found a contribution from northeasterly flows originating in the subtropical North Pacific. Further examples of extratropical influences on ISV of the region are discussed in Section 5.11.

5.10 MODULATION OF TROPICAL CYCLONES

Much interest exists in the intraseasonal modulation of TCs due to their obvious large impact on society and the potential for applying that modulation for intraseasonal prediction of TC activity. Early results pertaining to the modulation of TCs by ISV in the region were presented by Liebmann *et al.* (1994). They looked specifically at modulation by the MJO across the Indian and Western Pacific Oceans, a broad region that includes the Australasian monsoon region. They computed an approximately 2 : 1 modulation of the occurrence of TCs using a 35 to 95-day filtered definition of the MJO (i.e., TCs were found to occur twice as often during the enhanced convective phase of the MJO compared with the opposite phase). The hypothesis for such a modulation is that the MJO alters "climatologically favorable factors" for TCs (warm sea surface temperatures, large values of absolute vorticity in the lower troposphere, weak vertical wind shear, high mid-level humidity, mean upward motion; Gray, 1979) on scales that are large enough and long enough to significantly influence TC development and TC lifespan.

Further results on the modulation of southern hemisphere TCs by the MJO were presented by Hall *et al.* (2001) and Bessafi and Wheeler (2006). Hall *et al.* defined four different categories of the MJO and found the TC modulation to be as great as 4 : 1 to the northwest of Australia and 3 : 1 to the northeast, considerably greater than the overall 2 : 1 result of Liebmann *et al.* (1994). Figure 5.18 demonstrates this modulation using the Wheeler and Hendon (2004) RMM definition of MJO phases. During the "weak MJO" category, TC tracks are evenly spread across the ocean basins and, when taking into account the number of days in the category, the chance

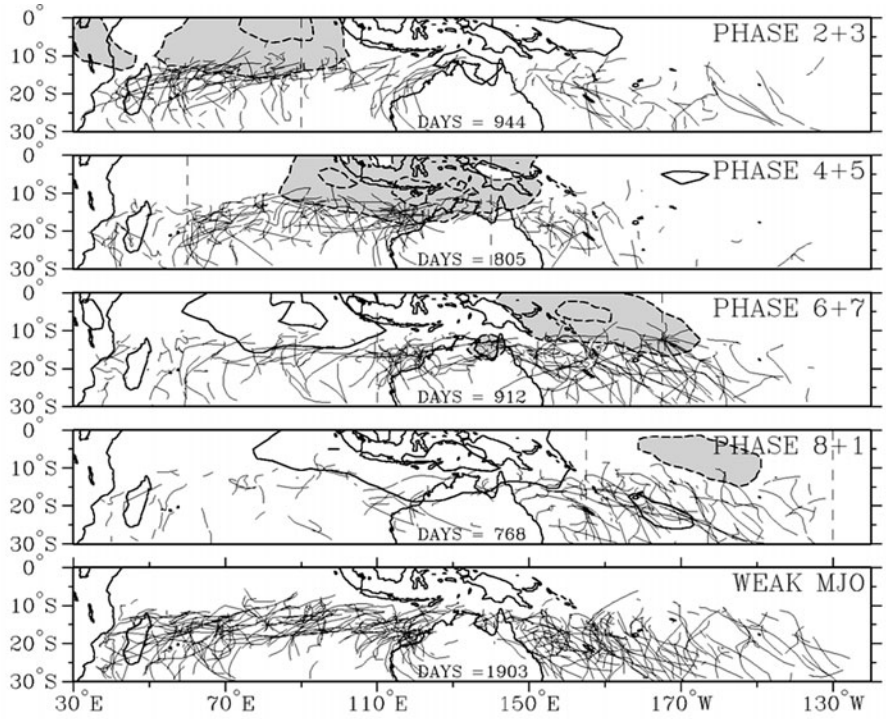

Figure 5.18. Tropical cyclone (TC) tracks (defined using a threshold of estimated central pressure of 995 hPa) stratified according to the phase of the MJO as described by the RMM index of Wheeler and Hendon (2004). November through April data used for years from 1974 to 2003. "Weak MJO" refers to days when the amplitude of the (RMM1, RMM2) vector is less than 1.0. The number of days counted within each of the MJO categories is provided. Also shown (with contours and shading) is the composite OLR anomaly for the corresponding MJO phases: the contour interval is 10 W m^{-2}, with negative contours dashed, the zero contour omitted, and values less than -10 W m^{-2} shaded.

of TC occurrence is not significantly altered from normal. During MJO phase categories, on the other hand, there is a shift in the location of TC tracks from the west to east which follows the shift in convection (as indicated by negative OLR anomalies) with the MJO. To the west of Australia (west to about 90°E), TC occurrence is significantly enhanced in phases 4 and 5 and reduced in phases 8 and 1. To the east of Australia (east to about the dateline), TC occurrence is significantly enhanced in phases 6 and 7. When compared with composite OLR anomalies (see also Figure 5.8), TC genesis locations tend to cluster slightly poleward and westward of the main large-scale equatorial convective anomaly. It is there that the low-level cyclonic vorticity anomalies of the MJO tend to be greatest. This is consistent with the fact that the low-level cyclonic anomalies were found by Hall *et al.* (2001) to provide the best match (of the variables they considered) with variations in TC activity.

Application of this MJO–TC connection to forecast TC activity has been made by Leroy and Wheeler (2008). Using the RMM indices as predictors, together with the seasonal cycle and large-scale sea surface temperatures (SSTs), Leroy and Wheeler demonstrated the skill obtainable from statistical predictions of TC activity. In particular, they made forecasts of the probability of TC genesis and occurrence in specified domains for weeks 1, 2, 3, and 4, showing usable skill up to week 3 (see also Vitart *et al.*, 2010).

The mechanism involved in the MJO's modulation of TCs was systematically studied by Camargo *et al.* (2009). Using the genesis potential (GP) index of Emanuel and Nolan (2004), Camargo *et al.* (2009) found that—of the four environmental variables that enter the GP index—mid-level relative humidity is the most important for MJO-associated variations. The second most important is low-level absolute vorticity, and only very minor contributions come from vertical wind shear and potential intensity (which is a function of SST).

Other forms of ISV, besides the MJO, have also been found to modulate TCs. Liebmann *et al.* (1994) computed the modulation by a higher frequency band than the MJO and found a similar relationship (i.e., with more TCs occurring during the convectively active phase of ISV). Hence, they suggested that any form of low-frequency large-scale (relative to the TC) variability, that alters the dynamical factors favorable for cyclogenesis, can modulate TC activity. In fact, investigation of the modulation of TCs by other defined modes of ISV in the region is proving to be a fruitful avenue of current research. Of those modes, the convectively coupled $n = 1$ ER wave has been found to provide the most significant modulation (e.g., Bessafi and Wheeler, 2006; Frank and Roundy, 2006), in accordance with its relatively large-amplitude perturbations in low-level vorticity.

5.11 EXTRATROPICAL–TROPICAL INTERACTION

A number of papers have presented evidence that the extratropics have an effect on convection in the Australasian monsoon. In their study of monsoon onset during winter MONEX, Davidson *et al.* (1983) suggested that the trigger mechanism lies in the evolution of highs and lows over the oceans to the south and west of Australia. In particular, they hypothesized that "prior to onset the seasonal buildup of planetary-scale land–sea temperature gradients has reached a critical stage such that the troposphere is in a state of readiness for the monsoon. Before the onset can take place, however, it must wait for the southern hemisphere midlatitude traveling highs and lows to be in such a configuration that trade wind easterlies are prevalent across the Australian continent" (Davidson *et al.*, 1983). While not invoking the exact same mechanism, 20 years later Hung and Yanai (2004) also listed the "intrusion of midlatitude troughs" as one of the four major factors contributing to onset of the Australian monsoon. Other evidence for a role played by extratropical systems was discussed in Keenan and Brody (1988). They showed evidence for modulation of tropical convection by upper-level troughs in the higher latitude westerly flow. More recently, Davidson *et al.* (2007) provided a

general framework for interpreting these extratropical influences, with the suggested key being high-latitude cyclogenesis over the southwest Indian Ocean.

Several of the case studies for the year of the AMEX–EMEX experiments also provide evidence for an influence from the extratropics. McBride and Frank (1999) found that the AMEX break period coincided with horizontal advection of dry air from higher latitudes at the levels of the mid to lower troposphere. Danielsen (1993) proposed that the passage of midlatitude cold fronts south of the Australian continent spreads cold air northward across the continent which in turn interacts with the continental-scale sea breeze lying across the northern part of the continent. Such a description bares much similarity to that for the South China Sea cold surges mentioned in Section 5.9 above (see also Love, 1985). Danielsen showed that changes in lower tropospheric stability and low-level convergence—factors that contribute to the triggering of convection—were synchronized with the passage of these higher latitude cold fronts.

None of the abovementioned observational papers on the extratropics influencing the tropics discriminates between "synoptic" and "intraseasonal" timescales, however. Another note is that—even though they are consistent in the view that tropical convection responds to higher latitude systems—there appears little consistency from paper to paper on the actual mechanisms involved. Besides the gravity current–like mechanism involved in the propagation of low-level cold surges to the equator (e.g., Love, 1985; Compo *et al.*, 1999; Section 5.9), one other obvious theoretically derived mechanism is the meridional propagation of upper-level extratropical Rossby wave energy into the tropics. Although such Rossby wave propagation should primarily be limited to regions of upper-level westerlies (e.g., Webster and Holton, 1982), eastward-moving extratropical forcings have been shown to be capable of generating an equatorial response in the presence of upper-level easterlies, as is the case in the Australasian region (Hoskins and Yang, 2000). This mechanism was invoked by Straub and Kiladis (2003), when explaining the observed connection between eastward extratropical Rossby wave activity in the southern hemisphere subtropical jet and the initiation of convectively coupled Kelvin waves over Indonesia. Another theoretical mechanism is found in the work of Frederiksen and Frederiksen (1997). Based on normal mode analysis employing the basic state of January 1979, they demonstrated a link between intraseasonal activity in the Australasian monsoon and baroclinic instability of the higher latitude flow. Little has been done, however, to employ this latter theoretical mechanism in understanding the observations of ISV in the monsoons.

We turn now to influence in the opposite direction (i.e., the influence of the tropics on the extratropics). Here we concentrate our discussion on the near-field response, specifically near the longitudes of Australia. The interaction most commonly noted in the early monsoon-specific papers is the southward shift in the location of the southern hemisphere subtropical jet at the time of monsoon onset. This was first shown by Troup (1961) and later by Murakami and Sumi (1982), McBride (1983), Davidson *et al.* (1983), and Hendon and Liebmann (1990a). Again, however, these results only apply to ISV to the extent that monsoon onset is occurring on the intraseasonal timescale.

Since those early papers, more specific work has been done on the extratropical response to tropical convection on the intraseasonal timescale. Among the most pertinent work is that of Kiladis and Weickmann (1992), Berbery and Nogués-Paegle (1993), and Tyrrell *et al.* (1996). As is well documented in the review by Kiladis and Mo (1998), the strong relationship between tropical convection and the Australian subtropical jet, as described for the monsoon onset above, holds for the intraseasonal timescale of the MJO (namely, 30 to 80 days) as well. During the phase of the MJO when convection is at the longitudes of northern Australia (phase 5 in Figure 5.8), the response at the 200 hPa level (in summer) is that of an anomalous anticyclone centered at the latitude of about 30°S and stretching in the zonal direction from the central Indian Ocean to Australia (not shown) (i.e., an upper-level anticyclone located poleward and westward of tropical heating, not too dissimilar to the response expected from the theoretical equilibrium solution of Gill, 1980). When compared with the seasonal mean flow in summer, this represents an expansion of upper-level equatorial easterlies, and a strengthening of the jet south of 30°S. At higher intraseasonal frequencies than the MJO (namely, less than 30 days), the result appears similar, albeit more localized near the region of convection (Kiladis and Weickmann 1992, 1997).

Another example of tropical–extratropical interaction that has been mentioned in this chapter is the extratropical cloudiness signal in southern and central Australia placed to the southeast of the main tropical convective signal of the MJO (as seen in Figure 5.8, phases 3 and 4). This extratropical cloud signature is associated with enhanced rainfall in these locations (Wheeler and Hendon, 2004; Wheeler *et al.*, 2009) and bears a resemblance to what is commonly known as a northwest Australian cloud band. Although northwest cloud bands may occur in any season, the link to the MJO appears strongest in the summer (Wheeler *et al.*, 2009). In Figure 5.8 the cloud band can be seen to be accompanied by anomalous northerly winds at the 850 hPa level, and at the 500 hPa level the northerlies are associated with a mid-latitude wavetrain emanating from the tropical Indian Ocean (Wheeler *et al.*, 2009). This suggests a role for moisture transport from the tropics for this enhanced extratropical rainfall, induced by a tropically forced extratropical Rossby wavetrain. As with all work on extratropical–tropical interaction processes, however, configuration of the basic state appears to be crucial for the timing and location of this extratropical impact. Consistent with this notion, Wheeler *et al.* (2009) found the extratropical response to the MJO to be highly seasonally dependent.

5.12 PREDICTION

ISV prediction has received an upswing in attention in the last 5–10 years, and now there are a number of prediction products routinely available that have relevance for the Australasian monsoon region. One example product that has already been mentioned is the statistical forecasts of weekly TC activity of Leroy and Wheeler (2008). This prediction product has filled some of the gap that has traditionally

existed between the high-resolution numerical forecasts of TCs that extend out several days and seasonal TC prediction products. It has now been available through the World Wide Web for a number of years (*http://www.meteo.nc/espro/previcycl/cyclA.php*). The original Leroy–Wheeler scheme produced probabilistic forecasts of TC genesis and occurrence in four zones across the southern hemisphere, but it has since been improved to provide forecasts for an overlapping grid and has been shown to provide comparable skill with a modern extended range numerical forecast model (Vitart *et al.*, 2010).

Leroy–Wheeler TC forecasts concentrate on one specific aspect of ISV (i.e., intraseasonal modulation of TCs). More generally, it is also of great interest to forecast intraseasonal monsoon bursts and breaks. Given the prominence of the MJO on the intraseasonal timescale, most effort has concentrated on it. The MJO also provides the greatest source of predictability on this timescale, with estimates suggesting the theoretical predictability limit for the MJO should be greater than 30 days (Waliser, 2005).

One of the first intraseasonal prediction products to become routinely available for forecasters in the region was that of Wheeler and Weickmann (2001). Using Fourier filtering in two dimensions applied to satellite OLR data, the scheme extrapolates the signals of the MJO and convectively coupled equatorial waves forward in time as a forecast. Useful intraseasonal skill is achievable for the MJO with convectively coupled equatorial waves providing much shorter range skill due to their high frequency. Nevertheless, the diagnosis of both the MJO and convectively coupled equatorial waves employing this technique has remained useful for forecasters in the region as an additional piece of input for their forecast process.

Another frequently applied tool for intraseasonal forecasting in the Australasian monsoon region is the RMM index of Wheeler and Hendon (2004). Although it does not provide predictions in itself, it does when coupled with other statistical and/or numerical models. One natural extension of the RMM index is the generation of forecasts using lagged linear regression with RMM1 and RMM2 as predictors. This is described and tested by Jiang *et al.* (2008), with a version provided through the World Wide Web at *http://cawcr.gov.au/staff/mwheeler/maproom/RMM/*. Forecast fields include maps of OLR and wind anomalies associated with the MJO. As with most MJO-based forecast products, the skill is greatest in the Australasian monsoon region during austral summer.

The RMM index has also been used for tracing the MJO in the output of global numerical prediction models. The numerical model output fields of OLR and zonal winds are projected onto the same EOF spatial structures derived by Wheeler and Hendon (2004), as shown here in Figure 5.7a. It is then possible to more easily see the predicted future evolution of the MJO in those numerical models. Two websites currently exist that show this forecast information (*http://www.cpc.noaa.gov/products/precip/CWlink/MJO/CLIVAR/clivar_wh.shtml* and *http://tparc.mri-jma.go.jp/TIGGE/tigge_MJO.html*); the practice of using this display in the decision process for weather forecasters in Australasia is becoming widespread. Forecasters combine these forecasts of the phase and amplitude of the MJO with their local knowledge of

its impacts (e.g., Hidayat and Kizu, 2009; Wheeler *et al*., 2009). Statistical forecasts of the RMM index are also available (e.g., Maharaj and Wheeler, 2005; Seo *et al*., 2009).

5.13 CONCLUSIONS

This chapter has reviewed and discussed research on the intraseasonal variability (ISV) of the Australasian monsoon region, concentrating on the extended austral summer season. As with other monsoon regions, there is a significant body of older literature addressing active and break periods of the monsoon. Since the realization in the late 1980s of the importance of the Madden Julian Oscillation (MJO) in the monsoon, there is some confusion in the literature as to the relationship between active–break cycles and the MJO. Hence, a large component of this chapter has addressed this issue.

In consideration of the research presented in this review, the following key points can be made:

(1) Compared with other frequency bands, the seasonal cycle, and other regions of the globe, the intraseasonal frequency range has a large amplitude in the Australasian monsoon. Consequently, the presence of ISV appears necessary for many of the defining characteristics of the monsoon (e.g., the monsoon's sudden onset, its breaks, and deep westerly bursts).
(2) The frequency-only power spectra of most monsoon parameters (excluding rainfall) show the robust signature of the MJO, but are otherwise predominantly "red" with no spectral gap between intraseasonal and higher frequencies with which to distinguish them. There is, however, high coherence between monsoon parameters (e.g., zonal wind vs. rain) on intraseasonal scales, particularly beyond a period of 20 days, which is not seen at higher frequencies. This high coherence provides a dynamical distinction for the intraseasonal frequency range.
(3) The phase of the zonal wind vs. rain cross-spectra demonstrates the similarity in structure between the seasonal cycle and ISV (i.e., both frequency bands share the useful and traditional concept of a two-state system: wet westerlies vs. dry easterlies). This disappears at higher frequencies and provides a further point of distinction for the intraseasonal frequency range.
(4) Convection studies over northern Australia have revealed that, while large-scale monsoon bursts involve more rain, the individual convective cells within the bursts are generally less intense than their counterparts in the breaks.
(5) The MJO is the strongest mode of ISV within the Australasian region, with a discernible impact on many aspects of the monsoon. For rainfall, the greatest MJO-associated anomalies occur over far northern Australia and the seas to its north, with new research showing a relatively smaller signal over the islands of Sumatra, Borneo, Java, Sulawesi, and New Guinea owing to the complications of topography and the diurnal cycle.

(6) Using the framework of the Wheeler–Hendon (RMM1, RMM2) measure of the MJO, the influence of the MJO on ISV can be quantified. Case studies of the 1983/1984 and 1987/1988 summers reveal large differences. The 1987/1988 season was characterized by three large-amplitude intraseasonal events which corresponded to cycles of the MJO. In contrast the 1983/1984 summer had a similar level of ISV activity, but no strong MJO signal.

(7) There have been a number of studies of the influence of the MJO on monsoon onset with conclusions ranging from "no MJO influence" to "a one-to-one correspondence with MJO passage". We discuss the methodologies of each of them. Using the (RMM1, RMM2) framework we show onset almost always occurs across Wheeler–Hendon phases 4–7, which can be interpreted as the locally active half of the MJO cycle. Thus, it appears that, while the planetary-scale MJO is limiting monsoon onset to within its active half-cycle lasting for a few weeks, the actual day of onset is set by other shorter timescale phenomena.

(8) Other well-defined modes of ISV also exist and have an impact in the region. Of particular note are the convectively coupled Kelvin and $n = 1$ ER waves, both of which can be identified in plots of total fields in some illustrative cases. Many cases of the sometimes westward propagation of large-scale convection over the region can be identified with ER waves.

(9) Besides that accounted for by the abovementioned modes of tropical ISV, there is still much variance in the intraseasonal band. Given its close correspondence to the red spectrum of a lag 1 autoregressive model, some of this variance appears best described as simply a consequence of the continuum of scales from "weather" to "climate". An isolated TC, for example, given its large amplitude, will project significantly onto intraseasonal frequencies.

(10) The intrusion of disturbances and energy from the extratropics is yet another source of ISV in the Australasian monsoon. Likewise, there is an influence of the region's tropical ISV on the extratropics.

(11) The intraseasonal modulation of TCs provides an interesting avenue for our dynamical understanding and application for extended range TC forecasts.

(12) The increased understanding of ISV in the Australasian monsoon has led to a new era of application work focusing on ISV prediction, with many ISV prediction products now available.

5.14 REFERENCES

Berbery, E. H. and J. Nogués-Paegle (1993) Intraseasonal interactions between the Tropics and extratropics in the Southern Hemisphere. *J. Atmos. Sci.*, **50**, 1950–1965.

Berlage, H. P. (1927) *East-Monsoon Forecasting in Java* (Verhandelingen No. 20). Koninklijk Magnetisch en Meteorologisch Observatorium te Batavia, 42 pp.

Bessafi, M. and M. C. Wheeler (2006) Modulation of south Indian Ocean tropical cyclones by the Madden–Julian oscillation and convectively-coupled equatorial waves. *Mon. Wea. Rev.*, **134**, 638–656.

Bowman, D. M. J. S., G. K. Brown, M. F. Braby, J. R. Brown, L. G. Cook, M. D. Crisp, F. Ford, S. Haberle, J. Hughes, Y. Isagi *et al.* (2009) Biogeography of the Australian monsoon tropics. *J. Biogeogr.*, **37**(2), 201–216.

Braak, C. (1919) *Atmospheric Variations of Short and Long Duration in the Malay Archipelago and Neighbouring Regions, and the Possibility to Forecast Them* (Verhandelingen No. 5). Koninklijk Magnetisch en Meteorologisch Observatorium te Batavia, 57 pp.

Camargo, S. J., M. C. Wheeler, and A. H. Sobel (2009) Diagnosis of the MJO modulation of tropical cyclogenesis using an empirical index. *J. Atmos. Sci.*, **66**, 3061–3074.

Compo, G. P., G. N. Kiladis, and P. J. Webster (1999) The horizontal and vertical structure of east Asian winter monsoon pressure surges. *Quart. J. Roy. Meteorol. Soc.*, **125**, 29–54.

Danielsen, E. F. (1993) In situ evidence of rapid, vertical irreversible transport of lower tropospheric air into the lower tropical stratosphere by convective cloud turrets and by large-scale upwelling in tropical cyclones. *J. Geophys. Res.*, **98**, 8665–8681.

Davidson, N. E. (1984) Short term fluctuations in the Australian monsoon during winter MONEX. *Mon. Wea. Rev.*, **112**, 1697–1708.

Davidson, N. E. and H. H. Hendon (1989) Downstream development in the Southern Hemisphere monsoon during FGGE/WMONEX. *Mon. Wea. Rev.*, **117**, 1458–1470.

Davidson, N. E., J. L. McBride, and B. J. McAvaney (1983) The onset of the Australian monsoon during Winter MONEX: Synoptic aspects. *Mon. Wea. Rev.*, **111**, 496–516.

Davidson, N. E., K. J. Tory, M. J. Reeder, and W. L. Drosdowsky (2007) Extratropical–tropical interaction during onset of the Australian monsoon: Reanalysis diagnostics and idealized dry simulations. *J. Atmos. Sci.*, **64**, 3475–3498.

de Boer, H. J. (1947) *On Forecasting the Beginning and End of the Dry Monsoon in Java and Madura* (Verhandelingen No. 32). Koninklijk Magnetisch en Meteorologisch Observatorium te Batavia, 20 pp.

Drosdowsky, W. (1996) Variability of the Australian summer monsoon at Darwin: 1957–1992. *J. Climate*, **9**, 85–96.

Dunkerton, T. J. and F. X. Crum (1995) Eastward propagating ∼2- to 15-day equatorial convection and its relation to the tropical intraseasonal oscillation. *J. Geophys. Res.*, **100**, 25781–25790.

Emanuel, K. A. and D. S. Nolan (2004) Tropical cyclone activity and global climate. Preprints of the *26th Conference on Hurricanes and Tropical Meteorology, Miami, FL*. American Meteorological Society, Boston, pp. 240–241.

Flinders, M. (1814) *A Voyage to Terra Australia*. G. & W. Nicol, London. (Edited reproduction available as *Terra Australis*, edited by Tim Flannery, and published by Text Publishing, Melbourne, in 2000.)

Frank, W. M. and J. L. McBride (1989) The vertical distribution of heating in AMEX and GATE cloud clusters. *J. Atmos. Sci.*, **46**, 3464–3478.

Frank, W. M. and P. E. Roundy (2006) The role of tropical waves in tropical cyclogenesis. *Mon. Wea. Rev.*, **134**, 2397–2417.

Frederiksen, J. S. and C. S. Frederiksen (1997) Mechanisms of the formation of intraseasonal oscillations and Australian monsoon disturbances: The roles of latent heat, barotropic, and baroclinic instability. *Contributions to Atmospheric Physics*, **70**, 39–56.

Gill, A. E. (1980) Some simple solutions for heat induced tropical circulations. *Quart. J. Roy. Meteorol. Soc.*, **106**, 447–462.

Gray, W. M. (1979) Hurricanes: Their formation, structure and likely role in the tropical circulation. In: D. B. Shaw (Ed.), *Meteorology over the Tropical Oceans*. Royal Meteorological Society, Bracknell, U.K., pp. 155–218.

Gunn, B. W., J. L. McBride, G. J. Holland, T. D. Keenan, N. E. Davidson, and H. H. Hendon (1989) The Australian summer monsoon circulation during AMEX Phase II. *Mon. Wea. Rev.*, **117**, 2554–2574.

Hall, J. D., A. J. Matthews, and D. J. Karoly (2001) The modulation of tropical cyclone activity in the Australian region by the Madden–Julian oscillation. *Mon. Wea. Rev.*, **129**, 2970–2982.

Hamilton, K., R. A. Vincent, and P. T. May (2004) Darwin Area Wave Experiment (DAWEX) field campaign to study gravity wave generation and propagation, *J. Geophys. Res.*, **109**, D20S01, doi: 10.1029/2003JD004393.

Hastenrath, S. (1987) Predictability of Java monsoon rainfall anomalies: A case study. *J. Climate Appl. Meteorol.*, **26**, 133–141.

Hayashi, Y. and T. Nakazawa (1989) Evidence of the existence and eastward motion of superclusters at the equator. *Mon. Wea. Rev.*, **117**, 236–243.

Hendon, H. H. and B. Liebmann (1990a) A composite study of onset of the Australian summer monsoon. *J. Atmos. Sci.*, **47**, 2227–2240.

Hendon, H. H. and B. Liebmann (1990b) The intraseasonal (30–50 day) oscillation of the Australian summer monsoon. *J. Atmos. Sci.*, **47**, 2909–2923.

Hendon, H. H. and B. Liebmann (1994) Organization of convection within the Madden–Julian oscillation. *J. Geophys. Res.*, **99**, 8073–8083.

Hendon, H. H. and M. L. Salby (1994) The life cycle of the Madden–Julian oscillation. *J. Atmos. Sci.*, **51**, 2225–2237.

Hendon, H. H., N. E. Davidson, and B. Gunn (1989) Australian summer monsoon onset during AMEX 1987. *Mon. Wea. Rev.*, **117**, 370–390.

Hendon, H. H., C. Zhang, and J. D. Glick (1999) Interannual variation of the Madden–Julian oscillation during austral summer. *J. Climate*, **12**, 2538–2550.

Hendon, H. H., E. Lim, and M. C. Wheeler (2011) Seasonal prediction of Australian summer monsoon rainfall. In: C.-P. Chang, Y. H. Ding, R. Johnson, G. N.-C. Lau, B. Wang, and T. Yasunari (Eds.), *The Global Monsoon System: Research and Forecast* (Second Edition) (World Scientific Series on Asia–Pacific Weather and Climate Vol. 5). World Scientific, Singapore, pp. 73–84.

Hidayat, R. and S. Kizu (2009) Influence of the Madden–Julian Oscillation on Indonesian rainfall variability in austral summer. *Int. J. Climatol.*, **30**, 1816–1825, doi: 10.1002/joc.2005.

Holland, G. J. (1986) Interannual variability of the Australian summer monsoon at Darwin: 1952–82. *Mon. Wea. Rev.*, **114**, 594–604.

Hoskins, B. J. and G.-Y. Yang (2000) The equatorial response to higher-latitude forcing. *J. Atmos. Sci.*, **57**, 1197–1213.

Hoyos, C. D. and P. J. Webster (2007) The role of intraseasonal variability in the nature of Asian monsoon precipitation. *J. Climate*, **20**, 4402–4424.

Hung, C.-W. and M. Yanai (2004) Factors contributing to the onset of the Australian summer monsoon. *Quart. J. Roy. Meteorol. Soc.*, **130**, 739–758.

Hunt, H. A., G. Taylor, and E. T. Quayle (1913) *The Climate and Weather of Australia*. Commonwealth Bureau of Meteorology, Melbourne, Australia, 93 pp.

Ichikawa, H. and T. Yasunari (2008) Intraseasonal variability in diurnal rainfall over New Guinea and the surrounding oceans during austral summer. *J. Climate*, **21**, 2852–2868.

Jiang, X., D. E. Waliser, M. C. Wheeler, C. Jones, M.-I. Lee, and S. D. Schubert (2008) Assessing the skill of an all-season statistical forecast model for the Madden–Julian oscillation. *Mon. Wea. Rev.*, **136**, 1940–1956.

Keenan, T. D. and L. R. Brody (1988) Synoptic-scale modulation of convection during the Australian summer monsoon. *Mon. Wea. Rev.*, **116**, 71–85.

Keenan, T. D. and R. E. Carbone (1992) A preliminary morphology of precipitation systems in tropical northern Australia. *Quart. J. Roy. Meteorol. Soc.*, **118**, 283–326.

Keenan, T. D. and S. A. Rutledge (1993) Mesoscale characteristics of monsoonal convection and associated stratiform precipitation. *Mon. Wea. Rev.*, **121**, 352–374.

Keenan, T., S. Rutledge, R. Carbone, J. Wilson, T. Takahashi, P. May, N. Tapper, M. Platt, J. Hacker, S. Sekelsky *et al.* (2000) The Maritime Continent Thunderstorm Experiment (MCTEX): Overview and some results. *Bull. Amer. Meteorol. Society*, **81**, 2433–2455.

Kiladis, G. N. (1998) Observations of Rossby waves linked to convection over the eastern tropical Pacific. *J. Atmos. Sci.*, **55**, 321–339.

Kiladis, G. N. and K. C. Mo (1998) Interannual and intraseasonal variability in the Southern Hemisphere. In: D. Karoly and D. Vincent (Eds.), *Meteorology of the Southern Hemisphere*. American Meteorological Society, Boston, pp. 307–336.

Kiladis, G. N. and K. M. Weickmann (1992) Circulation anomalies associated with tropical convection during northern winter. *Mon. Wea. Rev.*, **120**, 1900–1923.

Kiladis, G. N. and K. M. Weickmann (1997) Horizontal structure and seasonality of large-scale circulations associated with submonthly tropical convection. *Mon. Wea. Rev.*, **125**, 1997–2013.

Kiladis, G. N. and M. Wheeler (1995) Horizontal and vertical structure of observed tropospheric equatorial Rossby waves. *J. Geophys. Res.*, **100**, 22981–22997.

Kiladis, G. N., M. C. Wheeler, P. T. Haertel, K. H. Straub, and P. E. Roundy (2009) Convectively coupled equatorial waves. *Rev. Geophys.*, **47**, RG2003, doi: 10.1029/2008RG000266.

Knutson, T. R. and K. M. Weickmann (1987) 30–60 day atmospheric oscillations: Composite life cycles of convection and circulation anomalies. *Mon. Wea. Rev.*, **115**, 1407–1436.

Lau, K.-M. and P. H. Chan (1985) Aspects of the 40–50 day oscillation during the northern winter as inferred from outgoing longwave radiation. *Mon. Wea. Rev.*, **113**, 1889–1909.

Lau, K.-M. and P. H. Chan (1988) Intraseasonal and interannual variations of tropical convection: A possible link between the 40–50 day oscillation and ENSO? *J. Atmos. Sci.*, **45**, 506–521.

Lau, K. M. and C.-P. Chang (1987) Planetary scale aspects of the Winter monsoon and atmospheric teleconnections. In: C. P. Chang and T. N. Krishnamurti (Eds.), *Monsoon Meteorology*. Oxford University Press, Oxford, U.K., pp. 161–202.

Lawrence D. M. and P. J. Webster (2002) The boreal summer intraseasonal oscillation: Relationship between northward and eastward movement of convection. *J. Atmos. Sci.*, **59**, 1593–1606.

Leroy, A. and M. C. Wheeler (2008) Statistical prediction of weekly tropical cyclone activity in the Southern Hemisphere. *Mon. Wea. Rev.*, **136**, 3637–3654.

Liebmann, B., H. H. Hendon, and J. D. Glick (1994) The relationship between tropical cyclones of the western Pacific and Indian Oceans and the Madden–Julian oscillation. *J. Meteorol. Soc. Japan*, **72**, 401–412.

Lo, F., M. C. Wheeler, H. Meinke, and A. Donald (2007) Probabilistic forecasts of the onset of the north Australian wet season. *Mon. Wea. Rev.*, **135**, 3506–3520.

Love, G. (1985) Cross-equatorial influence of winter hemisphere subtropical cold surges. *Mon. Wea. Rev.*, **113**, 1487–1498.

Madden, R. A. and P. R. Julian (1971) Detection of a 40–50 day oscillation in the zonal wind in the tropical Pacific. *J. Atmos. Sci.*, **28**, 702–708.

Madden, R. A. and P. R. Julian (1972) Description of global-scale circulation cells in the tropics with a 40–50-day period. *J. Atmos. Sci.*, **29**, 1109–1123.

Madden, R. A. and P. R. Julian (1994) Observations of the 40–50-day tropical oscillation: A review. *Mon. Wea. Rev.*, **122**, 814–837.

Maharaj, E. A. and M. C. Wheeler (2005) Forecasting an index of the Madden-oscillation. *Int. J. Climatol.*, **25**, 1611–1618.

Manton, M. J. and J. L. McBride (1992) Recent research on the Australian monsoon. *J. Meteorol. Soc. Japan*, **70**, 275–284.

Mapes, B. and R. A. Houze, Jr. (1992) An integrated view of the 1987 Australian monsoon and its mesoscale convective systems, I: Horizontal structure. *Quart. J. Roy. Meteorol. Soc.*, **118**, 927–963.

Masunaga, H. (2007) Seasonality and regionality of the Madden–Julian oscillation, Kelvin wave, and equatorial Rossby Wave. *J. Atmos. Sci.*, **64**, 4400–4416.

Matsuno, T. (1966) Quasi-geostrophic motions in the equatorial area. *J. Meteorol. Soc. Japan*, **44**, 25–43.

Matthews, A. J. (2000) Propagation mechanisms for the Madden–Julian oscillation. *Quart. J. Roy. Meteorol. Soc.*, **126**, 2637–2652.

Matthews, A. J. and H. Y. Y. Li (2005) Modulation of station rainfall over the western Pacific by the Madden–Julian oscillation. *Geophys. Res. Lett.*, **32**, L14827, doi: 10.1029/2005GL023595.

May, P. T. and A. Ballinger (2007) The statistical characteristics of convective cells in a monsoon regime (Darwin, northern Australia). *Mon. Wea. Rev.*, **135**, 82–92.

May, P. T., J. H. Mather, G. Vaughan, K. N. Bower, C. Jakob, G. M. McFarquhar, and G. G. Mace (2008) The Tropical Warm Pool International Cloud Experiment. *Bull. Amer. Meteorol. Society*, **89**, 629–645.

May, P. and D. K. Rajopadhyaya (1999) Vertical velocity characteristics of deep convection over Darwin, Australia. *Mon. Wea. Rev.*, **127**, 1056–1071.

McBride, J. L. (1983) Satellite observations of the southern hemisphere monsoon during Winter MONEX. *Tellus*, **35A**, 189–197.

McBride, J. L. (1987) The Australian summer monsoon. In: C. P. Chang and T. N. Krishnamurti (Eds.), *Monsoon Meteorology*. Oxford University Press, Oxford, U.K. pp. 203–231.

McBride, J. L. (1995) Tropical cyclone formation. *Global Perspectives on Tropical Cyclones* (WMO Tech. Doc. WMO/TD 693). World Meteorological Organization, Geneva, pp. 63–105.

McBride, J. L. (1998) Indonesia, Papua New Guinea, and tropical Australia: The Southern Hemisphere monsoon. In: D. Karoly and D. Vincent (Eds.), *Meteorology of the Southern Hemisphere*. American Meteorological Society, Boston, pp. 89–99.

McBride, J. L. and W. M. Frank (1999) Relationships between stability and monsoon convection. *J. Atmos. Sci.*, **56**, 24–36.

McBride, J. L. and T. D. Keenan (1982) Climatology of tropical cyclone genesis in the Australian region. *J. Climatol.*, **2**, 13–33.

Meehl, G. A. (1987) The annual cycle and interannual variability in the tropical Pacific and Indian Ocean regions. *Mon. Wea. Rev.*, **115**, 27–50.

Murakami, T. and A. Sumi (1982) Southern Hemisphere monsoon circulation during the 1978–79 WMONEX, Part II: Onset, active and break monsoons. *J. Meteorol. Soc. Japan*, **60**, 649–671.

Murata, F., M. D. Yamanaka, H. Hashiguchi, S. Mori, M. Kudsy, T. Sribimawati, B. Suhardi, and Emrizal (2006) Dry intrusions following eastward-propagating synoptic-scale cloud systems over Sumatera island. *J. Meteorol. Soc. Japan*, **84**, 277–294.

Nakazawa, T. (1986) Mean features of 30–60 day variations as inferred from 8-year OLR data. *J. Meteorol. Soc. Japan*, **64**, 777–786.

Nakazawa, T. (1988) Tropical super clusters within intraseasonal variations over the western Pacific. *J. Meteorol. Soc. Japan*, **66**, 823–839.

Naylor, R. L., W. P. Falcon, D. Rochberg, and N. Wada (2001) Using El Nino/Southern Oscillation climate data to predict rice production in Indonesia. *Clim. Change*, **50**, 255–265.

Nicholls, N. (1981) Air–sea interaction and the possibility of long-range weather prediction in the Indonesian Archipelago. *Mon. Wea. Rev.*, **109**, 2435–2443.

Numaguti, A. (1995) Characteristics of 4- to 20-day-period disurbances observed in the equatorial Pacific during the TOGA COARE IOP. *J. Meteorol. Soc. Japan*, **73**, 353–377.

Pires, P., J.-L. Redelsperger, and J.-P. Lafore (1997) Equatorial atmospheric waves and their association to convection. *Mon. Wea. Rev.*, **125**, 1167–1184.

Pope, M., C. Jakob, and M. J. Reeder (2009) Regimes of the North Australian wet season. *J. Climate*, **22**, 6699–6715.

Rauniyar, S. P. and K. J. E. Walsh (2011) Scale interaction of the diurnal cycle of rainfall over the Maritime Continent and Australia: Influence of the MJO. *J. Climate*, **24**, 325–348.

Roundy, P. E. and W. M. Frank (2004) A climatology of waves in the equatorial region. *J. Atmos. Sci.*, **61**, 2105–2132.

Rutledge, S. A., E. R. Williams, and T. D. Keenan (1992) The Down Under Doppler and Electricity Experiment (DUNDEE): Overview and preliminary results. *Bull. Amer. Meteorol. Society*, **73**, 3–16.

Salby, M. L. and H. H. Hendon (1994) Intraseasonal behavior of clouds, temperature and motion in the Tropics. *J. Atmos. Sci.*, **51**, 2207–2224.

Seo, K.-H., W. Wang, J. Gottschalck, Q. Zhang, J.-K. Schemm, W. Higgins, and A. Kumar (2009) Evaluation of MJO forecast skill from several statistical and dynamical forecast models. *J. Climate*, **22**, 2372–2388.

Sikka, D. R. and S. Gadgil (1980) On the maximum cloud zone and the ITCZ over Indian longitudes during the southwest monsoon. *Mon. Wea. Rev.*, **108**, 1840–1853.

Slingo, J. M., D. P. Rowell, K. R. Sperber, and F. Nortley (1999) On the predictability of the interannual behavior of the Madden–Julian oscillation and its relationship with El Nino. *Quart. J. Roy. Meteorol. Soc.*, **125**, 583–609.

Straub, K. H. and G. N. Kiladis (2002) Observations of a convectively coupled Kelvin wave in the eastern Pacific ITCZ. *J. Atmos. Sci.*, **59**, 30–53.

Straub, K. H. and G. N. Kiladis (2003) Extratropical forcing of convectively coupled Kelvin waves during austral winter. *J. Atmos. Sci.*, **60**, 526–543.

Sumathipala, W. L. and T. Murakami (1988) Intraseasonal fluctuations in low-level meridional winds over the south China Sea and the western Pacific and monsoonal convection over Indonesia and northern Australia. *Tellus*, **A40**, 205–219.

Suppiah, R. (1992) The Australian summer monsoon: A review. *Progress in Physical Geography*, **16**, 283–318.

Takayabu, Y. N. (1994) Large-scale cloud disturbances associated with equatorial waves, Part I: Spectral features of the cloud disturbances. *J. Meteorol. Soc. Japan*, **72**, 433–448.

Takayabu, Y. N. and M. Murakami (1991) The structure of super cloud clusters observed on 1–20 June 1986 and their relationship to easterly waves. *J. Meteorol. Soc. Japan*, **69**, 105–125.

Tanaka, M. (1994) The onset and retreat dates of the austral summer monsoon over Indonesia, Australia and New Guinea. *J. Meteorol. Soc. Japan*, **72**, 255–267.

Troup, A. J. (1961) Variations in upper tropospheric flow associated with the onset of the Australian summer monsoon. *Indian J. Meteorol. Geophys.*, **12**, 217–230.

Tyrrell, G. C., D. J. Karoly, and J. L. McBride (1996) Links between tropical convection and variations of the extratropical circulation during TOGA COARE. *J. Atmos. Sci.*, **53**, 2735–2748.

Vitart, F., A. Leroy, and M. C. Wheeler (2010) A comparison of dynamical and statistical predictions of weekly tropical cyclone activity in the Southern Hemisphere. *Mon. Wea. Rev.*, **138**, 3671–3682.

Waliser, D. E. (2005) Predictability and forecasting. In: W. K. M. Lau and D. E. Waliser (Eds.), *Intraseasonal Variability in the Atmosphere–Ocean Climate System*. Springer/Praxis, Heidelberg, Germany/Chichester, U.K., pp. 389–423.

Waliser, D. E., K. M. Lau, W. Stern, and C. Jones (2003) Potential predictability of the Madden–Julian oscillation. *Bull. Amer. Meteorol. Society*, **84**, 33–50.

Wallace, A. R. (1891) *The Malay Archipelago; The Land of the Orang-utan and the Bird of Paradise; A Narrative of Travel with Studies of Man and Nature* (Tenth Edition), Macmillan & Co., London. (Reprinted as *The Malay Archipelago*, published by Periplus, Hong Kong in 2000.)

Wang, B. and H. Rui (1990) Synoptic climatology of transient tropical intraseasonal convection anomalies: 1975–1985. *Meteorol. Atmos. Phys.*, **44**, 43–61.

Webster, P. J. and J. R. Holton (1982) Cross-equatorial response to middle-latitude forcing in a zonally-varying basic state. *J. Atmos. Sci.*, **39**, 722–733.

Webster, P. J. and R. A. Houze, Jr. (1991) The Equatorial Mesoscale Experiment (EMEX): An overview. *Bull. Amer. Meteorol. Society*, **72**, 1481–1505.

Webster, P. J., V. O. Magana, T. N. Palmer, J. Shukla, R. A. Tomas, M. Yanai, and T. Yasunari (1998) Monsoons: Processes, predictability, and the prospects for prediction. *J. Geophys. Res.*, **103**, 14451–14510.

Weickmann, K. M. (1983) Intraseasonal circulation and outgoing longwave radiation modes during Northern Hemisphere winter. *Mon. Wea. Rev.*, **111**, 1838–1858.

Weickmann, K. M., G. R. Lussky, and J. E. Kutzbach (1985) Intraseasonal (30–60 day) fluctuations of outgoing longwave radiation and 250 mb streamfunction during Northern Winter. *Mon. Wea. Rev.*, **113**, 941–961.

Wheeler, M. C. and H. H. Hendon (2004) An all-season real-time multivariate MJO index: Development of an index for monitoring and prediction. *Mon. Wea. Rev.*, **132**, 1917–1932.

Wheeler, M. and G. N. Kiladis (1999) Convectively coupled equatorial waves: Analysis of clouds and temperature in the wavenumber–frequency domain. *J. Atmos. Sci.*, **56**, 374–399.

Wheeler, M. C. and J. L. McBride (2005) Australian–Indonesian monsoon. In: W. K. M. Lau and D. E. Waliser (Eds.), *Intraseasonal Variability in the Atmosphere–Ocean Climate System*. Springer/Praxis, Heidelberg, Germany/Chichester, U.K., pp. 125–173.

Wheeler, M. and K. M. Weickmann (2001) Real-time monitoring and prediction of modes of coherent synoptic to intraseasonal tropical variability. *Mon. Wea. Rev.*, **129**, 2677–2694.

Wheeler, M., G. N. Kiladis, and P. J. Webster (2000) Large-scale dynamical fields associated with convectively coupled equatorial waves. *J. Atmos. Sci.*, **57**, 613–640.

Wheeler, M. C., H. H. Hendon, S. Cleland, H. Meinke, and A. Donald (2009) Impacts of the Madden–Julian oscillation on Australian rainfall and circulation. *J. Climate*, **22**, 1482–1498.

Williams, M. (1981) Interhemispheric interaction during winter MONEX (Global Atmospheric Research Program). *Proceedings of the WMO International Conference on Early Results of FGGE and Large-Scale Aspects of its Monsoon Experiments* (N82-23851 14-47, 5 pp.).

Williams, E. R., S. A. Rutledge, S. G. Geotis, N. Renno, E. Rasmussen, and T. Rickenbach (1992) A radar and electrical study of tropical "hot towers". *J. Atmos. Sci.*, **49**, 1386–1395.

Wu, C.-H. and H.-H. Hsu (2009) Topographic influence on the MJO in the Maritime Continent. *J. Climate*, **22**, 5433–5448.

Yano, J.-I. and J. L. McBride (1998) An aqua-planet monsoon. *J. Atmos. Sci.*, **55**, 1373–1399.

Yasunari, T. (1979) Cloudiness fluctuations associated with the Northern Hemisphere summer monsoon. *J. Meteorol. Soc. Japan*, **57**, 227–242.

6

The oceans

William S. Kessler

6.1 INTRODUCTION

There is a very wide variety of intraseasonal variability (ISV) in the oceans, due to many different processes beyond forcing by tropical intraseasonal winds and heat fluxes. The main focus of this chapter, however, is on the upper-ocean response to the tropical atmospheric ISV discussed in the other chapters of this book and is most germane in this context. The prominent oceanic ISV signatures generated by other mechanisms (largely intrinsic to the ocean) and those found in other regions are briefly reviewed in Section 6.7.

Episodic wind events on intraseasonal timescales affect the ocean through three main mechanisms: increased evaporation, the generation of equatorial jets and waves that produce advective changes remotely, and enhanced mixing and entrainment. As Webster and Lukas (1992) note, these responses are proportional to the windspeed u, u^2, and u^3, respectively, and therefore depend very differently on the background wind and the structure of its variance. Much of the forcing by tropical intraseasonal oscillations (TISOs) occurs over the warm pools of the Indian and West Pacific Oceans where the thermocline is usually deeper than the mixed layer. Thus, the near surface density structure is relatively unconstrained by large-scale ocean dynamics and can easily be modulated by the winds and the heat and moisture fluxes due to the ISV, providing the opportunity for air–sea feedbacks, nonlinear effects, and the retention of an oceanic memory of previous forcing. The dynamic response depends on the thickness of the accelerating layer, which is a function both of background stratification and of local precipitation and mixing. Thus, a principal focus of this chapter (Sections 6.2 and 6.3) is the factors controlling upper-ocean stratification under rapidly changing windspeed and precipitation sufficient for salinity variation to determine the mixed layer depth. The correlation of the ISV of solar shortwave forcing with wind fluctuations can also lead to significant effects

W. K. M. Lau and D. E. Waliser (Editors), *Intraseasonal Variability in the Atmosphere–Ocean Climate System* (Second Edition).

on the mixed layer temperature structure, with a variety of consequences (Section 6.5 and Chapter 7).

Because most of the work on oceanic ISV has been done in the Pacific, while the Indian Ocean is relatively poorly sampled, the processes of the oceanic response are described in the Pacific context and factors specific to the Indian Ocean are discussed in Section 6.6.

Much of the interest in tropical ISV in recent years has concerned its possible interaction with the El Niño Southern Oscillation (ENSO) cycle, which has been a controversial element of the debate over the nature of ENSO. While coupled models without realistic ISV have been successful in reproducing aspects of ENSO statistics, it remains in question whether ENSO is a disturbance to a stable background state, in which case an initiating perturbation would be required, or is a self-sustained mode on an unstable background. After satellite sampling established the occurrence of strong Madden Julian Oscillation (MJO) events penetrating into the Western Pacific during the onset stages of El Niños, several mechanisms have been proposed by which rectification of intraseasonal forcing in the ocean could interact constructively with the ENSO cycle; these are discussed in Section 6.5. (see also Chapters 9 and 12 for additional discussion of ISV–ENSO interactions).

6.2 HEAT FLUXES

Intraseasonal ocean–atmosphere heat fluxes are discussed in several other parts of this book, especially Chapters 7, 10, and 11. This section will focus on changes in the structure of the ocean in response to those fluxes, especially within the West Pacific warm pool which has been extensively studied—see Godfrey *et al.*, 1998, for a review of the Tropical Ocean Global Atmosphere (TOGA) Coupled Ocean–Atmosphere Response Experiment (COARE) program. The West Pacific warm pool differs from most other open ocean regions because its heavy precipitation and generally weak winds mean that the seasonal background mixed layer depth is often controlled by salinity stratification. Net precipitation minus evaporation over the warm pool is $1\,\mathrm{m\,yr^{-1}}$ to $2\,\mathrm{m\,yr^{-1}}$ (Anderson *et al.*, 1996), leading to low surface salinity which plays a major role in determining the vertical stability of the warm pool. As a result, the thick warm layer above the thermocline can be split by a halocline and its lower part is thereby uncoupled from surface forcing. Much of the precipitation occurs during convection associated with TISO events, which also produce strong shortwave and windspeed variability as convective systems pass across the region (see Figure 1.2 and Chapter 7).

6.2.1 Salinity and the barrier layer

The isothermal layer beneath the halocline has become known as the "barrier layer" (Lukas and Lindstrom, 1991; Sprintall and Tomczak, 1992) since it inhibits the communication between the surface and the thermocline that dominates sea

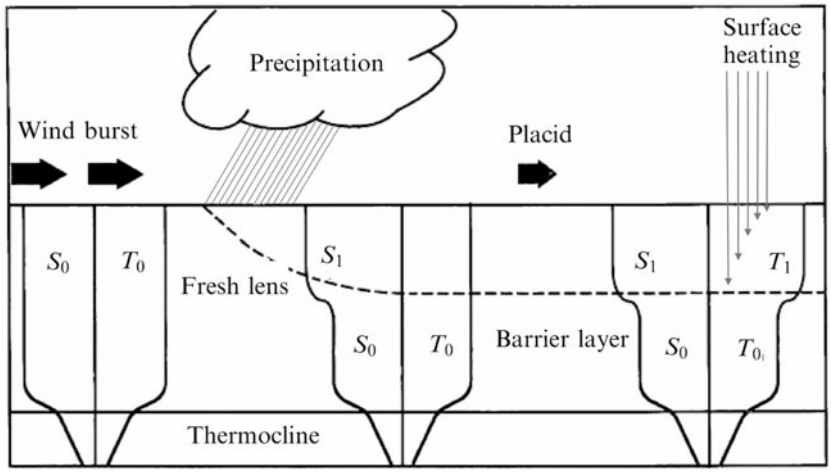

Figure 6.1. Schematic diagram showing the Lukas–Lindstrom "barrier layer" theory. During a strong wind burst, the surface mixed layer extends down to the top of the thermocline. Following the wind burst, the additional buoyancy from precipitation and strong surface heating act to form a relatively warm and fresh thin surface layer. Below this thin layer is a strong halocline, which effectively decouples surface forcing from deeper waters. Further heating is trapped by vertical mixing above the barrier formed by the halocline (after Anderson *et al.*, 1996).

surface temperature (SST) change in the central and eastern equatorial Pacific (e.g., Kessler and McPhaden, 1995b; Zhang, 2001). A thin mixed layer tends to trap surface fluxes of heat and momentum within it, enhancing both SST variability in response to heat fluxes and the acceleration of surface currents in response to winds. Figure 6.1 shows a schematic of barrier layer formation and erosion (Anderson *et al.*, 1996). Under strong winds, the upper layer can become well mixed down to the deep thermocline of the West Pacific (typically 150 m; e.g., Figure 6.2). Following heavy precipitation, as long as the winds are not strong enough to mix it away, a fresh lens can cap the top of the isothermal layer (Figure 6.1, middle). If this stratification is maintained, subsequent surface heating under clear skies will mostly occur within this relatively thin layer (≤ 50 m), because shortwave attenuation with depth is exponential (Figure 6.1, right), and will not be mixed over the entire above-thermocline layer, as would generally occur in other regions. However, if the surface layer is very thin, some radiation will penetrate into the barrier layer (see next section). Because the halocline inhibits mixing and because additional heating enhances its stability, the barrier layer tends to persist until winds (often in the form of intraseasonal westerlies) are strong enough to mix it away. Model experiments based on the situation during TOGA COARE suggest that the observed stratification produces close to the maximum possible SST: increased precipitation or weaker winds would result in a shallower mixed layer that would lose heat through its base by penetrative radiation, whereas decreased precipitation or

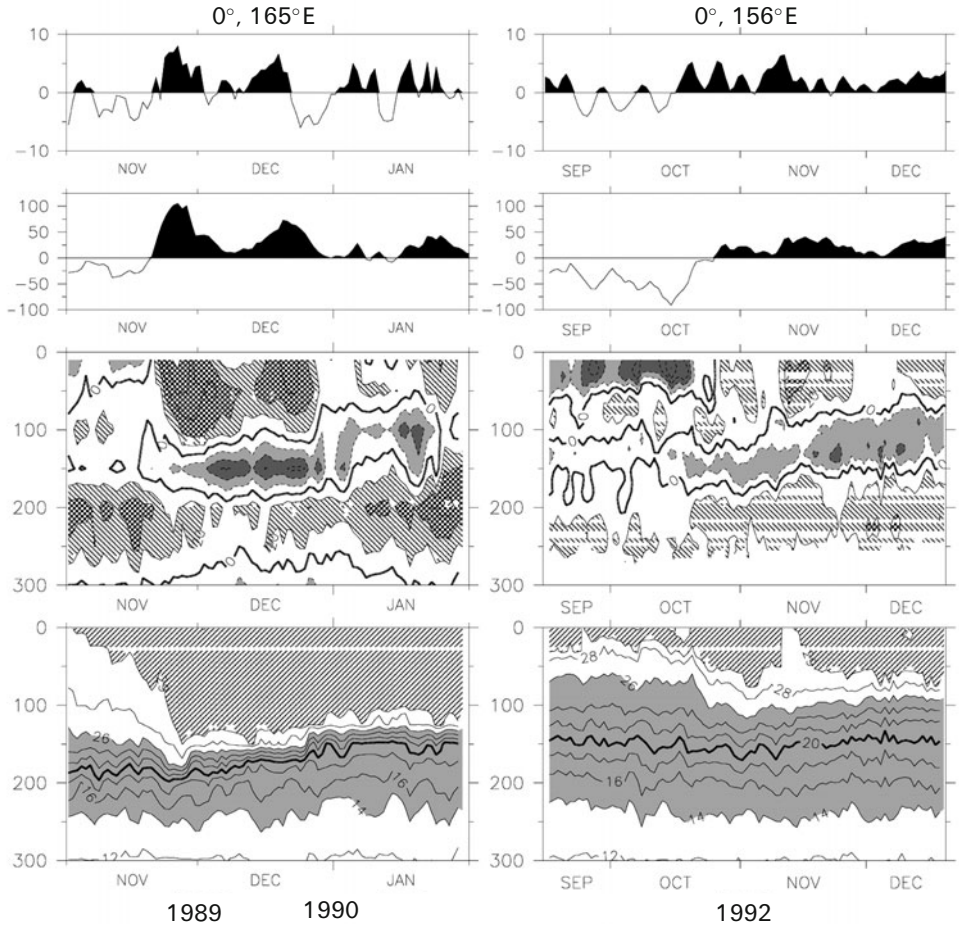

Figure 6.2. Zonal wind (top), 10-m zonal current (upper middle), zonal current (lower middle), and temperature (bottom) at 0°, 165°E during 1989–1990 (left panels) and at 0°, 156°E during 1992 (right panels). In the upper panels westerly winds and eastward currents are shaded. In the lower middle panels hatching indicates eastward currents, gray shading westward currents with a contour interval of 20 cm s^{-1}. In the bottom panels, hatching indicates temperatures greater than 29°C and gray shading indicates the thermocline with temperatures between 14°C and 26°C.

stronger winds would lead to fewer barrier layer occurrences and, thus, more entrainment cooling (Anderson *et al*., 1996). Recent work has suggested other mechanisms that can produce or intensify barrier layers on intraseasonal timescales. For example, since West Pacific surface salinity is lower than that farther east, if a rain-produced halocline and westerly winds lead to a surface-intensified eastward jet (see Section 6.3), then the resulting shear will tend to tilt the zonal salinity gradient by causing the fresh lens to run over the saltier eastern layer (Roemmich *et al*., 1994;

Cronin and McPhaden, 2002). Similarly, Ekman convergence in response to westerly winds can bring fresher northern hemisphere surface water to the equator (Cronin and McPhaden, 2002). However it is caused, the existence of a barrier layer enhances the local ocean response to both heat and momentum fluxes by concentrating it in a thin surface layer.

6.2.2 A 1-D heat balance?

Numerous studies have shown that, although advection can on occasion be important in determining near surface temperature change, a 1-D balance dominated by surface fluxes is the principal influence determining warm pool SST variability (McPhaden and Hayes, 1991; McPhaden *et al.*, 1992; Webster and Lukas, 1992; Sprintall and McPhaden, 1994; Anderson *et al.*, 1996; Cronin and McPhaden, 1997; Shinoda and Hendon, 1998, 2001; Zhang and McPhaden, 2000). The principal surface flux terms on intraseasonal timescales are latent heat flux, which varies mostly due to windspeed since the SST is always high (Cronin and McPhaden, 1997), and shortwave radiation, varying mostly due to the thick cloudiness of convective systems; both of these have strong signatures as TISO events pass across the region (Shinoda *et al.*, 1998). Since the highest windspeeds occur during westerly wind bursts (Weller and Anderson, 1996; Zhang and McPhaden, 2000), which are themselves associated with the convective phase of TISOs (Zhang, 1996; Shinoda and Hendon, 2002), the shortwave and latent heat flux terms are approximately in phase on intraseasonal timescales (Figure 7.1), and a convective event produces strong cooling (McPhaden *et al.*, 1988, 1992; Ralph *et al.*, 1997; Zhang and McPhaden, 2000). Figure 6.3 shows episodes of cooling under the intraseasonal westerly wind bursts during the growth of the 1997/1998 El Niño. The implications of net cooling of the far Western Pacific as a result of TISO events will be discussed in Section 6.5. In addition to attempts to directly estimate the heat balance terms, several types of overview evidence indicate the dominance of surface flux forcing in the upper-layer intraseasonal heat balance. First, the meridional scale of cooling under strong westerly winds has been observed to have the relatively broad scale of the wind, rather than that of the ocean dynamical response, which is more closely trapped to the equator (Ralph *et al.*, 1997; Shinoda and Hendon, 2001). Second, temperature anomalies subsequent to surface fluxes associated with the MJO are observed to propagate downwards and are not in phase with deeper temperature variability (Zhang, 1997).

Entrainment from below might also contribute to SST change in a 1-D balance, and this has been considered by several investigators, although it cannot be measured directly and is often inferred from the residual of other terms (e.g., McPhaden and Hayes, 1991; Cronin and McPhaden, 1997). Entrainment could be fostered by dynamical processes like Ekman divergence–caused upwelling bringing cooler water within the reach of wind mixing, as occurs in the Eastern Pacific, or due to wind mixing itself against shallow stratification (e.g., mixing away a halocline and exposing a cooler barrier layer as would occur in Figure 6.1). The thickness of the

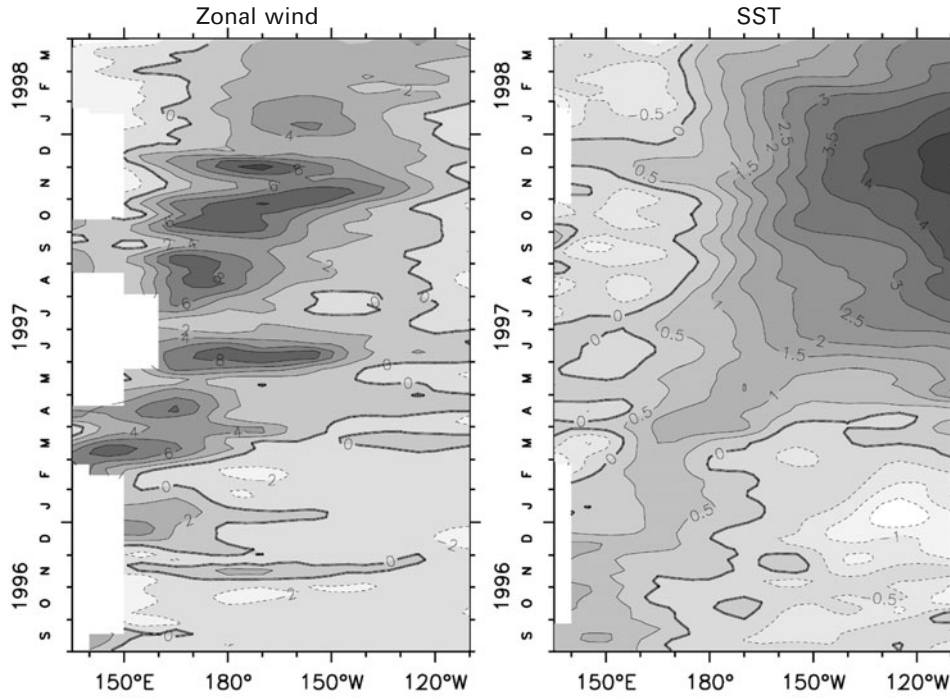

Figure 6.3. Zonal wind (left) and SST (right) anomalies along the equator, based on data from Tropical Atmosphere Ocean (TAO) moorings. Dark shading and solid contours indicate westerly wind and high SST anomalies. Contour intervals are $2\,\mathrm{m\,s^{-1}}$ and 0.5°C.

warm layer and its frequent stabilization by salinity make entrainment relatively ineffective at cooling the SST in the West Pacific warm pool most of the time (Meyers *et al.*, 1986; McPhaden and Hayes, 1991; Eldin *et al.*, 1994). Exceptions have been noted, however. Cronin and McPhaden (1997) use a steady-state turbulence model to show that entrainment was a cooling tendency during a period of shallow pycnocline early in COARE, though it was apparently not the main reason for changes in pycnocline depth. Sprintall and McPhaden (1994) find that during La Niñas in 1988/1989, with stronger than normal trades and weak rainfall at 0°, 165°E, there was no barrier layer. In this situation, SST changes were significantly influenced by upwelling (downwelling) in response to easterly (westerly) wind anomalies, much as occurs in the Eastern and Central Pacific. Although entrainment is generally a cooling term, salinity stratification can result in entrainment warming. Under low wind and clear sky conditions, a very shallow halocline can lead to heating of the barrier layer by penetrative radiation (which remains stable because of low surface salinity). With the turn to the cloudy–windy phase, surface flux cooling reduces vertical stability while wind mixing strengthens; the result can be that entrainment produces heating of the surface (Anderson *et al.*, 1996; Shinoda and Hendon, 1998; Schiller and Godfrey, 2003).

6.2.3 The role of advection

The importance of intraseasonal heat advection in the warm pool has been controversial. On one hand, as noted above, many investigators have concluded that a 1-D balance represents the dominant physics; these arguments appear reasonable since mean SST gradients in the warm pool are small. However, several examples have demonstrated that advection can be a significant contributor to heat balance in certain cases, involving different processes under both easterly and westerly winds. Despite the uniformity of mean SST in the warm pool, remnants of anomalous SST patches due to preceding conditions can leave significant, if transient, gradients for currents to work on and, as discussed in Section 6.3, equatorial currents can spin up rapidly in response to intraseasonal wind reversals. Two examples from the COARE experiment suggest the range of possibilities. During the early part of COARE in October 1992, cooler SSTs lay at and west of the 156°E mooring, presumably the residual of a westerly wind event in September. Moderate easterly winds (Figure 6.2, top right) spun up a strong westward surface current (Figure 6.2, right middle) which produced advective warming of about 1°C during the first 3 weeks of October (Cronin and McPhaden, 1997). Two months later, the strongest intraseasonal westerly event during COARE occurred in late December 1992, with stresses as high as $0.4\,\mathrm{N\,m^{-2}}$ (Weller and Anderson, 1996). Currents spun up by the December winds were well observed by surface drifters, which are drogued to move with the current at a 15 m depth and had been seeded extensively around the region (Ralph *et al.*, 1997). During the event, drifters within at least 2°S to 2°N converged on the equator and accelerated eastward. The surface jet extended at least to 180° and was about 300 km wide (Figures 7.10 and 7.11). Surface layer cooling under the strong winds was substantial, with a temperature drop of as much as 1°C along drifter trajectories. Ralph *et al.* (1997) find that this heat loss resulted in a positive SST gradient with SSTs warmer by at least 1°C near 180°E than at 145°E and, consequently, eastward advection was a cooling term in the eastern part of the warm pool. They noted that the strong latent heat and shortwave cooling under the cloudy westerly phase of TISO events means that eastward surface currents tend to be correlated with positive SST gradients ($\overline{u'T'_x} > 0$). This correlation suggests that long-term mean zonal advection is not negligible despite small mean SST gradients, and that the time-averaged effect of TISO winds and clouds is cooling at the east edge of the warm pool (Ralph *et al.,* 1997). Both these examples contradict the conventional idea that mean SST advection along the equator is due to the westward mean South Equatorial Current (SEC) working on the mean negative SST gradient. They indicate the potential for ISV to produce low-frequency changes in SST (see Section 6.5).

6.3 VERTICAL STRUCTURE UNDER WESTERLY WINDS

The complex and rapidly varying vertical structure of West Pacific zonal currents has been noticed from the earliest cruises in the region (Hisard *et al.*, 1970). During a

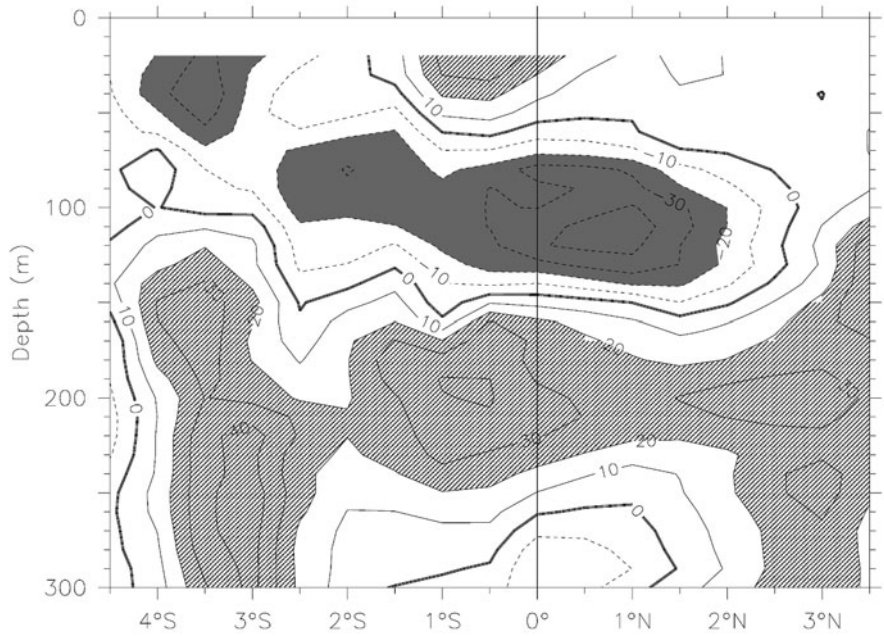

Figure 6.4. Zonal current example illustrating the subsurface westward jet (SSWJ) sandwiched between a frictional surface eastward current and the eastward EUC at 200 m. Hatching and solid contours indicate eastward currents, gray shading and dashed contours indicate westward currents. The contour interval is 10 cm s^{-1}. The measurements were made by a shipboard acoustic doppler current profiler (ADCP) along 156°E over December 8–11, 1992 from the R/V *Le Noroit*. Only data obtained while the ship was on station were used to construct the section.

cruise along 170°E in March 1967, trade winds prevailed and equatorial currents had a two-layer structure, with a westward SEC above 60 m depth and an eastward equatorial undercurrent (EUC) below. This is typical of the trade wind regime of the Central Pacific; in the mean it has been shown to be the result of a directly wind-forced frictional current in the surface layer, with a baroclinic pressure gradient due to thermocline tilt producing an eastward current below (McPhaden and Taft, 1988). In the following month a westerly wind burst occurred, and Hisard *et al.* (1970) observed a three-layer structure with an eastward flow above 60 m depth, a westward flow from 60 m to 175 m, and an eastward EUC below that (similar to Figure 6.4); these have become known as "reversing jets" and the sandwiched westward current has been called the subsurface westward jet (SSWJ).

Since the Hisard *et al.* (1970) study, there have been numerous reports of such reversing jets in the western equatorial Pacific (McPhaden *et al.*, 1988, 1990, 1992; Delcroix *et al.*, 1993; Cronin *et al.*, 2000). In general, they are not found in the Central or Eastern Pacific, despite decades-long moored velocity time series at several locations; however, Weisberg and Wang (1997) show one example of a

brief reversing jet at 170°W during the eastwardmost penetration of westerly winds in January 1992, at the height of the El Niño of that year. It seems likely that a deep thermocline and a thick weakly stratified surface layer is necessary for the complex structure of velocity to exist, thus restricting reversing jets to the warm pool, except occasionally during El Niños when these conditions spread eastward.

It was soon recognized that the surface eastward current associated with reversing jets was an example of a Yoshida jet (Yoshida, 1959). A Yoshida jet has the simple, accelerating balance:

$$u_t - fv = \tau^x/h \tag{6.1a}$$

$$fu = -p_y \tag{6.1b}$$

$$p_t + hv_y = 0 \tag{6.1c}$$

where (u, v) are zonal and meridional velocity components; f is the Coriolis parameter; τ^x is zonal wind stress; h is thickness of the accelerating layer; and p is the pressure (both τ and p have been divided by density for simplicity of notation). The zonal jet that is the solution to (6.1) decays exponentially away from the equator with a meridional scale of the equatorial Rossby radius (typically 300 km). Away from the equator, meridional transport in (6.1a) is approximately Ekman convergence (for westerly winds), which feeds the accelerating zonal jet and produces equatorial downwelling (6.1c) which provides the meridional pressure gradient to geostrophically balance the jet (6.1b). For a westerly wind burst magnitude of $7.5\,\mathrm{m\,s^{-1}}$ (e.g., Figure 6.2, top) the stress anomalies would be about $0.1\,\mathrm{N\,m^{-2}}$. Taking a 100 m layer thickness, the zonal acceleration at the equator indicated by (6.1a) is of the order of $10\,\mathrm{cm\,s^{-1}\,day^{-1}}$, comparable with observations under these conditions and indicating that a very rapid current can be spun up within the timescale of a westerly wind burst (McPhaden *et al.*, 1988, 1992; Ralph *et al.*, 1997; Cronin *et al.*, 2000). Yoshida jets appear to be a common and robust feature of the West Pacific under westerly wind bursts and are frequently observed (McPhaden *et al.*, 1990; Delcroix *et al.*, 1993). Since the Yoshida balance does not consider zonal variability, the jet is assumed to occur everywhere under the wind; an unresolved question concerns the possible convergence at the east edge of the jet (Richardson *et al.*, 1999; Cronin and McPhaden, 2002; Lengaigne *et al.*, 2002).

Cronin *et al.* (2000) diagnosed zonal momentum terms in the COARE region during March 1992–April 1994. Figure 6.5, from that paper, shows that near surface zonal acceleration was nearly in phase with the wind and that the jet reaches maximum velocity within about 3 days from the peak of the wind. Examples of rapid acceleration of surface currents under westerly wind bursts are common (e.g., Figure 6.2). One model of the response to impulsive forcing simplified the situation by assuming linear frictional dynamics in a homogeneous mixed layer above a sharp thermocline (McPhaden *et al.*, 1988). With switched-on zonal wind forcing, their solution for shear flow was a parabolic velocity profile accelerating in the direction of the wind, maximum at the surface, and decaying to zero at the base of the mixed layer. With vertical eddy viscosity estimated from observed shear profiles, the shear profile was set up within several days.

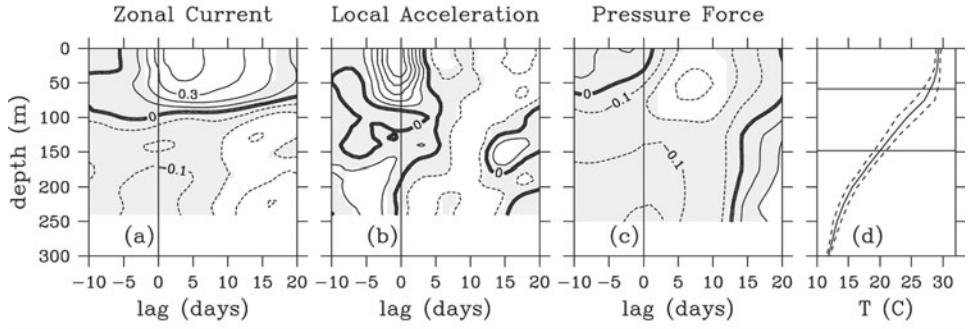

Figure 6.5. Lagged correlation between local zonal wind stress and (a) zonal current, (b) local zonal current acceleration, and (c) zonal pressure gradient force as a function of depth at 0°, 156°E. A positive lag implies that wind stress variability occurs prior to the respective variable anomaly. (d) Mean temperature and its standard deviation envelope at 0°, 156°E. The two horizontal lines show the mean depths of the 28°C and 20°C isotherms, which define the surface, intermediate, and EUC layers. Correlations that are not significant at the 90% confidence level are shaded. The contour interval is 0.1 (after Cronin *et al*., 2000).

The Yoshida jet would accelerate without bound except that the zonal pressure gradient term, omitted from (6.1a), becomes important in days to weeks and results in equatorial Kelvin and Rossby waves being emitted from the edges of the wind patch (McCreary, 1985). The meridional profile of the wind determines the mix of Kelvin and Rossby waves (see Richardson *et al*., 1999). The Kelvin wave part of the response has no effect west of the wind patch but carries a downwelling signal to the east, such that the thermocline tilts down to the east under the (westerly) wind patch and is flat from its eastern edge to the back of the advancing wave. The Rossby part of the response has no role east of the patch but carries an upwelling signal westward. If the westerly wind remains steady (and ocean boundaries are unimportant), the fully adjusted solution has a flat upwelled thermocline to the west, a downward slope under the wind, and a flat downwelled thermocline to the east. Under the wind patch itself, the vertically integrated zonal pressure gradient reaches Sverdrup balance with the wind stress and the acceleration stops; in effect, the waves carry the wind input momentum away from the forcing region. The result is a downwind jet at the surface, decaying with depth, and a pressure gradient–driven upwind current below, as the frictional influence declines with depth. For steady easterly winds, this two-layer structure describes the mean situation in the Central Pacific, with a westward SEC at the surface and an EUC beneath. For a discussion of the nonlinearities associated with these circulations, see among many others Philander and Pacanowski (1980), Johnson and McPhaden (1993a, b), Johnson and Luther (1994), Yu and Schopf (1997), Zhang and Rothstein (1998), Cronin *et al*. (2000), Lengaigne *et al*. (2002), Kessler *et al*. (2003). The key questions for westerly wind bursts, therefore, are the timescale on which the waves establish the pressure gradient and how the vertical structure that allows *three* stacked jets to exist is set up.

The pressure gradient timescale depends primarily on the width of the wind patch compared with the propagation time of the waves. For typical westerly wind burst forcing with fetch of a few thousand kilometers and first baroclinic mode Kelvin waves with speeds of $2\,m\,s^{-1}$ to $3\,m\,s^{-1}$, the pressure gradient setup takes about 10 days, which is borne out by observation (Figure 6.5c, and see Cronin *et al.*, 2000). Model experiments with idealized winds have shown the strong sensitivity of ocean response to wind fetch and zonal profile (Richardson *et al.*, 1999).

Yoshida dynamics alone can only set up shear of one sign and, therefore, only two stacked jets. The reversing jets observed under westerly wind bursts, however, demonstrate the possibility of a surface eastward Yoshida jet, an eastward EUC in the center of the thermocline, and a westward flow (the reversing jet or SSWJ) in the weakly stratified upper thermocline between them (Figures 6.2 and 6.4). In fact, Figure 6.2 shows that a quite complicated vertical structure can occur with rapid wind changes; note that the zonal current at 156°E in September and early October, 1992, under easterly winds, has a surface westward current varying in phase with the wind, a subsurface eastward current near 80 m that is apparently driven by the shallow pressure gradient response to the easterlies, a remnant of a SSWJ at 130 m generated by early-September westerlies, and an EUC at 240 m below that. This suggests that the relatively diffuse West Pacific thermocline can support pressure gradient reversals in the vertical (Cronin *et al.*, 2000). Observations show examples of an EUC flowing nearly undisturbed during the occurrence of significant westerly winds with the formation of a Yoshida jet and SSWJ lasting for several months (e.g., Figure 6.2, right-hand panels) and, conversely, of a reversed pressure gradient extending into the central thermocline and slowing an EUC as the SSWJ develops (McPhaden *et al.*, 1992; see Figure 6.2, left-hand panels). On average, the pressure gradient and zonal current at the EUC level are weakly correlated with local zonal winds with a lag of about 15 days (Cronin *et al.*, 2000; see also Figure 6.5a, c). One can imagine that the different responses depend sensitively on the pre-existing stratification and current structure: in particular, the thickness of the SEC, how far it extends into the thermocline, and whether the upper thermocline above the EUC can adjust to produce a pressure gradient to bring the Yoshida jet to a steady state and thereby create a SSWJ without involving the lower isotherms. Model experiments to try to isolate these effects have been performed by Zhang and Rothstein (1998) and Richardson *et al.* (1999).

This raises the deeper issue of what determines the vertical structure of ocean adjustment to time-varying winds. On the basin scale at low frequency (say 6 months or more), the entire thermocline slope reaches Sverdrup balance with the wind stress (McPhaden and Taft, 1988). In the Eastern Pacific—where the thermocline is sharp and shallow and the winds are relatively steady easterlies that provide via upwelling for quick communication of thermocline anomalies to the surface—there is little opportunity for a complex vertical structure to occur. But in the warm pool—where the upper layer can be more than 100 m thick, the thermocline can extend over 200 m or more, and the winds commonly change sign in a month or less—a more elaborate structure is possible. For example, Zhang (1997) notes that, although

intraseasonal temperature variability at 0°, 165°E is large down to at least 300 m, the signal is incoherent across about 75 m depth. The factors setting the vertical scales of these reversals presumably are related to the pre-existing stratification, but this is not well understood.

6.4 REMOTE SIGNATURES OF WIND-FORCED KELVIN WAVES

The propagation of equatorial Kelvin waves is so efficient at carrying wind-forced signals eastward along the equator that the first recognition of intraseasonal timescales in the tropical Pacific Ocean was in sea level records along the coast of the Americas (Enfield and Lukas, 1983). Spillane *et al.* (1987) and Enfield (1987) document coherent 30 to 70-day period coastal sea level variability from Peru to northern California. They quickly realized that nothing in the local winds could produce such a signal and found a lag relation with West Pacific island sea levels that clearly showed Kelvin wave propagation at speeds of about 2.5 m s^{-1}. More recently, Hormazabal *et al.* (2002) made a similar diagnosis for sea level at 30°S on the Chilean coast (see also Clarke and Ahmed, 1999 for an analysis of the role of the continental shelf in determining the phase speed of coastal propagation).

Since the TAO mooring array (Hayes *et al.*, 1991; McPhaden, 1995) has provided adequate temporal resolution, observation of prominent intraseasonal Kelvin waves has become routine. Kelvin waves due to intraseasonal westerly wind events are seen as a thermocline downwelling that commonly can be 50 m or more (Figure 6.6), well east of the wind itself, and accompanied by an eastward surge of surface current that can be as large as 1 m s^{-1}. Their effects on SST in the Central and Eastern Pacific have been noted many times. Under some conditions, SST change at 140°W can be dominated by intraseasonal zonal advection due to West Pacific Kelvin waves (Kessler *et al.*, 1995). Vecchi and Harrison (2000) stratify westerly wind bursts by location and by the low-frequency background state of ENSO. They showed that, on average, the largest East Pacific SST effects were found when equatorial westerlies occurred with climatologically normal SST—not during El Niño events—apparently because zonal advection is more efficient at changing SST when a large background zonal gradient exists. Westerly wind-driven Kelvin waves can also remotely modulate Eastern Pacific SST by lowering the thermocline (Figure 6.6) and changing the effect of background upwelling on SST, which Zhang (2001) argues is the dominant mechanism (see also Belamari *et al.*, 2003). Giese and Harrison (1991) suggest that another possible SST effect could be due to the passage of a downwelling Kelvin wave, with a meridional scale of 2°–3°, accelerating the EUC and thereby increasing shear with the surrounding SEC. In their model, the resulting amplification of tropical instability waves (see Section 6.7.2) resulted in an equatorward heat flux that was as large as the zonal advection warming.

The TAO moorings have also allowed the vertical structure of intraseasonal Kelvin waves to be dissected and diagnosed. McPhaden and Taft (1988) use moorings at 140°W, 125°W, and 110°W, where there is little intraseasonal wind

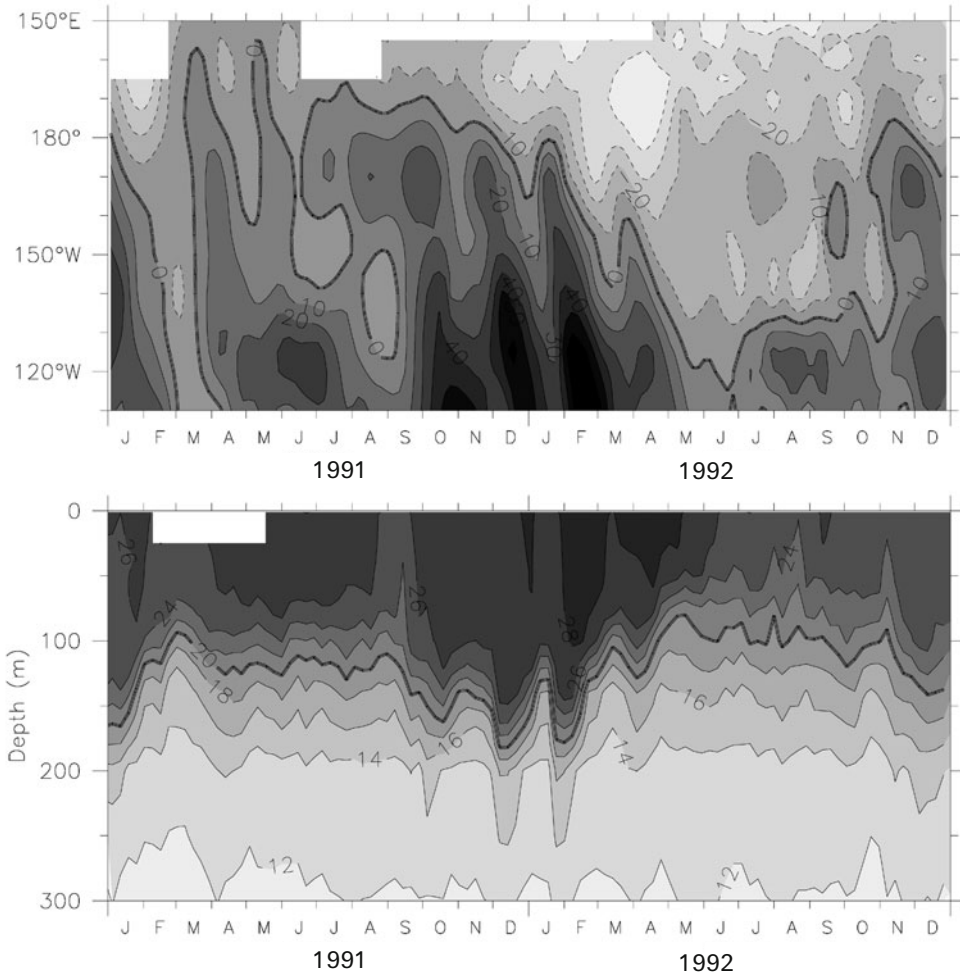

Figure 6.6. (Top) Anomalous depth of the 20°C isotherm along the equator. Dark shading indicates deep anomalies, with a contour interval of 10 m. Intraseasonal Kelvin waves are evident as tilted bands, especially during September 1991–February 1992. (Bottom) Temperature at 0°, 140°W. Dark shading indicates higher temperature, with a contour interval of 2°C. The 20°C isotherm is shown as the thick line. Kelvin waves arriving from the Western Pacific produce the sharp downwelling events. For both panels data come from TAO moorings.

forcing, to show that the principal intraseasonal signals in zonal current, temperature, and dynamic height had the characteristics of a remotely forced first baroclinic mode Kelvin wave, with a speed about 2.1 m s^{-1}, and that this variability had an amplitude as large as that of the annual cycle. They also comment that the dominant intraseasonal period observed in these oceanic variables is 60–90 days, longer than the apparent MJO forcing (see Section 6.5 for further discussion of this issue).

Although their results suggested that the waves were approximately linear, the fact that the EUC speed is typically $1\,\mathrm{m\,s^{-1}}$ or more raised the question of mean current modifications of wave modes. Johnson and McPhaden (1993b) analyzed time series of temperature and zonal current from moorings along 140°W and compared them with a meridionally symmetric model that included an idealized mean flow comparable with the EUC, as well as a SEC centered near 3° latitude at the surface. Relatively little direct Doppler shifting was found, because wave vertical scales are so much larger than those of mean currents, and the main modifications to linear dynamics were the occurrence of a temperature amplitude minimum on the equator and an amplification of wave zonal currents below the EUC core (see also Lengaigne *et al.,* 2002 who emphasizes that Kelvin advection of the mean EUC is responsible for this). Both these effects were due to wave vertical advection of the background temperature and current fields. Considering these studies, a linear diagnosis of remotely forced Kelvin waves seems to be first-order appropriate.

Theory suggests that many vertical Kelvin modes would be excited by the observed wind forcing, and several studies have noted evidence for modal structures. Busalacchi and Cane (1985) show that—while both the first and second vertical modes are a significant contribution to sea level variability in the eastern Pacific—higher modes are not. Giese and Harrison (1990) find that in an OGCM with a realistically sloping equatorial thermocline, second baroclinic mode Kelvin wave surface currents would be amplified relative to that of the first mode and would be the dominant velocity signal at the South American coast. Kutsuwada and McPhaden (2002) point out that during El Niño events, when the thermocline is flatter than usual, this effect would be moderated and the first baroclinic mode more prominent. They also show evidence of upward phase propagation in the free-wave region, suggesting formation of a downward beam of energy (McCreary, 1984). Kindle and Phoebus (1995) find that a model including three modes gave a better simulation of sea level at the American coast. Cravatte *et al.* (2003) show evidence of energy transfer from the first to the second baroclinic mode for intraseasonal Kelvin waves during 1992/1999. In light of these results—suggesting the importance of at least the second baroclinic mode—the apparent success of single active layer (reduced gravity) models in simulating much of observed wave-mediated variability (Metzger *et al.*, 1992; Wu *et al.*, 2000) is puzzling. Kessler and McPhaden (1995a) examine the signatures of the first four baroclinic modes in thermocline depth at 140°W and find that—although in a strict modal decomposition two modes were needed—in fact. reasonable choices of reduced gravity (thus single-mode) parameters gave a very similar solution, at least in the Central Pacific not too far from the forcing region. The reason is that the typical choice for wave speed in reduced gravity models ($c = 2.5\,\mathrm{m\,s^{-1}}$) is appropriate to a true first mode of about 250 m thickness (where $c^2 = g'h$, with g' being reduced gravity and h layer thickness). In fact, however, these models are often taken to let h be a realistic thermocline depth of about 150 m. These choices therefore artificially pump up the mode 1 amplitude and, thereby, compensate to produce a fairly realistic representation of the total Kelvin signal (Kessler and McPhaden, 1995a).

Although Kelvin waves propagate non-dispersively with a simple velocity and thermocline depth anomaly structure that has u and h in phase, they can produce much more complex phasing of SST variability. Indeed, Kessler and McPhaden (1995a) note, but could not explain, the intraseasonal warming and cooling events that occurred nearly simultaneously over a wide longitude range during the onset and decay of the El Niño of 1991/1992. McPhaden (2002) interprets this by showing that—while Kelvin wave zonal advection dominates the intraseasonal SST balance in the Central Pacific—vertical advection and entrainment are more important in the east where the thermocline is very shallow. If Kelvin wave vertical velocity is assumed to be due to thermocline motion ($w \approx dh/dt$), then upwelling leads the westward current anomaly by 1/4 of a cycle as the wave passes a point. Thus, cooling due to upwelling also leads cooling due to wave zonal advection of the mean SST gradient by 1/4 of a cycle. Depending on the relative importance of each of these processes to the SST balance at different longitudes, the phasing of SST due to intraseasonal Kelvin waves can appear to propagate in either direction or occur in phase. McPhaden (2002) shows that the growing dominance of vertical entrainment as the Kelvin wave propagates eastward leads to the nearly simultaneous intraseasonal SST anomalies over a broad longitude range observed throughout the 1990s.

Although equatorial Kelvin waves can have arbitrary shape in (x, t), two factors combine to make the MJO fraction of ISV the dominant contribution to the oceanic Kelvin signal. First, since the ocean integrates wind forcing along Kelvin wave characteristics (Kessler *et al.*, 1995; Hendon *et al.*, 1998), organized large-scale forcing is favored over more incoherent variability. Second, wind forcing that moves eastward will project more strongly onto the Kelvin mode (Weisberg and Tang, 1983), because it is partly resonant. Over the West Pacific warm pool, the MJO propagates east at a speed of about $5\,\mathrm{m\,s^{-1}}$ (Hendon and Salby, 1994; Shinoda *et al.*, 1998), which is comparable with the oceanic Kelvin speed (about $2.5\,\mathrm{m\,s^{-1}}$ for the first vertical mode). Hendon *et al.* (1998) note that as the MJO speeds up east of the dateline, it gets ahead of the oceanic Kelvin wave and by about 130°W it is out of phase with Kelvin current anomalies and thus serves to damp the wave.

In addition to the effects discussed in this section, intraseasonal Kelvin waves have also been related to the ENSO cycle and rectification mechanisms through a variety of processes. These will be discussed in Section 6.5.

6.5 EL NIÑO AND RECTIFICATION OF ISV

The question of a role for ISV, especially the MJO, in the ENSO cycle has been a hotly debated topic in the climate community (Zhang *et al.*, 2001), and no definitive resolution has thus far been reached (see Chapter 9). Although intraseasonal signatures in the ocean during El Niños can be impressively large, comparable with the amplitude of the seasonal cycle or ENSO (e.g., Figure 6.6), a nonlinear mechanism would be required to couple intraseasonal to lower frequencies, and this has been

difficult to demonstrate. In addition, the usual indices of global MJO activity are uncorrelated with indices of the ENSO cycle (Hendon *et al.*, 1999; Slingo *et al.*, 1999), which has led some to argue that a systematic connection is unlikely. Nevertheless, the frequent observation of strong intraseasonal (especially MJO) variability in the Western Pacific during the onset stage of recent El Niños (Gutzler, 1991; Kessler *et al.*, 1995; McPhaden, 1999; McPhaden and Yu, 1999; Zhang and Gottschalck, 2002) has generated a variety of speculation about this possibility. The spectacular failure of all ENSO forecast models to predict the magnitude or rapid growth of the 1997/1998 El Niño, which occurred subsequent to a series of large MJO events in boreal winter/spring 1996/1997 (McPhaden, 1999; Barnston *et al.*, 2000; van Oldenborgh, 2000) brought the problem to the fore. The question of the role of ISV in the ENSO is part of a fundamental debate that revolves around the distinction between two views: the ENSO seen as a quasi-cyclic mode of oscillation of the Pacific climate system (see Neelin *et al.*, 1998 for a review), or as an initial value problem in which each El Niño is a largely independent event (Moore and Kleeman, 1999; Kessler, 2002b). In the first case, ISV is a source of noise that may contribute to irregularity of the cycle but is not fundamental to it (Roulston and Neelin, 2000). In the second case an initiating perturbation external to the ENSO itself is an essential element and ISV could potentially provide it. However, no one suggests that ISV *causes* the ENSO cycle itself, as is clear from the fact that coupled models without anything resembling the MJO develop fairly realistic ENSO cycles and statistics. Recently, theories have arisen that combine elements of these two viewpoints, arguing that the spatial characteristics of West Pacific westerlies associated with the MJO produce climate noise that is especially suited to influencing a developing El Niño (Moore and Kleeman, 1999; Fedorov, 2002).

The occurrence of intraseasonal signatures in the ocean associated with El Niños was first noticed by Lukas *et al.* (1984), looking at Central Pacific island sea levels, and others have followed using a variety of observed quantities (Enfield, 1987; McPhaden *et al.*, 1988; Kessler and McPhaden, 1995a, b; Kutsuwada and McPhaden, 2002; Zhang and Gottschalck, 2002). As described in the sections above, ocean signatures include cooling under the strong winds and cloudiness of the West Pacific warm pool (e.g., Figure 6.3), and Kelvin wave–mediated eastward advection and thermocline downwelling in the equatorial regions to the east.

There is no doubt that strong MJO activity is regularly seen during non-El Niño years, including its ocean signatures (Kessler *et al.*, 1995). Global interannual variability of the MJO is dominated by changes in the core region centered at 90°E, which are unrelated to the ENSO (Hendon *et al.*, 1999; see also Figure 6.7, left-hand panel). Differences in MJO characteristics during El Niños have been noted, however. Several investigators have shown that MJO convection and surface zonal winds shift eastward during El Niño onset, from the far Western Pacific to the eastern edge of the expanding warm pool (Gutzler, 1991; Fink and Speth, 1997; Hendon *et al.*, 1999; Kessler, 2001). Figure 6.7 shows that intraseasonal OLR in the warm pool region (150°–180°E) has a large amplitude during El Niños that is not well correlated with the core intraseasonal OLR region over the Indian Ocean. During El Niños, ISV extends eastward (Figure 6.3) and its warm pool

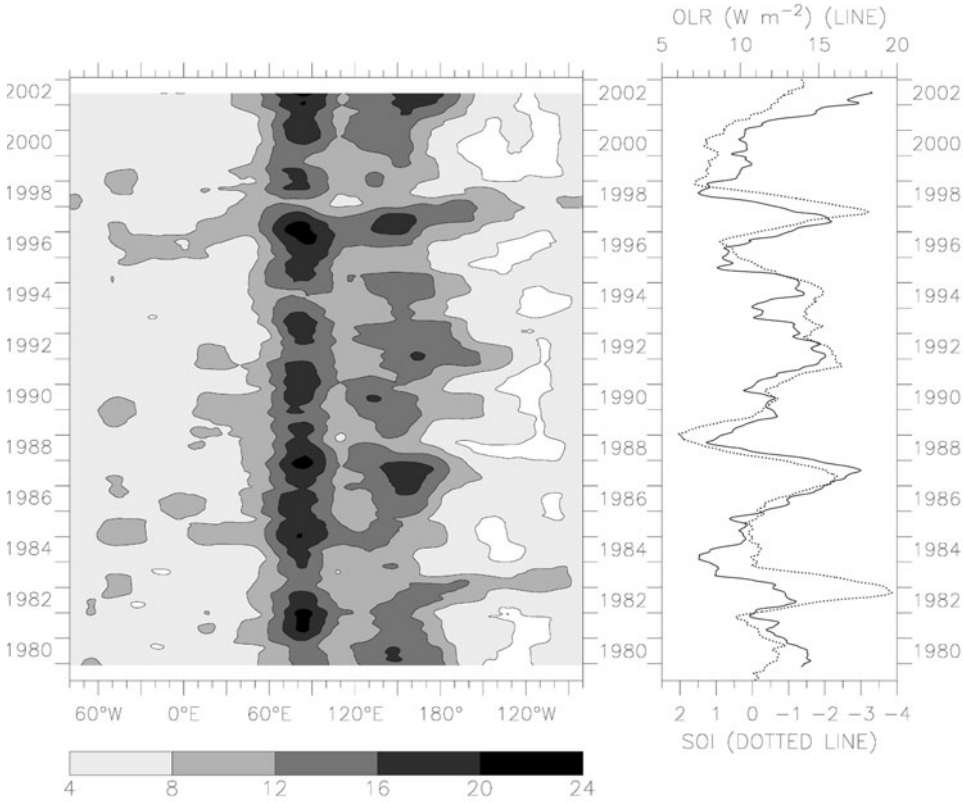

Figure 6.7. Interannual amplitude of intraseasonal outgoing longwave radiation (OLR) (5°S–5°N) (W m^{-2}), defined as the 1-year running standard deviation of intraseasonally bandpassed OLR. (Left) Amplitude in the global tropical strip, centered on the major region of variance at 100°E (the abscissa extends around the world, broken at the South American coast at 80°W). (Right) Time series of OLR amplitude averaged over the Western Pacific (150°E–180°) (solid line, scale at top) compared with the SOI (dotted line, scale at bottom). Year ticks on each panel are at January 1 of each year, with year labels centered at mid-year (after Kessler, 2001).

activity is in fact strongly correlated with the Southern Oscillation Index (SOI) ($r = -0.58$, see Figure 6.7, right-hand panel). Kessler (2001) shows that the eastward shift was not just incoherent ISV, which makes up perhaps half of the variance in this frequency band (Hendon *et al.*, 1999), but a systematic component of the organized MJO (note the large-scale events in Figure 6.3). The eastward shift is crucial to MJO/ENSO interaction because it can greatly increase the fetch of MJO winds over the Pacific (perhaps by a factor of 2), thereby increasing the magnitude of ocean signatures during those times.

The observed shift in the MJO envelope and its effect on the ocean is quantified by Zhang (2001) and Zhang and Gottschalck (2002), who suggest that an

appropriate index could be based on the integral of MJO-filtered winds along oceanic Kelvin wave characteristics. The index constructed in this way encompasses changes in the spatial pattern of the MJO as felt by ocean dynamics (though it does not consider changes in heat fluxes under the winds themselves). Zhang and Gottschalck (2002) use this technique to show that the MJO accounted for a significant fraction of interannual East Pacific SST variability and that stronger El Niños (since 1980) were preceded by stronger MJOs. Although this work indicates a statistical relation between intraseasonal and interannual frequencies, the rectifying mechanism still needs to be explained. If the MJO is simply an oscillation with zero mean and the ocean feels this forcing linearly, there would be no interaction between frequencies. Several attempts have been made to elucidate such a mechanism.

One approach asks whether the occurrence of MJO events changes the background winds and heat fluxes over the Pacific. Ordinary statistical techniques used to extract MJO signatures from observations assume a linear separation between frequencies by bandpass filtering in some form to isolate intraseasonal variance. The resulting zero mean time series are often taken to represent MJO anomalies with equal magnitude positive and negative phases. However, the realism of such representations has been questioned. If, for example, MJO events have systematically higher windspeed or westerly winds than the background, then anomalies defined to have zero mean will not adequately describe the effect on the ocean.

In the western Pacific, where the background winds are often weak, the occurrence of large MJO wind oscillations implies a stronger windspeed during *both* its easterly and westerly phases than in the absence of an MJO event, with correspondingly higher evaporation averaged over a cycle. Shinoda and Hendon (2002) show that this process has an interannual modulation: MJOs represented in the U.S. National Center for Environmental Prediction–National Center for Atmospheric Research (NCEP–NCAR) reanalysis were more active over the warm pool during periods when low-frequency winds were weak (probably because MJOs are restricted to the far western Pacific during La Niñas when strong trade winds extend westward), and thus on average the mean windspeed over a complete MJO cycle is enhanced by about $1\,\mathrm{m\,s^{-1}}$, with an average increased latent heat flux of about $23\,\mathrm{W\,m^{-2}}$. Zhang (1997) notes the difference in the effect of westerly anomalies on different backgrounds: during periods of mean easterlies (La Niña) a westerly wind burst represents a weakening of wind speed that will reduce latent heat fluxes, whereas on a westerly background the same wind burst increases the windspeed and is a cooling term. Ocean models often use an ad hoc "gust factor" to represent disorganized small-scale wind speeds in the calculation of latent heat and mixing; this also tends to increase the windspeed produced by intraseasonal wind anomalies imposed in a model by limiting it on the low end. Kessler and Kleeman (2000) force an ocean GCM with equal-amplitude easterly and westerly zonal wind anomalies (and a gust factor minimum of $4\,\mathrm{m\,s^{-1}}$) and find that the resulting higher windspeed produced SST cooling of about 0.6°C over an MJO cycle, compared with a climatological run. Although the gust factor influenced

these results, SST cooling under stronger-than-climatology oscillating winds appears to be a robust feature of the MJO over the warm pool.

There are many other possibilities for rectifying interactions among the ocean responses to intraseasonal forcing, and these are just beginning to be explored. Waliser *et al.* (2003, 2004) force an Indo-Pacific OGCM with realistic composite MJO and ISO anomalies and emphasize the potential for interaction between intraseasonal solar shortwave forcing and the ocean mixed layer. During the suppressed convection phase of the MJO, positive shortwave anomalies occur in conjunction with low wind forcing; both of these act to stabilize and shoal the mixed layer and can produce SST warming. During the active convection phase, the mixed layer deepens due to stronger winds and weaker solar heating; the result is that the cool anomaly is spread over a thicker layer and the negative SST change is not as large as the positive change of the opposite phase, so the rectified signal is a warming. This appears to explain their results in the maritime continent region where ocean dynamical processes play a minor role.

Some have explicitly argued that MJO winds do not in fact have zero mean: the MJO composites of Waliser *et al.* (2003, 2004) showed that the westerly phase of MJO winds averaged about $0.5\,\mathrm{m\,s^{-1}}$ stronger than the easterly phase over the warm pool. Raymond (2001) presents a model of the MJO in which convective systems were associated with westerly wind bursts without a corresponding easterly anomaly—when there is no MJO there are no bursts (see also Clarke, 1994 for a discussion of the preference for westerly winds under equatorial convection). In such a model, the occurrence of MJOs changes mean winds and, thus, intraseasonal events have a low-frequency component. It is difficult to objectively define from observations what the background winds would be "without the MJO" and, therefore, what is the net signature of the MJO, especially because of their frequent occurrence during El Niño onset phases, when low-frequency winds are turning westerly. Does the occurrence of a particular background foster more or stronger MJOs? Or, conversely, does the chance occurrence of more MJOs add up to a different background? It appears that the answer to both questions is "yes", and that makes definition of the total effect of intraseasonal forcing a fuzzy concept. The best answer that can be given today is that the passage of an MJO across a large region of the West Pacific appears to be more likely during El Niño onset, when warming SST is spreading eastward, and the result of this passage is an increase in both westerly winds and wind speed over a wide zonal extent. This leads to the question: How might these forcing changes interact with the coupled dynamics of the ENSO cycle?

One of the earliest attempts to quantify the effect of a short-term westerly event on the Pacific was by Latif *et al.* (1988). They forced a coupled GCM with a single 30-day "westerly wind burst", with $10\,\mathrm{m\,s^{-1}}$ winds extending over 10°S–10°N, from the western boundary to 180°, after the model had achieved a stable climatology. Following the imposed burst, the coupled model was allowed to evolve freely. While the response of an uncoupled ocean model to such an event is short-lived, the coupled system developed long-term changes. An eastward shift of the area of warmest water to about 160°W led to an eastward shift of convection. The model

atmosphere responded with persistent westerlies blowing into the convection, in a self-sustaining feedback which maintained the eastward-shifted SST and convection for more than a year. The Latif *et al.* (1988) experiment suggested that the coupled system is capable of rectifying short-term wind anomalies into a low-frequency change because the rapid response of the atmosphere to SST changes can reinforce ocean anomalies before they have dissipated.

Around the same time, an experiment with a simple coupled model came to the opposite conclusion. Zebiak (1989) added intraseasonal noise to the model-generated zonal wind field in the Zebiak and Cane (1987; hereafter ZC) coupled model and found little impact on evolution of the modeled ENSO cycle. The imposed ISV produced only a spread to the forecasts—not a systematic change in ENSO amplitude. Moore and Kleeman (2001) note the insensitivity of the ZC model to perturbations in the Western Pacific and attribute it to the way atmospheric latent heating (which spurs the growth of convection) is treated over the warm pool where in reality small SST anomalies can produce a strong flowering of convection. This process is inhibited in the ZC model and is a major difference from the coupled GCM of Latif *et al.* (1988). Another difference is that SST anomalies in ZC are closely tied to thermocline depth fluctuations, which is appropriate in the Central and Eastern Pacific but much less so in the west, where the background thermocline is very deep and surface fluxes dominate (McPhaden, 2002; see Section 6.2.2). Although the ZC model has shown notable success in forecasting the ENSO cycle, it is probably the wrong tool to investigate the effects of ISV.

A simple model of MJO rectification under zero mean winds was proposed by Kessler *et al.* (1995), based on a similar idea to that of Latif *et al.* (1988) discussed above: the atmosphere responds within days to SST changes by shifting the location of convection and associated westerlies, but the ocean's response to winds is lagged because it integrates the forcing. The rapid atmospheric shift is seen in Figure 6.3 as intraseasonal winds following the maximum SST gradient eastward. Kessler *et al.* (1995) modeled this in highly idealized form by assuming that organized intraseasonal winds occur only over the warm pool and that the wind fetch responds instantly to changes in warm pool zonal width. Westerly winds generate Kelvin wave currents that advect the east edge of the warm pool eastward and easterly winds do the opposite. As the with of the warm pool changes, so does the region of convection and the fetch of oscillating winds: westerly winds increase the width and easterly winds decrease it. Thus, westerly winds increase their own fetch and easterlies decrease it, thus the ocean feels the eastward advection more strongly. The net effect of oscillating intraseasonal winds is to push the warm pool slowly eastward; in the idealized Kessler *et al.* (1995) model this was found to resemble the stepwise eastward expansion of warm SST seen during El Niños. The fact that the east edge of the warm pool is also a salinity front contributes an additional positive pressure gradient term that can enhance eastward advection (Lengaigne *et al.*, 2002).

Kessler and Kleeman (2000) explore the consequences of the net latent heat cooling produced by high windspeeds due to oscillating winds on a weak background. In an intermediate coupled model, slightly cool SST (presumed to have

been generated by a series of MJOs) was imposed on the Pacific west of about 160°E during the time the 1997/1998 El Niño was beginning. In fact, observations showed cooling of the far West Pacific at this time (Figure 6.3, see also McPhaden, 1999). Hindcasts of the 1997/1998 event were made with and without imposed cooling. The control run produced a weak El Niño, typical of the forecasts made by many models before the event. The imposed cooling run developed persistent westerlies blowing out of the cool western region; these increased El Niño SST anomalies by about 30%, which improved the realism of the hindcast. They suggested that the MJO can thus act constructively on the ENSO as a stochastic amplifier and that the weather-like unpredictable nature of MJOs may make forecasting the amplitude of an oncoming El Niño event more difficult than predicting the occurrence of the event itself.

A different sort of rectifying process has been proposed to explain the perplexing discrepancy between the 40 to 50-day MJO signals observed in the atmosphere (Madden and Julian, 1994) and the 60 to 70-day periods that dominate the ocean Kelvin wave response (Enfield, 1987; Kessler *et al*., 1995, among others). Figure 6.8 shows the variance-preserving spectra of two atmospheric quantities at 165°E (OLR and zonal winds measured by the TAO buoy there) and two ocean quantities at 140°W (thermocline depth and zonal current at undercurrent level), which experience little local intraseasonal forcing, but strongly feel ISV through Kelvin wave propagation from the Western Pacific. The intraseasonal variance of both atmospheric quantities falls off sharply at periods longer than about 55 days, while the corresponding peak for both ocean quantities is clearly shifted to a lower frequency. As noted above, the Kelvin wave amplitude east of a patch of oscillating zonal winds depends on the integral of the forcing along the wave characteristic. For steady winds, this is proportional to the time it takes the Kelvin wave to cross the patch, L/c, where L is the patch width and c is the wave speed (about $2.5\,\mathrm{m\,s^{-1}}$), but for oscillating winds the response is smaller because the winds may change sign while the wave is still traversing the patch. As the frequency of the wind increases to the point where the Kelvin wave crosses the patch in one period ($P = L/c$), the wave feels an equal amount of easterlies and westerlies, so the forcing integral cancels exactly and the response east of the patch falls to zero. Kessler *et al*. (1995) show that, for a 5,000 km width patch, there is a rapid falloff in Kelvin wave amplitude between roughly 100 and 30-day period oscillations, and suggest that this would account for the preference for lower intraseasonal frequencies in the ocean east of the warm pool (Figure 6.8). Hendon *et al*. (1998) improve on this crude fixed patch model by considering the more realistic eastward propagation of MJO forcing over the warm pool, which moves at speeds similar to the Kelvin wave (Hendon and Salby, 1994). When the MJO speed equals the Kelvin wave speed, the forcing is resonant and the Kelvin amplitude is the same as for steady winds; in other cases it is less. For a realistic MJO wind, this maximum occurs at periods of about 70 days and falls off very rapidly at higher frequencies. They conclude that the observed frequency offset between atmosphere and ocean is due to these linear Kelvin wave dynamics as a consequence of the spatial and temporal characteristics of MJO winds.

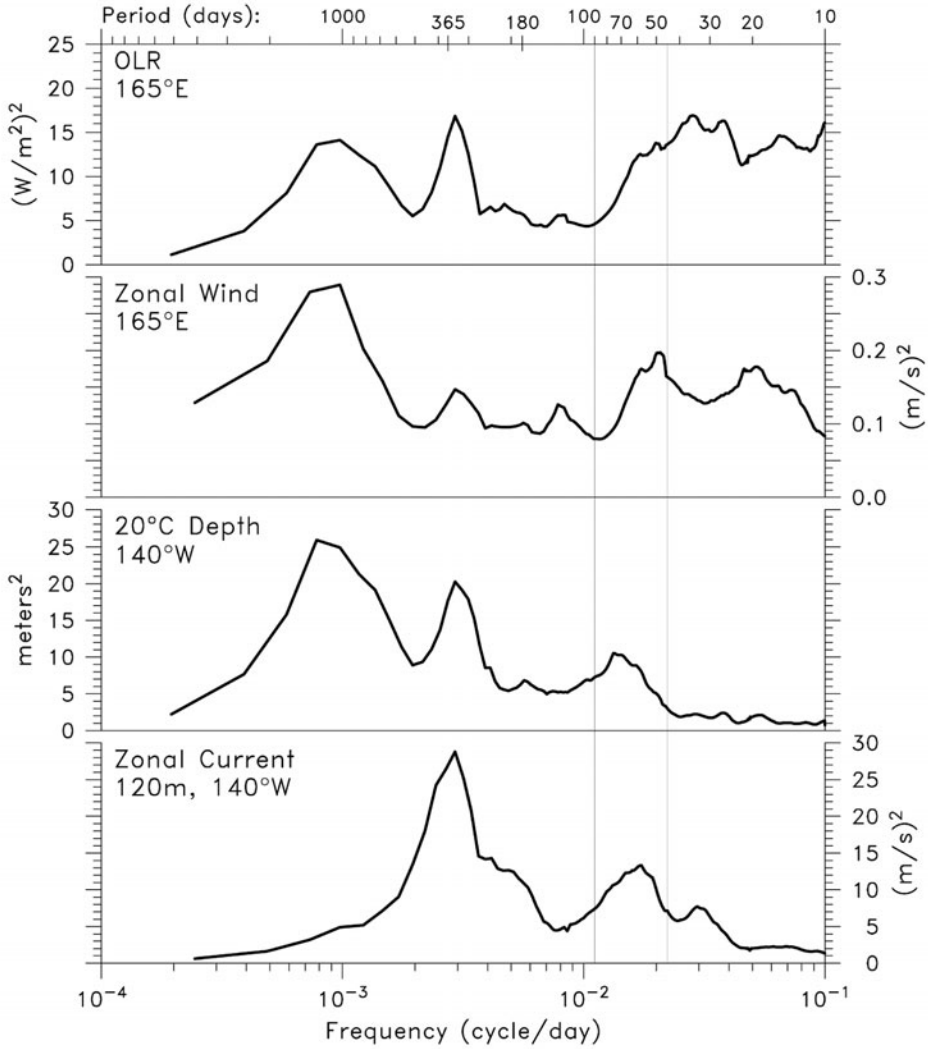

Figure 6.8. Variance-preserving spectra of OLR at 165°E, zonal wind at 165°E, 20°C depth at 140°W, and EUC speed at 140°W, 120 m depth, all at the equator. Each variable has a separate scale as indicated. The spectra are calculated for the 10-year period April 1983–April 1993 for all quantities except zonal wind, for which only 7 years of data, July 1986–July 1993, were available (after Kessler *et al.*, 1995).

6.6 ISV IN THE INDIAN OCEAN

The Indian Ocean is much more poorly observed than the Pacific; as a result much of the diagnosis has been done in models, often without adequate observational confirmation. Many hypotheses have been raised in model studies that cannot be fully

substantiated and remain speculative. This situation is slowly being rectified through large-scale sampling (e.g., the Argo array of profiling floats, Gould *et al.*, 2004) and through regional programs (e.g., JASMINE, see Webster *et al.*, 2002). Schott and McCreary (2001) give a comprehensive review of the present state of knowledge of Indian Ocean circulation, focusing on the dynamics of large-scale and low-frequency signals. Another useful overview is the textbook of Tomczak and Godfrey (1994), while Swallow (1983) reviews in situ observations of Indian Ocean eddies.

6.6.1 Differences between the Indian and Pacific Ocean warm pools and their consequences

The physical processes by which the Indian Ocean responds to intraseasonal forcing are the same as those of the Pacific, but differences in the background conditions have a large influence on oceanic consequences. The shape of the Indian Ocean basin has an important effect because it is closed in the northern subtropics. In the Pacific (or Atlantic), equatorial Kelvin waves reflect along the eastern boundary to coastal signals that propagate poleward; as a result, intraseasonal wind forcing becomes "lost" to the tropics in those basins. In the Indian Ocean, in contrast, coastal waves are directed into the Bay of Bengal (and from the Bay around the southern tip of India into the Arabian Sea), providing an important source of remote forcing to the off-equatorial tropics originating in equatorial winds (Potemra *et al.*, 1991; McCreary *et al.*, 1993; Schott *et al.*, 1994; Eigenheer and Quadfasel, 2000; Somayajulu *et al.*, 2003; Yu, 2003; Waliser *et al.*, 2004).

The fact that the climatological semi-annual wind forcing is much stronger than the mean winds in the Indian Ocean distinguishes it from the other basins that have permanent equatorial easterlies and, thus, a permanent zonally sloping thermocline and EUC, with their accompanying warm pool in the west and cold tongue due to upwelling in the east. The shallow East Pacific thermocline allows remotely forced thermocline depth changes to quickly and easily affect SST and thereby provide the potential for coupled interaction. Figure 6.9 shows the mean zonal thermocline slope associated with the mean easterlies in the Pacific and Atlantic, and the contrasting flat deep thermocline of the Indian Ocean. Because of this profound difference in structure, the fluent communication between ocean dynamical processes and the atmosphere as occurs in the Pacific (Sections 6.4 and 6.5) is much more difficult to accomplish in the equatorial Indian Ocean. However, an interannual "Indian Ocean zonal mode" has been proposed that depends on such changes in the narrow upwelling region close to the coast of Java (see Webster *et al.*, 1999; Saji *et al.*, 1999; Murtugudde *et al.*, 2000; Annamalai *et al.*, 2003).

The semi-annual equatorial zonal winds spin up eastward Yoshida jet–like features in May and November (Wyrtki jets; Figure 6.10) in response to westerly maxima during the monsoon transition seasons (Wyrtki, 1973; Reverdin, 1987; Han *et al.*, 1999). Although the climatological picture suggests two well-defined jets, observational (Reppin *et al.*, 1999) and modeling studies (Masson *et al.,* 2003) show that each semi-annual jet is broken up into oscillations with timescales of a month or less. As the zonal pressure gradient adjusts to monsoon transition winds

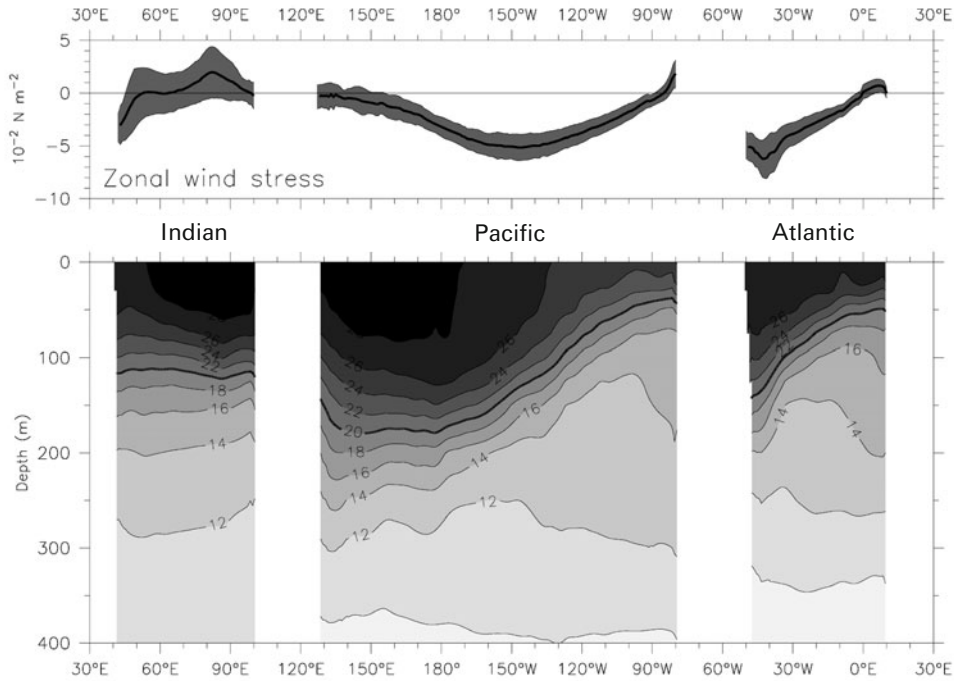

Figure 6.9. Mean zonal wind stress (top) and upper-ocean temperature (bottom) along the equator. The winds are from the ERS scatterometer during 1992–2000, averaged over 5°S–5°N. The heavy line shows the mean and the gray shading around it shows the standard deviation of the annual cycle. Ocean temperatures are from the Levitus (1994) *World Ocean Atlas*, with a contour interval of 2°C and a supplemental contour at 29°C.

(see Section 6.3), semi-annual Kelvin waves are generated that contribute to seasonally reversing boundary currents in the Bay of Bengal (see references above) and, by interacting with the locally generated flow field there, contribute to its rich intraseasonal eddy field (Vinayachandran and Yamagata, 1998). This source of semi-annual remote forcing adds to the local intraseasonal forcing in boreal summer (Waliser *et al.*, 2004) to produce variability throughout the year, which may be one reason that Bay of Bengal eddies do not appear to be strongly seasonally modulated (Somayajulu *et al.*, 2003).

In the central equatorial Pacific, meridional winds are weak compared with zonal winds, and zonal winds are relatively uniform in latitude within 5°N–5°S. Thus, the meridional circulation there is largely symmetric with a nodal point at the equator, and cross-equatorial oceanic heat transport occurs principally through mixing and small-scale processes (Blanke and Raynaud, 1997). In the Indian Ocean, by contrast, meridional winds are strong and seasonally reversing, and zonal winds are antisymmetric across the equator. This allows significant mid-basin cross-equatorial (mean southward) Ekman mass transport (Miyama *et al.*, 2003) which balances large cross-equatorial western boundary current mass transport driven by

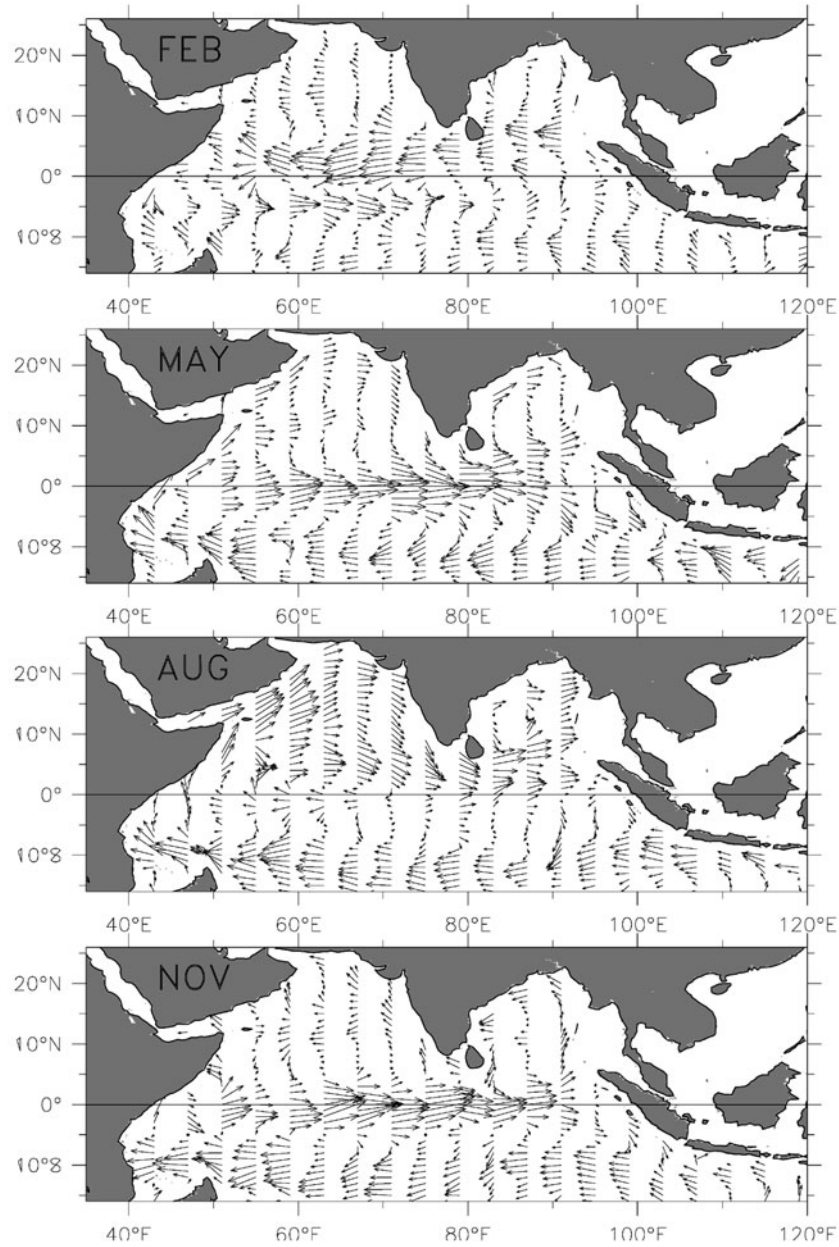

Figure 6.10. Seasonal cycle of Indian Ocean surface currents from historical ship drift data (Mariano *et al*., 1995). North of about 8°S the annual and semi-annual variation of most currents is much larger than the mean. The Wyrtkijets are the equatorially trapped eastward currents during May and November. The dramatic seasonal reversals of circulation in the Arabian Sea, the Bay of Bengal, and along the African Coast (Somali Current) are also evident.

monsoon winds (the Somali Current, see Section 6.7.3); such a circulation has no counterpart in the other oceans. Similarly, in the West Pacific warm pool, the annual cycle of SST is damped by the tendency for convective cloudiness to increase with surface temperature (Ramanathan and Collins, 1991). In the North Indian Ocean, by contrast, shortwave heat flux has a strong annual cycle because convection is absent during boreal spring. However, the annual cycle of SST there (east of the Somali Current region) is also small (Murtugudde and Busalacchi, 1999), comparable with that of the Pacific warm pool. Loschnigg and Webster (2000) suggest that this requires seasonally reversing oceanic cross-equatorial heat transport of the order of ± 1.5 PW, northward in winter and southward in summer, to maintain the SST (Figure 6.11). In their model, this transport was produced by a combination of western boundary and interior Ekman flows, driven by monsoon winds. It was strongly intraseasonally modulated. On the other hand, Waliser *et al.* (2004) find a similar seasonal but much smaller intraseasonal cross-equatorial transport oscillation in their ocean GCM and comment that the simplicity of the Loschnigg and Webster (2000) 2.5-layer ocean model might have led to an overestimate by neglecting complex baroclinic variations.

The extreme rainfall and riverine input to the Bay of Bengal give it a surface salinity at least 1 p.s.u. fresher than the West Pacific warm pool (Bhat *et al.*, 2001) and low surface salinity extends across the equator in the eastern basin (Sprintall and Tomczak, 1992; Han *et al.*, 2001b). The resulting barrier layer is much stronger than in the Pacific warm pool (Section 6.2), especially in the western part of the Bay of Bengal (Shetye *et al.,* 1996), and enlarges down to the equator most prominently in boreal fall (Masson *et al.*, 2002). As in the West Pacific warm pool, the barrier layer enhances the surface speed of the boreal fall Wyrtki jet by trapping wind momentum in a thin surface layer (Section 6.2); Han *et al.* (1999) estimate this effect at $0.3\,\mathrm{m\,s^{-1}}$. In a model forced by observed precipitation, Masson *et al.* (2002, 2003) further suggest that advection of a subsurface salinity maximum by the jet contributes to intensification of the barrier layer in the eastern equatorial Indian Ocean.

The Indonesian Throughflow (ITF) exerts a fundamental control on the Indo-Pacific warm pool; coupled model experiments suggest that it results in a warming of the Indian Ocean while cooling the Pacific and shifting the warm pool to the west (Schneider, 1998). Therefore, factors that influence ITF mass and property transport variability are of great interest. Velocities through the narrow ITF outflow straits can be significantly affected by Kelvin waves forced by equatorial winds and propagating along the Java coast at intraseasonal and semi-annual frequencies (Qiu *et al.,* 1999; Potemra *et al.*, 2002; Waliser *et al.*, 2003). These waves modulate the sea level at the ends of Indian Ocean straits and, therefore, change along-strait pressure gradients; there may also be property effects due to changing the baroclinic structure of the outflows (Potemra *et al.*, 2003; Sprintall *et al.*, 2003). Qiu *et al.* (1999) and Durland and Qiu (2003) also show that intraseasonal Kelvin waves enter Indonesian seas at the Lombok Strait (a major outflow into the Indian Ocean) and modulate sea level in the Makassar Strait; this means that the straits further east (Timor and Omboi) are much less affected by Indian Ocean equatorial ISV. Although intraseasonal equatorial forcing is a major influence on the velocity at

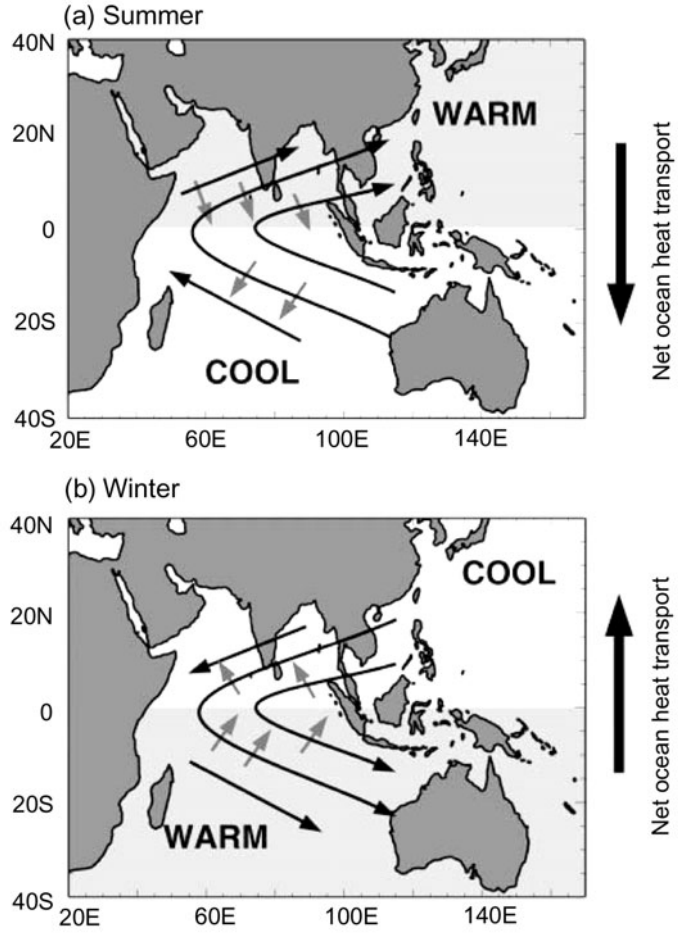

Figure 6.11. A regulatory model of the annual cycle of the Indian Ocean monsoon system depicted for (a) summer (June–September) and (b) winter (December–February). Curved black arrows denote the wind forced by large-scale differential heating denoted by ''warm'' and ''cool''. The small gray arrows are Ekman transport forced by the winds. The large vertical black arrows to the right show the net ocean heat transport that reverses between summer and winter. The net effect of the combined wind-forced ocean circulation is to transport heat to the winter hemisphere, thus modulating SST differences between the hemispheres (after Loschnigg and Webster, 2000).

Lombok, it is not yet clear whether this variability has a significant effect on properties on the Indian Ocean side that would contribute to subsequent variability (Sprintall *et al.*, 2003).

It is worth noting that Qiu *et al.* (1999) also identify an ISO in the Celebes Sea that is unrelated to TISO winds. Their model results suggest that as the Mindanao

Current retroflects into the Pacific at about 4°N, it sheds eddies into the Celebes Sea that closely match the gravest Rossby mode of this semi-enclosed basin, leading to resonance.

6.6.2 Oscillations lasting about 60 days in the western equatorial Indian Ocean

Meridional current oscillations concentrated on a narrow band of periods near 26 days were first observed by moorings in the western equatorial Indian Ocean in 1979–1980 (Luyten and Roemmich, 1982). There was very little zonal current signal in this band. Subsequently, similar oscillations were found in drifter tracks just north of the equator (Reverdin and Luyten, 1986), which raised the possibility that these were tropical instability waves (TIWs; see Section 6.7.2) similar to those in the Pacific and Atlantic. However, the close association of TIWs with zonal current shear was not seen in the Indian Ocean. Models forced with smoothly varying monthly winds were able to reproduce the 26-day waves and showed that their dispersion properties (wavelength, westward phase propagation, and eastward group velocity) were consistent with Yanai wave kinematics (Kindle and Thompson, 1989). Tsai *et al.* (1992) use satellite SST to examine the spatial and temporal properties of oscillations in this frequency band. These data confirmed the 26-day period, and its characteristics were consistent with westward-phase-propagating Yanai waves. The oscillations were found from 52°E to 60°E, about 1,000 km east of the coast. There have been two explanations proposed for the generation of these waves, which are apparently not forced by anything in the local winds. Moore and McCreary (1990) suggest that periodic wind stress along the slanting western boundary could produce such Yanai waves propagating into the interior. However, several models (e.g., Kindle and Thompson, 1989) have produced 26-day Yanai waves when forced with climatological monthly winds alone. In these models, the waves were generated as an instability of the Somali Current system southern gyre (Schott and McCreary, 2001), a completely different mechanism than that which produces TIWs. It is not known why there is a preference for the apparently robust 26-day period.

6.6.3 Recent models of wind-forced ISV in the Indian Ocean

Using the detailed new satellite wind and SST products, modelers have begun to attempt simulations of Indian Ocean ISV forced with realistic winds and compared with realistic SSTs. Although many of the processes found are similar to those previously diagnosed in the Pacific, several studies have tried to disentangle oceanic ISV due to TISO wind forcing vs. that due to internal instabilities.

Han *et al.* (2001a) note the occurrence of two distinct peaks in simulated zonal currents in the central and eastern Indian Ocean, at 40–60 days and at 90 days. Comparing model runs with and without intraseasonal winds showed that the 40 to 60-day signals were a predominantly linear ocean response to direct wind forcing. In the central and eastern basin, much of this variability was associated with

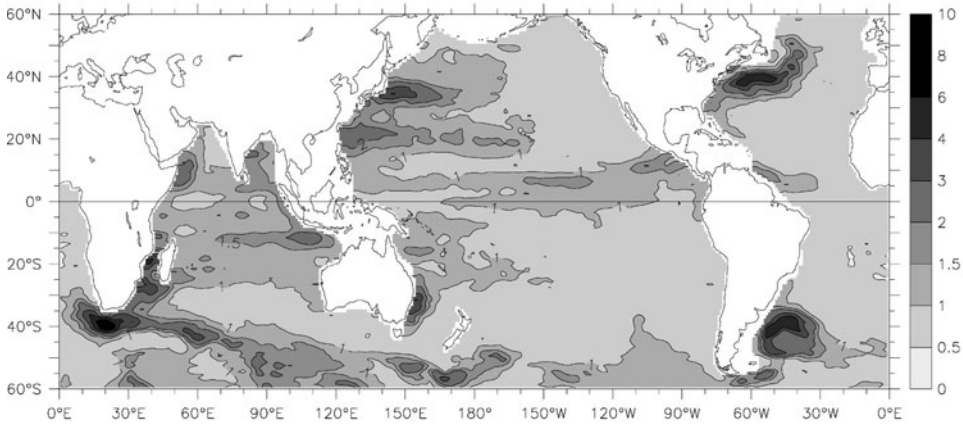

Figure 6.12. RMS of bandpassed (35 to 85-day half-power) sea level from the TOPEX/Poseidon satellite altimeter, for data during January 1992–July 2003. Dark shading indicates high sea level RMS with a stretched contour interval (values indicated in the scale on the right).

organized, eastward-propagating MJO winds. The 90-day current peak, however, was significantly different from the forced linear solution. Part of the difference could be explained by a mechanism similar to that found in the Pacific by Kessler *et al.* (1995) and Hendon *et al.* (1998), in which the ratio between the period of the forcing and the time it takes a wave to cross the wind patch can lead to lower frequencies being preferentially felt by the ocean (see Section 6.5). However, in the Indian Ocean reflected Rossby waves can be an additional influence because the distance from the region of strong intraseasonal winds and the eastern boundary is much shorter than it is in the Pacific. Han *et al.* (2001a) show that a second baroclinic mode equatorial Kelvin/reflected Rossby wave is nearly resonant in the Indian Ocean basin when forced with 90-day period winds (see also Jensen, 1993), and thereby enhances the eastern ocean response at that period.

Sengupta *et al.* (2001) compare the results of an OGCM forced with full wind variability and with filtered seasonal cycle winds. Even when forced with smooth seasonal cycle winds, their model developed intraseasonal current variability in the western boundary region (see Section 6.7.3) and also south of Sri Lanka in the central basin, similar to observations (e.g., Figure 6.12). Tracing individual Kelvin waves and their Rossby reflections showed that Sri Lankan ISV in this model was due to intraseasonal vortices generated when the eastern boundary Rossby reflections of semi-annual Wyrtki jet Kelvin waves meet the background eastward-moving South Monsoon Current (Vinayachandran and Yamagata, 1998; Schott and McCreary, 2001). The fact that Sri Lankan ISV in a complete forcing run agreed in phase with observed velocities strongly suggested that, despite the development of instabilities, these signals were predictable and, thus, at least quasi-linear responses to the winds.

6.7 OTHER INTRINSIC OCEANIC ISV

6.7.1 Global ISV

There is such a large variety of intrinsic ISV in the oceans—caused by many processes other than intraseasonal atmospheric forcing—that a review of the entire subject is well beyond the scope of this chapter. In addition, much of this variability is not germane to the principal thrust of this book. We will therefore focus on the most common signals that are likely to be intermingled with wind-forced ISV in the tropics and that could therefore cause confusion in the interpretation of ocean observations connected with TISOs. Other regional ISV signals will be discussed only briefly.

As an index of the occurrence of ISV in the global ocean, Figure 6.12 shows the RMS of the intraseasonally bandpassed sea level—sea surface height (SSH)—from the TOPEX/Poseidon altimeter (Fu *et al.*, 1994). It shows distinct regions with strong SSH ISV in many parts of the world ocean; most are not associated with the tropical ISOs that are the principal subject of this book. Note that the equatorial region discussed above does not appear as a strong maximum of SSH ISV. That principally reflects the fact that small pressure gradients are more effective at driving currents near the equator because of the small value of the Coriolis parameter. Many investigators have studied altimetric SSH as an index of eddy variability, sometimes using it to estimate eddy kinetic energy through a geostrophic assumption which emphasizes the tropics (Stammer, 1997). Also note that the TOPEX altimeter does not sample small-scale signals very near the coast very well, which is probably why the coastal Kelvin waves mentioned in Section 6.4 do not appear in Figure 6.12.

6.7.2 Non-TISO-forced ISV in the tropical Indo-Pacific

Two important intraseasonal phenomena that are not forced by TISOs are observed in the tropical Pacific: the Tehuantepec and Papagayo eddies that produce the bands of high ISV extending southwest from Central America in Figure 6.12 and the tropical instability waves that are seen as the strip of SSH variability along 5°N. Although these two signals appear continuous in Figure 6.12, they are entirely separate phenomena (Giese *et al.*, 1994).

Central American eddies

The Tehuantepec eddies are generated by episodic winds blowing through the mountain pass at the isthmus of Tehuantepec in southern Mexico (Chelton *et al.*, 2000b; Kessler, 2002a). High pressure behind winter cold fronts transiting North America causes a cross-mountain pressure gradient that funnels an intense wind jet through the pass and over the Pacific, on timescales of a few days (Hurd, 1929; Roden, 1961; Chelton *et al.,* 2000a). These winds produce locally strong mixing and SST fluctuations (Trasviña, 1995) and also generate a series of typically three to five anticyclonic (warm core) eddies each winter that propagate approximately westward as free Rossby waves (Giese *et al.*, 1994), leading to the strip of high SSH variance in Figure 6.12. Individual eddies can be tracked in SSH along 11°N—on

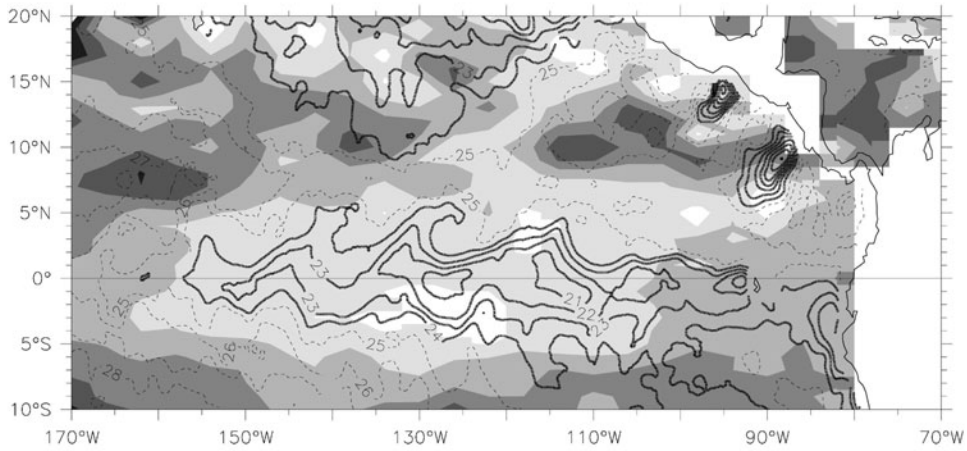

Figure 6.13. Example of the sea surface topography (shading) and temperature (contours) observed by satellite during January 2000, illustrating the signatures of Central American eddies and tropical instability waves (Section 6.7.2). The eddies are visible as the four dark patches lined up along 8°N–12°N; these are warm-core (anticyclonic) vortices produced by episodic mountain gap winds through the Central American Cordillera. They propagate west at a speed of about 15 cm s^{-1} (400 km $month^{-1}$). The direct SST effects of the winds are seen as the packed dark (cool) contours that indicate the location of the strongest winds at Tehuantepec and Papagayo. The dark SST contours along the equator show the cold tongue (SSTs greater than 25°C are indicated by dashed contours). The cusps along the tight SST gradient on the north side of the tongue are the signatures of tropical instability waves. These waves propagate west at a speed of about 1,000 km $month^{-1}$.

occasion as far west as the dateline (Perigaud, 1990; Giese *et al*., 1994; see also Figure 6.13). Ocean color is a useful technique for remotely sensing these eddies because their SST signal may be small, but the associated plankton blooms can still be evident (McClain *et al*., 2002). While forcing occurs on a timescale much shorter than intraseasonal, the fact that the wind events occur episodically several times each winter results in the apparent intraseasonal timescale. The observed preference for anticyclonic rotation was explained by McCreary *et al*. (1989): although eddies of both signs are generated by the wind jet (downwelling under the negative curl region on the right flank of the jet axis, upwelling on the left flank to the east), high winds quickly mix away the upwelled thermocline of the cyclonic eddy.

Winds blowing through the lowlands of Nicaragua (known as Papagayo winds) are less variable than those through Tehuantepec, and not apparently associated with midlatitude cold fronts, though they are still stronger in winter (Müller-Karger and Fuentes-Yaco, 2000; Chelton *et al*., 2000a, 2000b). A different explanation for the eddies west of Nicaragua (seen as the southern strip of high intraseasonal variance west of Central America in Figure 6.12) is proposed by Hansen and Maul (1991), who estimate a propagation speed greater than that of free Rossby waves and diagnose the eddies as strongly nonlinear and similar to Gulf Stream rings. They suggest that the Papagayo eddies, which are also anticyclonic, could be due entirely

to ocean dynamics, without any influence of mountain gap winds. Instead, they point to conservation of potential vorticity as the North Equatorial Countercurrent (NECC), which is strongest in boreal winter, turns sharply northward when it meets the coast. They propose that the anticyclonic relative vorticity gained in the northward flow results in eddy shedding. This hypothesis has been questioned (Giese *et al.*, 1994) and the possible difference in generation mechanism between the Papagayo and Tehuantepec eddies has not been resolved. Eddies are also seen west of a third wind jet through the lowlands of Panama (Müller-Karger and Fuentes-Yaco, 2000; note the third weaker strip of ISV in Figure 6.12), but these have been studied even less.

The offshore passage of these eddies, however generated, is documented by Giese *et al.* (1994) using TOPEX altimetry and by Hansen and Maul (1991) using surface drifter tracks. Confusingly, the Tehuantepec eddies appear to first move southwest and then follow the same track along 11°N as the Papagayo eddies westward from Central America (Giese *et al.*, 1994; see also Figure 6.12); it is not known why this behavior occurs. Their speed along 11°N is about 17 cm s^{-1}, which is close to the theoretical first baroclinic mode Rossby wave speed at that latitude. The spatial scale of the eddies is a few hundred kilometers and they tend to be zonally elongated (Giese *et al.*, 1994; see also Figure 6.13). It is unlikely that offshore eddies would interact with ocean variability due to TISO forcing, because they are far enough from the equator to be well poleward of the Kelvin wave–influenced region and they die out east of the warm pool where TISO signals have a wider meridional span. However, near the coast an interaction is possible, because TISO-forced equatorial Kelvin waves (Section 6.4) produce strong intraseasonal velocity and thermocline depth variability as their reflection leaves poleward-propagating coastal waves (note that TISO Kelvin waves also display a preference for downwelling). An apparent coincidence between the arrival of TISO-origin Kelvin waves and the shedding of offshore-propagating eddies led to speculation that perhaps some Central American eddies were in fact triggered or modulated by TISOs (B. Kessler, pers. commun., 1998), though the mechanism is unclear. Linear wave theory does not encompass the dynamics of coastal Kelvin wave propagation when a zonally oriented coast is part of the picture, as occurs at the isthmus of Tehuantepec; this problem has been glossed over (see the appendix to Kessler *et al.*, 2003).

Tropical instability waves

TIWs were recognized as soon as satellites began observing SST as the cusps in the sharp front near 2°N between the East Pacific cold tongue and warmer water along the North Equatorial Countercurrent (Legeckis, 1977). They are particularly obvious in their SST patterns (Chelton *et al.*, 2000c; Contreras, 2002), distorting the front into 1,000 km to 1,500 km long cusp shapes (rounded to the south, pointed to the north; Figure 6.13). Since then, they have also been observed in satellite altimetry (Musman, 1989; Weidman *et al.*, 1999), surface drifter tracks (Hansen and Paul, 1984; Flament *et al.*, 1996; Baturin and Niiler, 1997), satellite ocean color (McClain *et al.,* 2002), and moored temperature and velocity time series

(Halpern *et al.*, 1988; McPhaden, 1996). They are a robust and commonly observed aspect of the eastern tropical Pacific (and Atlantic). In addition, they are a ubiquitous feature of ocean GCMs (Cox, 1980; Philander *et al.*, 1986; Kessler *et al.*, 1998; Masina and Philander, 1999). With very large meridional velocity fluctuations, of the order of $\pm 50\,\mathrm{cm\,s^{-1}}$, TIWs are a substantial source of noise that pose difficult aliasing problems in typically sparse ocean observations, even in sampling the mean (Johnson *et al.*, 2001). TIWs arise in the far eastern Pacific and propagate west with speeds of about $30\,\mathrm{cm\,s^{-1}}$ to $60\,\mathrm{cm\,s^{-1}}$ (about 10° longitude per month), weakening west of about 150°W. It has not been clear how far west they penetrate, since as the SST front weakens to the west their SST signature that is easiest to observe dies away. Their frequency spans 20–35 days. A feature that has caused confusion is the apparent difference in frequency depending on the quantity being observed, with SST (whose signature is seen in the SST front near 2°N) showing a dominant period of about 25 days (Legeckis, 1977), whereas the altimetric sea level (seen near 4°–6°N) appears to have a period near 35 days (Chelton *et al.*, 2003) and equatorial velocity a period near 21 days (Halpern *et al.*, 1988). These discrepancies may be the result of a fairly broadband instability shedding quasi-linear Yanai waves preferentially at certain frequencies (e.g., Weisberg *et al.*, 1979). Although TIWs were first identified north of the equator, and their strongest signals continue to be found there, recent work has shown the existence of TIWs to the south (Chelton *et al.*, 2000c).

The principal mechanism producing TIWs is thought to be barotropic (shear) instability, as first explained by Philander (1976, 1978). Since it is very difficult to diagnose energetics from sparse ocean observations, most of this work has been done in numerical models of various types. Hhowever, see Luther and Johnson (1990) and Qiao and Weisberg (1998) for observational analyses. Meridional shear in the equatorial Pacific is complex, with several strong oppositely directed zonal currents in close proximity (Luther and Johnson, 1990; Johnson *et al.*, 2002), and there has been an evolution in thinking about this problem. The original Philander analysis concluded that the relevant shear was near 4°N between the westward SEC and the eastward NECC. More recent work points to the shear close to the equator between the SEC and the EUC; in addition, the possibility of baroclinic instabilities associated either with spreading isotherms around the EUC or with the sharp temperature front appears to be important as well (Yu *et al.*, 1995; Masina *et al.*, 1999). The sources of energy conversion driving TIWs remains an active area of research, and it is likely that different mechanisms come into play at different latitudes, perhaps explaining the multiple frequency structure seen. However, the fact that ocean GCMs of diverse types easily generate TIWs, whether forced with realistic or highly simplified winds, suggests that near equatorial zonal shear is the dominant factor. The contribution to variability by free wave propagation out of the instability growth region is another current area of research. It has not been clear exactly how far east the TIWs begin, nor what is the initiating perturbation. All three currents involved are weaker in the far east (Lagerloef *et al.*, 1999; Johnson *et al.*, 2002), but note that the Costa Rica dome circulation may provide more shear east of 95°W (see Kessler, 2002a).

Because TIWs depend on background conditions, which vary seasonally and interannually, their low-frequency modulation is expected. The entire upper-equatorial circulation quickens when winds are strongest in June–December: the westward SEC and eastward NECC are largest in boreal fall, as is equatorial upwelling (Kessler *et al*., 1998). These conditions produce both the strongest meridional shears and sharpest temperature front, so it is not surprising to find that TIWs appear in May or June and persist through the following February–March. Similarly, during El Niño events both the SEC and cold tongue weaken dramatically, and TIWs are found to be absent (Baturin and Niiler, 1997). It is possible that TISO-generated Kelvin waves have an effect on TIWs by increasing eastward current speeds on the equator. Giese and Harrison (1991) find that in their OGCM the resulting increase in meridional shear amplifies TIWs and produces a transient equatorward heat flux that is as large as zonal advective warming due to Kelvin waves.

Equatorward heat flux due to TIW mixing across the sharp SST front is a first-order term in the low-frequency East Pacific heat balance, as large as upwelling or surface fluxes (Hansen and Paul, 1984; Bryden and Brady, 1989; Kessler *et al*., 1998; Swenson and Hansen, 1999; Wang and McPhaden, 1999). In the annual cycle it tends to counter the cooling due to wind-driven upwelling, which is also largest in June–December. TIWs accomplish a substantial momentum flux as well by mixing the shear between the SEC and EUC. The magnitude of mean zonal transport due to this poleward flux of eastward momentum is comparable with wind-driven Sverdrup transport (Kessler *et al*., 2003). Thus, TIWs pose a substantial sampling challenge for observations and a corresponding requirement for high temporal resolution in the diagnosis of ocean models in order to properly represent these very large rectified signatures.

With the advent of high-resolution scatterometer winds, the cusp-like TIW SST pattern was found to be imprinted on the cross-equatorial southeasterlies of the eastern equatorial Pacific (Chelton *et al*., 2001). This occurs because the cold tongue SST stabilizes and decouples the atmospheric planetary boundary layer from the free atmosphere above, leading to a slow surface wind speed. As southeasterlies blow across the distorted front and over the warm SST, convection develops that mixes momentum downward and increases the windspeed. Chelton *et al*. (2001) show that, because the wind direction is quite consistent, this feedback produces a systematically positive curl and divergence signal along the SST front, raising the possibility of a coupled interaction that could further impact the ocean.

6.7.3 ISV outside the equatorial Indo-Pacific

Large intraseasonal signatures are prominent in several regions outside the equatorial Indo-Pacific which are unconnected to the TISO signals that form the main subject of this book. This large topic is sketched here very briefly, giving the bare picture and providing references for those who wish to delve more deeply.

ISV associated with western boundary currents

The poleward western boundary currents closing the Atlantic, Pacific, and South Indian Ocean subtropical gyres generate significant variability in the intraseasonal to interannual frequency bands (Figure 6.12) (the North Indian Ocean is discussed below). ISV associated with western boundary currents has its origin in the fact that when these currents separate from the coast and are injected into the relatively quiescent open ocean the strong jets become unstable and form meanders which may grow to become closed-core eddies or rings containing water pinched off from north or south of the jet axis. Bottom topography is an important influence on the path of the current and the regions of meander formation. Rings have scales of a few hundred kilometers, reach depths of more than one kilometer, and may persist for several years as identifiable water mass features. Each of these currents sheds typically three to ten rings each year, resulting in an apparent intraseasonal timescale. Once generated, the rings tend to drift westward with some characteristics of Rossby wave dynamics, though nonlinear terms are usually significant, and they can also be swept eastward with the current or reabsorbed by it. Because the rings "contain" the water within them, substantial transport of heat and water properties can be accomplished by this drift. Such western boundary current ISV is seen in Figure 6.12 at the separation regions of the Gulf Stream and Brazil Current in the Atlantic, the Kuroshio and East Australia Current in the Pacific, and the Mozambique/Agulhas Current in the South Indian Ocean. Useful overviews of western boundary current structure and eddy generation mechanisms can be found in Olson (1991), Hogg and Johns (1995), and Ridgway and Dunn (2003). Analyses of eddies in the various regions include Willson and Rees (2000), Ducet and LeTraon (2001), Goni and Wainer (2001), Tilburg *et al.* (2001), and Qiu (2002).

The Mozambique/Agulhas Current system differs from the others because the South Indian Ocean subtropical gyre extends south of the Cape of Good Hope and, as a result, the western boundary current cannot close the gyre within the Indian basin. According to linear Sverdrup theory, the western boundary current would extend across the South Atlantic to the coast of South America (Godfrey, 1989), but this is not realized because of the instability of the strong jet injected into the South Atlantic, combined with the background eastward flow around the Southern Ocean. The Agulhas Current retroflects (i.e., turns around) developing an eddy at its western loop; this pinches off and the eddy usually drifts northwestward into the South Atlantic, accomplishing a large water property transport into that ocean, and producing the ISV maximum south of Africa in Figure 6.12. Agulhas eddies are discussed by Schouten *et al.* (2002) and references cited therein.

The Somali Current is distinguished from the other poleward western boundary currents by being present for only part of the year (see the May and August panels of Figure 6.10), a consequence of the fact that winds over the North Indian Ocean do not consist of permanent tropical trades and midlatitude westerlies and, thus, this basin does not have a permanent subtropical gyre. Nevertheless, during intense summer monsoon winds, the western boundary current that arises along the Somali coast is comparable in speed and transport with other major systems. ISV

associated with the Somali Current is again due to instabilities as it turns offshore near 5°N, as well as further eddies near the tip of Somalia known as the Great Whirl and Socotra Eddy that are spun up with the boundary current (Figure 6.12). Schott and McCreary (2001) provide a comprehensive review of the Somali Current and its stationary and transient eddies.

ISV in the Southern Ocean

A strip of high ISV runs along the axis of the Antarctic Circumpolar Current (ACC; Figure 6.12), where meridional eddy fluxes have long been seen as a principal process of both its heat and momentum balance (Bryden, 1983). Eddy kinetic energy along this band is the most energetic in the world ocean. The poleward heat transport across the Southern Ocean required to maintain the steady state is large and, because there are no meridional boundaries to support a gyre circulation, the eddies are the dominant mechanism by which this is accomplished (Gille, 2003). Zonal momentum from strong and persistent westerly winds must be removed, presumably by vertical transport to be balanced by topographic drag. However, there has been considerable debate about whether eddy momentum fluxes accelerate or decelerate the mean flow (e.g., Morrow *et al.*, 1994; Hughes and Ash, 2001). The ACC appears to be broken up into interleaved jets that flow along quasi-permanent temperature and salinity fronts, some of which are evident at the surface (Belkin and Gordon, 1996). This complex structure tends to be anchored to topography and much eddy variance is generated as strong nearly barotropic current flows over bottom features (Morrow *et al.*, 1992). The regions of intense eddy generation are visible in Figure 6.12 and include the ridges south of New Zealand, Drake Passage, and the mid-ocean ridges in the central Indian and Pacific Oceans.

Because of the extreme difficulty of working in these distant and dangerous waters, much of the early work on Southern Ocean eddies took place in the Drake Passage where a decades-long observational program took place (Bryden, 1983), but since satellite altimetry has allowed the production of maps of SSH variability, statistics of the global picture have become possible (Morrow *et al.*, 1992, 1994; Gille and Kelly, 1996). Although large-scale wind forcing might be expected to produce a large-scale response, Southern Ocean SSH variance is dominated by scales less than 1,000 km. Timescales were found to be about 34 days (Gille and Kelly, 1996). It is not known what produces this frequency structure.

ISV due to baroclinic instability

Currents on the westward limb (equatorial side) of subtropical gyres (i.e., the North and South Equatorial Currents) in all oceans typically present conditions favorable for the development of baroclinic instability. At the surface, especially in winter, temperatures are cooler with increasing latitude, but at the thermocline level temperatures become warmer moving poleward into the deep bowels of the gyres. The resulting poleward tilt of the gyres with depth implies a change of sign in the vertical of the meridional gradient of potential vorticity, which is a necessary (though not sufficient) condition for such instabilities to grow (see Pedlosky, 1987, for a review of

these dynamics). Linear stability analysis suggests that such disturbances should have the preferred size of 2π times the first baroclinic mode Rossby radius (a few hundred kilometers in the subtropics) and disperse as baroclinic Rossby waves; these characteristics will produce an intraseasonal timescale in subtropical time series (Qiu, 1999). Two such regions stand out in the bandpassed SSH variability map of Figure 6.12: in the Eastern Indian Ocean along 12°S and in the Western Pacific Ocean along 20°N. In both cases, although these are regions potentially influenced by intraseasonal wind and heat flux forcing, prominent ISV maxima have been shown to be due to internal oceanic phenomena unconnected to the TISO.

The band of high ISV roughly along 12°S in the Indian Ocean (Figure 6.12) occurs along the axis of the westward SEC, which carries low-salinity Pacific water from the ITF into the Central Indian Ocean. Feng and Wijffels (2002) show that the high-variance signal shown in Figure 6.12 has strong seasonal modulation, being larger by a factor of about 2 in July–September when the SEC itself is largest (as is the ITF which partly feeds it). They note that this seasonality is inconsistent with ISV forced by equatorial winds, which brings strong ISV to the Indonesian coast via Kelvin wave propagation, but peaks in January–June (see Section 6.6). Instead, ISV observed along 12°S was found to be an internally generated baroclinic instability of the SEC itself. Feng and Wijffels (2002) further show propagating sea level features, arising near 115°E, with a period of 40–80 days, a lengthscale of 100 km to 150 km, and a westward phase speed of 15 cm s^{-1} to 19 cm s^{-1}, consistent with the first-mode baroclinic Rossby wave speed in this region, and conclude that the observed ISV maximum was produced as an internal instability in the ocean.

A band of high ISV extends along 20°N from Hawaii to Taiwan (Figure 6.12), following the path of the eastward Subtropical Countercurrent (STCC) in the North Pacific. The STCC overlies the subsurface part of the westward North Equatorial Current (NEC) which extends poleward to the center of the gyre at the thermocline level. As in the Indian Ocean signal discussed above, the 20°N ISV has a pronounced seasonal modulation, with its maximum in boreal spring about 50% larger than its boreal fall minimum (Qiu, 1999). Qiu showed that as the vertical shear between the STCC and the NEC increases in boreal winter the vertical–meridional structure becomes baroclinically unstable and eddies develop. Roemmich and Gilson (2001) use temperature profiles along a ship track roughly at 20°N to show that their subsurface structure produced an overturning circulation and substantial poleward heat flux. The eddies propagate westward as baroclinic Rossby waves with a phase speed of about 10 cm s^{-1}, a wavelength of about 500 km, and thus a period of about 60 days. Although there is substantial intraseasonal forcing in this region, it occurs primarily in boreal summer, and the ISV maximum seen in Figure 6.12 appears to be due to internal ocean processes.

6.8 CONCLUSION

The literature reviewed here has shown that tropical intraseasonal forcing leads to a wide complex of dynamic and thermodynamic effects in the ocean, some of which

have the potential to produce subsequent effects on the evolution of the tropical climate system. A principal driver of the present enthusiasm for tropical oceanic ISV has been the possibility of oceanic rectification leading to a connection between the MJO and the ENSO cycle, but progress in observing and modeling the Eastern Indian Ocean and the development of the Asian monsoon suggests that some of the same mechanisms might be operating there as well.

The MJO/ENSO question revolves around the still unquantified net effect of intraseasonally oscillating forcing on the West Pacific warm pool. As reviewed in Sections 6.2 and 6.3, it is clear that the results of TISO heat, moisture, and wind forcing profoundly affect the character and composition of the West Pacific warm pool, producing its commonly stacked velocity structure with several layers of reversing jets and its frequent salinity-stratified barrier layer. These dynamic and thermodynamic consequences are tied together because the result of precipitation is to enhance the response to wind forcing by concentrating it in a thin surface layer. While the possibilities for rectification are rife, the quantification of suggested mechanisms is hindered by the difficulty of modeling these processes, which depend sensitively on the mixed layer depth and the vertical structure of momentum mixing, among the least believable aspects of present generation OGCMs. Indeed, similar models come to opposite conclusions about even the sign of some of the important rectified terms (e.g., the sign of the rectified current in the model of Kessler and Kleeman, 2000 compared with that of Waliser *et al*., 2003). In addition, the paucity of salinity observations means that the spatial structure of the mixed and barrier layers is only barely known.

6.9 REFERENCES

Anderson, S. P., R. A. Weller, and R. B. Lukas (1996) Surface buoyancy forcing and the mixed layer of the western equatorial Pacific warm pool: Observations and 1-D model results. *J. Climate*, **9**, 3056–3085.

Annamalai, H., R. Murtugudde, J. Potemra, S. P. Xie, P. Liu, and B. Wang (2003) Coupled dynamics over the Indian Ocean: Spring initiation of the Zonal Mode. *Deep-Sea Res. II*, **50**, 2305–2330.

Barnston, A. G., Y. He, and D. A. Unger (2000) A forecast product that maximizes utility for state-of-the-art seasonal climate prediction. *Bull. Amer. Meteorol. Soc.*, **81**, 1271–1290.

Baturin, N. G. and P. P. Niiler (1997) Effects of instability waves in the mixed layer of the equatorial Pacific. *J. Geophys. Res.*, **102**, 21771–21793.

Belamari, S., J.-L. Redelsperger, and M. Pontaud (2003) Dynamic role of a westerly wind burst in triggering an equatorial Pacific warm event. *J. Climate*, **16**, 1869–1890.

Belkin, I. M. and A. L. Gordon (1996) Southern Ocean fronts from the Greenwich Meridian to Tasmania. *J. Geophys. Res. Oceans*, **101**, 3675–3696.

Bhat, G. S., S. Gadgil, P. V. H. Kumar, S. R. Kalsi, P. Madhusoodanan, V. S. N. Murty, C. V. K. P. Rao, V. R. Babu, L. V. G. Rao, and R. R. Raos (2001) BOBMEX: The Bay of Bengal monsoon experiment. *Bull. Amer. Meteorol. Soc.,* **82**, 2217–2243.

Blanke, B. and S. Raynaud (1997) Kinematics of the Pacific equatorial undercurrent: An Eulerian and Lagrangian approach from GCM results. *J. Phys. Oceanogr.*, **27**, 1038–1053.

Bryden, H. L. (1983) The Southern Ocean. In: A. R. Robinson (Ed.), *Eddies in Marine Science*, Springer-Verlag, New York, pp. 265–277.

Bryden, H. L. and E. C. Brady (1989) Eddy momentum and heat fluxes and their effects on the circulation of the equatorial Pacific Ocean. *J. Mar. Res.*, **47**, 55–79.

Busalacchi, A. J. and M. A. Cane (1985) Hindcasts of sea level variations during the 1982–83 El Niño. *J. Phys. Oceanogr.*, **15**, 213–221.

Chelton, D. B., M. H. Freilich, and S. K. Esbensen (2000a) Satellite observations of the wind jets off the Pacific coast of Central America, Part I: Case studies and statistical characteristics. *Mon. Wea. Rev.*, **128**, 1993–2018.

Chelton, D. B., M. H. Freilich, and S. K. Esbensen (2000b) Satellite observations of the wind jets off the Pacific coast of Central America, Part II: Regional relationships and dynamical considerations. *Mon. Wea. Rev.*, **128**, 2019–2043.

Chelton, D. B., F. J. Wentz, C. L. Gentemann, R. A. deSzoeke, and M. G. Schlax (2000c) Satellite microwave SST observation of transequatorial Tropical Instability Waves. *Geophys. Res. Lett.*, **27**, 1239–1242.

Chelton, D. B., S. K. Esbensen, M. G. Schlax, N. Thum, M. H. Freilich, F. J. Wentz, C. L. Gentemann, M. J. McPhaden, and P. S. Schopf (2001) Observations of coupling between surface wind stress and sea surface temperature in the eastern tropical Pacific. *J. Climate*, **14**, 1479–1498.

Chelton, D. B., M. G. Schlax, J. M. Lyman, and G. C. Johnson (2003) Equatorially trapped Rossby waves in the presence of meridionally sheared baroclinic flow in the Pacific Ocean. *Prog. Oceanogr.*, **56**, 323–380.

Clarke, A. J. (1994) Why are surface equatorial ENSO winds anomalously westerly under anomalous large-scale convection? *J. Climate*, **7**, 1623–1627.

Clarke, A. J. and R. Ahmed (1999) Dynamics of remotely forced intraseasonal oscillations off the western coast of South America. *J. Phys. Oceanogr.*, **29**, 240–258.

Contreras, R. F. (2002) Long-term observations of tropical instability waves. *J. Phys. Oceanogr.*, **32**, 2715–2722.

Cox, M. D. (1980) Generation and propagation of 30-day waves in a numerical model of the Pacific. *J. Phys. Oceanogr.*, **10**, 1168–1186.

Cravatte, S., J. Picaut, and G. Eldin (2003) Second and first baroclinic modes in the equatorial Pacific at intraseasonal timescales. *J. Geophys. Res.*, **108**, 3226, doi: 10.1029/2002JC001511.

Cronin, M. F. and M. J. McPhaden (1997) The upper ocean heat balance in the western equatorial Pacific warm pool during September–December 1992. *J. Geophys. Res.*, **102**, 8533–8553.

Cronin, M. F. and M. J. McPhaden (2002) Barrier layer formation during westerly wind bursts. *J. Geophys. Res.*, **107**, 8020, doi: 10.1029/2001JC001171.

Cronin, M. F., M. J. McPhaden, and R. H. Weisberg (2000) Wind-forced reversing jets in the western equatorial Pacific. *J. Phys. Oceanogr.*, **30**, 657–676.

Delcroix, T., G. Eldin, M. J. McPhaden, and A. Morliere (1993) Effects of westerly wind bursts upon the western equatorial Pacific Ocean, February–April 1991. *J. Geophys. Res.*, **98**, 16379–16385.

Ducet, N. and P. Y. LeTraon (2001) A comparison of surface eddy kinetic energy and Reynolds stresses in the Gulf Stream and the Kuroshio Current systems from merged TOPEX/Poseidon and ERS-1/2 altimetric data. *J. Geophys. Res.*, **106**, 16603–16662.

Durland, T. S. and B. Qiu (2003) Transmission of subinertial Kelvin waves through a strait. *J. Phys. Oceanogr.*, **33**, 1337–1350.

Eigenheer, A. and D. Quadfasel (2000) Seasonal variability of the Bay of Bengal circulation inferred from TOPEX/Poseidon altimetry. *J. Geophys. Res.*, **105**, 3243–3252.

Eldin, G., T. Delcroix, C. Henin, K. Richards, Y. duPenhoat, J. Picaut, and P. Rual (1994) Large-scale current and thermohaline structures along 156° during the COARE intensive observing period. *Geophys. Res. Lett.*, **21**, 2681–2684.

Enfield, D. B. (1987) The intraseasonal oscillation in eastern Pacific sea levels: How is it forced? *J. Phys. Oceanogr.*, **17**, 1860–1876.

Enfield, D. B. and R. Lukas (1983) Low-frequency sea level variability along the South American coast in 1981–83. *Trop. Ocean–Atmos. Newslett.*, **28**, 2–4.

Fedorov, A. V. (2002) The response of the coupled tropical ocean–atmosphere to westerly wind bursts. *Quart. J. Roy. Meteorol. Soc.*, **128**, 1–23.

Feng, M. and S. Wijffels (2002) Intraseasonal variability in the South Equatorial Current of the east Indian Ocean. *J. Phys. Oceanogr.*, **32**, 265–277.

Fink, A. and P. Speth (1997) Some potential forcing mechanisms of the year-to-year variability of the tropical convection and its intraseasonal (25–70-day) variability. *Int. J. Climatol.*, **17**, 1513–1534.

Flament, P. J., S. C. Kennan, R. A. Knox, P. P. Niiler, and R. L. Bernstein (1996) The three-dimensional structure of an upper-ocean vortex in the tropical Pacific Ocean. *Nature*, **383**, 610–613.

Fu, L.-L., E. J. Christensen, C. A. Yamarone, M. Lefebvre, Y. Menard, M. Dorrer, and P. Escudier (1994) TOPEX/POSEIDON mission overview. *J. Geophys. Res.*, **99**, 24369–24382.

Giese, B. S. and D. E. Harrison (1990) Aspects of the Kelvin wave response to episodic wind forcing. *J. Geophys. Res. Oceans*, **95**, 7289–7312.

Giese, B. S. and D. E. Harrison (1991) Eastern equatorial Pacific response to three composite westerly wind types. *J. Geophys. Res.*, **96**, 3239–3248.

Giese, B. S., J. A. Carton, and L. J. Holl (1994) Sea level variability in the eastern Pacific as observed by TOPEX and Tropical Ocean Global–Atmosphere Tropical Atmosphere–Ocean experiment. *J. Geophys. Res.*, **99**, 24739–24748.

Gille, S. T. (2003) Float observation of the Southern Ocean, Part II: Eddy fluxes. *J. Phys. Oceanogr.*, **33**, 1182–1196.

Gille, S. T. and K. A. Kelly (1996) Scales of spatial and temporal variability in the Southern Ocean. *J. Geophys. Res.*, **101**, 8759–8773.

Godfrey, J. S. (1989) A Sverdrup model of the depth-integrated flow for the world ocean, allowing for island circulations. *Geophys. Astrophys. Fluid Dyn.*, **45**, 89–112.

Godfrey, J. S., R. A. Houze, R. H. Johnson, R. Lukas, J.-L. Redelsperger, A. Sumi, and R. Weller (1998) Coupled Ocean–Atmosphere Response Experiment (COARE): An interim report. *J. Geophys. Res.*, **103**, 14395–14450.

Goni, G. J. and I. Wainer (2001) Investigation of the Brazil Current front variability from altimeter data. *J. Geophys. Res.*, **106**, 31117–31128.

Gould, J., D. Roemmich, S. Wijffels, H. Freeland, M. Ignaszewsky, X. Jianping, S. Pouliquen, Y. Desaubies, U. Send, and K. Radhakrishman (2004) Argo profiling floats bring new era of in situ ocean observations. *EOS, Trans. Amer. Geophys. Union*, **85**, 179–191.

Gutzler, D. S. (1991) Interannual fluctuations of intraseasonal variance of near-equatorial zonal winds. *J. Geophys. Res.*, **96**, 3173–3185.

Halpern, D., R. A. Knox, and D. S. Luther (1988) Observations of 20-day period meridional current oscillations in the upper ocean along the Pacific equator. *J. Phys. Oceanogr.*, **18**, 1514–1534.

Han, W., J. P. McCreary, D. L. T. Anderson, and A. J. Mariano (1999) On the dynamics of the eastward surface jets in the equatorial Indian Ocean. *J. Phys. Oceanogr.*, **29**, 2191–2209.

Han, W., D. M. Lawrence, and P. J. Webster (2001a) Dynamical response of equatorial Indian Ocean to intraseasonal winds: Zonal flow. *Geophys. Res. Lett.*, **28**, 4215–4218.

Han, W., J. P. McCreary, and K. E. Kohler (2001b) Influence of precipitation minus evaporation and Bay of Bengal rivers on dynamics, thermodynamics, and mixed layer physics in the upper Indian Ocean. *J. Geophys. Res.*, **106**, 6895–6916.

Hansen, D. V. and G. A. Maul (1991) Anticyclonic current rings in the eastern tropical Pacific Ocean. *J. Geophys. Res.*, **96**, 6965–6979.

Hansen, D. V. and C. A. Paul (1984) Genesis and effect of long waves in the equatorial Pacific. *J. Geophys. Res.*, **89**, 10431–10440.

Hayes, S. P., L. J. Mangum, J. Picaut, A. Sumi, and K. Takeuchi (1991) TOGA-TAO: A moored array for real-time measurements in the tropical Pacific Ocean. *Bull. Amer. Meteorol. Soc.*, **72**, 339–347.

Hendon, H. H. and M. L. Salby (1994) The life cycle of the Madden–Julian Oscillation. *J. Atmos. Sci.*, **51**, 2225–2231.

Hendon, H. H., B. Liebmann, and J. D. Glick (1998) Oceanic Kelvin waves and the Madden–Julian Oscillation. *J. Atmos. Sci.*, **55**, 88–101.

Hendon, H. H., C. Zhang, and J. D. Glick (1999) Interannual variability of the Madden–Julian Oscillation during austral summer. *J. Climate*, **12**, 2358–2550.

Hisard, P., J. Merle, and B. Voituriez (1970) The equatorial undercurrent observed at 170°E in March and April 1967. *J. Mar. Res.*, **28**, 281–303.

Hogg, N. G. and W. E. Johns (1995) Western boundary currents. *Rev. Geophys.*, **33**, 1311–1334.

Hormazabal, S., G. Shaffer, J. Letelier, and O. Ulloa (2001) Local and remote forcing of sea surface temperature in the coastal upwelling system off Chile. *J. Geophys. Res. Oceans*, **106**(C8), 16657–16671.

Hormazabal, S., G. Shaffer, and O. Pizarro (2002) Tropical Pacific control of intraseasonal oscillations off Chile by way of oceanic and atmospheric pathways. *Geophys. Res. Lett.*, **29**, Art. 1081.

Hughes, C. W. and E. R. Ash (2001) Eddy forcing of the mean flow in the Southern Ocean. *J. Geophys. Res.*, **106**, 2713–2722.

Hurd, W. E. (1929) Northers of the Gulf of Tehuantepec. *Mon. Wea. Rev.*, **57**, 192–194.

Jensen, T. G. (1993) Equatorial variability and resonance in a wind-driven Indian Ocean model. *J. Geophys. Res.*, **98**, 22533–22552.

Johnson, E. S. and D. S. Luther (1994) Mean zonal momentum balance in the upper and central equatorial Pacific Ocean. *J. Geophys. Res.*, **99**, 7689–7705.

Johnson, E. S. and M. J. McPhaden (1993a) Structure of intraseasonal Kelvin waves in the equatorial Pacific Ocean. *J. Phys. Oceanogr.*, **23**, 608–625.

Johnson, E. S. and M. J. McPhaden (1993b) Effects of a 3-dimensional mean flow on intraseasonal Kelvin waves in the equatorial Pacific Ocean. *J. Geophys. Res. Oceans*, **98**, 10185–10194.

Johnson, G. C., M. J. McPhaden, and E. Firing (2001) Equatorial Pacific Ocean horizontal velocity, divergence and upwelling. *J. Phys. Oceanogr.*, **31**, 839–849.

Johnson, G. C., B. M. Sloyan, W. S. Kessler, and K. E. McTaggart (2002) Direct measurements of upper ocean currents and water properties across the equatorial Pacific during the 1990s. *Prog. Oceanogr.*, **52**, 31–61.

Kessler, W. S. (2001) EOF representations of the Madden–Julian Oscillation and its connection with ENSO. *J. Climate*, **14**, 3055–3061.

Kessler, W. S. (2002a) Mean three-dimensional circulation in the northeast tropical Pacific. *J. Phys. Oceanogr.*, **32**, 2457–2471.

Kessler, W. S. (2002b) Is ENSO a cycle or a series of events? *Geophys. Res. Lett.*, **29**, 2125, doi: 1029/2002GL015924.

Kessler, W. S. and R. Kleeman (2000) Rectification of the Madden–Julian Oscillation into the ENSO cycle. *J. Climate*, **13**, 3560–3575.

Kessler, W. S. and M. J. McPhaden (1995a) Oceanic equatorial waves and the 1991–93 El Niño. *J. Climate*, **8**, 1757–1774.

Kessler, W. S. and M. J. McPhaden (1995b) The 1991–93 El Niño in the central Pacific. *Deep-Sea Res. II*, **42**, 295–333.

Kessler, W. S., M. J. McPhaden, and K. M. Weickmann (1995) Forcing of intraseasonal Kelvin waves in the equatorial Pacific. *J. Geophys. Res.*, **100**, 10613–10631.

Kessler, W. S., L. M. Rothstein, and D. Chen (1998) The annual cycle of SST in the eastern tropical Pacific, diagnosed in an ocean GCM. *J. Climate*, **11**, 777–799.

Kessler, W. S., G. C. Johnson, and D. W. Moore (2003) Sverdrup and nonlinear dynamics of the Pacific equatorial currents. *J. Phys. Oceanogr.*, **33**, 994–1008.

Kindle, J. C. and P. A. Phoebus (1995) The ocean response to operational wind bursts during the 1991–92 El Niño. *J. Geophys. Res.*, **100**, 4803–4920.

Kindle, J. C. and J. D. Thompson (1989) The 26- and 50-day oscillations in the western Indian Ocean: Model results. *J. Geophys. Res.*, **94**, 4721–4736.

Kutsuwada, K. and M. J. McPhaden (2002) Intraseasonal variations in the upper equatorial Pacific Ocean prior to and during the 1997–98 El Niño. *J. Phys. Oceanogr.*, **32**(4), 1133–1149.

Lagerloef, G. S. E., G. T. Mitchum, R. B. Lukas, and P. P. Niiler (1999) Tropical Pacific near-surface currents estimated from altimeter, wind and drifter data. *J. Geophys. Res.*, **104**, 23313–23326.

Latif, M., J. Biercamp, and H. von Storch (1988) The response of a coupled ocean–atmosphere general circulation model to wind bursts. *J. Atmos. Sci.*, **45**, 964–979.

Legeckis, R. (1977) Long waves in the eastern equatorial ocean: A view from a geostationary satellite. *Science*, **197**, 1179–1181.

Lengaigne, M., J. P. Boulanger, C. Menkes, S. Masson, G. Madec, and P. Delecluse (2002) Ocean response to the March 1997 westerly wind event. *J. Geophys. Res. Oceans*, **107**(C12), Art. 8015.

Levitus, S. (1994) *Climatological Atlas of the World Ocean* (NOAA Prof. Pap. No. 13). U.S. Government Printing Office.

Loschnigg, J. and P. J. Webster (2000) A coupled ocean–atmosphere system of SST modulation for the Indian Ocean. *J. Climate*, **13**, 3342–3360.

Lukas, R. and E. Lindstrom (1991) The mixed layer of the western equatorial Pacific. *J. Geophys. Res.*, **96**, 3343–3357.

Lukas, R., S. P. Hayes, and K. Wyrtki (1984) Equatorial sea level response during the 1982–1983 El Niño. *J. Geophys. Res.*, **89**, 10425–10430.

Luther, D. S. and E. S. Johnson (1990) Eddy energetics in the upper equatorial Pacific during the Hawaii-to-Tahiti Shuttle Experiment. *J. Phys. Oceanogr.*, **20**, 913–944.

Luyten, J. R. and D. H. Roemmich (1982) Equatorial currents at semi-annual period in the Indian Ocean. *J. Phys. Oceanogr.*, **12**, 406–413.

Madden, R. A. and P. A. Julian (1994) Observations of the 40–50-day tropical oscillation: A review. *Mon. Wea. Rev.*, **122**, 814–837.

Mariano, A. J., E. H. Ryan, B. D. Perkins, and S. Smithers (1995) *The Mariano Global Surface Velocity Analysis 1.0* (Technical Report, CG-D-34-95). U.S. Coast Guard.

Masina, S. and S. G. H. Philander (1999) An analysis of tropical instability waves in a numerical model of the Pacific Ocean, Part 1: Spatial variability of the waves. *J. Geophys. Res.*, **104**, 29613–29635.

Masina, S., S. G. H. Philander, and A. B. G. Bush (1999) An analysis of tropical instability waves in a numerical model of the Pacific Ocean, Part 2: Generation and energetics of the waves. *J. Geophys. Res.*, **104**, 29637–29661.

Masson, S., P. Delecluse, J.-P. Boulanger, and C. Menkes (2002) A model study of the seasonal variability and formation mechanisms of the barrier layer in the eastern equatorial Indian Ocean. *J. Geophys. Res.*, **107**, 8017, doi: 10.1029/2001JC000832.

Masson, S., P. Delecluse, and J.-P. Boulanger (2003) Impacts of salinity on the eastern Indian Ocean during the termination of the fall Wyrtki Jet. *J. Geophys. Res.*, **108**, doi: 10.1029/2001JC00083.

McClain, C. R., J. R. Christian, S. R. Signorinin, M. R. Lewis, I. Asanuma, D. Turk, and C. Dupouy-Douchement (2002) Satellite ocean color observations of the tropical Pacific Ocean. *Deep-Sea Res. II*, **49**, 2533–2560.

McCreary, J. P. (1984) Equatorial beams. *J. Mar. Res.*, **42**, 395–430.

McCreary, J. P. (1985) Modeling equatorial ocean circulation. *Ann. Rev. Fluid Mech.*, **17**, 359–409.

McCreary, J. P., H. S. Lee, and D. B. Enfield (1989) Response of the coastal ocean to strong offshore winds: With application to circulations in the Gulf of Tehuantepec and Papagayo. *J. Mar. Res.*, **47**, 81–109.

McCreary, J. P., P. K. Kundu, and R. L. Molinari (1993) A numerical investigation of dynamics, thermodynamics and mixed-layer processes in the Indian Ocean. *Prog. Oceanogr.*, **31**, 181–244.

McPhaden, M. J. (1995) The Tropical Atmosphere–Ocean array is completed. *Bull. Amer. Meteorol. Soc.*, **76**, 739–741.

McPhaden, M. J. (1996) Monthly period oscillations in the Pacific North Equatorial Countercurrent. *J. Geophys. Res.*, **101**, 6337–6360.

McPhaden, M. J. (1999) Genesis and evolution of the 1997–98 El Niño. *Science*, **283**, 950–954.

McPhaden, M. J. (2002) Mixed layer temperature balance on intraseasonal timescales in the equatorial Pacific Ocean. *J. Climate*, **15**, 2632–2647.

McPhaden, M. J. and S. P. Hayes (1991) On the variability of winds, sea surface temperature and surface layer heat content in the western equatorial Pacific. *J. Geophys. Res.*, **96**(Suppl.), 3331–3342.

McPhaden, M. J. and B. A. Taft (1988) Dynamics of seasonal and intraseasonal variability in the eastern equatorial Pacific. *J. Phys. Oceanogr.*, **18**, 1713–1732.

McPhaden, M. J. and X. Yu (1999) Equatorial waves and the 1997–98 El Niño. *Geophys. Res. Lett.*, **26**, 2961–2964.

McPhaden, M. J., H. P. Freitag, S. P. Hayes, B. A. Taft, Z. Chen, and K. Wyrtki (1988) The response of the equatorial Pacific Ocean to a westerly wind burst in May 1986. *J. Geophys. Res.*, **93**, 10589–10603.

McPhaden, M. J., S. P. Hayes, L. J. Mangum, and J. M. Toole (1990) Variability in the western equatorial Pacific Ocean during the 1986–87 El Niño/Southern Oscillation event. *J. Phys. Oceanogr.*, **20**, 190–208.

McPhaden, M. J., F. Bahr, Y. duPenhoat, E. Firing, S. P. Hayes, P. P. Niiler, P. L. Richardson, and J. M. Toole (1992) The response of the western equatorial Pacific Ocean to westerly wind bursts during November 1989 to January 1990. *J. Geophys. Res.*, **97**, 14289–14303.

Metzger, E. J., H. E. Hurlburt, J. C. Kindle, Z. Sirkes, and J. M. Pringle (1992) Hindcasting of wind-driven anomalies using a reduced gravity global ocean model. *Mar. Tech. Soc. J.*, **26**, 23–32.

Meyers, G., J.-R. Donguy, and R. Reed (1986) Evaporative cooling of the western equatorial Pacific. *Nature*, **312**, 258–260.

Miyama, T., J. P. McCreary, T. G. Jensen, J. Loschnigg, S. Godfrey, and A. Ishida (2003) Structure and dynamics of the Indian Ocean cross-equatorial cell. *Deep-Sea Res. II*, **50**, 2023–2047.

Moore, A. M. and R. Kleeman (1999) Stochastic forcing of ENSO by the intraseasonal oscillation. *J. Climate*, **12**, 1199–1220.

Moore, A. M. and R. Kleeman (2001) The differences between the optimal perturbations of coupled models of ENSO. *J. Climate*, **14**, 138–163.

Moore, D. W. and J. P. McCreary (1990) Excitation of intermediate-frequency equatorial waves at a western ocean boundary: With application to observations from the Indian Ocean. *J. Geophys. Res.*, **95**, 5219–5231.

Morrow, R., J. Church, R. Coleman, D. Chelton, and N. White (1992) Eddy momentum flux and its contribution to the Southern Ocean momentum balance. *Nature*, **357**, 482–484.

Morrow, R., R. Coleman, J. Church, and D. Chelton (1994) Surface eddy momentum flux and velocity variances in the Southern Ocean from Geosat altimetry. *J. Phys. Oceanogr.*, **24**, 2050–2071.

Müller-Karger, F. E. and C. Fuentes-Yaco (2000) Characteristics of wind-generated rings in the eastern tropical Pacific Ocean. *J. Geophys. Res.*, **105**, 1271–1284.

Murtugudde, R. and A. J. Busalacchi (1999) Interannual variability of the dynamics and thermodynamics of the tropical Indian Ocean. *J. Climate*, **12**, 2300–2326.

Murtugudde, R., J. P. McCreary, and A. J. Busalacchi (2000) Oceanic processes associated with anomalous events in the Indian Ocean with relevance to 1997–1998. *J. Geophys. Res.*, **105**, 3295–3306.

Musman, S. (1989) Sea height wave form in equatorial waves and its interpretation. *J. Geophys. Res.*, **94**, 3303–3309.

Neelin, J. D., D. S. Battisti, A. C. Hirst, F.-F. Jin, Y. Wakata, T. Yamagata, and S. E. Zebiak (1998) ENSO theory. *J. Geophys. Res.*, **103**, 14261–14290.

Olson, D. B. (1991) Rings in the ocean. *Ann. Rev. Earth Planet Sci.*, **19**, 283–311.

Pedlosky, J. (1987) *Geophysical Fluid Dynamics* (Second Edition). Springer-Verlag, New York. 710 pp.

Perigaud, C. (1990) Sea level oscillations observed with Geosat along the two shear fronts of the Pacific North Equatorial Countercurrent. *J. Geophys. Res.*, **95**, 7239–7248.

Philander, S. G. H. (1976) Instabilities of zonal equatorial currents. *J. Geophys. Res.*, **81**, 3725–3735.

Philander, S. G. H. (1978) Instabilities of zonal equatorial currents, 2. *J. Geophys. Res.*, **83**, 3679–3682.

Philander, S. G. H. and R. C. Pacanowski (1980) The generation of equatorial currents. *J. Geophys. Res.*, **85**, 1123–1136.

Philander, S. G. H., W. J. Hurlin, and R. C. Pacanowski (1986) Properties of long equatorial waves in models of the seasonal cycle in the tropical Atlantic and Pacific Oceans. *J. Geophys. Res.*, **91**, 14207–14211.

Potemra, J. T., M. E. Luther, and J. J. O'Brien (1991) The seasonal circulation of the upper ocean in the Bay of Bengal. *J. Geophys. Res.*, **96**, 12667–12683.

Potemra, J. T., S. L. Hautala, J. Sprintall, and W. Pandoe (2002) Interaction between the Indonesian Seas and the Indian Ocean in observations and numerical models. *J. Phys. Oceanogr.*, **32**, 1838–1854.

Potemra, J. T., S. L. Hautala, and J. Sprintall (2003) Vertical structure of the Indonesian Throughflow in a large-scale model. *Deep-Sea Res. II*, **50**, 2143–2161.

Qiao, L. and R. H. Weisberg (1998) Tropical instability wave energetics: Observations from the Tropical Instability Wave Experiment. *J. Phys. Oceanogr.*, **28**, 345–360.

Qiu, B. (1999) Seasonal eddy field modulation of the North Pacific Subtropical Countercurrent: TOPEX/Poseidon observations and theory. *J. Phys. Oceanogr.*, **29**, 2471–2486.

Qiu, B. (2002) The Kuroshio Extension system: Its large-scale variability and role in the midlatitude ocean–atmosphere interaction. *J. Oceanogr.*, **58**, 57–75.

Qiu, B., M. Mao, and Y. Kashino (1999) Intraseasonal variability in the Indo-Pacific Throughflow and the regions surrounding the Indonesian Seas. *J. Phys. Oceanogr.*, **29**, 1599–1618.

Ralph, E. A., K. Bi, P. P. Niiler, and Y. duPenhoat (1997) A Lagrangian description of the western equatorial Pacific response to the wind burst of December 1992: Heat advection in the warm pool. *J. Climate*, **10**, 1706–1721.

Ramanathan, V. and W. Collins (1991) Thermodynamic regulation of ocean warming by cirrus clouds deduced from observations of the 1987 El Niño. *Nature*, **351**, 27–32.

Raymond, D. J. (2001) A new model of the Madden–Julian Oscillation. *J. Atmos. Sci.*, **58**, 2807–2819.

Reppin, J., F. A. Schott, J. Fischer, and D. Quadfasel (1999) Equatorial currents and transports in the upper central Indian Ocean: Annual cycle and interannual variability. *J. Geophys. Res.*, **104**, 15495–15514.

Reverdin, G. (1987) The upper equatorial Indian Ocean: The climatological seasonal cycle. *J. Phys. Oceanogr.*, **17**, 903–927.

Reverdin, G. and J. Luyten (1986) Near-surface meanders in the equatorial Indian Ocean. *J. Phys. Oceanogr.*, **16**, 1088–1100.

Richardson, R. A., I. G. Ginnis, and L. M. Rothstein (1999) A numerical investigation of the local ocean response to westerly wind burst forcing in the western equatorial Pacific. *J. Phys. Oceanogr.*, **29**, 1334–1352.

Ridgway, K. R. and J. R. Dunn (2003) Mesoscale structure of the mean East Australian Current System and its relationship with topography. *Prog. Oceanogr.*, **56**, 189–222.

Roden, G. I. (1961) On the wind-driven circulation in the Gulf of Tehuantepec and its effect on surface temperatures. *Geofis. Int.*, **1**, 55–72.

Roemmich, D. and J. Gilson (2001) Eddy transport of heat and thermocline waters in the North Pacific: A key to interannual/decadal climate variability? *J. Phys. Oceanogr.*, **31**, 675–687.

Roemmich, D., M. Morris, W. R. Young, and J. R. Donguy (1994) Fresh equatorial jets. *J. Phys. Oceanogr.*, **24**, 540–558.

Roulston, M. S. and J. D. Neelin (2000) The response of an ENSO model to climate noise, weather noise and intraseasonal forcing. *Geophys. Res. Lett.*, **27**, 3723–3726.

Saji, N. H., B. N. Goswami, P. N. Vinayachandran, and T. Yamagata (1999) A dipole mode in the tropical Indian Ocean. *Nature*, **401**, 360–363.

Schiller, A. and J. S. Godfrey (2003) Indian Ocean intraseasonal variability in an ocean general circulation model. *J. Climate*, **16**, 21–39.

Schneider, N. (1998) The Indonesian Throughflow and the global climate system. *J. Climate*, **11**, 676–689.

Schott, F. A. and J. P. McCreary (2001) The monsoon circulation of the Indian Ocean. *Prog. Oceanogr.*, **51**, 1–123.

Schott, F., J. Reppin, and J. Fischer (1994) Currents and transports of the Monsoon Current south of Sri Lanka. *J. Geophys. Res.*, **99**, 25127–25141.

Schouten, M. W., W. P. M. de Ruijter, and P. J. van Leeuwen (2002) Upstream control of Agulhas ring shedding. *J. Geophys. Res.*, **107**, doi: 10.1029/2001JC000804.

Sengupta, D., R. Senan, and B. N. Goswami (2001) Origin of intraseasonal variability of circulation in the tropical central Indian Ocean. *Geophys. Res. Lett.* **28**, 1267–1270.

Shetye, S. R., A. D. Gouveia, D. Shankar, S. S. C. Shenoi, P. N. Vinayachandran, D. Sundar, G. S. Michael, and G. Nampoothiri (1996) Hydrography and circulation in the western Bay of Bengal during the northeast monsoon. *J. Geophys. Res.*, **101**, 14011–14025.

Shinoda, T. and H. H. Hendon (1998) Mixed layer modeling of intraseasonal variability in the tropical western Pacific and Indian Oceans. *J. Climate*, **11**, 2668–2685.

Shinoda, T. and H. H. Hendon (2001) Upper-ocean heat budget in response to the Madden–Julian oscillation in the western equatorial Pacific. *J. Climate* **14**(21), 4147–4165.

Shinoda, T. and H. H. Hendon (2002) Rectified wind forcing and latent heat flux produced by the Madden–Julian Oscillation. *J. Climate*, **15**(23), 3500–3508.

Shinoda, T., H. H. Hendon, and J. D. Glick (1998) Intraseasonal variability of surface fluxes and sea surface temperature in the tropical western Pacific and Indian Oceans. *J. Climate*, **11**, 1685–1702.

Slingo, J. M., D. P. Rowell, K. R. Sperber, and F. Nortley (1999) On the predictability of the inter annual behavior of the Madden–Julian Oscillation and its relationship with El Niño. *Quart. J. Roy. Meteorol. Soc.*, **125**, 583–609.

Somayajulu, Y. K., V. S. N. Murty, and Y. V. B. Sarma (2003) Seasonal and interannual variability of surface circulation in the bay of Bengal from TOPEX/Poseidon altimetry. *Deep-Sea Res. II*, **50**, 867–880.

Spillane, M. C., D. B. Enfield, and J. S. Allen (1987) Intraseasonal oscillations in sea level along the west coast of the Americas. *J. Phys. Oceanogr.*, **17**, 313–325.

Sprintall, J. and M. J. McPhaden (1994) Surface layer variations observed in multiyear time series measurements from the western equatorial Pacific. *J. Geophys. Res.*, **99**, 963–979.

Sprintall, J. and M. Tomczak (1992) Evidence of the barrier layer in the surface layer of the tropics. *J. Geophys. Res.*, **97**, 7305–7316.

Sprintall, J., J. T. Potemra, S. L. Hautala, N. A. Bray, and W. W. Pandoe (2003) Temperature and salinity variability in the exit passages of the Indonesian Throughflow. *Deep-Sea Res.* II, **50**, 2183–2204.

Stammer, D. (1997) Global characteristics of ocean variability estimated from regional TOPEX/Poseidon altimeter measurements. *J. Phys. Oceanogr.*, **27**, 1743–1769.

Stommel, H. M. (1960) Wind-drift near the equator. *Deep-Sea Res.*, **6**, 298–302.

Swallow, J. C. (1983) Eddies in the Indian Ocean. In: A. R. Robinson (Ed.), *Eddies in Marine Science*. Springer-Verlag, New York, pp. 200–218.

Swenson, M. S. and D. V. Hansen (1999) Tropical Pacific Ocean mixed layer heat budget: The Pacific cold tongue. *J. Phys. Oceanogr.*, **29**, 69–82.

Tilburg, C. E., H. E. Hurlburt, J. J. O'Brien, and J. F. Shriver (2002) The dynamics of the East Australian Current system: The Tasman Front, the East Auckland Current, and the East Cape Current. *J. Phys. Oceanogr.*, **31**, 2917–2943.

Tomczak, M. and J. S. Godfrey (1994) *Regional Oceanography: An Introduction*. Pergamon Press, Oxford, U.K., 422 pp.

Trasviña, A. (1995) Offshore wind forcing in the Gulf of Tehuantepec, Mexico: The asymmetric circulation. *J. Geophys. Res.*, **96**, 12599–12618.

Tsai, P. T. H., J. J. O'Brien, and M. E. Luther (1992) The 26-day oscillation observed in satellite sea surface temperature measurements in the equatorial western Indian Ocean. *J. Geophys. Res.*, **97**, 9605–9618.

van Oldenborgh, G. J. (2000) What caused the onset of the 1997–98 El Niño? *Mon. Wea. Rev.*, **128**, 2601–2607.

Vecchi, G. A. and D. E. Harrison (2000) Tropical Pacific sea surface temperature anomalies, El Niño, and westerly wind bursts. *J. Climate*, **13**, 1814–1830.

Vinayachandran, P. N. and T. Yamagata (1998) Monsoon response of the sea around Sri Lanka: Generation of thermal domes and anticyclonic vortices. *J. Phys. Oceanogr.*, **28**, 1946–1960.

Waliser, D. E., R. Murtugudde, and L. E. Lucas (2003) Indo-Pacific ocean response to atmospheric intraseasonal variability, Part I: Austral summer and the Madden–Julian Oscillation. *J. Geophys. Res.*, **108**, 3160, doi: 10.1029/2003JC001620.

Waliser, D. E., R. Murtugudde, and L. E. Lucas (2004) Indo-Pacific ocean response to atmospheric intraseasonal variability, Part II: Boreal summer and the intraseasonal oscillation. *J. Geophys. Res.*, **109**, C03030, doi: 10.1029/2003JC002002.

Wang, W. and M. J. McPhaden (1999) The surface-layer heat budget in the equatorial Pacific Ocean, Part I: Mean seasonal cycle. *J. Phys. Oceanogr.*, **29**, 1812–1831.

Webster, P. J. and R. Lukas (1992) TOGA-COARE: The coupled ocean–atmosphere response experiment. *Bull. Amer. Meteorol. Society*, **73**, 1377–1416.

Webster, P. J., A. M. Moore, J. P. Loschnigg, and R. R. Leben (1999) Coupled ocean–atmosphere dynamics in the Indian Ocean during 1997–98. *Nature*, **401**, 356–360.

Webster, P. J., E. F. Bradley, C. W. Fairall, J. S. Godfrey, P. Hacker, R. A. Houze, R. Lukas, Y. Serra, J. M. Hummon, T. D. M. Lawrence *et al.* (2002) The JASMINE pilot study. *Bull. Amer. Meteorol. Society*, **83**, 1603–1630.

Weidman, P. D., D. L. Mickler, B. Dayyani, and G. H. Born (1999) Analysis of Legeckis eddies in the near-equatorial Pacific. *J. Geophys. Res.*, **104**, 7865–7887.

Weisberg, R. H. and T. Y. Tang (1983) Equatorial ocean response to growing and moving wind systems, with application to the Atlantic. *J. Mar. Res.*, **41**, 461–486.

Weisberg, R. H. and C. Wang (1997) Slow variability in the equatorial west–central Pacific in relation to ENSO. *J. Climate*, **10**, 1998–2017.

Weisberg, R. H., A. M. Horigan, and C. Colin (1979) Equatorially-trapped variability in the equatorial Atlantic. *J. Mar. Res.*, **37**, 67–86.

Weller, R. A. and S. P. Anderson (1996) Surface meteorology and air–sea fluxes in the western equatorial Pacific warm pool during the TOGA coupled ocean–atmosphere response experiment. *J. Climate*, **9**, 1959–1990.

Willson, H. R. and N. W. Rees (2000) Classification of mesoscale features in the Brazil–Falkland Current confluence zone. *Prog. Oceanogr.*, **45**, 415–426.

Wu, L., Z. Liu, and H. E. Hurlburt (2000) Kelvin wave and Rossby wave interaction in the extratropical–tropical Pacific. *Geophys. Res. Lett.*, **27**, 1259–1262.

Wyrtki, K. (1973) An equatorial jet in the Indian Ocean. *Science*, **181**, 262–264.

Yoshida, K. (1959) A theory of the Cromwell Current (the equatorial undercurrent) and of equatorial upwelling. *J. Oceanogr. Soc. Japan*, **15**, 159–170.

Yu, L. S. (2003) Variability of the depth of the 20°C isotherm along 6°N in the Bay of Bengal: Its response to remote and local forcing and its relation to satellite SSH variability. *Deep-Sea Res. II*, **50**, 2285–2304.

Yu, Z. J. and P. S. Schopf (1997) Vertical eddy mixing in the tropical upper ocean: Its influence on zonal currents. *J. Phys. Oceanogr.*, **27**, 1447–1458.

Yu, Z. J., J. P. McCreary, and J. A. Proehl (1995) Meridional asymmetry and energetics of tropical instability waves. *J. Phys. Oceanogr.*, **25**, 2997–3007.

Zebiak, S. E. (1989) On the 30–60 day oscillation and the prediction of El Niño. *J. Climate*, **2**, 1381–1387.

Zebiak, S. E. and M. A. Cane (1987) A model El Niño-Southern Oscillation. *Mon. Wea. Rev.*, **115**, 2262–2278.

Zhang, C. (1996) Atmospheric intraseasonal variability at the surface in the tropical western Pacific Ocean. *J. Atmos. Sci.*, **53**, 739–758.

Zhang, C. (1997) Intraseasonal variability of the upper-ocean thermal structure observed at 0° and 165°E. *J. Climate*, **10**, 3077–3092.

Zhang, C. (2001) Intraseasonal perturbations in sea surface temperatures of the equatorial eastern Pacific and their association with the Madden–Julian Oscillation. *J. Climate*, **14**(6), 1309–1322.

Zhang, C. D. and J. Gottschalck (2002) SST anomalies of ENSO and the Madden–Julian oscillation in the equatorial Pacific. *J. Climate*, **15**, 2429–2445.

Zhang, C. and M. J. McPhaden (2000) Intraseasonal surface cooling in the equatorial western Pacific. *J. Climate*, **13**, 2261–2276.

Zhang, C., H. H. Hendon, W. S. Kessler, and A. J. Rosati (2001) A workshop on the MJO and ENSO: Meeting summary. *Bull. Amer. Meteorol. Society*, **82**, 971–976.

Zhang, K. Q. and L. M. Rothstein (1998) Modeling the oceanic response to westerly wind bursts in the western equatorial Pacific. *J. Phys. Oceanogr.*, **28**, 2227–2249.

7

Air–sea interaction

Harry Hendon

7.1 INTRODUCTION

Air–sea interaction associated with tropical intraseasonal variability (ISV) and, particularly, the Madden–Julian Oscillation (MJO) is of interest for three reasons. First, variations in the air–sea fluxes of heat and moisture may be fundamental to the mechanisms involved in tropical ISV. For instance, air–sea interaction may promote the slow eastward propagation of the MJO and its northward propagation in the Indian summer monsoon. Besides playing a critical role for the interplay between convection and dynamics, surface fluxes of heat, moisture, and momentum drive sea surface temperature (SST) perturbations that may feed back to surface fluxes and, ultimately, to atmospheric dynamics—thus, for instance, contributing to growth of the MJO. Second, the episodic variations of surface momentum, heat, and freshwater fluxes driven by atmospheric ISV may play a role in the maintenance and low-frequency variability of the warm pool in the tropical Indian and Pacific Oceans. For example, the MJO induces transports in the equatorial West Pacific that act in the mean to remove about the same amount of heat from the warm pool as is provided by mean surface heat flux (Ralph *et al.*, 1997). From the opposite perspective of the ocean driving the atmosphere, interannual variations of SST in the warm pool may also drive interannual variations in MJO activity, which may bear on the ability to predict seasonal variations of MJO activity. Third, the MJO forces surface currents that drive SST variations at the eastern edge of the warm pool (e.g., Kessler *et al.*, 1995). Kelvin waves are also efficiently excited by the MJO (e.g., Hendon *et al.*, 1998), which radiate into the Eastern Pacific where they can perturb the SST (e.g., Giese and Harrison, 1991; Zhang, 2001; McPhaden, 2002). These intraseasonal SST variations may lead to a rectified coupled response, which plays a role in the evolution of the El Niño Southern Oscillation (ENSO) (e.g., Bergman *et al.*, 2001; Zhang and Gottschalck, 2002).

W. K. M. Lau and D. E. Waliser (Editors), *Intraseasonal Variability in the Atmosphere–Ocean Climate System* (Second Edition).

The focus in this chapter is on observations of air–sea interaction that may be relevant to the mechanism and variability of the MJO. Interactions relevant to the evolution of ENSO are only briefly discussed but are covered in detail in Chapters 6 and 9. Diagnostic studies of the response in the upper ocean to intraseasonal surface flux variations, which provides insight into the processes that control the associated SST variability in the warm pool, are also covered. Theory and modeling studies of the role of air–sea interaction for the mechanism for the MJO are touched upon briefly but are treated in detail in Chapters 10 and 11.

7.2 AIR–SEA FLUXES FOR THE EASTWARD MJO

The evolution of surface heat, moisture, and momentum fluxes associated with the eastward-propagating MJO has been described in the Western Pacific using satellite and in situ observations (e.g., Zhang, 1996; Lau and Sui, 1997; Zhang and McPhaden, 2000) and across the entire warm pool using global analyses (e.g., Flatau *et al*., 1997; Hendon and Glick, 1997; Jones *et al*., 1998; Shinoda *et al*., 1998; Woolnough *et al*., 2000). The basic structure of the fluxes is schematically illustrated in Figure 7.1. The abscissa (in kilometers) spans one half the wavelength of the MJO, which is an equivalent duration of $\sim$30 days at a given point as the MJO systematically propagates eastward. This schematic is typical for the MJO (with some minor shifts in phasing as discussed below) across the entire warm pool of the Indian and Western Pacific Oceans.

In the convectively active phase, which has a zonal extent of about 8,000 km and meridional width of about 2,000 km, increased deep convection is associated with increased cloud cover, increased rainfall, and decreased surface insolation. Enhanced deep convection slightly leads (by $\sim$1 week) enhanced surface westerlies. In the warm pool region where the basic state wind is weak westerly, these anomalous westerlies act to increase the surface windspeed, hence increasing the flux of latent and sensible heat. In the convectively suppressed phase, which has a slightly larger zonal extent (and longer duration) than the active phase, reduced westerlies act to reduce the windspeed, thus reducing latent and sensible heat flux. Decreased convection is also associated with decreased cloud cover and increased surface insolation.

The observed phase lag ($\sim$1 week) of latent heat flux with respect to enhanced convection is counter to that assumed in some simple "quasi-equlibrium" models of the MJO, whereby enhanced latent heat flux to the east of enhanced convection acts to intensify convection to the east (e.g., Emanuel, 1987). Such models presume an easterly basic state so that easterly anomalies in advance of enhanced convection act to increase the windspeed and latent heat flux. While such a simple theory is at odds with the observed phase lag of latent heat flux with respect to convection, a positive impact of wind-induced latent heat flux variations has been demonstrated in some models (e.g., Neelin *et al*., 1987; Lin *et al*., 2000; Raymond, 2001; Colón *et al*., 2002).

The magnitudes of fluxes at the extrema of a large MJO event are indicated in Figure 7.1. The sensible heat flux anomaly is not shown, as it is about one tenth the size of the latent heat flux anomaly and has similar phasing. The net surface

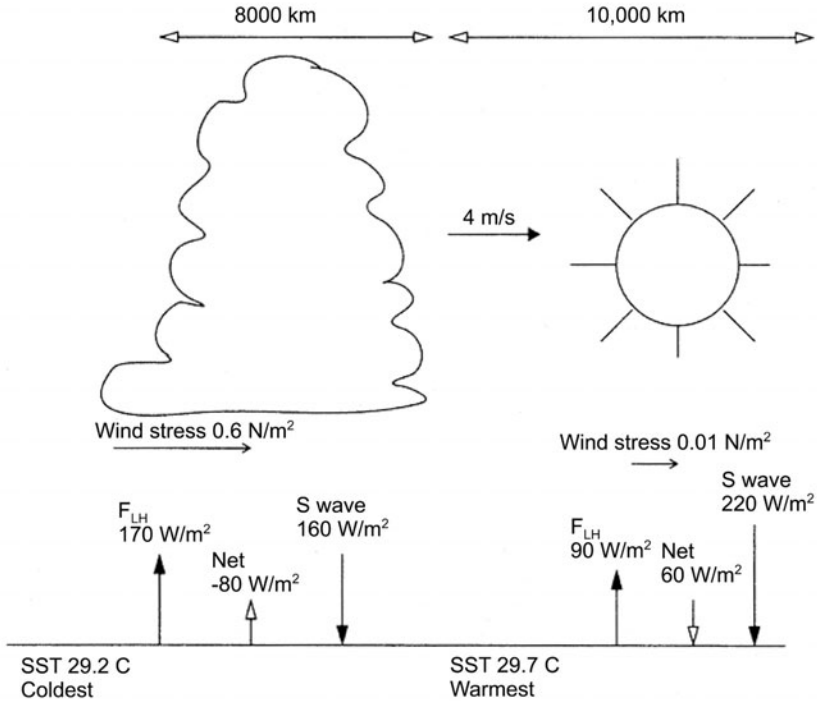

Figure 7.1. Schematic diagram showing the magnitude and phase relationship relative to the convective anomaly of surface fluxes and SST variations produced by the canonical MJO. The asymmetric zonal scale of the cloudy windy phase and suppressed calm phase as well as the eastward phase speed ($4\,m\,s^{-1}$) of the joint atmosphere–ocean disturbance across the warm pool are indicated. Typical extrema of surface fluxes and SST over the lifecycle of the MJO are shown for the Western Pacific (from Shinoda *et al.*, 1998).

longwave radiation (also not shown) tends to oppose the surface insolation anomaly but is much smaller. Hence, the surface heat flux variation is dominated by insolation and latent heat flux variations.

Enhanced convection and associated enhanced cloud cover typically reduce surface insolation by about $20\,W\,m^{-2}$ to $40\,W\,m^{-2}$. Shortly thereafter ($\sim$7-day lag), latent heat flux, in association with enhanced surface westerlies, peaks with a similar magnitude. This near collocation implies that latent heat flux and the insolation anomaly act together to produce a peak surface cooling of $40\,W\,m^{-2}$ to $80\,W\,m^{-2}$, which propagates coherently eastward across the equatorial warm pool in conjunction with convection and surface westerly anomalies. In the suppressed convective phase, insolation is increased by $10\,W\,m^{-2}$ to $30\,W\,m^{-2}$ and the reduced surface westerlies act to decrease latent heat flux by $10\,W\,m^{-2}$ to $30\,W\,m^{-2}$. Together, insolation and latent heat flux anomalies produce a peak surface warming of about $20\,W\,m^{-2}$ to $60\,W\,m^{-2}$ during the suppressed phase. Note that in this analysis the peak amplitude of the warming during the suppressed

convective phase is weaker than the cooling during the enhanced convective phase. However, the suppressed phase is of longer duration (greater zonal extent) than the enhanced phase. Hence, averaged over a lifecycle, net heat flux is weakly positive into the warm pool.

As the convective anomaly approaches the dateline, induced easterly anomalies east of the convection act to increase the windspeed and latent heat flux (e.g., Hendon and Glick, 1997; Woolnough *et al*., 2000) because the mean (trade) winds are easterly in the Eastern Pacific. Because enhanced latent heat flux now occurs east of enhanced convection (i.e., in a region of enhanced insolation) and convective anomalies weaken as the MJO propagates into the Eastern Pacific (hence producing weaker surface insolation anomalies), the surface heat flux perturbation is generally small east of the dateline. However, during northern summer, the MJO perturbs convection in the Intertropical Convergence Zone (ITCZ) north of the equator and coherent surface heat flux perturbations of similar phasing and magnitude to those in the warm pool are observed in the Eastern Pacific (e.g., Maloney and Kiehl, 2002).

The MJO also perturbs freshwater and surface momentum fluxes. Over the warm pool, Shinoda *et al*. (1998) estimate rainfall to increase by $5\,\mathrm{mm\,day^{-1}}$ to $7\,\mathrm{mm\,day^{-1}}$ during the enhanced convective phase and decrease by a similar amount during the calm-suppressed convective phase. Similarly, westerly stress increases to about $0.05\,\mathrm{N\,m^{-2}}$ during the westerly-convective phase and decreases to about $0.01\,\mathrm{N\,m^{-2}}$ during the suppressed convective phase. A hallmark of the MJO is that the maximum (westerly) stress nearly coincides with the highest flux of freshwater into the ocean. Hence, their individual influences on the buoyancy forcing of the warm pool mixed layer will tend to cancel (e.g., Anderson *et al*., 1996; Zhang and Anderson, 2003).

The phasing and relative magnitude of the fluxes in Figure 7.1 are observed to vary systematically as the MJO traverses the Indian and Western Pacific Oceans. When convection is developing in the Indian Ocean, the convective anomaly tends to be near the node of the surface zonal wind anomaly (e.g., Hendon and Salby, 1994), which is consistent with a Gill-type response to equatorially symmetric diabatic heating. As the convection moves into the Western Pacific, the surface zonal wind anomaly shifts eastward relative to the convection so that anomalous westerlies blow entirely through the region of anomalous convection. Hendon and Salby (1994) interpret this changing phase as indicative of the evolution of the energetics of the MJO through its lifecycle. However, a simple dynamical explanation is that the convective anomaly tends to be equatorially centered in the Indian Ocean but shifts off the equator into the South Pacific Convergence Zone (SPCZ) in the West Pacific. Hence, the phasing of the surface zonal wind relative to convection in the Indian Ocean is consistent with an equatorial symmetric heat source. In the Western Pacific, however, the phasing of surface zonal winds is consistent with an equatorial asymmetric heat source displaced into the southern hemisphere.

The changing phase of surface zonal winds relative to the convective anomaly implies that the phasing of surface fluxes will change as the active convective phase propagates eastward from the Indian Ocean. In the Western Pacific, the surface

insolation anomaly will be more in phase with the latent heat flux anomaly because the surface westerlies coincide with increased convection. But, in the Indian Ocean, there will be less cooperation. Shinoda *et al.* (1998) further diagnose the latent heat flux anomaly to contribute less to the total surface heat flux anomaly in the Indian Ocean. Hence, surface heat flux variation in the Indian Ocean is dominated by insolation variation whereas latent heat and insolation anomalies make equal contributions in the Western Pacific.

7.3 AIR–SEA FLUXES ASSOCIATED WITH NORTHWARD PROPAGATION IN THE INDIAN SUMMER MONSOON

During boreal summer, the eastward-propagating MJO is notably weaker (e.g., Salby and Hendon, 1994), while the dominant intraseasonal mode exhibits pronounced northward propagation ($\sim 1^\circ$ lat day^{-1}) from the equatorial Indian Ocean into the Indian monsoon (e.g., Sikka and Gadgil, 1980; Wang and Rui, 1990; Kemball-Cook and Wang, 2001). The dominant period is shorter as well (35 days as compared with 50 days during winter). There is some debate as to whether northward propagation occurs independent of the eastward-propagating MJO along the equator (e.g., Lawrence and Webster, 2002; Jiang *et al.*, 2004). Nonetheless, the northward-propagating events during boreal summer significantly perturb the surface fluxes of heat, moisture, and momentum. The associated coherent SST anomalies are indicative of robust air–sea interaction (e.g., Bhat *et al.*, 2001; Sengupta and Ravichandran, 2001; Vecchi and Harrison, 2002; Webster *et al.*, 2002). While dynamical mechanisms for the poleward propagation away from the equator, which involve emitted Rossby waves, have been suggested (Chapter 10), air–sea interaction appears to foster northward propagation in much the same fashion as it fosters eastward propagation along the equator (e.g., Fu *et al.*, 2003).

Figure 7.2 displays the structure of air–sea fluxes for the typical northward-propagating intraseasonal oscillation (ISO) in the Indian Ocean sector during boreal summer. The abscissa spans about 20°–25° latitude, representative of a section of the Indian Ocean from the equator to 20°–25°N. Equivalently, a span of about 20 days is displayed at a given point in the Indian Ocean as the oscillation propagates to the north.

To the north of the developing convective anomaly, reduced convection acts to increase surface insolation. In the suppressed region, anomalous easterlies act on the westerly basic state of the summer monsoon, thereby reducing windspeed and latent heat flux. During the convective phase, enhanced convection acts to decrease insolation, while anomalous westerlies act on the westerly basic state to increase windspeed and latent heat flux. Typical magnitudes of these intraseasonal variations are $\sim 5\,\mathrm{m\,s^{-1}}$ for the zonal wind and $\sim 25\,\mathrm{W\,m^{-2}}$ for latent heat flux and insolation. These anomalies can increase by a factor of 3 to 4 for individual events (e.g., Webster *et al.*, 2002).

As for the eastward-propagating MJO, the maximum latent heat flux anomaly occurs slightly after the maximum convection, which again brings into question the

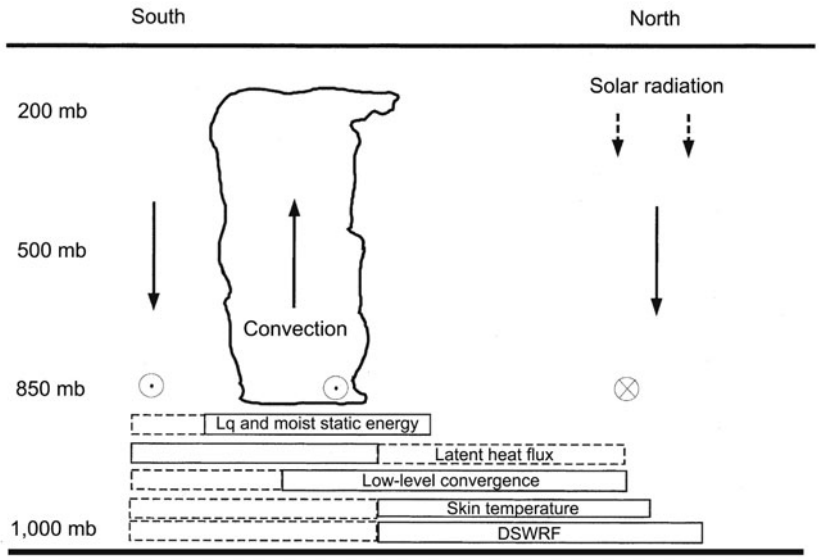

Figure 7.2. Schematic of air–sea interaction in the northward propagation of convective anomalies associated with the ISO during boreal summer in the Indian and Western Pacific Oceans. Dark vertical lines indicate the mid-troposphere vertical velocity anomaly. The cloud indicates deep precipitating convection. DSWRF is downward shortwave radiative flux and Lq is the latent heat of vaporization times the humidity anomaly q. The boxes represent the approximate locations of anomalies relative to the convection. Solid boxes indicate a positive anomaly and dashed boxes a negative anomaly. Circles indicate the direction of the 850 mb zonal wind anomaly with the $\odot$ ($\otimes$) representing easterlies (westerlies) (from Kemball-Cook and Wang, 2001).

relevance of simple "quasi-equilibrium" theories for explaining intraseasonal behavior during boreal summer. The insolation anomaly slightly leads the latent heat flux anomaly, but they still add constructively to perturb net surface heat flux, which can result in significant SST perturbations.

7.4 SST VARIABILITY

For the ocean to play an active role in the dynamics of the eastward-propagating MJO and the northward-propagating variability in the Indian monsoon, surface flux variations must induce a SST variation. Krishnamurti *et al.* (1988), motivated by the need to explain the long timescale of the MJO, were the first to examine SST variability associated with the MJO. Using data from the First GARP Global Experiment (FGGE) year, they showed that intraseasonal (30 to 60-day period) SST variability was most prominent across the equatorial Indian and Western Pacific Oceans and had temporal phasing indicative of atmospheric forcing of the ocean on the intraseasonal timescale (i.e., minimum SST lagged maximum surface

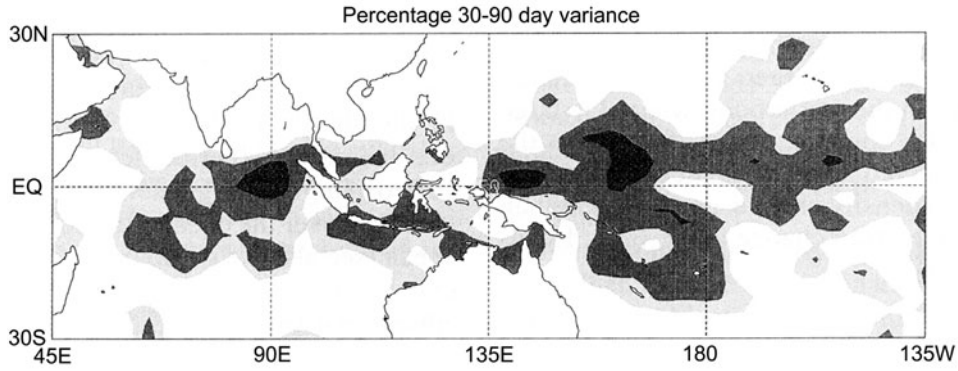

Figure 7.3. Ratio (percentage) of intraseasonal (30 to 90-day period) SST variance to total subseasonal (10 to 200-day period) SST variance for the period July 1, 1986–June 30, 1993. Shading levels begin at 45%, 50%, and 60% (from Hendon and Glick, 1997).

westerlies by $\sim 1/4$ of a cycle). Hendon and Glick (1997), using 7 years of weekly SST analyses from Reynolds and Smith (1994), confirm their results. Figure 7.3 displays the ratio (as a percentage) of intraseasonal (30 to 90-day period) to subseasonal (10 to 200-day period) SST variance. Regions in the Indian and Western Pacific with a ratio greater than 50% are also regions where SST variability exhibits a significant spectral peak near 60 days (Zhang, 1996; Hendon and Glick, 1997). These regions are also where the signal in convection and surface winds associated with the MJO is the strongest (e.g., Salby and Hendon, 1994). Note that ISV in the northern Indian Ocean may be underestimated in the satellite-based SST data used to create Figure 7.3 due to retrieval problems in regions of persistent precipitating convection (Harrison and Vecchi, 2001; Sengupta and Ravichandran, 2001).

For the eastward-propagating MJO, warm SST anomalies develop after passage of the calm-suppressed phase, when surface heat flux is most positive into the ocean and cold SST anomalies develop after passage of the windy convective phase, when the surface heat flux is mostly negative (Figure 7.1). The typical SST anomaly has an amplitude of $\sim 1/3$ K (Flatau *et al.*, 1997; Hendon and Glick, 1997; Zhang, 1997; Shinoda *et al.*, 1998; Woolnough *et al.*, 2000; Kemball-Cook and Wang, 2001), although strong MJO events often produce SST swings of more than 1 K in the western equatorial Pacific (e.g., Weller and Anderson, 1996).

Pronounced SST anomalies in the Indian Ocean are also observed during boreal summer when the ISO is propagating northward. To the north of the developing convective anomaly in the equatorial Indian Ocean, clear skies (enhanced insolation) and reduced latent heat flux (easterly anomalies) act to warm the Arabian Sea and Bay of Bengal (e.g., Kimball-Cook and Wang, 2001; Vecchi and Harrison, 2002). During the convective phase, increased cloud cover reduces insolation and anomalous westerlies act to increase windspeed and latent heat flux, thereby producing surface cooling. Hence, a warm SST anomaly leads the northward-propagating convective anomaly by 1–2 weeks (1/4 of a cycle) and a cold SST anomaly follows the convective anomaly by a similar lag. The magnitude of these

SST anomalies, especially in the Bay of Bengal (1–3 K), can be much larger than for the near equatorial SST anomalies associated with the eastward-propagating MJO (e.g., Sengutpa and Ravichandran, 2001). The freshness of the mixed layer in the Bay of Bengal, where mean precipitation and river runoff is high, results in a shallower and more stably stratified mixed layer with a deeper barrier layer than in the western equatorial Pacific (e.g., Bhat *et al.*, 2001; Sengupta and Ravichandran, 2001; Webster *et al.*, 2002). Hence, the mixed layer in the Bay of Bengal remains shallow in the presence of stronger winds and is more sensitive to intraseasonal surface heat flux variations.

7.5 MECHANISMS OF SST VARIABILITY

Understanding how SST and the upper-ocean mixed layer vary intraseasonally is important both for successful coupled simulation and for validation of the air–sea interaction theories of ISV. The focus in this section is on mechanisms of near equatorial SST variability associated with the eastward MJO. Much less work has been done on the mechanisms of SST variability in the northern Indian Ocean associated with northward-propagating ISOs during boreal summer, probably due to a lack of quality observations of upper-ocean and surface meteorology. However, recent field campaigns (e.g., JASMINE and BOBMEX) and new satellite SST products (e.g., Vecchi and Harrison, 2002) have revealed some similarities and differences in the behavior of the near equatorial warm pool, which are commented on at the end of this section.

The near equatorial warm pool is a region of weak winds and horizontal SST gradient, a deep thermocline (~ 100 m), and a shallow (~ 25 m) fresh (stable) mixed layer that overlays a deeper more saline isothermal layer (e.g., Lukas and Lindstrom, 1991). The layer between the halocline, which typically defines the base of the mixed layer, and the thermocline is referred to as the barrier layer, because it effectively shields the mixed layer from colder sub-thermocline water. These conditions of weak horizontal temperature gradient and strong vertical stability mean that 1-D processes primarily govern intraseasonal SST variations in the warm pool. The relatively weak wind fluctuations produced by the MJO are typically not sufficient to mix through the barrier layer. Hence, the SST variation associated with the MJO is primarily accounted for by surface heat flux variation (Anderson *et al.*, 1996; Flatau *et al.*, 1997; Hendon and Glick, 1997; Lau and Sui, 1997; Jones *et al.*, 1998; Shinoda and Hendon, 1998; Woolnough *et al.*, 2000; Schiller and Godfrey, 2003; Zhang and Anderson, 2003). The largest heat flux out of the ocean occurs at about the time of maximum convection (Figure 7.1), resulting in a minimum SST about 1/4 of a cycle later (about 2 weeks for a typical MJO event). Similarly, the largest heat flux into the ocean occurs at the time of most suppressed convection, resulting in a warmest SST about 1/4 of a cycle prior to onset of deep convection.

Detailed observations in the western equatorial Pacific during the Tropical Ocean Global Atmosphere–Coupled Ocean Atmosphere Response Experiment (TOGA–COARE) (Webster and Lukas, 1992), however, suggest complex

evolution of the upper ocean through the lifecycle of the MJO. TOGA–COARE ran from November 1992 to February 1993. The experiment was fortunate in that two major MJO events traversed the intensive flux array (IFA) located in the equatorial Western Pacific (roughly spanning 2°N–2°S, 152°S–157°E) in December 1992 and January 1993 (e.g., Gutzler *et al.*, 1994). Hourly observations of surface fluxes and SST at the Improved Meteorology (IMET) mooring (located at 1.45°S, 156°E; Weller and Anderson, 1996) are shown in Figure 7.4 (Anderson *et al.*, 1996). During the suppressed convective phase, SST gradually warms in the presence of a positive surface heat flux and weak surface wind. A pronounced diurnal cycle of SST is evident. During the convective phase, when winds strengthen and become westerly, surface heat flux is negative and SST rapidly cools with an absence of a diurnal cycle. The westerlies at this time are seen to be highly variable, which is a hallmark of the so-called westerly "wind bursts" that tend to occur within the large-scale envelope of enhanced convection during the MJO (e.g., Hendon and Liebmann, 1994). These wind bursts could potentially play an important role in the evolution of the warm pool mixed layer because wind stirring of the mixed layer does not simply increase linearly with windspeed.

High-resolution modeling of the mixed layer indicates that 1-D processes govern this SST behavior provided that accurate surface fluxes are utilized (Figure 7.4; see also Shinoda and Hendon, 1998). However, for this TOGA–COARE period at the IMET site, a cumulative systematic bias is apparent (Figure 7.4), which is only accounted for by considering horizontal and vertical advection (e.g., Cronin and McPhaden, 1997; Feng *et al.*, 1998, 2000). Except within the oceanic equatorial radius of deformation ($\sim$2–3° latitude; e.g., Ralph *et al.*, 1997; Feng *et al.*, 2000; Shinoda and Hendon, 2001; Schiller and Godfrey, 2003), horizontal and vertical advection appear not to be coherent on the scale of the MJO. Hence, advection does not play a systematic role in governing the meridionally broad SST variation associated with the MJO (Shinoda and Hendon, 1998, 2001). While advective processes are clearly important at some places for individual events, they depend critically on the initial state of the upper ocean (e.g., pre-existing anomalous horizontal temperature gradient) and atmospheric noise (non-spatially coherent circulation). Thus, the magnitude and sign of advective tendencies vary significantly from one MJO event to another. Systematic advection in the near equatorial belt is returned to shortly.

The mixed layer depth does vary systematically over the lifecycle of the MJO (Hendon and Glick, 1997; Shinoda and Hendon, 1998), which will affect the sensitivity of the mixed layer to surface heat flux variations and the amount of shortwave radiation that penetrates through the mixed layer. Mixed layer deepening is also indicative of entrainment, which may act to additionally cool or warm the mixed layer depending on the stratification.

Typical evolution of the ocean mixed layer from the suppressed calm phase to the convective windy phase of the MJO is illustrated in Figure 7.5. During the calm clear phase of the MJO (days 36–48)—which corresponds to November 26 to December 8, 1992 during COARE—a shallow mixed layer forms above a deep barrier layer in response to positive surface heat flux and small turbulent mixing.

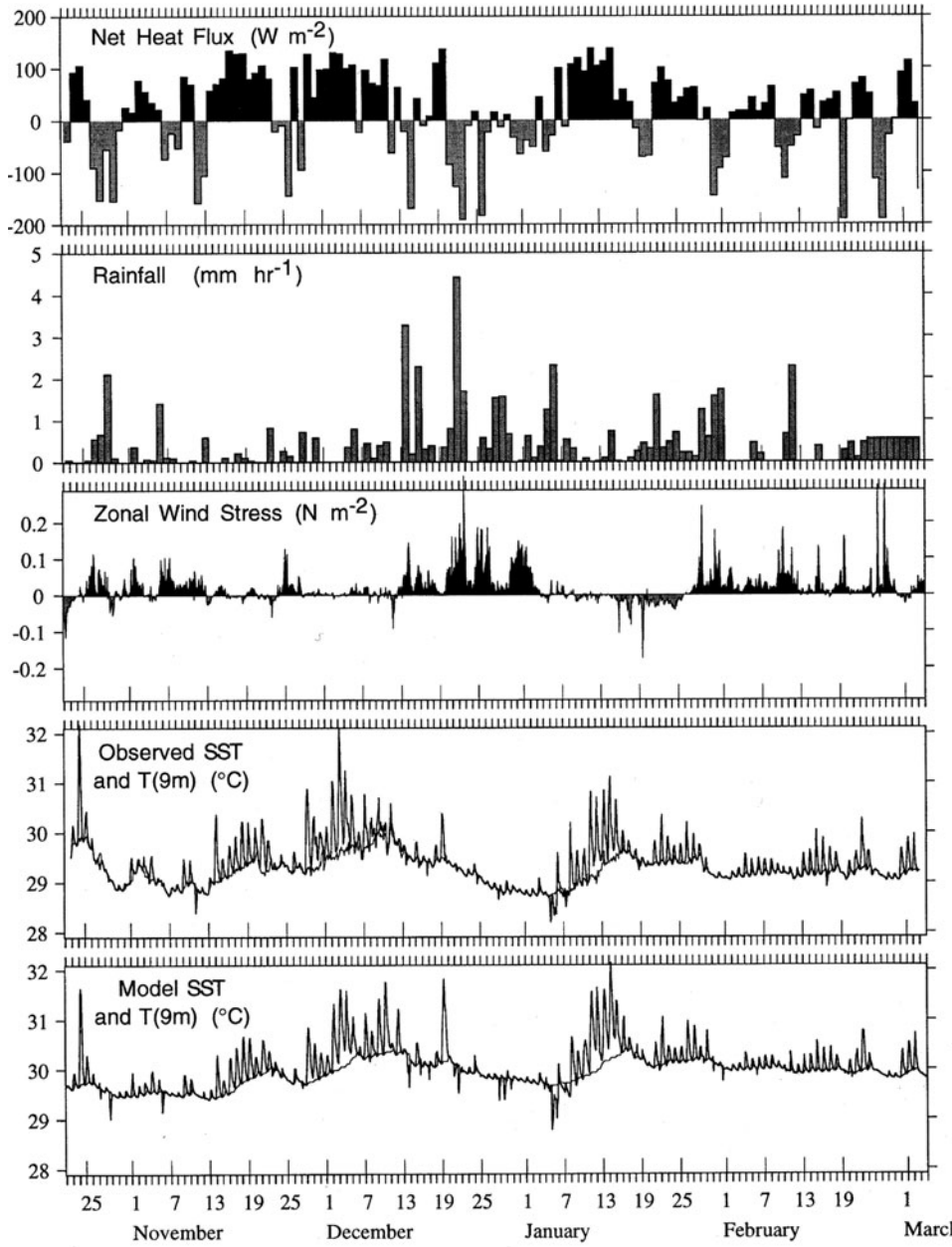

Figure 7.4. Time series of air–sea fluxes and SST from the WHOI–IMET mooring located in the IFA during TOGA–COARE (October 25, 1992–March 1, 1993). Net heat flux and rainfall were averaged over 24 hours. Wind stress and observed SST were smoothed over 2 hours. Modeled SST was estimated using a 1-D mixed layer model forced with observed surface fluxes from the IMET mooring (from Anderson *et al.*, 1996).

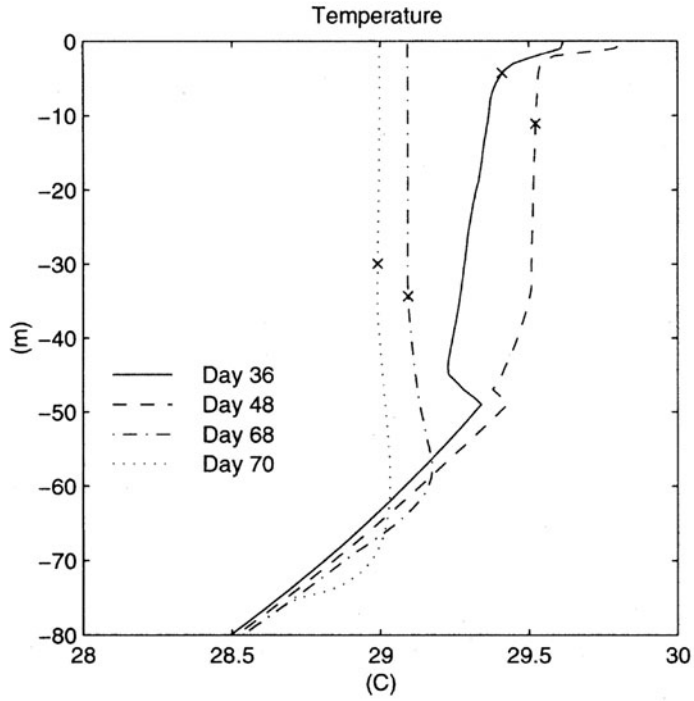

Figure 7.5. Daily average temperature profile simulated in the equatorial Western Pacific using a 1-D mixed layer model driven by observed surface fluxes for the MJO event that traversed the IFA in late December 1992 (see Figure 7.4). The crosses indicate the mixed layer depth each day. Day 36 corresponds to November 26, 1992 (suppressed convective phase) and day 70 corresponds to December 30, 1992 (post convective phase) (from Shinoda and Hendon, 1998).

A strong diurnal cycle of mixed layer depth and temperature develops (Figure 7.6), with night-time convection acting to spread intense daytime warming to a deeper layer. The shallowness of the mixed layer during this warming phase (<10 m) also results in significant ($>10\,\mathrm{W\,m^{-2}}$) penetration of shortwave radiation through the base of the mixed layer. Absorption of this radiation below the mixed layer results in a stable inversion owing to the freshness of the mixed layer (Lukas and Lindstrom, 1991; Sprintall and Tomczak, 1992; Anderson *et al.*, 1996; Shinoda and Hendon, 1998; Schiller and Godfrey, 2003; Zhang and Anderson, 2003).

During the cloudy windy phase (days 68–70)—which corresponds to December 26–28, 1992)—the surface heat flux is negative, the mixed layer deepens, and the diurnal cycle of radiation is weak. The negative surface heat flux initially cools the mixed layer more than the sub–mixed layer and the mixed layer begins to deepen, eroding the barrier layer. Entrainment of sub–mixed layer water into the mixed layer initially acts to warm the mixed layer because of the slight (but stable) temperature inversion in the barrier layer. Thus, entrainment of the heat flux into the mixed layer tends to be out of phase with the surface heat flux (Shinoda and Hendon, 1998);

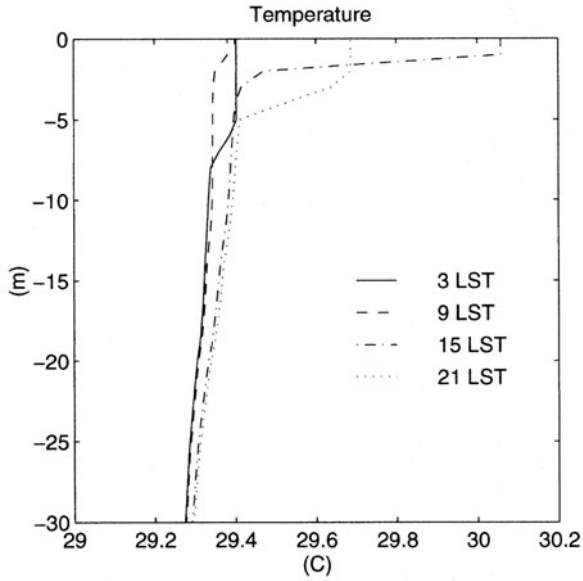

Figure 7.6. Diurnal cycle of vertical temperature profile simulated during the suppressed convective phase of the MJO in the equatorial Western Pacific on November 26, 1992 (from Shinoda and Hendon, 1998).

diurnal entrainment (night-time convection) during the surface warming phase cools the mixed layer, while entrainment of warm sub–mixed layer water during the surface cooling phase tends to warm the mixed layer.

In the experiments of Shinoda and Hendon (1998), cold sub-thermocline water was never entrained into the mixed layer during the windy convective phase because of the weakness of large-scale MJO-induced winds, strong stratification at the thermocline under initial conditions, and development of a barrier layer during the calm clear phase. However, entrainment of sub-thermocline water into the mixed layer is observed to occur in the Western Pacific during some strong westerly wind bursts (e.g., Feng *et al.*, 1998). The results of Shinoda and Hendon (1998) suggest that over the large spatial scale of a typical MJO, entrainment cooling during the cloudy windy phase of the MJO is not systematic, but may be important during some intense events.

The phasing of the mixed layer depth (deepest during the cloudy windy phase and shallowest during the calm clear phase) does result in enhanced sensitivity of mixed layer temperature to surface heat flux forcing during the warming phase and reduced sensitivity during the cooling phase. Enhanced sensitivity during the warming phase is partially offset by an increased amount of shortwave radiation that penetrates through the base of the shallow mixed layer. However, if the mean mixed depth is used to simulate MJO-induced SST variation, then the cooling phase is overpredicted and the warming phase is underpredicted by 25% to 50% (Shinoda and Hendon, 1998).

Lukas and Lindstrom (1991) and Anderson *et al.* (1996) suggest that intraseasonal variation of the flux of freshwater may also play a role in governing mixed layer evolution over the course of the MJO. They envision intense precipitation prior to the windy cooling phase generating a very stable fresh mixed layer, hence preventing the mixing of cold water into the mixed layer during the windy cooling phase. While such behavior has been observed at individual locations throughout the warm pool (e.g., Sprintall and Tomczak, 1992), the phasing of the flux of freshwater relative to surface cooling and maximum surface windspeed for the MJO (Figure 7.1) suggests that it is not an important process for a typical MJO event. That is, the bulk of rainfall during the MJO tends to fall during the windiest period, thus preventing formation of a shallow fresh layer (e.g., Zhang and Anderson, 2003).

Shinoda and Hendon (1998) show the lack of sensitivity to the MJO's freshwater flux variation by driving the mixed layer model with composite surface fluxes from 10 well-defined MJO events. Two simulations were conducted. The control run used full surface fluxes for each MJO event, while the other run prescribed freshwater flux to be held constant at its mean value. Very little difference in mixed layer temperature is predicted. Hence, while mean freshwater flux is critical for maintaining the freshness and stratification of the warm pool (e.g., Lukas and Lindstrom, 1991; Anderson *et al.*, 1996), intraseasonal variation of the flux of freshwater over the lifecycle of the MJO appears not to be systematically important. Zhang and Anderson (2003) point out that accurate simulation in climate models of the phasing of rainfall and winds for the MJO is challenging. Hence, coupled models may erroneously simulate sensitivity to freshwater flux simply by simulating an MJO with unrealistic phasing of rainfall relative to the windspeed maximum.

Inclusion of the diurnal cycle of insolation, on the other hand, does have a large systematic impact on the evolution of mixed layer temperature. Figure 7.7 shows the daily mean mixed layer temperature predicted at the IMET mooring during TOGA–COARE for simulations using hourly surface fluxes and daily mean surface fluxes. During calm clear phases of the MJO, when the diurnal cycle of mixed layer temperature is large, inclusion of the diurnal cycle of insolation increases daily mean mixed layer temperature by 0.2 K to 0.5 K. More heat is absorbed in a shallower mixed layer during daylight hours when insolation and mixed layer depth vary diurnally, even though night-time convection tends to spread this heat out over a deeper layer. Hence, mean SST during the calm phase increases. The amplitude of intraseasonal variation of SST over the lifecycle of the MJO also increases by 20% to 30% (see also Schiller and Godfrey, 2003). The impact of this amplified intraseasonal SST variation on the atmosphere and, specifically, on the dynamics of the MJO has yet to be determined. On the other hand, the diurnal cycle of SST during the suppressed phase has been postulated to drive shallow convection in the afternoon that acts to progressively moisten the lower troposphere, setting up conditions that are favorable for the onset of organized convection within the MJO (Godfrey *et al.*, 1998).

The broad-scale surface wind perturbations associated with the MJO, though typically weak ($<5\,\mathrm{m\,s^{-1}}$), do act to rapidly spin up a near equatorial surface current

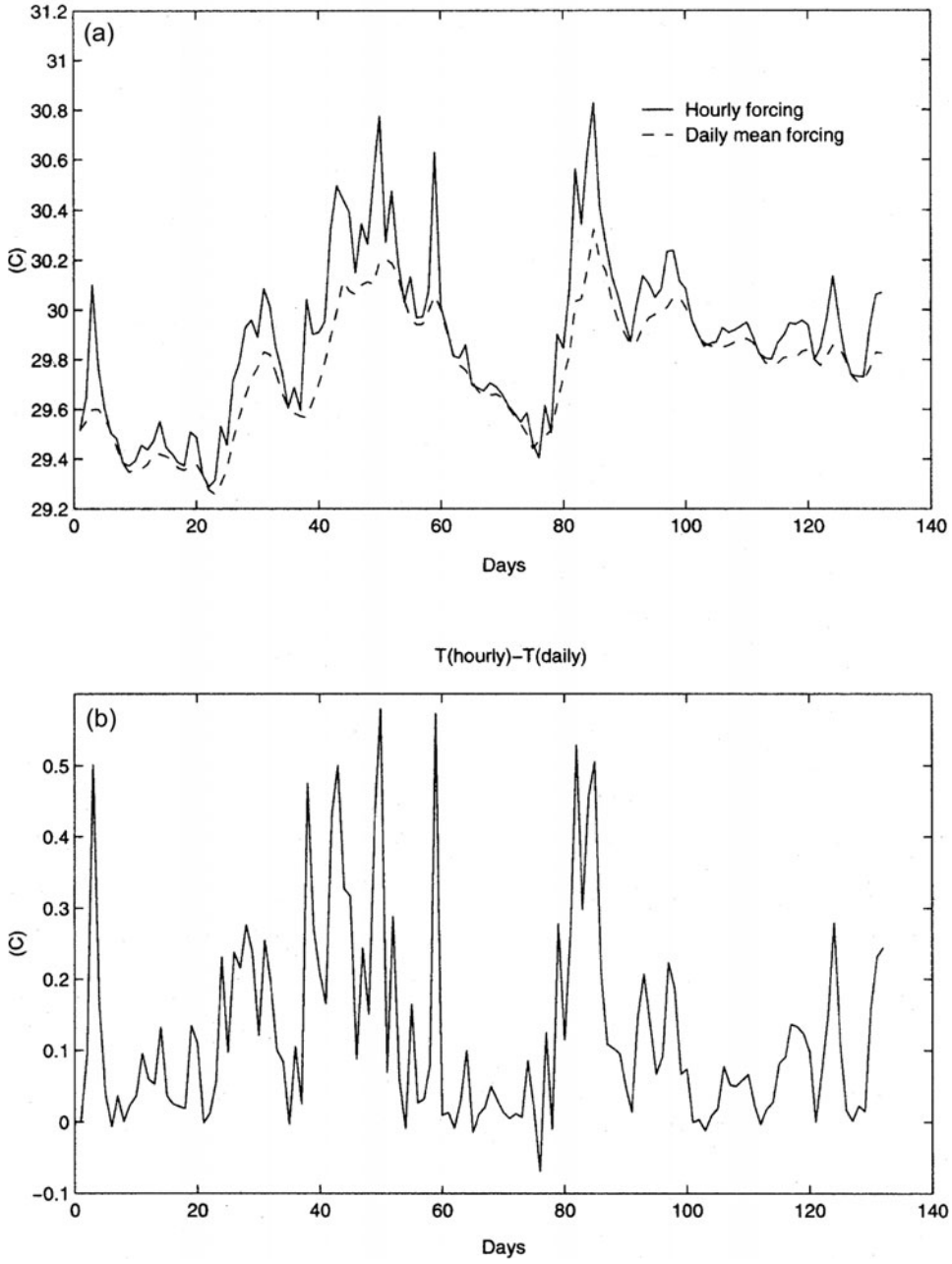

Figure 7.7. (a) Predicted SST at the IMET site for October 22, 1992–March 2, 1993 using hourly surface fluxes from IMET mooring data (thick curve) and daily mean fluxes (dashed curve). (b) SST difference between the two experiments shown in (a) (from Shinoda and Hendon, 1998).

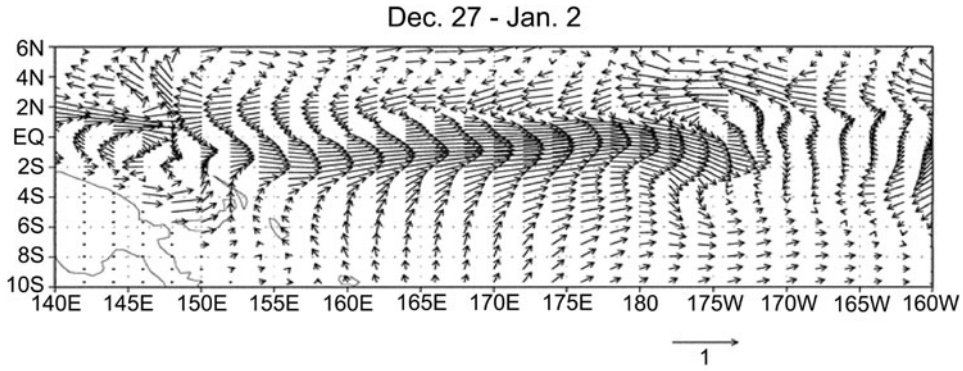

Figure 7.8. Surface currents simulated for the week beginning December 27, 1992, using an OGCM driven by observed surface fluxes. The maximum velocity vector has a magnitude of $1\,\mathrm{m\,s^{-1}}$ (from Shinoda and Hendon, 2001).

(e.g., McPhaden *et al.*, 1988; Maes *et al.*, 1998; Cronin *et al.*, 2000; Shinoda and Hendon, 2001). These currents may then advect both the mean zonal SST gradient on the eastern edge of the warm pool (which may be relevant to the initiation of an El Niño as discussed in Chapters 6 and 9) and the anomalous zonal SST gradient in the warm pool induced by the MJO via surface heat flux variations (Ralph *et al.*, 1997). An example of such a narrow equatorial jet (i.e., Yoshida, 1959) was observed with drifters during TOGA–COARE (Ralph *et al.*, 1997). This strong eastward current developed in response to surface westerlies associated with the MJO event that traversed the Western Pacific in late December 1992. The narrow meridionally convergent jet is well simulated by an OGCM forced with observed surface stress for this period (Figure 7.8).

Ralph *et al.* (1997) demonstrate that this jet advected eastward the anomalous cold SST that developed in the equatorial Western Pacific in response to MJO-induced surface cooling. They further diagnose that, in the long-term mean, such nonlinear advection cools the equatorial Western Pacific warm pool at just the rate that it is warmed by net surface heat flux ($\sim 10\,\mathrm{W\,m^{-2}}$). Hence, episodic nonlinear advection generated by the MJO helps to maintain the mean state of the warm pool. Shinoda and Hendon (2001) qualitatively confirm this result by driving an OGCM with observed intraseasonal surface fluxes. But, the simulated mean cooling produced by the MJO was underestimated, presumably due to difficulties in predicting subtle changes to the weak zonal SST gradient.

Much less work has been done on the mechanisms involved in SST variability in the northern Indian Ocean associated with northward-propagating intraseasonal activity during boreal summer. Analysis of limited observations in the Bay of Bengal reveal a near quadrature relationship between net surface heat flux variations associated with ISOs in convection and SST, consistent with the notion that SST variation is primarily driven by surface heat flux variation (Sengupta and Ravichandran, 2001). Taking into account the variation of mixed layer depth and

the penetration of shortwave radiation, Sengupta and Ravichandran (2001) show qualitative agreement between surface heat flux variation and observed intraseasonal SST tendency. Despite the fact that mean winds are strong ($\sim 10\,\mathrm{m\,s^{-1}}$), the abundance of rainfall and runoff in the region maintains a stable mixed layer upon a deep barrier layer, which prevents the mixing of cold sub-thermocline water into the mixed layer (Bhat *et al.*, 2001). On the other hand, model results from Loschnigg and Webster (2000) suggest oceanic poleward heat transport integrated across the entire Indian Ocean varies in association with poleward-propagating intraseasonal events. Their results imply that the ISO drives changes in the wind-driven circulation of the Indian Ocean, but it is not clear how or whether these changes in heat transport relate to associated SST changes.

7.6 SST–ATMOSPHERE FEEDBACK

One consequence of induced intraseasonal SST variations is that surface fluxes will be modified. The induced SST anomaly associated with the MJO (Figure 7.1) has been diagnosed to cause a slight eastward shift of the latent heat flux anomaly relative to the wind speed anomaly because of the temperature effect on surface saturation humidity (e.g., Zhang, 1996; Hendon and Glick, 1997). This eastward shift causes maximum latent heat flux to be more collocated with maximum convection, rather than lagging it by a few days. This subtle phase difference has important ramifications for the mechanisms involved in an eastward-propagating MJO (e.g., Raymond, 2001). However, the quality of current global surface flux and humidity datasets prohibits a more definitive description at this time.

The induced SST anomaly will also act to reduce the sensible and latent heat fluxes driven by the MJO (Hendon and Glick, 1997; Shinoda *et al.*, 1998). That is, SST will warm in response to reduced latent heat flux in the suppressed phase, but a warmer SST will act to increase latent heat flux. The opposite happens in the suppressed phase. Shinoda *et al.* (1998) estimate that the induced SST anomaly acts to reduce the amplitude of the latent heat flux by 10% to 15%. How this reduction affects the dynamics of the MJO is not obvious, but in some atmospheric models coupled to shallow slab mixed layers (so that a large SST anomaly is induced) the MJO amplitude is diminished because the wind–evaporation feedback is effectively eliminated (E. Maloney, pers. commun., 2004).

The phasing of SST anomalies relative to the convective anomaly—whereby warm SST precedes enhanced convection by ~1–2 weeks and cold SST precedes suppressed convection by a similar lag—is also suggestive of a positive feedback. Various mechanisms for a positive feedback of SST perturbations onto the eastward-propagating MJO have been proposed. Wang and Xie (1998), Waliser *et al.* (1999), Kemball-Cook *et al.* (2002), and Maloney and Kiehl (2002) propose that the warm SST in advance of the convective anomaly hydrostatically acts to lower surface pressure, thereby promoting more moisture convergence in advance of the convective phase and helping to destabilize the MJO. This thermodynamically driven enhancement is estimated to directly account for about a 10% reduction in

surface pressure and a similar increase in surface convergence. However, due to feedbacks between moisture convergence, diabatic heating, and circulation, the total effect of this slight pressure reduction could be much larger. In the Waliser *et al.* (1999) and Kemball-Cook *et al.* (2002) studies, SST-induced surface convergence acts to amplify a pre-existing MJO mode in the models. On the other hand, in the Wang and Xie (1998) study, SST-induced convergence acts to destabilize the MJO mode under conditions where the model otherwise does not support an MJO.

Flatau *et al.* (1997), Hendon and Glick (1997), and Lau and Sui (1997) propose that the warm SST anomaly directly destabilizes the atmospheric column in advance of convection by acting to raise the surface equivalent potential temperature (or moist static energy). At 30°C, a 0.5°C swing in SST is associated with a $0.8\,\mathrm{g\,kg^{-1}}$ change in saturation mixing ratio or about a 3°C change in saturation equivalent potential temperature. In the Flatau *et al.* (1997) model, where the SST tendency was simply parameterized to be negative (cool)—when surface winds were westerly (which encompasses enhanced windspeed and reduced insolation due to enhanced convection) and positive (warm) when the surface winds were easterly (which encompasses reduced windspeed and enhanced insolation due to reduced convection)—coupling with the SST acted to amplify, slow down, and better organize an existing MJO-like mode.

Judging the realism of these coupled model studies is difficult. In the Flatau *et al.* (1997) study, induced SST anomalies are three to four times bigger than observed. Though coupling did dramatically improve the intraseasonal organization of convection and its eastward propagation, the impact of induced SST anomalies may be overestimated. Waliser *et al.* (1999), using a slab mixed layer coupled to a GCM, and Kemball-Cook *et al.* (2002), using an intermediate ocean model coupled to a GCM, report more positive impacts whereby coupling slowed down and strengthened an existing MJO-like mode. While more realistic intraseasonal SST anomalies were simulated (amplitudes $\sim 0.1\,\mathrm{K}$), it is difficult to assess the robustness of these results based on short (10 to 15-year) integrations due to large internal variability of the MJO in the absence of coupling. However, coupling is certainly not a panacea for simulation of the MJO. Hendon (2000) finds little impact of coupling in a GCM that produces a robust MJO-like mode when uncoupled. The uncoupled mode in this particular model appears to be promoted by evaporation–wind feedback (Neelin *et al.*, 1987), with enhanced evaporation unrealistically occurring in easterlies to the east of the convective anomaly. As a result, the latent heat flux and insolation anomalies in this model do not constructively add to perturb the net surface heat flux, thus little SST anomaly is generated. The conclusion from these GCM studies, then, is that coupling at best improves simulation of the MJO, but only if it is reasonably simulated in uncoupled models.

The near quadrature relationship between northward-propagating convection during boreal summer and SST suggests that the ocean is primarily being forced by the atmosphere, similar to the situation for the eastward-propagating MJO. But, as for eastward MJO events, the warm SST anomaly in advance of the poleward-propagating convective anomaly acts to hydrostatically decrease surface pressure, thereby increasing surface convergence and humidity, which acts to destabilize the

atmosphere in advance of convection (e.g., Kemball-Cook *et al.*, 2002; Fu *et al.*, 2003). While northward propagation of the MJO is simulated in some models to occur in the absence of air–sea coupling, inclusion of coupling increases the amplitude of northward-propagating events by $\sim 50\%$ (Fu *et al.*, 2003). In fact, the impact of air–sea coupling on northward propagation in the Indian summer monsoon appears to be more robust than that on eastward propagation of the MJO along the equator.

7.7 IMPACT OF SLOW SST VARIATIONS ON MJO ACTIVITY

The interaction between the MJO and the ocean has been discussed from the perspective of the atmosphere driving the ocean with the possibility of coupled feedback. One-way interaction—in which a slowly varying SST influences the behavior of the MJO—does play an important role in seasonal and interannual variation of MJO activity. The seasonal variation in MJO activity, with the strongest eastward propagation occurring near the vernal equinox (e.g., Salby and Hendon, 1994), is partially explained by the seasonal cycle of SST and mean convection (e.g., Li and Wang, 1994; Salby *et al.*, 1994). The most zonally extensive warm pool and region of active convection develops after the austral solstice, but is displaced into the southern hemisphere. The strongest MJO activity tends to occur at this time because near equatorial convection can develop in the Indian Ocean and propagate farther east into the Pacific. At the autumnal equinox, intraseasonal convection is observed to peak again in the Indian Ocean (Salby and Hendon, 1994), but because SSTs have not yet warmed in the equatorial Western Pacific, MJO activity tends to be not as strong as near the vernal equinox.

Large year-to-year variability in the strength of MJO activity is also observed (e.g., Salby and Hendon, 1994; Hendon *et al.*, 1999; Slingo *et al.*, 1999). This variability—at least at the time of year when the MJO is strongest as measured by globally integrated indices—is not clearly connected to interannual variation in SST. For instance, Hendon *et al.* (1999) and Slingo *et al.* (1999) find little relationship between year-to-year variations of the level of global MJO activity and SST variations—particularly, those associated with the ENSO. A possible exception is an apparent tendency for global MJO activity to weaken at the peak of the strongest El Niño events. Figure 7.9 (top panel), which is an updated version of the plot shown in Hendon *et al.* (1999), confirms the lack of a simple relationship between MJO activity in austral summer (the season when MJO activity is strongest) and the ENSO. This result has been confirmed by GCM studies where observed SST is prescribed for a number of years (e.g., Gualdi *et al.*, 1999; Slingo *et al.*, 1999; Waliser *et al.*, 2001). However, simulation of the MJO in these models is far from perfect. Thus, there is ample scope for further study of seasonal predictability of the MJO once reliable simulations of the MJO are achieved.

On the other hand, a significant relationship between global MJO activity in boreal summer and the ENSO is apparent (Figure 7.9, bottom panel). Despite the fact that this occurs at the time of year when the MJO is weakest along the equator,

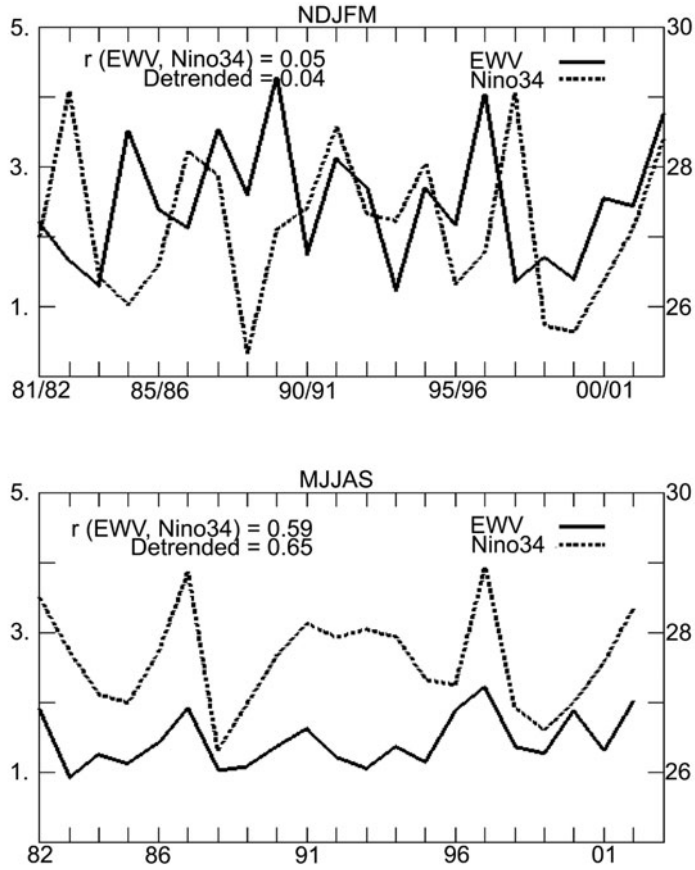

Figure 7.9. Time series of tropically averaged (15°S–15°N) outgoing longwave radiation (OLR) variance filtered to eastward wavenumbers 1–4 and periods of 30–90 days. (top panel) The 5-month period November–March. (bottom panel) May–September. Also shown is the Niño34 SST index for the same 5-month periods. Simultaneous correlations, with and without linear trend, are indicated (filtered OLR data were kindly supplied by M. Wheeler, BMRC).

it is during this time of the year when MJO activity may have its greatest impact on the evolution of the coupled system in the Pacific (e.g., Fedorov, 2002). A simple explanation for the enhanced MJO activity in boreal summer during developing El Niño events is that the total SST field is then similar to the normal SST field during late boreal winter. In particular, the cold tongue in the Central and Eastern Pacific, which normally acts to reduce eastward propagation along the equator during boreal summer (e.g., Li and Wang, 1994) is absent during a warm event. Thus, MJO activity can propagate farther east and maintain its strength longer. The lack of a relationship between the strength of global MJO activity and the ENSO during boreal winter results because, as warm events peak in boreal winter,

anomalous convection then often shifts so far east in the Pacific that suppressed conditions develop in the Western Pacific. Thus, the MJO experiences less of a fetch on which to grow.

MJO activity, along with all other intraseasonally varying convective activity, does shift eastward in the Pacific during warm events and contracts westward during cold events (Gutzler, 1991; Anyamba and Weare, 1995; Fink and Speth, 1997; Hendon *et al*., 1999; Kessler, 2001). This eastward shift appears to simply reflect the eastward shift of warm SST as an El Niño develops: warming SST provides the basis for MJO activity to develop farther eastward. Kessler (2001) points out that this apparently diagnostic relationship may still be supportive of an active role of the MJO in the development of an El Niño, especially if the MJO produces a rectified response in the Western Pacific (e.g., Shinoda and Hendon, 2002), where the coupled system is especially sensitive (e.g., Kessler and Kleeman, 2000; see also Chapters 6 and 9).

7.8 CONCLUDING REMARKS

This chapter has focused on observations of the air–sea interaction associated with eastward and northward propagation of the MJO. Specifically, air–sea interactions that are relevant to the mechanisms involved in and variability of the MJO were addressed. Two areas of future research will shed more light on the role of air–sea interaction for ISV throughout the global tropics. First, improved global datasets from new observing platforms and refined reanalysis of surface fluxes, SST, and rainfall will allow more comprehensive study of the delicate interplay of convection, SST, and oceanic and atmospheric circulation. Second, improved simulation of tropical ISV in climate models will allow careful study of the mechanisms involved and the importance of active coupling on intraseasonal timescales.

7.9 ACKNOWLEDGMENTS

While this chapter is purportedly a comprehensive review of tropical intraseasonal air–sea interaction, the perspective is a personal one. I thank S. Anderson, S. Kemball-Cook, and the American Meteorological Society for allowing me to reproduce Figures 7.2 and 7.4. Comments on an earlier version of this chapter by C. Zhang and the editors led to improvements in its presentation and scope.

7.10 REFERENCES

Anderson, S. P., R. A. Weller, and R. Lukas (1996) Surface buoyancy forcing and the mixed layer in the western Pacific warm pool: Observation and 1D model results. *J. Climate*, **9**, 3056–3085.

Anyamba, E. K. and B. C. Weare (1995) Temporal variability of the 40–50 day oscillation in tropical convection. *Int. J. Climatol.*, **15**, 379–402.

Bergman, J. W., H. H. Hendon, and K. M. Weickmann (2001) Intraseasonal variation of west Pacific convection at the onset of the 1997–98 El Niño. *J. Climate.*, **14**, 1702–1719.

Bhat, G. S., S. Gadgil, P. U. Hareesh Kumar, S. R. Kalse, P. Madhusoodanan, V. S. N. Muriz, C. U. K. Prasada Rao, V. Ramosh Babu, L. U. G. Rao., R. R. Rao *et al.* (2001) BOBMEX: The Bay of Bengal Monsoon Experiment. *Bull. Amer. Meteorol. Society*, **82**, 2217–2243.

Colón, E., J. Lindesay, and M. J. Suarez (2002) The impact of surface flux- and circulation-driven feedbacks on simulated Madden–Julian Oscillations. *J. Climate*, **15**, 624–641.

Cronin, M. F. and M. J. McPhaden (1997) The upper ocean heat balance in the western equatorial Pacific warm pool during September–December 1992. *J. Geophys. Res.*, **102**, 8533–8553.

Cronin, M. F., M. J. McPhaden, and R. H. Weisberg (2000) Wind-forced reversing jets in the western equatorial Pacific. *J. Phys. Ocean.*, **30**, 657–676.

Emanuel, K. A. (1987) An air–sea interaction model of intraseasonal oscillations in the Tropics. *J. Atmos. Sci.*, **44**, 2324–2340.

Fedorov, A. V. (2002) The response of the coupled tropical ocean–atmosphere to westerly wind bursts. *Quart. J. Roy. Meteorol. Soc.*, **128**, 1–23.

Feng, M., P. Hacker, and R. Lukas (1998) Upper ocean heat and salt balances in response to a westerly wind burst in the western equatorial Pacific during TOGA COARE. *J. Geophys. Res.*, **103**, 10289–10311.

Feng, M., R. Lukas, P. Hacker, R. A. Weller, and S. P. Anderson (2000) Upper-ocean heat and salt balances in the western equatorial Pacific in response to the intraseasonal oscillation during TOGA COARE. *J. Climate*, **13**, 2409–2427.

Fink, A. and P. Speth (1997) Some potential forcing mechanisms of the year-to-year variability of the tropical convection and its intraseasonal (25–70 day) variability. *Int. J. Climatol.*, **17**, 1513–1534.

Flatau, M., P. J. Flatau, P. Phoebus, and P. P. Niiler (1997) The feedback between equatorial convection and local radiative and evaporative processes: The implications for intraseasonal oscillations. *J. Atmos. Sci.*, **54**, 2373–2386.

Fu, X., B. Wang, T. Li, and J. P. McCreary (2003) Coupling between northward propagating intraseasonal oscillations and sea surface temperature in the Indian Ocean. *J. Atmos. Sci.*, **60**, 1733–1753.

Giese, B. S. and D. E. Harrison (1991) Eastern equatorial Pacific response to three composite westerly wind types. *J. Geophys. Res.*, **96**(Suppl.), 3239–3248.

Godfrey, J. S., R. A. Houze, R. H. Johnson, R. Lukas, J. L. Redelsperger, A. Sumi, and R. Weller (1998) Coupled Ocean–Atmosphere Response Experiment (COARE): An interim report. *J. Geophys. Res.*, **103C**, 14395–14450.

Gualdi, S., A. Navarra, and G. Tinarelli (1999) The interannual variability of the Madden–Julian Oscillation in an ensemble of GCM simulations. *Climate Dynamics*, **15**, 643–658.

Gutzler, D. S. (1991) Interannual fluctuations of intraseasonal variance of near-equatorial zonal winds. *J. Geophys. Res.*, **96**, 3173–3185.

Gutzler, D. S., G. N. Kiladis, G. A. Meehl, K. M. Weickmann, and M. Wheeler (1994) The global climate of December 1992–February 1993, Part II: Large-scale variability across the tropical western Pacific during TOGA COARE. *J. Climate*, **7**, 1606–1622.

Harrison, D. E. and G. A. Vecchi (2001) January 1999 Indian Ocean cooling event. *Geophys. Res. Lett.*, **28**, 3717–3720.

Hendon, H. H. (2000) Impact of air–sea coupling on the Madden–Julian oscillation in a general circulation model. *J. Atmos. Sci.*, **57**, 3939–3952.

Hendon, H. H. and J. Glick (1997) Intraseasonal air–sea interaction in the tropical Indian and Pacific Oceans. *J. Climate*, **10**, 647–661.

Hendon, H. H. and B. Liebmann (1994) Organization of convection within the Madden–Julian Oscillation. *J. Geophys. Res.*, **99**, 8073–8083.

Hendon, H. H. and M. L. Salby (1994) The life cycle of the Madden–Julian Oscillation. *J. Atmos. Sci.*, **51**, 2225–2237.

Hendon, H. H., B. Leibmann, and J. Glick (1998) Oceanic Kelvin waves and Madden–Julian Oscillation. *J. Atmos. Sci.*, **55**, 88–101.

Hendon, H. H., C. Zhang, and J. D. Glick (1999) Interannual variability of the Madden–Julian Oscillation during austral summer. *J. Climate.*, **12**, 2538–2550.

Jiang, X., T. Li, and B. Wang (2004) Structures and mechanisms of the northward propagating boreal summer intraseasonal oscillation. *J. Climate*, **17**, 1022–1039.

Jones, C., D. E. Waliser, and C. Gautier (1998) The influence of the Madden–Julian oscillation on ocean surface heat fluxes and sea surface temperature. *J. Climate*, **11**, 1057–1072.

Kemball-Cook, S. and B. Wang (2001) Equatorial waves and air–sea interaction in the boreal summer intraseasonal oscillation. *J. Climate*, **14**, 2923–2942.

Kemball-Cook, S., B. Wang, and X. Fu (2002) Simulation of the intraseasonal oscillation in ECHAM-4 model: The impact of coupling with an ocean model. *J. Atmos. Sci.*, **59**, 1433–1453.

Kessler, W. S. (2001) EOF representations of the Madden–Julian Oscillation and its connection with ENSO. *J. Climate*, **14**, 3055–3061.

Kessler, W. S. and R. Kleeman (2000) Rectification of the Madden–Julian Oscillation into the ENSO cycle. *J. Climate*, **13**, 3560–3575.

Kessler, W. S., M. J. McPhaden, and K. M. Weickmann (1995) Forcing of intraseasonal Kelvin waves in the equatorial Pacific. *J. Geophys. Res.*, **100**, 10613–10631.

Krishnamurti, T. N., D. K. Oosterhof, and A. V. Metha (1988) Air–sea interaction on the timescale of 30–50 days. *J. Atmos. Sci.*, **45**, 1304–1322.

Lau, K. M. and C.-H. Sui (1997) Mechanisms of short-term sea surface temperature regulation: Observations from TOGA COARE. *J. Climate*, **10**, 465–472.

Lawrence, D. M. and P. J. Webster (2002) The boreal summer intraseasonal oscillation: Relationship between northward and eastward movement of convection. *J. Atmos. Sci.*, **59**, 1593–1606.

Li, T. and B. Wang (1994) The influence of sea surface temperature on the tropical intraseasonal oscillation: A numerical study. *Mon. Wea. Rev.*, **122**, 2349–2362.

Lin, J. W.-B., J. D. Neelin, and N. Zeng (2000) Maintenance of tropical intraseasonal variability: Impact of evaporation–wind feedback and midlatitude storms. *J. Atmos. Sci.*, **57**, 2793–2823.

Loschnigg, J. and P. J. Webster (2000) A coupled-atmosphere system of SST modulation for the Indian Ocean. *J. Climate*, **13**, 3342–3360.

Lukas, R., and E. Lindstrom (1991) The mixed layer of the western equatorial Pacific ocean. *J. Geophys. Res.*, **96**(Suppl.), 3343–3357.

Maes, C., P. Delecluse, and G. Madec (1998) Impact of westerly wind bursts on the warm pool of the TOGA COARE domain in an OGCM. *Climate Dynamics*, **14**, 55–70.

Maloney, E. D. and J. T. Kiehl (2002) MJO-related SST variations over the tropical Eastern Pacific during Northern Hemisphere summer. *J. Climate*, **15**, 675–689.

McPhaden, M. J. (2002) Mixed layer temperature balance on intraseasonal timescales in the equatorial Pacific Ocean. *J. Climate*, **15**, 2632–2647.

McPhaden, M. J., H. P. Freitag, S. P. Hayes, B. A. Taft, Z. Chen, and K. Wyrtki (1988) The response of the equatorial Pacific Ocean to a westerly wind burst in May 1986. *J. Geophys., Res*., **93**, 10589–10603.

Neelin, J. D., I. M. Held, and K. H. Cook (1987) Evaporation–wind feedback and low-frequency variability in the tropical atmosphere. *J. Atmos. Sci*., **44**, 2341–2348.

Ralph, E. A., K. Bi, and P. P. Niiler (1997) A Lagrangian description of the western equatorial Pacific response to the wind burst of December 1992. *J. Climate*, **10**, 1706–1721.

Raymond, D. J. (2001) A new model of the Madden–Julian Oscillation. *J. Atmos. Sci*., **58**, 2807–2819.

Reynolds, R. W. and T. M. Smith (1994) Improved global sea surface temperature analyses using optimum interpolation. *J. Climate*, **7**, 929–948.

Salby, M. L. and H. H. Hendon (1994) Intraseasonal behavior of clouds, temperature, and winds in the Tropics. *J. Atmos. Sci*., **51**, 2207–2224.

Salby, M. L., G. Rolando, and H. H. Hendon (1994) Planetary-scale circulations in the presence of climatological and wave-induced heating. *J. Atmos. Sci*., **51**, 2344–2367.

Sengupta, D. and M. Ravichandran (2001) Oscillations of Bay of Bengal sea surface temperature during the 1998 summer monsoon. *Geophys. Res. Lett*., **28**, 2033–2036.

Schiller, A. and J. S. Godfrey (2003) Indian Ocean intraseasonal variability in an ocean general circulation model. *J. Climate*, **16**, 21–39.

Shinoda, T. and H. H. Hendon (1998) Mixed layer modeling of intraseasonal variability in the tropical western Pacific and Indian Oceans. *J. Climate*, **11**, 2668–2685.

Shinoda, T. and H. H. Hendon (2001) Upper-ocean heat budget in response to the Madden–Julian Oscillation in the western equatorial Pacific. *J. Climate*, **14**, 4147–4165.

Shinoda, T. and H. H. Hendon (2002) Rectified wind forcing and latent heat flux produced by the Madden–Julian Oscillation. *J. Climate*, **15**, 3500–3508.

Shinoda, T., H. H. Hendon, and J. Glick (1998) Intraseasonal variability of surface fluxes and sea surface temperature in the tropical western Pacific and Indian Oceans. *J. Climate*, **11**, 1685–1702.

Sikka, D. R. and S. Gadgil (1980) On the maximum cloud zone and the ITCZ over Indian longitudes during the southwest monsoon. *Mon. Wea. Rev*., **108**, 1840–1853.

Slingo, J. M., D. P. Rowell, K. R. Sperber, and F. Nortley (1999) On the predictability of the interannual behaviour of the Madden–Julian Oscillation and its relationship to El Niño. *Quart. J. Roy. Meteorol. Soc*., **125**, 583–609.

Sprintall, J. and M. Tomczak (1992) Evidence of the barrier layer in the surface layer of the tropics. *J. Geophys. Res*., **97**, 7305–7316.

Vecchi, G. A. and D. E. Harrison (2002) Monsoon breaks and subseasonal sea surface temperature variability in the Bay of Bengal. *J. Climate*, **15**, 1485–1493.

Waliser, D. E., K.-M. Lau, and J. H. Kim (1999) The influence of coupled sea surface temperatures on the Madden–Julian Oscillation: A model perturbation experiment. *J. Atmos. Sci*., **56**, 333–358.

Waliser, D. E., Z. Zhang, K. M. Lau, and J.-H. Kim (2001) Interannual sea surface temperature variability and the predictability of tropical intraseasonal variability. *J. Atmos. Sci*., **58**, 2596–2615.

Wang, B. and H. Rui (1990) Synoptic climatology of transient tropical intraseasonal convection anomalies: 1975–1985. *Meteorol. Atmos. Phys*., **44**, 43–61.

Wang, B. and X. Xie (1998) Coupled modes of the warm pool climate system, Part I: The role of air–sea interaction in maintaining Madden–Julian Oscillation. *J. Climate*, **11**, 2116–2135.

Webster, P. J. and R. Lukas (1992) TOGA COARE: The Coupled Ocean–Atmosphere Response Experiment. *Bull. Amer. Meteorol. Society*, **73**, 1377–1416.

Webster, P. J., E. F. Bradley, C. W. Fairall, J. S. Godfrey, P. Hacker, R. A. Houze, R. Lukas, Y. Serra, J. M. Hummon, T. D. M. Lawrence *et al.* (2002) The JASMINE pilot study. *Bull. Amer. Meteorol. Society*, **83**, 1603–1630.

Weller, R. A. and S. P. Anderson (1996) Surface meteorology and air–sea fluxes in the western equatorial Pacific warm pool during the TOGA coupled ocean–atmosphere response experiment. *J. Climate*, **9**, 1959–1990.

Woolnough, S. J., J. M. Slingo, and B. J. Hoskins (2000) The relationship between convection and sea surface temperature on intraseasonal timescales. *J. Climate*, **13**, 2086–2104.

Yoshida, K. (1959) A theory of the Cromwell current and of the equatorial upwelling: An interpretation in a similarity to a coastal circulation. *J. Oceanogr. Society Japan*, **15**, 159–170.

Zhang, C. (1997) Intraseasonal variability of the upper-ocean thermal structure observed at 0° and 165°E. *J. Climate*, **10**, 3077–3092.

Zhang, C. (1996) Atmospheric intraseasonal variability at the surface in the tropical western Pacific Ocean. *J. Atmos. Sci.*, **53**, 739–758.

Zhang, C. (2001) Intraseasonal perturbations in sea surface temperatures of the equatorial eastern Pacific and their association with the Madden–Julian Oscillation. *J. Climate*, **14**, 1309–1322.

Zhang, C. and S. P. Anderson (2003) Sensitivity of intraseasonal perturbations in SST to the structure of the MJO. *J. Atmos. Sci.*, **60**, 2196–2207.

Zhang, C. and J. Gottschalck (2002) SST anomalies of ENSO and the Madden–Julian Oscillation in the equatorial Pacific. *J. Climate*, **15**, 2429–2445.

Zhang, C. and M. J. McPhaden (2000) Intraseasonal surface cooling in the equatorial western Pacific. *J. Climate*, **13**, 2261–2276.

8

Mass, momentum, and geodynamics

Benjamin F. Chao and David A. Salstein

8.1 INTRODUCTION

While other chapters of this book describe meteorological intraseasonal variability (ISV) phenomena in the atmosphere–ocean system and examine the possible causes of ISV or the dynamic interactions between the meteorological components that are involved, in this chapter we will study certain global geodynamic effects that relate to the *mass transport* associated with ISV, which for the most part occurs in the atmosphere–ocean system. In particular, we will discuss the angular momentum variability of the atmosphere and its influences on Earth's rotation and visit the associated mass-induced gravity variations. Observations of these can help improve our understanding of, and our modeling capability for, atmospheric–oceanic circulations in general, including those related to ISV.

The transport of mass and energy are key processes that determine the dynamics of our Earth system. Mass transport occurs in all the *geophysical fluid* components of the Earth system—the atmosphere, hydrosphere, cryosphere, biosphere, lithosphere, and the deep interior of the mantle and core, on a wide range of temporal and spatial scales. In the atmosphere, variations in the position and strength of pressure systems, as found on weather maps as well as in wind systems indicate that different masses of air move around the planet; dynamical fluctuations result as part of this atmospheric general circulation. Mass transport also occurs in the oceans, resulting mainly from forcing by the surface wind, pressure, thermohaline fluxes, and tides, but also by internal ocean modes. Numerical models of these circulations allow the response of the atmosphere and oceans to these processes to be investigated in detail. Mass transport near the Earth's land surface in the cryosphere and hydrological reservoirs varies due to both natural and anthropogenic influences. Hydrological modeling, in combination with observations, can supplement atmospheric and ocean models to determine global mass variability. These mass transport components may all have strong ISV signals, and studying them is undoubtedly the most interdisciplinary field in Earth sciences.

W. K. M. Lau and D. E. Waliser (Editors), *Intraseasonal Variability in the Atmosphere–Ocean Climate System* (Second Edition).

However, mass transport has not received due attention. For example, many current ocean general circulation models (GCMs) do not conserve water mass correctly, instead they conserve water volume under the Boussinesq approximation (e.g., Da Szoeke and Samelson, 2002), although some modern models have investigated aspects of mass conservation (Griffies and Adcroft, 2008). Although atmospheric GCMs largely conserve dry air mass—including many that are used daily for weather forecasting—like ocean models not all do. A most critical piece in the global water mass puzzle, the large-scale land hydrological and cryospheric water mass cycle budget that is constantly under direct exchange with the atmosphere, remains least known (e.g., IPCC, 2001), although information from both hydrosphere models and gravity missions has increased our knowledge of the time-variable mass field, mostly from moisture in the air, for geodetic purposes (Nastula *et al*., 2007).

There is, of course, mass transport that occurs in interior geophysical fluids as well (e.g., in the mantle associated with post-glacial rebound and tectonic movements and in the fluid core under forcing by the geodynamo). These occur, however, on markedly different timescales than ISV.

As mass moves or redistributes in geophysical fluids, three distinct geodynamic effects occur as a consequence (e.g., Chao *et al*., 2000):

(i) *Temporal variation in the solid Earth's rotation*. By virtue of the conservation of angular momentum of the closed Earth system, the angular momentum variation associated with any geophysical mass transport has to be balanced by a change with the same magnitude but with a sign change in the angular momentum of the rest of the Earth, essentially the solid Earth. In this sense, the former (or more accurately the combined sum of all such angular momentum changes) manifests itself in variation of the solid Earth's rotation. As will be discussed below, mass transport imparts angular momentum not only by virtue of the actual motion of the mass, but also by the resultant change in mass distribution and, hence, in the inertia tensor of the geophysical fluid. Note also that the rotation of the Earth is a 3-D quantity; all three components vary as a result of angular momentum exchange.

(ii) *Temporal variations in the Earth's gravity field*. The redistributed mass in question modifies slightly the global gravitational attraction force, as dictated by Newton's gravitational law, thereby changing the gravity field in both time and space. This time-variable gravity signal, coming from all geophysical fluids, is superimposed on the background static gravity field.

(iii) *Temporal variation in the solid Earth's center of mass (CM)*. The conservation of linear momentum dictates a motion in the CM of the solid Earth resulting from a net shift of the CM of the fluid envelope in such a way that the CM of the whole Earth (the "geocenter") remains stationary (or, more accurately, stays in its orbit about the Sun according to celestial mechanics).

In this chapter we will mainly discuss variation of the Earth's rotation (i), which is the most mature subject of the three as far as observation and modeling is concerned. We shall, however, give some discussion on time-variable gravity (ii) and, to a lesser

extent, geocenter motion (iii) keeping in mind that observations of geocenter motion are still early in development.

Although relatively minute—typically, no larger than 1–10 parts per billion in relative terms—the aforementioned geodynamic signals have become observable through very precise space-geodetic techniques (e.g., AGU, 1993). Efforts have now been updated in the Global Geodetic Observing System (Plag and Pearlman, 2009). For over three decades, space-geodetic measurement precision has improved at the rate of one order of magnitude per decade (something of a space-geodetic "Moore's law"; see, e.g., Chao, 2003). Today, observations come from several advanced geodetic techniques, whose development has been primarily led by NASA but incorporating extensive international cooperation. The earliest such technique was based on pulsed laser ranging to retro-reflectors placed on the Moon by the Apollo Mission circa 1970, though it was soon supplemented and all but replaced since the late 1970s by similar ranging to retro-reflectors onboard the now dozen or so geodetic satellites in very stable orbits at various altitudes and inclinations—the technique is known as satellite laser ranging (SLR). Another space-geodetic technique beginning in the early 1980s, very long baseline interferometry (VLBI) uses signals from remote radio sources in the universe for geometrical determination of the precise baseline length between pairs of radio-telescopes. Earth's orientation at a given instant in relation to inertial space can be derived. Since the 1990s the Global Positioning System (GPS) came on the scene using a whole constellation of artificial satellites as a reference system, within which the position of places on the Earth's surface can be precisely determined "anywhere, anytime". Somewhat more recently, the French Doppler Orbitography and Radio positioning Integrated by Satellite (DORIS) system uses a tracking system providing range rate measurements of signals from a dense network of ground-based radio beacons. Together these observing systems define precisely our celestial and terrestrial reference frames (among many other observables) and, more importantly for our present study, the link between the two reference systems. This link, primarily simply a uniform daily Earth rotation, also contains slight variations in rotation, which is the main target of our study. The origin of the terrestrial reference frame is defined relative to the geocenter. In addition, satellites' dynamic orbit determinations from SLR are used to determine the Earth's gravity field and have been precise enough to detect temporal *variations* in gravity (e.g., Cox and Chao, 2002).

Variability in the Earth's rotation, geocenter, and gravity parameters represents the sum total of contributions from all mass transport taking place in geophysical fluids, as mentioned above. In this sense, the space geodesy system has become an integrating, effective, and unique tool for remote sensing of global mass transport, subject naturally to its precision/accuracy and temporal/spatial resolutions. With respect to ISV in the meteorological system, we only examine a focused component within an otherwise extensive and interdisciplinary subject. Specifically, we emphasize the interactions and connections of ISV with Earth rotation parameters and related geodynamic signals which occur as a result of ISVs themselves.

8.2 ANGULAR MOMENTUM VARIATIONS AND EARTH ROTATION

The distribution of atmospheric mass and its changing motions have been known for quite some time. The basic structure of zonal general circulation—westerly winds in midlatitudes, easterlies in low and high latitudes—was well appreciated in the 19th century, as was meridional circulation featuring the direct Hadley circulation of rising air in the tropics and descending air further poleward. More structure was noted when it was determined that the mean cells in midlatitudes, known as Ferrel cells, are indirect. Both zonal mean motion and eddy motions are responsible for transporting momentum meridionally. Using the network of radiosondes, annual and interannual signals in these large-scale circulation systems were synthesized (see Peixoto and Oort, 1992 for a summary, although they only treated the axial component of atmospheric angular momentum). Similar results were obtained from various operational meteorological series as well as reanalyses.

Remarkably, the atmosphere changes its overall atmospheric angular momentum (AAM) substantially (especially with season). Between northern hemisphere winter and summer, relative AAM changes by a factor of 2, with strong winter winds at the jetstream level of the winter hemisphere being particularly strong. Whereas westerly winds, with maxima in the jets at levels near 200 hPa in the subtropics and midlatitudes of both hemispheres, carry most of the axial AAM, variations on interannual, seasonal, and intraseasonal scales are distributed somewhat differently. Rosen and Salstein (1983) note that ISV is more distributed in lower latitudes of the hemispheres.

An important question arose early on as to how changes in AAM can occur so quickly and dramatically. Physically, angular momentum in a system can only be changed by torques. The search for torques affecting terrestrial AAM led to two particular mechanisms: one from normal pressure forces against topography, and another from tangential friction along the boundary. We discuss these torques and their implications later in the chapter. For ISV in particular, detailed studies of angular momentum torques on such timescales have been performed and related to other elements. Lau *et al.* (1989) and Kang and Lau (1990) consider how those elements of already known ISV whose contributions peak in the upper troposphere could impact global angular momentum. They link variations in the effects of heating, dynamics, and convection—particularly over the tropical Pacific—with concomitant transfer of angular momentum across the ocean boundary as frictional torques. More recent understanding of the momentum budget connected to ISV can be found in Lin *et al.* (2005), in which maintenance of the momentum budget requires damping in the upper levels, advection by vertical motions, as well as damping in the lower levels. Local fluctuations in ISV timescales are noted in mountain and friction torques. The overall role of global winds in the Madden–Julian Oscillation have been updated by Weickmann and Berry (2009). With the transfer of angular momentum from the atmosphere to the solid Earth—in the form of the Earth's rotation—it is important to understand the concepts underlying its rotational variability and how it is measured.

As stated above, the Earth's rotation—linking so-called terrestrial and celestial

reference frames—is simply the uniform daily rotation of the Earth plus some very small variations. As with any rotation in our 3-D world, Earth's rotation can be represented as a 3-D vector. Note that the tensor dimension of the rotation vector in an n-D space is $n(n-1)/2$. The departure of the Earth's rotation from a uniform rotation in space can thus be conveniently divided into two parts: (i) the magnitude of the (1-D) axial component along the mean rotation z-axis that pierces the surface at the mean north and south poles, determining *length-of-day* variation (ΔLOD); and (ii) the (2-D) equatorial component in the x–y plane, giving the orientation of the rotational axis as seen on the Earth, known as *polar motion*.

SLR, VLBI, GPS, and more recently DORIS have been, of the group of techniques measuring the Earth's rotation, the major techniques relied upon. The dataset we use here is an optimal combination of these techniques (as described by Gross *et al.*, 1998a). Submilliarcsecond precision (1 milliarcsecond, or mas, corresponds to about 3 cm if projected onto the Earth's surface) is now routinely achieved in quasi-daily measurements.

8.2.1 Length-of-day variation and axial angular momentum

As stated, Earth's rotation varies as a result of angular momentum variations in geophysical fluids. Among these, AAM is a fundamental and important quantity in the atmospheric circulation system; in addition to exchanges internal to the atmosphere, its total amount is constantly changing, so that angular momentum is transferred to and from the solid Earth, modifying the (solid) Earth's rotation. Let us first focus on the (1-D) axial component—the AAM_z on the atmospheric side of the balance and ΔLOD on the geodetic side. A modern perspective on complete LOD variations can be found in, for example, Chao (2003) and more recently in the annual reports of the International Earth Rotation and Reference Systems Service. The formulation by which one computes AAM (or any angular momentum due to mass transport in geophysical fluids) was clearly laid out in the seminal work by Munk and MacDonald (1960) and later brought up to date using increasingly more appropriate Earth parameters by, for example, Barnes *et al.* (1983), Eubanks (1993), and Zhou *et al.* (2006).

In general, when moving the mass of a geophysical fluid produces an angular momentum variation that consists of two parts: one part due to the actual motion of that mass relative to the Earth, plus another part due to change in the inertia tensor as a consequence of mass redistribution (participating with the planet in its solid body rotation). For the axial z-component of AAM, we have approximately:

$$\text{Motion term for } \mathrm{AAM}_z \text{ (or the ``wind term'')} = \frac{1.00a^3}{C\omega g}\iiint u\cos\theta\, d\Omega\, dp \quad (8.1a)$$

$$\text{Mass term of } \mathrm{AAM}_z \text{ (or the ``pressure term'')} = \frac{0.70a^4}{Cg}\iint p\cos^2\theta\, d\Omega \quad (8.1b)$$

Physically, (8.1a) is analogous to what happens to a log floating on water as a lumberjack ''races'' (i.e., balances himself) on it, while (8.1b) is analogous to the

spinning skater phenomenon whereby a skater speeds up her spinning as she draws her arms closer to her body and slows down as she does the opposite.

In the equations u and p are the (zonal) westerly-wind field and the surface pressure field, respectively; a, ω, and g are the mean radius, mean rotation rate, and mean gravitational acceleration of the Earth, respectively; Ω is an abbreviation for $(\theta, \lambda) = (\text{latitude, longitude})$, where $d\Omega = \cos\theta \, d\theta \, d\lambda$ is the surface element. The dp can be converted into the vertical distance element dh by the hydrostatic relation $dp = -\rho g \, dh$, where ρ is air density. The multiplicative coefficients in front account for some subtle but important effects including Earth's elastic yielding under surface loading. C is the mean axial moment of inertia of the mantle; the cores are excluded in C because it is approximately true that they do not participate in the mantle's rotational variation on ISV timescales (see Barnes *et al.*, 1983). In other words, we assume zero core–mantle coupling strength, on timescales that are much shorter than the decadal or longer scales associated with core–mantle coupling (Jault and Le Mouel, 1988). Note that for simplicity we have normalized the AAM terms with respect to Earth parameters, so that they are in non-dimensional *excitation* units relative to the length of the mean solar day: 86,400 s. The resultant change in LOD due to AAM_z is

$$\text{AAM}_z(\text{sum of } 8.1\text{a} + 8.1\text{b}) = -\Delta\text{LOD}/\text{LOD}. \tag{8.2}$$

Note that an increase in AAM_z slows the spinning planet, causing LOD to increase. In absolute units, a change of 1 millisecond (ms) of ΔLOD is equivalent to 15 milliarcseconds (mas) in Earth orientation or $\sim$45 cm at the Earth's surface, the rotation angle and distance subtended in that time, which in turn corresponds to a transfer of 5.95×10^{25} kg m^2 s^{-1} of AAM.

Not all LOD changes come from AAM_z of course (e.g., Chao, 2003). Period-specific tidal signals in LOD data do not behave according to relation (8.2), because they are a result of external lunar and solar torques and resultant internal interactions (which are in themseves sets of very complex phenomena). For example, the long-period tidal signals (such as fortnightly and monthly tides) in ΔLOD arise from solid Earth tidal deformations and, to a lesser extent, ocean tides, which on the other hand are the main causes for diurnal and semidiurnal ΔLOD. For seasonal (annual + semiannual) signals, though the majority are related to AAM, many come from tides and non-atmospheric mass transport. Oceanic angular momentum and land hydrological angular momentum are examples of the latter, now determined from models, ocean data assimilation systems, and hydrological models, including the effects of soil moisture and ice. There is also a large, slow (decadal) fluctuation in ΔLOD resulting primarily from core angular momentum variation and a secular increase in LOD due to "tidal braking" where the Moon slows down the Earth's rotation via tidal energy dissipation, while the distance between the two bodies increases—a phenomenon long discussed since George Darwin discovered it in the 19th century (e.g., Cartwright, 1999); these, too, will not be discussed here.

It should be mentioned that evaluation of the mass term of AAM is subject to an important uncertainty related to the ocean's behavior: namely, the inverted barometer (IB) assumption. The IB assumption stipulates that the world ocean

adjusts its level instantaneously and isostatically to overlying atmospheric pressure variations. Dynamically, the net effect is that the ocean simply smooths out atmospheric pressure variation evenly over the entire ocean area. An idealization—which is a good approximation to reality especially on timescales longer than 10 days or so such as is the case for ISV—shows the IB effect leading to significantly reduced variability in the mass (pressure) terms for LOD and, for that matter, for polar motion, time-variable gravity, and geocenter motion. The pure IB assumption has been found to be generally valid at lower frequencies and in particular areas (Ponte, 2006), but may be more complex and related to temporal scales in a dynamic way (Dickman, 1998).

Among the first detailed results concerning the AAM_z–ΔLOD relationship were those of Hide *et al.* (1980) and Langley *et al.* (1981). The linear relationship between the two quantities was later firmly demonstrated by Rosen and Salstein (1983) and a number of subsequent investigations in the following two decades, based on progressively improved AAM estimation and LOD observation, which, reassuringly, led to ever improving correlation between them (e.g., Eubanks, 1993; Dickey, 1993). The linear relationship was observed over a wide range of timescales from interannual, to intraseasonal, to as short as a few days (Rosen *et al.* 1990; Dickey *et al.*, 1992), approaching the limiting resolving power of modern LOD data.

Thus, the close relation between the zonal atmospheric circulation system and ΔLOD on a range of timescales between a few days and years (Figure 8.1) became very evident, once high-quality high-temporal-resolution data became available. This was owing to the following facts: (i) ΔLOD on timescales of several days to interannual is dominated, among all contributing sources, by AAM_z; (ii) AAM_z in turn is dominated by the contribution made by the motion term determined by the zonal u-wind field (8.1a); (iii) the zonal u-wind is the dominant feature in the atmospheric circulation field; and (iv) the mass term (8.1b) contributes relatively less, so its uncertainly regarding "IB vs. non-IB" is only of secondary influence. Similar close relationships, though, were more difficult to establish about the other geodetic observables (e.g., polar motion, time-variable gravity, or geocenter motion), as their corresponding relationships turned out to be more elusive; they were only made possible later via better observations, analysis, and improvements in atmospheric models.

Today, the AAM_z is routinely computed according to (8.1) at weather prediction centers such as the U.S. National Centers for Environmental Prediction (NCEP) and the European Centre for Medium-range Weather Forecasts (ECMWF), using output from their respective atmospheric analyses, typically at 6-hour intervals. The mass terms are evaluated both ways: with and without the IB assumption. These datasets are available from the Special Bureau for Atmosphere of the International Earth Rotation and Reference Systems Service's Global Geophysical Fluids Center (Salstein *et al.*, 1993, 2001; Chao *et al.*, 2000). An example is given in Figure 8.1 showing a 2-year span of excellent agreement between variations in LOD and AAM_z, although, by using this agreement, an indication of the underestimation in AAM of atmospheric GCMs by about 10% has been demonstrated numerically (Chao and Yan, 2010). This is true in both the seasonal signature and

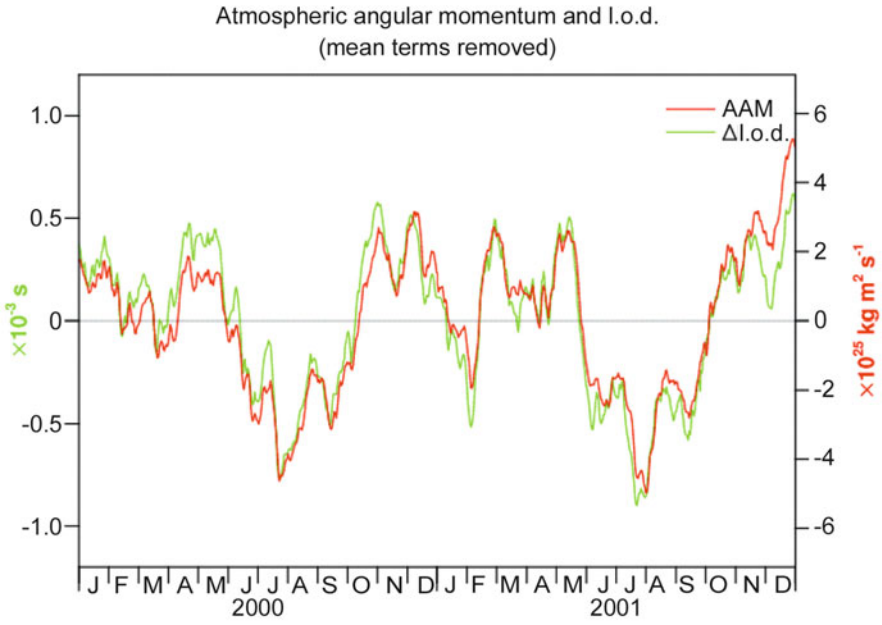

Figure 8.1. Axial angular momentum of the atmosphere AAM_z (green) computed using NCEP–NCAR reanalysis, compared with the length of day (red) from a combined geodetic solution in equivalent units for 2 years. Atmospheric excitation AAM_z is the sum of wind terms and pressure terms with the IB effect assumed for the ocean. Mean values have been removed. Note the very good agreement of the two series; discrepancies signify non-atmospheric contributions to length-of-day change. In addition to the seasonal signature note the very prominent ISV.

contemporaneous intraseasonal variations (as becomes clear by close examination of Figure 8.1). Other than that, the small differences between variations in LOD and AAM_z suggest the existence of non-AAM contributions to DLOD, given small errors in the datasets. In fact, such remaining signals have been linked to variations in oceanic angular momentum (e.g., Marcus *et al.*, 1998; Johnson *et al.*, 1999)..

Langley *et al.* (1981) specifically examine the near 50-day (ISV) oscillation in ΔLOD, making a connection to the AAM_z possibly associated with the Madden–Julian Oscillation (MJO; Madden and Julian, 1971, 1972) and the discovery of LOD variability with similar timescales (Feissel and Gambis, 1980). A series of investigations has since examined ISV in both AAM_z and ΔLOD, notably those of Anderson and Rosen (1983) relating the oscillation to convection in the Central Pacific, and Weickmann and Sardeshmukh (1994) and Weickmann *et al.* (1997) who broaden the investigation to consider activity in the Indian Ocean as well and tie the dynamics of angular momentum to wavetrains across the Pacific Ocean. In fact, even confinement of an intraseasonal oscillation to the tropical area was being questioned with the suggestion that there are angular momentum signatures from an independent extra-tropical oscillation (Dickey *et al.*, 1991). Lau *et al.* (1989) study the relation of AAM_z

and outgoing longwave radiation in terms of tropical ISV modes. Gutzler and Ponte (1990) examine the coherences among tropical zonal winds, near equatorial sea level, AAM_z, and ΔLOD, all of which exhibit a broad ISV including the MJO. Rosen *et al.* (1991) separate variability in AAM_z in terms of frequency bands and geographic zonal bands, and find in particular that ISV is mostly the result of behavior in the tropics and subtropics. Itoh (1994) further specify the subtropics as the source region of AAM_z ISV. Hendon (1995) confirms the 50-day peak in LOD is associated with active phases of the MJO. Marcus *et al.* (2001) report the correlation of ISV in AAM_z and ΔLOD with the ENSO, but no direct relationship between the MJO and the ENSO.

For a fuller diagnostic analysis—revealing the temporal dependence of the strength of different frequency signals—we can decompose the time series using a time–frequency wavelet spectrum. This special technique basically shows a "contour" of spectral power, using a running shortwave packet ("wavelet") of a given shape to pick out the power within any given (narrow) frequency band over a given (short) time period (see Chao and Naito, 1995). Naturally, such a spectrum is subject to limited resolution in both frequency and time, but it does provide an effective overview to a time series that has broadband spectral content. Thus, in the case of ISV signals with varying frequency–time characteristics, the full evolution of ISV is visible.

To produce the wavelet spectrum of the ΔLOD time series (Figure 8.2, upper panel), the strongest signals (i.e., the seasonal terms: annual and semi-annual) have been removed beforehand by subtracting least squares fits in order to reveal other signals of interest. Clearly seen, though not the subject under discussion here, are the long-period tidal terms (mostly the fortnightly M_f at 13.66 days and the monthly M_m at 27.55 days, modulated at the 18.6-year period related to the tide at the lunar precession period, as well as semi-annual tidal periods as expected). Here we only plot the real part (the cosine term of the wavelet transform) so that the positive–negative polarity of the undulations is shown. It is interesting to note the long decadal-scale undulations in the period exhibited by the strongest (sequence with shading contrast) ISV signals (e.g., the strongest subseasonal signals that occur in the last part of the record, around 2001–2002). In comparison, Figure 8.2 (lower panel) shows the computed non-seasonal AAM_z. Close examination of the ISV portion of the two spectra reveals remarkably good agreement, corroborating what was evident in the time–domain comparison (Figure 8.1). Also evident is the agreement in the interannual band, demonstrating that interannual ΔLOD is caused by the changing AAM_z (primarily in the *u*-wind fields) related to important ENSO (El Niño Southern Oscillation) and QBO (Quasi-Biennial Oscillation) signals (e.g., Chao, 1989); the alternating signs around 1980–1985 and 1995–2000 are such examples.

8.2.2 Polar motion excitation and equatorial angular momentum

Next we shall study 2-D equatorial *x*–*y* components, AAM_{xy} (in the equatorial plane orthogonal to AAM_z) on the atmospheric side and polar motion, rotational wobble of the Earth, on the geodetic side. The direction to which the Earth's rotational axis

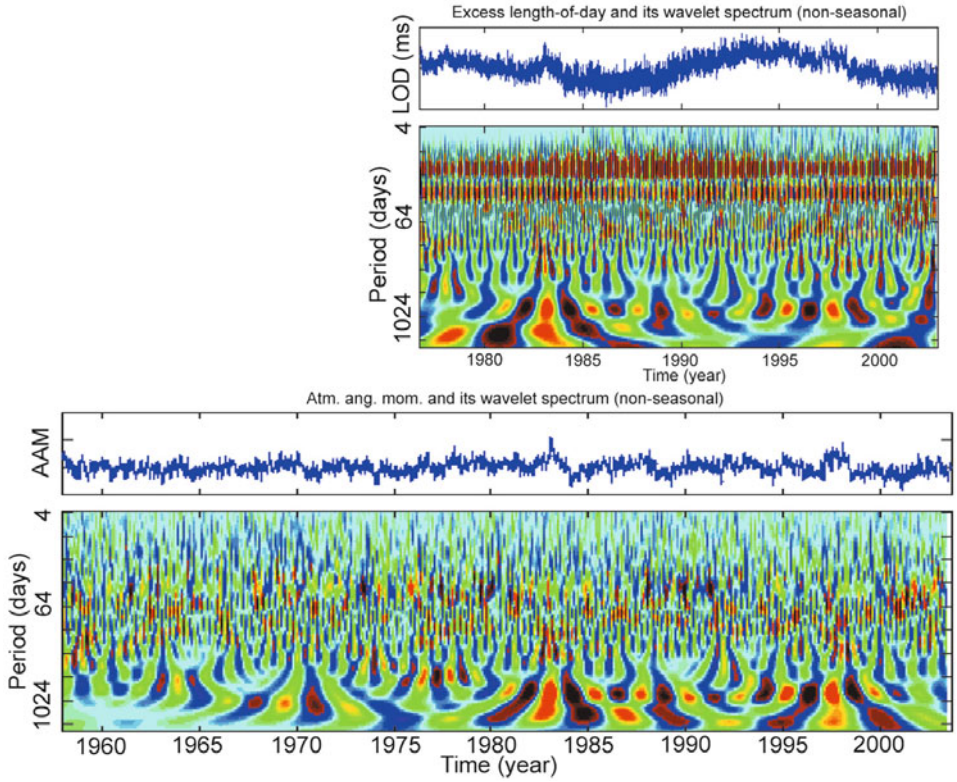

Figure 8.2. Comparison of the time–frequency wavelet spectrum of (upper panel) the geodetically observed ΔLOD time series with (lower panel) the computed AAM_z time series. Seasonal terms have been removed beforehand; the plot gives the real part (the cosine term of the wavelet transform) so that the positive–negative polarity of undulations is shown. Note the similarity between the two spectra. The contour amplitude in both plots is normalized and dimensionless and, hence, only shows relative strength (in fact, the contour shade has been saturated on the high end so as to bring out more moderate signals).

points (near the mean poles) varies due to a number of astronomical and geophysical processes. When observed from space absolute variations, similar to those of a spinning (and gyrating) top, are known as *nutation* (including the familiar astronomical precession). On the other hand, *polar motion* is that of the same rotation axis direction but relative to an observer sitting on Earth and hence rotating with the terrestrial reference frame. The observer sees polar motion even though the absolute momentum of the entire planet is conserved. An analogy of this motion is that felt by an ant on a poorly thrown wobbling frisbee. The important fact relevant to us here is that, in contrast to nutation which magnifies external astronomical influences, polar motion magnifies *internal geophysical* influences such as angular momentum exchanges among geophysical fluids.

Unlike the z-component, which is dominated by the atmospheric zonal wind field, the x–y components of atmospheric dynamics have a more subtle interplay and

have commanded somewhat less attention by atmospheric scientists, though the modes that cause polar motion have been noted in idealized atmospheric models (Feldstein, 2003). Corresponding to (8.1), the expressions for the x–y component of (normalized non-dimensional) AAM are approximately (Munk and MacDonald, 1960; Barnes *et al.*, 1983):

$$\text{Motion term of AAM}_{xy} = \frac{-1.43a^3}{(C-A)\omega g}\iiint (u\sin\theta + iv)\, e^{i\lambda}\, d\Omega\, dp \qquad (8.3a)$$

$$\text{Mass term of AAM}_{xy} = \frac{-1.00a^4}{(C-A)g}\iint p\cos\theta\sin\theta\, e^{i\lambda}\, d\Omega \qquad (8.3b)$$

where C is the mantle's principal momentum of inertia as in (8.1); and A is its mean moment of inertia pointing in the equatorial plane.

Note that now the motion term involves v, the meridional wind field, as well as u. The pressure term dominates the wind term for polar motion excitation. This term results from the (degree = 2, order = 1) term in spherical harmonics favoring zonal wavenumber 1 waves with the largest amplitudes and opposite phases in the two midlatitude regions of each hemisphere. Such uneven mass distributions in either latitude or longitude, causing imbalances of mass in opposite parts of the globe, are excitations for polar motion. In terms of our spinning skater analogy, if she draws in her two arms in an asymmetric way (e.g., one arm higher than the other), she would wobble while continuing to spin. Loading near the equator and the poles (0, 90°N, and 90°S latitude) creates no polar motion, as these latitudes are the nodes of the (2, 1) excitation term; hence strong ISV across the globe needs to occur in midlatitudes to have an appreciable effect on polar motion.

In contrast to (8.1), we now allow the *difference* between the axial and equatorial moment of inertia, $C - A$, to come into play. The relative difference $(C - A)/C$, about 1 part in 300, represents the Earth's oblateness, which in turn is a result of the Earth's rotation. It is the stabilizing factor that keeps polar motion in check and prevents the Earth's axis from, say, undergoing a disastrous change in position. In fact, modified by a factor related to the elasticity of the Earth and the participation/non-participation of the core and the ocean, it is responsible for Earth's resonance oscillation, known as the Chandler wobble, that occurs naturally at $p_c = 434$ days. As a damped oscillator, the Chandler wobble also has a natural damping factor, or quality factor Q_c, estimated to be upward of 50 (e.g., Furuya and Chao, 1996).

Observed polar motion is a relatively largely prograde motion (counterclockwise if viewed from above the north pole) of the rotation axis around the nominal north pole, with an amplitude of several meters consisting mainly of a forced annual wobble plus an excited Chandler wobble. The equation of motion that relates the AAM_{xy} to its excited polar motion P, expressed in radians, is:

$$\text{AAM}_{xy}(\text{sum of } 8.3\text{a} + 8.3\text{b}) = P - \frac{1}{i\omega_c}\frac{d}{dt}P \qquad (8.4)$$

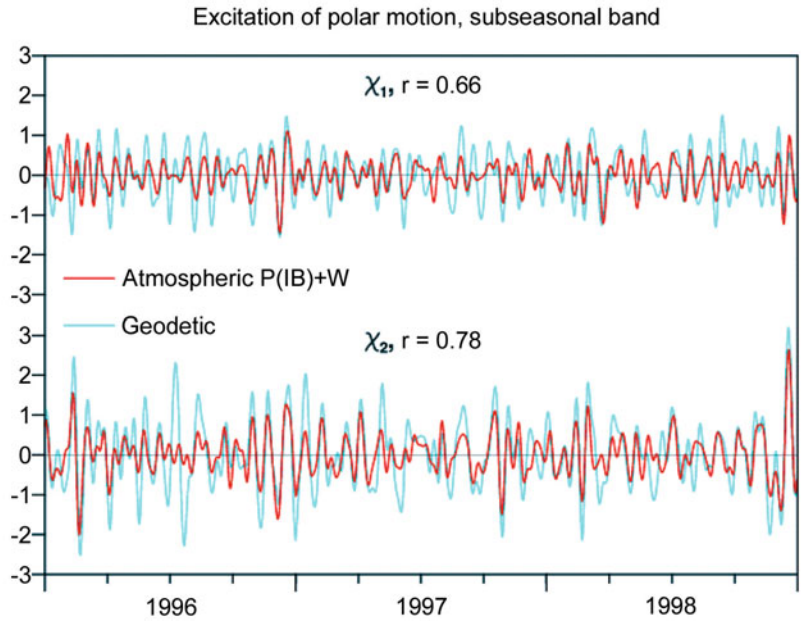

Figure 8.3. Comparison of the excitation function for polar motion: red is the equatorial AAM_{xy} computed using the NCEP–NCAR reanalysis system; blue is from a deconvolution of geodetically observed polar motion data off of the free Chandler resonance for the x and y components. The atmospheric excitation AAM_{xy} is the sum of wind terms and pressure terms with the inverted barometer effect assumed for the ocean. Units are $\times 10^{-7}$ radian (1 radian $= 2.06 \times 10^8$ mas). Here the series are filtered in the ISV band and have relatively good phase relationship at that timescale. Correlation coefficients, r, are indicated.

where the Chandler frequency $\omega_c \equiv 2\pi(1 + i/2Q_c)/p_c$ is given as a complex number to allow for the damping. In (8.3) and (8.4), the real and imaginary parts represent the x-component along the Greenwich meridian and the y-component along the 90°E longitude.

Equation (8.4) describes an excited 2-D linear resonance system, with the excitation function on the left side in the form of AAM_{xy}. When solved, polar motion P is the temporal convolution of the polar motion excitation function AAM_{xy} with the Earth's resonance as the free Chandler wobble. Conversely, the right-hand side operation of (8.4) represents the deconvolution of observed polar motion P from the free Chandler wobble. The result, often expressed as a χ-function (see Figure 8.3), is then the observed *excitation* of polar motion. It consists of a broadband signal (including ISV), plus strong seasonal (annual + semiannual) terms mostly of atmospheric origin, and a long-term secular drift primarily due to the post-glacial rebound of the solid Earth resulting from the unloading of the ice sheets since the last glacial age 10,000 years ago. The broadband signal in χ is thus directly comparable with the non-seasonal AAM_{xy}.

Figure 8.3 shows, for a selected few years, a comparison of such polar motion excitations in the ISV band; here we have removed the seasonal and secular terms similarly to the earlier ΔLOD example, as they are outside the temporal scale of our present interest. Again, a good agreement is evident; the broad ISV band correlation coefficients are as high as 0.66 for the x-component and 0.78 for the y-component.

Such a correlation was first reported by Eubanks *et al.* (1988) and then by a number of other studies. Note, however, that this agreement is not as good as for the axial case for ΔLOD. This difference relates to the different physical mechanisms at work. For example, unlike for ΔLOD, the mass (pressure) term has a larger contribution than the motion (wind) term, hence the IB effect—which reduces effective surface pressure excitations—introduces a larger uncertainty in the evaluation of AAM_{xy}. In the axial case, forced mostly by westerly winds, the prevailing zonal circulation of the atmosphere projects strongly onto the excitation of ΔLOD. Regarding agreement between atmospheric and geodetic polar motion signals, the amplitude of meteorological signal exceeds that of geodetic signals when the IB is not taken into account, but is too small when it is included (as shown in Figure 8.3); hence a state somewhat in between no IB effect and full IB effect appears likely to be closer to reality. Also, non-atmospheric sources prove to be relatively important in contributing their own χ, especially oceanic angular momentum, as demonstrated by, for example, Ponte *et al.* (1998) and Johnson *et al.* (1999); see also the review by Gross *et al.* (2003).

Understanding the meteorological origins of polar motion variability is instructive. The variance of the excitation term has its greatest power in regions of variability that often strongly feature fluctuating low pressures, like the North Pacific, North Atlantic, and regions of the southern oceans (Salstein and Rosen, 1989). Though the atmospheric excitation for polar motion from pressure variations over oceanic regions are largely reduced by the IB effect on ISV timescales, over the continents the strong semi-permanent high-pressure regions fluctuate, mainly over Siberia and secondarily over North America, impacting polar motion (Nastula and Salstein, 1999). Fluctuations at higher frequencies, though, may be related to Rossby waves excited by latent heating.

Some further insight into ISV can be acquired from the power spectrum of the observed polar motion excitation χ given in Figure 8.4. Since the input time series in this case is complex valued, both positive and negative frequencies are meaningful—the positive frequency refers to the circularly prograde component (i.e., the same direction as the prevailing polar motion), while the negative frequency refers to the retrograde component. Here one sees a broadband red spectrum which shows a very distinctive asymmetry between the positive (prograde) and negative (retrograde) frequencies all across the broad ISV band. Thus, a considerably larger partition of AAM_{xy} power resides over the retrograde band with periods longer than a few days than in the opposite prograde direction. It has been demonstrated that this asymmetry does indeed come from AAM_{xy}, as it disappears once the AAM_{xy} is subtracted from the time series (Gross *et al.*, 1998b). Superimposed are the long-period peak (at the central approximately zero frequency), four seasonal peaks

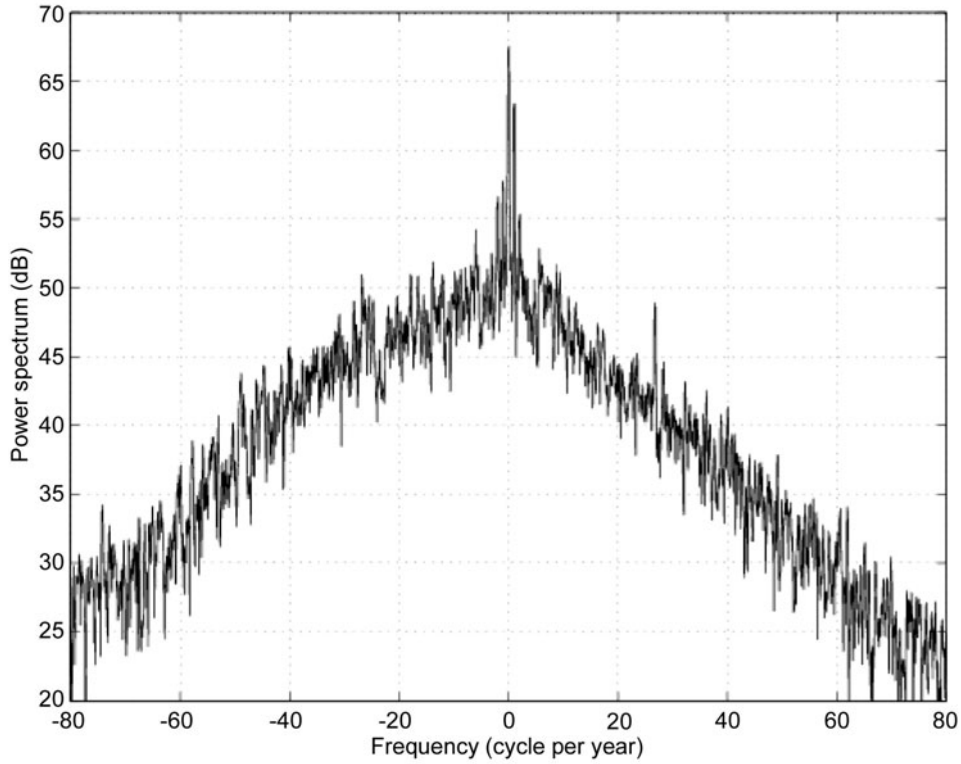

Figure 8.4. Power spectrum of the polar motion excitation obtained from a deconvolution of geodetically observed polar motion data off of the free Chandler resonance, 1976–2003. The positive frequency refers to the circularly prograde component, the negative frequency the retrograde component. Note the distinctive asymmetry in the spectrum where considerably higher power resides in negative rather than positive frequencies all across the broad ISV band.

(prograde + retrograde for annual + semiannual, next to the central peak, with the strongest one being the prograde annual term), and a few isolated tidal peaks (e.g., at monthly and fortnightly periods due to ocean tides); all are on timescales quite distant from the ISV scales of interest here.

8.2.3 Angular momentum and torques

The transfer of angular momentum between the solid Earth and its fluid envelope is accomplished dynamically by torques from forces acting on the fluid–solid Earth interfaces. The torque vector, of course, is the cross-product of the force and radius vectors. Formulation of the relation between angular momentum and torques can be found in Munk and MacDonald (1960) and Wahr (1982). Basically, in treating Earth rotation problems, one can rely solely on the conservation of angular momentum and equate the opposite changes in the AAM and that of the solid Earth, without

any prior knowledge of the actual torques that actually transfer angular momentum. On the other hand, one can endeavor to model and compute the appropriate torques, which in principle should affect the said transfer of angular momentum in exactly the same way (and conserve total angular momentum) as found in the angular momentum approach. The angular momentum and torque approaches are dynamically equivalent, but they have different formulations and face different data availability and uncertainty issues. In particular, the torque approach is less of an "exact science" at present because of our insufficient knowledge about torque mechanisms and hence larger uncertainties in their modeling.

In the case of the atmosphere and ocean, there are two major types of torques, the study of which dates back to White (1949) and Newton (1971). The first is a frictional torque, which is derived from a tangential force in the form of wind stress over land and ocean surfaces as well as ocean bottom drag; the second is a pressure torque based on a normal force acting against topography. At the atmosphere–land and ocean–land boundaries, the pressure torque is known as the mountain torque and the continental torque, respectively. For the atmosphere, they are calculated by models within a data assimilation scheme (e.g., Madden and Speth, 1995; Huang and Weickmann, 2008). Similarly, oceanic torques affecting Earth's rotation are reviewed and computed from models by Fujita *et al.* (2002).

Fundamentally, actions occurring at smaller than the grid scale of most general circulation models generate an additional torque based on gravity wave drag. The torque has been adapted as an additional torque though it is small on the timescales considered here. Such gravity waves may be viewed as presenting an accumulation of the effect of horizontal pressure gradients; when described in a model, though, they resemble frictional torques. We show in Figure 8.5 two larger torques—the fiction and mountain torques—for the axial case, based on the NCEP reanalysis system. It may be noted that the mountain torque has power at high frequencies related to synoptic activity of storm and fair weather systems crossing mountainous terrain (Iskenderian and Salstein, 1998), leading to the pressure gradients mentioned above. On such rapid synoptic scales, friction torque has low temporal variability, as prevailing winds near the surface do not change so markedly on those timescales. A power spectrum in time (not shown) reveals that around ISV timescales the friction and mountain torques are of comparable magnitudes. Madden (1987) indicates that friction torque from anomalies to the east of areas of convection may be responsible for interactions on 40 to 50 day timescales. Feldstein (2001) notes the presence of convection and its interaction with friction torques in this context.

In principle, there is an additional gravitational torque acting at distance on density anomalies between the fluid and solid Earth (de Viron *et al.*, 1999). The mass, and hence gravity, anomaly of a mountain range would cause an additional force on the atmospheric mass above it that would project onto a torque. Variable atmospheric mass surrounding the mountain would have an uneven effect, yielding a residual force in a particular direction. This effect has an extremely small magnitude in the axial case and so is not plotted in Figure 8.5. However, for signals in the equatorial plane that excite polar motion, the gravitational

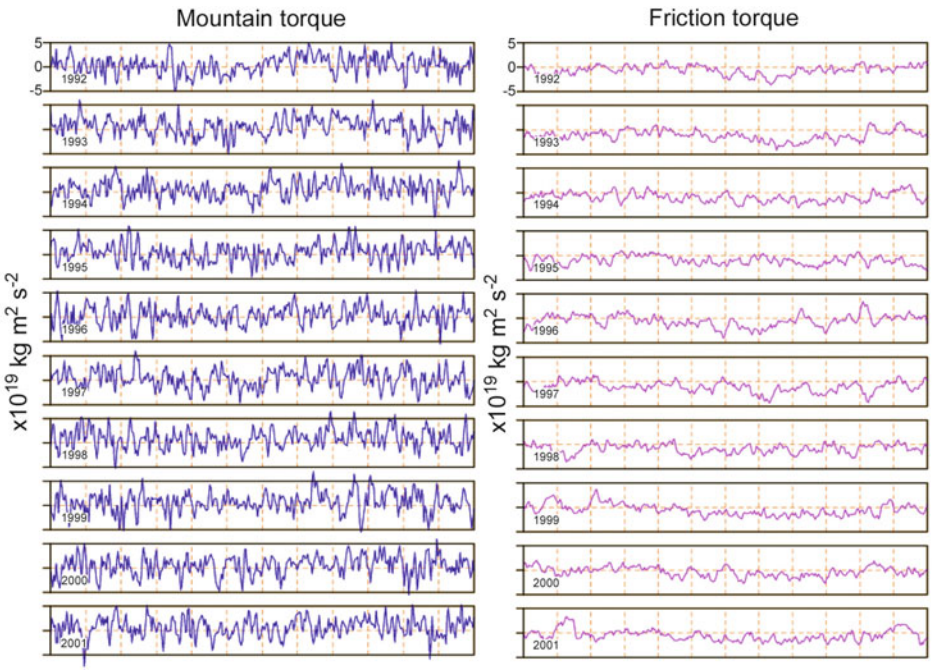

Figure 8.5. Two different atmospheric torques exerted upon the solid Earth in the axial component related to ΔLOD, including the normal mountain torque and the tangential friction torque. Note the prominence of the highest frequencies in mountain torques, though for ISV timescales mountain and friction torques have comparable power.

torque related to the oblate bulge of the Earth is important because of the large latitude-dependent mass anomaly that is the Earth's oblateness. This gravitational torque counterbalances to a considerable extent the pressure "mountain" torque obtained when considering the equatorial bulge as a huge mountain on the Earth (Wahr, 1982; Bell, 1994). Such gravitational torques, however, have relatively small variability on ISV timescales, even in the equatorial polar motion–related direction. Nevertheless, on ISV timescales the net bulge torque dominates the atmospheric effect on polar motion (Marcus *et al.*, 2004).

8.3 TIME-VARIABLE GRAVITY

Little was known about Earth's global gravity field beyond a nominal value of g until 1957 when the Sputnik satellites ushered in the space age. From space, the type of data used to solve the gravity "anomaly" involved the actual satellite orbit itself, determined by tracking from ground stations. Putting a gravimeter into orbit is fruitless as far as measuring gravity is concerned, because the gravimeter would always be in a free fall, experiencing weightlessness along with the satellite body

itself. Deep down this is a consequence of the equivalence principle between gravitational mass and inertia mass and, hence, between gravity and acceleration, a unique property of gravity according to general relativity. This situation makes gravity much different from, and its space measurement so much harder than, other physical properties that are conducive to direct remote sensing from space. Nevertheless, the orbit of a satellite does contain information about the gravity field through which the satellite traverses—the overall mean elliptic orbit gives the main spherically symmetric (the "monopole") part, whereas departures therefrom signify gravity *anomalies*. Taking enough orbits of different satellites, the complete gravity field could in principle be determined.

Over the years, the tracking of more and more satellites began to provide just such data, and ever higher spatial degree harmonic components of the gravity field were recovered (higher harmonics mean shorter "wavelengths" or higher spatial resolution, see below). Satisfying the Laplace equation, the gravity potential field U has the closed-form solution, customarily expressed as (e.g., Kaula, 1966):

$$U(r,\theta,\phi) = \frac{GM}{a}\sum_{l=0}^{\infty}\sum_{m=0}^{l}\left(\frac{a}{r}\right)^{l+1} P_{lm}(\cos\theta)(C_{lm}\cos m\lambda + S_{lm}\sin m\lambda) \tag{8.5}$$

where M is the Earth's mass; and P_{lm} is the 4π-normalized Legendre function. The coefficients C_{lm} and S_{lm} are known as the (normalized) harmonic *Stokes coefficient* of degree $l\,(=0,1,2,\ldots,\infty)$ and order $m\,(=0,1,2,\ldots,l)$; they constitute a basic set of functions which at a given truncation specify a gravity model. On the other hand, from Newton's gravitational law and so-called multipole expansion of the field U (e.g., Jackson, 1975), one realizes that Stokes coefficients are simply normalized multipoles of the density distribution of the body (e.g., Chao and Gross, 1987; Chao, 1994):

$$C_{lm}(t) + iS_{lm}(t) = \frac{1}{(2l+1)Ma^l}\iiint \rho(\mathbf{r};t)r^l Y_{lm}(\Omega)\,dV \tag{8.6}$$

where $Y_{nm}(\Omega) = P_{nm}(\cos\theta)\exp(im\lambda)$. When there is mass redistribution $\Delta\rho(\mathbf{r};t)$ in the body, the external gravity field would change accordingly. In particular, for mass redistributions $\Delta\sigma(\Omega;t)$ that can be considered as happening approximately on a spherical surface $r=a$, (8.6) reduces from a volume integral to a surface integral (see Chao, 2005):

$$\Delta C_{lm}(t) + i\Delta S_{lm}(t) = \frac{a^2}{(2l+1)M}\iint \Delta\sigma(\Omega;t)\,Y_{lm}(\Omega)\,d\Omega \tag{8.7}$$

Again, for loading the atmospheric mass over the ocean, $\Delta\sigma(\Omega;t)$ is modified greatly by the oceanic IB effect. For the atmosphere (or oceans), $\Delta\sigma(\Omega;t)$ can be easily converted from the surface (or ocean bottom) pressure field assuming hydrostatic equilibrium: $p = g\Delta\sigma$. Similarly to the procedure for angular momentum, one employs pressure datasets provided by weather centers such as NCEP or ECMWF.

As with Earth's rotation, contributions to time-variable gravity (8.7) come from mass transport in all geophysical fluids. Therefore, ultimately our study pertains to

all mass redistribution as a function of space and time. So, in principle, variations of gravity would be related to ISV if masses are redistributed on that timescale. In Section 8.2, variation in Earth's rotation represents a globally integrated angular momentum quantity; the small spatial resolution that exists is afforded by the kernel function in (8.1) and (8.3) during integration (e.g., Legendre functions of degree 2 in the case of mass terms). Note that the Stokes coefficient of degree 2, order 1 $(2, 1)$ is identical to the mass term of polar motion excitation (apart from a constant factor), and so is the (2,0) coefficient to the mass term of ΔLOD excitation. It should be noted that studying gravity allows the analysis of higher spatial harmonics than the study of Earth rotation. If the maximum harmonic degree that can be supported by the available data is L, then the nominal spatial resolution is the Earth's circumference (40,000 km) divided by $2L$.

SLR techniques have detected relatively minute but important time-variable gravity signals on the largest spatial scales; variations longer than monthly can now be clearly identified. Many studies have shown a clear connection between these signals and atmospheric and oceanic mass redistributions (e.g., Chao and Au, 1991; Johnson *et al.*, 2001). In another example, Cox and Chao (2002) report and speculate on possible meteorological causes for a positive anomaly in the Earth's oblateness, corresponding to the negative of the $(2, 0)$ Stokes coefficient, during 1998–2001, superimposed on the well-known secular decrease due primarily to post-glacial rebound. However, SLR data are intrinsically limited in resolution: monthly sampling may not be very useful in studying ISV in mass redistribution, and the geographical resolution associated with low-degree harmonics (say, below degree 4 or 5) is rather low.

On the other hand, the space gravity missions of CHAMP (launched in July 2000), GRACE (launched in March 2002), and GOCE (launched in March, 2009) are yielding gravity information at much higher precision and geographical resolution than ever before, certainly the earlier SLR-based information. In particular, the GRACE (Gravity Recovery And Climate Experiment) mission, now with an expected lifetime of over 5–10 years, promises to be able to detect subcentimeter–millimeter level equivalent water thickness (EWT) mass changes over an area of a few hundred kilometers across every month or so (Wahr *et al.*, 1998, 2004; Tapley *et al.*, 2004), yielding invaluable information about mass transport in all geophysical fluids under global changes (Tapley *et al.*, 2004; Luthcke *et al.*, 2006; Ramillien *et al.*, 2008; Rodell *et al.*, 2009; Chen *et al.*, 2009).

At monthly and longer time resolutions, both the classic SLR and the new GRACE time-variable gravity data are barely capable of resolving many interesting ISV signals. In the near future, though, GRACE solutions at time intervals as short as 10 days will become available (Bruinsma *et al.*, 2010) through tradeoffs between temporal resolution, spatial resolution and precision.

An indicative example of what GRACE can elucidate about intraseasonal mass redistribution is given in Figure 8.6. From these GRACE observations, the effect of atmospheric mass redistribution including its high temporal resolution, based on ECMWF analyses, is removed, as are oceanic contributions according to a nominal barotropic ocean model (see Ali and Zlotnicki, 2003). This process is

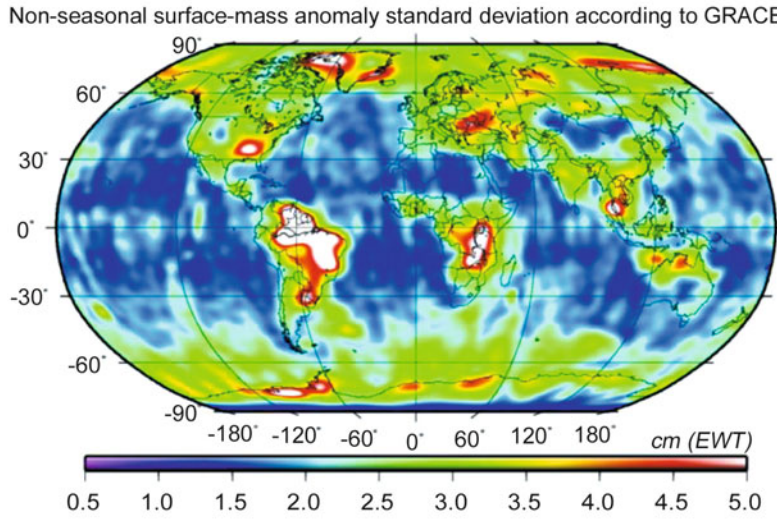

Figure 8.6. The ISV mass anomaly in terms of equivalent water thickness (EWT) standard deviation up to degree 60, order 60 harmonics, according to GRACE satellite data (fan filtered at 350 km) over the 7-year period from January 2003 through December 2009. These signals are first corrected for atmospheric mass redistribution (based on the ECMWF GCM model) and oceanic contributions (according to a mass-conserving baroclinic ocean model), while any further seasonal or linear trend signals are also removed numerically. Note the low ISV signal level over the oceans (except the Arctic Ocean), implying that the applied ocean model did a fair job in modeling mass redistribution (and hence removing signals).

needed to de-alias the signal, as observed by GRACE at shorter timescales, and leaves an approximately monthly time resolution for gravity signals. The map contours in Figure 8.6 show the strength of the residual intraseasonal mass anomaly in terms of EWT standard deviation after removal of any remaining seasonal signals and linear trends. The map is made by superposing up to (10,10) harmonics (hence a geographical resolution of about 2,000 km) and averaged over 18 monthly solutions spanning the period between August 2002 and May 2004. The most prominent signals with the strongest intraseasonal variability are land hydrology. In particular, the moderate ISV signal level over the oceans implies at face value that the applied ocean model did a preliminary job in modeling (and hence removing signals) of mass redistribution in the oceans up to harmonic degree 10. However, more complete scientific results await further and more detailed analyses to higher degrees based on longer and more accurate observations.

8.4 GEOCENTER MOTION

The degree $l = 0$ term in (8.5) corresponds to the gravity generated by the spherically symmetric Earth or, conceivably, the "monopole" as if the total mass of the Earth

was collapsed into a singular point. The next higher components, the three $l = 1$ terms or the dipoles, correspond to the position vector of the geocenter or the CM of the Earth system. This vector would of course be identically zero if the coordinate origin is always fixed at the geocenter. In practice, however, observatories fixed on the surface of the solid Earth tracking dynamic satellites define a slightly different reference system, where the CM of the solid Earth deviates slightly from the geocenter; these slight shifts lead to so-called geocenter motion. This apparent motion is the result of mass shifts in the moving geophysical fluid, as dictated by the conservation of linear momentum. Its observed amplitude is on the order of 1 cm, smaller than the size of a cherry, with strong seasonality and ISV.

In much the same way as for any other Stokes coefficients (8.7), geocenter motion due to the atmosphere (in particular), ISV, or otherwise can be readily evaluated given the global datasets from, say, NCEP or ECMWF. Together with additional contributions from the oceans and land hydrology (if similarly evaluated via global data or model outputs), they should be able to explain actual geocenter motion (e.g., Chen *et al*., 1999). The space-geodetic observation of geocenter motion is currently in its infancy; the solutions sometimes have systematic differences from those determined by different techniques that are as large as the signal level (IERS, 1999). However, the three components of geocenter motion in principle contain as much (independent) information about global mass redistribution as the three components of variation in Earth rotation. Monitoring the geocenter thus promises great utility in studying global mass changes, as in fact has already been demonstrated by Blewitt *et al*. (2001), and is a capability of gravity-observing satellites (Kang *et al*., 2009).

8.5 CONCLUSIONS

The conservation of angular momentum is the physical principle that governs the influence of AAM on Earth's rotation. This is of course true for any angular momentum variation in any geophysical fluid on any timescale. The practical significance of knowing the Earth's rotation is of great interest because of navigational needs, both for near Earth and for interplanetary spacecraft applications, for timekeeping, and for understanding the geophysical balances of the planet. Besides practical applications in monitoring and predicting variation in Earth's rotation, the scientific significance of the study of this relationship as presented above is manifold: at the root level, we have quantitative "confirmation" of the validity of the principle of angular momentum conservation on planetary scales; but, more importantly, to the extent permitted by the error bounds of the data, we have quantitative confirmation of the validity of measurement of Earth's rotation and the validity of calculated angular momentum based on GCM outputs. Conversely, discrepancies as a function of frequency and time contain information about angular momentum variation from secondary sources not already accounted for, whether meteorological, geophysical, or even anthropogenic (as in the case of major diversions of water mass, say, by building dams). In addition, they can lead to

quantitative improvement of models and geophysical formulations employed in angular momentum calculations, thereby providing useful constraints leading to a better understanding of mass transport in geophysical fluids.

The same argument is valid with respect to other global geodynamic observables due to mass transport in geophysical fluids. In this sense, variation in Earth's rotation, as well as time-variable gravity and geocenter motion all contain information about ISV in particular. An important and unique feature is that these observables pertain to mass, a quantity not readily derived by the usual remote-sensing observations.

Nevertheless, these geodynamic observables have intrinsic limitations due to their integrating nature, despite the triumphant progress seen in increasingly accurate space-geodetic techniques in the last two to three decades. For one thing, geodynamic effects sense the sum total of all mass transport—not discriminating meteorological/geophysical sources. To effectively distinguish the processes, geographical identification comes into play. While Earth rotation and geocenter observations have little spatial resolution to speak of, as integrated global quantities, the reasonably high resolution afforded by time-variable gravity provides a powerful identification of actual sources at any given time. Such is the case shown in Figure 8.6, where knowledge of time-variable gravity can have dramatic effects on monitoring various mass transport processes.

Another key consideration related to the usefulness of geodetic techniques—as applied in research of ISV—is the timescale and temporal resolution of observations. Meteorological and geophysical processes are typically characterized by distinct timescales, but there are exceptions, such as a number of geophysical/climatic changes that are broadband phenomena having timescales upwards from decadal to secular (e.g., ice sheet dynamics, post-glacial rebound, core flows). One such resolution, ISV, has been noted in geodetic signals and appears simply linked to the MJO discussed in other chapters. For the broad range of timescales, however—other than tidal variations, which have specific and well-defined periods—the only significant sources are meteorological, and some oceanic, forcing as discussed here. Relative to ISV, Earth rotation and geocenter observations can (and do) have reasonably high temporal resolutions, whereas time-variable gravity currently has temporal resolutions inadequate for ISV but is potentially capable of reaching higher resolutions. There are challenges and at the same time exciting prospects ahead of us in interpreting and making optimal applications of geodynamic observations in the study of ISV in the Earth system.

8.6 ACKNOWLEDGMENTS

Supported by NASA's Solid Earth Sciences programs, the space geodesy techniques that resulted in the Earth rotation, gravity, and geocenter data have been developed over decades under a truly international effort. The geophysical fluid data used in this chapter were provided by the IERS Global Geophysical Fluids Center (in particular, its Special Bureaus for the Atmosphere and for the Oceans). Earth rotation

data were kindly provided by Richard Gross of JPL; Figure 8.6 was made available by Zizhan Zhang from newly released GRACE data by the Center for Space Research, University of Texas, courtesy of the joint U.S.–German project of GRACE. The U.S. National Science Foundation provided partial support for this work, most recently through grant ATM-0913780.

8.7 REFERENCES

AGU (1993) *Contributions of Space Geodesy to Geodynamics: Technology* (Geodynamics Series 25, edited by D. E. Smith and D. L. Turcotte). American Geophysical Union, Washington, D.C.

Ali, A. H. and V. Zlotnicki (2003) Quality of wind stress fields measured by the skill of a barotropic ocean model: Importance of stability of the Marine Atmospheric Boundary Layer. *Geophys. Res. Lett.*, **30**(3): Art. #1129, February 11.

Anderson, J. R. and R. D. Rosen (1983) The latitude–height structure of the 40–50 day variations in the atmospheric angular momentum. *J. Atmos. Sci.*, **40**, 1584–1591.

Barnes, R. T. H., R. Hide, A. A. White, and C. A. Wilson (1983) Atmospheric angular momentum fluctuations, length-of-day changes and polar motion. *Proc. Royal Society London A*, **387**, 31–73.

Bell, M. J. (1994) Oscillations in the equatorial components of the atmosphere's angular momentum and torques on the earth's bulge. *Quart. J. Roy. Meteorol. Soc.*, **120**, 195–213.

Bettadpur, S. (2007) *CSR Level-2 Processing Standards Document for Product Release 04* (GRACE 327-742, The GRACE Project). Center for Space Research, University of Texas at Austin.

Blewitt, G., D. Lavallee, P. Clarke, and K. Nurutdinov (2001) A new global mode of Earth deformation: Seasonal cycle detected. *Science*, **294**, 2342–2345.

Bruinsma, S., J. M. Lemoine, R. Biancale, and N. Vales (2010) CNES/GRGS 10-day gravity field models (release 2) and their evaluation. *Adv. Space Res.*, **45**(4), 587–601.

Cartwright, D. E. (1999) *Tide: A Scientific History*. Cambridge University Press, Cambridge, U.K.

Chao, B. F. (1989) Length-of-day variations caused by El Niño–Southern Oscillation and Quasi-Biennial Oscillation. *Science*, **243**, 923–925.

Chao, B. F. (1994) The geoid and Earth rotation. In: P. Vanicek and N. Christou (Eds.), *Geophysical Interpretations of Geoid*. CRC Press, Boca Raton, FL.

Chao, B. F. (2003) Geodesy is not just for static measurements any more. *EOS, Trans. Amer. Geophys. Union*, 84, 145–156.

Chao, B. F. (2005) On inversion for mass distribution from global (time-variable) gravity field. *J. Geodynamics*, **39**, 223–230, doi: 10.1016/j.jog.2004.11.001.

Chao, B. F. and A. Y. Au (1991) Temporal variation of Earth's zonal gravitational field caused by atmospheric mass redistribution: 1980–1988. *J. Geophys. Res.*, **96**, 6569–6575.

Chao, B. F. and Gross, R. S. (1987) Changes in the Earth's rotation and lo-degree gravitational field induced by earthquakes. *Geophys. J. Royal Astron. Society*, **91**, 569–596.

Chao, B. F. and I. Naito (1995) Wavelet analysis provides a new tool for studying Earth's rotation. *EOS, Trans. Amer. Geophys. Union*, **76**, 161–165.

Chao, B. F. and H. M. Yan (2010) Relation between length-of-day variation and angular momentum of geophysical fluids. *J. Geophys. Res.*, doi: 10.1029/2009JB007024.

Chao, B. F., V. Dehant, R. S. Gross, R. D. Ray, D. A. Salstein, M. M. Watkins, and C. R. Wilson (2000) Space geodesy monitors mass transports in global geophysical fluids. *EOS, Trans. Amer. Geophys. Union*, **81**, 247–250.

Chen, J. L., C. R. Wilson, R. J. Eanes, and R. S. Nerem (1999) Geophysical interpretation of observed geocenter variations. *J. Geophys. Res.*, **104**, 2683–2690.

Chen, J. L., C. R. Wilson, D. Blankenship, and B. D. Tapley (2009) Accelerated Antarctic ice loss from satellite gravity measurements. *Nature Geoscience*, **2**, 859–862, doi: 10.1038/ngeo694.

Cox, C. M. and B. F. Chao (2002) Detection of a large-scale mass redistribution in the terrestrial system since 1998. *Science*, **297**, 831–833.

Da Szoeke, R. A. and R.M. Samelson (2002) The duality between the Boussinesq and non-Boussinesq hydrostatic equations of motion. *J. Phys. Oceanogr.*, **32**, 2194–2303.

de Viron, O., C. Bizouard, D. A. Salstein, and V. Dehant (1999) Atmospheric torque on the Earth and comparison with atmospheric angular momentum variations. *J. Geophys. Res.*, **104**, 4861–4875.

Dickey, J. O. (1993) Atmospheric excitation of the Earth's rotation: Progress and prospects via space geodesy. In: D. E. Smith and D. L. Turcott (Eds.), *Contributions of Space Geodesy to Geodynamics: Earth Dynamics* (pp. 55–70). American Geophysical Union, Washington, D.C.

Dickey, J. O., M. Ghil, and S. L. Marcus (1991) Extratropical aspects of the 30–60 day oscillation in length-of-day and atmospheric angular momentum. *J. Geophys. Res.*, **96**, 22643–22658.

Dickey, J. O., S. L. Marcus, J. A. Steppe, and R. Hide (1992) The Earth's angular momentum budget on subseasonal time scales. *Science*, **255**, 321–324.

Dickman, S. R. (1998) Determination of oceanic dynamic barometer corrections to atmospheric excitation of Earth rotation. *J. Geophys. Res.*, **103**, 15127–15143, doi: 10.1029/98JB00614.

Eubanks, T. M. (1993) Variations in the orientation of the Earth. In: D. E. Smith and D. L. Turcott (Eds.), *Contributions of Space Geodesy to Geodynamics: Earth Dynamics* (pp. 1–54). American Geophysical Union, Washington, D.C.

Eubanks, T. M., J. A. Steppe, J. O. Dickey, R. D. Rosen, and D. A. Salstein (1988) Causes of rapid motions of the Earth's pole. *Nature*, **334**, 115–119.

Feissel M. and D. Gambis (1980) La mise en evidence de variations rapides de la durée du jour. *C. R. Hebdomadaires Séances Acad. Sci.*, Ser. B, **291**, 271–273 [in French].

Feldstein, S. B. (2001) Friction torque dynamics associated with intraseasonal length-of-day variability. *J. Atmos. Sci.*, **58**, 2942–2953.

Feldstein, S. B. (2003) The dynamics associated with equatorial atmospheric angular momentum in an aquaplanet GCM. *J. Atmos. Sci.*, **60**, 1822–1834.

Fujita, M., B. F. Chao, B. V. Sanchez, and T. J. Johnson (2002) Oceanic torques on solid Earth and their effects on Earth rotation: Results from the Parallel Ocean Climate Model. *J. Geophys. Res.*, **107**(B8), doi: 10.1029/2001JB000339.

Furuya, M. and B. F. Chao (1996) Estimation of period and Q of the Chandler wobble. *Geophys. J. Int.*, **127**, 693–702.

Griffies, S. M. and A. Adcroft (2008) Formulating the equations of ocean modeling in an eddying regime. *Geophys. Monograph Ser.*, **177**, doi: 10.1029/177GM.8.

Gross, R. S., T. M. Eubanks, J. A. Steppe, A. P. Freedman, J. O. Dickey, and T. F. Runge (1998a) A Kalman-filter-based approach to combining independent Earth-orientation series. *J. Geodesy*, **72**, 215–235.

Gross, R. S., B. F. Chao, and S. D. Desai (1998b) Effect of long-period ocean tides on the Earth's polar motion. *Prog. in Oceanography*, **40**, 385–397.

Gross, R. S., I. Fukumori, and D. Menemenlis (2003) Atmospheric and oceanic excitation of the Earth's wobbles during 1980–2000. *J. Geophys. Res.*, **108**(B8), 2370, doi: 10.1029/2002JB002143.

Gutzler, D. S. and R. M. Ponte (1990) Exchange of momentum, among atmosphere, ocean, and solid Earth associated with the Madden–Julian Oscillation. *J. Geophys. Res.*, **95**, 18679–18686.

Hendon, H. H. (1995) Length of day changes associated with the Madden–Julian oscillation. *J. Atmos. Sci.*, **52**, 2373–2383.

Hide, R., N. T. Birch, L. V. Morrison, D. J. Shea, and A. A. White (1980) Atmospheric angular momentum fluctuations and changes in the length of the day. *Nature*, **286**, 114–117.

Huang, H.-P. and K. M. Weickmann (2008) On the computation of mountain torque from gridded global datasets. *Mon. Wea. Rev.*, **136**, 4005–4009.

IERS (1999) *IERS Analysis Campaign to Investigate Motions of the Geocenter* (IERS Tech. Note #25, edited by J. Ray). International Earth Rotation Service, Paris.

IPCC (2001) Climate Change 2001. In: R. T. Watson and the Core Writing Team (Eds.), *The Climate System: An Overview* (a contribution of Working Groups I, II, and III to the Third Assessment Report of the Intergovernmental Panel on Climate Change). Cambridge University Press, Cambridge, U.K., 398 pp.

Iskenderian, H. and D. A. Salstein (1998) Regional sources of mountain torque variability and high-frequency fluctuations in atmospheric angular momentum. *Mon. Wea. Rev.*, **126**, 1681–1694.

Itoh, H. (1994) Variations of atmospheric angular momentum associated with intraseasonal oscillations forced by zonally moving prescribed heating. *J. Geophys. Res.*, **99**, 12981–12998.

Jackson, J. D. (1975) *Classical Electrodynamics* (Second Edition). John Wiley & Sons, New York.

Jault, D. and J. L. Le Mouel (1989) The topographic torque associated with the tangentially geostrophic motion at the core surface and inferences on the flow inside the core. *Geophys. Astrophys. Fluid Dynamics*, **48**, 273–296.

Johnson, T. J., C. R. Wilson, and B. F. Chao (1999) Oceanic angular momentum variability estimated from the Parallel Ocean Climate Model, 1988–1998. *J. Geophys. Res.*, **104**, 25183–25196.

Johnson, T. J., C. R. Wilson, and B. F. Chao (2001) Non-tidal oceanic contributions to gravitational field changes: Predictions of the Parallel Ocean Climate Model. *J. Geophys. Res.*, **106**, 11315–11334.

Kang, I.-S. and K. M. Lau (1990) Evolution of tropical circulation anomalies associated with 30–60 day oscillation of globally averaged angular momentum during northern summer. *J. Meteorol. Soc. Japan*, **68**, 237–249.

Kang, Z., B. Tapley, J. Chen, J. Ries, and S. Bettadpur (2009) Geocenter variations derived from GPS tracking of the GRACE satellites. *J. Geodesy*, **83**, 895–901.

Kaula, W. M. (1966) *Theory of Satellite Geodesy*. Blaisdell Publishing, Waltham, MA.

Langley, R. B., R. W. King, I. I. Shapiro, R. D. Rosen, and D. A. Salstein (1981) Atmospheric angular momentum and length of day: A common fluctuation with a period near 50 days. *Nature*, **294**, 730–733.

Lau, K. M., I. S. Kang, and P. J. Sheu (1989) Principal modes of intraseasonal variations in atmospheric angular momentum and tropical convection. *J. Geophys. Res.*, **94**, 6319–6332.

Lin, J.-L., M. Zhang, and B. Mapes (2005) Zonal momentum budget of the Madden–Julian Oscillation: The source and strength of equivalent linear damping. *J. Atmos. Sci.*, **62**, 2172–2188, doi: 10.1175/JAS3471.1.

Luthcke, S. B., H. J. Zwally, W. Abdalati, D. D. Rowlands, R. D. Ray, R. S. Nerem, F. G. Lemoine, J. J. McCarthy, and D. S. Chinn (2006) Recent Greenland ice mass loss by drainage system from satellite gravity observations. *Science*, **314**(5803), 1286–1289, doi: 10.1126/science.1130776.

Madden, R. A. (1987) Relationships between changes in the length of day and the 40–50 day oscillation in the tropics. *J. Geophys. Res.*, **44**, 8391–8399.

Madden, R. A. and P. R. Julian (1971) Description of a 40–50 day oscillation in the zonal wind in the tropical Pacific. *J. Atmos. Sci.*, **28**, 702–708.

Madden, R. A. and P. R. Julian (1972) Description of global-scale circulation cells in the tropics with a 40–50 day period. *J. Atmos. Sci.*, **29**, 1109–1123.

Madden, R. A. and P. Speth (1995) Estimates of atmospheric angular momentum, friction, and mountain torque during 1987–1988. *J. Atmos. Sci.*, **52**, 3681–3694.

Marcus, S. L., Y. Chao, J. O. Dickey, and P. Gegout (1998) Detection and modeling of nontidal oceanic effects on Earth's rotation rate. *Science*, **281**, 1656–1659.

Marcus, S. L., J. O. Dickey, and O. de Viron (2001) Links between intraseasonal (extended MJO) and ENSO timescales: Insights via geodetic and atmospheric analysis. *Geophys. Res. Lett.*, **28**, 3465–3458.

Marcus, S. L., O. de Viron, and J. O. Dickey (2004) Atmospheric contributions to Earth nutation: Geodetic constraints and limitations of the torque approach. *J. Atmos. Sci.*, **61**, 352–356.

Munk, W. H. and G. J. F. MacDonald (1960) *The Rotation of the Earth*. Cambridge University Press, New York.

Nastula, J. and D. A. Salstein (1999) Regional atmospheric angular momentum contributions to polar motion excitation. *J. Geophys. Res.*, **104**, 7347–7358.

Nastula, J., R. Ponte, and D. Salstein (2007) Comparison of polar motion excitation series derived from GRACE and from analyses of geophysical fluids. *Geophys. Res. Lett.*, **34**, L11306, doi: 10.1029/2006GL028983.

Newton, C. W. (1971) Mountain torques in the global angular momentum balance. *J. Atmos. Sci.*, **28**, 623–628.

Peixoto, J. P. and A. H. Oort (1992) *Physics of Climate*. American Institute of Physics, Melville, New York.

Plag, H.-P. and M. Pearlman (2009) *Global Geodetic Observing System* (ISBN-978-3-642-02686-7). Springer-Verlag, Berlin.

Ponte, R. M. (2006) Low-frequency sea level variability and the inverted barometer effect. *J. Atmos. Oceanic Technol.*, **23**, 619–629.

Ponte, R. M., D. Stammer, and J. Marshall (1998) Oceanic signals in observed motions of the Earth's pole of rotation. *Nature*, **391**, 476–479.

Ramillien, G., J. S. Famiglietti, and J. Wahr (2008) Detection of continental hydrology and glaciology signals from GRACE: A review. *Surv. Geophys.*, **29**(4/5), 361–374.

Rodell, M., I. Velicogna, and J. S. Famiglietti (2009) Satellite-based estimates of groundwater depletion in India. *Nature*, **460**, 999–1002, doi: 10.1038/nature08238.

Rosen, R. and D. Salstein (1983) Variations in atmospheric angular momentum on global and regional scales and the length of day. *J. Geophys. Res.*, **88**, 5451–5470.

Rosen, R. D., D. A. Salstein, and T. M. Wood (1990) Discrepancies in the Earth–atmospheric angular momentum budget. *J. Geophys. Res.*, **95**, 265–279.

Rosen, R. D., D. A. Salstein, and T. M. Wood (1991) Zonal contributions to global momentum variations on intraseasonal through interannual time scales. *J. Geophys. Res.*, **96**, 5145–5151.

Salstein, D. A. and R. D. Rosen (1989) Regional contributions to the atmospheric excitation of rapid polar motion. *J. Geophys. Res.*, **94**, 9971–9978.

Salstein, D. A., D. M. Kann, A. J. Miller, and R. D. Rosen (1993) The sub-bureau for Atmospheric Angular Momentum of the International Earth Rotation Service (IERS): A meteorological data center with geodetic applications. *Bull. Amer. Meteorol. Society*, **74**, 67–80.

Salstein, D. A., O. de Viron, M. Yseboodt, and V. Dehant (2001) High-frequency geophysical fluid modeling necessary to understand Earth rotation variability. *EOS, Trans. Amer. Geophys. Union*, **82**, 237–238.

Swenson, S. and J. Wahr (2006) Post-processing removal of correlated errors in GRACE data. *Geophys. Res. Lett.*, **33**, L08402, doi: 10.1029/2005GL025285.

Tapley, B. D. (2002) The GRACE mission: Status and performance assessment. *American Geophysical Union Fall Meeting, San Francisco*.

Tapley, B. D., S. Bettadpur, J. C. Ries, P. F. Thompson, and M. M. Watkins (2004) GRACE measurements of mass variability in the earth system. *Science*, **305**(5683), 503–505, doi: 10.1126/science.1099192.

Wahr, J. M. (1982) The effects of the atmosphere and oceans on the Earth's wobble, I: Theory. *Geophys. J. Royal Astron. Society*, **70**, 349–372.

Wahr, J., M. Molenaar, and F. Bryan (1998) Time variability of the Earth's gravity field: Hydrological and oceanic effects and their possible detection using GRACE. *J. Geophys. Res.*, **103**, 30205–30230.

Wahr, J., S. Swenson, V. Zlotnicki, and I. Velocogna (2004) Time-variable gravity from GRACE: First results. *Geophys. Res. Lett.*, **31**, L11501, doi: 10.1029/2004GL019779.

Weickmann, K. and E. Berry (2009) The tropical Madden–Julian Oscillation and the global wind oscillation. *Mon. Wea. Rev.*, **137**, 1601–1614.

Weickmann, K. and P. Sardeshmukh (1994) The atmospheric angular momentum budget associated with a Madden–Julian Oscillation. *J. Atmos. Sci.*, **51**, 3194–3204.

Weickmann, K., G. Kiladis, and P. Sardeshmukh (1997) The dynamics of intraseasonal atmospheric angular momentum oscillations. *J. Atmos. Sci.*, **54**, 1445–1461.

White, R. M. (1949) The role of the mountains in the angular momentum balance of the atmosphere. *J. Meteorol.*, **6**, 353–355.

Zhang, Z. Z., B. F. Chao, Y. Lu, and H. T. Hsu (2009) An effective filtering for GRACE time-variable gravity: Fan filter. *Geophys. Res. Lett.*, **36**, L17311, doi: 10.1029/2009GL039459.

Zhou, Y. H., D. A. Salstein, and J. L. Chen (2006) Revised atmospheric excitation function series related to Earth's variable rotation under consideration of surface topography. *J. Geophys. Res.*, **111**, D12108, doi: 10.1029/2005JD006608.

9

El Niño Southern Oscillation connection

William K. M. Lau

9.1 INTRODUCTION

The Madden–Julian Oscillation (MJO) is the most pronounced signal in tropical intraseasonal (20–90 days) variability, and the El Niño Southern Oscillation (ENSO) is the most dominant interannual climate phenomenon in the tropical ocean–atmosphere system. Both the MJO and the ENSO involve major shifts in tropical convection, large-scale circulation, and weather patterns around the world. The hypothesis that the MJO and the ENSO may be intrinsically linked was first proposed in the mid-1980s by Lau (1985a, b). Subsequently, many observational and modeling studies have appeared in the literature debating the merits of the hypothesis. Today, while the MJO–ENSO connection is still a topic of active research (Zhang *et al.*, 2001), knowledge gained from better understanding of the causes and evolution of the MJO and the ENSO has been incorporated into long-range weather forecasting and climate prediction schemes, resulting in improved forecasts not only in the tropics but also in many extratropical regions. A key factor in the prediction improvement is the recognition that MJO and ENSO events do not act independently, but may interact with each other to provide the long-term preconditions and the short-term fine tuning needed for better skill in long-range ($>$ month) predictions. How can the MJO and the ENSO—two phenomena with widely separate timescales—be physically linked and interact with each other? This critical question and related issues will be addressed in this chapter.

Here, as in other chapters of this book, the MJO is considered in the context of tropical intraseasonal variability (TISV). In Section 9.2, a historical perspective of the TISV–ENSO connection will be presented. This is followed in Sections 9.3–9.6 by discussions, in terms of four major phases, about the development and evolution of the paradigm of the TISV–ENSO relationship from 1980 to the present day. Note that the phases have much overlap and do not strictly follow chronological order.

W. K. M. Lau and D. E. Waliser (Editors), *Intraseasonal Variability in the Atmosphere–Ocean Climate System* (Second Edition).

- *Phase 1*: this is the embryonic stage beginning in the early 1980s consisting of mostly observational studies based on emerging satellite data and operational analyses, with somewhat sketchy descriptions and rudimentary ideas. This stage also included observational and theoretical work, documenting the hierarchical structure of the MJO, westerly wind bursts, and coupling instability of the tropical ocean–atmosphere.
- *Phase 2*: this is the exploratory stage from the late 1980s to mid-1990s, represented by a large number of more in-depth observational and modeling studies, focusing on the understanding of possible mechanisms. These studies generally did not find strong statistical evidence of an MJO–ENSO link, but yet could not exclude the possible relevance of such a connection.
- *Phase 3*: this phase encompassed many case studies of El Niño and La Niña, including the oceanic remote response to TISV forcings carried out in the mid-1990s to early 2000s. The strong TISV forcings associated with the onset and demise of the 1997/1998 El Niño lended definitive support to and rejuvenated the debate on the MJO–ENSO connection. This period also covers work on the development of a more comprehensive and dynamical framework, including the concept of optimal stochastic forcings and rectification of the MJO into ENSO cycles.
- *Phase 4*: this phase covers recent developments including new observational insights, many studies focused on realistic simulation of the MJO in atmospheric models and coupled climate models, and the effects of TISV and MJO on the predictability of ENSO.

Studies conducted in Phases 2 and 3 have considerable overlap with material covered in Chapters 6 and 7 of this book. Here, we shall only concentrate on the aspects relevant to the TISV–ENSO connection and refer details of TISV to those chapters. For Phase 4, we also include results from recent observations to shed new light on the TISV–ENSO relationship. The chapter ends with a discussion in Section 9.7 on the role of TISV in ENSO predictability.

9.2 A HISTORICAL PERSPECTIVE

The MJO, originally known as the 40 to 50-day oscillation of the tropical atmosphere, was first reported in two seminal papers by Madden and Julian (1971, 1972; see Chapter 1). However, the importance of the discovery was largely left unnoticed for almost a decade. It was not until the early 1980s, when the phenomenon was ''re-discovered'' almost serendipitously, that its paramount importance was recognized, thanks to the convergence of several major events in the field of atmospheric and oceanic sciences.

The first was the launch of the First GARP Global Experiment (FGGE) in 1978/1979, which was the first global-scale observation and field program undertaken by the international meteorological and oceanographic communities in an attempt to provide a complete description of the general circulation of the atmosphere with the

objective to improve weather prediction (McGovern and Fleming, 1977; Kalnay *et al.*, 1981). One of the special observing periods in FGGE was the Monsoon Experiment (MONEX), in which regional field campaigns were conducted to provide better observations of Asian summer and winter monsoons. FGGE and MONEX led to the discovery of pronounced intraseasonal oscillations (ISOs), with quasi-biweekly and 30 to 60-day timescales in the global tropics and in the monsoon regions (Lorenc, 1984; Krishnamurti and Subramanyan, 1983; Krishnamurti *et al.*, 1985). These studies led some scientists to believe in the early 1980s that the Asian monsoon was responsible for exciting the MJO (Yasunari, 1982; Murakami *et al.*, 1984; Murakami and Nakazawa, 1985). Today, it is recognized that the MJO is an intrinsic phenomenon of the tropical atmosphere, but subject to modulation by air–sea interaction, as well as regional land and oceanic processes associated with the Asian–Australian monsoon.

The second major event was the abrupt occurrence of the major El Niño of 1982/1983. In view of the influential work of Wyrtki (1975, 1979), who postulated a sea level rise in the Western Pacific as a precondition for the onset of El Niño, everyone was caught by surprise by the sudden onset of the 1982/1983 El Niño, which occurred without a major buildup phase (Cane, 1983; Gill and Rasmusson, 1983). Many scientists came to realize that they did not understand the mechanisms involved in El Niño at all and that more observations and better models were needed. The frustration at being fooled by nature had provided the impetus for many scientists to start looking for better explanations of El Niño, including coupled instability of the tropical ocean–atmosphere and the role of atmospheric transients. This impetus led to the establishment of the very successful Tropical Ocean Global Atmosphere (TOGA) program in 1985–1995 for monitoring and improving the prediction capability of the ENSO (NRC, 1996).

The third event that influenced the underlying ideas of an MJO–ENSO connection was the commencement of the modern satellite era in the late 1970s, coupled with the development of the Global Telecommunication System (GTS) enabling operational weather services around the world to use and produce satellite products for weather forecasting. Indeed, recognition of the importance of using and sharing satellite information for weather forecasting was the driving force behind the World Weather Watch (WWW), a component of the FGGE. One of the first and most important satellite products used for climate research was the advanced very high resolution radiometer (AVHRR) flown onboard the NOAA TIROS satellite since 1974. By the early 1980s, almost 10 years of daily AVHRR data were archived and available to the research community. The most widely used AVHRR product was outgoing longwave radiation (OLR), which provided a broadband measure of the total flux of longwave radiation loss to space at the top of the atmosphere (Gruber and Krueger, 1984). Deep convective clouds in the tropics have cold cloud tops and, therefore, a low OLR value. Typically, a value less than 200 $W\,m^{-2}$ signals the presence of deep convection in the tropics (Waliser *et al.*, 1993). Because of this simple but unique property of OLR, it has been widely used as a proxy for deep convection over the tropical oceans, where the background longwave radiation from low clouds or from the ocean surface is much higher

($>220\,\mathrm{W\,m^{-2}}$). In the early to mid-1980s, a series of observational papers on the MJO (at the time still referred to as the 40 to 50-day or 30 to 60-day oscillation) using OLR and wind analyses from the U.S. National Meterological Center (NMC) appeared (e.g., Lau and Chan, 1983a, b, 1985, 1986a, b; Weickmann, 1983; Murakami and Nakazawa, 1985; Weickmann *et al.*, 1985; Knutson and Weickmann, 1987). These papers helped to bring the MJO to the attention of the scientific community.

9.3 PHASE 1: THE EMBRYONIC STAGE

The basic concept of an MJO–ENSO connection was first proposed in Lau (1985a, b). Noting the similar spatial scales but vastly different timescales of variability associated with the MJO and the ENSO, Lau proposed a theoretical framework in which three basic elements (unstable air–sea interaction, the seasonal cycle, and stochastic forcing from high-frequency transients such as the MJO) were identified to be crucial factors leading to the ENSO cycle and its long-term behavior. Using a simple nonlinear oscillator model, Lau demonstrated that interplay of the aforementioned processes could produce many salient features of ENSO variability including the 2 to 5-year recurrence interval, autocorrelation, and spectral characteristics, as well as phase locking with the seasonal cycle. In a series of subsequent papers, the basic paradigm was bolstered by further observational and theoretical studies (Lau and Chan, 1986a, b, 1988; Lau and Shen, 1988; Hirst and Lau, 1990).

9.3.1 OLR time–longitude sections

Figure 9.1a shows the time–longitude section, also known as a Hovmöller diagram, of 7-day mean OLR along the equator covering the entire Indo-Pacific basin, reproduced from Lau and Chan (1986a) for the period 1974–1984. Data were missing and never recovered for 1978. This figure provided for the first time a vivid depiction of the episodic onset of El Niño, juxtaposed against a backdrop of spacetime evolution of deep convection associated with the MJO year after year. It provided convincing evidence of the intrinsic nature of the MJO in the tropical atmosphere and its possible transformation during the ENSO. Notable features in Figure 9.1a included the almost continuous streams of eastward propagation of convective pulses from the western Indian Ocean to the Central Pacific. During El Niño of 1982/1983, deep convection began to shift eastward to the Eastern Pacific in June 1982 and remained active there until June 1983, when convection abruptly ceased and the coupled system began to enter La Niña phase. Lau and Chan also noted increased MJO activity in the Indian Ocean and Western Pacific several months prior to the onset of El Niño in 1982/1983. Interestingly, Figure 9.1a suggested that the MJO is present all year round, with a stronger signal (along the equator) during spring and fall, but the weakest signal in the northern summer. This helped dispel the notion that the Asian summer monsoon was the cause of the MJO. Based

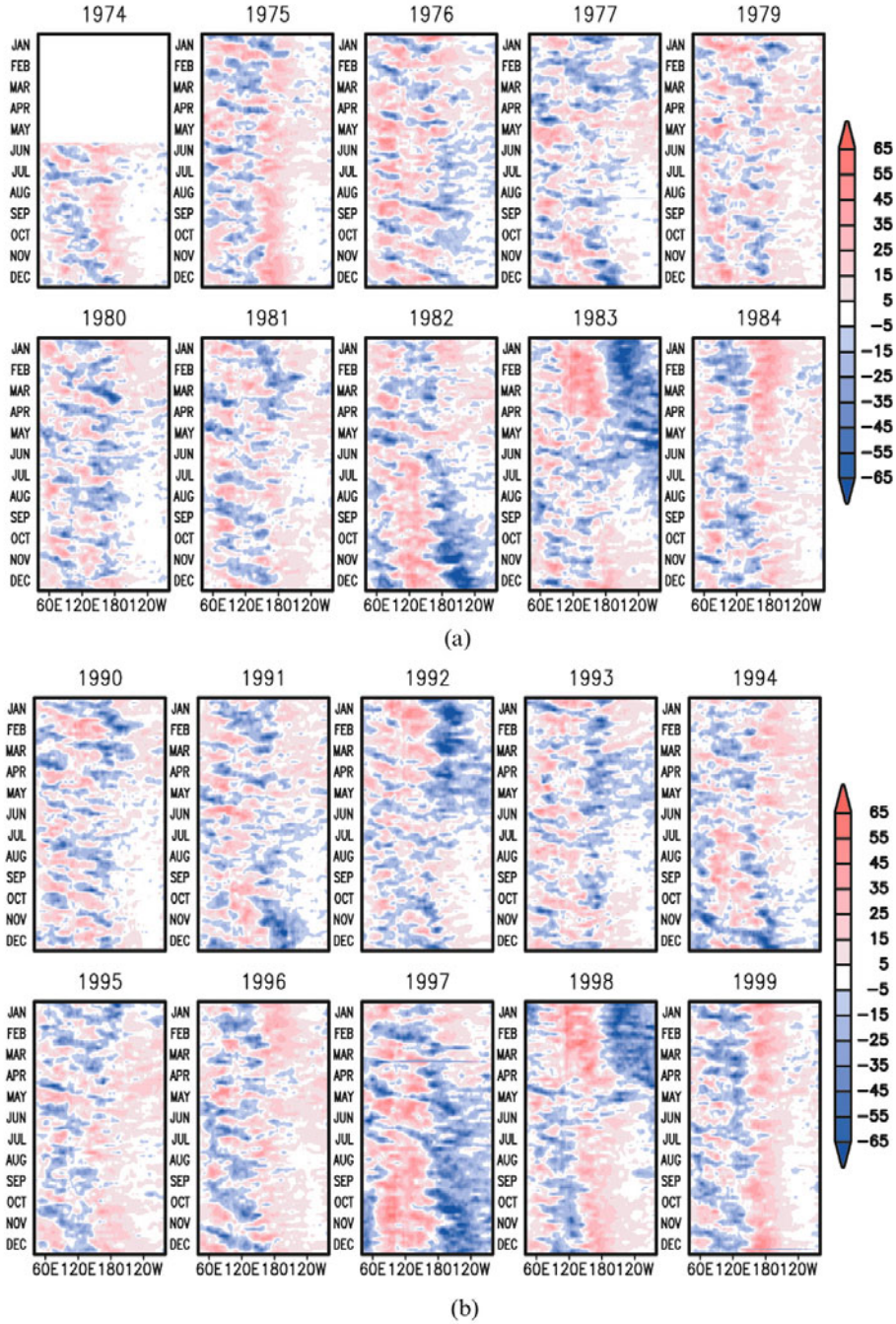

Figure 9.1. Time–longitude section of 5-day mean OLR ($W\,m^{-2}$) averaged between 5°S–5°N, for (a) 1974–1984 and (b) 1990–1999. Negative values (shaded blue) indicate enhanced deep convection, and positive values (shaded red) reduced deep convection.

on observations such as these, a number of authors went on to develop basic theories of atmospheric low-frequency oscillations arising from moisture convergence and latent heating feedback from tropical convection in an aqua-planet (i.e., an Earth completely covered by ocean) (Hayashi and Sumi, 1986; Lau and Peng, 1987; Chang and Lim, 1988; Wang and Rui, 1990; Hendon, 1988). Readers are referred to Chapter 10 for discussions of theories of the MJO.

Figure 9.1b shows a time–longitude section similar to that used in Lau and Chan (1986a), but for the period 1990–1999. Two El Niños occurred during the period in 1991/1992 and in 1997/1998. The latter has been referred to as El Niño of the century, because of its exceptional strength and impact on weather and climate worldwide. In normal years, pronounced MJO convection signals were more or less confined to the Indian Ocean and Western Pacific warm pool ($>28^{\circ}$C) of the tropical Western Pacific. Near the dateline, MJO convective activities appear to stop just at the eastern extreme of the warm pool, except during El Niño, when the warm pool expands to the Eastern Pacific, setting up conditions for deep convection there. Compared with the period 1974–1984, the general similarity in variability associated with the MJO and the ENSO is striking. Even more remarkable is the similarity of MJO propagation and ENSO evolution during the two decades, as if nature had a memory to repeat itself through the entire MJO–ENSO evolution, even after more than 10 years. Increased MJO activity in the Indian Ocean and Western Pacific during the first part of 1997 and other definitive observations of oceanic Kelvin wave signals from the TOGA tropical atmosphere and ocean (TAO) array suggested strong MJO impacts on the onset of El Niño in 1997/1998 and provided the impetus for renewed interest in studies of an MJO–ENSO connection (see discussion in Section 9.5).

9.3.2 Seasonality

The seasonal cycle was recognized as an important factor in the interaction between the MJO and the ENSO, because of the strong phase locking of the ENSO to the annual cycle (Lau, 1985a, b). Lau and Chan (1988) show that the tropical averaged root-mean-square fluctuation of OLR associated with the annual cycle is about 1.5 times that of the TISV, which is about 3 times stronger than the interannual component. Figure 9.2 shows the amplitude and spatial distribution of TISV of OLR in different seasons. TISV centers of activity stretch from the Indian Ocean to the Western Pacific, with an obvious minimum over the maritime continent. The reason for the minimum is not clear, but may be related to the effects of topography, which inhibit large-scale organization of deep convection, or to strong land heating (cooling) during the day (night) which tends to favor strong diurnal variability over low-frequency variability. Also, the maritime continent is frequently impacted by midlatitude and subtropical disturbances such as cold air intrusion from the East Asian continent, which inhibits the development of deep convection (Chang and Lau, 1980; Lau *et al.*, 1983). The TISV is strongest and most extensive in DJF, with a pronounced signal in the southern tropics between the equator and 20°S. In MAM, the MJO appears more symmetric about the equator, with centers of

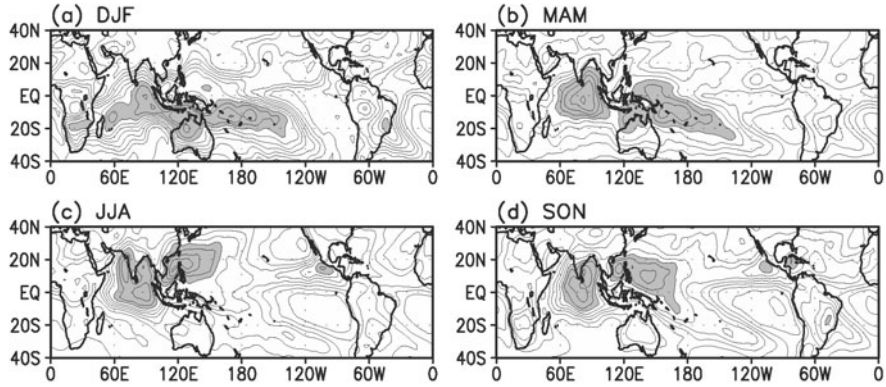

Figure 9.2. Spatial distribution of variance of 20 to 70-day bandpassed OLR for the four seasons: (a) DJF, (b) MAM, (c) JJA, and (d) SON. The unit is $(\mathrm{W\,m^{-2}})^2$. Regions of deep convection are highlighted.

activity well separated between the Indian Ocean and the Western Pacific. During JJA, TISV activity shifts to the Asian monsoon region, with centers around the eastern Arabian Sea, the Bay of Bengal, the South China Sea, and the subtropical Western Pacific. The SON pattern is similar to JJA, except for signs of TISV activity in the South Pacific Convergence Zone (SPCZ) and the South Atlantic Convergence Zone (SACZ) in the southern hemisphere. As will be discussed in Section 9.5, in terms of remote forcing and possible triggering of the onset of ENSO anomalies by surface winds, TISV in MAM may be most effective through excitation of oceanic Kelvin waves in the equatorial oceanic waveguide which is within approximately 2° of the equator (Harrison and Schopf, 1984; Giese and Harrison, 1990; Hendon *et al.*, 1998). However, not all TISV in MAM will lead to onset of El Niño. To increase the probability of triggering a full-blown warm event, preconditioning (e.g., increased heat content in the tropical Pacific) in the preceding winter season may be required.

9.3.3 Supercloud clusters

In addition to coherent eastward propagation, the MJO is associated with a hierarchy of different scales of atmospheric motion, which may provide stochastic forcing of El Niño. Nakazawa (1988) shows that westward-propagating high-frequency convective systems are embedded in the eastward-propagating MJO envelope, along the equator, to form a large-scale organized convective complex known as a "supercloud cluster" (SCC). The SCC constitutes the eastward-propagating convective envelope of the MJO (see Chapter 1 and Figure 1.4). Lau *et al.* (1991) find that substructures within the SCC possessed a hierarchy of spatial and temporal scales ranging from a few tens to hundreds and thousands of kilometers, with multiple periodicities from diurnal to 2–3 days and 10–15 days. Associated with SCC substructures are fluctuations of surface westerly winds over a variety of timescales over the Western and Central Pacific. Westerly wind

fluctuations and related twin cyclone activities belong to the phenomenon known as westerly wind bursts (Keen, 1982; Harrison, 1984). Lau *et al.* (1989) propose a unified dynamical framework for studying the mechanisms of SSC, MJO, twin cyclones, westerly wind bursts, and the ENSO, in terms of atmospheric moist dynamics and coupled air–sea interactions over the tropical oceans. Today, the term "westerly wind event" (WWE) is used to refer to a broad-spectrum TISV in surface westerly wind fluctuations from days to weeks over the western and central equatorial Pacific with no preferred periodicity. Discussions of the relationship that WWEs and sea surface temperature (SST) variations have with WWEs as a stochastic forcing of the tropical coupled ocean–atmosphere will follow in Sections 9.4 and 9.5.

9.3.4 Early modeling framework

During the early 1980s, simple coupled ocean–atmosphere models of El Niño began to appear (Lau, 1981; Zebiak, 1982; McCreary and Anderson, 1984; Gill, 1984). Cane and Zebiak (1985) and Zebiak and Cane (1987) pioneered the development of an intermediate model of El Niño coupling a dynamical ocean to a steady-state atmosphere, with convergence feedback. Lau and Shen (1988) and Hirst and Lau (1990) reason that, besides providing stochastic forcing, the MJO may fundamentally contribute to El Niño. They argue that to study the effect of MJOs and WWE forcings on the coupled system, it is necessary to include interactive moist convection in coupled models, as opposed to steady-state atmosphere or "slave-atmosphere" coupled models. For the atmosphere, they use the following shallow-water system:

$$U_t - \beta y V + D_m U = \theta_x \tag{9.1}$$

$$V_t + \beta y U + D_m V = \theta_y \tag{9.2}$$

$$\theta_t - c_a^2 (U_x + V_y) + D_T \theta = \lambda c_a^2 P \tag{9.3}$$

$$m q_o (U_x + V_y) = E - P \tag{9.4}$$

where the subscripts t, x, and y denote differentiation with respect to time and space; U and V are the zonal and meridional perturbation velocity of the lower atmosphere; and θ is the perturbation tropospheric potential temperature. Equation (9.3) is scaled by the factor gH_a/θ_a with H_a and θ_a representing the mean depth and mean potential temperature of the lower troposphere, respectively; c_a is the equivalent phase speed of the shallow-water system; and λ is a dimensional factor relating to the densities of air, water, heat capacity of air, and c_a. D_m and D_T represent the damping coefficients in momentum and temperature, respectively. The perturbation precipitation rate P is related to background moisture q_o, precipitation efficiency m, and surface evaporation E by (9.4). Lau and Shen (1988) use the following expression for evaporation:

$$E = -\alpha_a U + \alpha_o T \tag{9.5}$$

where T is the SST anomaly. The wind-coupling coefficient α_a is derived from a

linearized form of the bulk aerodynamic formula for surface momentum and is positive for mean easterlies and negative for mean westerlies. The SST-coupling coefficient α_o is always positive. Basic state moisture q_o is related to basic state SST through a standard formula relating saturation moisture to temperature. Equations (9.1–9.4) for the tropical atmosphere are coupled through surface latent heat and momentum fluxes to a similar system of equations for the tropical ocean (Hirst, 1986; Hirst and Lau, 1990):

$$u_t - \beta y v - h_x = \gamma U \tag{9.6}$$

$$v_t + \beta y u - h_y = \gamma V \tag{9.7}$$

$$h_t - c_o^2(u_x + v_y) = 0 \tag{9.8}$$

$$T_t + T_x^* u - K_T h + d_o T = 0 \tag{9.9}$$

where u and v are the eastward and northward perturbation currents; γ is the coefficient for wind stress; h is dynamic height perturbation of the upper ocean; c_o is the oceanic gravity wavespeed parameter; T^* is basic state SST of the ocean; K_T is a coefficient governing SST changes associated with thermocline depth variations; and d_o is thermal dissipation of the upper ocean.

Lau and Shen (1988) find that the presence of interactive moisture (i.e., condensation–convergence feedback in the tropical atmosphere) causes atmospheric motions to slow down through reduction of the effective moist static stability of the lower troposphere. This influence becomes increasingly strong as the saturated moisture content of the lower troposphere increases in warmer SSTs, especially when damping is weak. When atmospheric waves are slowed to timescales commensurate with tropical intraseasonal oscillations (TISOs), due to reduced moist static stability from the interaction between dynamics with moist convection, ocean–atmosphere coupling can destablize both TISO and low-frequency (interannual) modes. As a special solution for coupled Kelvin waves ($V = v = 0$) in equations (9.1–9.9), two basic unstable modes can be identified in the intermediate coupled moist atmosphere–ocean system (i.e., an advective mode and an upwelling mode) (see Figure 9.3). The advective mode stems from destabilization of atmospheric waves, identifiable as MJOs, by the air–sea interaction and east–west SST advection of anomalous zonal currents in the equatorial waveguide. This mode is characterized by eastward propagation with the region of deep convection found to the west of the anomalous SST maximum (Figure 9.3a). It slows down and becomes increasingly unstable over warmer background SST, due to enhanced condensation–convergence feedback. Lau and Shen suggested that this mode may be responsible for the initial growth of El Niño in 1982/1983. The upwelling mode arises from destabilization of oceanic Kelvin waves by air–sea interaction through oceanic upwelling and moisture convergence feedback in the atmosphere (Figure 9.3b). The upwelling mode corresponds to the unstable coupled mode for slave-atmosphere models of El Niño (Lau, 1981; Philander *et al.*, 1984; Cane and Zebiak, 1985; Hirst, 1986; and many others). This mode has no east–west displacement between SST and deep convection, and is stationary. The inclusion of evaporation–wind feedback in the presence of mean

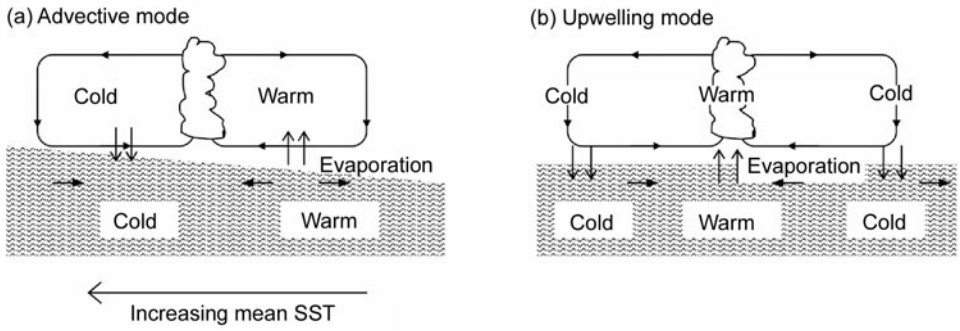

Figure 9.3. Schematic showing the structure of two unstable coupled ocean–atmosphere modes: (a) advective mode and (b) upwelling mode (from Lau and Shen, 1988).

surface easterly wind causes the upwelling mode to move eastward (Emanuel, 1988). Evaporation–wind feedback may have been operative during the amplifying stage of El Niño in 1982/1983. Hirst and Lau (1990) further analyze coupled modes, including contributions from Rossby waves, and confirm the importance of non-equilibrium atmospheric dynamics in the ocean–atmosphere interaction, which is capable of amplifying ISV of internal atmospheric origin through evaporation–wind feedback.

9.4 PHASE 2: THE EXPLORATORY STAGE

This stage is characterized by a large number of in-depth diagnostic and modeling studies in attempts to establish a long-term statistical and more physically based TISV–ENSO connection. Establishing a long-term statistical relationship between the MJO and the ENSO proved to be elusive. One indisputable feature is that the MJO and associated convection are strongly modulated by ENSO cycles. MJO wind signals extend eastward to the equatorial Eastern Pacific as the mean convection and warm water spread eastward along the equator during El Niño (Gill and Rasmusson, 1983; Lau and Chan, 1988; Weickmann, 1991; Schrage *et al.*, 1999). Yet, over the extreme Western Pacific and the Indian Ocean, there is no noticeable overall change in the amplitudes of MJO convection and wind activities during El Niño (Fink and Speth, 1997). A number of subsequent studies find that, statistically, the overall interannual variability (IAV) of MJO activity is not related to ENSO cycles (Hendon *et al.*, 1999; Slingo *et al.*, 1999; Waliser *et al.*, 2001). Some studies show that introducing TISV as white-noise forcings into intermediate coupled models do not significantly alter the model's El Niño response (Zebiak, 1989). In general, results from SST-forced atmospheric general circulation models suggest that reproducibility of IAV of the MJO was poor (Gualdi *et al.*, 1999; Slingo *et al.*, 1999). These results have often been taken to mean that the MJO and the ENSO do not interact in a substantial way.

It is important to note that MJO–ENSO interactions may also be dependent on the use of definitions of MJO activities. The most common method of defining an MJO is to decompose bandpassed (e.g., 20–70 days) OLR or wind fields (e.g., 200 mb velocity potential) into empirical orthogonal functions (EOFs). Typically, the first two eigenmodes that appear as a quadrature pair in both space and time can be interpreted as signals of coherent eastward propagation of the MJO. Compositing or regression analyses of the large-scale fields of wind, temperature, and moisture are then carried out with respect to an index of MJO activity from the first two principal components (Knutson and Weickman, 1987; Lau and Chan, 1988; Zhang and Hendon, 1997). Kessler (2001) suggests the use of the third EOF to capture signals over the Central Pacific where interaction between the MJO and the ENSO was likely to occur. In the following, we provide a description of MJO–ENSO interactions based on one of the aforementioned popular definitions. In Section 9.6, we introduce a new index specially designed to study MJO–ENSO interactions.

9.4.1 MJO and ENSO interactions

A sense of how the ENSO modulates the MJO as well as possible MJO–ENSO interactions can be gleaned from an EOF analysis of pentad (5-day running mean) OLR. The analysis is conducted separately for (i) normal, (ii) La Niña (cold), and (iii) El Niño (warm) states of the tropical Pacific, defined respectively as periods in which area-averaged monthly SST in the Niño 3 region (5°N–5°S; 150°W–90°W) (i) has an absolute value less than 0.5°C, (ii) is less than 0.5°C, and (iii) is greater than 0.5°C. The pentads are defined with respect to the climatological seasonal cycle at each gridpoint, which has been removed before EOF analysis. The spatial distributions of the dominant EOFs for the three categories, representing eastward-propagating components of the MJO, are shown in Figure 9.4. For normal (Figure 9.4a, b) and cold events (Figure 9.4c, d), these components are represented by the first two EOFs, which together explain up to 6.8% and 7.1% of total anomalous variance, respectively. For warm events (Figure 9.4e, f), the propagating modes are represented by the second and third EOFs, which together explain 6.4% of total variance. The first EOF for warm events, which will be described separately later, represents the MJO–ENSO interaction mode, which explains in its own right 6.1% of total anomalous variance.

For all three categories, a pair of east–west dipoles in anomalous convection associated with eastward-translating centers of action of the MJO from the Indian Ocean to the Central Pacific is quite clear. The spatial distributions of the dipoles are quite similar between the normal and cold states, except that the dipoles appear to be more compressed over the western Indo-Pacific region and weakened over the Central Pacific during cold events. These features are consistent with the westward extension of the cold tongue in the equatorial Eastern Pacific during La Niña. During warm events (Figure 9.4e, f), while still maintaining the dipole structure over the western Indo-Pacific, OLR anomalies expand eastward over the equatorial Eastern Pacific and the Atlantic, consistent with the spread of warm water over these

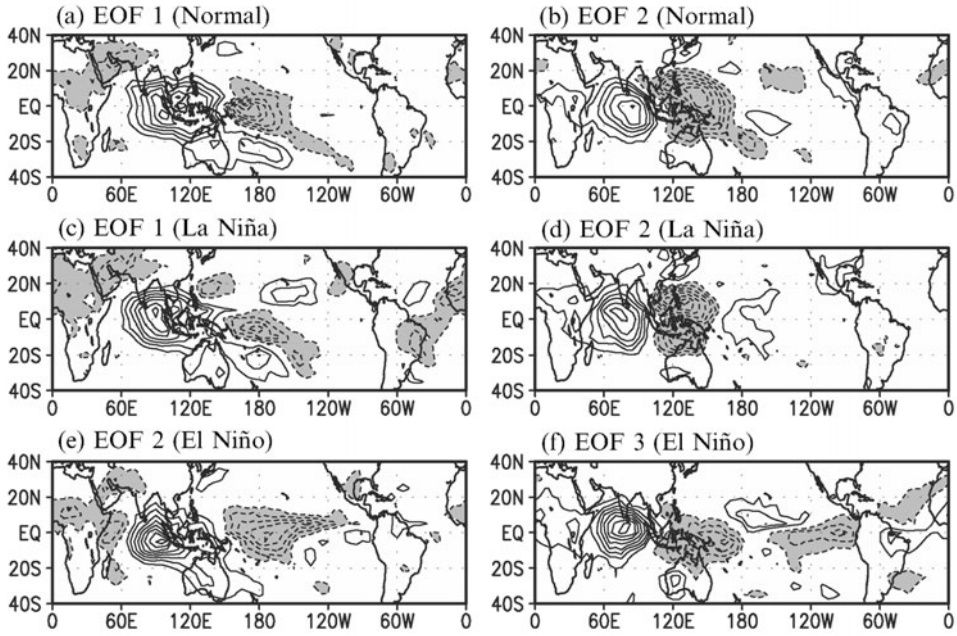

Figure 9.4. Spatial patterns of dominant EOFs of pentad OLR for (a, b) normal state, (c, d) La Niña state, and (e, f) El Niño state for the period 1979–1999. Units are non-dimensional.

regions. Also noticeable is an east–west dipole structure over the Indian Ocean (Figure 9.4e), not found in normal or cold states. However, there appears to be no noticeable difference in the magnitude of variance of the MJO signal over the Indo-Pacific region between normal, warm, and cold oceanic states, implying that the intensity of the MJO is somewhat independent of the interannual variation of SST. However, this does not imply that air–sea interactions are not important on MJO timescales. In fact, there is now increasing evidence from observations and modeling studies that the structure and propagation of MJOs are strongly modulated by air–sea interactions (Flatau *et al.*, 1997; Lau and Sui, 1997; Wang and Xie, 1998; Waliser *et al.*, 1999; Fu *et al.*, 2003).

Returning to the MJO–ENSO mode (first EOF mode) for warm events (Figure 9.5), we find that this mode has a pattern over the Central and Eastern Pacific similar to that found during the ENSO (Gill and Rasmusson, 1983). The MJO–ENSO mode is unique in the sense that it possesses both interannual and intraseasonal timescales. It is not found in normal or cold events and represents an extension of the MJO signal when the tropical Pacific is in its warm state. Strictly speaking, this mode should not be considered part of the intrinsic MJO mode, as it does not exist under normal or cold ocean states. The above description is in agreement with previous results indicating that the amplitude of MJO activity over the Indian Ocean and the Western Pacific is relatively independent of the state of the ocean. An alternate interpretation is that the MJO–ENSO connection does

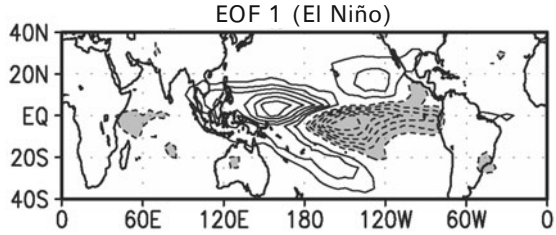

Figure 9.5. Same as in Figure 9.4, except for the spatial distribution of EOF 1 of pentad OLR, showing the mixed MJO–ENSO mode.

not occur all the time and, when it does, it is concentrated over the central and eastern tropical Pacific. Note that the percent variance explained by the propagating modes is relatively small (6–7%) compared with total pentad anomalous variance. This means that there are substantial portions of TISV variability not captured by eastward-propagating MJO signals, which may have to be included when considering possible TISV–ENSO interactions (see discussion in Section 9.6).

9.4.2 WWEs

Westerly wind anomalies in the Western and Central Pacific—regardless of whether they stem from an eastward-propagating MJO or from other sources such as Asian monsoons or cold air intrusion from the extratropics (Lau *et al.*, 1983; Yu and Reinecker, 1998)—are important agents for remote forcing of the ENSO. Hence, a more direct way of examining the TISV–ENSO connection is through the impact of WWEs on SST. WWEs are defined here as surface wind fluctuations in the Western and Central Pacific, between 110°E–170°W, within 15° latitude on either side of the equator. They can occur singly or in succession, typically with zonal wind anomalies spanning 30°–40° longitude, and lasting from 7 to 10 days (Luther *et al.*, 1983; Harrison, 1984; Luther and Harrison, 1984; Harrison and Giese, 1988; Harrison and Vecchi, 1997). As discussed in Section 9.3, some WWE signals may be associated with the hierarchical supercloud structure of the MJO. A large number of observations and modeling studies have shown that WWEs can induce downwelling oceanic Kelvin waves that propagate eastward along the equator, induce zonal SST advection, suppress upwelling along the equator, and possibly trigger the onset of El Niño (Harrison and Schopf, 1984; Harrison and Giese, 1988; Giese and Harrison, 1990; Kindle and Phoebus, 1995; Kessler *et al.*, 1996; Belamari *et al.*, 2003; and many others). Meyer *et al.* (1986) show that there was substantial cooling of the Western Pacific Ocean induced by WWEs during El Niño in 1982/1983. Kessler and Kleeman (2000) suggest that cooling of the Western Pacific associated with MJO passage can alter east–west SST and hence pressure gradients across the entire Pacific, thus providing a rectifying effect on the ENSO (see also Chapter 6).

Vecchi and Harrison (2000) conduct a comprehensive study of the relationship between WWEs and SST variation. They find, in the absence of WWEs, that SST

perturbations in the equatorial Central and Eastern Pacific tend to relax back to climatology. While WWEs west of the dateline lead to local surface cooling in the Western Pacific (Meyer *et al.*, 1986), those east of the dateline spawn warming in the equatorial waveguide when the ocean is in a normal state. When the Pacific Ocean is in a warm state, equatorial WWEs may be important in sustaining warming of the equatorial Eastern Pacific. Figure 9.6 shows composites of initial SST anomalies (SSTAs) and changes in SSTAs at 20-day intervals, before and after WWEs over the western Central Pacific, during normal and warm states of the ocean, respectively. The changes in SSTAs are with respect to initial SSTAs. In the normal state, 20 days prior to strong WWEs (Figure 9.6a), SST is above normal in the Central Pacific and below normal in the Western Pacific in large areas of the tropics and extratropics. The most pronounced features are the warming that develops over the southeastern Pacific and the equatorial waveguide starting from day 10 to day 20 (Figure 9.6c). The warming spreads to the coast of South America by day 80 (Figure 9.6f) and reaches an amplitude of 1.0°C to 1.5°C. WWEs produce local cooling in the Western Pacific ranging between 0.25°C and 0.5°C. In the warm state, changes in SSTAs subsequent to WWEs are relatively small compared with the normal state. WWE-induced local cooling is found over the Western Pacific from day 0 to day 20 (Figure 9.6e). Enhanced warming in the waveguide region and cooling in the southeastern Pacific are found to start on day 20, but all induced SST changes are less than 0.25°C. Hence, the impact of WWEs appears to be strongly dependent on the ambient state of the ocean–atmosphere system. The above results suggest that WWEs may be instrumental in transitioning the tropical ocean–atmosphere from a normal to a warm state, by providing initial warming in the equatorial waveguide and then in the coastal region of South America. The result also illustrates the importance of initial warming of the Central Pacific, even in the normal category, suggesting that El Niño may already be underway in order for WWE wind forcing to be effective.

9.5 PHASE 3: ENSO CASE STUDIES

From the mid-1990s through to early 2000, there were many case studies of El Niño documenting the impact of WWEs and the excitation of oceanic Kelvin waves which were believed to have triggered the onset of El Niño (e.g., McPhaden *et al.*, 1988; Kindle and Phoebus, 1995; Kessler *et al.*, 1996; Yu and Reinecker, 1998; McPhaden, 1999; Kutsuwada and McPhaden, 2002). Nakazawa (2000) documents various atmospheric conditions associated with the MJO and tropical cyclone activities during El Niño in 1997/1998. Indeed, definitive observations of atmospheric MJO signals and oceanic Kelvin wave responses from satellites and TOGA–TAO moorings, prior to onset of El Niño in 1997/1998, re-invigorated the debate on the role of the MJO in possibly leading to abrupt onset and termination of ENSO cycles (McPhaden and Yu, 1999; Takayabu *et al.*, 1999).

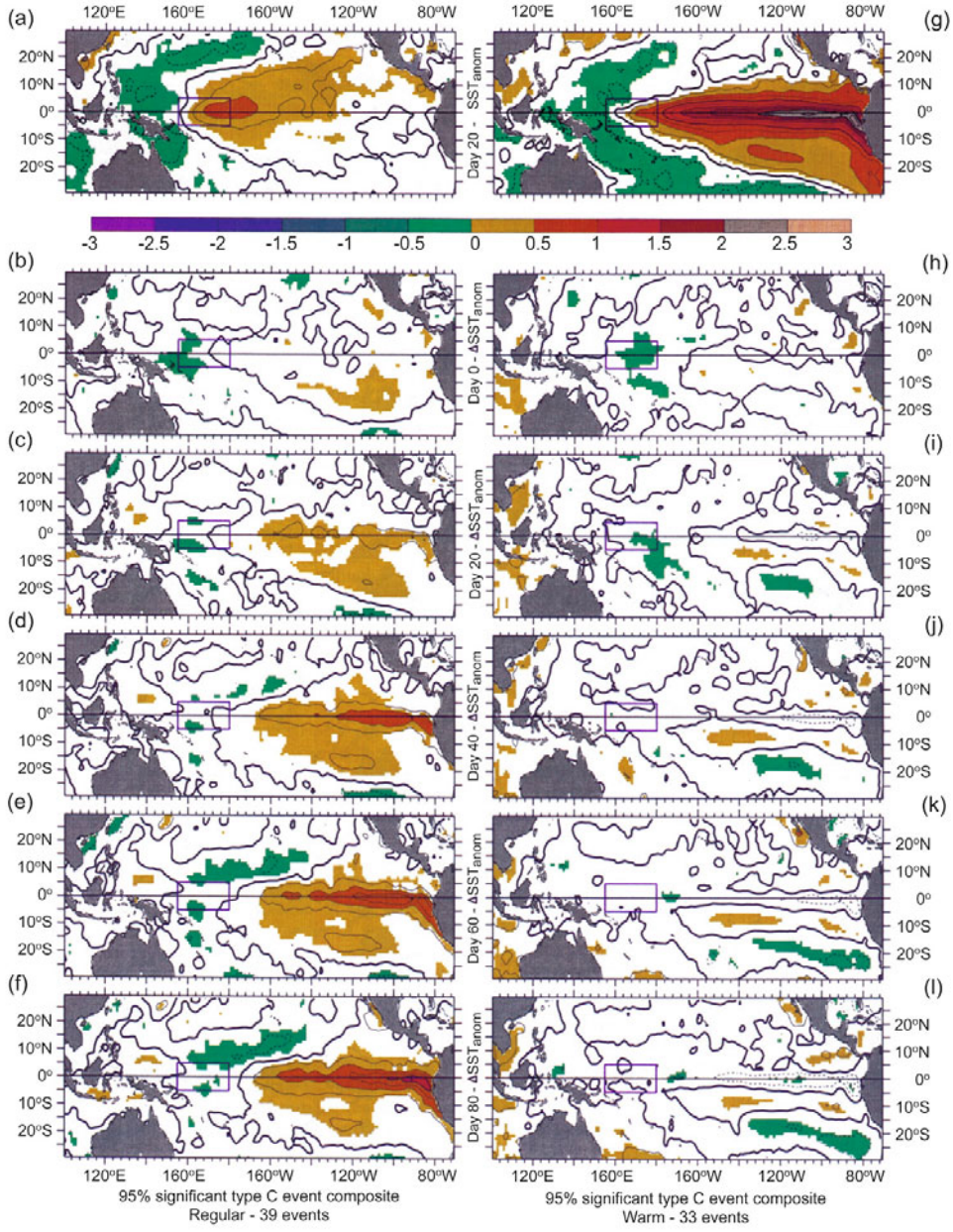

Figure 9.6. Composites of SSTA and changes in SSTA (ΔSSTA) from day −20 for a WWE in the western Central Pacific (shown as square rectangle) under normal conditions (left panels): (a) day −20, (b) day 0, (c) day 20, (d) day 40, (e) day 60, and (f) day 80. The same composites are shown in (g)–(l) except for warm ocean states. Values exceeding the 95% confidence level are color shaded. The contour interval is in 0.25°C. Shading contours are 0.5°C (adapted from Vecchi and Harrison, 2000).

9.5.1 El Niño of 1997/1998

El Niño of 1997/1998 was the strongest on record (McPhaden, 1999). It began in the spring of 1997 when SST in the Central and Eastern Pacific rose rapidly (Figure 9.7d) in conjunction with the appearance of extensive surface westerly wind anomalies signaling the collapse of the trade winds in the equatorial Central and Eastern Pacific (Figure 9.7b). El Niño was terminated even more abruptly than the onset in May 1998, with an unprecedented 8°C drop in SST in a 30-day period (Figure 9.7d). Almost a year prior to the onset, there were pronounced WWEs over the Indian Ocean and the Western Pacific (60°E–160°E), as well as a buildup of sea

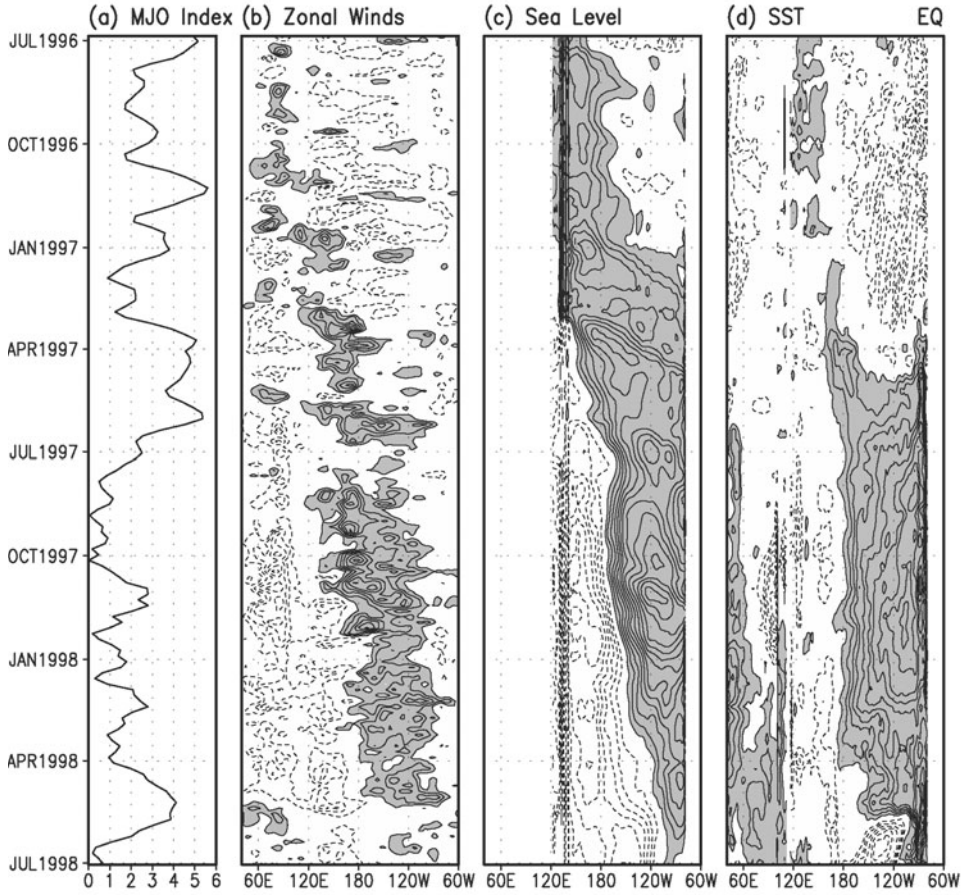

Figure 9.7. Spacetime evolution of oceanic–atmospheric variables associated with the onset and termination of El Niño in 1997/1998: (a) Time series of an MJO index (see Section 9.6), and equatorial time–longitude sections of anomalies spanning the Indian Ocean and the Pacific, (b) pentad 850 mb zonal wind ($m\,s^{-1}$), (c) weekly sea level height (cm), and (d) weekly SST (°C). Anomalies are defined for the period July 1996–July 1998. The contour interval for wind is $0.5\,m\,s^{-1}$, for the sea level it is in centimeters, and for SST it is 0.2°C.

level in the Western Pacific (Figure 9.7c). Increased WWEs prior to El Niño onset were also captured in an MJO index based on variability of the 850 mb stream-function (Figure 9.7a; see definition in Section 9.6). During this buildup phase, the Eastern Pacific cold tongue was well developed with noticeable signals of westward-propagating tropical instability waves in the equatorial Eastern Pacific (Figure 9.7d, see Chapter 6). In the Indo-Pacific region, three major MJO signals—occurring in October–November 1996, December–January 1997, and March–April 1997—can be identified in the 850 mb wind, propagating from the Indian Ocean to the Western and Central Pacific. Figure 9.7c clearly shows the Kelvin wave signal in sea level anomalies propagating across the entire Pacific to the coast of South America, excited by the last two MJOs in December–January and in March–April. Downwelling Kelvin waves led to rapid deepening of the thermocline and abrupt warming in the Eastern Pacific, caused by a combination of warm advection and cessation of upwelling (McPhaden, 1999). As shown in Figure 9.8 (left panels), warm water was already well developed in the Central Pacific below the surface in January 1997. The strong MJO/WWE forced the warm water to migrate eastward and upward to the Eastern Pacific, reaching the coast of South America in early March. By mid-April, the result of MJO wind forcing was to trigger a transition of the entire Pacific from the cold to the warm state. During the peak of El Niño in January 1998, easterly

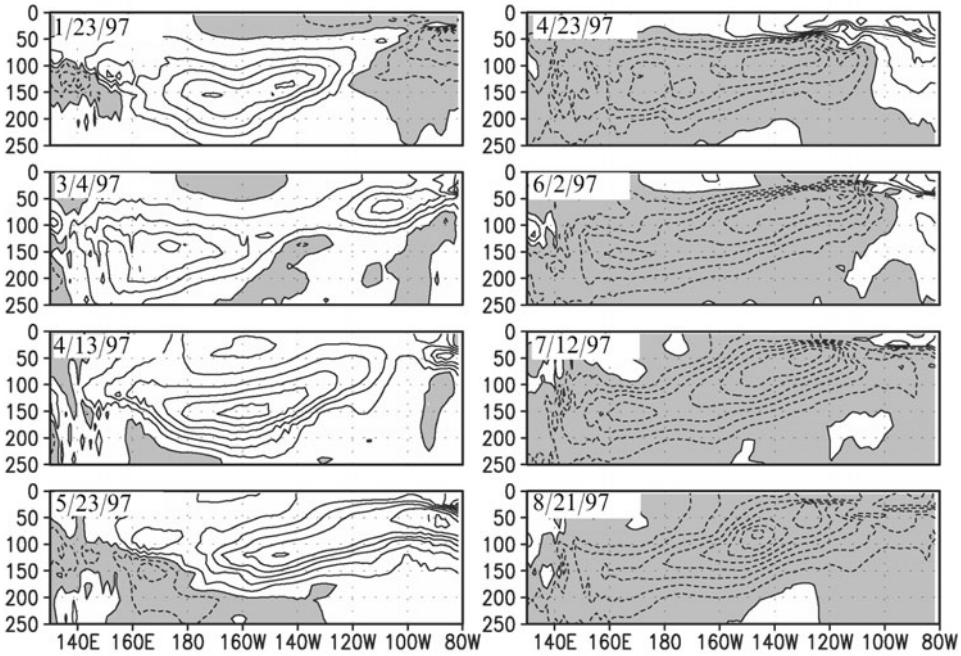

Figure 9.8. Depth–longitude cross-sections showing the evolution of water temperature during the onset (left panels) and termination (right panels) phases of El Niño in 1997/1998. The contour interval is 0.5°C (data from NCEP Ocean Data Assimilation, see Ji *et al.*, 1995).

wind anomalies emerged over the far Western Pacific, leading to thermocline shoaling, sea level depression, and development of cold subsurface water. Shoaling and cooling progressed steadily eastward and upward from April through June, as El Niño ran its course (Figure 9.8, right panels), in a manner similar to reversal of the onset phase. Termination of the 1997/1998 El Niño appeared to be pre-destined by the appearance of cold water below the surface over the Western and Central Pacific in the boreal spring of 1998, and was accomplished by rapid shoaling of the thermocline that first appeared in the open ocean of the eastern Pacific in May to June. From July to August, transition to La Niña was complete. Note that the MJO index showed a substantial drop in activity during El Niño (Figure 9.7a). However, it appears to increase in activity, due to an easterly impulse of the MJO, just prior to termination. Takayabu *et al.* (1999) suggest the easterly MJO impulse may have led to sudden shoaling of the thermocline, return of upwelling, and hence abrupt SST drop, terminating the 1997/1998 El Niño.

9.5.2 Stochastic forcings

Since the 1982/1983 El Niño, there have been great advances in our understanding of the nature of the ENSO, with the delayed oscillator as the linchpin of the modern theory of the ENSO (Suarez and Schopf, 1988; Battisti and Hirst, 1989). The theory of the ENSO is outside the scope of this chapter. For a review of ENSO dynamics, readers are referred to Latif *et al.* (1994) and Neelin *et al.* (1998). However, the delayed oscillator cannot explain the quasi-irregularity of ENSO cycles, their timing and relationship to ISV. Toward the latter part of the 1990s, the idea of stochastic forcing of the ENSO by TISV was gaining momentum (Penland and Sardeshmukh, 1995; Penland, 1996; Kleeman and Moore, 1997). Moore and Kleeman (1999) formulate a generalized dynamical framework to examine the spatial structure of noise forcing which is most effective in forcing ENSO variability in the coupled ocean–atmosphere system.

They propose the concept of a "stochastic optimal" defined as the most effective spatial structure that would give rise to the fastest growth of El Niño from stochastic forcings. Their results show that the spatial structure of the surface-heating functions and surface wind stress of the stochastic optimal from an intermediate coupled ocean–atmosphere model are similar to the east–west dipole structure in OLR and wind stress associated with the MJO (Lau and Chan, 1985, 1988; Hendon *et al.*, 1999). Experiments with various stochastic forcings due to single or multiple WWEs suggest that: (a) when forced by white noise, the onset of an ENSO-like large-amplitude perturbation is most favored when the forcing has the structure of the stochastic optimal—such optimal stochastic forcings can effectively trigger the ENSO or disrupt developing ENSO episodes; (b) the history of noise forcing and its integral effects are important in amplifying or restricting the growth of the ENSO mode in the coupled ocean–atmosphere system; and (c) the effectiveness of stochastic forcing is dependent on the phase of the seasonal cycle and the evolving state of the ocean and atmosphere.

These results are in agreement with observations that groups of MJOs and associated WWEs may have contributed to development of El Niño events, such as the 1997/1998 event. If stochastic forcings are not applied at the right phase of the seasonal cycle or the right phase of El Niño itself, their impact may be minimal. However, because the ENSO is an intrinsic mode in the tropical coupled ocean–atmosphere, El Niño and La Niña events may be generated even without WWE perturbations. These characteristics of forcings by the stochastic optimal are consistent with those originally proposed by Lau (1985a, b) and Lau and Chan (1986a, b, 1988).

9.6 PHASE 4: RECENT DEVELOPMENT

At present, the TISV–ENSO relationship is still a subject of debate. While better observations of oceanic Kelvin waves have certainly provided strong evidence of the importance of TISV, particularly the MJO, in triggering El Niño of 1997/1998, there are still many uncertainties in determining under what conditions the relationship will or will not hold (Bergman *et al.*, 2001). Zhang *et al.* (2001) propose an index for measuring Kelvin wave forcings by the wind stress associated with the MJO and find evidence that strong Kelvin wave forcing in the Western Pacific preceded greater SSTAs in the equatorial Pacific by 6–12 months during 1980–1999. However, no such evidence can be found for the period 1950–1979. While some studies show substantial impact of stochastic forcings (Penland and Sardeshmukh, 1995; Moore and Kleeman, 1999), others have suggested that power in the ISV range cannot be effectively channeled from subannual frequencies to the low frequencies associated with the ENSO, but rather more likely through reddening of the frequency spectrum through SST processes outside the tropics (Roulston and Neelin, 2000). Further progress in better understanding the MJO–ENSO connection is hampered by the inability of models to reproduce the realistic structure and statistics of MJOs (Slingo *et al.*, 1997; Sperber *et al.*, 1997; Maloney and Hartmann, 2000; Waliser *et al.*, 2003). For an assessment of the capability of models to simulate the MJO, readers are referred to Chapter 11.

Motivated by the need to assess the scientific controversy and to improve models of the MJO and the ENSO for climate prediction, an MJO–ENSO workshop was convened at the National Oceanic and Atmospheric Administration's (NOAA) Geophysical Fluid Dynamics Laboratory (GFDL) in Princeton, New Jersey, in March 2000. Over 70 scientists from 8 countries attended the workshop. During the workshop, scientists discussed a wide range of topics from the dynamics and air–sea interaction associated with MJOs, oceanic response to westerly wind bursts, stochastic forcings of ENSO, MJO predictability, regional manifestations of MJOs, and impacts on ENSO prediction skills (Zhang *et al.*, 2001). Workshop participants noted the lack of skill of state-of-the-art climate models to simulate the MJO/ISV and its possible interactions with the ENSO in coupled ocean–atmosphere models. They summarized the broad spectrum of opinions, into three competing hypotheses:

- *Hypothesis I.* ISV, as with other weather systems, provides a source of irregularity of the ENSO and limits ENSO predictability. ISV is no different from noise forcing (i.e., inherent chaotic behavior in the coupled system) and ISV is not required for ENSO prediction.
- *Hypothesis II.* The influence of ISV on the ENSO is unique and distinct from other weather systems. The timing and strength of an ENSO event may be sensitive to ISV forcing and alter the phase of ENSO cycles. The MJO/ISV is a necessary component of the coupled ocean–atmosphere system. A better understanding of the mechanisms involved in the MJO/ISV interaction should lead to improved prediction.
- *Hypothesis III.* Stochastic forcings of the MJO/ISV are essential for maintaining ENSO variability. This implies that the coupled ocean–atmosphere is damped and that ENSO prediction with long lead times will be extremely difficult since it is dependent only on stochastic forcings.

Further discussion of these hypotheses with regard to ENSO predictability will be presented in Section 9.7. Suffice it to point out here that there is not yet definitive observational evidence nor modeling studies to confirm or reject any one of the hypotheses. As noted in the workshop, the debate on the MJO–ENSO relationship is partly aggravated by the lack of clear statistical evidence of such a relationship.

One of the problems in previous studies of the MJO–ENSO relationship may have arisen from too great a focus on the MJO in one season, either boreal winter or summer, especially as MJO wind forcings are likely to be imposed on the ocean throughout the year. Oceanic Kelvin waves forced by the MJO are likely to be most effective when forcing is confined to the equatorial waveguide and symmetric with respect to the equator during the spring and fall, but less so during boreal winter or summer. Furthermore, the MJO has pronounced signals not only in the tropics, but also in the extratropics. Some studies suggest the possible forcing of the MJO from the extratropics (Lau *et al.*, 1983; Hsu, 1996). Hence, identifying the full spectrum of variability associated with the MJO—including all seasons, tropical and extratropical variability, and separating the modes of ISV with respect to SST forcings and responses—is essential in understanding the MJO–ENSO relationship.

9.6.1 A new ISO index

In this section, we re-examine the MJO–ENSO relationship, by identifying the dominant spacetime modes of ISOs in the tropics and extratropics and their possible separate roles in triggering or responding to the ENSO. Using 50 years of the U.S. National Center for Environmental Prediction (NCEP) wind reanalysis, we have computed the spacetime extended empirical orthogonal functions (EEOFs) of 20 to 70-day filtered 850 mb streamfunctions to identify the modes of ISV that predominate throughout the year. EEOF analysis, also known as multichannel singular decomposition (M-SSA), is a powerful technique for identifying temporal and spatial structures in large-scale geophysical fields. Oscillatory modes are represented as a pair of eigenvectors approximately in quadrature (Vautard and Ghil,

1989). The rotational component of wind in the lower atmosphere is used because it is closely linked not only to surface wind forcing in the tropics but also extratropical cyclone–anticyclone development, both of which may be linked to ENSO development. The first two EEOF modes describe an eastward circum-global propagating planetary pattern with equatorial surface wind buildup and propagation from the Indian Ocean to the Eastern Pacific, in tandem with the development of large-scale cyclonic and anticyclonic wind circulation patterns over the North and South Pacific (Figure 9.9, EEOF 1 only; see also Weickmann *et al.*, 1985). The pattern is only a part of the large-scale circulation variability within the 20 to 70-day window, which we shall refer to as the eastward-propagating mode (EPM). The third and fourth modes depict a quasi-stationary but oscillatory component associated with wave signals emanating from the Indo-Pacific region along the subtropical jetstreams of

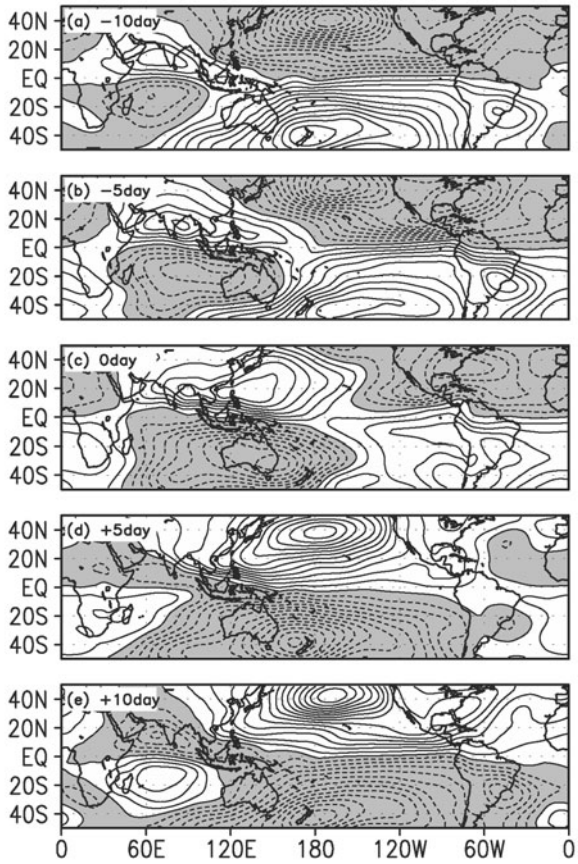

Figure 9.9. Spacetime structure of the first dominant EEOF mode of the 20 to 70-day bandpassed 850 mb streamfunction, representing the eastward-propagating component of the ISO: EEOF 1 for (a) −10 days, (b) −5 days, (c) center day, (d) +5 days, and (e) +10 days. The data period is 1956–1999. The unit is non-dimensional.

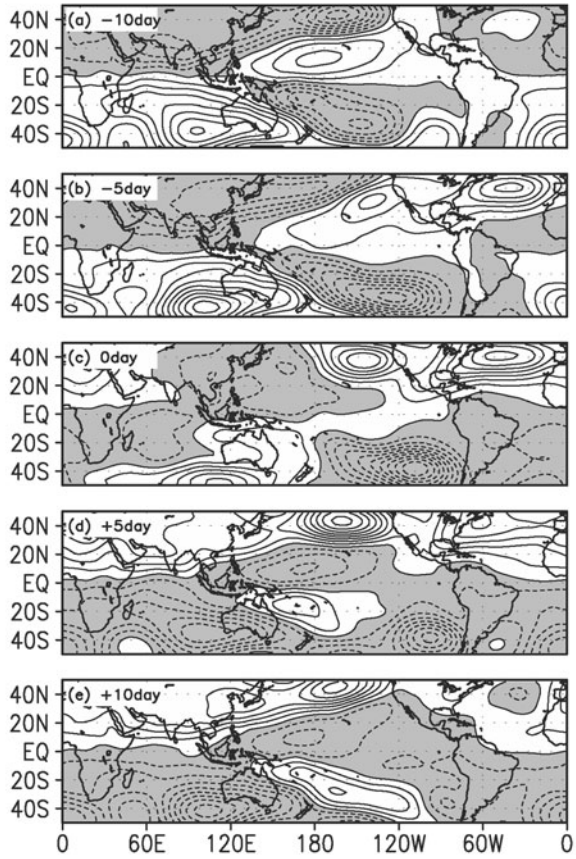

Figure 9.10. Same as Figure 9.9, except for the third EEOF mode, which represents the quasi-stationary component of the ISO signal.

East Asia and northern Australia, to the subtropics and extratropics of both hemispheres (Figure 9.10, EEOF 3 only). The centers of action appear to be anchored over the eastern South Indian Ocean, the eastern South Pacific, the North Atlantic, and the North Pacific. Hereafter, these modes will be referred to as the quasi-stationary mode (QSM). EEOF 2 and EEOF 4 (not shown) have spatial structures similar to but shifted approximately one quarter of a wavelength relative to EEOF 1 and EEOF 3, respectively.

Figure 9.11 compares the time series of a new ISO index, formed by the square root of the sum of the squares of the two principal components for the EPM (EEOF 1 and EEOF 2), with several commonly used indices of the MJO (Hendon *et al.*, 1999; Slingo *et al.*, 1999). It can be seen that the new index is significantly correlated with those derived using the 200 mb velocity potential and streamfunction (Figure 9.11c, d) as well as those using OLR (Figure 9.11e). Correlation with the 200 mb velocity potential index (Figure 9.11c) is highest and lowest using the zonal wind

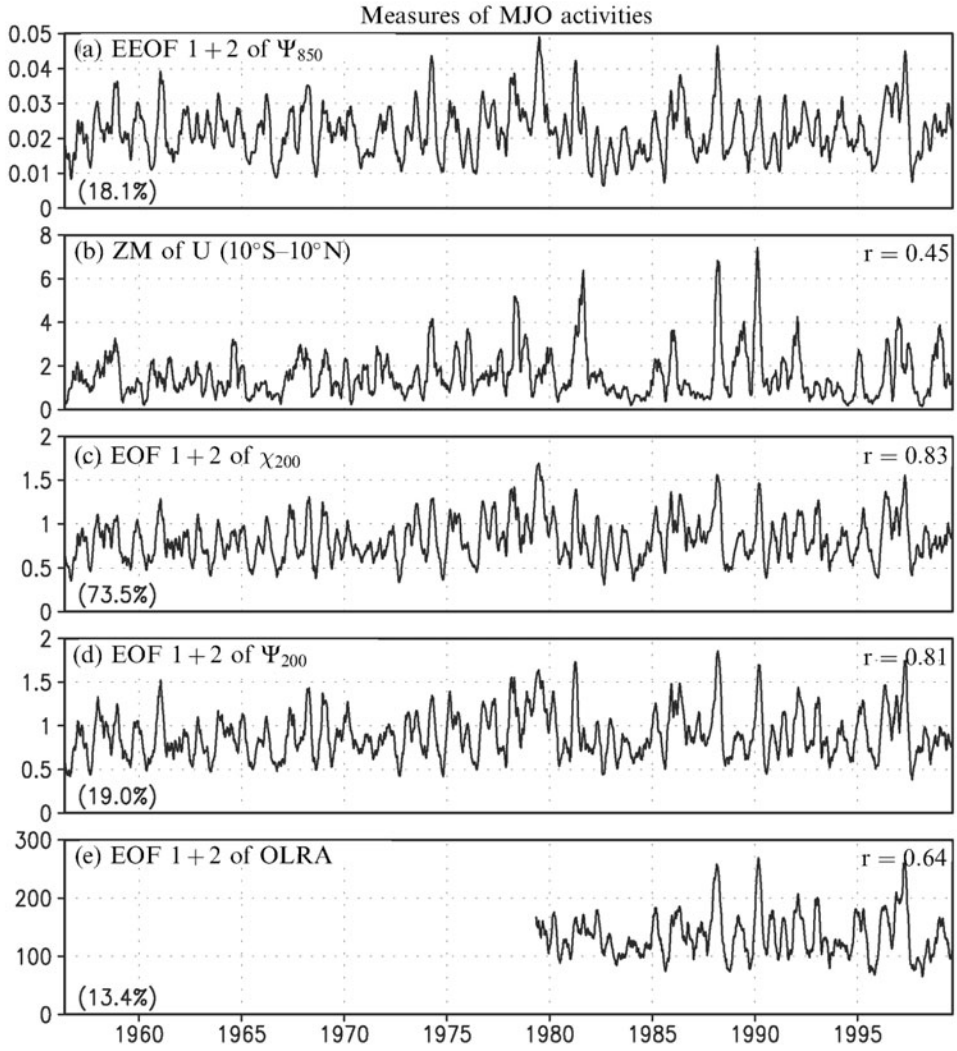

Figure 9.11. A comparison of time series of MJO indices: (a) the EPM index used in this chapter, (b) 20 to 70-day bandpassed zonal mean 200 mb zonal wind averaged from 10°S to 10°N, (c) an index derived from the first two EOFs of 200 mb velocity potential, (d) 200 mb streamfunction, and (e) OLR anomalies. Numbers in brackets denote variance explained by the first two dominant EOFs used for the index. Correlation coefficient (r) with the EPM index is shown on upper right-hand corner of each panel. The unit for zonal wind is m s^{-1}. All other indices have non-dimensional units.

index (Figure 9.11b). Because the velocity potential index is dominated by the first two EEOFs (>73% variance), it contains almost exclusively tropical signals associated with divergent wind components and deep convection. On the other hand, the new ISO index contains a much wider spectrum of variability including the effects of

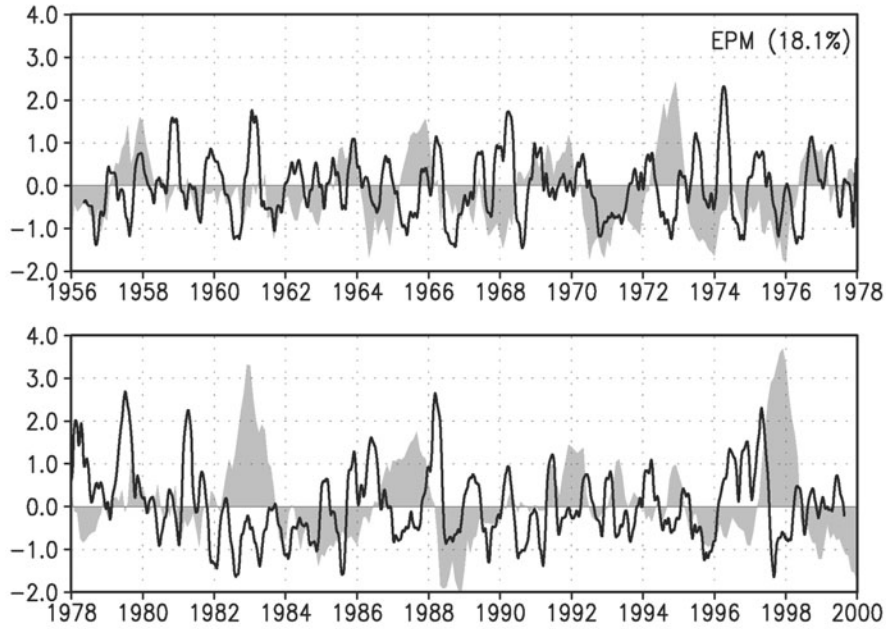

Figure 9.12. EPM activity index (see text for definition) shown as the solid line. Number in brackets shows percentage variance explained. Niño 3 SST anomaly shown as shaded plots. Units of SST are in °C.

rotational and divergent winds from the tropics and extratropics and, therefore, is a more inclusive index for describing ISO–ENSO relationships.

Two indices of ISO activities have been constructed based on 90-day window variances of the principal components of the first two EEOFs and of the third and the fourth EEOFs, respectively, for the EPM and QSM. Both modes show strong seasonality, with the EPM peaking in March–April and the QSM in January–February (not shown). Figure 9.12 shows the indices of EPM activity (EEOF 1 and EEOF 2) superimposed on the monthly time series of the Niño 3 SST anomaly. For most El Niño events (i.e., 1997/1998, 1987/1988, 1982/1983, 1972/1973, 1969/1970), there was an increase in EPM activity prior to the abrupt rise in Niño 3 SST, followed by a decrease in EPM activity when Niño 3 SST was substantially above normal. For 1982/1983, the relationship was not as strong, because the increased EPM occurred more than a year before the initial warming. Notably, there were El Niño events that were not clearly preceded by enhanced EPM (i.e., 1957/1958, 1976/1977, and the series of warm episodes in 1991–1995). Conversely, there were strong EPMs that were not followed by onset of major warm events. These features are in agreement with the impact of stochastic forcing of El Niño events by the MJO (see Section 9.5.2). Figure 9.13 shows the QSM index with Niño 3 SST. Here, with few exceptions, enhanced (reduced) QSM activity was found when Niño 3 SST was substantially above (below) normal. This feature can

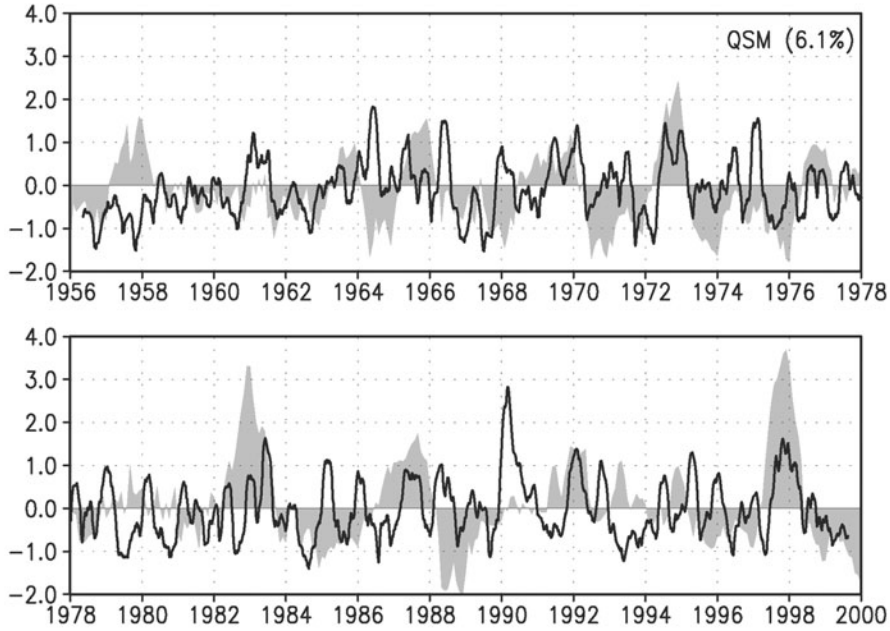

Figure 9.13. Same as Figure 9.12 except for QSM.

be clearly seen in all the major El Niño–La Niña events of 1997–2000, 1982–1985, and 1972–1974.

9.6.2 Composite events

Figure 9.14 shows a composite of EPM and QSM activities and Niño 3 SST for all past major El Niño events as a function of the calendar month centered on January during the peak of a warm event. Increased EPM activity from the previous fall through the antecedent spring is evident prior to onset of a warm event, which typically occurs in April–June. The most pronounced pulse of increased EPM occurs in April–May. As the warm event grows in June–July, the EPM abruptly drops off to a very low level in August–September and remains suppressed throughout the warm phase, only to recover during development of the cold phase in the following spring. In contrast to the EPM, the QSM is suppressed prior to and during the initial warming phase from the previous winter to late fall. QSM activity notably increases after the peak of Niño 3 SST is reached in December and remains enhanced for the rest of the winter through late spring, with a second peak in April. The QSM becomes suppressed during La Niña phase. Overall, there is a 3 to 6-month lag between the peak of Niño 3 SST and maximum activity in the QSM.

The ISO–ENSO relationships implied by Figure 9.14 are coherent across the Indo-Pacific, as is evident in Figures 9.15 and 9.16 which show the time–longitude sections of lagged covariance of the 850 mb zonal wind and SST anomalies with

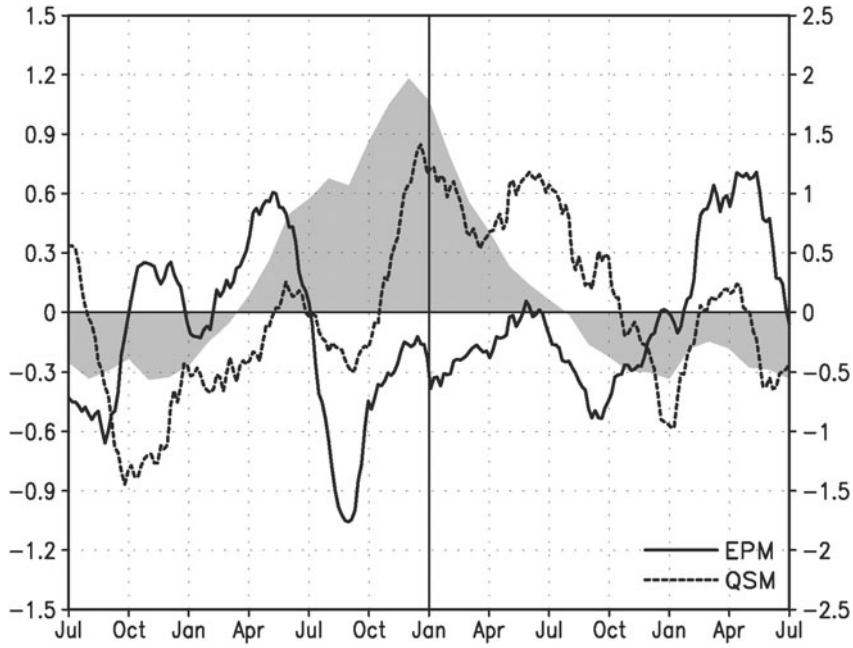

Figure 9.14. Composite of Niño 3 SST (shaded) superimposed on windowed variance of EPM (solid) and QSM (dashed), normalized by standard deviation.

reference to EPM and QSM, respectively. EPM maximum activity occurs at a time equal to zero ($T = 0$) when the Eastern Pacific is colder than normal (Figure 9.15b), with anomalous easterlies over the Central Pacific and anomalous westerlies over the Indian Ocean (Figure 9.15a). The wind anomalies propagate eastward to the Central Pacific about 12 months later and lead to a warm event in the Eastern Pacific (Figure 9.15b). Following the maximum EPM at $T = 0$, SST and wind structures exhibit well-defined alternating warm (cold) events coupled to 850 mb westerlies (easterlies) in the Central Pacific, occurring at approximately 12 to 14-month intervals. Before $T = -12$, the wind and SST structures are not very well organized. Temporal asymmetry suggests that enhanced EPM activities may be responsible for the excitation of warm and cold SSTAs, but not necessarily the converse. The timescale of SST oscillation shown in Figure 9.16b is quasi-biennial (i.e., 24–26 months) and not the dominant ENSO cycle timescale of 36–48 months. As evident in the relatively small regions with 95% statistical signifiance (indicated by the shaded area in Figure 9.16), the coherence in winds and SST variations with EPM on interannual timescales is not very high. This is consistent with the stochastic nature of the MJO–ENSO interaction, occurring only episodically, during a preferred phase in seasonal and ENSO cycles. Figure 9.16 shows that QSM variability is strongly linked to variation of the ENSO cycle. The maximum QSM signal is preceded—approximately 2–3 months earlier—by the development of a warm event manifested as an east–west wind dipole with surface westerlies over the Central Pacific, easterlies over the Indian

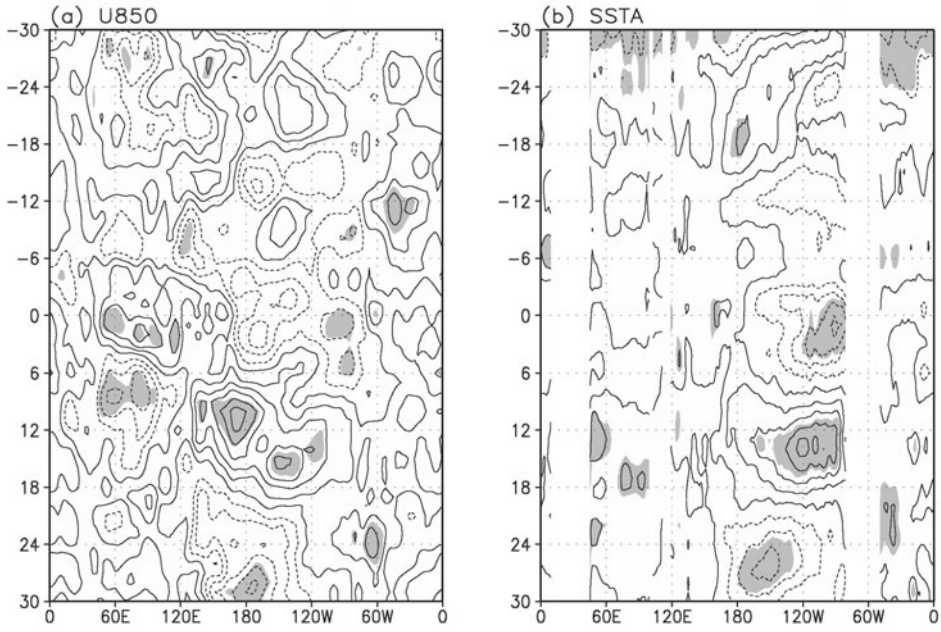

Figure 9.15. Time–longitude section across the Indo-Pacific Ocean along the equator of lagged covariance with reference to EPM activity: (a) 850 mb zonal wind anomalies and (b) SST anomalies. Values exceeding the 95% significance level are highlighted.

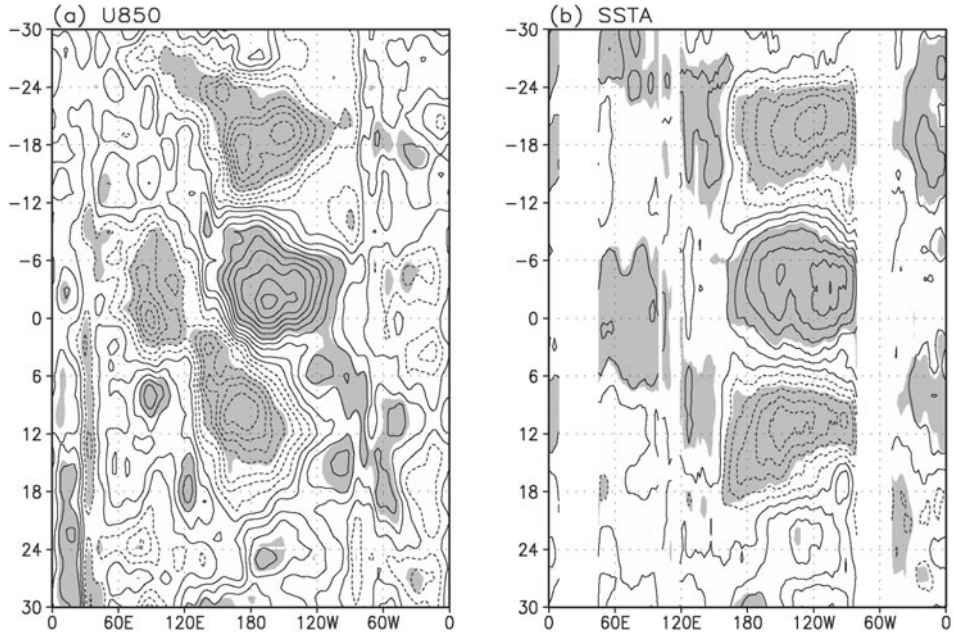

Figure 9.16. Same as Figure 9.15 except for the QSM.

Ocean (Figure 9.16a), and above-normal SST in the Eastern Pacific (Figure 9.16b). Each warm (cold) episode in the equatorial Eastern Pacific is coupled to westerly (easterly) wind anomalies over the Central Pacific, which can be traced to eastward wind propagation originating from the Indian Ocean. Clearly, the QSM component is associated with teleconnection signals transmitted from the tropics to the extratropics and is an integral part of the ENSO cycling process.

9.6.3 The ISV–ENSO biennial rhythm

Based on the new observational evidence, we present a new scenario of ISV–ENSO biennial cycle interaction (Figure 9.17). In this scenario, the tropical ocean–atmosphere system is considered to possess two climate states: one cold and one warm. In the absence of MJO/WWE forcing, transition to warm and cold states occurs at the basic ENSO time intervals of 4–5 years, as determined by the time

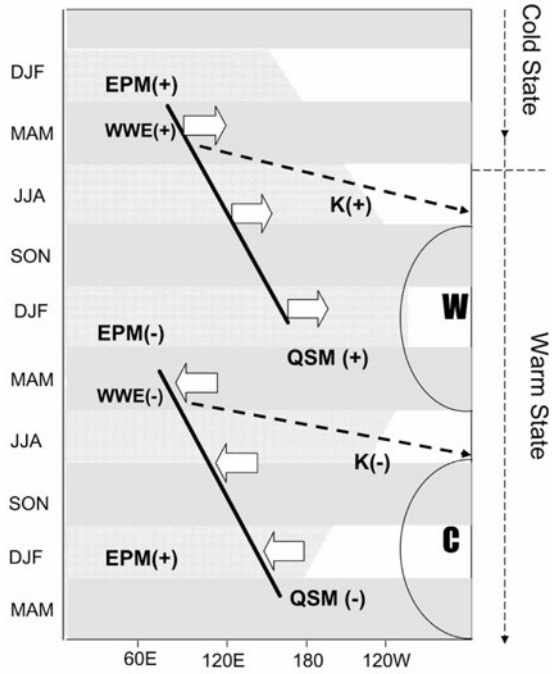

Figure 9.17. A schematic time–longitude section showing the interaction of EPM, QSM, and WWEs in setting up a biennial oscillation in the tropical ocean–atmosphere system along the equator. The phases of EPM and QSM are indicated by the positive and negative signs. The slanting thick solid lines indicate eastward migration of the center of ENSO–MJO activities, labeled as WWE(+) and WWE(−). The thick dashed lines denote propagation of downwelling oceanic Kelvin waves K(+) initiating the warm state (W) and upwelling oceanic Kelvin waves K(−) initiating the cold state (C). The region of anomalous westerly winds is indicated by the stippled background.

required for charge and discharge of heat content in the tropical ocean, with each state lasting for approximately 2 years (Wang *et al.*, 2003). Enhanced EPM activity denoted by EPM(+) in Figure 9.17 and associated westerly wind forcings denoted by WWE(+) in boreal spring may induce oceanic downwelling Kelvin waves denoted by K(+), initiating rapid warming of the equatorial waveguide and the coastal region of South America. If EPM(+) occurs when the ocean is preconditioned for a warm event (i.e., heat content is already accumulating in the tropical Pacific Ocean)—as indicated by the transition from a cold to warm state in Figure 9.17—the EPM wind will accelerate the coupled air–sea interaction, advance the timing and amplify the warming process, and increase the likelihood of a full-blown warm event (**W**). As the warm event (**W**) develops, the region of surface westerlies expands eastward with enhanced convection over the equatorial Eastern Pacific and suppressed convection over the Western Pacific (see also Figure 9.5). During this phase, the excess oceanic heat content accumulated during the previous 9–12 months will be transported from the tropics to the extratropics, as manifested in part by increased QSM(+) activity following the peak of the warm event. In the Indo-Pacific monsoon region (60°E–120°E), subsidence associated with suppressed convection will induce over the eastern Indian Ocean anomalous surface easterly events denoted by EPM(−), which propagate eastward to the Western and Central Pacific as a coupled system. The ISV easterly wind anomalies denoted by WWE(−) embedded within the EPM(−) will drive upwelling Kelvin waves K(−) along the equatorial waveguide, arrest the Eastern Pacific warming, and initiate a cold event (C). Subsequently, similar interactions, but with opposite signs to the warm event, take place. Hence, a consequence of the MJO–ENSO interaction is production of a pronounced biennial tendency for the ENSO cycle. However, it is unlikely that the biennial rhythm will continue for more than two half-cycles, because if the biennial tendency reinforces the quasi-4-year basic ENSO cycle in the first half-cycle (W), the second half-cycle (C) will oppose it. Thus, the MJO–ENSO interacting with the seasonal cycle may sow the seeds of its own destruction, through suppression and enhancement of westerly wind forcing in the western Indo-Pacific monsoon region. The scenario proposed here is consistent with the results of recent model studies which stressed the importance of Western Pacific wind forcing in generating the biennial tendency in the ENSO cycle (Weisberg and Wang, 1997; Kim and Lau, 2001).

9.7 TISV AND PREDICTABILITY

This chapter would not be complete without a discussion of the relationship between TISV and ENSO predictability. While MJO/WWE signals undoubtedly provide useful information, which can be harnessed to improve ENSO prediction, it is clear from previous discussions in this chapter that TISV is also a source of climate noise, limiting the potential predictability of the climate system on interannual and longer timescales. It has been suggested that a useful analogy of TISV–ENSO coupling is that of a slightly damped oscillator subject to both external periodic forcing (the annual cycle), internal dynamics (ENSO mode), and

random noise forcings (TISV) (Lau, 1985a; Fedorov *et al*., 2003). Noise forcing renders the oscillation irregular. In the absence of such random forcings, the ENSO would be perfectly predictable. However, for ENSO, the response of the system to noise forcing is sensitive to the phase of the annual cycle and the ENSO cycle itself. During boreal spring, the MJO and related WWEs are confined to the proximity of the equator and are therefore more effective, compared with other seasons, in driving Kelvin waves along the equatorial waveguide, triggering the onset of El Niño.

The impact of stochastic forcing in limiting the potential predictability of the ENSO has been investigated by many authors. Eckert and Latif (1997) find that the effectiveness of ISV noise forcing typically leads to loss of predictability before a cycle period has elapsed. Moore and Kleeman (1998) show that ISV forcing associated with statistical optimals in a coupled system can be used to mimic the presence of initial condition errors and high-frequency stochastic noise to provide a measure of reliability and skill in ensemble forecasts. Blanke *et al*. (1997) find that periodic states in a seasonally varying coupled ocean–atmosphere model can be modified by WWE forcings to produce irregular behavior as well as strong phase locking to subharmonics of the annual cycle, in particular the biennial tendency. Broadening of model ENSO spectral peaks by noise forcing provides a much richer spatial and temporal pattern consistent with observations.

More recently, Fedorov *et al*. (2003) provide an insightful analysis of the predictability of ENSO and ISV forcings, which is re-captured in the following. Figure 9.18 shows the possible responses of coupled ocean–atmosphere states to an initial burst of a WWE in the coupled system of Neelin (1990), depending on whether the model ENSO state is: (a) damped; (b) has periodic oscillations that are affected by ISV; or (c) exhibits chaotic behavior. These situations correspond to hypotheses III, II, and I discussed in the previous subsection. It is argued that if the ENSO state is damped (hypothesis III), then the ENSO can only be generated by WWE stochastic forcings. But, hypothesis III does not explain why some El Niño events are generated by WWEs and others are not, and why there is a quasi-periodic 4 to 5-year ENSO cycle. On the other hand, if the system is chaotic (hypothesis I), like that shown in Figure 9.18c, the role of ISV forcing is irrelevant, because it is just like any other noise component, including those generated by the chaotic behavior inherent in the coupled system. Under this hypothesis, predictability is limited and ISV plays no unique role. Figure 9.18b may well describe a system which is quasi-periodic, but also responds to MJO/WWE forcings in ways that are dependent on the phase of the annual cycle and the phase of the ENSO cycle itself (hypothesis II). This scenario is the most consistent with observations so far. In fact, the variation of SST here is similar to those portrayed in Figure 9.16, following strong activity in MJO/WWE events. It is likely that predictability of the ENSO depends on the interplay of two sets of phenomena: a low-frequency signal that governs the timescale of ENSO cycles (years) and a high-frequency component that readjusts the actual time of onset and amplitude of the event in a statistical sense. Readjustment could sometimes be amplified to substantially accelerate onset time or to abort an ongoing warming event. For this reason, dynamical ENSO forecasts should be

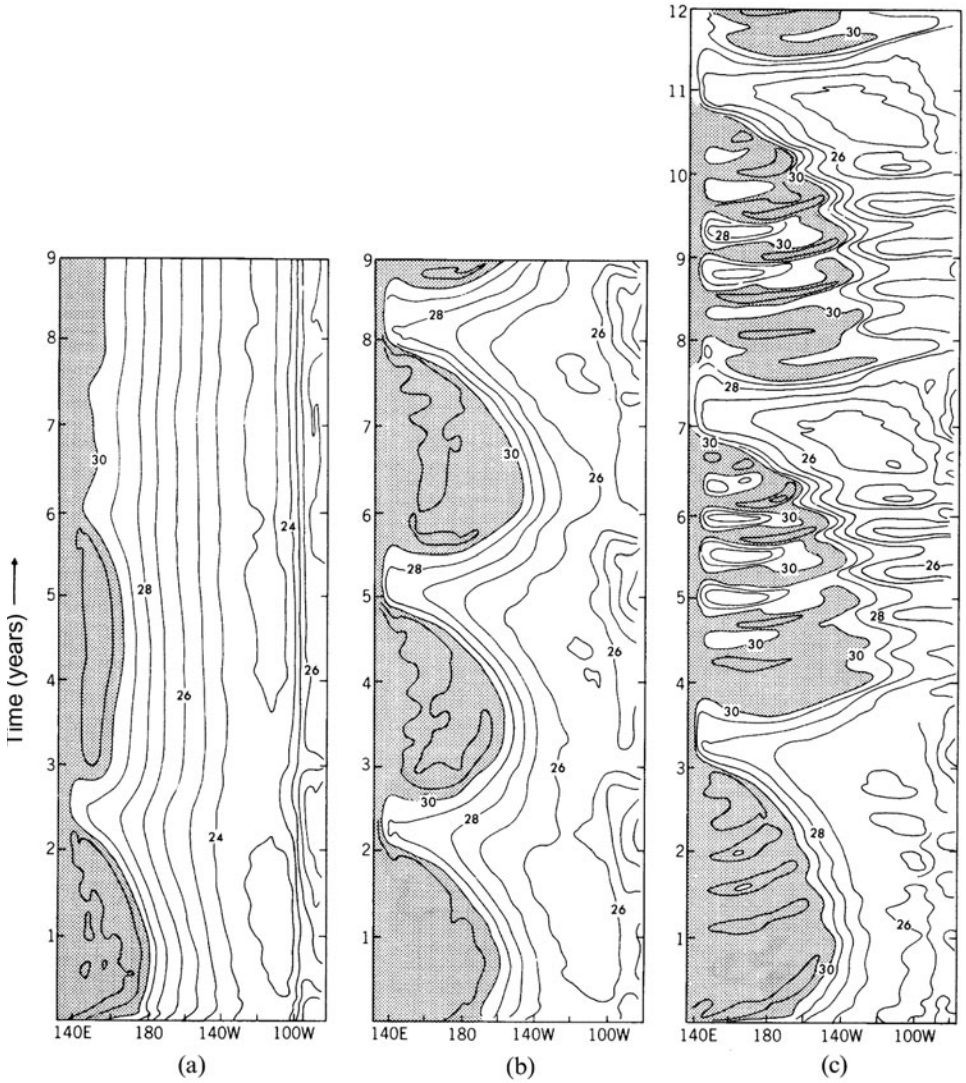

Figure 9.18. Time–longitude section along the equator, showing the evolution of SST (°C) in response to a westerly wind burst imposed at $T = 0$ in a coupled model, which (a) is damped, (b) has periodic oscillations, and (c) exhibits chaotic behavior (from Fedorov *et al.*, 2003).

probabilistic, with large ensembles, so that the shift in probability distribution functions, with respect to wind and convection fluctuations in the Indo-Pacific region, can be detected. There is now increasing observational evidence that ENSO predictions can benefit from inclusion of realistic MJO/ISV precursory signals in the Indo-Pacific region, in addition to those that describe the slowly evolving ocean–atmosphere states such as sea level, SST, and heat content (Kessler and Kleeman, 2000).

Curtis *et al*. (2002) find enhanced precipitation and wind gradients in the east equatorial Indian Ocean associated with MJO fluctuation, 3–9 months preceding the five strongest El Niño events since 1979 (1982/1983, 1986/1987, 1991/1992, 1994/1995, and 1997/1998). They successfully predicted the development of the 2001–2002 El Niño using a thresholding technique with an index based on MJO signals. Clarke and Van Gorder (2003) show that updating the most current spacetime information on Indo-Pacific winds and equatorial Pacific upper-ocean heat content associated with the MJO/WWE can lead to improved empirical forecasts of El Niño. Zhang and Gottschalck (2002) find a lead signal of 6–12 months before major El Niño onset in a wind stress index in the equatorial Pacific related to oceanic Kelvin wave forcing associated with the MJO. To improve dynamical prediction, the challenging tasks are to harness these observational precursory signals by including realistic representations of ocean–atmosphere coupling across the whole spectrum of spatial and temporal scales from intraseaonal to interannual and by including accurate initial conditions for the ocean–atmosphere states associated with the MJO/WWEs to carry out probabilistic forecasts using ensemble methods.

9.8 ACKNOWLEDGMENTS

This work was supported by the NASA Global Modeling and Analysis Program, the TRMM Project of the NASA Earth Science Enterprise. Dr. K. M. Kim provided valuable literature search and programming support.

9.9 REFERENCES

Battisti, D. S. and A. C. Hirst (1989) Interannual variability in a tropical atmosphere–ocean model: Influences of the basic state, ocean geometry and nonlinearity. *J. Atmos. Sci*., **46**, 1687–1712.

Belamari, S., J. Redelsperger, and M. Pontaud (2003) Dynamic role of a westerly wind burst in triggering equatorial Pacific warm event. *J. Climate*, **16**, 1869–1890.

Bergman, J. W., H. H. Hendon, and K. M. Weickmann (2001) Intraseasonal air–sea interaction at the onset of El Niño. *J. Climate*, **14**, 1702–1719.

Blanke, B., J. D. Neelin, and D. Gutzler (1997) Estimating the effect of stochastic wind stress forcing on ENSO irregularity. *J. Climate*, **10**, 1473–1486.

Cane, M. (1983) Oceanographic events during El Niño. *Science*, **222**, 1189–1195.

Cane, M. A. and S. E. Zebiak (1985) A theory of El Niño and the Southern Oscillation. *Science*, **228**, 1085–1087.

Chang, C. P and K. M. Lau (1980) Northeasterly cold surges and near-equatorial disturbances over the winter MONEX area during December, Part II: Large-scale aspects. *Mon. Wea. Rev*., **108**, 298–312.

Chang, C. P. and H. Lim (1988) Kelvin wave CISK: A plausible mechanism for the 30–50 day oscillation. *J. Atmos. Sci*., **45**, 1709–1720.

Clarke, A. J. and S. Van Gorder (2003) Improving El Niño prediction using a space–time integration of Indo-Pacific winds and equatorial Pacific upper ocean heat content. *Geophys. Res. Lett.*, **30**(7), 1399, doi: 10.1029/2002GL-16673.

Curtis, S., G. J. Huffman, and R. F. Adler (2002) Precipitation anomalies in the tropical Indian Ocean and their relationship to initiation of El Niño. *Geophys. Res. Lett.*, **29**(10), 1441.

Eckert, C. and M. Latif (1997) Predictability of a stochastically forced hybrid coupled model of El Niño. *J. Climate*, **10**, 1488–1504.

Emanuel, K. (1988) An air–sea interaction model of intraseasonal oscillations in the tropics. *J. Atmos. Sci.*, **44**, 2324–2340.

Fedorov, A. V., S. L. Harper, S. G. Philander, B. Winter, and A. Wittenberg (2003) How predictable is El Niño? *Bull. Amer. Meteorol. Society*, **84**, 911–919.

Fink, A. and P. Speth (1997) Some potential forcing mechanisms of the year-to-year variability of the tropical convection and its intraseasonal (25–70 day) variability. *Int. J. Climatol.*, **17**, 1513–1534.

Flatau, M., P. J. Flatau, P. Phoebus, and P. P. Niiler (1997) The feedback between equatorial convection and local radiative and evaporative processses: The implications for intraseasonal oscillations. *J. Atmos. Sci.*, **54**, 2373–2386.

Fu, X., B. Wang, T. Li, and J. McCreary (2003) Coupling between northward propagating boreal summer ISO and Indian Ocean SST revealed in an atmosphere–ocean coupled model. *J. Atmos. Sci.*, **60**, 1733–1753.

Giese, B. S. and D. E. Harrison (1990) Aspects of Kelvin wave response to episodic wind forcing. *J. Geophys. Res.*, **95**(C5), 7289–7312.

Gill, A. E. (1984) Elements of coupled ocean–atmosphere models for the tropics. In: J. C. J. Nihoul (Ed.), *Coupled Ocean Atmosphere Models* (Elsevier Oceanography Series 40). Elsevier, Amsterdam, 767 pp.

Gill, A. and E. M. Rasmusson (1983) The 1982/83 climate anomaly in the equatorial Pacific. *Nature*, **306**, 229–234.

Gruber, A. and A. F. Krueger (1984) The status of the NOAA outgoing longwave radiation data set. *Bull. Amer. Meteorol. Society*, **65**, 958–962.

Gualdi, S., A. Navarra, and G. Tinarelli (1999) The interannual variability of the Madden–Julian Oscillation in an ensemble of GCM simulations. *Climate Dynamics*, **15**, 643–658.

Harrison, D. E. (1984) On the appearance of sustained equatorial westerlies during the 1982 Pacific warm event. *Science*, **225**, 1099–1102.

Harrison, D. E. and B. S. Giese (1988) Remote westerly wind forcing of the eastern equatorial Pacific: Some model results. *Geophys. Res. Lett.*, **15**, 804–807.

Harrison, D. E. and P. Schopf (1984) Kelvin-wave induced anomalous advection and the onset of surface warming in El Niño events. *Mon. Wea. Rev.*, **112**, 923–933.

Harrison, D. E. and G. A. Vecchi (1997) Westerly wind events in the tropical Pacific: 1986–95. *J. Climate*, **10**, 3131–3156.

Hayashi, Y. Y. and A. Sumi (1986) The 30–60 day oscillations simulated in an aqua-planet model. *J. Meteorol. Soc. Japan*, **64**, 451–467.

Hendon, H. H. (1988) A simple model of the 40–50 day oscillation. *J. Atmos. Sci.*, **45**, 569–584.

Hendon, H. H., B. Liebmann, and J. D. Glick (1998) Oceanic Kelvin waves and the Madden–Julian Oscillation. *J. Atmos. Sci.*, **55**, 88–101.

Hendon, H. H., C. Zhang, and J. D. Glick (1999) Interannual variation of the Madden–Julian Oscillation during austral summer. *J. Climate*, **12**, 2538–2550.

Hirst, A. C. (1986) Unstable and damped equatorial modes in simple coupled ocean–atmosphere models. *J. Atmos. Sci.*, **43**, 606–630.

Hirst, A. and K. M. Lau (1990) Intraseasonal and interannual variability in coupled ocean–atmosphere models. *J. Climate*, **3**, 713–725.

Hsu, H. H. (1996) A global view of intraseasonal oscillation during northern winter. *J. Climate*, **9**, 2396–2406.

Ji, M. A., A. Leetmaa, and J. Derber (1995) An ocean analysis system for seasonal to interannual climate study. *Mon. Wea. Rev.*, **123**, 460–481.

Kalnay, E., M. Halem, and W. E. Baker (1981) The FGGE observing system during SOP-2. *Bull. Amer. Meteorol. Society*, **62**, 897–898.

Keen, R. A. (1982) The role of cross-equatorial cyclone pairs in the Southern Oscillation. *Mon. Wea. Rev.*, **110**, 1405–1416.

Kessler, W. S. (2001) EOF representations of the Madden–Julian Oscillation and its connection with ENSO. *J. Climate*, **14**, 3055–3061.

Kessler, W. S. and R. Kleeman (2000) Rectification of the Madden–Julian Oscillation into the ENSO cycle. *J. Climate*, **13**, 3560–3575.

Kessler, W. S., M. J. McPhaden, and K. M. Weickmann (1996) Forcing of intraseasonal Kelvin waves in the equatorial Pacific. *J. Geophys. Res.*, **100**, 10613–10631.

Kim, K. M. and K. M. Lau (2001) Monsoon induced biennial variability in ENSO. *Geophys. Res. Lett.*, **28**, 315–318.

Kindle, J. C. and P. A. Phoebus (1995) The ocean response to operational wind bursts during the 1991–1992 El Niño. *J. Geophys. Res.*, **100**(C3), 4803–4920.

Kleeman, R. and A. M. Moore (1997) A theory for the limitations of ENSO predictability due to stochastic atmospheric transients. *J. Atmos. Sci.*, **54**, 753–767.

Knutson, T. R. and K. M. Weickmann (1987) 30–60 day atmospheric oscillation: Composite cycles of convection and circulation anomalies. *Mon. Wea. Rev.*, **115**, 1407–1436.

Krishnamurti, T. N. and D. Subramanyan (1983) The 30–50 day mode at 850 mb during MONEX. *J. Atmos. Sci.*, **39**, 2088–2095.

Krishnamurti, T. N., P. K. Jayakumar, J. Shen, N. Surgi, and A. Kumar (1985) Divergent circulation on the 30–50 day time scale. *J. Atmos. Sci.*, **42**, 364–374.

Krishnamurti, T. N., D. K. Oosterhof, and A. V Mehta (1988) Air–sea interaction on the time scale of 30–60 days. *J. Atmos. Sci.*, **45**, 1304–1322.

Kutsuwada, K. and M. McPhaden (2002) Intraseasonal variations in the upper equatorial Pacific Ocean prior to and during the 1997–98 El Niño. *J. Phys. Oceanogr.*, **32**, 1133–1149.

Latif, M., T. P. Barnett, M. A. Cane, M. Flugel, N. E. Graham, H. Von Storch, J. S. Xu, and S. E. Zebiak (1994) A review of ENSO prediction studies. *Climate Dynamics*, **9**, 167–179.

Lau, K. M. (1981) Oscillations in a simple equatorial climate system. *J. Atmos. Sci.*, **38**, 248–261.

Lau, K. M. (1985a) Elements of a stochastic–dynamical theory of the long-term variability of the El Niño/Southern Oscillation. *J. Atmos. Sci.*, **42**, 1552–1558.

Lau, K. M. (1985b) Subseasonal scale oscillations, bimodal climate state and the El Niño/Southern Oscillation. In: J. C. J. Nihoul (Ed.), *Coupled Atmosphere–Ocean Models* (Elsevier Oceanographic Series 40). Elsevier, Amsterdam, 767 pp.

Lau, K. M. and P. H. Chan (1983a) Short-term climate variability and atmospheric teleconnection as inferred from satellite derived outgoing longwave radiation, Part I: Simultaneous correlations. *J. Atmos. Sci.*, **40**, 2735–2750.

Lau, K. M. and P. H. Chan (1983b) Short-term climate variability and atmospheric teleconnection from satellite derived outgoing longwave radiation, Part II: Lagged correlations. *J. Atmos. Sci.*, **40**, 2752–2767.

Lau, K. M. and P. H. Chan (1985) Aspects of the 40–50 day oscillation during northern winter as inferred from outgoing longwave radiation. *Mon. Wea. Rev.*, **113**, 1889–1909.

Lau, K. M. and P. H. Chan (1986a) The 40–50 day oscillation and the El Niño/Southern Oscillation: A new perspective. *Bull. Amer. Meteorol. Society*, 533–534.

Lau, K. M. and P. H. Chan (1986b) Aspects of the 40–50 day oscillation during northern summer as inferred from outgoing longwave radiation. *Mon. Wea. Rev.*, **114**, 1354–1367.

Lau, K. M. and P. H. Chan (1988) Intraseasonal and interannual variability of tropical convection: A possible link between the 40–50 day oscillation and ENSO. *J. Atmos. Sci.*, **45**, 506–521.

Lau, K. M. and L. Peng (1987) Origin of low frequency (intraseasonal) oscillation in the tropical atmosphere, Part I: Basic theory. *J. Atmos. Sci.*, **44**, 950–972.

Lau, K. M. and S. Shen (1988) Dynamics of intraseasonal oscillations and ENSO. *J. Atmos. Sci.*, **45**, 1781–1797.

Lau, K. M. and C.-H. Sui (1997) Mechanisms of short-term sea surface temperature regulation: Observations during TOGA–COARE. *J. Climate*, **9**, 465–472.

Lau, K. M., C. P. Chang, and P. H. Chan (1983) Short-term planetary scale interactions over the tropics and midlatitudes, Part II: Winter-MONEX period. *Mon. Wea. Rev.*, **111**, 1372–1388.

Lau, K. M., L. Peng, C. H. Sui, and T. Nakazawa (1989) Super cloud clusters, westerly wind burst, 30–60 day oscillations and ENSO: A unified view. *J. Meteorol. Soc. Japan*, **67**, 205–219.

Lau, K. M., T. Nakazawa, and C. H. Sui (1991) Observations of cloud cluster hierarchies over the tropical western Pacific. *J. Geophys. Res.*, **96**, 3197–3208.

Lorenc, A. C. (1984) The evolution of planetary scale 200 mb divergences during the FGGE year. *Quart. J. Roy. Meteorol. Soc.*, **110**, 427–442.

Luther, D. S. and D. E. Harrison (1984) Observing long-period fluctuations of surface winds in the tropical Pacific: Initial results from island data. *Mon. Wea. Rev.*, **112**, 285–302.

Luther, R. S., D. E. Harrison, and R. A. Knox (1983) Zonal winds in the central equatorial Pacific and El Niño. *Science*, **222**, 327–330.

Madden, R. (1986) Seasonal variations of the 40–50 day oscillation in the tropics. *J. Atmos. Sci.*, **43**, 3138–3158.

Madden, R. and P. Julian (1971) Detection of a 40–50 day oscillation in station pressure and zonal winds in the tropical Pacific. *J. Atmos. Sci.*, **28**, 702–708.

Madden, R. and P. Julian (1972) Description of global scale circulation cells in the tropics with a 40–50 day period. *J. Atmos. Sci.*, **29**, 1109–1123.

Maloney, E. D. and D. L. Hartmann (2000) The sensitivity in intraseasonal variability in the NCAR CCM3 to changes in convective parameterization. *J. Climate*, **14**, 2015–2034.

McCreary, J. P. and D. L. T. Anderson (1984) A simple model of El Niño and the Southern Oscillation. *Mon. Wea. Rev.*, **112**, 934–946.

McGovern, W. and R. Fleming (1977) FGGE and its implications for numerical weather prediction. *Bull. Amer. Meteorol. Society*, **58**, 113.

McPhaden, M. J. (1999) Genesis and evolution of the 1997–98 El Niño. *Science*, **283**, 950–954.

McPhaden, M. J. and X. Yu (1999) Equatorial waves and the 1997–98 El Niño. *Geophys. Res. Lett.*, **26**, 2961–2964.

McPhaden, M. J., H. P. Freitag, S. P. Hayes, B. A. Taft, Z. Chen, and K. Wyrtki (1988) The response of the equatorial Pacific Ocean to a westerly wind burst in May 1986. *J. Geophys. Res.*, **93**(C9), 10589–10603.

Meyer, G., J. R. Donguy, and R. K. Reed (1986) Evaporative cooling of the western equatorial Pacific ocean by anomalous winds. *Nature*, **323**, 523–526.

Moore, A. M. and R. Kleeman (1998) Skill assessment of ENSO using ensemble prediction. *Quart. J. Roy. Meteorol. Soc.*, **124**, 557–584.

Moore, A. M. and R. Kleeman (1999) Stochastic forcing of ENSO by the intraseasonal oscillation. *J. Climate*, **12**, 1199–1220.

Murakami, T. and T. Nakazawa (1985) Tropical 45-day oscillations during the 1979 northern hemisphere summer. *J. Atmos. Sci.*, **42**, 1107–1122.

Murakami, T., T. Nakazawa, and J. He (1984) On the 40–50 day oscillations during the 1979 northern hemisphere summer, Part I: Phase propagation. *J. Meteorol. Soc. Japan*, **62**, 440–468.

Nakazawa, T. (1988) Tropical super clusters within intraseasonal variations over the western Pacific. *J. Meteorol. Soc. Japan*, **66**, 823–839.

Nakazawa, T. (2000) MJO and tropical cyclone activity during 1997/98 ENSO. *Adv. Space Res.*, **25**, 953–958.

Neelin, J. D. (1990) A hybrid coupled general circulation model for El Niño studies. *J. Atmos. Sci.*, **47**, 674–693.

Neelin, J. D., D. S. Battisti, A. C. Hirst, F. F. Jin, Y. Wakata, T. Yamagata, and S. E. Zebiak (1998) ENSO theory. *J. Geophys. Res.*, **103**, 14261–14290.

NRC (1996) *Learning to Predict Climate Variations Associated with El Niño and the Southern Oscillation: Accomplishments and Legacies of the TOGA Program* (National Research Council report). National Academy Press, Washington, D.C., 235 pp.

Penland, C. (1996) A stochastic model of Indo-Pacific sea surface temperature anomalies. *Physica D*, **98**, 534–558.

Penland, C. and P. D. Sardeshmukh (1995) The optimal growth of tropical sea surface temperature anomalies. *J. Climate*, **8**, 1999–2024.

Philander, S. G. H., T. Yamagata, and C. Pacanowski (1984) Unstable air–sea interactions in the tropics. *J. Atmos. Sci.*, **41**, 604–613.

Roulston, M. S. and J. D. Neelin (2000) The response of an ENSO model to climate noise, weather noise and intraseasonal forcing. *Geophys. Res. Lett.*, **27**, 3723–3726.

Schrage, J. M., D. G. Vincent, and A. H. Fink (1999) Modulation of intraseasonal (25–70 day) processes by the superimposed ENSO cycle across the Pacific basin. *Meteorol. Atmos. Phys.*, **70**, 15–27.

Slingo, J. M. and AMIP collaborators (1997) Intraseasonal oscillations in 15 atmospheric general circulation mdoels: Results from an AMIP diagnostic subproject. *Climate Dynamics*, **12**, 325–357.

Slingo, J. M., D. P. Rowell, and K. R. Sperber (1999) On the predictability of the interannual behavior of the Madden–Julian Oscillation and its relationship with El Niño. *Quart. J. Roy. Meteorol. Soc.*, **125**, 583–609.

Sperber, K. R., J. M. Slingo, P. M. Inness, and K. M. Lau (1997) On the maintenance and initiation of intraseasonal oscillation in the NCEP/NCAR reanalysis and the GLA and UKMO AMIP simulations. *Climate Dynamics*, **13**, 769–795.

Suarez, M. and P. Schopf (1988) A delayed action oscillator for ENSO. *J. Atmos. Sci.*, **45**, 3283–3287.

Takayabu, Y. N., T. Iguchi, M. Kachi, A. Shibata, and H. Kanzawa (1999) Abrupt termination of the 1997–98 El Niño in response to a Madden–Julian Oscillation. *Nature*, **402**, 279–282.

Vautard, R. and M. Ghil (1989) Singular spectrum analysis in nonlinear dynamics with applications to paleoclimatic time series. *Physica*, **35D**, 395–424.

Vecchi, G. A. and D. E. Harrison (2000) Tropical Pacific sea surface temperature anomalies, El Niño and equatorial westerly wind events. *J. Climate*, **13**, 1814–1830.

Waliser, D. E., N. E. Graham, and C. Gautier (1993) Comparison of the highly reflective cloud and outgoing longwave radiation datasets for use in estimating tropical deep convection. *J. Climate*, **6**, 331–353.

Waliser, D. E., K. M. Lau, and J. H. Kim (1999) The influence of coupled sea surface temperatures on the Madden–Julian Oscillation: A model perturbation experiment. *J. Atmos. Sci.*, **56**, 333–358.

Waliser, D., Z. Zhang, K. M. Lau, and J. H. Kim (2001) Interannual sea surface temperature variability and the predictability of tropical intraseasonal variability. *J. Atmos. Sci.*, **58**, 2595–2615.

Waliser, D. E., K. Jin, I. S. Kang, W. F. Stern, S. D. Schubert, M. L. Wu, K. M. Lau, M. I. Lee, J. Shukla, V. Krishnamurthy *et al.* (2003) AGCM simulations of intraseasonal variability associated with the Asian summer monsoon. *Climate Dynamics*, **21**, 423–446.

Wang, B. and H. Rui (1990) Dynamics of the coupled moist Kelvin–Rossby wave on an equatorial β-plane. *J. Atmos. Sci.*, **47**, 397–413.

Wang, B. and X. Xie (1998) Coupled modes of the warm pool climate system, Part I: The role of air–sea interaction in maintaining the Madden–Julian Oscillation. *J. Climate*, **11**, 2116–2135.

Wang, X. C., F. F. Jin, and Y. Q. Wang (2003) A tropical ocean recharge mechanism for climate variability, Part I: Equatorial heat content changes induced by off-equatorial wind. *J. Climate*, **16**, 3585–3598.

Weickmann, K. M. (1983) Intraseasonal circulation and outgoing longwave radiation modes during northern hemisphere winter. *Mon. Wea. Rev.*, **111**, 1838–1858.

Weickmann, K. M. (1991) El Niño/Southern Oscillation and Madden and Julian (30–60 day) oscillations during 1981–82. *J. Geophys. Res. Oceans*, **96**, 3187–3195.

Weickmann, K. M., G. R. Lussky, and J. E. Kutzbach (1985) Intraseasonal (30–60 day) fluctuations of outgoing longwave radiation and 250 mb streamfunction during northern winter. *Mon. Wea. Rev.*, **113**, 941–961.

Weisberg, R. H. and C. Wang (1977) A western Pacific oscillator paradigm for the El Niño/Southern Oscillation. *Geophys. Res. Lett.*, **24**, 770–782.

Wyrtki, K. (1975) El Niño: The dynamic response of the equatorial Pacific Ocean to atmospheric forcing. *J. Phys. Oceanogr.*, **5**, 572–584.

Wyrtki, K. (1979) Sea level variations: Monitoring the breath of the Pacific. *EOS, Trans. Amer. Geophys. Union*, **60**, 25–27.

Yasunari, T. (1982) Structure of the Indian summer monsoon system with a period around 40 days. *J. Meteorol. Soc. Japan*, **60**, 336–354.

Yu, L. and M. M. Reinecker (1998) Evidence of an extratropical atmospheric influence during the onset of the 1997–98 El Niño. *Geophys. Res. Lett.*, **25**, 3537–3540.

Zebiak, S. E. (1982) A simple atmospheric model of relevance to El Niño. *J. Atmos. Sci.*, **39**, 2017–2027.

Zebiak, S. (1989) On the 30–60 day oscillation and the prediction of ENSO. *J. Climate*, **2**, 1381–1387.

Zebiak, S. and M. Cane (1987) A model El Niño Southern Oscillation. *Mon. Wea. Rev.*, **115**, 2262–2278.

Zhang, C. and J. Gottschalck (2002) SST anomalies of ENSO and the MJO in the equatorial Pacific. *J. Climate*, **15**, 2429–2445.

Zhang, C. and H. Hendon (1997) Propagating and standing components of the intraseasonal oscillation in tropical convection. *J. Atmos. Sci.*, **54**, 741–752.

Zhang, C., H. H. Hendon, W. S. Kessler, and A. Rosati (2001) A workshop on the MJO and ENSO. *Bull. Amer. Meteorol. Society*, **82**, 971–976.

10

Theories

Bin Wang

10.1 INTRODUCTION

Since the late 1980s, many studies have been devoted to developing our theoretical understanding of the tropical ISO in order to improve model simulations and predictions. Significant progress has been achieved, although some aspects of theories remain disputable and incomplete.

One of the purposes of this chapter is to review the basic ideas and limitations of existing theories and hypotheses. These invoke a broad range of processes and mechanisms to account for the growth and maintenance of low-frequency tropical disturbances. The major mechanisms that have been proposed are categorized based on their key feedback processes. They are discussed in Section 10.2.

Much of the work in this chapter is aimed at identifying the essential physics of the ISO and to formulate a general theoretical framework. The proposed theoretical model is simplistic but integrates several key mechanisms, providing a prototype model for describing the basic dynamics relevant to both the MJO and its boreal summer counterpart—referred to here as the boreal summer ISO (BSISO) or monsoon ISO. The essential physical processes involved in the model and their mathematical description are presented in Section 10.3.

An account is given of a series of previous and current theoretical studies with the view of *promoting* our understanding of the large-scale dynamics behind the MJO (Section 10.4) and BSISO (Section 10.5). Section 10.6 is devoted to enlightening the roles played by air–sea coupling in MJO dynamics. The physical explanations presented in these sections primarily reflect the author's personal view. The effort to explain the phenomenon is perhaps more significant than the explanation itself, because one of the purposes of this chapter is to stimulate better and deeper insights into the physics of the phenomenon.

Despite all the work that has been undertaken, some aspects of the ISO are still not adequately understood and continue to present the scientific community with a

W. K. M. Lau and D. E. Waliser (Editors), *Intraseasonal Variability in the Atmosphere–Ocean Climate System* (Second Edition).

challenge. Section 10.7 discusses the success and limitations of the theories presented in this chapter and outstanding issues to be taken into consideration in improving theories and models.

The ultimate goal of a meteorological theory is to explain an observed phenomenon and to predict it. For this purpose, it is useful to review the fundamental characteristics of the ISO that the theory should explain. Given the complexity of the phenomenon and limitations of current observations, determining these features is not easy. Nevertheless, such a list is necessary and useful for validating models and defining theoretical targets. The following set of statistical features is proposed as defining the horizontal scale, spatial structure, propagation (direction and phase speed), and annual variation of the ISO: (1) planetary-scale circulation coupled with a large-scale convective complex (Madden and Julian, 1972); (2) horizontal circulation comprising equatorial Kelvin and Rossby waves (Rui and Wang, 1990) and baroclinic circulation with boundary layer convergence preceding the major convection region (Hendon and Salby, 1994); (3) slow eastward propagation (about $5\,\mathrm{m\,s^{-1}}$) in the eastern hemisphere (Knutson *et al.*, 1986) and longitudinal dependence of amplification (Wang and Rui, 1990a); and (4) prominent northward propagation (Yasunari, 1979, 1980) and off-equatorial westward propagation (Murakami, 1980) during boreal summer in the summer monsoon region. More stringent validation characteristics include (5) the multiscale structure of the convective complex (Nakazawa, 1988) and the role of multiscale interaction in MJO dynamics, and (6) the associated interaction with SST variability (Krishnamurti *et al.*, 1988; and many others). The above characteristics provide focal points for theoretical analyses and discussions. For a more detailed summary of observed features the reader is referred to Zhang (2005).

10.2 REVIEW OF ISO THEORIES

Madden and Julian's (1971, 1972) pioneering work not only discovered the 40 to 50-day oscillation, but also went beyond the pure descriptive to propose a hypothesis for the origin of the oscillation. They visualized an equatorial eastward-propagating planetary-scale circulation anomaly that couples with a convection anomaly of a few thousand kilometers (see Chapter 1). Thus, their studies laid down a hypothesis for understanding the nature of the 40 to 50-day oscillation. The vertical structure and eastward propagation of the MJO visualized by Madden and Julian stimulated an earliest explanation in terms of Kelvin waves. But the gravest vertical mode (''free'') Kelvin wave propagates five times too fast to account for the slow timescale of the MJO. To account for the slow propagation, Chang (1977) proposes convectively driven Kelvin waves that are subject to a damping arising from Newtonian cooling or cumulus friction. In the early 1980s, the horizontal structure of the MJO was further documented in detail (e.g., Weickmann, 1983; Lau and Chan, 1985; Knutson *et al.*, 1986). Perhaps motivated by Gill's (1980) theory, some scientists interpreted the MJO as an atmospheric response to a localized heat source that pulsates with a 40 to 50-day period (e.g., Yamagata and Hayashi, 1984; Anderson, 1987; Hayashi

and Miyahara, 1987; Yamagata, 1987) or to a mobile heat source with a given speed (Chao, 1987). These "Gill response" hypotheses, however, could not explain what selects the oscillation frequency or what causes the movement of the heat source.

Based on the key processes, the MJO theories/hypotheses are summarized in the following categories.

10.2.1 Wave CISK

In the mid to late 1980s, a number of general circulation models (GCMs) had shown the capability to realistically simulate some features of the observed MJO—in particular, the eastward propagation of large-scale circulation and convective anomalies (e.g., Hayashi and Sumi, 1986; Lau and Lau, 1986). It was soon recognized that a key to explanation of the MJO is the interaction between large-scale motion and convective processes. Lau and Peng (1987) invoke an instability arising from the interaction between convective heating and large-scale wave motion, known as wave CISK (convective instability of the second kind). The term CISK dates back to Ooyama (1964) and Charney and Eliassen (1964) who explain hurricane formation by a cooperative feedback between the collective effect of small-scale convection and large-scale low-level convergence due to Ekman pumping. This idea was consequently applied to the cooperative interaction between tropical wave convergence and organized convection (i.e., wave CISK; Yamasaki, 1969; Hayashi, 1970; Lindzen, 1974).

In their five-level model with positive condensational heating (also known as conditional heating or nonlinear heating), Lau and Peng (1987) find equatorial Kelvin waves being selectively amplified. The periodicity of the oscillation is determined by the time taken by a moist Kelvin wave to complete one circuit around the globe. Their linear analysis shows that both the growth rate and phase speed depend on the vertical structure of the heating profile and the static stability of the basic state.

Many wave CISK models produce faster than observed eastward propagation. The slow phase propagation of wave CISK was attributed to the reduction in effective static stability and the coupling of two internal modes that are locked in phase vertically (Chang and Lim, 1988). Slow propagation was also attributed to the specified heating maximized in the lower troposphere in multilayer models (e.g., Takahashi, 1987; Sui and Lau, 1989), but this remains controversial. For example, Cho and Pendlebury (1997) show that an unstable large-scale mode emerges only when the heating profile is sufficiently top heavy; the model results of Mapes (2000) support this point of view (i.e., unstable mode occurs when the specified heating contains a sufficient amount of the second vertical mode of the troposphere).

Most wave CISK models used Kuo (1965, 1974)-type cumulus parameterization; some used the Arakawa–Schubert (1974) scheme. When other schemes were used, the unstable wave CISK mode might not be found. Neelin and Yu (1994) find that under the Betts–Miller (1986) scheme a sufficiently long Kelvin wave becomes a slowly decaying mode under reasonable conditions. Introduction of a finite

convective adjustment timescale has the property of selectively damping the smallest scales while certain vertical modes at planetary-scales decay only slowly.

A caveat of the wave CISK theory is that the *linear* theory does not explain how the disturbance can maintain the planetary-scale structure against the explosive growth of shortwave components (Chao, 1995). Lim *et al*. (1990) claim that positive-only heating may remedy this catastrophe in a finite-resolution numerical model. However, analytical solutions show that positive-only heating may result in planetary-scale descending regions on both sides of a concentrated convective region, but the convective region of the most unstable mode has an infinitesimal width (Dunkerton and Crum, 1991; Wang and Xue, 1992). Hendon (1988), in his two-level model study, finds that the effects of nonlinear advection cause the growing CISK modes to rapidly stabilize the atmosphere. The stability increases greatest to the west of CISK heating. It appears that nonlinear advection supports eastward-propagating disturbances with finite wavelengths.

10.2.2 Wind–evaporation feedback or WISHE

Emanuel (1987) and Neelin *et al*. (1987) propose that the waves producing the MJO arise from an instability driven by wind-induced surface latent heat flux. This mechanism was called the wind–evaporation feedback in Neelin *et al*. (1987) and wind-induced surface heat exchange (WISHE) in Yano and Emanuel (1991). In Emanuel's conceptual model (Emanuel, 1987), no cumulus convective scheme was involved. Entropy is redistributed through the troposphere by local convection because the atmosphere is assumed to be neutrally stratified. A basic assumption is that mean surface winds are easterlies. Thus, the enhancement of mean easterlies ahead of an eastward-propagating trough leads to enhanced transfer of entropy from the ocean and the associated atmospheric warming lowers pressure and moves the trough eastward. Similar to wave CISK, the linear WISHE mechanism favors shortwave growth. Emanuel (1993) introduces a time lag between the large-scale forcing of convection and its response, which damps shortwaves. But the time lag in the vertical transport of water vapor is shown to make the phase speed too large by a factor of 4 to 5 (Brown and Bretherton, 1995).

WISHE instability has been examined in models with different cumulus parameterization schemes. Brown and Bretherton (1995) investigate WISHE with a simple two-dimensional non-rotational model on the equatorial plane. They find that evaporationally driven unsaturated downdrafts play a major role in damping shortwaves and only the longwavelength WISHE mode is unstable, although the phase speed is too large. On the other hand, Lin *et al*. (2000) investigate the ISO using their intermediate tropical circulation model in which nonlinearity, radiative–convective feedback, and the Betts–Miller scheme are included. Their experiments with specified SST show that wind–evaporation feedback partially organizes model intraseasonal variability by reducing damping, but it is not by itself sufficient to sustain the oscillation for the most realistic parameters.

Without invoking wave dynamics, the WISHE mechanism on its own has difficulty explaining the slow eastward propagation. The eastward propagation of

the WISHE mode in the Emanuel (1987) model is driven by the asymmetry of surface heat fluxes: enhanced surface evaporation in the perturbation easterly phase and suppressed heat fluxes in the westerly phase. Such an asymmetric heat flux pattern relies on the existence of mean surface easterlies. Yet, observed mean winds are equatorial westerlies over the Indian and Western Pacific where the MJO is most active (Wang, 1988b). TOGA/COARE observations have revealed that the surface evaporation associated with the MJO has an opposite zonal asymmetry (i.e., large anomalous latent heat flux occurs in the westerly phase behind the convection; e.g., Jones and Weare, 1996; Lin and Johnson, 1996; Zhang and Anderson, 2003).

The WISHE mechanism accounts for an important energy source for the ISO. Neelin *et al.* (1987) find that evaporation is important for the intraseasonal oscillation in a GCM with a zonally symmetric climate, although the existence of an energy peak on the intraseasonal timescale does not depend on it. Furthermore, when equatorial wave dynamics are included in simple models with conditional heating parameterization, the WISHE mechanism is found to lead to instability and to enhance eastward propagation, which does not necessarily require the existence of mean easterlies (Xie *et al.*, 1993; Wang and Li, 1994). Nonlinear WISHE is shown to be able to produce a coherent signal in westerly winds and convection that travels eastward at $4\,\mathrm{m\,s^{-1}}$ to $10\,\mathrm{m\,s^{-1}}$ through the interaction between eastward-propagating Yanai waves and Kelvin waves in the presence of mean easterlies (Solodoch *et al.*, 2011).

10.2.3 Frictional convergence instability (FCI)

Wang (1988a) proposes that the MJO is driven by an instability arising from boundary layer friction-induced moisture convergence associated with large-scale equatorial waves. Frictional moisture convergence can couple equatorial Kelvin and Rossby waves through frictionally organized convective heating and select a frictional convergence instability (FCI) mode that is slowly moving eastward (Wang and Rui, 1990a). The unstable FCI mode is characterized by a boundary layer convergence ahead of the free tropospheric wave convergence and major precipitation anomaly. Different from wave CISK, FCI emphasizes that wave-induced moisture convergence does not result in instability (Wang, 1988a; Xie and Kubakawa, 1990).

The FCI mechanism has been further examined in more complex models using different convective parameterization schemes. Salby *et al.* (1994) use column-integrated moisture flux convergence to represent convection. They show that friction-induced convergence renders the gravest zonal dimensions most unstable. In an equatorial β-plane very high–resolution (1 km) model without cumulus parameterization, Ohuchi and Yamasaki (1997) show that boundary layer convergence exhibits a phase shift slightly eastward relative to the convergence aloft, which is key to effective feedback between convection and wave motion. They find that resultant unstable wave and supercloud clusters are characterized by a slow phase speed of less than $10\,\mathrm{m\,s^{-1}}$ and its growth rate by a weak dependence on wavelength. Moskowitz

and Bretherton (2000) use a Betts–Miller-like convective parameterization. Friction is found to be modestly destabilizing for the moist Kelvin mode and the gravest moist Rossby mode. Frictionally forced boundary layer convergence promotes wave amplification by enhancing convective heating along the equator in the warm sector of the wave. With a radiation condition at the upper boundary, the longest wave has the largest growth rate. The effect of frictional convergence feedback is reported to be fairly insensitive to the convective parameterization used (Moskowitz and Bretherton, 2000).

The key feature of FCI (i.e., frictional moisture convergence ahead of precipitation in the MJO) has been observed and documented using a variety of datasets (Hendon and Salby, 1994; Jones and Weare, 1996; Maloney and Hartmann, 1998; Matthews, 2000; Sperber, 2003; Lin *et al*., 2004; Tian *et al*., 2006; Yang *et al*., 2008). Maloney and Hartmann (1998) analyze column-integrated water vapor from the surface to 300 hPa that is associated with the MJO lifecycle and find that a significant correlation exists between surface convergence and column water vapor anomalies in the Western Pacific Ocean and Indian Ocean. They show that frictional moisture convergence fosters the growth of positive water vapor anomalies to the east of convection. The frictional convergence in front of convection helps to slowly moisten the atmosphere to a state that is favorable for convection (preconditioning). A number of diagnostic studies of model simulations have also confirmed the importance of boundary layer frictional convergence in various GCMs with different cumulus parameterization schemes (Lau and Lau, 1986; Lau *et al*., 1988; Kuma, 1994; Maloney, 2002; Lee *et al*., 2003; Liu *et al*., 2005) and in coupled GCMs (Waliser *et al*., 1999).

A concern with FCI is the value of the Rayleigh friction coefficient E in the boundary layer. Wang (1988a) takes $E = 3 \times 10^{-5}\,\mathrm{s}^{-1}$. Moskowitz and Bretherton (2000) suggest this value is an order of magnitude too large, although their use of a small value yields qualitatively similar results. Worthy of note is that—for low-frequency motions—the Rayleigh friction coefficient represents not only friction but also other damping effects such as high-frequency transient Reynolds stress. Calculations of tropical winds from sea level pressure fields indicate that an adequate value for E is $O(10^{-5}\,\mathrm{s}^{-1})$ (Murphree and van den Dool, 1988; Murakami *et al*. 1992). If E is $O(10^{-6}\,\mathrm{s}^{-1})$, the observed surface pressure would yield unrealistically large boundary layer wind fields for tropical low-frequency variability. Diagnosis of the surface momentum balance over the tropical Pacific Ocean suggests that the Rayleigh friction coefficient in the meridional direction should be three times larger or $O(3 \times 10^{-5}\,\mathrm{s}^{-1})$ (Deser, 1993; Li and Wang, 1994).

10.2.4 Cloud–radiation feedback

Hu and Randall (1994, 1995) suggest that nonlinear interactions among radiation, convection, the surface flux of moisture, and sensible heat might result in a non-propagating intraseasonal oscillation rather than a steady state. Radiative cooling and surface moisture flux tend to destabilize model atmosphere, while convection tends to maintain a convectively neutral state by reducing boundary layer moisture

and the lapse rate. Oscillations are favored by a warm sea surface and a weak surface windspeed. Their model, however, excluded large-scale dynamics and fixed the surface windspeed and SST in calculating surface heat flux (thus, the WISHE mechanism is also excluded). This mechanism is speculated to play a role in explaining the stationary component of the MJO over the Western Pacific Ocean and Indian Ocean warm pool (e.g., Lau and Chan, 1985; Zhu and Wang, 1993), although the results of Zhang and Hendon (1997) suggest there is not much of a stationary component.

Raymond (2001) proposes another model of radiative–convective instability. The large-scale convective overturning given by a combination of latent heat release and radiative heating anomalies induced by cloud–radiation interactions are thought to be the primary driving mechanism of the model ISO. A pre-existing precipitation anomaly has a region of mid-to-upper level stratiform cloudiness associated with it. The suppression of outgoing longwave radiation results in a heating anomaly relative to its surroundings, which causes lifting and further precipitation. The effects of surface heat flux variability also substantially modify the behavior of the unstable mode. The cumulus parameterization used in the model assumed a lag of several days to exist between the strongest surface heat flux into the column and the subsequent development of heavy precipitation in that column. One could argue that this lag mimics the time to moisten the free atmosphere, but the processes responsible for the delay should be clarified because the model oscillation depends on this lag.

Cloud–radiation feedback has been studied using atmospheric GCMs. High clouds with thick optical depth play a significant role in driving large-scale diabatic circulations in the tropics (Slingo and Slingo, 1988; Randall *et al*., 1989). In addition to condensational heating, the radiation process, which is affected by cloud properties, also contributes to the vertical distribution of diabatic heating and static stability, thus affecting the convective instability and vertical distribution of latent heating. Slingo and Madden (1991) find that longwave cloud radiative forcing is not crucial in simulating the MJO and suggest that the intensity of the simulated MJO depends on cloud–radiation interaction but the period is not significantly affected. In later studies, the role of longwave radiation becomes controversial. For instance, Mehta and Smith (1997) suggest the importance of longwave cooling in maintaining the MJO. In contrast, Lee *et al*. (2001) find that the inclusion of cloud–radiation weakens the model MJO, since the magnitude of longwave cooling is greater than that of shortwave cooling in MJO-related tropospheric radiative heating. The roles played by longwave interaction and the processes by which cloud–radiation feedback influences the MJO are subjects that call for further studies.

10.2.5 Convection–water vapor feedback and the moisture mode

The role played by moisture variation in MJO dynamics has been noted as important. Blade and Hartmann (1993) propose a "discharge–recharge" hypothesis whereby the 40-day recurrence period in their model is set by the growth and

duration times of a convective episode together with the recharge time for the instability. Kemball-Cook and Weare (2001), based on the analysis of radiosonde data, suggest that—prior to the onset of MJO convection—the atmosphere has been destabilized through a combination of low-level moist static energy buildup and concurrent drying of the middle atmosphere by subsidence in the wake of the previous cycle of MJO convection. In a model study, Goswami and Mathew (1994) suggest that large-scale flow is not in exact quasi-equilibrium with precipitation heating and that a time-dependent moisture equation is necessary. In his numerical experiments using a model that treats moisture budget explicitly, Itoh (1989) finds that—in order to obtain a ''supercloud cluster'' and an associated wavenumber 1 circulation—the cumulus convection scheme has to restrain the occurrence of deep convection so that dry regions occur over wide areas of the tropics where weak moisture convergence exists. In these dry regions, the accumulation of moisture presumably preconditions MJO deep convection.

Moisture anomalies can interact with convection. The feedback between convection and water vapor appears to be important in regulating the strength and propagation speed of the MJO (Woolnough *et al*., 2000). Tompkins (2001) proposes that the water vapor–convection feedback can cause self-aggregation (i.e., the occurrence of convection makes future convection more likely to occur in the same location through an organized positive feedback between convection and water vapor). Bretherton *et al*. (2005) find that—in a large-domain cloud-resolving model—convection undergoes self-aggregation when gross moist stability (GMS; Neelin *et al*., 1987) is negative. Using a global model that applies a cloud-resolving convection parameterization, Grabowski (2003) finds that replacing cumulus parameterization in a large-scale model by an embedded cloud-resolving model (''superparameterization'') strengthens an MJO-like large-scale organization of convection. Khairoutdinov *et al*. (2005) use such a superparameterization in their CAM (community atmospheric model), which also results in a much improved MJO. The buildup of humidity in a convective region is key to producing this disturbance. If large-scale fluctuations of convectively generated free atmospheric moisture are removed on a timescale of a few hours, the coherent structure of MJO-like disturbance does not develop (Grabowski, 2003).

The moisture–convection feedback is considered the backbone of stationary or slowly propagating convectively coupled modes in the tropics (Fuchs and Raymond, 2005). Raymond and Fuchs (2007) develop a two-dimensional linearized model of convectively coupled disturbances. Convection is forced by precipitable water anomalies and the relaxation of convective inhibition (CIN). The model yields stationary moisture mode instabilities, which occur in the tropical oceanic atmosphere when precipitation is a strongly increasing function of the saturation fraction (precipitable water divided by saturated precipitable water) and when convection acts to further moisten the atmosphere. Raymond and Fuchs (2009) further build a numerical model with idealized SST distribution in which a cumulus adjustment scheme was used. Convection in this model exhibits the strong dependence of precipitation on the saturation fraction and acts to increase moisture, thus the moisture mode instability is satisfied. The model produced eastward-moving equa-

torial westerly anomalies (an MJO-like disturbance), suggesting that the MJO may be driven in part by moisture mode instability.

The multicloud heating acting on high-frequency disturbances may produce instability. Observations have shown that the MJO and embedded disturbances involve the multicloud structure: a deep convection core preceded by shallow convection or congestus clouds and tailed by upper-tropospheric stratus clouds (Lin and Johnson, 1996; Johnson *et al*., 1999; Houze *et al*., 2000; Mapes *et al*., 2006). By considering two vertical modes—the gravest baroclinic mode and the second baroclinic mode (the stratiform/congestus mode)—Kuang (2008) shows that a moisture stratiform instability can produce most unstable waves of a few thousand kilometers, which is stronger than the direct stratiform instability (top-heavy heating profile) (Mapes, 2000).

10.2.6 Multiscale interaction theory

The convective complex—which is coupled with planetary-scale circulation and brings an active (wet) phase of the MJO—can be viewed as an envelope of myriad mesoscale and synoptic-scale systems with multiple cloud heating involved. The systems can move either eastward—such as convectively coupled Kelvin waves or supercloud clusters (SCCs)—or westward (2-day waves and squall lines) (Nakazawa, 1988; Straub and Kiladis, 2003; Haertel and Kiladis, 2004; Moncrieff, 2004). These disturbances have a backward-tilted vertical structure against its propagation direction, which is valid for a hierarchy of cloudiness, temperature, and humidity within convectively coupled equatorial waves, from the mesoscale to the MJO scale (Mapes *et al*., 2006; Kiladis *et al*., 2009). This generic backward tilt is rooted in multicloud heating (Khouider and Majda, 2006, 2007) and planetary boundary layer convergences which lead free tropospheric wave convergence (Wang and, Liu, 2011). The vertically tilted structures of these meso-synoptic systems allow for nonzero upscale eddy momentum transfer (EMT) converting eddy available potential energy to large-scale horizontal kinetic energy. Krishnamurti *et al*. (2003) show that about 30% to 50% of total surface heat flux on the MJO timescale comes from the triad interaction of the MJO with two other synoptic timescales. Moncrieff (2004) proposes that upscale momentum and heat transfer may play an important role in maintaining the MJO.

Recent theoretical studies of the MJO have focused on understanding the roles played by scale interaction by developing multiscale models (Majda and Klein, 2003; Majda and Biello, 2004; Biello and Majda, 2005; Majda and Stechmann, 2009). Majda and Biello (2004) demonstrate that the EMT generated by rearward-tilted SCCs may make an MJO-like system. An improved multiscale model developed by Biello and Majda (2005) includes both congestus clouds and SCCs, which are located, respectively, in the eastern and western part of the convective complex. This model reproduced a quadrupole vortex structure that is similar to the MJO (Rui and Wang, 1990; Hendon and Salby, 1994). These MJO kinematic models are built on the feedback of synoptic activity on planetary-scale motion, but do not include modulation of the MJO on synoptic-scale disturbances.

Majda and Stechmann (2009) further study the interaction between zonal mean flow and EMT on the equator without considering Earth's rotation. The model produced an intraseasonal oscillation in mean flow, but left eastward propagation unexplained. To capture the dynamics of the MJO envelope, Majda and Stechmann (2009) propose a minimal dynamical model for the MJO "skeleton" through an implicit representation of synoptic activity in the *thermodynamic* equation. The model was able to capture some fundamental features of the skeleton of the MJO, such as slow phase speed, horizontal quadrupole vortex structure, and wave dispersion relationship. But, the effect of upscale momentum transport, which was recognized as more important than eddy heat transport (Majda and Biello, 2004), is not explicitly represented in this "skeleton" model. The model produced both an eastward and westward-propagating low-frequency mode. The lack of selection of propagation direction may be rectified if boundary layer moisture convergence is included.

Wang and Liu (2011) propose a multiscale interaction model which consists of a frictional convergence instability that mimics the planetary-scale component of the MJO and an explicit representation of EMT effects based on Biello and Majda's (2005) model. FCI controls the locations and regulates the strength of EMT, which in turn feedbacks to FCI by upscale westerly/easterly momentum transport. Multiscale interaction (MSI) instability stems from cooperative FCI or EMT mechanisms; a growing MSI mode has a horizontal quadrupole and rearward-tilted structure and prefers slow eastward propagation, which resembles the observed MJO. FCI sets the eastward propagation, while EMT slows down the propagation speed. Model results will be discussed in detail in Section 10.4.4.

10.2.7 Mechanisms of the boreal summer intraseasonal oscillation

During boreal summer, the eastward-propagating MJO mode substantially weakens (Madden, 1986; Wang and Rui, 1990b), whereas northward propagation becomes a prominent feature of the ISO in the Indian summer monsoon region (Chapter 2; Yasunari, 1979, 1980; Sikka and Gadgil, 1980; Krishnamurti and Subrahmanyam, 1982).

Several mechanisms have been suggested to account for northward propagation over the Indian Ocean sector. Webster (1983) proposes that land surface heat fluxes into the boundary layer can destabilize the atmosphere ahead of an ascending zone, causing a northward shift of the convection zone. Goswami and Shukla (1984) find the low-frequency oscillation simulated in their axially symmetric atmospheric model results from a convective–thermal relaxation feedback. Convective activity increases atmospheric stability, which would depress convection; meanwhile, dynamic and radiative relaxation brings the atmosphere to a new convectively unstable state.

Based on a boreal summer ISO model in which the ISO is controlled by the climatological July mean basic state including vertical shear and surface moist static energy distribution, Wang and Xie (1997) find that the northward-propagating rainband associated with the ISO is a consequence of continuous northwestward

emanation of Rossby waves from an equatorial Kelvin–Rossby wave packet (an MJO-like disturbance) when the latter passes through a maritime continent. More prominent emanation occurs in the western North Pacific when the equatorial disturbance rapidly decays in the equatorial Central Pacific. This model result agrees with the observed northwestward propagation of ISO convective anomalies over both the North Indian Ocean and the western North Pacific.

The westward propagation generated over the monsoon region may be a manifestation of equatorial Rossby waves destabilized by easterly vertical shear and interactive convective heating (Wang and Xie, 1996; Xie and Wang, 1996). These disturbances may emanate from and be modulated by an equatorial eastward-propagating ISO (Wang and Xie, 1997; Kemball-Cook and Wang, 2001) or be formed by merging an equatorial eastward-moving convective system with a westward-propagating low-level convergence anomaly located in the subtropics (Hsu and Weng, 2001). However, why the Rossby wave propagation has a northward component was not addressed.

The works of Jiang *et al*. (2004) and Drbohlav and Wang (2005) further identify and elaborate how easterly vertical shears and boundary layer moisture advection could contribute to the northward propagation component. This vertical shear theory will be explained in detail in Section 10.5. This theory explains why poleward propagation preferably occurs in the monsoon region where vertical easterly shears prevail. This poleward propagation is observed not only in the Asian–Western Pacific summer monsoon region but also in the North American summer monsoon region (Jiang and Waliser, 2008) and the Australian summer monsoon region when monsoon easterly vertical shears exist.

In addition to the vertical shear theory, the air–sea interaction is found to significantly affect northward propagation. Fu and Wang (2004) point out that, on the one hand, an ISO convective anomaly in the equatorial Indian Ocean can generate a positive SST anomaly to the northeast of the convection through reducing total monsoon westerly and evaporation cooling. On the other hand, positive SST anomalies ahead (northeast) of the convection can promote convection through destabilization of moist Rossby waves and local adjustment of convection to SST anomalies, thus enhancing the northeastward-propagating ISO. In the western North Pacific, eddy momentum transport from synoptic systems may also contribute to northward propagation of the BSISO (Hsu *et al*., 2011; Hsu and Li, 2011). Based on a cloud-resolving model, Boos and Kuang (2010) suggest that the beta drift of synoptic motion may induce northward propagation of the ISO.

Understanding the origin and perpetuation of the monsoon intraseasonal cycle has eluded scientists for decades. Effort has been made recently to address these issues. Using a suite of unprecedented satellite measurements, Wang *et al*. (2005) show that antecedents of active/break monsoon periods emerge in the western equatorial Indian Ocean (EIO). The initiation of a new rainy phase in the western EIO is preceded by in situ surface wind convergence and central EIO warming, both induced by subdued conditions over the eastern EIO set up in the previous cycle. Thus, a self-induction mechanism appears to be operating to maintain the Indian monsoon intraseasonal oscillation. The finding offers a focus for prediction of the

active/break Indian monsoon periods with potential predictability about 4 weeks in advance.

10.2.8 Atmosphere–ocean interaction

TOGA COARE has provided firm evidence that active air–sea interaction occurred during the two MJO events in late 1992 and early 1993. The coupled structure of MJO and oceanic mixed layer variability were documented in the mid-1990s (see Section 10.6 and Chapter 8). Stimulated by these observations, there has been a surge of theoretical and numerical model studies of the nature of the air–sea interaction in the Indo-Pacific warm oceans and its role in the development of the ISO.

In theoretical model studies, Wang and Xie (1998) introduce a simple coupled atmosphere–ocean model suitable for study of the coupled instability of the warm pool climate system. This model emphasizes oceanic mixed layer physics and its thermodynamic coupling (through surface heat exchanges) with transient atmospheric motion. The fastest growing coupled mode in the model has a planetary zonal scale and an intraseasonal timescale, as well as a realistic SST–convection relationship. The wind–evaporation and entrainment feedback plays a primary role in generating the coupled instability, while the contribution of cloud–SST coupling becomes significant when the wind is weak (see Section 10.6). Sobel and Gildor (2003) introduce a simple model for the evolution of SST in a localized region of a warm ocean. The model consists of a zero-dimensional atmosphere coupled to an ocean mixed layer. For plausible parameter values, the steady state of the system can oscillate with periods ranging from intraseasonal to subannual. The basic mechanism behind the instability and oscillation comes from cloud–radiative and wind–evaporation feedbacks, which agree qualitatively with the model results of Wang and Xie (1998). In their model, however, these two processes play the same roles. This difference may be due to atmospheric dynamics. In the regions of active interaction associated with these two feedback processes, they would have a spatial phase shift due to dynamical processes and their roles would be different (as discussed by Wang and Zhang, 2002).

In numerical model studies, Flatau *et al.* (1997) use an AGCM with a parameterized empirical relationship between windspeed and SST tendency to examine the effect of SST feedback on equatorial convection on an aqua-planet. Model MJO-like fluctuations were slowed down and became more organized than those with a fixed SST distribution. Waliser *et al.* (1999), using a GCM coupled to a slab ocean mixed layer, show that air–sea coupling increased MJO variability, more closely matched the timescale of the oscillation with observations, reduced the eastward phase speed in the eastern hemisphere, and increased the seasonal signature in the MJO with more events occurring in the December–May period. Subsequent numerical model studies have generally confirmed the positive contributions of the air–sea interaction in enhancing the eastward-propagating MJO and the northward propagation of boreal summer ISO. For instance, analysis of the European Centre for Medium-range Weather Forecast-Hamburg atmospheric

model (ECHAM4) and its coupled version with the University of Hawaii 2.5-layer tropical ocean model, Kemball-Cook *et al.* (2002) find—upon coupling—pronounced northward propagation of convection and circulation anomalies appear in the May–June Asian monsoon season.

However, it has also been recognized that—for the air–sea interaction to enhance the ISO—realistic simulation of the mean state in the coupled model appears to be necessary (Gualdi *et al.*, 1999; Hendon, 2000). Inness and Slingo (2003) also find that air–sea coupling improves eastward propagation of convection across the Indian Ocean, but there was no eastward propagation in the Western Pacific, because errors in the mean low-level zonal wind component there prevented the MJO from propagating into this region (Inness *et al.* 2003).

In the coupled model of Waliser *et al.* (1999), SST variation is primarily due to changes in latent heat flux and, to a lesser degree, changes in surface shortwave flux. However, the slab ocean model might be too simple to address the question of what causes intraseasonal SST variation. The cause of SST variability was further studied using a coupled atmosphere–ocean general circulation model by Cubukcu and Krishnamurti (2002), who find that intraseasonal SST oscillations in the warm pool are primarily caused by the variation of solar radiation, while evaporative cooling was of secondary importance.

How SST anomalies feed back to the MJO is key to understanding the oscillation, but is a more complex issue. Waliser *et al.*'s (1999) coupled model shows enhanced SST to the east of convection reinforces the meridional convergence associated with frictional moisture convergence. The resulting increase in moist static energy helped destabilize the disturbance and maintain it against dissipation more effectively than in the case without coupling. Kemball-Cook *et al.* (2002) confirm this conclusion and attribute the improved northward propagation of the BSISO to increased low-level convergence in regions where a positive SST anomaly exists (i.e., ahead of the convective anomaly).

Observed positive SST anomalies tend to lead convective anomalies by about one quarter of a wavelength. What creates this phase lag is controversial. Woolnough *et al.* (2001) investigate the response of convection to an idealized imposed mobile intraseasonal SST anomaly in an atmospheric GCM on an aqua-planet. Convection is found to be organized on the spatial and temporal scales of imposed SST anomalies and the location of maximum precipitation relative to SST anomalies is in good agreement with observations. They suggest that free tropospheric humidity plays a critical role in determining the location and magnitude of the precipitation response. On the other hand, Wu *et al.* (2002) compare an observed strong case of the MJO and its counterparts simulated by 10 different atmospheric GCMs forced using the same observed weekly SST. In the observations, positive SST anomalies develop upstream of the main convection center while in simulations the forced component is in phase with the SST.

The coupled modeling study by Fu and Wang (2004) demonstrates that the air–sea interaction significantly enhances northward propagation of the ISO compared with the forced run in which the same atmospheric model is forced by the daily SST produced by the coupled model. They point out that the coupled and forced

solutions are fundamentally different. Without coupling, the SST and convection anomalies are nearly in phase, but in the coupled run the SST–convection relationship has a structure similar to that observed. Neglecting atmospheric feedback makes the forced solution depart from the coupled solution in the presence of initial noises or tiny errors in the lower boundary.

10.3 A GENERAL THEORETICAL FRAMEWORK

10.3.1 Fundamental physical processes

What is the energy source behind MJO disturbances? Wang (1988a) presents a scale analysis for the MJO. If the observed baroclinic wind circulation (5 m/s) of the MJO is maintained, the required divergence is on the order of $(5 \times 10^{-7}\ s^{-1})$, which has to be sustained by a diabatic heating rate on the order of $2\ mm\ day^{-1}$ to $3\ mm\ day^{-1}$. This diabatic heating rate is only 20% to 30% of the total precipitation heating rate in the tropics and the remaining percentage of precipitation heating is presumably consumed by meso-synoptic-scale systems. It is conceivable that the ISO is primarily driven by the latent heat released in precipitation, though some studies have suggested the roles played by extratropical forcing (e.g., Hsu *et al.*, 1990; Blade and Hartmann, 1993; Lin *et al.*, 2000) in exciting and maintaining the MJO.

Figure 10.1 presents a schematic summary of the fundamental processes relevant to the ISO. Of central importance is convective interaction with dynamics (CID)

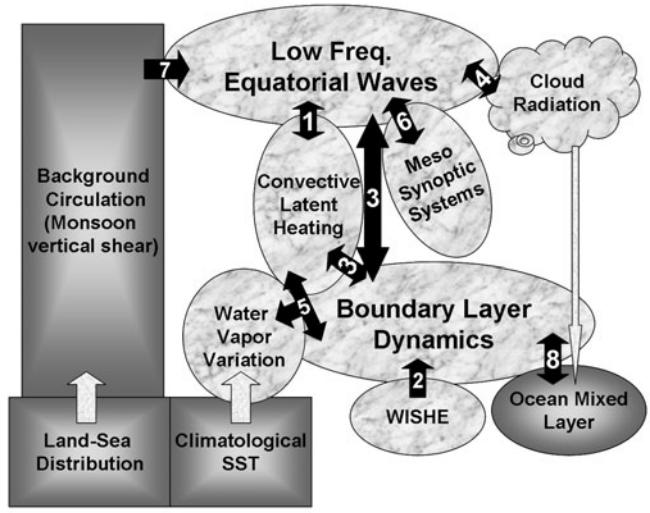

Figure 10.1. Essential physical processes involved in theoretical modeling of the ISO. These processes are numbered in this figure in an order consistent with the reviews in Section 10.2.

(following Neelin and Yu, 1994). CID processes are marked by marbled shadings in Figure 10.1, which comprises (a) the collective effects of convective heating, (b) low-frequency equatorial Kelvin and Rossby waves, (c) planetary boundary layer dynamics, (d) surface heat and momentum exchanges (WISHE) with the lower boundary, (e) the moisture feedback between convection and its dynamics, and (f) upscale momentum and heat transfer. These feedback processes integrate the following mechanisms (reviewed in Section 10.2): convection–wave convergence feedback, frictional moisture convergence feedback, evaporation–wind feedback, moisture feedback, and meso-synoptic-scale feedback. CID is considered essential for understanding the basic internal dynamics of the MJO.

Planetary boundary layer processes are of central importance in CID. Dynamically, CID provides large-scale control of the moisture that fuels convection and contributes to the accumulation of moist static energy and the triggering of shallow and deep convections with the "self-similarity" property (Mapes *et al*., 2006; Kiladis *et al*., 2009). Thermodynamically, WISHE is key to change in moist static energy in the boundary layer, thus providing an energy source for the MJO (Emanuel, 1993). Besides the potential role in determining the location and strength of precipitation heating, boundary layer friction is also an efficient energy sink for low-frequency motion. The roles of these CID feedback processes will be discussed in Section 10.4.

Other processes include cloud–radiation feedback, impacts of seasonal mean flows, and air–sea interaction (Figure 10.1). The tropospheric radiative heating associated with the MJO is dominated by longwave radiative cooling (Lee *et al*. 2001), which in turn is determined by the properties of clouds. In the following formulation, simplistic Newtonian cooling is adopted to represent the net radiative heating effect. Keep in mind that (as suggested by Lin *et al*.. 2004) net radiative heating may be slightly positive in the cloud region, which could enhance latent heating to the first order. In addition, the radiative heating/cooling by shortwave and longwave radiation at upper level clouds associated with MJO convection might be important in destabilizing the atmosphere and leading to deep convection, thus Newtonian cooling may be an oversimplified parameterization of radiation processes.

The seasonality of the ISO suggests possible regulation of moist wave dynamics by seasonally varying background flows. The amplitude of MJO circulation variations is typically small compared with that of seasonal variations of tropical circulations, such as monsoon circulation. Also, transient momentum and heat fluxes tend to play a negligible role in determining tropical mean circulation (Ting, 1994; Hoskins and Rodwell, 1995). Thus, to the first approximation the ISO is treated as a perturbation motion. ISO disturbances are influenced by seasonal mean circulation and the climatological distribution of moisture through SST (Figure 10.1). The impact of background circulation is essential in explaining the seasonal behavior of the MJO (Section 10.5).

While the ISO is, to a large extent, determined by atmospheric internal dynamics, its coupling to the oceanic mixed layer may have a considerable impact on its behavior. The coupled formulation will be presented in Section 10.6.

10.3.2 Governing equations

The basic equations governing hydrostatic *perturbation* motion consist of conservations of momentum, mass, thermodynamic energy, and water vapor. These can be written as pressure coordinates on an equatorial β-plane:

$$\frac{\partial u}{\partial t} + \beta y v = -\frac{\partial \phi}{\partial x} + F_x + M(u) + F^U \tag{10.1a}$$

$$\frac{\partial v}{\partial t} - \beta y u = -\frac{\partial \phi}{\partial y} + F_y + M(v) \tag{10.1b}$$

$$\frac{\partial u}{\partial x} + \frac{\partial v}{\partial y} + \frac{\partial \omega}{\partial p} = 0 \tag{10.1c}$$

$$\frac{\partial}{\partial t}\frac{\partial \phi}{\partial p} + S(p)\omega = -\mu \frac{\partial \phi}{\partial p} - \frac{R}{C_p p} Q_c(p) + M\left(\frac{\partial \phi}{\partial p}\right) + \frac{R}{p} F^T \tag{10.1d}$$

$$\frac{\partial}{\partial t} M_c + \frac{1}{g}\int_{p_u}^{p_s} \nabla \cdot (\bar{q}\vec{V})\, dp = E_v - P_r + M(q) \tag{10.1e}$$

where $M(u)$, $M(v)$, $M(\partial\phi/\partial p)$, and $M(q)$ represent the following mean flow terms in which quantities with overbars denote basic state quantities:

$$M(u) = \left(-\bar{u}\frac{\partial u}{\partial x} - u\frac{\partial \bar{u}}{\partial x} - \bar{v}\frac{\partial u}{\partial y} - v\frac{\partial \bar{u}}{\partial y} - \bar{\omega}\frac{\partial u}{\partial p} - \omega\frac{\partial \bar{u}}{\partial p}\right) \tag{10.2a}$$

$$M(v) = \left(-\bar{u}\frac{\partial v}{\partial x} - u\frac{\partial \bar{v}}{\partial x} - \bar{v}\frac{\partial v}{\partial y} - v\frac{\partial \bar{v}}{\partial y} - \bar{\omega}\frac{\partial v}{\partial p} - \omega\frac{\partial \bar{v}}{\partial p}\right) \tag{10.2b}$$

$$M\left(\frac{\partial \phi}{\partial p}\right) = -\bar{u}\frac{\partial^2 \phi}{\partial x\, \partial p} - u\frac{\partial^2 \bar{\phi}}{\partial x\, \partial p} - \bar{v}\frac{\partial^2 \phi}{\partial y\, \partial p} - v\frac{\partial^2 \bar{\phi}}{\partial y\, \partial p} \tag{10.2c}$$

$$M(q) = -\int_{p_u}^{p_s}\left(\bar{u}\frac{\partial q}{\partial x} + \bar{v}\frac{\partial q}{\partial y}\right)\frac{dp}{g} \tag{10.2d}$$

In Equation (10.1) the dependent variables, u, v, ω, and ϕ, denote zonal and meridional wind, vertical pressure velocity, and geopotential height, respectively; β is meridional variation of the Coriolis parameter; $S(p)$ is the static stability parameter; F_x and F_y denote frictions; F^U and F^T are nonlinear interaction terms between the MJO and synoptic-scale systems. In the thermodynamic equation (10.1d), two diabatic heating terms are included—condensational latent heat and longwave radiation—in which μ denotes a constant coefficient for Newtonian cooling; Q_c expresses the condensational heating rate per unit mass; and R and C_p are the gas constant of the air and the specific heat at constant pressure, respectively.

Conservation of column-integrated water vapor M_c in (10.1e) requires the perturbation precipitation rate P_r to be balanced by the sum of the perturbation surface evaporation rate E_v, column-integrated moisture convergence, and the local rate of change of M_c. In the moisture convergence term, $\vec{V}$ represents horizontal wind and p_u and p_s are pressures at the upper boundary and the surface, respectively. Moisture

convergence depends on basic state specific humidity $\bar{q}$, which provides latent energy for perturbation motion and can be expressed as a function of pressure and mean SST over the ocean. Assume that the absolute humidity of the basic state atmosphere falls off with height exponentially with a water scale height $H_1 = 2.2\,\text{km}$. The mean specific humidity in an arbitrary vertical layer between pressure p_1 and p_2 where $p_2 > p_1$ is (Wang, 1988a):

$$\bar{q}(p_1, p_2) = q_0 \frac{(p_2^m - p_1^m)}{m(p_2 - p_1)} \tag{10.3a}$$

where $m = H/H_1$ is the ratio of the density scale height H to the water vapor scale height H_1; and q_0 is air specific humidity at the surface. Over ocean and on the timescale of a month or so, q_0 is well correlated with SST and may be approximated by the following empirical formula (Li and Wang, 1994):

$$q_0 = q_0(\text{SST}) = (0.94 \times \text{SST}(^\circ\text{C}) - 7.64) \times 10^{-3} \tag{10.3b}$$

The condensational heating rate Q_c must be constrained by the precipitation rate (i.e., the column-integrated condensational heating rate is linked to the precipitation rate):

$$\delta L_c P_r = \frac{1}{g} \int_{p_u}^{p_s} Q_c(p)\, dp \tag{10.3c}$$

where L_c is the latent heat of condensation; and δ represents a switch-on tracer for nonlinear heating in the absence of basic state rainfall: δ equals unity in the region of positive precipitation and zero otherwise. The heating is linear when $\delta \equiv 1$.

10.3.3 Boundary layer dynamics near the equator

In view of the importance of frictional moisture convergence in CID, in this subsection we derive the barotropic boundary layer dynamics in detail. The perturbation equations for a slab mixed layer flow have the form:

$$\frac{\partial u}{\partial t} + \beta y v = -\frac{\partial \phi_e}{\partial x} + g \frac{\partial \tau_{xp}}{\partial p} \tag{10.4a}$$

$$\frac{\partial v}{\partial t} - \beta y u = -\frac{\partial \phi_e}{\partial y} + g \frac{\partial \tau_{yp}}{\partial p} \tag{10.4b}$$

$$\frac{\partial \omega}{\partial p} = -\left(\frac{\partial u}{\partial x} + \frac{\partial v}{\partial y}\right) \tag{10.4c}$$

where ϕ_e is the geopotential at p_e (see Figure 10.3 on p. 354). Matching conditions require that vertical velocity and turbulent Reynolds stresses (τ_{xp}, τ_{yp}) are continuous at p_e; the latter implies

$$(\tau_{xp}, \tau_{yp}) = 0, \quad \text{at } p = p_e \tag{10.5a}$$

At the lower boundary, $p = p_s$, the Reynolds stress is related to surface wind by a simple linearized stress relationship, that is,

$$(\tau_{xp}, \tau_{yp}) = -\rho_e K_D (u_s, v_s), \quad \text{at } p = p_e \tag{10.5b}$$

where ρ_e is the air density in the boundary layer; K_D is a measure of surface drag; and $u_s = u(p_s), v_s = v(p_s)$. To determine K_D, we subdivide the boundary layer into a surface layer and an outer boundary layer (Blackadar and Tennekes, 1968). In the outer boundary layer, Equation (10.4) applies while in the surface layer the Reynolds stress is nearly constant and the wind profile is logarithmic. Matching the outer boundary layer with the surface layer at their interface leads to $K_D = A_z/[h_0 \ln(h_0/Z_0)]$, where A_z is the turbulent viscosity, h_0 the depth of the surface layer, and Z_0 is surface roughness length. Integrating Equations (10.4a–c) with respect to p from p_e to p_s, dividing the resulting equations by $(p_s - p_e)$, and using conditions (10.5a, b), we obtain

$$\frac{\partial u_b}{\partial t} + \beta y v_b = -\frac{\partial \phi_e}{\partial x} - E u_b \tag{10.6a}$$

$$\frac{\partial v_b}{\partial t} - \beta y u_b = -\frac{\partial \phi_e}{\partial y} - E v_b \tag{10.6b}$$

where u_b and v_b are vertical averaged boundary layer winds; and E is the friction coefficient in the boundary layer, where $E = \rho_e g K_D/(p_s - p_e)$. For typical parameter values, E is $O(10^{-5}\ \mathrm{s}^{-1})$ (Table 10.1).

Due to a change in sign of the Coriolis force at the equator, the dynamics of the equatorial boundary layer is at odds with quasi-geostrophic Ekman theory. In the subtropics or extratropics, the vertical velocity induced by boundary layer friction (Ekman pumping) is determined by vorticity at the top of the boundary layer (Eliassen, 1971). Near the equator, however, the solution of Equation (10.6) for steady motions yields

$$D = -\frac{E}{E^2 + \beta^2 y^2}\left(\nabla^2 \phi_e + \beta u_b + \frac{\beta^2}{E} y v_b\right) \tag{10.7}$$

where D is boundary layer divergence. Thus, frictional convergence in the deep tropics is determined by the Laplacian of the pressure at the top of the boundary layer and the strengths of eastward and poleward surface winds. This explains why the boundary layer convergence zone often occurs on the equatorward side of an off-equatorial monsoon trough. To the equatorward side of a monsoon trough the winds have an eastward and poleward component. The beta effect acting on both components causes convergence according to the second and third terms on the right-hand side of (10.7).

Table 10.1. Model parameter values used in Sections 10.4 and 10.5.

P_e	Pressure at the top of the boundary layer	900 hPa
Δ_P	Half-pressure depth of the free troposphere	400 hPa
SST	Sea surface temperature	29°C
C_0	Dry gravity wavespeed of baroclinic mode	$50\,\mathrm{m\,s^{-1}}$
r	Horizontal momentum diffusion coefficient	$10^6\,\mathrm{m^2\,s^{-1}}$
b	Precipitation efficiency coefficient	0.9
A_z	Vertical turbulent viscosity in the boundary layer	$10\,\mathrm{m^2\,s^{-1}}$
h_0	Depth of the atmospheric surface layer	40 m
z_0	Surface roughness depth	0.01 m
C_E	Heat exchange coefficient	1.5×10^{-3}
I	Heating coefficient due to wave convergence	0.84
B	Heating coefficient due to friction convergence	1.73
F	Heating coefficient due to evaporation	0.59
E	Ekman number in the boundary layer	3×10^{-5}
d	Non-dimensional boundary layer depth	0.25
h	Half-depth of the free troposphere	3.6 km

10.3.4 The 1.5-layer model for the MJO

In this subsection, a simplistic model for the ISO is formulated that includes the effects of the boundary layer. This model will be used to simulate the basic dynamics of the MJO in Section 10.4.

To simplify the vertical resolution of the model, we begin by analyzing the structure of vertical normal modes in the governing equation (10.1). For this purpose, let us consider the linear frictionless adiabatic motion of the dry atmosphere in a quiescent environment—namely, the friction terms, mean flow terms, all heating terms, and the moisture equations neglected in (10.1). The static stability parameter $S(p)$ is a function of pressure only. With these approximations, the vertical modes that satisfy the rigid boundary condition at the surface and at the top of the atmosphere (e.g., $\omega = 0$ at $p = p_u$ and p_s) are separable; each satisfies the so-called "shallow-water equation" with differing equivalent depth (or gravity wave speed) (e.g., Gill, 1980). The vertical structures of these modes are solely determined by basic state stratification.

For an idealized yet realistic dry atmosphere (an isothermal atmosphere, for example), the static stability parameter, $S(p)$, is proportional to the inverse of the pressure square. For such a stratified atmosphere, the vertical structures and phase speeds of vertical modes were derived analytically (Wang and Chen, 1989). The phase speed for the lowest four ($m = 1$, 2, 3, and 4) modes are approximately 50 m/s, 26 m/s, 18 m/s, and 13 m/s, respectively. Higher vertical modes have smaller equivalent depth and slower phase speed. The vertical velocity profiles for the lowest four vertical modes are shown in Figure 10.2. The gravest baroclinic mode has maximum vertical velocity in the middle of the atmosphere. The higher baroclinic modes have more nodes and shorter wavelengths. Since the vertical structure of the MJO is dominated by the gravest baroclinic mode, the simplest model of the MJO should consist of two layers in the free troposphere (Figure 10.3).

In the absence of basic flows, all terms in Equation (10.2) vanish. One can obtain a two-level free atmosphere system by writing the horizontal momentum and continuity equations (10.1a–c) at p_1 and p_3 and the thermodynamic equation (10.1d) at mid-level p_2 of the model free atmosphere. Motion in the two-level system can be alternatively represented by a baroclinic and a barotropic mode. In the presence of

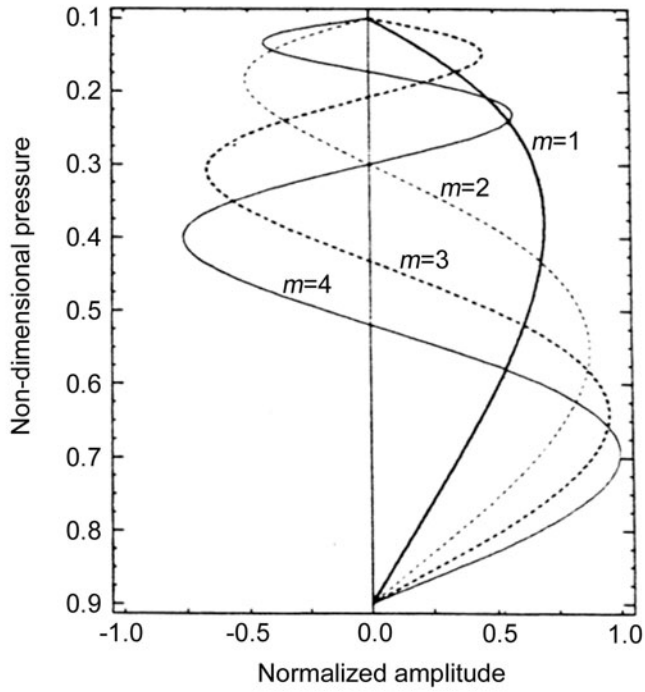

Figure 10.2. The vertical structures of the vertical pressure velocity for the first four internal modes computed for an isothermal atmosphere in which the static stability parameter is proportional to the inverse of the pressure square. The vertical pressure velocity vanishes at the upper ($p = 0.1$) and lower ($p = 0.9$) boundary (adapted from Wang and Chen, 1989).

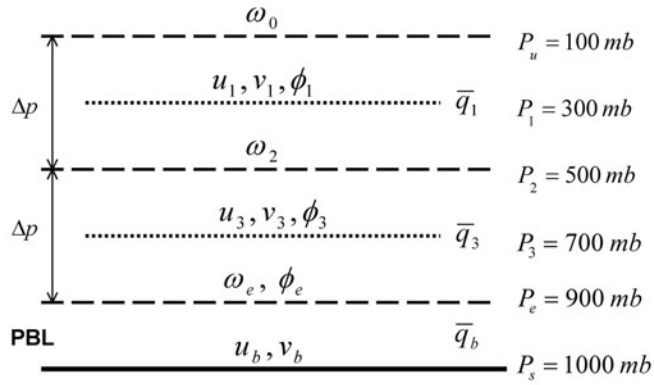

Figure 10.3. Schematic vertical structure of the 2.5-layer model of the ISO.

boundary layer friction, these two vertical modes are coupled through frictional convergence–induced vertical motion at p_e. To save space, the equations for this two-level system are not given here. Interested readers can find them in Wang and Rui (1990a). Note that only baroclinic mode is subjected to diabatic heating. Condensational heating is linked to the precipitation rate (Equation 10.3c). With the limited vertical resolution of the two-level system, the precipitation rate is expressed by

$$\delta P_r' = \delta b\{[-\omega_2 \bar{q}_3 - \omega_e(\bar{q}_e - \bar{q}_3)]/g + \rho_s C_E |V_b|(q_s - q_0)\} \tag{10.8}$$

where ω_e and ω_2 represent, respectively, vertical pressure velocities at the top of the boundary layer (p_e) and the mid-troposphere (p_2); g, ρ_s, and C_E are gravity, surface air density, and the heat exchange coefficient, respectively; V_b is windspeed at the surface $p = p_s$ that will be approximated by model boundary layer wind; q_s is the saturation specific humidity of SST, which can be calculated from the Clausius–Clapeyron equation. Equation (10.8) enables the governing equations to be a closed system.

It has been demonstrated that *in the absence of basic flows* the magnitude of barotropic mode is an order of magnitude smaller than that of baroclinic mode (Wang and Rui, 1990a; Wang and Li, 1993). Thus, a simplification can be made to neglect the barotropic mode by assuming a vanishing column integral of divergence in the free troposphere. Baroclinic mode in the free troposphere is governed by the following equations on an equatorial β-plane, after ω_2 and ω_e are eliminated by using the continuity equation:

$$\frac{\partial u}{\partial t} + \beta y v = -\frac{\partial \phi}{\partial x} \tag{10.9a}$$

$$\frac{\partial v}{\partial t} - \beta y u = -\frac{\partial \phi}{\partial y} \tag{10.9b}$$

$$C_0^{-2}\frac{\partial \phi}{\partial t} + (1 - \delta I)\nabla \cdot \vec{V} = d(\delta B - 1)\nabla \cdot \vec{V}_b - \delta F C_E |\vec{V}_b|/h \tag{10.9c}$$

where u, v, and ϕ represent lower-troposphere zonal and meridional wind and geopotential height, respectively (upper-tropospheric zonal and meridional wind are $-u$ and $-v$, respectively); $\vec{V}_b$ denotes boundary layer barotropic wind whose components (u_b, v_b) satisfy Equations (10.6a, b); $C_0 = 50\,\mathrm{m\,s^{-1}}$ denotes the dry gravity wavespeed of free troposphere baroclinic mode (corresponding to the gravest baroclinic mode in a vertically continuous model); $d = (p_s - p_e)/\Delta p$ is the dimensionless depth of the boundary layer; and $h = \Delta p/\rho_e g$, where Δp is half the pressure depth of the free troposphere. In the thermodynamic equation (10.9c) there are three non-dimensional heating parameters, which are defined by

$$I = \bar{q}_3/q_c \qquad \text{heating coefficient due to wave convergence} \tag{10.10a}$$

$$B = \bar{q}_e/q_c \qquad \text{heating coefficient due to frictional convergence} \tag{10.10b}$$

$$F = (q_s - q_0)/q_c \qquad \text{heating coefficient associated with evaporation} \tag{10.10c}$$

where $q_c = 2C_p p_s C_0^2/(bR\Delta p L_c)$ stands for vertical mean specific humidity in the lower-tropospheric layer, which corresponds to a vanishing effective static stability in the presence of convective heating. The standard values of model parameters used in this chapter are given in Table 10.1.

Equations (10.9a–c) and (10.6a, b) (with the assumption $\phi_e = \phi$) consist of a closed set of equations, which describes the moist dynamics of a single free troposphere baroclinic mode that is coupled with boundary layer motion. This model is an extension of the Matsuno (1966) model by including diabatic heating and the effects of the boundary layer. Such a model is referred to as a 1.5-layer model.

Note that, in a two-level free atmospheric model, heating is released in the middle of the troposphere; the closure assumption for condensational heating is provided solely by conservation laws of moisture and thermal energy through the linkage between the vertical integrated condensational heating rate and the precipitation rate in the same column (10.3c). Any type of cumulus parameterization, when boiled down to a two-level approximation, must obey the same physical principles. Therefore, use of (10.8) should not be considered a version of Kuo or any other specific parameterization schemes. The only approximation made in (10.8) is that the local change of moisture and moisture in the upper-tropospheric layer is neglected. An adjustable parameter b is introduced to compensate for the omission of moisture storage in the atmosphere. Parameter b represents condensation efficiency and measures the fraction of total moisture convergence that condenses out as precipitation. This simplification facilitates eigenvalue analysis. A two-level version of the time-dependent moisture equation (10.1e) and a transient boundary layer (rather than a steady boundary layer) have also been used; the results are not qualitatively different from those derived using these simplifications.

10.3.5 The 2.5-layer model including the effects of basic flows

As shown by Wang and Xie (1996), the presence of a mean flow directly couples baroclinic and barotropic modes and barotropic mode has a significant magnitude that can no longer be neglected. Thus, in the presence of mean flows, a full two-level

free troposphere is required. Similar to the formulation of the 1.5-layer model, one can obtain a two-level free atmosphere system by writing the horizontal momentum and continuity equations (10.1a–c) at p_1 and p_3 and the thermodynamic equation (10.1d) at mid-level p_2 of the model free atmosphere. In this case, the mean flow terms in (10.2) are included. Motion in this two-level system can be alternatively represented by a baroclinic mode and a barotropic mode. To save space, the equations for barotropic and baroclinic components are not shown here. Interested readers should refer to Wang and Xie (1996).

The ω_e in the free tropospheric equations is provided as a lower boundary condition and is determined from the boundary layer equations (10.6a, b). For a steady boundary layer, it can be shown that

$$\omega_e = D_1 \frac{\partial^2 \phi_e}{\partial x^2} + D_2 \frac{\partial \phi_e}{\partial x} + D_3 \frac{\partial^2 \phi_e}{\partial y^2} + D_4 \frac{\partial \phi_e}{\partial y} \tag{10.11}$$

where coefficients D_1 through D_4 are functions of latitude and model parameters (for details refer to Wang and Xie, 1997). Here ω_e is related to free atmospheric convergence by mass conservation in a vertical column, giving:

$$\omega_e = -\Delta p \sum_{k=1}^{2} \left(\frac{\partial u_k}{\partial x} + \frac{\partial v_k}{\partial y} \right) \tag{10.12}$$

By assuming $\phi_e = \phi_3$, Equations (10.11) and (10.12) along with the two-level finite difference versions of Equations (10.1) and (10.2) constitute a closed set of equations. Since the barotropic boundary layer is included in this two-level system, this set of equations will be referred to as a 2.5-layer system. For numerical details that solve the system, readers are referred to Wang and Xie (1997). This 2.5-layer model will be used in Section 10.5 when we study the seasonal behavior of the ISO.

10.4 DYNAMICS OF THE MJO

The elementary dynamics of the low-frequency disturbances producing MJO may be elucidated by examining the behavior of convectively interactive low-frequency motion in a quiescent atmosphere with underlying uniform SST. The simplest 1.5-layer model described in Section 10.3.4 is used. The simplicity of the model allows us to focus on basic atmospheric internal dynamics, such as frictional convergence instability (FCI) and multiscale interaction (MSI). The model is solved for both boundary value and initial value problems. The behavior of moist low-frequency motion will be compared against observed features of the MJO.

10.4.1 Low-frequency equatorial waves and the associated Ekman pumping

Let us begin by analyzing the basic wave motions relevant to MJO disturbances. For clarity, let us neglect diabatic heating for the time being in (10.9a–c) (i.e., $\delta = 0$).

The resulting equation describing the adiabatic baroclinic motion of the free troposphere becomes a shallow-water equation (e.g., Matsuno, 1966).

Because of the observed anisotropic lengthscales (the zonal scale is an order of magnitude larger than the meridional scale) of the MJO, geostrophic approximation can be applied to the v-momentum equation. This approximation is known as the longwave approximation (Gill, 1980). This approximation rules out high-frequency inertia–gravity waves. Thus, only low-frequency Kelvin and Rossby waves are relevant wave motions and communicators in the MJO.

Figure 10.4a illustrates the horizontal structure of the pressure fields for the Kelvin wave and the most equatorially trapped Rossby wave. These waves are slightly damped due to the presence of boundary layer friction (Equations 10.6a–b). The eastward-propagating Kelvin waves are strongly trapped to the equator and owe their existence to the vanishing Coriolis parameter there. Away from the equator, the geostrophic balance between the pressure gradient force and the Coriolis force dominates the frictionless atmospheric motion, which is a

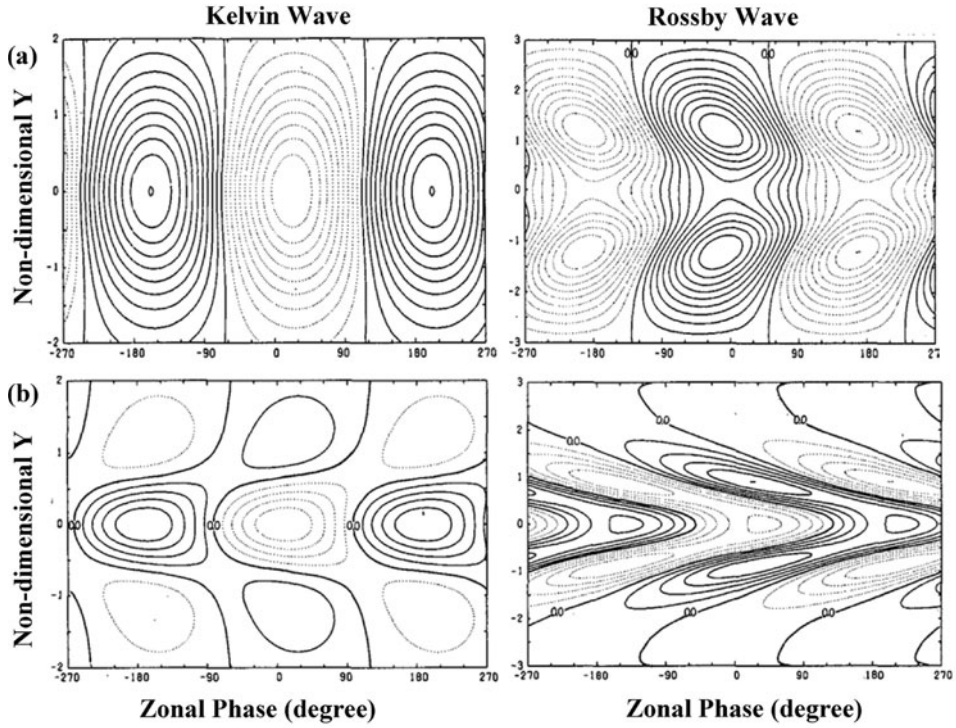

Figure 10.4. Horizontal structures of the equatorial Kelvin wave (left) and the most trapped equatorial Rossby wave (right) in the presence of boundary layer damping: (a) geopotential height (upper panels), and (b) vertical pressure velocity at the top of the boundary layer (lower panels). The meridional scale is the Rossby radius of deformation, whose unit corresponds to about 1,500 km.

characteristic of Rossby waves. The meridional variation of the Coriolis force strongly constrains the speed of westward propagation of Rossby waves. Overall, the structures are similar to their corresponding inviscid counterparts (Matsuno, 1966). A notable modification of Rossby waves is the equatorward and eastward slant of troughs and ridges.

Figure 10.4b shows vertical motions at the top of the boundary layer associated with the Kelvin wave and the most trapped symmetric Rossby wave shown in Figure 10.4a. The calculations were based on a steady version of Equation (10.6). For these waves, the Laplacian of pressure terms generally dominates frictional convergence (Equation 10.7). Thus, for Kelvin waves the friction-induced upward motion is located in its low pressure or easterly phase, while for the most trapped equatorial Rossby waves, the ascent occurs in both off-equatorial low pressures and the equatorial trough between the two off-equatorial high pressures. As a result, along the equator the maximum ascent (descent) leads the corresponding westerly (easterly) by about one eighth of a wavelength. Overall, upward motion in the Rossby wave is generally shifted eastward compared with the minimum pressure and strongest equatorial westerlies. This has important ramifications for Kelvin and Rossby wave coupling and selection of the eastward-propagating unstable mode in the presence of heating.

10.4.2 Frictional convergence instability (FCI)

Here we further consider the effect of convective heating (terms with the tracer δ) in the 1.5-layer model (Section 10.3.4). In the presence of interactive convective heating, the latent heat that drives equatorial waves is associated, respectively, with free tropospheric wave convergence, boundary layer frictional convergence, and surface evaporation (Equation 10.10). The wave-induced heating measured by parameter I can be estimated from Equations (10.10a), (10.3a), and (10.3b). I is a function of SST: $I = 0.72$ for SST $= 26^{\circ}$C and $I = 0.88$ for SST $= 30^{\circ}$C are typical parameter values of the tropical atmosphere listed in Table 10.1. The condition $I < 1$ means that the latent heating rate due to free tropospheric wave convergence is smaller than the adiabatic cooling rate arising from ascending motion in the mid-level of the model. Thus, the wave-induced convergence feedback in this model does not produce instability per se (no wave CISK). Note that if there were no boundary layer, the same set of parameters would yield a parameter $I > 1$ when SST exceeds 29°C. Thus, this stable regime is not due to artificial parameter tuning, rather it reflects the fact that free tropospheric wave convergence can only control a portion of moisture convergence, which in reality cannot produce wave CISK.

In a dynamic regime that is stable to wave CISK, the growth or maintenance of low-frequency waves has to rely on destabilization by other mechanisms such as frictional convergence feedback (B), surface wind–evaporation feedback (F), or cloud–radiative enhancement. When boundary layer moisture concentration is sufficiently high (or the underlying SST exceeds a critical value), the positive contribution of boundary layer frictional moisture convergence to wave growth would exceed its dissipative effect. Frictional moisture convergence thus acts to generate instability

(FCI). Unstable FCI mode was originally termed "frictional wave CISK mode" (Wang, 1988a). Since this unstable mode occurs in a dynamic regime stable to wave CISK, it is more meaningful to call this type of unstable mode "unstable FCI mode".

To investigate the nature of FCI mode, we first examine the behavior of the normal modes of the 1.5-layer model using linear heating ($\delta = 1$). The parameters used in the analysis are listed in Table 10.1. Normal mode analysis shows that an unstable eastward-propagating FCI mode exists as long as the basic state SST exceeds a critical value (Figure 10.5a). The growth rate of the unstable mode

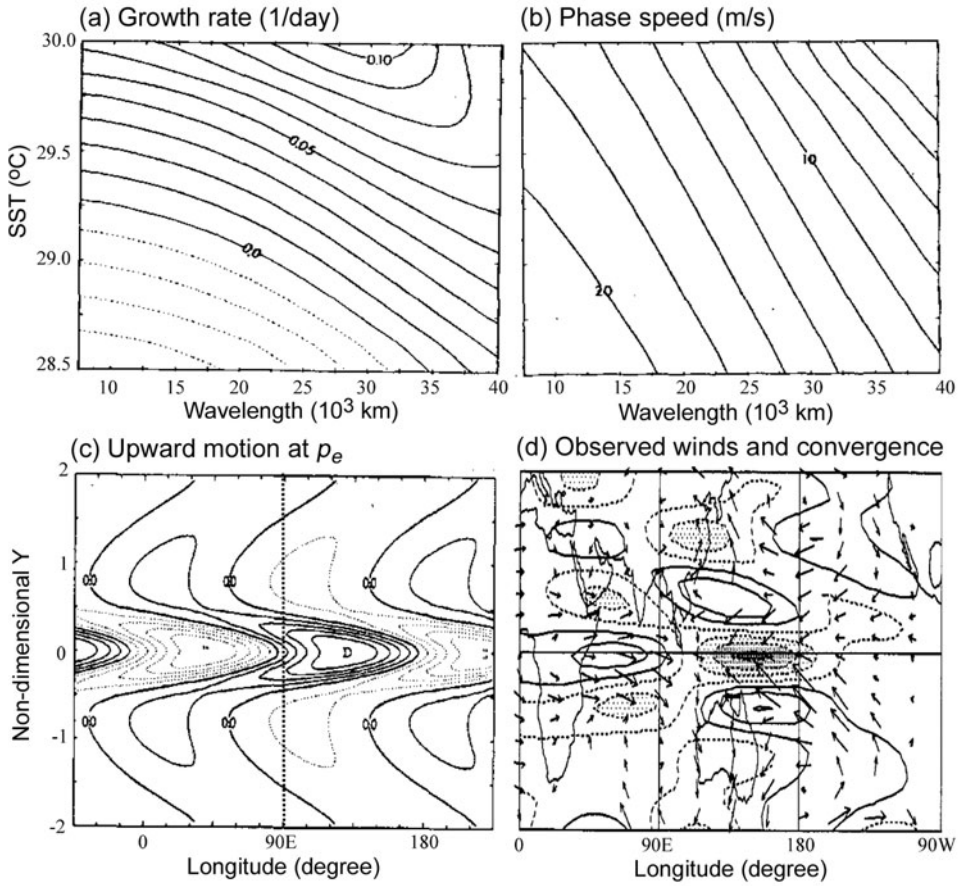

Figure 10.5. Behavior of FCI mode associated with the model MJO. (a) Growth rate and (b) zonal phase speed as functions of wavelength and maximum SST at the equator. (c) Normalized upward motion at the top of the boundary layer computed for the growing FCI mode under SST = 29.5°C. (d) Observed surface winds and convergence (contours). The meridional scale in (c) is the Rossby radius of deformation (about 1,500 km) ((a)-(c) adapted from Wang and Rui, 1990a and (d) from fig. 3 of Hendon and Salby, 1994).

increases with increasing background SST. In contrast to the shortwave blow-up of wave CISK, the longest wave is most unstable until the equatorial SST exceeds 29.5°C, above which the wavelength of the fastest growing wave shifts to 30,000 km. The propagation speed decreases with increasing SST and wavelength (Figure 10.5b). The phase speeds of the fastest growing waves are slow, about $5\,m\,s^{-1}$ to $10\,m\,s^{-1}$.

The growing mode exhibits equatorial symmetric and trapped geopotential and zonal wind fields, which resemble Kelvin waves. But it also has a significant meridional wind component, which is antisymmetric about the equator and resembles that of the most equatorially trapped Rossby waves. Thus, friction-induced ascending motion comprises mixed Kelvin and Rossby waves; along the equator it is located to the east of free tropospheric precipitation and rising motion (Figure 10.5c). This horizontal and vertical structure compares favorably with observations (Figure 10.5d), so do the spatial scales, slow propagation, and amplification.

Why does the unstable mode in the 1.5-layer model have a low-frequency growth rate and favor planetary scales? A fundamental reason is that frictional convergence, which supplies a large amount of moisture, is not in phase with wave-induced moisture convergence. This effectively reduces the strength of the interaction between wave-induced heating and overturning circulation, prohibiting unstable wave CISK. The energy source driving the instability comes from generation of eddy-available potential energy, which is proportional to the covariance between warming and heating. The frictional convergence to the east of major convection induces condensational heating, which overlaps the positive temperature anomaly, thereby generating eddy-available potential energy for growth of the unstable mode. Wang (1988a) has shown that the rate of generation of eddy energy by frictional moisture convergence increases with increasing zonal scale so that the planetary-scale mode is preferred.

What mechanism can hold eastward-propagating Kelvin waves and westward-propagating waves together and select eastward propagation? Why does it have a rearward tilt of rising motion against the direction of propagation? Again, the frictional convergence paradigm can address these questions. In a model without boundary layer convergence, it can be shown that a region of organized condensational heating may generate both Kelvin and Rossby waves. The convectively interactive Kelvin and Rossby waves would soon decouple and propagate in opposite directions (e.g., Li and Cho, 1997). As shown in Figure 10.4, Rossby wave–induced boundary layer convergence favors in part the development of moist Kelvin waves by producing equatorial convergence at the easterly phase, but Kelvin wave–induced frictional convergence favors its own growth. Therefore, the frictional organization of convective heating couples Kelvin and Rossby waves together but favors the Kelvin wave and selects eastward propagation. As such, frictional coupling creates a realistic mixed Kelvin and Rossby wave structure. In addition, boundary layer convergence coincides with the low-pressure (easterly) Kelvin wave response to the east of precipitation heating, thus boundary layer convergence leads to eastward-propagating precipitation anomalies.

What gives rise to the slow propagation speed such that the oscillation has an intraseasonal timescale? A primary cause is that wave convergence–induced heating, as measured by parameter I (Equation 10.10a), acts to reduce effective static stability by a factor of $(1-I)^{1/2}$ (about 0.35 at 30°C of SST), hence reducing the propagation speed of equatorial waves by a factor of 3. The results in Figure 10.5b indicate that the speed of the unstable mode is much slower than the pure moist gravity wave speed, which is $C_0(1-I)^{1/2}$ (about $17\,\mathrm{m\,s^{-1}}$), suggesting that the frictional coupling of Kelvin and Rossby waves operates as a brake on eastward movement. The reason is that the coupling-induced off-equatorial twin cyclonic cells resist eastward movement because the meridional transport of planetary vorticity constantly generates a westward-moving tendency for Rossby waves.

10.4.3 FCI mode under nonlinear heating

In Section 10.4.2, normal mode behavior under linear heating was examined using the 1.5-layer model. In this subsection, we further investigate the behavior of the time evolution of low-frequency motion in the same model but with nonlinear heating by solving the initial value problem. In the time integration of Equations (10.9a–c) and (10.6a–b), positive-only and SST-dependent nonlinear heating is used. This nonlinear SST-dependent heating is not only controlled by positive-only precipitation but also by the underlying SST. This SST-dependent heating is motivated by the observed relationship between SST and deep convection (Wang and Li, 1993). Physically, this formulation reflects the impact of the underlying SST on deep convection through changing the convective instability of the atmosphere. SST-dependent heating assumes that when the SST is below 26°C no convective heating occurs; when the SST increases from 26°C to 28°C the heating coefficient increases linearly from 0 to 1; and when the SST exceeds 28°C the heating coefficient equals 1. In order to eliminate small-scale numerical noise, two momentum diffusion terms—proportional to the Laplacian of u and v—are added, respectively, to Equations (10.9a–b) with the horizontal momentum diffusion coefficient r being $10^6\,\mathrm{m^2\,s^{-1}}$ (Table 10.1). All other parameter values used in the computation are given in Table 10.1. Integration is initiated by a pure Kelvin wave perturbation in the free troposphere. While the results confirm major conclusions derived from linear analysis, some new features are notable.

As is shown in Figure 10.6, the initial dry disturbance rapidly evolves into a multiscale wave packet: global-scale circulation coupled with a large-scale (several thousand kilometer) convective complex, which consists of a few synoptic-scale precipitation cells. Thus, nonlinear heating renders model low-frequency waves as having a planetary circulation scale with a concentrated precipitation region, a feature resembling the observed MJO structure.

Why does the circulation have a planetary wavenumber 1 structure, while precipitation is confined? Positive-only heating creates a precipitation core and widespread dry descending regions away from the core. The precipitation core moves slowly due to reduced effective static stability, but in descending regions the dry Kelvin wave moves eastward at a speed of $C_0 = 50\,\mathrm{m\,s^{-1}}$ and the dry Rossby

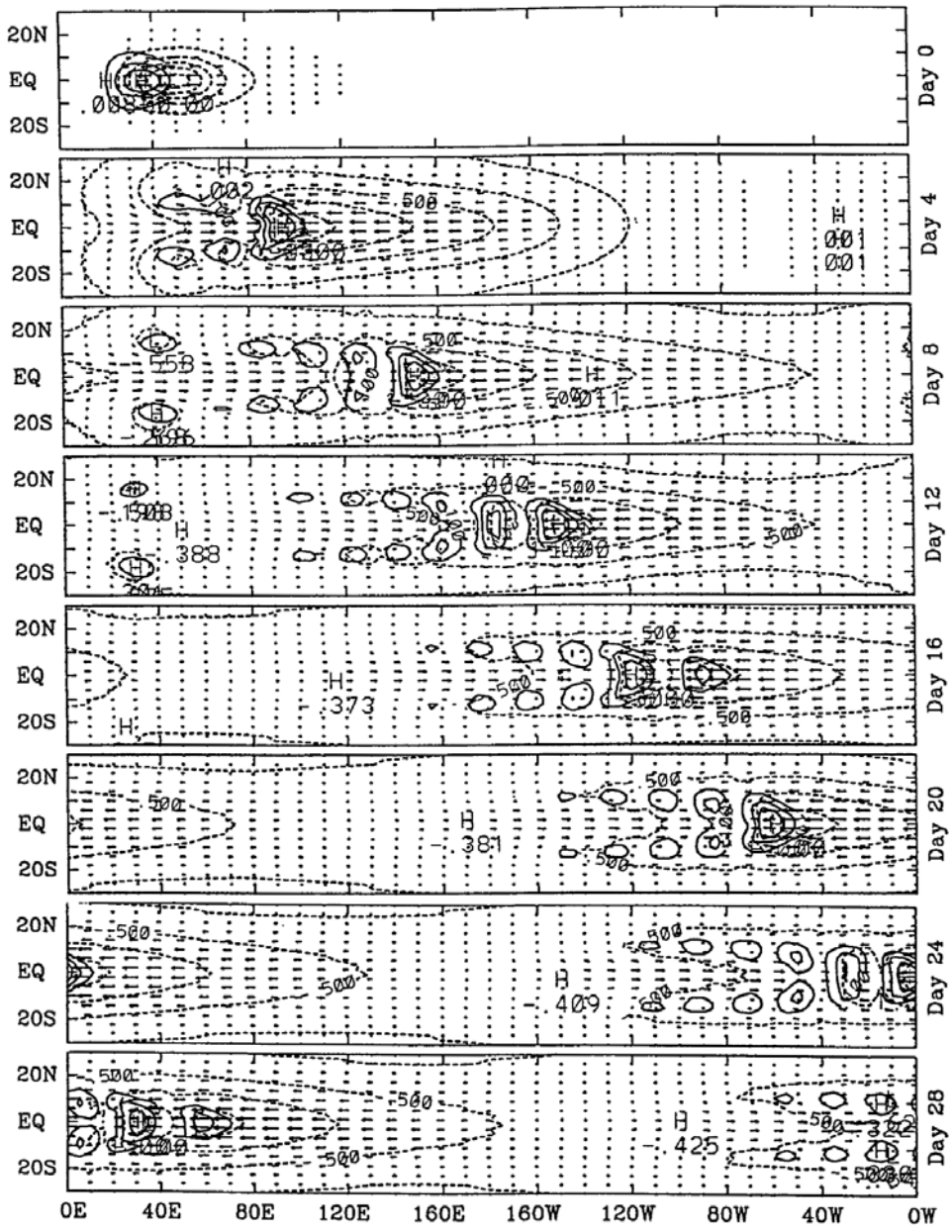

Figure 10.6. Sequential maps of the precipitation rate (solid contours) and lower-troposphere geopotential perturbation (dashed contours) and winds (arrows) for the Kelvin–Rossby wave packet induced by frictional convergence under nonlinear (positive-only and SST-dependent) heating. All three fields are normalized by their respective maxima at each panel. The contour starts from 0.1 and the interval is 0.2 (adapted from Wang and Li, 1994).

wave moves westward at a speed of $17\,\mathrm{m\,s^{-1}}$ (about one third the Kelvin wave speed). These dry waves expand dry regions until they are constrained by Earth's finite geometry. Thus, the spreading of energy by fast-propagating dry Kelvin and Rossby waves away from the precipitation complex forms the planetary circulation scale. Fast Kelvin waves have been seen in data (Milliff and Madden, 1996) and in AGCM experiments (Matthews *et al.*, 1999).

Heating released in the precipitation complex couples with equatorial waves, forming a *dispersive* wave packet in which energy propagation is slower than that of the individual cells within the complex (Figure 10.6). This offers a mechanism for slowing down the MJO in addition to reducing effective static stability and the coupling of Kelvin and Rossby waves. In the boundary layer, notable westerlies are located beneath major precipitation cells and convergence occurs to the east of the precipitation complex (figure not shown, see Wang and Li, 1994). Without boundary layer friction, the multiscale structure would disappear.

Wang and Li (1994) compare the growth rates that are induced by wave CISK (I), frictional moisture convergence feedback (B), and evaporation–wind feedback (F), using the same 1.5-layer model with the SST-dependent positive-only heating and the same parameter values given in Table 10.1. It was found that both the wind–evaporation feedback and wave CISK favor a synoptic-scale growth rate of $O(10^{-5}\,\mathrm{s^{-1}})$ in the absence of boundary layer friction, while the instability generated by frictional feedback has a low frequency with a typical growth rate of $O(10^{-6}\,\mathrm{s^{-1}})$. Observed development of the MJO over the Indian Ocean, for instance, takes a week or so to double the amplitude, which is much slower than synoptic-scale growth. When both frictional moisture convergence and wind–evaporation feedback are included, the resulting growth rate and other properties are very close to those of the FCI mode without WISHE. For more details, interested readers are referred to Wang and Li (1994).

Nonlinear FCI can help in understanding the pronounced longitudinal variability of propagation speed (Knutson *et al.*, 1986), development and decay (Wang and Rui, 1990b), as well as seasonality of the MJO. These longitudinal and seasonal variations are primarily due to underlying SST variations. Climatological SSTs determine the atmospheric convective instability and availability of moist energy (Figure 10.1). The longitudinal variation of SST has a major impact over cold sectors of the tropics where the atmosphere is sufficiently stable, and MJO disturbances propagate in the form of a damped moisture-modified Kelvin wave. In general, the MJO perturbation could travel around the globe and periodically regenerate and amplify over the warm ocean pools in response to a local buildup of instability (as shown by Salby *et al.*, 1994).

During northern winter and spring, the MJO shows a most coherent eastward propagation along the equator. The reason is that the SST distribution is largely symmetric about the equator and the background flow effect is not critical except for modulation by the ITCZ of the MJO. It has been shown that the greatest amplification of the equatorial Kelvin wave and associated subtropical Rossby gyres occurs when the maximum SST is located at the equator (Wang and Rui, 1990a) and when atmospheric heating is strongest at the equator (Salby *et al.* 1994).

10.4.4 The role of multiscale interaction (MSI) in MJO dynamics

In this subsection two types of synoptic systems are considered as interacting with the MJO: eastward-propagating supercloud clusters (SCCs) and westward-propagating 2-day waves—or westward-propagating inertial–gravity (WIG) waves (as observed by Nakazawa, 1988). The interaction between the planetary-scale MJO (represented by FCI) and synoptic disturbances is illustrated schematically in Figure 10.7. Based on observations, eastward-propagating SCCs tilt westward with height ("rearward tilt" with respect to the MJO), while westward-propagating 2-day waves tilt eastward with height ("frontward tilt" with respect to the MJO) (Johnson and Lin, 1997; Moncrieff and Klinker, 1997; Houze *et al*., 2000; Kiladis *et al*. 2005). SCCs prevail in the rear (low-level westerly) part of the MJO convective complex (Kiladis *et al*., 2005). Westward-propagating 2-day waves are assumed to prevail in the front part of the MJO convective complex, as found by Kikuchi and Wang (2010) using the spatiotemporal (2-D) wavelet transform. With the multiscale structure shown in Figure 10.7, SCCs in the rear part of the MJO complex can generate upscale low-level westerly momentum flux, while the frontward-tilted 2-day waves (WIGs) can induce upscale low-level easterly momentum flux. Thus, the upscale easterly/westerly momentum transfer occurring in the front/rear portion of the convective complex is in phase with the MJO easterly/westerly in the lower troposphere (Figure 10.7). Eddy

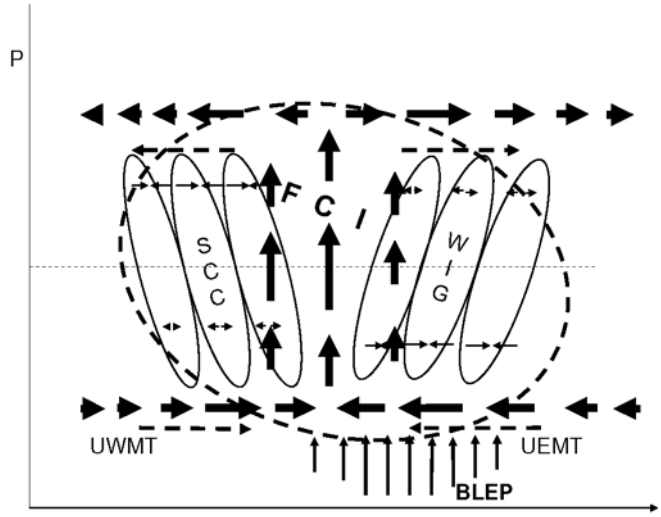

Figure 10.7. Schematic diagram describing the multiscale structure and interaction associated with the model MJO. The solid ellipse and short thin arrows denote vertically tilted synoptic disturbances (SCCs in the rear part and 2-day waves in the front part of the MJO convection center) and associated convergence/divergence, respectively. The long dashed arrows represent eddy-induced upscale easterly/westerly momentum transfer (UEMT/UWMT). The dashed ellipse and thick arrows represent, respectively, the convective complex and planetary scale zonal circulations associated with the MJO. The long thin arrows represent boundary layer Ekman pumping (BLEP) (modified from Wang and Liu, 2011).

momentum transfer (EMT) can be expressed as (Biello and Majda, 2005; Wang and Liu, 2011)

$$F^U = \frac{1}{2}\frac{U(P)}{|U_{\max}(P)|} AF(X)^2\alpha(1-\alpha)\sin(\phi_0)V(p)M(Y) \tag{10.13}$$

where $U(P)/|U_{\max}(P)| > 0$ for the westerly and $U(P)/|U_{\max}(P)| < 0$ for the easterly in the lower troposphere. Here A represents dimensional amplitude; $F(X)$ is the envelope function of synoptic-scale motions; and α stands for the relative strength of deep convection to total heating. The strength of stratiform and congestus heating are assumed to be equal (i.e., $(1-\alpha)/2$). The vertical structure $V(p) = \cos(1-p/p_e)\pi - \cos 3(1-p/p_e)\pi$ results from the interaction between stratiform/congestus and deep convective heating. $M(Y) = 2H^2 + YHH_Y$ with $H = e^{-2Y^2}$ denoting the meridional structure of synoptic waves.

Assuming that planetary-scale moisture convergence in the lower troposphere, $\bar{q}_F$, determines the location and strength of synoptic disturbances, the zonal structure of F^U in (10.13) is $F(X)^2 = \bar{q}_F$; here the square term was used to keep MSI instability at the same order of magnitude as FCI. The meridional structure of F^U can also be represented by that of large-scale moisture convergence $\bar{q}_F$, thus $M(Y)$ is no longer necessary and (10.13) becomes

$$F^U = \frac{1}{2}\frac{U(P)}{|U_{\max}(P)|} A\alpha(1-\alpha)\sin(\phi_0)V(p)\bar{q}_F \tag{10.14}$$

Large-scale motion in the free troposphere is dominated by the first baroclinic mode. For simplicity, we project the vertical structures of EMT to the first baroclinic mode in a two-layer model. Since the first baroclinic mode of temperature and deep convective heating have a maximum at the middle troposphere P_m, upscale EMT (as depicted by (10.14)) is simplified as $F_1^U \approx 4U/|U_{\max}|A\alpha(1-\alpha)\sin(\phi_0)\bar{q}_F/3\pi$.

Using a characteristic velocity scale $C_0 = \sqrt{S\Delta p^2/3} \approx 49\ \mathrm{m\ s^{-1}}$ (the gravest internal gravity wavespeed, Wang 1988a), lengthscale $L_c = \sqrt{C_0/\beta} \approx 1{,}460\ \mathrm{km}$, timescale $T_c = 1/\sqrt{\beta}C_0 = 0.34\ \mathrm{day}$, and geopotential height scale C_0^2, the dimensionless governing equation for the MSI model becomes (Wang and Liu, 2011):

$$U_t - YV + \Phi_X = c_1\frac{U}{|U_{\max}|}\alpha(1-\alpha)\bar{q}_F - dU \tag{10.15a}$$

$$YU + \Phi_Y = 0 \tag{10.15b}$$

$$\Phi_t + (U_X + V_Y) = -\alpha(\bar{q}_E + \bar{q}_F) - d\Phi \tag{10.15c}$$

$$\bar{q}_E = c_2(\nabla^2\Phi - \Phi_X) \tag{10.15d}$$

$$\bar{q}_F = -c_3(U_X + V_Y) \tag{10.15e}$$

where non-dimensional coefficients c_1, c_2, c_3 and all other parameters are explained in Table 10.2. The terms involving c_1, c_2, and c_3 denote, respectively, the magnitudes of EMT, boundary layer moisture convergence, and lower free troposphere moisture convergence.

Table 10.2. List of MSI model parameters for wavenumber 1.

Parameter	*Description*	*Value*
β	Meridional variation of the Coriolis parameter	$2.3 \times 10^{-11}\ \mathrm{m^{-1}\ s^{-1}}$
C_0	Gravity wave speed of the gravest baroclinic mode	49 m/s
d	Momentum and heat damping (dimensional) coefficient in the free troposphere	$3 \times 10^{-7}\ \mathrm{s^{-1}}$
E	Ekman damping coefficient	$3 \times 10^{-5}\ \mathrm{s^{-1}}$
ϕ_0	Spatial lag between stratiform and deep convective heating	$\pi/4$
α	Ratio of deep convective heating to total heating	1–0.5
A	Dimensional amplitude of the EMT	$0.1\ \mathrm{m\ s^{-2}}$
ΔP_b	Depth of the boundary layer	$P_s - P_e$
q_c	Mean specific humidity in the lower free troposphere	$\frac{1}{\Delta p}\int_{P_s}^{P_e} q(P)\,dP$
q_b	Mean specific humidity in the boundary layer	$\frac{1}{\Delta p_b}\int_{P_e}^{P_s} q(P)\,dP$
c_1	Constant associated with EMT	$4A\sin(\phi_0)/(3\pi C_0\sqrt{\beta C_0})$
c_2	Constant associated with boundary layer moisture convergence	$\frac{\sqrt{\beta C_0}}{E}\frac{\Delta p_b}{P_M}(q_b - q_c)\frac{L_q R}{C_0^2 C_p}$
c_3	Constant associated with lower-tropospheric moisture convergence	$\frac{\Delta P}{P_M} q_c \frac{L_q R}{C_0^2 C_p}$

The values listed here were used in the numerical computation unless otherwise noted. Parameters not listed here take the same values as in the standard case (Table 10.1).

In terms of model parameters, three distinct dynamic regimes can be identified: (1) a pure FCI regime with $P_e < P_s$ (presence of boundary layer) and $\alpha = 1$ (i.e., only deep convective cloud is present), and EMT vanishes because of the absence of vertical tilt of synoptic systems; (2) a pure EMT regime with $P_e = P_s$, and $c_2 = 0$, which means the absence of boundary layer frictional convergence (or FCI). In this case, the solution corresponds to a pure EMT regime if $\alpha < 1$; (3) an MSI regime with $\alpha < 1$ and $c_2 > 0$, which represents a general case involving both FCI and EMT mechanisms.

The MSI model (10.15) was solved as an initial value problem. The initial perturbation was a small-amplitude, equatorial Kelvin wave depression centered at 90°E. For simplicity, only a single vertical mode was considered and the role of barotropic mode was neglected.

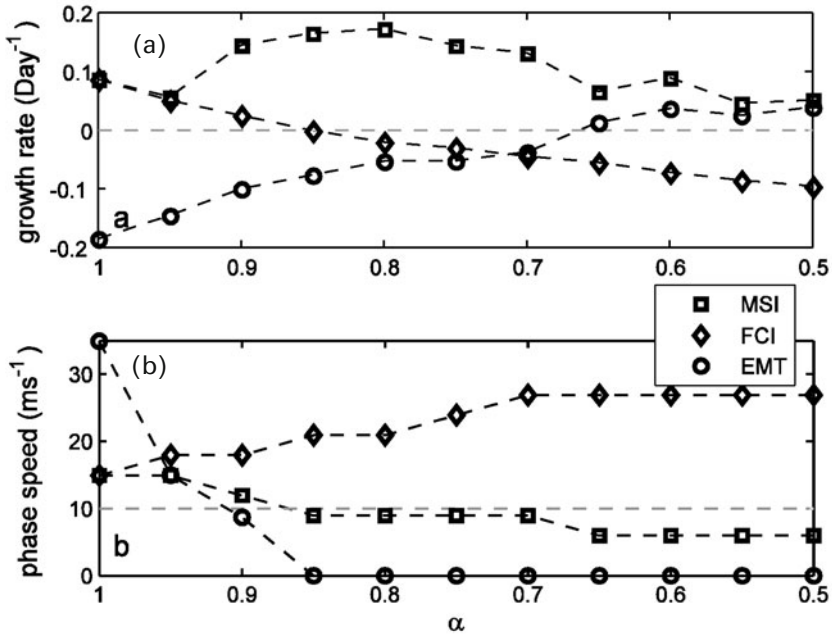

Figure 10.8. The properties of FCI, EMT, and MSI modes for wavenumber 1. (a) Growth rate and (b) phase speed as functions of α (the ratio of deep convective vs. total condensation heating). Other parameter values used are listed in Table 10.2 (modified from Wang and Liu, 2011).

The growth rate and phase speed of the MSI mode are expected to vary with the cloud aspect ratio α, which represents the fraction of deep convective vs. total heating for synoptic systems and the MJO. Note that α also depicts the proportion of condensational heating that is projected onto the gravest baroclinic mode of FCI (10.15c) and affects the strength of EMT feedback and the coupling between FCI and EMT (10.15a). In Section 10.4.2, the unstable FCI mode corresponds to $\alpha = 1.0$. When the amount of stratiform/congestus clouds equals that of deep convection, α is 0.5. It is seen from (10.15a) that EMT feedback reaches its maximum when $\alpha = 0.5$.

Figure 10.8 shows the growth rate and zonal propagation speed as a function of α for wavenumber 1. The growth rate of FCI mode decreases, but the phase speed increases with decreasing α because when α decreases the amount of deep convective heating that is projected to FCI mode decreases, thus the effective static stability of the basic state would increase.

In sharp contrast, the growth rate of EMT mode increases with decreasing α, or with increasing amount of non-deep convective clouds (Figure 10.8a). When $\alpha \geq 0.9$, EMT mode is strongly damped and propagates fast (Figure 10.8b) because the stratiform/congestus cloud heating is too weak to support instability and the phase speed is dominated by the eastward-propagating dry Kelvin wave. When the stratiform/congestus heating rate increases, EMT mode starts growing at

$\alpha < 0.7$, meanwhile eastward propagation decreases rapidly and at $\alpha < 0.85$ EMT mode becomes stationary.

What is most interesting about Figure 10.8 is that MSI mode—driven by the interaction between FCI and EMT—produces growing modes regardless of the value of α. MSI mode shows fast growth when $0.7 < \alpha < 0.9$ for which the FCI or EMT mechanism alone produces damped modes, suggesting that FCI and EMT interact cooperatively to contribute to MSI instability.

It is also interesting that the phase speed of MSI mode follows that of FCI mode when $\alpha = 1$ or 0.9 but then rapidly decreases and remains below $10\,\mathrm{m\,s^{-1}}$ thereafter, indicating that the EMT mechanism plays an effective role in slowing down eastward propagation. EMT mode displays enhanced Rossby wave responses (Figure 10.9b), which can efficiently slow down eastward propagation of MSI mode. Observed slow propagation often occurs when stratiform/congestus clouds are fully developed. The results shown in Figure 10.8b indicate that the phase speed of MSI mode is comparable with observations of an MJO (0–$10\,\mathrm{m\,s^{-1}}$) that had a fully developed stratiform/congestus in its convective complex.

The horizontal structure of FCI mode resembles a Gill-like pattern (Gill, 1980) with a very weak Rossby wave component (Figure 10.9a). The horizontal structure is basically consistent with the previous results (Wang and Li, 1994), but the Kelvin wave component has a stronger intensity than the Rossby wave component. EMT mode arising from multicloud interaction alone is a stationary Rossby wave-like system. There is strong convergence between the prominent equatorial westerly and easterly anomalies. In off-equatorial regions, a pair of weak anticyclones associated with equatorial easterlies leads a pair of strong cyclones that are associated with equatorial westerlies (Figure 10.9b). In contrast to FCI mode, EMT mode has an enhanced Rossby wave component in the equatorial westerly region of the MJO.

The unstable MSI mode exhibits a horizontal quadrupole–vortex structure (Figure 10.9c) with a pair of relatively weak anticyclones—leading a pair of strong cyclones—that propagate eastward at a slow speed of $6\,\mathrm{m\,s^{-1}}$. MSI mode has a convective envelope similar to that of FCI mode and a quadrupole–vortex structure similar to that of EMT mode. MSI mode overcomes the unrealistic structure of FCI mode (in which a large part of convection occurs in the easterly region) and the unrealistic propagation of EMT mode (stationary), leading to improved agreement with the observed MJO.

In much the same way as FCI mode, MSI mode has boundary layer convergence leading free tropospheric heating. Overall, MSI mode resembles the observed MJO in its slow eastward propagation, its quadrupole–vortex horizontal structure, and its backward-tilted vertical structure (in which boundary convergence leads wave convergence), all of which are essential features of the MJO.

Because a pure growing EMT mode is stationary, the eastward propagation of MSI mode comes from the FCI mechanism, suggesting that the FCI mechanism is essential for selecting eastward propagation. FCI also supports the backward-tilted vertical structure. While the EMT mechanism alone does not explain eastward propagation, it favors a quadrupole–vortex structure with an enhanced Rossby

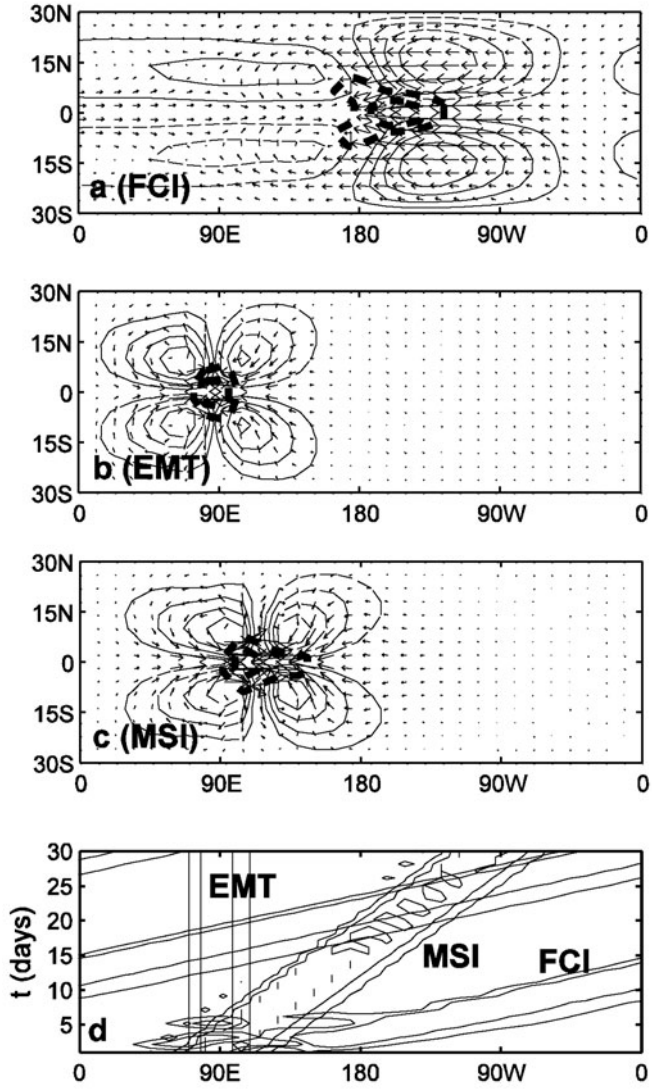

Figure 10.9. Horizontal structures of three unstable modes arising from (a) frictional convergence instability (FCI), (b) eddy momentum transfer (EMT), (c) multiscale interaction (MSI) and their movements along the equator (d). Here the structures were made for $\alpha = 0.6$ and at day 7 and shown by planetary-scale winds (vectors) and areas of convective heating (thick contour), as well as the streamline (thin contours). The vectors and convective heating contours are scaled to their respective maximum magnitudes: (a) $1.5\,\mathrm{m\,s^{-1}}$, $0.2\,\mathrm{K\,day^{-1}}$; (b) $3.7\,\mathrm{m\,s^{-1}}$, $0.45\,\mathrm{K\,day^{-1}}$; (c) $4.0\,\mathrm{m\,s^{-1}}$, $0.6\,\mathrm{K\,day^{-1}}$. The movements are shown by the time–longitude diagram of the simulated core heating associated with the FCI, EMT, and MSI modes. Contour interval is 0.4 for the heating rate and 0.2 for the streamfunctions, respectively. Zero contours are not drawn and negative streamfunctions are dashed. The amplitude is a growing function of time (adapted from Wang and Liu, 2011).

wave component and plays a critical role in slowing down the eastward propagation of the MJO convective complex.

In this model, only the first baroclinic mode is considered such that all moisture convergence produced by boundary layer Ekman pumping stimulates only the first baroclinic mode. This oversimplified representation neglects the coupling effect of boundary layer convergence on vertical modes and cannot favor longwave growth (Wang, 1988a). The inclusion of higher vertical modes in the description of the EMT mechanism and the role of boundary layer moisture preconditioning would provide a more realistic model for MJO dynamics. We have also assumed a fixed phase lag between synoptic activity (EMT) and the MJO convective complex and an equal number of stratiform and congestus clouds, which yields a stationary EMT mode. Further consideration of wavelength-dependent phase lags and study of the impact on phase propagation of EMT mode under different multicloud structures are warranted.

10.5 DYNAMICS OF BOREAL SUMMER ISO

During boreal summer, MJO disturbances weaken significantly and major centers of ISO variability in convection and precipitation move to the northern hemisphere Asian–Pacific summer monsoon region. Prominent northward propagation takes place in the Indian monsoon region. In the off-equatorial regions of the western North Pacific (WNP), westward and northwestward propagation prevails (Murakami, 1980; Lau and Chan, 1986; Chen and Murakami, 1988; Wang and Xu, 1997). In addition, there exists a stationary component, a convective seesaw between the equatorial Indian Ocean and the WNP (Zhu and Wang, 1993; Zhang and Hendon, 1997). Therefore, boreal summer ISO behaves in a much more complicated manner than the MJO (see Chapters 3 and 4). This section aims to explain the complex behavior of boreal summer ISO.

Recent observations have established two fundamental features of boreal summer ISO. First, the dominant mode of the ISO exhibits an eastward-moving precipitation band that is tilted northwestward from the equator, tailing the main center of equatorial convection associated with the MJO (Ferranti *et al.*, 1997; Annamalai and Slingo, 2001; Waliser *et al.*, 2003b). Second, the equatorial eastward-propagating MJO tends to bifurcate poleward near Sumatra (Maloney and Hartmann, 1998; Kemball-Cook and Wang, 2001; Lawrence and Webster, 2002; Wang *et al.*, 2005). It is important to get a grip on what is responsible for these observed features. This is the aim of the current analysis.

10.5.1 Effects of mean flows on the ISO

Wang and Xie (1997) propose that the complexity of the ISO during summer (see Chapters 2 and 3) could be understood as consequences of the impact of seasonal mean circulations and SST (or surface specific humidity). Based on this premise, they

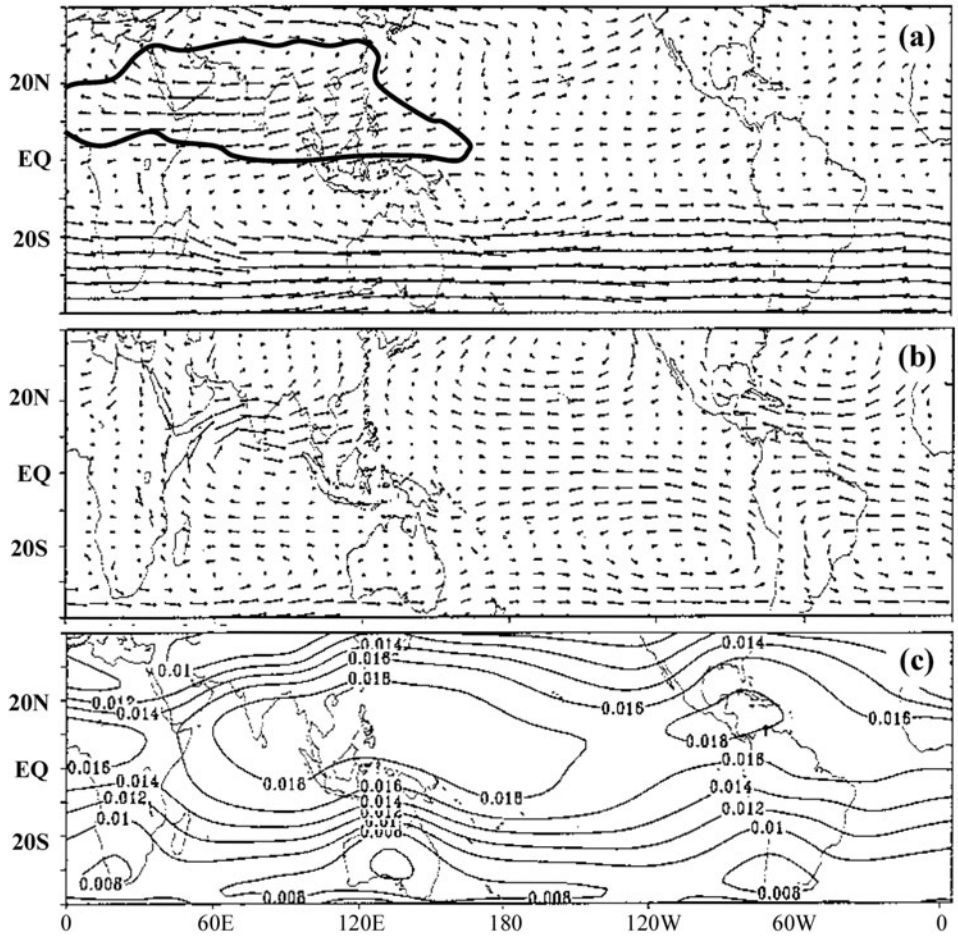

Figure 10.10. Climatological July mean winds at 200 hPa (a) and 850 hPa (b) and July mean specific humidity at 1,000 hPa (c). The thick contour in panel (a) represents the contour of $-4\,\mathrm{m\,s^{-1}}$ of July mean U_{200}–U_{850}, which outlines the regions with significant easterly vertical shears. The data used were derived from ECMWF reanalysis for the period 1979–1992.

construct a prototype model for explaining the seasonal behavior of the ISO, which was described in Section 10.3.5. In their model, they prescribe climatological July mean flows and surface specific humidity (or, equivalently, SST) as the typical boreal summer basic state. Model upper-layer and lower-layer basic flows and surface specific humidity are shown in Figure 10.10. An initial perturbation is a Kelvin wave-like zonal wind perturbation with a circular shape and a diameter of 4,000 km centered at 40°E on the equator. Wind variations follow a cosine function in both the zonal direction and the meridional direction. The geopotential field and the temperature field are determined by semi-geostrophic and hydrostatic balance, respectively.

Figure 10.11 shows snapshot views of the lower-tropospheric wind and precipitation rate every 4 days. Bear in mind that upper-tropospheric perturbation winds in this model are nearly 180° out of phase with lower-tropospheric winds. The initial disturbance moves eastward along the equator, as its major component is an equatorial Kelvin wave (Figure 10.11a). Because boundary layer friction generates a meridional flow that feeds back to convection, by day 4 the perturbation develops into a precipitation complex consisting of an equatorial cell and two off-equatorial cells, indicating that the perturbation evolves into a Kelvin–Rossby wave packet coupled with convective heating similar to that shown in Figure 10.6. When the wave packet approaches the maritime continent, it weakens because of a reduction in basic state specific humidity (Figure 10.10c), meanwhile Rossby wave cells—having a typical zonal scale of 2,000 km to 4,000 km—emanate from the packet and move northwestward. By day 6 these Rossby wave cells produce a northwest–southeast-tilted rainband from India to Borneo (Figure 10.11b). When the equatorial packet arrives at the Western Pacific at day 10, it starts emanating Rossby cells again (Figure 10.11c). By day 14 the equatorial disturbance weakens and stalls east of the dateline (Figure 10.11d) while sending fast eastward-propagating Kelvin waves that cross the Eastern Pacific (Figure 10.11e) and South America (Figure 10.11f) and dissipate in the Atlantic (Figure 10.11g). On the other hand, the moist Rossby cells emanating over the Philippine Sea at day 10 continuously migrate northwestward through the South China Sea and back to India. When the northern cell decays in the Arabian Sea due to "blocking" of the sinking dry airmass over North Africa, the southern cell re-initiates equatorial perturbation (Figure 10.11f) and starts the next cycle. The whole lifecycle spans about 4 weeks. It is worthy of note that intraseasonal disturbances in this model experience development and decay locally due to variations in basic state moisture distribution (as reflected by surface specific humidity) and the influences of basic state circulation. While this idealized lifecycle exaggerates the strength of off-equatorial westward propagation, there are some notable features that provide useful hints in our efforts to understand observed boreal summer ISO.

First, model low-frequency disturbances invoke not only equatorial trapped Kelvin–Rossby wave packets but also off-equatorial Rossby wave activity. The result here suggests that boreal summer mean circulation and spatial variations in the moist static energy of mean flows can trap moist Kelvin and Rossby waves within the northern summer monsoon domain, which is defined as a region with easterly vertical shear (Figure 10.10a) and surface specific humidity exceeding $18\,g\,kg^{-1}$ (Figure 10.10c). The westward-propagating perturbations in the model are readily identified as the gravest meridional mode of moist equatorial Rossby waves that are destabilized and modified by monsoon easterly vertical shears. Wang and Xie (1996) and Xie and Wang (1996) show that easterly vertical shear and convective heating can destabilize equatorial Rossby waves; the resulting most unstable wavelength is about 4,000 km; furthermore, when easterly shear is confined to the northern hemisphere as in the case of the northern summer monsoon, the structure of Rossby waves can become remarkably asymmetric about the equator with the southern cell severely suppressed and close to the equator. Krishnan *et al.* (2000) suggest that rapid northwestward-propagating Rossby waves from the central Bay of

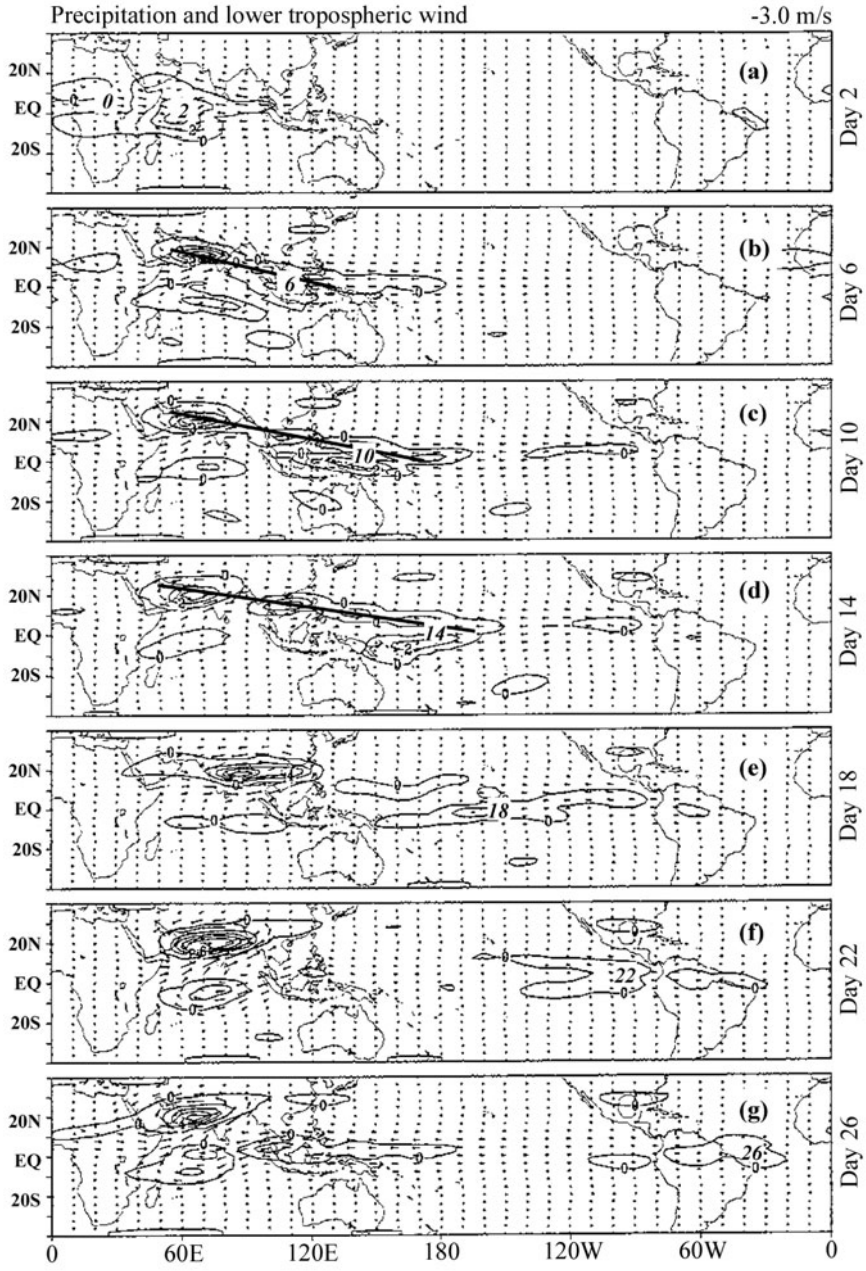

Figure 10.11. Sequential maps of the lower-tropospheric winds and precipitation rate (contour interval 2 mm day^{-1}) for the Kelvin–Rossby wave packet induced by frictional convergence under nonlinear heating and in the July mean basic state. The straight line indicates tilted precipitation bands. The numbers denote the day of model integration, which traces the locations of major precipitation centers (modified from Wang and Xie, 1997).

Bengal toward northwest India and the decoupling of the eastward-propagating equatorial anomaly determine the transition from a wet phase to a break phase of the Indian summer monsoon.

Second, the model is able to simulate the northwest–southeastward-tilted rainband (Figure 10.11; see also Figure 2.11). Model results suggest that this tilted rainband consists of emanated moist Rossby cells moving west-northwestward. The radiation of moist Rossby waves is longitudinally phase-locked to weakening or disintegration of equatorial wave packets over Indonesia and over the equatorial Central Pacific due to decrease in SST or mean state latent energy. The decay of equatorial eastward-propagating disturbances over these two longitudes is an observed feature. The decay near the dateline is due mainly to the sharp decrease in SST. However, the die-out over Indonesia is not solely due to reduction of mean state latent energy, it might involve multifactors that are not included in the model. The topographic blocking of Sumatra Island (a mountain range higher than 2 km) could be destructive to the boundary layer organization of MJO convection. The strong diurnal cycle over Indonesia is also an unfavorable condition for the MJO because it constantly releases convective energy and destroys the energy accumulation needed on the MJO timescale. Destructive land effects on the air–sea interaction that is a positive contributor to the MJO represent another possibility.

Third, model results are instrumental for understanding the nature of northward propagation over the northern Indian Ocean. The longitude–time diagrams along 90°E and 110°E show slow northward migration of precipitation (Figure 10.12). Model northward propagation over the eastern Indian Ocean and north of Indonesia is an integrated part of the movement of the northwest–southeast-tilted rainband. The northwestward propagation of moist Rossby waves that is modulated by the equatorial eastward MJO mode is also relevant in explaining the observed northwestward propagation of low-frequency cloud and vorticity anomalies on bi-weekly and 30-day periods observed over the western North Pacific (Nitta, 1987; Lau and Lau, 1990).

Fourth, the lifecycle shown in Figure 10.11 tends to repeat itself in the 90-day model integration (figure not shown, see Wang and Xie, 1997). This recurrence of the ISO cycle suggests a self-sustaining mechanism of monsoon ISO. The results obtained from a suite of reduced physics experiments in Wang and Xie (1997) suggest that basic state meridional and Walker circulations play a critical role in regeneration of disturbances over the equatorial Indian Ocean. When these mean circulations are removed from model basic flows, the southern cell of Rossby waves is suppressed and re-initiation of the equatorial perturbation is so weak that the ISO cannot be sustained.

10.5.2 Mechanism of northward propagation

A critical question in explaining the northwest–southeast tilt of the precipitation band and associated northward propagation of the ISO is what causes Rossby waves to have a northward propagation component. Obviously, without mean flows, emanated Rossby waves move only westward as shown in Figure 10.6. It is

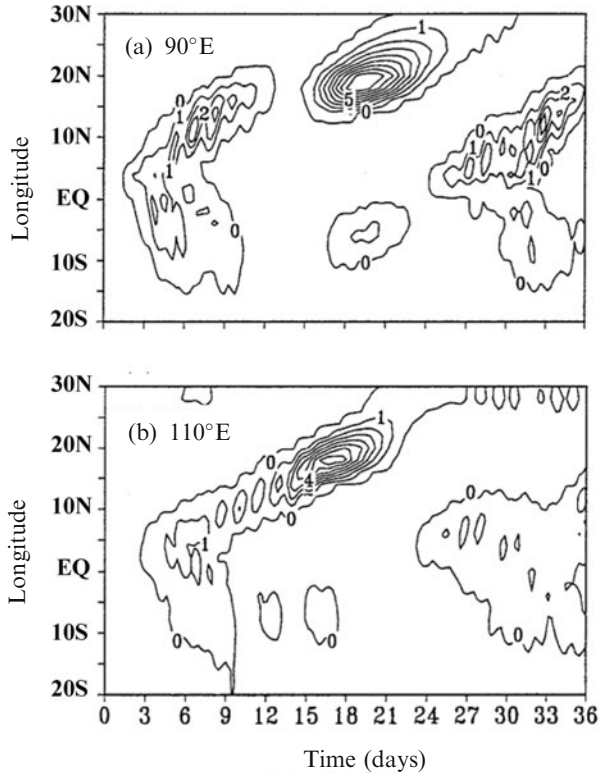

Figure 10.12. Time–longitude cross-sections of the precipitation rate along (a) 90°E and (b) 110°E for the experimental results shown in Figure 10.11. The contour interval is 1 mm day^{-1} (modified from Wang and Xie, 1997).

the presence of the basic flow that induces the northward propagation component. However, what specific factors in summer mean circulation are responsible for the northward propagation? This remains an issue. The works of Jiang *et al.* (2004) and Drbohlav and Wang (2005) identify the effect of easterly vertical shear as an important internal dynamic factor.

To illustrate this mechanism, let us consider a simplified 2-D version of the model of Wang and Xie (1996) in which zonal variations of the basic state and dependent variables are neglected. The vorticity equation for the barotropic component (denoted by the subscript "+") is (see Wang and Xie, 1996 for derivation)

$$\frac{\partial \zeta_+}{\partial t} = -\beta v_+ - U_T\left(\frac{\partial \omega}{\partial y}\right) \tag{10.16}$$

where U_T denotes the constant vertical shear of basic zonal flow. Equation 10.16

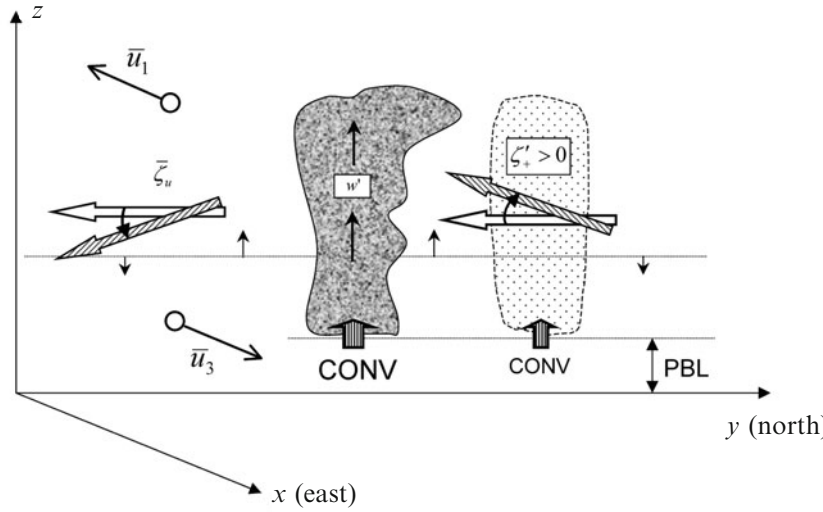

Figure 10.13. Schematic diagram showing the vertical shear mechanism by which monsoon easterly vertical shear generates northward propagation of ISO convective anomalies.

indicates that, in the presence of vertical easterly shear $U_T < 0$, a northward decrease in perturbation upward motion can generate positive barotropic vorticity to the north of convection.

This process is illustrated in Figure 10.13. A mean flow with easterly vertical shear has equatorward relative vorticity, from which the perturbation motion can tap energy. Rossby wave–induced heating generates a perturbation vertical motion field that decreases northward to the north of convection. This vertical motion field twists mean flow horizontal vorticity and generates a vorticity with a positive vertical component north of the convection region. Positive vorticity in turn induces convergence in the boundary layer, which would destabilize the atmosphere and trigger new convection to the north of convection. Based on a similar argument, negative vorticity and boundary layer divergence would develop and suppress convection south of the convection region. Thus, the twisting of mean flow horizontal vorticity by the vertical motion field associated with Rossby waves creates conditions that favor northward movement of enhanced rainfall.

This conclusion is supported by observations made by Jiang *et al.* (2004) who show that barotropic vorticity in the free troposphere is located about 4° to the north of northward-propagating convection anomalies. Jiang *et al.* (2004) also argue that the advection of mean state specific humidity by meridional winds of the ISO in the boundary layer favors northward propagation. The third factor that may enhance northward propagation is intraseasonal variation of SST, which is shown to guide convection in the northward-propagating ISO (Kemball-Cook and Wang, 2001; Fu *et al.*, 2003). The SST feedback to convection is essentially the same mechanism as that for the MJO, which is discussed in the next section.

10.6 ROLE PLAYED BY ATMOSPHERIC–OCEAN INTERACTION

Figure 10.14a presents a schematic summary of the observed structure of the MJO and the associated oceanic mixed layer based on TOGA COARE observations. The "wet" region of the MJO in the equatorial zonal plane features a large-scale convective envelope whose core consists of supercloud clusters. This convective region is accompanied by large-scale rising motion and planetary-scale equatorial upper-level easterly and low-level westerly anomalies (Lin and Johnson, 1996). The core of low-level and surface westerly anomalies, however, lags behind enhanced convection by slightly less than one quarter of a wavelength (e.g., Chen *et al*., 1996; Chou *et al*., 1995; Fasullo and Webster, 1995). The westerly wind bursts associated with the convective phase of the MJO cause the SST to drop more than one degree and profoundly change the mixed layer structure and currents (Webster, 1994; Weller and Anderson, 1996; Lau and Sui, 1997; Jones *et al*., 1998; Shinoda *et al*., 1998; Shinoda and Hendon, 1998; Zhang and Anderson, 2003). SST decreases under and to the west of enhanced convection due to enhanced evaporation and latent heat flux that nearly coincides with low-level westerly anomalies. To the east of convection in the MJO low-level easterly phase, SST rises due to reduced windspeed, the shallow mixed layer, and increased insolation in the suppressed convection region (Jones and Weare, 1996; Zhang, 1996; Lin and Johnson, 1996). Thus, positive SST anomalies lead enhanced convection by about one quarter of a wavelength.

Over the Indian Ocean and during boreal summer, coherent negative/positive SST anomalies generated by surface heat fluxes that move northward were found to follow regions of active and suppressed convection anomalies (Kemball-Cook and Wang, 2001; Sengupta *et al*., 2001). In the western North Pacific, SST anomalies associated with northwestward propagation of the ISO and their possible feedbacks were also noted (Kemball-Cook and Wang, 2001; Hsu and Weng, 2001).

As reviewed in Section 10.2.8, these observational analyses have stimulated numerous theoretical and numerical modeling studies. In this section, an attempt is made to elucidate the nature and impacts of air–sea interaction on the MJO in terms of a simple theoretical coupled model.

As shown by Hirst and Lau (1990), unstable coupled modes on the intraseasonal timescale result from atmospheric waves, which contrasts the coupled ENSO modes that arise from oceanic wave adjustment (Philander *et al*., 1984) or slow SST variation (Neelin, 1990). In Hirst and Lau's model formulation, however, the atmosphere–ocean interaction is essentially the same as that used for ENSO studies except for the inclusion of atmospheric transient waves. ENSO-type models are not suitable for study of the warm pool of the tropical Indian Ocean and Western Pacific Ocean, because both the climatological mean state and the processes of atmosphere–ocean coupling in the warm pool differ fundamentally from those in the cold tongue of SST in the eastern tropical Pacific.

The theoretical coupled model of Wang and Xie (1998) consists of a single vertical mode atmospheric model coupled to a linearized ocean mixed layer model. The ocean component differs from that used in the previous coupled stability analysis for the Eastern Pacific (e.g., Hirst and Lau, 1990), which

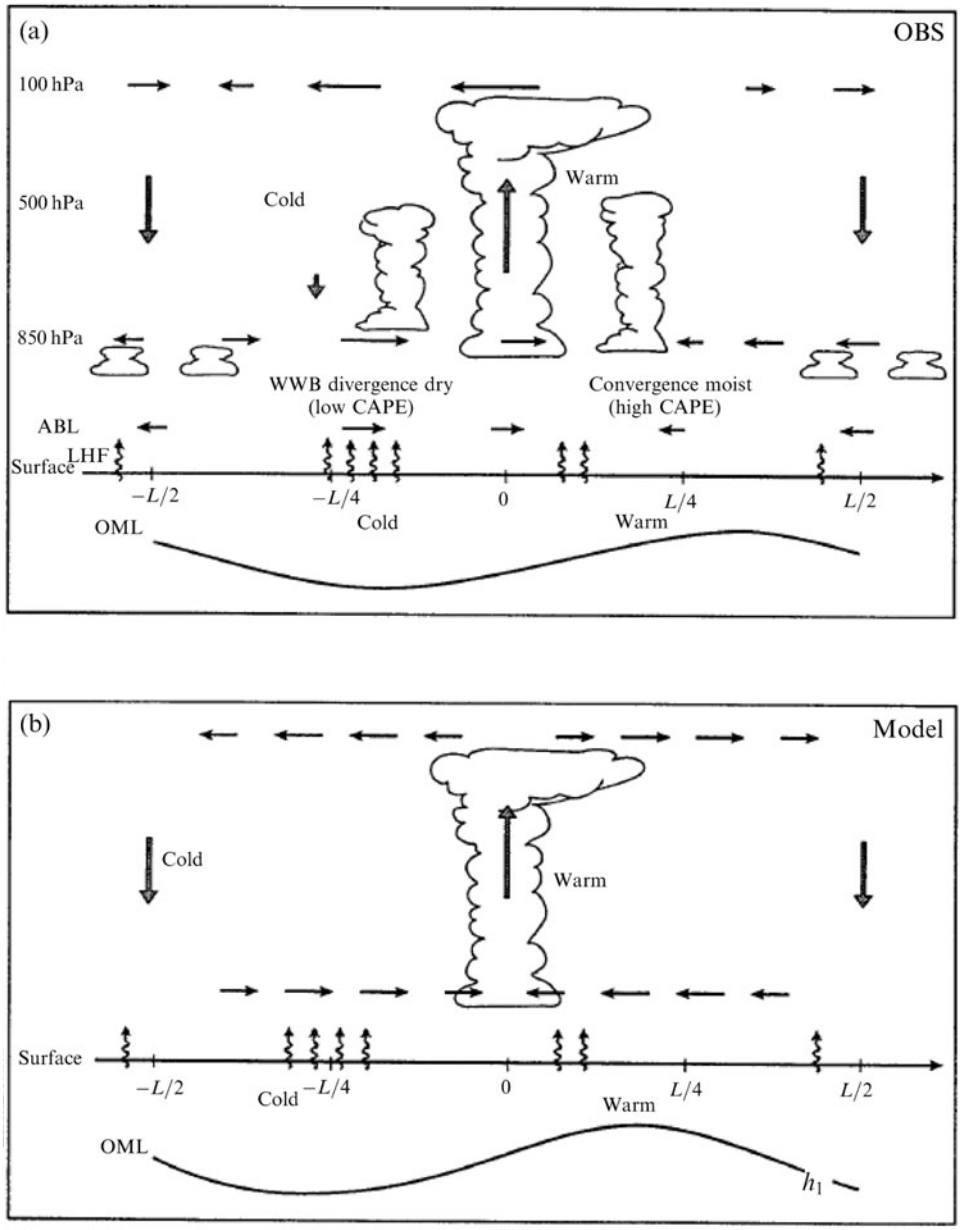

Figure 10.14. Schematic diagram illustrating the equatorial vertical structure of the MJO observed in TOGA/COARE (a) and the most unstable coupled mode in the theoretical model (b). Wavy lines denote surface latent heat flux. Symbols ABL, OML, LHF, WWB, CAPE, and L represent, respectively, atmospheric boundary layer, ocean mixed layer, latent heat flux, westerly wind burst, convective available potential energy, and wavelength (adapted from Wang and Xie, 1998).

describes ocean mixed layer physics and thermodynamic coupling of the atmosphere and ocean through surface heat exchanges. Dynamical coupling which plays an essential role in the eastern Pacific is neglected, because it is unimportant regarding changing SST in warm pool oceans. The ocean mixed layer is described by the following linearized equations:

$$\frac{\partial h_1}{\partial t} = \varepsilon \bar{U} U + \bar{w}_e \left(\frac{3U}{\bar{U}} - \frac{h_1}{H_1} \right) \tag{10.17a}$$

$$\frac{\partial T}{\partial t} = D_{\text{rad}} \left(\frac{\partial U}{\partial x} + \frac{\partial V}{\partial y} \right) - (3D_{\text{ent}} + D_{\text{eva}}) \frac{U}{\bar{U}} + D_{\text{ent}} \frac{h_1}{H_1} - dT \tag{10.17b}$$

where h_1 and T denote the mixed layer depth and temperature, respectively; $H_1 = 50\,\text{m}$ is the mean depth of the mixed layer; $\bar{U}$ is mean surface wind; $\bar{w}_e$ is the mean entrainment rate; d is the thermal damping coefficient; and the coefficients D_{rad}, D_{ent}, and D_{eva} measure the heating rate associated with, respectively, downward shortwave radiation, entrainment, and evaporation processes. Here, downward solar radiation flux is assumed to decrease with increasing atmospheric moisture convergence (hence atmospheric cloudiness); surface evaporation is assumed to enhance over regions of anomalous westerly because the mean surface winds are from the west. Expressions for all coefficients and the derivation of (10.17a, b) are given in Wang and Xie (1998).

The atmospheric component of the coupled model describes the linear motion of the lowest baroclinic mode, which is similar to findings by Davey and Gill (1987) except that the local rate of changes of momentum and temperature are added. The equations take the shallow-water form:

$$\frac{\partial u}{\partial t} + \varepsilon_a U - \beta y V = -\frac{\partial \phi}{\partial x} \tag{10.18a}$$

$$\frac{\partial V}{\partial t} + \varepsilon_a V + \beta y U = -\frac{\partial \phi}{\partial y} \tag{10.18b}$$

$$\frac{\partial \phi}{\partial t} + \mu_a \phi + C_a^2 (1 - I) \left(\frac{\partial U}{\partial x} + \frac{\partial V}{\partial y} \right) = -\frac{Rg}{2C_p p_2} \alpha T \tag{10.18c}$$

where U, V, and ϕ are the lower-tropospheric zonal wind, lower-tropospheric meridional wind, and geopotential, respectively; ε_a and μ_a are, respectively, coefficients for Rayleigh friction and Newtonian cooling; C_a is the speed of a dry atmospheric Kelvin wave; α is the latent heating coefficient; T is the SST anomaly or the ocean mixed layer temperature anomaly. As in Equation (10.9), the speed of a moist atmospheric Kelvin wave is $C_a(1 - I)^{1/2}$.

Figure 10.15 shows results derived from instability analysis of the coupled system (10.17) and (10.18): how the growth rate and phase speed of the fastest growing coupled mode vary with the two coupling coefficients (i.e., the cloud–SST coupling coefficient D_{rad} and the wind–SST coupling coefficient $D_{\text{wind}} = D_{\text{eva}} + 3D_{\text{ent}}$). The fastest growing coupled mode has a planetary zonal scale (Figure 10.15a). Obviously, wind–SST coupling plays a primary role in

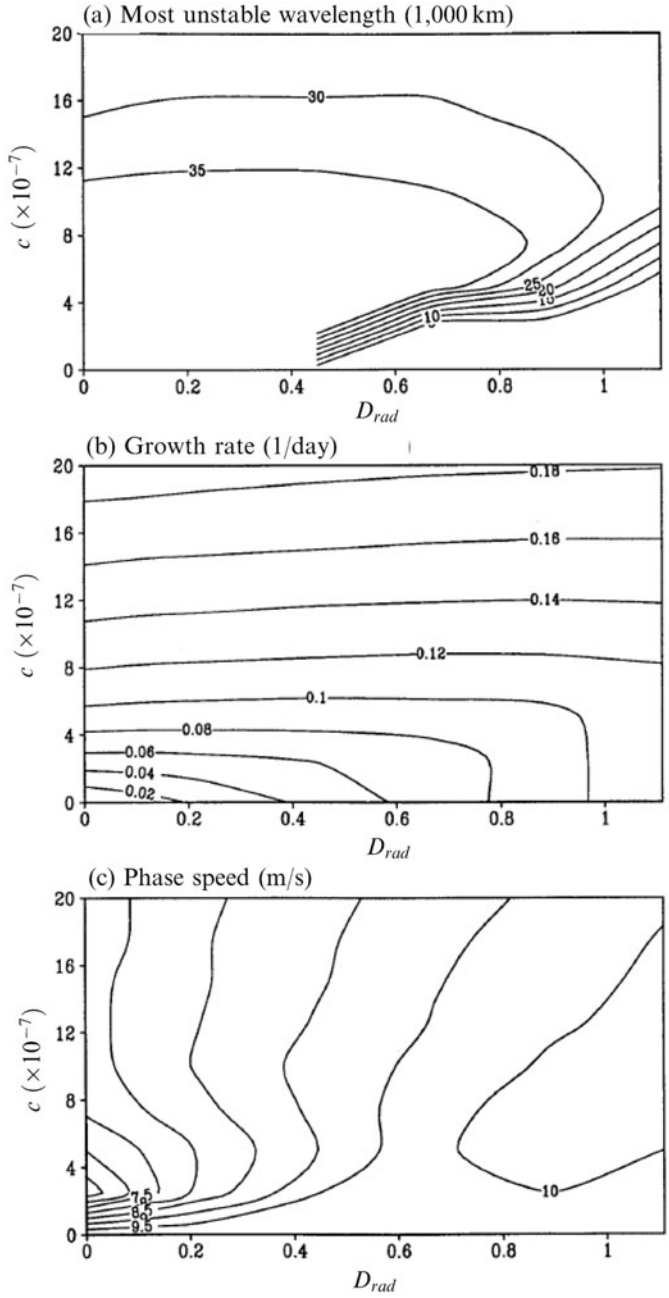

Figure 10.15. The wavelength (a), growth rate (b), and phase speed (c) of the most unstable coupled mode as functions of the cloud–SST coupling coefficient D_{rad} (K) and wind–SST coupling coefficient D_{wind} (K s^{-1}) in a coupled atmosphere–ocean model for the warm pool climate system (adapted from Wang and Xie, 1998).

generating the coupled instability (Figure 10.15b). Cloud–SST coupling can significantly contribute to growth only when the wind effect is relatively weak. Coupled modes have an eastward phase speed less than $10\,m\,s^{-1}$ (Figure 10.15c). The unstable coupled mode originates from atmospheric moist Kelvin waves. These results indicate that the warm pool basic state is conducive to the coupled unstable mode on intraseasonal timescales.

The structure of the unstable coupled mode is illustrated in Figure 10.14b. This schematic diagram was strictly based on model results (figure not shown, see Wang and Xie, 1998). The coupled mode in the model has a realistic SST–convection relationship: Positive SST anomalies are located to the east of convection anomalies by about one sixth of a wavelength, but lag behind surface easterly wind anomalies by about one twelfth of a wavelength. Note, however, the phase relationship between equatorial zonal wind (lower and upper level) and convection anomalies is not correctly captured. This appears to be a common weakness of current theoretical models of the MJO.

In the model, SST anomaly–induced heating tends to increase atmospheric temperature (or thickness) locally so that the positive covariance between heating and warming generates perturbation available potential energy for the growing coupled mode. It is shown that coupling effects are more effective for planetary-scale perturbations because planetary-scale disturbance can have a sufficiently long time to change SST; also, the larger the change in SST the stronger the feedback from SST.

Coupled model results suggest that while atmospheric internal dynamics are primary causes for the MJO, ocean mixed layer thermodynamic processes interacting with the atmosphere may play a significant part in sustaining the MJO by adding instability to atmospheric moist low-frequency perturbations and by providing a mechanism for longwave selection and slow eastward propagation.

10.7 SUMMARY AND DISCUSSION

10.7.1 Understanding gained from the FCI theory

Based on a review of existing theories, the essential physics of the ISO is illustrated in Figure 10.1 and discussed in Section 10.3.1. A general dynamic framework for theoretical study of ISO dynamics is put forward in Section 10.3.2. This simple ISO model is a time-dependent primitive equation model on an equatorial β-plane that has two levels: a free troposphere and a well-mixed planetary boundary layer (Figure 10.3).

At the very heart of the ISO model are nonlinear interactions among (1) condensational heating, (2) low-frequency equatorial (Kelvin and Rossby) waves, (3) boundary layer dynamics, (4) convection–moisture feedback and wind-induced heat exchanges at the surface (Figure 10.1). These nonlinear interactions result in frictional convergence instability (FCI). At a higher level, the model can be extended to include (5) the interaction between the MJO and embedded synoptic

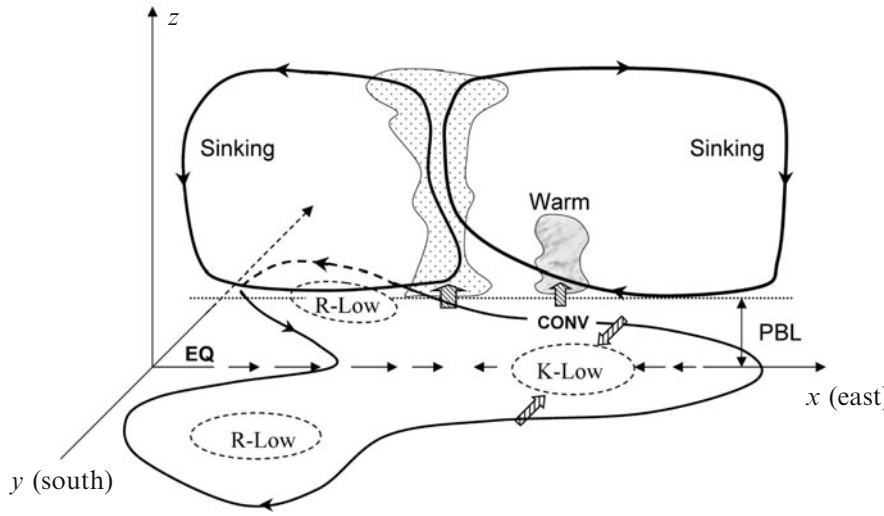

Figure 10.16. Schematic structure of FCI mode, which is the counterpart of observed MJO mode. In the horizontal plane the "K-low" and "R-low" represent the low-pressure anomalies associated with moist equatorial Kelvin and Rossby waves, respectively. Arrows indicate the wind directions. In the equatorial vertical plane. free tropospheric wave circulation is highlighted. Wave-induced convergence is in phase with major convection, whereas frictional moisture convergence in the "K-low" region is ahead of major convection due primarily to meridional wind convergence.

systems, (6) the impacts of three-dimensional background circulations as well as (7) the effect of interactive SST feedback. Thus, the model physics integrate, to varying degrees, the mechanisms listed in the review section (Section 10.2) except that simple Newtonian cooling was used to represent net cloud–radiative heating. Regardless of its simplicity, the model is able to reproduce atmospheric disturbances that closely resemble features of the observed MJO and the boreal summer ISO, thus providing a unifying framework for the tropical ISO.

The ISO theory based on this general framework without considering multiscale interaction, mean states, and ocean feedback is termed, in short, "frictional convergence instability" (FCI). The structure of FCI mode is schematically presented in Figure 10.16. Among the four feedback processes (convection–wave convergence feedback, frictional moisture convergence feedback, evaporation–wind feedback, and moisture feedback), frictional moisture convergence feedback is emphasized because the low-frequency convectively coupled Kelvin–Rossby wave packet that characterizes the MJO is essentially coupled through frictional moisture convergence. As shown in Figure 10.4, Kelvin wave–induced frictional convergence favors itself while Rossby wave–induced boundary layer convergence also partially favors Kelvin waves. Thus, frictional moisture convergence–induced heating couples equatorial Kelvin and Rossby waves and selects the eastward-moving unstable mode. Condensational heating induced by free tropospheric waves reduces

effective static stability and slows down eastward propagation, but in isolation does not produce instability. The slow eastward propagation is also attributed to frictional coupling of moist Kelvin and Rossby waves.

The nature and role of multiscale interaction (MSI) is one of the elusive aspects of MJO dynamics. The basic FCI model can be extended to include the effects of upscale eddy momentum transfer (EMT) and heat transfer. In this extended FCI model, the interaction between planetary-scale wave motion and synoptic-scale systems (eastward-propagating supercloud clusters and westward-propagating 2-day waves) is described (Figure 10.7). EMT alone tends to yield a stationary mode with an enhanced Rossby wave component. Multiscale interaction instability stems from corporative FCI and EMT mechanisms. With increasing stratiform and congestus heating, FCI weakens while EMT becomes more effective. A growing MSI mode has a horizontal quadrupole and rearward-tilted structure and prefers slow eastward propagation, which resemble the observed MJO. FCI sets up eastward propagation, while EMT provides another slowdown mechanism.

Northward propagation of the ISO in the Asian–Pacific summer monsoon region, as suggested by the FCI model with basic flows included, is due to northwestward propagation of moist Rossby waves that emanate from equatorial disturbances when the latter decay over Indonesia and near the dateline. What induces the northward propagation component for emanated moist Rossby waves? Model experiments suggest that monsoon easterly vertical shear provides such an atmospheric internal dynamic mechanism. This vertical shear mechanism (Jiang *et al.*, 2004; Drbohlav and Wang, 2005), as illustrated in Figure 10.13, is essentially due to the twisting of mean flow horizontal vorticity by the vertical motion field associated with Rossby waves. This twisting process generates positive vorticity north of convection in the troposphere, thus creating boundary layer moisture convergence that favors northward movement of enhanced rainfall (Section 10.5.2). Interactive SST and surface heat fluxes also contribute to northward propagation (Fu *et al.*, 2003; Fu and Wang, 2004).

The results of the coupled FCI–ocean mixed layer model suggest that—while atmospheric internal dynamics are essential in generating the MJO—the interaction between the atmosphere and ocean mixed layer may further enhance and better organize the eastward-propagating MJO through additional coupled instability amplifying moist atmospheric low-frequency perturbations. The basic state of the warm pool is conducive to the occurrence of the coupled unstable mode on intraseasonal timescales. The wind–evaporation–SST feedback is central to the coupled instability (Figure 10.15).

In summary, the FCI theory provides a reasonable explanation of the essential characteristics of the observed ISO listed in the introduction including: (1) global-scale circulation that is coupled to a large-scale complex of convective cells; (2) baroclinic structure, with winds converging in the boundary layer in front of the main precipitation; (3) horizontal circulation consisting of both equatorial Kelvin and Rossby waves, (4) the slow eastward (about 5–10 $\mathrm{m\,s^{-1}}$) movement that gives rise to the intraseasonal timescale (Figure 10.5), (5) the multiscale structure of the convective complex involving eastward-propagating supercloud

clusters and westward-propagating 2-day waves, (6) longitudinal variation and seasonal variation in the activity center and propagation, especially the prominent northward propagation and off-equatorial westward propagation of disturbances in the Asian monsoon region during boreal summer (Figure 10.11), and (7) SST anomalies lead and the strongest surface heat exchange lags behind a major convective complex (Figure 10.14).

10.7.2 Model limitations

The crude vertical resolution of the FCI model confines the description of heating-induced baroclinic motion to the gravest baroclinic mode and can only describe vertical-integrated condensational heating that is constrained by water vapor conservation. This oversimplified representation neglects the coupling effect of boundary layer convergence on vertical modes. The higher vertical modes are necessary to explain the realistic vertical structure: namely, the magnitude of wind anomalies at the upper level is considerably larger than its low-level counterpart and the rearward tilt of large-scale vertical velocity against its direction of propagation. The higher modes have slower phase speeds and may be important in explaining the slow eastward propagation of the MJO (Mapes, 2000). The inclusion of higher vertical modes to describe the EMT mechanism and the role of boundary layer moisture preconditioning would provide a more realistic model for investigating MJO dynamics.

The model's simplicity does not allow description of the complex cloud–radiation feedback process, which may play a significant role in sustaining oscillations on intraseasonal timescales (Hu and Randall, 1994; Raymond, 2001). The simple ocean mixed layer model used in Section 10.6 neglected the effect of the salinity barrier layer, which can potentially provide much stronger local coupling between the atmosphere and ocean. In the FCI-based multiscale interaction model, a fixed phase lag between synoptic activity (EMT) and the MJO convective complex and the equal number of stratiform and congestus clouds were assumed. Further consideration of wavelength-dependent phase lags and study of the impact on phase propagation of the EMT effect under different multicloud structures is warranted.

10.7.3 Outstanding issues

Accurate modeling and prediction of the ISO may improve seasonal-to-interannual climate prediction and bridge the gap between weather forecast and seasonal prediction (Waliser *et al.*, 2003a; see also Chapter 12). Unfortunately, current global circulation models still have great difficulty in simulating the properties of the tropical oscillation correctly (Slingo *et al.*, 1996; Wu *et al.*, 2002; Waliser *et al.*, 2003b; Lin *et al.*, 2006). One might wonder whether the FCI theory is the key to the ISO and why would some AGCMs that have well-constrained formulations of similar processes perform poorly when simulating the ISO?

In simple models, such as the basic FCI model, the direct linkage between large-scale low-frequency wave motion and the collective effect of convective heating was

established through moisture and heat energy conservation without getting involved in the details when resolving vertical heating distribution or scale interactions. Such models have little difficulty in producing MJO-like low-frequency oscillations because they avoid the complex interactions among many physical processes that take place on different timescales. Modeling the ISO in complex models, however, must entail a series of interactive parameterizations including moisture transport, cloud and convection, and radiation transfer. Uncertainties in mathematical descriptions of these interactive parameterizations jeopardize the capability of models to simulate the ISO.

These theoretical model results suggest that—in order to simulate the MJO realistically—the cumulus parameterization schemes in complex models have to allow large-scale low-frequency waves (and associated boundary layer motion) to be affected by parameterized convective heating and to allow these low-frequency waves to have some effect on parameterized heating either directly (through grid-scale precipitation, for example) or indirectly (through correct description of multiscale interactions). If all convective heating was consumed by high-frequency small-scale disturbances and if there was no appropriate description of upscale transport of energy, how could the model maintain the low-frequency MJO?

In complex GCMs, one does not know what the correct heating partitioning is between convective and stable precipitation and between small-scale high-frequency and large-scale low-frequency disturbances. Recent Tropical Rainfall Measuring Mission precipitation radar measurements show that stratiform precipitation contributes more to intraseasonal rainfall variations than it does to seasonal mean rainfall (Lin *et al.*, 2004). Numerical experiments with general circulation models (GCMs) have demonstrated that stratiform rain plays a critical role in maintaining the MJO (Tompkins and Jung, 2003; Fu and Wang, 2009). In summary, inadequate treatment of cumulus parameterization and multiscale interaction processes could be the major hurdles to realistic simulation of the MJO.

The sensitivity of ISO simulations to various cumulus parameterization schemes has been evaluated using a single model with differing cumulus schemes. Both Chao and Deng (1998) and Lee *et al.* (2003) compare three different schemes: the moist convective adjustment (MCA) scheme (Manabe *et al.*, 1965), the Kuo (1974) scheme, and the modified Arakawa–Schubert (1974) (AS) scheme. Both studies find that the MCA scheme produces the strongest ISO variability and the AS scheme the smallest. What causes this sensitivity deserves further investigation. Wang and Schlesinger (1999) use the University of Illinois AGCM with the above three types of cumulus parameterization schemes to simulate the MJO. For each parameterization the relative humidity criterion (RHC) for convection or convective heating to occur was used. They find that—as the RHC increases—the simulated ISO gets stronger for all three parameterizations. They suggest that—when large values of RHC are used—the triggering convection requires moist static energy in the lower troposphere to be accumulated by a certain amount through moisture convergence; this elevated RHC weakens the interaction between circulation and heating for small-scale perturbations and allows the ISO to occur at low frequencies. On the other hand, Maloney and Hartmann (2001) find that the ISO in the NCAR Community Climate

Model (CCM3) using the relaxed AS scheme is not improved by increasing the RHC. They report that the ISO is highly sensitive to parameterization of convective precipitation evaporation in unsaturated environmental air and saturated downdraft. Concerning improvement of the cumulus scheme, three interesting aspects have emerged: the vertical profile of diabatic heating, closure assumptions used in parameterization, and the role of shallow vs. deep cumulus clouds.

A new generation of cloud system–resolving GCMs has recently been developed without cumulus parameterization. The NICAM (Nonhydrostatic Icosahedral Atmospheric Model) is an example (Satoh *et al*., 2008). The first aqua-planet experiment performed in 2004 with a mesh size of approximately 3.5 km has successfully simulated systematic eastward propagation of supercloud cluster–like signals with the multiscale structure of convective systems embedded in large-scale organized convective systems (Tomita *et al*., 2005). An MJO hindcast simulation was then performed that took the topography, land process, and specified sea surface temperature into account and successfully simulated a realistic MJO event up to 30 days (Miura *et al*., 2007; Liu *et al*., 2009). The hierarchical structure of the MJO was simulated including synoptic-scale convectively coupled eastward-propagating and westward-propagating disturbances as frequently detected in observations (Nasuno *et al*., 2009). It was suggested that spontaneous organization of the eastward-propagating MJO is prompted by the westward-propagating disturbance that helps transport the moisture necessary for the buildup of MJO-associated convection (Miura *et al*., 2007). Seasonal simulation using NICAM successfully simulated the multiscale precipitation features and accompanied circulation in the mature Asian monsoon season. Comparison of the Indian monsoon index (Wang *et al*., 2004) between the model-derived index and observations revealed the fair level of skill that the 7 km mesh NICAM has in predicting the monsoon cycle up to 30–40 days in advance including northward propagation (Oouchi *et al*., 2009).

Theoretical results learned from the multiscale interaction (MSI) model have important ramifications. First, the boundary layer moisture convergence and multicloud heating associated with synoptic systems are essential for creating vertical tilts of meso-synoptic-scale disturbances or upscale EMT to affect planetary-scale wave dynamics. In this regard, documentation of vertical heating profiles and multicloud structures should be encouraged. Further, adequate simulation of the MJO in general circulation models may depend on the ability of models to reproduce the correct partitioning of cloud amounts among deep convective and stratiform/congestus clouds. Many general circulation models (GCMs) tend to simulate a considerably higher percentage of deep convective clouds compared with satellite observations. In this case, the EMT mechanism and MSI may be underrepresented.

Validating theories and developing new ideas rely on improved observations. Different from other weather systems, the MJO or intraseasonal variation in general is a ''broad-frequency band'' phenomenon (Madden and Julian, 1994). Current observational analyses of the MJO have often focused on its statistical behavior or averaged features of many events. TOGA/COARE provided invaluable observations of two MJO events. Analyses of these observations have greatly advanced our knowledge of the structure of the MJO and its associated surface heat flux exchanges

and air–sea interaction. The information gained from these analyses has been extremely useful for validating theories and furthering our theoretical understanding. Yet, we still do not have sufficient information on the differences among individual events, which may be as important as their common features. Most observed features have been derived using temporal or spatially filtered data, which tends to artificially separate high-frequency and intraseasonal variations in a linear fashion that might undermine the inherent nonlinearity. In addition, due to a lack of accurate observation over tropical oceans, we do not have sufficient information about the spatial structure and the nature of the clouds and diabatic heating that drives the MJO, which is critical for improving theories and numerical simulations.

Current theoretical model results are useful in the sense that they provide clues to understanding the basic mechanisms that are active in nature. However, to improve representation of the MJO in GCMs, numerical experiments with full physical representations are necessary, which should establish the sensitivity of the MJO to various processes and validate these processes with observations. At present, thorough understanding of the complex interactive processes involved in the initiation and maintenance of the ISO and faithful simulation of it by GCMs remains elusive.

10.8 ACKNOWLEDGMENTS

The author thanks anonymous reviewers and Drs. R. Madden, B. Mapes, D. Waliser, K.-M. Lau, P. V. Joseph for their critical comments on an earlier version of the manuscript which has resulted in a significant improvement of the chapter. Drs. F. Liu and H. Taniguchi helped with the revision. This work was supported by Climate Dynamics Program National Science Foundation award ATM03-29531 and AGS-1005599.

10.9 REFERENCES

Anderson, J. R. (1987) Response of the tropical atmosphere to low-frequency thermal forcing. *J. Atmos. Sci.*, **44**, 676–686.

Anderson, J. R. and D. E. Stevens (1987) Presence of linear wavelike modes in a zonally symmetric model of the tropical atmosphere. *J. Atmos. Sci.*, **44**, 2115–2117.

Annamalai, H. and J. M. Slingo (2001) Active/break cycles: Diagnosis of the intraseasonal variability of the Asian Summer Monsoon. *Climate Dynamics*, **18**, 85–102.

Arakawa, A. and W. H. Schubert (1974) Interaction of a cumulus cloud ensemble with the large-scale environment, Part I. *J. Atmos. Sci.*, **31**, 674–701.

Betts, A. K. and M. J. Miller (1986) New convective adjustment scheme, Part 2: Single column tests using GATE wave, BOMEX, ATEX, and Arctic air-mass data sets. *Quart. J. Roy. Meteorol. Soc.*, **112**, 693–709.

Biello, J. A. and A. J. Majda (2005) A new multiscale model for the Madden–Julian oscillation. *J. Atmos. Sci.*, **62**, 1694–1721.

Blackadar, A. K. and H. Tennekes (1968) Asymptotic similarity in neutral barotropic planetary boundary layers. *J. Atmos. Sci.*, **25**, 1015–1020.

Blade, I. and D. L. Hartmann (1993) Tropical intraseasonal oscillations in a simple nonlinear model. *J. Atmos. Sci.*, **50**, 2922–2939.

Boos, W. R. and Z. Kuang (2010) Mechanisms of poleward propagating, intraseasonal convective anomalies in cloud system–resolving models. *J. Atmos. Sci.*, **67**, 3673–3691.

Bretherton, C., P. Blossey, and M. Khairoutdinov (2005) An energy-balance analysis of deep convective self-aggregation above uniform SST. *J. Atmos. Sci.*, **62**, 4237–4292.

Brown, R. G. and C. S. Bretherton (1995) Tropical wave instabilities: Convective interaction with dynamics using the Emanuel convective parameterization. *J. Atmos. Sci.*, **52**, 67–82.

Chang, C.-P. (1977) Some theoretical problems of the planetary-scale monsoons. *Pure Appl. Geophys.*, **115**, 1089–1109.

Chang, C.-P. and H. Lim (1988) Kelvin wave-CISK: A possible mechanism for the 30–50 day oscillations. *J. Atmos. Sci.*, **45**, 1709–1720.

Chao, W. C. (1987) On the origin of the tropical intraseasonal oscillation. *J. Atmos. Sci.*, **44**, 1940–1949.

Chao, W. C. (1995) A critique of wave-CISK as an explanation for the 40–50 day tropical intraseasonal oscillation. *J. Meteorol. Soc. Japan*, **73**, 677–684.

Chao, W. C. and L. Deng (1998) Tropical intraseasonal oscillation, super cloud clusters, and cumulus convection schemes. Part II: 3D aquaplanet simulations. *J. Atmos. Sci.*, **55**, 690–709.

Charney, J. G. and A. Eliassen (1964) On the growth of the hurricane depression. *J. Atmos. Sci.*, **21**, 68–75.

Chen, S. S., R. A. Houze Jr., and B. E. Mapes (1996) Multiscale variability of deep convection in relation to large-scale circulation during TOGA COARE. *J. Atmos. Sci.*, **53**, 1380–1409.

Chen, T. C. and M. Murakami (1988) The 30–50 day variation of convective activity over the western Pacific Ocean with the emphasis on the northwestern region. *Mon. Wea. Rev.*, **116**, 892–906.

Cho, H. R. and D. Pendlebury (1997) Wave CISK of equatorial waves and the vertical distribution of cumulus heating. *J. Atmos. Sci.*, **54**, 2429–2440.

Chou, S. H., C. L. Shie, R. M. Atlas, and J. Ardizzone (1995) The December 1992 westerly wind burst and its impact on evaporation determined from SSMI data. paper presented at *Proc. Int. Scientific Conf. on the Tropical Ocean Global Atmosphere Program, Melbourne, Australia*. World Meteorological Organization, Geneva, pp. 489–493.

Cubukcu, N. and T. N. Krishnamurti (2002) Low-frequency controls on the thresholds of sea surface temperature over the western tropical Pacific. *J. Climate*, **15**, 1626–1642.

Davey, M. K. and A. E. Gill (1987) Experiments on tropical circulation with a simple moist model. *Quart. J. Roy. Meteorol. Soc.*, **113**, 1237–1269.

Deser, C. (1993) Diagnosis of the surface momentum balance over the tropical Pacific Ocean. *J. Climate*, **6**, 64–74.

Drbohlav, H.-K. L. and B. Wang (2005) Mechanism of the northward propagating intraseasonal oscillation in the south Asian monsoon region: Results from a zonally averaged model. *J. Climate*, **18**, 952–972.

Dunkerton, T. J. and F. X. Crum (1991) Scale selection and propagation of wave-CISK with conditional heating. *J. Meteorol. Soc. Japan*, **69**, 449–458.

Eliassen, A. (1971) On the Ekman layer in a circular vortex. *J. Meteorol. Soc. Japan*, **49** (Special Issue), 784–789.

Emanuel, K. A. (1987) Air–sea interaction model of intraseasonal oscillations in the Tropics. *J. Atmos. Sci.*, **44**, 2324–2340.

Emanuel, K. A. (1993) The effect of convective response time on WISHE modes. *J. Atmos. Sci.*, **50**, 1763–1776.

Fasullo, J. and P. J. Webster (1995) Ocean–atmosphere energetics during westerly wind bursts: The development of a conceptual model. paper presented at *Proc. 20th Climate Diagnnostics Workshop, Seattle, WA, October 23–27*. U.S. Department of Commerce. Springfield, VA, p. 41.

Ferranti, L., J. M. Slingo, T. N. Palmer, and B. J. Hoskins (1997) Relations between interannual and intraseasonal monsoon variability as diagnosed from AMIP integrations. *Quart. J. Roy. Meteorol. Soc.*, **123**, 1323–1357.

Flatau, M., P. J. Flatau, P. Phoebus, and P. P. Niiler (1997) The feedback between equatorial convection and local radiative and evaporative processes: The implication for intraseasonal oscillations. *J. Atmos. Sci.*, **54**, 2373–2386.

Fu, X. and B. Wang (2004) Different solutions of intraseasonal oscillation exist in atmosphere–ocean coupled model and atmosphere-only model. *J. Climate*, **17**, 1263–1271.

Fu, X. and B. Wang (2009) Critical roles of the stratiform rainfall in sustaining the Madden Julian Oscillation: GCM experiments. *J. Climate*, **22**, 3939–3959.

Fu, X., B. Wang, T. Li, and J. P. McCreary (2003) Coupling between northward propagating intraseasonal oscillations and sea-surface temperature in the Indian Ocean. *J. Atmos. Sci.*, **60**, 1733–1753.

Fuchs, Z. and D. J. Raymond (2005) Large-scale modes in a rotating atmosphere with radiative–convective instability and WISHE. *J. Atmos. Sci.*, **62**, 4084–4094.

Fuchs, Z. and D. J. Raymond (2007) A simple, vertically resolved model of tropical disturbances with a humidity closure. *Tellus*, **59A**, 344–354.

Gill, A. E. (1980) Some simple solutions for heat-induced tropical circulation. *Quart. J. Roy. Meteorol. Soc.*, **106**, 447–462.

Goswami, B. N. and J. Shukla (1984) Quasi-periodic oscillations in a symmetric general circulation model. *J. Atmos. Sci.*, **41**, 20–37.

Goswami, P. and V. Mathew (1994) A mechanism of scale selection in tropical circulation at observed intraseasonal frequencies. *J. Atmos. Sci.*, **51**, 3155–3166.

Grabowski, W. W. (2003) MJO-like coherent structures: Sensitivity simulations using the cloud-resolving convection parameterization (CRCP). *J. Atmos. Sci.*, **60**, 847–864.

Gualdi, S., A. Navarra, and M. Fischer (1999) The tropical intraseasonal oscillation in a coupled ocean–atmosphere general circulation model. *Geophys. Res. Lett.*, **26**, 2973–2976.

Haertel, P. T. and G. N. Kiladis (2004) Dynamics of 2-day equatorial waves. *J. Atmos. Sci.*, **61**, 2707–2721.

Hayashi, Y. (1970) A theory of large scale equatorial waves generated by condensation heat and accelerating the zonal wind. *J. Meteorol. Soc. Japan*, **48**, 140–160.

Hayashi, Y. and S. Miyahara (1987) Three-dimensional linear response model of the tropical intraseasonal oscillation. *J. Meteorol. Soc. Japan*, **65**, 843–852.

Hayashi, Y. and A. Sumi (1986) 30–40-day oscillations simulated in an "aqua planet" model. *J. Meteorol. Soc. Japan*, **64**, 451–467.

Hendon, H. H. (1988) Simple model of the 40–50 day oscillation. *J. Atmos. Sci.*, **45**, 569–584.

Hendon, H. H. (2000) Impact of air–sea coupling on the Madden–Julian Oscillation in a general circulation model. *J. Atmos. Sci.*, **57**, 3939–3952.

Hendon, H. H. and M. L. Salby (1994) The life cycle of the Madden–Julian Oscillation. *J. Atmos. Sci.*, **51**, 2225–2237.

Hirst, A. C. and K. M. Lau (1990) Intraseasonal and interannual oscillations in coupled ocean–atmosphere models. *J. Climate*, **3**, 713–725.

Hoskins, B. J. and M. J. Rodwell (1995) A model of the Asian summer monsoon, Part I: The global scale. *J. Atmos. Sci.*, **52**, 1329–1340.

Houze, R. A., S. S. Chen, D. K. Kingsmill, Y. Serra, and S. E. Yuter (2000) Convection over the Pacific warm pool in relation to the atmospheric Kelvin–Rossby wave. *J. Atmos. Sci.*, **57**, 3058–3089.

Hsu, H. H. and C. H. Weng (2001) Northwestward propagation of the intraseasonal oscillation in the western north Pacific during the boreal summer: Structure and mechanism. *J. Climate*, **14**, 3834–3850.

Hsu, H. H., B. J. Hoskins, and F.-F. Jin (1990) The 1985/86 intraseasonal oscillation and the role of the extratropics. *J. Atmos. Sci.*, **47**, 823–839.

Hsu, P.-C. and T. Li (2011) Interactions between boreal summer intraseasonal oscillations and synoptic-scale disturbances over the western North Pacific, Part II: Apparent heat and moisture sources and eddy momentum transport. *J. Climate*, **24**, 942–961.

Hsu, P.-C., T. Li, and C.-H. Tsou (2011) Interactions between boreal summer intraseasonal oscillations and synoptic-scale disturbances over the western North Pacific, Part I: Energetics diagnosis. *J. Climate*, **24**, 927–941.

Hu, Q. and D. A. Randall (1994) Low-frequency oscillations in radiative–convective systems. *J. Atmos. Sci.*, **51**, 1089–1099.

Hu, Q. and D. A. Randall (1995) Low-frequency oscillations in radiative–convective systems, Part II: An idealized model. *J. Atmos. Sci.*, **52**, 478–490.

Inness, P. M. and J. M. Slingo (2003) Simulation of the Madden–Julian Oscillation in a coupled general circulation model, Part I: Comparison with observations and an atmospheric only GCM. *J. Climate*, **16**, 345–364.

Inness, P. M., J. M. Slingo, E. Guilyardi, and C. Jeffrey (2003) Simulation of the Madden–Julian Oscillation in a coupled general circulation model, Part II: The role of the basic state. *J. Climate*, **16**, 365–382.

Itoh, H. (1989) The mechanism for the scale selection of tropical intraseasonal oscillations, Part I: Selection of wavenumber 1 and the three-scale structure. *J. Atmos. Sci.*, **46**, 1779–1798.

Jiang, X. and D. E. Waliser (2008) Northward propagation of the subseasonal variability over the East Pacific Warm Pool. *Geophys. Res. Lett.*, **35**, L09814, doi: 10.1029/2008GL033723.

Jiang, X., T. Li, and B. Wang (2004) Structures and mechanisms of the northward propagating boreal summer intraseasonal oscillation. *J. Climate*, **17**, 1022–1039.

Johnson, R. H. and X. Lin (1997) Episodic trade wind regimes over the western Pacific warm pool. *J. Atmos. Sci.*, **54**, 2020–2034.

Johnson, R. H., T. M. Rickenbarch, S. A. Rutledge, P. E. Ciesielski, and W. H. Schubert (1999) Trimodal characteristics of tropical convection. *J. Climate*, **12**, 2397–2417.

Jones, C. and B. C. Weare (1996) The role of low-level moisture convergence and ocean latent heat fluxes in the Madden–Julian Oscillation: An observational analysis using ISCCP data and ECMWF analyses. *J. Climate*, **9**, 3086–3104.

Jones, C., D. E. Waliser, and C. Gautier (1998) The influence of the Madden-Julian Oscillation on ocean surface heat fluxes and sea surface temperature. *J. Climate*, **11**, 1057–1072.

Kemball-Cook, S. and B. Wang (2001) Equatorial waves and air–sea interaction in the boreal summer intraseasonal oscillation. *J. Climate*, **14**, 2923–2942.

Kemball-Cook, S. and B. C. Weare (2001) The onset of convection in the Madden–Julian Oscillation. *J. Climate*, **14**, 780–793.

Kemball-Cook, S., B. Wang, and X. Fu (2002) Simulation of the intraseasonal oscillation in ECHAM4 model: The impact of coupling with an ocean model. *J. Atmos. Sci.*, **59**, 1433–1453.

Khairoutdinov, M., D. A. Randall, and C. DeMott (2005) Simulation of the atmospheric general circulation using a cloud-resolving model as a super-parameterization of physical process. *J. Atmos. Sci.*, **62**, 2136–2154.

Khouider, B. and A. J. Majda (2006) A simple multicloud parameterization for convectively coupled tropical waves, Part I: Linear analysis. *J. Atmos. Sci.*, **63**, 1308——1323.

Khouider, B. and A. J. Majda (2007) A simple multicloud parameterization for convectively coupled tropical waves, Part II. Nonlinear simulations. *J. Atmos. Sci.*, **64**, 381–400.

Kikuchi, K. and B. Wang (2010) Spatiotemporal wavelet transform and the multiscale behavior of the Madden–Julian Oscillation. J. Climate, 23, 3814–3834.

Kikuchi, K. and Y. N. Takayabu (2004) Equatorial circumnavigation of moisture signal associated with the Madden-Julian Oscillation (MJO) during the boreal winter. *J. Meteorol. Soc. Japan*, **81**, 851–869.

Kiladis, G. N., K. H. Straub, and P. T. Haertel (2005) Zonal and vertical structure of the Madden–Julian Oscillation. *J. Atmos. Sci.*, **62**, 2790–2809.

Kiladis, G. N., M. C. Wheeler, P. T. Haertel, K. H. Straub, and P. E. Roundy (2009) Convectively coupled equatorial waves. *Rev. Geophys.*, **47**, RG2003.

Knutson, T. R., K. M. Weickmann, and J. E. Kutzbach (1986) Global-scale intraseasonal oscillations of outgoing longwave radiation and 250 mb zonal wind during northern hemisphere summer. *Mon. Wea. Rev.*, **114**, 605–623.

Krishnamurti, T. N. and D. Subrahmanyam (1982) The 30–50 day mode at 850 mb during MONEX. *J. Atmos. Sci.*, **39**, 2088–2095.

Krishnamurti, T. N., P. K. Jayakumar, J. Sheng, N. Surgi, and A. Kumar (1985) Divergent circulations on the 30 to 50 day time scale. *J. Atmos. Sci.*, **42**, 364–375.

Krishnamurti, T. N., D. K. Oosterhof, and A. V. Mehta (1988) Air–sea interaction on the time scale of 30 to 50 days. *J. Atmos. Sci.*, **45**, 1304–1322.

Krishnamurti, T. N., D. R. Chakraborty, N. Cubukcu, L. Stefanova, and T. S. V. Kumar (2003) A mechanism of the Madden–Julian Oscillation based on interactions in the frequency domain. *Quart. J. Roy. Meteorol. Soc.*, **129**, 2559–2590.

Krishnan, R., C. Zhang, and M. Sugi (2000) Dynamics of breaks in the Indian summer monsoon. *J. Atmos. Sci.*, **57**, 1354–1372.

Kuang, Z. (2008) A moisture–stratiform instability for convective coupled waves. *J. Atmos. Sci.*, **65**, 834–854.

Kuma, K.-I. (1994) The Madden–Julian oscillation and tropical disturbances in an aqua-planet version of JMA global model with T63 and T159 resolution. *J. Meteorol. Soc. Japan*, **72**, 147–172.

Kuo, H. L. (1965) On formation and intensification of tropical cyclones through latent heat release by cumulus convection. *J. Atmos. Sci.*, **22**, 40–63.

Kuo, H. L. (1974) Further studies of the parameterization of the influence of cumulus convection on large-scale flow. *J. Atmos. Sci.*, **31**, 1232–1240.

Lau, K. H. and N. C. Lau (1990) Observed structure and propagation characteristics of tropical summertime synoptic scale disturbances. *Mon. Wea. Rev.*, **118**, 1888–1913.

Lau, K. M. and P. H. Chan (1985) Aspects of the 40–50 day oscillation during northern winter as inferred from OLR. *Mon. Wea. Rev.*, **113**, 1889–1909.

Lau, K. M. and P. H. Chan (1986) Aspects of the 40–50 day oscillation during northern summer as inferred from OLR. *Mon. Wea. Rev.*, **114**, 1354–1367.

Lau, K. M. and L. Peng (1987) Origin of low-frequency (intraseasonal) oscillations in the tropical atmosphere, Part I: Basic theory. *J. Atmos. Sci.*, **44**, 950–972.

Lau, K. M. and L. Peng (1990) Origin of low-frequency (intraseasonal) oscillations in the tropical atmosphere, Part III: Monsoon dynamics. *J. Atmos. Sci.*, **47**, 1443–1462.

Lau, K. M. and C. H. Sui (1997) Mechanisms of short-term sea surface temperature regulation: Observations during TOGA–COARE. *J. Climate*, **10**, 465–472.

Lau, K. M. and H.-T. Wu (2003) Warm rain processes over the tropical ocean and climate implications. *Geophys. Res. Lett.*, **30**(24), 2290, doi: 10.1029/2003GL018567.

Lau, K. M., L. Peng, C. H. Sui, and T. Nakazawa (1989) Dynamics of super cloud clusters, westerly wind bursts, 30–60 day oscillations and ENSO: A unified view. *J. Meteorol. Soc. Japan*, **67**, 205–219.

Lau, N.-C. and K. M. Lau (1986) The structure and propagation of intraseasonal oscillation appearing in a GFDL general circulation model. *J. Atmos. Sci.*, **43**, 2023–2047.

Lau, N.-C., I. M. Held, and J. D. Neelin (1988) The Madden–Julian Oscillation in an idealized GCM model. *J. Atmos. Sci.*, **45**, 3810–3832.

Lawrence, D. M. and P. J. Webster (2002) The boreal summer intraseasonal oscillation: Relationship between northward and eastward movement of convection. *J. Atmos. Sci.*, **59**, 1593–1606.

Lee, M. I., I. S. Kang, J. K. Kim, and B. E. Mapes (2001) Influence of cloud–radiation interaction on simulating tropical intraseasonal oscillation with an atmospheric general circulation model. *J. Geophys. Res.*, **106**, 14219–14233.

Lee, M. I., I. S. Kang, and B. E. Mapes (2003) Impacts of cumulus convection parameterization on aqua-planet AGCM simulations of tropical intraseasonal variability. *J. Meteorol. Soc. Japan*, **81**, 963–992.

Li, T. and B. Wang (1994) A thermodynamic equilibrium climate model for monthly mean surface winds and precipitation over the tropical Pacific. *J. Atmos. Sci.*, **51**, 1372–1385.

Li, X. and H. R. Cho (1997) Development and propagation of equatorial waves. *Adv. Atmos. Sci. China*, **14**, 323–338.

Lim, H., T. K. Lim, and C.-P. Chang (1990) Reexamination of wave–CISK theory: Existence and properties of nonlinear wave–CISK modes. *J. Atmos. Sci.*, **47**, 3078–3091.

Lin, J. W.-B., J. Neelin, and N. Zeng (2000) Maintenance of tropical intraseasonal variability: Impact of evaporation–wind feedback and midlatitude storms. *J. Atmos. Sci.*, **57**, 2793–2823.

Lin, J., B. E. Mapes, M. Zhang, and M. Newman (2004) Stratiform precipitation, vertical heating profiles, and the Madden–Julian Oscillation. *J. Atmos. Sci.*, **61**, 296–309.

Lin, J.-L., G. N. Kiladis, B. E. Mapes, K. M. Weickmann, K. R. Sperber, W. Lin, M. C. Wheeler, S. D., Schubert, A. Del Genio, L. J. Donner *et al.* (2006) Tropical intraseasonal variability in 14 IPCC AR4 climate models, Part I: Convective signals. *J. Climate*, **19**, 2665–2690, doi: 10.1175/JCLI3735.1.

Lin, X. and R. H. Johnson (1996) Kinematic and thermodynamic characteristics of the flow over the western Pacific warm pool during TOGA–COARE. *J. Atmos. Sci.*, **53**, 695–715.

Lindzen, R. S. (1974) Wave–CISK and tropical spectra. *J. Atmos. Sci.*, **31**, 1447–1449.

Liu, P., B. Wang, K. R. Sperber, T. Li, and G. A. Meehl (2005) MJO in the NCAR CAM2 with the Tiedtke convective scheme. *J. Climate*, **18**(15), 3007–3020.

Liu, P., M. Satoh, B. Wang, H. Fudeyasu, T. Nasuno, T. Li, H. Miura, H. Taniguchi, H. Masunaga, X. Fu *et al.* (2009) An MJO simulated by the NICAM at 14-km and 7-km resolutions. *Mon. Wea. Rev.*, **137**, 3254–3268, doi: 10.1175/2009MWR2965.1.

Madden, R. A. (1986) Seasonal variations of the 40–50 day oscillation in the tropics. *J. Atmos. Sci.*, **43**, 3138–3158.

Madden, R. A. and P. R. Julian (1971) Detection of a 40–50 day oscillation in the zonal wind in the tropical Pacific. *J. Atmos. Sci.*, **28**, 702–708.

Madden, R. A. and P. R. Julian (1972) Description of global-scale circulation cells in the tropics with a 40–50 day period. *J. Atmos. Sci.*, **29**, 1109–1123.

Madden, R. A. and P. R. Julian (1994) Observations of the tropical 40–50 day oscillation: Review. *Mon. Wea. Rev.*, **122**, 814–837.

Majda, A. J. and J. A. Biello (2004) A multiscale model for tropical intraseasonal oscillations. *Proceedings of the National Academy of Sciences U.S.A.*, **101**, 4736–4741.

Majda, A. J. and J. A. Biello (2009) The skeleton of tropical intraseasonal oscillations. *Proceedings of the National Academy of Sciences U.S.A.*, **106**, 8417–8422.

Majda, A. J. and R. Klein (2003) Systematic multiscale models for the tropics. *J. Atmos. Sci.*, **60**, 393–408.

Majda, A. J. and S. N. Stechmann (2009) A simple dynamical model with features of convective momentum transport. *J. Atmos. Sci.*, **66**, 373–392.

Maloney, E. D. (2002) An intraseasonal oscillation composite life cycle in the NCAR CCM3.6 with modified convection. *J. Climate*, **15**, 964–982.

Maloney, E. D. and D. L. Hartmann (1998) Frictional moisture convergence in a composite life cycle of the Madden–Julian Oscillation. *J. Climate*, **11**, 2387–2403.

Maloney, E. D. and D. L. Hartmann (2001) The sensitivity of intraseasonal variability in the NCAR CCM3 to changes in convective parameterization. *J. Climate*, **14**, 2015–2034.

Manabe, S., J. Smagorinsky, and R. F. Strickler (1965) Simulated climatology of a general circulation model with a hydrologic cycle. *Mon. Wea. Rev.*, **93**, 769–798.

Mapes, B. E. (2000) Convective inhibition, subgrid-scale triggering energy, and stratiform instability in a toy tropical wave model. *J. Atmos. Sci.*, **57**, 1515–1535.

Mapes, B. E., S. Tulich, J. Lin, and P. Zuidema (2006) The mesoscale convection life cycle: Building block or prototype for large scale tropical waves? *Dyn. Atmos. Oceans*, **42**, 3–29.

Matsuno, T. (1966) Quasigeostrophic motions in the equatorial area. *J. Meteorol. Soc. Japan*, **44**, 25–43.

Matthews, A. J. (2000) Propagation mechanisms for the Madden–Julian Oscillation. *Quart. J. Roy. Meteorol. Soc.*, **126**, 2637–2651.

Matthews, A. J., J. M. Slingo, B. J. Hoskins, and P. M. Inness (1999) Fast and slow Kelvin waves in the Madden–Julian Oscillation of a GCM. *Quart. J. Roy. Meteorol. Soc.*, **125**, 1473–1498.

Mehta, A. V. and E. A. Smith (1997) Variability of radiative cooling during the Asian summer monsoon and its influence on intraseasonal waves. *J. Atmos. Sci.*, **54**, 941–966.

Moncrieff M. W. (2004) Analytic representation of the large-scale organization of tropical convection. *J. Atmos. Sci.*, **61**, 1521–1538.

Moncrieff, M. W. and E. Klinker (1997) Organized convective systems in the tropical western Pacific as a process in general circulation models: A TOGA COARE case study. *Quart. J. Roy. Meteorol. Soc.*, **123**, 805–827.

Moskowitz, B. M. and C. S. Bretherton (2000) An analysis of frictional feedback on a moist equatorial Kelvin mode. *J. Atmos. Sci.*, **57**, 2188–2206.

Milliff, R. F. and R. A. Madden (1996) The existence and vertical structure of the fast, eastward-moving disturbances in the equatorial troposphere. *J. Atmos. Sci.*, **53**, 586–597.

Miura, H., M. Satoh, T. Nasuno, A. T. Noda, and K. Oouchi (2007) A Madden–Julian Oscillation event realistically simulated by a global cloud-resolving model. *Science*, **318**, 1763–1765.

Murakami, T. (1980) Empirical orthogonal function analysis of satellite observed out-going longwave radiation during summer. *Mon. Wea. Rev.*, **108**, 205–222.

Murakami, T., B. Wang, and S. W. Lyons (1992) Summer monsoons over the Bay of Bengal and the eastern North Pacific. *J. Meteorol. Soc. Japan*, **70**, 191–210.

Murphree, T. and H. van den Dool (1988) Calculating winds from time mean sea level pressure fields. *J. Atmos. Sci.*, **45**, 3269–3281.

Nakazawa, T. (1988) Tropical super clusters within intraseasonal variations over the western Pacific. *J. Meteorol. Soc. Japan*, **66**, 823–839.

Nasuno, T., H. Miura, M. Satoh, A. T. Noda, and K. Oouchi (2009) Multi-scale organization of convection in a global numerical simulation of the December 2006 MJO event using explicit moist processes. *J. Meteorol. Soc. Japan*, **87**, 335–345.

Neelin, J. D. (1990) A hybrid coupled general circulation model for El Niño studies. *J. Atmos. Sci.*, **47**, 674–693.

Neelin, J. D. and J.-Y. Yu (1994) Modes of tropical variability under convective adjustment and the Madden–Julian Oscillation, Part I: Analytical theory. *J. Atmos. Sci.*, **51**, 1876–1894.

Neelin, J. D., I. M. Held, and K. H. Cook (1987) Evaporation–wind feedback and low-frequency variability in the tropical atmosphere. *J. Atmos. Sci.*, **44**, 2341–2348.

Nitta, T. (1987) Convective activities in the tropical western Pacific and their impact on the Northern Hemisphere summer monsoon. *J. Meteorol. Soc. Japan*, **65**, 373–390.

Ohuchi, K. and M. Yamasaki (1997) Kelvin wave–CISK controlled by surface friction: A possible mechanism of super cloud cluster. *J. Meteorol. Soc. Japan*, **75**, 497–511.

Oouchi, K., A. T. Noda, M. Satoh, B. Wang, S.-P. Xie, H. G. Takahashi, and T. Yasunari (2009) Asian summer monsoon simulated by a global cloud-system-resolving model: Diurnal to intra-seasonal variability. *Geophys. Res. Lett.*, **36**, L11815, doi: 10.1029/2009GL038271.

Ooyama, K. (1964) A dynamic model for the study of tropical cyclone development. *Geofits. Int. (Mexico)*, **4**, 187–198.

Pedlosky, J. (1979) *Geophysical Fluid Dynamics*. Springer-Verlag, New York, 710 pp.

Philander, S. G. H., T. Yamagata, and R. C. Pacanowski (1984) Unstable air–sea interactions in the Tropics. *J. Atmos. Sci.*, **41**, 604–613.

Randall, D. A., Harshvardhan, D. A. Dazlich, and T. G. Corsetti (1989) Interactions among radiation, convection, and large-scale dynamics in a general circulation model. *J. Atmos. Sci.*, **46**, 1943–1970.

Raymond, D. J. (2001) A new model of the Madden–Julian Oscillation. *J. Atmos. Sci.*, **58**, 2807–2819.

Raymond, D. J. and Z. Fuchs (2007) Convectively coupled gravity and moisture modes in a simple atmospheric model. *Tellus*, **59A**, 627–640.

Raymond, D. J. and Z. Fuchs (2009) Moisture modes and Madden–Julian Oscillation. *J. Climate*, **22**, 3031–3046.

Rui, H. and B. Wang (1990) Development characteristics and dynamic structure of tropical intraseasonal convection anomalies. *J. Atmos. Sci.*, **47**, 357–379.

Salby, M. L., R. R. Garcia, and H. H. Hendon (1994) Planetary-scale circulations in the presence of climatological and wave-induced heating. *J. Atmos. Sci.*, **51**, 2344–2367.

Satoh, M., T. Matsuno, H. Tomita, H. Miura, T. Nasuno, and S. Iga (2008) Nonhydrostatic Icosahedral Atmospheric Model (NICAM) for global cloud resolving simulations. *J. Comp. Phys.*, **227**, 3486–3514.

Sengupta, D., B. N. Goswami, and R. Senan (2001) Coherent intraseasonal oscillations of ocean and atmosphere during the Asian summer monsoon. *Geophys. Res. Lett.*, **28**, 4127–4130.

Shinoda, T. and H. H. Hendon (1998) Mixed layer modeling of intraseasonal variability in the tropical western Pacific and Indian Ocean. *J. Climate*, **11**, 2668–2685.

Shinoda, T., H. H. Hendon, and J. Glick (1998) Intraseasonal variability of surface fluxes and sea surface temperature in the tropical Western Pacific and Indian Oceans. *J. Climate*, **11**, 1685–1702.

Short, D. and K. Nakamura (2000) TRMM radar observations of shallow precipitation over tropical oceans. *J. Climate*, **13**, 4107–4124.

Sikka, D. R. and S. Gadgil (1980) On the maximum cloud zone and the ITCZ over Indian longitudes during the southwest monsoon. *Mon. Wea. Rev.*, **108**, 1840–1853.

Slingo, A. and J. M. Slingo (1988) Response of a general circulation model to cloud long-wave radiative forcing, Part 1: Introduction and initial experiments. *Quart. J. Roy. Meteorol. Soc.*, **114**, 1027–1062.

Slingo, J. M. and R. A. Madden (1991) Characteristics of the tropical intraseasonal oscillation in the NCAR community climate model. *Quart. J. Roy. Meteorol. Soc.*, **117**, 1129–1169.

Slingo, J. M., J. S. Boyle, J.-P. Ceron, M. Dix, B. Dugas, W. Ebisuzaki, J. Fyfe, D. Gregory, J.-F. Gueremy, J. Hack *et al.* (1996) Intraseasonal oscillations in 15 atmospheric general circulation models: Results from an AMIP diagnostic subproject. *Climate Dynamics*, **12**, 325–357.

Slingo, J. M., P. Inness, R. Neale, S. Woolnough, and G.-Y. Yang (2003) Scale interaction on diurnal to seasonal timescales and their relevance to model systematic errors. *Geophys. Ann.*, **46**, 139–155.

Sobel, A. H. and H. Gildor (2003) A simple time-dependent model of SST hot spas. *J. Climate*, **16**, 3978–3992.

Solodoch, A., W. R. Boos, Z. Kuang, and E. Tziperman (2011) Excitation of intraseasonal variability in the equatorial atmosphere by Yanai wave groups via WISHE-induced convection. *J. Atmos. Sci.*, **68**, 210–225.

Sperber, K. R. (2003) Propagation and vertical structure of the Madden–Julian Oscillation. *Mon. Wea. Rev.*, **131**, 3018–3037.

Straub, K. H. and G. N. Kiladis (2003) Interactions between the boreal summer intraseasonal oscillation and higher-frequency tropical wave activity. *Mon. Wea. Rev.*, **131**, 945–960.

Sui, C. H. and K. M. Lau (1989) Origin of low-frequency (intraseasonal) oscillations in the tropical atmosphere, Part 2: Structure and propagation of mobile wave–CISK modes and their modification by lower boundary forcings. *J. Atmos. Sci.*, **46**, 37–56.

Takahashi, M. (1987) Theory of the slow phase speed of the intraseasonal oscillation using the wave–CISK. *J. Meteorol. Soc. Japan*, **65**, 43–49.

Tian, B., D. E. Waliser, E. J. Fetzer, B. H. Lambrigtsen, Y. L. Yung, and B. Wang (2006) Vertical moist thermodynamic structure and spatial–temporal evolution of the MJO in AIRS observations. *J. Atmos. Sci.*, **63**, 2462–2485.

Ting, M. (1994) Maintenance of northern summer stationary waves in a GCM. *J. Atmos. Sci.*, **51**, 3286–3308.

Tomita, H., H Miura, S. Iga, T. Nasuno, and M. Satoh (2005) A global cloud-resolving simulation: Preliminary results from an aqua planet experiment. *Geophys. Res. Lett.*, **32**, L08805, doi: 10.1029/2005GL022459.

Tompkins, A. M. (2001) On the relationship between tropical convection and sea surface temperature. *J. Atmos. Sci.*, **58**, 529–545.

Tompkins, A. M. and T. Jung (2003) Influence of process interactions on MJO-like convective structures in the IFS model. Available at *http://www.ecmwf.int/publications/library/ecpublications/_pdf/workshop/2003/MJO/ws_mjo_tompkins.pdf*

Waliser, D. E., K. M. Lau, and J. H. Kim (1999) The influence of coupled sea surface temperatures on the Madden-Julian Oscillation: A model perturbation experiment. *J. Atmos. Sci.*, 56, 333-358.

Waliser, D. E., K. M. Lau, W. Stern, and C. Jones (2003a) Potential predictability of the Madden–Julian Oscillation. *Bull. Amer. Meteorol. Society*, **84**, 33–50.

Waliser, D. E., K. Jin, I. S. Kang, W. F. Stern, S. D. Schubert, M. L. Wu, K. M. Lau, M. I. Lee, J. Shukla, V. Krishnamurthy *et al.* (2003b) AGCM simulations of intraseasonal variability associated with the Asian summer monsoon. *Climate Dynamics*, **21**, 423–446.

Wang, B. (1988a) Dynamics of tropical low-frequency waves: An analysis of the moist Kelvin wave. *J. Atmos. Sci.*, **45**, 2051–2065.

Wang, B. (1988b) Comments on "An air–sea interaction model of intraseasonal oscillation in the tropics." *J. Atmos. Sci.*, **45**, 3521–3525.

Wang, B. and J. K. Chen (1989) On the zonal-scale selection and vertical structure of equatorial intraseasonal waves. *Quart. J. Roy. Meteorol. Soc.*, **115**, 1301–1323.

Wang, B. and T. Li (1993) A simple tropical atmosphere model of relevance to short-term climate variations. *J. Atmos. Sci.*, **50**, 260–284.

Wang, B. and T. Li (1994) Convective interaction with boundary-layer dynamics in the development of a tropical intraseasonal system. *J. Atmos. Sci.*, **51**, 1386–1400.

Wang, B. and F. Liu (2011) A model for scale interaction in the Madden–Julian Oscillation. *J. Atmos. Sci.* (accepted).

Wang, B. and H. Rui (1990a) Dynamics of the coupled moist Kelvin–Rossby wave on an equatorial beta-plane. *J. Atmos. Sci.*, **47**, 397–413.

Wang, B. and H. Rui (1990b) Synoptic climatology of transient tropical intraseasonal convection anomalies: 1975–1985. *Meteorol. Atmos. Phys.*, **44**, 43–61.

Wang, W. and M. E. Schlesinger (1999) The dependence on convective parametrization of the tropical intraseasonal oscillation simulated by the UIUC 11-layer atmospheric GCM. *J. Climate*, **12**, 1423–1457.

Wang, B. and X. Xie (1996) Low-frequency equatorial waves in vertically sheared zonal flow, Part I: Stable waves. *J. Atmos. Sci.*, **53**, 449–467.

Wang, B. and X. Xie (1997) A model for the boreal summer intraseasonal oscillation. *J. Atmos. Sci.*, **54**, 72–86.

Wang, B. and X. Xie (1998) Coupled modes of the warm pool climate system, Part I: The role of air–sea interaction in maintaining Madden–Julian Oscillation. *J. Atmos. Sci.*, **11**, 2116–2135.

Wang, B. and X. Xu (1997) Northern Hemisphere summer monsoon singularities and climatological intraseasonal oscillation. *J. Climate*, **10**, 1071–1085.

Wang, B. and Y. Xue (1992) Behavior of a moist Kelvin wave packet with nonlinear heating. *J. Atmos. Sci.*, **49**, 549–559.

Wang, B. and Q. Zhang (2002) Pacific–East Asian teleconnection, Part II: How the Philippine Sea anticyclone established during development of El Niño. *J. Climate*, **15**, 3252–3265.

Wang, B., I.-S. Kang, and J.-Y. Lee (2004) Ensemble simulations of Asian–Australian monsoon variability by 11 AGCMs. *J. Climate*, **17**, 803–818.

Wang, B., P. J. Webster, and H. Teng (2005) Antecedents and self-induction of the active-break Indian summer monsoon. *Geophys. Res. Lett.*, **32**, L04704.

Webster, P. J. (1983) Mechanisms of monsoon low-frequency variability: Surface hydrological effects. *J. Atmos. Sci.*, **40**, 2110–2124.

Webster, P. J. (1994) The role of hydrological processes in ocean–atmosphere interactions. *Rev. Geophys.*, **32**, 427–476.

Weickmann, K. M., (1983) Intraseasonal circulation and outgoing longwave radiation modes during Northern Hemisphere winter. *Mon. Wea. Rev.*, **111**, 1838–1858.

Weller, R. A. and S. P. Anderson (1996) Surface meteorology and air–sea fluxes in the western equatorial Pacific warm pool during the TOGA Coupled Ocean–Atmosphere Response Experiment. *J. Climate*, **9**, 1959–1990.

Woolnough, S. J., J. M. Slingo, and B. J. Hoskins (2000) The relationship between convection and sea surface temperature on intraseasonal timescales. *J. Climate*, **13**, 2086–2104.

Woolnough, S. J., J. M. Slingo, and B. J. Hoskins (2001) The organization of tropical convection by intraseasonal sea surface temperature anomalies. *Quart. J. Roy. Meteorol. Soc.*, **127**, 887–907.

Wu, M. L. C., S. Schubert, I. S. Kang, and D. E. Waliser (2002) Forced and free intraseasonal variability over the south Asian monsoon region simulated by 10 AGCMs. *J. Climate*, **15**, 2862–2880.

Wu, Z. (2003) A shallow CISK, deep equilibrium mechanism for the interaction between large scale convection and large scale circulations in the tropics. *J. Atmos. Sci.*, **60**, 377–392.

Xie, S.-P. and A. Kubokawa (1990) On the wave-CISK in the presence of a frictional boundary layer. *J. Meteorol. Soc. Japan*, **68**, 651–657.

Xie, S.-P., A. Kubokawa, and K. Hanawa (1993) Evaporation–wind feedback and the organizing of tropical convection on the planetary scale, Part II: Nonlinear evolution. *J. Atmos. Sci.*, **50**, 3884–3893.

Xie, X. and B. Wang (1996) Low-frequency equatorial waves in vertically sheared zonal flows, Part II: Unstable waves. *J. Atmos. Sci.*, **53**, 3589–3605.

Yamagata, T. (1987) Simple moist model relevant to the origin of intraseasonal disturbances in the Tropics. *J. Meteorol. Soc. Japan*, **65**, 153–165.

Yamagata, T. and Y. Hayashi (1984) Simple diagnostic model for the 30–50 day oscillation in the Tropics. *J. Meteorol. Soc. Japan*, **62**, 709–717.

Yamasaki, M. (1969) Large-scale disturbances in the conditionally unstable atmosphere in low latitudes. *Papers Meteorol. Geophys.*, **20**, 289–336.

Yang, B, X. Fu, and B. Wang (2008) Atmosphere–ocean conditions jointly guide convection of the boreal-summer intraseasonal oscillation: Satellite observations. *J. Geophys. Res.*, **113**, D11105, doi: 10.1029/2007JD009276.

Yano, J.-I. and K. Emanuel (1991) An improved model of the equatorial troposphere and its coupling with the stratosphere. *J. Atmos. Sci.*, **48**, 377–389.

Yasunari, T. (1979) Cloudiness fluctuations associated with the Northern Hemisphere summer monsoon. *J. Meteorol. Soc. Japan*, **57**, 227–242.

Yasunari, T. (1980) A quasi-stationary appearance of 30–40 day period in the cloudiness fluctuations during the summer monsoon over India. *J. Meteorol. Soc. Japan*, **58**, 225–229.

Zhang, C. D. (1996) Atmospheric intraseasonal variability at the surface in the tropical western Pacific Ocean. *J. Atmos. Sci.*, **53**, 739–758.

Zhang, C. D. (2005) Madden–Julian Oscillation. *Rev. Geophys.*, **43**, 1–36.

Zhang, C. D. and S. P. Anderson (2003) Sensitivity of intraseasonal perturbations in SST to the structure of the MJO. *J. Atmos. Sci.*, **60**, 2196–2207.

Zhang, C. D. and H. H. Hendon (1997) Propagating and standing components of the intraseasonal oscillation in tropical convection. *J. Atmos. Sci.*, **54**, 741–752.

Zhu, B. and B. Wang (1993) The 30–60 day convection seesaw between the tropical Indian and western Pacific Oceans. *J. Atmos. Sci.*, **50**, 184–199.

11

Modeling intraseasonal variability

K. R. Sperber, J. M. Slingo, and P. M. Inness

11.1 INTRODUCTION

The Madden–Julian Oscillation (MJO) has long been an aspect of the global climate that has provided a challenging test for the climate modeling community. Since the 1980s there have been numerous studies of simulation of the MJO and boreal summer intraseasonal variability (BSISV) in general circulation models (GCMs), ranging from Hayashi and Golder (1986, 1988) and Lau and Lau (1986), through to more recent studies such as Zhang *et al*. (2006), Sperber and Annamalai (2008), and Kim *et al*. (2009). Of course, attempts to reproduce the MJO in climate models have proceeded in parallel with developments in our understanding of what the MJO is and what drives it. In fact, many advances in understanding the MJO have come through modeling studies. In particular, the failure of climate models to simulate various aspects of the MJO has prompted investigations into the mechanisms that are important to its initiation and maintenance, leading to improvements both in our understanding of, and ability to simulate, the MJO.

Most of the early studies concentrated on the ability of models to simulate the signal of the MJO in upper-level winds (e.g., Swinbank *et al*., 1988), partly because these were the fields in which the MJO was originally identified in observations, and partly because the dynamical signal of the MJO has often been more reliable in GCMs than its convective signal. Many quite simple GCMs with coarse resolution were shown to produce a peak at approximately the right frequency in the spectrum of upper-tropospheric wind variability, along with many of the characteristics of the observed oscillation (e.g., Slingo and Madden, 1991; Hayashi and Golder, 1993). Furthermore, these studies showed that the simulated oscillation resembled the observed structure of a Kelvin wave coupled to a forced Rossby wave, and with the typical baroclinic structure in the vertical (e.g., Knutson and Weickmann, 1987; Sperber *et al*., 1997; Matthews *et al*., 1999). However, there remained some substantial deficiencies; in particular, the periodicity of the simulated oscillation tended

W. K. M. Lau and D. E. Waliser (Editors), *Intraseasonal Variability in the Atmosphere–Ocean Climate System* (Second Edition).

to be too short, nearer 25–30 days than 40–50 days, and the eastward propagation of the convective anomaly across the warm pool of the Indian and West Pacific Oceans was poorly simulated.

In the 1990s, following the more limited intercomparison of Park *et al.* (1990), a comprehensive study of the ability to simulate the MJO by the then state-of-the-art atmospheric models was carried out by Slingo *et al.* (1996) as part of the first Atmospheric Model Intercomparison Project (AMIP I; Gates *et al.*, 1999). In that study, the following key questions for simulation of the MJO were addressed:

- Can characteristics of the convective parameterization, such as the vertical profile of heating, closure (e.g., moisture convergence), be identified, which might influence the existence of intraseasonal variability?
- How does the intraseasonal oscillation depend on aspects of a model's basic climate?
- What seasonal and interannual variability in the activity of the MJO is simulated? How does it compare with reality?

Slingo *et al.* (1996) showed that, although there were GCMs that could simulate some aspects of the MJO, all the models in their survey were deficient in some respect. In particular, the period of the oscillation was too fast in many models, and the amplitude of the MJO signal in upper-level winds was often too weak. No model was able to capture the pronounced spectral peak associated with the observed MJO. In reality, the MJO is strongest and most coherent in northern winter/spring, whereas many models showed no seasonality for the MJO. Furthermore, as the envelope of enhanced convection associated with variations in the upper wind field develops over the Indian Ocean and propagates eastwards into the West Pacific, the propagation speed of the oscillation is observed to slow down. Many models failed to capture this geographical dependence. In an extension of the study of Slingo *et al.* (1996), Sperber *et al.* (1997) focused on the most skilful models in AMIP I and showed that, at best, the models produced a pattern of standing oscillations, with convective anomalies developing and decaying over the Indian Ocean on intraseasonal timescales, with out-of-phase oscillations occurring over the West Pacific.

More recent intercomparisons have shown that most models are still unable to reproduce the observed concentration of power at the 40 to 50-day timescale with the precipitation signal being too weak in most models (Wu *et al.*, 2002; Lin *et al.*, 2006, 2008; Zhang *et al.*, 2006; Kim *et al.*, 2009). However, progress in simulating the MJO is being made. At a workshop on simulation and prediction of subseasonal variability in 2003 (Waliser *et al.*, 2003c), most of the models presented were able to simulate at least some aspects of the MJO. In contrast to the study of Slingo *et al.* (1996), some of the modeling results presented at this workshop showed an MJO that was actually too strong or propagated more slowly than the observed oscillation. More recently, Sperber and Annamalai (2008) demonstrated that virtually all the Coupled Model Intercomparison Project-3 (CMIP3) models produce eastward propagation of intraseasonal convective anomalies over the Indian Ocean, a

demonstrative improvement compared with previous generations of models. Even so, the questions posed in 1996 by Slingo *et al.* are still very relevant.

The initial focus of this chapter will be on modeling the MJO during northern winter, when it is characterized as a predominantly eastward-propagating mode as seen in observations. Aspects of simulation of the MJO will be discussed in the context of its sensitivity to formulation of the atmospheric model, and the evidence that it may be a coupled ocean–atmosphere phenomenon. Later, we will discuss the challenges regarding simulation of boreal summer intraseasonal variability, which is more complex since it is a combination of the eastward-propagating MJO and the northward propagation of the tropical convergence zone. Finally, some concluding remarks on future directions in modeling the MJO and its relationship with other timescales of variability in the tropics will be made.

11.2 MODELING THE MJO IN BOREAL WINTER

11.2.1 Interannual and decadal variability of the MJO

Slingo *et al.* (1996) introduced an index of MJO activity based on the near-equatorial zonal wind at 200 hPa, to provide a preliminary measure of MJO variability in models and to describe interannual and decadal variations in MJO activity (Figure 11.1). This index uses the fact that the MJO projects on to the zonal mean

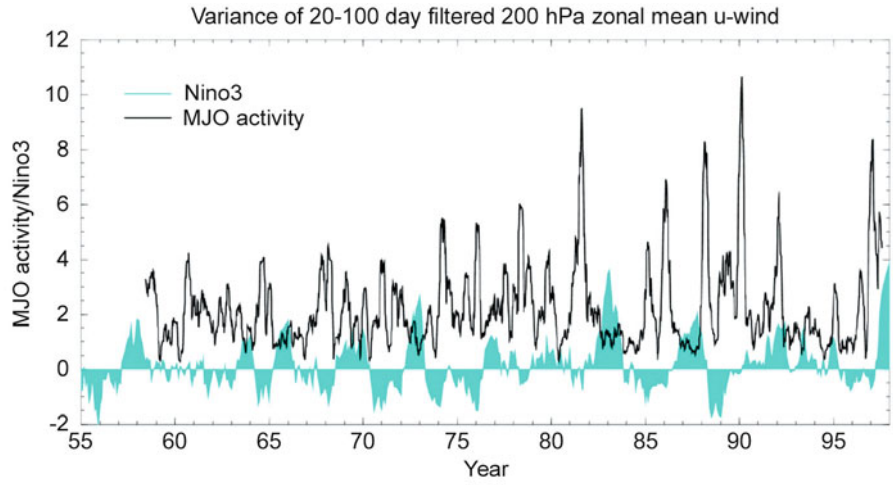

Figure 11.1. Interannual variability in the activity of the MJO as depicted by the time series of the variance ($m^2\ s^{-2}$) of the 20 to 100-day bandpass-filtered zonal mean zonal wind from the recent ECMWF reanalysis for 1958 to 1997 (ERA-40). A 100-day running mean has been applied to the variance time series. The lower, shaded curve is the sea surface temperature anomaly (K) for the Niño-3 region (5°N–5°S, 90°W–150°W) (see Slingo *et al.*, 1999 for more details on calculation of the MJO index).

of the equatorial zonal wind component through its Kelvin and Rossby wave characteristics (Slingo *et al.*, 1999).

This index also shows that there is substantial interannual variability in the activity of the MJO, which Slingo *et al.* (1999) and Hendon *et al.* (1999) found was not strongly related to sea surface temperatures (Figure 11.1 also includes the time series of the Niño-3 region SST anomaly). This lack of predictability was also seen in a four-member ensemble of 45-year integrations with the Hadley Centre climate model (HADAM2a), forced by observed SSTs for 1949 to 1993, suggesting that the interannual behavior of the MJO is not controlled by the phase of El Niño and would appear to be mainly chaotic in character. In a related study, Gualdi *et al.* (1999b) also showed that only with a very large ensemble was it possible to detect any predictability for the interannual behavior of the MJO. These results may have important implications for the predictability of the coupled system through the influence of the MJO on westerly wind activity and hence on the development and amplification of El Niño (e.g., McPhaden, 1999; Kessler and Kleeman, 2000; Lengaigne *et al.*, 2004; see Chapter 6 herein).

Also evident in Figure 11.1 is a marked decadal change in the activity of the MJO. Prior to the mid-1970s, the activity of the MJO was consistently lower than during the latter part of the record. This may be related to either inadequate data coverage, particularly over the tropical Indian Ocean prior to the introduction of satellite observations, or to the real effects of a decadal timescale warming in the tropical SSTs. However, as described by Slingo *et al.* (1999), the ensemble of integrations with the Hadley Centre model were able to reproduce the low-frequency decadal timescale variability of MJO activity seen in Figure 11.1. The activity of the MJO is consistently lower in all realizations prior to the mid-1970s, suggesting that the MJO may indeed become more active as tropical SSTs become warmer with implications for the effects of global warming on the coupled tropical atmosphere–ocean system. Zveryaev (2002) also notes interdecadal changes in intraseasonal variability during the Asian summer monsoon. Slingo *et al.* (1999) based their results on NCEP/NCAR reanalyses. The fact that very similar results have been obtained from the ECMWF 40-year reanalysis (ERA-40), as shown in Figure 11.1, adds credence to the decadal variability identified earlier.

11.2.2 Sensitivity to formulation of the atmospheric model

In the 1980s, the resolution of GCMs was low (typically spectral T21, R15, equivalent to a grid of $\sim 5^{\circ}$) by comparison with the current generation of models, and much of the early success in simulating an eastward-propagating mode was achieved with models whose resolution was not sufficient to resolve tropical synoptic systems. Since the active phase of the MJO is often characterized by smaller scale organized convection associated with tropical synoptic systems, this lack of resolution was considered a possible cause for the errors in simulation of the MJO. In the early 1990s, Slingo *et al.* (1992) analyzed tropical variability in high-resolution (spectral T106, $\sim 1^{\circ}$) simulations with the ECMWF model and showed that the various aspects of tropical synoptic variability, such as easterly waves, could

be captured with considerable skill. Their integrations were not long enough, however, to say anything conclusive about the MJO.

In AMIP I, the majority of models were run at resolutions capable of capturing synoptic variability (typically spectral T42, equivalent to a grid of at least 3°, and above). However, the results from the study by Slingo *et al.* (1996) suggested that horizontal resolution did not play an important role in determining a model's intraseasonal activity. Even at much higher resolutions, up to as much as T576, evidence from ECMWF suggested no improvement in simulation of the MJO (Jung and Tompkins, 2003). Rather, Bechtold *et al.* (2008) indicated that improvements to convection and diffusion were responsible for an improved representation of the MJO in the ECMWF Integrated Forecast System. Similarly, improved physics and dynamics in coarse-resolution climate models has led to better fidelity in representing the MJO (e.g., Ringer *et al.*, 2006), and importantly other GCMs that use convective parameterization have been able to produce credible simulations of the MJO (e.g., Kemball-Cook *et al.*, 2002; Sperber *et al.*, 2005, 2008; Sperber and Annamalai, 2008). Hence, at this stage there is no clear evidence that increasing the horizontal resolution in the atmospheric model will improve simulation of the MJO, possibly because of more fundamental errors in representing convection and its interaction with dynamics. Support for this hypothesis has come recently from the studies of Grabowski (2003) and Randall *et al.* (2003) in which the convective parameterization has been replaced by a two-dimensional cloud-resolving model (CRM)—the "cloud-resolving convective parameterization" or super-parameterization approach. By representing the interaction between convective clouds and the dynamics more completely, their studies have shown dramatic improvements in the organization of convection on both synoptic and intraseasonal timescales. Use of a CRM in this way provides useful insights into fundamental aspects of organized convection in the tropics and how to address sub-gridscale processes. For example Thayer-Calder (2008) and Thayer-Calder and Randall (2009) noted that the relationship between column moisture and precipitation intensity is similar to observations in the Super-parameterized Community Atmospheric Model (SPCAM), which has a realistic simulation of the MJO (Benedict and Randall, 2009; Kim *et al.*, 2009). However, this relationship was poorly represented in models that had problematic MJO simulations (Kim *et al.*, 2009). Similar benefits are obtained by explicitly resolving cloud systems in ultra high–resolution global model simulations/hindcasts of the MJO (Miura *et al.*, 2007, 2009) with Masunaga *et al.* (2008) gaining insight into shortcomings in model-parameterized cloud microphysics by comparing with Tropical Rainfall Measuring Mission (TRMM) and CloudSat observations. The ultra high–resolution approach also provides insight into multiscale interactions that are embedded in the MJO, which are not otherwise resolved in coarse-resolution GCMs (Oouchi *et al.*, 2009), including MJO conditions under which the generation of tropical cyclones is favorable (Taniguchi *et al.*, 2010).

Even though there is no compelling evidence to suggest that horizontal resolution is important for simulation of the MJO, this appears not be the case for vertical resolution. Experiments with the Met Office Unified Model (UM,

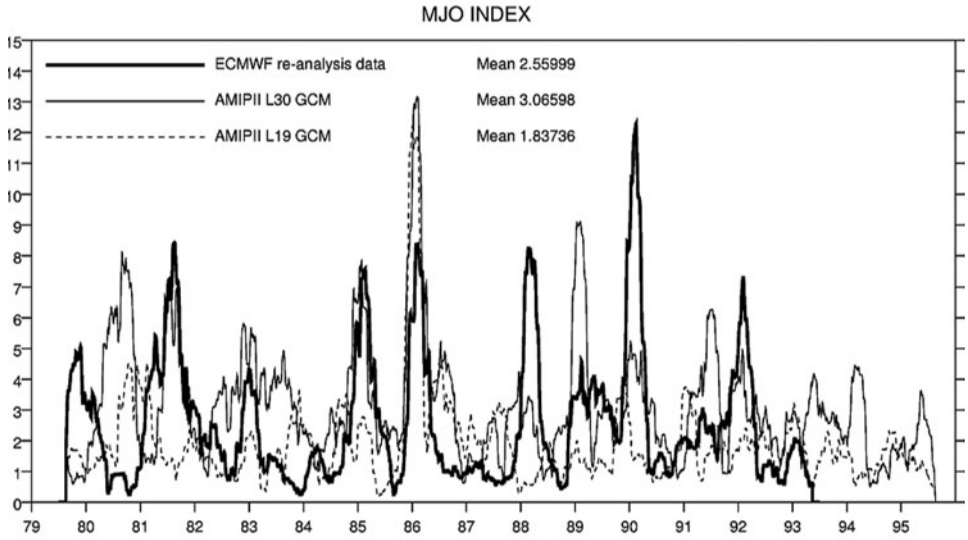

Figure 11.2. Influence of changing the vertical resolution in the Hadley Centre's atmospheric model (HadAM3) on the strength of the MJO as described by the index used in Figure 11.1. Note the increased amplitude of MJO activity in the L30 version of the model and the improved seasonality with respect the ECMWF reanalyses (from Inness *et al*., 2001).

version HadAM3) using two different vertical resolutions (19 and 30 levels) have shown significant differences in the amount of variability in the tropical upper-tropospheric zonal wind component associated with the MJO (Inness *et al*., 2001; Figure 11.2).

Most of the extra levels were placed in the middle and upper troposphere, decreasing the layer thickness in the mid-troposphere from 100 hPa to 50 hPa, and giving a much better representation of the temperature and humidity structure around the freezing level. The model results suggested a change in the temporal organization of convection which was investigated further using an aqua-planet version of the UM. These experiments, described in detail in Inness *et al*. (2001), showed that when the vertical resolution was increased in the UM, the spectrum of tropical cloud top heights changed from a bimodal to a tri-modal distribution, with the third peak in the mid-troposphere, near the freezing level. Associated with periods when these mid-level clouds were dominant, the detrainment from these clouds significantly moistened the mid-troposphere. In comparison, the 19-level version of the model shows no evidence of a tri-modal distribution in convection and no such moistening events.

Many conceptual models of tropical convection are based on a bimodal cloud distribution, emphasizing shallow "trade wind" or boundary layer cumuli and deep cumulonimbi. However, TOGA-COARE results have shown the dominance of cumulus congestus clouds, and point to a tri-modal cloud distribution in which freezing level inversion is the key. Observational studies have shown that, during

the suppressed phase of the MJO, tropical convection is dominated by clouds that terminate around the stable layer at the 0°C level (Johnson *et al*., 1999), and that these clouds provide a source of moisture to the mid-troposphere (Lin and Johnson, 1996). Inness *et al*. (2001) argued that the development of a stable layer around the tropical melting level, which is frequently observed over the tropical oceans, acts to reinforce the transition from the enhanced convective phase to the suppressed phase of the MJO. Subsequently, the moistening of the mid-troposphere during the suppressed phase acts to reinforce the transition back to the active phase. This is consistent with the ''recharge–discharge'' theory for the MJO proposed by Bladé and Hartmann (1993) in which the MJO timescale may be set by the time it takes for the moist static energy to build up following the decay of the previous convective event. It may be that the recharging of the moist static energy is achieved in part by the injection of moisture into the mid-troposphere by the cumulus congestus clouds that dominate during the suppressed phase of the MJO.

The appearance of these congestus clouds has been postulated as the reason for the improvement in simulation of the MJO in the 30-level version of the UM since observations indicate that shallow and cumulus congestus cloud dominate during the early-stage development of the MJO (Morita *et al*., 2006; Benedict and Randall, 2007). This is shown to be partly due to improved resolution of the freezing level and of the convective processes occurring at this level. However, the results also suggest that convection and cloud microphysics schemes must be able to represent cumulus congestus clouds which, being neither shallow nor deep cumulus as well as often weakly precipitating, tend not to be explicitly represented in current schemes. In addition, this study has highlighted the importance of understanding and modeling the suppressed phase of the MJO; over the last two decades most of the attention has been given, understandably, to the active phase of the MJO, but with limited success. Further evidence of the importance of cumulus congestus in the lifecycle of the MJO comes from a theoretical and simple modeling study by Wu (2003). This study presents a ''shallow CISK, deep equilibrium'' mechanism for the interaction of convection and large-scale circulations in the tropics, emphasizing the role of heating by congestus clouds as a precursor to the outbreak of deep convection corresponding to the active phase of the MJO.

The results of Inness *et al*. (2001) highlighted the importance of vertical resolution, in line with the study of Tompkins and Emanuel (2000), as well as the need to properly represent the tri-modal structure of tropical convection. The importance of the cumulus congestus stage of tropical convection is being stressed here as a potentially important ingredient for the MJO. This means that vertical resolution in the free troposphere must be adequate to resolve formation of the freezing level inversion and the cooling associated with melting precipitation. In the absence of resolving the tri-model distribution of clouds and the contribution of low-level clouds in moistening the atmosphere ahead of deep MJO convection, models can compensate by exacerbating other interactions, such as lower-tropospheric moistening due to reduced eddy moisture advection between the equator and poleward latitudes (Maloney, 2009).

That the MJO is intimately linked to convection is undeniable, and numerous modeling studies have demonstrated that changes to the convection scheme can produce radical changes in simulation of the MJO. For example, Slingo *et al.* (1994) replaced the Kuo convection scheme (Kuo, 1974; closed on moisture convergence) with the convective adjustment scheme of Betts and Miller (Betts, 1986; closed on buoyancy) and showed extreme sensitivity in the representation of organized tropical convection at synoptic to intraseasonal timescales, with the Kuo scheme unable to capture realistic levels of tropical variability. This suggested that a dependence of convective activity on moisture convergence might be a factor in the poor simulation of the MJO. This was further supported by Nordeng (1994), who showed that when the moisture convergence dependence of the ECMWF convection scheme was replaced by a buoyancy criterion, there was a marked improvement (i.e., increase) in transient activity in the tropics of the ECMWF model.

Subsequently, the closure of the convection scheme of the Australian Bureau of Meteorology Research Center's seasonal prediction GCM has been modified from moisture convergence to convective available potential energy (CAPE) relaxation, with a resulting increase in eastward-moving power at MJO frequencies (Wheeler, 2003). At a broader level, Slingo *et al.* (1996) also suggested that those models in AMIP I with a reasonable level of intraseasonal activity use convection schemes that were closed on buoyancy rather than moisture supply. However, as Wang and Schlesinger (1999) demonstrated, it is possible to change the strength of the MJO substantially by modifying the particular closure used within the convection scheme, as well as the fundamental design of the convection scheme itself. But, as they point out, some configurations of convection schemes did not produce realistic mean climates which, as will be discussed later, can compromise simulation of the MJO. Studies such as those of Maloney and Hartmann (2001) and Lee *et al.* (2003) also demonstrated that considerable changes to the simulation of the MJO can be brought about by modifications to the convective parameterization. In this case, the imposition of a minimum entrainment rate for deep convective plumes in the Arakawa–Schubert convection scheme (Arakawa and Schubert, 1974; Tokioka *et al.*, 1988) in an aqua-planet configuration of the Seoul National University GCM resulted in a much stronger MJO-like signal.

Many schemes use an equilibrium approach to convection, which assumes that instabilities are removed completely at each time step. Sensitivity experiments with non-equilibrium closures suggest that improvements in the intraseasonal organization of convection can be achieved, but often at the expense of the quality of the mean climate. Indeed, separating the effects of changes to the convection scheme on the organization of convection, from the effects on the mean climate of the tropics has been notoriously difficult. For example, Inness and Gregory (1997) showed that the inclusion of the vertical transport of momentum by the convection scheme considerably weakened the upper-tropospheric signal of the MJO in the UM, possibly due to changes in basic state winds in tropical latitudes.

Although much of the focus of attention for simulation of the MJO has been on the convective parameterization, there are other aspects of the physics that deserve attention. For example, Salby *et al.* (1994) suggested that the oscillation may be very

sensitive to boundary layer friction in which the sympathetic interaction between convection and large-scale circulation, through frictional wave CISK (see Chapter 10), can explain many aspects of the observed behavior of the MJO in the eastern hemisphere. Due to frictional effects, surface convergence is shifted some 40° to 50° to the east of the heating, towards low pressure and in-phase with the temperature anomaly associated with the Kelvin wave. This study also emphasized the importance of the Rossby gyres generated by the heating. In the amplifying phase of the MJO their position reinforces moisture convergence to the east of the heating, so providing the necessary conditions for the heating to amplify and propagate eastwards. Salby *et al.* (1994) showed that their solutions were very sensitive to boundary layer friction, suggesting that this may be an important factor in GCMs. The most skilful models in AMIP I did not employ frictional wave CISK or wind-induced surface heat exchange (WISHE; Emanuel, 1987) for maintaining the MJO (Sperber *et al.*, 1997). On the other hand, Waliser *et al.* (1999) note that when coupling between the atmosphere and ocean was introduced (see Section 11.2.3), then frictional wave CISK was enhanced and became an important factor in the improved simulation of the MJO.

With low-level moisture convergence leading convection, as suggested by Salby *et al.* (1994), there is a pronounced westward vertical tilt in divergence, vertical velocity, zonal wind, and specific humidity, as demonstrated by Sperber (2003) and Seo and Kim (2003) using the NCEP/NCAR reanalysis. More recent GCMs represent this process and these vertical structures as part of the mechanism for MJO propagation (Sperber *et al.*, 2005; Benedict and Randall, 2009). The strongest zonal inflow into the convective region occurs in the free troposphere between 600 hPa and 700 hPa. Conditions to the east of the center of convection promote eastward propagation of the MJO, while to the west they erode convection. Thus, free tropospheric interactions are also an essential component of the MJO that models need to represent. The ability of models to represent these features will be sensitive to the simulated diabatic heating profile, and thus to the aforementioned sensitivities to convection scheme and vertical resolution. Unfortunately, such detailed analyses of models are not the norm due to the extensive archive of data required. However, further progress in understanding a model's ability to capture the MJO will necessitate more comprehensive model output to become routine (see Section 11.5).

Raymond (2001) suggested that cloud–radiation interaction might be important for simulation of the MJO. Slingo and Madden (1991), in their study of the MJO simulated by the NCAR Community Climate Model, investigated the role of atmospheric cloud longwave forcing in the behavior of the MJO. They showed that cloud–radiation interaction had little effect on the periodicity of the MJO and its basic characteristics. Without cloud–radiation interaction, the simulated MJO was slightly more regular. However, this issue probably deserves revisiting with the current models that have a more sophisticated representation of cloud microphysics. In fact, this area is indeed being investigated more fully in the context of the super-parameterization approach discussed earlier in this chapter (e.g., Grabowski and Moncrieff, 2002), with initial results indicating that the interaction between clouds

and radiation does indeed have a part to play in the large-scale organization of convection.

Tropical channel atmospheric models have also provided insight into mechanisms by which the MJO can be initiated. In these models, boundary conditions are specified at predetermined latitudes in the northern hemisphere and southern hemisphere, while equatorward the system is free to develop on its own at all longitudes. Using the tropical channel version of the National Center for Atmospheric Research Mesoscale Model, Ray *et al.* (2009) found that extratropical disturbances from the southern hemisphere that propagate into the western Indian Ocean were the most important influence for initiating observed MJOs. The results were robust at lead times of >30 days, suggesting the potential for long-lead forecasts of the MJO beyond that estimated from perfect predictability experiments (Waliser *et al.* 2003b; see Chapter 12). Although latent heating and moist processes play an important role in eastward propagation of the MJO, these processes were not found to be important in the initiation phase. Similarly, specification of time-varying SST had no impact on initiation of the MJO, though coupled air–sea interactions, which might amplify a local perturbation, were not considered by Ray *et al.* (2009). This suggestion of an extratropical trigger is consistent with the observed result of Matthews (2008), though in both studies the trigger was related to perturbations arising from an immediate predecessor MJO event but were not influential in initiating primary (spontaneously generated) MJO events.

11.2.3 Modeling the MJO as a coupled ocean–atmosphere phenomenon

One of the biggest advances in modeling the MJO has been in the recognition that it almost certainly involves coupling with the ocean (as discussed in Chapter 7 and references cited therein). There is now convincing evidence from observations that the MJO interacts with the upper ocean in such a way for it to be a coupled phenomenon, and which may therefore require an interactive ocean system for its proper simulation.

In a comprehensive analysis of observational and reanalysis data, Woolnough *et al.* (2000) showed that, for the Indian Ocean and West Pacific, a coherent relationship exists between MJO convection, surface fluxes, and sea surface temperature (SST), in which SSTs are warmer than normal about 10 days prior to, and east of, the maximum in convective activity (Figure 11.3). As shown in Figure 11.3, this warming is associated with increased solar radiation, reduced surface evaporation, and light winds, which reduces vertical mixing. To the west of the convective maximum, SSTs cool due to reduced solar radiation and enhanced evaporation associated with stronger winds. A key requirement for the observed temporal and spatial phase relationship between latent heat flux, winds, and convection is the presence of a surface westerly basic state, an issue that emerges later as being crucial for improved simulation of the MJO in coupled models. In addition to the SST anomaly pattern, Figure 11.3 also shows the phasing of surface flux and wind stress anomalies relative to the convective maximum.

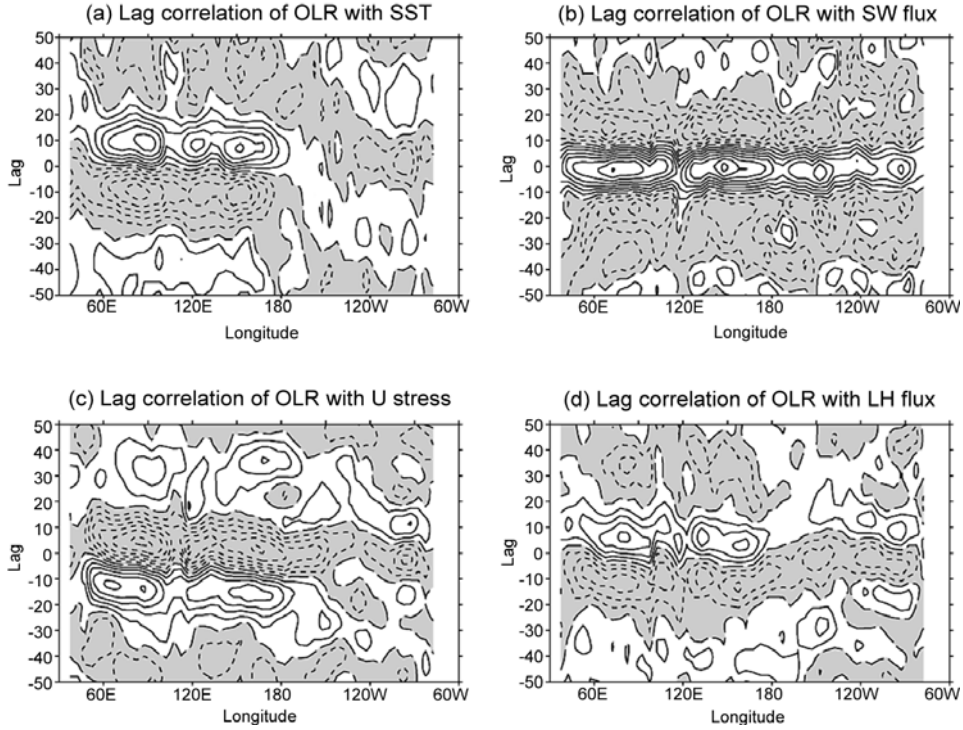

Figure 11.3. Lag correlations between observed outgoing longwave radiation (OLR; convection) and surface fields: (a) sea surface temperature (SST), (b) shortwave radiation, (c) zonal wind stress, and (d) latent heat flux. Negative lags indicate that convection lags the surface field, positive lags indicate that convection leads surface fields. The sign convention is such that positive correlations indicate that enhanced convection (a negative OLR anomaly) is correlated with a negative SST anomaly, reduced shortwave radiation at the surface, enhanced evaporation, or an easterly wind stress anomaly (from Woolnough *et al*., 2000).

Having established that the surface fluxes and winds associated with the MJO can force intraseasonal variations in SSTs, which can typically reach 1 K in individual events, it then needs to be confirmed that the atmosphere can respond to these SST variations. In a related study, Woolnough *et al*. (2001) therefore used the observed SST perturbations associated with the MJO to form the basis of a series of experiments with the aqua-planet version of the UM to investigate, first, the organization of tropical convection by these intraseasonal anomalies and, second, how this organization depends on the temporal behavior of these SST anomalies. The study showed that boundary layer humidity adjusts rapidly to the presence of the SST anomaly. However, the free atmosphere takes longer to adjust. Initial convective plumes triggered by the presence of warm SSTs are rapidly eroded by entrainment of dry air in the free troposphere and so terminate relatively low down

in the troposphere. However, detrainment of the terminating plumes moistens the atmosphere allowing subsequent convective plumes to penetrate further before decaying. Eventually, the atmosphere is moist enough to support deep convection through most of the depth of the troposphere. This type of preconditioning behavior means that the most intense convection occurs, not directly over the warm SST anomaly, but to the west over the maximum gradient in SST between the warm and cold anomalies, as observed in the MJO. The timescale of about 5 days for preconditioning of the tropical atmosphere for deep convection has been confirmed in a detailed study of reanalysis data by Sperber (2003). Associated with this adjustment timescale, the experiments of Woolnough *et al.* (2001) also showed that intraseasonal SST anomalies could potentially organize convection in a manner that favors the longer timescales ($\sim$60 days) typical of the observed MJO, and which produces a phase relationship between convection and SST, consistent with the observed structure over the Indian and West Pacific Oceans.

Sperber *et al.* (1997) had already suggested that a possible reason for the lack of realistic propagation of convective anomalies in atmospheric models used in AMIP I was that the MJO may be, at least in part, a coupled mode. The results of Woolnough *et al.* (2000, 2001) appeared to support this hypothesis. Flatau *et al.* (1997) also proposed that the eastward propagation of MJO convection might involve a coupled mechanism, and performed a simple numerical experiment to test their hypothesis. Using a low-resolution (spectral R15) GCM, configured as an aqua-planet model, they modeled the dependence of SST on surface fluxes empirically by relating SST fluctuations to changes in the strength of low-level winds, based on observed SST changes and windspeeds from drifter buoys in the tropical Pacific. Their results showed that oscillations in low-level winds on intraseasonal timescales became more organized when the variations of SST with windspeed were included, producing a coherent eastward-propagating signal which resembled the MJO in some respects.

A similar modeling study was carried out by Waliser *et al.* (1999), but using a more complex GCM and a more realistic parameterization of SST anomalies in the tropics, based on a slab ocean model of fixed depth in which SST anomalies developed in association with changes in net surface heat flux according to the formula:

$$dT'/dt = F'/(\rho C_p H) - \gamma T'$$

where T' is the SST anomaly; F' is the surface flux anomaly; H is the depth of the mixed layer (fixed at 50 m); and γ is a damping factor, set to $(50 \text{ days})^{-1}$. Changes in SST due to this formula were small, however, being of the order of 0.1°C to 0.15°C and were due largely to changes in latent heat flux ahead of and behind the convective region, and to changes in shortwave flux associated with variations in convective cloudiness. It is worth noting that in their study the use of a fixed mixed layer depth underestimated the SST variability associated with the MJO since the warming during the suppressed phase is, in reality, strongly amplified by the shoaling of the mixed layer under light wind conditions (e.g., Weller and Anderson, 1996). Nevertheless, their results showed that MJO simulation was improved in a number

of respects. The period of the oscillation slowed down to be closer to the observed period, the variability of upper-level winds and convective activity on intraseasonal timescales became stronger, the number of MJO events occurring during northern hemisphere winter and spring increased significantly, and the phase speed of the oscillation slowed in the eastern hemisphere in association with more organized convection.

The results of Waliser *et al*. (1999) were very encouraging and suggested that a more comprehensive and realistic approach to simulating the coupled aspects of the MJO might be fruitful. Until ~2005, with the availability of the CMIP3 database, there were only a limited number of studies of the MJO in coupled GCMs in the literature. This arose since (until quite recently) the cost of running coupled GCMs was prohibitively high for many research centers and so their use had been limited to a few institutes. Second, the development of coupled GCMs has historically been motivated by the requirements of long-term climate prediction and, more recently, seasonal prediction, so the ability of models to capture variability on timescales of less than a season had not been a primary consideration to the groups involved. Third, it has only been recently that coupled GCMs have been developed without the need for flux adjustment to maintain a stable mean climate (e.g., Gordon *et al*., 2000), and there had been concerns that the flux adjustment of the coupled system might compromise simulation of intraseasonal variability.

Initial studies by Gualdi *et al*. (1999a) and Hendon (2000) using fully coupled models concluded that an interactive ocean did not improve MJO simulation. Instead, they found that accompanying changes in the mean climate of the model and deficiencies in the representation of surface flux anomalies were the main factors affecting the behavior of the MJO. However, Kemball-Cook *et al*. (2002), Inness and Slingo (2003), Inness *et al*. (2003), and Sperber *et al*. (2005) demonstrated that the coupling improves the organization and propagation characteristics of the MJO in comparison with results from atmosphere-only models, at least for the boreal winter (Figure 11.4). Whereas the atmosphere-only model had a predominantly standing oscillation in convection (Figure 11.4b), the coupled model produced a more realistic eastward-propagating signal (Figure 11.4a). This was associated with coherent variations in SST (Figure 11.4c), which showed a similar phase relationship with convection as in observations, with warmer SSTs preceding the maximum in convection by 5–10 days.

Due to the increased number of degrees of freedom in a fully coupled GCM, it is much more likely that there will be errors in the basic state than in an atmosphere-only GCM constrained by realistically prescribed SSTs. This has emerged as a crucial factor in simulation of the MJO in coupled models. In particular, the low-level climatological westerlies across the Indo-Pacific warm pool associated with the austral monsoon are critical for the air–sea interaction mechanism of the MJO. It is only when these winds are westerly that the wind perturbations associated with the MJO can give enhanced latent heat fluxes (i.e., cooling the ocean) to the west of convection and reduced fluxes to the east (i.e., warming the ocean). Inness *et al*. (2003) showed conclusively that the easterly bias over the West Pacific, typical of the majority of coupled models, acts to restrict eastward propagation of the MJO by

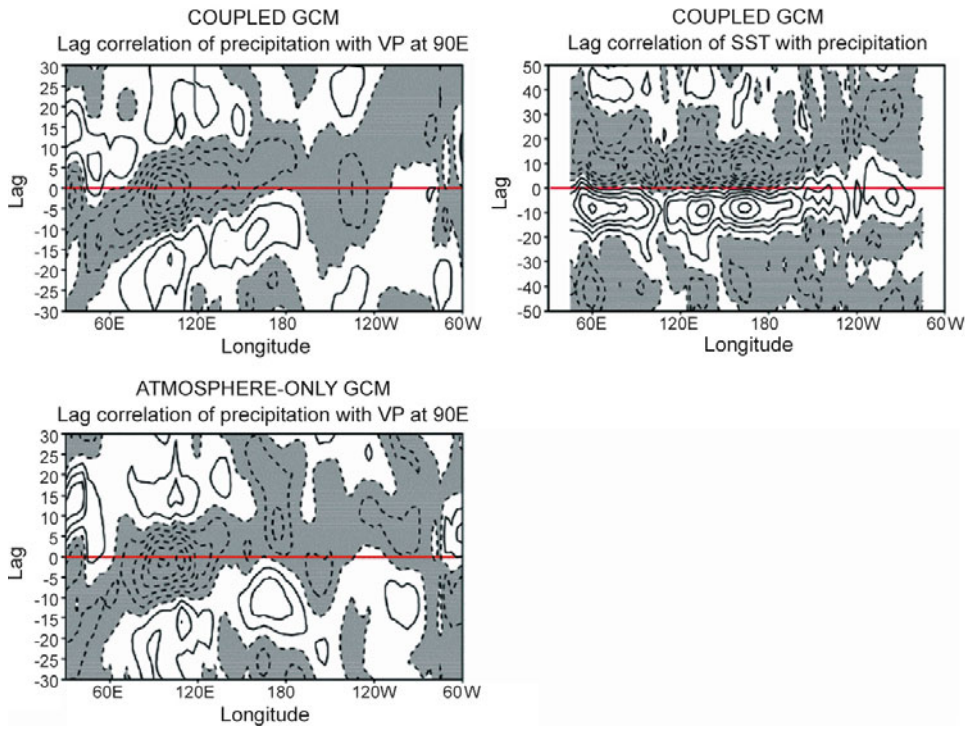

Figure 11.4. Lag correlations between precipitation at every longitude and an index of MJO activity at 90°E, based on the 20 to 100-day filtered 200 hPa velocity potential, from (a) a version of the coupled ocean–atmosphere model, HadCM3, and (b) the equivalent atmosphere-only model, HadAM3. (c) Simulated lag correlations between precipitation and SST at every longitude (as in Figure 11.3a) from HadCM3 (from Slingo *et al.*, 2003).

disabling the air–sea interaction mechanism. Consequently, improving the mean simulation in coupled models is a major issue facing future improvements in modeling the MJO.

11.3 BOREAL SUMMER INTRASEASONAL VARIABILITY

As noted in the introduction (Section 11.1), the MJO during boreal summer is much more complex, and eastward propagation is often accompanied by northward propagation over the Indian Ocean sector. A brief discussion of boreal summer intraseasonal variability (BSISV) follows in order to characterize the basic challenges to the modeling community. A more comprehensive discussion of observed variability is presented in Chapters 2 and 3. BSISV is important because it is intimately related to the active/break cycles of the Asian summer monsoon (Krishnamurti and Bhalme, 1976; Sikka, 1980; Gadgil and Asha, 1992; Webster *et al.*, 1998; Annamalai

and Sperber, 2005). Observed years of below-normal Indian monsoon rainfall tend to be associated with prolonged breaks in the monsoon and, conversely, fewer breaks of shorter duration tend to occur during years of normal or above-normal monsoon rainfall. During northern summer, the MJO is modified substantially by the off-equatorial heating associated with the Asian summer monsoon. It has a mixed character of both northward and eastward propagation. Northward propagation of the tropical convergence zone on timescales of 30–50 days over Indian longitudes was initially identified by Yasunari (1979, 1980) and Sikka and Gadgil (1980), and over the West Pacific by Murakami *et al.* (1984) and Lau and Chan (1986). Wang and Rui (1990) classified intraseasonal propagating events over the monsoon domain, including isolating northward propagation that occurred independent of eastward propagation. Later, Lawrence and Webster (2002) found that 78% of northward-propagating intraseasonal events were accompanied by eastward propagation, and it is mainly on these events that we concentrate. Figure 11.5a shows the composite OLR from observations corresponding to active convection/rainfall over India, extending to the southeast into the Western Pacific. As this tilted rainband propagates to the east, rainfall occurs farther north at about 1° latitude per day at a given longitude.

Lau and Peng (1990) proposed that northward propagation is due to coupled Kelvin wave–Rossby wave interactions. The theory of tropical intraseasonal oscillations is discussed in Chapter 10. The intermediate complexity model of Wang and Xie (1997) replicated the northwest–southeast tilt of the rainband due to Kelvin wave–Rossby wave interactions. Observational evidence that the tilt is due to emanation of Rossby waves has been found by Annamalai and Slingo (2001), Kemball-Cook and Wang (2001), and Lawrence and Webster (2002). Annamalai and Sperber (2005) used a linear barotropic model forced with heating proportional to the rainfall rate for different phases of the BSISV lifecycle. They were able to reproduce the observed low-level circulation and showed that the development of forced Rossby waves could only occur in the presence of easterly zonal shear, as suggested by Lau and Peng (1990) and Wang and Xie (1997). The importance of forced Rossby waves for the tilted rainband was also highlighted in a full GCM by Wu *et al.* (2006). Annamalai and Sperber (2005) also concluded that the intraseasonal variability over the Indian Ocean and the West Pacific are mutually dependent systems. That is, the eastward extension of equatorial convection over the eastern Indian Ocean is important for setting up the tilted rainband, while subsequent convection over the West Pacific helps initiate the monsoon break over India and Indian Ocean convection can modulate the active and break phase over the West Pacific.

As during boreal winter, low-level moisture convergence is important for maintaining eastward propagation of near-equatorial convection as it destabilizes the atmosphere ahead of the main center of convection. In boreal summer, northward propagation also exhibits the tendency for low-level moisture convergence to lead convection (Kemball-Cook and Wang, 2001). Thus, the mechanisms involved in boreal summer intraseasonal variability are akin to those during the boreal winter MJO. Additionally, over the western North Pacific it has been

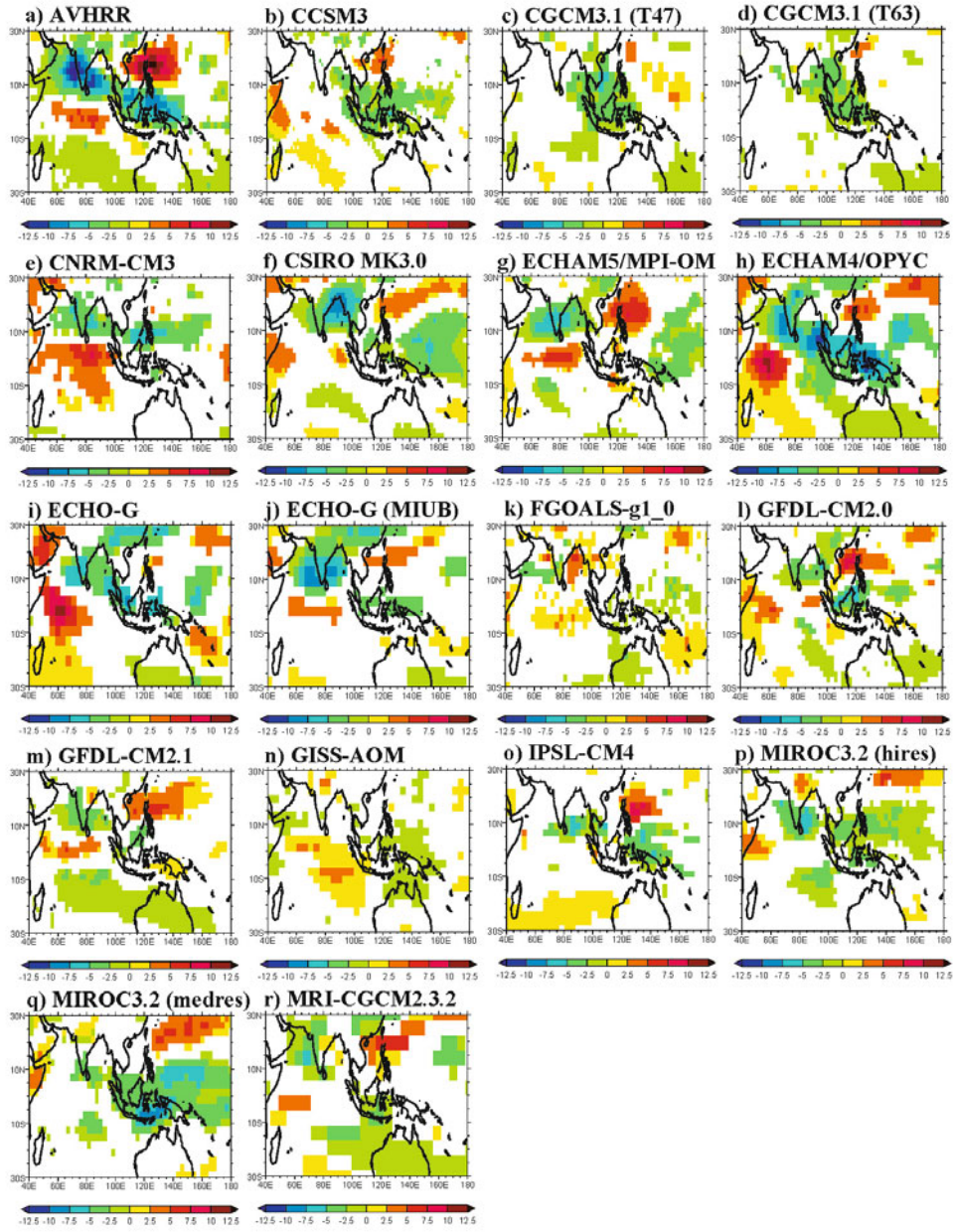

Figure 11.5. Simulated BSISV convective anomalies relative to the observed day 10 pattern. (a) Observations (AVHRR outgoing longwave radiation), (b) CCSM3, (c) CGCM3.1 (T47), (d) CGCM3.1 (T63), (e) CNRM-CM3, (f) CSIRO MK3.0, (g) ECHAM5/MPI-OM, (h) ECHAM4/OPYC, (i) ECHO-G, (j) ECHO-G (MIUB), (k) FGOALS-g1_0, (l) GFDL-CM2.0, (m) GFDL-CM2.1, (n) GISS-AOM, (o) IPSL-CM4, (p) MIROC3.2 (hires), (q) MIROC3.2 (medres), and (r) MRI-CGCM2.3.2 (after Sperber and Annamalai, 2008).

suggested that subtropical westward-propagating low-level convergence anomalies contribute to the northwestward propagation of the rainband (Hsu and Weng, 2001). Thus, the complex nature of BSISV makes it especially challenging to simulate.

11.3.1 GCM simulations

Modeling studies of BSISV have been relatively limited partly due to the difficulties in simulating both the mean monsoon and its variability (Sperber and Palmer, 1996, Sperber *et al.*, 2000). Given the complex orography over the summer monsoon domain, deficiencies in simulating rainfall were noted by Hahn and Manabe (1975) and Gilchrist (1977). Subsequently, numerous studies have evaluated monsoon sensitivity to horizontal resolution, though most studies concentrated on time mean behavior (e.g., Tibaldi *et al.*, 1990). Typical results indicated a better representation of rainfall along the western Ghats and their downwind rainshadow effect, as well as improvement in the foothills of the Himalayas.

As with the boreal winter MJO, studies of the sensitivity of BSISV to horizontal resolution have been inconclusive. Using the Geophysical Fluid Dynamics Laboratory GCM, Hayashi and Golder (1986) found that R30 ($\sim 3^\circ$) represented the spacetime spectra of rainfall better than the R15 ($\sim 5^\circ$) model version. Of special note was the ability of the model to simulate the poleward propagation of rainfall over the monsoon domain, including the observed asymmetry, with the northern hemisphere propagation being stronger than that in the southern hemisphere. Using a T21 ($\sim 5^\circ$) model from the European Centre for Medium-range Weather Forecasts (ECMWF), Gadgil and Srinivasan (1990) found that this model produces northward propagation of the rainbelt over the Bay of Bengal. However, using a later version of the ECMWF model, Sperber *et al.* (1994) find that a resolution of T106 ($\sim 1^\circ$) was needed to represent northward propagation of the tropical convergence zone and the sudden jump of the Meiyu front over China, although later work has suggested coarser resolution models with may have similar capabilities (Lau and Yang, 1996; Martin, 1999). In fact, the differences among models are mainly associated with combinations of, improvement in, and the addition of physical parameterizations.

The ability of models to simulate the dominant BSISV convective pattern has remained problematic (as shown in Figure 11.5). This result, from a CMIP3 study by Sperber and Annamalai (2008), demonstrated that only two models (Figures 11.5h–i, ECHAM4/OPYC and ECHO-G) represent the tilted convection that extends from India to the Maritime Continent. While many of the CMIP3 models exhibited northward propagation of intraseasonal convective anomalies (Lin *et al.*, 2008), Sperber and Annamalai (2008) showed that only the two aforementioned models simulated the northward propagation that is observed to occur in conjunction with the eastward propagation of near-equatorial convection (Annamalai and Sperber, 2005); that is, properly generating the tilted rainband due to the forced Rossby wave response described in Section 11.3. Despite this limited success at capturing the off-equatorial convective signal, all of the CMIP3 models simulated eastward

propagation of intraseasonal equatorial convective anomalies over the Indian Ocean (Sperber and Annamalai, 2008). This is a demonstrable improvement compared with the older models analyzed by Waliser *et al.* (2003a), in which none of the models exhibited any systematic intraseasonal rainfall variability over the Indian Ocean.

11.3.2 Air–sea interaction and boreal summer intraseasonal variability

Observations indicate that systematic SST changes over the Bay of Bengal occur in conjunction with the northward propagation of intraseasonal convection (Vecchi and Harrison, 2002). The tendency is for warm (cold) anomalies to lead enhanced (suppressed) convection, suggesting that air–sea interaction may be important for northward propagation of BSISV, in addition to the Kelvin wave/Rossby wave interactions discussed in Section 11.3. Modeling of BSISV has also benefited from an understanding of the important role that air–sea interaction has played in representing the boreal winter MJO. For example, using the ECHAM4 model in coupled and uncoupled configurations, Kemball-Cook *et al.* (2002) show that with air–sea feedback the spacetime spectra of OLR display a more realistic partitioning of variance between eastward and westward propagation near the equator. They also find that "coupling is helping to destabilize the northward moving mode by enhancing low-level convergence into the positive SST anomaly." However, unlike the reanalysis, the model shortwave surface heat flux was more important than the latent heat flux for forcing the SST anomalies that are in quadrature with convection. In addition, the model also overestimated the strength of low-level convergence. Thus, the model appears to compensate for the weak latent heat flux anomalies, suggesting that the BSISV is arising from the wrong combination of interactions. Despite this, the indication is that net surface heat flux is important for generating realistic SST anomalies, which in turn are important for modulating the propagation of BSISV.

Kemball-Cook *et al.* (2002) also found that the failure to generate easterly wind shear in the late summer precluded the emanation of Rossby waves and prohibited the northwestward propagating mode. As in the boreal winter case, this attests to the importance of simulating a realistic basic state to properly capture the dynamics important for simulating intraseasonal variability. In cases where there is an eastward-propagating equatorial convective component, Kelvin wave/Rossby wave interactions and air–sea interaction both promoted the northward propagation of precipitation resulting in the tilted rainband.

Further support that both dynamical processes and air–sea interaction are important for generating boreal summer northward propagation in climate models has been reported by Rajendran *et al.* (2004) and Rajendran and Kitoh (2006) using the Meteorological Research Institute CGCM2. The presence of northward propagation in the prescribed SST simulations indicated that dynamical processes play an important role for their development. However, the inclusion of air–sea feedback in the coupled model resulted in 50% more northward-propagating events, and exhibited surface flux, convection, and SST feedbacks that resulted in a more realistic lifecycle of BSISV. Wang *et al.* (2009) also found an improved representa-

tion of northward propagation in case study experiments with the National Centers for Environmental Prediction (NCEP) coupled atmosphere–ocean Climate Forecast System (CFS) compared with the NCEP Global Forecast System (GFS) in which the SST is prescribed. Thus, it appears that air–sea interaction gives rise to more accurate simulation of intraseasonal variability, provided the model has a realistic mean state (Inness *et al*., 2003; Seo *et al*., 2005). An important question for the future is: What are the relative contributions of the Kelvin wave/Rossby interactions vs. the air–sea interaction for promoting northward propagation? Fu *et al*. (2003) suggested that air–sea interaction is the most important process. They note cases of northward propagation that occur independently of an eastward equatorial propagating convective component such that northward propagation occurs solely due to air–sea interaction rather than with a contribution from Kelvin wave/Rossby wave interactions. Conversely, numerous GCM studies have shown some ability to generate northward propagation using prescribed SST (e.g., Ajayamohan *et al*. 2010), suggesting that internal processes can also dominate. What is needed is a better understanding of the hierarchy of subseasonal modes of monsoon variability (e.g., Wang and Rui, 1990; Sperber *et al*., 2000), and the mechanisms that control them, including land surface processes that may affect the land–sea temperature gradient which could promote or diminish northward propagation.

11.3.3 Modeling studies of the links between boreal summer intraseasonal and interannual variability

In the mid-1990s, modeling studies of BSISV and its possible link to interannual variations outpaced our ability to firmly establish such a link in observations. Fennessy and Shukla (1994) used the Center for Ocean Land Atmosphere (COLA) atmospheric general circulation model to simulate the weak (strong) Indian monsoon of 1987 (1988). They found that the spatial pattern of interannual rainfall difference was nearly identical to the difference due to break and active phases of the monsoon. Ferranti *et al*. (1997) found a similar result with the ECMWF model in AMIP simulations forced with observed SST for 1979–1988. Using canonical correlation analysis (CCA), they found the 850 hPa relative vorticity exhibited a common mode of variability on interannual and intraseasonal timescales, being characterized by alternation of the tropical convergence zone between the tropical Indian Ocean and over the continental landmass, centered at about 15°N. However, the oceanic and continental locations of the tropical convergence zone were regime transitions that were not associated with northward-propagating intraseasonal events.

With the advent of reanalysis, it became possible to investigate the link between intraseasonal and interannual variability based on a dynamically consistent representation of the atmosphere using a uniform model and data assimilation system (Gibson *et al*., 1996, 1997; Kalnay *et al*., 1996). Reanalysis winds and vorticity are more reliable than rainfall or OLR (Kalnay *et al*., 1996), and they provide a longer record than satellite-derived OLR, and are more spatially complete compared with observed rainfall. Using 850 hPa relative vorticity, Annamalai *et al*. (1999) showed

that both the ECMWF and NCEP/NCAR reanalyses had nearly identical dominant modes of intraseasonal variability, characterized by a northwest to southeast tilt and northward propagation. Additionally, these modes were linked to the active and break monsoon over India. Compared with the results of Annamalai *et al.* (1999), the aforementioned model results of Ferranti *et al.* (1997) and Martin (1999) exhibit intraseasonal patterns that are too zonal, with the transition from ocean to the continent being more regime-like rather than propagating. Furthermore, the first mode in the models explained far more of the subseasonal variance than in the observations.

Observational evidence for a common mode of intraseasonal and interannual variability was found by Sperber *et al.* (2000) and Goswami and Ajaya Mohan (2001). This mode, shown in Figure 11.6c, is characterized by cyclonic flow at 850 hPa over India and an anticyclone to the south over the Indian Ocean. It shows a strong link to all-India rainfall manifested as a systematic shift in the mean of the frequency distribution of the principal component time series when

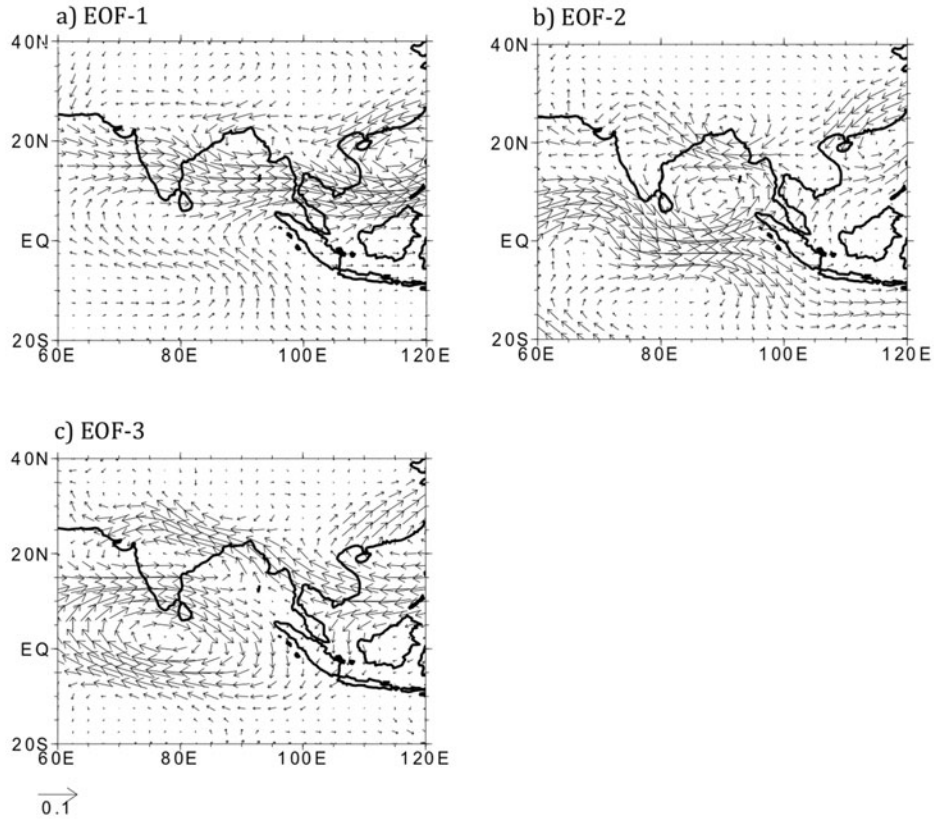

Figure 11.6. The dominant modes of boreal summer intraseasonal variability in the 850 hPa winds from the NCEP/NCAR reanalysis (after Sperber *et al.*, 2000).

stratified between years of above-normal and below-normal all-India rainfall (Sperber *et al*. 2000). Unfortunately, a direct link of this mode to slowly varying boundary conditions, which could be a source of predictability, has remained elusive. EOFs 1 and 2 in the 850 hPa wind are associated with northward propagation of the tropical convergence zone (Figures 11.6a and 11.6b), with EOF 2 being linked to the phase of the El Niño/Southern Oscillation (Sperber *et al*., 2000). While encouraging from the viewpoint of predictability, this is not the dominant mode of intraseasonal variability and, thus, the chaotic nature of the other components of the BSISV can obscure a boundary forced signal.

The ability of atmospheric general circulation models to simulate the dominant modes of BSISV in the 850 hPa winds using hindcast experiments run with observed SST was evaluated by Sperber *et al*. (2001). While the models were largely successful at representing the observed patterns, seen in Figure 11.6, they overemphasized the role of EOF 1 and, unlike the observations, most models linked this mode to boundary forcing. As a result the models were predisposed to incorrectly project subseasonal variability onto seasonal rainfall, thus poorly representing interannual variability. Similar to Ferranti *et al*. (1997), Molteni *et al*. (2003) found zonally oriented anomalies to be common between interannual and intraseasonal timescales using a more comprehensive suite of hindcast experiments with a later version of the ECMWF model. Though the principal component of the dominant mode was not correlated with the ENSO, it did exhibit "multiple-regime behavior" related to the strength of zonal asymmetry in equatorial Pacific SST, a characteristic yet to be seen in observations. As in Sperber *et al*. (2001), they note "significant discrepancies from observations in the partition of variance between modes with different regional characteristics."

Overall, models show some ability to represent the observed spatial patterns of the 850 hPa intraseasonal wind field, and poorer ability to represent the northward and eastward-propagating rainband associated with 30 to 50-day BSISV. Numerous factors complicate dynamical seasonal predictability of the summer monsoon. These include, but are not limited to, (i) the inability of models to realistically partition the relative importance of the dominant modes, (ii) the failure of models to link these modes to the boundary forcing as observed, and (iii) the fact that the ENSO forced mode is not the dominant mode of variability.

In the last several years modeling studies of BSISV have become more frequent as we push our models to excel over a broader range of capabilities. Success in simulating the BSISV, with its poleward-propagating component, is an even more sensitive test of a GCM's capability than simulating the MJO, which is dominated by near-equatorial propagation. This partly arises because simulation of the mean climate of the Asian summer monsoon continues to prove a challenge. Furthermore, our basic understanding of what drives the BSISV and its northward vs. eastward propagation is not so advanced, and we do not fully understand the role that land surface processes and the Tibetan Plateau may play in the evolution of BSISV. Yet, the social and economic benefits from extended range prediction of BSISV could be huge and thus makes this a major challenge for the modeling community in the coming years.

11.4 THE IMPACT OF VERTICAL RESOLUTION IN THE UPPER OCEAN

There is good evidence that the MJO in both boreal winter and summer manifestations is, at least to some extent, a coupled ocean–atmosphere mode (Sections 11.2.3 and 11.3.2). Whilst coupled models are capable of producing the correct relationship between convection and SST on intraseasonal timescales, these models still underestimate the activity of the MJO (e.g., Inness *et al.*, 2003; Lin *et al.*, 2006, 2008) and the magnitude of SST perturbations is smaller than observed. This occurs despite variations in surface fluxes being similar to those observed and suggests that the representation of the upper layers of the ocean may not be responding realistically to subseasonal variations in winds and fluxes.

Most coupled climate models have a relatively coarse vertical resolution in the upper ocean, typically of the order of 10 meters. But observations by tethered buoys, such as the Woods Hole IMET buoy during TOGA–COARE (e.g., Anderson *et al.*, 1996), have shown that the upper ocean has a very complex structure, which undergoes dramatic changes during the lifecycle of the MJO. A particularly noteworthy aspect of these buoy observations is the diurnal variation in SST that only occurs during suppressed phases of the MJO, when winds are light, net heat flux into the ocean is large, and the mixed layer is very shallow. In a study with a very high vertical resolution mixed layer model, Shinoda and Hendon (1998) and Bernie *et al.* (2005) showed that rectification of these diurnal variations on to intraseasonal timescales is significant and accounts for a large proportion of the intraseasonal warming of the ocean during the suppressed phase of the MJO. Clearly, the coarse resolution of the upper ocean in current coupled models and the lack of resolution of the diurnal cycle in the coupling frequency means that these diurnal variations in SST and their rectification on to intraseasonal timescales are not represented. Bernie *et al.* (2005, 2007) concluded that a resolution of 1 meter for the skin layer of the ocean and a coupling frequency of at least every 3 hours are needed to adequately capture diurnal and intraseasonal SST variability, leading to stronger and more coherent MJOs (Bernie *et al.*, 2008). As Figure 11.7 shows, only simulations with high-frequency coupling and a shallow top layer are capable of reproducing the observed signal.

Diurnal SST variations may also be important for the MJO in other ways. For example, Johnson *et al.* (1999) showed that cumulus congestus clouds are most prevalent during light wind conditions in the presence of a strong diurnal cycle in SST. These clouds occur most frequently in the late afternoon, with a behavior that resembles more closely the diurnal cycle in land convection, suggesting that they may be triggered by the diurnal cycle in SST. The fact that these clouds appear to be key players during the suppressed phase of the MJO adds further weight to the need for taking a complete atmosphere–upper ocean approach to simulating the MJO.

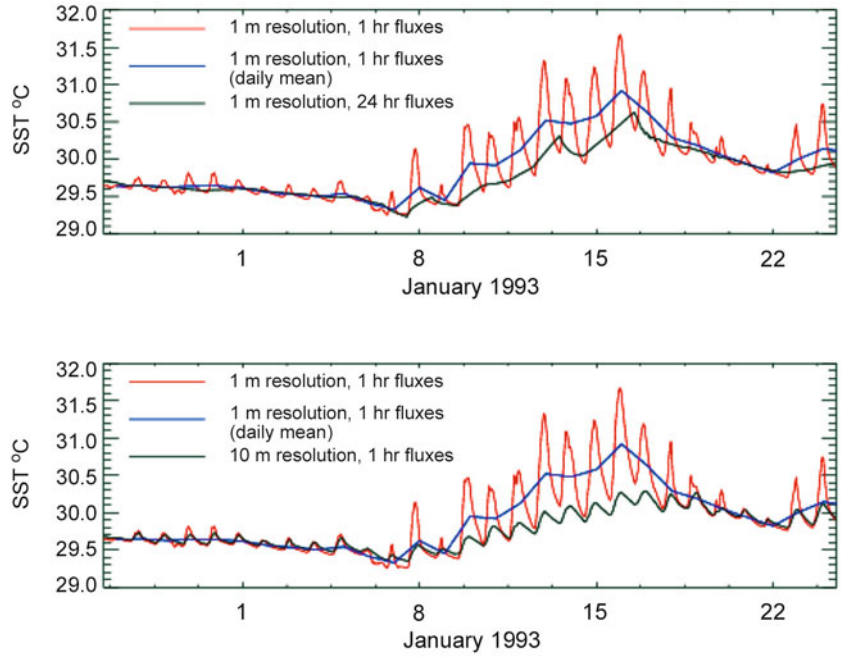

Figure 11.7. Impact of coupling frequency (upper panel) and resolution of the uppermost ocean (lower panel) on simulations of diurnal and intraseasonal variations in SST for TOGA–COARE using a mixed layer ocean model. The observed SSTs are very close to the red curves (from Bernie *et al.*, 2005).

11.5 CONCLUDING REMARKS

It is certainly true that simulation of the MJO by general circulation models is improving, along with our understanding of what are the key processes for its initiation and maintenance. However, it is still not the case that a good representation of all aspects of the MJO is inherent in the majority of recent CMIP3 GCMs. Research has pointed to possible avenues that might lead to improvements in simulation of the MJO in the coming years. First, greater emphasis is being placed on understanding the suppressed phase of the MJO and the processes that recharge the tropical troposphere for the next period of active convection. Steps are being taken to improve the representation of cumulus congestus clouds in convection schemes, including warm rain processes, which are key to the lifecycle of these clouds.

Furthermore, other aspects of subseasonal tropical variability need to be considered. Interactions between multiple timescales of variability in the tropics have been the subject of several papers (e.g., Nakazawa, 1988; Lau *et al.*, 1991), suggesting that synoptic-scale higher frequency modes of convective activity are modulated by the MJO. How much the synoptic and mesoscale activity embedded within the MJO is responsible for the evolution of the oscillation itself remains an open question (e.g., Hendon and Liebmann, 1994). More generally, investigating the

importance of equatorial wave modes for organizing tropical convection (Wheeler and Kiladis, 1999; Yang *et al*., 2003) deserves more attention. In fact, the results of Yang *et al*. (2003) suggest that the majority of tropical convection is associated with equatorial Kelvin, Rossby, and mixed Rossby–gravity waves, which undergo Doppler shifting and changes in vertical structure depending on the basic state wind and vertical shear. Yang *et al*. (2003) also showed that the structure of waves is substantially modified over the Indo-Pacific warm pool by equatorial convection induced through wind–evaporation feedbacks. However, analysis of these waves in the CMIP2 and CMIP2+ models (AchutaRao *et al*., 2004) and in the Hadley Centre's climate model (Ringer *et al*., 2006) has shown major deficiencies in their structure and their coupling with convection. Since these waves are the building blocks of the tropical climate and are fundamental to simulation of the MJO, future efforts to model the MJO must also address the more general issue of convectively coupled equatorial waves.

The measures used to determine the quality of MJO simulation are very important. Early GCM studies of the MJO tended to concentrate on the signal in upper-tropospheric tropical winds or velocity potential. It could be that *in situ* intraseasonal modulation of the main convective region over the Indo-Pacific warm pool produces an equatorially trapped Kelvin wave response, which resembles the MJO signal in upper-level winds, without actually being accompanied by eastward propagation of the main convective region through the Indian Ocean and into the West Pacific. The need to use a reasonable range of diagnostics to determine the quality of a MJO simulation is clearly important, in which the signal of the MJO in upper-tropospheric winds should be regarded as a bare minimum indication of the presence of the MJO. The evolution of convection through the lifecycle of the MJO, with particular emphasis on eastward propagation, and in boreal summer also northward propagation, must be further examined. Recent research has emphasized the complex three-dimensional structure of the MJO, in particular the vertical distribution of the humidity field, and these should provide stringent tests for model simulations (Sperber, 2003; Kiladis *et al*., 2005; Tian *et al*., 2006; Thayer-Calder, 2008). Finally, the intraseasonal variability of surface fluxes and their impact on SST should be diagnosed, ensuring that the coupled nature of the simulated MJO is properly represented.

With these goals in mind, the limited lifetime U.S. CLIVAR MJO Working Group (MJOWG) was established in 2006 (Sperber and Waliser, 2008). The MJOWG developed (1) a set of standard diagnostics to track progress in modeling the MJO (CLIVAR MJOWG, 2009; Kim *et al*., 2009) with the latter authors also beginning to explore process-oriented diagnostics, and (2) initiated a World Climate Research Program/Working Group on Numerical Experimentation (WCRP/WGNE) endorsed effort of making experimental operational MJO forecasts (Gottschalck *et al*., 2010). The Year of Tropical Convection MJO Task Force (YOTC MJOTF) is the follow-on group to the MJOWG and is sponsored by the WCRP and the World Weather Research Program (WWRP). The MJOTF is (1) developing process-oriented diagnostics, (2) developing boreal summer intraseasonal diagnostics and metrics, (3) further developing MJO forecast tech-

niques, and (4) assessing impacts of the MJO on tropical cyclones and other phenomena.

Additional resources are currently being brought to bear in the investigation of the MJO, including the YOTC project (Waliser and Moncrieff, 2008) which consists of a 2-year period (May 2008–April 2010) "of coordinated observing, modeling, and forecasting of organized tropical convection." This effort will include numerous sources of high-resolution NWP analyses, exploit new satellite capabilities (e.g., CloudSat), and include numerical experimentation of case study periods "with the objective of advancing the characterization, diagnosis, modeling, parameterization and prediction of multi-scale convective/dynamic interactions," including the MJO/BSISV. Comparisons of coarse-resolution and cloud system–resolving GCMs in conjunction with observational process studies—for example, Asian monsoon years (AMY), Wang *et al*., 2010; the Cooperative Indian Ocean Experiment on intraseasonal variability in Year 2011 (CINDY2011), Yoneyama *et al*., 2009; Dynamics of the Madden–Julian Oscillation (DYNAMO), Zhang *et al*., 2010)—will help foster improved parameterization for coarse-resolution models and expand our basic understanding and ability to model the MJO.

As our understanding of the MJO has increased, we are setting more stringent tests for our GCMs and NWP models in terms of what constitutes a "good" MJO simulation, and we are testing experimental methods of forecasting the MJO/BSISV (see Chapter 12) due to its importance for medium-range and seasonal forecasts and the impact it has on the lives of those who live within the domain of its influence.

11.6 ACKNOWLEDGMENTS

Julia Slingo acknowledges support through the NERC Centres for Atmospheric Science. K. R. Sperber was supported under the auspices of the U.S. Department of Energy Office of Science, Regional and Global Climate Modeling Program by Lawrence Livermore National Laboratory under contract DE-AC52-07NA27344. K.R.S. would like to thank Drs. H. Annamalai and X. Fu for helpful discussions.

11.7 REFERENCES

AchutaRao, K., C. Covey, C. Doutriaux, M. Fiorino, P. Gleckler, T. Phillips, K. Sperber, and K. Taylor (2004) An appraisal of coupled climate model simulations. In: D. Bader (Ed.), *Program for Climate Model Diagnosis and Intercomparison* (UCRL-TR-202550). Lawrence Livermore National Laboratory, Livermore, CA, 183 pp.

Ajayamohan, R. S., H. Annamalai, J.-J. Luo, J. Jafner, and T. Yamagata (2010) Poleward propagation of boreal summer intraseasonal oscillations in a coupled model: Role of internal processes. *Climate Dynamics*, doi: 10.1007/s00382-010-0839-6.

Anderson, S. P., R. A. Weller, and R. B. Lukas (1996) Surface buoyancy forcing and the mixed layer of the Western Pacific warm pool: Observations and 1D model results. *J. Climate*, **9**, 3056–3085.

Annamalai, H. and J. M. Slingo (2001) Active/break cycles: Diagnosis of the intraseasonal variability of the Asian summer monsoon. *Climate Dynamics*, **18**, 85–102.

Annamalai, H. and K. R. Sperber (2005) Regional heat sources and the active and break phases of boreal summer intraseasonal variability. *J. Atmos. Sci.*, **62**, 2726–2478.

Annamalai, H., J. M. Slingo, K. R. Sperber, and K. Hodges (1999) The mean evolution and variability of the Asian summer monsoon: Comparison between ECMWF and NCEP–NCAR reanalyses. *Mon. Wea. Rev.*, **127**, 1157–1186.

Arakawa, A. and W. H. Schubert (1974) Interaction of a cumulus cloud ensemble with the large-scale environment, Part I. *J. Atmos. Sci.*, **31**, 674–701.

Bechtold, P., M. Kohler, T. Jung, F. Doblas-Reyes, M. Leubecher, M. J. Rodwell, F. Vitart, and G. Balsamo (2008) Advances in simulation atmospheric variability with the ECMWF model: From synoptic to decadal time-scales. *Quart. J. Roy. Meteorol. Soc.*, **134**, 1337–1351, doi: 10.1002/qj.289.

Benedict, J. J. and D. A. Randall (2007) Observed characteristics of the MJO relative to maximum rainfall. *J. Atmos. Sci.*, **64**, 2332–2354.

Benedict, J. J. and D. A. Randall (2009) Structure of the Madden–Julian oscillation in the superparameterized CAM. *J. Atmos. Sci.*, **66**, 3277–3296.

Bernie, D. J., S. J. Woolnough, J. M. Slingo, and E. Guilyardi (2005) Modeling diurnal and intraseasonal variability of the ocean mixed layer. *J. Climate*, **18**, 1190–1202.

Bernie, D. J., E. Guilyardi, G. Madec, J. M. Slingo, and S. J. Woolnough (2007) Impact of resolving the diurnal cycle in an ocean-atmosphere GCM, Part 1: A diurnally forced OGCM. *Climate Dynamics*, **29**, 575–590, doi: 10.1007/s00382-007-0249-6.

Bernie, D. J., E. Guilyardi, G. Madec, J. M. Slingo, S. J. Woolnough, and J. Cole (2008) Impact of resolving the diurnal cycle in an ocean–atmosphere GCM, Part 2: A diurnally coupled CGCM. *Climate Dynamics*, **31**, 909–925, doi: 10.1007/s00382-008-0429-z.

Betts, A. K. (1986) A new convective adjustment scheme, Part I: Observational and theoretical basis. *Quart. J. Roy. Meteorol. Soc.*, **112**, 677–691.

Bladé, I. and D. L. Hartmann (1993) Tropical intraseasonal oscillations in a simple nonlinear model. *J. Atmos. Sci.*, **50**, 2922–2939.

CLIVAR Madden–Julian Oscillation Working Group (2009) MJO simulation diagnostics. *J. Climate*, **22**, 3006–3030, doi: 10.1175/2008JCLI2731.1.

Emanuel, K. A. (1987) An air–sea interaction model of intraseasonal oscillations in the tropics. *J. Atmos. Sci.*, **44**, 2324–2340.

Fennessy, M. J. and J. Shukla (1994) GCM simulations of active and break periods. Paper presented at *Proceedings of the International Conference on Monsoon Variability and Prediction. Trieste, Italy* (WCRP-84, WMO/TD-No. 619, Vol. 2, pp. 576–585).

Ferranti, L., J. M. Slingo, T. N. Palmer, and B. J. Hoskins (1997) Relations between interannual and intraseasonal variability as diagnosed from AMIP integrations. *Quart. J. Roy. Meteorol. Soc.*, **123**, 1323–1357.

Flatau, M., P. J. Flatau, P. Phoebus, and P. P. Niiler (1997) The feedback between equatorial convection and local radiative and evaporative processes: The implications for intraseasonal oscillations, *J. Atmos. Sci.*, **54**, 2373–2386.

Fu, X., B. Wang, T. Li, and J. P. McCreary (2003) Coupling between northward propagation, intraseasonal oscillations and sea surface temperature in the Indian Ocean. *J. Atmos. Sci.*, **60**, 1733–1753.

Gadgil, S. and G. Asha (1992) Intraseasonal variation of the summer monsoon, I: Observational aspects. *J. Meteorol. Soc. Japan*, **70**, 517–527.

Gadgil, S. and J. Srinivasan (1990) Low frequency variation of tropical convergence zones. *Meteorol. Atmos. Phys.*, **44**, 119–132.

Gates, W. L. (1992) AMIP: The atmospheric model intercomparison project. *Bull. Amer. Meteorol. Society*, **73**, 1962–1970.

Gates, W. L., J. S. Boyle, C. Covey, C. G. Dease, C. M. Doutriaux, R. S. Drach, M. Fiorino, P. J. Gleckler, J. J. Hnilo, S. M. Marlais *et al.* (1999) An overview of the results of the atmospheric model intercomparison project (AMIP I). *Bull. Amer. Meteorol. Society*, **80**, 29–55.

Gibson, J. K., P. Kallberg, and S. Uppala (1996) The ECMWF ReAnalysis (ERA) project. *ECMWF Newsletter*, **73**, 7–17.

Gibson, J. K., P. Kallberg, S. Uppala, A. Hernandez, A. Nomura, and E. Serrano (1997) *ECMWF ReAnalysis Project Report* (Series 1). ECMWF, Shinfield Park, Reading, U.K., 77 pp.

Gilchrist, A. (1977) The simulation of the Asian summer monsoon by general circulation models. *Pageoph*, **115**, 1431–1448.

Gordon, C., C. Cooper, C. A. Senior, H. Banks, J. M. Gregory, T. C. Johns, J. F. B. Mitchell, and R. A. Wood (2000) The simulation of SST, sea ice extents and ocean heat transports in a version of the Hadley Centre coupled model without flux adjustments. *Climate Dynamics*, **16**, 147–168.

Goswami, B. N. and R. S. Ajaya Mohan (2001) Intraseasonal oscillations in interannual variability of the Indian summer monsoon. *J. Climate*, **14**, 1180–1198.

Gottschalck, J., M. Wheeler, K. Weickmann, F. Vitart, N. Savage, H. Lin, H. Hendon, D. Waliser, K. Sperber, M. Nakagawa *et al.* (2010) Establishing and assessing operational model MJO forecasts: A project of the CLIVAR Madden–Julian Oscillation Working Group. *Bull. Amer. Meteorol. Society*, **91**, 1247–1258.

Grabowski, W. W. (2003) MJO-like coherent structures: Sensitivity simulations using the Cloud-Resolving Convection Parameterization (CRCP). *J. Atmos. Sci.*, **60**, 847–864.

Grabowski, W. W. and M. W. Moncrieff (2002) Large-scale organization of tropical convection in two-dimensional explicit numerical simulations: Effects of interactive radiation. *Quart. J. Roy. Meteorol. Soc.*, **128**, 2349–2375.

Gualdi, S., A. Navarra, and M. Fischer (1999a) The tropical intraseasonal oscillation in a coupled ocean–atmosphere general circulation model. *Geophys. Res. Lett.*, **26**, 2973–2976.

Gualdi, S., A. Navarra, and G. Tinarelli (1999b) The interannual variability of the Madden Julian Oscillation in an ensemble of GCM simulations. *Climate Dynamics*, **15**, 643–658.

Hahn, D. G. and S. Manabe (1975) The role of mountains in the south Asian monsoon circulation. *J. Atmos. Sci.*, **32**, 1515–1541.

Hayashi, Y-Y. and D. G. Golder (1986) Tropical intraseasonal oscillations appearing in a GFDL general circulation model and FGGE data. Part I: Phase propagation. *J. Atmos. Sci.*, **43**, 3058–3067.

Hayashi, Y-Y. and D. G. Golder (1988) Tropical intraseasonal oscillations appearing in a GFDL general circulation model and FGGE data, Part II: Structure. *J. Atmos. Sci.*, **45**, 3017–3033.

Hayashi, Y-Y. and D. G. Golder (1993) Tropical 40–50 and 25–30 day oscillations appearing in realistic and idealized GFDL climate models and ECMWF dataset. *J. Atmos. Sci.*, **50**, 464–494.

Hendon, H. H. (2000) Impact of air–sea coupling on the Madden–Julian Oscillation in a general circulation model. *J. Atmos. Sci.*, **57**, 3939–3952.

Hendon, H. H. and B. Liebmann (1994) Organization of convection within the Madden–Julian Oscillation. *J. Geophys. Res.*, **99**, 8073–8083.

Hendon, H. H., C. D. Zhang, and J. D. Glick (1999) Interannual variation of the Madden–Julian Oscillation during austral summer. *J. Climate*, **12**, 2538–2550.

Hsu, H.-H. and C.-H. Weng (2001) Northwestward propagation of the intraseasonal oscillation in the western north Pacific during the boreal summer: Structure and mechanism. *J. Climate*, **14**, 3834–3850.

Inness, P. M. and D. Gregory (1997) Aspects of the intraseasonal oscillation simulated by the Hadley Centre Atmosphere Model. *Climate Dynamics*, **13**, 441–458.

Inness, P. M. and J. M. Slingo (2003) Simulation of the MJO in a coupled GCM, I: Comparison with observations and an atmosphere-only GCM. *J. Climate*, **16**, 345–364.

Inness, P. M., J. M. Slingo, S. J. Woolnough, R. B. Neale, and V. D. Pope (2001) Organization of tropical convection in a GCM with varying vertical resolution: Implications for the simulation of the Madden–Julian Oscillation. *Climate Dynamics*, **17**, 777–793.

Inness, P. M., J. M. Slingo, E. Guilyardi, and J. Cole (2003) Simulation of the MJO in a coupled GCM, II: The role of the basic state. *J. Climate*, **16**, 365–382.

Johnson, R. H., T. M. Rickenbach, S. A. Rutledge, P. E. Ciesielski, and W. H. Schubert (1999) Trimodal characteristics of tropical convection. *J. Climate*, **12**, 2397–2418.

Jung, T. and A. Tompkins (2003) *Systematic Rrrors in the ECMWF Forecasting System* (ECMWF Technical Memorandum No. 422). ECMWF, Shinfield Park, Reading, U.K.

Kalnay, E., M. Kanamitsu, R. Kistler, W. Collins, D. Deaven, L. Gandin, M. Iredell, S. Saha, G. White, J. Woollen *et al.* (1996) The NCEP/NCAR 40-year reanalysis project. *Bull. Amer. Meteorol. Society*, **77**, 437–471.

Kemball-Cook, S. and B. Wang (2001) Equatorial waves and air–sea interactions in the boreal summer intraseasonal oscillation. *J. Climate*, **14**, 2923–2942.

Kemball-Cook, S., B. Wang, and X. Fu (2002) Simulation of the intraseasonal oscillation in the ECHAM-4 model: The impact of coupling with an ocean model. *J. Atmos. Sci.*, **59**, 1433–1453.

Kessler, W. S. and R. Kleeman (2000) Rectification of the Madden–Julian oscillation into the ENSO cycle. *J. Climate*, **13**, 3560–3575.

Kiladis, G. N., K. H. Straub, and P. T. Hartel (2005) Zonal and vertical structure of the Madden–Julian oscillation. *J. Atmos. Sci.*, **62**, 2790–2809.

Kim, D., K. Sperber, W. Stern, D. Waliser, I.-S. Kang, E. Maloney, W. Wang, K. Weickmann, J. Benedict, M. Khairoutdinov *et al.* (2009) Application of MJO simulation diagnostics to climate models. *J. Climate*, **22**, 6413–6436, doi: 10.1175/2009JCLI3063.1.

Krishnamurti, T. N. and H. N. Bhalme (1976) Oscillations of the monsoon system, Part 1: Observational aspects. *J. Atmos. Sci.*, **33**, 1937–1954.

Knutson, T. R. and K. M. Weickmann (1987) 30–60 day atmospheric oscillations: Composite life-cycles of convection and circulation anomalies. *Mon. Wea. Rev.*, **115**, 1407–1436.

Kuo, H. L. (1974) Further studies of the parameterization of the influence of cumulus convection on large-scale flow. *J. Atmos. Sci.*, **31**, 1232–1240.

Lau, K. M. and P. H. Chan (1986) Aspects of the 40–50 day oscillation during the northern summer as inferred from outgoing longwave radiation. *Mon. Wea. Rev.*, **114**, 1354–1367.

Lau, K. M. and L. Peng (1990) Origin of low frequency (intraseasonal) oscillations in the tropical atmosphere, Part III: Monsoon dynamics. *J. Atmos. Sci.*, **47**, 1443–1462.

Lau, K. M. and S. Yang (1996) Seasonal variation, abrupt transition, and intraseasonal variability associated with the Asian summer monsoon in the GLA GCM. *J. Climate*, **9**, 965–985.

Lau, K. M., Nakazawa, T., and Sui, C. H. (1991) Observations of cloud cluster hierarchies over the tropical western Pacific. *J. Geophys. Res.*, **96**, 3197–3208.

Lau, N. C. and K. M. Lau (1986) Structure and propagation of intraseasonal oscillations appearing in a GFDL GCM. *J. Atmos. Sci.*, **43**, 2023–2047.

Lawrence, D. M. and P. J. Webster (2002) The boreal summer intraseasonal oscillation: Relationship between northward and eastward movement of convection. *J. Atmos. Sci.*, **59**, 1593–1606.

Lee, M. I., Kang, I. S., and Mapes, B. E. (2003) Impacts of convection parametrization on aqua-planet AGCM simulations of tropical intraseasonal variability. *J. Meteorol. Soc. Japan*, **81**, 963–992.

Lengaigne, M., E. Guilyardi, J.-P. Boulanger, C. Menkes, P. Inness, P. Delecluse, P. Inness, J. Cole, and J. M. Slingo (2004) Triggering of El Niño by westerly wind events in a coupled general circulation model. *Climate Dynamics*, **23**, 601–620, doi: 10.1007/s00382-004-0457-2.

Lin, J.-L., G. Kiladis, B. E. Mapes, K. M. Weickmann, K. R. Sperber, W. Lin, M. C. Wheeler, S. D. Schubert, A. DelGenio, L. J. Donner *et al.* (2006) Tropical intraseasonal variability in 14 IPCC AR4 climate models, Part 1: Convective signals. *J. Climate*, **19**, 2665–2690.

Lin, J.-L., K. M. Weickmann, G. N. Kiladis, B. E. Mapes, S. D. Schubert, M. J. Suarez, J. T. Bacmeister, and M.-I. Lee (2008) Intraseasonal variability associated with the Asian summer monsoon simulated by 14 IPCC AR4 coupled GCMs. *J. Climate*, **21**, 4541–4567, doi: 10.1175/2008JCLI1816.1.

Lin, X. and R. H. Johnson (1996) Heating, moistening and rainfall over the western Pacific warm pool during TOGA COARE. *J. Atmos. Sci.*, **53**, 3367–3383.

Maloney, E. D. (2009) The moist static energy budget of a composite tropical intraseasonal oscillation in a climate model. *J. Climate*, **22**, 711–729, doi: 10.1175/2008JCLI2542.1.

Maloney, E. D. and D. L. Hartmann (2001) The sensitivity of intraseasonal variability in the NCAR CCM3 to changes in convective parameterization. *J. Climate*, **14**, 2015–2034.

Martin, G. (1999) The simulation of the Asian summer monsoon, and its sensitivity to horizontal resolution, in the UK Meteorological Office Unified Model. *Quart. J. Roy. Meteorol. Soc.*, **125**, 1499–1525.

Masunaga, H., M. Satoh, and H. Miura (2008) A joint satellite and global cloud-resolving model analysis of a Madden–Julian Oscillation event: Model diagnosis. *J. Geophys. Res.*, **113**, D17210, doi: 10.1029/2008JD009986.

Matthews, A. J. (2008) Primary and successive events in the Madden–Julian oscillation. *Quart. J. Roy. Meteorol. Soc.*, **134**, 439–453.

Matthews, A. J., J. M. Slingo, B. J. Hoskins, and P. M. Inness (1999) Fast and slow Kelvin waves in the Madden–Julian Oscillation of a GCM. *Quart. J. Roy. Meteorol. Soc.*, **125**, 1473–1498.

McPhaden, M. J. (1999) Genesis and evolution of the 1997–1998 El Niño. *Science*, **283**, 950–954.

Miura, H., M. Satoh, T. Nasuno, A. T. Noda, and K. Oouchi (2007) A Madden–Julian oscillation event realistically simulated by a global cloud resolving model. *Science*, **318**, 1763–1765, doi: 10.1126/science.1148443.

Miura, H., M. Satoh, and M. Katsumata (2009) Spontaneous onset of a Madden-Julian oscillation event in a cloud-system-resolving simulation. *Geophys. Res. Lett.*, **36**, L13802, doi: 10.1029/2009GL039056.

Molteni, F., S. Corti, L. Ferranti, and J. M. Slingo (2003) Predictability experiments for the Asian summer monsoon: Impact of SST anomalies on interannual and intraseasonal variability. *J. Climate*, **16**, 4001–4021.

Morita, J., Y. N. Takayabu, S. Shige, and Y. Kodama (2006) Analysis of rainfall characteristics of the Madden–Julian oscillation using TRMM satellite data. *Dynamics Atmos. Oceans*, **42**, 107–126.

Murakami, T., T. Nakazawa, and J. He (1984) On the 40–50 day oscillations during the 1979 northern hemisphere summer, I: Phase propagation. *J. Meteorol. Soc. Japan*, **62**, 440–468.

Nordeng, T. E. (1994) *Extended Versions of the Convective Parametrization Scheme at ECMWF and Their Impact on the Mean and Transient Activity of the Model in the Tropics* (ECMWF Technical Memorandum No. 206). ECMWF, Shinfield Park, Reading, U.K.

Nakazawa, T. (1988) Tropical superclusters within intraseasonal variations over the western Pacific. *J. Meteorol. Soc. Japan*, **66**, 823–839.

Oouchi, K., A. T. Noda, M. Satoh, B. Wang, S.-P. Xie, H. G. Takahashi, and T. Yasunari (2009) Asian summer monsoon simulated by a global cloud-system-resolving model: Diurnal to intra-seasonal variability. *Geophys. Res. Lett.*, **36**, L11815, doi: 10.1029/2009GL038271.

Park, C. K., D. M. Straus, and K. M. Lau (1990) An evaluation of the structure of tropical intraseasonal oscillations in three general circulation models. *J. Meteorol. Soc. Japan*, **68**, 403–417.

Rajendran, K. and A. Kitoh (2006) Modulation of tropical intraseasonal oscillations by ocean–atmosphere coupling. *J. Climate*, **19**, 366–391.

Rajendran, K., A. Kitoh, and O. Arakawa (2004) Monsoon low-frequency intraseasonal oscillation and ocean–atmosphere coupling over the Indian Ocean. *Geophys. Res. Lett.*, **31**, doi: 10.1029/2003GL019031.

Randall, D., M. Khairoutdinov, A. Arakawa, and W. Grabowski (2003) Breaking the cloud parameterization deadlock. *Bull. Amer. Meteorol. Society*, **84**, 1547–1564.

Ray, P., C. Zhang, J. Dudhia, and S. Chen (2009) A numerical case study of the initiation of the Madden–Julian oscillation. *J. Atmos. Sci.*, **66**, 310–331, doi: 10.1175/2008/JAS2701.1.

Raymond, D. J. (2001) A new model of the Madden–Julian Oscillation. *J. Atmos. Sci.*, **58**, 2807–2819.

Ringer, M. A., G. M. Martin, C. Z. Greeves, T. J. Hinton, P. M. James, V. D. Pope, A. A. Scaife, and R. A. Sutton (2006) The physical properties of the atmosphere in the new Hadley Centre global environmental model (HadGEM1), Part II: Aspects of variability and regional climate. *J. Climate*, **19**, 1302–1326.

Salby, M. M., H. H. Hendon, and R. R. Garcia (1994) Planetary-scale circulations in the presence of climatological and wave-induced heating. *J. Atmos. Sci.*, **51**, 2344–2367.

Seo, K. H. and K. Y. Kim (2003) Propagation and initiation mechanisms of the Madden–Julian oscillation. *J. Geophys. Res.*, **108**, doi:10.1029/2002JD002876.

Seo, K.-H., J.-K. Schemm, W. Wang, and A. Kumar (2005) Boreal summer intraseasonal oscillation simulated in the NCEP climate forecast system: The effect of sea surface temperature. *Mon. Wea. Rev.*, **135**, 1807–1827, doi: 10.1175/MWR3369.1.

Shinoda, T. and H. H. Hendon (1998) Mixed layer modeling of intraseasonal variability in the tropical Western Pacific and Indian Oceans. *J. Climate*, **11**, 2668–2685.

Sikka, D. R. (1980) Some aspects of the large-scale fluctuations of summer monsoon rainfall over India in relation to fluctuations in planetary and regional scale circulation parameters. *Proc. Indian Acad. Sci. (Earth Planet. Sci.)*, **89**, 179–195.

Sikka, D. R. and S. Gadgil (1980) On the maximum cloud zone and the ITCZ over Indian longitudes during the southwest monsoon. *Mon. Wea. Rev.*, **108**, 1840–1853.

Slingo, J. M. and R. A. Madden (1991) Characteristics of the tropical intraseasonal oscillation in the NCAR community climate model. *Quart. J. Roy. Meteorol. Soc.*, **117**, 1129–1169.

Slingo, J. M., K. R. Sperber, J-J. Morcrette, and G. L. Potter (1992) Analysis of the temporal behavior of convection in the tropics of the ECMWF model. *J. Geophys. Res.*, **97**, 18119–18135.

Slingo, J. M., M. Blackburn, A. Betts, R. Brugge, K. Hodges, B. Hoskins, M. Miller, L. Steenman-Clark, and J. Thuburn (1994) Mean climate and transience in the tropics of the UGAMP GCM: Sensitivity to convective parameterization. *Quart. J. Roy. Meteorol. Soc.*, **120**, 881–922.

Slingo, J. M., K. R. Sperber, J. S. Boyle, J.-P. Ceron, M. Dix, B. Dugas, W. Ebisuzaki, J. Fyfe, D. Gregory, J.-F. Gueremy *et al.* (1996) Intraseasonal oscillations in 15 atmospheric general circulation models: Results from an AMIP diagnostic subproject. *Climate Dynamics*, **12**, 325–357.

Slingo, J. M., D. P. Rowell, K. R. Sperber, and F. Nortley (1999) On the predictability of the interannual behaviour of the Madden–Julian Oscillation and its relationship with El Niño. *Quart. J. Roy. Meteorol. Soc.*, **125**, 583–609.

Slingo, J. M., P. M. Inness, R. B. Neale, S. J. Woolnough, and G-Y. Yang (2003) Scale interactions on diurnal to seasonal timescales and their relevance to model systematic errors. *Ann. Geophys.*, **46**, 139–155.

Sperber, K. R. (2003) Propagation and the vertical structure of the Madden–Julian Oscillation. *Mon. Wea. Rev.*, **131**, 3018–3037.

Sperber, K. R. and H. Annamalai (2008) Coupled model simulations of boreal summer intraseasonal (30–50 day) variability, Part 1: Systematic errors and caution on use of metrics. *Climate Dynamics*, **31**, 345–372, doi: 10.1007/s00382-008-0367-9.

Sperber, K. R. and T. N. Palmer (1996) Interannual tropical rainfall variability in general circulation model simulations associated with the atmospheric model intercomparison project. *J. Climate*, **9**, 2727–2750.

Sperber, K. R. and D. E. Waliser (2008) New approaches to understanding, simulating and forecasting the Madden–Julian oscillation. *Bull. Amer. Meteorol. Society*, **89**, 1917–1920, doi: 10.1175/2008BAMS2700.1.

Sperber, K. R., S. Hameed, G. L. Potter, and J. S. Boyle (1994) Simulation of the northern summer monsoon in the ECMWF model: Sensitivity to horizontal resolution. *Mon. Wea. Rev.*, **122**, 2461–2481.

Sperber, K. R., J. M. Slingo, P. M. Inness, and W. K-M. Lau (1997) On the maintenance and initiation of the intraseasonal oscillation in the NCEP/NCAR reanalysis and the GLA and UKMO AMIP simulations. *Climate Dynamics*, **13**, 769–795.

Sperber, K. R., J. M. Slingo, and H. Annamalai (2000) Predictability and the relationship between subseasonal and interannual variability during the Asian summer monsoon. *Quart. J. Roy. Meteorol. Soc.*, **126**, 2545–2574.

Sperber, K. R., C. Brankovic, M. Deque, C. S. Frederiksen, R. Graham, A. Kitoh, C. Kobayashi, T. Palmer, K. Puri, W. Tennant *et al.* (2001) Dynamical seasonal prediction of the Asian summer monsoon. *Mon. Wea. Rev.*, **129**, 2226–2248.

Sperber, K. R., S. Gualdi, S. Legutke, and V. Gayler (2005) The Madden–Julian oscillation in ECHAM4 coupled and uncoupled general circulation models. *Climate Dynamics*, **25**, 117–140, doi: 10.1007/s00382-005-0026-3.

Sperber, K. R., J. M. Slingo, D. E. Waliser, and P. M. Inness (2008) Coarse-resolution models only partly cloudy. *Science*, **320**, 612.

Swinbank, R., T. N. Palmer, and M. K. Davey (1988) Numerical simulations of the Madden Julian Oscillation. *J. Atmos. Sci*, **45**, 774–788.

Taniguchi, H., W. Yanase, and M. Satoh (2010) Ensemble simulation of Cyclone Nargis by a global cloud-system-resolving model with modulation of cyclogenesis by the Madden–Julian oscillation. *J. Meteorol. Soc. Japan*, **88**, 571–591.

Thayer-Calder, K. (2008) The role of moisture in the MJO: A comparison of tropical convection processes in the CAM and super-parameterized CAM. M.Sc. thesis, Department of Atmospheric Science, Colorado State University, 74 pp.

Thayer-Calder, K. and D. A. Randall (2009) The role of convective moistening in the Madden–Julian Oscillation. *J. Atmos. Sci.*, **66**, 3297–3312, doi: 10.1175/2009JAS3081.1.

Tian, B., D. E. Waliser, E. J. Fetzer, B. Lambrigsten, Y. L. Yung, and B. Wang (2006) Vertical moist thermodynamic structure and spatial-temporal evolution of the MJO in AIRS observation. *J. Atmos. Sci.*, **63**, 2462–2485.

Tibaldi, S., T. N. Palmer, C. Brankovic, and U. Cubasch (1990) Extended-range predictions with ECMWF models: Influence of horizontal resolution on systematic model error and forecast skill. *Quart. J. Roy. Meteorol. Soc.*, **116**, 835–866.

Tokioka, T., K. Yamazaki, A. Kitoh, and T. Ose (1988) The equatorial 30–60 day oscillation and the Arakawa–Schubert penetrative cumulus parametrization. *J. Meteorol. Soc. Japan*, **66**, 883–901.

Tompkins, A. M. and K. A. Emanuel (2000) The vertical resolution sensitivity of simulated equilibrium tropical temperature and water vapour profiles. *Quart. J. Roy. Meteorol. Soc.*, **126**, 1219–1238.

Vecchi, G. A. and D. E. Harrison (2002) Monsoon breaks and subseasonal sea surface temperature variability in the Bay of Bengal. *J. Climate*, **15**, 1485–1493.

Waliser, D. and M. Moncrieff (2008) *Year of Tropical Convection (YOTC): The YOTC Science Plan* (WMO/TD-No. 1452). World Meteorological Organization, Geneva, 26 pp. Available at *http://www.ucar.edu/yotc/*

Waliser, D. E., K. M. Lau, and J.-H. Kim (1999) The influence of coupled sea surface temperatures on the Madden–Julian oscillation: A model perturbation experiment. *J. Atmos. Sci.*, **56**, 333–358.

Waliser, D. E., K. Jin, I.-S. Kang, W. F. Stern, S. D. Schubert, M. L. C. Wu, K.-M. Lau, M.-I. Lee, V. Krishnamurty, A. Kitoh *et al.* (2003a) AGCM simulations of intraseasonal variability associated with the Asian summer monsoon. *Climate Dynamics*, **21**, 423–446.

Waliser, D. E., K. M. Lau, W. Stern, and C. Jones (2003b) Potential predictability of the Madden–Julian oscillation. *Bull. Amer. Meteorol. Society*, **84**, 33–50.

Waliser, D. E., S. Schubert, A. Kumar, K. Weickmann, and R. Dole (2003c) *Modeling, Simulation, and Forecasting of Subseasonal Variability* (Technical Report Series on Global Modeling and Data Assimilation, NASA/CP-2003-104606, Vol. 25). NASA, Washington, D.C., 66 pp.

Wang, B. and H. Rui (1990) Synoptic climatology of transient tropical intraseasonal convection anomalies: 1975–1985. *Meteorol. Atmos. Phys.*, **44**, 43–61.

Wang, B. and X. Xie (1997) A model for the boreal summer intraseasonal oscillation. *J. Atmos. Sci.*, **54**, 72–86.

Wang, B., J. Matsumoto, G. Wu, and J. Li (2010) *The Science Plan for Asian Monsoon Years (AMY 2007–2012): A Cross-cutting WCRP Initiative*. China Meteorological Press, Beijing, 67 pp.

Wang, W. Q. and M. E. Schlesinger (1999) The dependence on convective parameterization of the tropical intraseasonal oscillation simulated by the UIUC 11-layer atmospheric GCM. *J. Climate*, **12**, 1423–1457.

Wang, W., M. Chen, and A. Kumar (2009) Impacts of the ocean surface on the northward propagation of the boreal summer intraseasonal oscillation in the NCEP climate forecast system. *J. Climate*, **22**, 6561–6576, doi: 10.1175/2009JCLI3007.1.

Webster, P. J., V. O. Magana, T. N. Palmer, J. Shukla, R. A. Tomas, M. Yanai, and T. Yasunari (1998) Monsoons: Processes, predictability, and the prospects for prediction. *J. Geophys. Res.*, **103**(C7), 14451–14510.

Weller, R. A. and S. P. Anderson (1996) Surface meteorology and air–sea fluxes in the western equatorial Pacific warm pool during the TOGA coupled ocean–atmosphere experiment. *J. Climate*, **9**, 1959–1992.

Wheeler, M. (2003) MJO modeling and simulation: Rectifying shortcomings. In: D. E. Waliser, S. Schubert, A. Kumar, K. Weickmann, and R. Dole (Eds.), *Modeling, Simulation, and Forecasting of Subseasonal Variability* (Technical Report Series on Global Modeling and Data Assimilation, NASA/CP-2003-104606, Vol. 25). NASA, Washington, D.C., 66 pp.

Wheeler, M. and G. N. Kiladis (1999) Convectively coupled equatorial waves: Analysis of clouds and temperature in the wavenumber–frequency domain. *J. Atmos. Sci.*, **56**, 374–399.

Woolnough, S. J., J. M. Slingo, and B. J. Hoskins (2000) The relationship between convection and sea surface temperature on intraseasonal timescales. *J. Climate*, **13**, 2086–2104.

Woolnough, S. J., J. M. Slingo, and B. J. Hoskins (2001) The organization of tropical convection by intraseasonal sea surface temperature anomalies. *Quart. J. Roy. Meteorol. Soc.*, **127**, 887–907.

Wu, M. L. C., S. Schubert, I. S. Kang, and D. E. Waliser (2002) Forced and free intraseasonal variability over the South Asian Monsoon region simulated by 10 AGCMs. *J. Climate*, **15**, 2862–2880.

Wu, M.-L. C., S. D. Schubert, M. J. Suarez, P. J. Pegion, and D. E. Waliser (2006) Seasonality and meridional propagation of the MJO. *J. Climate*, **19**, 1901–1921.

Wu, Z. (2003) A shallow CISK, deep equilibrium mechanism for the interaction between large-scale convection and large-scale circulations in the tropics. *J. Atmos. Sci.*, **60**, 377–392.

Yang, G.-Y., B. J. Hoskins, and J. M. Slingo (2003) Convectively coupled equatorial waves: A new methodology for identifying wave structures in observational data. *J. Atmos. Sci.*, **60**, 1637–1654.

Yasunari, T. (1979) Cloudiness fluctuations associated with the northern hemisphere summer monsoon. *J. Meteorol. Soc. Japan*, **57**, 227–242.

Yasunari, T. (1980) A quasi-stationary appearance of 30 to 40 day period in cloudiness fluctuations during the summer monsoon over India. *J. Meteorol. Soc. Japan*, **58**, 225–229.

Yoneyama, K., M. Katsumata, K. Yasunaga, T. Nasuno, C. Zhang, M. J. McPhaden, C. Fairall, R. H. Johnson, E. D. Maloney, M. Wheeler *et al.* (2009) *CINDY2011: Cooperative Indian Ocean Experiment on Intraseasonal Variability in the Year 2011*. Available at *http://www.jamstec.go.jp/iorgc/cindy/docs/CINDY2011_Plan_Ver1-2.pdf*

Zhang, C., M. Dong, S. Gualdi, H. H. Hendon, E. D. Maloney, A. Marshall, K. R. Sperber, and W. Wang (2006) Simulations of the Madden-Julian oscillation in four pairs of coupled and uncoupled global models. *Climate Dynamics*, **27**, 573–592, doi: 10.1007/s00382-006-0148-2.

Zhang, C., C. Fairall, and J. Moore (2010) *DYNAMO: Dynamics of the Madden–Julian Oscillation*. Available at *https://www.eol.ucar.edu/projects/dynamo/documents/DYNAMO_SPO_v10.pdf*

Zveryaev, I. (2002) Interdecadal changes in the zonal wind and the intensity of intraseasonal oscillations during boreal summer Asian monsoon. *Tellus*, **54**, 288–298.

12

Predictability and forecasting

Duane Waliser

12.1 INTRODUCTION

In April 2002, a workshop was held that brought together participants with a wide range of geophysical expertise to focus on the problem of intraseasonal predictability (Schubert *et al*., 2002). This workshop marked a relatively important milestone in the development of our predictive capability of the atmosphere, ocean, and land systems. The fact that it lured scientists with expertise in modeling, theory, and observations, as well as operational forecasters and funding agency administrators indicated that we had reached the point where intraseasonal variability (ISV) presented itself as more than a theoretical concern or vaguely observed set of phenomena. In fact, the need for such a workshop was based on the recognition that a number of intraseasonal features could likely provide near term opportunities for improving long-lead forecast skill. One of the keynote speakers, H. van den Dool, brought to the participants' attention the early foresight that John von Neumann (1955) had of the expected progress to be made in the area of "long-range" forecasting. In terms of present day terminology, von Neumann recognized (see the Appendix on p. 467 for an excerpt) that the first gains to be made in the area of (atmospheric) prediction were likely to be made at the short range where the initial conditions are expected to play an important role (i.e., 1950s–1970s). Following progress in this area, substantial gains would next be likely made at the very long range, meaning climate prediction, where surface boundary conditions (e.g., large-scale sea surface temperature) are expected to play the most important role (i.e., 1980s–1990s). Then, only after considerable understanding was obtained in each of these two extreme regimes could progress be made at the intraseasonal timescale (e.g., 2 weeks to 2 months) where both initial conditions and boundary conditions are expected to be important. The occurrence of the above workshop, followed by no fewer than five closely related workshops (Waliser *et al*., 2003c; ECMWF, 2004; Moncrieff *et al*., 2007; Sperber and Waliser, 2008b; Hendon *et al*., 2011) and the

W. K. M. Lau and D. E. Waliser (Editors), *Intraseasonal Variability in the Atmosphere–Ocean Climate System* (Second Edition).

establishment of the MJO Working Group (MJOWG) in 2007[1] and subsequently the follow-on MJO Task Force (MJOTF) in 2010[2] indicates that, by virtue of our progress with both "weather" and "climate" prediction problems, we had reached a point where it was feasible to consider the intermediary problem of the intraseasonal timescale. Illustrative of this progress is the inclusion of "intraseasonal" in the now commonly used acronym "ISI" (i.e., intraseasonal to interannual prediction) and the focus on ISI prediction of a recent report from the U.S. National Academy of Sciences (NAS, 2010).

While the workshops mentioned above included presentations and discussion of a number of intraseasonal phenomena, including the Pacific North America pattern, North Atlantic Oscillation, Arctic Oscillation, and blocking, it was clear that the Madden–Julian Oscillation (MJO) was one of the most underexploited in terms of the likely potential for near term gains in the area of intraseasonal prediction, including its impacts on other climate and weather processes. This was not only due to the characteristics of the phenomenon itself (e.g., Chapter 10) and the direct impact it has on a broad region of the tropics but because of the role it plays, via tropical diabatic heating variability, on the evolution of the extratropics (e.g., see Chapters 2–5 and 13). In order to fully exploit the possible benefits from MJO/intraseasonal prediction, it is obvious from the discussion in Chapter 11 that the biggest hurdle to overcome has been, and is still—albeit with significant signs of improvement—the development of forecasting systems (i.e., data assimilation schemes and forecast models) that properly represent the phenomenon itself. As this is becoming a reality, it facilitates progress in both weather and climate prediction. For weather, the MJO and the intraseasonal timescale offer the hope for extending (at least occasionally) the range of useful forecasts of weather and/or weather statistics, while for the seasonal and longer term climate prediction problem, the proper representation of the intraseasonal timescale is a key component of the atmospheric "noise" that influences, for example, the evolution of the ENSO (e.g., Chapter 10) and the occurrence of extreme events (e.g., tropical cyclones, blocking, atmospheric rivers).

In addition to making progress in weather and/or climate prediction via the MJO, and other ISV, are the implications for providing a means to develop more seamless prediction capabilities (e.g., Hurrell *et al.*, 2009; Brunet *et al.*, 2010; Hazeleger *et al.*, 2010; NAS, 2010). For example, it is perceived that useful skill associated with deterministic prediction of most "weather" phenomena is on the order of 6–10 days (e.g., Thompson, 1957; Lorenz, 1965, 1982; Palmer, 1993; van den Dool, 1994; Bougeault *et al.*, 2010; Froude, 2010; Gelaro *et al.*, 2010). Similarly, actualized predictability for the ENSO is on the order of 6–12 months (e.g., Cane *et al.*, 1986; Graham and Barnett, 1995; Kirtman *et al.*, 1997; Barnston *et al.*, 1999; Kirtman and Pirani, 2009; NAS, 2010). Conveniently lying between these two

[1] Sponsored by the U.S. component of the World Climate Research Program (WCRP)'s Climate Variability and Prediction (CLIVAR) activity; *www.usclivar.org/mjo.php*

[2] Sponsored by the World Climate Research Program (WCRP) and World Weather Research Program (WWRP)/THORPEX; *www.ucar.edu/yotc/mjo.html*

timescale regimes is that associated with the MJO, a somewhat well-behaved and recurring tropical phenomenon, with indications that useful predictive skill for the MJO exists out to at least 2–3 weeks. Support for this comes from dynamic and empirical predictability studies and, more recently, from operational dynamic prediction models. The combination of natural predictive phenomena with timescales on the order of days (e.g., cyclones), weeks (e.g., the MJO), and then months (e.g., the ENSO), along with unified and/or seamless approaches to prediction offer broad new capabilities in the area of environmental and socially relevant predictions (e.g., Shukla *et al*., 2009, 2010; Martin *et al*., 2010; NAS, 2010; Nobre *et al*., 2010; Shapiro *et al*., 2010)—with the MJO and ISV making a critical contribution.

This chapter will review the progress that has been made regarding our capabilities of predicting the MJO via empirical and dynamical means and our understanding of its predictability characteristics. Note that there are a number of studies that indicate an influence of the MJO on the prediction and predictability of remote (extratropics) and/or secondary circulations (e.g., tropical cyclones). Some reference will be made to this material but more direct discussion can be found in other chapters (e.g., Chapters 2, 3, 6, 13). In the following section, a review of empirical methods for forecasting the MJO will be presented. In Section 12.3, an analogous discussion will be presented for forecasts based on dynamical (e.g., numerical weather prediction) models. In Section 12.4, issues regarding the inherent predictability of the MJO will be discussed. In Section 12.5, present day efforts of real time/operational MJO forecasting will be described. Section 12.6 concludes with a discussion of the outstanding issues and questions regarding future progress in this area.

12.2 EMPIRICAL MODELS

By the late 1980s, many characteristics of the MJO were fairly well documented and it was clear that it was a somewhat well-defined phenomenon with a number of reproducible features from one event to another as well as in events from one year to the next. Given this, and the degree to which research had shown a number of important interactions of the MJO with other features of our weather and climate system, it was an obvious step to begin to consider MJO forecasting in more earnest. Since numerical weather and climate models typically had a relatively poor representation of the MJO at the time, a natural avenue to consider was the development of empirical models. Along with likely providing more skillful forecasts than the numerical methods available at the time, this avenue also provided a means to establish an estimate of the predictability for the MJO—at least one that could be ascertained from the observations alone.

The first study along these lines was by von Storch and Xu (1990) who examined the principal oscillating patterns (POPs) of equatorial 200 mb velocity potential anomalies from a 2-year subinterval of a 5-year dataset. Upon verifying against the dataset as a whole (as well as against the remaining 3 years of data), they found that forecasts based on the first pair of POPs—which tended to emphasize

the variability in boreal winter (e.g., Figures 4.5, 5.8)—produced forecasts that were better than persistence and appeared to have useful skill out to at about 10–15 days (Figure 12.1). While this was an encouraging result—at least relative to "weather"—the limited length of data used combined with the non-stationary characteristics of the MJO over interannual timescales (e.g., Salby and Hendon, 1994; Hendon *et al.*, 1999) necessitated some caution in overinterpreting it. Moreover, given the smoothly varying nature of the 200 hPa velocity potential, and the fact that it is only loosely related to near surface meteorological variables (e.g., precipitation), also suggested caution in generalizing this result to other years, variables, and/or different techniques. In this regard, one might hope that given the roughly 50-day timescale of the MJO that it might be possible to have useful skill out to one half of a period (van den Dool and Saha, 2002)—particularly for upper-level flow (e.g., 200 hPa velocity potential). Subsequent to the above, Kousky and Kayano (1993) suggested that real time monitoring of the MJO could be achieved by projecting anomalies of a number of fields (e.g., OLR, 200 hPa velocity potential, surface pressure, etc.) onto their leading combined extended empirical orthogonal function patterns which would indicate the present phase and strength of the MJO in the tropical atmosphere and its likely evolution. It turns out that a number of later developments in the area of empirical MJO prediction tended to follow this suggestion in one form or another (e.g., Wheeler and Hendon, 2004).

After a relatively long hiatus in this area, Waliser *et al.* (1999a) developed an empirical MJO forecasting method in order to use the skill results as a benchmark by which to judge the predictive skill of numerical long-range forecasts and to begin exploring the feasibility of employing such a model to augment operational long-range forecasting procedures. The model was based on a field-to-field singular value decomposition that used previous and present pentads of OLR to predict future pentads of OLR (Figure 12.2). Separate models were developed for austral and boreal summer conditions (e.g., Figures 4.10 and 4.5, respectively) using 30 to 70-day filtered OLR data from 1979 to 1989 and validated on data from 1990 to 1996. For the validation period, the model exhibited temporal correlations to filtered observations of about 0.5–0.9 over a significant region of the eastern hemisphere at lead times from 15 to 20 days, after which the correlation dropped rapidly with increasing lead time. Correlations against observed total anomalies were on the order of 0.3 to 0.5 over a smaller region of the eastern hemisphere. While this was an equally, if not more, encouraging result than that of Storch and Xu discussed above, the fact that the model utilized filtered data limited its real time applicability and in this case warranted caution in considering the result too optimistic (see fig. 10 and associated discussion in Jiang *et al.*, 2008a). In concluding their study, the authors provided a number of avenues for addressing this filtering problem (i.e., being able to isolate the MJO signal from both the "weather" and interannual climate variations). For example, it was suggested that low-frequency variations (i.e., ENSO variability) might be removed using projections on low-order empirical orthogonal functions from coarser (e.g., monthly) data, and high-frequency signals could be removed by using longer time averages, that could even overlap to retain some aspect of the high temporal resolution (e.g., overlapping

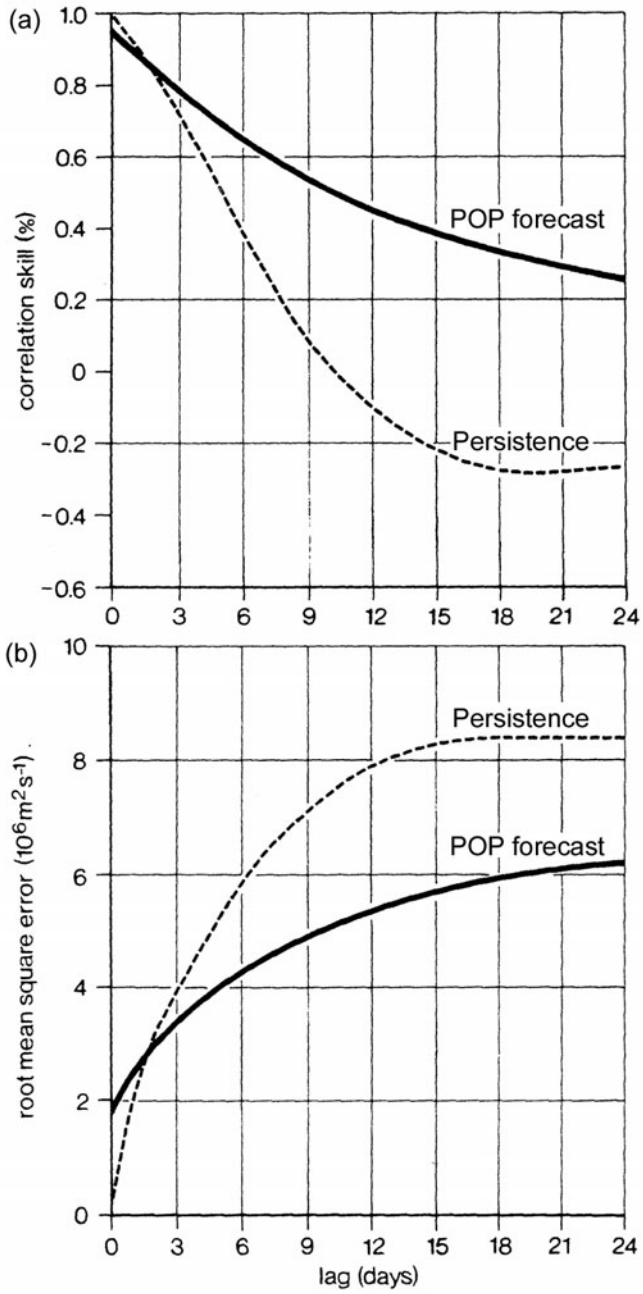

Figure 12.1. Measures of (a) correlation and (b) root mean square error forecast skill for persistence and the POP-based forecasting scheme developed by von Storch and Xu (1990). The skills have been derived from daily forecast experiments for the period May 1984 to April 1989. Note the model itself was developed on data between May 1986 to April 1988.

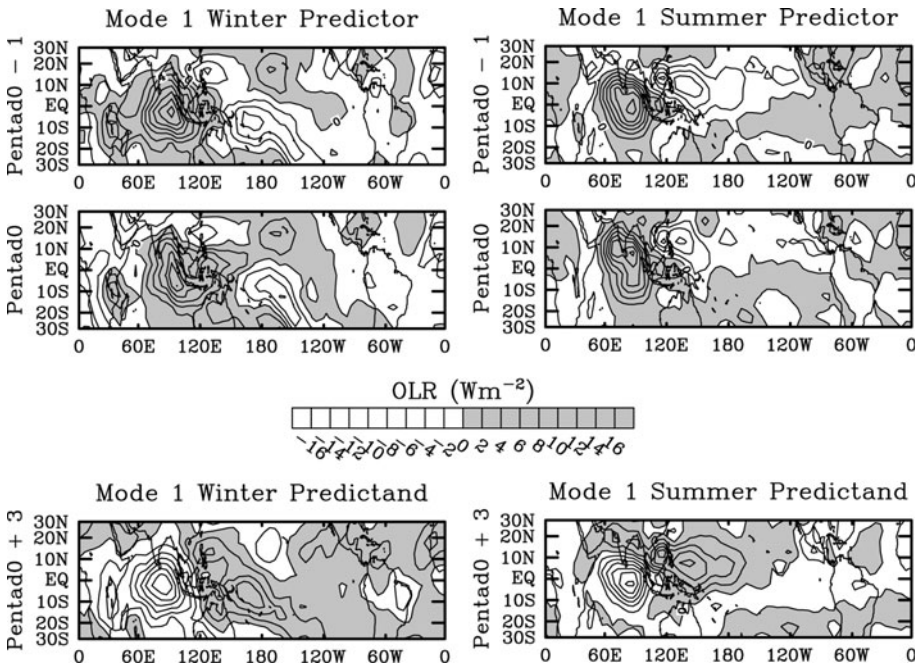

Figure 12.2. (left column) Mode 1 from the singular value decomposition (SVD)–based MJO-forecasting scheme developed by Waliser *et al*. (1999b) for the northern hemisphere winter and a three-pentad lead forecast. The top panel shows the predictor patterns for Pentad0 (the current pentad) and Pentad0 − 1 (the previous pentad). The bottom panel shows the associated predictand patterns for Pentad0 + 3 (i.e., three pentads in the future). (right column) The same, except for northern hemisphere summer. Here winter (summer) is defined as November 17 to May 15 (May 16 to November 16). Note that mode 2 for each season looks similar to mode 1 but tends to be spatially in quadrature.

10-day averages every 5 days). In addition, it was noted that, once low-frequency variability was removed, low-pass spatial filtering might serve as a useful mechanism for low-pass temporal filtering given that MJO variability tends to be isolated to wavenumbers 1–3 and periods of about 40–60 days.

Following the above study, there were a number of empirical MJO-forecasting efforts that each produced a unique and useful approach to the problem. Lo and Hendon (2000) developed a lag regression model that uses as predictors the first two and first three principal components of spatially filtered OLR and the 200 hPa streamfunction (Ψ), respectively, to predict the evolution of OLR and 200 hPa streamfunction anomalies associated with the austral summer MJO. In order to address the filtering problem discussed above regarding real time application, the data had the annual cycle, interannual, and high-frequency (i.e., $<$30 days) components removed separately. The annual cycle was removed by subtracting out the first three annual harmonics pointwise. The interannual (e.g., ENSO) variability was

removed by developing regression equations between the OLR (and Ψ) anomalies and the principal component time series from the first two EOFs of tropical SST anomalies. Based on these regressions and daily SST values (interpolated from weekly data), the low-frequency components of OLR (and Ψ) that could plausibly be attributed to the ENSO were removed. Subsequent to this, the high-frequency temporal components of the data were removed by subjecting the data to a T12 spectral truncation—utilizing the notion that high-frequency temporal and high-wavenumber spatial variations tended to occur concomitantly. The resulting intra-seasonally filtered OLR and Ψ anomalies were then subjected to EOF decomposition and then time-lagged regression equations were developed for predicting, at a given lead, the principal component values for the EOF modes that define the MJO (e.g., modes 1 and 2). When tested on independent data, the model exhibited useful skill (correlation $\sim$0.5) for predictions of these principal components out to about 15 days, with greater skill during active vs. quiescent MJO periods. In comparison with filtered observed OLR data, the model exhibited correlation values around 0.3–0.4 in a fairly broad region of the equatorial Indian Ocean and maritime continent.

A somewhat different approach was taken by Mo (2001) who utilized empirical basis functions in time for the forecasting procedure. This was done by using a combination of singular spectrum analysis (SSA) (Vautard and Ghil, 1989) for the filtering and identification of the principal modes of variability and the maximum entropy method (MEM) (Keppenne and Ghil, 1992) for the forecasting component. The procedure was applied to monitor and forecast outgoing longwave radiation anomalies (OLRAs) in the intraseasonal band over both the Indian–Pacific sector as well as the pan-American region. This included variability such as the MJO, higher frequency intraseasonal modes associated with the Asian monsoon (see Chapters 2 and 3) and variability related to both of these that occurs over the U.S. west coast (see Chapter 4). For example, in the Pacific and the pan-American region, there were three leading modes (T-EOFs) identified with periods near 40, 22, and 18 days. In this method, the leading SSA modes (T-EOFs) are determined from a training period. OLRA time series are then projected onto T-EOFs to obtain the principal components (T-PCs). To obtain fluctuations in a given frequency band of interest (i.e., perform filtering), a subset of the T-EOFs and the related T-PCs associated with that band are summed. This filtering procedure, based on the SSA modes, is data adaptive and there is no loss of endpoints. This aspect makes it particularly well suited for real time monitoring. To perform forecasts, the MEM is used to determine the autoregressive coefficients from the training period. These coefficients are used to forecast the T-PCs at future leads. The summation of the T-EOFs and T-PCs related to three retained modes used in the filtering process gives the predicted OLRAs. When tested on 8 years of independent December–February and June–August OLRA data, the averaged correlation over the tropics between the predicted and the observed anomalies was 0.65 (range 0.48–0.78) at the lead times of four pentads (20 days). Although the model amplitudes are weaker than the observations, a feature not uncommon amongst the empirical models, the spatiotemporal structure is well captured out to the four-pentad forecast.

In a quite different approach, Wheeler and Weickmann (2001) utilize tropical wave theory (Matsuno, 1966) as the basis for their filtering and forecasting technique. Essentially, spacetime Fourier analysis is performed on daily OLR data for a given time–longitude section of interest in the tropics. In a previous study, Wheeler and Kiladis (1999) showed that the spectrum from such an analysis exhibits variability that is associated with the modes that one would expect from theoretical considerations (e.g., Kelvin and mixed Rossby–gravity waves), as well as the expected peak of variability around wavenumbers 1–3 and 40–60 days associated with the MJO. In order to monitor and predict the evolution of a given mode of interest, the specific zonal wavenumbers and frequencies associated with the mode(s) of interest are retained and then the modified spectrum is inverse-Fourier-analyzed. Figure 12.3 shows how the filtered values obtained for times before the end of the dataset can be used for monitoring the activity of a given mode, while the filtered fields obtained for times after the endpoint may be used as a forecast. This idea is akin to an ocean tidal forecast, which in that case is based on harmonic analysis in time only and of course much sharper frequencies of variability. For prediction, the method exhibits useful skill for the MJO out to about 15–20 days. An advantage is that the method readily provides predictions of other well-defined, typically higher frequency, modes of large-scale tropical variability.

In an effort that focused on the active and break conditions of the Indian summer monsoon, Goswami and Xavier (2003) note that all active (break) conditions go over to a break (active) phase after about 15–20 days (see Figure 2.3). The events would be highly predictable if the transitions from active to break (or vice versa) were all identical. However, the rate of transition, the magnitude of the next minimum (or maximum), and the timing of achieving the minimum (maximum) of the next phase vary from event to event. Using the rainfall-based index illustrated in Figure 2.3 and their definition of active and break conditions (see Chapter 2), Goswami and Xavier calculated the typical (i.e., ensemble average) transition from active to break (and break to active) conditions as a function of lead time. The typical size of these transitions—referred to as the "signal"—and their associated intra-ensemble variance—referred to as the (ensemble) "spread"—are shown in the upper panel of Figure 12.4. While the variability among break to active transitions become as large as the associated signal in fewer than 10 days, it takes more than 20 days for the variance among active to break transitions to become as large as the signal. Circulation parameters such as the 850 hPa relative vorticity over the monsoon trough region also lead to the same conclusion (not shown). These results indicate that monsoon breaks are intrinsically more predictable than active monsoon conditions. Similar results were found by Waliser *et al.* (2003d) using an ensemble of twin-predictability GCM experiments (see Section 12.4). To explore the practical consequences of these results, Goswami and Xavier constructed an empirical multiple regression model for the first four principal components (PCs) of 10 to 90-day filtered CMAP using the first four PCs of filtered rainfall data and the first two PCs of filtered surface pressure as predictors and showed that useful prediction of monsoon breaks up to 18 days in advance could be made while useful forecast of active conditions could be made with a lead time of only about 10 days.

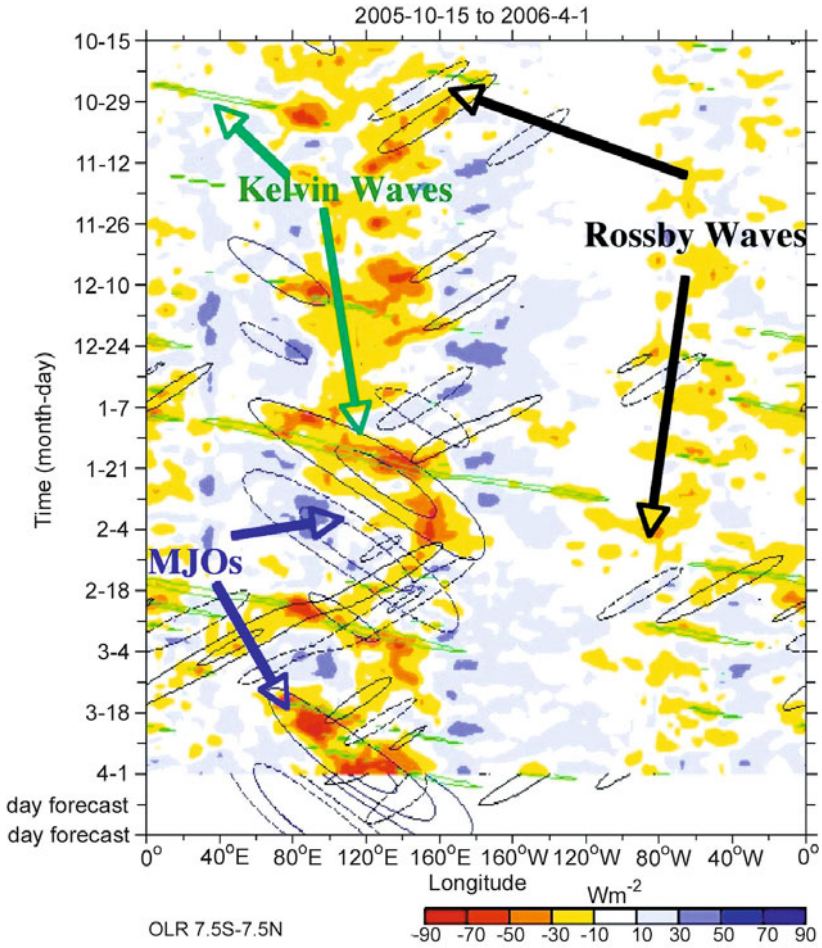

Figure 12.3. (a) Time–longitude plot of the total OLR anomalies and filtered OLR anomalies averaged between 7.5°S and 7.5°N during late 2005 to early 2006. Shading is for total OLR anomalies and contours are for the diagnostically filtered anomalies for the MJOs (blue/eastward), Kelvin waves (green) and mode 1 equatorial Rossby waves (black/westward). Solid contours represent negative OLR anomalies, while dashed contours are for positive anomalies, with the contour interval for wave-filtered bands being $10\,\mathrm{W\,m^{-2}}$, and the zero contour omitted. Note that the filtering was performed with the last day of data being on April 1, 2006. After April 1, when the real time filtered anomalies are continued into the future as a forecast, the contour interval is halved (based on Wheeler and Weickman, 2001).

The lower panel of Figure 12.4 shows 18-day forecasts of filtered precipitation averaged over central India and northern Bay of Bengal (70°E–85°E, 10°N–22°N) for June to September 2000.

Another technique contributing to empirical forecasting builds on what is referred to as all season real time multivariate MJO (RMM) modes and their

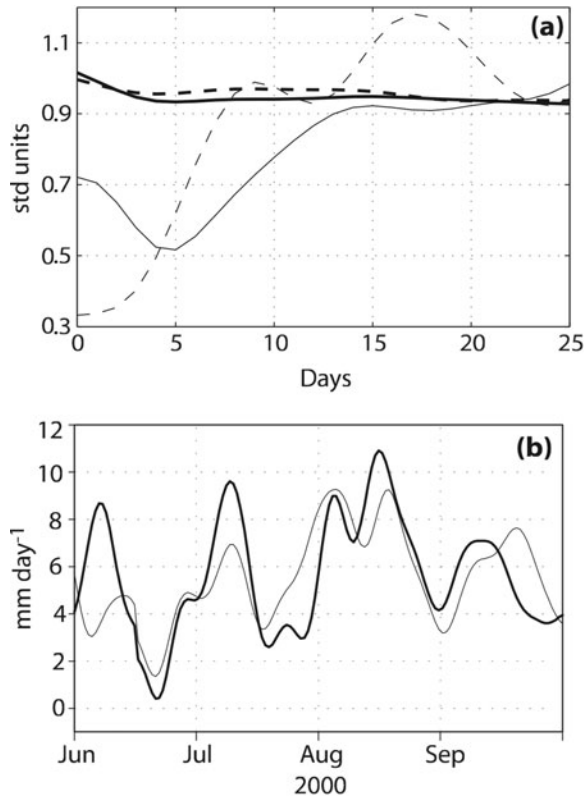

Figure 12.4. (a) The thick dashed (solid) line is the monsoon ISO "signal" starting from troughs (peaks) of the index (see Figure 2.4). The thin dashed (solid) line is the variance (or spread) of ensemble members as a function of days from the initial date corresponding to all troughs (peaks) of the index representing transitions from break to active (active to break). (b) Time series of 18-day predictions (thin line) and observations (thick line) of rainfall (mm day^{-1}) averaged over the monsoon trough region for June to September of 2000 (from Goswami and Xavier, 2003).

associated indices (Wheeler and Hendon, 2004)[3] (for more discussion, see Chapter 5). The indices result from projecting daily data onto the first two modes of a combined EOF of tropical (15°N–15°S) OLR, and zonal winds at 850 hPa and 200 hPa. This projection onto the EOF pair, along with the prior removal of an estimate of the data's very low-frequency components (e.g., the ENSO) via their relationship to interannual SST variability, remove the need to perform time filtering to identify the MJO. The values of the two indices, one for mode 1 (RMM1) and one for mode 2 (RMM2), at any given time can be used for MJO monitoring. In addition, seasonally and time lag–dependent regression can be used

[3] *http://www.bom.gov.au/climate/mjo/*

to forecast the evolution of these indices or any associated field, using as predictors RMM1 and RMM2 at the initial day. Jiang *et al.* (2008a) provide a skill assessment for this type of RMM-based regression model, including a number of sensitivity tests regarding number of modes retained, quantity being compared, seasonality, strong vs. weak MJO, applications of filtering, etc. Figure 12.5 shows a subset of these sensitivity tests. Figure 12.6 shows the temporal correlation values for this model when compared with EOF-filtered (i.e., low-frequency/wavenumber MJO) observations of OLR (upper left) and when compared with total anomalies (upper right), along with a more specific example of a hindcast during 2003–2004. Note that correlations with wind, particularly 200 hPa zonal wind, have considerably larger correlation values over a broader expanse of the tropics relative to those shown for

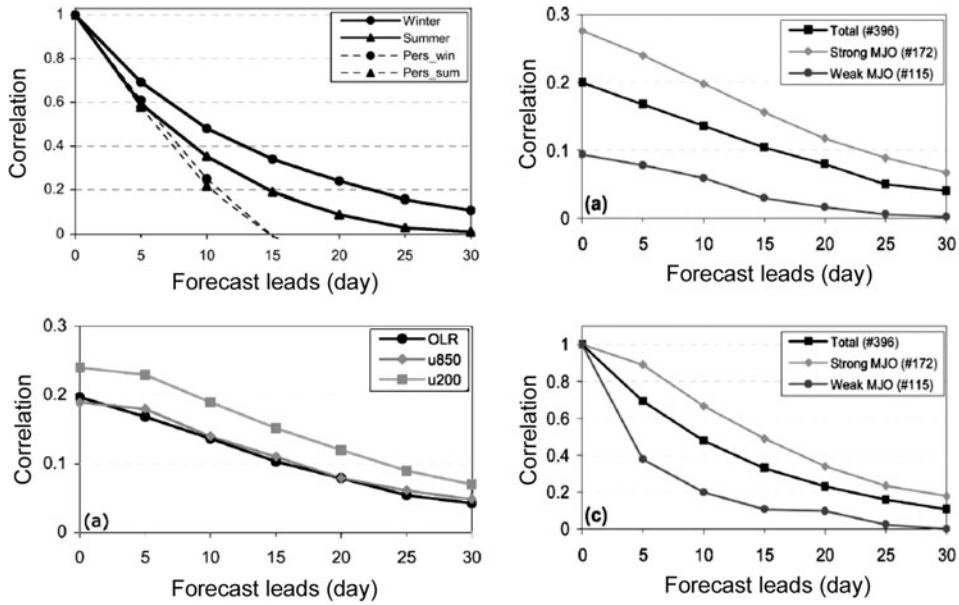

Figure 12.5. (upper left) Pattern correlation of OLR over global tropics between predicted and observed EOF-filtered OLR perturbation patterns for boreal winter (solid line with circles) and summer (solid line with triangles) predictions. The observed EOF-filtered OLR perturbation patterns are reconstructed based on the simultaneous regression relationship between OLR and two leading PCs of combined EOFs. Dashed lines denote the predictive skill obtained by persistence for winter (circles) and summer (triangles) predictions. (lower left) Pattern correlation between forecasts and observed unfiltered perturbation patterns of OLR, u850, and u200 for boreal winter. (right) Pattern correlation between forecasts and observed (top) unfiltered and (bottom) EOF-filtered OLR perturbation patterns based on the predictions for all cases (squares; i.e., Ctrl_exp), and strong (circles) and weak (diamonds) MJO events for boreal winter predictions. Strong and weak MJO events are defined by the combined amplitude of PC1 and PC2 with amplitude exceeding 1.5 for strong MJOs (black line) and less than 1 for weak MJOs (gray line) (from Jiang *et al.*, 2008).

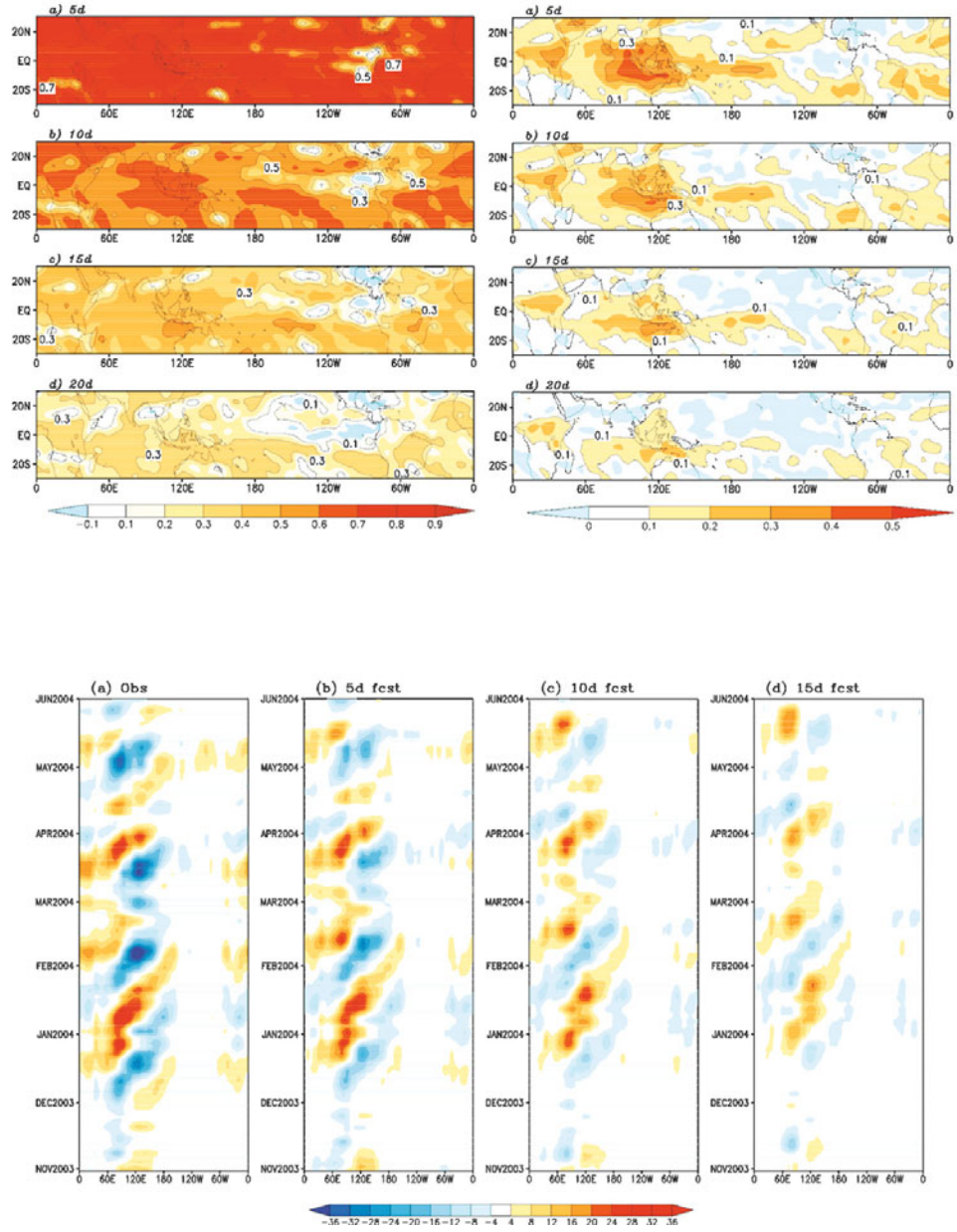

Figure 12.6. (upper left) Temporal correlation between forecasts and observed EOF-filtered OLR perturbations at various forecast leads from 5 to 20 days for boreal winter. (upper right) Same, but for temporal correlation between forecasts and observed unfiltered OLR perturbations. (lower) Hovmöller diagram of OLR (averaged over 10°S–10°N) during 2003/2004 winter for the (a) observed EOF-filtered field and forecasts at the lead time of (b) 5 days, (c) 10 days, and (d) 15 days ($W\,m^{-2}$) (from Jiang *et al.*, 2008).

OLR in the upper panel of Figure 12.6, including much of the western hemisphere (not shown).

The above discussion gives a flavor of the types of empirical MJO modeling that have been developed to date and their associated levels of forecast skill. Figure 12.7 shows direct comparisons of skill from a number of empirical models conducted by Kang and Kim (2010) and by Seo *et al*. (2009), with the indication that relatively low-order RMM-based regression models tend to outperform other comparably

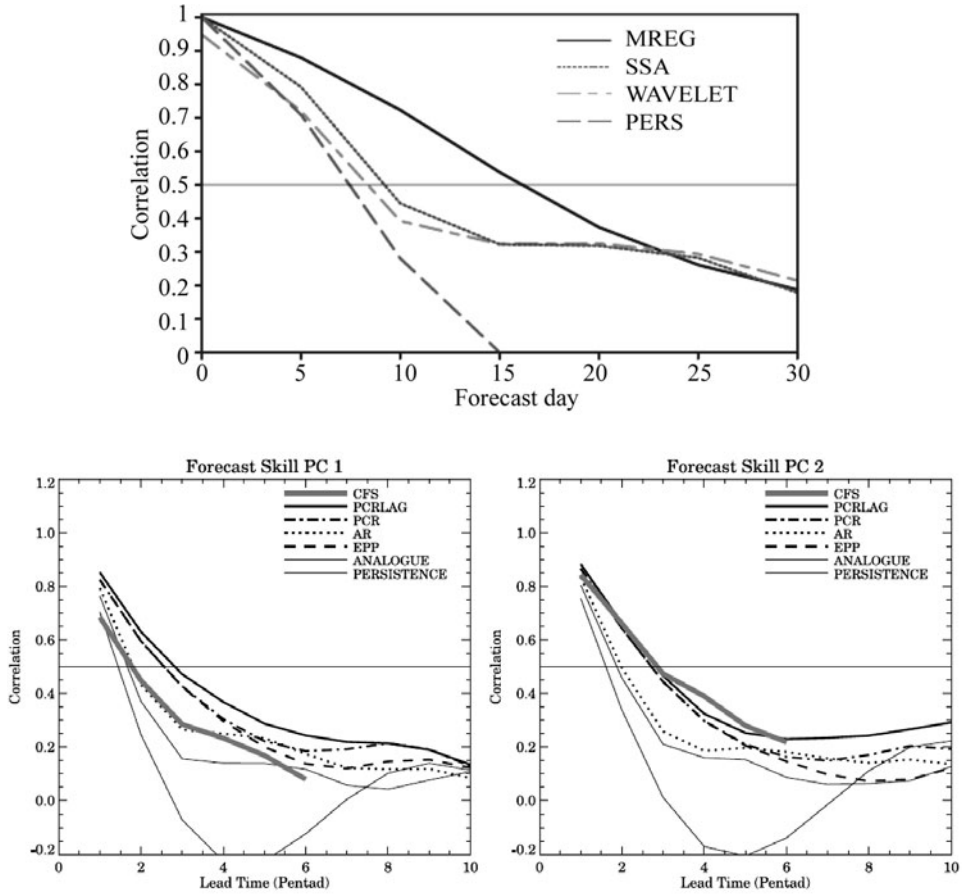

Figure 12.7. Comparisons of skill for various statistical models. (top) Correlation values for RMM1 for an SSA-based model (dotted line), a regression model (MREG; solid line), and a wavelet-based model (long and short-dashed line), and persistence of the initial condition (dashed line) (Kang and Kim, 2010). (bottom) Correlation skill for RMM-like calculated values of MJO indices as a function of forecast time (pentad) for (left) PC1 and (right) PC2 for a number of statistical forecasts—multiple linear regression (PCRLAG, PCR), auto-regressive (AR), empirical phase propagation (EPP), analogue, and persistence. The NCEP Coupled Forecast System (CFS) is also shown (Seo *et al*., 2009).

simple empirical methods. There are a number of additional empirical modeling studies worth describing that have been associated with real time efforts and these are discussed in Section 12.5 below. In addition, it is worth highlighting that in no cases are the above schemes physical in nature or based on very complex techniques and that they are all based on linear methods. Thus, it is likely that we may have yet not developed and demonstrated models that have saturated the skill potential for empirical forecasting methods. In addition, it is also worth highlighting that MJO events are at best quasi-periodic in nature, meaning here that the atmosphere can be relatively quiescent regarding MJO variability and then an event suddenly develops. Most of the models above would tend to perform relatively poorly at forecasting this initial development, as they all tend to rely on the periodic nature of the MJO to forecast its evolution. For these scenarios, as well as for dealing with the heterogeneity of MJO events, it will be vital to improve our dynamic models, as they are likely to be the best means of dealing with these sorts of issues. In any case, the above sorts of studies provide a useful benchmark in forecast skill for our dynamical models and suggest, based on the observations alone, that the MJO should be predictable with lead times of at least 2–3 weeks. It is worth noting that the following statement appeared in this chapter in the first edition of this book: "The skill associated with the techniques above in almost all cases has yet to be demonstrated by numerical forecast techniques." It is encouraging to report in this second edition of this book that this is no longer the case; these developments will be highlighted below.

12.3 DYNAMICAL FORECAST MODELS

Prior to the last several years, there had only been a handful of studies that had examined forecast skill (i.e., verified against observations) from dynamical models. This stemmed from what amounted to: (a) considerably less overall interest in forecasting the intraseasonal timescale relative to weather and the ENSO, (b) the difficulty and resources required to produce an adequate sample of very long–range weather forecasts (at least 30 days), (c) the pessimism and known challenges associated with tropical weather forecasting in general, and (4) the indications that our forecast or climate simulation models were not very adept at simulating the MJO (see Chapter 11). In any case, as part of a more generalized forecast skill study of planetary-scale divergent circulation, Chen and Alpert (1990) examine the MJO forecast skill from one year (June 1987–May 1988) of daily 10-day forecasts from the U.S. National Meteorological Center's (NMC; now National Center for Environmental Prediction or NCEP) medium-range forecast (MRF) model (based partly on MRF86 and MRF87) in terms of the 200 hPa velocity potential. In their analysis, the MRF's forecast skill, measured in terms of spatial correlations of 200 hPa velocity potential between 50°N–50°S, declined to about 0.6 by forecast day 6 and 0.4 by forecast day 9. This relatively poor skill was attributed to: (1) the inability of the model to maintain MJO variability during a forecast (thus the model probably did not intrinsically exhibit or support an MJO of its own), and

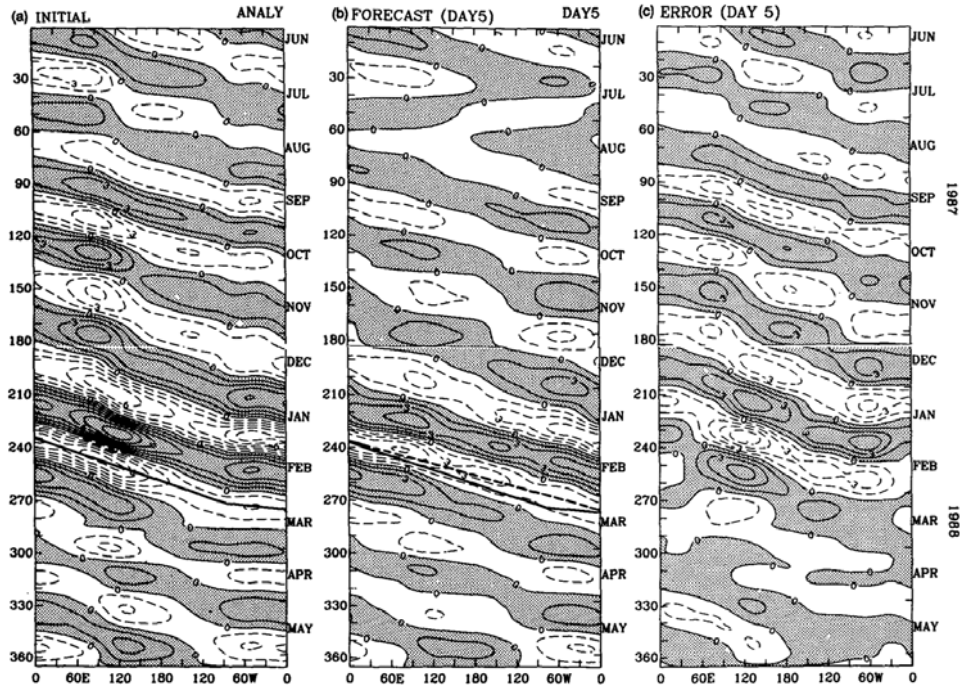

Figure 12.8. Equatorial time–longitude diagram of 200 hPa velocity potential anomalies constructed from the first two EOF modes of the data. In this case, the EOF was done separately for each lead time. Values are shown for (a) initial conditions, (b) day 5 forecasts, and (c) day 5 forecast errors. The solid line connects maximum initial condition 200 hPa velocity potential anomalies for a half lifecycle of the intraseasonal oscillation during winter in (a). The dashed line connects maximum 200 hPa velocity potential anomalies of day 5 forecast in (b). The solid line of (a) is also shown in (b) for comparison. The contour interval is 1.0×10^6 m^2/s (from Chen and Alpert, 1990).

(2) the model's tendency to propagate MJO anomalies too fast. This latter aspect is illustrated in Figure 12.8. The left panel illustrates the observed 200 hPa velocity potential with a line overlaid to indicate the observed phase speed of one of the stronger events. The middle panel illustrates the model forecast values at a lead time of 5 days with the same line overlaid from the left panel that shows quite clearly the model propagating the anomalies too fast. Lau and Chang (1992) analyze one season (December 14, 1986 through March 31, 1987) of 30-day global forecasts derived from a set of dynamical extended range forecasts (DERFs) from a research version of the MRF86 model mentioned above. Their results showed that the forecast model had significant skill in predicting the global pattern of intraseasonal variability in 200 hPa velocity potential and streamfunction for up to a 10-day lead time, with the error growth of tropical and extratropical low-frequency modes less than persistence when the amplitude of the MJO was large and vice versa when the amplitude was small.

Both Hendon *et al.* (2000) and Jones *et al.* (2000) analyze a more recent DERF experiment which used a reanalysis version (Kalnay *et al.*, 1996) of the NCEP medium-range forecast (MRF) model (Schemm *et al.*, 1996). This experiment included 50-day forecasts made once a day for the period January 1985 to February 1990. In both studies, the focus was on the northern hemisphere winter season. Using different analysis and filtering techniques for identifying the MJO within the forecasts and, thus, for assessing forecast skill against observations, both studies concluded that this version of the NCEP MRF model also exhibited rather poor MJO forecast skill. Jones *et al.* show that the anomaly correlations of intraseasonally filtered values of 200 hPa zonal wind, zonally averaged along the equator, declined from about 0.6 on day 3 to 0.2 by day 10. Moreover, that model exhibited a forecast skill that was slightly better (worse) when the MJO was particularly active (weak; i.e., null case) and that model skill might have some dependence on the phase of the MJO. The rather poor forecast skill was attributed to the development of systematic errors in forecast upper-level winds, particularly over the Eastern Pacific and, as above, due to the inability of this model to maintain/simulate a robust MJO phenomenon itself. For example, a diagnosis of the model's representation of the MJO from a 10-year simulation using the same model showed an MJO-like phenomenon but one that was significantly less intense and propagated considerably faster than the observed phenomenon (Jones *et al.*, 2000).

The detailed analysis by Hendon *et al.* (2000) shows that forecasts initialized during very active episodes of the MJO did not reproduce the observed eastward propagation of the tropical convection and circulation anomalies, rather the anomalies would typically weaken in place and even retrograde in some cases. Typically, it was found that convective anomalies would decay almost completely by day 7 of the forecast, and in nearly the same time systematic errors in the extratropical 200 hPa streamfunction became fully developed. They argue that the errors in the latter developed due to the collapse of tropical heating anomalies and, thus, the development of an error in the Rossby wave source emanating from the tropics. Due to the types of errors, which are greatest for the largest MJO anomalies, and likely due to their categorization of active events, their analysis showed that forecast skill in the tropics and northern hemisphere extratropics was actually worse during active MJO events than periods that exhibited very little MJO activity (Figure 12.9).

Progress in improving NCEP's forecast skill of the MJO was demonstrated in an updated DERF analysis by Seo *et al.* (2005). The experiments were done with the NCEP Global Forecast System (GFS) that was operational in the early to mid-2000s. GFS DERF 30-day hindcasts were carried out for the 1998 through 2002 period with T126L28 resolution for the first 7 days and with T62L28 resolution afterwards. Changes to a number of physics processes and the increased horizontal resolution were deemed important changes in this model compared with the previous DERF model (used in the studies above). Similar to the previous DERF, SST was damped from its initial observed value to climatology with a 90-day e-folding time. Figure 12.10 shows anomaly correlation values versus the lead time for zonal wind at 200 hPa, with the indication of an improvement of forecast skill by a few days. Along

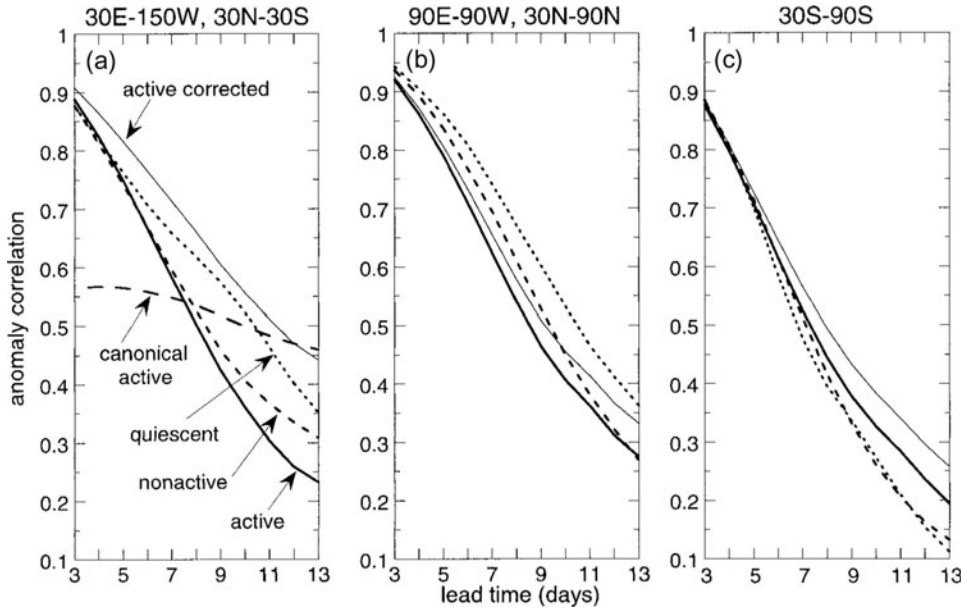

Figure 12.9. Anomaly correlations between forecasts, as functions of lead time, and verification of the 200 hPa streamfunction for (a) the tropical region 30°N–30°S, 30°E–150°W, (b) the northern hemisphere extratropical region 30°N–90°N, 90°E–90°W, and (c) the southern hemisphere extratropics 30°S–90°S. Forecast data are based on the DERF experiment (Schemm *et al.*, 1996) which used the reanalysis version (Kalnay *et al.*, 1996) of the NCEP medium-range forecast (MRF) model. This experiment included 50-day forecasts made once a day for the period January 1985 to February 1990. Correlations are shown for all forecasts initialized when the MJO was active and quiescent and for times when the MJO was non-active (i.e., neither active nor quiescent). Active and quiescent MJO periods were selected using the principal component values of the first two EOFs of intraseasonally filtered OLR. Empirically corrected (lead-dependent systematic MJO error estimated and removed) anomaly correlations are also shown for forecasts initialized when the MJO was active (labeled "active corrected"). Also shown in (a) is the anomaly correlation for the canonical MJO (i.e., a simple empirical model), which is formed by lag regression of the verifying analyses onto the leading two principal components of OLR at the initial forecast time (from Hendon *et al.*, 2000).

similar lines, the representation of the MJO in ECMWF's Integrated Forecast System has undergone remarkable improvement in the time since the writing of the first edition of this book. Figure 12.11 illustrates model hindcast performance in terms of OLR for the TOGA–COARE period (i.e., winter of 1992–1993) verified at a lead time of 15 days. The model cycles (i.e., versions) are operational versions of the IFS starting in 2004 and extending to 2010. Evident is the substantial improvement in model fidelity, arising from a varied combination of model resolution, model physics, and data assimilation improvements (Bechtold *et al.*, 2008; cf. Agudelo *et al.*, 2009). In addition, model improvements to GCMs used for weather prediction and climate studies in Canada have led to additional demonstrations of viable MJO

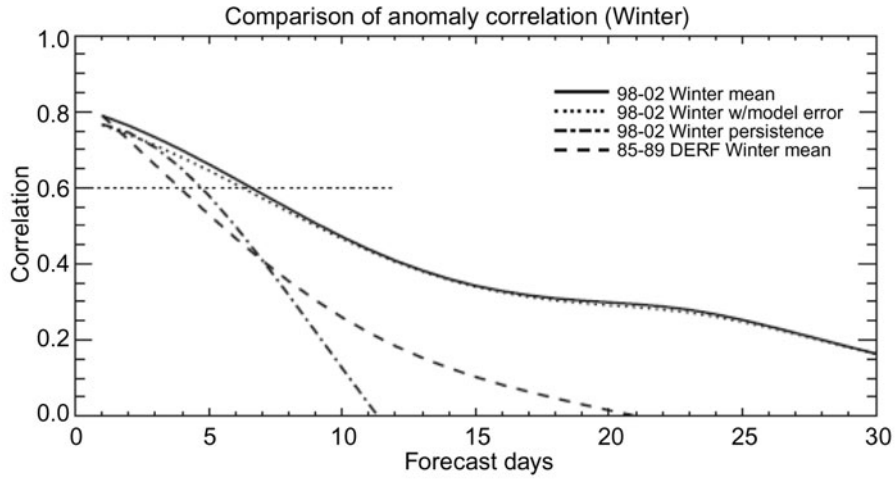

Figure 12.10. Anomaly correlation of U200 as a function of forecast lead time averaged over 20°S–20°N for 5-year winter average (thick), the case with model error retained (dotted), persistence forecast (dash-dotted), and previous (1985–1989) dynamic extended range forecast experiments (DERF; dashed) (from Seo *et al*., 2009).

forecast skill from dynamical models (Lin *et al*., 2008). Additional discussion of how this increasing model fidelity translates into the improvement of operational MJO predictions will be discussed in the next section.

In an early and entirely independent line of research, T. N. Krishnamurti produced a number of studies in the early 1990s that examined MJO forecast skill as it relates to active and break periods of the Asian summer monsoon. Underlying these studies was the importance of intraseasonal SST anomalies and the development and application of a unique and potentially promising avenue for forecasting "low-frequency modes" (as they are referred to in these studies). In the first study, Krishnamurti *et al*. (1990) laid the groundwork for the method which argues that part of the loss of forecast skill associated with low-frequency modes, such as the MJO, during a forecast comes about from the errors and evolution of high-wavenumber/frequency variability. If the forecast objective is primarily the prediction of low-frequency variability (e.g., active and break periods of the monsoon), then it is plausible to filter the initial state in order to remove all but the relevant/recent "mean" state (e.g., 45-day average conditions prior to forecast) and the low-frequency modes of interest (in this case, obtained via time filtering). Krishnamurti *et al*. argue that this will delay the "contamination of the low-frequency modes as a result of the energy exchanges from the higher frequency modes".

The above idea was tested using a T21 version of the Florida State University (FSU) global spectral model (Krishnamurti *et al*., 1990). Observed SST anomalies, filtered to include only 30 to 50-day variability (Krishnamurti *et al*., 1988) and multiplied by a factor of 3.5 to help account for the coarse vertical/boundary

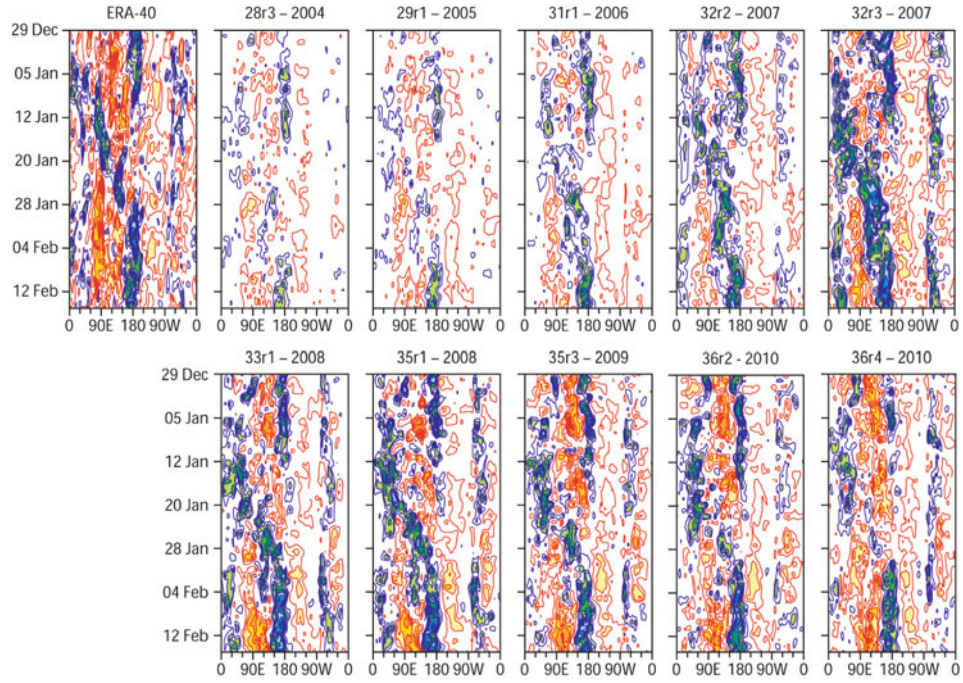

Figure 12.11. Hovmöller diagrams of averaged outgoing longwave radiation (OLR) between 10°S and 10°N from December 29, 1992 to February 15, 1993 as analyzed by ERA-40 and obtained from daily forecasts with ECMWF IFS cycles Cy28r3 (~2004) to Cy32r3 ~2010). Each forecast verifies at the 15-day lead time. Red shading denotes warm OLR anomalies (suppressed phase of the MJO) and blue shading cold anomalies (convectively active phase of the MJO). Courtesy of F. Vitart and P. Bechtold, ECMWF.

layer structure (i.e., eight total layers), were specified in addition to the mean annual cycle of SST. While the latter specification certainly provides the hindcast with information that a true forecast would not have, the results from the 270-day forecast case study performed from July 31, 1979 were still encouraging given that intraseasonal SST anomalies are not a dominant control at this timescale (Chapters 7, 10, 11). Figure 12.12 shows that the model forecast exhibited considerable skill at predicting the meridional motion of the 850 hPa trough–ridge system over the Indian Ocean and the eastward propagation of the 200 hPa divergence anomaly out to about 4 weeks. A control experiment—which included all frequencies and wavenumbers associated with the initial conditions (that the model would accommodate) and which did not include the SST anomalies—actually performed quite poorly in the first few days. In addition, it was found that when just the mean annual cycle of SST is specified, the amplitude of the low-frequency wave motion degrades considerably, thus indicating the importance of such SST anomalies in such an experiment. In Krishnamurti *et al.* (1992, 1995), analogous experiments using two select case studies were performed for low-frequency "wet and dry spells" over China and

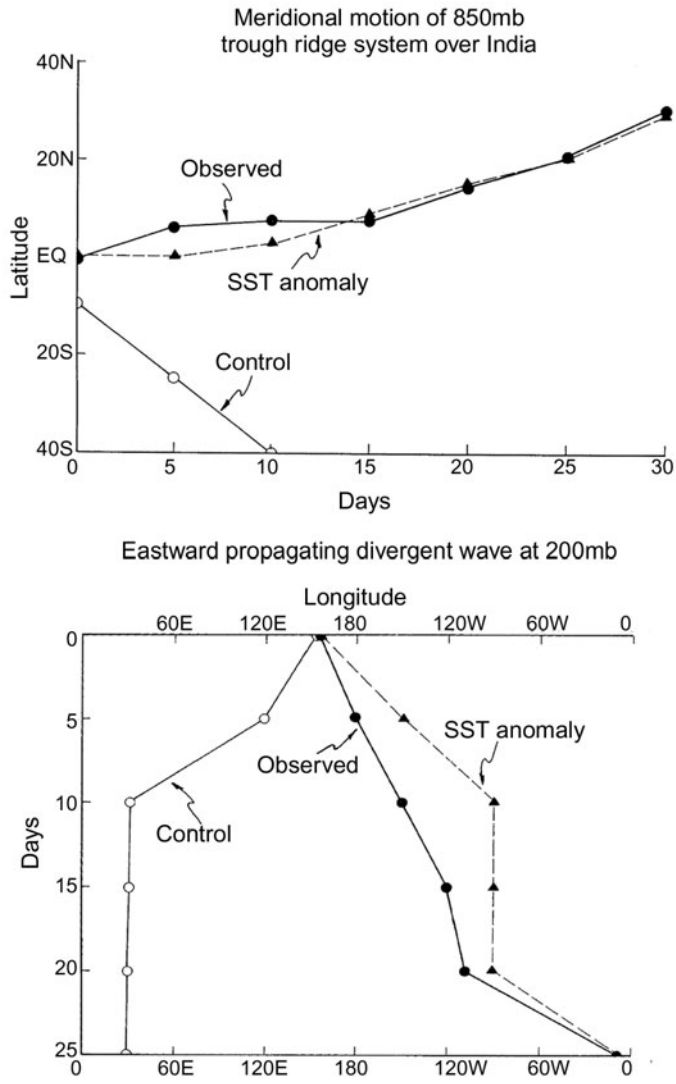

Figure 12.12. (top) A $y - t$ diagram of the monsoonal low-frequency ridge line at 850 hPa. The results are shown for observations, control experiment (no SST anomaly and complete initialized state), and the SST anomaly experiment (SST anomaly specified and initialized state includes time mean and low-frequency mode only. (bottom) Same as (top), except an $x - t$ diagram of the position of the 200 hPa divergent center. See text for details of experimental setup and dates of forecast (from Krishnamurti *et al.*, 1990).

Australia for each of their associated summer monsoons with essentially the same results as that indicated. As in the first study, the SST anomalies were found to be vital to retaining forecast skill. In both of these studies, simple empirical prediction of the SST anomalies was incorporated and found to provide much of the necessary

SST information to retain most of the long-lead forecast skill found in this suite of experiments.

Following from Krishnamurti's modeling studies discussed above, in addition to his initiating observational work in the same area (Krishnamurti *et al.*, 1988), a number of studies noted the potential importance that coupled ocean–atmosphere feedbacks may have on the initiation, propagation, and maintenance of the MJO (Chapter 7, 8, 13) (e.g., Waliser *et al.*, 1999b; Woolnough *et al.*, 2000; Fu and Wang, 2004; Zheng *et al.*, 2004). Given the progress in dynamical and coupled model improvements, recent studies have been able to more directly explore the ramifications of ocean coupling on forecast still. For example, Woolnough *et al.* (2007) perform a number of boreal winter MJO hindcast experiments with the ECMWF monthly forecast system using a number of coupling strategies and sensitivity experiments that included a full dynamical ocean model and a 1-D ocean mixed layer model. These experiments demonstrated (Figure 12.13) improvements in forecast skill arising from ocean coupling, primarily from high vertical resolution—O(1 m)—in the near surface ocean and high-frequency temporal coupling—O(hour)—each of which allowed better representation of the intraseasonal and diurnal modulations of SST. Similarly, Kim *et al.* (2010) show a modest (i.e., 1-day) improvement in hindcast skill for the boreal winter MJO when comparing an ocean–atmosphere coupled GCM with the atmosphere-only version of a GCM. For additional evidence for the importance of intraseasonal SST variability to the proper representation of the MJO in a forecasting context, see Reichler and Roads (2005), Kim *et al.* (2008), and Pegion and Kirtman (2008b).

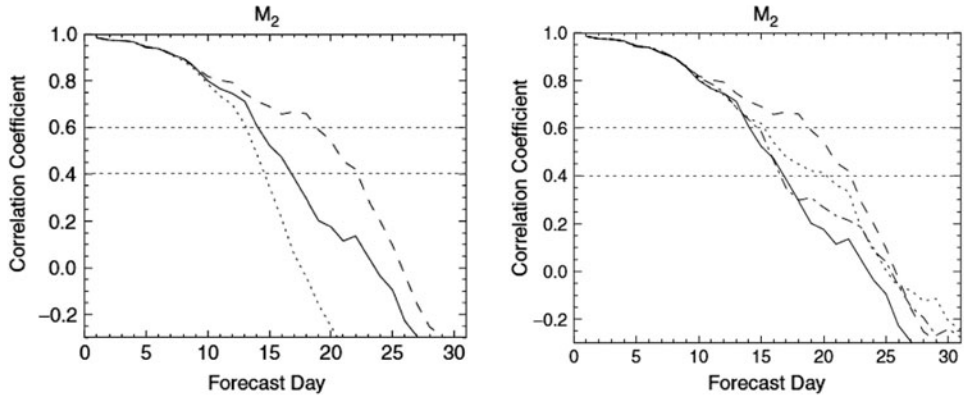

Figure 12.13. (left) Correlation of the observed M_2 MJO-combined EOF time series—similar to the Wheeler and Hendon (2004) RMM2 but using OLR, 850 hPa zonal wind, and 200 hPa velocity potential; see Chapter 6—with the ensemble mean forecast time series, based on 47 start dates for the control experiment (full coupled model; solid line), the mixed layer experiment (1 m vertical resolution non-interacting colums, dashed line), and the persisted SST experiment (dotted line). (right) Same, except for the case when the vertical resolution of the mixed layer experiment is degraded to 10 m—the same as the full coupled model (dot-dashed)—and the case where the coupling for the mixed layer experiment is done once every 24 hours (dotted) (from Woolnough *et al.*, 2007).

The studies discussed above point to the need for forecast models to not only have a proper representation of MJO anomalies via adequate resolution and realistic physical processes but also to produce an unbiased mean state so initialization errors and their subsequent evolution/adjustment do not contaminate the forecast over these relatively long lead times.

12.4 PREDICTABILITY

The previous two sections provide some indication of what the inherent predictability limit might be for the MJO. From the empirical model studies, this limit might be ascertained to be at least 2–3 weeks, depending on the variable. However, as with any empirical model, these models are limited in the totality of the weather/climate system they can predict, their ability to adapt to arbitrary conditions, and their ability to take advantage of known physical constraints. Thus, one might conclude that if dynamical models had a realistic representation of the MJO, this limit might be extended somewhat. However, the information that can be ascertained from many of the above dynamical studies is limited due to the fact that they were either based on models with poor, or less than perfect, representations of the MJO (e.g., weak amplitude, fast phase propagation) or they were based on only a few select cases. Moreover, since all the dynamical studies discussed above were verified against observations, their degradation in skill with lead time includes the component associated with the natural limit of predictability of the MJO phenomenon as well as a model's systematic bias associated with the MJO. For this reason, dynamical as well as empirical forecast skill studies—those measured against observations—might always be considered as providing plausible lower bounds to predictability (NAS, 2010).

A complimentary avenue of research for ascertaining the upper bounds of prediction skill for the MJO utilizes so-called "twin-predictability" experiments in which the model employed is presumed to be "perfect" and forecast experiments are verified against others that only differ in the initial conditions (e.g., Lorenz, 1965; Shukla, 1985). This approach was taken in two studies by Waliser *et al.* (2003b, 2003d); see also Reichler and Roads (2005). The important consideration for a study such as this is that the model provides a relatively realistic representation of the phenomenon of interest. In this case, the experiments were performed with the NASA Goddard Laboratory for Atmospheres (GLA) GCM (Kalnay *et al.*, 1983; Sud and Walker, 1992). In a number of studies, this model has been shown to exhibit a relatively realistic MJO (Slingo *et al.*, 1996; Sperber *et al.*, 1997; Waliser *et al.*, 2003a) with reasonable amplitude, propagation speed, surface flux properties, seasonal modulation, and interannual variability (Waliser *et al.*, 1999b, 2001). One of its principal deficiencies is its relatively weak variability in the equatorial Indian Ocean, a problem quite common in AGCMs (Waliser *et al.*, 2003a).

For these studies, a 10-year control simulation using specified annual cycle SSTs was performed in order to provide initial conditions from which to perform an ensemble of twin-predictability experiments. Note that this analysis was performed

separately on northern hemisphere winter MJO activity (i.e., that which typically travels eastward along the equator and the SPCZ; e.g., Figure 4.5) and northern hemisphere summer MJO activity (i.e., that which typically travels northeastward into India/South East Asia; e.g., Figure 4.10). The following discussion describes the northern hemisphere winter study (Waliser *et al.*, 2003b) but the methods and results are quite similar for the northern hemisphere summer analog (Waliser *et al.*, 2003d). Initial conditions were taken from periods of strong MJO activity identified via extended empirical orthogonal function (EOF) analysis of 30 to 90-day bandpassed tropical rainfall during the October–April season. From the above analysis, 15 cases were chosen when MJO convection was located over the Indian Ocean, maritime continent, Western Pacific Ocean, and Central Pacific Ocean, respectively, making 60 cases in total. In addition, 15 cases were selected which exhibited very little to no MJO activity. Two different sets of small random perturbations, determined in a rather ad hoc and simplistic manner, were added to these 75 initial states. Simulations were then performed for 90 days from each of these 150 perturbed initial conditions.

A measure of potential predictability was constructed based on a ratio of the signal associated with the MJO, in terms of bandpassed (30 to 90-day filtered) rainfall or 200 hPa velocity potential (VP200), and the mean square difference between sets of twin (bandpassed) forecasts. Predictability was considered useful if this ratio was greater than one, and thus if the mean square error was less than the signal associated with the MJO. The results indicate that useful predictability for this model's MJO extends out to about 20 to 30 days for VP200 and to about 10 to 15 days for rainfall (Figure 12.14). This is in contrast to the timescales of useful predictability for the model's weather, or for cases in which the MJO is absent, which is about 12 days for VP200 and 7 days for rainfall. Note that these latter two regimes are related in that, when the MJO is quiescent, the model lacks a low-frequency component that might help it retain predictability over long timescales and is in a regime where the processes and timescales of weather are the only phenomena left to give predictability. In addition to the above, the predictability measure exhibited modest dependence on the phase of the MJO, with greater predictability for the convective phase at short ($<\sim$5 days) lead times and for the suppressed phase at longer ($>\sim$15 days) lead times.

While the results from these studies are encouraging from the viewpoint of subseasonal prediction and are not entirely inconsistent with the sorts of complimentary studies mentioned above, there are a number of issues to consider that might impact the limit of predictability estimate they provide. First, the model has been shown to have too much high-frequency low-wavenumber activity (Slingo *et al.* 1996). Relative to the MJO, this variability would be considered to be unorganized errant convective activity that may erode the relatively smooth evolution of the MJO and thus diminish its predictability. Second, these simulations were carried out with fixed climatological SST values. A previous study with this model showed that coupled SSTs tend to have an enhancing and organizing influence on the MJO, making it stronger and more coherent (Waliser *et al.*, 1999b). Thus, the exclusion of SST coupling may lead to an underestimate of the predictability as well. Both of

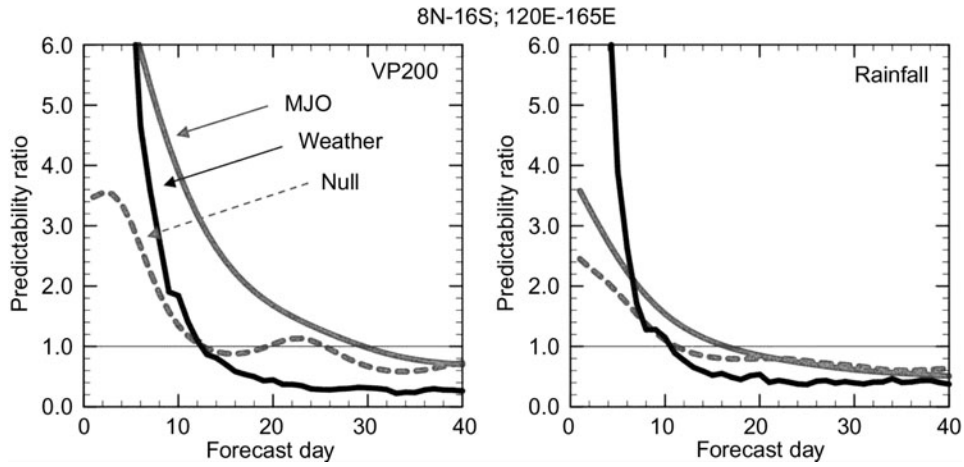

Figure 12.14. Predictability measure (defined as the ratio of the MJO "signal" and the MJO forecast error; see Waliser *et al*. 2003b) vs. lead time based on 120 northern hemisphere winter MJO twin-predictability forecast cases for VP200 (left) and rainfall (right) from the NASA/GLA model for 120 active/strong MJO cases (solid black), 30 weak/null MJO cases (dashed gray), and for unfiltered "weather" variations (using the 120 active MJO cases; solid gray) for the region 8°N–16°S and 120°E–165°E.

these issues would appear to have a direct relation to the methods and results associated with the Krishnamurti *et al*. studies discussed in the previous section.

There are also a number of aspects associated with the model and/or analysis to suggest that the above results might overestimate the predictability of the MJO. The first is that the model's coarse resolution and inherent reduced degrees of freedom relative to the true atmosphere may limit the amount of small-scale variability that would typically erode large timescale and spacescale variability. However, it is important to note in this regard that the low-order EOFs of intraseasonally filtered model output typically do not capture as much variability as analogous EOFs of observed quantities. Thus, the model's MJO itself still has room to be more robust and coherent which would tend to enhance predictability. In addition to model shortcomings, the simple manner in which perturbations were added to the initial conditions may also lead to an overestimate of the predictability. The perturbation structure and the size of the perturbations may be too conservative and not adequately represent the type of initial condition error that would be found in an operational context. However, even if that is the case, it would seem that adequate size "initial" errors would occur in the forecast in a matter of a day or two and, thus, one would expect this aspect to overestimate the predictability by only a couple days, if at all.

In order to address some of the uncertainties mentioned above, an analogous study for boreal summer conditions using the ECHAM AGCM has been undertaken (Liess *et al*., 2005). The modeling and analysis framework is similar to that described

above with two important exceptions. First, rather than select a large number of events (i.e., ~15-20) for each of the four phases of the boreal summer ISO (i.e., convection in India, the maritime continent, the Western Pacific, and the Central Pacific) and performing only a few (i.e., two) perturbation experiments with each, this study has selected three relatively strong events and performs a larger ensemble of forecasts for each of the four phases (i.e., 15). In addition, rather than use somewhat simply determined perturbations, this study uses the breeding method (Toth and Kalnay, 1993; Cai *et al.*, 2003). The left panels of Figure 12.15 show the precipitation (upper) and 200 hPa velocity potential (right) from the individual members of one of the 15-member ensembles (i.e., one phase of one event). Evident is

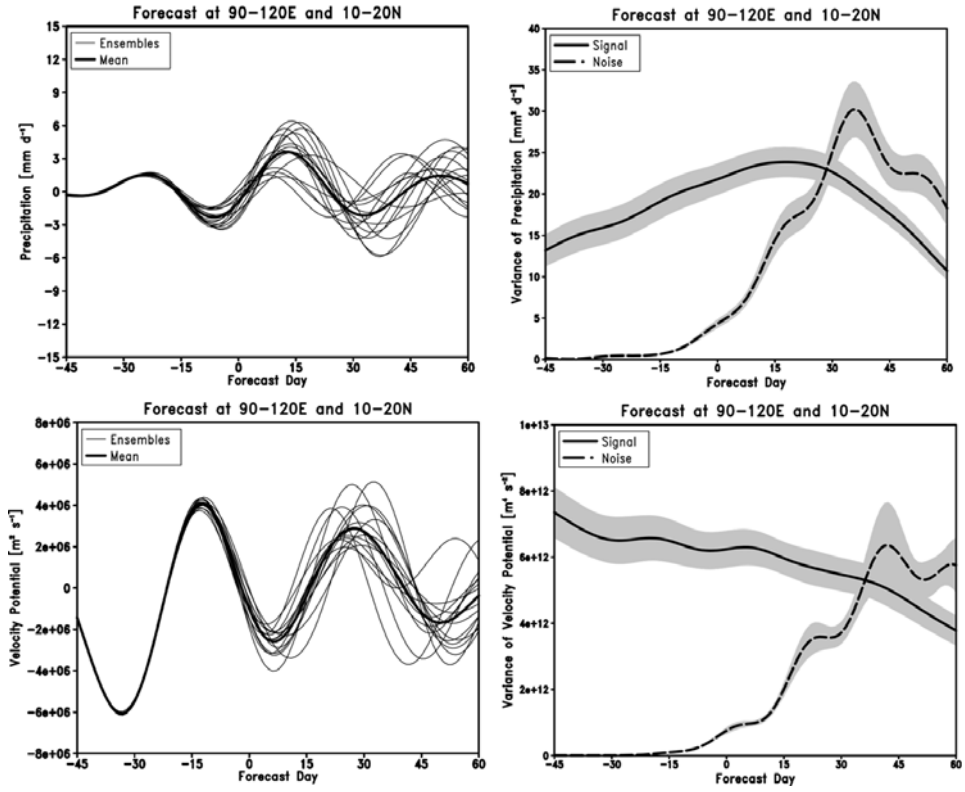

Figure 12.15. (left) Fifteen-member ensemble forecast of a boreal summer ISO event, in a given phase of the event (out of four defined phases), using the ECHAM5 AGCM. Data are taken from 90°E–120°E and 10°N–20°N and are 30 to 90-day filtered precipitation (upper) and 200 hPa velocity potential (lower) anomalies. (right) The signal-to-noise ratios (using the methods in Waliser *et al.*, 2003b; see discussion in Section 12.4) for precipitation (upper) and 200 hPa velocity potential (lower) anomalies when combining 15-member ensembles from three different model ISO events and including all four phases of each event (i.e., $N = 168$) (from Liess *et al.*, 2005).

the expected spread of the forecasts with lead time. The right panels of Figure 12.15 quantify this spread in terms of a "signal-to-noise" ratio, defined as in the Waliser *et al*. (2003b) study described above. These results suggest that the boreal summer ISO exhibits dynamical predictability with lead times potentially up to and beyond 30 days. These lead times are at least as large, if not larger, than those found in the Waliser *et al*. studies highlighted above. However, it should be noted that the events analyzed here are the strongest three events in a 10-year model simulation record, and those above were based on both strong and moderate size events which could account for the difference.

Consistent with the demonstration of improved MJO forecast skill with the incorporation of ocean coupling are findings that such coupling enhances measures of the potential predictability limits of the MJO. Using the twin-predictability experimental approach using the University of Hawaii coupled model (ECHAM4 and an intermediate ocean model), Fu *et al*. (2007) demonstrate that ocean coupling extended the estimate of useful predictability for boreal summer ISV from about 2 weeks to 3 weeks when ocean coupling was included. Similarly, using the NCEP Coupled Forecast System (CFS) and a twin-predictability framework, Pegion *et al*. (2008a) demonstrate increased values (by several days) of the upper bound of MJO predictability through the inclusion of coupling. In their results, upper limits were as great as 4 weeks for intraseasonal filtered precipitation and OLR and 5 weeks and longer for dynamical quantities. While the above twin-predictability experiments can, at best, be considered plausible estimates for the upper bound on MJO forecast due to their inherent deficiencies of representing the full complexity of the MJO, nonetheless, they strongly suggest substantial benefit is still to be gained in the area of MJO forecasting.

12.5 REAL TIME FORECASTS

Based on the qualified success of some of the MJO empirical and dynamical hindcast studies discussed above, a number of forecast schemes have been implemented in real time. The first of these was associated with the Wheeler and Weickmann (2001) scheme described in Section 12.2.[4] This scheme has been operational for about 9 years and provides forecasts out to about 2–3 weeks lead time for not only the MJO but other coherent modes of tropical variability (e.g., Kelvin, mixed Rossby, gravity). A second, somewhat related effort, and already alluded to above and discussed in Chapter 6, utilizes lag regression and the all season Real-time Multivariate MJO (RMM) index (Wheeler and Hendon, 2004).[5] Skill scores for model MJO forecasts in terms of spatial correlation are about 0.5 for 10-day forecasts (Jiang *et al*., 2008b). In addition, Charles Jones and his colleagues have produced real time predictions of the MJO for about 8 years.[6] The scheme is

[4] *http://cawcr.gov.au/staff/mwheeler/maproom/OLR_modes/*
[5] *http://cawcr.gov.au/staff/mwheeler/maproom/RMM/*
[6] *http://www.icess.ucsb.edu/asr/mjo_forecasts.htm*

described in Jones *et al*. (2004a) and is based on bandpassed (20–90 days) OLR and zonal winds at 850 hPa and 200 hPa. Upon filtering, a combined EOF of the three fields is computed and then the principle components (PCs) are separated into summer and winter. A seasonally dependent regression model is then formed at every given lead between 1 and 10 pentads. The model utilizes the first five principle components (PCs) from the EOF analysis and the five most recent values of the PCs. The model is found to exhibit winter and summer skill scores comparable with the other empirical models described above and in Section 12.2.

In quite a different approach, stemming from a somewhat different and/or more comprehensive objective, Matt Newman and his colleagues developed and implemented a real time forecasting scheme[7] that has applicability to the MJO based on what is often referred to as the Linear Inverse Model (i.e. LIM, Winkler *et al*., 2001; Newman *et al*., 2003). The LIM is based on NCEP/NCAR reanalysis data (Kalnay *et al*., 1996) that have had the annual cycle removed, been smoothed with a 7-day running mean filter, gridded to T21 spatial resolution, and been reduced by EOF decomposition. The specific fields used include global 250 hPa and 750 hPa streamfunctions and tropical column-integrated diabatic heating. For the northern hemisphere winter (summer) model, the first 30 (30) streamfunction and 7 (20) diabatic heating EOFs are used. In this model, historical data are used to define the relationship between a given state (i.e., a weekly average) and conditions 1 week later, with the process being iterated to produce multiweek forecasts). The advantage of the model is that it includes both tropical (in terms of diabatic heating—hence a prediction of the MJO) and extratropical (in terms of streamfunction) forecasts. In this way, the interaction between them can be more readily examined and diagnosed. For tropical forecasts of diabatic heating, the LIM slightly outperforms an older research version of the NCEP MRF model at lead times of 2 weeks, for both northern hemisphere summer and winter, particularly in regions where the MJO is most strongly affecting the diabatic heating field (Figure 12.16).

Van den Dool and Qin (1996) develop a generalized wave-propagating forecasting technique that they refer to as "empirical wave propagation" (EWP). EWP is a "phase-shifting" technique that allows one, in the diagnostic step, to determine the amplitude-weighted average climatological phase speed of anomaly waves (e.g., equatorial MJO), where the waves are represented as either zonal or spherical harmonics. The diagnostic step results in a table of phase speed (or 1-day displacement) for waves in the anomaly field as a function of zonal wavenumber, calendar month, and latitude, based on a specified (model or observed) dataset. Its first application was to midlatitude Rossby waves as diagnosed from 500 hPa geopotential height fields (Qin and van den Dool, 1996). EWP has been applied to the MJO (van den Dool and Saha, 2002) and implemented in real time.[8] Based on analysis of 5 years of 200 hPa velocity potential data for all seasons, the diagnostic step produces a wavenumber 1 disturbance that propagates at about 5 m/s with an amplitude of about 5×10^6 m^2/s. In the forecast step, the anomaly field under initial

[7] *http://www.esrl.noaa.gov/psd/forecasts/clim/*
[8] *http://www.cpc.noaa.gov/products/precip/CWlink/MJO/mjo.shtml*

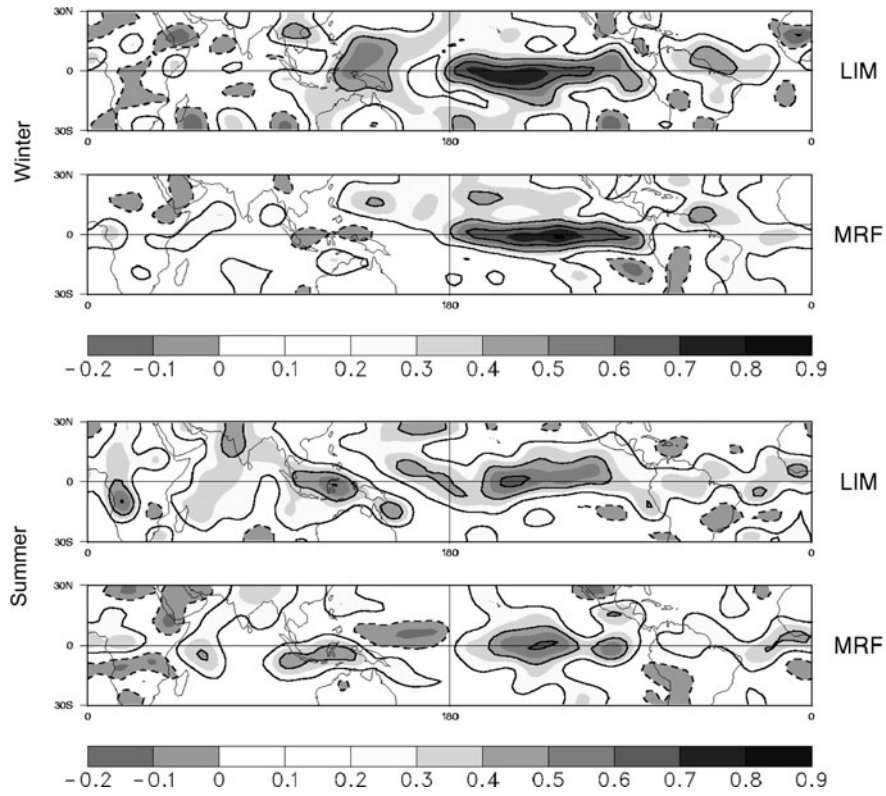

Figure 12.16. Anomaly correlations between forecast and verification column-integrated diabatic heating using the LIM forecast model (see Winkler *et al*., 2001 and Newman *et al*., 2003) and a research version of the NCEP MRF model (i.e., MRF98) for both the northern hemisphere winter (top) and summer (bottom). Forecasts were made for June–August periods for the years 1979–2000. Solid (dashed) contours indicate positive (negative) values.

conditions is projected onto sines and cosines or spherical harmonics, then each wave component is propagated over the longitude displacement provided by the table and then transformed back to physical space. This technique is particularly well suited for empirically forecasting large-scale upper-level anomalies associated with the MJO.

It is almost a certainty that the MJO's greatest impact based on sheer numbers of people and the severity of losses in agriculture and economics is associated with the Asian summer monsoon. Motivated by this, Webster and Hoyos (2004) developed an empirical model for predicting Indian district rainfall and Brahmaputra and Ganges river discharge into Bangladesh on 20 to 25-day timescales. The empirical model is physically based with predictors drawn from the composite structure of monsoon intraseasonal variability (e.g., Indian Ocean SST, precipitation over India, upper-level easterly jet, surface winds over the Arabian Sea). In essence, the model is

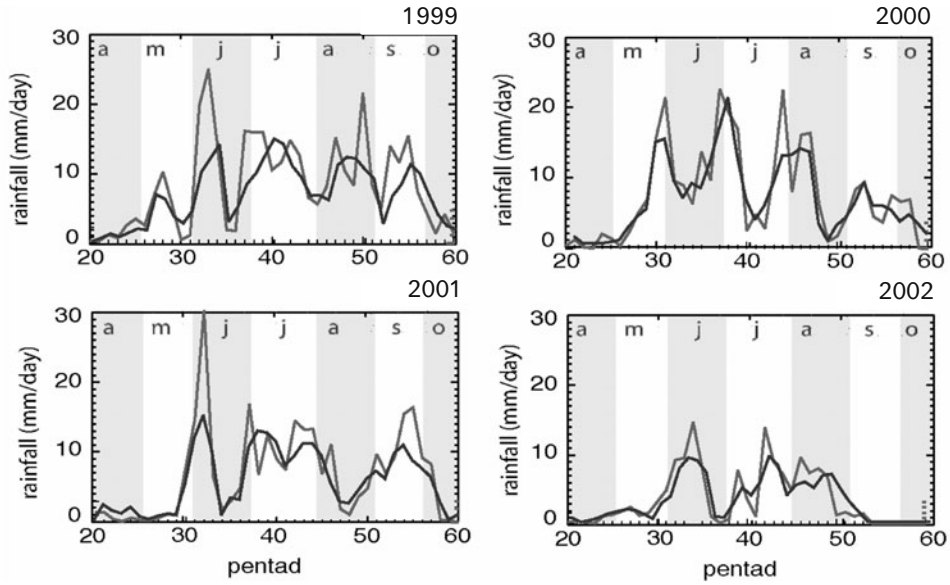

Figure 12.17. Gray lines indicate forecasts at 20-day (four pentads) lead times based on the empirical model of Webster and Hoyas (2003) of precipitation averaged over the Ganges Valley for the summers of 1999–2002. Black lines indicate observations. Gray and white background denotes months.

Bayesian and uses a wavelet technique to separate significant spectral bands. The model has been used to predict rainfall in hindcast mode. For example, Figure 12.17 shows observed and 20-day forecasts of 5-day average rainfall amounts over the Ganges Valley for the summers of 1999–2002. From these hindcasts, it appears the model is very adept at capturing seasonal, interannual, and subseasonal rainfall variability. The model was also used for the first time during the summer of 2003 in real time operational mode in the Climate Forecast Application in Bangladesh project as part of a three-tier forecasting system wherein seasonal outlooks are given every month for the ensuing 6 months, a 20 to 25-day forecast is prepared every 5 days and a 1 to 5-day forecast is prepared daily. At the time of writing this chapter for the First Edition, these forecasts of precipitation and river discharge had been integrated into the Bangladesh forecasting system on an experimental basis.

Based on the sorts of activities and preliminary successes described above, along with the need to take a more systematic approach to diagnosing problems in dynamical forecasts of the MJO, an experimental MJO prediction program was formulated and implemented (Waliser *et al.*, 2006). The formal components of this program arose from two parallel streams of activity. The first was the occurrence of the subseasonal workshop mentioned in the introduction (Schubert *et al.*, 2002) and the recognition of the importance of the MJO regarding the potential skill to be had from subseasonal predictions. The second stream of activity ensued from the

priorities and recommendations of the U.S. CLIVAR Asian–Australian Monsoon Working Group. In their 2001 research prospectus (AAMWG/U.S.-CLIVAR *et al.*, 2001) as well as in subsequent deliberations with the U.S. CLIVAR Scientific Steering Committee, recommendations were made to develop an experimental prediction program due to the significant influence that the MJO has on the character and evolution of Asian–Australian monsoons. These streams of activity led to an informal (email) discussion among a number of MJO forecast enthusiasts during the summer and fall of 2002 that helped to formulate the framework for such a program and to the identification of a sponsor that could provide scientific and technical support as well as serve as the data host/server (i.e., NOAA's Climate Diagnostics Center). Invitations to participate in the program were subsequently sent out to a number of empirical modelers and international forecasting agencies and an implementation meeting was held in June 2003 (Waliser *et al.*, 2003c). Over the subsequent 2 years, the experimental system was implemented and it remained quasi-operational until about 2009 (Waliser *et al.*, 2006).

From the growing recognition of the MJO's importance to subseasonal and seamless prediction problems, along with the success of the community efforts described above, the U.S. Climate Variability and Predictability (CLIVAR) program supported the formation of a (limited lifetime) MJO working group[9] (MJOWG) in early 2006 (Sperber and Waliser, 2008a). The objectives of the MJOWG included the development (Waliser *et al.*, 2009) and application (Kim *et al.*, 2009) of model diagnostics for the MJO and fostering a strategy to expand and formalize the experimental MJO prediction effort discussed above. The latter primarily centered around the development and adoption of a *uniform* forecast metric for the MJO akin to, for example, the pattern correlation of the 500 hPa geopotential heights for midlatitude weather forecasts or the Niño-3.4 SST index utilized for ENSO forecasts. The motivation for having such a metric is that it allows for a more quantitative assessment of forecast quality, the ability to track model forecast quality over time, the capability to measure potential model improvements relative to the MJO, and the means to develop a multimodel ensemble forecast of the MJO. Once the MJO forecast metric was selected (an adaptation of Wheeler and Hendon, 2004), an invitation letter from the MJOWG and the Working Group on Numerical Experimentation (WGNE) was distributed to operational centers around the world outlining the project and requesting participation in the activity, with the U.S. Climate Prediction Center (CPC) of NCEP/NOAA serving as a host (Gottschalck *et al.*, 2010).

MJO forecast metric activity has been an unqualified success. At least 10 operational centers are participating with at least 20 streams of forecasts being operationally sent to CPC/NOAA, where the forecasts get aggregated, displayed, and disseminated in a uniform manner in real time. The forecast streams include both single deterministic forecasts as well as a number of ensembles (up to 51 in one case), with forecast lead times ranging between 7 and 45 days. Figure 12.18 shows an

[9] See *www.usclivar.org/Organization/MJO_WG.html*. The MJO Working Group also received support from International CLIVAR, *www.clivar.org*

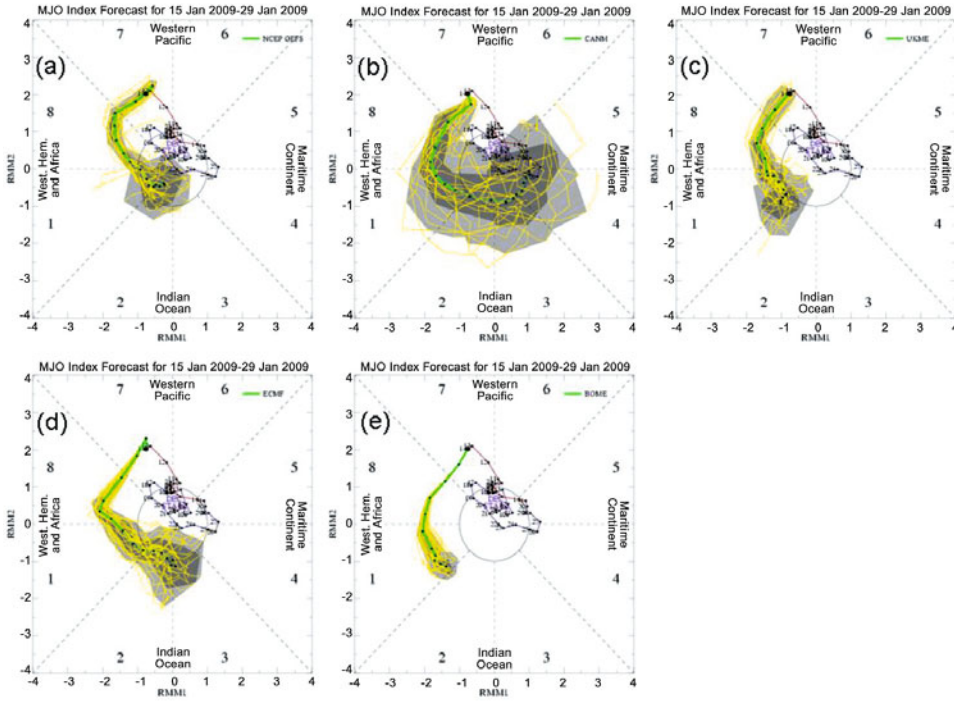

Figure 12.18. RMM phase space plots for five different ensemble forecasting systems: (a) NCPE, (b) CANM, (c) UKME, (d) ECMF, and (e) BOME (10 days). RMM1 and RMM2 are the *x*-axis and *y*-axis, respectively. The numbers within each octant (from 1 to 8) are the defined MJO phase and the words on each side of the diagram describe the approximate location of MJO-associated convection along the equator. The red and blue lines show the last 40 days of observations (red—January 2009, blue—December 2008). The green line is the model ensemble mean (thick—first 7 days, thin—second 8 days) and yellow lines are individual ensemble member forecasts. The light (dark) gray shading indicates that 90% (50%) of the members fell within the highlighted region, respectively. The larger dot is the last observation point (from Gottschalck *et al.*, 2010).

example of the type of information that has been developed and is presented on the activity's website.[10] Specifically, the figure shows forecasts from five of the activity's participants initialized during an active MJO. The lines and shading on each panel indicate the observed state of the MJO up to the forecast period, and the evolution, average, and spread of the ensemble members. For this case, most of the models consistently forecast a continuation of the active state for several days, albeit with considerable differences in the ensemble spreads.

A number of outstanding issues still need to be addressed with regard to improving the utility of this activity. These include the development of multimodel ensemble strategies, issues concerning how to deal with and/or remove the lead-

[10] *http://www.cpc.noaa.gov/products/precip/CWlink/MJO/CLIVAR/clivar_wh.shtml*

dependent background climatology for a given modeling system (particularly in cases when this is not routinely available upon revision to the operational model/models), and the development, posting, and use of more validation measures. At the communitywide level, the continuation of this effort is now being shepherded by the MJOWG's follow-on entity, the WCRP-WWRP/THORPEX and Year of Tropical Convection[11] MJO Task Force.[12] The specific objectives for the MJOTF are to develop process-oriented MJO model diagnostics, continue to foster the above forecasting activity including a focus on boreal summer ISV, and coordinate experimentation and activities across national and international agencies and programmatic activities (Hendon *et al.*, 2011). In addition to the above CLIVAR-supported effort, Dr. M. Matsueda and Dr. T. Nakazawa have developed a similar multimodel operational MJO prediction resource from the THORPEX Interactive Grand Global Ensemble (TIGGE) operational database of 15-day forecasts.[13]

As a means of illustrating the vast strides made since the writing of this chapter for the First Edition, Figure 12.19 illustrates *present day* forecast still from three different operational forecast systems—each of which contributes to the above two community forecasting activities. These include the ECMWF Integrated Forecasting System, the Predictive Ocean–Atmosphere Model for Australia (POAMA), and the NCEP Coupled Forecast System (CFS). For the ECMWF and NCEP cases, there are comparisons between present day and previous versions of their forecasting systems. The overall message from these plots is that, as a community, we have developed MJO forecast based on dynamical prediction models with skill that extends out to at least 2 weeks and in some cases 3 weeks. This is a remarkable achievement, as this capability was simply not evident nor seemingly on the near term horizon during the writing of the first edition.

12.6 DISCUSSION

The review of the studies examined in this chapter was meant to summarize the historical developments associated with MJO forecasting and provide a brief description of the current state of affairs regarding MJO prediction capability and what is known of its inherent limits of predictability. Overall, there is enough evidence to suggest that MJO prediction can be considerable with great optimism due to the fact that our capabilities, on the one hand, have grown considerably in the last few years and are demonstrating skill—yet, on the other hand, seem far from saturating their potential. This operational capability, and its expected improvement and expansion, is providing a unique and important link between our more mature areas of fore-

[11] *www.ucar.edu/yotc* and Waliser, D. E. and M. Moncrieff (2008) *The Year of Tropical Convection (YOTC) Science Plan: A Joint WCRP–WWRP/THORPEX International Initiative* (WMO/TD No. 1452, WCRP-130, WWRP/THORPEX No 9). WMO, Geneva, Switzerland.

[12] *www.ucar.edu/yotc/mjo.html*

[13] *tparc.mri-jma.go.jp/TIGGE/tigge_MJO.html*

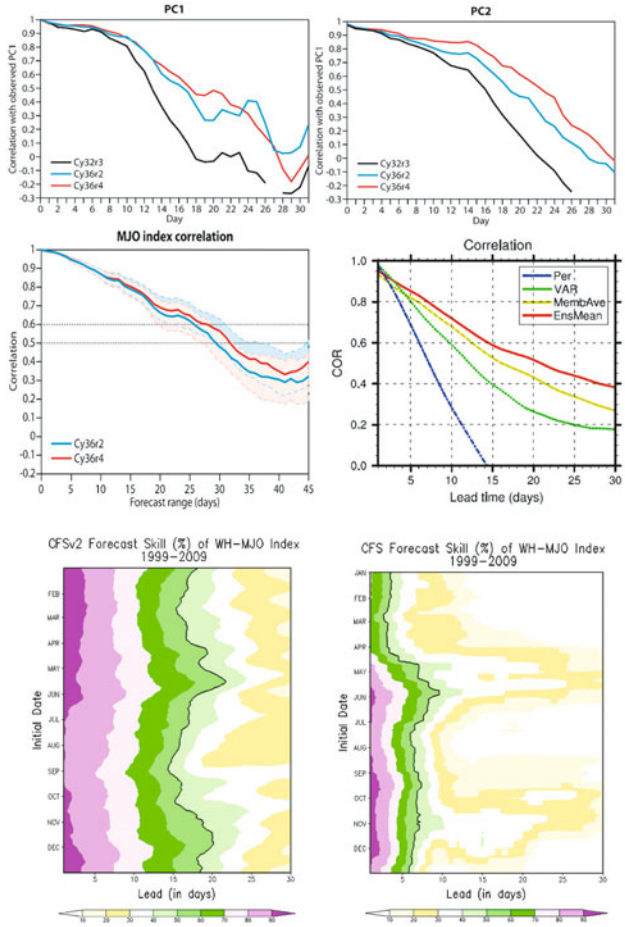

Figure 12.19. (upper and middle left panels) The top panels show the correlation of the observed RMM1 and RMM2 time series with the ensemble mean ECMWF IFS Cy36r4 (~2010) forecasts, based on 48 start dates (daily from December 15, 1992 to January 31, 1993). The middle left panel shows the bivariate correlation between ensemble mean forecast and observations, based on 80 dates (February 1, May 1, August 1, and November 1, 1989–2008) (pers. commun., Frederic Vitart of ECMWF). (middle right panel) The bivariate anomaly correlation (BAC) for RMM1 and RMM2 for the POAMA seasonal forecast model, as a function of forecast lead time for all hindcasts initialized from 1980 to 2006. Displayed in (a) and (b) are scores for the ensemble mean (red curve), an empirical forecast scheme (green curve), the persistence forecast (blue curve), and the average value of the correlation of the 10 individual ensemble members (light green curve). All curves are smoothed with a three-point running mean before plotting (Rashid *et al.*, 2010). (lower panels) The NCEP Climate Forecast System (Version 1 and Version 2) skill in predicting the MJO for period 1999–2009, as expressed by the BAC × 100 for RMM1 and RMM2. On the left is CFSv2 and on the right is CFSv1. Both predictions have a systematic error correction as described by Zhang and van den Dool (2011). The black lines indicate BAC = 0.5 (pers. commun., Steve Lord (NCEP/NOAA) and Saha *et al.*, 2010).

casting (namely, weather and ENSO). As identified in this chapter and book, and in many other studies and reports (NAS, 2010), a remaining challenge to achieving full potential is still to develop more robust and realistic representations of the MJO in our weather and climate forecast models (Chapter 11). As these model capabilities are developed and implemented, we not only have a means to improve predictions of low-frequency weather variations in the tropics that are directly impacted by the MJO, including the onsets and breaks of the Asian and Australian summer monsoons (e.g., Yasunari, 1980; Lau and Chan, 1986; Hendon and Liebmann, 1990a, b, see also Chapters 2, 3, and 5), but we will also likely improve forecasts associated with a number of processes remote to the MJO (see Chapters 4 and 13). These include *wintertime midlatitude circulation anomalies* (e.g., Weickmann, 1983; Liebmann and Hartmann, 1984; Weickmann *et al*., 1985; Lau and Phillips, 1986; Ferranti *et al*., 1990; Higgins and Schubert, 1996; Higgins and Mo, 1997; Jones *et al*., 2004b; Vecchi and Bond, 2004), *summertime precipitation variability over Mexico and South America as well as to austral wintertime circulation anomalies over the Pacific–South American sector* (e.g., Nogues-Paegle and Mo, 1997; Mo and Higgins, 1998a; Jones and Schemm, 2000; Mo, 2000a; Paegle *et al*., 2000; Jiang and Waliser, 2009), *extreme events in rainfall variability along the western United States* (e.g., Mo and Higgins, 1998b, c; Higgins *et al*., 2000; Jones, 2000; Whitaker and Weickmann, 2001), *the development of tropical storms/hurricanes in both the Atlantic and Pacific sectors* (Maloney and Hartmann, 2000a, b; Mo, 2000b; Higgins and Shi, 2001; Vitart *et al*., 2010), *and a number of socially relevant quantities related to biology and chemistry* (Waliser *et al*., 2005; Tian *et al*., 2007, 2008; Wong and Dessler, 2007; Li *et al*., 2010).

From the discussion in this chapter, as well as that in Chapters 7, 10, 11, and 13, a number of areas of research and development present themselves. This includes a more complete understanding of the role that coupling to the ocean plays in maintaining and, in particular, forecasting the MJO (e.g., Flatau *et al*., 1997; Wang and Xie, 1998; Waliser *et al*., 1999b; Kemball-Cook *et al*., 2002; Woolnough *et al*., 2007; Pegion and Kirtman, 2008a; Fu *et al*., 2006). For example, a number of studies have indicated an error in the phase relation between the convection and SST anomalies associated with the MJO in GCM simulations using specified SSTs, whereas coupled simulations tend to reproduce the observed phase relationship (Wu *et al*., 2002; Fu *et al*., 2003; Zheng *et al*., 2004). These sorts of studies not only imply the importance of incorporating MJO-related SST anomalies but also necessitate they be coupled (i.e., forecast) as well. Issues still to be better understood and implemented include the representation of the diurnally varying mixed layer (Woolnough *et al*., 2007), the impact and representation of the maritime continent, and the role of and interactions with freshwater and barrier layers. In addition, there has still been very little research done on model initialization/data assimilation issues in terms of what are the critical criteria to meet in order to adequately initialize the state of the MJO (e.g., Liess *et al*., 2005; Vintzileos and Behringer, 2008; Fu *et al*., 2009) or the best strategies for constructing multimodel ensembles. Related to this are issues regarding the importance of the basic state of the forecast model and how an incorrect basic state might negatively impact the maintenance and propagation of the MJO (Inness *et al*., 2003;

Sperber *et al.*, 2003; Liess and Bengtsson, 2004; Liess *et al.*, 2004). In addition to the above, there is clearly a need for additional dynamical predictability studies of the MJO using other GCMs as well as sensitivity studies to test the effects of SST coupling and ENSO state, the impacts from/on midlatitude variability, and the influence of the size and type of initial condition perturbations and definition of predictability.

While the signs are positive for having and exploiting useful MJO/ISV forecasts, the above list is still a tall order of challenges to overcome. However, at the time of this writing there are a number of programmatic efforts in place to facilitate addressing these questions and challenges. These include the WCRP–WWRP MJO Task Force mentioned above that will continue work to develop and apply model diagnostics to achieve better model fidelity of the MJO, as well as develop and foster the use of new and more comprehensive MJO forecast metrics and forecasting frameworks and applications. In addition, the joint WCRP and WWRP/THORPEX research program, Year of Tropical Convection (YOTC),[14] includes the MJO as a high-priority focus area. This program brings together a rich set of high-resolution analysis products, satellite data resources, high-resolution global to limited area process/cloud system–resolving models, and a focus period approach to improve our understanding and forecast representations of tropical convection. An additional activity that will lead to advancing understanding regarding present day prediction skill, predictability estimates, and MME forecast strategies is the Intraseasonal Variability Hindcast Experiment (ISVHE)—the first coordinated, multimodel hindcast experiment explicitly tailored for ISV and the MJO.[15] Finally, the DYNAMO/CINDY2011 field campaign(s)[16] will be conducted in the Indian Ocean in late 2011 through early 2012. These international collaborations are primarily designed to advance our understanding of MJO dynamics and initiation processes necessary for improving MJO simulation and prediction.

12.7 APPENDIX

Excerpt from John von Neumann (1955):

> "It seems quite plausible from general experience that in any mathematical problem it is easiest to determine the solution for shorter periods, over which the extrapolation parameter is small. The next most difficult problem to solve is that of determining the asymptotic conditions—that is, the conditions that exist over periods for which the extrapolation parameter is very large, say near infinity.

[14] *www.ucar.edu/yotc* and Waliser, D. E. and M. Moncrieff (2008) *The Year of Tropical Convection (YOTC) Science Plan: A Joint WCRP–WWRP/THORPEX International Initiative* (WMO/TD No. 1452, WCRP-130, WWRP/THORPEX No 9). WMO, Geneva, Switzerland.

[15] *www.ucar.edu/yotc/iso.html*

[16] *http://www.eol.ucar.edu/projects/dynamo/* and *http://www.jamstec.go.jp/iorgc/cindy/*

Finally, the most difficult is the intermediate range problem, for which the extrapolation parameter is neither very small nor very large. In this case the neglect of either extreme is forbidden. On the basis of these considerations, it follows that there is a perfectly logical approach to any computational treatment of the problem of weather prediction. The approach is to try first short-range forecasts, then long-range forecasts of those properties of the circulation that can perpetuate themselves over arbitrarily long periods of time (other things being equal), and only finally to attempt forecast for medium–long time periods which are too long to treat by simple hydrodynamic theory and too short to treat by the general principles of equilibrium theory''.

12.8 ACKNOWLEDGMENTS

The first edition of this work was supported by the National Science Foundation (ATM-0094416), the National Oceanographic and Atmospheric Administration (NA16GP2021), and the National Atmospheric and Aeronautics Administration (NAG5-11033). Work on the Second Edition was carried out on behalf of the Jet Propulsion Laboratory, California Institute of Technology, under a contract with the National Aeronautics and Space Administration.

12.9 REFERENCES

AAMWG/U.S.-CLIVAR, W. K. M. Lau, S. Hastenrath, B. Kirtman, T. N. Krishnamurti, R. Lukas, J. McCreary, J. Shukla, J. Shuttleworth, and D. Waliser (2001) *Asian–Australian Monsoon Research Prospectus*. Asian-Australian Monsoon Working Group, Location of publisher, 46 pp.

Agudelo, P. A., C. D. Hoyos, P. J. Webster, and J. A. Curry (2009) Application of a serial extended forecast experiment using the ECMWF model to interpret the predictive skill of tropical intraseasonal variability. *Climate Dynamics*, **32**(6), 855–872.

Barnston, A. G., M. H. Glantz, and Y. X. He (1999) Predictive skill of statistical and dynamical climate models in SST forecasts during the 1997–98 El Niño episode and the 1998 La Niña onset. *Bull. Amer. Meteorol. Society*, **80**(2), 217–243.

Bechtold, P., M. Kohler, T. Jung, F. Doblas-Reyes, M. Leutbecher, M. J. Rodwell, F. Vitart, and G. Balsamo (2008) Advances in simulating atmospheric variability with the ECMWF model: From synoptic to decadal time-scales. *Quart. J. Roy. Meteorol. Soc.*, **134**(634), 1337–1351.

Bougeault, P., Z. Toth, C. Bishop, B. Brown, D. Burridge, D. H. Chen, B. Ebert, M. Fuentes, T. M. Hamill, K. Mylne *et al.* (2010) The THORPEX Interactive Grand Global Ensemble. *Bull. Amer. Meteorol. Society*, **91**(8), 1059–1072.

Brunet, G., M. Shapiro, B. Hoskins, M. Moncrieff, R. Dole, G. N. Kiladis, B. Kirtman, A. Lorenc, B. Mills, R. Morss *et al.* (2010) Collaboration of the weather and climate communities to advance subseasonal-to-seasonal prediction. *Bull. Amer. Meteorol. Society*, **91**(10), 1397–1406.

Cai, M., E. Kalnay, and Z. Toth (2003) Bred vectors of the Zebiak–Cane model and their potential application to ENSO predictions. *J. Climate*, **16**, 40–56.

Cane, M. A., S. E. Zebiak, and S. C. Dolan (1986) Experimental forecasts of El Niño. *Nature*, **321**(6073), 827–832.

Chen, T. C. and J. C. Alpert (1990) Systematic errors in the annual and intraseasonal variations of the planetary-scale divergent circulation in NMC medium-range forecasts. *J. Atmos. Sci.*, **118**, 2607–2623.

ECMWF (2004) *ECMWF/CLIVAR Workshop on Simulation and Prediction of Intra-Seasonal Variability with Emphasis on the MJO, November 3–6, 2003*. ECMWF, Reading, U.K.

Ferranti, L., T. N. Palmer, F. Molteni, and K. Klinker (1990) Tropical–extratropical interaction associated with the 30–60-day oscillation and its impact on medium and extended range prediction. *J. Atmos. Sci.*, **47**, 2177–2199.

Flatau, M., P. J. Flatau, P. Phoebus, and P. P. Niiler (1997) The feedback between equatorial convection and local radiative and evaporative processes: The implications for intraseasonal oscillations. *J. Atmos. Sci.*, **54**(19), 2373–2386.

Froude, L. S. R. (2010) TIGGE: Comparison of the prediction of northern hemisphere extratropical cyclones by different ensemble prediction systems. *Weather and Forecasting*, **25**(3), 819–836.

Fu, X. and B. Wang (2004) Differences of boreal-summer intraseasonal oscillations simulated in an atmosphere–ocean coupled model and an atmosphere-only model. *J. Climate*, **17**(6), 1263–1271, doi: 10.1175/1520-0442(2004).

Fu, X., B. Wang, T. Li, and J. P. McCreary (2003) Coupling between northward-propagating, intraseasonal oscillations and sea surface temperature in the Indian Ocean. *J. Atmos. Sci.*, **60**(15), 1733–1753.

Fu, X., B. Wang, D. E. Waliser, and T. Li (2006) Impact of atmosphere–ocean coupling on the predictability of monsoon intraseasonal oscillations (MISO). *J. Atmos. Sci.* **64**, 157–174.

Fu, X., B. Wang, D. E. Waliser, and L. Tao (2007) Impact of atmosphere–ocean coupling on the predictability of monsoon intraseasonal oscillations. *J. Atmos. Sci.*, **64**(1), 157–174.

Fu, X., B. Wang, Q. Bao, P. Liu, and J. Y. Lee (2009) Impacts of initial conditions on monsoon intraseasonal forecasting. *Geophys. Res. Lett.*, **36**.

Gelaro, R., R. H. Langland, S. Pellerin, and R. Todling (2010) The THORPEX Observation Impact Intercomparison Experiment. *Mon. Wea. Rev.*, **138**(11), 4009–4025.

Goswami, B. N. and P. Xavier (2003) Potential predictability and extended range prediction of Indian summer monsoon breaks. *Geophys. Res. Lett.*, **30**(18), 1966, doi: 1910.1029/2003GL1017,1810.

Gottschalck, J., M. Wheeler, K. Weickmann, F. Vitart, N. Savage, H. Lin, H. Hendon, D. Waliser, K. Sperber, M. Nakagawa *et al.* (2010) A framework for assessing operational Madden–Julian Oscillation forecasts: A CLIVAR MJO Working Group project. *Bull. Amer. Meteorol. Society*, **91**(9), 1247–1258.

Graham, N. E. and T. P. Barnett (1995) ENSO and ENSO-related predictability, 2: Northern-hemisphere 700-mb height predictions based on a hybrid coupled ENSO model. *J. Climate*, **8**(3), 544–549.

Hazeleger, W., C. Severijns, T. Semmler, S. Stefanescu, S. Yang, X. Wang, K. Wyser, E. Dutra, J. M. Baldasano, R. Bintanja *et al.* (2010) EC-Earth: A seamless Earth-system prediction approach in action. *Bull. Amer. Meteorol. Society*, **91**(10), 1357–1363.

Hendon, H. H. and B. Liebmann (1990a) A composite study of onset of the Australian summer monsoon. *J. Atmos. Sci.*, **47**(18), 2227–2240.

Hendon, H. H. and B. Liebmann (1990b) The intraseasonal (30–50 day) oscillation of the Australian summer monsoon. *J. Atmos. Sci.*, **47**(24), 2909–2923.

Hendon, H. H., C. D. Zhang, and J. D. Glick (1999) Interannual variation of the Madden–Julian oscillation during austral summer. *J. Climate*, **12**(8), 2538–2550.

Hendon, H. H., B. Liebmann, M. Newman, J. D. Glick, and J. E. Schemm (2000) Medium-range forecast errors associated with active episodes of the Madden–Julian oscillation. *Mon. Wea. Rev.*, **128**(1), 69–86.

Hendon, H., K. Sperber, D. Waliser, and M. Wheeler (2011) Modelling monsoon intra-seasonal variability: From theory to operational forecasting. A meeting summary for *The Workshop on Modelling Monsoon Intraseasonal Variability, June 15–18, 2010, APEC Climate Center, Busan, Republic of Korea*. Submitted to *Bull. Amer. Meteorol. Society*. Available at *http://www.ucar.edu/yotc/documents/mjo/KoreaWkshp.html*

Higgins, R. W. and K. C. Mo (1997) Persistent North Pacific circulation anomalies and the tropical intraseasonal oscillation. *J. Climate*, **10**(2), 223–244.

Higgins, R. W. and S. D. Schubert (1996) Simulations of persistent North Pacific circulation anomalies and interhemispheric teleconnections. *J. Atmos. Sci.*, **53**(1), 188–207.

Higgins, R. W. and W. Shi (2001) Intercomparison of the principal modes of interannual and intraseasonal variability of the North American Monsoon System. *J. Climate*, **14**(3), 403–417.

Higgins, R. W., J. K. E. Schemm, W. Shi, and A. Leetmaa (2000). Extreme precipitation events in the western United States related to tropical forcing. *J. Climate*, **13**(4), 793–820.

Hurrell, J., G. A. Meehl, D. Bader, T. L. Delworth, B. Kirtman, and B. Wielicki (2009) A unified modeling approach to climate system prediction. *Bull. Amer. Meteorol. Society*, **90**(12), 1819–1832.

Inness, P. M., J. M. Slingo, E. Guilyardi, and J. Cole (2003) Simulation of the Madden-Julian oscillation in a coupled general circulation model, Part II: The role of the basic state. *J. Climate*, **16**(3), 365–382.

Jiang, X. and D. E. Waliser (2009) Two dominant subseasonal variability modes of the eastern Pacific ITCZ. *Geophys. Res. Lett.*, **36**.

Jiang, X., D. E. Waliser, M. Wheeler, C. Jones, M.-I. Lee, and S. Schubert (2008) Assessing the skill of an all-season statistical forecast model for the Madden-Julian Oscillation. *Mon. Wea. Rev.*, **136**, 1940–1956.

Jones, C. (2000) Occurrence of extreme precipitation events in California and relationships with the Madden–Julian oscillation. *J. Climate*, **13**(20), 3576–3587.

Jones, C. and J. K. E. Schemm (2000) The influence of intraseasonal variations on medium- to extended-range weather forecasts over South America. *Mon. Wea. Rev.*, **128**(2), 486–494.

Jones, C., D. E. Waliser, J. K. E. Schemm, and W. K. M. Lau (2000) Prediction skill of the Madden and Julian Oscillation in dynamical extended range forecasts. *Climate Dynamics*, **16**(4), 273–289.

Jones, C., L. M. V. Carvalho, R. W. Higgins, D. E. Waliser, and J.-K. E. Schemm (2004a) A statistical forecast model of tropical intraseasonal convective anomalies. *J. Climate*, **17**, 2078–2095.

Jones, C., D. E. Waliser, K. M. Lau, and W. Stern (2004b) Global occurrences of extreme precipitation and the Madden–Julian oscillation: Observations and predictability. *J. Climate*, **17**(23), 4575–4589.

Kalnay, E., R. Balgovind, W. Chao, D. Edelmann, J. Pfaendtner, L. Takacs, and K. Takano (1983) *Documentation of the GLAS Fourth Order General Circulation Model* (Vol. 1, NASA Tech. Memo. No. 86064). NASA Goddard Space Flight Center, Greenbelt, MD.

Kalnay, E., M. Kanamitsu, R. Kistler, W. Collins, D. Deaven, L. Gandin, M. Iredell, S. Saha, G. White, J. Woollen *et al.* (1996) The NCEP/NCAR 40-year reanalysis project. *Bull. Amer. Meteorol. Society*, **77**(3), 437–471.

Kang, I.-S. and H.-M. Kim (2010) Assessment of MJO predictability for boreal winter with various statistical and dynamical models. *J. Climate*, **23**(9), 2368–2378.

Kemball-Cook, S., B. Wang, and X. Fu (2002) Simulation of the ISO in the ECHAM4 model: The impact of coupling with an ocean model. *J. Atmos. Sci.*, **59**(9), 1433–1453.

Keppenne, C. L. and M. Ghil (1992) Adaptive filtering and prediction of the Southern Oscillation Index. *J. Geophys. Res.-Atmospheres*, **97**(D18), 20449–20454.

Kim, D., K. Sperber, W. Stern, D. Waliser, I. S. Kang, E. Maloney, W. Wang, K. Weickmann, J. Benedict, M. Khairoutdinov *et al.* (2009) Application of MJO simulation diagnostics to climate models. *J. Climate*, **22**(23), 6413–6436.

Kim, H. M., C. D. Hoyos, P. J. Webster, and I. S. Kang (2008) Sensitivity of MJO simulation and predictability to sea surface temperature variability. *J. Climate*, **21**(20), 5304–5317.

Kim, H. M., C. D. Hoyos, P. J. Webster, and I. S. Kang (2010) Ocean–atmosphere coupling and the boreal winter MJO. *Climate Dynamics*, **35**(5), 771–784.

Kirtman, B. and A. Pirani (2009) The state of the art of seasonal prediction outcomes and recommendations from the First World Climate Research Program Workshop on Seasonal Prediction. *Bull. Amer. Meteorol. Society*, **90**(4), 455–458.

Kirtman, B. P., J. Shukla, B. H. Huang, Z. X. Zhu, and E. K. Schneider (1997) Multiseasonal predictions with a coupled tropical ocean–global atmosphere system. *Mon. Wea. Rev.*, **125**(5), 789–808.

Kousky, V. E. and M. T. Kayano (1993) Real-time monitoring of intraseasonal oscillations. Paper presented at *18th Annual Climate Diagnostics Workshop, November 1–5, Boulder, CO*, pp. 66–69.

Krishnamurti, T. N., D. K. Oosterhof, and A. V. Mehta (1988) Air sea interaction on the time scale of 30 to 50 days. *J. Atmos. Sci.*, **45**(8), 1304–1322.

Krishnamurti, T. N., M. Subramaniam, D. K. Oosterhof, and G. Daughenbaugh (1990) Predictability of low-frequency modes. *Meteorol. Atmos. Phys.*, **44**, 63–83.

Krishnamurti, T. N., M. Subramaniam, G. Daughenbaugh, D. Oosterhof, and J. H. Xue (1992) One-month forecasts of wet and dry spells of the monsoon. *Mon. Wea. Rev.*, **120**(7), 1191–1223.

Krishnamurti, T. N., S. O. Han, and V. Misra (1995) Prediction of the dry and wet spell of the Australian monsoon. *Int. J. Climatol.*, **15**(7), 753–771.

Lau, K. M. and P. H. Chan (1986) Aspects of the 40–50 day oscillation during the northern summer as inferred from outgoing longwave radiation. *Mon. Wea. Rev.*, **114**(7), 1354–1367.

Lau, K. M. and F. C. Chang (1992) Tropical intraseasonal oscillation and its prediction by the NMC operational model. *J. Climate*, **5**(12), 1365–1378.

Lau, K. M. and T. J. Phillips (1986) Coherent fluctuations of extratropical geopotential height and tropical convection in intraseasonal time scales. *J. Atmos. Sci.*, **43**(11), 1164–1181.

Li, K. F., B. J. Tian, D. E. Waliser, and Y. L. Yung (2010) Tropical mid-tropospheric CO_2 variability driven by the Madden–Julian oscillation. *Proceedings of the National Academy of Sciences U.S.A.*, **107**(45), 19171–19175.

Liebmann, B. and D. L. Hartmann (1984) An observational study of tropical midlatitude interaction on intraseasonal time scales during winter. *J. Atmos. Sci.*, **41**(23), 3333–3350.

Liess, S. and L. Bengtsson (2004) The intraseasonal oscillation in ECHAM4, Part II: Sensitivity studies. *Climate Dynamics*, **22**, 671–688.

Liess, S., L. Bengtsson, and K. Arpe (2004). The intraseasonal oscillation in ECHAM4, Part I: Coupled to a comprehensive ocean model. *Climate Dynamics*, **22**, 653–688.

Liess, S., D. E. Waliser, and S. D. Schubert (2005) Predictability studies of the intraseasonal oscillation with the ECHAM5 GCM. *J. Atmos. Sci.*, **62**(9), 3320–3336.

Lin, H., G. Brunet, and J. Derome (2008) Forecast skill of the Madden-Julian Oscillation in two Canadian atmospheric models. *Mon. Wea. Rev.*, **136**(11), 4130–4149.

Lo, F. and H. H. Hendon (2000) Empirical extended-range prediction of the Madden-Julian oscillation. *Mon. Wea. Rev.*, **128**(7), 2528–2543.

Lorenz, E. N. (1965) A study of the predictability of a 28-variable atmospheric model. *Tellus*, **17**, 321–333.

Lorenz, E. N. (1982) Atmospheric predictability experiments with a large numerical model. *Tellus*, **34**(6), 505–513.

Maloney, E. D. and D. L. Hartmann (2000a) Modulation of hurricane activity in the Gulf of Mexico by the Madden-Julian oscillation. *Science*, **287**(5460), 2002–2004.

Maloney, E. D. and D. L. Hartmann (2000b) Modulation of eastern North Pacific hurricanes by the Madden-Julian oscillation. *J. Climate*, **13**(9), 1451–1460.

Martin, G. M., S. F. Milton, C. A. Senior, M. E. Brooks, S. Ineson, T. Reichler, and J. Kim (2010) Analysis and reduction of systematic errors through a seamless approach to modeling weather and climate. *J. Climate*, **23**(22), 5933–5957.

Matsuno, T. (1966) Quasi-geostrophic motions in the equatorial area. *J. Meteorol. Soc. Japan*, **44**, 25–43.

Mo, K. C. (2000a) Intraseasonal modulation of summer precipitation over North America. *Mon. Wea. Rev.*, **128**(5), 1490–1505.

Mo, K. C. (2000b) The association between intraseasonal oscillations and tropical storms in the Atlantic basin. *Mon. Wea. Rev.*, **128**(12), 4097–4107.

Mo, K. C. (2001) Adaptive filtering and prediction of intraseasonal oscillations. *Mon. Wea. Rev.*, **129**(4), 802–817.

Mo, K. C. and R. W. Higgins (1998a) The Pacific–South American modes and tropical convection during the Southern Hemisphere winter. *Mon. Wea. Rev.*, **126**(6), 1581–1596.

Mo, K. C. and R. W. Higgins (1998b) Tropical influences on California precipitation. *J. Climate*, **11**(3), 412–430.

Mo, K. C. and R. W. Higgins (1998c) Tropical convection and precipitation regimes in the western United States. *J. Climate*, **11**(9), 2404–2423.

Moncrieff, M. W., M. Shapiro, J. Slingo, and F. Molteni (2007) Collaborative research at the intersection of weather and climate. *WMO Bull.*, **56**, 204–211.

NAS (2010) *Assessment of Intraseasonal to Interannual Climate Prediction and Predictability*. Board on Atmospheric Sciences and Climate, The National Academies Press, Washington, D.C. Available at *http://www.nap.edu*

Newman, M., P. D. Sardeshmukh, C. R. Winkler, and J. S. Whitaker (2003) A study of subseasonal predictability. *Mon. Wea. Rev.*, **131**, 1715–1732.

Nobre, C., G. P. Brasseur, M. A. Shapiro, M. Lahsen, G. Brunet, A. J. Busalacchi, K. Hibbard, S. Seitzinger, K. Noone, and J. P. Ometto (2010) Addressing the complexity of the Earth system. *Bull. Amer. Meteorol. Society*, **91**(10), 1389–1396.

Nogues-Paegle, J. and K. C. Mo (1997) Alternating wet and dry conditions over South America during summer. *Mon. Wea. Rev.*, **125**(2), 279–291.

Paegle, J. N., L. A. Byerle, and K. C. Mo (2000) Intraseasonal modulation of South American summer precipitation. *Mon. Wea. Rev.*, **128**(3), 837–850.

Palmer, T. N. (1993) Extended-range atmospheric prediction and the Lorenz model. *Bull. Amer. Meteorol. Society*, **74**(1), 49–65.

Pegion, K. and B. P. Kirtman (2008a) The impact of air–sea interactions on the predictability of the tropical intraseasonal oscillation. *J. Climate*, **21**(22), 5870–5886.

Pegion, K. and B. P. Kirtman (2008b) The impact of air–sea interactions on the simulation of tropical intraseasonal variability. *J. Climate*, **21**(24), 6616–6635.

Qin, J. and H. M. van den Dool (1996) Simple extensions of an NWP model. *Mon. Wea. Rev.*, **124**(2), 277–287.

Rashid, H. A., H. H. Hendon, M. C. Wheeler, and O. Alves (2010) Prediction of the Madden–Julian Oscillation with the POAMA dynamical prediction system. *Climate Dynamics*, **36**(3/4), 649–661, doi: 10.1007/s00382-010-0754-x.

Reichler, T. and J. O. Roads (2005) Long-range predictability in the tropics, Part II: 30–60-day variability. *J. Climate*, **18**(5), 634–650.

Saha, S., S. Moorthi, H-L. Pan, X. Wu, J. Wang, S. Nadiga, P. Tripp, R. Kistler, J. Woollen, D. Behringer *et al.* (2010) The NCEP Climate Forecast System Reanalysis. *Bull. Amer. Meteorol. Society*, **91**, 1015–1057, doi: 10.1175/2010BAMS3001.1.

Salby, M. L. and H. H. Hendon (1994) Intraseasonal behavior of clouds, temperature, and motion in the tropics. *J. Atmos. Sci.*, **51**(15), 2207–2224.

Schemm, J. E., H. van den Dool, and S. Saha (1996) A multi-year DERF experiment at NCEP. Paper presented at *11th Conference on Numerical Weather Prediction, August 19–13, Norfolk, VA*.

Schubert, S., R. Dole, H. van den Dool, M. Suarez, and D. Waliser (2002) *Proceedings of a Workshop on Prospects for Improved Forecasts of Weather and Short-term Climate Variability on Subseasonal (2 week to 2 month) Time Scales, April 16–18, Mitchellville, MD* (NASA/TM 2002-104606, vol. 23(XX), 171 pp.). NASA, Washington, D.C.

Seo, K. H., J. K. E. Schemm, C. Jones, and S. Moorthi (2005) Forecast skill of the tropical intraseasonal oscillation in the NCEP GFS dynamical extended range forecasts. *Climate Dynamics*, **25**(2/3), 265–284.

Seo, K. H., W. Q. Wang, J. Gottschalck, Q. Zhang, J. K. E. Schemm, W. R. Higgins, and A. Kumar (2009) Evaluation of MJO forecast skill from several statistical and dynamical forecast models. *J. Climate*, **22**(9), 2372–2388.

Shapiro, M., J. Shukla, G. Brunet, C. Nobre, M. Beland, R. Dole, K. Trenberth, R. Anthes, G. Asrar, L. Barrie *et al.* (2010). An Earth-system prediction initiative for the twenty-first century. *Bull. Amer. Meteorol. Society*, **91**(10), 1377–1388.

Shukla, J. (1985) Predictability. *Adv. Geophys.*, **28B**, 87–122.

Shukla, J., R. Hagedorn, M. Miller, T. N. Palmer, B. Hoskins, J. Kinter, J. Marotzke, and J. Slingo (2009) Strategies: Revolution in climate prediction is both necessary and possible—A declaration at the World Modelling Summit for Climate Prediction. *Bull. Amer. Meteorol. Society*, **90**(2), 175–178.

Shukla, J., T. N. Palmer, R. Hagedorn, B. Hoskins, J. Kinter, J. Marotzke, M. Miller, and J. Slingo (2010) Toward a new generation of world climate research and computing facilities. *Bull. Amer. Meteorol. Society*, **91**(10), 1407–1412.

Slingo, J. M., K. R. Sperber, J. S. Boyle, J. P. Ceron, M. Dix, B. Dugas, W. Ebisuzaki, J. Fyfe, D. Gregory, J. F. Gueremy *et al.* (1996) Intraseasonal oscillations in 15 atmospheric general circulation models: Results from an AMIP diagnostic subproject. *Climate Dynamics*, **12**(5), 325–357.

Sperber, K. R. and D. Waliser (2008a) New approaches to understanding, simulating, and forecasting the Madden–Julian Oscillation. *Bull. Amer. Meteorol. Society*, 1917–1920, doi: 10.1175/2008BAMS2700.1.

Sperber, K. R. and D. E. Waliser (2008b) New approaches to understanding, simulating, and forecasting the Madden–Julian Oscillation. *Bull. Amer. Meteorol. Society*, **89**(12), 1917–1920.

Sperber, K. R., J. M. Slingo, P. M. Inness, and W. K. M. Lau (1997) On the maintenance and initiation of the intraseasonal oscillation in the NCEP/NCAR reanalysis and in the GLA and UKMO AMIP simulations. *Climate Dynamics*, **13**(11), 769–795.

Sperber, K. R., J. M. Slingo, P. M. Inness, S. Gualdi, W. Li, P. J. Gleckler, and C. Doutriaux (2003) The Madden-Julian Oscillation in GCMs. In: *Research Activities in Atmospheric and Oceanic Modelling* (Report No. 33, WMO/TD-No. 1161). World Meteorological Organization, Geneva, p. 09-01.

Sud, Y. C. and G. K. Walker (1992) A review of recent research on improvement of physical parameterizations in the GLA GCM. In: D. R. Sikka and S. S. Singh (Eds.), *Physical Processes in Atmospheric Models*. Wiley Eastern, New Delhi, pp. 422–479.

Thompson, P. D. (1957) Uncertainty of initial state as a factor in the predictability of large scale atmospheric flow patterns. *Tellus*, **9**(3), 275–295.

Tian, B., Y. L. Yung, D. E. Waliser, T. Tyranowski, L. Kuai, E. J. Fetzer, and F. W. Irion (2007) Intraseasonal variations of the tropical total ozone and their connection to the Madden–Julian Oscillation. *Geophys. Res. Lett.*, **34**, L08704, doi: 08710.01029/02007GL029471.

Tian, B. J., D. E. Waliser, R. A. Kahn, Q. Li, Y. L. Yung, T. Tyranowski, I. V. Geogdzhayev, M. I. Mishchenko, O. Torres, and A. Smirnov (2008) Does the Madden-Julian Oscillation influence aerosol variability? *J. Geophys. Res.*, **113**, D12215, doi: 10.1029/2007JD009372.

Toth, Z. and E. Kalnay (1993) Ensemble forecasting at NMC: The generation of perturbations. *Bull. Amer. Meteorol. Society*, **74**, 2330–2371.

van den Dool, H. M. (1994) Long-range weather forecasts through numerical and empirical-methods. *Dyn. Atmos. Oceans*, 20(3), 247–270.

van den Dool, H. M. and J. Qin (1996) An efficient and accurate method of continuous time interpolation of large-scale atmospheric fields. *Mon. Wea. Rev.*, **124**, 964–971.

van den Dool, H. M. and S. Saha (2002) Analysis of propagating modes in the tropics in dhort AMIP runs. Paper presented at *AMIPII Workshop, Toulouse, France, November 12–15*. World Meteorological Organization, Geneva.

Vautard, R. and M. Ghil (1989) Singular spectrum analysis in nonlinear dynamics, with applications to paleoclimatic time-series. *Physica D*, **35**(3), 395–424.

Vecchi, G. A. and N. A. Bond (2004) The Madden-Julian Oscillation (MJO) and northern high latitude wintertime surface air temperatures. *Geophys. Res. Lett.*, **31**(4).

Vintzileos, A. and D. Behringer (2008) On the importance of atmospheric and oceanic initial conditions for forecasting the MJO. Paper presented at *Fall AGU Meeting, San Francisco*. American Geophysical Union, Washington, D.C.

Vitart, F., A. Leroy, and M. C. Wheeler (2010) A comparison of dynamical and statistical predictions of weekly tropical cyclone activity in the southern hemisphere. *Mon. Wea. Rev.*, **138**(9), 3671–3682.

von Neumann, J. (1955) Some remarks on the problem of forecasting climate fluctuations. Paper presented at *Dynamics of Climate: The Proceedings of a Conference on the Application of Numerical Integration Techniques to the Problem of the General Circulation*. Pergamon Press, Oxford, U.K. (published 1960).

von Storch, H. and J. Xu (1990) Principal oscillation pattern analysis of the 30- to 60-day oscillation in the tropical troposphere. *Climate Dynamics*, **4**, 175–190.

Waliser, D. E. and M. Moncrieff (2008) *The Year of Tropical Convection (YOTC) Science Plan: A Joint WCRP–WWRP/THORPEX International Initiative* (WMO/TD No. 1452, WCRP-130, WWRP/THORPEX No 9). World Meteorological Organization, Geneva.

Waliser, D. E., C. Jones, J. K. E. Schemm, and N. E. Graham (1999a) A statistical extended-range tropical forecast model based on the slow evolution of the Madden–Julian oscillation. *J. Climate*, **12**(7), 1918–1939.

Waliser, D. E., K. M. Lau, and J. H. Kim (1999b) The influence of coupled sea surface temperatures on the Madden–Julian oscillation: A model perturbation experiment. *J. Atmos. Sci.*, **56**(3), 333–358.

Waliser, D., Z. Zhang, K. M. Lau, and J. H. Kim (2001) Interannual sea surface temperature variability and the predictability of tropical intraseasonal variability. *J. Atmos. Sci.*, **58**, 2595–2614.

Waliser, D. E., K. Jin, I. S. Kang, W. F. Stern, S. D. Schubert, M. L. C. Wu, K. M. Lau, M. I. Lee, V. Krishnamurthy, A. Kitoh *et al.* (2003a) AGCM simulations of intraseasonal variability associated with the Asian summer monsoon. *Climate Dynamics*, **21**(5/6), 423–446.

Waliser, D. E., K. M. Lau, W. Stern, and C. Jones (2003b) Potential predictability of the Madden–Julian Oscillation. *Bull. Amer. Meteorol. Society*, **84**(1), 33–50.

Waliser, D. E., S. Schubert, A. Kumar, K. Weickmann, and R. Dole (2003c) Paper title. Paper presented at *Proceedings of a Workshop on Modeling, Simulation and Forecasting of Subseasonal Variability, June 4–5, College Park, MD* (NASA/TM 2003-104606, vol. 25). NASA, Washington, D.C., p. 67.

Waliser, D. E., W. Stern, S. Schubert, and K. M. Lau (2003d) Dynamic predictability of intraseasonal variability associated with the Asian summer monsoon. *Quart. J. Roy. Meteorol. Soc.*, **129**, 2897–2925.

Waliser, D. E., R. Murtugudde, P. Strutton, and J. L. Li (2005) Subseasonal organization of ocean chlorophyll: Prospects for prediction based on the Madden–Julian Oscillation. *Geophys. Res. Lett.*, **32**(23).

Waliser, D., K. Weickmann, R. Dole, S. Schubert, O. Alves, C. Jones, M. Newman, H. L. Pan, A. Roubicek, S. Saha, C. Smith, H. van den Dool, F. Vitart, M. Wheeler, and J. Whitaker (2006) The experimental MJO prediction project. *Bull. Amer. Meteorol. Society*, **87**(4), 425–431.

Waliser, D., K. Sperber, H. Hendon, D. Kim, M. Wheeler, K. Weickmann, C. Zhang, L. Donner, J. Gottschalck, W. Higgins *et al.* (2009) MJO simulation diagnostics. *J. Climate*, **22**(11), 3006–3030.

Wang, B. and X. S. Xie (1998) Coupled modes of the warm pool climate system, Part 1: The role of air–sea interaction in maintaining Madden–Julian oscillation. *J. Climate*, **11**(8), 2116–2135.

Webster, P. J. and C. D. Hoyos (2004) Prediction of monsoon rainfall and river discharge on 15–30-day time scales. *Bull. Amer. Meteorol. Society*, **85**(11), 1745–1765.

Weickmann, K. M. (1983) Intraseasonal circulation and outgoing longwave radiation modes during northern hemisphere winter. *Mon. Wea. Rev.*, **111**(9), 1838–1858.

Weickmann, K. M., G. R. Lussky, and J. E. Kutzbach (1985) Intraseasonal (30–60 day) fluctuations of outgoing longwave radiation and 250-mb stream-function during northern winter. *Mon. Wea. Rev.*, **113**(6), 941–961.

Wheeler, M. C. and H. H. Hendon (2004) An all-season real-time multivariate MJO index: Development of an index for monitoring and prediction. *Mon. Wea. Rev.*, **132**(8), 1917–1932.

Wheeler, M. and G. N. Kiladis (1999) Convectively coupled equatorial waves: Analysis of clouds and temperature in the wavenumber–frequency domain. *J. Atmos. Sci.*, **56**(3), 374–399.

Wheeler, M. and K. M. Weickmann (2001) Real-time monitoring and prediction of modes of coherent synoptic to intraseasonal tropical variability. *Mon. Wea. Rev.*, **129**, 2677–2694.

Whitaker, J. S. and K. M. Weickmann (2001) Subseasonal variations of tropical convection and week-2 prediction of wintertime western North American rainfall. *J. Climate*, **14**(15), 3279–3288.

Winkler, C. R., M. Newman, and P. D. Sardeshmukh (2001) A linear model of wintertime low-frequency variability, Part I: Formulation and forecast skill. *J. Climate*, **14**, 4474–4494.

Wong, S. and A. E. Dessler (2007) Regulation of H_2O and CO in tropical tropopause layer by the Madden–Julian Oscillation. *J. Geophys. Res.-Atmospheres*, **112**, D14305, doi: 14310.11029/12006JD007940.

Woolnough, S. J., J. M. Slingo, and B. J. Hoskins (2000) The relationship between convection and sea surface temperature on intraseasonal timescales. *J. Climate*, **13**(12), 2086–2104.

Woolnough, S. J., F. Vitart, and M. A. Balmaseda (2007) The role of the ocean in the Madden–Julian Oscillation: Implications for MJO prediction. *Quart. J. Roy. Meteorol. Soc.*, **133**(622), 117–128.

Wu, M. L. C., S. Schubert, I. S. Kang, and D. E. Waliser (2002) Forced and free intra-seasonal variability over the South Asian monsoon region simulated by 10 AGCMs. *J. Climate*, **15**, 2862–2880.

Yasunari, T. (1980) A quasi-stationary appearance of the 30–40 day period in the cloudiness fluctuations during the summer monsoon over India. *J. Meteorol. Soc. Japan*, **59**, 336–354.

Zhang, Q. and H. M. van den Dool (2011) Relative merit of model improvement versus availability of retrospective forecasts: The case of CFS MJO prediction. *Geophys. Res. Lett.*, submitted.

Zheng, Y., D. E. Waliser, W. F. Stern, and C. Jones (2004) The role of coupled sea surface temperatures in the simulation of the tropical intraseasonal oscillation. *J. Climate*, **17**, 4109–4134.

13

Africa and West Asia

Mathew Barlow

13.1 OVERVIEW

Several studies, which are reviewed in the following sections, have identified a Madden–Julian Oscillation (MJO) influence on precipitation in both Africa and West Asia, consistent with the maximum of MJO tropical convection in the adjacent Indian Ocean basin (e.g., Wang and Rui, 1990). In Africa, as a result of the complexity of precipitation seasonality, the existence of multiple pathways for MJO influence, and data limitations, previous studies have tended to focus regionally on several distinct areas: the West Africa monsoon region, the highlands and coastal regions of eastern Africa, and Southern Africa, which are shown schematically in Figure 13.1. In western Asia, the largest influence appears to be in the southwestern part of the region, which is also shown in Figure 13.1. This identification of areas of primary influence should be regarded as still somewhat provisional and will likely be subject to further refinement and possible expansion.

For context, an estimate of the MJO influence on convection for individual seasons is shown in Figure 13.2. The estimate is calculated by compositing normalized daily outgoing longwave radiation (OLR) anomalies by phase of the MJO for each season, taking the absolute value, and then averaging over all composites. Such an estimate provides a general overview, but does not account for lagged relationships and is limited by the indirect relationship between OLR and convection; some direct analysis of station precipitation data is presented in Section 13.4. The Wheeler and Hendon (2004) index is used to define the daily MJO phase. A boreal cold season signal is well defined over southwestern Asia and eastern Africa, with somewhat patchy and more diffuse influence over the rest of Africa. The lack of exact correspondence between the OLR-based estimate in Figure 13.2 and the regions in Figure 13.1 is likely due to several factors, including the imperfect relationship between OLR and precipitation, data scarcity problems that have limited

W. K. M. Lau and D. E. Waliser (Editors), *Intraseasonal Variability in the Atmosphere–Ocean Climate System* (Second Edition).

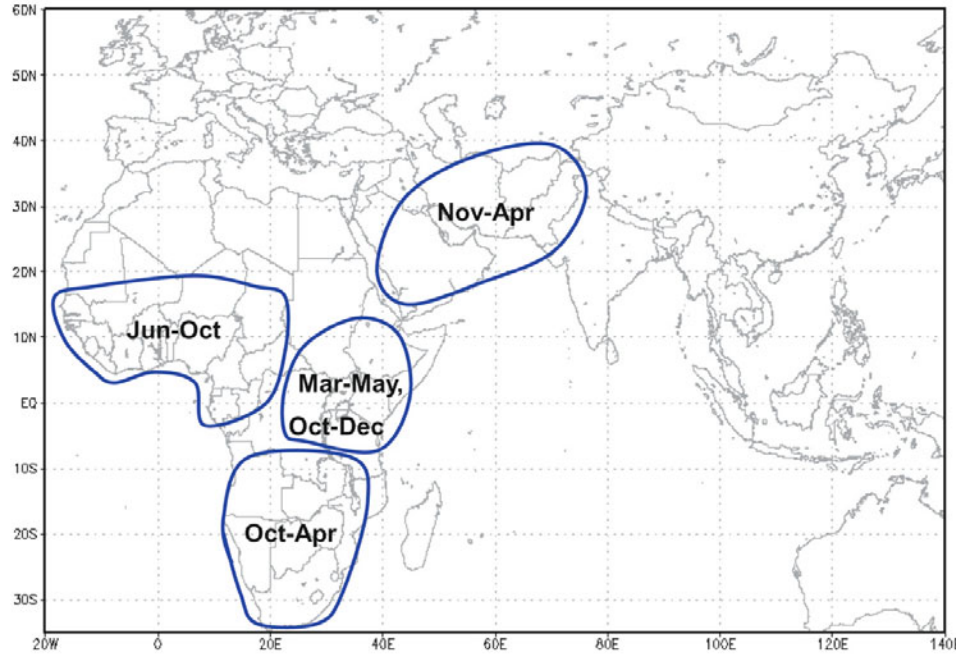

Figure 13.1. Areas and primary seasonality of MJO influence in Africa and Western Asia that have been identified in previous studies, as reviewed in Sections 13.2 and 13.3.

the possibility for a comprehensive analysis of African influence, and the importance of seasonality and regional dynamics, including lagged relationships, in determining the strength of the influence.

The previous African studies are reviewed, by region, in Section 13.2 and the western Asia studies are reviewed in Section 13.3. To provide some context on how the MJO influence is realized at the individual station level, two stations, one from eastern Africa (Nairobi, Kenya) and one from western Asia (Riyadh, Saudia Arabia) are analyzed in Section 13.4. While a considerable number of dynamical questions pertaining to MJO influence in the two regions remain to be fully answered, one very basic question arises: How realistic are the simple Gill–Matsuno dynamics (Matsuno, 1966; Gill, 1980) that are usually invoked to qualitatively explain the large-scale wind patterns? While the general conceptual relevance of Gill–Matsuno dynamics to the MJO is well established, the presence of several potential complicating factors—including the propagating component of the MJO, the regional presence in boreal winter of a strong westerly jet in the midlatitudes, the asymmetric pattern of tropical MJO convection, and the possible influence of transients—raises the question of exactly how realistic the simple dynamics are in this case, and this is examined in Section 13.5. Finally, in Section 13.6, a summary is given and some of the outstanding issues and questions are discussed.

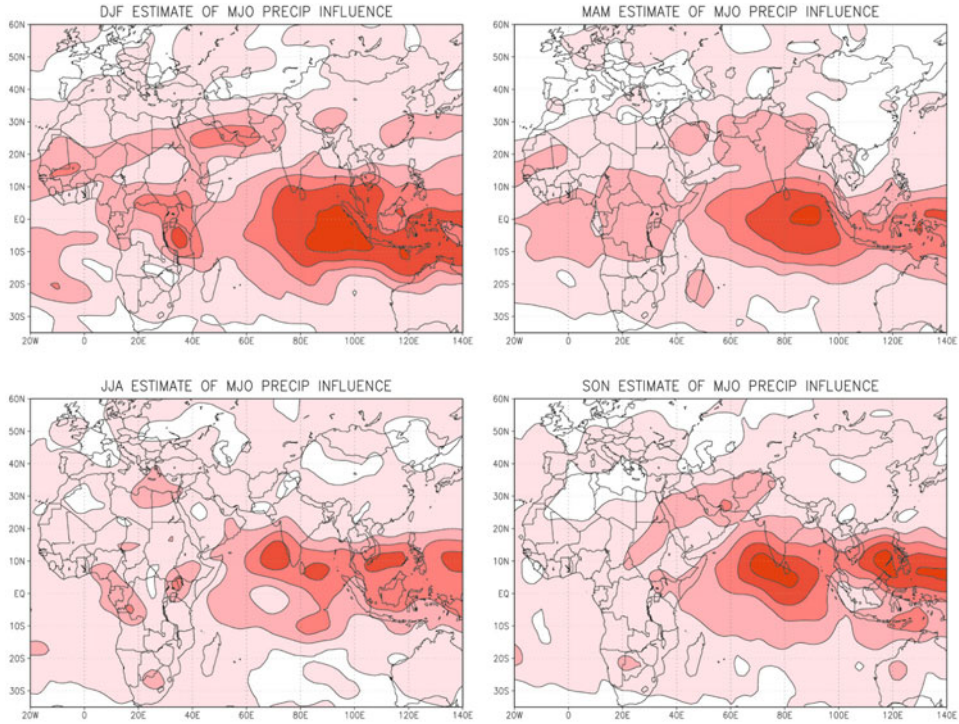

Figure 13.2. Estimated strength of MJO influence on convection for: (a) December–February, (b), March–May, (c) June–August, and (d) September–November. The estimate is based on normalized daily OLR anomalies, which are composited within each season over the eight Wheeler and Hendon MJO phases. After the composites are made, the average of the absolute values over all composites is taken. A nine-point spatial smoother has been applied (weights: 1.0 at center, 0.5 at sides, and 0.3 at diagonals), and the contour interval is 0.08 standard deviations.

13.2 SUMMARY OF AFRICA RESEARCH

13.2.1 West Africa

The dominant large-scale precipitation system in western Africa is the West Africa monsoon (e.g., Hastenrath, 1995), which is active from approximately June to October. The variability of the West African monsoon has a prominent spectral peak at MJO timescales at 25–60 days (Janicot and Sultan, 2001; Sultan *et al.*, 2003; Gu and Adler, 2004; Mounier *et al.*, 2008), although only about a third of the associated variability may be directly linked to the MJO (Maloney and Shaman, 2008). As the overall intraseasonal variability, from 10 to 60 days, itself accounts for about 30% of the seasonal totals (Sultan *et al.*, 2003), the overall influence of the MJO is likely somewhat modest in this region.

The local MJO influence appears to come in large part as a lagged response to the primary area of MJO convective activity in the warm pool regions of the Indian and Western Pacific Oceans (Matthews, 2004; Maloney and Shaman, 2008; Pohl *et al*., 2009), with local conditions perhaps playing an important role in modulating the remote response (Pohl *et al*., 2009). The link is robust and can be established both from local analysis and from warm pool–based analysis (Pohl *et al*., 2009). Modeling studies have reproduced the influence of remote forcing (Lavender and Matthews, 2009) and also highlighted the importance of related changes in the Indian monsoon and associated forcing (Janicot *et al*., 2009). Convective activity over the warm pool appears to generate both an eastward-moving Kelvin wave and a westward-moving Rossby wave which meet over Africa approximately 3 weeks later (Matthews, 2004). The Rossby wave may be the more important factor (Janicot *et al*., 2009; Pohl *et al*., 2009), with a stronger influence during the dry phase than the wet phase.

The dynamical mechanisms controlling the local changes in precipitation are not yet entirely clear, as several important changes take place, including in boundary layer moisture, shear of the African Easterly Jet, and mid-level temperatures and potential vorticity gradient (Matthews, 2004), as well as tropical cyclone activity (Matthews, 2004; Maloney and Shaman, 2008) and synoptic eddies (Maloney and Shaman, 2008). However, there is some evidence that boundary layer moisture and shear in the easterly jet are responding to convection rather than forcing it, and the strongest support appears to be for Matthews' (2004) hypothesis relating changes in mid-level temperature and associated stability to forcing by remotely generated waves (Maloney and Shaman, 2008; Janicot *et al*., 2009; Lavender and Matthews, 2009). Additionally, there is the possibility of land–atmosphere coupling at intraseasonal timescales in the region (Taylor, 2008).

MJO-related predictability in the region appears to be somewhat modest (Sultan *et al*., 2009), although perhaps consideration of multiple factors may yield some improvements.

13.2.2 Eastern Africa

Eastern Africa has two primary rainy seasons, the "short rains" in October to December and the "long rains" in March to May, generally following the seasonal movement of the Intertropical Convergence Zone (ITCZ) (e.g., Hastenrath, 1995). An MJO influence has been identified in several parts of the region (Mutai and Ward, 2000; Mpeta and Jury, 2001; Pohl and Camberlin, 2006a, b). There is a notable contrast between the influence in the western highlands and in the coastal areas of the region. In the western highlands, changes in rainfall appear to be associated with deep-convective processes and westerly moisture transport, and track the large-scale convection changes over Africa and the Indian Ocean. In the eastern coastal regions, however, changes in rainfall appear to be more related to shallow-convective or stratiform processes and easterly moisture transport, and are out of phase with the large-scale convective changes (Pohl and Camberlin, 2006a). As expected for an area where precipitation is not deep convective in nature, OLR

(e.g., as in Figure 13.2) is not a good proxy for precipitation in the eastern coastal regions.

Pohl and Camberlin (2006b) have estimated the MJO contribution to seasonal variability to be 44% in the most affected part of the region during the long rains, although there is large year-to-year variability in the strength of the contribution, and they have also shown a strong influence on extreme events. In years with a strong MJO influence, there are upper-level temperature anomalies consistent with Kelvin wave dynamics and upward vertical motion. Lead–lag analysis shows a strong signal in upper-level westerlies in the 2-week period preceding the largest local changes (Mutai and Ward, 2001; Pohl and Camberlin, 2006a).

El Niño considerably modulates the MJO influence (Mutai and Ward, 2001; Kijazi and Reason, 2005; Pohl and Camberlin, 2006b), and Mutai and Ward (2001) suggest that El Niño signals may actually be realized through modulation of intraseasonal variability.

13.2.3 Southern Africa

All but the southern tip of Southern Africa receives the bulk of its precipitation during the austral warm season, approximately October to April, with most falling from December to February (Buckle, 1996; Bartman *et al.*, 2003). A significant portion of the precipitation is associated with tropical temperate troughs (TTTs), which link tropical convection with midlatitude transients (Harrison, 1984; Todd and Washington, 1999). An MJO influence has been identified (Levey and Jury, 1996; Pohl *et al.*, 2007; Pohl *et al.*, 2009) and accounts for about 35% of intraseasonal variance (Pohl *et al.*, 2007). The MJO appears to modulate the Mascarene High and associated moisture transport into Southern Africa (Pohl *et al.*, 2007). There is strong year-to-year variation in the strength of the MJO influence, at least partially in association with El Niño (Pohl *et al.*, 2007, 2009). The Normalized Difference Vegetation Index (NDVI) also exhibits intraseasonal timescales in this region and may have a feedback relationship at those timescales with moisture flux and precipitation (Chikoore and Jury, 2010).

13.3 SUMMARY OF WEST ASIA RESEARCH

The primary precipitation mechanism for much of southwestern Asia is eastward-moving synoptic storms during the boreal cold season, November to April (Martyn, 1992; Barlow *et al.*, 2005). The November to April MJO influence, calculated as before, and the November to April cold season contribution to the annual precipitation total are shown in Figure 13.3. For much of Southwest Asia, the area of strongest cold-season MJO influence coincides with the area of largest cold-season contribution to precipitation, suggesting that MJO-related predictability may be of particular relevance in this region.

A strong MJO influence on precipitation in the region has been shown by Barlow *et al.* (2005) and Nazemosadat and Ghaedamini (2010), with rainfall at

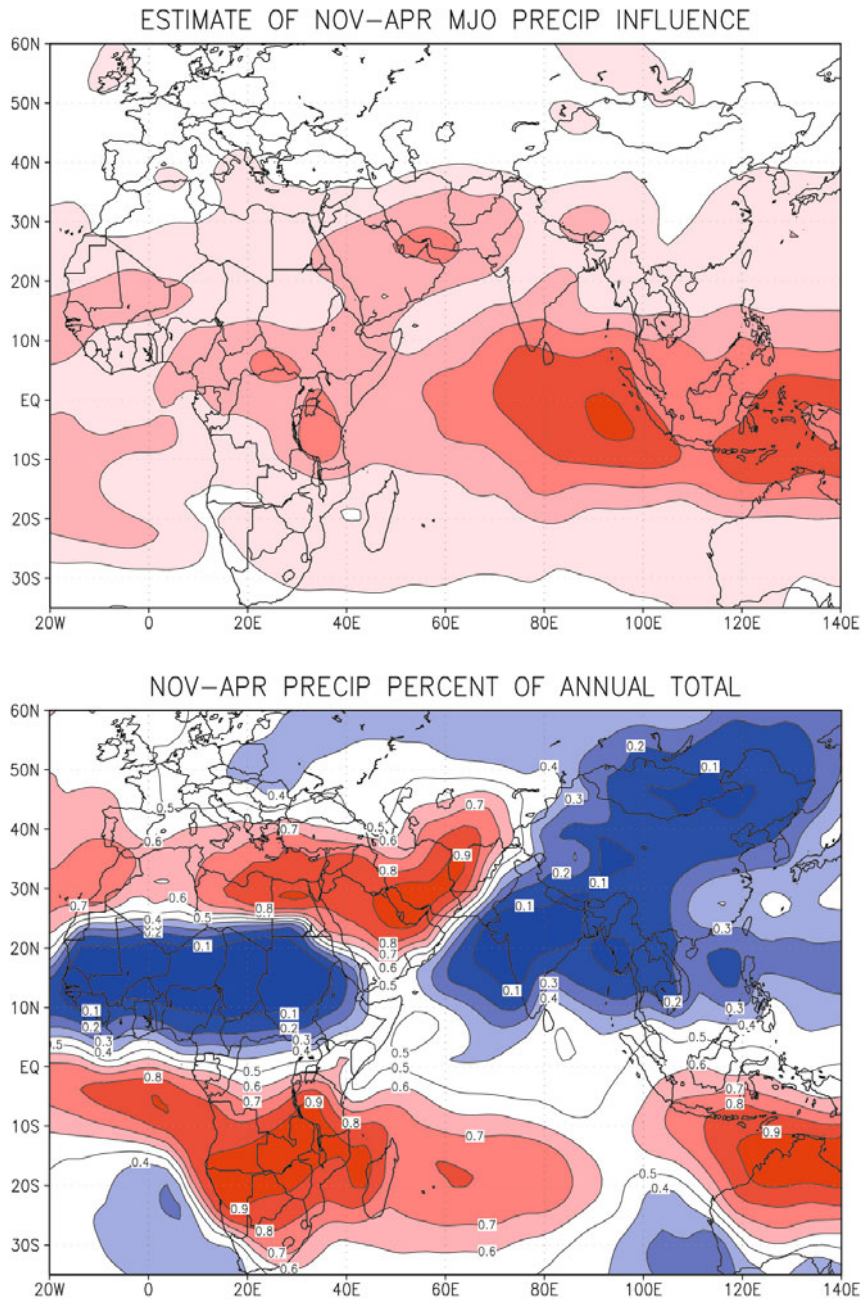

Figure 13.3. (a) OLR-based November–April estimate of MJO influence and (b) contribution of November–April precipitation to annual total, with a contour interval of 0.1 (10%) and red shading for more than 60% and blue shading for less than 40%. The estimate of MJO influence is produced as in Figure 13.2, and the same nine-point smoother is used.

some stations in the region changing by more than a factor of 2 depending on the MJO phase. The occurrence of extreme events is also modulated by the MJO (Jones *et al*., 2004; Barlow *et al*., 2005).

One pathway for MJO influence on the region is dynamic–thermodynamic: a large area of mid-level warm temperature anomalies is generated by tropical MJO convection, as part of a Gill–Matsuno-like response, and the intersection of these anomalies with the westerly jet results in cold temperature advection and subsidence (isentropic downgliding) over Southwest Asia (Barlow *et al*., 2005), similar to the "desert–monsoon" hypothesis of Rodwell and Hoskins (1996, 2001). A full physics atmospheric model is able to reproduce these dynamics when forced by additional diabatic heating in the peak tropical MJO region (Barlow *et al*., 2007). Changes to moisture transport also appear to be important (Nazemosadat and Ghaedamini. 2010). The MJO pattern is similar to the regional pattern associated with severe drought in Southwest Asia during 1999–2001 (Barlow *et al*., 2002), although the similarity of the dynamics remains to be fully explored.

In terms of predictability, the year-to-year strength of the influence is fairly consistent and there appears to be at least some predictability extending beyond week 2 (Barlow *et al*., 2005), consistent with the strength of the relationship in this area, although a comprehensive analysis of forecast skill remains to be done.

An interesting question is the strength of the MJO influence on the coastal Middle East. The region is at the margin of the area of strong influence (Figure 13.3) and has not been identified as having a large MJO signal. However, a subset of flooding events in the region have been linked to tropical moisture plumes (Rubin *et al*. 2007) and preliminary analysis suggests that tropical plumes occur preferentially during MJO phases 5–8 by a ratio of more than 2 to 1.

13.4 STATION DATA ANALYSIS

13.4.1 Methodology and data

To provide some context for how the MJO influence is realized at the individual station level, daily data from two stations, one in eastern Africa and one in western Asia, are analyzed here. Data limitations are severe in both regions so, while both stations are from strongly influenced regions, the locations were determined in large part based on data availability and may not represent the largest strength of influence. A Monte Carlo approach, described further below, is used to assess statistical significance.

Nairobi, Kenya is chosen for eastern Africa and Riyadh, Saudia Arabia, is chosen for western Asia. For each station, daily precipitation is composited based on the eight phases of the Wheeler and Hendon MJO index for the period of available data, and then year-to-year variations in the difference between the peak phases are examined. Averaging precipitation over the different phases provides a simple estimate of MJO influence, but it should be borne in mind that other measures of influence—including changes to the start and end of the wet season,

duration of dry or wet spells, or extremes—may be more important in terms of societally relevant impacts.

The daily station data for precipitation was obtained from the Global Historical Climatology Network (GHCN) daily database (NCDC, 2004) and have undergone several quality controls (Durre *et al.*, 2010). Data from the Global Summary of the Day (GSOD), as archived by NCDC, were also obtained but appear to require in-depth examination to assess validity, so were not used here. Daily data for Nairobi were examined for a 25-year period (1979–2003), with a 65% reporting rate during that time, including nine completely missing months (January–September 1999). A 14-year period (1985–1998) was examined for Riyadh, with a 98% reporting rate.

13.4.2 Nairobi

The MJO composites for Nairobi were calculated separately for the two main rainy seasons, the "short rains" in October to December and the "long rains" in March to May, and are shown in Figure 13.4. The eight MJO phases are taken from the Wheeler and Hendon (2004) index, only including phases when the amplitude of the index was greater or equal to 1.0. The frequency of occurrence for each phase varies somewhat by season; for March to May, the frequencies of the eight phases, respectively, were 8.5%, 7.9%, 7.9%, 7.6%, 7.1%, 7.7%, 9.3%, 9.4% and for October to December they were 6.8%, 7.4%, 8.1%, 7.5%, 9.2%, 8.5%, 7.5%, 6.3%. Statistical significance was estimated by repeating the composite calculations 1,000 times, with the phases randomly determined but maintaining their relative frequency of occurrence.

For March to May, the composites show only a single phase (4) significant at the 95% level and no phases significant at the 99% level. Given the somewhat limited data, it is perhaps not surprising that high statistical significance is difficult to obtain when compositing is done for all eight phases separately. Considering the enhanced (3, 4, 5) and suppressed phases (6, 7, 8) as groups gives values of 6.92 mm and 3.88 mm and the difference between these groups is, indeed, significant at higher than 99%.

For October to December, the signal appears more robust, and two phases (3 and 5) are individually significant at the 99% level, with a more than sixfold difference between the precipitation in the two phases.

To assess the year-to-year consistency of these relationships, the seasonal means for each year were calculated for precipitation during the enhanced and suppressed phases and are shown in Figure 13.5 for March to May and in Figure 13.6 for October–December. For March to May, precipitation during phases 3–5 exceeds precipitation in phases 6–8 for 70% of the years (missing values indicate seasons where the phases were not observed). Precipitation averages 77% larger during the enhanced phase compared with the suppressed phase. For October to December, precipitation during phases 1–3 exceeds precipitation phases 4–6 for 67% of the years. Average precipitation during phases 1–3 is more than double over this period compared with phases 4–6, although a considerable part of that is due to

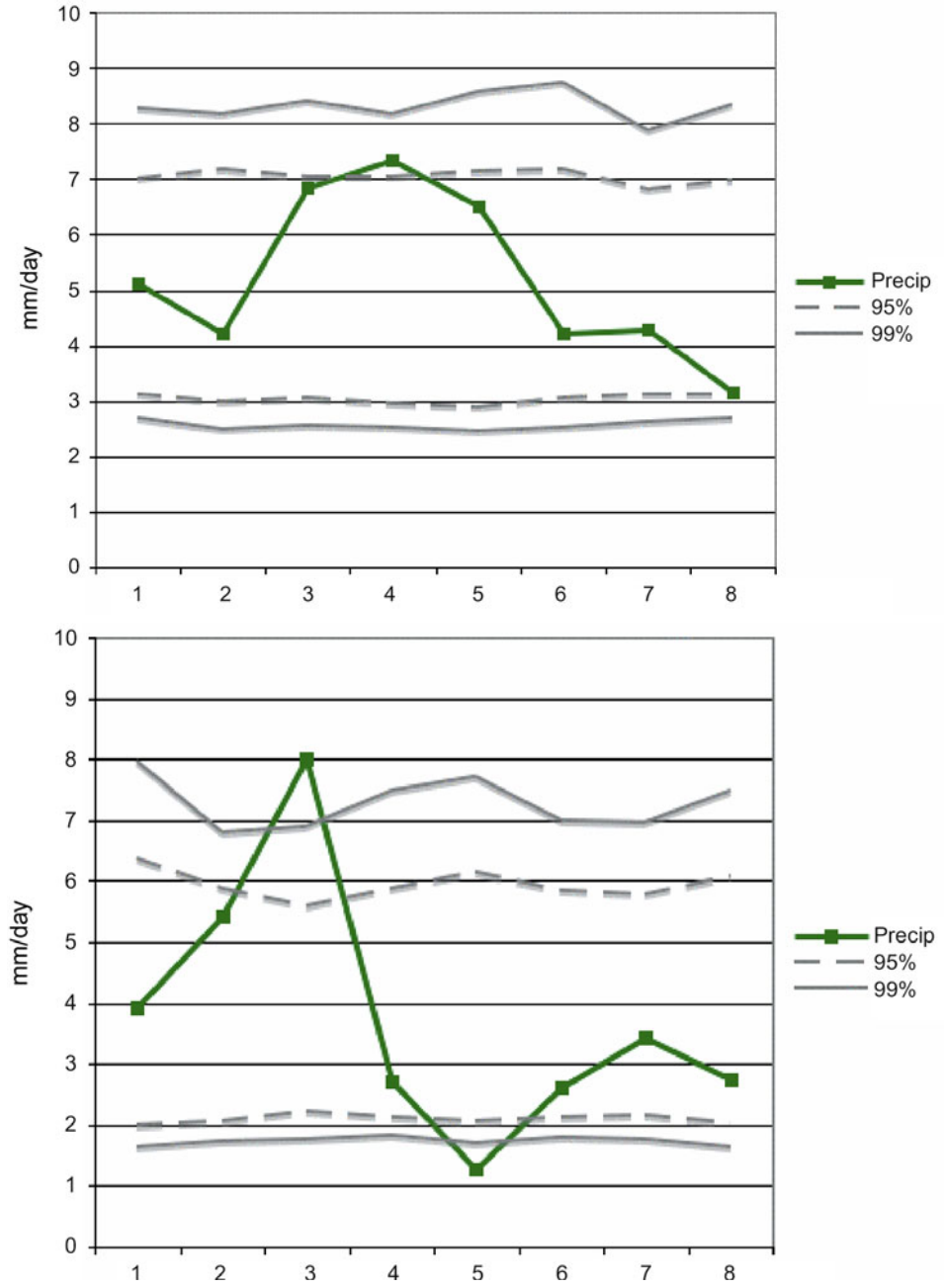

Figure 13.4. Nairobi daily precipitation, 1979–2003, composited by MJO phase for (a) March–May, and (b) October–December. The Wheeler and Hendon index is used to determine the MJO phase and statistical significance is assessed through 1,000 iterations of the composites with randomly distributed phases.

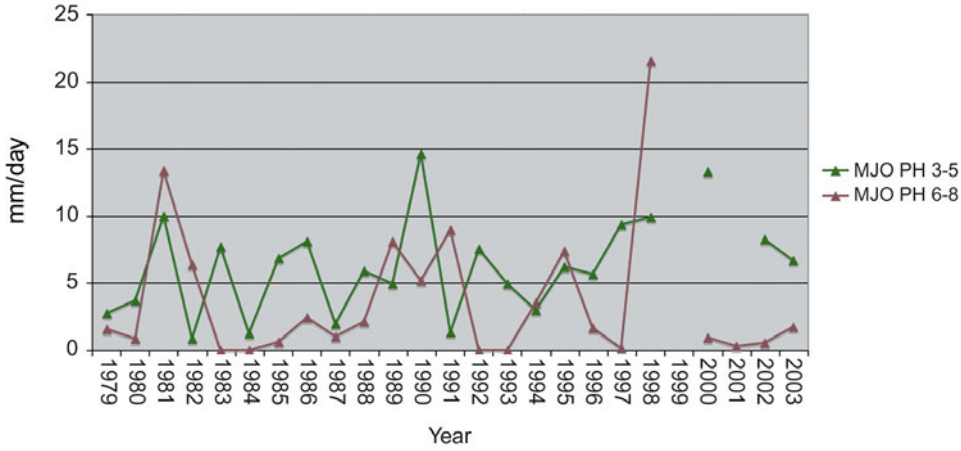

Figure 13.5. Nairobi precipitation for March–May of each year is shown for MJO phases 3–5 in green and phases 6–8 in brown. Missing values indicate seasons where the phases were not observed.

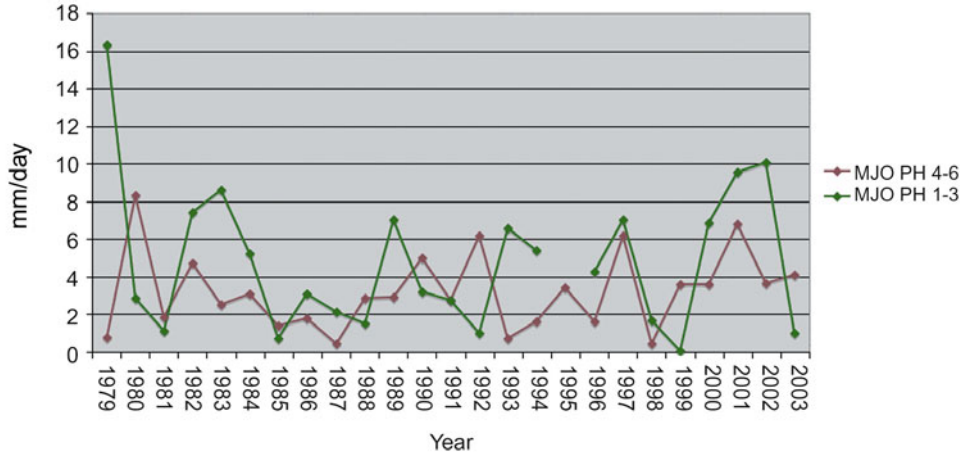

Figure 13.6. Nairobi precipitation for October–December of each year is shown for MJO phases 1–3 in green and phases 4–6 in brown. Missing values indicate seasons where the phases were not observed.

the large difference during 1979. Excluding 1979, however, still yields 30% greater precipitation during phases 1–3.

As expected from previous work, there is considerable variation in the strength of the MJO influence from year to year. Using the difference between October to December precipitation during phases 1–3 and 4–6 as a simple index of the strength

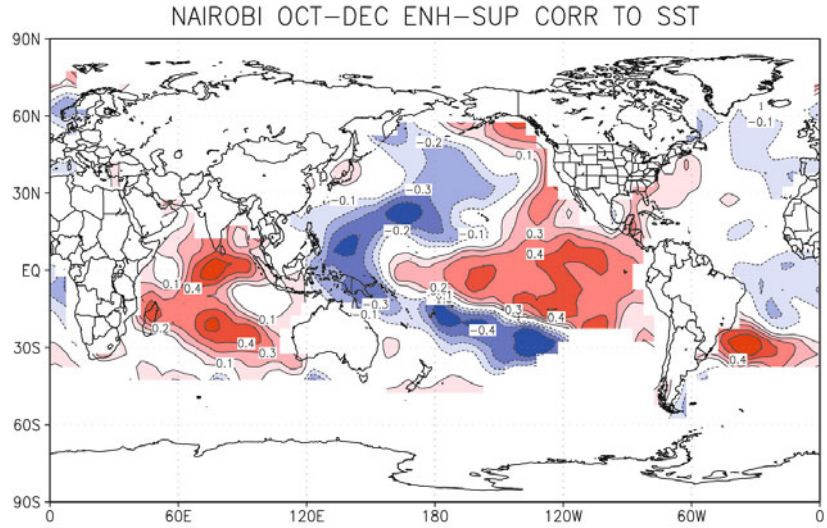

Figure 13.7. Correlation between October–December SSTs and the difference between Nairobi precipitation in the MJO-enhanced and MJO-suppressed phases.

of the MJO influence, the correlation to global SSTs is shown in Figure 13.7. While the correlation does capture a pattern consistent with a mature ENSO, the magnitude over the Pacific, at least with this measure, is somewhat modest. Correlations are higher in the Indian Ocean and, interestingly, in the South Atlantic, and merit further analysis.

13.4.3 Riyadh

The MJO composite of Riyadh precipitation for November to April, the primary local wet season, is shown in Figure 13.8. Four of the eight phases are individually statistically significant at the 99% level and show a very large difference. The frequency of occurrence for the eight phases during November to April is 6.5%, 7.8%, 9.4%, 8.2%, 7.4%, 8.4%, 9.2%, and 7.5%, respectively.

The year-to-year consistency of this relationship, shown in Figure 13.9, is quite robust: precipitation during the enhanced phases is greater than or equal to precipitation during the suppressed phases in every year of the record. Averaged over the whole period, precipitation is more than six times larger during the enhanced phase. Even removing the 2 years with the largest difference, precipitation is still more than four times greater than during the enhanced phase. The causes underlying the large year-to-year variations in precipitation amount are not yet known.

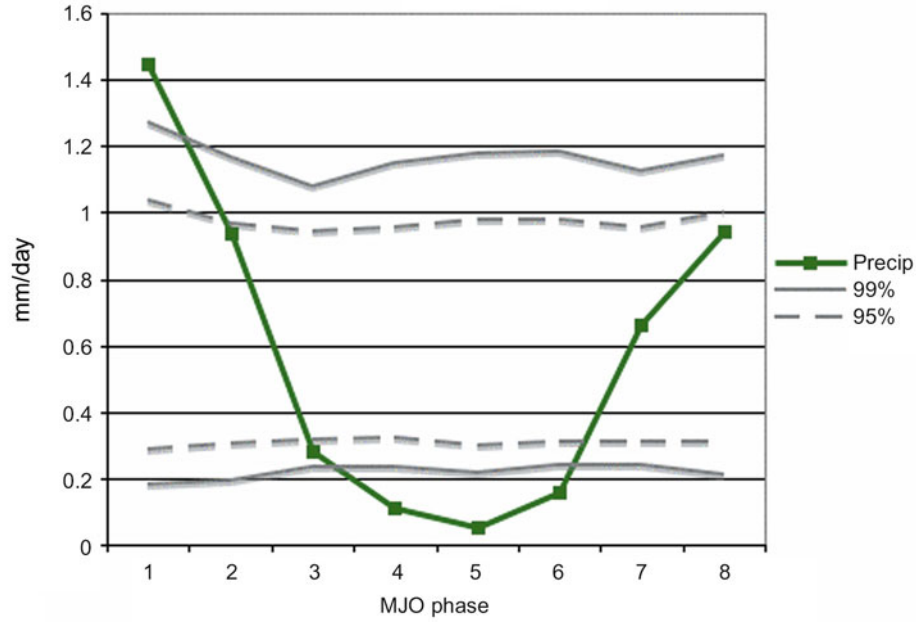

Figure 13.8. Riyadh daily precipitation, 1985–1998, composited by MJO phase for November–April.

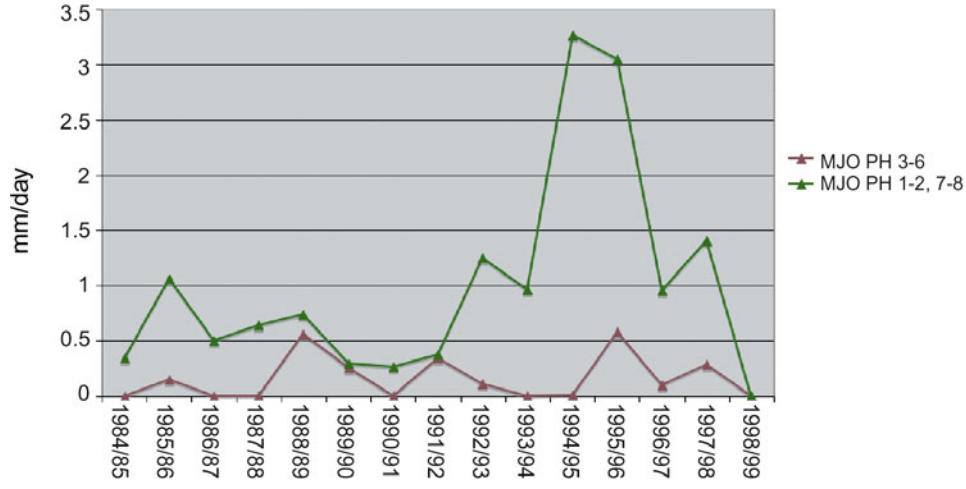

Figure 13.9. Riyadh precipitation for November–April of each year is shown for MJO phases 1, 2, 7, and 8 in green and phases 3–6 in brown.

13.5 RELEVANCE OF GILL–MATSUNO DYNAMICS AND THE ROLE OF MEAN WIND

The conceptual importance of Gill–Matsuno tropical dynamics to the MJO has long been recognized (e.g., Madden and Julian, 1994), and is often used as the starting point for many theoretical studies (e.g., Wang and Rui, 1990). However, the simplicity of the Gill–Matsuno framework and the complexity of the actual situation raises the question of whether the model can realistically capture the large-scale dynamics or whether it is primarily useful as a conceptual tool. As the intersection of the tropically forced response with the westerly jet is a key part of extratropical influence (Barlow *et al.*, 2005, 2007), it is important to ascertain how well the simplest set of dynamics explains the response and whether any additional dynamical mechanisms need to be considered. Given the presence of a strong westerly jet, the extent to which the mean wind affects the Gill–Matsuno dynamics, which assume a resting basic state, is a key question. Here, the observed MJO circulation at the time of peak strength is compared with three versions of Gill–Matsuno dynamics: the basic Gill–Matsuno equations forced by idealized heating (equivalent to the usual analytical solution), the basic equations forced by the observed pattern of heating, and an extension of the equations that includes the mean wind.

Matsuno (1966) and Gill (1980) both consider the response of the first-baroclinic mode of a Bousinesq atmosphere on an equatorial β-plane, linearized about a resting basic state, to tropical forcing. The basic equations have the form of shallow-water equations (although they are not derived by assuming the atmosphere is a single shallow layer) and may be written:

$$\frac{\partial u_s}{\partial t} = f v_s - \frac{\partial \phi_s}{\partial x} - \varepsilon u_s$$

$$\frac{\partial v_s}{\partial t} = -f u_s - \frac{\partial \phi_s}{\partial y} - \varepsilon v_s$$

$$\frac{\partial \phi_s}{\partial t} = -H\left(\frac{\partial u_s}{\partial x} + \frac{\partial v_s}{\partial y}\right) + Q - \varepsilon \phi_s$$

Which is the same as Matsuno (1966) and Gill (1980) before non-dimensionalization, but with geopotential instead of pressure and the full Coriolis force instead of the equatorial β-plane approximation. The use of geopotential is justified as the equations may also be derived from a linearized rigid lid two-layer pressure level model (without assuming quasi-geostrophy), in which case the variables are interpreted as the difference between the upper and lower levels (subscript "s" for shear). We use that interpretation here for simplicity and to facilitate comparison with observed pressure level data. The equations can also be derived from a two-layer shallow-water model with a rigid lid and no mean wind, with the same shear interpretation of variables.

Matsuno and Gill went on to solve for a single equation (neglecting some small terms) and analytically solve the system for some simple cases. Here we consider the

governing equations above as the "Gill–Matsuno model"; that is, slightly generalized from the original analyses to consider any forcing pattern. A justification for the strong linear drag in this model is given in Lin *et al*. (2008). This dynamical framework has been reinterpreted as a boundary layer model (Neelin, 1989; Battisti *et al*., 1999), but here we consider its realism in terms of the free troposphere, as originally formulated.

The observed November to April convection (OLR, shaded) and upper-level streamfunction (contoured) anomalies are shown in Figure 13.10a for the MJO at its peak strength of tropical convection anomalies (Wheeler and Hendon phases 3 and 4 minus phases 7 and 8). The idealized Gill (1980) response to symmetric heating is shown in Figure 13.10b and, qualitatively, has very good correspondence with the idealized model in getting the right scale and similar pattern and placement of the response. The main limitation of the idealized response is that it is trapped somewhat too close to the equator and is not shifted as far to the west as observations. However, the idealized forcing covers a wider range of latitudes than the observed tropical MJO convective forcing, so a more realistic comparison would be to examine the Gill–Matsuno response to the actual pattern of MJO forcing; this is shown in Figure 13.10c. The forcing is specified based on the OLR anomalies in the tropical eastern Indian Ocean (50°E–120°E, 20°S–20°N). The westward shift of the Rossby response is better captured with the realistic forcing pattern, but the response is even more equatorially constrained, at least near the heating. Thus, the simple Gill–Matsuno dynamics realistically capture the general sense of the observed upper-level circulation, but do not fully capture the northward displacement of the upper-level anticyclone into the midlatitudes and the westerly jet stream, which is a critical part of the regional dynamics. The observed lower-level (700 hPa) response (not shown) is not displaced as far poleward, so the realism of the Gill–Matsuno model in terms of the lower-level response is even better, consistent with its success in simulating surface winds as part of simple coupled models of ENSO (e.g., Cane and Zebiak, 1985).

A key limitation of the Gill–Matsuno model is the lack of mean wind. Given that the westerly jet directly impinges on the Rossby response, the question of its influence naturally arises. The simplest way to add mean wind is in a two-layer shallow-water model (e.g., Vallis, 2006); the upper-level response of such a model linearized about the observed November to April wind is shown in Figure 13.10d. Values of the drag parameter are kept the same as in the Gill–Matsuno model, for simplicity. Inclusion of mean wind puts the maximum of the wind response in almost exactly the right place, although the zonal orientation of the observed response is not fully captured. Adding the rest of the forcing in the region, especially the negative values over Southwest Asia, further improves the model response (not shown) but here we focus on tropical forcing, to emphasize the direct response as considered by Matsuno and Gill.

Thus, while the idealized Gill–Matsuno dynamics are sufficient to give a good qualitative description of the observed anomalies, the addition of mean wind is necessary to capture the correct northward displacement of upper-level anticyclones. While the response is still not perfect, the addition of mean wind to Gill–Matsuno

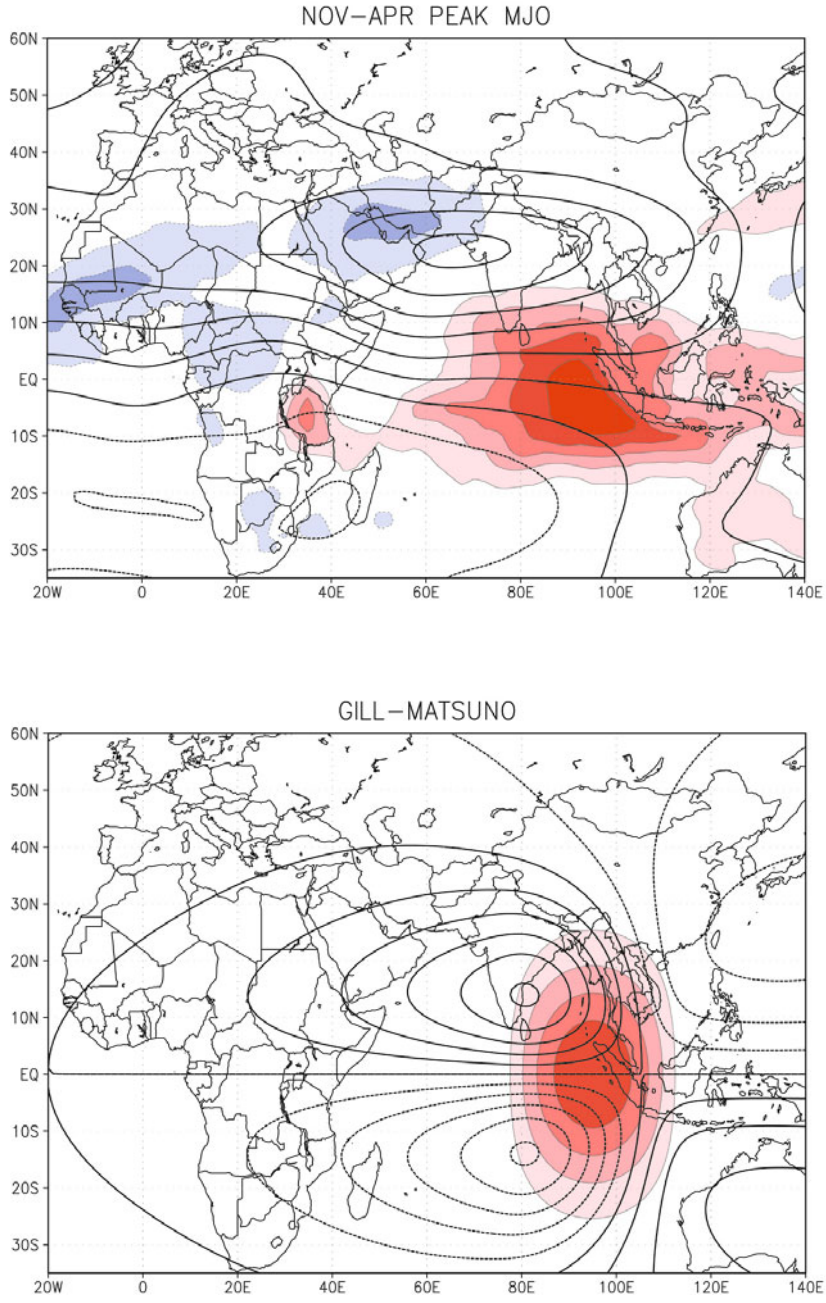

Figure 13.10. Convection (shaded) and upper-level streamfunction (contour) anomalies for (a) peak strength of the MJO, November–April; (b) same variables from the Gill–Matsuno model with idealized forcing. The MJO composite is Wheeler and Hendon phases 3 and 4 minus phases 7 and 8.

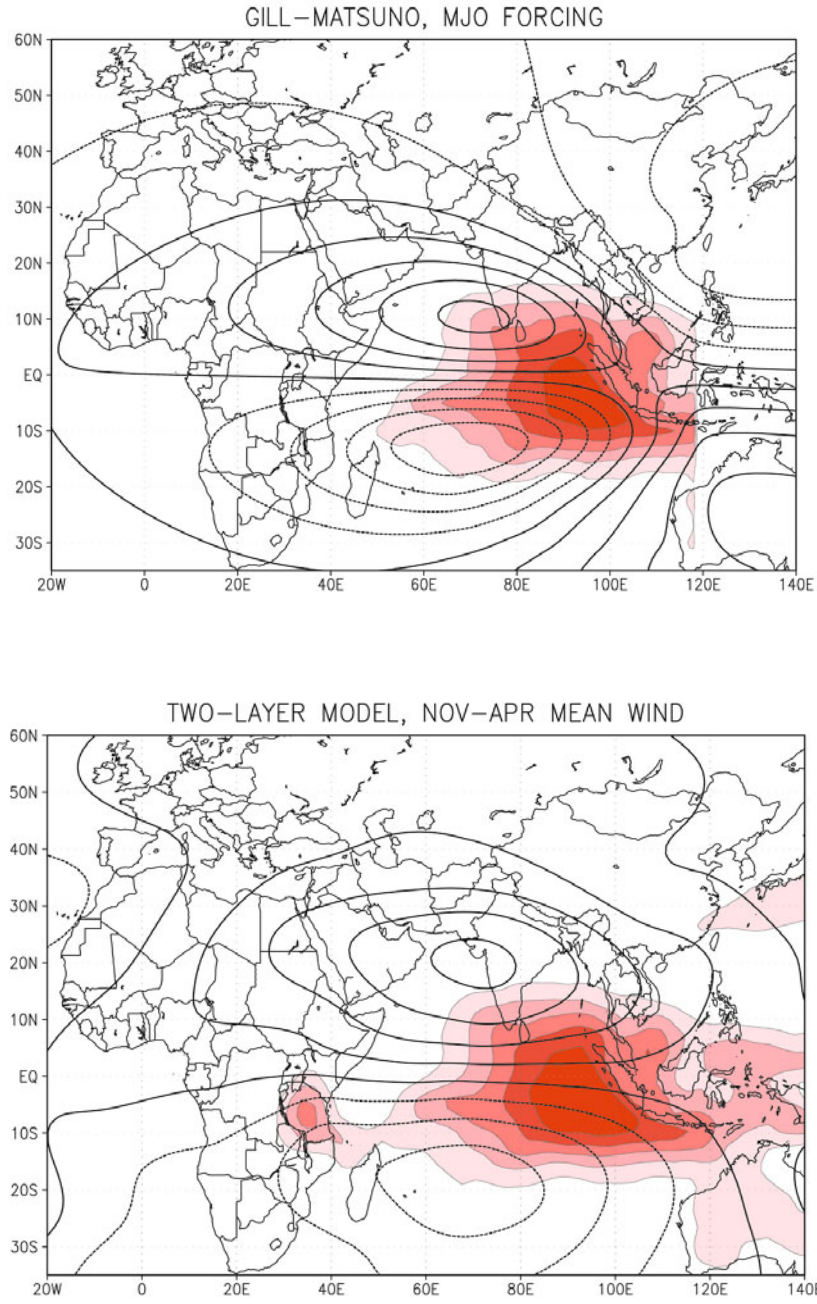

Figure 13.10 (*cont.*). (c) Same variables from the Gill–Matsuno model with forcing based on the observed convection anomalies in the Indian Ocean; and (d) same variables from a two-layer shallow-water model linearized about a zonally varying November–April mean state and forced by the observed convection anomalies in the Indian Ocean.

dynamics does capture the basic aspects of the upper-level circulation response in a fairly realistic fashion.

13.6 SUMMARY AND DISCUSSION

The MJO has been shown to influence precipitation over much of Africa and the southern part of western Asia. Based on the analyses conducted so far, the strength of the influence appears to be largest in southwestern Asia and eastern Africa. The associated predictability has not yet been extensively studied, but appears promising, at least in some of the more affected areas. However, large year-to-year changes in the strength of the influence in some regions presents a challenging forecast problem. A number of dynamical mechanisms for the influence have been suggested for each of the regions but a common thread is the influence of large-scale equatorial waves and the importance of local conditions. The complex seasonality of African precipitation further complicates the interpretation of the dynamics. When MJO convection is at its peak in boreal winter, the main features of large-scale circulation are generally well described by simple Gill–Matsuno dynamics when the influence of mean wind is included.

Due in part to data scarcity and the complexity of the climate system in these regions, our understanding of MJO influence and the extent to which that influence can be exploited for useful predictions is still in relatively early stages for these regions. More comprehensive analyses aimed at robustly identifying the strength and extent of MJO influence over large areas would be useful in guiding future work. More dynamical analysis is needed to distinguish between the different possible mechanisms suggested thus far in the various regions. A particularly important question is the relationship between the MJO and interannual variability. It appears that ENSO can modulate the MJO and there are some suggestions that the ENSO signal, in turn, may actually be realized through modulation of the MJO in some areas. This is important to understand both from a dynamical perspective as well as from a prediction standpoint. Finally, it does not appear that we have come near to utilizing the full predictive potential in these very precipitation-sensitive parts of the world. The identification of key forecast targets (variable, lead time, domain) for each of the regions would facilitate forecast development and a robust assessment of skill.

13.7 REFERENCES

Barlow, M., H. Cullen, and B. Lyon (2002) Drought in Central and Southwest Asia: La Niña, the Warm Pool, and Indian Ocean precipitation. *J. Climate*, **15**, 697–700.

Barlow, M., M. Wheeler, B. Lyon, and H. Cullen (2005) Modulation of daily precipitation over Southwest Asia by the Madden–Julian Oscillation. *Mon. Wea. Rev.*, **133**, 3579–3594.

Barlow, M., A. Hoell, and F. Colby (2007) Examining the wintertime response to tropical convection over the eastern Indian Ocean by modifying atmospheric heating in a global atmospheric model. *Geophys. Res. Lett.*, **34**, L19702, doi: 10.1029/2007GL030043.

Bartman, A. G., W. A. Landman, and C. J. De W. Rautenbach (2003) Recalibration of general circulation model output to austral summer rainfall over Southern Africa. *Int. J. Climatol.*, **23**, 1407–1419.

Battisti, D. S., E. S. Sarachik, and A. C. Hirst (1999) A consistent model for the large scale steady atmospheric circulation in the tropics. *J. Climate*, **12**, 2956–2964

Buckle, C. (1996) *Weather and Climate in Africa*. Longman, Harlow, U.K., 312 pp.

Cane, M. A. and S. E. Zebiak (1985) A theory for El Niño and the Southern Oscillation. *Science*, **228**, 1085–1087.

Chikoore, H. and M. R. Jury (2010) Intraseasonal variability of satellite-derived rainfall and vegetation over Southern Africa. *Earth Interactions*, **14**, 1–26

Durre, I., M. J. Menne, B. E. Gleason, T. G. Houston, and R. S. Vose (2010) Comprehensive automated quality assurance of daily surface observations. *J. Appl. Meteorol. Climatol.*, **49**, 1615–1633.

Gill, A. E. (1980) Some simple solutions for heat-induced tropical circulation. *Quart. J. Roy. Meteorol. Soc.*, **106**, 447–462.

Gu, G. and R. F. Adler (2004) Seasonal evolution and variability associated with the West African monsoon system. *J. Climate*, **17**, 3364–3377.

Harrison, M. (1984) A generalized classification of South African summer rain-bearing synoptic systems. *Int. J. Climatol.*, **4**, 547–560.

Hastenrath S. (1995) *Climate Dynamics of the Tropics* (Second Printing). Kluwer, Dordrecht, The Netherlands, 488 pp.

Janicot, S. and B. Sultan (2001) Intra-seasonal modulation of convection in the West African monsoon. *Geophys. Res. Lett.*, **28**, 523–526.

Janicot, S., F. Mounier, N. Hall, S. Leroux, B. Sultan, and G. Kiladis (2009) Dynamics of the West African monsoon, Part IV: Analysis of 25–90-day variability of convection and the role of the Indian monsoon. *J. Climate*, **22**, 1541–1565.

Jones, C., D. E. Waliser, K. M. Lau, and W. Stern (2004) Global occurrences of extreme precipitation and the Madden–Julian Oscillation: Observations and predictability. *J. Climate*, **17**, 4575–4589.

Kijazi, A. and C. J. C. Reason (2005) Relationships between intreaseasonal rainfall variability of coastal Tanzania and ENSO. *Theor. Appl. Climatol.*, **82**, 153–176, doi: 10.1007/s00704-005-0129-0.

Lavender, S. L. and A. J. Matthews (2009) Response of the West African monsoon to the Madden–Julian oscillation. *J. Climate*, **22**, 4097–4116.

Levey, K. M. and M. R. Jury (1996) Composite intraseasonal oscillations of convection over Southern Africa. *J. Climate*, **9**, 1910–1920.

Lin, J.-L., B. E. Mapes, W. Han (2008) What are the sources of mechanical damping in Matsuno–Gill-type models? *J. Climate*, **21**, 165–179

Madden, R. A. and P. R. Julian (1994) Observations of the 40–50 day tropical oscillation: A review. *Mon. Wea. Rev.*, **122**, 814–837.

Maloney, E. D. and J. Shaman (2008) Intraseasonal variability of the West African monsoon and Atlantic ITCZ. *J. Climate*, **21**, 2898–2918.

Martyn, D. (1992) *Climates of the World*. Elsevier, Amsterdam, 436 pp.

Matsuno, T. (1966) Quasi-geostrophic motions in the equatorial area. *J. Meteorol. Soc. Japan*, **44**, 25–43.

Matthews, A. J. (2004) Intraseasonal variability over tropical Africa during northern summer. *J. Climate*, **17**, 2427–2440.

Mounier, F. and S. Janicot (2004) Evidence of two independent modes of convection at intraseasonal timescale in the West African summer monsoon. *Geophys. Res. Lett.*, **31**, L16116, doi: 10.1029/2004GL020665.

Mounier, F., S. Janicot, and G. N. Kiladis (2008) The West African monsoon dynamics, Part III: The quasi-biweekly zonal dipole. *J. Climate*, **21**, 1911–1928.

Mpeta, E. J. and M. Jury (2001) Intra-seasonal convective structure and evolution over tropical east Africa. *Climate Res.*, **17**, 83–92.

Mutai, C. C. and M. N. Ward (2000) East African rainfall and the tropical circulation/convection on intraseasonal to interannual timescales. *J. Climate*, **13**, 3915–3939.

Nazemosadat, M. J. and H. Ghaedamini (2010) On the relationships between the Madden–Julian Oscillation and precipitation variability in southern Iran and the Arabian Peninsula: Atmospheric circulation analysis. *J. Climate*, **23**, 887–904

NCDC (2004) *National Climatic Data Center Data Documentation for Data Set 9300 (DSI-9300) Global Historical Climatology Network—Daily, V1.0*. National Climatic Data Center, Asheville, NC, 17 pp.

Neelin, J. D. (1989) On the interpretation of the Gill model. *J. Atmos. Sci.*, **46**, 2466–2468.

Pohl, B. and P. Camberlin (2006a) Influence of the Madden–Julian Oscillation on East African rainfall, Part I: Intraseasonal variability and regional dependency. *Quart. J. Roy. Meteorol. Soc.*, **132**, 2521–2539, doi: 10.1256/qj.05.104.

Pohl, B. and P. Camberlin (2006b) Influence of the Madden–Julian Oscillation on East African rainfall, Part II: March–May season extremes and interannual variability. *Quart. J. Roy. Meteorol. Soc.*, **132**, 2541–2558, doi: 10.1256/qj.05.223.

Pohl, B., Y. Richard and N. Fauchereau (2007) Influence of the Madden–Julian Oscillation on Southern African summer rainfall. *J. Climate*, **20**, 4227–4242, doi: 10.1175/JCLI4231.1.

Pohl, B., S. Janicot, B. Fontaine, and R Marteau (2009) Implication of the Madden–Julian Oscillation in the 40-day variability of the West African monsoon. *J. Climate*, **22**, 3769–3785.

Rodwell, M. J. and B. J. Hoskins (1996) Monsoons and the dynamics of deserts. *Quart. J. Roy. Meteorol. Soc.*, **122**, 1385–1404.

Rodwell, M. J. and B. J. Hoskins (2001) Subtropical anticyclones and summer monsoons. *J. Climate*, **14**, 3192–3211.

Rubin, S., B. Ziv, and N. Paldor (2007) Tropical plumes over eastern North Africa as a source of rain in the Middle East. *Mon. Wea. Rev.*, **35**(12), 4135–4148.

Sultan, B., S. Janicot, and A. Diedhiou (2003) The West African monsoon dynamics, Part I: Documentation of intraseasonal variability. *J. Climate*, **16**, 3389–3406.

Sultan, B., S. Janicot, and C. Correia (2009) Medium lead-time predictability of intraseasonal variability of rainfall in West Africa. *Weather and Forecasting*, **24**, 767–784.

Taylor, C.M. (2008) Intraseasonal land–atmosphere coupling in the West African monsoon. *J. Climate*, **21**, 6636–6648.

Todd, M. C. and Washington, R. (1999) Circulation anomalies associated with tropical-temperate troughs over Southern Africa and the South West Indian Ocean. *Climate Dynamics*, **15**, 937–951.

Vallis, G. K. (2006) *Atmospheric and Oceanic Fluid Dynamics*. Cambridge University Press, Cambridge, U.K., 745 pp.

Wang, B. and H. Rui (1990) Synoptic climatology of transient tropical intraseasonal convection anomalies. *Meteorol. Atmos. Phys.*, **44**(1/4), 43–61.

Wheeler, M. and Hendon, H. H. (2004), An all-season real-time multivariate MJO index: Development of the index for monitoring and prediction in Australia. *Mon. Wea. Rev.*, **132**, 1917–1932.

14

Tropical–extratropical interactions

Paul E. Roundy

14.1 INTRODUCTION

Intraseasonal anomalies of moist deep convection in the tropics evolve together with the global atmospheric circulation. Some of the coherence between tropical convection and extratropical weather is a consequence of redistribution of mass by convection, which is associated with broad-scale overturning circulations, global and regional cycles of atmospheric angular momentum (Anderson and Rosen, 1983; Weickmann and Sardeshmukh, 1994; Weickmann and Berry, 2009), and Rossby wavetrains that extend eastward and poleward across the midlatitudes (Sardeshmukh and Hoskins, 1988; Jin and Hoskins, 1995; Bladé and Hartmann, 1995). Another portion of this coherence is associated with modulation of tropical convection by extratropical waves (Lim and Chang, 1981; Webster and Holton, 1982; Hoskins and Yang, 2000; Allen *et al*., 2008). Thus, the tropical and extratropical patterns influence each other, yielding profound associations between tropical intraseasonal oscillations and extratropical storm tracks. These associations frequently express themselves as global teleconnection patterns (Wallace and Gutzler, 1981; Ferranti *et al*., 1990; Higgins and Mo, 1997, Matthews and Meredith, 2004; Cassou, 2008; L'Heureux and Higgins, 2008; Roundy and Verhagen, 2010). Prediction of midlatitude weather at lead times longer than 4 or 5 days thus depends on the geographical distribution and temporal evolution of moist deep convection in the tropics (Wallace and Gutzler, 1981; Ferranti *et al*., 1990; Weickmann *et al*., 1997; Mo and Higgins, 1998; Hendon *et al*., 2000; Higgins *et al*., 2000; Jones *et al*., 2000; Nogues-Paegle *et al*., 2000; Mo, 2000; Branstator, 2002; Jones *et al*., 2004a,b; Weickmann and Berry, 2007). The global footprint of tropical intraseasonal oscillations allows them to influence or otherwise evolve with a broad range of high-impact weather events at high latitudes, including droughts and floods (Mo and Higgins, 1998; Jones, 2000; Higgins *et al*., 2000; Whitaker and Weickmann, 2001; Jones *et al*., 2004b; Donald *et al*., 2006), extreme temperature events (Vecchi

W. K. M. Lau and D. E. Waliser (Editors), *Intraseasonal Variability in the Atmosphere–Ocean Climate System* (Second Edition).

and Bond, 2004; Lin and Brunet, 2009), and even the general timing and locations of outbreaks of severe thunderstorms and tornados.

Although convection in the tropics varies across a broad spectrum, the earliest analyses of connections between organized convection in the tropics and the flow throughout the global atmosphere were performed to study seasonal circulation patterns associated with El Niño and the Southern Oscillation (ENSO). More recently, interest has risen in the intraseasonal band. This band includes the Madden–Julian Oscillation (MJO), various convectively coupled equatorial waves, oceanic waves that might couple to atmospheric convection (e.g., Lau and Shen, 1988), and other disturbances. Some authors have demonstrated that equatorial Rossby waves and convectively coupled atmospheric and oceanic Kelvin waves are associated with variations in extratropical circulation (e.g., Kiladis and Wheeler, 1995; Straub and Kiladis, 2003; Roundy, 2008; Roundy *et al.*, 2010). However, much of the research that has associated tropical convection organized on intraseasonal timescales with the global flow has focused on the MJO, leading to a similar focus for this chapter.

Teleconnection patterns around the global extratropics have been analyzed for decades, but only since the early 1980s have the connections between these patterns and the MJO been manifest in the literature. Weickmann (1983) initiated analysis of observed connections between tropical convection organized on intraseasonal timescales and extratropical flow. He calculated the leading empirical orthogonal functions (EOFs) of pentad-averaged outgoing longwave radiation (OLR) anomalies in the tropics as well as the leading EOFs of pentad-averaged wind data from the upper and lower troposphere. He observed that during some northern hemisphere winters, eastward-moving convective anomalies in the tropics evolve together with anomalies in extratropical flow. Subsequently, Weickmann *et al.* (1985) applied cross-spectrum analysis between OLR anomalies and the 250 hPa streamfunction. Their results demonstrate, for example, that the circumpolar vortex expands southward along the longitudes of enhanced convection in the equatorial region and retracts northward along the longitudes of suppressed convection.

Following the initial work of Weickmann (1983) and Weickmann *et al.* (1985), Lau and Phillips (1986) showed coherent fluctuations between extratropical flow and eastward-moving anomalies of convection in the tropics of the eastern hemisphere. Observational and model analyses from the same decade and since have added further detail to the nature of observed associations between intraseasonal tropical convection and the flow throughout the global atmosphere (e.g., Knutson and Weickmann, 1987; Hsu *et al.*, 1990; Hendon and Salby, 1994; Hsu, 1996; Matthews *et al.*, 2004). Hsu (1996) argues—in agreement with Lau and Phillips (1986)—that the intraseasonal oscillation is a global phenomenon and that it is inadequate to treat it as either purely tropical or purely extratropical. Thus, the extratropical patterns associated with the oscillation in tropical convection might evolve as part of the fundamental anatomy of the oscillation itself, a possibility largely ignored in many of the simple models that have attempted to describe the MJO.

14.2 A BOREAL WINTER COMPOSITE OF THE GLOBAL FLOW ASSOCIATED WITH THE MJO

The seasonally varying global weather patterns associated with the MJO are easily diagnosed from observed and reanalysis data. The simplest demonstration of the general association of the MJO with the flow in the global atmosphere is a composite average of variables that characterize that flow, based on periods of time when the MJO evolved through particular phases. The Wheeler–Hendon (2004) real time multivariate MJO (RMM) indices offer a convenient basis for such composites, especially since these indices have been applied widely in recent years (for an overview, see Chapter 12).

Composites of the global flow associated with particular phases of the RMM indices during a particular season are easily calculated by averaging fields of data over the dates when the RMM indices suggest a given phase and when the MJO is active as suggested by the square root of the sum of the squares of the two indices exceeding 1 standard deviation (in practice, this occurs roughly 62% of the time in the 1974–2009 data, as shown by direct analysis of the two indices). We include here, for reference, such a composite for events during December through February. Figure 14.1 shows composite 300 hPa geopotential height (contours) together with OLR anomalies (shaded, with negative anomalies in blue, plotted only in the tropics, for simplicity). Panels (a)–(h) give the results for RMM phases 1–8, respectively. The pair of composites in each row represent nearly opposite phases of the oscillation. The regions shaded blue (suggestive of enhanced convection) tend to progress eastward with increasing phase number. The largest composite height anomalies exceed 100 m. Composite height anomaly fields do not always appear to evolve continuously from one RMM phase to the next. However, most of the associated patterns evolve continuously and smoothly between the phases when observed in daily means (not shown). Height anomalies move generally eastward through the tropics, with ridges amplifying over time poleward of the regions of enhanced convection and troughs amplifying poleward of the regions of suppressed convection. For example, during phases 1–5, convection begins and amplifies eastward across the Indian Ocean basin and the maritime continent. As this convection amplifies, a trough anomaly over southern Asia is gradually replaced by a ridge anomaly that later extends eastward across the Pacific following the convection. Similarly, during phases 5–8, a ridge that occurs north of a region of amplifying suppressed convection over the Indian Ocean basin (phase 5) decays during phase 6 and then a trough anomaly amplifies and extends eastward following the region of suppressed convection.

These ridge and trough anomalies across the subtropics associate with wavetrains that frequently extend away from the tropics even to near the poles. Many authors have thus demonstrated large signals associated with the MJO in the Arctic and Antarctic oscillations (Carvalho *et al.*, 2005; Zhou and Miller, 2005; L'Heureux and Higgins, 2008), the Pacific North America pattern (e.g., Mori and Watanabe, 2008), and the North Atlantic oscillation (e.g., Cassou, 2008; Roundy *et al.*, 2010). Figure 14.1 suggests that the highest amplitude anomalies of

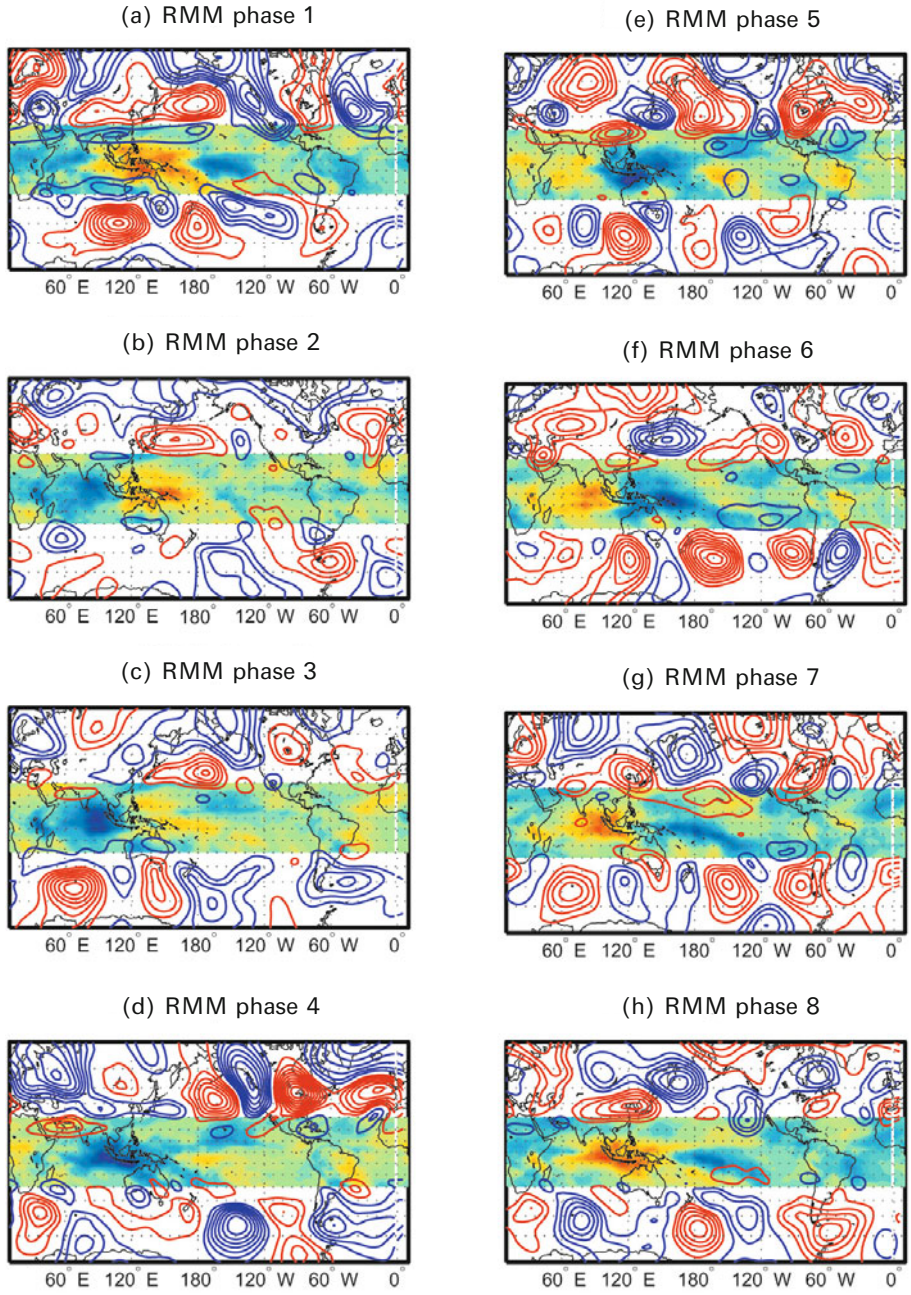

Figure 14.1. Composite OLR anomalies averaged over December through February (shaded, with negative anomalies suggestive of active convection in blue), and 300 hPa geopotential height anomalies (positive in red and negative in blue, with a contour interval of 15 m, and the zero anomaly is omitted). Panels (a)–(h) represent RMM phases 1–8, respectively.

300 hPa geopotential height associated with the MJO occur over the North Pacific and North Atlantic Oceans. The extratropical patterns associated with the MJO vary dramatically in both phase and amplitude with the status of ENSO and its temporal trend, as illustrated by the finding that composite signals in extratropical circulation associated with the MJO are substantially and significantly larger and found in different geographical locations when MJO events included in the averages are further sorted according to the ENSO phase in which they occur (Roundy *et al.* 2010).

Although the signals in OLR and geopotential height in Figure 14.1 are usually roughly opposite for the opposite panels within each row, some exceptions occur. These exceptions suggest asymmetries about the MJO cycle. However, some such asymmetries also result from a slightly different set of events averaged into the different phases. For example, some individual events might only attain the 1 standard deviation threshold during one or two phases, so the global pattern associated with those events would be included only in those phases. Such variation in RMM amplitude across the different phases during the same MJO event can sometimes be quasi-systematic. For example, the high-amplitude signals associated with one RMM phase at a given geographical location might occur during one ENSO state but not another. During development of La Niña conditions, high-amplitude expressions of RMM 6 and 7 are relatively infrequent, whereas phases 2–5 occur more often. Since the structure of the MJO and its associated global patterns change with ENSO (Roundy *et al.*, 2010), these changes would be expressed in Figure 14.1 as signals that are not opposite between opposite phases.

This composite analysis diagnoses the association between the MJO and extratropical signals, but it does not explain how these signals became associated with the MJO in the first place. Such associations could arise from a response of the global flow to heating in convection and/or from a response of convection to variations in extratropical flow. Most authors who have analyzed associations between flow in the extratropical atmosphere and the MJO have addressed this issue from one of these perspectives or the other rather than considering both directions of action simultaneously.

14.3 RESPONSE OF THE GLOBAL ATMOSPHERE TO HEATING IN TROPICAL CONVECTION

The global atmospheric circulation responds to heating in organized convection moving through the tropics (e.g., Bladé and Hartmann, 1995; Jin and Hoskins, 1995; Hendon and Salby, 1996; Matthews *et al.*, 2004). This response pattern includes overturning circulations through the tropics and Rossby wavetrains that extend poleward and around the globe. Jin and Hoskins (1995) force a simple model atmosphere in a DJF background state by a heat source fixed in space, with heating distributed in the vertical with a maximum heating rate near the 0.4 sigma level centered near the intersection of the equator and the dateline. Figure 14.2 shows the resulting equatorial cross-section of perturbation zonal flow after the heating

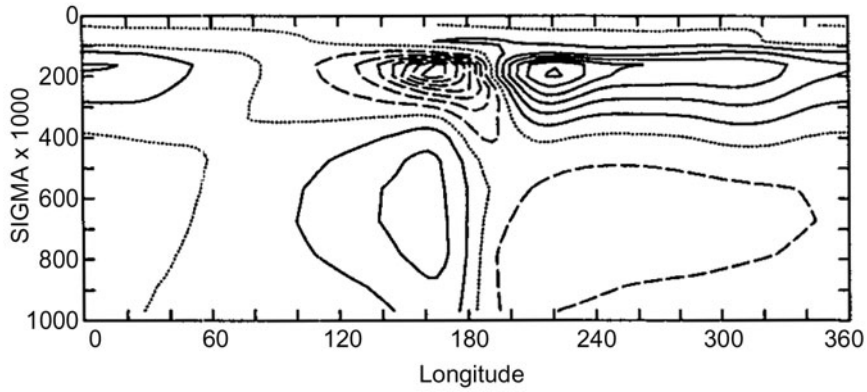

Figure 14.2. Vertical profile of a model response of zonal winds to heating on the equator (from Jin and Hoskins, 1995). This pattern develops after 15 days of heating, with a heating rate that increases with height from the surface of the earth to 0.4 sigma then decreases in intensity to zero near the tropopause. Heating is centered on the equator at the dateline. A background state equivalent to that of December through February is also assumed. Solid lines indicate westerly anomalies and dashed lines easterly anomalies.

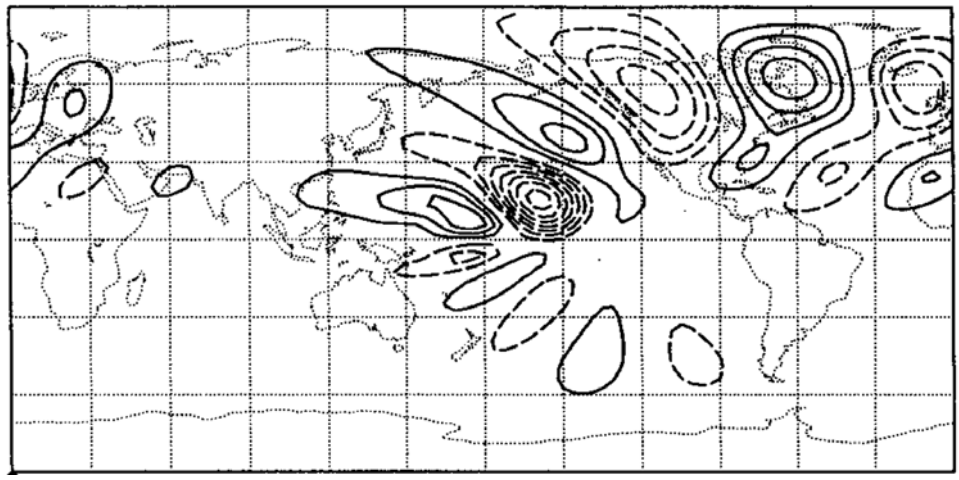

Figure 14.3. The horizontal pattern of streamfunction on the 0.24 sigma surface corresponding to the vertical cross-section shown in Figure 14.2. A northern hemisphere anticyclone is indicated by solid contours (from Jin and Hoskins, 1995).

continued for 15 days. Figure 14.2 demonstrates that the primary result of such heating in the equatorial plane is a vertical overturning circulation with an ascending branch in the vicinity of the heat source. Figure 14.3 shows the corresponding global pattern of streamfunction on the 0.24 sigma surface. This result indicates that upper-tropospheric ridges develop on the poleward sides of the heat

source. These ridges are a consequence of mass redistributed as the atmosphere expands in response to the heating. As the upper-level flow accelerates poleward in response to associated pressure gradient forces, the Coriolis force and the beta effect induce anticyclinic upper-level flow (the beta effect may be larger because of the proximity to the equator). This geostrophic adjustment process also yields development of a trough downstream from the ridge. This pattern of downstream development is manifest as Rossby wave dispersion from the heat source toward the poles, deflected eastward by the prevailing westerly flow. The amplitude of the Rossby wave response is greatest across the winter hemisphere.

To diagnose the more specific response to patterns of convection more like those of the observed MJO, Matthews *et al.* (2004) force a primitive equation spectral transform model in a DJF background state with patterns of prescribed heating characteristic of the observed MJO. The flow in the model tropics characteristic of the MJO developed after a few days of initiating the prescribed heating and anomalies developed across the extratropics after about 2 weeks. The resulting global response to that heating is similar in many respects to the regression models and composite averages of observed data that show the actual weather patterns that associate with the MJO. However, the model result for the midlatitude circulation is shifted roughly 20 degrees of longitude from the observed pattern. Matthews *et al.* (2004) suggest that this phase shift might be associated with lack of a damping process in the regions of convective heating in their model.

14.4 INFLUENCE OF EXTRATROPICAL WAVES ON TROPICAL CONVECTION

Analysis of the influence of extratropical waves on tropical convection commenced before Weickmann (1983) diagnosed associations between tropical intraseasonal oscillations and the extratropical flow. Early works demonstrated that extratropical waves propagate into the tropics through regions of westerly wind (Lim and Chang, 1981; Webster and Holton, 1982), where they modulate tropical convection over a range of timescales that include those of the MJO (e.g., Matthews and Kiladis 1999a). Liebmann and Hartmann (1984) demonstrate large correlations between tropical convection and extratropical wave patterns and argue that most of the covariance in 5 and 10-day averaged data is associated with forcing of tropical convection by the extratropical flow, rather than the other way around. Hoskins and Yang (2000) further show that extratropical waves that merely propagate parallel to the tropics can also disturb the equatorial waveguide and help organize convection in the tropics, even if extatropical waves do not propagate directly into the tropics through regions of westerly wind. In an intermediate complexity model, Lin *et al.* (2000) show that extratropical wave activity could interact with wind–evaporation feedback in the tropics to generate patterns in the tropics that evolve like the MJO. More recently, Ray *et al.* (2009) and Ray and Zhang (2010) showed that a dry-channel model of the tropical atmosphere developed MJO-like signals in tropical wind fields when forced by reanalysis fields at poleward boundaries, but did

not develop such signals internally when forced at the periphery by climatological winds. These results suggested to Ray *et al*. that extratropical patterns might force the organization of the MJO itself.

Extratropical waves also influence the organization of convection in the tropics on timescales shorter than those of the MJO. Such waves might influence progression of the MJO through some rectification process. For example, Rossby waves in the 6 to 30-day band propagate equatorward into the eastern equatorial Pacific basin, where they trigger convection along the ITCZ (Kiladis and Weickmann, 1992). Matthews and Kiladis (1999a) demonstrate that the convection that develops in the East Pacific ITCZ region in association with these extratropical waves rectifies back onto MJO timescales. This rectified signal in active convection moves eastward across the East Pacific to the east of the core of the MJO active convection, which occurs simultaneously over the West Pacific. In addition to the tropical convection organized by direct propagation of extratropical waves into the tropics through regions of westerly wind, further observational analyses show that convectively coupled Kelvin waves develop in association with extratropical waves, even in regions of easterly background flow that would prevent direct propagation into the tropics (Straub and Kiladis 2002), consistent with the model analysis of Hoskins and Yang (2000).

14.5 TWO-WAY INTERACTIONS BETWEEN THE TROPICS AND EXTRATROPICS

Some early authors acknowledged the possibility of two-way interactions between organized convection in the tropics and circulation in the extratropical atmosphere. Such interactions might facilitate the development of coherent circulation anomalies across the two regions (e.g., Lau and Phillips, 1986). The vast majority of more recent works, however, have emphasized either forcing of the tropics by extratropical waves or forcing of extratropical waves by tropical convection. Coherent circulation anomalies that bridge the tropics and the extratropics might be possible in part because the midlatitude response to tropical convection in one region can subsequently influence the evolution of convection elsewhere in the tropics. For example, a Rossby wavetrain forced by convection over Indonesia during the local active convective phase of the MJO acts to enhance convection farther east within the South Pacific Convergence Zone (Matthews and Meredith, 2004). Extratropical waves propagate into the tropics of the eastern equatorial Pacific as the MJO and ENSO combine to induce westerly winds across the region (Matthews and Kiladis, 1999a). Such extratropical wavetrains occasionally develop in association with the MJO and convectively coupled Kelvin wave activity farther west. In summary, these results suggest that:

(1) The MJO and other phenomena of organized tropical convection can induce extratropical waves.

(2) The circulation associated with the combination of the MJO and the background state can later guide the extratropical waves in (1) back into or parallel to the tropics in other geographical regions.
(3) These extratropical waves disturb the equatorial waveguide and further influence the local development and organization of convection associated with the MJO.
(4) The tropical convection influenced by extratropical waves can then redistribute mass, yielding Rossby wave dispersion to the extratropics, resulting in a continuously interactive feedback loop.

Consistent with this view, Moore *et al.* (2010) demonstrate that Rossby waves initially forced by convection within the MJO frequently break across the subtropics and in turn modulate further development of tropical convection. Figure 14.4 illustrates how the active convective phase of the MJO approaching the maritime continent region is associated with Rossby wave development near South East Asia and extension of a subtropical jet stream eastward across the Central Pacific basin (figure adapted from Moore *et al.*, 2010). An anticyclonic wave-breaking event frequently develops across the Central Pacific basin at this stage of the MJO, which yields an upper-level trough in the deep tropics. Although this trough enhances convection on its eastern side, it suppresses convection on its western side, reinforcing the suppressed convective phase of the MJO over the west central Pacific basin.

The above works taken together suggest that the MJO might influence extratropical flow and then in turn be modulated thereby. Apparent dependence of the MJO on baroclinic instability along the subtropical jet stream (e.g., Straus

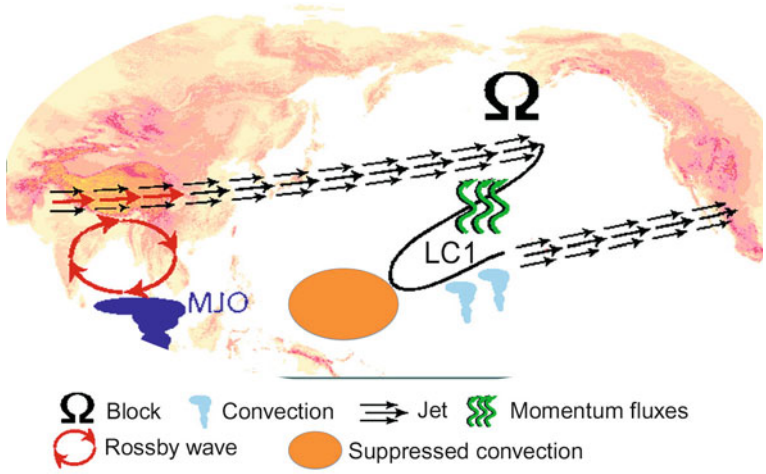

Figure 14.4. Schematic representation of the MJO and its associated patterns across higher latitudes as its active convection approaches the maritime continent, highlighting its association with breaking Rossby waves across the Central Pacific basin. LC1 refers to an anticyclonic wave-breaking event (adapted from Moore *et al.*, 2010).

and Lindzen, 2000) suggests that these types of interactions between the MJO and the global flow might even be fundamental to the structure and evolution of the MJO itself (consistent with the model results of Lin *et al.*, 2000). In the context of the above results in which planetary waves respond to heating in convection within the MJO, the MJO-like wind signals in the tropical channel models of Ray *et al.* (2009) and Ray and Zhang (2010) might have developed at least in part because of extratropical signals in the reanalysis data that were forced by the MJO itself.

Accounting for such two-way interactions between the tropics and extratropics might help explain some discrepancies between model experiments and observations when authors assume that observed patterns might be forced exclusively by the tropics or exclusively by the midlatitudes. For example, part of the phase shift between the global response to MJO convection in the model of Matthews *et al.* (2004) and observed extratropical patterns might be associated with a lack of modulation of tropical convection by the extratropical flow in their model.

In spite of strong associations between tropical convection and higher latitude flow, both convection in the tropics and flow in the extratropical atmosphere contain substantial signals not explained by the other. Distinguishing the portion of the global flow anomaly that is associated with the MJO from the portion that is apparently not would benefit forecasters and other stakeholders. Some authors have developed algorithms for tracking the evolution of the MJO and extratropical patterns that frequently evolve with it. For example, Weickmann and Berry (2009) demonstrate that convection in the MJO frequently evolves together with a portion of the activity in a broader spectrum ''global wind oscillation''. They have developed indices for tracking the progress of this wind oscillation in near real time. The patterns commonly associated with the extratropical response to MJO convection are among the broader set of structures of this global wind oscillation.

14.6 MJO INFLUENCE ON THE PREDICTABILITY OF THE GLOBAL FLOW

The gradual evolution of tropical intraseasonal oscillations together with an understanding of the global circulation patterns that tend to evolve with them suggests that these oscillations might be applied to predict the evolution of a portion of the flow throughout the global atmosphere (Ferranti *et al.*, 1990). Traditional weather forecasting in the midlatitudes has developed one focus based largely on numerical weather prediction, which has generally been deemed most effective for forecast lead times shorter than roughly 1 week, and a second focus based on monthly (e.g., Vitart, 2004) or seasonal (e.g., Livezey and Timofeyeva, 2008; Preisendorfer and Mobley, 1984) prediction of the background climate state. Some forecasters have begun to apply understanding of tropical intraseasonal oscillations and their associations with midlatitude flows to help make predictions of midlatitude weather at lead times between the weekly and monthly forecast regimes.

Increased understanding of the observed teleconnection patterns associated with organized intraseasonal convection in the tropics has led to extension of skillful predictions of the evolving background state weather conditions around the globe into week 2 and beyond (e.g., Jiang *et al*., 2008; Vitart *et al*., 2008). By predicting the gradual evolution of the MJO (e.g., Waliser *et al*., 1999; Jiang *et al*., 2008; Gottschalk *et al*., 2010), it might be possible to use empirical means to predict the associated extratropical patterns. Such predictions straddle the weather–climate interface and have thus become of great interest in both private and government sectors.

Most empirical approaches to predict the extratropical patterns associated with tropical intraseasonal oscillations require first some choice of indices of the oscillations. Composite or linear regression analyses relate the selected indices to the corresponding "expectation values" of global weather patterns. Forecasts of future global patterns can be generated simply by introducing time lags into the composite or regression analyses or by predicting the indices themselves and referencing the corresponding favored global pattern for the target season (e.g., Jiang *et al*., 2008; Kang and Kim, 2010). Such predictions are more effective when global patterns are estimated based on events from similar ENSO states (e.g., Roundy *et al*., 2010).

Many of the statistical models applied for such prediction simply capitalize on observed patterns, regardless of the causes of those patterns. Such empirical prediction schemes are necessary because a consensus does not exist on the fundamental dynamics of the MJO itself and because most numerical models poorly simulate the MJO. Our apparent lack of understanding of the physics of the MJO thus does not prevent us from capitalizing on its signals to predict the evolutions of associated global flows. On the other hand, our lack of understanding of the dynamics of the MJO and our inability to simulate it properly is reflected in our lack of ability to predict the MJO beyond 30 days, or only about one half of an MJO cycle.

14.7 DISCUSSION

The MJO is associated with significant signals that extend around the globe and throughout the seasonal cycle. Organized convection in its active convective phase results in a planetary wave response that modulates teleconnection patterns around the globe. Convection organized in the tropics associated with the MJO is also strongly modulated by extratropical waves, including those that previously originated within the MJO itself. Such associations suggest the possibility that coupling between the tropics and the extratropics might be fundamental to the evolution and structure of the MJO. The associated global signals modulate extreme weather events. Since numerical weather prediction models tend to poorly simulate the MJO, MJO modulation of extreme events would reduce our ability to predict such events at long range by deterministic means until simulation of the MJO improves.

14.8 REFERENCES

Allen, G., G. Vaughan, D. Brunner, P. T. May, W. Heyes, P. Minnis, and J. K. Ayers (2008) Modulation of tropical convection by breaking Rossby waves. *Quart. J. Roy. Meteorol. Soc.*, **135**(638), 125–137, doi: 10.1002/qj.349.

Anderson, J. R. and R. D. Rosen (1983) The latitude–height structure of 40–50 day variations in atmospheric angular momentum. *J. Atmos. Sci.*, **40**, 1584–1591.

Arkin, P. and P. J. Webster (1985) Annual and interannual variability of tropical–extratropical interaction: An empirical study. *Mon. Wea. Rev.*, **113**, 1510–1523.

Bladé, I. and D. L. Hartmann (1995) The linear and nonlinear extratropical response to tropical intraseasonal heating. *J. Atmos. Sci.*, **52**, 4448–4471.

Brankovic, C., T. Palmer, and L. Ferranti (1994) Predictability of seasonal atmospheric variations. *J. Climate*, **7**, 217–237.

Branstator, G. W. (2002) Circumglobal teleconnections, the jet stream waveguide, and the North Atlantic Oscillation. *J. Climate*, **15**, 1893–1910.

Carvalho, L. M. V., C. Jones, and T. Ambrizzi (2005) Opposite phases of the Antarctic oscillation and relationships with intraseasonal to interannual activity in the tropics during austral summer. *J. Climate*, **18**, 702–718.

Cassou, C. (2008) Intraseasonal interaction between the Madden–Julian Oscillation and the North Atlantic Oscillation. *Nature*, **455**, 523–527.

Charney, J. and J. Shukla (1981) Predictability of monsoons. In: J. Lighthill and R. Pearce (Eds.), *Monsoon Dynamics*. Cambridge University Press, Cambridge, U.K., chap. 6.

Donald, A., H. Meinke, B. Power, M. C. Wheeler, A. de H.N. Maia , R. C. Stone, J. Ribbe, and N. White (2006) Near-global impact of the Madden–Julian Oscillation on rainfall. *Geophys. Res. Lett.*, **33**, L09704, 4 pp, doi: 10.1029/2005GL025155.

Ferranti, L., T. N. Palmer, F. Molteni, and K. Klinker (1990) Tropical–extratropical interaction associated with the 30–60 day oscillation and its impact on medium and extended range prediction. *J. Atmos. Sci.*, **47**, 2177–2199.

Frank, W. M. and P. E. Roundy (2006) The relationship between tropical waves and tropical cyclogenesis. *Mon. Wea. Rev.*, **134**, 2397–2417.

Frederiksen, J. S. and C. S. Frederiksen (1997) Mechanisms of the formation of intraseasonal oscillations and Australian monsoon disturbances: The roles of convection, barotropical and baroclinic instability. *Beitr. Phys. Atmos.*, **70**, 39–56.

Gottschalck, J., M. Wheeler, K. Weickmann, F. Vitart, N. Savage, H. Lin, H. Hendon, D. Waliser, K. Sperber, M. Nakagawa *et al.* (2010) A framework for assessing operational Madden–Julian Oscillation forecasts: A CLIVAR MJO Working Group project. *Bull. Amer. Meteorol. Society*, **91**, 1247–1258.

Gruber, A. (1974) The wavenumber–frequency spectra of satellite-measured brightness in the tropics. *J. Atmos. Sci.*, **31**, 1675–1680.

Hendon, H. H. and B. Liebmann (1991) The structure and annual variation of antisymmetric fluctuations of tropical convection and their association with Rossby–gravity waves. *J. Atmos. Sci.*, **48**, 2127–2140.

Hendon, H. H. and M. L. Salby (1994) The life cycle of the Madden–Julian Oscillation. *J. Atmos. Sci.*, **51**, 2225–2237.

Hendon, H. H. and M. L. Salby (1996) Planetary-scale circulations forced by intraseasonal variations of observed convection. *J. Atmos. Sci.*, **53**, 1751–1758.

Hendon, H. H., B. Liebmann, M. Newman, J. D. Glick, and J. E. Schemm (2000) Medium-range forecast errors associated with active episodes of the Madden–Julian oscillation. *Mon. Wea. Rev.*, **128**, 69–86.

Higgins, R. W. and K. C. Mo (1997) Persistent North Pacific circulation anomalies and the tropical intraseasonal oscillation. *J. Climate*, **10**, 223–244.

Higgins, R. W., J.-K. E. Schemm, W. Shi, and A. Leetmaa (2000) Extreme precipitation events in the western United States related to tropical forcing. *J. Climate*, **14**, 403–417.

Hoskins, B. J. and G.-Y. Yang (2000) The equatorial response to higher latitude forcing. *J. Atmos. Sci.*, **57**, 1197–1213.

Hsu, H.-H. (1996) Global view of the intraseasonal oscillation during northern winter. *J. Climate*, **9**, 2386–2406.

Hsu, H.-H., B. J. Hoskins, and F.-F. Jin (1990) The 1985/86 intraseasonal oscillation and the role of the extratropics. *J. Atmos. Sci.*, **47**, 823–839.

Jiang, X., D. E. Waliser, M. Wheeler, C. Jones, M.-I. Lee, and S. Schubert (2008) Assessing the skill of an all-season statistical forecast model for the Madden–Julian Oscillation. *Mon. Wea. Rev.*, **136**, 1940–1956.

Jin, F. and B. J. Hoskins (1995) The direct response to tropical heating in a baroclinic atmosphere. *J. Atmos. Sci.*, **52**, 307–319.

Jones, C. (2000) Occurrence of extreme precipitation events in California and relationships with the Madden–Julian Oscillation. *J. Climate*, **13**, 3576–3587.

Jones, C. and J.-K. E. Schemm (2000) The influence of intraseasonal variations on medium-range weather forecasts over South America. *Mon. Wea. Rev.*, **128**, 486–494.

Jones, C. (2000) Occurrence of extreme precipitation events in California and relationships with the Madden–Julian Oscillation. *J. Climate*, **13**, 3576–3587.

Jones, C., D. E. Waliser, K. M. Lau, and W. Stern (2004a) Global occurrences of extreme precipitation and the Madden–Julian Oscillation: Observations and predictability. *J. Climate*, **17**, 4575–4589.

Jones, C., D. E. Waliser, K. M. Lau, and W. Stern (2004b) The Madden–Julian oscillation and its impact on Northern Hemisphere weather predictability. *Mon. Wea. Rev.*, **132**, 1462–1471.

Kang, I.-S. and H.-M. Kim (2010) Assessment of MJO predictability for boreal winter with various statistical and dynamical models. *J. Climate*, **23**, 2368–2378.

Kiladis, G. N. and K. M. Weickmann (1992) Extratropical forcing of tropical Pacific convection during northern winter. *Mon. Wea. Rev.*, **120**, 1924–1938.

Kiladis, G. N. and M. C. Wheeler (1995) Horizontal and vertical structure of observed tropospheric equatorial Rossby waves. *J. Geophys. Res.*, **100**, 22981–22997.

Kiladis, G. N., C. D. Thorncroft, and N. M. J. Hall (2006) Three-dimensional structure and dynamics of African easterly waves, Part I: Observations. *J. Atmos. Sci.*, **63**, 2212–2230.

Kiladis, G. N., M. C. Wheeler, P. T. Haertel, K. H. Straub, and P. E. Roundy (2009) Convectively coupled equatorial waves. *Rev. Geophys.*, **47**, RG2003, doi: 10.1029/2008RG000266.

Knutson, T. R. and K. L. Weickmann (1987) 30–60 day atmospheric oscillations: Composite life cycles of convection and circulation anomalies. *Mon. Wea. Rev.*, **115**, 1407–1435.

Krishnamurti, T. N., P. K. Jayakumar, J. Sheng, N. Surgi, and A. Kumar (1985) Divergent circulations on the 30 to 50 day time scale. *J. Atmos. Sci.*, **42**, 364–375.

Lau, K.-M. and T. J. Phillips (1986) Coherent fluctuations of extratropical geopotential height and tropical convection in intraseasonal timescales. *J. Atmos. Sci.*, **43**, 1164–1181.

Lau, K.-M. and S. Shen (1988) On the dynamics of intraseasonal oscillations and ENSO. *J. Atmos. Sci.*, **25**, 1781–1797.

Liebmann, B. and D. L. Hartmann (1984) An observational study of tropical–midlatitude interaction on intraseasonal time scales during winter. *J. Atmos. Sci.*, **41**, 3333–3350

Liebmann, B. and H. H. Hendon (1990) Synoptic-scale disturbances near the equator. *J. Atmos. Sci.*, **47**, 1463–1479.

Liebmann, B. and C. A. Smith (1996) Description of a complete (interpolated) outgoing longwave radiation dataset. *Bull. Amer. Meteorol. Society*, **77**, 1275–1277.

Lim, H. and C. P. Chang (1981) A theory of midlatitude forcing of tropical motions during the winter monsoon. *J. Atmos. Sci.*, **41**, 3333–3350.

Lin, J.-L., G. N. Kiladis, B. E. Mapes, K. M. Weickmann, K. R. Sperber, W. Lin, M. C. Wheeler, S. D. Schubert, A. D. Genio, L. J. Donner *et al.* (2006) Tropical intraseasonal variability in 14 IPCC AR4 climate models, Part I: Convective signals. *J. Climate*, **19**, 2665–2690.

Lin, J. W.-B., J. D. Neelin, and N. Zeng (2000) Maintenance of tropical intraseasonal variability: Impact of evaporation–wind feedback and midlatitude storms. *J. Atmos. Sci.*, **57**, 2793–2823.

Lin, H., G. Brunet, and J. Derome (2009) An observed connection between the North Atlantic oscillation and the Madden–Julian oscillation. *J. Climate*, **22**, 364–380.

Lindzen, R. S. (1967) Planetary waves on beta planes. *Mon. Wea. Rev.*, **95**, 441–451.

Livezey, R. E. and M. M. Timofeyeva (2008) The first decade of long-lead U.S. seasonal forecasts: Insights from a skill analysis. *Bull. Amer. Meteorol. Society*, **89**, 843–854.

L'Heureux, M. L. and R. W. Higgins (2008) Boreal winter links between the Madden–Julian oscillation and the Arctic Oscillation. *J. Climate*, **21**, 3040–3050.

Madden, R. A. and P. R. Julian (1994) Observations of the 40–50-day tropical oscillation: A review. *Mon. Wea. Rev.*, **122**, 814–837.

Majda, A. J., B. Khouider, G. N. Kiladis, K. H. Straub, and M. G. Shefter (2004) A model for convectively coupled tropical waves: Nonlinearity, rotation, and comparison with observations. *J. Atmos. Sci.*, **61**, 2188–2205.

Matsuno, T. (1966) Quasi-geostrophic motions in the equatorial area. *J. Meteorol. Soc. Japan*, **44**, 25–43.

Kiladis, G. N. and Wheeler, M. (1995) Horizontal and vertical structure of observed tropospheric equatorial Rossby waves. *J. Geophys. Res.*, **100**, 22981–22997.

Matthews, A. J. and G. N. Kiladis (1999a) The tropical–extratropical interaction between high-frequency transients and the Madden–Julian oscillation. *Mon. Wea. Rev.*, **127**, 661–677.

Matthews, A. J. and G. N. Kiladis (1999b) Interactions between ENSO, transient circulation, and tropical convection over the eastern tropical Pacific. *J. Climate*, **12**, 3062–3086.

Matthews, A. J. and G. N. Kiladis (2000) A model of Rossby waves linked to submonthly convection over the eastern tropical Pacific. *J. Atmos. Sci.*, **57**, 3785–3798.

Matthews, A. J. and M. P. Meredith (2004) Variability of Antarctic circumpolar transport and the Southern Annual Mode associated with the Madden–Julian Oscillation. *Geophys. Res. Lett.*, **31**, L24312, doi: 10.1029/2004GL021666.

Matthews, A. J., B. J. Hoskins, J. M. Slingo, and M. Blackburn (1996) Development of convection along the SPCZ within a Madden–Julian Oscillation. *Quart. J. Roy. Meteorol. Soc.*, **122**, 669–688.

Matthews, A. J., B. J. Hoskins, and M. Masutani (2004) The global response to tropical heating in the Madden–Julian oscillation during northern winter. *Quart. J. Roy. Meteorol. Soc.*, **130**, 1991–2011.

Mo, K. C. (2000) Intraseasonal modulation of summer precipitation over North America. *Mon. Wea. Rev.*, **128**, 1490–1505.

Mo, K. C. and R. W. Higgins (1998) Tropical influences on California precipitation. *J. Climate*, **11**, 412–430.

Molteni, F. and L. Ferranti (2000) *Non-linear Aspects of Systematic Errors of the ECMWF Coupled Model* (technical report). European Centre for Medium-Range Weather Forecasts, Reading, U.K.

Moore, R. W., O. Martius, and T. Spengler (2010) The modulation of the subtropical and extratropical atmosphere in the Pacific Basin in response to the Madden Julian Oscillation. *Mon. Wea. Rev.*, in press.

Mori, M. and M. Watanabe (2008) The growth and triggering mechanisms of the PNA: A MJO–PNA coherence. *J. Meteorol. Soc. Japan*, **86**, 213–236.

Nogues-Paegle, J., L. A. Byerle, and K. C. Mo (2000) Intraseasonal modulation of South American summer precipitation. *Mon. Wea. Rev.*, **128**, 837–850.

Pohl, B. and A. J. Matthews (2007) Observed changes in the lifetime and amplitude of the Madden–Julian oscillation associated with interannual ENSO sea surface temperature anomalies. *J. Climate*, **20**, 2659–2674.

Preisendorfer, R. W. and C. D. Mobley (1984) Climate forecast verifications: United States mainland, 1974–1983. *Mon. Wea. Rev.*, **112**, 809–825.

Ray, P. and C. Zhang (2010) A case study on the mechanisms of extratropical influence on the Madden–Julian Oscillation. *J. Atmos. Sci.*, **67**, 515-528.

Ray, P., C. Zhang, J. Dudhia, and S. S. Chen (2009) A numerical case study on the initiation of the Madden–Julian Oscillation. *J. Atmos. Sci.*, **66**, 310-331.

Roundy, P. E. (2008) Analysis of convectively coupled Kelvin waves in the Indian Ocean MJO. *J. Atmos. Sci.*, **65**, 1342–1359.

Roundy, P. E. and G. N. Kiladis (2006) Observed relationships between oceanic Kelvin waves and atmospheric forcing. *J. Climate*, **19**, 5253–5272.

Roundy, P. E. and J. R. Kravitz (2009) The association of the evolution of intraseasonal oscillations with ENSO phase. *J. Climate*, **22**, 381–395.

Roundy, P. E. and L. G. Verhagen (2010) Variations in the flow of the global atmosphere associated with a composite convectively coupled oceanic Kelvin wave. *J. Climate*, **23**, 4192–4201.

Roundy, P. E., K. MacRitchie, J. Asuma, and T. Melino (2010) Modulation of the global atmospheric circulation by combined activity in the Madden–Julian Oscillation and the El Niño/Southern Oscillation during boreal winter. *J. Climate*, **23**, 4045–4059.

Sardeshmukh, P. D. and B. J. Hoskins (1988) The generation of global rotational flow by steady idealized tropical divergence. *J. Atmos. Sci.*, **45**, 1228–1251.

Shinoda, T. and H. H. Hendon (2002) Rectified wind forcing and latent heat flux produced by the Madden–Julian Oscillation. *J. Climate*, **15**, 3500–3507.

Straub, K. H. and G. N. Kiladis (2002) Observations of a convectively coupled Kelvin wave in the eastern Pacific ITCZ. *J. Atmos. Sci.*, **59**, 30–53.

Straub, K. H. and G. N. Kiladis (2003) Interactions between the boreal summer intraseasonal oscillation and higher frequency tropical wave activity. *Mon. Wea. Rev.*, **131**, 945–960.

Straus, D. M. and R. S. Lindzen (2000) Planetary-scale baroclinic instability and the MJO. *J. Atmos. Sci.*, **57**, 3609–3626.

Vecchi, G. A. and N. A. Bond (2004) The Madden–Julian Oscillation (MJO) and northern high latitude wintertime surface air temperatures. *Geophys. Res. Lett.*, **31**, L24312, doi: 10.1029/2004GL021666.

Vitart, F. (2004): Monthly forecasting at ECMWF. *Mon. Wea. Rev.*, **132**, 2761–2779.

Vitart, F. *et al.* (2008) The new VAREPA-monthly forecasting system: A first step toward seemless prediction. *Quart. J. Roy. Meteorol. Soc.*, **134**, 1789–1799.

Waliser, D. E., K. M. Lau, and J.-H. Kim (1999) Influence of coupled sea surface temperatures on the Madden Julian Oscillation: A model perturbation experiment. *J. Atmos. Sci.*, **56**, 333–358.

Wallace, J. M. and D. S. Gutzler (1981) Teleconnections in the geopotential height field during Northern Hemisphere winter. *Mon. Wea. Rev.*, **109**, 784–812.

Webster, P. J. and J. R. Holton (1982) Cross-equatorial response to middle-latitude forcing in a zonally varying basic state. *J. Atmos. Sci.*, **39**, 722–733.

Weickmann, K. M. (1983) Intraseasonal circulation and outgoing longwave radiation modes during northern winter. *Mon. Wea. Rev.*, **111**, 1838–1858.

Weickmann, K. M. and E. Berry (2007) A synoptic–dynamic model of subseasonal atmospheric variability. *Mon. Wea. Rev.*, **135**, 449–474.

Weickmann, K. and E. Berry (2009) The tropical Madden–Julian oscillation and the global wind oscillation. *Mon. Wea. Rev.*, **137**, 1601–1614.

Weickmann, K. M. and P. D. Sardeshmukh (1994) The atmospheric angular momentum cycle associated with the Madden–Julian oscillation. *J. Atmos. Sci.*, **51**, 3194–3208.

Weickmann, K. M., G. R. Lussky, and J. E. Kutzbach (1985) A global scale analysis of intraseasonal fluctuations of outgoing longwave radiation and 250 mb streamfunction during northern winter. *Mon. Wea. Rev.*, **113**, 941–961.

Weickmann, K. M., G. N. Kiladis, and P. D. Sardeshmukh (1997) The dynamics of intraseasonal atmospheric angular momentum oscillations. *J. Atmos. Sci.*, **54**, 1445–1461.

Wheeler, M. and H. H. Hendon (2004) An all-season real-time multivariate MJO index: Development of an index for monitoring and prediction. *Mon. Wea. Rev.*, **123**, 1917–1932.

Wheeler, M. and G. N. Kiladis (1999) Convectively coupled equatorial waves: Analysis of clouds and temperature in the wavenumber–frequency domain. *J. Atmos. Sci.*, **56**, 374–399.

Wheeler, M. C. and K. M. Weickmann (2001) Real time monitoring and prediction of modes of coherent synoptic to intraseasonal tropical variability. *Mon. Wea. Rev.*, **129**, 2677–2694.

Whitaker, J. S. and K. M. Weickmann (2001) Subseasonal variations of tropical convection and week two prediction of wintertime western North American rainfall. *J. Climate*, **14**, 1524–1534.

Wilks, D. S. (2006) *Statistical Methods in the Atmospheric Sciences*. Academic Press, San Diego, CA, 627 pp.

Zhang, C. (2005) The Madden–Julian Oscillation. *Rev. Geophys.*, **43**, RG2003, doi: 10.1029/2004RG000158.

Zangvil, A. (1975) Temporal and spatial behavior of large-scale disturbances in tropical cloudiness deduced from satellite brightness data. *Mon. Wea. Rev.*, **103**, 904–920.

Zangvil, A. and M. Yanai (1981) Upper tropospheric waves in the tropics, Part II: Association with clouds in the wavenumber–frequency domain. *J. Atmos. Sci.*, **38**, 939–953.

Zhou, S. and A. J. Miller (2005) The interaction of the Madden–Julian Oscillation and the Arctic Oscillation. *J. Climate*, **18**, 143–159.

15

Oceans and air–sea interaction

Jean Philippe Duvel

15.1 INTRODUCTION

Since the publication of the First Edition of this book, many new studies have focused on the role of air–sea interaction in tropical atmospheric intraseasonal variability (ISV). The aim of this section is to summarize the results of these new studies and to extract their main conclusions. This chapter is thus an update of Chapters 6 (W. Kessel) and 7 (H. Hendon) and is also a complement to the revised Chapter 9 (W. Lau).

The interaction between the upper-ocean thermal structure and large-scale organized convective perturbations is probably key to understanding the physical source of tropical ISV. These large-scale organized convective perturbations have typical horizontal scales of several thousand kilometers and correspond to the super-cloud clusters (SCCs) examined by Nakazawa (1988) or, more recently, by Yamada *et al*. (2010). Recent progress has been achieved in the analysis of intraseasonal perturbations of the upper-ocean structure related to these SCCs—in particular, through the use of new measurements of sea surface temperature (SST) from the Tropical Rainfall Measuring Mission (TRMM) microwave imager (TMI) and through new in situ measurements given by the floats of the Array for Real-time Geostrophic Oceanography (ARGO) and by the deployment of the Research moored Array for African–Asian–Australian Monsoon Analysis and Prediction (RAMA) (McPhaden *et al*., 2009) in the Indian Ocean.

Other advances were achieved concerning scale interactions—in particular, for the potential importance of the diurnal cycle in amplifying the ISV of SST. Ocean diurnal warm layers (DWLs) do indeed develop at the ocean surface under low wind conditions—in particular, during the convectively suppressed phase of ISV. These DWLs thus increase average SST and surface turbulent fluxes prior to the intra-seasonal convective phase and may influence the simulation and forecast of ISV. Concerning the relation between ISV and interannual variability, new results were

W. K. M. Lau and D. E. Waliser (Editors), *Intraseasonal Variability in the Atmosphere–Ocean Climate System* (Second Edition).

reported on the link between ISV and the Indian Ocean Dipole (IOD). The influence of ISV on the triggering and termination of El Niño events is discussed in Chapter 9.

The impact of air–sea interaction on the initiation and evolution of atmospheric ISV has also been studied in more detail using general circulation models (GCMs). Recent studies confirm that coupling with the ocean may improve the amplitude (e.g., Zheng *et al*., 2004) or the predictability (e.g., Fu *et al*., 2008) of ISV. However, this coupling is not absolutely necessary for a reasonable description of ISV, and the ability of a given coupled GCM (CGCM) to simulate ISV generally reflects mostly the skill of the atmospheric GCM (AGCM) (see also Section 7.6). Some studies based on idealized models even show that the coupling might damp ISV under some circumstances (e.g., Grabowski, 2006). In addition, the simulation of ISV is very variable from one coupled model to another (Lin *et al*., 2006; Zhang *et al*., 2006; Xavier *et al*., 2010). While a few CGCMs represent ISV well, most of them simulate wrong ISV amplitude and perturbation patterns (i.e., maps of amplitude and propagation characteristics). Should we conclude that coupling with the ocean has only a marginal impact on tropical intraseasonal variability? This point is discussed at the end of this chapter.

15.2 THE SOURCE OF SST INTRASEASONAL PERTURBATIONS

15.2.1 Observed ISV of the SST

Several new observational studies on the ISV of SST are based on measurements from the Tropical Rainfall Measuring Mission (TRMM) microwave imager (TMI). The main advantage of TMI is to give a good estimate of the day-to-day variability of SST, even under cloudy conditions (Wentz *et al*., 2000). An illustration is given here on the basis of daily TMI OI SST time series on a 0.25×0.25 degree grid. With this good spatial resolution, it is possible to separate the ISV of SST due to small-scale (i.e., $<$10 degrees) internal ocean waves and eddies from the ISV of SST due to large-scale atmospheric perturbations. This point is illustrated in Figure 15.1 showing the tropical SST field for August 1, 1998 (Figure 15.1a), and the corresponding intraseasonal SST anomaly for the same day obtained by filtering SST in time using a 20 to 100-day passband Lanczos filter (Figure 15.1b). This filtered SST field exhibits small-scale structures such as eddies related to the great whirls off the Somalia coast or tropical instability waves (TIWs) over the eastern Pacific Ocean and the Atlantic Ocean. Large-scale intraseasonal SST anomalies are visible in Figure 15.1b, such as the cold band over the northern Indian Ocean and the warm area in the eastern equatorial Indian Ocean. In order to estimate the part of the ISV of the SST due to intraseasonal atmospheric perturbations, this large-scale signal is extracted using a very simple box average smoothing technique (continental regions are ignored for coastal areas). The size of the box (12×12 degrees), although somewhat arbitrary, allows filtering out most of the TIW signal, as shown on Figure 15.1c. The hypothesis is that these large-scale structures (Figure 15.1c) are mostly generated by large-scale intraseasonal atmospheric perturbations

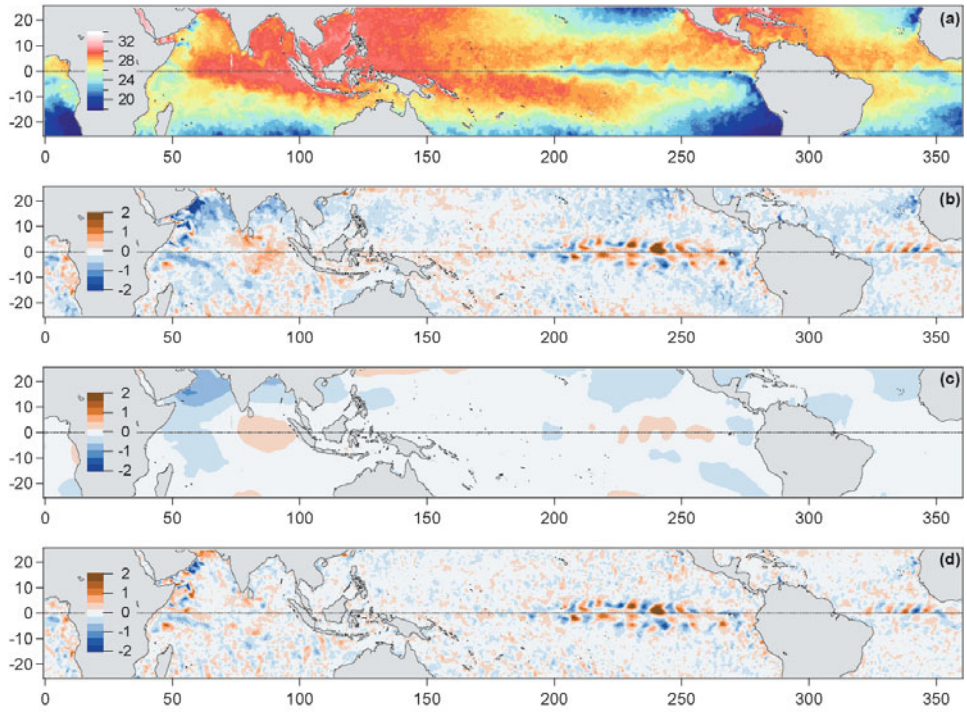

Figure 15.1. The SST field and its intraseasonal anomaly for August 1, 1998: (a) original TMI OI SST data with a $0.25 \times 0.25^{\circ}$ resolution; (b) intraseasonal SST anomaly resulting from temporal filtering between 20 and 100 days; (c) spatial smoothing of field (b) using a box of $12 \times 12^{\circ}$, which extracts the large-scale organized intraseasonal SST anomaly; (d) residual small-scale intraseasonal SST anomaly obtained by the difference between fields (b) and (c).

and that the residual intraseasonal signal (Figure 15.1d) is mostly due to oceanic waves and eddies. The small-scale ISV of SST is obtained by computing the standard deviation among these residual fields (Figure 15.2), while the large-scale organized ISV of the SST is obtained by computing the standard deviation among smoothed SST fields (Figure 15.3).

Many known features are apparent in Figure 15.2, such as the large TIW signals in the eastern Pacific Ocean and Atlantic Ocean, the "great whirl" gyre of the Somali Current during boreal summer (e.g., Schott *et al.*, 2009), or the Tehuantepec and Papagayo Eddies west of Central America with maximum activity during boreal winter (see Section 6.7). SST perturbations, related mostly to TIWs over the equatorial Pacific and Atlantic Oceans, are largest during boreal summer and autumn. As shown by Han *et al.* (2008), SST variability in the Atlantic could also result in part from first and second baroclinic mode equatorial Kelvin waves that are forced by intraseasonal zonal winds. Due to their small scale, these SST perturbations, while forced in part by the atmosphere, are not supposed to play a significant role in the triggering and evolution of large-scale organized tropical atmospheric ISV. Note

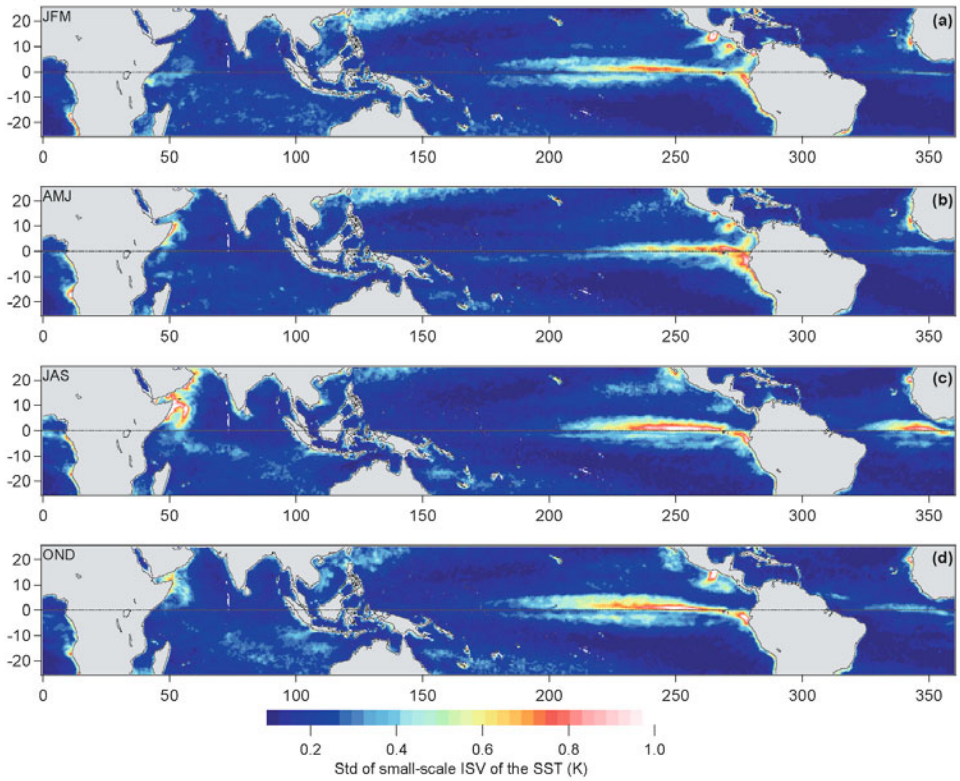

Figure 15.2. ISV of SST at the small scale (i.e., $<10^{\circ}$) obtained by computing for each $0.25 \times 0.25^{\circ}$ region the temporal standard deviation among the ensemble of residual fields (e.g., Figure 15.1d) for (a) January–March, (b) April–June, (c) July–September, and (d) October–December.

that this spatial smoothing approach may also smooth out possible SST perturbations confined at the equator, but due to the ocean dynamical response to large-scale atmospheric forcing, such as those appearing in an OGCM in the Eastern Pacific (Lucas *et al.*, 2010), and not to internal ocean dynamics.

The large-scale organized ISV of SST reported in Figure 15.3 is assumed to be forced mostly by large-scale organized intraseasonal atmospheric perturbations and further assumed to have a potential feedback on these perturbations. As already reported in previous studies based on TMI data (e.g., Saji *et al.*, 2006; Duvel and Vialard, 2007), the ISV of SST during boreal winter (Figure 15.3a) is large over the Indian Ocean south of the equator, especially in its western part (west of 75°E) where a shallow thermocline induces a shallow ocean mixed layer of around 20 m to 25 m (de Boyer Montégut *et al.*, 2004). This region is sometimes called the Seychelles–Chagos Thermocline Ridge (SCTR) (Hermes and Reason, 2008). For this season, the ISV of SST is largest over an area covering the eastern Indian Ocean (east of 115°E),

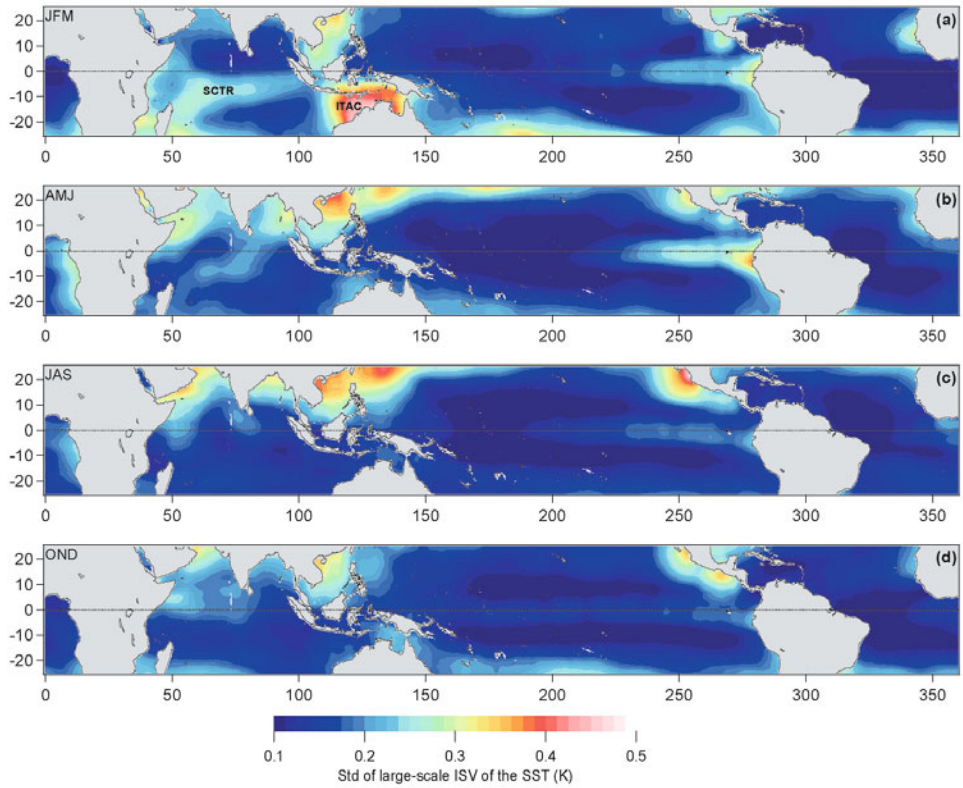

Figure 15.3. ISV of SST at the large scale (i.e., $>10^{\circ}$) obtained by computing for each $0.25 \times 0.25^{\circ}$ region the temporal standard deviation among the ensemble of spatially smoothed fields (e.g., Figure 15.1c) for (a) January–March, (b) April–June, (c) July–September, and (d) October–December.

the Timor and Arafura Seas and the Gulf of Carpentaria (ITAC). This ITAC region also has a shallow ocean mixed layer of around 25 m to 30 m. Over the southwestern Pacific Ocean, the ocean mixed layer is deeper and the ISV of SST is weak, especially north of 15°N. During boreal winter, the ISV of SST and its potential feedback on the atmosphere are thus more important for the Indian Ocean and the ITAC region than for the Western Pacific Ocean. This ISV of SST over the south Indian Ocean—in particular, over the ITAC region—is large only during boreal winter months (JFM). The ISV of SST is weak almost everywhere during the preceding autumn season (OND, Figure 15.3d).

On average during boreal spring (AMJ), the ISV of SST is relatively large north of the equator with larger values in the western Arabian Sea and in the eastern Bay of Bengal (Figure 15.3b). During boreal summer (JAS), the ISV of SST is more concentrated in the northern Arabian Sea and Bay of Bengal. For both seasons (AMJ and JAS), maximum ISV of SST is observed over the China Sea and the

northwestern Pacific Ocean, with larger ISV during JAS. At this time the large ISV of SST, forced by large-scale intraseasonal oscillation of wind and convection, is also observed over the tropical northeast Pacific (e.g., Maloney and Esbensen, 2007).

During boreal spring and summer, some intraseasonal events are associated with large SST perturbations over the Bay of Bengal (Vecchi and Harrison, 2002; Roxy and Tanimoto, 2007), with a positive SST anomaly associated with boundary layer moistening (Jiang *et al.*, 2004; Fu *et al.*, 2006) north of the convective occurrence. This process is likely to play a role in the northward propagation of the intraseasonal disturbance. However, the corresponding average ISV of SST is relatively small south of 10°N during the heart of the monsoon season in JAS (Figure 15.3c). This can be related to wind stress related to the setting of the low-level monsoon jet that deepens the ocean mixed layer in JAS compared with AMJ. This deepening of the mixed layer over the Arabian Sea and the southern Bay of Bengal gives an SST less reactive to atmospheric forcing. Over the northern Bay of Bengal, the mixed layer depth (MLD) remains relatively small over a barrier layer generated by freshwater gathering (e.g., Thadathil *et al.*, 2007). The barrier layer tends to reduce cooling due to vertical mixing but the small MLD tends to amplify the effect of intraseasonal surface heat flux perturbations on SST (Duncan and Han, 2009). Over the western Arabian Sea, the ISV of SST (Figures 15.3b and 15.3c) could result partly from modulation of the Somali–Oman upwelling (Duvel and Vialard, 2007). These SST perturbations impact local evaporation and water vapor transport toward the Western Ghats (Izumo *et al.*, 2008) and could thus be an important source of variability for the Indian monsoon.

The ISV of convection is maximal over the northern Indian Ocean in May and June and over the northwest Pacific Ocean in July–September (Kemball-Cook and Wang, 2001). As shown in Bellenger and Duvel (2007), there is also a specific "pre-monsoon ISV pattern" in May and a specific "monsoon onset ISV pattern" in June. This shows the very sharp seasonality of ISV during boreal spring and summer. The eastward shift of the ISV amplitude between the northern Indian Ocean in MJ and the northwest Pacific Ocean in JAS could be related to seasonal evolution of the MLD. After setup of the low-level monsoon jet, the mixed layer deepens over the northern Indian Ocean in JAS while it remains small for both boreal spring and summer over the China Sea and the northwestern Pacific Ocean (Bellenger and Duvel, 2007). The potential mechanisms linking MLD to ISV (Sobel and Gildor, 2003; Maloney and Sobel, 2004) are discussed later in this chapter (see p. 525).

15.2.2 Source of the ISV of SST

Various parameters influence the amplitude of the ISV of SST, such as surface turbulent and radiative fluxes; mixed layer depth; ocean dynamics (lateral advection and diffusion, entrainment and mixing at the base of the mixed layer); the presence of a barrier layer; and the formation of a DWL during the warm phase. One may thus expect the ISV of SST to be quite dependent on region and season and on characteristics of the intraseasonal event (especially its duration). More details on the different physical sources of the ISV of the SST are given below (see p. 519).

Before discussing these details, it is interesting to report some large-scale statistics on radiative and turbulent surface heat fluxes which are major sources of the ISV of SST (e.g., Woolnough *et al*., 2000; Duvel and Vialard, 2007, §7.2). The ISV of net surface energy flux is dominated by solar radiative fluxes (mainly the screening of solar radiation by convective clouds) and turbulent fluxes (mainly evaporation due to surface wind). The phasing between convection and surface wind perturbations is thus an important characteristic for the amplitude of the ISV of SST. This phasing is not an intrinsic attribute of ISV, but varies with region and season.

A typical large-scale dynamical response to convective heating near the equator (i.e., a Gill-type response) gives a maximum westerly (easterly) wind perturbation west (east) of convection. In addition, wind gustiness increases surface turbulent fluxes under the ensemble of convective systems embedded in the SCC envelope (e.g., Chuda *et al*., 2008). For a large-scale convective perturbation moving eastward in an average low-level westerly flow (as over the Indian Ocean), the maximum windspeed is delayed with regard to maximum convection. Over the Indian Ocean and the ITAC region, this lag varies typically between 0 and 1/4 of a period (i.e., around 10 days). Convection is more in phase with windspeed over the western Pacific (150°E–210°E), maybe because the eastward propagation of the convective perturbation is not as reproducible as for the Indian Ocean (Duvel and Vialard, 2007). This propagation is even westward for some large intraseasonal events of the western Pacific. During boreal summer (JJA), the windspeed is maximal under convection near the equator (Li *et al*., 2008) but lags convection over the Arabian Sea and the Bay of Bengal where the propagation is northward.

For an ocean mixed layer temperature controlled by quasi-periodic surface flux perturbations, the expected lag between the mixed layer temperature and the surface flux is 1/4 of a period (flux forcing is in phase with the SST derivative). Detailed maps of the lag between SST and convection (i.e., maximum extinction of surface solar flux and cooling by wind gustiness under convective systems) reveal that the maximum convection generally precedes the minimum SST by about 1/4 to 1/8 of a period (Duvel and Vialard, 2007). The lag between SST and windspeed is generally smaller than 1/8 of a period. SST thus responds more hastily than expected (if surface evaporation is the main forcing) to surface wind and sometimes quasi-instantly with regard to intraseasonal timescales. Part of this rapid surface cooling could be due to vanishing ocean DWLs as soon as the windspeed rises. This fast cooling could also result from vertical mixing with cold water at the base of the ocean mixed layer.

These studies show that the amplitude and phase of SST perturbations associated with the ISV of convection are quite variable from one ocean basin to another and from one season to another. This variability must be taken into account in order to analyze the physical source of the ISV of SST and its potential feedback on atmospheric intraseasonal variability. The next section will present recent results on the perturbation of the ocean mixed layer structure by atmospheric intraseasonal forcing over the Indian Ocean. This is especially interesting if one considers that this basin is a major source of intraseasonal variability and an initiation region for the MJO. These new studies complement well the detailed in situ measurements of the

Tropical Ocean Global Atmosphere Coupled Ocean–Atmosphere Response Experiment (TOGA COARE) obtained over the western equatorial Pacific region.

15.2.3 SST perturbations over the SCTR

The large SST perturbations over the Indian Ocean during boreal winter are related to a thermocline ridge located south of the equator between roughly 5°S and 10°S. This ridge is more pronounced west of 75°E but is also present in the eastern Indian Ocean. This feature, also called the Seychelles–Chagos Thermocline Ridge (SCTR) (Hermes and Reason, 2008) or simply the Seychelles Dome (SD) (Yokoi *et al.*, 2008), is forced by both wind stress and wind stress curl which generate local Ekman upwelling and lift the thermocline. This results in semiannual thermocline depth variation with minima around June and January (Yokoi *et al.*, 2008). SST is maximal (28–29°C) between January and March, giving a warm surface temperature above a shallow thermocline for this season. This is a unique feature of the SCTR region that generates deep convection over a relatively thin and reactive ocean mixed layer during boreal winter (Vialard *et al.*, 2009). This is associated with the clear asymmetry about the equator during boreal winter accompanied by a stronger ISV of convection, wind, and SST south of the equator and south of the average position of the Intertropical Convergence Zone (ITCZ).

Using TMI measurements, Harrison and Vecchi (2001) report an SST perturbation of more than 3°C for a large region (20° longitude by 10° latitude) in the south equatorial Indian Ocean around 85°E. This ISV of SST was related to the strong intraseasonal event of January–February 1999. Despite the suspected cold bias of TMI SST measurements during periods with deep convection or winds stronger than $10\,m\,s^{-1}$ (Bhat *et al.*, 2004), comparison between TMI measurements and in situ surface drifters showed no clear bias for this cooling event (Duvel *et al.*, 2004). An ocean general circulation model (OGCM) forced by observed surface radiative and turbulent fluxes produces a realistic SST perturbation pattern for this 1999 episode (Duvel *et al.*, 2004). However, the SST perturbation was too small in the OGCM, mostly because of an underestimate of about 1°C of SST during the warm phase due to the absence of a DWL (see Section 15.4.1 on diurnal variations). The realistic SST perturbation pattern given by the OGCM gives confidence in tracing the source of intraseasonal SST variability. SST perturbation of the forced OGCM is mostly due to surface fluxes. Exchanges with the subsurface and lateral exchanges play a secondary role for these particular events. Considering the latitudinal distribution of the perturbations, the net heat flux perturbation is maximal near the equator and the wind stress perturbation is maximal at 5°S (Figure 15.4). At the equator, the surface current response and the associated vertical shear deepen the ocean mixed layer. At 5°S, the MLD is still modulated by the wind burst by more than 20 m, but at 10°S the modulation is less than 10 m. This southern region near 10°S is thus more reactive to surface heat flux perturbations than regions closer to the equator. The latitudinal distribution of the various surface perturbations and of the various ocean dynamical responses produces a maximum ISV of SST near 7°S. Other studies report a

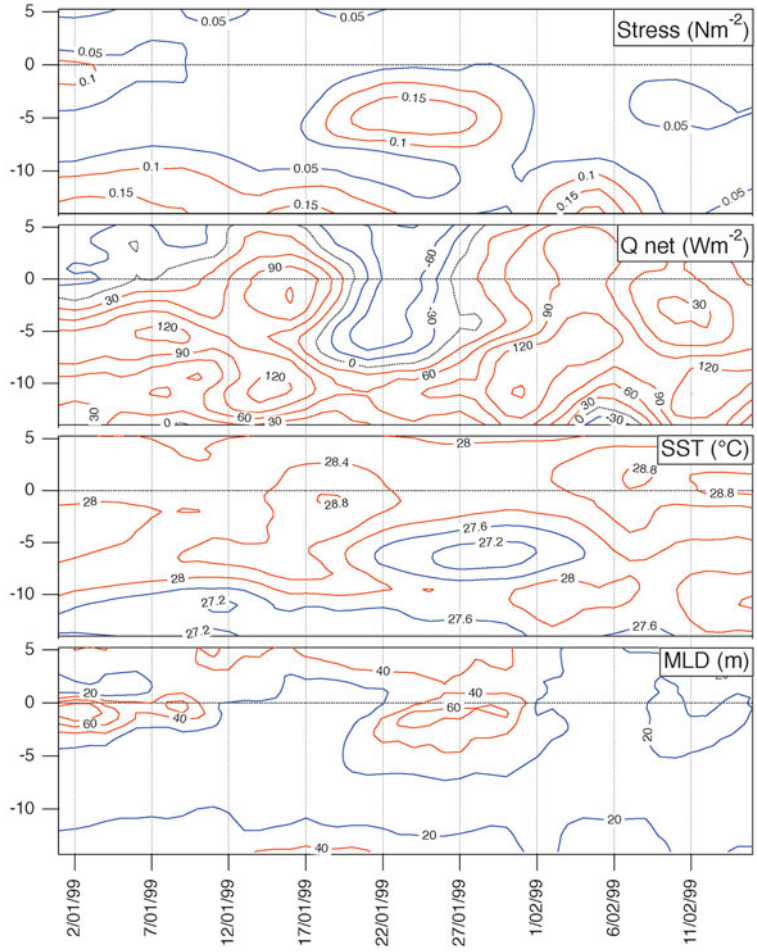

Figure 15.4. Time–latitude diagrams of the evolution of (top) wind stress in pascals and (middle top) net surface flux in watts per square meter used to force an OGCM. The response of the OGCM is shown for (middle bottom) the temperature of the mixed layer in degrees Celsius and (bottom) the mixed layer depth in meters. Values are averaged between 80°E and 90°E (from Duvel *et al.*, 2004).

larger role played by ocean dynamics in intraseasonal SST variability. For example, Waliser *et al.* (2003) analyze the simulation of an OGCM forced with a canonical MJO and find that vertical and meridional advection also plays a role in modulation of the mixed layer heat budget for a small region centered at 5°S–80°E. Also, Han *et al.* (2007), using an OGCM forced by observations, find that the MLD was modulated by the January 1999 event and that entrainment plays a role in the ISV of SST south of the equator.

As noted in Lloyd and Vecchi (2010), the ISVs of SST over the SCTR have a significant negative skew and can be regarded as cooling events. These cooling events

are sometimes so large over this shallow thermocline region that one may indeed suspect vertical mixing and entrainment (subsurface processes) to supplement surface forcing. Using measurements from a RAMA moored buoy at 8°S–67°E for four winter months, Vialard *et al.* (2008) show first that average upper-ocean heat balance is dominated by heating due to surface forcing (2.0 ± 0.3°C/month) and cooling due to subsurface processes (-2.2 ± 0.8°C/month). This shows the average impact of Ekman pumping. However, at intraseasonal timescales, only the surface forcing term has an evolution consistent with evolution of the mixed layer temperature. This suggests that the ISV of subsurface processes has only a marginal impact, at least for these events and neglecting any possible bias due to missing data. Other studies indeed demonstrate that some cooling events involve subsurface processes. Vinayachandran and Saji (2008), using the sea-viewing wide-field-of-view sensor (SeaWiFS), ARGO observations, and an OGCM, and Resplandy *et al.* (2009), using SeaWiFS observations and biophysical ocean simulations, conclude that (as suggested in Waliser *et al.*, 2005) the observed chlorophyll blooms associated with cooling events are generated by wind-induced subsurface processes. Also, Lloyd and Vecchi (2010) show that the strongest cooling events (not necessarily related to the MJO) in the western part of the SCTR (50–70°E) are due in equal part to surface fluxes and to subsurface processes, while moderate cooling events are mostly due to surface fluxes.

There is no fundamental contradiction between these different studies which all conclude that the maximum ISV of SST over the SCTR is due to the shallow thermocline. The fact that subsurface processes are more or less important depending on the location (e.g., also in latitude, cf. Figure 15.4) and the strength of surface forcing is physically sound. These studies show that variations in thermocline depth over the SCTR can modulate the impact of both surface flux and subsurface processes on the ISV of SST. Interannual modulation of this thermocline depth may thus have consequences for the strength of air–sea coupling and, thus, possibly for ISV and its predictability.

15.3 AIR–SEA PROCESSES FOR THE SIMULATION AND PREDICTABILITY OF ISV

15.3.1 Passive response of the atmosphere to the ISV of SST

Section 15.2 focused on intraseasonal perturbation of the ocean mixed layer by atmospheric forcing. It is also interesting to analyze the ISV generated by an AGCM forced by SST fields containing an intraseasonal signal. Since, as shown above, this intraseasonal SST signal is in fact the result of air–sea interaction, the aim of these AGCM simulations is not to explain the source of atmospheric ISV, but to quantify the potential feedback of SST on atmospheric ISV. In particular, the objective is to show whether observed intraseasonal SST variations can initiate realistic intraseasonal convective perturbations and dynamical response. This is not obvious since the atmospheric response depends on the characteristics of SST

anomalies (amplitude, size, duration) and, as shown above, these characteristics may be distorted with regard to initial atmospheric forcing. Such an exercise has been carried out using idealized SST perturbations (Woolnough *et al.*, 2001) and observed SST for the boreal winter (Matthews, 2004; Kim *et al.*, 2008; Bellenger *et al.*, 2009) or the boreal summer (Wu *et al.*, 2002; Klingaman *et al.*, 2008). These studies used different AGCMs and different sources of observed SST such as the Reynolds *et al.* (2002) dataset, TMI, or a combination of different measurements (e.g., Donlon *et al.*, 2007). Despite these differences, all these experiments report generation of a more realistic atmospheric ISV compared with AGCMs forced by slow seasonal evolution of the SST. This shows that feedback of the ISV of SST to the atmosphere is potentially important in explaining the dynamics of tropical intraseasonal perturbations. As discussed above, one-way forcing of the atmosphere by the ISV of SST is however unphysical and does not enable precise analysis of the origin of ISV. In particular, as discussed in numerous analyses (e.g., Wu *et al.*, 2002; Matthews, 2004; Fu and Wang, 2004; Zheng *et al.*, 2004), convection tends to be in phase with the SST in these experiments compared with the observed lag of 1/4 of a period. This too fast convective response to SST could result from inaccurate triggering or closure assumptions for the convective parameterization that tend to give maximum convection for the maximum static instability of the column and thus, in most cases, above the warmest surface. For these forced simulations, part of the discrepancy may also relate to the inadequacy between the local atmospheric state (e.g. convective instability, low-level divergence field) and the SST field. In observations, the SST rising phase occurs under dry, subsiding, and convectively suppressed large-scale conditions, while it may appear under different large-scale conditions in an AGCM (including local low-level convergence) forced by observed SST. Different members of an ensemble of forced simulations will thus also have different convective responses to SST forcing since the local atmospheric state will vary from one member to another. Warm surface forcing occurring under unstable and/or low-level convergence conditions will tend to give maximum convection close to the maximum SST and not with the expected lag of 1/4 of a period.

As discussed above, the SST response to intraseasonal atmospheric forcing is quite variable from one region to another. For example, in the Indian Ocean during boreal winter the maximum SST perturbation is located in the western part of the basin (on the SCTR) while the maximum convective perturbation is in the eastern part of the basin. An AGCM forced using observed daily SST will thus exhibit larger ISV of convection, but with some bias in the spatial perturbation patterns (westward shift in the Indian Ocean). However, these forced simulations may point out interesting processes. For example, as shown in Bellenger *et al.* (2009), intraseasonal SST anomalies tend to be organized at a relatively large spatial scale and trigger large-scale organized convective perturbations. The resulting convective heating generates a Gill-type dynamical response close to observed dynamical intraseasonal perturbations. As a result, the aggregation of convection into a few large-scale organized intraseasonal events gives a nonlinear response modifying the average large-scale circulation of the AGCM compared with convection that is more disseminated in space and time. This suggests that correct representation of convective ISV, with

such an aggregation of convective events, is necessary for correct simulation of average large-scale tropical circulation.

15.3.2 Coupled simulations, air–sea fluxes, and SST feedback

Recent ISV assessment studies (e.g., Lin *et al.*, 2006; Xavier *et al.*, 2010) show that most current CGCMs still have problems in simulating realistic ISV. However, these CGCMs are the only tool representing the complex nature of tropical ISV. These models are thus useful in assessing the potential role of air–sea interaction in the simulation and predictability of ISV. Many recent studies are based on comparing the coupled and forced simulations of a given AGCM (e.g., Fu and Wang, 2004, Zheng *et al.*, 2004; Rajendran and Kitoh, 2006; Zhang *et al.*, 2006; Seo *et al.*, 2007; Pegion and Kritman, 2008). In order to focus on the impact of air–sea coupling, the SST used to force the AGCM in most of these experiments is taken from CGCM simulations themselves, either with a daily time step (to conserve the ISV of SST) or with monthly mean values. Note that this may be a handicap for a CGCM that represents climatology poorly since the positive impact of air–sea coupling also depends on correct representation of the average SST field by the CGCM (Seo *et al.*, 2007) or, more generally, its background state (Zhang *et al.*, 2006). Despite the different GCMs and the different approaches used to assess simulation of ISV, these coupled simulations generally show some improvements in the characteristics of ISV, either in the amplitude, the period, or in propagative properties (see also Chapter 11). For example, Marshall *et al.* (2008) find that coupling of an AGCM with a slab ocean reduces the period of the oscillation to a more realistic value. In agreement with results reported in Waliser *et al.* (1999), the improvement of the ISV in the coupled simulation studied in Marshall *et al.* (2008) is due to increased low-level moisture east of the maximum convection contributing to eastward propagation of the convective anomaly.

Coupling with the ocean also extends the predictability of intraseasonal perturbations (e.g., Vitart *et al.*, 2007; Woolnough *et al.*, 2007; Fu *et al.*, 2008; Wang *et al.*, 2009; see also Chapter 12). These sensitivity experiments are based on comparison between hindcasts done by the CGCM and those done by the AGCM forced using either persistent SST or observed bulk SST. For example, Fu *et al.* (2008) show that predictability is similar (30 days according to their metrics) for coupling with a full ocean model or for forcing with the SST of a coupled model. This predictability decreases for coupling with a slab ocean (25 days) and is minimal for forcing with a persistent SST (20 days). In addition, Krishnamurti *et al.* (2007) show that the inclusion of subsurface ARGO profiler measurements during the assimilation phase of a coupled model improves the forecast of intraseasonal perturbation in both the ocean and the atmosphere. This gives further evidence of the role played by the ocean in the evolution of intraseasonal perturbations.

Due to the complexity of these models, it is not trivial to trace the physical source of the various improvements due to air–sea coupling. As underlined by Goulet and Duvel (2000) and by Sperber and Annamalai (2008), ISV is also a complex and intermittent phenomenon and it is thus difficult to elaborate a con-

venient and unambiguous approach to evaluate its simulation in global models. The interpretation of sensitivity experiments and the analysis of the impact of a particular physical process can be facilitated by the use of simplified models. For example, Maloney and Sobel (2004) use an AGCM coupled to slab ocean with a fixed mixed layer depth (MLD) and show that the ISV of precipitation is maximum for an MLD at around 20 m and a minimum for a small (2 m) or very large MLD. The highly simplified model of Sobel and Gildor (2003) was used to interpret this result. Following this model, the MLD may have some optimal value (around 20–30 m) in order to be sufficiently small to respond to atmospheric forcing at the intraseasonal timescale (warming and cooling phases) and sufficiently large to contain the energy necessary to sustain convection during the warm phase. Using an idealized coupled model, Bellon *et al.* (2008) reproduce and analyze the physical origin of northward propagation of monsoon ISV and also find damped amplitude for an MLD lower than about 10 m. As suggested in Bellenger and Duvel (2007), and despite the methodological difficulties inherent in these types of observational analyses, part of the seasonal evolution of intraseasonal activity can be related to the seasonal march of the Indo-Pacific monsoon through such a variation of MLD. For example, over the northern Indian Ocean, intraseasonal events are strong in May and June when the average MLD is relatively small (20–30 m), but decrease in amplitude during the heart of the monsoon season when the average MLD is increased (60–70 m) by the strong low-level monsoon jet.

As advocated in two recent papers (Sobel *et al.*, 2008, 2010), variation of the surface moist enthalpy fluxes in the different phases of intraseasonal disturbances may play a fundamental role in driving intraseasonal oscillations. Sobel *et al.* (2010) show that an AGCM initially representing a realistic ISV is degraded when a constant value of surface wind is considered in the computation of surface turbulent fluxes (this eliminates so-called wind-induced surface heat exchange or WISHE). Turbulent air–sea flux is also modulated by disturbances at submonthly and synoptic timescales. For example, synoptic-scale wave activity and tropical cyclone activity that occur during certain phases of ISV significantly modulate turbulent air–sea fluxes (e.g., Batstone *et al.*, 2005; Maloney and Esbensen, 2007; Han *et al.* 2007; Katsumata *et al.*, 2009; Zhou and Li, 2010). It is worth noting that the air–sea flux feedback to ISV is mostly related to wind perturbation and may thus exist even with a constant SST. However, the ISV of SST may intensify or lessen air–sea flux feedback. As discussed in Maloney and Sobel (2004) and Marshall *et al.* (2008), a too fast SST response to surface forcing can, for example, damp the air–sea flux feedback and the ISV amplitude.

The amplitude of the ISV of SST is generally underestimated in OGCMs because of the relatively coarse (10 m) vertical resolution near the surface. The peak-to-peak intraseasonal amplitude of SST perturbation in OGCMs is indeed generally on the order of a few tenths of a degree Celsius and thus well below the observed ISV of SST that may be of a few degrees Celsius. Wang *et al.* (2009) suggest that the amplitude of SST perturbation should be two to three times larger than the simulated SST in order to correctly simulate northward propagation of boreal summer intraseasonal disturbances. Other experiments have been performed (e.g.,

Vitart *et al.*, 2007; Woolnough *et al.*, 2007; Bernie *et al.*, 2008) to explore the potential role that better representation of ocean mixed layer processes, including DWL, could play in MJO simulation and forecast skill. This is reported in the next section.

15.4 AIR–SEA PROCESSES AND SCALE INTERACTION

15.4.1 The diurnal cycle

Earlier studies, partly based on TOGA–COARE measurements, pointed out the role played by ocean diurnal warm layers (DWL) on the amplitude of the ISV of SST (e.g., Anderson *et al.*, 1996; Lau and Sui, 1997; Shinoda, 2005; Bernie *et al.*, 2005; see also Section 7.5 in this book). These DWLs (0–3 m) form under low wind stress conditions when vertical turbulent mixing is insufficient to break the vertical stratification generated by daily solar flux. These DWLs may have daily amplitude of more than 3 K and may increase average daily SST by as much as 1 K. This must be considered to correctly diagnose the ISV of SST in climate models since the surface layer of the OGCM is 10 m thick and cannot generate DWLs. This partly explains why the intraseasonal SST perturbation is too weak in OGCMs compared with observations (e.g., Xavier *et al.*, 2008).

DWLs could also play a role in atmospheric ISV. Using a diagnostic DWL scheme forced using the 40-year ECMWF reanalysis (ERA-40), Bellenger and Duvel (2009) show that DWLs can indeed cover areas of a few thousand kilometers in radius and persist for more than 5 days. Strong DWLs tend to appear in regions of large ISV of SST, like the SCTR and the ITAC region during boreal winter. It is suggested that, due to these large spacescales and timescales, these DWLs trigger shallow and mid-level convection during the afternoon over large regions during the suppressed phase of the MJO. This gives a preconditioning of the troposphere by injecting moisture into the free troposphere prior to the convectively active phase of the MJO. The triggering of convection in the afternoon by DWLs was confirmed by Bellenger *et al.* (2010) using in situ observations from the *Mirai* Indian Ocean cruise for the study of the Madden–Julian Oscillation (MJO)–Convection Onset (MISMO) experiment (Yoneyama *et al.*, 2008).

The impact of better vertical resolution of surface ocean layers (1 m instead of 10 m) and of diurnal variation of solar flux on the ISV of SST has been tested using a forced OGCM (Bernie *et al.*, 2007). The resulting SST response, including the diurnal cycle, increases the intraseasonal SST amplitude in the forced OGCM. However, the simulated diurnal SST amplitude is small compared with in situ or TMI observations (Gentemann *et al.*, 2003). This is because a resolution of 1 m near the surface is still not sufficient to estimate the amplitude of the DWL. As shown in Soloviev and Lukas (1997), the vertical temperature gradient around 13:00 LT can be sharp near the surface for very low wind stress. This generates a large diurnal amplitude difference between the surface and a depth of a few tenths of a meter (typically a factor of 2 between the surface and 0.25 m). This fact, together with the

high computing cost resulting from high vertical resolution of the OGCM, prompted Zeng and Beljaars (2005) and Bellenger and Duvel (2009) to propose and test DWL schemes to estimate the skin temperature in GCMs. These schemes improve SST estimation and, thus, the computation of air–sea fluxes under low-wind conditions.

Coupled GCM simulations with a diurnal cycle of solar flux and with a better vertical resolution near the ocean surface (around 1 m) were also done to test the impact of DWLs on atmospheric ISV (Bernie *et al.*, 2008) and on its forecast (Woolnough *et al.*, 2007). The first study shows that DWLs slightly reduce MJO activity, but also enhance the SST response to the MJO, leading to a more coherent and structured MJO. Woolnough *et al.* (2007) investigate the role of coupled processes in the forecast of the MJO in the European Centre for Medium-Range Weather Forecasts (ECMWF) monthly forecasting system. They perform various forecast experiments considering either a persistent SST, a full OGCM, or a 1-D mixed layer model with better vertical resolution ($\sim$1 m), with or without the diurnal cycle of solar flux. Coupling with the 1-D mixed layer model increases the ISV of SST, but has no significant impact on the characteristic loss of amplitude of the MJO during the forecast. However, both better vertical resolution of the mixed layer and inclusion of the diurnal cycle of solar flux increase the forecast skill of the phase of the MJO by up to a week regarding forecasts done using a mixed layer model with a 10 m vertical resolution. Further studies based on the same ECMWF monthly forecasting system (Vitart *et al.*, 2007) demonstrate that the positive impact of mixed layer processes on forecast skill may be additive to MJO amplitude improvements resulting from enhanced convective (CAPE threshold for the activation of deep convection) and cloud (radiative processes favoring low-level convergence in the convective area) parameterizations.

The inclusion of a DWL may in some cases degrade simulation of ISV. For example, Brunke *et al.* (2008) use the DWL scheme of Zeng and Beljaars (2005) in the Community Atmosphere Model (CAM3.1) and find that the diurnal cycle in skin SST slightly reduces the amplitude of the simulated MJO. Duvel *et al.* (2008) show that inclusion of a DWL scheme in the LMD-Z AGCM increases the ISV of SST, but decreases the ISV of precipitation over the Indian Ocean. This smaller ISV of precipitation is due to the excessive diurnal response of convection during DWL episodes that tends to increase deep convective activity during (normally) suppressed conditions. This shows that the convective scheme must be able to correctly respond (shallow and mid-level convection) to the instability generated by warm SST during the afternoon. Too responsive convection will tend to degrade simulated ISV when a DWL scheme, or an improved mixed layer representation, is introduced. The correct response of shallow, mid-level, and deep convection to DWLs in AGCMs—in particular, for the warm suppressed phase preceding MJO initiation—certainly is a constraining and interesting model diagnostic.

15.4.2 Interannual variability and the Indian Ocean Dipole

The Indian Ocean Dipole (IOD) is an interannual mode of variability of the air–sea coupled system. A positive IOD phase is related to a cold-ocean anomaly in the

southeastern Indian Ocean and warm anomaly in the western Indian Ocean (Saji *et al.*, 1999). This is associated with a zonal wind anomaly over the central equatorial basin, indicating that Bjerknes feedback might be important for its development. The corresponding SST anomaly starts in May and is maximum at the end of the Indian monsoon (October). The IOD is related to interannual variations of the Indian monsoon (e.g., Ashok *et al.*, 2004) and can be used as a predictor for El Niño (e.g., Izumo *et al.*, 2010).

Recent studies showed interactions between the IOD and ISV for both summer and winter seasons. In particular, surface westerly wind events associated with boreal winter ISV excite downwelling oceanic Kelvin waves that tend to destroy positive IOD anomalies (Rao and Yamagata, 2004; Han *et al.*, 2006). During boreal summer (JJAS), poleward propagation of the intraseasonal convective anomaly tends to be more organized for negative IOD years (warm anomaly in the eastern Indian Ocean), compared with positive IOD years (Ajayamohan *et al.*, 2008) in relation to enhanced air–sea interaction (Ajayamohan *et al.*, 2009). The relation between the IOD and the Indian monsoon, and even the direction of causality, is however unclear and complicated by some correlation between the IOD and ENSO (e.g., Krishnamurthy and Kirtman, 2009) and the role played by other modes of interannual SST variability of the Indian Ocean (e.g., Yang *et al.*, 2010). The potential role of ISV in this relation is thus difficult to estimate.

Near the equator, the ocean structure can be modified by zonal and meridional current fluctuations forced by intraseasonal wind stress fluctuations. For the Indian Ocean, these intraseasonal fluctuations of the equatorial current are larger than the semi-annual Wyrtki jet modulation (Masumoto *et al.*, 2005). Sengupta *et al.* (2007) show that the spring Wyrtki jet is in fact related to a single intraseasonal wind event, while the fall Wyrtki jet is actually a succession of two or more intraseasonal events. At intraseasonal timescales, these jets deepen the MLD and locally reduce ocean temperature reactivity near the equator (see above and Figure 15.4). At longer timescales, these jets redistribute water mass, heat, and salt. The resulting modification of the ocean structure—in particular, in the eastern Indian Ocean—may affect the IOD and, more generally, regional climate through the modification of SST. The depth of the thermocline over the SCTR and, thus, the potential reactivity of the upper ocean to intraseasonal surface flux forcing are also modulated at the interannual timescale by slow biannual oceanic Rossby waves (Chowdary *et al.*, 2009; Gnanaseelan and Vaid, 2010).

15.5 DISCUSSION

Maps of intraseasonal variance show that the strongest ISV of precipitation occurs over three basins: the Indian Ocean, the maritime continent, and the West Pacific. Considering each basin separately, observations show that intraseasonal perturbation patterns for precipitation, surface wind, and SST are quite reproducible from one intraseasonal event to another (Duvel and Vialard, 2007). This reproducibility is a necessary condition for analyzing the physical source of the disturbance, especially

if this analysis is based on average perturbation patterns. However, for most of the 19 CGCMs participating in phase 3 of the Coupled Model Intercomparison Project (CMIP3), the reproducibility of intraseasonal perturbation patterns is poor over the Indian Ocean during northern hemisphere summer (Xavier *et al.*, 2010). In addition, the intraseasonal signal is more a result of local and unorganized precipitation variability than of quasi-periodic perturbations organized at the scale of the basin. As shown by Lin at al. (2006), and confirmed using a very different approach by Xavier *et al.* (2010), the lack of ISV in these models is indeed associated with an over-reddened spectrum, revealing a lack of both intraseasonal (i.e., 20–90 days) and synoptic (i.e., 2–12 days) variability. In these CGCMs, the precipitation field is too persistent and mostly follows the slow seasonal evolution of the SST field. On the other hand, a few CGCMs present a better ISV simulation with better scores concerning the average ISV pattern (for both amplitude and propagation characteristics), the reproducibility of ISV patterns, the redness of the spectrum, the large-scale organization of perturbations, and the average precipitation pattern.

The fact that a few coupled GCMs reasonably represent ISV shows that the basic physical processes at the origin of ISV are already included in current models. However, the correct representation of ISV by a given model depends sometimes on relatively small modification of the physical parameterization. A very efficient modification consists in suppressing or reducing deep convection under some boundary layer conditions (small depth, low humidity, divergence, etc.). Such inhibition of deep convection allows accumulation of low-level moist air in some phase of the perturbation that leads to larger ISV amplitude (Tokioka *et al.* 1988, Wang and Schlesinger, 1999). A recent paper by Zhang and Mu (2005) also confirms that by inhibiting convection the ISV amplitude of the precipitation increases. This point is discussed here because it may shed light on the CGCM diagnostic of Xavier *et al.* (2010) and on the potential role of air–sea interaction on ISV. The over-reddened precipitation spectrum and the lack of large-scale organization of convective perturbation in some CGCMs could result from quasi-equilibrium closure of the convective scheme. In such a case, there is virtually no accumulation of low-level moist air since the convective scheme very rapidly eliminates column instability. If no large-scale dynamical disturbance comes to organize convection in such a model, local convection thus simply tends to follow the slow seasonal evolution of SST, in agreement with the unorganized and over-reddened variability of precipitation in these CGCMs. The main effect of convective inhibition (obtained through some triggering threshold or specific closure) is to allow convectively suppressed conditions over a warm ocean. The hypothesis is that the resulting accumulation of low-level moist air is susceptible to triggering large-scale organized (i.e., on several model gridpoints) convective surges that, associated with a Gill-type dynamical response, can initiate an intraseasonal event (Maloney and Sobel, 2007; Bellenger *et al.*, 2009) or participate in its evolution (Marshall *et al.*, 2008). While somewhat speculative, this hypothesis is in very good agreement with the CGCM diagnostics done by Xavier *et al.* (2010) and is consistent with the view of Waliser (1996) recently revisited by Stephens *et al.* (2004). Moreover, this local or basin-scale hypothesis of

the origin of ISV is comforted by the analysis of Duvel and Vialard (2007) showing that many intraseasonal events actually occur over a single basin.

In agreement with the concluding remark of Woolnough *et al.* (2007), coupling with the ocean will possibly have a greater impact on the simulation of ISV as long as some shortcomings of the AGCM can be overcome. With the hypothesis discussed above, coupling with the ocean may have a positive impact on the realism of ISV only if the convective scheme of the AGCM does not systematically release the convective instability of the column while SST rises under certain large-scale atmospheric conditions (subsidence, dry intrusion). This could be a necessary condition to initiation of large-scale organized convective perturbations at the origin of ISV. Note that, as discussed in Tokioka *et al.* (1988) and Wang and Schlesinger (1999), this process could also be relevant for forced AGCMs because of some accumulation of low-level moist air even for constant or seasonally varying SST fields. Other physical processes not related to air–sea coupling, such as cloud radiative forcing (not discussed here), may also increase the organization of convection by increasing low-level convergence into the convective region (Vitart *et al.*, 2007). Coupling with the ocean is thus not strictly required for the existence of ISV in GCMs. However, coupling can be critical to determining both the location and timing of the initiation of intraseasonal disturbances. The subsequent evolution of these disturbances may also depend significantly on air–sea flux perturbations and feedbacks with some regional and seasonal modulations depending on the upper-ocean structure. As a consequence, air–sea coupling at intraseasonal timescales is thus certainly necessary to improve the realism of the simulations of a given GCM, including its forecast skill and its representation of average climate.

15.6 ACKNOWLEDGMENTS

Discussions with the editors and additional comments from two reviewers led to appreciable improvements in the content and the presentation of this chapter.

15.7 REFERENCES

Ajayamohan, R. S., S. Rao, and T. Yamagata (2008) Influence of Indian Ocean Dipole on poleward propagation of boreal summer intraseasonal oscillations. *J. Climate*, **21**, 5437–5454.

Ajayamohan, R. S., S. A. Rao, J.-J. Luo, and T. Yamagata (2009) Influence of Indian Ocean Dipole on boreal summer intraseasonal oscillations in a coupled general circulation model. *J. Geophys. Res.*, **114**, D06119, doi: 10.1029/2008JD011096.

Anderson, S. P., R. A. Weller, and R. B. Lukas (1996) Surface buoyancy forcing and the mixed layer of the Western Pacific Warm Pool: Observations and 1D model results. *J. Climate*, **9**, 3056–3085.

Ashok, K., Z. Guan, N. H. Saji, and T. Yamagata (2004) Individual and combined influences of ENSO and Indian Ocean dipole on the Indian summer monsoon. *J. Climate*, **17**, 3141–3155.

Batstone, C. P., A. J. Matthews, and D. P. Stevens (2005) Coupled ocean–atmosphere interactions between the Madden–Julian oscillation and synoptic-scale variability over the warm pool. *J. Climate*, **18**, 2004–2020.

Bhat, G. S., G. A. Vecchi, and S. Gadgil (2004) Sea surface temperature of the Bay of Bengal derived from the TRMM Microwave Imager. *J. Atmos. Oceanic Technol.*, **21**, 1283–1290.

Bellenger, H. and J. P. Duvel (2007) Intraseasonal convective perturbations related to the seasonal march of the Indo-Pacific monsoons. *J. Climate*, **20**, 2853–2863.

Bellenger, H. and J. P. Duvel (2009) An analysis of tropical ocean diurnal warm layers. *J. Climate*, **22**, 3629–3646.

Bellenger, H., J. P. Duvel, M. Lengaigne, and P. Levan (2009) Impact of organized intraseasonal convective perturbations on the tropical circulation. *Geophys. Res. Lett.*, **36**, L16703, doi: 10.1029/2009GL039584.

Bellenger, H., Y. Takayabu, T. Ushiyama, and K. Yoneyama (2010) Role of diurnal warm layers in the diurnal cycle of convection over the tropical Indian Ocean during MISMO. *Mon. Wea. Rev.*, **138**, 2426–2433.

Bellon, G., A. H. Sobel, and J. Vialard (2008) Ocean–atmosphere coupling in the monsoon intraseasonal oscillation: A simple model study. *J. Climate*, **21**, 5254–5270.

Bernie, D. J., S. J. Woolnough, J. M. Slingo, and E. Guilyardi (2005) Modeling diurnal and intraseasonal variability of the ocean mixed layer. *J. Climate*, **18**, 1190–1202.

Bernie, D. J., E. Guilyardi, G. Madec, S. Woolnough, and J. Slingo (2007) Impact of resolving the diurnal cycle in an ocean–atmosphere GCM, Part 1: A diurnally forced OGCM. *Climate Dynamics*, **29**, 575–590.

Bernie, D. J., E. Guilyardi, G. Madec, J. Slingo, S. Woolnough, and J. Cole (2008) Impact of resolving the diurnal cycle in an ocean–atmosphere GCM, Part 2: A diurnally coupled CGCM. *Climate Dynamics*, **31**, 909–925.

Brunke, M. A., X. Zeng, V. Misra, and A. Beljaars (2008) Integration of a prognostic sea surface skin temperature scheme into weather and climate models. *J. Geophys. Res.*, **113**, D21117, doi: 10.1029/2008JD010607.

Chowdary, J. S., C. Gnanaseelan, and S. P. Xie (2009) Westward propagation of barrier layer formation in the 2006–07 Rossby wave event over the tropical southwest Indian Ocean. *Geophys. Res. Lett.*, **36**, L04607, doi: 10.1029/2008GL036642.

Chuda, T., H. Niino, K. Yoneyama, M. Katsumata, T. Ushiyama, and O. Tsukamoto (2008) A statistical analysis of surface turbulent heat flux enhancements due to precipitating clouds observed in the tropical western Pacific. *J. Meteorol. Soc. Japan*, **86**, 439–457.

de Boyer Montégut, C., G. Madec, A. S. Fischer, A. Lazar, and D. Iudicone (2004) Mixed layer depth over the global ocean: An examination of profile data and a profile-based climatology. *J. Geophys. Res.*, **109**, C12003, doi: 10.1029/2004JC002378.

Donlon, C., N. Rayner, I. Robinson, D. J. S. Poulter, K. S. Casey, J. Vazquez-Cuervo, E. Armstrong, A. Bingham, O. Arino, C. Gentemann *et al.* (2007) The Global Ocean Data Assimilation Experiment High-Resolution Sea Surface Temperature Pilot Project. *Bull. Amer. Meteorol. Society*, **88**, 1197–1213.

Duncan, B. and W. Han (2009) Indian Ocean intraseasonal sea surface temperature variability during boreal summer: Madden–Julian Oscillation versus submonthly forcing and processes. *J. Geophys. Res.*, **114**, C05002, doi: 10.1029/2008JC004958.

Duvel, J. P. and J. Vialard (2007) Indo-Pacific sea surface temperature perturbations associated with intraseasonal oscillations of the tropical convection. *J. Climate*, **20**, 3056–3082.

Duvel, J. P., R. Roca, and J. Vialard (2004) Ocean mixed layer temperature variations induced by intraseasonal convective perturbations over the Indian Ocean. *J. Atmos. Sci.*, **61**(9), 1004–1023.

Duvel, J. P., H. Bellenger, P. Xavier, and F. Doblas-Reyes (2008) Air–sea processes in the Indian Ocean and the intraseasonal oscillation. Paper presented at *Workshop on Atmosphere–Ocean Interaction, Reading, U.K.* European Centre for Medium-Range Weather Forecasts, Reading, U.K., pp. 83-92.

Fu, X. H. and B. Wang (2004) The boreal-summer intraseasonal oscillations simulated in a hybrid coupled atmosphere–ocean model. *Mon. Wea. Rev.*, **132**, 2628–2649.

Fu, X., B. Wang, and L. Tao (2006) Satellite data reveal the 3-D moisture structure of Tropical Intraseasonal Oscillation and its coupling with underlying ocean. *Geophys. Res. Lett.*, **33**, L03705, doi: 10.1029/ 2005GL025074.

Fu, X., B. Yang, Q. Bao, and B. Wang (2008) Sea surface temperature feedback extends the predictability of tropical intraseasonal oscillation. *Mon. Wea. Rev.*, **136**, 577–597.

Gentemann, C. L., C. J. Donlon, A. Stuart-Menteth, and F. J. Wentz (2003) Diurnal signals in satellite sea surface temperature measurements. *Geophys. Res. Lett.*, **30**, 1140, doi: 10.1029/2002GL016291.

Gnanaseelan, C. and B. H. Vaid (2010) Interannual variability in the Biannual Rossby waves in the tropical Indian Ocean and its relation to Indian Ocean Dipole and El Niño forcing. *Ocean Dynamics*, **60**, 27–40.

Goulet, L. and J.-P. Duvel (2000) A new approach to detect and characterize intermittent atmospheric oscillations: Application to the intraseasonal oscillations. *J. Atmos. Sci.*, **57**, 2397–2416.

Grabowski, W. W. (2006) Impact of explicit atmosphere–ocean coupling on MJO-like coherent structures in idealized aquaplanet simulations. *J. Atmos. Sci.*, **63**, 2289–2306.

Han, W., T. Shinoda, L-L. Fu, and J. P. McCreary (2006) Impact of atmospheric intraseasonal oscillations on the Indian Ocean dipole during the 1990s. *J. Phys. Oceanogr.*, **36**, 670–690.

Han, W., D. Yuan, W. T. Liu, and D. J. Halkides (2007) Intraseasonal variability of Indian Ocean sea surface temperature during boreal winter: Madden–Julian Oscillation versus submonthly forcing and processes. *J. Geophys. Res.*, **112**, C04001, doi: 10.1029/ 2006JC003791.

Han, W., P. J. Webster, J-L. Lin, W. T. Liu, R. Fu, D. Yuan, and A. Hu (2008) Dynamics of intraseasonal sea level and thermocline variability in the equatorial Atlantic during 2002–03. *J. Phys. Oceanogr.*, **38**, 945–967.

Harrison, D. E. and G. A. Vecchi (2001) January 1999 Indian Ocean cooling event. *Geophys. Res. Lett.*, **28**, 3717–3720.

Hermes, J. C. and C. J. C. Reason (2008) Annual cycle of the south Indian Ocean (Seychelles–Chagos) thermocline ridge in a regional ocean model. *J. Geophys. Res.*, **113**, C04035, doi: 10.1029/2007JC004363.

Izumo, T., C. D. Montégut, J. J. Luo, S. K. Behera, S. Masson, and T. Yamagata (2008) The role of the western Arabian Sea upwelling in Indian monsoon rainfall variability. *J. Climate*, **21**, 5603–5623.

Izumo, T., J. Vialard, M. Lengaigne, C. de Boyer Montégut, S. K. Behera, J. J. Luo, S. Cravatte, S. Masson, and T. Yamagata (2010) Influence of the state of the Indian Ocean Dipole on the following year's El Niño. *Nature Geoscience*, **3**, 168–172.

Jiang, X., T. Li, and B. Wang (2004) Structures and mechanisms of the northward propagating boreal summer intraseasonal oscillation. *J. Climate*, **17**, 1022–1039.

Katsumata, M., R. H. Johnson, and P. E. Ciesielski (2009) Observed synoptic-scale variability during the developing phase of an ISO over the Indian Ocean during MISMO. *J. Atmos. Sci.*, **66**, 3434–3448.

Kemball-Cook, S. and B. Wang (2001) Equatorial waves and air–sea interaction in the boreal summer intraseasonal oscillation. *J. Climate*, **14**, 2923–2942.

Kim, H. M., P. J. Webster, C. D. Hoyos, and I. S. Kang (2008) Sensitivity of MJO simulation and predictability to sea surface temperature variability. *J. Climate*, **21**, 5304–5317.

Klingaman, N. P., P. M. Inness, H. Weller, and J. M. Slingo (2008) The importance of high-frequency sea surface temperature variability to the intraseasonal oscillation of Indian monsoon rainfall. *J. Climate*, **21**, 2519–2539.

Krishnamurthy, V. and B. P. Kirtman (2009) Relation between Indian monsoon variability and SST. *J. Climate*, **22**, 4437–4458.

Krishnamurti, T. N., A. Chakraborty, R. Krishnamurti, W. K. Dewar, and C. A. Clayson (2007) Passage of intraseasonal waves in the subsurface oceans. *Geophys. Res. Lett.*, **34**, L14712, doi: 10.1029/2007GL030496.

Lau, K-M. and C-H. Sui (1997) Mechanisms of short-term sea surface temperature regulation: Observations during TOGA COARE. *J. Climate*, **10**, 465–472.

Li, T., F. Tam, X. Fu, T. Zhou, and W. Zhu (2008) Causes of the intraseasonal SST variability in the tropical Indian Ocean. *Atmos.–Ocean Sci. Lett.*, **1**, 18–23.

Lin, J., G. N. Kiladis, B. E. Mapes, K. M. Weickmann, K. R. Sperber, W. Lin, M. C. Wheeler, S. D. Schubert, A. Del Genio, L. J. Donner *et al.* (2006) Tropical intraseasonal variability in 14 IPCC AR4 climate models, Part I: Convective signals. *J. Climate*, **19**, 2665–2690.

Lloyd, I. D. and G. A. Vecchi (2010) Submonthly Indian Ocean cooling events and their interaction with large-scale conditions. *J. Climate*, **23**, 700–716.

Lucas, L. E., D. E. Waliser, and R. Murtugudde (2010) Mechanisms governing sea surface temperature anomalies in the eastern tropical Pacific Ocean associated with the boreal winter Madden Julian Oscillation. *J. Geophys. Res.*, **115**, C05012, doi: 10.1029/2009JC005450.

Maloney, E. D. and S. K. Esbensen (2007) Satellite and buoy observations of boreal summer intraseasonal variability in the tropical northeast Pacific. *Mon. Wea. Rev.*, **135**, 3–19.

Maloney, E. D. and A. H. Sobel (2004) Surface fluxes and ocean coupling in the tropical intraseasonal oscillation. *J. Climate*, **17**, 4368–4386.

Maloney, E. D. and A. H. Sobel (2007) Idealized hot spot experiments with a general circulation model. *J. Climate*, **20**, 908–925.

Marshall, A. G., O. Alves, and H. H. Hendon (2008) An enhanced moisture convergence–evaporation feedback mechanism for MJO air–sea interaction. *J. Atmos. Sci.*, **65**, 970–986.

Masumoto, Y., H. Hase, Y. Kuroda, H. Matsuura, and K. Takeuchi (2005) Intraseasonal variability in the upper layer currents observed in the eastern equatorial Indian Ocean. *Geophys. Res. Lett.*, **32**, L02607, doi: 10.1029/2004GL021896.

Matthews, A. J. (2004) Atmospheric response to observed intraseasonal tropical sea surface temperature anomalies. *Geophys. Res. Lett.*, **31**, L14107, doi: 10.1029/ 2004GL020474.

McPhaden, M. J., G. Meyers, K. Ando, Y. Masumoto, V. S. N. Murty, M. Ravichandran, F. Syamsudin, J. Vialard, L. Yu, and W. Yu (2009) RAMA: The Research Moored Array for African–Asian–Australian Monsoon Analysis and Prediction. *Bull. Amer. Meteorol. Society*, **90**, 459–480.

Nakazawa, T. (1988) Tropical super clusters within intraseasonal variations over the western Pacific. *J. Meteorol. Soc. Japan*, **66**, 823–839.

Pegion, K. and B. P. Kritman (2008) The impact of air–sea interactions on the simulation of tropical intraseasonal variability. *J. Climate*, **21**, 6616–6635.

Rajendran, K. and A. Kitoh (2006) Modulation of tropical intraseasonal oscillations by ocean–atmosphere coupling. *J. Climate*, **19**, 366–391.

Rao, S. A. and T. Yamagata (2004) Abrupt termination of Indian Ocean dipole events in response to intraseasonal disturbances. *Geophys. Res. Lett.*, **31**, L19306, doi: 10.1029/2004GL020842.

Resplandy, L., J. Vialard, M. Lévy, O. Aumont, and Y. Dandonneau (2009) Seasonal and intraseasonal biogeochemical variability in the thermocline ridge of the southern tropical Indian Ocean. *J. Geophys. Res.*, **114**, C07024, doi: 10.1029/2008JC005246.

Reynolds, R. W., N. A. Rayner, T. M. Smith, D. C. Stokes, and W.Wang (2002) An improved in situ and satellite SST analysis for climate. *J. Climate*, **15**, 1609–1625.

Roxy, M. and Y. Tanimoto (2007) Role of SST over the Indian Ocean in influencing the intraseasonal variability of the Indian summer monsoon. *J. Meteorol. Soc. Japan*, **85**, 349–358.

Saji, N. H., B. N. Goswami, P. N. Vinayachandran, and T. Yamagata (1999) A dipole mode in the tropical Indian Ocean. *Nature*, **401**, 360–363.

Saji, N. H., S.-P. Xie, and C.-Y. Tam (2006) Satellite observations of intense intraseasonal cooling events in the tropical south Indian Ocean. *Geophys. Res. Lett.*, **33**, L14704, doi: 10.1029/ 2006GL026525.

Schott, F. A., S.-P. Xie, and J. P. McCreary Jr. (2009) Indian Ocean circulation and climate variability. *Rev. Geophys.*, **47**, RG1002, doi: 10.1029/2007RG000245.

Sengupta, D., R. Senan, B. N. Goswami, and J. Vialard (2007) Intraseasonal variability of equatorial Indian Ocean zonal currents. *J. Climate*, **20**, 3036–3055, doi: 10.1175/JCLI4166.1.

Seo, K-H., J-K. Schemm, W-Q. Wang, and A. Kumar (2007) The boreal summer intraseasonal oscillation simulated in the NCEP Climate Forecast System: The effect of sea surface temperature. *Mon. Wea. Rev.*, **135**, 1807–1827.

Shinoda, T. (2005) Impact of the diurnal cycle of solar radiation on intraseasonal SST variability in the western equatorial Pacific. *J. Climate*, **18**, 2628–2636.

Sobel, A. H. and H. Gildor (2003) A simple time-dependent model of SST hot spots. *J. Climate*, **16**, 3978–3992.

Sobel, A. H., E. D. Maloney, G. Bellon, and D. M. Frierson (2008) The role of surface fluxes in tropical intraseasonal oscillations. *Nature Geoscience*, **1**, 653–657.

Sobel, A. H., E. D. Maloney, G. Bellon, and D. M. Frierson (2010) Surface fluxes and tropical intraseasonal variability: A reassessment. *J. Adv. Model. Earth Syst.*, **2**, Art. 2, 27 pp.

Soloviev, A. and R. Lukas (1997) Observation of large diurnal warming events in the near-surface layer of the western equatorial Pacific warm pool. *Deep-Sea Res. I*, **44**, 1055–1076.

Sperber, K. R. and H. Annamalai (2008) Coupled model simulations of boreal summer intraseasonal (30–50 day) variability, Part 1: Systematic errors and caution on use of metrics. *Climate Dynamics*, **31**, 345–372.

Stephens, G. L., P. J. Webster, R. H. Johnson, R. Engelen, and T. L'Ecuyer (2004) Observational evidence for the mutual regulation of the tropical hydrological cycle and tropical sea surface temperatures. *J. Climate*, **17**, 2213–2224.

Thadathil, P., P. M. Muraleedharan, R. R. Rao, Y. K. Somayajulu, G. V. Reddy, and C. Revichandran (2007) Observed seasonal variability of barrier layer in the Bay of Bengal. *J. Geophys. Res.*, **112**, C02009, doi: 10.1029/2006JC003651.

Tokioka, T., K. Yamazaki, A. Kitoh, and T. Ose (1988) The equatorial 30–60 day oscillation and the Arakawa–Schubert penetrative cumulus parameterization. *J. Meteorol. Soc. Japan*, **66**, 883–901.

Vecchi, G. A. and D. Harrison (2002) Monsoon breaks and subseasonal sea surface temperature variability in the Bay of Bengal. *J. Climate*, **15**, 1485–1493.

Vialard, J., G. R. Foltz, M. J. McPhaden, J. P. Duvel, and C. de Boyer Montégut (2008) Strong Indian Ocean sea surface temperature signals associated with the Madden–Julian Oscillation in late 2007 and early 2008. *Geophys. Res. Lett.*, **35**, L19608, doi: 10.1029/2008GL035238.

Vialard, J., J. P. Duvel, M. J. McPhaden, P. Bouruet-Aubertot, B. Ward, E. Key, D. Bourras, R. Weller, P. Minnett, A. Weill *et al.* (2009) Cirene: Air–sea interactions in the Seychelles–Chagos Thermocline Ridge Region. *Bull. Amer. Meteorol. Society*, **90**, 45–61.

Vinayachandran, P. N. and N. H. Saji (2008) Mechanisms of South Indian Ocean intraseasonal cooling. *Geophys. Res. Lett.*, **35**, L23607, doi: 10.1029/2008GL035733.

Vitart, F., S. Woolnough, M. A. Balmaseda, and A. M. Tompkins (2007) Monthly forecast of the Madden–Julian oscillation using a coupled GCM. *Mon. Wea. Rev.*, **135**, 2700–2715.

Waliser, D. E. (1996) Formation and limiting mechanisms for very high sea surface temperature: Linking the dynamics and the thermodynamics. *J. Climate*, **9**, 161–188.

Waliser, D. E., K. M. Lau, and J-H. Kim (1999) The influence of coupled sea surface temperatures on the Madden–Julian oscillation: A model perturbation experiment. *J. Atmos. Sci.*, **56**, 333–358.

Waliser, D. E., R. Murtugudde, and L. E. Lucas (2003) Indo-Pacific Ocean response to atmospheric intraseasonal variability, 1: Austral summer and the Madden–Julian Oscillation. *J. Geophys. Res.*, **108**(C5), 3160, doi: 10.1029/2002JC001620.

Waliser, D. E., R. Murtugudde, P. Strutton, and J.-L. Li (2005) Subseasonal organization of ocean chlorophyll: Prospects for prediction based on the Madden–Julian Oscillation, *Geophys. Res. Lett.*, **32**, L23602, doi: 10.1029/2005GL024300.

Wang, W. and M. E. Schlesinger (1999) The dependence on convection parameterization of the tropical intraseasonal oscillation simulated by the UIUC 11-layer atmospheric GCM. *J. Climate*, **12**, 1423–1457.

Wang, W., M. Chen, and A. Kumar (2009) Impacts of ocean surface on the northward propagation of the boreal summer intraseasonal oscillation in the NCEP climate forecast system, **22**, 6561–6576.

Wentz, F. J., C. Gentemann, D. Smith, and D. Chelton (2000) Satellite measurements of sea-surface temperature through clouds. *Science*, **288**, 847–850.

Woolnough, S. J., J. M. Slingo, and B. J. Hoskins (2000) The relationship between convection and sea surface temperature on intraseasonal timescales. *J. Climate*, **13**, 2086–2104.

Woolnough, S. J., J. M. Slingo, and B. J. Hoskins (2001) The organisation of tropical convection by intraseasonal sea surface temperature anomalies. *Quart. J. Roy. Meteorol. Soc.*, **127**, 887–907.

Woolnough, S. J., F. Vitart, and M. A. Balmaseda (2007) The role of the ocean in the Madden–Julian Oscillation: Implications for MJO prediction. *Quart. J. Roy. Meteorol. Soc.*, **133**, 117–128.

Wu, M. L. C., S. Schubert, I-S. Kang, and D. Waliser (2002) Forced and free intraseasonal variability over the South Asian monsoon region simulated by 10 AGCMs. *J. Climate*, **15**, 2862–2880.

Xavier, P. K., J. P. Duvel, and F. J. Doblas-Reyes (2008) Boreal summer intraseasonal variability in coupled seasonal hindcasts. *J. Climate*, **21**, 4477–4497.

Xavier, P. K., J. P. Duvel, P. Braconnot, and F. J. Doblas-Reyes (2010) An evaluation metric for intraseasonal variability and its application to CMIP3 Twentieth-Century simulations. *J. Climate*, **23**, 3497–3508.

Yamada, H., K. Yoneyama, M. Katsumata, and R. Shirooka (2010) Observations of a super cloud cluster accompanied by synoptic-scale eastward-propagating precipitating systems over the Indian Ocean. *J. Atmos. Sci.*, **67**, 1456–1473, doi: 10.1175/2009JAS3151.1.

Yang, J., Q. Liu, and Z. Liu (2010) Linking observations of the Asian Monsoon to Indian Ocean SST: Possible roles of Indian Ocean Basin mode and dipole mode. *J. Climate*, **23**, 5889–5902.

Yokoi, T., T. Tozuka, and T. Yamagata (2008) Seasonal variation of the Seychelles Dome. *J. Climate*, **21**, 3740–3754.

Yoneyama, K., M. Katsumata, K. Mizuno, M. Yoshizaki, R. Shirooka, K. Yasunaga, H. Yamada, N. Sato, T. Ushiyama, Q. Moteki *et al.* (2008) MISMO field experiment in the equatorial Indian Ocean. *Bull. Amer. Meteorol. Society*, doi: 10.1175/2008AMS2519.1.

Zeng, X. and A. Beljaars (2005) A prognostic scheme of sea surface skin temperature for modeling and data assimilation. *Geophys. Res. Lett.*, **32**, L14605, doi: 10.1029/2005GL023030.

Zhang, G. J. and M. Mu (2005) Simulation of the Madden–Julian oscillation in the NCAR CCM3 using a revised Zhang–McFarlane convection parameterization scheme. *J. Climate*, **18**, 4046–4064.

Zhang, C., M. Dong, S. Gualdi, H. H. Hendon, E. D. Maloney, A. Marshall, K. R. Sperber, and W. Wang (2006) Simulations of the Madden–Julian oscillation in four pairs of coupled and uncoupled models. *Climate Dynamics*, **27**, 573–592.

Zheng, Y., D. E. Waliser, W. F. Stern, and C. Jones (2004) The role of coupled sea surface temperatures in the simulation of the tropical intraseasonal oscillation. *J. Climate*, **17**, 4109–4134.

Zhou, C. and T. Li (2010) Upscale feedback of tropical synoptic variability to intraseasonal oscillations through the nonlinear rectification of the surface latent heat flux. *J. Climate*, **23**, 5738–5754.

16

Vertical structure from recent observations

Chidong Zhang

16.1 INTRODUCTION

This chapter discusses recent observations on the vertical structure of the MJO since 2005 when the First Edition of this book was published. Many studies have contributed to our knowledge of this subject. Earlier observations of the MJO were mainly based on limited rawinsonde data from operational sites and special field experiments, as well as previous global reanalysis products. Details of these observations and their references can be found in the other chapters of this book and in Zhang (2005). Sperber (2003) and Kiladis *et al.* (2005) provide systematic documentations of the vertical structure of the MJO in multiple variables. Results from these earlier studies are summarized only briefly here. Emphasis in this chapter will be given to results based on more recent and more advanced satellite observations and global reanalysis products.

The most fundamental vertical structure of the MJO is the reversal of its zonal wind anomalies resembling the first baroclinic mode, which converge toward an MJO convection center in the lower troposphere (e.g., 850 hPa) and diverge away from the convection center in the upper troposphere (e.g., 200 hPa). This vertical structure in the zonal wind of the MJO was clearly illustrated in the schematic of Madden and Julian (1972). Because of the Earth's rotation, the zonal wind anomalies are stronger west of the convection center than they are east of it. A first baroclinic structure also exists in meridional wind anomalies at the longitude of an MJO convection center. When MJO convection is not centered at the equator, a strong single overturning circulation is formed with its ascending branch in the hemisphere of the MJO convection center and the corresponding cross-equatorial meridional wind at the lower and upper troposphere. To the west of an MJO convection center, a pair of cyclonic (anticyclonic) circulation "gyres" can be found in the lower (upper) troposphere, giving the impression of a first baroclinic mode equatorial Rossby wave. The upward motion of this first baroclinic structure

W. K. M. Lau and D. E. Waliser (Editors), *Intraseasonal Variability in the Atmosphere–Ocean Climate System* (Second Edition).

in the wind is strongest in the upper troposphere (500–300 hPa) where the largest latent heating release often occurs in an MJO convection center. Because of the vertical density distribution, wind anomalies are much stronger in the upper troposphere than in the lower troposphere. All these basic features in the vertical structure of the wind associated with the MJO are similar to the Gill (1980) solution with a stationary and isolated heating source at or near the equator.

The temperature anomalies associated with the first baroclinic structure in the wind are positive in an MJO convection center or slightly to the east and negative outside. The largest anomalies are at the same levels of the strongest vertical motions (~300 hPa). These temperature signals extend through most of the troposphere but reverse their signs near 200 hPa to 150 hPa with greater amplitudes above (100 hPa) and near the surface with weaker amplitudes. Anomalies in specific humidity show a positive peak in an MJO convection center near the 700 hPa level and a negative peak to the west at the same level or slightly below. These humidity signals extend through most of the troposphere—to the maximum height where sounding measurement of humidity is mostly reliable (e.g., roughly 300 hPa).

The second most fundamental feature of the vertical structure of the MJO is a westward tilt from the lower to upper troposphere. This westward tilt has been observed in the first baroclinic structure in the zonal wind, which is more discernible in sounding data at certain sites in the tropical Indian and western Pacific regions than in global reanalyses. Similar westward tilts have also been found in the divergence field (convergence at low levels and especially in the boundary layer east of an MJO convection center), water vapor (low-level moist signals to the east of an MJO convection center), diabatic heating (low-level heating to the east of mid-level and high-level heating), and temperature (positive anomalies extending from the maximum level of ~400–300 hPa downward to the east). Temperature anomalies through the entire troposphere exhibit a more complicated structure. Above the maximum level (~400–300 hPa), temperature anomalies also tilt eastward with increasing height. These two branches of eastward tilts below and above the level of maximum anomalies are sometimes referred to as the ''boomerang pattern''. It is typical of the tropical atmosphere associated with propagating heating sources on a wide range of timescales, including convectively coupled equatorial waves (Wheeler *et al.*, 2000). The tilting upper branch of boomerang temperature anomalies indicates upward energy propagation from the level of maximum diabatic heating.

16.2 REMOTE-SENSING PRODUCTS

Since 2005, more observations on the vertical structure of the MJO have become available. Most new information has come from advanced satellite remote-sensing products that provide estimates of vertical profiles of the tropical atmosphere with better spatial coverage than limited sounding observations. Table 16.1 lists the satellite data that have been used in recent studies of the vertical structure of the MJO discussed in the rest of this chapter. In addition, advanced data assimilation

Table 16.1. Satellite data used in recent studies of MJO vertical structures.

Satellite data (supplements)	*Variable*	*Period*	*Vertical levels*	*Horizontal resolution*	*Temporal resolution*	*References*
TRMM (PR, TMI)	Latent and diabatic heating, radar echo top height, precipitation types	January 1, 1998–present	18 (1,000–100 hPa)	0.5°	Daily	Tao *et al.* (2006) Kummerow *et al.* (1998)
AIRS	Temperature, humidity	September 1, 2002–present	24 standard pressure levels (1,000–1 hPa) for temperature; 12 standard pressure layers (1,000–100 hPa) for humidity	1°	Twice daily	Susskind *et al.* (2006) Chahine *et al.* (2006)
CloudSat	Liquid water content, ice water content	2006–present	40	1°	Twice daily	Austin *et al.* (2009)
MLS	Ice water content, water vapor	August 26, 2004–February 22, 2007	6-surfaces-per-decade pressure from 316 to 0.1 hPa	4° × 8°	Twice daily	Wu *et al.* (2006)
ISCCP	Cloud regimes (based on cloud top pressure and optical thickness)	July 1, 1983–December 31, 2004	N/A	2.5°	3 hours	Rossow and Schiffer (1999)
QuickSCAT, MISR, SSM/I	Tropospheric column moisture transport and convergence	September 1, 1999–December 31, 2005	N/A	0.5°	Twice daily	Liu and Tang (2005)
QuickSCAT, AVHRR, TMI, SSM/I, AMSR-E (ERA-40, NCEP2)	Surface latent heat flux	January 1, 1981–December 31, 2002	N/A	1°	Daily	Yu and Weller (2007)

technology incorporating some of the satellite data has produced a new generation of global reanalysis datasets (e.g., MERRA, CFS-R). They provide information on the vertical structure of the MJO not available from previous reanalysis products (e.g., different components of diabatic heating).

Temperature anomalies associated with the MJO derived from satellite observations are mostly consistent with those based on sounding observations (Tian *et al.*, 2006, 2010). Maximum positive and negative anomalies are near 400 hPa, with low-level anomalies leading (to the east), at least over the Indian Ocean. Upper-level temperature anomalies are zonally confined over the Indian Ocean but are more widely spread across the Pacific. The vertical structure in temperature is more baroclinic (e.g., warm at 800–200 hPa, cold above and below) over the Indian Ocean than over the Pacific, where temperature anomalies tend to be of the same sign in the troposphere, with a reverse sign but smaller amplitude in the stratosphere.

Previous observations of the vertical structure of moisture based on limited soundings have also been discerned in satellite data (Tian *et al.*, 2006, 2010; Waliser *et al.*, 2009). During a convectively active (inactive) phase of the MJO, strong positive (negative) moisture anomalies extend from 850 hPa up to the 200 hPa level, with their peaks ($\pm$0.3–0.4 g/kg) between 800 hPa and 600 hPa. As a convection center of the MJO moves eastward from the Indian Ocean into the western Pacific, it tends to be preceded by positive anomalies in moisture in the lower troposphere (below 500 hPa) by 5–10 days. Negative anomalies in moisture also first occur in the lower troposphere immediately under or after (west of) the precipitation peak. During the transition period (between inactive and active phases), moisture anomalies evolve in the opposite sense in the lower and upper troposphere. Such structural changes constitute a westward tilt in moisture anomalies, consistent with the local moisture evolution associated with the MJO observed by sounding data (Lin and Johnson, 1996; Kemball-Cook and Weare, 2001; Kiladis *et al.*, 2005; Agudelo *et al.*, 2006; Yoneyama *et al.*, 2008; Katsumata *et al.*, 2009). This phase relationship between precipitation and low-level moisture apparently also exists in the northward-moving intraseasonal variability during the Asian summer monsoon (Jiang *et al.*, 2004, 2010a; Fu *et al.*, 2006).

It has been suggested that the low-level moisture increase prior to the precipitation maximum is instrumental in the development of deep convection in a convection center of the MJO (see Chapter 2). The causes of low-level moisture increase are likely to be related to a combination of factors. Possible processes involved include moisture convergence by large-scale circulation, surface evaporation, detrainment of shallow convective clouds, and synoptic-scale eddy transport. The first three have been supported by observations while the last was suggested by numerical simulation (Maloney, 2009). Diagnostics of global reanalysis products (Hendon and Salby, 1994; Jones and Weare, 1996; Weare, 2003; Benedict and Randall, 2009), sounding observations (Lin and Johnson, 1996; Kikuchi and Takayabu, 2004), and layered satellite data (Myers and Waliser, 2003) have shown boundary layer and low-level convergence preceding the precipitation maximum of the MJO as predicted by MJO theory (see Chapter 2). This phase relationship has

also been detected by diagnostics of recent satellite profiling data (Waliser *et al.*, 2009). A slight phase lead of total column moisture convergence exists when the MJO precipitation maximum is located over the Indian Ocean. The column-integrated water budget cannot, however, be closed using satellite-based data alone, indicating the need for a more reliable data source for this, such as improved data assimilation products. Possible connections between the low-level moisture fluctuation associated with the MJO and evolution of the cloud population will be discussed later (see p. 541).

The role played by surface evaporation in the MJO has been controversial (Zhang, 2005; Sobel *et al.*, 2010). Whether it may explain the increase in low-level moisture leading to an active phase of the MJO is even more uncertain. To first order, precipitation is balanced by total column moisture convergence and they covary in space and time according to sounding observations (Lin and, Johnson, 1996) and satellite estimates (Waliser *et al.*, 2009). The fluctuations in surface evaporation associated with the MJO follow those of the surface wind. Their peaks are located west of convection centers of the MJO and they are relatively weak east of convection centers (Zhang, 1996; Shinoda *et al.*, 1998). Surface evaporation may contribute to the increase in low-level moisture east of convection centers through zonal advection by strong surface and low-level westerlies, as suggested by a modeling study (Maloney *et al.*, 2010).

The possibility that detrainment of shallow convective cloud may help moisten the lower troposphere was suggested by the observed coexistence of abundant shallow convection and the increase in low-level moisture prior to an active phase of the MJO (Lin and Johnson, 1996; Johnson *et al.*, 1999). Advanced satellite remote-sensing products capable of detecting cloud properties seem to provide further evidence for this and also reveal other features of changes in cloud population through the lifecycle of the MJO (Masunaga *et al.*, 2006; Chen and Del Genio, 2009; Lau and Wu, 2009; Waliser *et al.*, 2009; Jiang *et al.*, 2010a; Tromeur and Rossow, 2010). Different types of clouds exist all the time but their dominance or occurrence frequency varies between MJO phases. In a convectively inactive phase of the MJO, non-precipitating, drizzling, or precipitating shallow liquid phase (warm) clouds are the most abundant (positive anomalous probability distribution function of low-brightness temperature and low echo-top height in P1 and P2 of Figure 16.1). During the transition phase from inactive to active phases, these shallow warm clouds are gradually replaced by more mixed phase cumulus congestus and isolated deep-convective clouds, both with various precipitation efficiencies (P3 and P4 in Figure 16.1). In an active phase of the MJO, the cloud population is dominated by supercooled liquid phase and mixed ice phase clouds, while deep convective and very optically thick clouds also reach their maximum amount (P5 and P6 in Figure 16.1). The transition from convectively active to inactive phases is marked by a reduction in mixed phase clouds, an increase in shallow warm clouds, with the remaining precipitating and non-precipitating high-level anvil clouds associated with mature and decaying mesoscale convective systems (P7 and P8 in Figure 16.1). This cloud evolution has also been observed by ground radar (e.g., Haertel *et al.*, 2009).

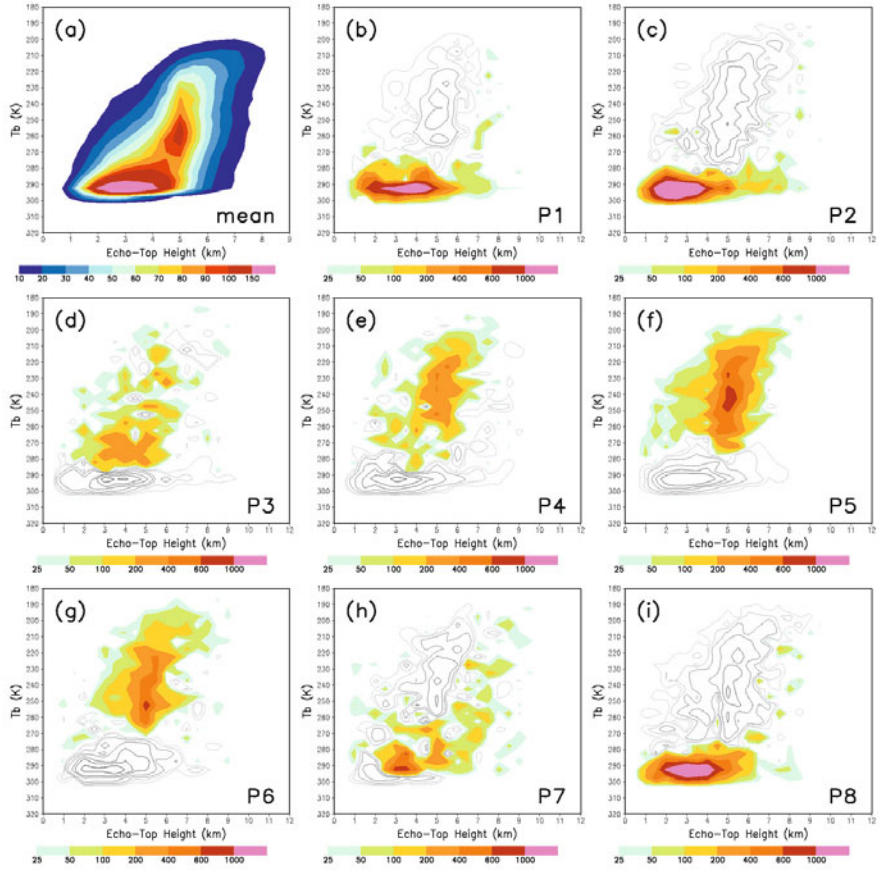

Figure 16.1. The joint probability distribution function of satellite-observed brightness temperature (Tb) and satellite radar echo-top height over the equatorial western Pacific: (a) mean state of the eight MJO phases and (b)–(i) difference between each of phases P1–P8 and the mean state. Positive values are color shaded and negative values are in clear contours. The unit for the mean state is in 0.01% of total occurrence counts. For P1–P8, the unit is the number of counts (from Lau and Wu, 2010).

Recent satellite observations of water vapor profiles and cloud properties allow conception of a schematic for the hydrological cycle associated with the MJO (Figure 16.2). Highlighted in this schematic are the relative phases between anomalies in low-level and high-level moisture, low-level moisture convergence, precipitation and surface evaporation, cloud liquid and ice water content. In particular, temporal vertical phase changes in moisture and cloud properties constitute a westward tilt when the schematic is considered to be moving eastward (toward the right) as does the MJO. The difference in cloud liquid water content between active and inactive phases is about 0.06 mm and the difference in total cloud ice water content is about 1 mg/m^3.

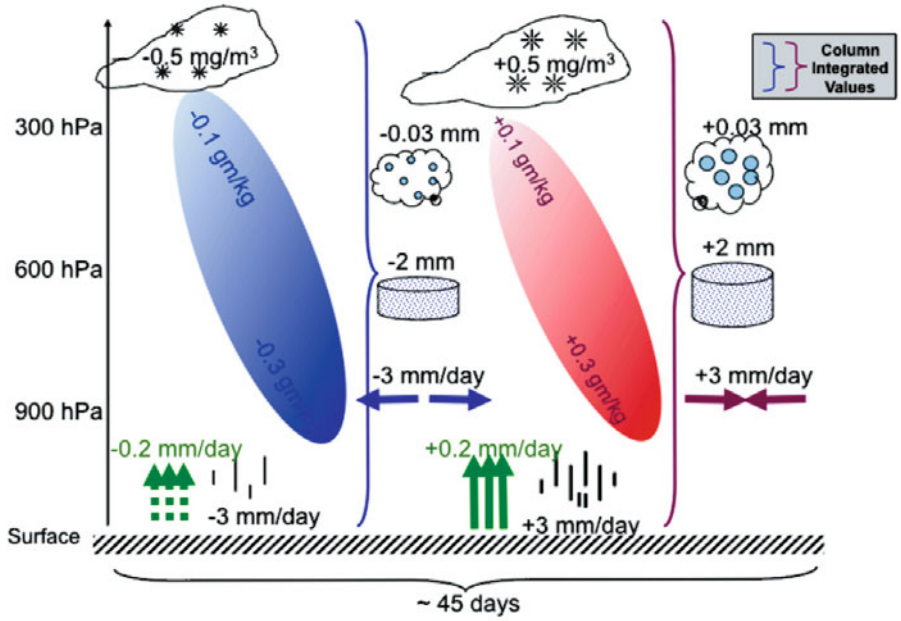

Figure 16.2. Schematic of the hydrological cycle associated with the MJO. Colored ovals indicate moisture anomalies. Asterisks mark cloud ice content. Total cloud liquid water content is symbolized by cyan circles. Horizontal arrows mark divergence (blue) and convergence (red). Vertical green arrows represent surface evaporation. Vertical black lines indicate precipitation. Shaded cylinders represent vertically integrated precipitable water (from Waliser *et al.*, 2009).

Another direct implication of changes in cloud population through the lifecycle of the MJO is the associated structural evolution of diabatic heating. Shallow precipitating cloud appearing prior to deep convective cloud indicates the elevation of latent heating from low to upper levels. This was first observed for MJO events during TOGA–COARE using diabatic heating estimated from sounding observations (Johnson *et al.*, 1999; Kikuchi and Takayabu, 2004; Lin *et al.*, 2004). For at least one major MJO event, heating maximum appeared at the 800 hPa to 700 hPa levels before deep heating (peaks at about the 400 hPa level) became dominant in the convectively active phase. If stratiform-like heating (peak in the upper troposphere, no heating or even cooling in the lower troposphere) dominates toward the end of a convectively active phase of the MJO, structural evolution in the heating profile yields a vertical tilt. Given the eastward motion of the MJO, this tilt is westward from a Lagrangian point of view in the same way as the tilt shown in Figure 16.2. The westward tilt of diabatic heating associated with the MJO—namely, the leading shallow heating and trailing stratiform-like heating relative to deep heating in the convection center—has also been shown in a composite using the NCEP–NCAR reanalysis (Lin *et al.*, 2004) and a composite and vertical mode decomposition using TOGA–COARE sounding data (Kiladis *et al.*, 2005).

Subsequent efforts at confirming the westward tilt in diabatic heating of the MJO have led to inconsistent results. Recent studies using two TRMM latent-heating datasets and two global reanalysis products over a season with multiple MJO events did not find any obvious shallow leading deep heating in latent or total diabatic heating profiles during individual MJO events (Jiang *et al.*, 2009). Neither did in situ sounding observations from the Indian Ocean for an MJO event (Katsumata *et al.*, 2009). A multiyear composite over the lifecycle of the MJO using a TRMM latent-heating estimate shows that the evolution of heat profiles is, instead of a gradual increase in the level of heating maximum as seen in a vertical tilt, a two-stage switch between low-level and high-level heating with the heating maxima fixed at 2 km and 8 km, respectively (Lau and Wu, 2009). A different TRMM latent-heating estimate reveals that peaks of convective and stratiform rain are in phase with two heating maxima in the convection center, one near 4 km and the other near 7 km. There is trailing heating in the upper troposphere (5–9 km) toward the western side of the convection center associated with the remaining stratiform rain, but there is no low-level heating leading (to the east) of the convection center (Morita *et al.*, 2006).

Studying the structural evolution of diabatic heating associated with the MJO currently faces difficulties from several sources: contamination of parameterized moist processes (including cloud microphysics as well as rainfall) in numerical models and data assimilation products, the infancy of latent-heating retrievals from satellite remote-sensing data, and limited sampling of sounding observations (covering four MJO events so far), which are always taken as the ground truth. Latent-heating fields derived by four TRMM algorithms exhibit clear spectral signals of the MJO in both deep and shallow heating. These heating retrievals agree well in their deep heating (with its peak above the melting level) of the MJO. Deep heating is at least an order of magnitude larger than shallow heating and its zonal propagating signals of the MJO are more robust than those of shallow heating. TRMM retrievals differ substantially in the structures and zonal distributions of their shallow heating. There is no consistent result from the four TRMM datasets in terms of shallow heating leading deep heating and the consequential tilt in latent heating of the MJO (Zhang *et al.*, 2010).

The new generation of global reanalyses—namely, ERA-Interim (ERAI), MERRA, and CFS-R—provide more advanced data assimilation products with higher resolutions than the previous ones. Direct heating fields are also available. A composite of latent-heating anomalies produced by MERRA clearly shows a westward tilt as the MJO convection center propagates from the Indian to the western Pacific Ocean (Figure 16.3). A similar tilt is also seen in diabatic heating estimated from ERAI and CFS-R (not shown). If the westward tilt in MJO heating is observed in these new global reanalysis products over the western Pacific (as seen in Figure 15.3), it is much less apparent at other longitudes (e.g., over the Indian Ocean) and not apparent in every MJO event (Ling and Zhang, 2010). These results illustrate the challenges we must face when studying the structure and evolution of the diabatic heating associated with the MJO: non-uniform quality in current diabatic and latent-heating data from global reanalyses and TRMM

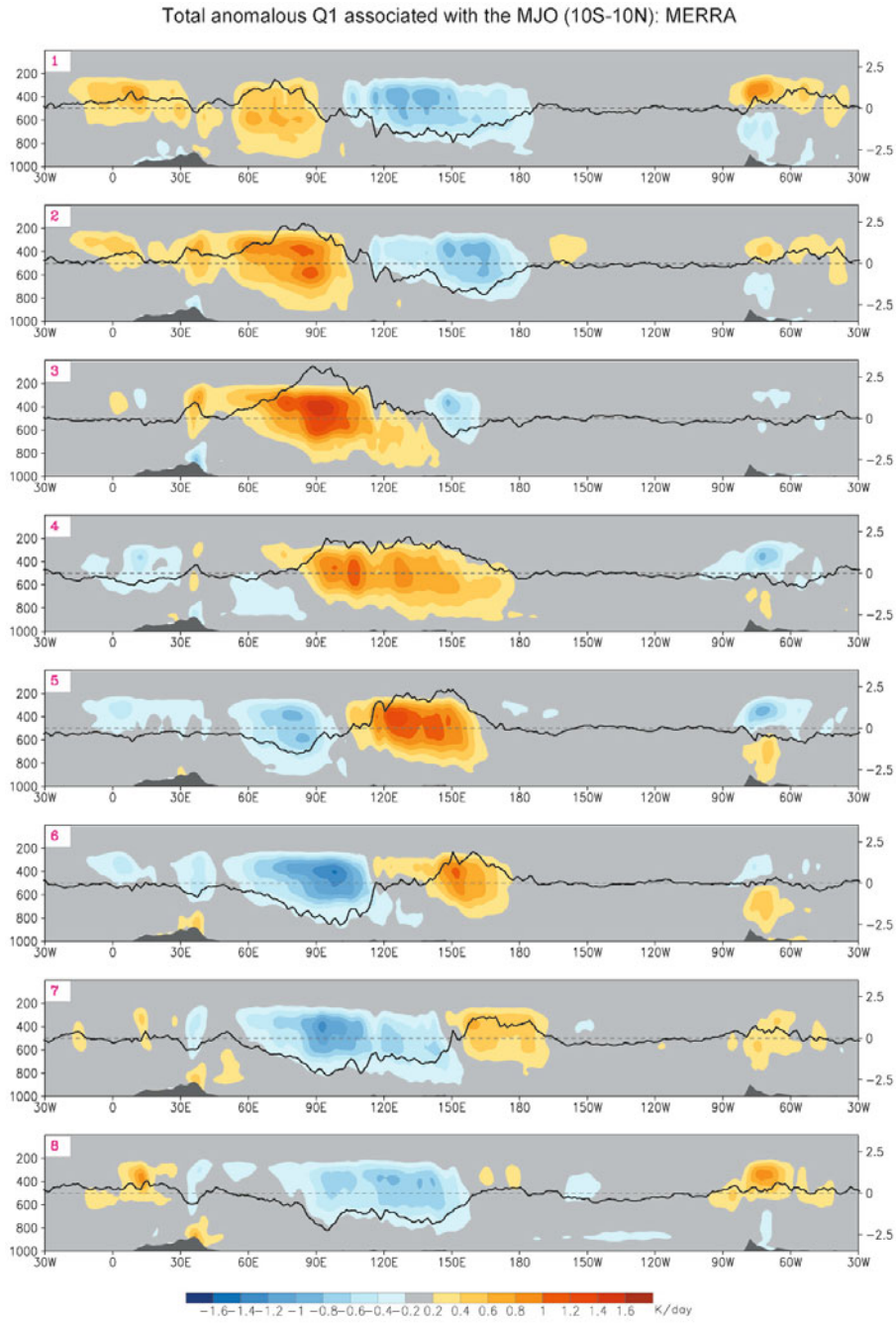

Figure 16.3. Composite of anomalous latent heating from MERRA for eight phases of the MJO (colors, K/day, left ordinate) and TRMM rainfall (curves, mm/day, right ordinate) (from Jiang *et al.*, 2010b).

retrievals and the small sample size of MJO events covered by in situ observations for validating heating data from global reanalyses and TRMM retrievals.

16.3 REFERENCES

Agudelo, P. A., J. A. Curry, C. D. Hoyos, and P. J. Webster (2006) Transition between suppressed and active phases of intraseasonal oscillations in the Indo-Pacific Warm Pool. *J. Climate*, **19**, 5519–5530.

Austin, R. T., A. J. Heymsfield, and G. L. Stephens (2009) Retievals of ice cloud microphysical parameters using the CloudSat millimeter-wave radar and temperature. *J. Geophys. Res.*, **114**, D00A23.

Benedict, J. J. and D. A. Randall (2009) Structure of the Madden–Julian Oscillation in the Superparameterized CAM. *J. Atmos. Sci.*, **66**, 3277–3296.

Chahine, M. T. *et al.* (2006) AIRS: Improving weather forecasting and providing new data on greenhouse gases. *Bull. Amer. Meteorol. Society*, **87**, 911–926, doi: 10.1175/BAMS-87-7-911.

Chen, Y. H. and A. D. Del Genio (2009) Evaluation of tropical cloud regimes in observations and a general circulation model. *Climate Dynamics*, **32**, 355–369, doi: 10.1007/S00382-008-0386-6.

Fetzer, E. J., W. G. Read, D. Waliser, B. H. Kahn, B. Tian, H. Vomel, F. W. Irion, H. Su, A. Eldering, M. de la Torre Juarez *et al.* (2008) Comparison of upper tropospheric water vapor observations from the Microwave Limb Sounder and Atmospheric Infrared Sounder. *J. Geophys. Res.*, **113**, D22110, doi: 10.1029/2008

Fu, X. H., B. Wang, and L. Tao (2006) Satellite data reveal the 3-D moisture structure of Tropical Intraseasonal Oscillation and its coupling with underlying ocean. *Geophys. Res. Lett.*, **33**.

Gill, A. E. (1980) Some simple solutions for heat-induced tropical circulation. *Quart. J. Roy. Meteorol. Soc.*, **106**, 447–462.

Haertel, P. T., G. N. Kiladis, A. Denno, and T. M. Rickenbach (2009) Vertical-mode decomposition of 2-day waves and the Madden–Julian oscillation. *J. Atmos. Sci.*, **65**, 813–833.

Hendon, H. H. and M. L. Salby (1994) The life-cycle of the Madden–Julian Oscillation. *J. Atmos. Sci.*, **51**(15), 2225–2237.

Jiang, X., T. Li, and B. Wang (2004) Structures and mechanisms of the northward propagating boreal summer intraseasonal oscillation. *J. Climate*, **17**, 1022–1039.

Jiang, X., D. E. Waliser, W. S. Olson, W.-K. Tao, T. S. L'Ecuyer, J.-L. Li, B. Tian, Y. L. Yung, A. M. Tompkins, S. E. Lang, and M. Grecu (2009) Vertical heating structures associated with the MJO as characterized by TRMM estimates, ECMWF Reanalyses and forecasts: A case study during 1998–99 winter. *J. Climate*, **22**, 6001–6020.

Jiang, X., D. E. Waliser, J.-L Li, and C. Woods (2010a) Vertical cloud structures of the boreal summer intraseasonal variability based on CloudSat observations and ERA-Interim reanalysis. *Climate Dynamics*, doi: 10.1007/s00382-010-0853-8.

Jiang, X., D. E. Waliser, W. S. Olson, W.-K. Tao, T. S. L'Ecuyer, S. Shige, K.-F. Li, Y. L. Yung, S. Lang, and Y. N. Takayabu (2011) Vertical diabatic heating structure of the MJO: Intercomparison between recent reanalyses and TRMM estimates. *Mon. Wea. Rev.* (in press).

Johnson, R. H., T. M. Rickenbach, S. A. Rutledge, P. E. Ciesielski, and W. H. Schubert (1999) Trimodal characteristics of tropical convection. *J. Climate*, **12**, 2397–2418.

Jones, C. and B. C. Weare (1996) The role of low-level moisture convergence and ocean latent heat flux in the Madden and Julian Oscillation: An observational analysis using ISCCP data and ECMWF analyses. *J. Climate*, **9**, 3086–3104.

Katsumata, M., R. H. Johnson, and P. E. Ciesielski (2009) Observed synoptic-scale variability during the developing phase of an ISO over the Indian Ocean during MISMO. *J. Atmos. Sci.*, **66**, 3434–3448.

Kemball-Cook, S. R. and B. C. Weare (2001) The onset of convection in the Madden Julian oscillation. *J. Climate*, **14**, 780–793.

Kikuchi, K. and Y. N. Takayabu (2004) The development of organized convection associated with the MJO during TOGA COARE IOP: Trimodal characteristics. *Geophys. Res. Lett.*, **31**, L10101, doi: 10.1029/2004GL019601.

Kiladis, G. N., K. H. Straub, and P. T. Haertel (2005) Zonal and vertical structure of the Madden–Julian Oscillation. *J. Atmos. Sci.*, **62**, 2790–2809.

Kummerow, C., W. Barnes, T. Kozu, J. Shiue, and J. Simpson (1998) The Tropical Rainfall Measuring Mission (TRMM) sensor package. *J. Atmos. Oceanic Technol.*, **15**, 809–817.

Lau, W. K. M. and M. Wu (2010) Characteristics of precipitation, cloud, and latent heating associated with the Madden and Julian Oscillation. *J. Climate*, **23**, 504–518.

Lin, J., B. E. Mapes, M. Zhang, and M. Newman (2004) Stratiform precipitation, vertical heating profiles, and the Madden–Julian Oscillation. *J. Atmos. Sci.*, **61**, 296–309.

Lin, X. and R. H. Johnson (1996) Heating, moistening, and rainfall over the western Pacific warm pool during TOGA COARE. *J. Atmos. Sci.*, **53**, 3367–3383.

Ling, J. and C. Zhang (2010) Structural evolution in heating profiles of the MJO in global reanalyses and TRMM retrievals. *J. Climate*, **24**, 825–842.

Liu, W. T. and W. Tang (2005) Estimating moisture transport over oceans using space-based observations. *J. Geophys. Res.*, **110**, D10101, doi: 10.1029/2004JD005300.

Madden, R. A. and P. R. Julian (1972) Description of global-scale circulation cells in the tropics with a 40–50 day period. *J. Atmos. Sci.*, **29**, 1109–1123.

Maloney, E. D. (2009) The moist static energy budget of a composite tropical intraseasonal oscillation in a climate model. *J. Climate*, **22**, 711–729

Maloney, E. D., A. H. Sobel, and W. M. Hannah (2010) Intraseasonal variability in an aquaplanet general circulation model. *J. Adv. Model. Earth Syst.*, **2**, Art. #5, 24 pp., doi: org/10.3894/JAMES.2010.2.5.

Masunaga, H., T. S. L'Ecuyer, and C. D. Kummerow (2006) The Madden–Julian Oscillation recorded in early observations from the Tropical Rainfall Measuring Mission (TRMM). *J. Atmos. Sci.*, **63**, 2777–2794.

Morita, J., Y. N. Takayabu, S. Shige, and Y. Kodama (2006) Analysis of rainfall characteristics of the Madden–Julian oscillation using TRMM satellite data. *Dyn. Atmos. Oceans*, **42**, 107–126.

Myers, D. S. and D. E. Waliser (2003) Three-dimensional water vapor and cloud variations associated with the Madden–Julian oscillation during Northern Hemisphere winter. *J. Climate*, **16**, 929–950.

Rossow, W. B. and R. A. Schiffer (1999) Advances in understanding clouds from ISCCP. *Bull. Amer. Meteorol. Society*, **80**, 2261–2287.

Shinoda, T., H. H. Hendon, and J. Glick (1998) Intraseasonal variability of surface fluxes and sea surface temperature in the tropical western Pacific and Indian oceans. *J. Climate*, **11**, 1685–1702.

Sobel, A. H., E. D. Maloney, G. Bellon, and D. M. Frierson (2010) Surface fluxes and tropical intraseasonal variability: A reassessment. *J. Adv. Model. Earth Syst.*, **2**, doi: 10.3894/JAMES.2010.2.2.

Sperber, K. R. (2003) Propagation and the vertical structure of the Madden–Julian Oscillation. *Mon. Wea. Rev.*, **131**, 3018–3037.

Susskind, J., C. Barnet, J. Blaisdell, L. Iredell, F. Kelta, L. Kouvaris, G. Molnar, and M. Chahine (2006) Accuracy of geophysical parameters derived from Atmospheric Infrared Sounder/Advanced Microwave Sounding Unit as a function of fractional cloud cover. *J. Geophys. Res.*, **111**, D09S17, doi: 10.1029/2005jd006272.

Tao, W.-K., E. Smith, R. Adler, Z. Haddad, A. Hou, T. Iguchi, R. Kakar, T. N. Krishnamurti, C. Kummerow, S. Lang *et al.* (2006) Retrieval of latent heating from TRMM measurements. *Bull. Amer. Meteorol. Society*, **87**, 1555–1572.

Tian, B., D. E. Waliser, E. J. Fetzer, B. H. Lambrigtsen, Y. L. Yung, and B. Wang (2006) Vertical moist thermodynamic structure and spatial–temporal evolution of the MJO in AIRS observations. *J. Atmos. Sci.*, **63**, 2462–2485.

Tian, B., D. E. Waliser, E. J. Fetzer, and Y. L. Yung (2010) Vertical moist thermodynamic structure of the Madden–Julian Oscillation in Atmospheric Infrared Sounder observations: An update and a comparison to ECMWF interim reanalysis. *Mon. Wea. Rev.*, **138**, 4576–4882.

Tromeur, E. and W. B. Rossow (2010) Interaction of tropical deep convection with the large-scale circulation in the MJO. *J. Climate*, **23**, 1837–1853.

Waliser, D. E., B. Tian, X. Xie, W. T. Liu, M. J. Schwartz, and E. J. Fetzer (2009) How well can satellite data characterize the water cycle of the Madden–Julian Oscillation? *Geophys. Res. Lett.*, **36**, L21803, doi: 10.1029/2009GL040005.

Weare, B. C. (2003) Composite singular value decomposition analysis of moisture variations associated with the Madden–Julian oscillation. *J. Climate*, **16**, 3779–3792.

Wheeler, M., G. N. Kiladis, and P. J. Webster (2000) Large-scale dynamical fields associated with convectively coupled equatorial waves. *J. Atmos. Sci.*, **57**, 613–640.

Wu, D. L. *et al.* (2006) EOS MLS cloud ice measurements and cloudy-sky radiative transfer model. *IEEE Trans. Geosci. Remote Sens.*, **44**(5), 1156–1165.

Yoneyama, K., Y. Masumoto, Y. Kuroda, M. Katsumata, K. Mizuno, Y. N. Takayabu, M. Yoshizaki, A. Shareef, Y. Fujiyoshi, M. J. McPhaden *et al.* (2008) MISMO field experiment in the equatorial Indian Ocean. *Bull. Amer. Meteorol. Society*, **89**, 1889–1903.

Yu, L. S. and R. A. Weller (2007) Objectively analyzed air–sea heat fluxes for the global ice-free oceans (1981–2005). *Bull. Amer. Meteorol. Society*, **88**(4), 527–539.

Zhang, C. (1996) Atmospheric intraseasonal variability at the surface in the western Pacific Ocean. *J. Atmos. Sci.*, **53**, 739–785.

Zhang, C. (2005) Madden–Julian Oscillation. *Rev. Geophys.*, **43**, RG2003, doi: 10.1029/2004RG000158.

Zhang, C., J. Ling, S. M. Hagos, W.-K. Tao, S. Lang, Y. N. Takayabu, S. Shige, M. Katsumata, W. S. Olson, and T. L'Ecuyer (2010) MJO signals in latent heating: Results from TRMM retrievals. *J. Atmos. Sci.*, **67**, 3488–3508.

17

Multiscale theories for the MJO

Andrew J. Majda and Samuel N. Stechmann

17.1 INTRODUCTION

In the equatorial troposphere, the Madden–Julian Oscillation (MJO) is a planetary-scale wave envelope of complex multiscale convection (see Figure 17.1 for a schematic illustration). It begins as a standing wave in the Indian Ocean and propagates eastward across the western Pacific Ocean at a speed of $\approx 5\,\mathrm{m/s}$. Due to its planetary-scale circulation anomalies, the MJO significantly affects monsoon development, intraseasonal predictability in midlatitudes, and the development of El Niño and the Southern Oscillation (ENSO) in the Pacific Ocean, which is one of the most important components of seasonal prediction (see Zhang, 2005 and any of the chapters in the current book). It is also known that the MJO is a superrotating planetary-scale wave (see Biello *et al.*, 2007 and references therein) and recent simulations suggest there may be enhanced MJO activity in a warmer climate, possibly leading to superrotating tropical mean circulation (Caballero and Huber, 2010).

Basic understanding of the MJO's features has been gained from observations, including statistical composites (Hendon and Liebmann, 1994; Hendon and Salby, 1994; Salby and Hendon, 1994; Wheeler and Kiladis, 1999; Roundy and Frank, 2004; Kiladis *et al.*, 2005) and case studies of individual MJO events (Lin and Johnson, 1996; Yanai *et al.*, 2000; Houze *et al.*, 2000). From these observations, the following fundamental features of the MJO have been identified relatively clearly:

I. Slow eastward phase speed of $\approx 5\,\mathrm{m/s}$.
II. Peculiar dispersion relation of $d\omega/dk \approx 0$.
III. Horizontal quadrupole vortex structure.

In the simplest theoretical model for the MJO, its vertical structure is given by the first baroclinic mode and its horizontal structure is given by the planetary-scale

W. K. M. Lau and D. E. Waliser (Editors), *Intraseasonal Variability in the Atmosphere–Ocean Climate System* (Second Edition).

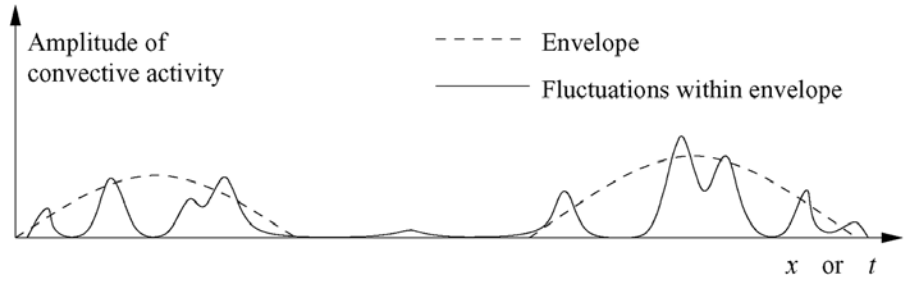

Figure 17.1. A large-scale envelope with fluctuations embedded within it.

response to a moving heat source whose velocity is prescribed at the MJO speed (Matsuno, 1966; Gill, 1980; Chao, 1987). This is called the Kelvin–Rossby wave paradigm by Houze *et al*. (2000), and they use it as a rough guideline for understanding observations, even though the structure of the model is different from and often at odds with actual observations (Houze *et al*., 2000). In fact, many theories have been proposed for the MJO, but they are all at odds with observations in various crucial ways, and no theory for the MJO has yet been generally accepted (see Majda and Stechmann, 2009a and Chapter 10 of the current book for overviews). The present chapter describes several recent theories and models for the MJO which focus on the multiscale structure of the MJO envelope (as described schematically in Figure 17.1).

This chapter begins with a minimal dynamical model for the MJO skeleton which captures all of the three key features (I–III) listed above. The following section deals with details of the MJO structure beyond the fundamental features of the skeleton, such as the vertical structure and the impact of multicloud and multiscale effects. Then we discuss the implications of these theories for improving global circulation model (GCM) simulations of the MJO.

17.2 THE MJO SKELETON

The MJO skeleton model is a minimal dynamical model that recovers robustly all three of the fundamental features (I–III) listed above. The fundamental mechanism of this model was proposed and developed in Majda and Stechmann (2009a, 2011), and it involves neutrally stable interactions between (i) planetary-scale lower-tropospheric moisture anomalies and (ii) sub-planetary-scale convection/wave activity (or, more precisely, the planetary-scale envelope of this sub-planetary-scale activity, which could be on synoptic scales and/or mesoscales).

The behavior of these two phenomena, moisture and wave activity, has been documented in numerous previous studies. Several studies have shown that the

lower troposphere tends to moisten during the suppressed convection phase of the MJO, and lower-tropospheric moisture appears roughly in quadrature with the MJO's heating anomaly (Kikuchi and Takayabu, 2004; Kiladis *et al.*, 2005; Tian *et al.*, 2006). Furthermore, it is well known that the low-level moisture content plays a key role in regulating mesoscale convection, and there is growing evidence that it also plays a key role in regulating convection on the scales of synoptic-scale convectively coupled waves and the MJO (Kikuchi and Takayabu, 2004; Kiladis *et al.*, 2005; Khouider and Majda, 2006, 2007, 2008a; Tian *et al.*, 2006; Majda *et al.*, 2007). A fundamental part of the model presented in Majda and Stechmann (2009a, 2011) is the effect of this low-level moisture on the envelope of sub-planetary-scale convection/wave activity.

The important role of synoptic-scale wave activity in driving the MJO is documented in a growing body of evidence in the form of observations (Hendon and Liebmann, 1994; Houze *et al.*, 2000; Masunaga *et al.*, 2006), simulations (Grabowski, 2001, 2003; Grabowski and Moncrieff, 2004; Khouider and Majda, 2007; Majda *et al.*, 2007; Majda and Stechmann, 2009b), and theory (Moncrieff, 2004; Majda and Biello, 2004; Biello and Majda, 2005, 2006; Biello *et al.*, 2007). This synoptic-scale wave activity is a complex menagerie of convectively coupled equatorial waves, such as 2-day waves, convectively coupled Kelvin waves, etc. (Khouider and Majda, 2006, 2008a; Kiladis *et al.*, 2009), and the envelope of this wave activity drives the MJO with its convective heating anomalies (Biello and Majda, 2005).

Based on the mechanisms outlined above, a dynamic model is designed for the MJO skeleton on intraseasonal/planetary scales. The model is formulated in terms of anomalies from a uniform base state of radiative–convective equilibrium, $\bar{R} = \bar{H}\bar{a}$, where $\bar{R} = 1\,\mathrm{K/day}$ is the fixed constant radiative cooling rate, $\bar{H}$ is a constant heating rate prefactor, and $\bar{a}$ is a constant (non-dimensional) amplitude of wave activity in the equilibrium state. The dry dynamical core of the model is the equatorial longwave equations (Majda, 2003; Majda and Biello, 2004; Biello and Majda, 2005, 2006), and two other dynamic variables are included to represent moist convective processes: q, lower-tropospheric moisture; and a, amplitude of the convection/wave activity envelope. The non-dimensional dynamical variable a parameterizes the amplitude of the planetary-scale envelope of sub-planetary-scale convection/wave activity (see Figure 17.1). It is noteworthy that, for the MJO skeleton model discussed here and in Majda and Stechmann (2009a, 2011), it is only the amplitude of the wave activity envelope that is needed—not any of the details of the particular synoptic-scale waves (Khouider and Majda, 2006, 2008a; Kiladis *et al.*, 2009) that make up the envelope. A key aspect of the model here is the interaction between a and q: as motivated by the discussion above, positive (negative) low-level moisture anomalies create a tendency to enhance (decrease) the envelope of equatorial synoptic-scale wave activity. The simplest equation for wave activity with these features is $a_t = \Gamma q(\bar{a} + a)$. The wave activity envelope then feeds back to the other variables through a heat source $\bar{H}a$ and—in accordance with conservation of moist static energy—a moisture sink $-\bar{H}a$. Thus, the model equations for anomalies from radiative–convective equilibrium take the

form

$$\left.\begin{aligned} u_t - yv &= -p_x \\ yu &= -p_y \\ 0 &= -p_z + \theta \\ u_x + v_y + w_z &= 0 \\ \theta_t + w &= \bar{H}a \\ q_t - \tilde{Q}w &= -\bar{H}a \\ a_t &= \Gamma q(\bar{a} + a) \end{aligned}\right\} \tag{17.1}$$

where u, v, and w are the zonal, meridional, and vertical velocities, respectively; and p and θ are the pressure and potential temperature, respectively. Notice that this model contains a minimal number of parameters: $\tilde{Q} = 0.9$, the (non-dimensional) mean background vertical moisture gradient; and $\Gamma = 1$, where Γq acts as the dynamic growth/decay rate of the wave activity envelope in response to moisture anomalies. In dimensional units, $\Gamma \approx 0.2\,\mathrm{day}^{-1}\,\mathrm{K}^{-1}$; see Stechmann *et al.* (2011) for a theoretical parameter estimate. These will be the standard parameter values used here unless otherwise noted. Also notice that the parameter $\bar{H}$ is actually irrelevant to the dynamics—as can be seen by rescaling (17.1) and recalling the equilibrium condition $\bar{R} = \bar{H}\bar{a}$—but it is written here for clarity of presentation.

The next step in obtaining the simplest dynamical model for the MJO skeleton is to use truncated vertical and meridional structures. The vertical structure is assumed to be first baroclinic—either $\cos(z)$ or $\sin(z)$—as in the Matsuno–Gill mean heating model (Majda, 2003; Biello and Majda, 2006). For instance, the zonal velocity u has a truncated vertical structure of $u(x, y, z, t) = \sum_j u_j(x, y, t)\sqrt{2}\cos(jz) \approx u_1(x, y, t)\sqrt{2}\cos z$. Truncated meridional structures are also used for simplicity. The meridional structure of a is assumed to simply be proportional to $\exp(-y^2/2)$. For the longwave-scaled equations, such a meridional heating structure is known to excite only Kelvin waves and first symmetric equatorial Rossby waves (Majda, 2003; Biello and Majda, 2006); hence one can write the resulting meridionally truncated equations as

$$\left.\begin{aligned} K_t + K_x &= -\frac{1}{\sqrt{2}}\bar{H}A \\ R_t - \frac{1}{3}R_x &= -\frac{2\sqrt{2}}{3}\bar{H}A \\ Q_t + \frac{1}{\sqrt{2}}\tilde{Q}K_x - \frac{1}{6\sqrt{2}}\tilde{Q}R_x &= \left(-1 + \frac{1}{6}\tilde{Q}\right)\bar{H}A \\ A_t &= \Gamma\bar{a}Q \end{aligned}\right\} \tag{17.2}$$

where K and R are the amplitudes of the Kelvin and equatorial Rossby wave structures, respectively, with their familiar meridional structures (Majda, 2003). In

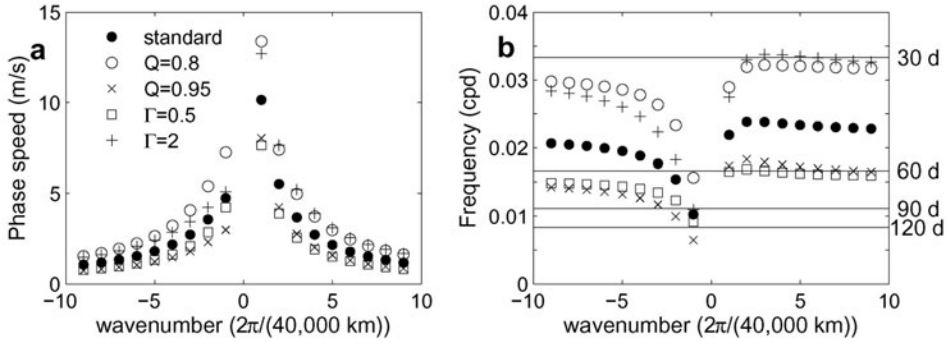

Figure 17.2. Phase speed (a) and oscillation frequency (b) as functions of wavenumber k for the low-frequency linear modes of the MJO skeleton model. Positive (negative) values of k represent eastward (westward) propagating modes. Different symbols represent different parameter choices (adapted from Majda and Stechmann, 2009a).

the absence of forcing, the "dry" longwave Kelvin and equatorial Rossby wave solutions of (17.2) are dispersionless waves that propagate at 50 m/s and 17 m/s, respectively (Majda, 2003; Biello and Majda, 2006). In the presence of dynamical forcing A in (17.2), Kelvin and equatorial Rossby wave structures can be coupled with each other and to Q and A, and these coupled modes can be dispersive.

Now the linear modes of the model are presented. Since the model (17.2) involves four dynamically coupled variables, there are four linear modes. The dispersion relation for the linear modes is shown in Figure 17.2. (Only the two low-frequency intraseasonal modes are shown. The other two modes are high-frequency modes and are only weakly coupled with wave activity.) Figure 17.2 shows that the skeleton model has eastward-propagating waves with phase speeds of roughly 5 m/s and the peculiar dispersion relation $d\omega/dk \approx 0$, in agreement with the MJO. Moreover, the phase speed and dispersion relation are robust over a wide range of parameter values, with the oscillation periods spanning the range of 30–60 days, which is the observed range of the MJO's oscillation period. Westward-propagating waves, on the other hand, which are plotted with positive ω and negative k, have variable ω, and their oscillation periods are seasonal—not intra-seasonal—for $k = 1$ and 2. This suggests the first piece of our explanation for the observed dominance of eastward-propagating intraseasonal variability: westward-propagating modes have seasonal oscillation periods, on which timescales other phenomena are expected to dominate over modulations of synoptic-scale wave activity. The second piece of the explanation is that eastward-propagating modes are more strongly coupled with equatorial moist convective processes than westward-propagating modes (Majda and Stechmann, 2009a).

The physical structure of the wavenumber-2 MJO mode is shown in Figure 17.3 for the standard parameter values. Horizontal quadrupole vortices are prominent, as in observations, and maximum wave activity is colocated with the maximum in equatorial convergence. Lower-tropospheric moisture leads and is in quadrature with wave activity, which is also roughly the relationship seen in observations

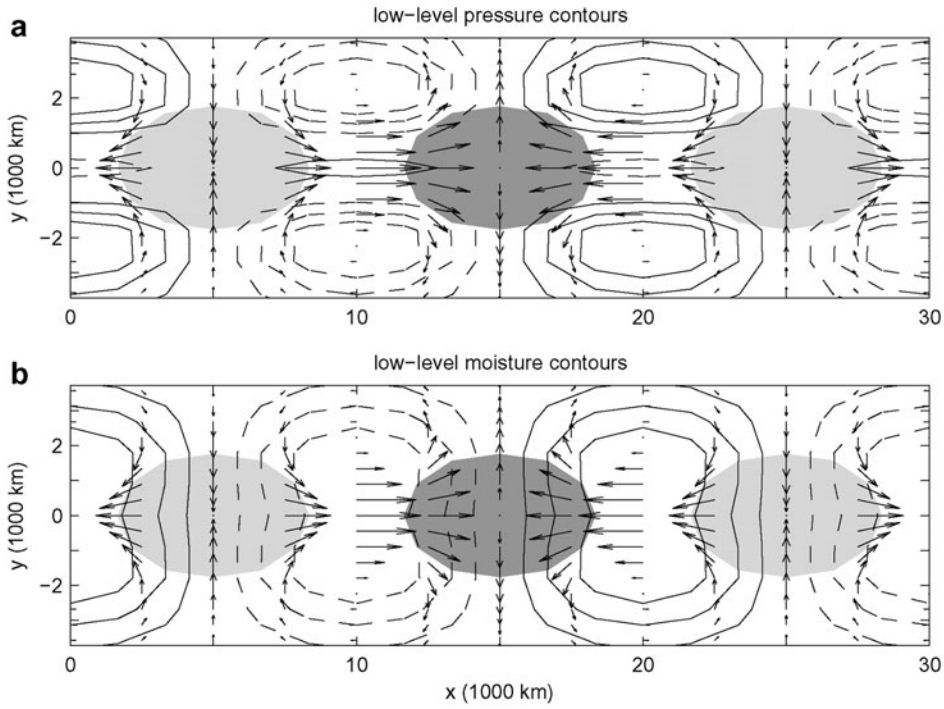

Figure 17.3. Horizontal structure of the wavenumber 2 MJO mode of the skeleton model. (a) Contours of lower-tropospheric pressure anomalies. (b) Contours of lower-tropospheric moisture anomalies. Solid (dashed) lines denote positive (negative) anomalies. Dark (light) shading denotes positive (negative) anomalies of convective activity (from Majda and Stechmann, 2009a).

(Kikuchi and Takayabu, 2004; Kiladis *et al.*, 2005; Tian *et al.*, 2006). The pressure contours clearly display the mixed Kelvin/Rossby wave structure of the wave. Equatorial high-pressure anomalies are colocated with the westerly wind burst as in Kelvin waves, and they are flanked by off-equatorial low-pressure anomalies and cyclonic Rossby gyres, in broad agreement with the observational record. Rectification of the vertical structure and some of the phase relationships is likely due to the effects of higher vertical modes (Majda and Biello, 2004; Biello and Majda, 2005; Khouider and Majda, 2007; Majda *et al.*, 2007), as discussed in the next section.

In addition to these illustrations, a formula for the intraseasonal oscillation frequency ω of the MJO skeleton can be obtained by considering the even simpler case of flow above the equator. In this case, v and y are set to zero and meridional derivatives are ignored. The result is a linear system of four equations for u, θ, q, a, and the system can be solved exactly due to the perfect east–west symmetry:

$$2\omega^2 = \Gamma\bar{R} + k^2 \pm \sqrt{(\Gamma\bar{R} + k^2)^2 - 4\Gamma\bar{R}k^2(1 - \tilde{Q})} \tag{17.3}$$

where k is the zonal wavenumber. For low-frequency waves, this is approximately

$$\omega \approx \sqrt{\Gamma \bar{R}(1-\tilde{Q})} \tag{17.4}$$

For the standard parameter values used here, the oscillation period corresponding to (17.3) is 45 days, in agreement with observations of the MJO. Notice that this formula is independent of wavenumber k; that is, this model recovers the peculiar dispersion relation $d\omega/dk \approx 0$ from the observational record and it relates the MJO frequency to the three parameters of the model.

For the nonlinear dynamics of the MJO skeleton model, see Majda and Stechmann (2011).

17.3 MULTICLOUD AND MULTISCALE EFFECTS

Beyond the fundamental features (I–III) explained by the MJO skeleton model, there are other observed details such as the refined vertical structure, multicloud progression, and multiscale convective processes. Regarding the refined vertical structure and multicloud effects, observations show a progression in the MJO through three cloud types above the boundary layer: in the initial phase, lower/middle-troposphere congestus cloud decks moisten and precondition the lower troposphere; then deep convection develops; and, finally, a trailing wake of upper-troposphere stratiform clouds follows (Lin and Johnson, 1996; Houze *et al*., 2000; Kikuchi and Takayabu, 2004; Kiladis *et al*., 2005). Concomitant with this progression in cloud types, the MJO envelope has a zonal–vertical tilt in heating, moisture, temperature, and circulation. For instance, in the initial phase, there is a low-level westerly onset region below easterlies; then strong westerlies develop in the deep-convective region; and, finally, the strongest westerlies form aloft in the lower/middle troposphere in the stratiform region. Regarding the multiscale structure, observations also reveal complex multiscale features within the propagating large-scale envelope of the MJO. These embedded smaller scale features include westward-propagating 2-day waves, eastward-propagating superclusters or convectively coupled Kelvin waves (Kiladis *et al*., 2009), and smaller scale squall line clusters that typically propagate westward (Nakazawa, 1988; Houze *et al*., 2000).

To account for these refined features of the MJO, we next describe multicloud and multiscale models and the theories behind them.

17.3.1 Kinematic models for the MJO

The multicloud aspects of the MJO are illustrated by a kinematic multiscale model for the MJO (Majda and Klein, 2003; Majda and Biello, 2004; Biello and Majda, 2005; Biello *et al*., 2007), which generalizes the Matsuno–Gill heating models in two significant ways. First, rather than a first baroclinic mode structure, a general heating structure in the vertical is utilized; and, second, upscale transport effects are modeled in a systematic multiscale fashion, including upscale transport of momentum and temperature from synoptic scales to planetary scales. In Figure 17.4, we illustrate the

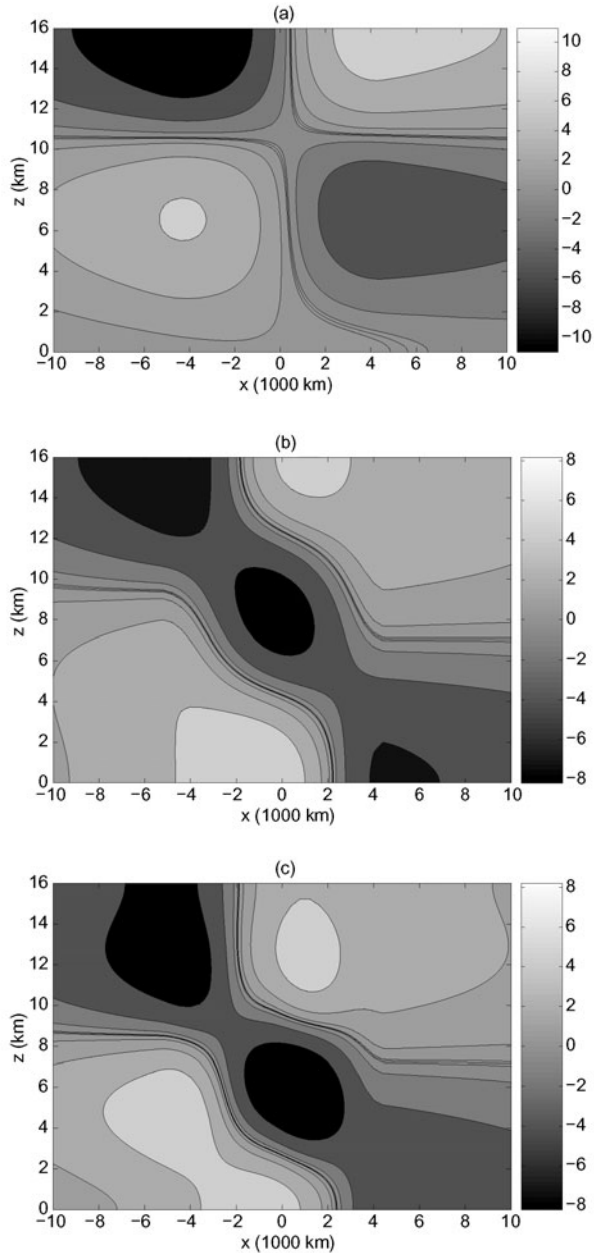

Figure 17.4. Summary of the kinematic model for the MJO. Contours of zonal velocity u as a function of latitude x and height z, with the leading edge of the MJO shown to the right of the domain. Stongest westerlies (easterlies) are shown in white (black). (a) Upright heating case. (b) Congestus/deep-stratiform tilted heating case. (c) Congestus/deep-stratiform tilted heating case plus the effect of upscale momentum transport from synoptic scales (adapted from Biello and Majda, 2005).

vertical structure of zonal winds along the equator for three cases of the model of Biello and Majda (2005), in order of increasing complexity and realism. Figure 17.4a shows results similar to the traditional Matsuno–Gill heating model; this case is different in that mean heating includes both deep convection and stratiform contributions, but it is similar in that the updraft is upright (as opposed to the tilted updrafts below), which occurs because deep convection and stratiform heating are colocated with each other in spacetime. Figure 17.4b shows results from a congestus/deep-stratiform mean heating model, where the three contributions lag each other in spacetime to create a tilted heating anomaly and a tilted updraft (Biello and Majda, 2005; Kiladis *et al*., 2005); note that the westerly wind burst begins at the bottom of the troposphere with easterly winds aloft as in observations (Lin and Johnson, 1996). Finally, in Figure 17.4c, besides congestus/deep-stratiform mean heating, we also include the additional effects of upscale momentum transport (Majda and Biello, 2004). The upscale transport is derived from a plausible multicloud model of synoptic variability within the MJO envelope. As shown in Figure 17.4c, the strongest winds in the westerly wind burst now occur aloft in the lower–middle troposphere as the strong phase of the MJO proceeds; this is in qualitative agreement with observations (Lin and Johnson, 1996). Thus, Figure 17.4c captures all the zonal and vertical qualitative aspects observed in the MJO; the model for Figure 17.4c also captures a number of observed features of the horizontal structure of the MJO (Biello and Majda, 2005; Biello *et al*., 2007).

An important aspect of the observational record for the MJO is that it is superrotating (Moncrieff, 2004); in other words, the large-scale vertically averaged zonal equatorial winds move faster than planetary rotation. According to Hide's Theorem, this observed superrotation implies that there necessarily must be upscale transport of momentum to sustain superrotation. Biello *et al*. (2007) use the multiscale MJO models discussed here to show that upscale fluxes from vertical transport of synoptic-scale momentum combined with positive planetary-scale heating drive this superrotation. In particular, there is no superrotation possible from planetary-scale heating alone in a Matsuno–Gill model—multiscale effects are needed.

17.3.2 Dynamic models for waves in the MJO

Kinematic models for the MJO, like those in Figure 17.4, are highly simplified in that the MJO's phase speed and heat source are specified. A more realistic approach should have an interactive heat source and should predict the MJO's phase speed, as in the MJO skeleton model of Section 17.1. An even more realistic approach should also resolve the smaller scale fluctuations embedded within the MJO envelope—not just the planetary-scale envelope itself. The goal of this section is to review current understanding of the dynamic interactions between the MJO envelope and fluctuations within the envelope. Since envelope–fluctuation interaction is a common generic topic, we first review this interactions in different contexts and then we review detailed results with application to the MJO specifically.

Envelope–fluctuation interaction is a common occurrence in the tropics, where the multiscale hierarchy of organized convection can be divided into three broad

categories: (i) the MJO on planetary spatial scales (roughly 20,000 km) and intraseasonal timescales (roughly 40 days) (see Zhang, 2005 and any of the chapters in the current book); (ii) convectively coupled waves (CCWs) on equatorial synoptic scales (roughly 2,000 km and 4 days) (Kiladis *et al*., 2009); and (iii) mesoscale convective systems (MCSs) on mesoscales (roughly 200 km and 0.4 days) (Houze, 2004). This hierarchy has a remarkable multiscale structure: the MJO is an envelope of smaller scale CCWs, and, in turn, the CCWs are envelopes of smaller scale MCSs. Figure 17.1 illustrates the structure of a generic large-scale envelope with smaller scale fluctuations embedded within it. For such a multiscale envelope, one can imagine three scenarios for its physical mechanisms: (i) Does the envelope drive the fluctuations within it? (ii) Do the fluctuations drive the large-scale envelope? (iii) Or do the two evolve cooperatively? This situation is reminiscent of the classic conundrum: Which came first—the chicken or the egg? In atmospheric science, such questions are most familiar from contexts such as midlatitude eddies and jets. Here, instead, the focus is on the tropical case described above, and the evidence will suggest that, in fact, there are cooperative interactions between the envelopes and the fluctuations within them (in addition to those interactions described earlier in the skeleton model).

Before reviewing any results in detail, we review recent and past results on convection–environment interactions. MCS–environment interactions are reviewed first in order to set the stage for the relatively new topic of CCW–environment interactions and in order to highlight their similarities and differences.

MCS–environment interactions have been studied in both "directions" (i.e., the effect of MCSs on the environment and vice versa). On the one hand, it is well known that MCSs can have important effects on the larger scale atmospheric state in which they exist (Houze, 2004). For example, precipitation and vertical transport of temperature and moisture can significanly alter the larger scale thermodynamic environment. A less understood effect of MCSs on their larger scale environment is convective momentum transport (CMT). A pervasive aspect of this is the idea of "cumulus friction"; however, many studies have also shown that the CMT of some MCSs can actually accelerate the background wind (LeMone and Moncrieff, 1994; Wu and Yanai, 1994; Tung and Yanai, 2002a, b). On the other hand, these interactions also proceed in the opposite direction: the background state—including wind shear and the moist thermodynamic state—affects the MCSs that form within it. The environmental thermodynamic state helps determine the intensity of MCSs, and the vertical wind shear $\partial u/\partial z$ helps determine their propagation direction and morphology (Barnes and Sieckman, 1984; LeMone *et al*., 1998; Liu and Moncrieff, 2001).

On larger scales than the MCS are synoptic-scale phenomena known as CCWs (Kiladis *et al*., 2009). With typical wavelengths of 2,000 km to 8,000 km and periods of 2–10 days, CCWs are the dominant synoptic-scale weather features in many regions in the tropics, but they are less understood than the smaller scale MCS. Just as MCSs interact with their larger scale environment, so do CCWs. However, CCW–environment interactions are in a relatively primitive stage of understanding.

On the one hand, one might suspect that CCWs can affect their larger scale environment as MCSs do. Some results using diagnostic models for CCWs have

demonstrated that this is true (see Haertel and Kiladis, 2004; Biello *et al.*, 2007, and references therein). For example, CCWs can act as heat sources and moisture sinks for their environment, as was represented by the $\bar{H}a$ terms of the MJO skeleton model in (17.1). Also, since they have tilts in the vertical/zonal direction (Takayabu *et al.*, 1996; Straub and Kiladis, 2003), CCW circulations can transport momentum to larger scales. That is to say, eddy flux divergences can accelerate or decelerate mean flow, where the CCWs are "eddies" in this context. This has important implications for the MJO, as shown in the kinematic multiscale models of Biello and Majda (2005) and Biello *et al.* (2007). As illustrated here in Figure 17.4, they show that the westerly jet of the MJO's westerly wind burst can be driven by momentum transport from synoptic-scale CCWs.

On the other hand, one might also suspect CCW–environment interaction to occur in the other direction (i.e., that the background state—including the background wind and moist thermodynamic state—can affect the CCWs that form within it). Unfortunately, while several studies have documented the properties of CCWs, few have documented them in different distinct background environments (exceptions to this include Roundy and Frank, 2004 and Yang *et al.*, 2007). Besides observations, computer simulations of CCWs have presently offered little insight into CCW–environment interaction, since GCMs do not adequately capture CCWs (Lin *et al.*, 2006) and simulations of CCWs using cloud-resolving models (CRMs) are challenging but not impossible (see Grabowski and Moncrieff, 2001; Tulich *et al.*, 2007, and the discussion below). One promising method for numerical simulation of CCWs is the so-called "multicloud model" in recent work of Khouider and Majda (2006, 2007, 2008a, b), which has been successful in capturing observed features of CCWs and in explaining their physical mechanisms. Building on earlier work, the multicloud model includes parameterization of the three cloud types (congestus, stratiform, and deep-convective clouds) and their different vertical structures (a deep-convective heating mode and a second vertical mode with low-level heating and cooling corresponding to congestus and stratiform clouds). Detailed linear stability analysis and nonlinear simulations reveal a mechanism for large-scale instability of moist gravity waves. The model reproduces key features of the observational record for CCWs (Kiladis *et al.*, 2009), including their phase speeds and their horizontal and vertical structures.

Since the multicloud model of Khouider and Majda (2006, 2007, 2008a, b) captures realistic CCWs, it can be used for studies of CCW–environment interaction. This has been done by Majda and Stechmann (2009b), who designed a multiscale framework for interactions of CCW and background wind shear (i.e., convectively coupled wave–mean flow interaction). Mean flow can affect CCWs through advection, and CCWs can drive changes in mean flow through CMT. Conceptually, the model then takes the form (using the zonal velocity as an example)

$$\frac{\partial \bar{U}}{\partial T} + \frac{\partial}{\partial z}\langle \overline{w'u'} \rangle = 0 \tag{17.5}$$

$$\frac{\partial u'}{\partial t} + \bar{U}\frac{\partial u'}{\partial x} + w'\frac{\partial \bar{U}}{\partial z} + \frac{\partial p'}{\partial x} = S'_{u,1} \tag{17.6}$$

where $\bar{U}$ is large-scale mean wind; and u' represents synoptic-scale waves. In mathematical form, the key interactions are (i) eddy flux convergence of wave momentum $\partial_z\langle\overline{w'u'}\rangle$ driving changes in mean flow $\bar{U}$, and (ii) advection of waves u' by mean flow $\bar{U}$. Also note that the timescale $T = \epsilon^2 t$ for the changes in zonal mean flows in (17.5) is longer than that for waves (i.e., intraseasonal rather than synoptic); this arises as part of a multiscale asymptotic derivation in Majda and Stechmann (2009b). While only large-scale mean wind $\bar{U}$ is displayed in (17.5)–(17.6), large-scale mean water vapor $\bar{Q}$ and potential temperature $\bar{\Theta}$ were also part of the model in Majda and Stechmann (2009b), but they had little effect (perhaps because there is no large-scale moisture convergence in this setup).

Results from the CCW–mean flow model (17.5)–(17.6) are shown in Figure 17.5 (see Majda and Stechmann, 2009b and Stechmann *et al.*, 2011 for further results). This figure shows the evolution of the CCW–mean flow system through one cycle, which proceeds on an intraseasonal timescale. Figures 17.5a and 17.5b show the evolution of mean wind, $\bar{U}(z,t)$, and Figure 17.5c shows the simultaneous evolution of CCWs. Initially, at time $t = 1{,}050$ days, an eastward-propagating CCW is favored in a background shear that resembles the westerly onset phase of the MJO, with strongest westerlies at the surface. As time progresses, the CMT from this CCW accelerates the strongest westerlies aloft by time $t = 1{,}070$ days, as in the westerly wind burst phase of the MJO (Lin and Johnson, 1996). In this way, the CCW essentially creates its own demise, since the eastward-propagating wave is unfavorable in the presence of this low-level westerly jet (as shown in Figure 17.5c) as it weakens, breaks up, and reforms as a westward-propagating wave from times $t = 1{,}065$–$1{,}085$ days. This westward-propagating wave, in turn, then decelerates the mean wind from $t = 1{,}085$–$1{,}100$ days, and the cycle continues, thereby demonstrating that momentum transport from CCWs can sometimes accelerate and sometimes decelerate the mean wind. The favorability of the eastward or westward-propagating wave in a given wind shear can be corroborated by linear theory, an example of which is shown in Figures 17.5d and 17.5e for jet shear at time $t = 1{,}080$. At this time, the westward-propagating wave has the largest growth rates on large scales, but the eastward-propagating waves have significant nonzero growth rates on smaller scales; this leads to the multi-scale wave structure at this time in Figure 17.5c, where CCWs appear as a westward-propagating envelope of smaller scale eastward-propagating features that resemble squall lines (see also Khouider *et al.*, 2011b). In summary, this model demonstrates CCW–mean flow interaction in a dynamical setting: mean wind determines the preferred propagation direction of the CCW and, simultaneously, CMT from CCWs can sometimes accelerate and sometimes decelerate mean wind, all on an intraseasonal timescale.

17.4 IMPLICATIONS FOR GLOBAL CIRCULATION MODELS

Given the wide range of interactions in the hierarchy of organized tropical convection, it is maybe not surprising that GCMs struggle with capturing CCWs and the MJO (Moncrieff and Klinker, 1997; Lin *et al.*, 2006). With grid spacings of

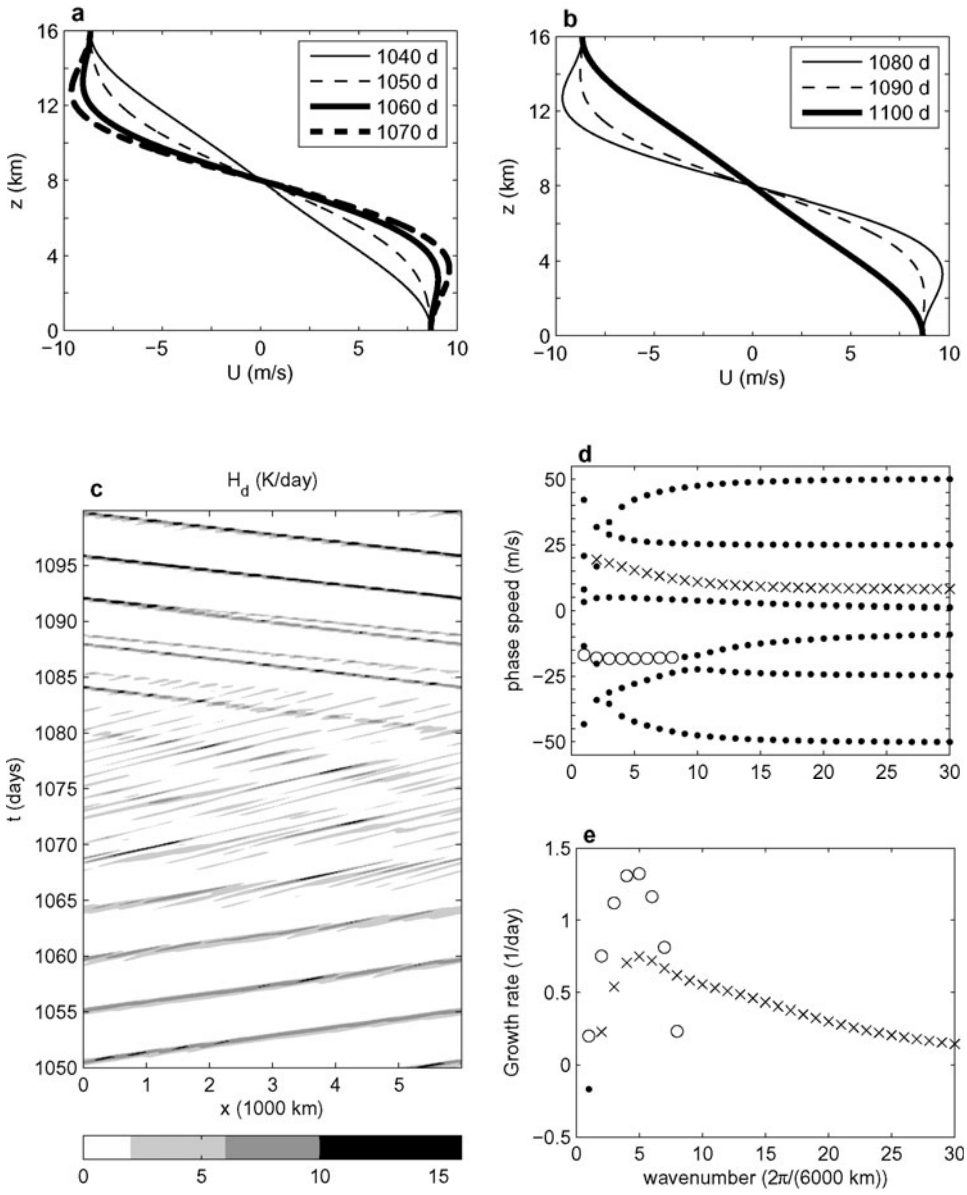

Figure 17.5. Summary of the dynamic model for waves in the MJO, with a demonstration of CCW–mean flow interaction on intraseasonal timescales. Snapshots of mean wind $\bar{U}(z,t)$ from (a) times $t = 1{,}040$–$1{,}070$ days, and (b) times $t = 1{,}080$–$1{,}100$ days. (c) Contours of deep convective heating $H_d(x,t)$ as a function of latitude x and time t. (d) Phase speeds of linear waves with background shear given by mean wind at time $t = 1{,}080$ days. (e) Growth rates of linear waves in this background shear. Unstable modes are plotted with "x" and "o" for eastward and westward-propagating modes, respectively (adapted from Majda and Stechmann, 2009b).

roughly 100 km, GCMs can at best hope to capture convection on scales of roughly 1,000 km and larger (i.e., CCWs and the MJO), assuming about 10 gridpoints are needed to properly resolve a given feature. This also implies that features with scales of 100 km to 1,000 km and smaller must be parameterized; MCSs fall within this category but are often ignored in parameterizations. These two problems—properly representing CCWs and properly parameterizing MCSs—are crucial to improving the MJO and the hierarchy of organized convection in GCMs (Moncrieff *et al.*, 2007).

A convective parameterization that captures realistic CCWs is the multicloud parameterization of Khouider and Majda (2006, 2007, 2008a, b), which includes several features that are not standard among contemporary convective parameterizations. The key aspect of this parameterization is representation of three different cloud types: congestus, deep convection, and stratiform clouds (Johnson *et al.*, 1999; Houze, 2004). Each of these different phases of convection plays a different role in the heat and moisture budgets, and it is important to include all three phases rather than just deep convection (Haertel and Kiladis, 2004; Khouider and Majda, 2006, 2008b). The congestus phase of convection appears to be important for moistening the lower troposphere during the MJO's suppressed stage (Kikuchi and Takayabu, 2004; Tian *et al.*, 2006). However, GCMs do not appear to properly represent congestus clouds and the accompanying moistening effects. It is possible that parameterizations with minimum entrainment parameters, which have improved the strength of intraseasonal variability in some GCMs, are employing a surrogate for congestus clouds and lower-tropospheric moistening (Tokioka *et al.*, 1988; Sobel *et al.*, 2010). In addition, the direct effect of the stratiform phase of convection is present in multicloud models but largely absent in contemporary GCMs, yet it is important due to unsaturated downdrafts in the stratiform region, which can cool and dry the lower troposphere and boundary layer and generate cold pools (Mapes, 2000).

While the earliest studies using the multicloud model employed a simplified dynamical core, multicloud model convective parameterization was recently coupled with NCAR's next-generation dry dynamical core GCM (Khouider *et al.*, 2011). With a coarse GCM resolution of 167 km in an aqua-planet setup, the multicloud parameterization succeeds in reproducing a realistic MJO with all of the features I–III and also dynamically consistent with the skeleton model (Majda and Stechmann, 2009a, 2011) described earlier. This model parameterization also produces realistic convectively coupled equatorial waves (Kiladis *et al.*, 2009; Khouider *et al.*, 2011). Furthermore, the computational overhead of the multicloud convective parameterization is less than 1% of the dry dynamical core. In comparison, features of the MJO are also captured by the superparameterization techniques pioneered by Grabowski (2001, 2004), and these techniques have recently improved the quality of MJO simulation beyond coarse GCM parameterization in realistic climate models (Khairoutdinov *et al.*, 2008; Benedict and Randall, 2009); of course, the computational overhead in such superparameterization algorithms is substantial beyond the dry dynamical core. An active area of research is the search for cheaper versions of superparameterization that retain

statistical fidelity of multiscale interactions (Jung and Arakawa, 2005; Grabowski, 2006; Xing *et al.*, 2009).

In addition to moist thermodynamic effects, unresolved MCSs can also affect resolved GCM dynamics in other ways. One way is convective momentum transport (CMT). It has been recognized that CMT can either accelerate or decelerate mean wind (LeMone and Moncrieff, 1994; Wu and Yanai, 1994), and representations of this feature have been included in parameterizations that have improved climatological-scale circulations (Wu *et al.*, 2007; Richter and Rasch, 2008). However, observations also show that the acceleration/deceleration due to CMT occurs in intense intermittent bursts (Tung and Yanai, 2002a, b), and including this intermittency should be important for the variability of resolved convection. A promising method for including the intermittent aspects of unresolved CMT is the stochastic parameterization of Majda and Stechmann (2008), which should help increase the variability of CCWs and the MJO, which tends to be significantly lower in GCMs than in observations (Lin *et al.*, 2006).

It is possible that lessons for GCMs can be learned from CRM simulations of multiscale convection, since CRMs are able to represent a CCW envelope and the MCSs within it, whereas GCMs struggle to capture the MJO envelope and the CCWs within it. For instance, the role of CMT and momentum damping can be seen in CRM simulations of CCWs. One subtle aspect of these CRM simulations is that the role played by *resolved* momentum transport appears to depend on the strength of *parameterized* momentum damping. The simulations of Grabowski and Moncrieff (2001) employ (parameterized) weak momentum damping with a timescale of 24 hours, and the results show that resolved CMT from MCSs plays an important role in driving the CCW envelope. On the other hand, the simulations of Tulich *et al.* (2007) employ (parameterized) stronger momentum damping with a timescale of 4 hours, and they find the role played by resolved CMT in driving the CCW envelope to be small; instead, the key mechanism involves interactions between MCSs and gravity waves generated by the MCSs (Mapes, 1993; Tulich and Mapes, 2008; Stechmann and Majda, 2009). Other CRM simulations of Held *et al.* (1993) show two extreme cases with (i) no CMT allowed and (ii) no momentum damping, and the results are completely different in the two cases. Given this variety of results, it is likely that parameterized CMT in GCMs strongly affects resolved waves (i.e., CCWs and the MJO) and the simulated mechanisms behind them.

17.5 SUMMARY

Observations show that the MJO is an envelope of smaller scale convective processes. Based on these observations, several multiscale theories and models for the MJO have been developed recently, and they have been reviewed here.

A simple model for the MJO skeleton predicts its fundamental features I–III on planetary/intraseasonal scales (Section 17.2), including a simple formula for MJO

frequency:

$$\omega \approx \sqrt{\Gamma \bar{R}(1 - \tilde{Q})}. \tag{17.7}$$

The fundamental mechanism for the MJO in this model involves neutrally stable interactions between (i) planetary-scale lower-tropospheric moisture anomalies and (ii) sub-planetary-scale convection/wave activity.

Many of the MJO's more refined features are captured by additional multicloud and multiscale effects (Section 17.3). Basic multicloud effects recover the tilted zonal–vertical structure of the MJO, as shown in a kinematic multiscale model. This model also demonstrates how westerly wind bursts can intensify aloft due to upscale momentum fluxes from synoptic-scale CCWs. Basic multiscale effects were further demonstrated with a dynamic multiscale model for interactions between CCWs and mean wind shear. This model also reproduces westerly wind burst intensification aloft, as did the kinematic model, but it does so in a dynamic setting where the waves can also respond to changes in mean wind (i.e., a dynamical setting of CCW–mean flow interaction).

Finally, based on the success of these multiscale models and theories in explaining features of the MJO, it was suggested that the key to simulating the MJO in GCMs is to properly represent the hierarchy of organized convection across all scales (Section 17.4). Ultimately, this means that GCMs must properly capture CCWs, which will require a proper parameterization of unresolved convection on mesoscales and smaller scales. Two key aspects of this are the parameterization of multiple cloud types—congestus, deep convection, and stratiform—and convective momentum transport. While some of these have long been challenging issues, recent results have suggested new ideas and shown further progress.

17.6 REFERENCES

Barnes, G. and K. Sieckman (1984) The environment of fast- and slow-moving tropical mesoscale convective cloud lines. *Mon. Wea. Rev.*, **112**(9), 1782–1794.

Benedict, J. and D. Randall (2009) Structure of the Madden–Julian Oscillation in the superparameterized CAM. *J. Atmos. Sci.*, **66**(11), 3277–3296.

Biello, J. A. and A. J. Majda (2005) A new multiscale model for the Madden–Julian oscillation. *J. Atmos. Sci.*, **62**, 1694–1721.

Biello, J. A. and A. J. Majda (2006) Modulating synoptic scale convective activity and boundary layer dissipation in the IPESD models of the Madden–Julian oscillation. *Dyn. Atmos. Oceans*, **42**, 152–215.

Biello, J. A., A. J. Majda, and M. W. Moncrieff (2007) Meridional momentum flux and superrotation in the multi-scale IPESD MJO model. *J. Atmos. Sci.*, **64**(5), 1636–1651.

Caballero, R. and M. Huber (2010) Spontaneous transition to superrotation in warm climates simulated by CAM3. *Geophys. Res. Lett.*, **37**(11), L11 701.

Chao, W. C. (1987) On the origin of the tropical intraseasonal oscillation. *J. Atmos. Sci.*, **44**, 1940–1949.

Gill, A. (1980) Some simple solutions for heat-induced tropical circulation. *Quart. J. Roy. Meteorol. Soc.*, **106**(449), 447–462.

Grabowski, W. W. (2001) Coupling cloud processes with the large-scale dynamics using the cloud-resolving convection parameterization (CRCP). *J. Atmos. Sci.*, **58**, 978–997.

Grabowski, W. W. (2003) MJO-like coherent structures: Sensitivity simulations using the cloud-resolving convection parameterization (CRCP). *J. Atmos. Sci.*, **60**, 847–864.

Grabowski, W. W. (2004) An improved framework for superparameterization. *J. Atmos. Sci.*, **61**, 1940–1952.

Grabowski, W. W. (2006) Comments on "Preliminary tests of multiscale modeling with a two-dimensional framework: Sensitivity to coupling methods." *Mon. Wea. Rev.*, **134**, 2021–2026.

Grabowski, W. W. and M. W. Moncrieff (2001) Large-scale organization of tropical convection in two-dimensional explicit numerical simulations. *Quart. J. Roy. Meteorol. Soc.*, **127**, 445–468.

Grabowski, W. W. and M. W. Moncrieff (2004) Moisture–convection feedback in the Tropics. *Quart. J. Roy. Meteorol. Soc.*, **130**, 3081–3104.

Haertel, P. T. and G. N. Kiladis (2004) Dynamics of 2-day equatorial waves. *J. Atmos. Sci.*, **61**, 2707–2721.

Held, I., R. Hemler, and V. Ramaswamy (1993) Radiative–convective equilibrium with explicit two-dimensional moist convection. *J. Atmos. Sci.*, **50**(23), 3909–3927.

Hendon, H. H. and B. Liebmann (1994) Organization of convection within the Madden–Julian oscillation. *J. Geophys. Res.*, **99**, 8073–8084, doi: 10.1029/94JD00045.

Hendon, H. H. and M. L. Salby (1994) The life cycle of the Madden–Julian oscillation. *J. Atmos. Sci.*, **51**, 2225–2237.

Houze, R. A. (2004) Mesoscale convective systems. *Rev. Geophys.*, **42**, G4003, doi: 10.1029/2004RG000150.

Houze, R. A., Jr., S. S. Chen, D. E. Kingsmill, Y. Serra, and S. E. Yuter (2000) Convection over the Pacific warm pool in relation to the atmospheric Kelvin–Rossby wave. *J. Atmos. Sci.*, **57**, 3058–3089.

Johnson, R. H., T. M. Rickenbach, S. A. Rutledge, P. E. Ciesielski, and W. H. Schubert (1999) Trimodal characteristics of tropical convection. *J. Climate*, **12**, 2397–2418.

Jung, J.-H. and A. Arakawa (2005) Preliminary tests of multiscale modeling with a two-dimensional framework: Sensitivity to coupling methods. *Mon. Wea. Rev.*, **133**(3), 649–662.

Khairoutdinov, M., C. DeMott, and D. Randall (2008) Evaluation of the simulated interannual and subseasonal variability in an AMIP-style simulation using the CSU Multiscale Modeling Framework. *J. Climate*, **21**(3), 413–431.

Khouider, B. and A. J. Majda (2006) A simple multicloud parameterization for convectively coupled tropical waves, Part I: Linear analysis. *J. Atmos. Sci.*, **63**, 1308–1323.

Khouider, B. and A. J. Majda (2007) A simple multicloud parameterization for convectively coupled tropical waves, Part II: Nonlinear simulations. *J. Atmos. Sci.*, **64**, 381–400.

Khouider, B. and A. J. Majda (2008a) Equatorial convectively coupled waves in a simple multicloud model. *J. Atmos. Sci.*, **65**, 3376–3397.

Khouider, B. and A. J. Majda (2008b) Multicloud models for organized tropical convection: Enhanced congestus heating. *J. Atmos. Sci.*, **65**, 895–914.

Khouider, B., A. St-Cyr, A. J. Majda, and J. Tribbia (2011a) MJO and convectively coupled waves in a coarse resolution GCM with a simple multicloud parameterization. *J. Atmos. Sci.*, **68**, 240–264.

Khouider, B., Y. Han, A. J. Majda, and S. N. Stechmann (2011b) Multiscale waves in an MJO background and CMT feedback. *J. Atmos. Sci.*, submitted.

Kikuchi, K. and Y. N. Takayabu (2004) The development of organized convection associated with the MJO during TOGA COARE IOP: Trimodal characteristics. *Geophys. Res. Lett.*, **31** (10.1029).

Kiladis, G. N., K. H. Straub, and P. T. Haertel (2005) Zonal and vertical structure of the Madden–Julian oscillation. *J. Atmos. Sci.*, **62**, 2790–2809.

Kiladis, G. N., M. C. Wheeler, P. T. Haertel, K. H. Straub, and P. E. Roundy (2009) Convectively coupled equatorial waves. *Rev. Geophys.*, **47**, RG2003, doi: 10.1029/2008RG000266.

LeMone, M. and M. Moncrieff (1994) Momentum and mass transport by convective bands: Comparisons of highly idealized dynamical models to observations. *J. Atmos. Sci.*, **51**(2), 281–305.

LeMone, M., E. Zipser, and S. Trier (1998) The role of environmental shear and thermodynamic conditions in determining the structure and evolution of mesoscale convective systems during TOGA COARE. *J. Atmos. Sci.*, **55**(23), 3493–3518.

Lin, J.-L., G. N. Kiladis, B. E. Mapes, K. M. Weickmann, K. R. Sperber, W. Lin, M. C. Wheeler, S. D. Schubert, A. Del Genio, and L. J. Donner (2006) Tropical intraseasonal variability in 14 IPCC AR4 climate models, Part I: Convective signals. *J. Climate*, **19**, 2665–2690.

Lin, X. and R. H. Johnson (1996) Kinematic and thermodynamic characteristics of the flow over the western Pacific warm pool during TOGA COARE. *J. Atmos. Sci.*, **53**, 695–715.

Liu, C. and M. Moncrieff (2001) Cumulus ensembles in shear: Implications for parameterization. *J. Atmos. Sci.*, **58**(18), 2832–2842.

Majda, A. J. (2003) *Introduction to PDEs and Waves for the Atmosphere and Ocean* (Courant Lecture Notes in Mathematics, Vol. 9). American Mathematical Society, Providence, RI, 234 pp.

Majda, A. J. and J. A. Biello (2004) A multiscale model for the intraseasonal oscillation. *Proceedings of the National Academy of Sciences U.S.A.*, **101**(14), 4736–4741.

Majda, A. J. and R. Klein (2003) Systematic multiscale models for the Tropics. *J. Atmos. Sci.*, **60**, 393–408.

Majda, A. J. and S. N. Stechmann (2008) Stochastic models for convective momentum transport. *Proceedings of the National Academy of Sciences U.S.A.*, **105**, 17614–17619.

Majda, A. J. and S. N. Stechmann (2009a) The skeleton of tropical intraseasonal oscillations. *Proceedings of the National Academy of Sciences U.S.A.*, **106**(21), 8417.

Majda, A. J. and S. N. Stechmann (2009b) A simple dynamical model with features of convective momentum transport. *J. Atmos. Sci.*, **66**, 373–392.

Majda, A. J. and S. N. Stechmann (2011) Nonlinear dynamics and regional variations in the MJO skeleton. *J. Atmos. Sci.*, in press.

Majda, A. J., S. N. Stechmann, and B. Khouider (2007) Madden–Julian Oscillation analog and intraseasonal variability in a multicloud model above the equator. *Proceedings of the National Academy of Sciences U.S.A.*, **104**(24), 9919–9924.

Mapes, B. (1993) Gregarious tropical convection. *J. Atmos. Sci.*, **50**(13), 2026–2037.

Mapes, B. E. (2000) Convective inhibition, subgrid-scale triggering energy, and stratiform instability in a toy tropical wave model. *J. Atmos. Sci.*, **57**, 1515–1535.

Masunaga, H., T. L'Ecuyer, and C. Kummerow (2006) The Madden–Julian oscillation recorded in early observations from the Tropical Rainfall Measuring Mission (TRMM). *J. Atmos. Sci.*, **63**(11), 2777–2794.

Matsuno, T. (1966) Quasi-geostrophic motions in the equatorial area. *J. Meteorol. Soc. Japan*, **44**(1), 25–43.

Moncrieff, M. W. (2004) Analytic representation of the large-scale organization of tropical convection. *J. Atmos. Sci.*, **61**, 1521–1538.

Moncrieff, M. W. and E. Klinker (1997) Organized convective systems in the tropical western Pacific as a process in general circulation models: A TOGA COARE case-study. *Quart. J. Roy. Meteorol. Soc.*, **123**(540), 805–827.

Moncrieff, M. W., M. Shapiro, J. Slingo, and F. Molteni (2007) Collaborative research at the intersection of weather and climate. *WMO Bull.*, **56**, 204–211.

Nakazawa, T. (1988) Tropical super clusters within intraseasonal variations over the western Pacific. *J. Meteorol. Soc. Japan*, **66**(6), 823–839.

Richter, J. and P. Rasch (2008) Effects of convective momentum transport on the atmospheric circulation in the Community Atmosphere Model, Version 3. *J. Climate*, **21**(7), 1487–1499.

Roundy, P. and W. Frank (2004) A climatology of waves in the equatorial region. *J. Atmos. Sci.*, **61**(17), 2105–2132.

Salby, M. and H. Hendon (1994) Intraseasonal behavior of clouds, temperature, and motion in the tropics. *J. Atmos. Sci.*, **51**(15), 2207–2224.

Sobel, A. H., E. D. Maloney, G. Bellon, and D. M. Frierson (2010) Surface fluxes and tropical intraseasonal variability: A reassessment. *J. Adv. Model. Earth Syst.*, **2**, art. #2, 27 pp.

Stechmann, S. N. and A. J. Majda (2009) Gravity waves in shear and implications for organized convection. *J. Atmos. Sci.*, **66**, 2579–2599.

Stechmann, S. N., A. J. Majda, and D. Skjorshammer (2011) Convectively coupled wave–environment interactions. *J. Fluid. Mech.*, submitted.

Straub, K. H. and G. N. Kiladis (2003) The observed structure of convectively coupled Kelvin waves: Comparison with simple models of coupled wave instability. *J. Atmos. Sci.*, **60**(14), 1655–1668.

Takayabu, Y. N., K. M. Lau, and C. H. Sui (1996) Observation of a quasi-2-day wave during TOGA COARE. *Mon. Wea. Rev.*, **124**(9), 1892–1913.

Tian, B., D. Waliser, E. Fetzer, B. Lambrigtsen, Y. Yung, and B. Wang (2006) Vertical moist thermodynamic structure and spatial–temporal evolution of the MJO in AIRS observations. *J. Atmos. Sci.*, **63**(10), 2462–2485.

Tokioka, T., K. Yamazaki, A. Kitoh, and T. Ose (1988) The equatorial 30–60 day oscillation and the Arakawa–Schubert penetrative cumulus parameterization. *J. Meteorol. Soc. Japan*, **66**(6), 883–901.

Tulich, S. and B. Mapes (2008) Multi-scale convective wave disturbances in the Tropics: Insights from a two-dimensional cloud-resolving model. *J. Atmos. Sci.*, **65**(1), 140–155.

Tulich, S. N., D. Randall, and B. Mapes (2007) Vertical-mode and cloud decomposition of large-scale convectively coupled gravity waves in a two-dimensional cloud-resolving model. *J. Atmos. Sci.*, **64**, 1210–1229.

Tung, W. and M. Yanai (2002a) Convective momentum transport observed during the TOGA COARE IOP, Part I: General features. *J. Atmos. Sci.*, **59**(11), 1857–1871.

Tung, W. and M. Yanai (2002b) Convective momentum transport observed during the TOGA COARE IOP, Part II: Case studies. *J. Atmos. Sci.*, **59**(17), 2535–2549.

Wheeler, M. and G. N. Kiladis (1999) Convectively coupled equatorial waves: Analysis of clouds and temperature in the wavenumber–frequency domain. *J. Atmos. Sci.*, **56**(3), 374–399.

Wu, X. and M. Yanai (1994) Effects of vertical wind shear on the cumulus transport of momentum: Observations and parameterization. *J. Atmos. Sci.*, **51**(12), 1640–1660.

Wu, X., L. Deng, X. Song, and G. Zhang (2007) Coupling of convective momentum transport with convective heating in global climate simulations. *J. Atmos. Sci.*, **64**(4), 1334–1349.

Xing, Y., A. J. Majda, and W. W. Grabowski (2009) New efficient sparse spacetime algorithms for superparameterization on mesoscales. *Mon. Wea. Rev.*, **137**, 4307–4324.

Yanai, M., B. Chen, and W.-W. Tung (2000) The Madden–Julian oscillation observed during the TOGA COARE IOP: Global view. *J. Atmos. Sci.*, **57**, 2374–2396.

Yang, G., B. Hoskins, and J. Slingo (2007) Convectively coupled equatorial waves, Part I: Horizontal and vertical structures. *J. Atmos. Sci.*, **64**(10), 3406–3423.

Zhang, C. (2005) Madden–Julian Oscillation. *Rev. Geophys.*, **43**, G2003+, doi: 10.1029/2004RG000158.

18

Chemical and biological impacts

Baijun Tian and Duane E. Waliser

18.1 INTRODUCTION

During the past three decades, many studies have been devoted to the interaction between the MJO and the dynamical components of the global climate system. For example, the MJO has been shown to have important influences on monsoon onsets and breaks (Chapters 2, 3, 4, 5, 13), the diurnal cycle (e.g., Tian *et al*., 2006a; Ichikawa and Yasunari, 2007; Suzuki, 2009), tropical hurricanes and cyclones (e.g., Maloney and Hartmann, 2000a, b; Bessafi and Wheeler, 2006; Camargo *et al*., 2009), extratropical and high-latitude weather patterns (Chapter 14), El Niño and the Southern Oscillation (ENSO) (Chapter 9), and oceans (Chapters 6, 7, 15). However, little attention has been paid to the impacts of the MJO on the chemical and biological components of the global climate system, despite many of these components being relevant to human life and society. Many studies have shown that the potential predictability of the MJO extends to 2–4 weeks (Waliser, 2005). Thus, if we can understand how the MJO systematically influences the chemical and biological components of the global climate system, then socially relevant prediction of composition and air quality with similar lead times may be possible. Furthermore, the MJO provides a robust intraseasonal "reference signal" that enables us to study how concentrations of various chemical species vary in response to changes in atmospheric circulation. These suggest the need for more characterization and understanding of the MJO's interactions with these non-dynamical components of our climate system. When more fully described, such interactions can also represent useful tests for the performance of Earth system models. Taking advantage of new and advanced satellite remote-sensing products of atmospheric composition and ocean surface chlorophyll, a number of studies have recently discovered that the MJO can also have important impacts on atmospheric composition and ocean biology. This chapter discusses these new findings. Table 18.1 lists the satellite

W. K. M. Lau and D. E. Waliser (Editors), *Intraseasonal Variability in the Atmosphere–Ocean Climate System* (Second Edition).

Table 18.1. Satellite data used in studies of MJO chemical and biological impacts.

Satellite instrument	*Variable*	*Period*	*Vertical resolution*	*Horizontal resolution*	*Temporal resolution*	*Reference*
TOMS/SBUV/ SBUV2	Total column ozone	January 1980–June 2006	N/A	10° longitude × 5° latitude	Daily	Tian *et al.* (2007)
AIRS	Total column ozone	September 2002–July 2006	N/A	1° × 1°	Twice daily	Tian *et al.* (2007)
MIPAS/GOMOS	Ozone profile	December 1–16, 2003	10–50 km, 1 km	L2	Daily	Liu *et al.* (2009)
EP TOMS/ UARS MLS	Tropospheric ozone	October 1991–April 1993	N/A	1° × 1°	Daily	Ziemke and Chandra (2003)
Aura OMI/MLS	Tropospheric ozone	September 2004–June 2006	N/A	5° × 5°	Daily	Ziemke *et al.* (2007)
Nimbus 7 TOMS	Aerosol index	January 1980–December 1992	N/A	1.25° longitude × 1° latitude	Daily	Tian *et al.* (2008)
Terra/Aqua MODIS	Aerosol optical thickness	February 2000–December 2005	N/A	1° × 1°	Daily	Tian *et al.* (2008)
NOAA AVHRR	Aerosol optical thickness	January 1982–June 2005	N/A	1° × 1°	Daily	Tian *et al.* (2008)
Aura MLS	Carbon monoxide	November 2004–May 2005	316, 215, 147, 100, and 68 hPa	5° longitude × 5° latitude	Daily	Wong and Dessler (2007)
SeaWiFS	Ocean surface chlorophyll	September 1997–September 2003	N/A	1° × 1°	Daily	Waliser *et al.* (2005)

data that have been used in studies of the chemical and biological impacts of the MJO discussed in the rest of this chapter.

18.2 OZONE

Ozone is one of the most important trace gases in the atmosphere. About 90% of total column ozone (TCO) (troposphere + stratosphere) resides in the stratosphere and accounts for the so-called ozone layer that protects human and other life on Earth via absorption of what would otherwise be harmful amounts of solar ultraviolet radiation. Although only about 10% of TCO is in the troposphere, tropospheric ozone is an important contributor to greenhouse radiative forcing and surface air quality (IPCC, 2007). The lifetime of ozone is about 1 year in the lower stratosphere, about 1 month in the upper troposphere, and about 1 week near the surface. Thus, lower-stratospheric and upper-tropospheric ozone is an important tracer for atmospheric circulation in addition to ozone chemistry. TCO and its variability have been extensively studied during the last few decades, such as its secular trend, annual cycle, and interannual variations including the quasi-biennial oscillation (QBO), ENSO, and solar cycle (e.g., Bowman, 1989; Shiotani, 1992; Hood, 1997; Camp *et al*., 2003). However, very few studies have investigated the intraseasonal variations of tropical TCO. Sabutis *et al*. (1987) first report evidence for 30 to 50-day variability in TCO data from the Nimbus 7 Total Ozone Mapping Spectrometer (TOMS) over specific locations in the southeast Pacific and southern Indian Oceans. Gao and Stanford (1990) find that low-frequency variations with periods of about 1–2 months exist in 8-year Nimbus 7 TOMS TCO data.

Recently, Tian *et al*. (2007) have more thoroughly characterized the spatial and temporal patterns of intraseasonal variations of tropical TCO and also described the connections between these patterns and the convective and dynamical features of the MJO. TCO data from the Atmospheric Infrared Sounder (AIRS) on the Aqua satellite, TOMS on Nimbus 7 and the Earth Probe satellites, Solar Backscatter Ultraviolet (SBUV) on the Nimbus 7 satellite, and SBUV2 on the NOAA 9, 11, and 16 satellites have played an important role in this study (Tian *et al*. 2007). Tian *et al*. find that tropical TCO intraseasonal variations are large ($\sim\pm$10 Dobson Units) and comparable with those on annual and interannual timescales, such as ENSO, QBO, and the solar cycle. Figure 18.1 shows intraseasonal variations of tropical TCO from the TOMS/SBUV/SBUV2 merged ozone dataset and 150 hPa geopotential height from the National Centers for Environmental Prediction (NCEP)/National Center for Atmospheric Research (NCAR) reanalysis reproduced from fig. 3 of Tian *et al*. (2007). Intraseasonal TCO anomalies are mainly evident in the subtropics over the Pacific and eastern hemisphere, while equatorial TCO anomalies are rather small. These subtropical TCO anomalies have a systematic relationship to the well-documented equatorial MJO convection and related wave dynamics (e.g., Wang and Rui, 1990; Hendon and Salby, 1994; Zhang, 2005; Chapters 10 and 17). Subtropical negative TCO anomalies typically flank or lie to the west of equatorial

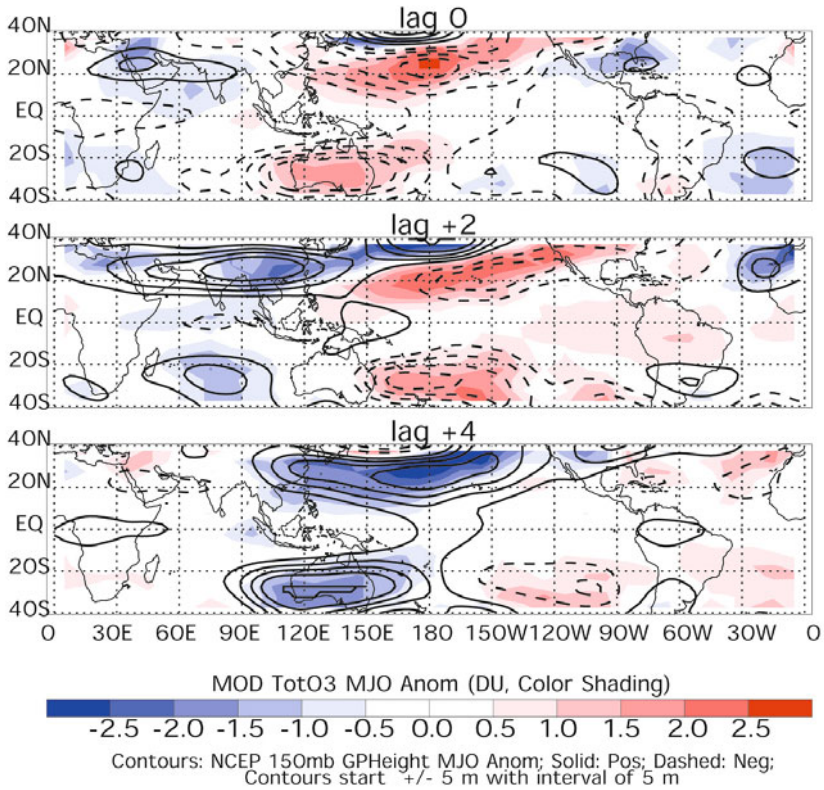

Figure 18.1. Composite maps of TCO anomalies from TOMS/SBUV/SBUV2 (color shading) and NCEP 150 hPa geopotential height anomalies (black contours). The lags 0, +2, and +4 are shown here (adapted from fig. 3 of Tian *et al.*, 2007).

enhanced convection and are co-located with the subtropical upper-tropospheric anticyclones generated by equatorial anomalous convective forcing. On the other hand, subtropical positive TCO anomalies generally lie to the east of equatorial enhanced convection and are co-located with the subtropical upper-tropospheric cyclones generated by equatorial anomalous convective forcing. Subtropical TCO anomalies are anticorrelated with geopotential height anomalies near the subtropical tropopause. These features strongly suggest that the variations in TCO evident in Figure 18.1 are strongly tied to the vertical movement of the subtropical tropopause and associated with stratospheric rather than tropospheric ozone variations. When the tropopause is lowered, more stratospheric ozone-rich air resides in the column yielding overall positive TCO anomalies, and vice versa when the tropopause is raised (Tian *et al.* 2007).

A number of additional studies have examined the vertical structure of ozone variation in the upper troposphere and lower stratosphere that may be related to the MJO. Based on ozonesonde data in Indonesia, Fujiwara *et al.* (1998) suggest that upper-tropospheric ozone enhancement is tied to the passage of Kelvin waves and

the MJO. In studying an "ozone mini-hole" (OMH) event over the Tibetan Plateau during December 2003, Liu *et al.* (2009) find that the majority of the ozone reduction of that OMH event was located in the upper troposphere and lower stratosphere based on the Michelson Interferometer for Passive Atmospheric Sounding (MIPAS) (Cortesi *et al.*, 2007) and Global Ozone Monitoring by Occultation of Stars (GOMOS) (Kyrola *et al.*, 2004) ozone profile data. Further analysis indicates that this ozone reduction in the upper troposphere and lower stratosphere is a result of the uplift of the tropopause by the upper-tropospheric anticyclone over the Tibetan Plateau induced by an MJO event over the equatorial Indian Ocean and western Pacific. These results appear to be consistent with the view of Tian *et al.* (2007) that subtropical intraseasonal TCO anomalies are mainly associated with vertical movement of the subtropical tropopause. Nevertheless, more precise quantification of the relative contributions from the stratosphere vs. troposphere to these subtropical TCO anomalies is still needed.

Tropospheric ozone has been very difficult to measure directly from space due to interference from extensive stratospheric ozone (Fishman *et al.*, 2008). However, tropical tropospheric ozone can be much more directly influenced by tropical convection (Dickerson *et al.*, 1987; Pickering *et al.*, 1990, 1995; Kley *et al.*, 1996; Lawrence *et al.*, 2003; Doherty *et al.*, 2005, 2006; Solomon *et al.*, 2005). There are three ways in which convection affects tropical tropospheric ozone. First, convection affects ozone by the vertical mixing of ozone itself. Convection lifts lower-tropospheric air to the upper troposphere where the ozone lifetime is longer, while mass balance subsidence mixes ozone-rich upper-tropospheric air downwards to the lower troposphere where the ozone lifetime is shorter. This tends to decrease upper-tropospheric ozone and the overall tropospheric column of ozone. Second, convection affects ozone by the vertical mixing of ozone precursors that influence tropospheric ozone chemical production and destruction. Where there are surface ozone precursor sources, such as short-lived isoprene (C_5H_8), NOx ($NO + NO_2$), carbon monoxide (CO), and hydrocarbons over polluted regions, convection significantly increases these precursor concentrations and, thus, ozone in the mid and upper troposphere at the expense of lower-tropospheric concentrations. For example, Lawrence *et al.* (2003) find that lofting of surface NOx is a significant driver of increases in ozone production over much of the tropospheric column in a chemical transport model. Third, lightning in the tropics is a major NOx source directly associated with convection, with most NOx added to the upper troposphere (Pickering *et al.*, 1998). There are also potential interactions between isoprene and lightning NOx emissions (von Kuhlmann *et al.*, 2004). An important isoprene degradation product is the peroxyacetyl radical (CH_3COO_2), which can affect NOx by promoting peroxyacyl nitrate (PAN) formation over land areas where isoprene and lightning NOx emissions are co-located. The net impact of convective mixing is thus sensitive to the profile of ozone and its precursors prior to convection, and is a complex balance between dynamical transport and a variety of chemical effects. Lawrence *et al.* (2003) find that convection increases tropospheric column ozone as the effect of convective changes in precursor emissions on the tropospheric ozone burden is more important than the

convective redistribution of ozone based on a chemical transport model. In contrast, Doherty *et al.* (2005) find that convection reduces tropospheric column ozone as the effect of convective overturning of ozone itself dominates over changes in ozone chemistry using a model of similar chemical complexity to that of Lawrence *et al.* (2003).

To date, very few studies have investigated the specific influence of the MJO on tropospheric ozone. From estimates of tropospheric column ozone using differential measurements of TCO from the Nimbus 7 TOMS and stratospheric column ozone from the Upper Atmosphere Research Satellite (UARS) Microwave Limb Sounder (MLS), Ziemke and Chandra (2003) suggest an influence from the MJO on tropospheric column ozone. They find that equatorial tropospheric column ozone decreases while equatorial upper-tropospheric humidity increases during enhanced phases of several MJO events. This suggests that convection during MJO events transports high-concentration water vapor and low-concentration ozone from the lower troposphere into the middle and upper troposphere. Relying on nearly 2 years of tropospheric ozone and water vapor data from the Aura Ozone-Monitoring Instrument (OMI) and MLS instruments, Ziemke *et al.* (2007) find a similar phenomenon to that of Ziemke and Chandra (2003). These studies have shed some light onto the MJO impact on tropospheric ozone. However, large uncertainties may exist in these tropospheric column ozone data as they were calculated as a small residual of two large quantities: TOMS or OMI TCO, and UARS or Aura MLS stratospheric column ozone. Thus, there are still many open questions regarding the MJO's impact on tropospheric ozone. For example, does the MJO systematically influence tropospheric ozone over the tropics? If it does, what is the dynamic (convective transport) vs. chemical (ozone production/destruction due to ozone precursors, such as isoprene, NOx, hydrocarbons, and lightning) contribution to tropospheric ozone variations? Further work, with the availability of new satellite data coupled with chemistry transport models, is needed to comprehensively address these questions. Such possibilities may exist by examining ozone profiles from the Tropospheric Emission Spectrometer (TES) (Worden *et al.*, 2007) onboard the Aura satellite as well as Southern Hemisphere ADditional OZonesonde (SHADOZ) (Thompson *et al.*, 2007) in situ data.

18.3 AEROSOLS

Aerosols exert a significant negative radiative forcing on the global climate system through their direct and indirect effects (IPCC, 2007). However, due to the heterogeneous spatial and temporal distributions of aerosols and the measurement challenges of global satellite and in situ aerosol observations, such as sampling issues and aerosol-type discrimination, the spatial and temporal variability of aerosols has not been comprehensively documented. Recently, a couple of studies (Tian *et al.*, 2008, 2011; Beegum *et al.*, 2009) have made such attempts. For example, Tian *et al.* (2008) documented the spatial and temporal variability of aerosols at the intraseasonal (30–90 day) timescale and explored its possible connection to the MJO using multiple

global satellite aerosol products. These satellite aerosol data include the aerosol index (AI) from the Nimbus 7 TOMS, aerosol optical thickness (AOT) from the Terra MODerate Resolution Imaging Spectroradiometer (MODIS), and the NOAA Advanced Very High Resolution Radiometer (AVHRR). A composite MJO analysis from that study shows large variations in TOMS AI and MODIS/AVHRR AOT over the equatorial Indian and western Pacific Oceans as well as over tropical Africa and the Atlantic Ocean.

Over the tropical Indian and western Pacific Oceans where MJO convection is active and the background aerosol level is low, a strong inverse linear relationship between TOMS AI and rainfall anomalies but a weaker less coherent positive correlation between MODIS/AVHRR AOT and rainfall anomalies were found. The exact mechanisms for these relationships are still unclear due to uncertainties about satellite-derived aerosol products (Tian *et al*., 2008). For example, the negative correlation between rainfall and aerosol anomalies exhibited by the TOMS AI data could plausibly be accounted for by aerosol scavenging by rainfall. On the other hand, TOMS tends to be sensitive only to absorbing aerosols above the highest cloud layer. Given the variations in cloud populations and height due to the MJO (e.g., Lau and Chan, 1985; Nakazawa, 1988), this negative correlation might also be accounted for simply by a sampling artifact of TOMS AI. Similarly, the (weak) positive correlation between rainfall and aerosol anomalies exhibited by MODIS/AVHRR data could plausibly be accounted for by an aerosol humidity effect due to moisture variations associated with the MJO (e.g., Tian *et al*., 2006b) or enhancements in sea spray and aerosol injection in the boundary layer due to westerly wind bursts. On the other hand, there is always concern that enhanced cloud amount, thin or small-scale clouds, can be incorrectly retrieved as aerosol and this positive correlation could be artificial. A preliminary look at the in situ Aerosol Robotic Network (AERONET) data suggests that the positive correlation between the AERONET/MODIS/AVHRR aerosol and rainfall anomalies is likely due to the cloud contamination effect.

By analyzing 6-year boreal winter in situ AOT data at a tropical semiarid location—Anantapur, India—Beegum *et al*. (2009) also show significant modulation of aerosols by planetary-scale atmospheric waves including the MJO. Juneng *et al*. (2009) analyze the spatiotemporal characteristics of atmospheric PM10 (particulate matter with an aerodynamic diameter of less than 10 μm) across Malaysia. Besides strong seasonal fluctuations, the PM10 concentration in Malaysia was also found to fluctuate at significant intraseasonal frequencies. Two different intraseasonal bands have been identified—the quasi-biweekly 10 to 20-day frequency and a lower frequency band of 30–60 days. These 10 to 20-day and 30 to 60-day oscillations of PM10 concentration are possibly indirectly induced by the boreal summer intraseasonal oscillation (ISO) (Chapter 10; Waliser, 2006).

Taken together, the results highlighted above indicate that the MJO and associated cloudiness and rainfall variability may systematically influence aerosol variability over the equatorial Indian Ocean and western Pacific although the degree and exact mechanisms are still unclear. As with ozone, there is a need for more studies in this area, with additional in situ and satellite datasets as well as

chemical transport models. The satellite datasets could include Multiangle Imaging Spectroradiometer (MISR) (Diner *et al.*, 1998; Kahn *et al.*, 2005) and Cloud–Aerosol Lidar and Infrared Pathfinder Satellite Observations (CALIPSO) (Winker *et al.*, 2003) aerosol products. Both datasets provide important new dimensions in terms of aerosol sampling and sensitivity such as aerosol vertical distribution and type information (e.g., particle size, shape, and single-scattering albedo) that will be useful to more robustly determine and understand the influence of the MJO on aerosols.

Over the equatorial Atlantic Ocean and Africa where MJO convection is weak but the background aerosol level is high, the spatiotemporal patterns of TOMS AI and MODIS AOT anomalies are rather similar. When enhanced MJO convection is located over the equatorial Indian Ocean and suppressed MJO convection is located over the equatorial western Pacific, the aerosol anomalies over the equatorial Atlantic Ocean and Africa are negative (see lag 0 of figs. 2 and 4 of Tian *et al.*, 2008). In contrast, when enhanced MJO convection is located over the equatorial western Pacific and suppressed MJO convection is located over the equatorial Indian Ocean, the aerosol anomalies over the equatorial Atlantic Ocean and Africa are positive (see lag +4 of figs. 2 and 4 of Tian *et al.*, 2008). To understand how the MJO impacts the aerosol over the equatorial Atlantic Ocean and Africa, 850 hPa wind anomalies from NCEP/NCAR reanalysis were plotted together with the MODIS AOT anomalies in Figure 18.2. When enhanced MJO convection is located over the equatorial Indian Ocean, the 850 hPa zonal wind anomalies over the equatorial Atlantic Ocean and Africa are predominantly westerlies. These low-level westerly anomalies can reduce the background aerosol transport by the trade winds from Africa to the Atlantic Ocean and can explain the negative AOT anomalies over the equatorial Atlantic Ocean and Africa (Figure 18.2a). When enhanced MJO convection is located over the equatorial western Pacific, the 850 hPa zonal wind anomalies over the equatorial Atlantic Ocean and Africa are predominantly easterlies. These low-level easterly anomalies can enhance the background aerosol transport by the trade winds from Africa to the Atlantic Ocean and can explain the positive AOT anomalies over the equatorial Atlantic Ocean and Africa (Figure 18.2b). This indicates that the MJO can modulate the equatorial Atlantic aerosol amount by modulating the low-level zonal wind anomalies over the equatorial Atlantic Ocean and Africa. Such a detailed analysis based on the MODIS/Aqua has been performed by Tian *et al.* (2011).

18.4 CARBON MONOXIDE

CO is another very important trace gas in the troposphere. Its presence in high concentrations affects the oxidizing capacity and self-cleansing ability of the atmosphere. In the presence of nitrogen oxides, it is a precursor to the formation of tropospheric ozone, which in turn leads to crop damage and human health problems through its effect on the respiratory system. Its principal sources arise from anthropogenic industrial emissions, biomass burning, and wildfires (Edwards

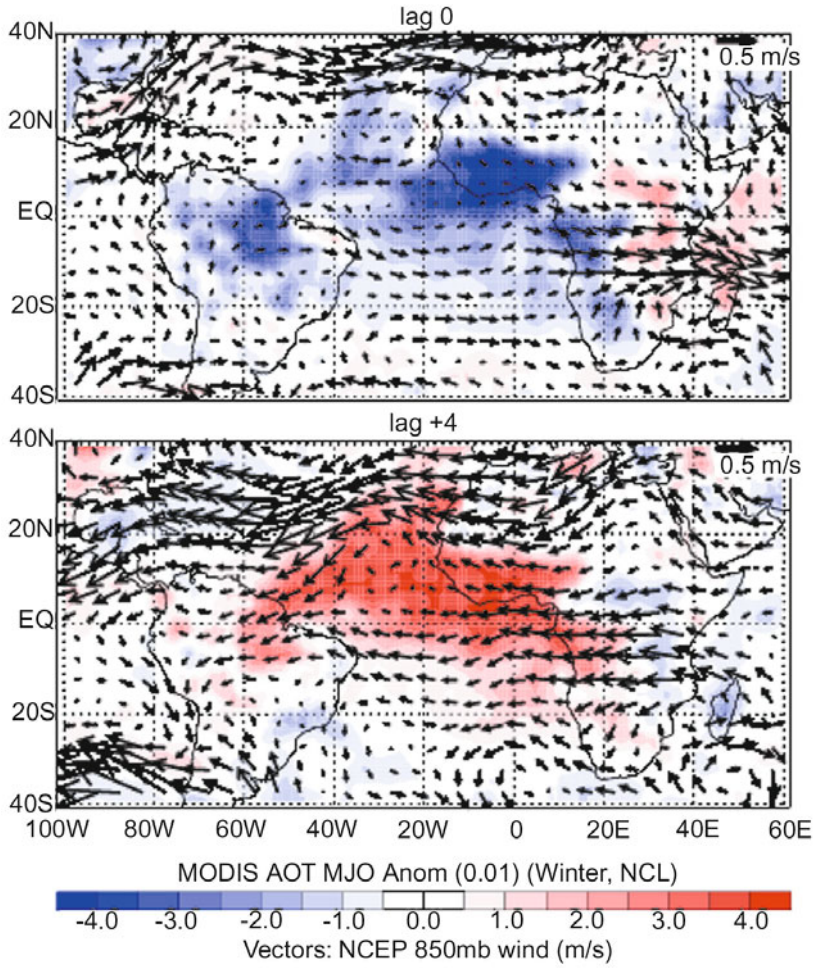

Figure 18.2. Composite maps of MODIS AOT anomalies (color shading) and 850 hPa NCEP/NCAR reanalysis vector wind anomalies (vectors) in two different phases of the MJO. The phases of the MJO are the same as those in Tian *et al.* (2008). For lag 0, enhanced MJO convection is located over the equatorial Indian Ocean and suppressed MJO convection is located over the equatorial western Pacific. For lag +4, vice versa (see figs. 2 and 4 of Tian *et al.*, 2008).

et al., 2004). The global average CO lifetime is about 2 months and varies with season and location. This makes CO an excellent tracer for tropospheric transport processes and the observed plumes from strong emission sources extend great distances. The global distribution of tropospheric column CO has been observed from space since 1999 by the Measurements of Pollution in the Troposphere (MOPITT) instrument onboard Terra (Edwards *et al.*, 2004). CO in the upper

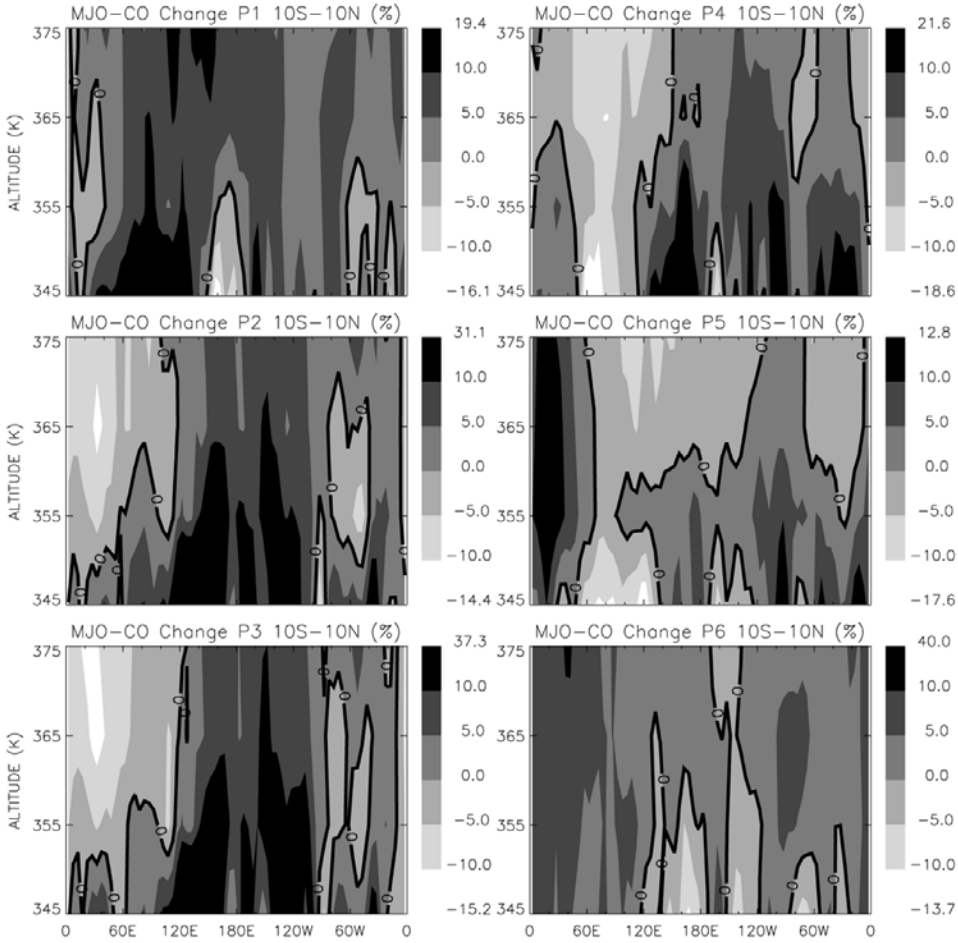

Figure 18.3. Longitude–altitude distribution of MLS CO anomalies averaged between 10°S and 10°N for phases of the MJO corresponding to different pentads. The anomalies are expressed as percentage change from mean values for November 2004–May 2005. The approximate locations of enhanced convection corresponding to different phases are: 80°E for P1, 120°E for P2, 140°E for P3, 160°E for P4, 40°W for P5, and 20°E for P6 (adapted from fig. 5 of Wong and Dessler, 2007).

troposphere and lower stratosphere has been observed by the Aura MLS (Waters *et al.*, 2006). The impacts of the MJO on CO abundances in the tropical tropopause layer were recently reported based on the Aura MLS CO data (Wong and Dessler, 2007). They found that positive (negative) CO anomalies in the TTL are co-located with the area of enhanced (suppressed) convection and propagate eastward (Figure 18.3). This indicates that the anomalous deep convection associated with the MJO can inject CO from the lower troposphere up to the TTL. Many studies are needed to further explore the relationship between intraseasonal CO variations and related

convection and large-scale circulation changes. One recent study by Li *et al.* (2010) has shown that the MJO can also impact the mid-tropospheric carbon dioxide (CO_2) based on the recently available mid-tropospheric CO_2 data from AIRS.

18.5 OCEAN CHLOROPHYLL

Ocean surface chlorophyll represents the measure of biomass at the lowest levels of the ocean food chain and can affect the distribution and viability of higher levels of the food chain. It is also an indicator of conditions conducive to the presence of cholera in coastal zones. For the physical system, chlorophyll influences solar penetration depth and the associated near surface heating distribution. Based on satellite-derived ocean surface chlorophyll data from the Sea-viewing Wide Field of View Sensor (SeaWiFS), Waliser *et al.* (2005) investigate the relationship between the MJO and satellite-derived chlorophyll. They find that the MJO produces systematic and significant variations in ocean surface chlorophyll in a number of regions across the tropical oceans, including the northern Indian Ocean, a broad expanse of the northwestern tropical Pacific Ocean, and a number of near coastal areas in the far eastern Pacific Ocean (Figure 18.4). Potential mechanisms for this modulation are examined with the result that wind-induced vertical entrainment at the base of the ocean mixed layer and Ekman pumping through their possible influence on nutrient availability appear to play important roles.

18.6 LOOKING AHEAD

The above studies have provided a wealth of new information on the MJO's chemical and biological impacts on the global climate system. However, this field is clearly in its infancy and tremendous opportunities still lie ahead. Several outstanding questions are still waiting to be answered. For example, over near equatorial/convective regions, does the MJO influence tropospheric ozone? If it does, what are the dynamic vs. chemical contributions to tropospheric ozone variations? Over the subtropics, do the ozone profiles from satellites and/or ozonesondes support the notion that the large and robust MJO-driven variations of TCO in the subtropics are mainly associated with dynamical changes in tropopause height? Does the MJO influence tropospheric CO and lightning? Why do different satellite aerosol products exhibit different relationships between MJO rainfall and aerosol variability over the equatorial Indian and western Pacific Oceans? Are these aerosol–rainfall relationships physical or an artifact due to cloud contamination? If they are physical, then what is the relative contribution of wet/dry deposition, aerosol humidity effect, upper vs. lower-tropospheric aerosols, absorbing vs. non-absorbing aerosols in these relationships? Can the state-of-the-art chemical transport model replicate the "observed" intraseasonal variations of atmospheric composition given the MJO-related forcing and can they be used to help us understand these variations? What are the specific physical mechanisms that influence chlorophyll in the ocean? Does

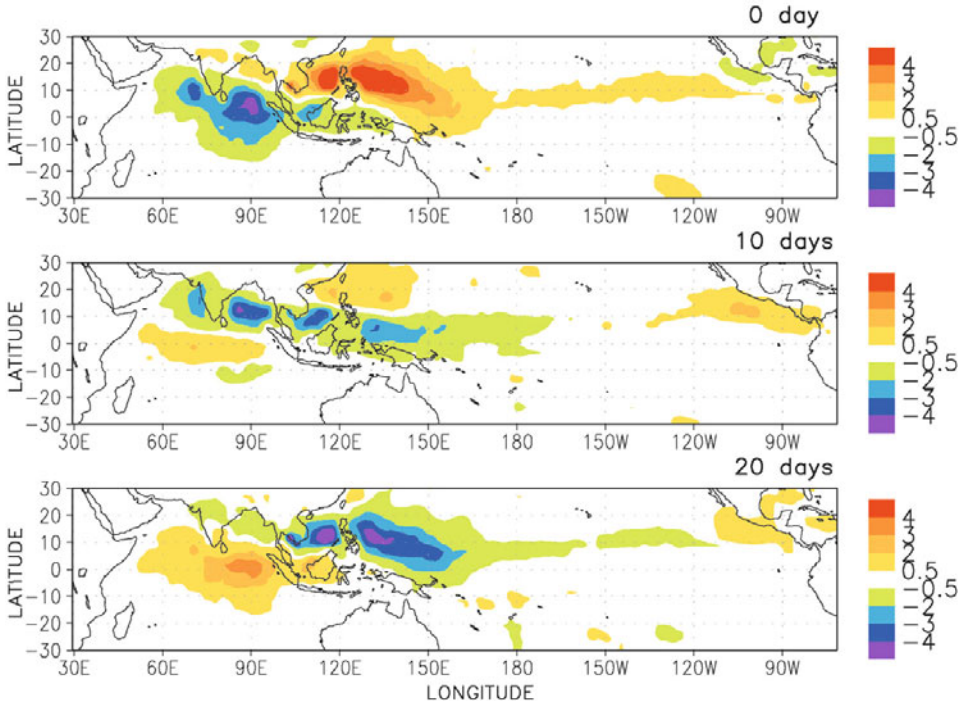

Figure 18.4. (left panel) Composite northern hemisphere (NH) summer rainfall anomalies (mm day^{-1}) associated with the Madden–Julian Oscillation (MJO). Lags start at 0 days (top), +10 days (middle), and +20 days (bottom), which together account for about one half of a complete MJO event(adapted from fig. 1 of Waliser *et al.*, 2005).

this influence and variability in chlorophyll impact higher levels of the foodchain that depend on it? Given the importance of the above-mentioned constituents to atmospheric and oceanic processes and their related societal impacts (e.g., air quality, ozone depletion, fishing, and cholera), coupled with the evidence that the MJO is predictable with 2 to 3-week lead times (Chapter 12), there is considerably more need for further investigation in this area.

18.7 ACKNOWLEDGMENTS

This research was carried out at the Jet Propulsion Laboratory (JPL), California Institute of Technology (Caltech), under a contract with the National Aeronautics and Space Administration (NASA) and also supported by the National Science Foundation (NSF) under grant No. 0840755 to University of California, Los Angeles (UCLA). Any opinions, findings, and conclusions or recommendations expressed in this material are those of the author(s) and do not necessarily reflect

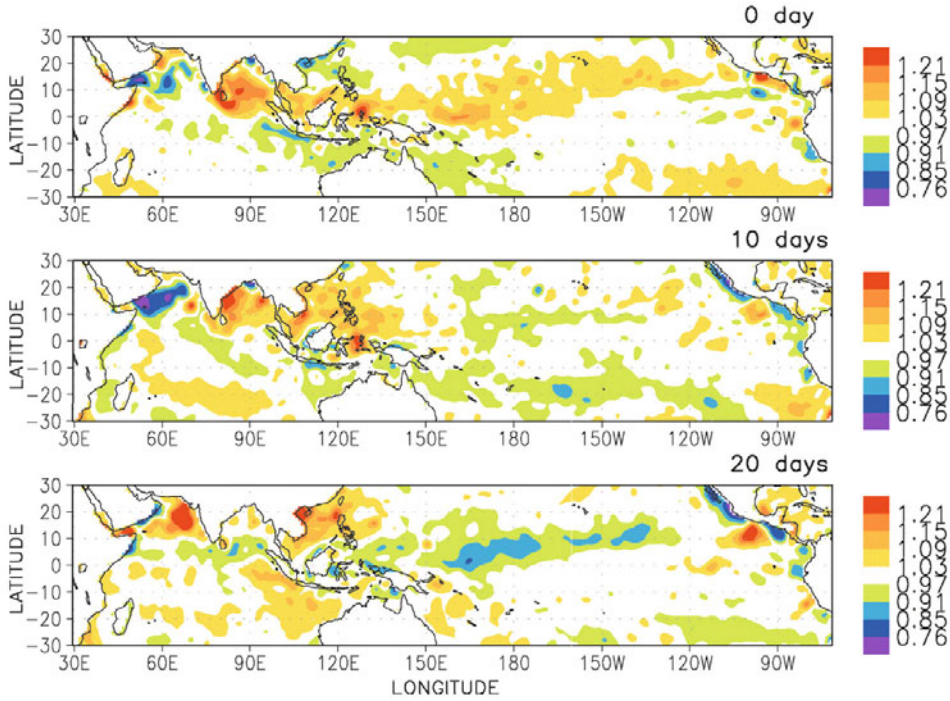

Figure 18.4 (*cont.*). (right panel) Same, except for ocean surface chlorophyll from SeaWiFS, where values are normalized by seasonal means (e.g., 1.2 indicates 120% of the northern hemisphere summer mean) (adapted from fig. 2 of Waliser *et al.*, 2005).

the views of the NSF or NASA. The authors want to thank Mike Wallace and Sun Wong for comments that helped to improve this chapter.

18.8 REFERENCES

Beegum, S. N., K. K. Moorthy, S. S. Babu, R. R. Reddy, and K. R. Gopal (2009) Large scale modulations of spectral aerosol optical depths by atmospheric planetary waves. *Geophys. Res. Lett.*, **36**, L03810, doi: 10.1029/2008gl036509.

Bessafi, M. and M. C. Wheeler (2006) Modulation of south Indian ocean tropical cyclones by the Madden–Julian oscillation and convectively coupled equatorial waves. *Mon. Wea. Rev.*, **134**, 638–656.

Bowman, K. P. (1989) Global patterns of the quasi-biennial oscillation in total ozone. *J. Atmos. Sci.*, **46**, 3328–3343.

Camargo, S. J., M. C. Wheeler, and A. H. Sobel (2009) Diagnosis of the MJO modulation of tropical cyclogenesis using an empirical index. *J. Atmos. Sci.*, **66**, 3061–3074, doi: 10.1175/2009jas3101.1.

Camp, C. D., M. S. Roulston, and Y. L. Yung (2003) Temporal and spatial patterns of the interannual variability of total ozone in the Tropics. *J. Geophys. Res.*, **108**, 4643, doi: 10.1029/2001JD001504.

Cortesi, U., J. C. Lambert, C. De Clercq, G. Bianchini, T. Blumenstock, A. Bracher, E. Castelli, V. Catoire, K. V. Chance, M. De Maziere *et al.* (2007) Geophysical validation of MIPAS–ENVISAT operational ozone data. *Atmos. Chem. Phys.*, **7**(18), 4807–4867.

Dickerson, R. R., G. J. Huffman, W. T. Luke, L. J. Nunnermacker, K. E. Pickering, A. C. D. Leslie, C. G. Lindsey, W. G. N. Slinn, T. J. Kelly, P. H. Daum *et al.* (1987) Thunderstorms: An important mechanism in the transport of air-pollutants. *Science*, **235**(4787), 460–464, doi: 10.1126/science.235.4787.460.

Diner, D. J., J. C. Beckert, T. H. Reilly, C. J. Bruegge, J. E. Conel, R. A. Kahn, J. V. Martonchik, T. P. Ackerman, R. Davies, S. A. W. Gerstl *et al.* (1998) Multi-angle Imaging SpectroRadiometer (MISR): Instrument description and experiment overview. *IEEE Trans. Geosci. Remote Sens.*, **36**(4), 1072–1087.

Doherty, R. M., D. S. Stevenson, W. J. Collins, and M. G. Sanderson (2005) Influence of convective transport on tropospheric ozone and its precursors in a chemistry–climate model. *Atmos. Chem. Phys.*, **5**, 3205–3218.

Doherty, R. M., D. S. Stevenson, C. E. Johnson, W. J. Collins, and M. G. Sanderson (2006) Tropospheric ozone and El Niño–Southern Oscillation: Influence of atmospheric dynamics, biomass burning emissions, and future climate change. *J. Geophys. Res.*, **111**, D19304, doi: 10.1029/2005jd006849.

Edwards, D. P., L. K. Emmons, D. A. Hauglustaine, D. A. Chu, J. C. Gille, Y. J. Kaufman, G. Petron, L. N. Yurganov, L. Giglio, M. N. Deeter *et al.* (2004) Observations of carbon monoxide and aerosols from the Terra satellite: Northern Hemisphere variability. *J. Geophys. Res.*, **109**(D24), D24202, doi: 10.1029/2004jd004727.

Fishman, J., K. W. Bowman, J. P. Burrows, A. Richter, K. V. Chance, D. P. Edwards, R. V. Martin, G. A. Morris, R. B. Pierce, J. R. Ziemke *et al.* (2008) Remote sensing of tropospheric pollution from space. *Bull. Amer. Meteorol. Society*, **89**(6), 805–821, doi: 10.1175/2008bams2526.1.

Fujiwara, M., K. Kita, and T. Ogawa (1998) Stratosphere–troposphere exchange of ozone associated with the equatorial Kelvin wave as observed with ozonesondes and rawinsondes. *J. Geophys. Res.*, **103**, 19173–19182.

Gao, X. H. and J. L. Stanford (1990) Low-frequency oscillations in total ozone measurements. *J. Geophys. Res.*, **95**, 13797–13806.

Hendon, H. H. and M. L. Salby (1994) The life-cycle of the Madden–Julian Oscillation. *J. Atmos. Sci.*, **51**, 2225–2237.

Hood, L. L. (1997) The solar cycle variation of total ozone: Dynamical forcing in the lower stratosphere. *J. Geophys. Res.*, **102**, 1355–1370.

Ichikawa, H. and T. Yasunari (2007) Propagating diurnal disturbances embedded in the Madden–Julian Oscillation. *Geophys. Res. Lett.*, **34**, L18811, doi: 10.1029/2007GL030480.

IPCC (2007) In: S. Solomon, D. Qin, M. Manning, Z. Chen, M. Marquis, K. B. Averyt, M. Tignor, and H. L. Miller (Eds.), *Climate Change 2007: The Physical Science Basis* (contribution of Working Group I to the Fourth Assessment Report of the Intergovernmental Panel on Climate Change). Cambridge University Press, Cambridge, U.K., 996 pp.

Juneng, L., M. T. Latif, F. T. Tangang, and H. Mansor (2009) Spatio-temporal characteristics of PM10 concentration across Malaysia. *Atmos. Environ.*, **43**, 4584–4594, doi: 10.1016/j.atmosenv.2009.06.018.

Kahn, R. A., B. J. Gaitley, J. V. Martonchik, D. J. Diner, K. A. Crean, and B. Holben (2005) Multiangle Imaging Spectroradiometer (MISR) global aerosol optical depth validation based on 2 years of coincident Aerosol Robotic Network (AERONET) observations. *J. Geophys. Res.*, **110**, D10S04, doi: 10.1029/2004JD004706.

Kley, D., P. J. Crutzen, H. G. J. Smit, H. Vomel, S. J. Oltmans, H. Grassl, and V. Ramanathan (1996) Observations of near-zero ozone concentrations over the convective Pacific: Effects on air chemistry. *Science*, **274**, 230–233.

Kyrola, E., J. Tamminen, G. W. Leppelmeier, V. Sofieva, S. Hassinen, J. L. Bertaux, A. Hauchecorne, F. Dalaudier, C. Cot, O. Korablev *et al.*; (2004) GOMOS on Envisat: An overview. *Adv. Space Res.*, **33**(7), 1020–1028, doi: 10.1016/s0273-1177(03)00590-8.

Lau, K. M. and P. H. Chan (1985) Aspects of the 40–50 day oscillation during the northern winter as inferred from outgoing longwave radiation. *Mon. Wea. Rev.*, **113**, 1889–1909.

Lawrence, M. G., R. von Kuhlmann, M. Salzmann, and P. J. Rasch (2003) The balance of effects of deep convective mixing on tropospheric ozone. *Geophys. Res. Lett.*, **30**, 1940, doi: 10.1029/2003gl017644.

Li, K. F., B. Tian, D. E. Waliser, and Y. L. Yung (2010) Tropical mid-tropospheric CO_2 variability driven by the Madden–Julian oscillation. *Proceedings of the National Academy of Sciences U.S.A.*, **107**(45), 19171–19175, doi: 10.1073/pnas.1008222107.

Liu, C. X., Y. Liu, Z. N. Cai, S. T. Gao, D. R. Lu, and E. Kyrola (2009) A Madden–Julian Oscillation-triggered record ozone minimum over the Tibetan Plateau in December 2003 and its association with stratospheric "low-ozone pockets". *Geophys. Res. Lett.*, **36**, L15830, doi: 10.1029/2009gl039025.

Maloney, E. D. and D. L. Hartmann (2000a) Modulation of eastern North Pacific hurricanes by the Madden–Julian oscillation. *J. Climate*, **13**, 1451–1460.

Maloney, E. D. and D. L. Hartmann (2000b) Modulation of hurricane activity in the Gulf of Mexico by the Madden–Julian Oscillation. *Science*, **287**, 2002–2004, doi: 10.1126/science.287.5460.2002.

Nakazawa, T. (1988) Tropical super clusters within intraseasonal variations over the western Pacific. *J. Meteorol. Soc. Japan*, **66**, 823–839.

Pickering, K. E., A. M. Thompson, R. R. Dickerson, W. T. Luke, D. P. McNamara, J. P. Greenberg, and P. R. Zimmerman (1990) Model-calculations of tropospheric ozone production potential following observed convective events. *J. Geophys. Res.*, **95**, 14049–14062.

Pickering, K. E., A. M. Thompson, W. K. Tao, R. B. Rood, D. P. McNamara, and A. M. Molod (1995) Vertical transport by convective clouds: Comparisons of 3 modeling approaches. *Geophys. Res. Lett.*, **22**, 1089–1092.

Pickering, K. E., Y. S. Wang, W. K. Tao, C. Price, and J. F. Muller (1998) Vertical distributions of lightning NOx for use in regional and global chemical transport models. *J. Geophys. Res.*, **103**, 31203–31216.

Sabutis, J. L., J. L. Stanford, and K. P. Bowman (1987) Evidence for 35–50-day low-frequency oscillations in Total Ozone Mapping Spectrometer data. *Geophys. Res. Lett.*, **14**, 945–947.

Shiotani, M. (1992) Annual, quasi-biennial, and El Niño–Southern Oscillation (ENSO) time-scale variations in equatorial total ozone. *J. Geophys. Res.*, **97**, 7625–7633.

Solomon, S., D. W. J. Thompson, R. W. Portmann, S. J. Oltmans, and A. M. Thompson (2005) On the distribution and variability of ozone in the tropical upper troposphere: Implications for tropical deep convection and chemical–dynamical coupling. *Geophys. Res. Lett.*, **32**, L23813, doi: 10.1029/2005GL024323.

Suzuki, T. (2009) Diurnal cycle of deep convection in super clusters embedded in the Madden–Julian Oscillation. *J. Geophys. Res.*, **114**, D22102, doi: 10.1029/2008jd011303.

Thompson, A. M., J. C. Witte, H. G. J. Smit, S. J. Oltmans, B. J. Johnson, V. Kirchhoff, and F. J. Schmidlin (2007) Southern Hemisphere Additional Ozonesondes (SHADOZ) 1998–2004 tropical ozone climatology, 3: Instrumentation, station-to-station variability, and evaluation with simulated flight profiles. *J. Geophys. Res.*, **112**, D03304, doi: 10.1029/2005JD007042.

Tian, B., D. E. Waliser, and E. J. Fetzer (2006a) Modulation of the diurnal cycle of tropical deep convective clouds by the MJO. *Geophys. Res. Lett.*, **33**, L20704, doi: 10.1029/2006GL027752.

Tian, B., D. E. Waliser, E. J. Fetzer, B. H. Lambrigtsen, Y. L. Yung, and B. Wang (2006b) Vertical moist thermodynamic structure and spatial–temporal evolution of the MJO in AIRS observations. *J. Atmos. Sci.*, **63**, 2462–2485, doi: 10.1175/JAS3782.1.

Tian, B., Y. L. Yung, D. E. Waliser, T. Tyranowski, L. Kuai, E. J. Fetzer, and F. W. Irion (2007) Intraseasonal variations of the tropical total ozone and their connection to the Madden–Julian Oscillation. *Geophys. Res. Lett.*, **34**, L08704, doi: 10.1029/2007GL029451.

Tian, B., D. E. Waliser, R. A. Kahn, Q. Li, Y. L. Yung, T. Tyranowski, I. V. Geogdzhayev, M. I. Mishchenko, O. Torres, and A. Smirnov (2008) Does the Madden–Julian Oscillation influence aerosol variability? *J. Geophys. Res.*, **113**(D12), D12215, doi: 10.1029/2007jd009372.

Tian, B., D. E. Waliser, R. A. Kahn, and S. Wong (2011) Modulation of Atlantic aerosols by the Madden–Julian Oscillation. *J. Geophys. Res.*, **116**, D15108, doi: 10.1029/2010JD015201.

von Kuhlmann, R., M. G. Lawrence, U. Poschl, and P. J. Crutzen (2004) Sensitivities in global scale modeling of isoprene. *Atmos. Chem. Phys.*, **4**, 1–17.

Waliser, D. E. (2005) Predictability and forecasting. In: W. K. M. Lau and D. E. Waliser (Eds.), *Intraseasonal Variability of the Atmosphere–Ocean Climate System*. Springer-Verlag, Berlin, pp. 389–424.

Waliser, D. E. (2006) Intraseasonal variability. In: B. Wang (Ed.), *The Asian Monsoon*. Springer/Praxis, Heidelberg, Germany/Chichester, U.K., pp. 203–257.

Waliser, D. E., R. Murtugudde, P. Strutton, and J. L. Li (2005) Subseasonal organization of ocean chlorophyll: Prospects for prediction based on the Madden–Julian Oscillation. *Geophys. Res. Lett.*, **32**, L23602, doi: 10.1029/2005GL024300.

Wang, B. and H. Rui (1990) Dynamics of the coupled moist Kelvin–Rossby wave on an equatorial beta-plane. *J. Atmos. Sci.*, **47**, 397–413.

Waters, J. W., L. Froidevaux, R. S. Harwood, R. F. Jarnot, H. M. Pickett, W. G. Read, P. H. Siegel, R. E. Cofield, M. J. Filipiak, D. A. Flower *et al.* (2006) The Earth Observing System Microwave Limb Sounder (EOS MLS) on the Aura satellite. *IEEE Trans. Geosci. Remote Sens.*, **44**(5), 1075–1092, doi: 10.1109/tgrs.2006.873771.

Winker, D. M., J. Pelon, and M. P. McCormick (2003) The CALIPSO mission: Spaceborne lidar for observation of aerosols and clouds. *Proc. Soc. Photo-opt. Inst. Eng.*, **4893**, 1–11.

Wong, S. and A. E. Dessler (2007) Regulation of H_2O and CO in tropical tropopause layer by the Madden–Julian oscillation. *J. Geophys. Res.*, **112**, D14305, doi: 10.1029/2006jd007940.

Worden, H. M., J. A. Logan, J. R. Worden, R. Beer, K. Bowman, S. A. Clough, A. Eldering, B. M. Fisher, M. R. Gunson, R. L. Herman *et al.* (2007) Comparisons of Tropospheric Emission Spectrometer (TES) ozone profiles to ozonesondes: Methods and initial results. *J. Geophys. Res.*, **112**(D3), D03309, doi: 10.1029/2006jd007258.

Zhang, C. D. (2005) Madden–Julian Oscillation. *Rev. Geophys.*, **43**, RG2003, doi: 10.1029/2004RG000158.

Ziemke, J. R. and S. Chandra (2003) A Madden–Julian Oscillation in tropospheric ozone. *Geophys. Res. Lett.*, **30**, 2182, doi: 10.1029/2003GL018523.

Ziemke, J. R., S. Chandra, M. R. Schoeberl, L. Froidevaux, W. G. Read, P. F. Levelt, and P. K. Bhartia (2007) Intra-seasonal variability in tropospheric ozone and water vapor in the tropics. *Geophys. Res. Lett.*, **34**, L17804, doi: 10.1029/2007gl030965.

Index